Unravelling the structural, metamorphic and strain history of the "Aegean Orogeny" Southern Greece, with a combined structural, petrological and geochronological approach

Thomas Neil Lamont

Thesis submitted to the University of Oxford
for the degree of Doctor of Philosophy
in
Geology and Mineralogy



Department of Earth Sciences
and University College,
University of Oxford

Trinity, 2018

Supervised by Prof. M.P. Searle, Dr. N.M.W. Roberts and Prof. D.J. Waters

Declaration

The contents of this thesis are all my own work, except where otherwise stated. The views and opinions expressed herein are mine and not necessarily those of any other person or body unless so attributed.

Citation: Thomas Neil Lamont (2018), Unravelling the structural, metamorphic and strain history of the "Aegean Orogeny" Southern Greece, with a combined structural, petrological and geochronological approach, D.Phil. Thesis, University of Oxford, Department of Earth Sciences, Oxford, UK.

Keywords: Tectonics, Metamorphism, Cyclades, Tinos, Naxos

This thesis has been typeset using LaTeX 2_ε.

Copyright ©, by Thomas Neil Lamont, 2018.
All rights reserved.

No part of the material protected by this copyright notice may be reproduced or utilised in any form or by any means, electronic or mechanical, including photocopying, recording or by any information storage and retrieval system, without written permission from the copyright owner.

Printed in the United Kingdom.

Abstract

Unravelling the structural, metamorphic and strain history of the "Aegean Orogeny" Southern Greece, with a combined structural, petrological and geochronological approach

Thomas Neil Lamont
University College, Oxford

Trinity, 2018

The Cycladic Islands in the Aegean region, southern Greece, has been indisputably under lithospheric extension throughout the last 10 Myrs but there remains a limited understanding of the regional tectono-metamorphic evolution prior to extension. In this thesis, new structural mapping, petrography, thermobarometry, phase equilibria modelling, U–Th–Pb and Lu–Hf garnet geochronology is presented from the islands of Tinos, Naxos and Delos and reveal the Cyclades have experienced a complete cycle of mountain building. The Tsiknias Ophiolite on Tinos formed at 161.9 ± 1.3 Ma and is underlaid by a metamorphic sole which displays a highly condensed and inverted temperature gradient, with partial melting directly below the ophiolite contact at P–T conditions of 8.5 kbar, 850°C. The timing of metamorphism is constrained as 74.0 ± 3.3 Ma from leucosomes and 66.6 ± 2.0 Ma from garnets in the underlying meta-sediments, and is interpreted to represent the initiation of a NE-dipping subduction zone that remained active for 20 Myrs associated with the closure of the Vardar Ocean to the NE. The arrival of the leading edge of the Cycladic continental margin caused high-pressure metamorphism (22–26 kbar, 500–570°C) at 46.4 ± 3.4 Ma on Tinos and 14.5 kbar, 470°C at 49–46 Ma on Naxos. Crustal thickening resulted in regional metamorphism and climaxed with kyanite-grade conditions (10 kbar, 670–730°C) at 18.5–16 Ma followed by sillmanite-grade anatexis (5–6 kbar, 690–730°C) at 15.5–14 Ma on Naxos. The transition from overall crustal shortening/thickening to extension is constrained to 15 Ma in the Naxos migmatite dome. I and S–type granites intruded contemporaneously between 14.6–12.2 Ma, suggesting a regional-scale partial melting event affected the deepest levels of the Cyclades, possibly associated with the onset of extension and exhumation.

Extended Abstract

Unravelling the structural, metamorphic and strain history of the "Aegean Orogeny" Southern Greece, with a combined structural, petrological and geochronological approach

Thomas Neil Lamont

University College, Oxford

Trinity, 2018

The Aegean Sea region has been considered a type locality for large-scale lithospheric extension, associated with Cordilleran-style metamorphic core complexes. Although lithospheric extension has undoubtedly occurred in the region since 15–10 Ma , the geodynamic history of the older, pre-extensional evolution is poorly understood. In this thesis, the Cyclades islands of Tinos and Naxos are studied in detail, integrating careful and detailed field mapping with petrology, whole rock and mineral chemistry, thermobarometry and equilibrium phase diagram modelling, together with U–Th–Pb allanite, monazite, zircon and rutile geochronology and Lu–Hf garnet geochronology. It is concluded that the Cyclades experienced a complete cycle of mountain building from the Late-Cretaceous to Middle Miocene, that is here termed the "Aegean Orogeny" prior to regional Aegean extension. This mountain belt formed as a result of prolonged crustal shortening associated with the closure of an ocean to the NE of the Cyclades in the present-day co-ordinates.

The Tsiknias Ophiolite exposed at the highest structural levels of Tinos Island, Greece comprises a succession of partially dismembered and structurally repeated ultramafic and mafic rocks. New field observations, an updated geological map of Tinos is, integrated with U–Pb zircon geochronology and whole-rock geochemistry from both magmatic ophiolitic and metamorphic rocks from a newly identified metamorphic sole accreted along the base of the peridotites. A plagiogranite dated at 161.9 ± 1.3 Ma, reveals the Tsiknias Ophiolite formed in a supra-subduction zone setting, comparable to the "East-Vardar Ophiolites", and was intruded by E-MORB gabbros at 144.4 ± 5.2 Ma. In contrast, the extremely deformed underlying metamorphic sole exhibits a condensed and inverted metamorphic gradient, from partially anatectic amphibolites to lower amphibolite-greenschist-facies oceanic meta-sediments over 300 m down structural section. Thermobarometry and equilibrium phase diagram modelling using THERMOCALC reveals the sole was metamorphosed at pressure (P) and temperature (T) conditions of ca. 8.5 kbar 850–600 °C, and represents a metamorphic field gradient of up-to 1000°C/km. Leucodioritic leucosomes were generated in the uppermost sole amphibolite, yielding a ca. 190 Ma protolith age, and reveal the timing of high-grade metamorphism and anatexis on the major subduction thrust (Tsiknias Thrust) occurred at ca. 74.0 ± 3.3 Ma, during the initial stages of SW-directed ophiolite obduction. The Tsiknias Ophiolite was therefore obducted some ca. 90 Myrs after it formed due to the initiation of a new NE-dipping intra-oceanic subduction system to the NE of the Cyclades. To generate such elevated P–T conditions in the sole with a 90 Myr old overlying ophiolite requires additional heat sources. It is speculated that shear heating on the Tsknias Thrust, and potentially rapid slip may supply important sources of additional heat, although this remains highly controversial. Metamorphism propagated down structural section with time as revealed by a Lu–Hf garnet age of 66.6 ± 2.0 Ma, thus supporting the metamorphic sole interpretation. Correlation with Vardar Zone rocks suggest this subduction zone was a regional feature and responsible

for Late Cretaceous ultra-high-pressure metamorphism in the Rhodope Massif.

Continued subduction during the closure of the Vardar Ocean, resulted in high-pressure metamorphism of the Adriatic (Cycladic) continental margin as it attempted to subduct some 20 Myrs later, and rocks associated with this subduction event are exposed in the Cycladic Blueschist Unit, which structurally lies below the ophiolite in the Lower Unit of Tinos. Together these rocks persevere ca. 20 Myrs of subduction zone history associated with the final closure of the Vardar Ocean is recorded over a structural thickness of less than three kilometres. The structures and petrography of these high pressure rocks on Tinos were integrated with Lu–Hf geochronology in order to constrain the *P*–*T*–*t*–*D*, M(H_2O) and M(O) history of eclogitic and blueschist-facies units. Equilibrium phase diagram modelling of newly discovered lawsonite-bearing garnet glaucophane schists that are exposed at the highest structural levels of the high-pressure rocks (Kionnia and Pygros Units), experienced ca. 22–27 kbar and 490–510°C under water saturated conditions, whereas adjacent mafic aegerine-bearing eclogites obtained 20–23 kbars and 530–570 °C under moderately oxidizing and hydrous conditions. Prograde garnets from these rocks yielded a Lu–Hf isochron age of 46.4 ± 3.4 Ma, which is interpreted as constraining the timing of peak M1 eclogite and blueschist-facies metamorphism on Tinos. Lawsonite breakdown upon the initial stages of isothermal decompression released between 3 and 6 % molar H_2O, facilitating growth of coarse and zoned secondary matrix glaucophanes. Water released through dehydration of lawsonite penetrated into the adjacent shear zones over a range of *P*–*T* conditions, causing retrogression, serpentinization, and weakening which facilitated the exhumation of high-pressure rocks to ca. 13 kbar 530–550 °C. In contrast, rocks at lower structural levels within the interior of the island record lower pressures of ca. 18.5 kbar and 480–510 °C and are overprinted by top-to-NE shearing that occurred during (M_1) blueschist to (M_2) greenschist-facies conditions. Upon exhumation to mid-crustal conditions, these rocks attained lower amphibolite conditions of ca. 7.3

$\pm$ 0.7 kbar and 536 $\pm$ 16 °C, which was related to (M_2) regional metamorphism of the middle crust. To produce these *P–T–t–D* relationships, it is suggested that the Cycladic Blueschist Unit, previously thought to be a single and coherent package of rocks, should be differentiated into a series of tectono-metamorphic units that each experienced different tectonic and thermal histories. These units were sequentially buried to variable depths at slightly different times and were sequentially emplaced during SW-directed syn-orogenic extrusion of the buoyant Cycladic continental margin. Exhumation occurred by coeval top-to-SW directed thrusting at the base and top-to-NE normal sensed movements at the top of the extruding units. During this extrusion stage, top-to-NE shearing was firstly highly localized on discrete passive roof normal sensed shear zones, but became more distributed as exhumation proceeded. All high-pressure and extrusion related features on Tinos are truncated by later normal sensed structures related to regional extension and doming. Finally, these data reveal that burial of the cycladic continental margin must have occurred a minimum rate of 4 mm/yr this subduction zone must have cooled rapidly following subduction initiation at ca. 74 Ma and obduction of the overlying Tsiknias Ophiolite some ca. 20 Myrs prior to high-pressure metamorphism. Together, these events suggest the final closure of the Vardar Ocean, NE of the Cyclades, during the Early Eocene and was associated with the NE–SW collision between Adria (Cyclades) and Eurasia.

Following this subduction phase, post-collisional crustal thickening resulted in regional Barrovian metamorphism that affected the middle and lower crust levels of the Cyclades. The geodynamic history of regional-scale (M_2 kyanite- and (M_3 sillimanite-grade metamorphic rocks that are exposed within the core of the Naxos dome, a classic metamorphic core complex. The pre-extensional prograde evolution of these rocks and the relative timing of peak metamorphism in relation to the onset of extension is poorly known. In this work new, detailed structural mapping is presented and integrated with petrography, phase equilibrium modelling and U–Th–Pb geochronology of

blueschists, kyanite gneisses and anatectic sillimanite migmatites, that provide constraints on the timing and rates of metamorphism and deformation. (M_2 Kyanite- M_3 sillimanite-grade gneisses within the core complex record a complex history of burial and compression, and did not form under conditions of crustal extension. Deformation and metamorphism was diachronous, and propagated down-structural section with time, resulting in the juxtaposition of several distinct tectonostratigraphic nappes that experienced contrasting metamorphic histories. Attempted northeast-directed subduction of the Cycladic (Adriatic) continental margin, dated at 49–46 Ma, is very similar to the Lu–Hf age of ca. 46 Ma from eclogites and blueschists within continental margin rocks on Tinos. This high-pressure unit was subsequently extruded towards the SW and overthrust onto the more proximal continental margin. This process resulted in crustal thickening and Barrovian metamorphism dated at ca. 40–15 Ma. These rocks underwent a clockwise P–T evolution and resulted in M_2 kyanite-grade conditions of ca. 10 kbar and 600–670 °C, between 22–17 Ma. At the deepest levels, kyanite-grade, fluid-fluxed melting at ca. 8–10 kbar occurred between 18.5–17 Ma, and was followed by isothermal decompression and sillimanite-grade, fluid-absent dehydration melting (ca. 5–6 kbar and 730 °C) at 16–14 Ma (M_3, facilitated by exhumation under a series of top-to-NNE passive roof normal faults. The migmatite dome formed at lower pressure conditions under horizontal constriction resulted in vertical boudinage and upright isoclinal folds, that refold the ductile shear zones.

U-Pb dating of zircons from cross-cutting leucogranite dykes, combined with young ages from sillimanite-grade gneisses constrain the timing of top-to-NNE shearing along these shear zones to 18–15.5 Ma, corresponding to an average exhumation rate of 6 km/Myr. These structures pre-date doming and are responsible for southwest-directed extrusion of gneisses and migmatites from 35 to 17.5 km depth in a compressional setting. The rocks were subsequently folded around the central migmatite dome on Naxos. North–south-oriented boudinaged leucogranite dykes and migmatites

dated at 15-13 Ma, alongside a U–Pb rutile cooling age of ca. 12.7 Ma, and published ^{40}Ar–^{39}Ar, fission track, and Rb–Sr ages, indicate that regional extension across the Aegean began at ca. 15 Ma. This was contemporaneous with a two-fold decrease in the convergence rate between Nubia and Eurasia that significantly accelerated cooling rates to 60–90 °C/Myr due to the onset of upper crustal normal faulting that truncates all earlier structures.

During this sillimanite grade metamorphic event, muscovite dehydration melting produced S-type garnet tourmaline and biotite-muscovite leucogranites, dated at ca. 18–13 Ma on Naxos. Similar leucogranites also occur on Tinos and Delos and intrude coeval with, or immediately prior to, adjacent I-type granitoids. On Tinos, a series of intrusions bracket the timing of motion on the Tinos Shear Zone, previously interpreted as representing a low-angle normal fault. U-Pb zircon geochronology was combined with whole rock ICP-MS geochemistry on cross-cutting dacite dykes, the Tinos hornblende biotite pluton and garnet bearing leucogranite sills that cut by brittle normal faults. The leucogranites are unlikely to be derived from the same parent magma as the adjacent I-type intrusions, and therefore formed during peak sillimanite-grade metamorphism and migmatization at deeper structural levels than currently exposed on Tinos. U–Pb dating also suggests that pervasive ductile movement on the Tinos Shear Zone ended by ca. 14.6 Ma, as ductile fabrics are cut by the granites and dacite dykes. A new strain localization, at structurally higher levels around the margins of the granite resulted in steep, brittle normal faults that cut the S-type leucogranite sills and yield ages between ca. 14.8 and 14.2 Ma. Brittle deformation associated with regional extension must therefore also be younger than 14.8–14.2 Ma. These features suggest that regional scale partial melting and exhumation affected the Cyclades concomitantly with the onset of regional extension at between ca. 15 and 14 Ma. It is also suggested that because the I-type granitoids are so localized in the Cyclades and occur over such a short duration (ca. 14.8–11 Ma) coeval with, or im-

mediately post-dating, S-type leucogranites, they could represent the partially melted products of a previous arc-related protolith (i.e. the Variscan basement), rather than the volcanic arc related to the Hellenic subduction zone.

In conclusion, the data in this thesis support a model of (1) early ophiolite obduction during the Late Cretaceous, followed by (2) attempted subduction of the continental margin to eclogite and blueschist facies condition during the Eocene, followed by (3) prolonged crustal shortening, thickening and regional metamorphism in the Cyclades. These data are incompatible with a continuous southward retreating Hellenic subduction zone. Rather, the Cyclades underwent a rapid switch from overall compressional to extensional tectonics at ca. 15 Ma, associated with the ending of the sillimanite-grade event, and therefore the extension is a relatively recent feature in the region and was responsible only for the final stages of exhumation.

Acknowledgements

I am truly indebted to my supervisors Mike Searle, Dave Waters and Nick Roberts for helping devise this project and therefore allowing me to continue my academic career at Oxford. They have all invested huge amounts of time during the last four years into discussing my (sometimes crazy) ideas, providing feedback on my work, sharing invaluable geological knowledge, as well as helping me think critically and approach problems in a logical and scientific way. Mike and Dave have been incredibly supportive both during my 4th year undergrad research project, and encouraged me to peruse a D.Phil to continue working on the Aegean region, for which I am extremely grateful for. Nick has been a constant source of help and discussion and on many occasions went far beyond the call of duty. He has provided huge amounts of time to help analyse an unbelievable number of samples, greatly improved my understanding of data acquisition and processing and had to "baby-sit" me on the SEM at the BGS whilst the Oxford Microprobe was getting set up. I like to think it was all good preparation for the birth of his first son, Joseph last year. I really could not have had three better supervisors.

Marc St-Onge was also an invaluable source of discussion and inspiration and I am truly grateful to have his advice and support on the Assynt trips and also on the Cyclades field-trip I organised during September 2017. I would also like to extend thanks to Richard Palin, Owen Weller, Andrew Smye and Dave Wallis, who have been extremely helpful with discussing various petrological, field, deformational ideas and thermodynamic modelling in THERMOCALC, and Phillip Gopon who joined me in the

field and trained me on the electron microprobe. They also provided critical feedback and acted as superb role models for me to strive to follow. I also extend thanks to Laurence Robb, Andy Parsons, Jon Wade, Philip England, Tony Watts, Bruce Level, Chris Ballhaus, Rolf Romer, Richard White and Lars Hansen for fruitful discussions, which helped crystallize my ideas.

I also acknowledge Adrian Wood for training and overseeing my sample preparation in NIGL and for the great soundtracks in the sample preparation lab, Gren Turner and Jeremy Rushmore for training me up on the Leo SEM and FEI Quanta SEM at the BGS. Ian Millar, who carried out the analysis of my garnet separates used for Lu–Hf garnet dating, and providing invaluable advice, Matt Horstwood, Simon Tappister, and Steve Noble for the valuable discussions which undoubtably helped improve my understanding of geochronology and how to date rocks, as well as making my visits NIGL a true pleasure. I would like to extend thanks to my brother and his housemates from Nottingham University for letting me stay in their house and making me feel inclusive during my regular visits to NIGL.

I would like to thank Owen Green for thorough advise on sample preparation and training, Jon Wells for always being super helpful and making (probably 100's) of thin-sections, and made particular exceptions if the odd ones needed to be finished quickly. I would like to thank Stanley Mertzman from the Franklin and Marshall College who ran my XRF for granite and ophiolitic samples, Ian Wyatt for carrying out the digestion of whole rock powders and finally Philip Holdship for setting up and running the mass-spectrometer to collect trace element data.

During my time as a post-grad, I have been extremely lucky to have worked closely with many MESci and D.Phil students in the Hard Rock Group. I would like to thank Eleni Wood, Robert Fox, Sam Cornish, John Henry Charles, Jacob Forshaw, Dianna Avidanii, Thomas Breithaupt, Will Mckenzie, Ethan Stamner Jones, Rellie Goddard and Brook Keats for allowing me to share ideas and have extremely useful

and stimulating discussions about their work and my own, commonly during the Hard Rock Group Lunches, which I will extremely miss. Greatest thanks go to my fellow post-grads and best friends Tyler Ambrose, who was a constant source of humour and banter, particularly on field trips such Assynt, Shetland, and in Oman and the UAE, and taught me how to wash my clothes in a bedet. Joshua Combs, who was my housemate at 39 Stanley Road and has always been there for support, discussion and good old rowing chat. Brendan Dyck who has always made time to discuss various topics and helped teach me petrological modelling during my final undergrad year and has been a great role model. I also thank Anna Bidgood and William Nash who joined me in the field. It has been a pleasure to work alongside my office mates Serjocha Evers, Gemma Bevenento, Mimi Harrison, David Ford and Sarah Lucas, even if my rock collection might have got in the way sometimes.

Outside of my studies, I would like to thank everyone at OUCCC for making my time in Oxford thoroughly enjoyable, through training, racing and socializing. Particular thanks go to club coach Kyle Bennet who helped me during my final year come back stronger than ever from glandular fever which resulted in me getting selected to run for Cheshire in the inter-counties XC in March 2018. I would also like to thank my good friends Callum Higgins, Bhavik Lodehia who have supported me throughout my work on the Aegean and were on my first visit to Naxos 6 years ago. I would like to thank my training buddies Alex Bampton, Joseph Woods and also Rahil Sachak-Patwa, for letting me stay at 31 Walton Well Road during the last month of writing up, as well as many many others for the good times during my studies at Oxford.

I would like to thank University College for the travel grants to persue field-work and the Natural Environment Research Council (Grant No. NE/L0021612/1) for providing the oportunity for me to carry out this work and the NERC Isotope Geo-sciences Laboratory for hosting me throughout the last 4 years which was funded by NIGFSC grant IP-1597-1115.

Finally, it has been a privilege to have been a student at Oxford and the last four years in Oxford have provided the best and also the most challenging experiences of my life to date. I could not have completed the D.Phil without the continual backing from my mum, dad, brother and close family. They have always believed in me and supported my passion for geology, put up with plenty of my geological conversations about Naxos and Tinos and even visited me in the field. This work is dedicated to them.

Contents

Declaration i
Abstract iii
Extended Abstract v
Acknowledgments xiii
Contents xxiv
List of Figures xxx
List of Tables xxxiii

1 Introduction **1**

1.1 Statement of the problem 1
1.2 Tectonic Setting 2
1.3 Geology of the Aegean region 6
1.4 Geological evolution 8
1.5 Geology of the Cyclades 13
1.6 Key aims and motivation 16
1.7 Thesis Structure 18

2 The age, origin and emplacement of the Tsiknias Ophiolite, Tinos, Greece **21**

2.1 Introduction 21
2.2 Geology of Tinos 24

2.3 Field Relations of the Tsiknias Ophiolite 27
2.3.1 Mantle and Gabbro - Moho Transition Zone: 28
2.3.2 Plagiogranites: 29
2.3.3 The Tsiknias Thrust 32
2.3.4 Metamorphic Sole 32
2.3.5 Mirsini Unit 36
2.3.6 Akrotiri Unit 40
2.3.7 Livada Detachment 40
2.3.8 Tinos Shear Zone 43
2.4 Petrography 43
2.4.1 Tsiknias Ophiolite 43
2.4.2 Metamorphic Sole 47
2.5 Pressure and Temperature Of Crystallization and Metamorphism . . . 58
2.5.1 Thermobarometry 59
2.5.2 Equilibrium Phase Diagrams 61
2.6 Trace Element Geochemistry 72
2.6.1 Results 72
2.7 Geochronology 81
2.7.1 U–Pb Geochronology 81
2.7.2 Lu–Hf Geochronology 86
2.8 Discussion 88
2.8.1 Formation of the Tsiknias Ophiolite 88
2.8.2 Timing of Ophiolite Emplacement and Sole Formation 93
2.8.3 Sole Formation: Subduction Initiation in Old Cold Oceanic Lithosphere? 94
2.8.4 The Cause of Metamorphism in the Sole: Thermal Conduction vs Shear Heating 96

2.8.5 Integrating the Tsiknias Ophiolite into the Tectonic Framework of Balkan Ophiolites 99
2.8.6 From Ophiolite Obduction to Attempted Subduction of the Cycladic Continental Margin 105
2.8.7 Final Closure of Vardar Ocean 106
2.8.8 Tectonic Model 106
2.9 Conclusions 109

3 Lawsonite eclogites and blueschists from Tinos, Greece 117

3.1 Introduction 117
3.2 Geological setting 119
3.2.1 Geology of Tinos 120
3.2.2 Overview of P–T–t data of the Cycladic Blueschists 123
3.3 Field Relationships of the Tinos High-Pressure Rocks 127
3.3.1 The Kionnia Unit 127
3.3.2 The Pygros Unit 130
3.3.3 Sostis Unit 133
3.3.4 Artemije and Efstathios Shear Zone (NW Tinos) (AESZ) 134
3.3.5 Tinos Shear Zone (TSZ) 134
3.3.6 Marlas Shear Zone (MSZ) 136
3.4 Petrography and Mineral Chemistry 138
3.4.1 Kionnia Unit 138
3.4.2 Pygros Unit 148
3.4.3 Sostis Unit 154
3.5 Pressure-Temperature (P–T) Conditions of Metamorphism 161
3.5.1 Thermobarometry 162
3.5.2 Equilibrium Phase Diagram Modelling 167
3.6 Geochronology 185

3.6.1 Lu-Hf Garnet Geochronology 185
3.6.2 Results 186
3.7 Discussion 188
3.7.1 Petrography 188
3.7.2 Tectonics 191
3.7.3 Implications for High-Pressure Metamorphism in the Cyclades . 203
3.7.4 Tectonic Model 206
3.8 Conclusions 209

4 Compressional origin to the Naxos metamorphic core complex: Structure and Metamorphism 213

4.1 Introduction 213
4.2 Geology of Naxos 216
4.3 Field Relationships 219
4.3.1 Tectono-Stratigraphy 219
4.3.2 Structures within the Metamorphic Core Complex 224
4.3.3 Extensional Shear Zones 238
4.3.4 Structures outside the Metamorphic Core Complex: 244
4.4 Petrography and mineral chemistry 246
4.4.1 Petrography of the Zas Unit 246
4.4.2 Petrography of the Koronos Unit (Kyanite-Grade Gneisses) . . . 252
4.4.3 Petrography of the Core Unit 256
4.4.4 Textures of Sillimanite-Grade Migmatites 261
4.4.5 Textures of Kyanite-Grade Migmatites 265
4.5 Pressure-Temperature Evolution of Metamorphism 270
4.5.1 TLN54: Retrogressed Blueschist (M_1 Zas Unit) 273
4.5.2 TL67: Kyanite Gneiss (M_2 Koronos Unit) 273

4.5.3 TL15: Kyanite Migmatite (Core Unit): Peak (M_2) Kyanite-Grade Conditions . . . 275
4.5.4 TL66: Sillimanite Migmatite (Core Unit): Peak (M_3) Sillimanite-Grade Conditions . . . 278
4.5.5 Melt re-integration (prograde evolution) . . . 281
4.5.6 Post-peak supra-solidus evolution . . . 282
4.5.7 Summary of P–T Results . . . 283
4.6 Palinspatic restoration of the Naxos Core Complex . . . 285
4.7 Discussion . . . 291
4.7.1 Integration of Structural, Petrographic and P–T–D Data . . . 291
4.7.2 Significance of E–W Shortening . . . 302
4.7.3 Possible Comparisons to Other Mountain Belts . . . 303
4.8 Conclusions . . . 305

5 Compressional origin of the Naxos metamorphic core complex: U-Th-Pb geochronology 309

5.1 Introduction . . . 309
5.2 Overview of Existing Geochronology . . . 313
5.2.1 Zas Unit: . . . 315
5.2.2 Koronos Unit: . . . 315
5.2.3 Core Unit: . . . 316
5.3 U–Th–Pb Geochronology . . . 319
5.4 Results . . . 328
5.4.1 Zas Unit (Blueschists) . . . 328
5.4.2 Koronos Unit . . . 331
5.4.3 Core Unit . . . 336
5.4.4 S-Type Leucogranites and Gneisses . . . 345
5.5 Discussion . . . 354

5.5.1 Interpreting Zircon Growth and Ages in S-Type Leucogranites . 354
5.5.2 Linking Ages to Metamorphic Histories and P–T–D Paths . . . 355
5.5.3 Relating Age Distributions to Tectonics Regime 364
5.5.4 Timing of Partial Melting, Top-to-NNE Shearing and Exhumation 367
5.5.5 Transition From Compression To Extension And Migmatite Doming 370
5.5.6 Post Peak Cooling and Exhumation 374
5.5.7 Mechanisms For The Switch From Compression to Extension: . 377
5.6 Tectonic Model 382
5.7 Conclusions 385

6 Coeval I and S-type granitoids on Tinos and Delos, Grecce 389
6.1 Introduction 389
6.2 I-Type And S-Type Magmatism in The Cyclades 390
6.3 Field Relations and Petrography 395
6.3.1 The North Cycladic Detachment System and Extensional Deformation on Tinos 395
6.3.2 Tinos Hornblende Biotite Monzogranite 396
6.3.3 Garnet Muscovite Leucogranite Sills 397
6.3.4 Dacite-Andesite Dykes 400
6.3.5 Delos Biotite-Tourmaline Leucogranites 402
6.3.6 Naxos Granodiorite 402
6.4 Geochemistry 404
6.4.1 Results 404
6.5 U–PB Geochronology 413
6.5.1 Results 414
6.6 Discussion 427
6.6.1 Relative Timing of Granite Intrusion 427

6.6.2 Timing of Deformation on Tinos 430
6.6.3 Origin of Cycladic I and S-Type Granitoids and Implications for Regional Tectonics 432
6.6.4 The Influence of Magmatism on Normal Faulting 434
6.6.5 Comparisons to Other I and S-Type Granite Terranes 435
6.6.6 Tectonic Model 436
6.7 Conclusions 439

7 Regional Synthesis, Conclusions and Further Work 441
7.1 Future Work 448

Bibliography 453

Appendices 519
1.1 Metamorphic Petrology 521
1.2 Thermodynamics 522
1.2.1 Thermobarometry 526
1.2.2 Limitations and uncertainities with using THERMOCALC and paractical thermobarometry 531
1.3 Electron microprobe analysis (EPMA) and operating conditions 535
2.1 Geochronology 547
2.1.1 The principles of radioactive decay 548
2.2 U–Th–Pb Geochronology 549
2.2.1 Sample preparation 551
2.2.2 Tinos samples analytical procedures 552
2.2.3 Naxos sampes analytical procedures 553
2.3 Lu-Hf geochronology 560
2.3.1 Lu–Hf garnet geochronology 561
2.3.2 Lu–Hf isochron method 561

2.3.3 Methodology 563
2.3.4 Additional U-Pb analysis 565
3.1 Whole Rock Geochemistry 567
3.1.1 Geochemical sample preparation and methods 567
3.1.2 X-Ray Fluorescence 567
3.1.3 Trace element geochemistry (ICP-MS) 568

List of Figures

1.1 Tectonic map of the Aegean 3

1.2 Present day deformation in the Aegean region 5

1.3 Ophiolite models 10

1.4 Slab roll-back model 12

1.5 Geological and Geochronological map of the Cyclades 15

2.1 Ophiolite map 23

2.2 Geological map of Tinos 26

2.3 Cross-sections of Tinos 30

2.4 Panoramic photographs and cross-sections 31

2.5 Tectonic section 33

2.6 Outcrop Photographs of gabbros 35

2.7 Outcrop photographs of the metamorphic sole 37

2.8 Outcrop deformation and anatexis in the sole amphibolites 39

2.9 Outcrop deformation in the metamorphic sole 41

2.10 Outcrop and thin section photographs of the plagiogranite sill 42

2.11 Photomicrographs 44

2.12 Gabbro mineral chemistry 46

2.13 Amphibolite sole mineral chemistry 48

2.14 Mirsini garnets line profiles 49

2.15 Tsiknias Ophiolite Gabbros thermobarometry 59

2.16 Sole thermobarometry 62
2.17 Sole thermobarometry 2 63
2.18 TLT63 Plagiogranite pseudosection 64
2.19 Amphibolite pseudosections 66
2.20 Mirsini Unit pseudosections 68
2.21 Summary P-T results 70
2.22 Spider diagrams 75
2.23 Tectonic discrimination diagrams 1 77
2.24 Tectonic discrimination diagrams 2 79
2.25 Zircons CL images 83
2.26 Plagiogranite and gabbro Tera-Wasserburg plots 84
2.27 Amphibolite Tera-Wasserburg plots 85
2.28 U-Pb age distributions 86
2.29 Lu–Hf isochron 87
2.30 Time chart 90
2.31 Summary temperature tectonic section through the metamorphic sole . 100
2.32 Paeleogeographic reconstruction 102
2.33 Tectonic model 114

3.1 Geological map of Tinos 122
3.2 Cross-sections of Tinos 123
3.3 Panoramic photographs of Tinos 125
3.4 Kionnia Unit photographs 129
3.5 Outcrop photographs 132
3.6 NW Tinos deformation 135
3.7 Mesoscale photographs of Tinos 137
3.8 Prograde photomicrographs 140
3.9 Retrograde photomicrographs 143

3.10 Mineral chemistry 153
3.11 Prograde garnets 156
3.12 Sostis garnets 161
3.13 Thermobarometry PT 166
3.14 TLTN26 pseudosections 170
3.15 TLTN26 pseudosections M(H_2O) 171
3.16 TLTN24 pseudosections 172
3.17 TLTN24 M(H_2O) pseudosections 174
3.18 TLTN33 pseudosections 175
3.19 TLTN33 pseudosections M(H_2O) 176
3.20 17TL104 pseudosections 178
3.21 Sostis Unit pseudos 179
3.22 Lu-Hf isochron 187
3.23 Lawsonite breakdown 190
3.24 Summary thermobarometry data and P-T paths 195
3.25 Extrusion 200
3.26 Tectonic Model 211

4.1 Schematic cartoon showing various metamorphic core complex models . 215
4.2 Geological map of Naxos 217
4.3 3-Dimensional model of Naxos 220
4.4 Panoramic photographs of Naxos 222
4.5 Meso-scale fold photographs 228
4.6 Upper Unit and NPDS photographs 231
4.7 Zas and Koronos Unit photographs 234
4.8 Zas and Koronos Unit photographs 237
4.9 CHSZ deformation 241
4.10 Zas Unit photomicrographs and mineral compositions 248

4.11 Koronos Unit photomicrographs 254
4.12 Core Unit photomicrographs and mineral compositions 260
4.13 Schematic cartoon of deformation in the Naxos MCC 264
4.14 Garnet EPMA maps and profiles 268
4.15 Thermobarometry Results 272
4.16 Zas Unit Pseudosections 274
4.17 Koronos Unit Pseudosections 276
4.18 Core Unit Pseudosections 279
4.19 Palinspastic pseudo-restoration of the Naxos MCC 288
4.20 N-S restoration of Naxos MCC 290
4.21 Summary *P-T-D* paths for Naxos MCC 294
4.22 Extrusion model for the Naxos MCC 301

5.1 Geological map of Naxos with U-Pb, Rb-Sr and fission track ages . . . 310
5.2 Outcrop photographs with cross-section of sample position 312
5.3 Age vs structural depth plots 314
5.4 Petrography and textural relationships of allanite and monazite 318
5.5 Monazite and garnet X-Ray maps 321
5.6 CL images of leucogranite zircons 323
5.7 Zas Unit Tera-Wasserburg diagrams 330
5.8 Koronos Unit Tera-Wasserburg diagrams part 1 333
5.9 Koronos Unit Tera-Wasserburg diagrams part 2 337
5.10 Core Unit Tera-Wasserburg diagrams part 1 340
5.11 Core Unit Tera-Wasserburg diagrams part 2 343
5.12 Leucogranites Tera-Wasserburg diagrams 353
5.13 Summary U-Pb age distributions 356
5.14 Summary geochronological map of Naxos contoured for U-Pb ages . . . 359
5.15 Petrochronolgy of Naxos samples 362

5.16 Naxos cooling history 366
5.17 Age-depth summary 369
5.18 Summary time chart 371
5.19 Annotated time chart of Naxos deformation and metamorphism 374
5.20 Migmatite dome models 375
5.21 Naxos P-T-t paths 378
5.22 Tectonic model for the Naxos MCC 381

6.1 Granitoids in the Cyclades 392
6.2 Geological map of Tinos with sample locations 394
6.3 Cross-sections of Tinos 395
6.4 Outcrop photographs of the Tinos granitoids 398
6.5 Cross-cutting relations of Tinos Granitoids 399
6.6 Delos and Naxos granites 401
6.7 Delos and Naxos granites 403
6.8 Discrimination diagrams part 1 406
6.9 Discrimination diagrams part 2 407
6.10 Harker diagrams 409
6.11 Trace element bivariate digrams 411
6.12 Spiderdiagrams 413
6.13 Zircon CL images 415
6.14 Dacite dyke Tera-Wasserburg plots and weighted mean 420
6.15 Tinos monzogranite Tera-Wasserburg plots and weighted mean 423
6.16 Tinos leucogranite Tera-Waserburg plots and weighted mean 425
6.17 Delos and Naxos leucogranite Tera-Wasserburg plots and weighted mean box plot 427
6.18 U-Pb geochronolgy of all granitoids and inhertitence age frequency plot 429
6.19 Hyndman diagrams 430

6.20 Tectonic model 437

List of Tables

2.1 Representative gabbro mineral compositions derived from electron microprobe 52

2.2 Representative mineral gabbro and plagiogranite compositions derived from electron microprobe 53

2.3 Representative metamorphic sole amphibolite mineral compositions derived from electron microprobe 54

2.4 Representative metamorphic sole mineral compositions derived from electron microprobe 55

2.5 Representative Amphibole Sole mineral compositions derived from electron microprobe 56

2.6 Representative Mirsini Unit metasediment mineral compositions derived from electron microprobe 57

2.7 Tsiknias Gabbro thermobarometry results 69

2.8 Sole thermobarometry results 71

2.9 Whole rock geochemistry results 73

2.10 SC-ICP-MS U–Pb zircon geochronology results for samples 17TL35 plagiogranite, 17TL27 gabbro and 17TL26 amphibolite samples 82

2.11 Lu-Hf geochronology results 88

3.1 Representative mineral compositions from the Kionnia Unit 149

3.2 Representative mineral compositions from the Kionnia Unit 150

3.3 Pygros Unit representative mineral compositions 157
3.4 Pygros Unit representative mineral compositions 160
3.5 Thermobaroetry results of Tinos HP rocks 168
3.6 Lu-Hf geochronology results 187

4.1 Compilation of previous P-T estimates for various stages of deformation and metamorphism on Naxos 246
4.2 Representative quatative mineral analysis of samples from the Zas Unit derived by electron microprobe 251
4.3 Representative quatative mineral analysis of samples from the Koronos UNit derived by electron microprobe 257
4.4 Representative quatative mineral analysis from the Core Unit samples . 266
4.5 Summary of P-T results from thermobarometry and THERMOCALC DS-62 Av-PT and pseudosection calculation for all Naxos samples . . . 284

5.1 Allanite and xenotime U-Th-Pb SC-ICP-MS geochroological results for the Zas Unit 324
5.2 Monazite U-Th-Pb SC-ICP-MS geochroological results for the Koronos Unit 325
5.3 Monazite U-Th-Pb SC-ICP-MS geochroological results for the Core Unit part 1 326
5.4 Monazite U-Th-Pb SC-ICP-MS geochroological results for the Core Unit part 2 327
5.5 Zircon U-Pb SC-ICP-MS geochroological results for leucogranites part 1 346
5.6 Zircon U-Pb SC-ICP-MS geochroological results for leucogranites part 2 347
5.7 Zircon U-Pb SC-ICP-MS geochroological results for leucogranites part 3 348
5.8 Zircon U-Pb SC-ICP-MS geochroological results for leucogranites part 4 349

6.1 XRF and ICP-MS results for Tinos, Naxos and Delos granitoids 405

6.2 SC-ICP-MS Zircon U-Pb results for Dacite Dykes on Tinos 416
6.3 SC-ICP-MS Zircon U-Pb results for the Hb-Bt monzogranite on Tinos . 417
6.4 SC-ICP-MS Zircon U-Pb results for garnet bearing leucogranites and granitic veins on Tinos and cross-cutting leucogranites on Tinos, Delos and Naxos 418

1.1 Calculated molar bulk compositions used in on samples in this thesis . 530
1.2 Zas Unit additional EMPA 538
1.3 Koronos Unit additional EMPA Part 1 539
1.4 Koronos Unit additional EMPA part 2 540
1.5 Core Unit additional EMPA Part 1 541
1.6 Core Unit additional EMPA Part 1 542
1.7 Core Unit additional EMPA Part 2 543
1.8 Core Unit additional EMPA Part 3 544
1.9 Naxos GASP thermobarometry results 545
2.10 Full Laboratory and analytical procedures for Tinos samples 554
2.11 Reproducibility of standards for U-Pb zircon on Tinos 555
2.12 Laboratory and Sample Preparation Table for Naxos Samples 558
2.13 Reproducibility of standards for U-Th-Pb geochronology 559
2.14 Sample 17TL43: North Tinos meta-psammite 566
3.15 ICP-MS Standards Data 570
3.16 All XRF whole rock analyses 571

Chapter 1

Introduction

1.1 Statement of the problem

Throughout its 4.55-billion-year history (Patterson et al., 1956; Allegre et al., 1995), the Earth has been expelling its internal heat into the cold vacuum of space. The most prominent geological result of this planetary cooling is the operation of plate tectonics (Hess, 1962; Vine and Matthews, 1963; Wilson, 1965). Plate tectonics describes the continual movement of numerous rigid fragments of the planet's outer shell – the lithosphere – above a more ductile, convecting asthenosphere (e.g Mckenzie, 1969) and provides a framework with which the evolution of the Earth's lithosphere maybe described and understood (Vine and Matthews, 1963). Tectonic plate motions are indeed the first order control for the rise and fall of mountain belts, the formation of economically valuable mineral resources, and devastating natural hazards, including volcanic activity and earthquakes. These geological phenomena commonly occur along plate boundaries, which by definition of plate tectonics, are characterized by narrow zones of deformation, seismicity or magmatism (Vine and Matthews, 1963). Although the oceanic lithosphere can be largely described by plate tectonics and is well understood (e.g. Mckenzie and Bickle, 1988), processes that control the evolution of the continental lithosphere remain debated. On the continents, deformation is not restricted to narrow plate boundaries and the effects of shortening (resulting in crustal thickening and

mountain building) and extension (resulting in crustal thinning and normal faulting) are distributed over wide zones (e.g. England et al., 1985; England and Houseman, 1986; Houseman and England, 1986; Searle, 2011). One such area associated with a broad zone of continental deformation is the Aegean region, in the Eastern Mediterranean (e.g. Mckenzie, 1978; Taymaz et al., 1991; Nyst and Thatcher, 2004; Shaw and Jackson, 2010; Floyd et al., 2010; England et al., 2016). The Cycladic Islands lie at the heart of this region (Fig. 1.1) and are geologically interesting as they have experienced a reversal from overall crustal shortening to extension is the recent geological record. The Cyclades also expose a variety of rock types including ophiolitic rocks, high-pressure metamorphic rocks that were buried in a subduction zone environment, Barrovian metamorphic rocks and migmatites that formed in the mid-lower crust, and I and S-type granites. Together these rocks provide insight into deep processes that cannot be directly observed at the surface. This thesis will therefore address the timing, duration and rates of deformation, metamorphism and exhumation prior to the onset of extension and in doing so attempt to constrain the timing and nature of this tectonic reversal.

1.2 Tectonic Setting

The Cycladic Islands in the central Aegean form part of the Attic–Cycladic Massif (Durr et al., 1978), which is a belt of thinned continental crust located to the north of the Hellenic subduction zone, where the Nubian plate is subducting northwards beneath Eurasia at approximately 10 mm/yr (Wortel and Spakman, 2000; Jolivet and Brun, 2010). Within this overall subduction setting, the Aegean region can be subdivided into the fore arc (Crete, Karpathos, Rhodes), the Hellenic arc (e.g. Santorini, Milos), and the back arc (Cyclades and crust to the NE). The active volcanoes of the Hellenic arc lie above the location where the subducted slab reaches about 125 km depth. The Aegean region is bounded to the south by the Nubian and Arabian plates and to the north by stable Eurasia, where there is neglegible contemporary deformation (Fig. 1.1). Present-

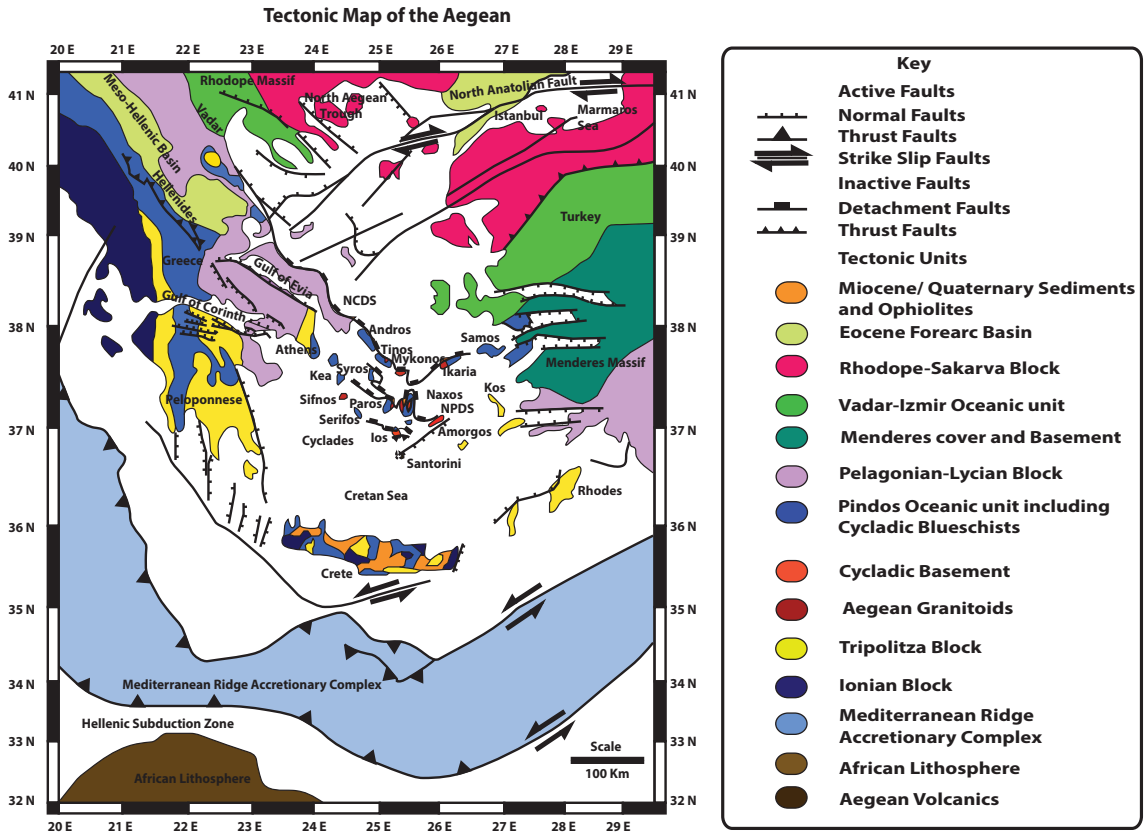


Figure 1.1: Simplified tectonic map of the Aegean region, after Jolivet et al., (2012) showing the major tectonic structures and rock types. Naxos lies in the Cycladic-Attic Massif in the central Cyclades. NCDS = North Cycladic Detachment System, NPDS = Naxos-Paros Detachment System, Yellow triangles represent current Hellenic volcanic arc.

day GPS velocities show that Nubia and Arabia move roughly northward, whereas Anatolia (along the eastern margin) moves northwest-to-westward, and western Turkey and Greece move west-to-southwestward (Fig. 1.2) (Aktuğ et al., 2009; Floyd et al., 2010; McClusky et al., 2000; Reilinger et al., 2006). The westward motion of Anatolia and the Aegean has been kinematically described by either westward "extrusion" or "escape" (e.g., Armijo et al., 1999, 2003; Şengör et al., 1985) or has been attributed to the "rollback" of the Nubian slab beneath the southern Aegean (e.g., Le Pichon, 1982; Le Pichon and Kreemer, 2010; Royden, 1993). Geodynamic explanations for this motion relate it to either gradients in gravitational potential energy between eastern Turkey and the southern Aegean (Fig. 1.2) (e.g. England et al., 2016), or to tractions applied to the base of the lithosphere by the underlying mantle flow due to "slab

rollback" (e.g., Faccenna et al., 2014; Le Pichon, 1982; Le Pichon and Angelier, 1979; Le Pichon and Kreemer, 2010; McKenzie, 1972, 1978). Although the large-scale motions of the Aegean and Anatolia relative to Eurasia can be approximately treated as a rigid-body rotation with a Euler pole situated near the Nile delta (Le Pichon and Kreemer, 2010; Reilinger et al., 2006). The region is cross-cut by active faults, and GPS velocities systematically increase across the region by 20 mm/yr from east to west, making it far from rigid by the plate tectonic definition (e.g., Aktuğ et al., 2009, 2013; Floyd et al., 2010; Goldsworthy and Jackson, 2000, 2001; Goldsworthy et al., 2002; Jackson, 1994; Jackson and McKenzie, 1988; Reilinger et al., 2006; Şaroglu et al., 1992; Shaw and Jackson, 2010; Taymaz et al., 1991a). Widespread large shallow earthquakes are the result of this deformation, whose focal mechanisms vary from thrust and reverse faulting along the western and southern margins of the region (Mediterranean Ridge Complex), to normal faulting throughout mainland Greece and western Turkey associated with regional crustal extension, to normal-plus-strike-slip faulting in the northern Aegean, and to strike-slip faulting on the north and southeastern margins of Anatolia associated with large strike slip fault systems such as the North Anatolian Fault that has been active since ca. 11 Ma (e.g. Şegnör et al., 2005). This concentrated strike-slip motion becomes more distributed towards the west into the Aegean Sea, and earthquakes with focal mechanisms of Mw >5 show no evidence of strike-slip motion within mainland Greece. An important point to note is that whereas the Aegean is often referred to as a region of back arc extension, most of the present day extension actually takes place in the fore arc, between the trench and the volcanic arc, and is associated with the formation of the sea of Crete (Fig. 1.2). Although the present-day deformation is reasonably well known, the deformation styles throughout the Cenozoic are largely disputed.

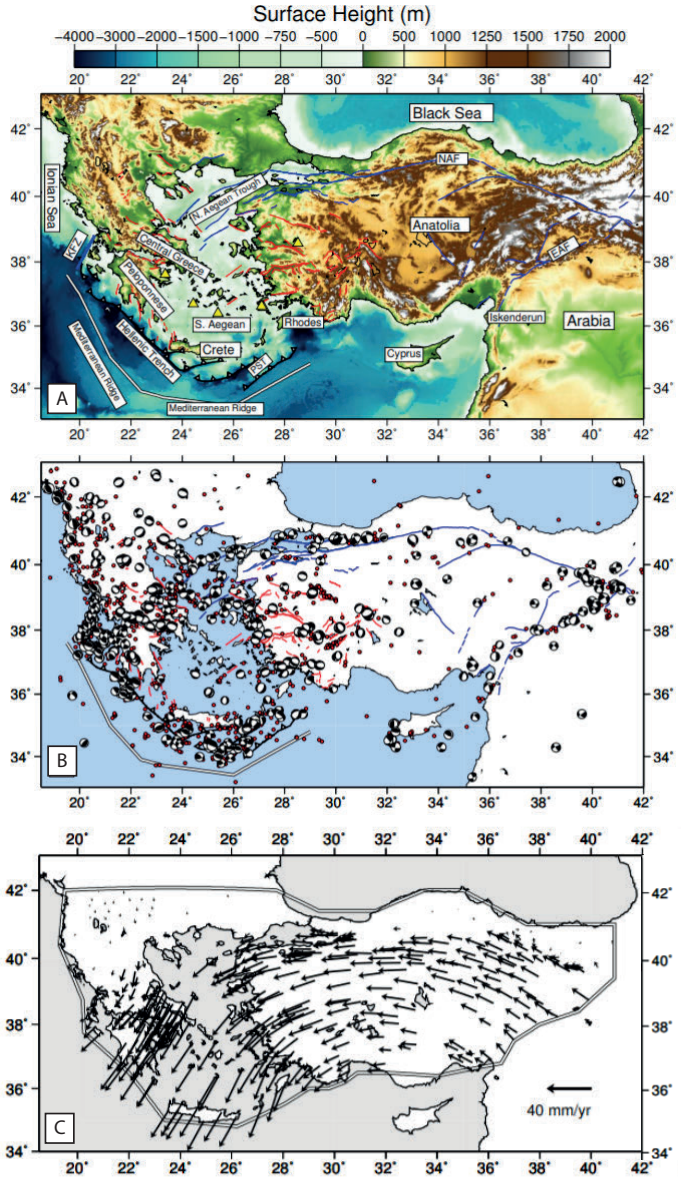


Figure 1.2: Presend day deformation in the Aegean region after England et al., 2016: A) Surface elevation false colour image showing the volcanic arc (yellow triangles), Hellenic subduction zone and major active structures; KFZ: Kefalonia Fault Zone; PST: Pliny and Strabo Trenches; NAF: North Anatolian Fault; EAF: East Anatolian Fault. Active faults of the region are shown in blue (strike-slip) or red (normal) (Goldsworthy and Jackson, 2000, 2001; Goldsworthy et al., 2002; Şaroglu et al., 1992). Yellow triangles indicate the locations of the active volcanoes of the Aegean arc. B) Seismic activity of the region. Dots show the epicenters of earthquakes between 1960 and 2007 with hypocenters shallower than 33 km (International Seismological Centre, 2011). Focal mechanisms from the GCMT catalogue (Dziewonski et al., 1981; Ekström et al., 2012) and from Jackson and McKenzie (1988); Shaw and Jackson (2010) note the Hellenic trench is located further south beyond the Mediterranean Ridge Complex. B) Compilation of earthquake focal mechanisms on active faults, showing dominantly normal faults associated with NE-SW extension. C) GPS velocities taken with respect to stable Eurasia, of 346 GPS sites in the Aegean and Anatolia from Nocquet, (2012) and 24 additional GPS studies (see England et al., 2016 for further discussion on selection of GPS sites). It shows rotation about a pole located just north of the Nile delta; velocites increase towards the SW across the Aegean region from 10-40 mm/yr

1.3 Geology of the Aegean region

The overall geology of the Aegean region is usually subdivided into several structural zones or terranes (e.g. Papanikolaou, 2013 and references therein) (Fig. 1.1). These zones reflect the successive tectonic shortening events which sequentially added new continental crust onto the southern margin of Eurasia in roughly NE–SW trending ribbons associated with the overall collision between Adria (to the SW) and Eurasia (to the NE) (e.g. Bijduval et al., 1977; Segnor, 1979, 1984; Dewey and Şegnör, 1979; Robertson and Dixon, 1984; Decourt et al., 1985; Robertson, 2002, Papanikolaou, 1984, 2013). In the western part of the region (the external zones), medium-to-low angle NE-dipping reverse faults represent the zone boundaries. Whereas in the northern and eastern parts of the region, the zone or terrane boundaries are marked by Tertiary normal faults (Leeder et al., 1991), and sometimes the Tertiary extension has re-activated earlier zone boundaries (e.g. Papakinlaou, 2013). The Tertiary extension of the region has disrupted the zones, mostly by a clockwise vertical axis rotation of the western Aegean, into an arcuate form (Fig. 1.1), so that, in Greece, the zones run roughly NW–SE. Moving across strike from NE to SW these zones include:

Rhodope Complex: The most easterly zone and comprises metamorphic and igneous rocks that represent the Eurasian margin with ages ranging from pre-Alpine into mid-Tertiary. Ultra-high-pressure (*UHP*) metamorphic rocks have recently been discovered with Lu–Hf garnet ages of ca. 70 Ma (Collings et al., 2017).

Serbo-Macedonian Zone: This is a Late Carboniferous aged metamorphic and igneous zone, associated with the Variscan Orogeny.

Vardar Zone: This zone comprises of Jurassic aged ophiolites and Mesozoic carbonates, which are cut by Late Cretaceous strike-slip faults and is referred to as a suture zone between Eurasia and Pelagonia/Adria (e.g. Brown and Robertson, 2004; Tremblay et al., 2015). It is bounded between the Serbo-Macedonian Zone to the east and the Pelagonian Zone to the west.

Pelagonian Zone: This zone is situated to the west of the Vardar Zone and to the east of the Pindos Zone and comprises continental 'Variscan' basement with Mesozoic

carbonate cover, locally metamorphosed in mid Mesozoic or later time. The origin of this continental fragment has been of considerable debate, some believe it represented a ribbon continent between the Vardar and Pindos Oceans (to the east and west respectively) (e.g. Robertson, 2002; Sharp and Robertson, 2006, Papakinlaou, 2013), whereas others suggest it belongs to Adria (e.g. van Hinsbergen et al., 2018).

Sub Pelagonian zone: This is a Mesozoic platform with presumed Variscan basement to the west of the Pelagonian Zone, it was deformed during ophiolite emplacement in Late Jurassic/Early Cretaceous time and was deformed again in Early Tertiary time.

Pindos Zone: This comprises Jurassic aged ophiolites (Pindos, Vourinos, Orthis and Mirdita Ophiolites), whose origin has been highly debated. The Pindos and Vourinos Ophiolites appear to have been thrusted towards the NE onto the Pelagonian zone (e.g. Sharp and Robertson, 2002), whereas the Mirdita Ophiolite shows thrusts with a westward vergence. This Unit also contains Mesozoic carbonates, Mesozoic pelagic cherts and carbonates overlain by Tertiary flysch, cut by Late Cretaceous strike-slip faults and deformed in the later Tertiary time.

The External Zones: This zone affects western Greece and includes the: Gavrovo-Tripolitza: Mesozoic platform carbonates overlain by Tertiary flysch, deformed in later Tertiary time. Ionian Zone: The most westerly zone on the Ionian Sea. It is made up of Mesozoic pelagic cherts and carbonates overlain by Tertiary flysch, then late Tertiary 'molasse', deformed in late Tertiary time. Collectively, these two zones are comparable to the present-day Florida platform, Tongue of the Ocean, Blake plateau and continental rise sequence of the western Atlantic continental margin.

The Attic–Cycladic Massif: This is the most southerly zone, that comprises of some exposures of ophiolitic rocks, underlain by continental margin sediments that have experienced high-pressure and Barrovian metamorphism during the Eocene-Miocene and is underlain by Hercynian continental basement. It is also the location of several metamorphic core complexes. These rocks have not been successfully correlated to other rocks on mainland Greece and are the subject of this study.

1.4 Geological evolution

The Aegean region has experienced a complicated geological evolution throughout the Mesozoic and Cenozoic, as summarised by the number of "structural zones" described above. It was firstly affected by the Variscan orogeny, which affects the metamorphic rocks of the northern Rhodope Massif, the Serbo-Macedonian Zone and the Pelagonian Zone but is also recognized in the basement rocks of the Cyclades (e.g. Naxos, Ios; Keay et al., 2001). Secondly, it was affected by the opening of the Tethys Ocean and formation of oceanic lithosphere during Jurassic times, which was associated with ophiolite formation between ca. 170 and 160 Ma. These ophiolites now form two distinct NNW–SSE trending belts running up the Balkan Peninsular and include the Vardar Ophiolites to the east (also referred to as the "East Vardar Ophiolites"; van Hinsbergen et al., 2018) and the Pindos, Vourinos, Orthis and Mirdita Ophiolites to the west (also referred to as the "West Vardar Ophiolites"; van Hinsbergen et al., 2018), which are separated by the Pelagonian Zone. The origin of these ophiolites has been a subject of debate for the last four decades and three end member models have been proposed:

1. **Single ocean and far travelled nappe model (Papanikolaou, 1984):** This model argues that the "West and East Vardar Ophiolites" i.e. all ophiolites are rooted from a single Neo-Tethyan Ocean Basin (Vardar Ocean) separating Adria to the west and Eurasia to the east. Ophiolites formed within this ocean either at a mid-ocean ridge or Supra Subduction Zone (SSZ)-type setting, or both. All the "West Vardar Ophiolites" were later were emplaced southwestwards onto the Adriatic continental margin (Aubouin et al., 1970) and the "East Vardar Ophiolites" were obducted eastwards onto the Eurasian Margin. This model requires the Mirdita–Pindos–Vourinos–Orthis Ophiolites to have been thrust >200 km to the SW over the Pelagonian Zone and subsequently back thrusted to the NE to produce eastward vergence directions particularly in the sole of the Pindos Ophiolite.

2. **Separate ocean model (Robertson, 2002):** This model suggests that the "West and East Vardar Ophiolites" formed in different oceanic basins separated by the Pelagonian ribbon continent and at different times. In this model, the eastern domain of the "West Vardar Ophiolites" formed in a different ocean basin to the western domain. The eastern domain formed above a NE dipping subduction zone and were thrust to the SW onto the Pelagonian ribbon continent. By contrast, the western domain of the "Western Vardar Ophiolites" (i.e. Mirdita–Pindos-Vourinos-Orthis Ophiolites) formed at ca. 170 Ma by SSZ-type spreading above a westerly dipping subduction zone to the SW of the Pelagonian ribbon continent and were thrust to the NE onto the Pelagonian continental margin during the closure of the Pindos Ocean.

3. **All the ophiolites formed in a single oceanic basin, but were later dissected into parallel belts as exotic terranes related to regional strike-slip faulting (Smith and Spray, 1984).** This scenario is not favorable, as there are strong differences in the tectono-stratigraphy of the ophiolites and related units within the Pindos and Vardar sutures, and therefore seems implausible the two sutures once represented the same structure.

Whichever of these three models is correct (discussed in Chapter 2), the net result of this shortening was to close the Jurassic ocean(s) (except for the tectonically emplaced ophiolites) and created a stack of thin-skinned internally deformed NE-dipping thrust sheets. Total shortening estimates from the west coast of Greece to the Pelagonian Zone are up to 500 km (within continental margin sediments) and therefore total amounts of shortening associated with closure of the Tethys Ocean could be much greater (Degnan and Robertson, 1998; Skourlis and Doutsos, 2003). Finally, Tertiary extension overprints the earlier shortening structures, and is responsible for the principal topographic features of the region. It is debated when the extension started. On mainland Greece, the extension appears to have initiated in the early to mid-Miocene time (e.g. Papakinlaou, 2013, Leeder et al., 1991). This also coincides with the timing of when ductile extensional shear zones in the Rhodope Massif (e.g. Dinter and Royden, 1993) and

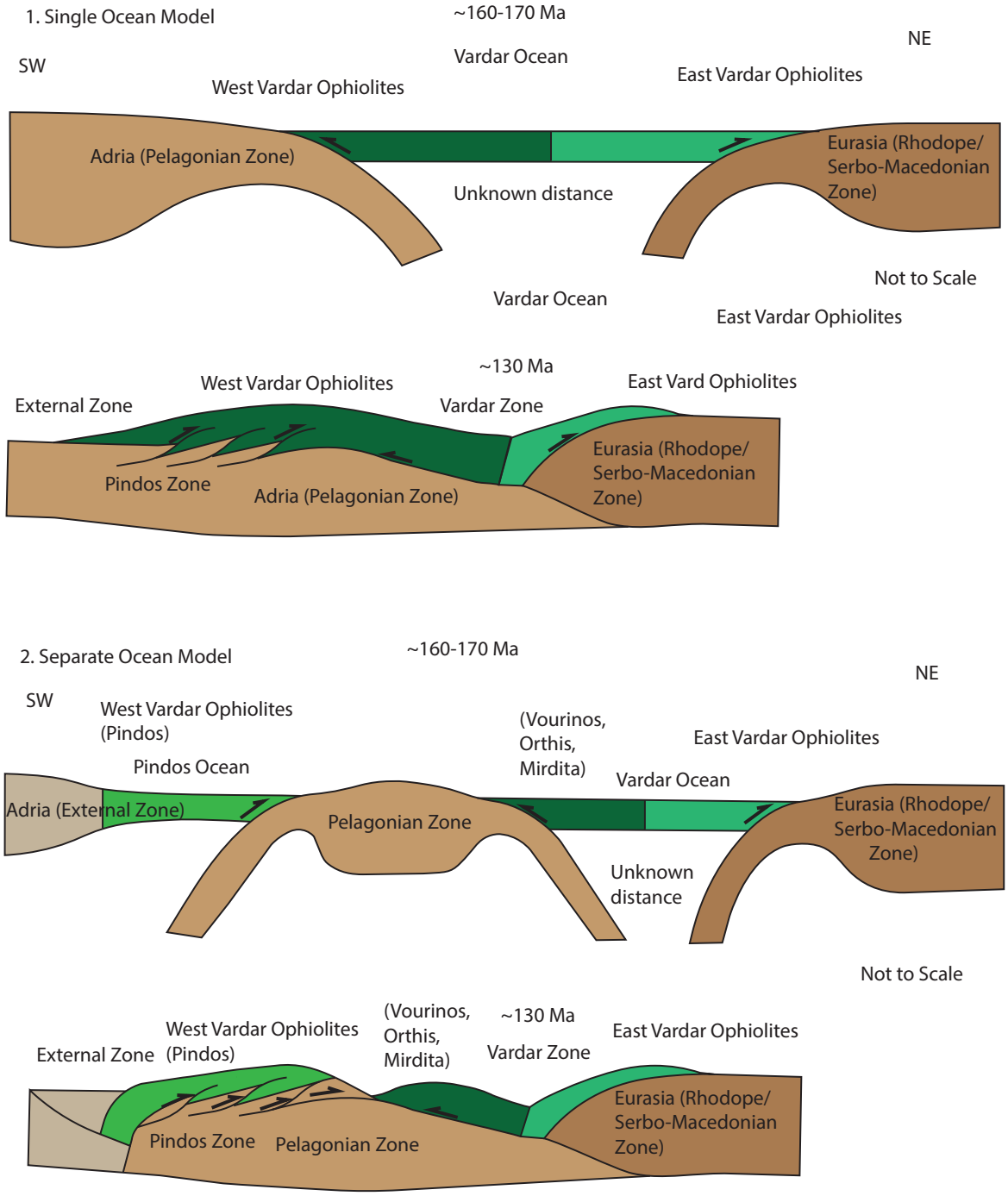


Figure 1.3: Tectonic end member models for Jurassic Ophiolite emplacement: A) Single ocean model, where the West Vardar Ophiolites are emplaced westward onto the Pelagonian zone and subsequently back-thrusted whereas the East Vardar Ophiolites are emplaced onto Eurasia. B) Separate ocean model where the western West Vardar Ophiolites (Pindos, Vourinos and Orthis Ophiolites) formed in a separate ocean basin and were emplaced to the NE onto the Pelagonian Zone.

Cyclades (e.g. Lister et al., 1984) were being exhumed (and is investigated in Chapter 4, 5 and 6), the formation of some major basins (e..g. the North Aegean Trough and the Sea of Crete; e.g. Koukouvelas and Aydin, 2002 and references therin), and the eruption of extension-related volcanics in the northern Aegean and Western Turkey (e.g. Perkins et al., 2018; Caran et al., 2016).

However, the relation between this ancient extension and the currently active extension is poorly understood (e.g. Jolivet, 2001). The major established geodynamic model to explain the ancient extension involves continuous slab rollback of the Hellenic subduction zone throughout the entire Cenozoic (e.g. LePichon and Kreemer, 2010; Jolivet and Brun, 2010; Jolivet et al., 2013; Fig. 1.4). In this model, the Hellenic subduction zone migrates further south west with time causing the Pelagonian, Pindos and External Zones (Gavro-tripolitzia and Ionian Zones) to be subducted and accreted from a lower plate position to an upper plate position. This model has also been used to explain the apparent southward migration of the Hellenic arc, apparent southwestward movement of the front of active thrusting, and the southwestward migration for the locus of high-pressure metamorphism across the Aegean through time (e.g. LePichon and Kremmer, 2010; Jolivet and Brun, 2010; Jolivet et al., 2013). This model also allows for high-pressure metamorphism to be followed by "back-arc extension", causing asthenospheric upwelling, Barrovian metamorphism and metamorphic core complex formation (e.g. Jolivet and Brun, 2010; Jolivet et al., 2010. 2013, 2015; Lister et al., 1984; Buick, 1991). Despite explaining several observations, this model of continuous extension and roll-back of the same Hellenic subduction zone throughout the entire Cenozoic exhibits several major problems. Firstly, it assumes that the entire continental crust between the Vardar Zone and the current Hellenic Trench was part of the subducting plate, and was accreted into the upper plate during subduction. As such, one would expect to find extensive high-pressure metamorphism throughout the entire Pelagonian, Pindos and External Zones, which is not observed. Because these rocks are of continental margin affinity, this also poses a major problem as it implies subduction of continental rocks continued for ca. 50 Ma, without a sufficient slab pull

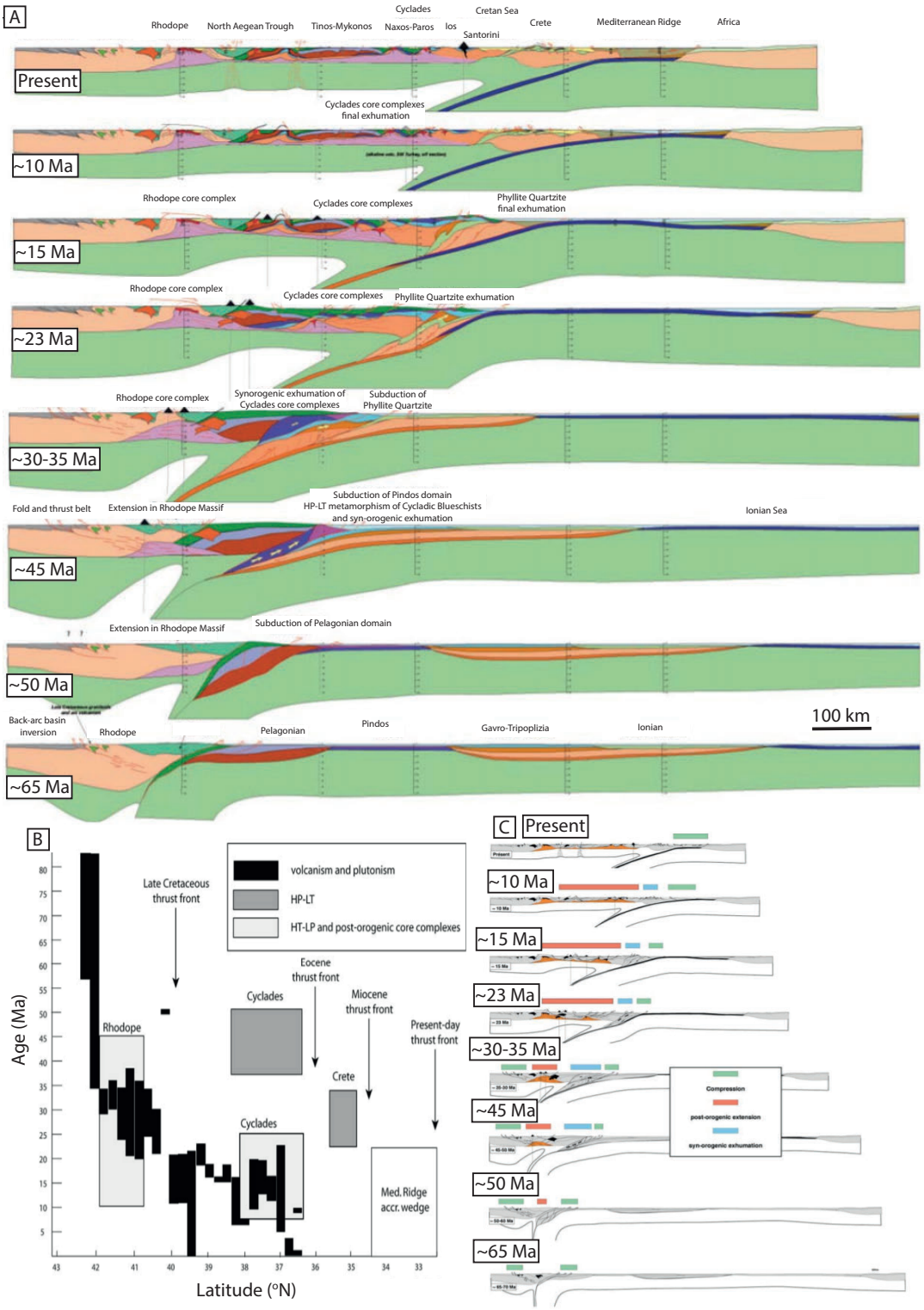


Figure 1.4: Slab roll-back model after Jolivet and Brun, 2010. A) tectonic reconstruction of slab roll-back to explain the locus of high-pressure metamorphism and magmatism to migrate southward throughout the Eocene. B) Time chart with lattitude showing high-pressure metamorphism occurs in two distinct episodes between ca. 50-40 in the Cyclades and ca. 35-20 Ma on Crete, and magmatism episodically get further south to the present day, interpretted to represent migration of the volcanic arc. C) Simplified tectonic reconstruction showing the zone of compression, syn-orogenic extension and back-arc extension

force. The arrival of continental crust into a subduction zone normally causes subduction to end in most orogenic belts due to the positive buoyancy of continental material (e.g. Agrad et al., 2009). Secondly, the present-day extension rate of ca. 40–50 mm/yr between southern Aegean and Europe clearly cannot have continued throughout the entire Cenozoic at present day rates. This is because ca. 15 million years of continuous extension would equate to at least ca. 600 km of extension using current GPS rates. The result is even more extreme assuming extension initiated at ca. 35–40 Ma (at least 1300 km of extension), as proposed by Jolivet and Brun., (2010) and Jolivet et al., (2013). This estimate for the onset of extension is based upon the timing of 'extensional' deformation fabrics in retrogressed high-pressure rocks and their exhumation histories, and mainly relies upon Ar–Ar isotopic ages for retrograde deformation. The origin of the "extensional fabrics" in these rocks is also a subject of considerable debate as they do not independently define an overall tectonic regime, but rather record the relative movement of material (e.g. Law et al., 2006; Searle, 2010; Lamont et al., in press). Furthermore, the processes driving the initiation of low-angle normal faulting, and whether this is associated with lithospheric-scale normal faulting in an overall extensional environment or localized extension in a compressional environment (e.g. Searle, 2010) are debated. Lastly, there are alternative explanations behind the cause of Aegean extension and involve either gravitational potential energy gradients between thick and thin crust (England et al., 2016) or changes in the angle of subduction (e.g. Shimon et al., 1989). Whether the extension was episodic, gradually accelerated through time, or did not initiate until much more recently than previously thought is largely unconstrained, and is investigated as part of this thesis.

1.5 Geology of the Cyclades

The Cycladic Islands, in the central Aegean Sea, have been previously regarded a type locality of subduction zone metamorphism, metamorphic core complexes, and low angle normal faults which are interpreted to have formed during regional lithospheric

extension. As such, the area has received intense investigation to further understand its complex geological evolution, and to gain insight into subduction zone processes (e.g. Lister et al., 1984; Kieter et al., 2004; Jolivet et al., 2010, 2013; Behr et al., 2018). The established framework for the Cenozoic evolution of the Cyclades has been linked to lithospheric extension in response to roll-back and retreat of the Hellenic slab (LePichon and Anglier, 1979; LePichon, 1982; LePichon and Kreemer, 2010; Jolivet and Brun, 2010; Jolivet et al., 2010, 2013) as described above. Many studies have suggested extension affected the area from the Oligiocene–Miocene until present day, and some estimate southward propagation of the Hellenic subduction zone on the order of 1000 km over this time period (e.g. John and Howard, 1995; Seward et al., 2009). It is proposed that NE–SW-oriented crustal extension rates within the last 15 Myrs may be up to twice as fast as present-day rates (Urai et al., 1990). In response to extension, three bivergent crustal-scale low-angle normal fault systems developed. The North Cycladic Detachment system (Fig. 1.5) exposed on the islands of Andros, Tinos and Mykonos displays top-to-NE sense of shear (Jolivet et al., 2010). The Naxos-Paros Detachment System (NPDS) exposed on Naxos and Paros displays top-to-NNE shear fabrics (Buick, 1991; Cao et al., 2013, 2017; Urai et al., 1991; Kruckenberg et al., 2010, 2011). The West Cycladic detachment system occurs on the islands of Kea, Kythnos, and Serifos, and shows top-to-SSW kinematics (Grasemann et al., 2012). Despite extensional deformation affecting all structural levels of the Cyclades, there remains a limited understanding of the geological evolution of the area prior to the initiation of extensional tectonics. Structural and metamorphic evidence from several islands suggests the Cyclades experienced a complicated tectonic evolution involving a complete cycle of mountain building (Ring and Lawyer 2003; Ring et al., 2007a; 2007b; Peillod et al., 2017). Remnant ophiolites crop out at the highest level on several islands, in the hanging walls of the low-angle normal fault systems (Katzir et al., 1996; Stouratti et al., 2017). These are underlain by (M_1) Eocene aged high-pressure eclogite–blueschist facies rocks of the Cycladic Blueschist Unit (CBU) that are exposed in the footwall of the detachment faults, dated at ca. 52.2–51.4 Ma by U–Pb zircon and

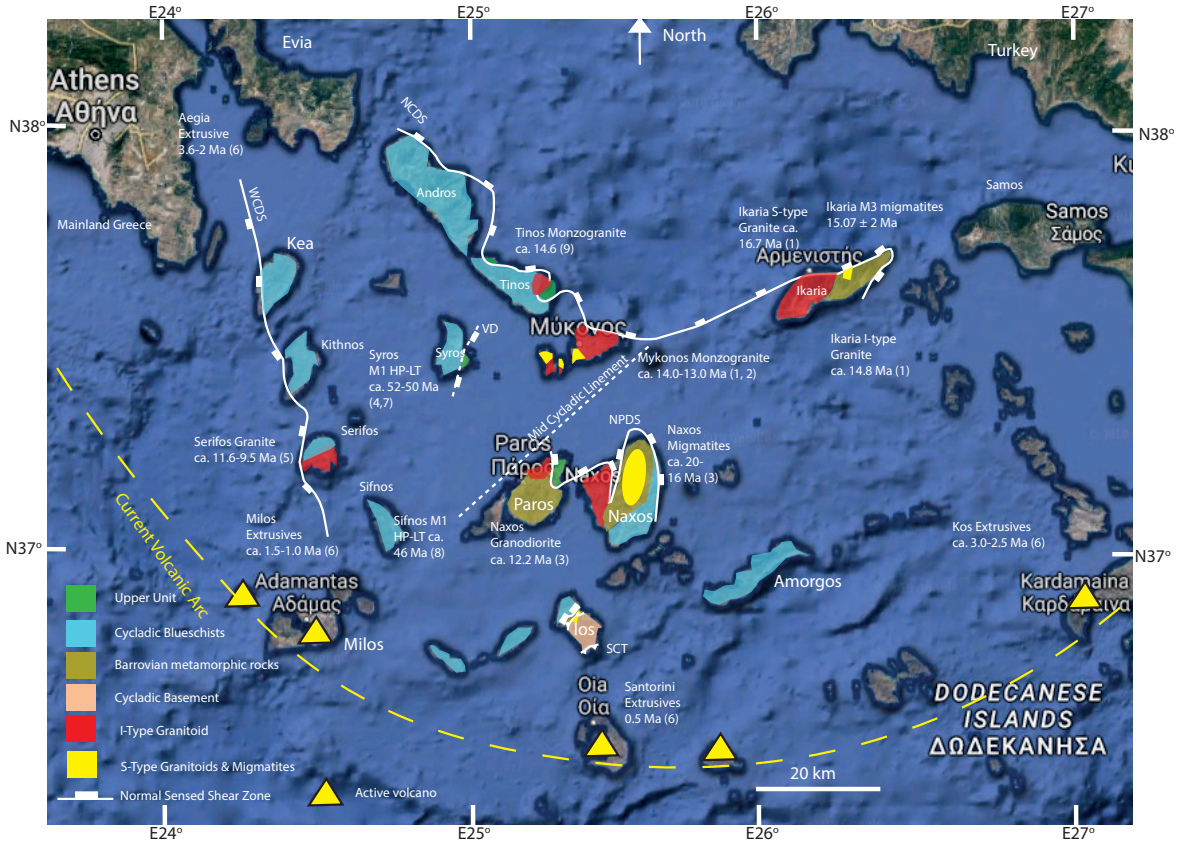


Figure 1.5: Simplified geological map of the Cyclades showing the main tectonic units and U-Pb or Lu-Hf garnet geochronology: NCDS=North Cycladic Detachment System, NPDS=Naxos-Paros Detachment System and WCDS=West Cycladic Detachment System. References: (1) Bolhar et al., (2010); (2) Brichau et al., (2010); Keay et al., (2001); (4) Tomaschek et al., (2003); (5) Igelseder et al., (2009); (6) Matsuda et al., 1999 (Ar-Ar volcanics); (7) Lagos et al., (2007); (8) Dragovic et al., 2012; (9) Brichau et al., (2007)

Lu–Hf garnet geochronology from Syros (Tomaschek et al., 2003; Lagos et al., 2007) and ca. 46 Ma from Sifnos eclogites (Dragovic et al., 2012). The area then experienced regional Barrovian metamorphism (M_2) during the Oligocene to early Miocene (40–18 Ma), followed by a sillimanite-grade event (M_3) at ca. 16 Ma that reached anatectic conditions on Naxos and Ios (Jansen and Schuiling 1976; Buick and Holland; 1989, Keay et al., 2001). I and S-type granites intruded during the late Miocene. The age of I-type granitoids get younger from north to south from ca. 14.6 Ma on Tinos to 12.2 Ma on Naxos. The origin of these granites and the coeval I and S-type nature is of significant geodynamic interest and is explored in Chapter 6.

1.6 Key aims and motivation

Although the above tectonic evolution for the Hellenides can account for many of the geological phenomenon observed across the Aegean region, the ophiolitic, metamorphic and magmatic rocks exposed in Cyclades do not easily conform to this framework. This is because the Cyclades experienced deformation and metamorphism during the Late Cretaceous – Miocene times (e.g. Keay et al., 2001) associated with high-pressure conditions (M_1) later followed by Barrovian-metamorphism (M_2). These tectono-metamorphic events are not recorded anywhere else on mainland Greece and therefore presumably represent a separate episode of orogenesis to what is observed on the mainland. Some workers have suggested the continental margin metamorphosed sediments of the Cyclades are equivalent to the Pindos Zone sediments and the Gavro-Tripolztia carbonates (e.g. Papakinlaou, 2013) although this remains highly debatable.

To obtain a thorough understanding of these tectonothermal events, the islands of Tinos and Naxos, which together provide the most complete structural cross section of the Cyclades, were the focus of this study. Tinos, which lies on the northern edge of the Cyclades, records the early stages of orogenesis associated with ocean closure and subduction. It exposes ophiolitic rocks and a newly identified metamorphic sole, which is underlain by high-pressure continental margin metamorphic rocks of the Cycladic Blueschist Unit that contain newly described outcrops of eclogites. Naxos was also subject to intense investigation, to gain insight into the prograde and peak (M_2) kyanite and (M_3) sillimanite-grade metamorphic evolution, partial melting, sequence of deformation and rates of exhumation. The island of Delos was also briefly visited, as this is also affected by (M_3) sillimanite-grade metamorphism, partial melting and I and S-type granites. The key aims of this thesis can therefore be summarised as follows:

1. To investigate the origin of ophiolitic rocks across the Cyclades, including deciphering their age of formation and emplacement. This will provide further constraints on the series of events that preceded high-pressure metamorphism of the Cycladic Blueschist Unit. It will also improve our understanding on the

timing of closure of the Tethys Ocean in the Aegean.

2. To gain an understanding of the relationship between ophiolitic rocks at the highest structural levels of the Cyclades, and the underlying Cycladic Blueschist Unit, which represents the attempted subduction of the leading edge of the continental margin down a Late Cretaceous to Eocene NE-dipping subduction zone.

3. To use field observations, thermobarometric and geochronological techniques to constrain the pressure (P), temperature (T) time (t) and deformation (D) evolution of the high-pressure rocks of the Cycladic Blueschist Unit on Tinos, and to gain an understanding of how these rocks were buried and exhumed.

4. To investigate the origin of and constrain the P–T–t–D evolution of the kyanite and sillimanite-grade metamorphic rocks and migmatites on Naxos. Key questions include how these rocks relate to the overlying high-pressure rocks of the Cycladic Blueschist Unit and how they were exhumed.

5. To provide constraints on the timing for the onset of regional extension in the Cyclades and the rates of exhumation on the low angle normal faults.

6. To constrain the timing of I and S-type magmatism in the Cyclades and in doing so, help address the timing for the onset of extension, exhumation and slab rollback of the Hellenic subduction zone.

To successfully accomplish these objectives, a combined approach was utilizing involving: 1. detailed field observations and mapping carried out over seven field seasons in total spanning 2012–2018 (five field seasons between 2015 and 2018 during the D.Phil); 2. detailed petrological observations, electron microprobe analysis, thermobarometric calculations using classical thermobarometry and THERMOCALC equilibrium phase diagram modelling to obtain precise P–T estimates for the prograde-peak and retrograde conditions of metamorphism; and 3. geochronological work to obtain precise absolute metamorphic and magmatic ages to constrain the timing of metamorphism and magma crystallization. This latter component was carried out on key samples from

Tinos, Naxos and Delos at the Natural Environment Isotope Geosciences Laboratory (NIGL) under the supervision of Dr. Nick Roberts. U–Pb zircon dating of ophiolitic rocks and granites from Tinos provide the age of ophiolite formation, obduction and metamorphism in the sole rocks, and the timing of granite intrusion. Lu–Hf garnet geochronology was performed on suitable samples from the metamorphic sole and the underlying eclogites and blueschists of the Cycladic Blueschist Unit and provide further timing constraints of metamorphic sole formation and high-pressure metamorphism. U–Th–Pb geochronology was performed on a complete range of metamorphic and magmatic samples from Naxos that include zircon, monazitite, allanite and rutile to provide constraints on the timing of deformation and exhumation.

1.7 Thesis Structure

The results of this thesis are presented as five research papers; chapters 2–6. Methodologies and background principles that are common in all studies are described once in the relevant chapters and included in the relevant appendix to avoid repetition. Each study starts with an introduction, followed by the presentation of new data obtained and its subsequent interpretation and discussion. Contributions to these studies made by collaborators or journal reviewers are clearly stated in the text; all other work is my own. The following chapters are summarised below:

Chapter 2 – In this chapter, the Upper Unit on Tinos is re-investigated. A detailed account of the field and petrological relations of the Tsinkias Ophiolite, a newly described metamorphic sole is presented, alongside trace element geochemistry, thermobaromery, equilibrium phase diagram modelling and U–Pb and Lu–Hf geochronology.

Chapter 3 – This chapter deals with the high-pressure rocks of the Lower Unit on Tinos. It includes detailed field and petrological descriptions of newly identified eclogites and blueschist outcrops, a new interpretation of the large-scale structures on Tinos, thermobarometry, equilibrium phase diagram modelling and Lu–Hf garnet geochronology.

Chapter 4 – This chapter presents the structural, petrological and thermobarometry results of a combined large-scale study of the Naxos metamorphic core complex.

Chapter 5 – This chapter provides the U–Th–Pb geochronological constraints to the data presented in Chapter 4 and integrates it into a new tectono-thermal model for the evolution of the Naxos metamorphic core complex.

Chapter 6 – This final research chapter presents the U–Pb geochronological and trace-element geochemistry results of I and S-type granites that intrude Tinos and Delos islands and provide timing constrains for the initiation of upper crustal extension and rates of exhumation.

Chapter 7 – This chapter summarises the work carried out during this D.Phil and provides a regional synthesis for the Aegean from the conclusions drawn from each chapter. This chapter also discusses the implications of this work and discusses future research directions.

Appendix – The appendices contain a variety of supplemental information of methods used to acquire data and results relevant to the studies on Tinos and Naxos and include an overview of metamorphic petrology and thermobaromtery, geochronology and whole rock geochemistry.

Chapter 2

The age, origin and emplacement of the Tsiknias Ophiolite, Tinos, Greece

2.1 Introduction

Ophiolites are scattered along the entire Alpine-Himalayan belt, and record oceanic spreading events within Neo-Tethys from late Jurassic to Eocene times. Together, these rocks have important implications for the regional scale geodynamics, as they are interpreted as fragments of oceanic lithosphere emplaced onto continental margins during orogenesis. In the Hellenides and Dinarides (Albania, Greece, Bulgaria, Croatia, Serbia; Fig. 1), most ophiolites (Dinaric–Mirdita–Pindos–Vourinous–Orthis and Guevgueli Ophiolites) have Jurassic U–Pb ages (e.g. Dilek et al., 2007; Zachardis, 2007; Liati et al., 2004; Froitzheim et al., 2014), whereas most ophiolites in the Turkish Taurides and Pontides are Cretaceous in age (e.g. Celic et al., 2006; Parlac et al., 2013; Karaoglan et al., 2013; Peters et al., 2017) (Fig. 2.1). Metamorphic soles underlie many of these ophiolites, and record the initial stages of their obduction histories. A range of ^{40}Ar–^{39}Ar, U–Pb, and Lu–Hf garnet ages (Jones et al., 1991; Celic et al., 2006; Parlac et al., 2013; Karaoglan et al., 2013; Peters et al., 2017) shows that

these features usually form at the same time as the ophiolites directly above them. Supra-subduction zone (SSZ) geochemical signatures of the ophiolites support a model whereby ophiolites formed above subduction zones, and were emplaced onto the respective continental margins during ocean closure (e.g. Schmid et al., 2008; Maffione and van Hinsbergen, 2018; Sharp and Robinson, 2006; Wakabashi and Dilek, 2000). In the Aegean Sea area (Fig. 2.1), several distinct ophiolite belts record traces ofsubduction zones that were active at different times during the closure of the Neo-Tethys Ocean. These include the Dinaric–Mirdita–Pindos–Vourinos–Orthis Ophiolites that make up the "Western Vardar Ophiolites" that sit on Adriatic continental crust and the Guevgueli and Serbo-Macedonian Ophiolites that make up the "Eastern Vardar Ophiolites" that lie on Eurasian continental crust (Schmidt, 2008). However, integrating these ophiolites into regional geodynamic models is often difficult as most occur as isolated fragments and have been overprinted by subsequent tectonic movements (e.g. Maffione and van Hinsbergen, 2018; Bortolotti et al., 2013; Sharp and Robertson, 2006). Topics of debate include: 1. How do the Balkan ophiolites relate to the younger Turkish ophiolites? 2. At what time did the Neo-Tethys Ocean close and was this associated with the closure of one, two or three basins? item Are ophiolitic rocks within the Aegean Sea related and can they be correlated to the surrounding well-studied ophiolite belts?

The Cycladic Islands in southern Greece (Figs. 2.1 and 2.2 inset), are a key area for addressing all these questions. Rocks of ophiolitic affinity crop out commonly along shear zones and mélanges within eclogite- and blueschist-facies rocks, or at higher levels bounded by low-angle normal faults associated with Miocene – present extension of the Aegean region (Jansen, 1973; Jansen and Schuiling, 1976; Melidonis, 1980; Avigad and Garfunkel, 1989, 1991; Katzir et al., 1996, 2002, 2007; Brichau et al., 2007; Jolivet et al., 2010; Stourati et al., 2017)). Studies on the most complete ophiolite sections from several islands (Tinos, Andros, Ikaria, Paros, Naxos, Mykonos, Samos and Skyros) that sit at high structural levels, indicate that these bodies have a range of geochemical affiliations, including supra subduction zone (SSZ) to ocean is-

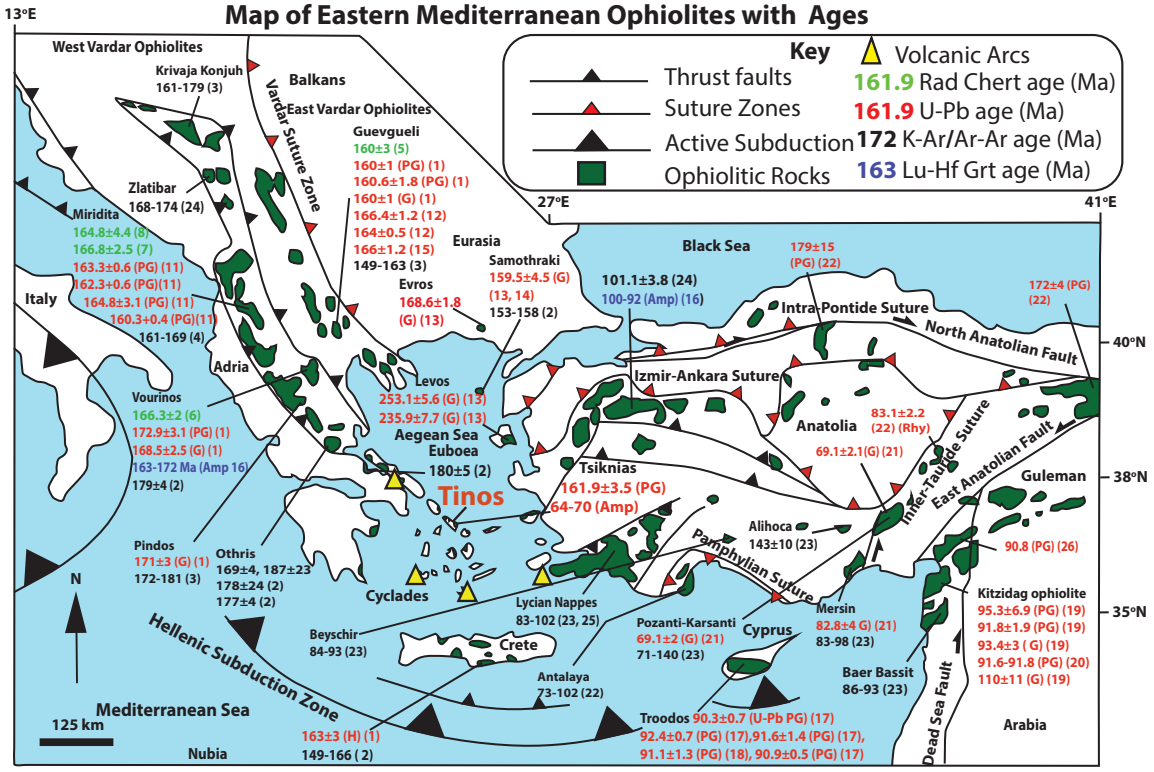


Figure 2.1: Summary map of Aegean Ophiolites with their reported geochronology ages and uncertainties. G = Gabbro, PG = Plagiogranite, Amp = Amphibolite from the metamorphic sole, H = Hornblendite. Reported ^{40}Ar–^{39}Ar, ^{40}K–^{39}Ar and Lu–Hf ages are from the ophiolite metamorphic soles. References: (1) Liati et al., 2004 (U–Pb); (2) Ferriére (1982) ^{40}Ar–^{39}Ar; (3) Spray et al., (1984) ^{40}Ar–^{39}Ar, (4) Dimo-Lahitte et al., (2001) ^{40}Ar–^{39}Ar; (5) Jones et al., (1991) ^{40}Ar–^{39}Ar (6) Danelian et al., (1996) (radiolarian cherts); (7) Chiari et al., (2003) (radiolarian cherts); (8) Prela et al., (2000) (radiolarian cherts); (9) Marcucci et al., (1994) and Chiari et al., (1994) (radiolarian cherts); (10) Zachariadis, (2007) (U–Pb) ; (11) Dilek et al., (2008); (12) Božović et al. (2013) U–Pb and ^{40}Ar–^{39}Ar; (13) Koglin, (2008) U–Pb; (14) Koglin et al., (2009) U–Pb; (14); (15) Kukoč et al. (2015) (radiolarian cherts); (16) Peters et al., (2017) Lu–Hf garnet; (17) Mukassa and Ludden (1987) U–Pb, (18) Konstantinou et al., (2007) U–Pb; (19) Karaoglan et al., (2013) U–Pb; (20) Dilek and Thy, (2009); (21) Parlak et al., (2013); (22) Topuz et al., (2012) U–Pb; (23) Thuizat et al., (1981) ^{40}K–^{39}Ar; (24) Harris et al., (1994) ^{40}K–^{39}Ar; (25) Okrusch et al., (1978) ^{40}K–^{39}Ar; (26) Sarıfakıoğlu et al., (2012) U–Pb.

land basalts (OIB). These sections are variably dismembered (Katzir et al., 1996, 2002, 2007; Stourati et al., 2017). Despite this work, there remains a limited understanding about how these rocks fit in with the current understanding of Aegean tectonics. As of yet, there is inadequate knowledge about their origin, emplacement mechanism(s), and their structural relationships to other metamorphic rocks of the Cyclades. It is

poorly understood whether they form part of the same ophiolite sequence and can be correlated with other Balkan or Anatolian ophiolites, or whether they represent completely separate ocean crust formation and obduction event(s) that are not recorded elsewhere in the eastern Mediterranean. To help answer these questions, we present a new structural map of Tinos and field relations, tied with petrology, thermobarometry, geochemistry and U–Pb and Lu–Hf geochronology, from the hitherto poorly understood Tsiknias Ophiolite exposed on Tinos. These data provide new constraints on the geodynamic history of the Aegean region since the Jurassic.

2.2 Geology of Tinos

Tinos lies along the northern margin of the Cycladic-Attic Massif (Fig. 2.2 inset). The island comprises of two distinct tectono-stratigraphic units that each experienced a different tectonic and metamorphic histories. The "Lower Unit" comprises continental margin lithologies that attained (M_1) blueschist- eclogite-facies conditions whereas the "Upper Unit" that incorporates continuous bodies of ophiolitic material, did not experience high-pressures. Pioneering work by Meloidis (1980), Avigad and Garfunkel (1989), and Katzir et al. (1996), highlighted that the island is a northwest-southeast striking elongate dome comprised of mainly retrogressed high-pressure rocks with variable amounts of intercalated fresh blueschists and some eclogite localities (e.g. Kionnia Peninsular see Fig. 2.2 and 2.3) that are bounded by a major greenschist-facies extensional shear zone with top-to-NE kinematics (Tinos Shear Zone). This shear zone (The Tinos Shear Zone) (Figs. 2 and 3) truncates and separates the high-pressure rocks in the footwall ("Lower Unit") against the "Upper Unit" (Melidonis, 1980; Patzak et al., 1994; Katzir et al., 1996). This structure has been interpreted to be part of the North Cycladic Detachment System (Jolivet et al., 2010; 2012), a series of low-angle normal faults and shear zones interpreted to be a result of Miocene extension of the central Aegean. However, this shear zone is folded around Tinos island (Fig. 2.3) and cross-cut by a 14.6 Ma I-type granite (Brichau et al., 2007), various ca. 15 Ma andesite-latite

dykes, and ca. 14–13 Ma leucogranite sills (Avigad and Garfunkel, 1989; Katzir et al., 1996, 2002, 2007; Ring et al., 2004; Jolivet et al., 2010). These relationships indicate that the shear zone was active prior to 14.6 Ma. The "Upper Unit" is comprised of a thrust sheet of ophiolitic material including peridotites, gabbros, low-grade schists and mafic phyllites, which are the subject of this paper. The Akrotiri Unit (Fig. 2 and 5g) crops out on the island's southern coastline near Tinos Town and exposes meta-basalts and metasedimentary rocks metamorphosed to upper amphibolite-facies conditions (Patzak et al., 1994). These rocks have been interpreted as a tectonically downthrown block of the "Upper Unit".

Previous ^{40}K–^{40}Ar and Rb–Sr ages of the "Upper Unit" spanned between 95 and 13 Ma and include 95–47 Ma ages for meta-gabbros from Mt Tsiknias, and a ^{40}K–^{40}Ar median age of ca. 72 Ma is for meta-basalts on Cape Fokos, SE Tinos (Fig. 2) (Zeffren et al., 2005). There are also ca. 70 Ma ^{40}K–^{40}Ar ages from the Akrotiri Unit, indicating a possible Late Cretaceous age of either formation, metamorphism or emplacement of meta-basalts and gabbros within the "Upper Unit". This contrasts with the Eocene aged high-pressure metamorphic rocks in the "Lower Unit", dated indirectly by correlative rocks on other islands at 52–45 Ma by U–Pb zircon (Tomaschek et al., 2003) and Lu–Hf in garnet (Lagos et al., 2007; Dragovic et al., 2012, 2015). However, due to the inherent problems of determining what part of the rock's complex history is actually being dated with the ^{40}K–^{40}Ar and Rb–Sr methods, open system behaviour and their large associated uncertainties, in what follows we present absolute U–Pb zircon and Lu–Hf ages for the timing of formation and emplacement of the Tsiknias Ophiolite within the "Upper Unit".

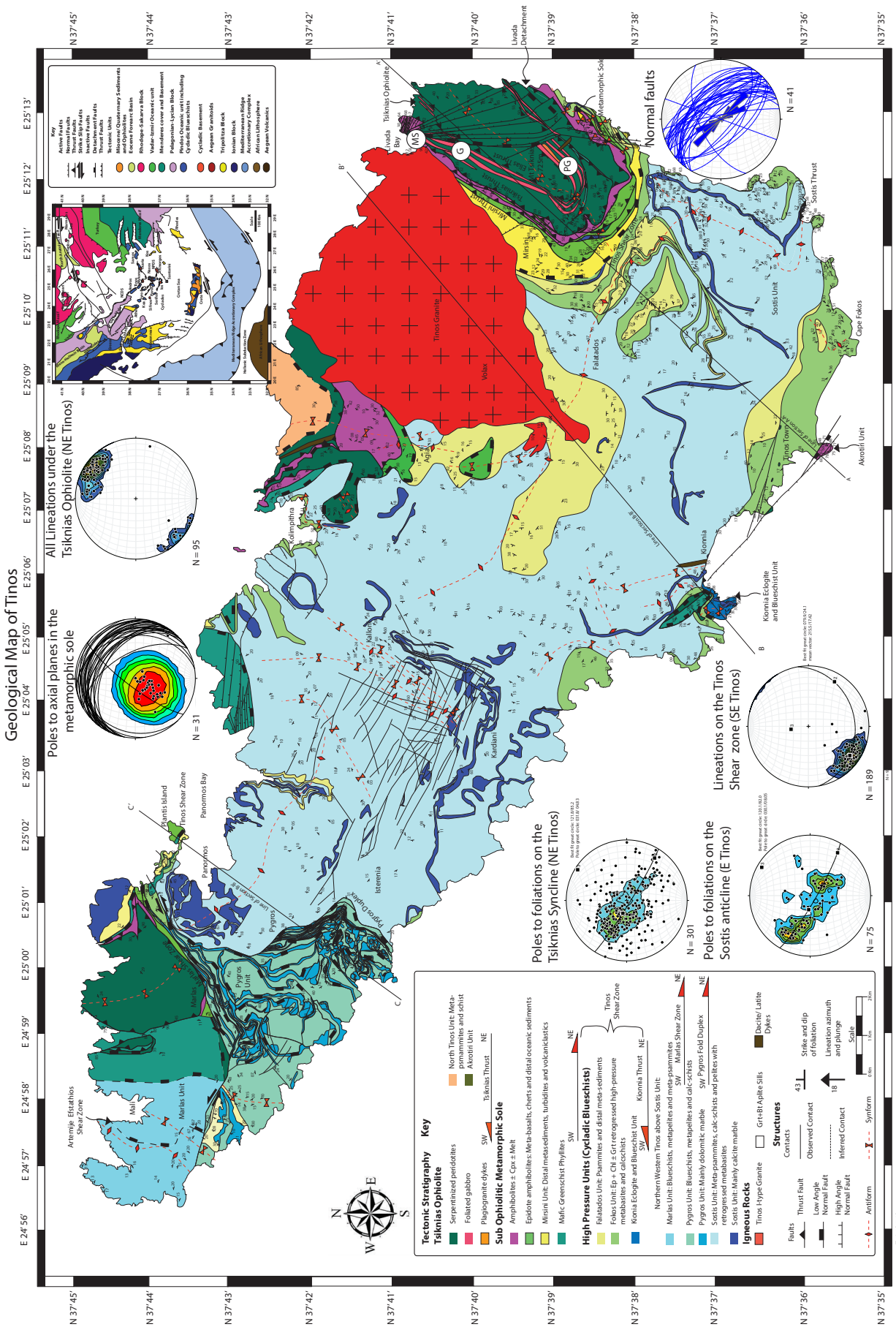

Geological Map of Tinos
Poles to axial planes in the metamorphic sole
N = 31
All Lineations under the Tsiknias Ophiolite (NE Tinos)
N = 95
Poles to foliations on the Tsiknias Syncline (NE Tinos)
N = 301
Poles to foliations on the Sostis anticline (E Tinos)
N = 75
Lineations on the Tinos Shear zone (SE Tinos)
N = 189
Normal faults
N = 41
Tectonic Stratigraphy Key
Tsiknias Ophiolite
Serpentinized peridotites
Foliated gabbro
Plagiogranite dykes
Sub Ophiolitic Metamorphic Sole
Amphibolites ± Cpx ± Melt
Epidote amphibolites: Meta-basalts, cherts and distal oceanic sediments
Mirsini Unit: Distal metasediments, turbidites and volcaniclastics
Mafic Greenschist Phyllites
High Pressure Units (Cycladic Blueschists)
Faladados Unit: Psammites and distal meta-sediments
Folos Unit: Ep + Chl ± Grt retrogressed high-pressure metabasites and calcschists
Kionia Eclogite and Blueschist Unit
Northern Western Tinos above Sostis Unit:
Marlas Unit: Blueschists, metapelites and meta-psammites
Pygros Unit: Blueschists, metapelites and meta-psammites
Pygros Unit: Mainly dolomitic marble
Sostis Unit: Meta-psammites, calc-schists and pelites with retrogressed metabasites
Sostis Unit: Mainly calcite marble
Igneous Rocks
Tinos I-type Granite
Grt+Bt Aplite Sills
Dacite/ Latite Dykes
Structures
Contacts
Observed Contact
Inferred Contact
Faults
Thrust Fault
Low Angle Normal Fault
High Angle Normal Fault
Antiform
Synform
Strike and dip of foliation
Lineation azimuth and plunge
Scale
Tsiknias Ophiolite
North Tinos Unit: Meta-psammites and schist
Akrotiri Unit
Tsiknias Thrust
Tinos Shear Zone
Kionia Thrust
Marlas Shear Zone
Pygros Fold Duplex
Tinos Granite
Volax
Livada Detachment
Livada Bay
Tsiknias Ophiolite
Metamorphic Sole
Sostis Thrust
Sostis Unit
Cape Fokos
Akrotiri Unit
Kionia Eclogite and Blueschist Unit
Panormos Bay
Panormos
Pantis Island
Isterenia
Kolimpithra
Kardiani
Agapi
Marsini
Falatados
Tinos Town
Artemis Efstathios Shear Zone
Marlas Unit
Mali
Pygros Unit
Pygros Dyke
Tinos Shear Zone
Panormos Shear Zone
Livada Detachment
Tsiknias Thrust
Kionia Thrust
Marlas Shear Zone
Pygros Fold Duplex
Sostis Thrust
Sostis Unit
Akrotiri Unit
Kionia Eclogite and Blueschist Unit
Tinos Granite
Volax
Faladados
Tinos Town
Cape Fokos
Kolimpithra
Kardiani
Agapi
Marsini
Isterenia
Pygros Dyke
Panormos Bay
Pantis Island
Panormos
Marlas Unit
Mali
Artemis Efstathios Shear Zone

Figure 2.2: New geological map of Tinos with accompanying cross-sections. The location of Plagiogranite, Gabbro and Amphibolite tonalitic melt sweat samples are labelled, with major thrusts, normal faults and fold axes. Inset shows a regional tectonic map of the Aegean showing with major units and structures Stereonets of structural data from various parts of Tinos "Upper Unit". NE plunging lineations in the sole of the Tsiknias Ophiolite, poles to fold axial planes in SW verging isoclinal folds in the metamorphic sole and Mirsini Unit in NE Tinos. Normal fault planes of normal faults in the "Upper Unit" commonly striking around 330/60 indicating ENE/WSW extension in present day coordinates. Km-scale upright open folds affecting both the "Lower Unit" and the "Upper Unit" with fold axial planes striking NE–SW indicating a component of E–W shortening e.g. Mt Tsinkias in NE Tinos represents an upright gently NE plunging synform. For cross sections A–A', B–B' and C–C' consult Fig. 2.3

2.3 Field Relations of the Tsiknias Ophiolite

New structural mapping of Tinos island was carried out at a 1:10,000 scale between 2015 and 2018. A new geological map of the entire island is presented in Fig. 2.2, with accompanying cross-sections in Fig. 2.3 and panoramic photographs in Fig. 2.4, an annotated tectono-stratigraphic column in Fig. 2.5, annotated outcrop photographs in Figs. 2.6-2.9, outcrop and photomicrographs of a large plagiogranite in Fig. 2.10 and thin section photomicrographs from the "Upper Unit" in Fig. 2.11. Ultramafic and gabbroic rocks crop out as part of the "Upper Unit" on Tinos (Avigad and Garfunkel, 1989, 1991; Katzir et al., 1996), and represent an incomplete ophiolite sequence, herein referred to as the Tsiknias Ophiolite, named after Mt Tsiknias, the highest mountain on Tinos.

The Tsinkias Ophiolite can be found at six exposures across Tinos, but the most complete is preserved as a klippe on Mt Tsiknias, NE of Kolimpritha Bay and NE of Marlas village (Fig. 2.2). There are no outcrops of upper crustal lithologies such as dykes and basalts in the ophiolite section and it is unknown whether they were originally there during ophiolite genesis. The ophiolite is structurally repeated by out-of-sequence thrusts and highly attenuated by late extensional normal faults. A newly discovered metamorphic sole is exposed along the base of the Mt Tsiknias section, and records the subduction-obduction history. The ophiolite and sole have been folded by gentle open upright folds with NNE trending axes after obduction and

metamorphism (see Fig. 2.2 stereonets). The "Upper Unit" and Tinos Shear Zone has been domed about a NW–SE axis that defines the island's elongate dome. Below, we give a systematic description of the ophiolite structure and key tectono-stratigraphic units from structurally high to low.

2.3.1 Mantle and Gabbro - Moho Transition Zone:

Massive serpentinites form the prominent slopes of Mt Tsiknias, NE of Kolimpratha Bay and the mountain to the NE of Marlas in NW Tinos (Fig. 2.2). There are two distinct horizons of serpentinized peridotites, both representing the mantle sequence of the Tsiknias Ophiolite. The first horizon occurs at the base of the ophiolite, directly above the metamorphic sole (see below and Fig. 2.7b-c and Fig. 2.7a), and shows extreme deformation directly above the basal sheared contact (The Tsiknias Thrust), similar to the banded ultramafic unit of the Semail Ophiolite (Searle and Cox, 2002). The degree of mylonitization decreases structurally up-section, where primary harzburgite and dunite precursors can be found (Fig. 2.2). Along the base of the ophiolite, particularly at Livada Bay, some localized channels of serpentinized dunites display transformation of primary olivine and minor pyroxene to antigorite, talc and asbestos group minerals (see Fig. 2.10a). These rocks are interpretted to represent a depleted mantle sequence underlying oceanic crust. We estimate there is approximate 100–400 m structural thickness of serpentinized mantle exposed today at the base of the ophiolite, beneath the first appearance of gabbro. The exposed upper levels of Mt Tsiknias, that overlay the serpentinites, represent a cross-section through the Moho Transition Zone and cumulate gabbro sequence, similar to the Moho Transition Zone of the Semail Ophiolite (Searle et al., 2015). The Moho Transition Zone is defined by a ca. 150 m thick section of alternating meter scale zones of foliated and tectonized hornblende-rich gabbros (Figs. 2.5b and 2.8) marked by the appearance of white saussurite (microcrystalline plagioclase + epidote) and almost completely serpentinized harzburgites, wehrlites, and pyroxenites (Fig. 2.11a-b). A large plagiogranite sill intrudes this sequence (see Fig. 2.10), is aligned with the gabbros and has a strong internal fabric.

Gabbro horizons vary from a few to over 50 meters in thickness, and are semi continuous bodies, with both leucocratic and mafic varieties, and locally display high-temperature magmatic-mylonitic fabrics (S_1), with top-to-NE kinematics, indicating they intruded during shearing. Another horizon of almost completely serpentinized wehrlites and harzburgites, representing depleted mantle, overlay the Moho Transition Zone gabbros possibly due to a major out-of-sequence thrust (Elias Thrust, dashed line Fig. 2.2), that structurally repeats the ophiolite sequence. This thrust must have been associated with the late stages of the ophiolite emplacement process. Similar out-of-sequence thrusts structurally repeat the metamorphic sole at Livada Bay (Fig. 2.4). On the west of Mt Tsiknias, close to the Tinos granite body, many of the primary assemblages have been recrystallized with hornfels textures due to contact metamorphism associated with the intrusion, (see Fig. 2.11c; actinolite rims on hornblende) Miocene imbricate normal faulting further disrupts the sequence, creating uplifted and domino rotated fault-blocks bounded by brittle faults rooting into the underlying Livada Detachment that cross-cuts the ophiolite (Fig. 2.5a). This has produced top-to-NE mylonite S–C fabrics throughout gabbro horizons within the ophiolite.

2.3.2 Plagiogranites:

A 50 m thick and 300 m long plagiogranite sill (Fig. 2.10) intrudes the Moho Transition Zone on the eastern flank of Mt Tsiknias (N37.580458, E25.231727) and has intrusive contacts clearly demonstrating that it was emplaced shortly after the host gabbros had crystallized. The plagiogranite is highly sausseritised and contains both large euhedral epidotes, that point to a magmatic origin, and secondary epidote that forms along its surfaces and fractures (see Fig. 2.10c). It displays irregular contacts and a black-wall reaction to chlorite and epidote, suggesting that it was emplaced late in the crystallization history and has subsequently experienced alteration. Plagiogranite is used to describe leucocratic rocks containing mainly quartz, plagioclase and rarely ferromagnesian minerals (e.g. Coleman and Peterman 1975; Coleman and Donato 1979). The formation of oceanic plagiogranite has been attributed primarily to either: 1. Late

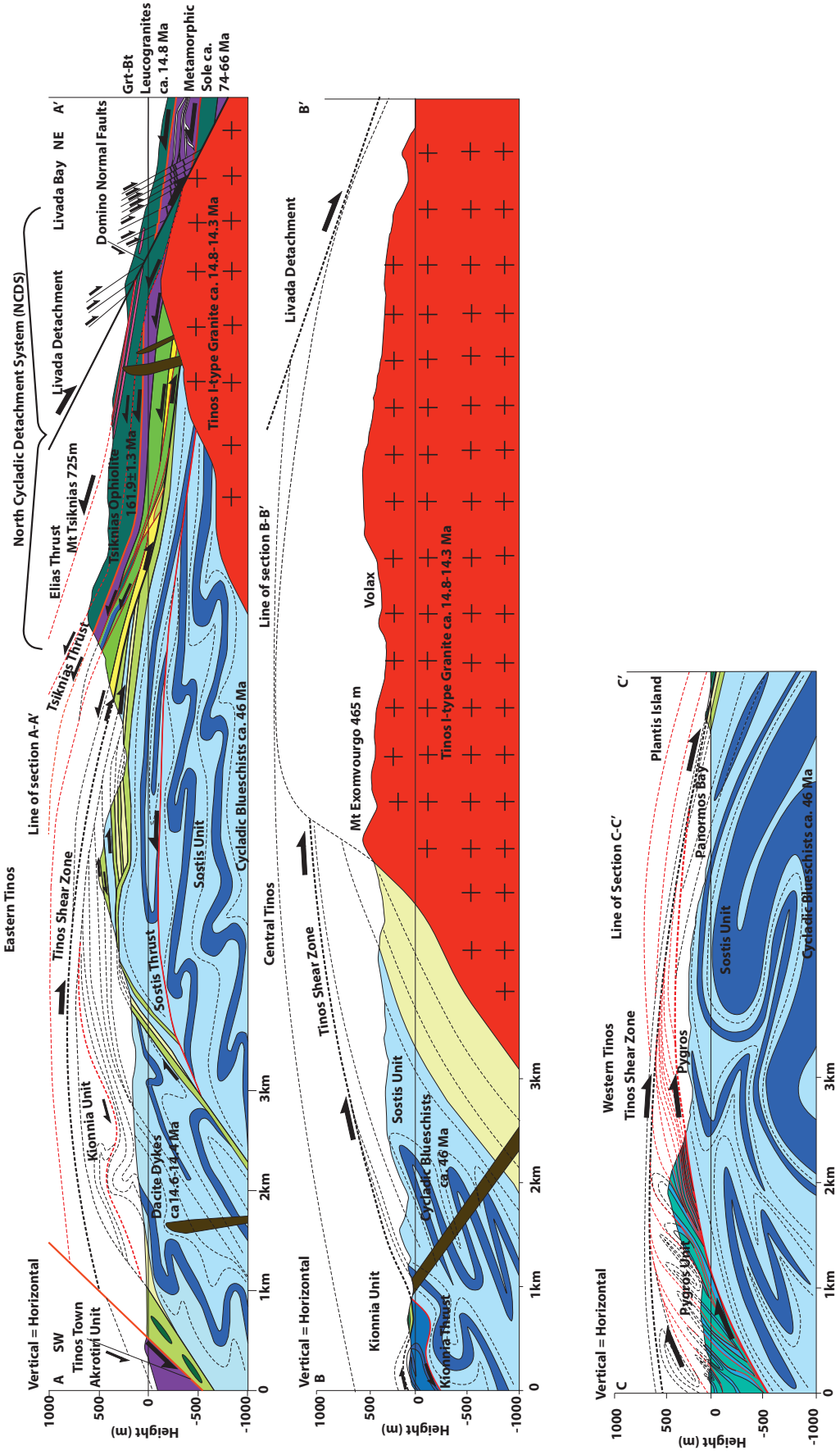


Figure 2.3: Cross sections through Tinos along the line of sections A–A', B–B', C–C'. For locations consult the geological map in Fig. 2.2

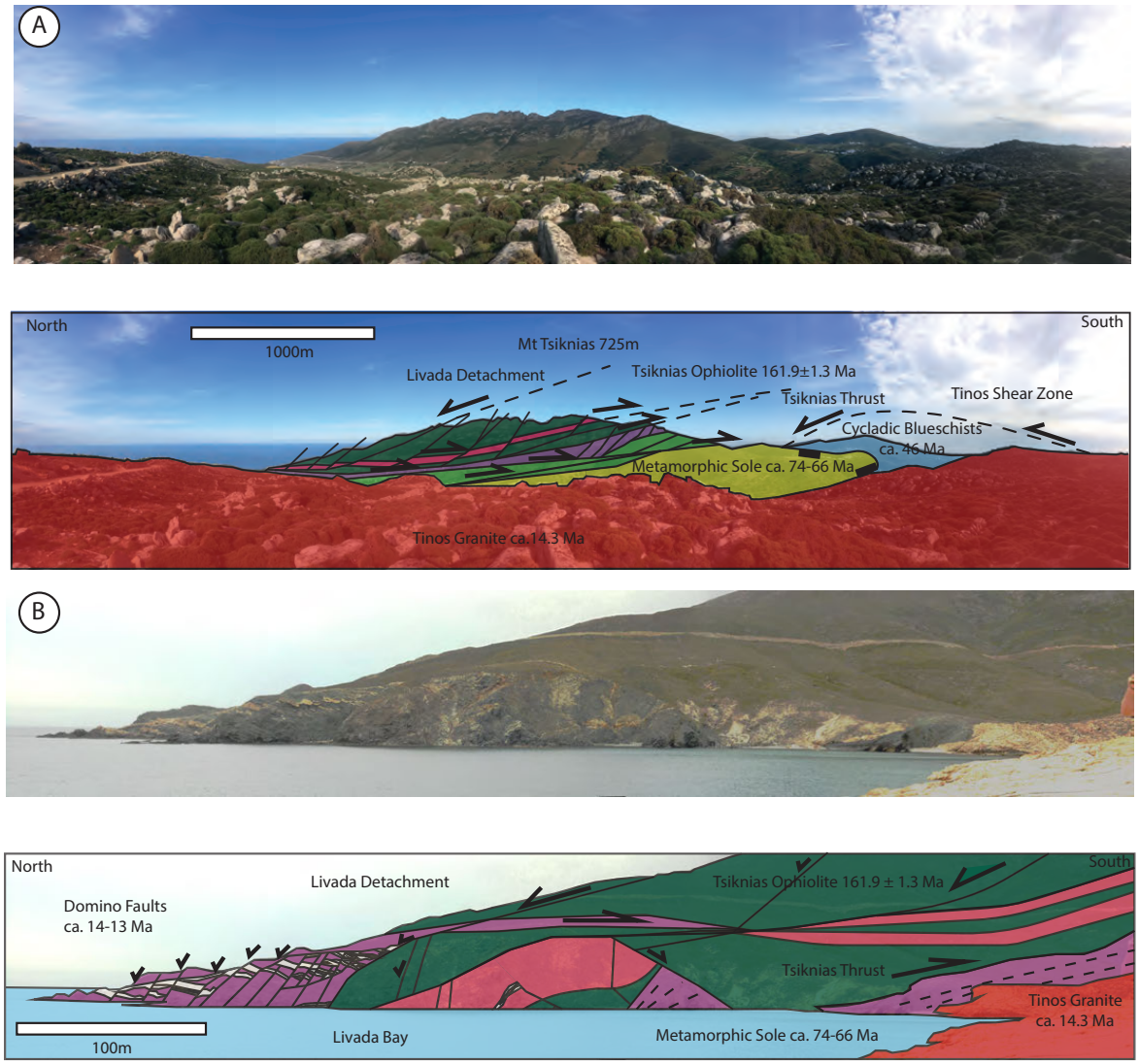


Figure 2.4: Panoramic photographs of the Tsiknias Ophiolite, metamorphic sole and Livada Detachments. A) Panoramic view of the Tsiknias Ophiolite and underlying sole illustrating its klippen structure on the Mt Tskinias ridge, with several imbricates structurally repeating and thickening the sole (taken from N37.595986, E25.206158). B) Panorama of Livada Bay showing the metamorphic Sole, structural repetition and out of sequence thrusting and I-type granite intrusion (taken from N37.611794, E25.236271)

stage differentiation of low-K tholeiitic MORB magmas (Coleman and Peterman 1975; Coleman and Donato 1979; Pallister and Knight 1981; Floyd et al. 2000), 2. Hydrous partial melting of gabbro or similar melts in a MOR setting (Gerlach et al. 1981; Spulber and Rutherford 1983; Floyd et al. 2000), or 3. Liquid immiscibility in an evolved MORB liquid (Phillpotts 1976; Dixon and Rutherford 1979; Floyd et al. 2000). In the subsequent discussion the viability of the first two processes are assessed in explaining

the major element and rare earth element (REE) data of plagiogranites.

2.3.3 The Tsiknias Thrust

At the base of the Tsiknias Ophiolite (Figs. 2.2-2.6), a major shear zone juxtaposes banded and mylonitised serpentinites and peridotites in the hanging-wall against dark and locally partially melted amphibolites in the footwall (see Figs. 2.5c and 2.7a, c, d 2.8). These structural relationships have been previously described by Katzir et al., (1996) and are best exposed in Livada Bay (N37.609704, E25.238715), near an intrusive contact between the Tinos I-Type granite and amphibolites (Fig. 2.8f). The structures we identified at this locality, however, seem to contradict previous geological explanations of this horizon, which propose that the contact represents part of the Livada Detachament, a low-angle normal fault forming part of the North Cycladic Detachment System (See Fig. 2.7) (Jolivet et al., 2010), and that metamorphism was due to intrusion of the adjacent I-type granite. However, several lines of evidence suggest that the structure actually represents the basal thrust of an intact ophiolite sequence (The Tsikinas Thrust). We note that towards the contact, the degree of mylonitization within the amphibolites drastically increases, consistently displaying top-to-SW kinematics, the opposite to the NCDS (see Figs. 2.5 and 2.6). The degree of isoclinal folding also increases and is associated with a SW-vergence. Finally, and most importantly, there is an inverted metamorphic gradient towards the contact (see metamorphic sole section), characteristic of placing hotter rocks above colder rocks. These features suggest this structure represents a SW-verging thrust that was responsible for emplacing the Tsinkias Ophiolite onto the amphibolite sole rocks. This thrust dips to the NE and preserves the Tsiknias Ophiolite as a klippe along the entire mountainside of Mt Tsiknias (Figs. 2.2-2.4).

2.3.4 Metamorphic Sole

A 300 m thick series of high-grade foliated meta-basalts crop out underlying the base of the Tsiknias Ophiolite (Figs. 2.4, 2.6-2.8), that are juxtaposed against highly ser-

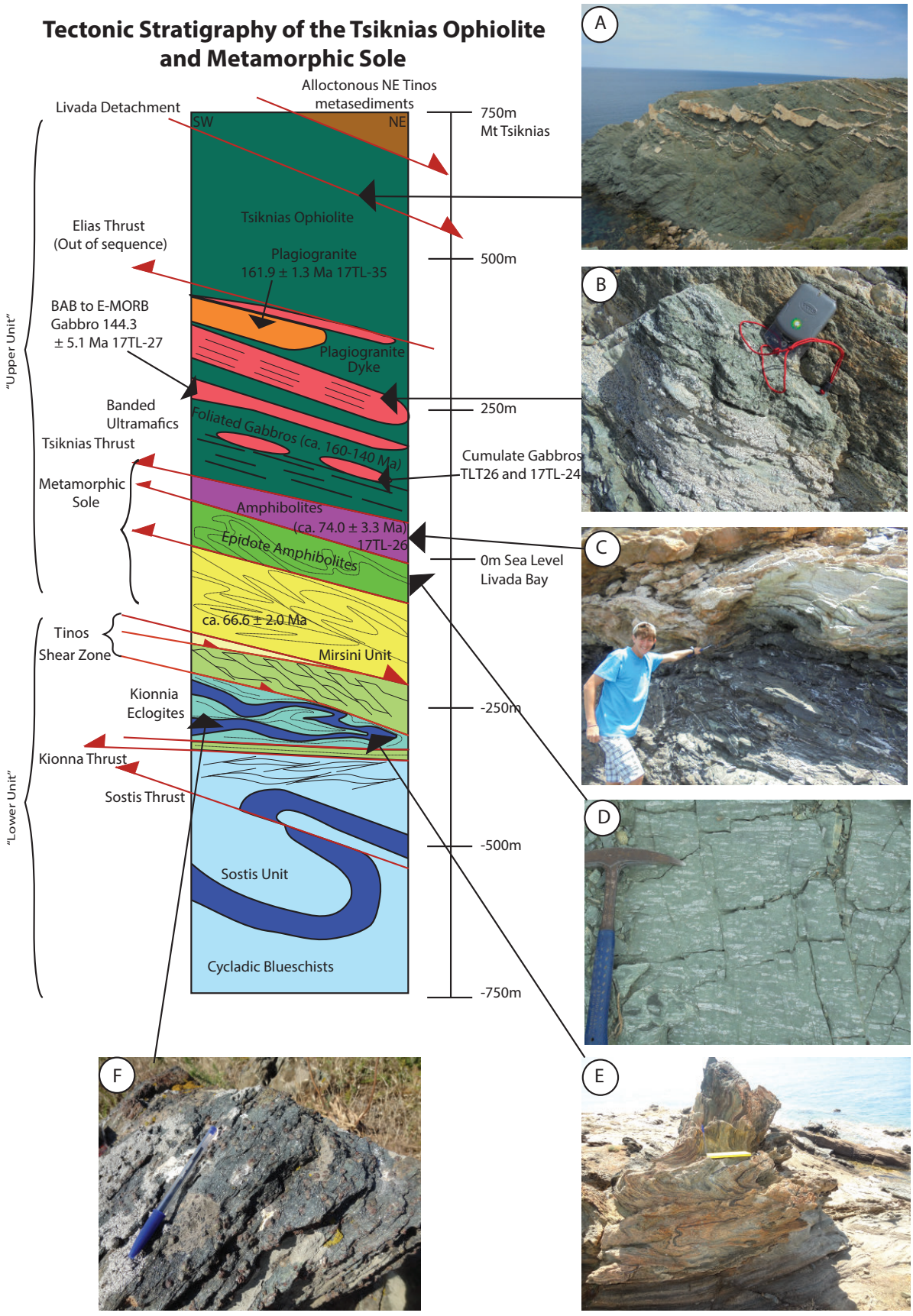


Figure 2.5: Continues on next page

Figure 2.5: Annotated stratigraphic section through the Tsiknias Ophiolite and metamorphic sole, with outcrop photographs. A) Domino style normal faults through the metamorphic sole at Livada Bay (N37.612559, E25.242034). Granite sills emanate from the I-type granite and are pre-tectonic, although in places some degree of plasticity minor rotation into the fault planes can be seen. B) Foliated hornblende rich gabbro bounded by serpentinized peridotites within the Moho-Transition Zone (N37.581116, E25.221087). C) The Tsinkias Thrust at Livada Bay with the author for scale (N37.609901, E25.238966). Dark amphibolites below with white leuco-diorite melt sweats emanating from the contact, and pale completely serpentinzed and sheared ultra-mafics above. D) Mylonitized amphibolite from the metamorphic sole with an exceptionally strong top-to-SW fabric and lineation defined by elongated plagioclase porphyroblasts indicating flattening strains of 4:1, taken at (N37.609616, E25.238603) in Livada Bay. E) Isoclinally folded eclogite-facies metasediments within the Kionnia Nappe of the Cycladic Blueschist Unit (Lamont et al., in prep) in the footwall of the Tinos shear zone (taken at N37.547897, E25.125450). F) Mafic eclogite within the Kionnia Nappe of the Cycladic Blueschist Unit, associated with attempted subduction down a NE dipping subduction zone (Lamont et al., in prep) in the footwall of the Tinos shear zone (taken at N37.550536, E25.124504).

pentinized foliated and sheared peridotites by a sharp contact (Tsiknias Thrust). An extremely condensed and inverted apparent metamorphic field gradient is also recorded across this zone with a drastic decrease in metamorphic grade from the ophiolite contact. Deformation within the sole is intense and characterized by a strong (S_{2b}) top-to-SW mylonite fabric with NE–SW trending lineation defined by hornblende and plagioclase porphyroclasts, a series of SW-verging recumbent isoclinal folds, and thrusts with top-to-SW shear fabrics on a range of scales. S_{2a} is locally preserved in lower strain domains and represents a spaced crenulation cleavage, particularly within some amphibole-rich domains. Within the uppermost five meters of the sole, directly below the contact with the ophiolite (Tsiknias Thrust), there are high temperature assemblages, including clinopyroxene and hornblende bearing amphibolites. Evidence for local anatexis is marked by the development of leucosomes and partial melt sweats emanating from the Tsiknias Thrust and the uppermost few meters of the amphibolites and are either aligned with or cross-cutting the mylonite fabrics, suggesting melting occurred during or after ductile shearing. Leucosomes have leuco-diorite compositions with dominantly plagioclase and hornblende with <3% quartz.

The metamorphic field gradient drastically decreases over less than 100 m to epidote-amphibolites and eventually to lower amphibolite to greenschist-facies my-

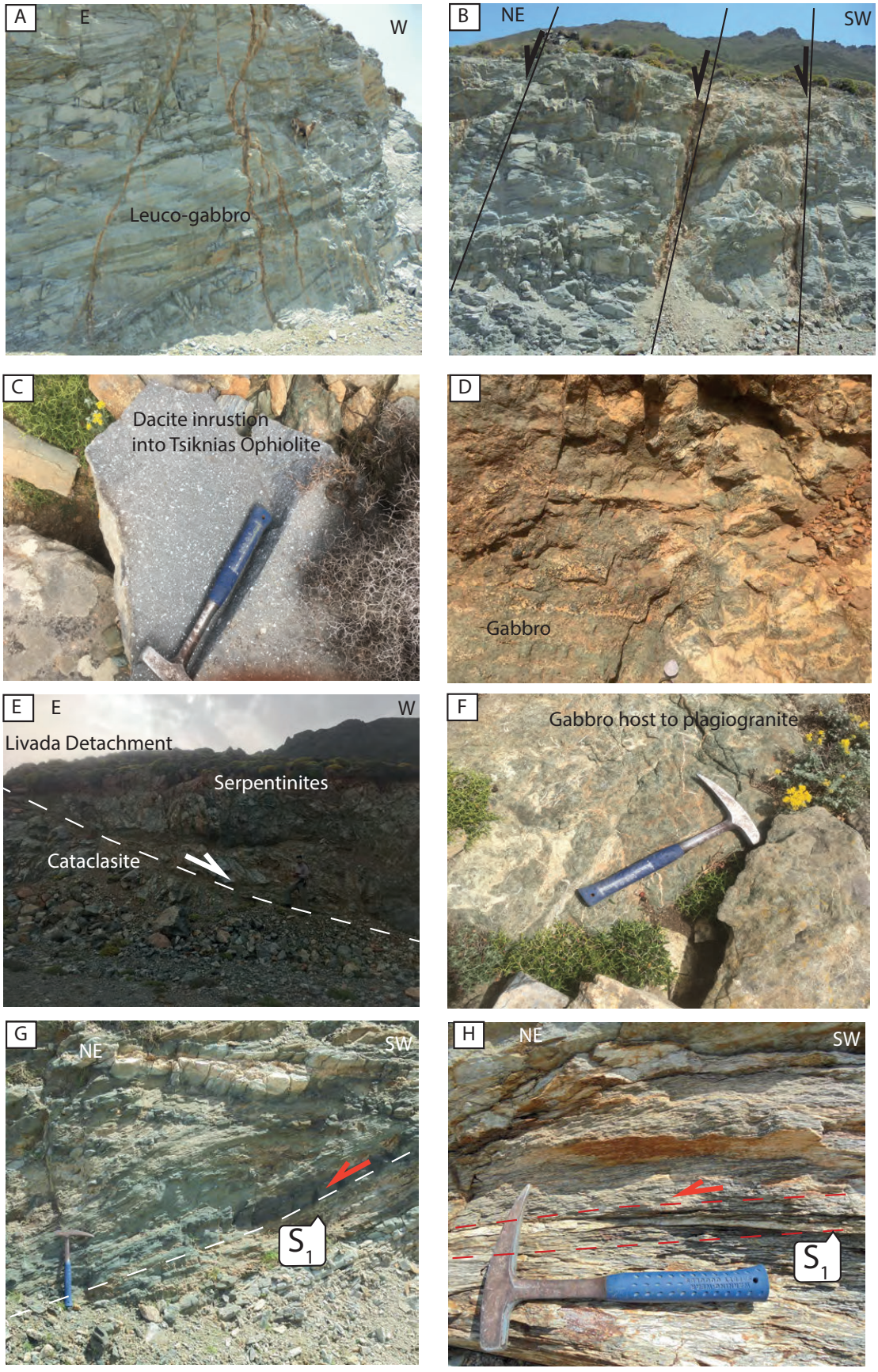


Figure 2.6: Continues on next page

Figure 2.6: Outcrop photographs of gabbros and deformation within the Tsiknias Ophiolite. A) Layered leuco-gabbros near the base of the ophiolite near Livada Bay. B) Normal faults cross-cutting leuco-gabbros. C) A Latite dyke intrusion into the Tsiknias ophiolite most likely associated with the I-type magmatism. D) Gabbros with some in-situ melt, leaving a cumulate residue. E) Possible outcrop of the Livada Detachment which cuts the eastern flank of Mt Tsiknias, associated with 3 m thick cataclasite zone. F) Gabbro from the Moho-transition zone, this is one of the host rocks to the large plagiogranite sill, with in-situ melt leaving a cumulate residue and tonalitic melt composition. G and H) Mylonitized gabbros associated with top-to-NE shear senses possibly representing the Livada Detachment on the western flank of Mt Tsiknias.

lonites (Figs. 2.5-2.10), which consists of: actinolite + albite + epidote + sphene ± chlorite ± hornblende ± clinopyroxene ± rodingitized garnet (e.g. Fig. 2.6e and 2.10h). A lithological zonation is also preserved within the sole, grading from meta-basalts and gabbros which form the uppermost and highest temperature lithologies, down to upper greenschist-facies distal oceanic meta-sediments and cherts with mm-sized Mn rich layers (S_0), that are characterized by tiny spessartine-rich garnet (e.g. Fig. 2.11j-l). This inverse structural sequence suggests the sole has been imbricated and thickened. On the western side of Mt Tsiknias, both the Tinos I-type granite and leucogranite sills intrude into the sole. This has highly altered the primary obduction (S_1 and S_2) microstructures and mineral assemblages and overprinted them with hornfels textures (S_3) including rims of actinolite and diopside on cores of higher temperature brown hornblende (see Fig. 2.11c).

2.3.5 Mirsini Unit

The Mirsini Unit represents the lowermost part of the metamorphic sole below the distinctive high-temperature amphibolites. The unit is exposed along the base of Mt Tsiknias (Figs. 2.4-2.6) representing a structural thickness of up-to 500 m. The unit is dominantly comprised of distal oceanic meta-sediments, interlayered with meta-volcanics, recrystallized quartzites and cherts, which have been metamorphosed to lower amphibolite facies, with no evidence for earlier high-grade conditions. Towards the base of this unit, metamorphosed turbidites suggest the lowermost levels of the Mirsini Unit formed on the distal continental slope. Deformation is highly penetrative

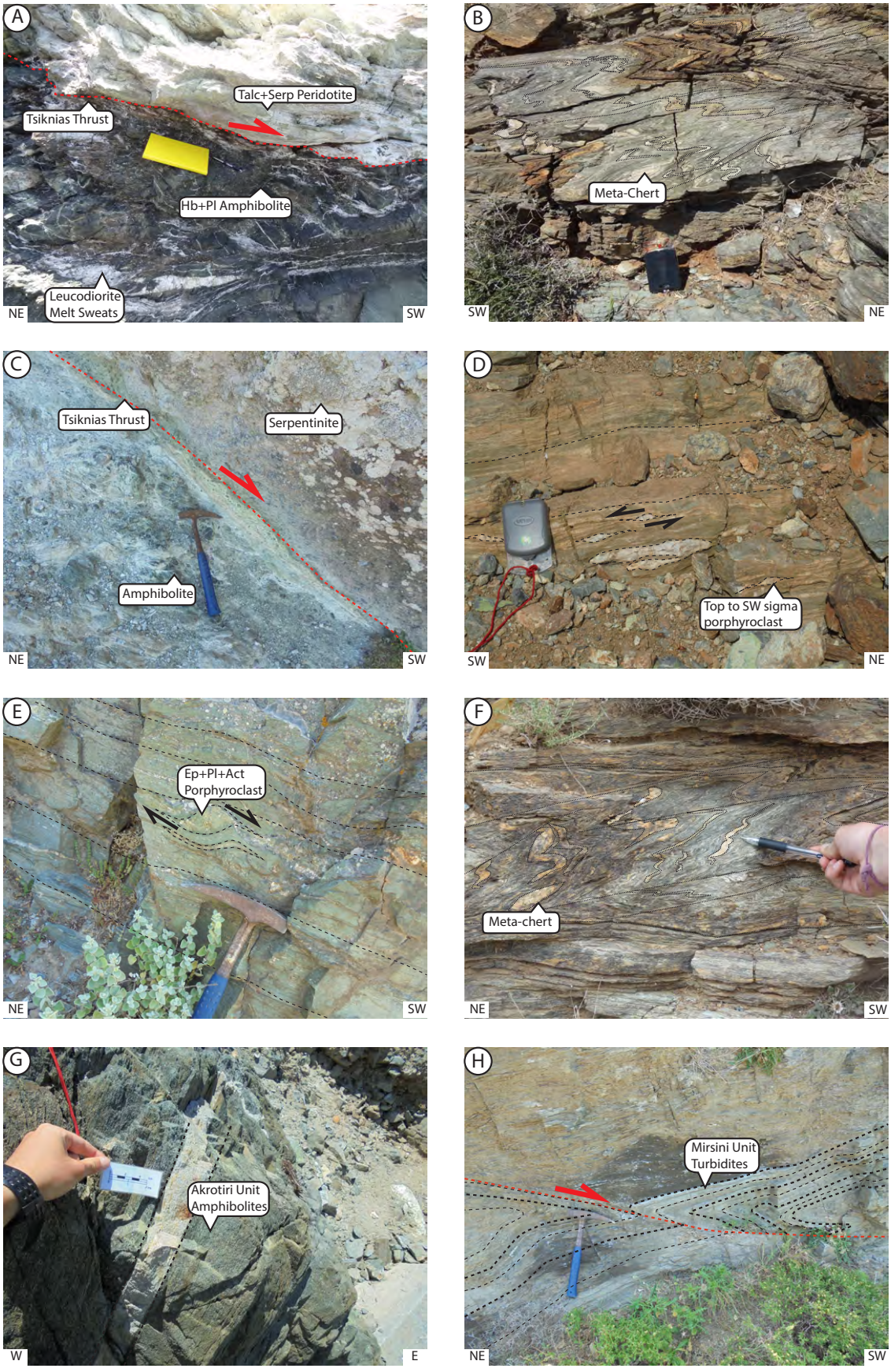


Figure 2.7: Continues on next page

Figure 2.7: Annotated outcrop photographs of the metamorphic sole and Mirsini Unit, showing the range in lithology and deformation in these units. A) The Tsiknias Thrust at Livada Bay (N37.609901, E25.238966), placing talc and serpentinized peridotites over anatectic clinopyroxene bearing amphibolites in the metamorphic sole. The extent of partial melting reaches up-to 20% of the rock volume within these upper five meters of the sole, with leuco-dioritic melt emanating from the thrusted contact. B) Meta-cherts and meta-basalts of the metamorphic sole (N37.573234, E25.237498), showing extreme deformation and intense isoclinal folding and ductile thrusting. C) The Tsinkias Thrust with a 5 cm thick cataclasite zone, indicative of intense localized ductile and brittle deformation (N37.582611, E25.216552). Completely serpentinized peridoties of the ophiolite adjacent to amphibolite mylonites with a heavy brittle overprint, suggesting the thrust has a long deformation history. D) High-temperature mylonitized amphibolites that have meta-gabbroic protoliths from east of Mt Tsiknias (N37.572140, E25.231410), with plagioclase porphyroclasts indicative of top-to-SW shearing. E) Epidote amphibolites with cm-scale porphyroclasts of epidote, plagioclase and actinolite, that possibly pseudomorph an earlier porphyroblast (N37.587169, E25.225783). The retrograde assemblage shows top-to-SW shearing, indicating syn-tectonic deformation during epidote-amphibolite to greenschist-facies conditions. F) Intensely deformed meta-chert and pelagic meta-sediments within the Mirsini Unit, with mylonitization overprinted by clear brittle-ductile thrusts with cm-scale offsets indicative of top-to-SW movement (N37.629003, E25.161868). G) Amphibolites with intercalated met-sediments with a strong steeply dipping foliation, with flattening strains of 10:1, from near Tinos Town (N37.529464, E25.163928). H) Recumbently folded and extremely deformed meta-turbidites and distal oceanic meta-sediments and meta-volcanics of the Mirsini Unit directly under the metamorphic sole. These rocks contain amphibole and garnet indicating upper-greenschist facies conditions with brittle-ductile thrusting overprinting blast-mylonite fabrics (N37.587198, E25.209995).

throughout this unit, with evidence for ductile thrusting and folding over a range of scales. This is interpreted to be related to the obduction of the overlying ophiolite (Figs. 2.4-2.6). At the top of the Mirsini Unit, the Sole Thrust is associated with top-to-SW kinematics and is interpreted to be responsible for overthrusting greenschists and amphibolite-facies meta-basalts and gabbros of the high-temperature sole during obduction. Contrastingly, along the base,the Mirsini Unit grades into greenschist-facies mylonites associated with top-to-NE kinematics of the Tinos Shear Zone, that separates the Mirsini Unit, metamorphic sole and Tsiknias Ophiolite ("Upper Unit") from the underlying Cycladic Blueschists (Lower Unit).

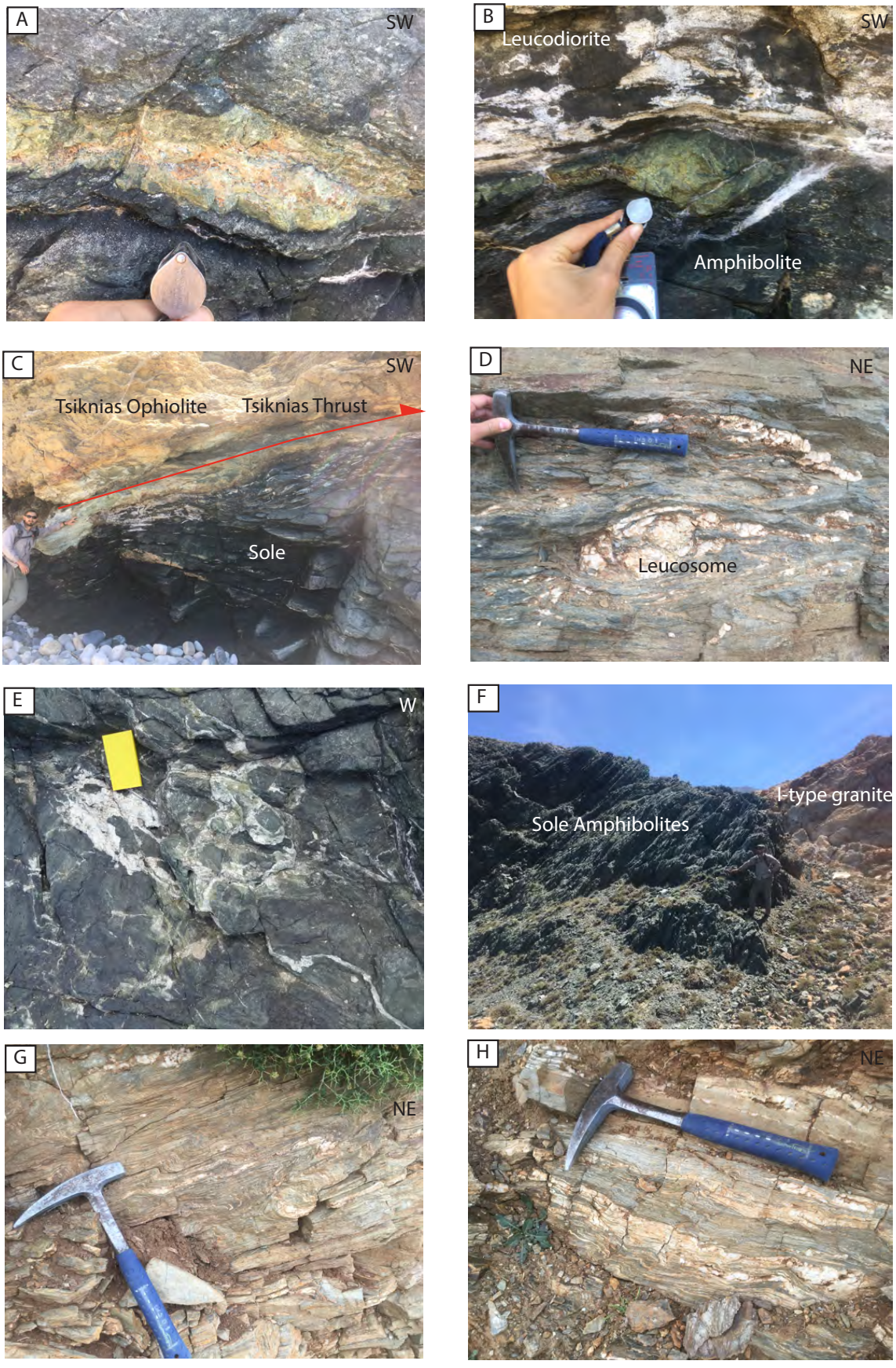


Figure 2.8: Continues on next page

Figure 2.8: Outcrop photographs of the amphibolite sole directly under the Tsiknias Thrust and the Tsiknias Ophiolite. A) Enclave of epidote + rhodingite within amphibolite. B) Leucosomes and epidote rich enclave possibly retrogressed pyroxene rich domain, the leucosomes make up 40% of the rock directly beneath (<30cm) from the Tsiknias Thrust. C) The Tsiknias Thrust and underlying high-grade metamorphic sole with leucosomes emanating from the contact at Livada Bay. D) Boudinaged and folded leucosome in amphibolite from the eastern side of Mt Tsiknias. E) Ponding of partial melt in a dilatant strain site within the amphibolite. F) Intrusive contact of the I-type granite and sole amphibolites at Livada Bay, note the truncation of the steep foliation in the amphibolites which pre-dates the flat lying foliation on the Tinos Shear Zone. G and H) small scale crenulations and isoclinal folds in amphibolite grade metasediments on the eastern side of Mt Tsiknias.

2.3.6 Akrotiri Unit

The Akrotiri Unit, exposed to the south of Tinos Town, is marked by steeply dipping (70/85°) amphibolites and intercalated meta-sediments associated with a steeply dipping lineation of ca. 70° recording top-to-WSW fabrics (Fig. 2.6g). It has experienced strong amphibolite-facies metamorphic conditions (Patzak et al., 1994) and has previously been interpreted as an allochthonous unit. However, these rocks have many similarities with the metamorphic sole exposed in northern Tinos and lie at a similar structural level. Although there is little context for this unit with the surrounding geology, one interpretation is that it represents a downthrown slice of the metamorphic sole (Fig. 2.3). Movement on this steep shear zone must have occurred after high-pressure metamorphism of the Lower Unit as it truncates the metamorphic foliation. Meta-gabbros and serpentinite outcrop to the west of Tinos Town, structurally along strike with this unit (Fig. 2.2), possibly supporting this interpretation. Blueschists ("Lower Unit").

2.3.7 Livada Detachment

The Tsiknias Ophiolite and metamorphic sole at Livada Bay (Fig. 2.4b-2.5a), have been attenuated by extension along the Livada Detachment, a low-angle normal fault associated with top-to-NNE shear fabrics. It cross-cuts several gabbro horizons, and results in extreme grain size reduction and S–C fabrics. At Livada Bay, a series of steep, domino-style normal faults root into the Livada Detachment, which cuts and

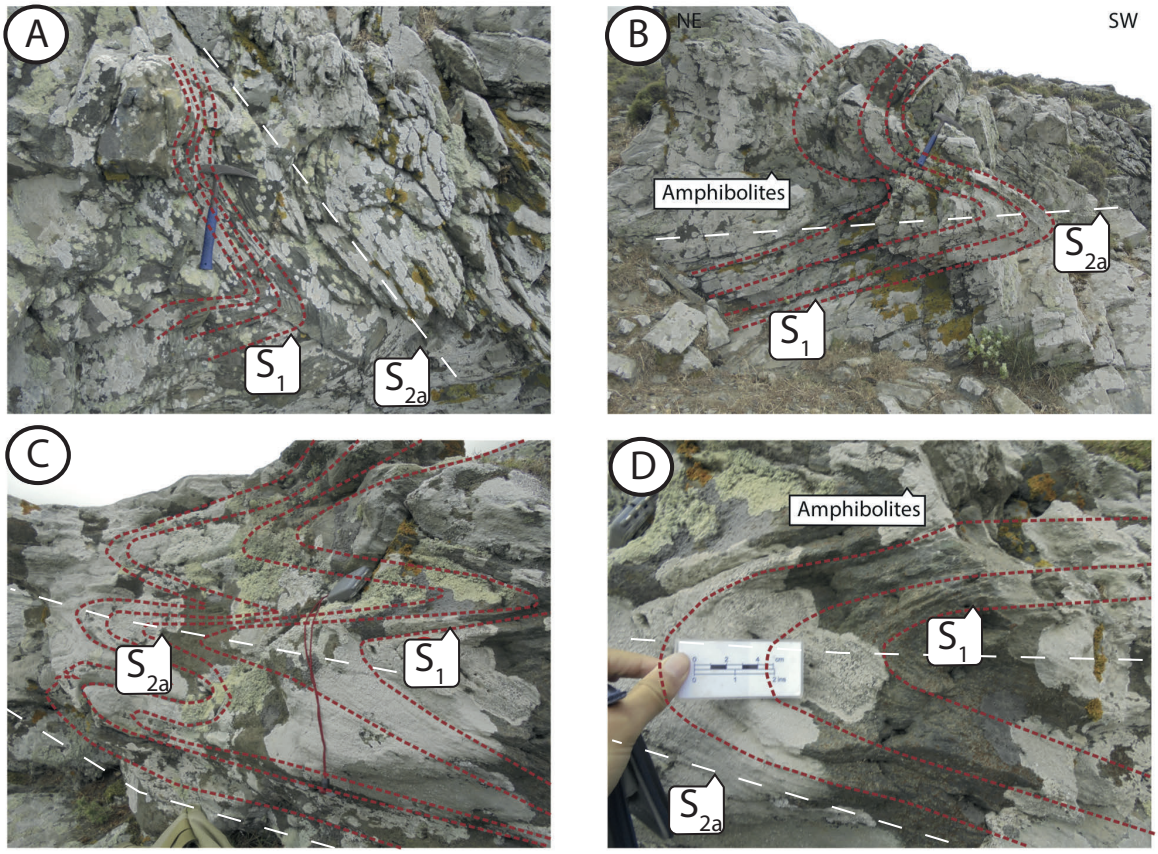


Figure 2.9: Deformation styles in the sole amphibolites showing intense isoclinal folding that verges towards the SW. The trace of the S_1 fabric is shown for clarity as the rocks are often weathered that is refolded into an S_{2a} foliation associated with obduction.

offsets the metamorphic sole and cross-cutting leucogranitic sills (Fig. 2.5a). These sills clearly pre-date many of the brittle normal faults, but in some occurrences show lobate margins and appear to propagate along the fault planes. Brittle normal faulting above the Livada Detachment must therefore be related to regional Aegean extension and immediately post-date the sill intrusion. These domino-style normal faults record the first definitive evidence for extension in the region and presumably represent the brittle-ductile transition at the time of granite intrusion (ca. 14.6 Ma) (Brichau et al., 2007)).

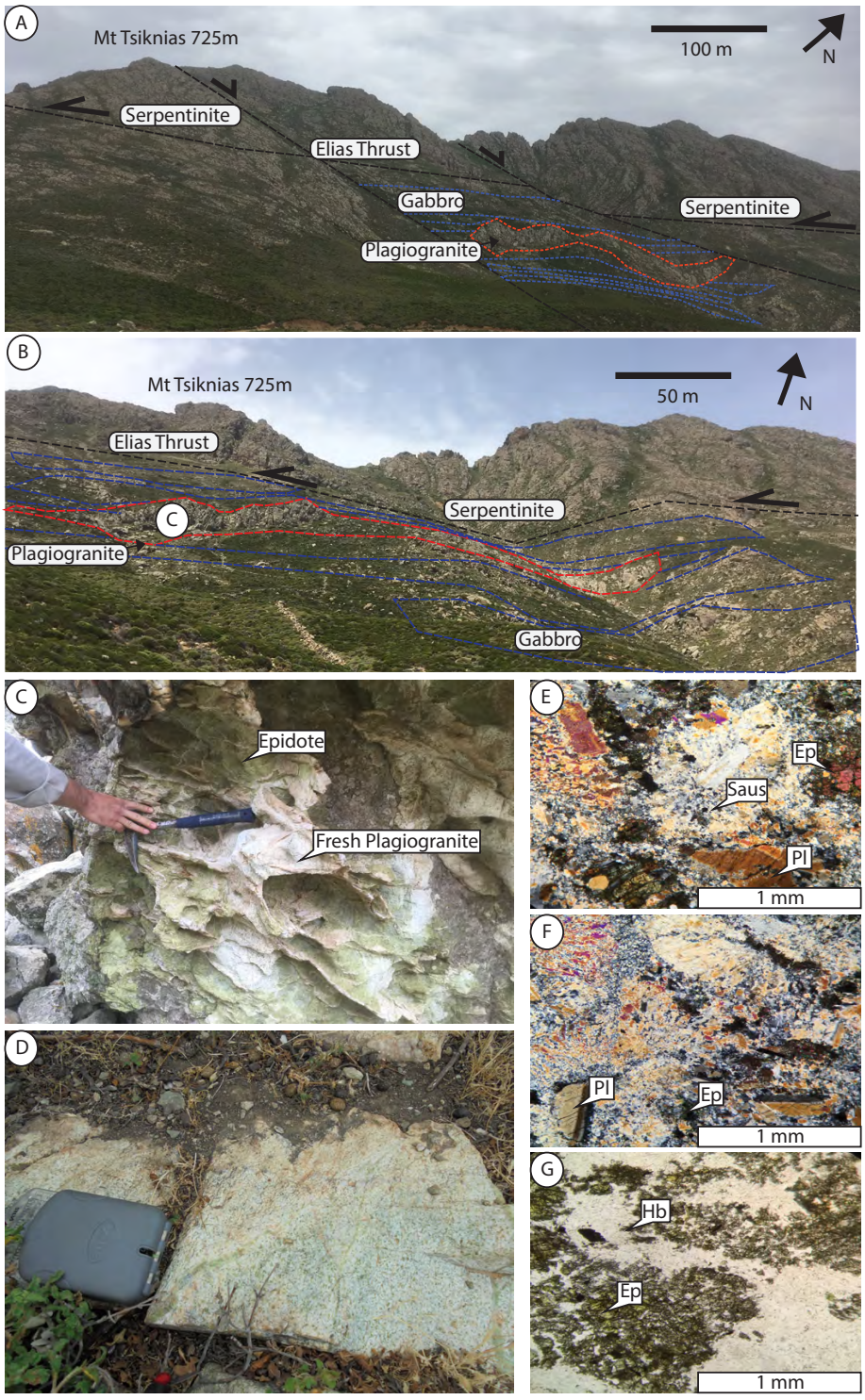


Figure 2.10: Representative photographs and photomicrographs of the plagiogranite body (N37.582399, E25.232871) intruding within the Moho Transition Zone on the eastern flank of Mt Tsiknias, it weathers proud against the surrounding highly serpentinized ultra-mafics and weathered gabbros (A and B). C) Large degrees of epidotization around the margins of the granite. Above it lies a large continuous body of ultra-mafics that have been structurally repeated due to the SW verging out of sequence thrust, the Elias Thrust (A and B). E and F) Somewhat fresh matrix of partially sausitized plagioclase graphitic groundmass with fresh phenocrysts of plagioclase with partial alignment of the phenocrysts defining a sub-horizontal magmatic fabric. Secondary epidote occurs in clusters nucleating of more sausertized zones.

2.3.8 Tinos Shear Zone

The Tinos Shear zone is a normal sense greenschist-facies structure that represents a major tectonic boundary separating the "Upper Unit" from the underlying high-pressure rocks of the Cycladic Blueschist Unit. It is associated with top-to-NE kinematics, and is domed around the island about a ENE–WSW axis. The gentle NNE dip of this structure on the island's north coast is responsible for the exposure of the "Upper Unit" as klippe on structurally high topography such as Mt. Tsiknias. This shear zone is cross-cut by the Tinos I-Type granite, indicating it was active prior to intrusion (ca. 14.6 Ma) and has subsequently been folded. It is unclear if this structure is related to crustal extension, as extensional shear fabrics only record the relative ductile exhumation of material and cannot be used to characterize a specific tectonic regime.

2.4 Petrography

2.4.1 Tsiknias Ophiolite

2.4.1.1 Plagiogranite

The large plagiogranite is characterized by plagioclase, quartz, muscovite, rutile, chlorite, ilmenite and sphene with <1% hornblende but contains abundant edudral epidote stubby phenocrysts that display ophitic textures. Epidotes also show embayments when in contact with the quartzofeldspathic matrix, suggesting they pre-date the leucocratic matrix. Epidotes also display allanite rich cores display mild zoning as pristicine content (Fe^{3+}/Fe_{total}) varies between 0.962-0.995 from core to rim. Together these features suggest epidote has a magmatic origin (Zen and Hammerstron, 1984; Schmidt and Poli, 2004). In the crystallization sequence of a plagiogranite epidote seems to appear in tonalite after hornblende but before or contemporaneous with biotite (Schmidt and Poli, 2004), indicating it is a relatively primary phase, and is consistent with these observations. Chlorite occurs as a secondary minor phase along fractures and as

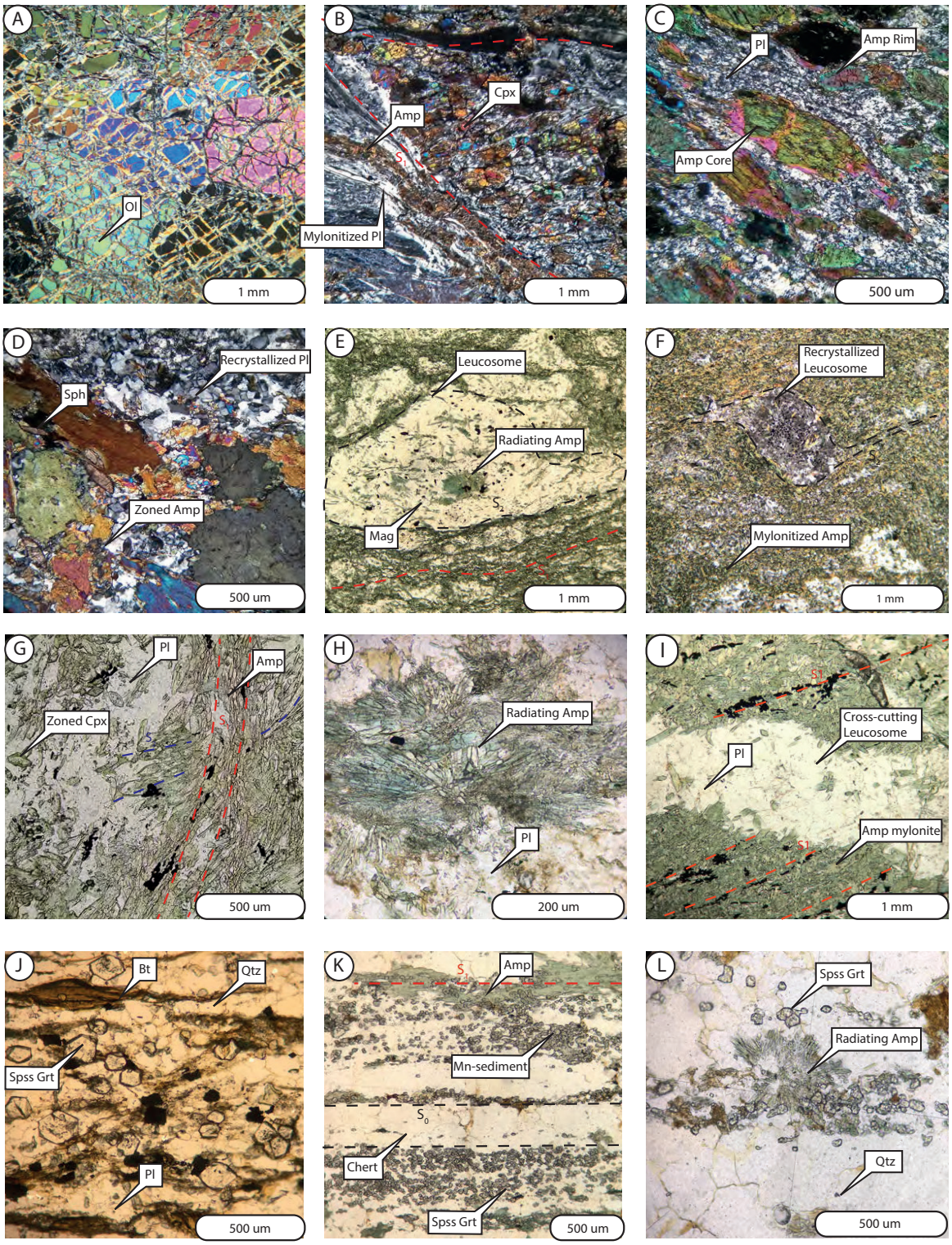


Figure 2.11: Continues on next page

breakdown of the primary epidote and biotite. Plagioclase is commonly saussertised but fresh grains are of albite in composition with XCa consistently <0.01.

Figure 2.11: A representative selection of photomicrographs from the Tsiknias Ophiolite, metamorphic sole and Mirsini Unit. A) 17TL-24, Serpentinized Dunite from a Dunite channel within the base of the ophiolite, with partially serpentinized olivine with concoidal fracture. B) TLT42, sheared and mylonitized gabbro within the moho-transition zone. C) TLT32, amphibolite from the metamorphic sole with overgrowths of actinolite amphibole and subgrain rotation in plagioclase. D) TLT3, amphibolite from the metamorphic sole, with titanite and large zoned amphiboles and extensive plagioclase dynamic recrystallization textures. E) 17TL-25, anatectic amphibolite from the uppermost five-meter melt zone, with leucosomes of dominantly plagioclase and radiating hornblende, with a high abundance of magnetite. This cross-cuts the mylonite amphibole fabric. F) 17TL-25, recrystallized leucosome, with top-to-SW asymmetry, indicating shearing deformation coeval with melt crystallization. G) TLT41 ampibolite textures with a strong S_2 fabric, with some radiaiting amphiboles (S_3), with some zoned metamorphic augite. H) TLT41 Radiating amphibole textures indicative of high temperatures outlasting deformation, with some degrees of static recrystallization in plagioclase. I) TLT49, migmatized amphibolite, with a sharp boundary marked by cross-cutting leuco-dioritic leucosome, that definitively post-dates S_{2b} mylonitization. J) TLT15, metasediment from the Mirsini Unit with macro-scale mylonite S–C fabrics, that are overgrown by small post-tectonic spessartine rich garnets. K) TLT13, cm-scale layers of meta-chert and Mn rich sediment, that have been metamorphosed to amphibolite-grade. Mn rich layers grown spessartine garnet in abundance, that cross-cut the previous mylonitization. L) TLT13, showing intergrown garnet and radiating amphibole (S_3, that are post-tectonic with respect to deformation, indicative of high-temperatures outlasting deformation.

2.4.1.2 Gabbros

Most of the gabbros comprise of >50% amphibole and dominantly plagioclase with <5% clinopyroxene, ilmenite and sphene. Amphiboles are generally zoned and coarse grained with compositions varying between hornblende to actinolite. Plagioclase shows a range of compositions from anorthite to pure albite probably due to retrogression. fresh plagioclase is characterized by XCa = 0.62–0.42, although most of the grains have been recrystallized and exhibit albite compositions with XNa = 0.90–0.99. Clinopyroxene is dominantly augite–diopside in composition, but commonly breaks down to amphibole, which sometimes forms actinolite rims. Primitive amphiboles are hornblende to paragasite in composition and display eccentric zoning with actinolite rims, with Ti varying from 0.10–0.01 p.f.u, K between 0.2–0.02 p.f.u. Along the Moho Transition zone, gabbros are intensely foliated (S_1) with top-to-NE kinematics. The gabbros show a complete spectrum of deformation textures in plagioclase from magmatic deformation to dynamic recrystallization and subgrain rotation, indicating deformation and top-to-NE shearing occurred over a wide temperature range during crystallization.

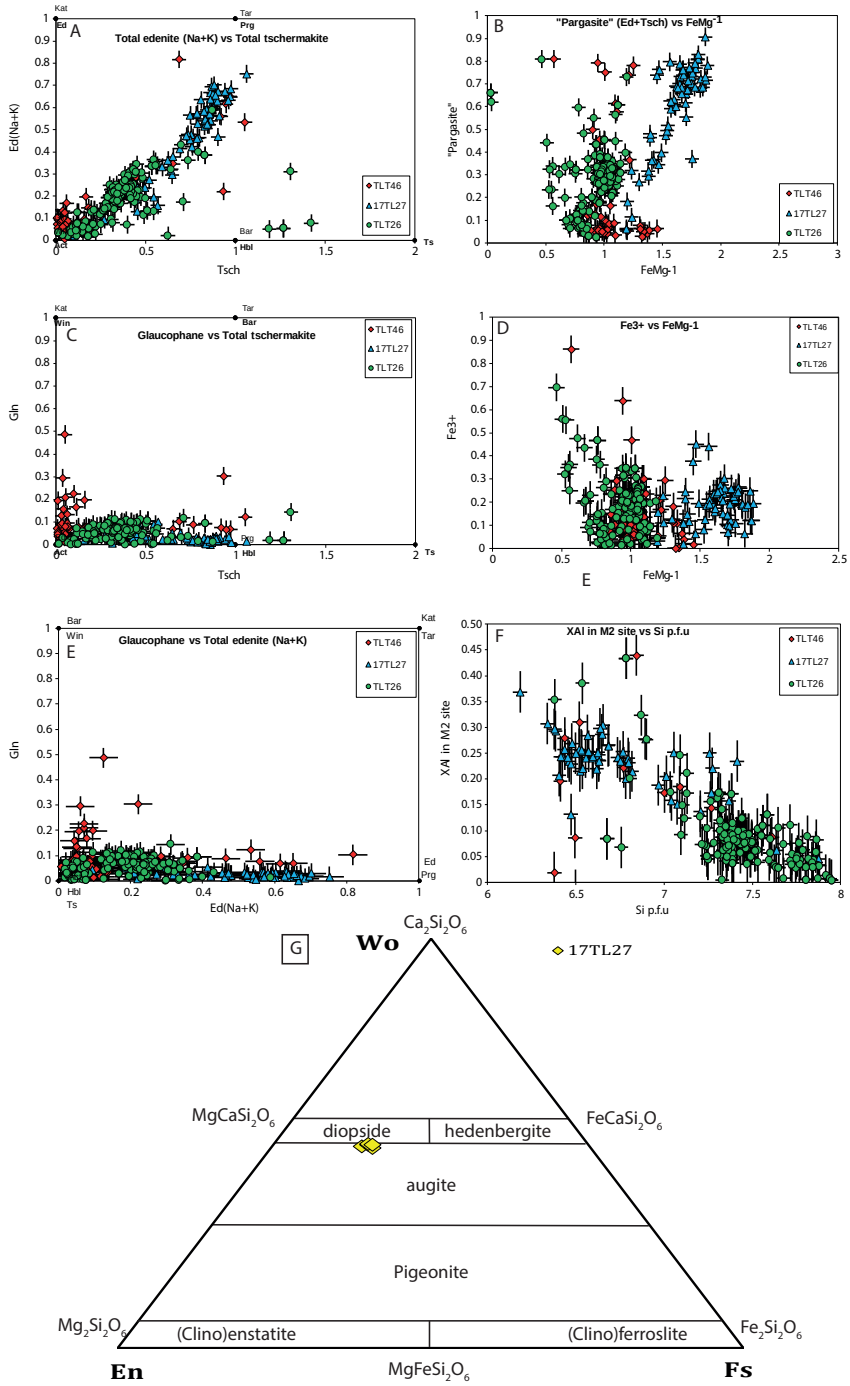


Figure 2.12: Gabbro mineral chemistry: A) Total edenite (Na+K) in the A site vs total Tschermakite exchange vectors showing amphiboles span from actinolite towards pargasite, with variation within and between samples, B) Pargasite vs $FeMg^{-1}$ exhange vectors showing a range in $FeMg^{-1}$ between samples but all trend towards pargasite lthough 17TL27 is pmost pargasite rich, C) Glaucophane (Na) in the B site vs total Tschermakite showing little variation in glaucophane content whereas amphibole trend from actinolite to hornblencde compositions, D) Fe^{3+} vs $FeMg^{-1}$ showing variable Fe^{3+} between 0.6-0.0 within samples although $FeMg^{-1}$ varies between samples, E) Glaucophane vs total edenite showing amphiboles are uniformly low in glaucophane but trend towards edenite/pargasite in samples 17TL27 and TLT46, F) XAl in M2 site vs Si p.f.u showing variable XAl in M2 site (a proxy for pressure) between samples, TLT26 has the largest range although lower values with increasing Si p.f.u associated with actinolite, G) pyroxene ternary plot pyroxenes composition varies between samples with 17TL27 being mostly diopside in composition, but TLT26 and TLT46 spans the augite-pigeonite divide

2.4.2 Metamorphic Sole

2.4.2.1 Amphibolites

The high-grade amphibolites (samples TL44, 17TL25, 17TL26, TLT10, TLT32) throughout the sole comprise of dominantly amphibole + plagioclase, with sphene and ilmenite, and contain enclaves of augitic clinopyroxene + amphibole with rare chromium spinel, with secondary chlorite and epidote. Amphiboles display a range of chemistry presented in fig. 2.12, and their peak composition is mainly pargasite to ferro-pargasite and grades down to fine grained actinolite, which is deformed with the S_{2b} mylonite fabric. Amphiboles are characterized by Ti between 0.18–0.03 and K between 0.11–0.03 p.f.u, with the most elevated Ti and K content associated with the most primitive high-temperature grains. These grains also exhibit the highest values of XAl in the M2 site = 0.35–0.28, suggesting the actinolite grew during decompression and is thus retrograde. Plagioclase is also extremely fine grained within the mylonite fabric and is in low abundance but occurs as $> 90\%$ of the leucosomes and melt veins, and shows a small range of XCa = 0.32–0.43. However, approximately 20 m below the Tsiknias Thrust, plagioclase forms rods up to 2 cm long that define the NE–SW trending lineation.

The amphibolites also display interesting microstructures. In rocks 50 m below the Tsiknias Thrust, where the rocks are not as intensely strained, the S_1 foliation is refolded into an S_{2a} crenulation cleavage defined by herringbone alignment of coarse amphiboles, and is associated with macro-scale isoclinal folding (Fig. 2.9). Top-to-SW S_{2b} mylonite fabrics overprint these earlier fabrics and increase in intensity towards the Tsiknias Thrust, where no trace of the earlier fabrics are observed.

Throughout the uppermost 10 m of the sole amphibolites under the Tsiknias Ophiolite, the degree of strain and partial melting sharply increases upwards towards the Tsiknias Thrust. A branching network of leucocratic veins emanate from

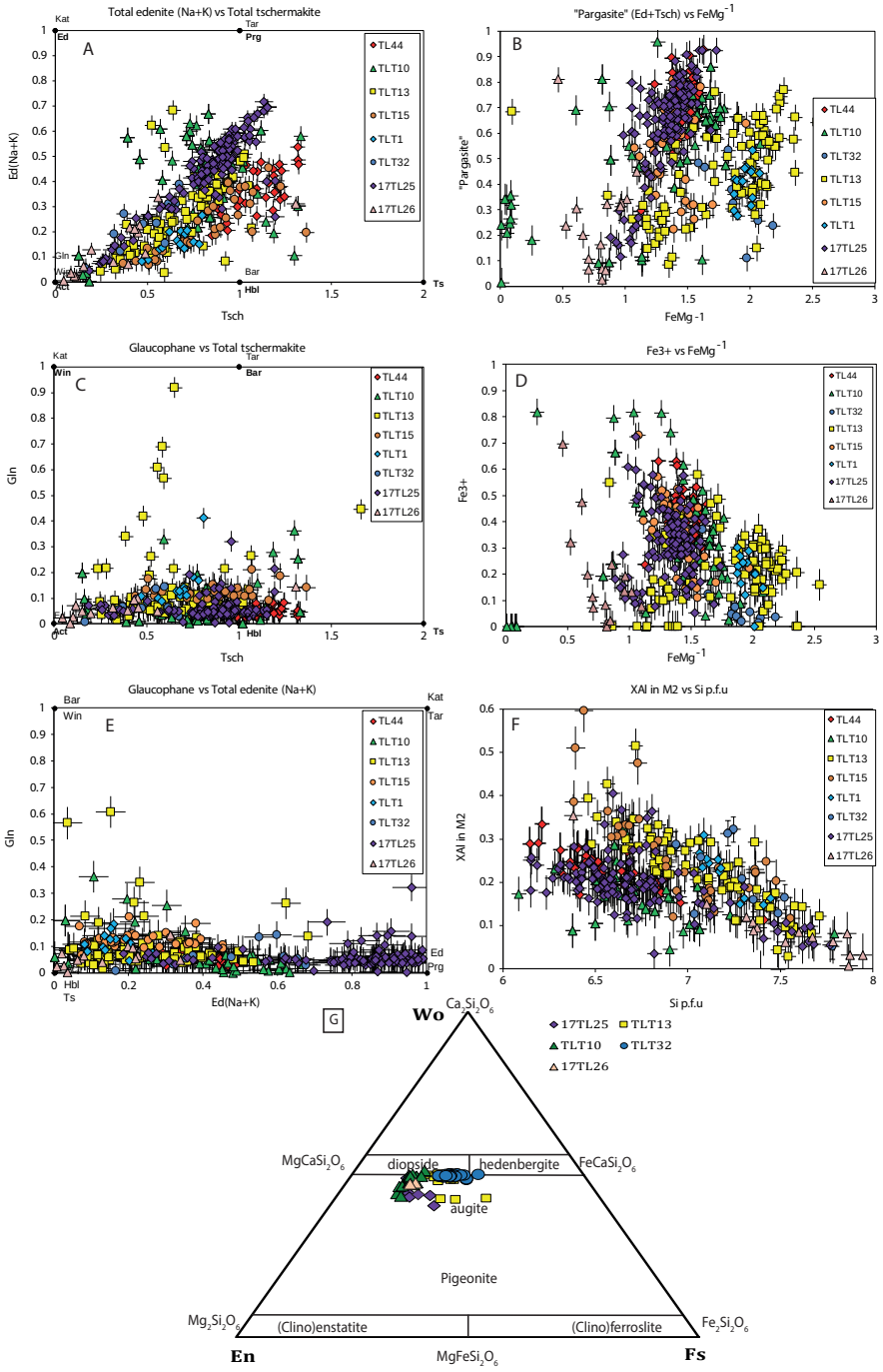


Figure 2.13: Amphibolite sole mineral chemistry: A) Total edenite (Na+K) in the A site vs total Tschermakite exchange vectors showing amphiboles span from actinolite towards pargasite within samples, B) Pargasite vs $FeMg^{-1}$ exhange vectors showing a range in $FeMg^{-1}$ between samples but all trend towards pargasite, C) Glaucophane (Na) in the B site vs total Tschermakite showing little variation in glaucophane content whereas amphibole trend towards tschermakite compositions, D) Fe^{3+} vs $FeMg^{-1}$, E) Glaucophane vs total edenite showing a trend towards edenite/pargasite in the highest grade amphiboles with little variation in glaucophane conent, F) XAl in M2 site vs Si p.f.u showing variable XAl in M2 site (a proxy for pressure) although lower values with increasing Si p.f.u associated with actinolite, G) pyroxene ternary plot showing most metamorphic pyroxenes are augite to diopside in composition

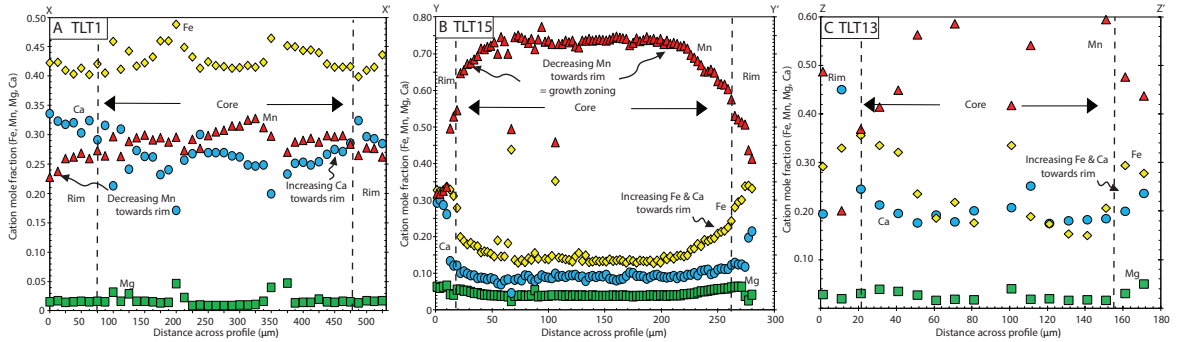


Figure 2.14: Line profiles of Mirsini garnets showing cation mole fractions almandine, grossular, pyrope and spessartine: A) TLT1, B) TLT15, C)TLT13

the thrust plane, alongside deformed leuco-dioritic leucosomes within the amphibolite. Structurally overlying this is a 2–3 m highly serpentinized cataclasite fault zone, comprised of ultra-mylonite talc tremolite schists with diverging networks of glassy magnesite and micro-crystalline plagioclase veins, clasts of Dunite and amphibolites accosiated with brittle fracture. Melt that emanates from the contact into the underlying amphibolites displays both syn and post-kinematic relationships with the S_{2b} top-to-SW ductile shearing fabrics. Leucocratic veins clearly cross-cut the S_{2b} mylonite fabrics and are composed of finely crystalline plagioclase with minor magnetite and hematite. Although many of the veins do not display microlite features (usually interpreted to indicate rapid quenching of melt; e.g. Del-Guidio et al., 2009), clear injection textures occur at the the vein margins, including rip clasts of host amphibole (see Fig. 2.10). Many of the melt veins have a preferential orientation down towards the SW; subparallel with the S_{2b} C' shear bands, which has been demonstrated to represent melt crystallization coeval with top-to-SW ductile shearing (Kolstead et al., 2004). In numerous samples, cross-cutting melt veins display dynamic re-crystallization of plagioclase, whereas in-situ leucosomes have augen geometries and are affected by consistent top-to-SW asymmetry, and therefore may represent previously boudinaged and deformed melt veins. Both these features are internally deformed in a ductile manner, indicating that deformation occurred at >550 °C during ambient conditions (Rosenberg and Stünitz, 2003) (Fig. 2.10). Brittle fracture is also superimposed on the amphibolite mylonite and these possibly influenced the migration of melt along distinct

linear geometries, and have also been subsequently deformed in a ductile fashion upon crystallization.

The observation that melt features and veins are both undeformed in regions near the contact (i.e. most recent melting) and highly deformed and boudinaged in more distal regions a few cm to few meters away from the Tsiknias Thrust (older melting), suggests anatexis occurred as a punctuated and episodic process and was associated with brittle fracture and melt injections, whereas ongoing ductile high-temperature creep was the dominant mode of deformation between melt episodes. These features suggest melting was episodic and a transient feature that affected rocks within close proximity to the Tsiknias Thrust. These features are consistent with repeated melting during rapid slip, overprinted by high-temperature ambient ductile flow. The preservation of undeformed melt veins indicates that deformation within the sole propagated to deeper structural levels as the sole was heated and metamorphosed. Therefore the upper part of the sole was accreted onto the base of the ophiolite during the initial stages of obduction. The large degree of epidotization and secondary mineralization indicates strong hydration persisted during retrogression and implies the dominant melting reaction was water saturated melting of amphibolite, characteristically occurring at temperatures above 680°C, with a negative P–T slope (e.g. Palin et al., 2016).

2.4.2.2 Mirsini Unit Metasediments

Pelagic metasediments (samples TLT1, TLT13 and TLT15) from the Mirsini Unit display a variety of protoliths including meta-turbidites, volcanic sediments and meta-cherts with significant Mn enrichment. All pelagic sediments are bi-domanial preserving their S_0 primary sedimentary layering defined by quartz rich domains (chert) separated from muddier domains defined by horizons of biotite, amphibole, sometimes Cpx and small (10–350 μm) spessartine rich garnets, which cross-cuts the dominant (S_{2b}) fabric. The S_1 fabric is defined by preferred orientation of micas and recrystallization of quartz, sub-parallel to S_0, and is refolded at outcrop scale into isoclinal folds and a mildly

formed crenulation cleavage (S_{2a}). A Top-to-SW planar fabric (S_{2b}) forms parallel along the cleavage domains to causing preferential alignment of matrix biotite and amphibole, however in some low strain domains they grow orthogonal to this fabric and display dessucate textures S_3.

Small garnets display hornfelic textures S_3 and also cross-cut this fabric, are inclusion free, and shows straight faces. The large abundance of small grains suggest it may have been kinetically favourable to nucleate lots of grains upon overstepping the garnet producing reaction (Waters and Lovegrove, 2002). This has been shown to be associated with either a rapid heating rate, fast reaction kinetics or large reaction overstep. The tight crystal size distribution suggest that it was probably a combination of these factors, although a rapid heating rate is likely. Garnet line profiles for samples TLT1, TLT13 and TLT15 (Fig. 2.14) reveal chemical zonation in garnet. Spessartine (XMn) content is extremely high >30% in all garnet cores and displays almost homogeneous patterns across the cores followed by a sharp decrease in the outer rims of all samples, suggesting a single stage of garnet growth. Similar albeit inverse patterns emerge in the grossular (XCa) and almandine although pyrope increases only slightly from core to rim. TLT1 shows slight zoning with spessartine content decreasing from 0.34 to 0.23 from core to rim whereas grossular increase from 0.24-0.34 and pyrope remains flat. Sample TLT15 is characterized by extreme spessartine content in the core that decreases to 0.30 on the rim, whereas grossular and almanidine increasing to 0.32 and 0.33 at 0.06-0.07 pyrope. Garnets in TLT13 display similar patterns with high spessartine cores, with outer rims with similar abundances of almandine, grossular and spessartine, at 0.06 pyrope. These features suggest that all Mn was consumed by garnets during grograde metamorphism whereas the last phase of garnet growth associated with the outermost rims had less available Mn. Matrix amphibolies range from actinolite to hornblende in composition (Fig. 2.13), with Ti between 0.08-0.003 pfu. Biotites have XMg values ranging between 0.39-0.67 and Ti between 0.06-0.36, suggesting they grew over a range of pressure and temperature.

Sample	TLT26	TLT26	TLT26	TLT26	TLT26	TLT26	TLT26	17TL27	17TL27	17TL27	17TL27	17TL27	17TL27	17TL27	17TL27	17TL27	17TL27
Min	Pl	Pl	Ep	Ep	Amp	Amp	Amp	Amph	Amp	Amp	Amp	Cpx	Cpx	Pl	Pl	Pl	Sph
Location	Matrix	Matrix	Matrix	Matrix	Core	Core	Rim	Core	Core	Core	Rim	Matrix	Matrix	Matrix	Matrix	Matrix	Matrix
SiO2	64.53	67.98	39.12	38.77	44.26	47.49	55.33	40.41	41.97	42.66	50.78	52.31	50.87	57.13	55.13	61.03	30.06
TiO2	0.00	0.00	0.07	0.05	0.22	0.17	0.01	0.95	0.79	0.63	0.33	0.10	0.09	0.00	0.00	0.00	38.65
Al2O3	23.73	21.36	32.02	30.34	13.69	12.37	1.55	14.15	12.78	11.35	5.55	1.27	5.27	27.34	28.57	24.52	1.06
FeO	0.12	0.06	2.45	4.28	9.63	9.52	7.12	15.55	15.82	15.97	12.26	8.60	9.29	0.23	0.07	0.20	0.43
MnO	0.02	-0.02	0.09	0.08	0.28	0.32	0.22	0.30	0.29	0.33	0.33	0.34	0.35	0.00	0.00	0.00	0.08
MgO	0.00	0.00	0.11	0.14	15.35	13.83	19.40	9.37	10.08	11.17	14.58	12.71	11.55	0.00	0.00	0.01	0.00
CaO	3.79	0.32	23.90	24.14	10.56	12.41	13.20	12.02	12.26	12.03	12.35	23.85	22.47	9.04	10.38	5.54	29.04
Na2O	8.42	10.31	0.02	0.02	1.38	1.54	0.24	1.95	1.87	1.79	0.68	0.38	0.38	6.57	5.64	8.21	0.01
K2O	0.08	0.06	0.01	0.02	0.38	0.28	0.07	0.96	0.75	0.77	0.25	0.01	0.02	0.12	0.15	0.10	0.01
Totals	100.69	100.07	97.80	97.84	95.74	97.94	97.16	95.67	96.60	96.68	97.11	99.57	100.30	100.42	99.93	99.60	99.34
Oxygens	8.00	8.00	12.50	12.50	23.00	23.00	23.00	23.00	23.00	23.00	23.00	6.00	6.00	8.00	8.00	8.00	5.00
Si	2.81	2.95	2.99	2.98	6.38	6.78	7.80	6.18	6.34	6.41	7.37	1.96	1.90	2.55	2.48	2.72	0.99
Ti	0.00	0.00	0.00	0.00	0.02	0.02	0.00	0.11	0.09	0.07	0.04	0.00	0.00	0.00	0.00	0.00	0.96
Al	1.22	1.09	2.88	2.75	2.33	2.08	0.26	2.55	2.28	2.01	0.95	0.06	0.23	1.44	1.52	1.29	0.04
Fe3+	0.00	0.00	0.11	0.25	0.70	0.02	0.06	0.12	0.19	0.44	0.11	0.04	0.00	0.01	0.00	0.01	0.00
Fe2+	0.00	0.00	0.05	0.03	0.46	1.12	0.78	1.87	1.81	1.56	1.38	0.23	0.29	0.00	0.00	0.00	0.01
Mn	0.00	0.00	0.01	0.01	0.03	0.04	0.03	0.04	0.04	0.04	0.04	0.01	0.01	0.00	0.00	0.00	0.00
Mg	0.00	0.00	0.01	0.02	3.30	2.94	4.08	2.14	2.27	2.50	3.15	0.71	0.64	0.00	0.00	0.00	0.00
Ca	0.18	0.02	1.96	1.99	1.63	1.90	1.99	1.97	1.98	1.94	1.92	0.96	0.90	0.43	0.50	0.26	1.03
Na	0.71	0.87	0.00	0.00	0.39	0.43	0.07	0.58	0.55	0.52	0.19	0.03	0.03	0.57	0.49	0.71	0.00
K	0.00	0.00	0.00	0.00	0.07	0.05	0.01	0.19	0.14	0.15	0.05	0.00	0.00	0.01	0.01	0.01	0.00
Sum	4.93	4.94	8.01	8.02	15.31	15.39	15.08	15.75	15.68	15.63	15.19	4.00	4.00	5.01	5.01	4.99	3.03
XMg	-	-	0.22	0.36	0.88	0.72	0.84	0.53	0.56	0.62	0.70	0.76	0.69	-	-	-	-
XCa	0.20	0.02	-	-	-	-	-	-	-	-	-	-	-	0.43	0.50	0.27	-
XMn	-	-	-	-	-	-	-	-	-	-	-	-	-	-	-	-	-
Al(iv)	-	-	-	-	-	-	-	-	-	-	-	-	-	-	-	-	-
Al(vi)	-	-	-	-	-	-	-	-	-	-	-	-	-	-	-	-	-
Alm	-	-	-	-	-	-	-	-	-	-	-	-	-	-	-	-	-
Prp	-	-	-	-	-	-	-	-	-	-	-	-	-	-	-	-	-
Grs	-	-	-	-	-	-	-	-	-	-	-	-	-	-	-	-	-
Spss	-	-	-	-	-	-	-	-	-	-	-	-	-	-	-	-	-
XFe3+	-	-	0.71	0.90	0.60	0.02	0.08	0.06	0.10	0.22	0.07	0.15	0.00	1.00	1.00	1.00	0.00
XPs	-	-	0.04	0.08	-	-	-	-	-	-	-	-	-	-	-	-	-

Table 2.1: Representative gabbro mineral compositions derived from electron microprobe

Sample Min Location	TLT46 Amp Core	TLT46 Amp Core	TLT46 Amp Rim	TLT46 ilm Matrix	TLT46 Pl Matrix	TLT46 Pl Matrix	TLT46 Pl Matrix	TLT63 Ep Matrix	TLT63 Ep Matrix	TLT63 Ep Matrix	TLT63 Ms Matrix	TLT63 Ms Matrix	TLT63 Chl Matrix	TLT63 Rt Matrix	TLT63 Ilm Matrix	TLT63 Pl Matrix	TLT63 Pl Matrix
SiO2	42.69	43.57	50.58	0.02	68.24	63.70	69.03	37.38	38.08	37.21	48.01	46.67	30.71	0.08	0.19	68.36	69.58
TiO2	0.65	0.73	0.40	0.01	0.01	2.76	0.00	0.37	0.03	0.11	0.59	0.35	0.07	96.82	62.09	0.11	0.00
Al2O3	9.35	12.18	6.04	0.00	20.16	18.06	21.18	23.92	21.74	20.83	33.40	35.68	19.86	0.02	0.05	20.53	20.35
FeO	11.60	12.50	11.53	90.55	0.01	0.10	0.00	10.83	13.08	14.38	4.42	2.28	21.99	1.73	33.22	0.15	0.04
MnO	0.47	0.69	0.64	0.06	0.00	0.01	0.41	0.10	0.14	0.01	0.00	0.00	0.10	0.00	0.02	0.00	0.01
MgO	15.99	12.67	15.18	0.00	0.01	0.03	0.00	0.05	0.00	0.02	1.16	0.38	12.56	0.00	0.00	0.00	0.00
CaO	9.12	11.84	12.06	0.02	0.16	2.76	0.01	23.43	22.70	23.35	0.12	0.02	0.33	0.03	0.03	0.03	0.05
Na2O	0.70	1.84	1.08	0.02	11.32	8.08	0.18	0.03	0.29	0.02	0.22	0.24	0.06	0.01	0.01	10.67	9.96
K2O	3.67	0.83	0.43	0.00	0.08	0.15	9.09	0.02	0.03	0.02	8.24	7.69	0.96	0.13	0.03	0.07	0.05
Totals	94.25	96.84	97.94	90.69	99.99	95.65	99.90	96.13	96.10	95.97	96.16	93.31	86.64	98.83	95.64	99.92	100.04
Oxygens	23.00	23.00	23.00	3.00	8.00	8.00	8.00	12.50	12.50	12.50	11.00	11.00	14.00	2.00	3.00	8.00	8.00
Si	6.50	6.44	7.27	0.00	2.98	2.92	2.98	2.99	3.06	3.01	3.14	3.11	3.19	0.00	0.01	2.99	3.01
Ti	0.07	0.08	0.04	0.00	0.00	0.10	0.00	0.02	0.00	0.01	0.03	0.02	0.01	0.99	1.15	0.00	0.00
Al	1.68	2.12	1.02	0.00	1.04	0.98	1.08	2.25	2.06	1.99	2.57	2.80	2.43	0.00	0.00	1.06	1.04
Fe3+	0.47	0.29	0.17	1.98	0.00	0.00	0.02	0.72	0.87	0.96	0.17	0.00	0.00	0.00	0.00	0.00	0.00
Fe2+	1.01	1.25	1.22	0.02	0.00	0.00	0.00	0.01	0.01	0.01	0.07	0.09	1.91	0.02	0.69	0.00	0.00
Mn	0.06	0.09	0.08	0.00	0.00	0.00	0.00	0.01	0.01	0.00	0.00	0.04	0.01	0.00	0.00	0.00	0.00
Mg	3.63	2.79	3.25	0.00	0.00	0.00	0.00	0.01	0.00	0.00	0.11	0.04	1.94	0.00	0.00	0.00	0.00
Ca	1.49	1.87	1.86	0.00	0.01	0.14	0.01	2.01	1.95	2.02	0.01	0.00	0.04	0.00	0.00	0.00	0.00
Na	0.21	0.53	0.30	0.00	0.96	0.72	0.76	0.00	0.05	0.00	0.03	0.03	0.01	0.00	0.00	0.87	0.84
K	0.71	0.16	0.08	0.00	0.01	0.01	0.00	0.00	0.00	0.00	0.69	0.65	0.13	0.00	0.00	0.00	0.00
Sum	15.82	15.62	15.28	2.01	4.98	4.86	4.85	8.01	8.00	8.01	6.82	6.77	9.66	1.01	1.85	4.92	4.89
XMg	0.78	0.69	0.73	-	-	-	-	0.46	0.00	0.23	0.61	0.29	0.50	0.00	0.00	-	-
XCa	-	-	-	-	0.01	0.16	0.01	-	-	-	-	-	-	-	0.00	0.00	
XMn	-	-	-	0.00	-	-	-	-	-	-	-	-	-	-	0.00	-	-
Al(iv)	-	-	-	-	-	-	-	-	-	-	0.86	0.89	-	-	-	-	-
Al(vi)	-	-	-	-	-	-	-	-	-	-	1.71	1.91	-	-	-	-	-
Alm	-	-	-	-	-	-	-	-	-	-	-	-	-	-	-	-	-
Prp	-	-	-	-	-	-	-	-	-	-	-	-	-	-	-	-	-
Grs	-	-	-	-	-	-	-	-	-	-	-	-	-	-	-	-	-
Spss	-	-	-	-	-	-	-	-	-	-	-	-	-	-	-	-	-
XFe3+	0.32	0.19	0.12	0.99	-	-	-	0.99	0.99	0.99	0.70	0.00	0.00	0.00	0.00	-	-
XPs	-	-	-	-	-	-	-	0.24	0.30	0.33	-	-	-	-	-	-	-

Table 2.2: Representative mineral gabbro and plagiogranite compositions derived from electron microprobe

Sample	17TL25	17TL25	17TL25	17TL25	17TL25	17TL25	17TL25	TLT10	TLT10	TLT10	TLT10	TLT10	TLT10	TLT10
Mn	Amp	Amp	Amp	Cpx	Pl	Pl	Ep	Amp	Amp	Amp	Cpx	Cpx	Pl	Pl
Location	Matrix	Matrix	Leucosome Matrix	Matrix	Matrix	Leucosome Matrix	Matrix	Matrix	Matrix	Matrix	Matrix	Matrix	Leucosome Matrix	Matrix
SiO2	40.47	41.12	41.66	42.57	52.85	53.02	64.77	59.98	61.93	38.99	4.82	42.30	40.43	43.86	44.20	52.33	52.44	52.60	58.68	60.70	58.35
TiO2	2.57	1.03	1.17	0.66	0.00	0.15	0.00	0.00	0.03	12.66	49.30	1.28	0.97	0.77	0.93	0.05	0.10	0.08	0.13	0.01	0.04
Al2O3	12.35	12.94	12.01	11.77	0.94	1.57	25.31	26.15	24.47	6.94	0.17	12.47	12.74	10.92	10.58	1.63	1.95	1.17	25.79	25.14	25.81
FeO	15.47	15.56	15.40	16.14	8.05	8.20	0.02	0.16	0.39	11.01	35.81	16.67	16.49	15.98	16.65	8.16	8.67	9.19	0.46	0.27	0.18
MnO	0.30	0.26	0.25	0.28	0.14	0.35	0.00	0.02	0.01	0.21	2.46	0.21	0.27	0.00	0.00	0.57	0.54	0.18	0.04	0.00	0.01
MgO	10.52	10.93	11.63	11.26	13.17	13.46	0.01	0.01	0.01	7.70	0.20	10.45	10.60	11.43	11.21	13.75	11.56	12.86	0.00	0.12	0.00
CaO	11.69	11.93	11.94	11.88	24.03	23.71	5.22	6.97	5.31	18.51	4.22	12.38	12.45	12.59	13.25	23.65	24.31	22.74	7.95	5.99	8.48
Na2O	2.25	2.21	2.19	1.71	0.46	0.46	3.99	3.55	8.39	1.21	0.00	1.83	1.71	1.00	1.50	0.16	0.75	0.38	6.24	7.67	7.39
K2O	0.55	0.41	0.41	0.61	0.00	0.00	0.03	2.37	0.07	0.33	0.02	0.48	0.66	1.02	0.75	0.00	0.00	0.05	0.05	0.04	0.17
Totals	96.16	96.40	96.67	96.88	99.63	100.91	99.36	99.21	100.61	97.55	97.01	98.07	96.32	97.57	99.07	100.30	100.31	99.26	99.35	99.94	100.43
Oxygens	23	23	23	23	6	6	8	8	8	12.5	3	23	23	23	23	6	6	6	8	8	8
Si	6.15	6.19	6.24	6.35	1.97	1.94	2.82	2.68	2.73	3.13	0.12	6.28	6.09	6.50	6.35	2.00	2.03	1.93	2.63	2.69	2.61
Ti	0.29	0.12	0.13	0.07	0.01	0.00	0.00	0.00	0.00	0.76	0.92	0.14	0.11	0.09	0.10	0.00	0.00	0.00	0.00	0.00	0.00
Al	2.21	2.29	2.12	2.07	0.06	0.07	1.30	1.38	1.29	0.66	0.01	2.18	2.26	1.91	1.79	0.06	0.04	0.07	1.36	1.32	1.36
Fe3+	0.23	0.46	0.52	0.58	0.00	0.00	0.01	0.01	0.00	0.73	0.00	0.39	0.81	0.44	1.40	0.00	0.00	0.10	0.02	0.01	0.01
Fe2+	1.74	1.49	1.40	1.44	0.23	0.25	0.00	0.00	0.00	0.01	0.74	1.68	1.27	1.54	0.60	0.25	0.28	0.16	0.00	0.00	0.00
Mn	0.04	0.03	0.03	0.04	0.01	0.02	0.00	0.00	0.00	0.01	0.05	0.03	0.03	0.00	0.00	0.01	0.01	0.01	0.00	0.00	0.00
Mg	2.38	2.45	2.60	2.50	0.74	0.76	0.00	0.00	0.00	0.92	0.01	2.31	2.38	2.53	2.40	0.74	0.73	0.71	0.00	0.01	0.00
Ca	1.90	1.92	1.92	1.90	0.97	0.94	0.24	0.33	0.26	1.59	0.11	1.97	2.01	2.00	2.04	0.90	0.89	0.96	0.38	0.29	0.41
Na	0.66	0.64	0.64	0.49	0.00	0.01	0.34	0.31	0.67	0.19	0.00	0.53	0.50	0.29	0.42	0.03	0.01	0.03	0.54	0.66	0.64
K	0.11	0.08	0.08	0.12	0.00	0.00	0.00	0.14	0.00	0.03	0.00	0.09	0.13	0.19	0.14	0.00	0.00	0.01	0.00	0.00	0.01
Sum	15.72	15.68	15.67	15.56	4.00	4.00	4.70	4.85	4.96	8.03	1.96	15.60	15.58	15.48	15.23	4.00	4.00	4.00	4.95	4.97	5.03
XMg	0.58	0.62	0.65	0.64	0.76	0.75	-	-	-	0.99	0.01	0.58	0.65	0.62	0.80	0.75	0.73	0.81	-	-	-
XCa	-	-	-	-	-	-	0.42	0.43	0.28			-	-	-	-	-	-	-	0.41	0.30	0.38
XMn	-	-	-	-	-	-	-	-	-	-	0.06	-	-	-	-	-	-	-	-	-	-
Al(iv)	-	-	-	-	-	-	-	-	-	-	-	-	-	-	-	-	-	-	-	-	-
Al(vi)	-	-	-	-	-	-	-	-	-	-	-	-	-	-	-	-	-	-	-	-	-
Alm	-	-	-	-	-	-	-	-	-	-	-	-	-	-	-	-	-	-	-	-	-
Prp	-	-	-	-	-	-	-	-	-	-	-	-	-	-	-	-	-	-	-	-	-
Grs	-	-	-	-	-	-	-	-	-	-	-	-	-	-	-	-	-	-	-	-	-
Spss	-	-	-	-	-	-	-	-	-	-	-	-	-	-	-	-	-	-	-	-	-
XFe3+	0.12	0.24	0.27	0.29	0.00	0.00	-	-	-	0.99	0.00	0.19	0.39	0.22	0.70	0.00	0.00	0.00	-	-	-
XPs	-	-	-	-	-	-	-	-	-	0.53	-	-	-	-	-	-	-	-	-	-	-

Table 2.3: Representative metamorphic sole amphibolite mineral compositions derived from electron microprobe

Sample	TL44	TL44	TL44	TL44	TL44	TL44	TL44	TL44	TLT1	TLT1	TLT1	TLT1	TLT1	TLT1	TLT1	TLT1	TLT1	TLT1	TLT1	TLT1	TLT1	TLT1	TLT1
Min	Amp	Amp	Amp	Amp	Amp	Chl	Pl	Pl	Grt	Grt	Grt	Grt	Amp	Amp	Amp	Bt	Bt	Bt	Ep	ilm	Ms	Ms	Pl	Pl
Location	Matrix	Matrix	Leucosome	Leucosome	Matrix	Matrix	Leucosome	Matrix	Outer Rim	Inner Rim	Intermediate	Core	Matrix	Matrix	Matrix	Matrix	Matrix	Matrix	Matrix	Matrix	Matrix	Matrix	Matrix	Matrix
SiO2	40.36	42.68	42.02	41.67	45.10	29.54	58.98	58.35	37.09	36.83	36.69	36.77	47.38	45.66	47.16	35.25	35.59	36.09	37.73	0.08	43.81	45.69	54.41	62.63
TiO2	1.35	0.91	1.11	1.21	1.41	0.16	0.00	0.04	0.05	0.08	0.04	0.06	0.70	0.46	0.49	2.75	2.69	3.16	0.08	52.56	0.70	3.10	0.00	0.00
Al2O3	13.54	12.10	12.65	13.62	11.61	17.40	25.03	25.81	21.17	20.77	20.78	20.92	7.76	9.10	7.86	17.31	17.36	17.74	26.15	0.00	18.27	15.68	28.53	23.23
FeO	16.47	16.62	15.70	16.21	16.39	18.70	0.21	0.18	19.42	17.96	20.61	20.49	17.75	17.47	17.55	17.88	18.37	16.82	7.75	40.50	10.56	15.28	0.01	0.05
MnO	0.31	0.31	0.31	0.33	0.19	0.17	0.02	0.01	9.92	11.76	13.04	12.94	0.77	0.70	0.80	0.35	0.35	0.21	0.26	4.02	0.18	0.25	0.01	0.00
MgO	9.53	10.48	10.46	10.16	11.16	19.70	0.00	0.00	0.38	0.33	0.34	0.98	9.60	9.39	10.01	7.80	8.71	9.42	0.00	0.12	7.65	7.56	0.00	0.00
CaO	11.82	11.97	12.06	12.23	12.15	0.18	6.80	8.48	11.58	11.38	8.11	6.85	11.48	11.47	11.32	0.95	0.13	0.09	23.08	0.01	0.78	0.15	10.77	4.33
Na2O	1.53	1.47	1.45	1.52	1.14	0.00	7.39	7.39	0.02	0.04	0.06	0.10	0.93	1.00	0.98	0.23	0.09	0.15	0.05	0.01	2.08	0.28	5.82	10.08
K2O	0.64	0.37	0.41	0.41	0.45	0.13	0.18	0.17	0.03	0.01	0.02	0.07	0.24	0.24	0.16	9.44	9.49	9.70	0.05	0.01	7.90	8.48	0.08	0.15
Totals	95.55	96.91	96.16	97.35	99.60	86.00	98.61	100.43	99.65	99.15	99.70	99.17	96.60	95.48	96.34	91.95	92.78	93.38	95.15	97.30	91.94	96.46	99.63	100.46
Oxygens	23	23	23	23	23	14	8	8	12	12	12	12	23	23	23	11	11	11	12.5	3	11	11	8	8
Si	6.15	6.37	6.31	6.19	6.52	2.94	2.72	2.61	2.97	2.97	2.97	2.98	7.11	6.94	7.08	2.78	2.78	2.78	3.01	0.00	3.16	3.17	2.47	2.77
Ti	0.15	0.10	0.13	0.13	0.15	0.01	0.01	0.00	0.00	0.01	0.00	0.00	0.08	0.05	0.06	0.16	0.16	0.18	0.01	1.02	0.04	0.16	0.00	0.00
Al	2.43	2.13	2.24	2.39	1.98	2.04	0.77	1.36	2.00	1.98	1.98	2.00	1.37	1.63	1.39	1.61	1.60	1.61	2.46	0.00	1.56	1.29	1.52	1.21
Fe3+	0.47	0.53	0.45	0.50	0.41	0.00	0.00	0.00	0.05	0.08	0.08	0.05	0.15	0.20	0.25	0.00	0.00	0.00	0.51	0.00	0.45	0.62	0.00	0.00
Fe2+	1.63	1.54	1.52	1.52	1.57	0.34	0.16	0.01	1.25	1.14	1.31	1.34	2.08	2.02	1.96	1.18	1.20	1.08	0.01	0.87	0.19	0.27	0.00	0.00
Mn	0.04	0.04	0.04	0.04	0.02	1.56	0.21	0.00	0.67	0.80	0.89	0.89	0.10	0.09	0.10	0.02	0.02	0.01	0.02	0.09	0.01	0.01	0.00	0.00
Mg	2.16	2.33	2.34	2.25	2.40	0.01	0.01	0.00	0.05	0.04	0.04	0.12	2.15	2.13	2.24	0.92	1.01	1.08	0.00	0.01	0.82	0.78	0.00	0.00
Ca	1.93	1.91	1.94	1.95	1.88	2.92	0.43	0.41	1.00	0.98	0.70	0.60	1.85	1.87	1.82	0.08	0.01	0.01	1.98	0.00	0.06	0.01	0.52	0.21
Na	0.45	0.42	0.42	0.44	0.32	0.02	0.34	0.64	0.00	0.01	0.01	0.02	0.27	0.29	0.28	0.04	0.01	0.02	0.01	0.00	0.29	0.04	0.51	0.86
K	0.12	0.07	0.08	0.08	0.08	0.00	0.31	0.01	0.00	0.00	0.00	0.01	0.05	0.05	0.03	0.95	0.95	0.95	0.01	0.00	0.73	0.75	0.00	0.01
Sum	15.54	15.45	15.47	15.49	15.34	9.85	4.96	5.05	8.00	8.00	8.00	8.00	15.20	15.26	15.21	7.74	7.74	7.73	8.00	1.98	7.31	7.11	5.03	5.06
XMg	0.57	0.60	0.61	0.60	0.60	0.04	-	-	0.03	0.03	0.03	0.08	0.51	0.51	0.53	0.44	0.46	0.50	0.00	0.01	0.81	0.75	-	-
XCa	-	-	-	-	-	-	0.40	0.38	-	-	-	-	-	-	-	-	-	-	-	-	-	-	0.50	0.19
XMn	-	-	-	-	-	-	-	-	-	-	-	-	-	-	-	-	-	-	-	-	-	-	-	-
Al(iv)	-	-	-	-	-	-	-	-	-	-	-	-	-	-	-	1.22	1.22	1.22	-	-	0.84	0.83	-	-
Al(vi)	-	-	-	-	-	-	-	-	-	-	-	-	-	-	-	0.39	0.38	0.39	-	-	0.72	0.46	-	-
Alm	-	-	-	-	-	-	-	-	0.42	0.38	0.44	0.45	-	-	-	-	-	-	-	-	-	-	-	-
Prp	-	-	-	-	-	-	-	-	0.02	0.01	0.01	0.04	-	-	-	-	-	-	-	-	-	-	-	-
Grs	-	-	-	-	-	-	-	-	0.34	0.33	0.24	0.20	-	-	-	-	-	-	-	-	-	-	-	-
Spss	-	-	-	-	-	-	-	-	0.23	0.27	0.30	0.30	-	-	-	-	-	-	-	-	-	-	-	-
XFe3+	0.22	0.26	0.23	0.25	0.21	0.00	-	-	0.04	0.06	0.06	0.04	0.07	0.09	0.11	0.00	0.00	0.00	0.99	0.00	0.70	0.70	-	-
XPs	-	-	-	-	-	-	-	-	-	-	-	-	-	-	-	-	-	-	0.17	-	-	-	-	-

Table 2.4: Representative metamorphic sole mineral compositions derived from electron microprobe

Sample	TLT32	TLT32	TLT32	TLT32	TLT32	TLT32	TLT32	17TL26	17TL26	17TL26	17TL26	17TL26	17TL26	17TL26	17TL26	17TL26
Min	Cpx	Cpx	Cpx	Amp	Amp	Kfs	Pl	Amp	Amp	Amp	Cpx	Cpx	Ep	Ep	Chl	Pl	Pl	Sph
Location	Matrix	Cpx	Matrix	Matrix	Matrix	Matrix	Matrix	Leucosome	Matrix	Matrix	Leucosome	Matrix	Matrix	Matrix	Matrix	Leucosome	Matrix	Matrix
SiO2	51.57	51.63	51.32	52.09	46.22	49.49	52.35	63.93	56.32	58.49	44.26	49.39	50.80	56.74	53.22	54.52	38.57	38.71	29.67	56.40	60.02	30.66
TiO2	0.01	0.02	0.02	0.01	0.36	0.35	0.06	0.04	0.01	0.00	0.22	1.06	0.69	0.00	0.44	0.15	0.14	0.04	0.02	0.12	0.40	34.27
Al2O3	0.42	0.24	0.30	0.24	9.27	5.51	1.84	18.33	27.29	25.71	13.69	7.05	5.43	1.14	1.31	1.86	26.53	29.51	21.90	21.09	24.21	3.46
FeO	12.51	12.13	13.44	12.20	14.95	15.34	16.36	0.07	0.09	0.08	9.63	9.78	9.54	7.50	7.43	7.41	5.72	4.93	13.32	2.85	0.41	0.79
MnO	0.46	0.57	0.53	0.55	0.31	0.38	0.41	0.00	0.02	0.02	0.28	0.29	0.20	0.21	0.31	0.26	0.14	0.08	0.31	0.02	0.00	0.00
MgO	9.98	10.46	9.41	10.38	11.10	12.18	12.70	0.00	0.00	0.00	15.35	15.85	16.53	19.53	13.40	12.88	1.76	0.03	22.39	2.81	0.11	0.04
CaO	24.00	23.87	24.10	23.95	12.17	12.08	12.48	0.02	9.33	7.47	10.56	12.52	12.30	13.42	24.48	23.60	22.58	24.24	0.22	7.05	6.54	28.90
Na2O	0.17	0.14	0.16	0.16	1.08	0.98	0.14	0.56	6.92	8.13	1.38	1.27	0.98	0.11	0.03	0.00	0.25	0.01	0.08	5.92	7.82	0.03
K2O	0.01	0.00	0.00	0.01	0.55	0.29	0.11	16.34	0.15	0.21	0.38	0.17	0.08	0.04	0.11	0.00	0.05	0.00	0.03	0.13	0.06	0.02
Totals	99.12	99.07	99.29	99.60	96.00	96.58	96.46	99.29	100.14	100.11	95.74	97.38	96.55	98.69	100.72	100.68	95.73	97.56	87.92	96.39	99.58	98.17
Oxygens	6	6	6	6	23	23	23	8	8	8	23	23	23	23	6	6	12.5	12.5	14	8	8	5
Si	1.99	1.99	1.98	1.99	6.94	7.36	7.78	2.98	2.53	2.62	6.38	7.10	7.32	7.88	1.95	1.95	3.04	2.99	2.90	2.64	2.69	1.02
Ti	0.00	0.00	0.00	0.00	0.04	0.04	0.01	0.00	0.00	0.00	0.02	0.12	0.08	0.00	0.00	0.00	0.01	0.00	0.00	0.00	0.01	0.86
Al	0.02	0.01	0.01	0.01	1.64	0.97	0.32	1.01	1.45	1.36	2.33	1.20	0.92	0.19	0.06	0.07	2.47	2.69	2.52	1.16	1.28	0.14
Fe3+	0.02	0.03	0.03	0.01	0.05	0.04	0.06	0.00	0.00	0.00	0.70	0.08	0.13	0.02	0.07	0.00	0.37	0.31	0.00	0.10	0.01	0.00
Fe2+	0.38	0.36	0.40	0.38	1.83	1.87	1.98	0.00	0.00	0.00	0.46	1.10	1.02	0.85	0.18	0.25	0.00	0.01	1.09	0.00	0.00	0.02
Mn	0.02	0.02	0.02	0.02	0.04	0.05	0.05	0.00	0.00	0.00	0.03	0.04	0.03	0.03	0.01	0.01	0.01	0.01	0.03	0.00	0.00	0.00
Mg	0.57	0.60	0.54	0.59	2.48	2.70	2.81	0.00	0.00	0.00	3.30	3.40	3.55	4.04	0.74	0.74	0.21	0.00	3.26	0.20	0.01	0.00
Ca	0.99	0.98	1.00	0.98	1.96	1.92	1.99	0.00	0.45	0.36	1.63	1.93	1.90	2.00	0.96	0.94	1.91	2.01	0.02	0.35	0.31	1.03
Na	0.01	0.01	0.01	0.01	0.31	0.28	0.04	0.05	0.60	0.71	0.39	0.36	0.27	0.03	0.04	0.03	0.04	0.00	0.02	0.54	0.68	0.00
K	0.00	0.00	0.00	0.00	0.11	0.06	0.02	0.97	0.01	0.01	0.07	0.03	0.02	0.01	0.00	0.00	0.01	0.00	0.00	0.01	0.00	0.00
Sum	4.00	4.00	4.00	4.00	15.39	15.27	15.05	5.02	5.05	5.06	15.31	15.34	15.23	15.04	4.00	4.00	8.06	8.01	9.84	5.00	5.00	3.06
XMg	0.60	0.62	0.57	0.61	0.58	0.59	0.59	-	-	-	0.88	0.76	0.78	0.83	0.81	0.75	0.98	0.33	0.75	1.00	1.00	0.09
XCa	-	-	-	-	-	-	-	0.00	0.42	0.33	-	-	-	-	-	-	-	-	-	0.39	0.32	-
XMn	-	-	-	-	-	-	-	-	-	-	-	-	-	-	-	-	-	-	-	-	-	-
Al(iv)	-	-	-	-	-	-	-	-	-	-	-	-	-	-	-	-	-	-	-	-	-	-
Al(vi)	-	-	-	-	-	-	-	-	-	-	-	-	-	-	-	-	-	-	-	-	-	-
Ahm	-	-	-	-	-	-	-	-	-	-	-	-	-	-	-	-	-	-	-	-	-	-
Prp	-	-	-	-	-	-	-	-	-	-	-	-	-	-	-	-	-	-	-	-	-	-
Grs	-	-	-	-	-	-	-	-	-	-	-	-	-	-	-	-	-	-	-	-	-	-
Spss	-	-	-	-	-	-	-	-	-	-	-	-	-	-	-	-	-	-	-	-	-	-
XFe3+	0.05	0.07	0.07	0.03	0.03	0.02	0.03	-	-	-	0.61	0.07	0.11	0.03	0.00	0.00	0.99	0.98	0.00	-	-	0.00
XPs																	0.13	0.10				

Table 2.5: Representative Amphibole Sole mineral compositions derived from electron microprobe

Sample	TLT13	TLT13	TLT13	TLT13	TLT13	TLT13	TLT13	TLT13	TLT13	TLT13	TLT13	TLT13	TLT13	TLT13	TLT13	TLT13	TLT13	TLT15	TLT15	TLT15	TLT15	TLT15	TLT15	TLT15	TLT15	TLT15	TLT15	TLT15	TLT15	TLT15
Min	Grt	Grt	Grt	Grt	Amp	Amp	Amp	Amp	Bt	Bt	Cpx	Cpx	Ep	Ms	Ms	Pl	Pl	Grt	Grt	Grt	Grt	Grt	Bt	Bt	Bt	Pl	Pl	Amp	Amp	Amp	Ep
Location	Inner Rim	Intermediate	Outer Rim	Core	Enclave	Matrix	Matrix	Matrix	Matrix	Enclave	Enclave	Enclave	Matrix	Matrix	Matrix	Matrix	Matrix	Outer Rim	Core	Inner Rim	Intermediate	Outer Rim	Matrix	Matrix	Enclave	Enclave	Matrix	Matrix	Matrix	Enclave	Matrix
SiO2	35.04	36.51	36.48	36.02	41.81	42.45	43.73	51.14	37.30	36.12	50.98	50.79	37.15	44.22	49.58	56.90	57.64	37.10	36.61	36.99	36.92	37.44	39.63	40.52	38.57	58.92	61.09	43.89	44.78	42.21	37.22
TiO2	5.91	0.04	0.06	0.14	0.36	0.20	0.62	0.17	2.69	2.96	0.08	0.07	0.02	1.75	0.15	0.00	0.00	0.01	0.09	0.02	0.08	0.02	1.68	1.25	1.59	0.00	0.00	0.46	0.16	0.13	0.05
Al2O3	17.24	20.20	20.21	19.58	12.76	11.62	12.76	2.95	14.55	14.30	0.67	0.95	22.42	11.56	28.70	26.22	25.91	20.60	19.36	20.29	20.04	20.69	15.34	15.21	15.01	26.36	24.80	12.29	11.40	14.71	22.37
FeO	8.40	13.14	15.32	6.62	19.13	17.29	21.01	14.45	19.98	19.71	12.17	12.79	12.85	18.28	1.97	0.03	0.07	13.13	6.98	12.20	6.90	14.79	13.62	13.97	14.63	0.25	0.16	17.11	14.52	14.38	12.48
MnO	23.83	22.86	18.87	33.96	0.95	1.25	0.68	1.17	0.56	0.47	1.62	1.73	0.81	0.66	0.10	0.00	0.01	22.28	33.69	23.53	31.51	19.10	0.37	0.36	0.35	0.00	0.01	0.96	1.03	0.95	0.61
MgO	0.45	0.86	1.04	0.56	6.99	9.25	5.31	13.75	7.75	8.17	10.00	9.23	0.00	8.73	3.17	0.00	0.00	1.58	0.50	1.09	0.80	0.66	12.24	13.27	12.89	0.00	0.03	8.93	11.20	9.42	0.01
CaO	8.76	6.69	7.38	3.79	11.61	11.29	9.90	12.28	1.00	0.23	23.45	23.29	22.57	4.30	0.01	8.59	8.00	4.28	2.55	4.92	3.57	6.86	0.39	0.39	0.43	8.27	6.28	8.70	11.08	10.53	22.67
Na2O	0.07	0.05	0.06	0.02	1.34	1.80	1.07	0.38	0.23	0.21	0.13	0.21	0.02	0.37	0.24	7.37	7.59	0.02	0.02	0.03	0.05	0.04	0.18	0.21	0.09	7.07	7.70	0.95	1.62	1.75	0.02
K2O	0.03	0.00	0.02	0.00	0.75	0.21	0.83	0.30	8.45	8.65	0.02	0.00	0.00	4.75	10.78	0.20	0.20	0.04	0.00	0.02	0.02	0.03	8.18	7.74	7.98	0.07	0.42	0.65	0.28	0.28	0.00
Totals	99.73	100.36	99.43	100.70	95.68	95.36	95.91	96.59	92.51	90.82	99.12	99.05	95.83	94.61	94.69	99.30	99.42	99.04	99.80	99.08	99.89	99.61	91.63	92.92	91.54	100.95	100.49	93.95	96.08	94.34	95.42
Oxygens	12	12	12	12	23	23	23	23	11	11	6	6	12.5	11	11	8	8	12	12	12	12	12	11	11	11	8	8	23	23	23	12.5
Si	2.86	2.94	2.96	2.93	6.46	6.48	6.72	7.54	2.94	2.90	1.97	1.97	3.00	3.16	3.33	2.58	2.60	3.02	3.01	3.02	3.01	3.03	3.01	3.03	2.96	2.61	2.70	6.73	7.06	7.45	3.01
Ti	0.36	0.00	0.00	0.01	0.04	0.02	0.07	0.02	0.16	0.18	0.00	0.00	0.00	0.09	0.01	0.00	0.00	0.00	0.01	0.00	0.01	0.00	0.10	0.07	0.09	0.00	0.00	0.05	0.06	0.04	0.00
Al	1.66	1.92	1.93	1.88	2.32	2.09	2.31	0.51	1.35	1.35	0.03	0.04	2.13	0.98	2.27	1.40	1.38	1.98	1.87	1.95	1.93	1.97	1.38	1.34	1.36	1.38	1.29	2.22	1.47	0.88	2.13
Fe3+	0.00	0.20	0.16	0.26	0.20	0.49	0.16	0.26	0.00	0.00	0.04	0.03	0.86	0.77	0.00	0.00	0.00	0.00	0.10	0.01	0.06	0.00	0.00	0.00	0.00	0.01	0.01	0.22	0.29	0.17	0.84
Fe2+	0.57	0.69	0.88	0.19	2.27	1.72	2.54	1.52	1.32	1.32	0.35	0.38	0.01	0.33	0.11	0.00	0.00	0.89	0.38	0.82	0.41	1.00	0.87	0.87	0.94	0.00	0.00	1.97	1.97	1.90	0.01
Mn	1.65	1.56	1.30	2.34	0.12	0.16	0.09	0.15	0.04	0.03	0.05	0.06	0.06	0.04	0.01	0.00	0.00	1.54	2.34	1.63	2.17	1.31	0.02	0.02	0.02	0.00	0.00	0.12	0.10	0.09	0.04
Mg	0.06	0.10	0.13	0.07	1.61	2.10	1.22	3.02	0.91	0.98	0.58	0.53	0.00	0.93	0.32	0.00	0.00	0.19	0.06	0.13	0.10	0.08	1.39	1.48	1.47	0.00	0.00	2.04	2.13	2.54	0.00
Ca	0.77	0.58	0.64	0.33	1.92	1.85	1.63	1.94	0.08	0.02	0.97	0.97	1.95	0.33	0.00	0.42	0.39	0.37	0.22	0.43	0.31	0.59	0.03	0.03	0.04	0.39	0.30	1.43	1.75	1.83	1.97
Na	0.01	0.01	0.01	0.00	0.40	0.53	0.32	0.11	0.04	0.03	0.01	0.02	0.00	0.05	0.03	0.65	0.66	0.00	0.00	0.00	0.01	0.01	0.03	0.03	0.01	0.61	0.66	0.28	0.28	0.16	0.00
K	0.00	0.00	0.00	0.00	0.15	0.04	0.16	0.06	0.85	0.89	0.00	0.00	0.00	0.43	0.92	0.01	0.01	0.00	0.00	0.00	0.00	0.00	0.79	0.74	0.78	0.00	0.02	0.13	0.04	0.03	0.00
Sum	7.95	8.00	8.00	8.00	15.51	15.49	15.22	15.13	7.67	7.70	4.00	4.00	8.01	7.11	7.00	5.05	5.05	8.00	8.00	8.00	8.00	7.99	7.61	7.61	7.67	5.00	4.99	15.20	15.15	15.08	8.00
XMg	0.09	0.13	0.12	0.26	0.41	0.55	0.32	0.67	0.41	0.42	0.62	0.58	0.00	0.74	0.74	-	-	0.18	0.14	0.14	0.19	0.07	-	-	-	-	-	0.51	0.52	0.57	0.11
XCa	-	-	-	-	-	-	-	-	-	-	-	-	-	-	-	0.39	0.36	-	-	-	-	-	-	-	-	0.39	0.30	-	-	-	-
XMn	-	-	-	-	-	-	-	-	-	-	-	-	-	-	-	-	-	-	-	-	-	-	-	-	-	-	-	-	-	-	-
Al(iv)	-	-	-	-	-	-	-	-	1.07	1.10	-	-	-	0.84	0.67	-	-	-	-	-	-	-	0.99	0.97	1.04	-	-	-	-	-	-
Al(vi)	-	-	-	-	-	-	-	-	0.29	0.25	-	-	-	0.14	1.61	-	-	-	-	-	-	-	0.39	0.37	0.32	-	-	-	-	-	-
Alm	0.19	0.23	0.30	0.07	-	-	-	-	-	-	-	-	-	-	-	-	-	0.30	0.13	0.27	0.14	0.34	-	-	-	-	-	-	-	-	-
Prp	0.02	0.04	0.04	0.02	-	-	-	-	-	-	-	-	-	-	-	-	-	0.06	0.02	0.04	0.03	0.03	-	-	-	-	-	-	-	-	-
Grs	0.25	0.20	0.22	0.11	-	-	-	-	-	-	-	-	-	-	-	-	-	0.12	0.07	0.14	0.10	0.20	-	-	-	-	-	-	-	-	-
Spss	0.54	0.53	0.44	0.80	-	-	-	-	-	-	-	-	-	-	-	-	-	0.51	0.78	0.54	0.73	0.44	-	-	-	-	-	-	-	-	-
XFe3+	0.00	0.22	0.15	0.57	0.08	0.22	0.06	0.15	0.00	0.00	0.11	0.08	0.99	0.70	0.00	-	-	0.00	0.22	0.02	0.13	0.00	0.00	0.00	0.00	-	-	0.10	0.13	0.08	0.99
XPs																															0.28

Table 2.6: Representative Mirsini Unit metasediment mineral compositions derived from electron microprobe

2.5 Pressure and Temperature Of Crystallization and Metamorphism

To determine the pressure (P) and temperature (T) evolution of the Tsiknias Ophiolite and metamorphic sole, conventional thermobarometry using THERMOCALC mode 2; Average P–T (Av-PT), Al in amphibole barometer, amphibole-plagioclase and Ti-in-biotite thermobarometry and where possible the garnet-Cpx thermometer (Holland and Powell, 2011; Schmidt, 1992; Anderson and Ross, 1996; Holland and Blundy, 1994; Henry et al., 2005; Powell, 1985 and Krough Ravana, 2000). Equilibrium phase diagram modelling was also performed using THERMOCALC v3.40i using dataset ds-62 (Powell and Holland, 1988; Holland and Powell, 2011; White et al., 2014a, 2014b, Green et al., 2016), to provide further constraints on peak metamorphic conditions and gain insight into the phase relations. This combined approach was performed on the plagiogranite and gabbros from the Tsiknias Ophiolite to constrain the depth of crystallization and hence provide an indication of the thickness of the ophiolite. It was also performed on high-grade amphibolites from immediately below the Tsiknias thrust (TLT10 and 17TL25), as well as the underlying meta-sediments 50–150 m structurally below (TLT1, TLT13 and TLT15). Although it is acknowledged that the timescales of transient heating and melting due to rapid slip may represent a disequilibrium process, the kinetics of rapid melting combined with elevated ambient conditions in the host-rocks (>550 °C), facilitate local equilibrium to be achieved. Thus, the conditions of the high-temperature hornblende-bearing assemblage were estimated by assuming an approach to equilibrium between coarse early brown or olive hornblende with plagioclase and with rim compositions. Analtical electron microprobe derived data are presented in Tables 2.1-2.6 with thermobarometry results in Table 2.7-2.8. For a full description of analytical procedures and overview of phase equilibria modelling please consult Appendix 1.

2.5.1 Thermobarometry

2.5.1.1 Tsiknias Ophiolite Gabbros

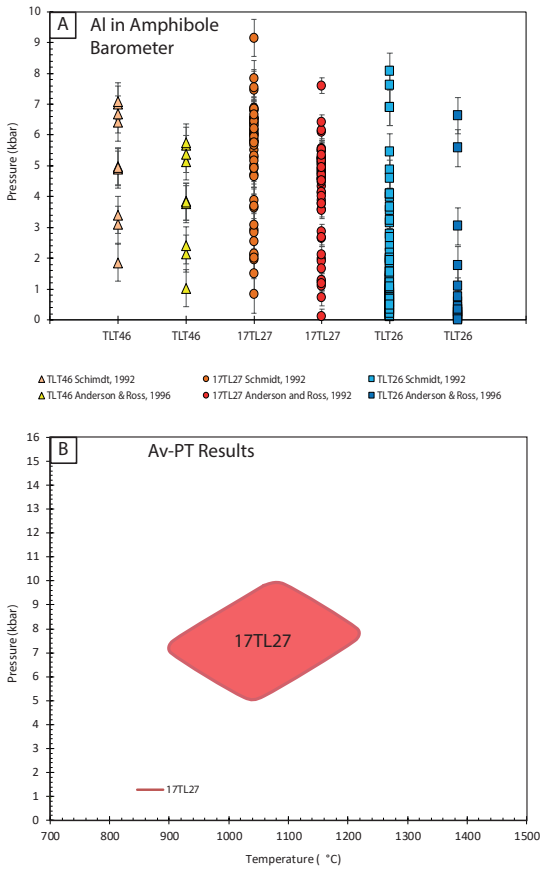


Figure 2.15: Thermobarometry results for the Tsiknias Gabbros: A) Al in amphibole barometry using both Schmidt, (1992) and Ross and Anderson, (1996) calibrations. The Anderson and Ross, (1996) calibration used the reference temperature results from independant Hbl-Pl thermometry B) Average P-T results derived from THERMOCALC

Tsiknias Ophiolite.

The Al in amphibole barometer using the calibrations of Schmidt, (1992) and Anderson and Ross, (1996) yields a range of pressures for amphibole rich gabbros ranging from 8.5 kbar to <1 kbar indicating sequential crystallization and metasomatism during decompression, with fairly consistent results, although the Anderson and Ross, (1996) calibration calculates consistently 1 kbar lower pressures for the amphiboles with the largest XAl in the M4 site. Inputing the most primitive phases (amphiboles with the largest Ti p.f.u and anorthite rich plagioglase) into Av-PT yields P–T conditions of 7.5 ± 1.9 kbar, 1059 ± 125 for gabbro 17TL27 using the end members shown in table 2.6. These independent results indicate high pressures of gabbro crystallization at high temperature, and although have large errors, a lower limit of 5 kbar can be placed on the intrusion depth within the exposed

2.5.1.2 Metamorphic Sole

All thermometers consistently demonstrate that peak metamorphic temperatures span from 600°C (e.g. TLT15) to >850 °C (TLT10) across the current exposure of the metamorphic sole and increase by 200 °C, over just ca. 150m directly below the Tsiknias Thrust. (Fig. 2.5). The hornblende-plagioclase thermometer was used in all samples and relies upon the two independent reactions: involving the Ca exchange between amphibole and plagioclase.

$$edenite + 4quartz \rightarrow tremolite + albite \tag{2.1}$$

$$edenite + albite \rightarrow richerite + anorthite \tag{2.2}$$

The second reaction is particularly useful as it does not rely on quartz, which in some amphibolite samples occurs in very low abundances, and is thus preferable in this instance. Although Holland and Blundy (1994) calibrations allow for portioning of Ca onto the M_1 and M3 sites in amphibole structure, in certain cases this can result in negative cummingtonite (D.J. Waters pers comms, 2014), because the IMA stoichiometric criterion requires <13 cations (excluding K+Na+Ca). This restricts Ca to the M4 site (e.g. Leake et al., 1997), whereas a limit of 12.9 is utilized by Holland and Blundy (1994), allowing Ca on the M_1 or M3 sites. To prevent this problem, formula recalculation was performed using spreadsheet HBPL94 (D.J. Waters pers comms, 2014) which prevents Ca underflow onto the M_1 or M3 sites and the cation total is reset to 13.

Because these reactions exhibit very small dT/dP 2–4 °C/kbar, pressure does not control the result significantly. Thus, a reference pressure of 8.5 kbar was chosen for final calculations based on Av-PT derived average pressure results (see below), yielding temperatures ranging between 910–510 °C (Ca underflow) and 890–530°C (no Ca underflow). Although there is a wide spectrum of amphibole compositions in each sample owing to variable degrees of retrogression, (Figs. 1.7 and 1.8) the peak temperature distribution determined by this method systematically reveals a decrease from 850 °C in samples TL44 and 17TL25 to 620 °C in sample TLT32, with the largest

temperature decrease directly beneath the Tsiknias Thrust. The Grt–Cpx thermometer was used exclusively for sample TLT13 and constrains the temperature to 608 ± 39 °C using the calibration of Powell, 1985 and 745 ± 52 °C using the calibration of Krough Ravna, (2000). The Ti in biotite thermometer was used in Mirsini samples TLT1, TLT13 and TLT15 and shows a range of maxium temperatures between samples from 692–617°C (TLT1-TLT15), with reported error of ± 24 °C (Henry et al., 2005) over 50 m depth interval. The Al in amphibole barometer reveals a range of pressures, however no amphibole exceeds 8.8 kbar consistently across all samples, and therefore provides a maximum estimate for the peak pressure of metamorphism. Average P–T calculations were performed for a range of water activities from 0.7–1.0, and fluid absent conditions and the results are plotted in Fig. 2.21 and Table 2.4 with activities of solid-solution end members calculated using AX (Holland, 2009). The results show that peak metamorphic pressure doesn't vary with structural position on the metamorphic sole. Although there are substantial errors with some P–T estimates (± 2 kbar, ± 100 °C), they consistently overlap between 6.5 and 9 kbar across the sole, implying the sole is affected by just a temperature gradient. The thermometry results also reveal that the temperature gradient is not linear and appears to get steeper within 50 m of the Tsiknias Thrust, where an apparent temperature difference of at least 150°C occurs.

2.5.2 Equilibrium Phase Diagrams

Equilibrium phase diagrams (pseudosections) were constructed over a wide range of pressures and temperatures. Due to reasonably high spessartine contents in garnets in meta-sediments, modelling of meta-sediments was performed in the MnO–Na_2O–CaO–K_2O–FeO– MgO–Al_2O_3–SiO_2–H_2O–TiO_2–O (MnNCKFMASHTO) system with dataset-62 using the White et al., (2014a, b) activity composition relations for the MnO system and the use of the omphacitic–clinopyroxene and amphibole activity–composition relations of Green et al., (2016). Whereas mafic rocks were modelled in the MnO free system (NCKFMASHTO) using the Green et al., (2016) activity-models for partial melting in mafic rocks. The pure phases andalusite, kyanite, sillimanite, rutile, quartz,

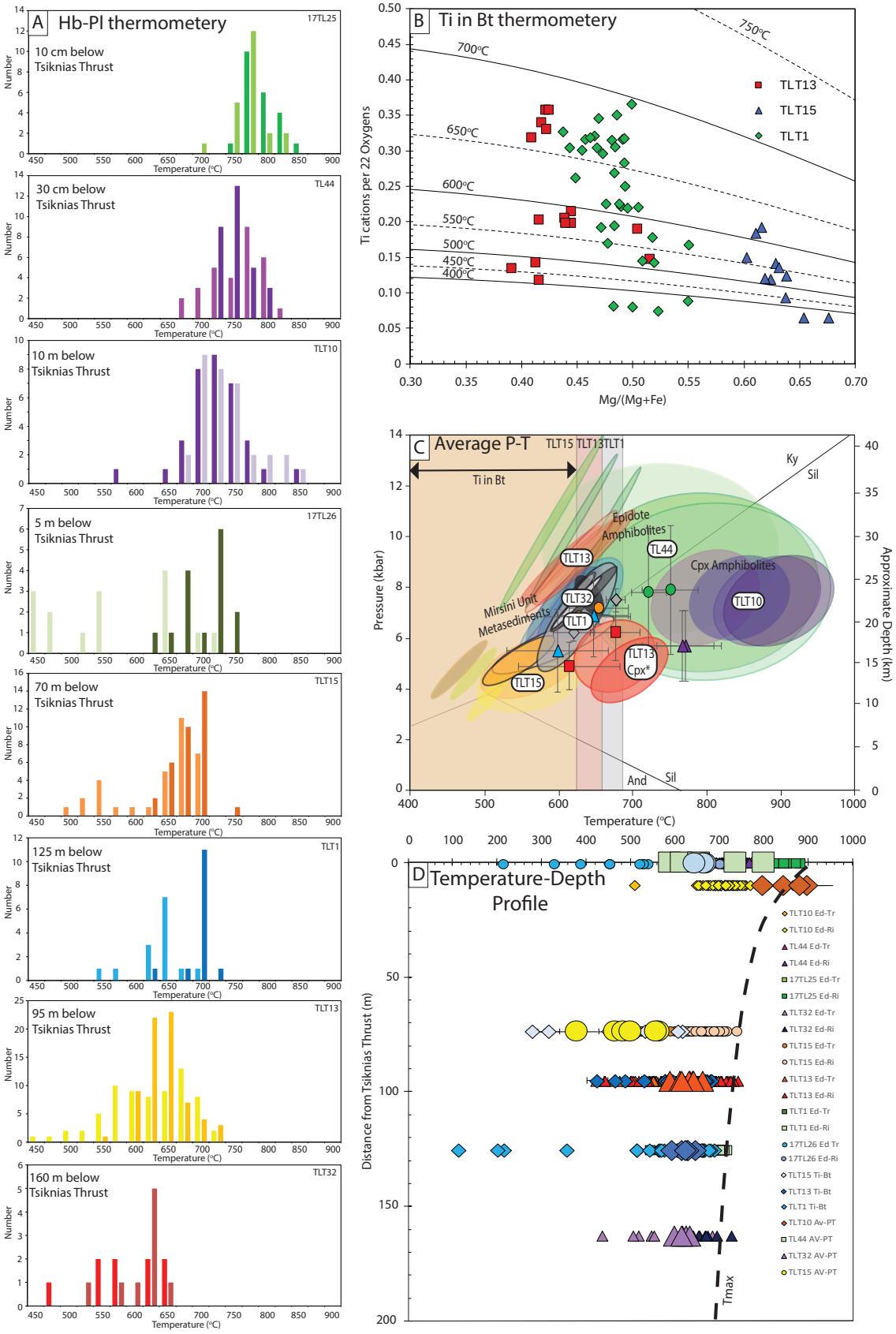


Figure 2.16: Continues on next page

Figure 2.16: Summary of thermobarometry results of the metamorphic sole: A) Hb-Pl temperature distributions across samples arranged in order of structural depth, B) Ti in Bt thermometry for metasediments from the Mirsini Unit, C) THERMOCALC Average *P-T* results with conventional thermobarometry.

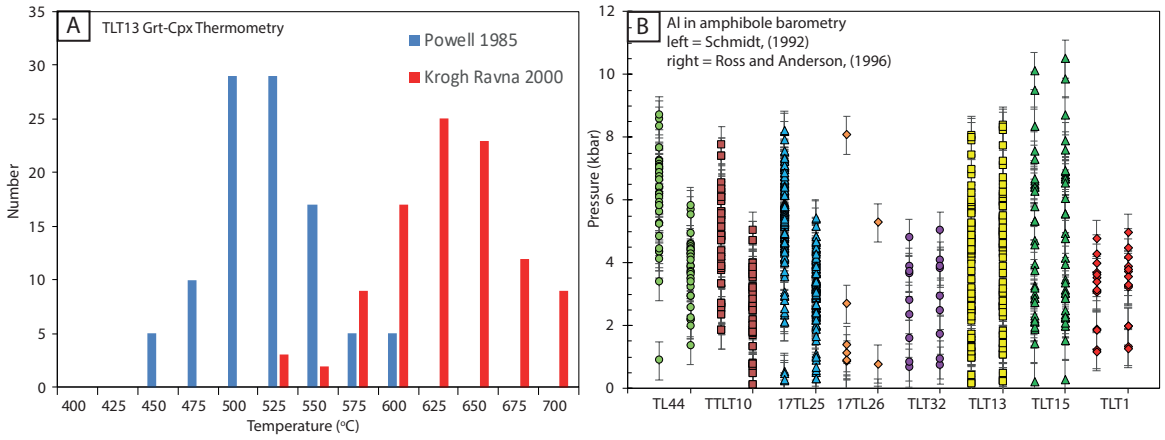


Figure 2.17: Thermobarometry continued: A) Grt-Cpx thermometer temperature distributions using a perturbed Monte-Carlo method to the original electron microprobe Grt and Cpx analysis (EMPA) for sample TLT13, B) distribution of pressures derived from the Al in amphibole barometer of Schmidt, (1992) and Anderson and Ross, (1996)

and H_2O were considered in all cases.

2.5.2.1 TLT63 (Plagiogranite)

An equilibrium phase diagram for sample TLT63 was constructed using the bulk rock composition derived from X-Ray fluorescence (XRF) (Table 2.9) converted into molar oxide % with the molar proportion of H_2O for the solidus to be just super saturated (4%) and FeO and O determined from the ferrous to ferric iron proportions. The phase diagram shows large areas of *P-T* space without a change in variance at low pressures and supra-solidus conditons, However, the appearence of magmatic epidote is constrained to the top left of the diagram. The intersection of epidote with the solidus occurs at ca. 8.5 kbar and thus constrains the minium crystallization depth of the plagiogranite, with the assemblage Pl + Qtz +Ep + Aug + ilm + Liq. Although no augite occurs in the sample it is likely this broke down to produce chlorite and muscovite alteration products.

2.5.2.2 TLT10 (Anatectic amphibolite)

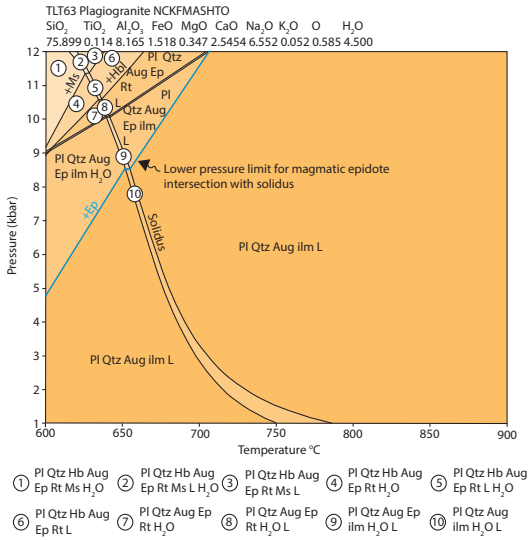


Figure 2.18: Equilibrium phase diagram of plagiogranite TLT63

An equilibrium phase diagram of TLT10 (Fig. 2.19 A and B) shows relatively complicated phase relationships at sub-solidus temperatures but simple topology supra-solidus. The observed peak assemblage Hb + Aug + Pl + ilm + Qtz + Liq lies over a wide range of P–T conditions 750 – 900 °C and 4–10 kbar along a positive P–T gradient, without a change in variance. Contours for y(amp) = XAl in M2 site and c(pl) = XCa show that aluminum content in amphibole increases with increasing pressure and increases in anorthite content with increasing temperature. Intersection of these isopleths (y(amp) = 0.28–0.35 corresponding to an c(pl) in plagioclase = 0.41 provide a P–T constraint of 6–9 kbar at 850–900 °C for peak metamorphic conditions corresponding to melt fraction of 11–12% in the phase field Hb + Aug + Pl + ilm + Qtz + Melt, consistent with the observed assemblage. The range of XAl in M2 site in amphibole suggest the rock decompressed whilst at high temperature, although the lack of Opx (predicted in the bottom right corner of the diagram) in the sample indicates it must have also cooled assuming it minated at least local equilibrium throughout. The range in observed data could also indicate the rock experienced disequilibrium. Sphene is predicted at lower temperatures indicating it is a retrograde phase. The appearance of garnet at 10.5–11 kbar provide an upper constraint for the P–T conditions. These predictions agree with thermobaromery results, although have a large uncertainty.

2.5.2.3 17TL25 (Anatectic amphibolite)

A calculated phase diagram of 17TL25 anatectic amphibolite (Fig. 2.19 C and D) reveals the observed peak assemblage Hb + Aug + Pl + ilm + Melt occurs over a large area of P–T space between 4–11 kbar and 750–900 °C, but is limited in pressure by the stability of garnet beyond 12 kbar. Consideration the intersection of y(amp) = 0.27–0.30 and c(pl) = 0.40–0.42 isopleths provide a further improved P–T constraint of ca. 840–890 °C at 5.6–7 kbars and corresponds to a similar melt fraction of 10–12% in the observed assemblage phase field, giving a good match with observations. However, at peak conditions, the models predict more augite and less amphibole compared to that observed, although this can be easily explained by retrogression and recrystallization during shearing causing augite to breakdown, it also may represent a disequilibrium process.

2.5.2.4 TLT1 (Mirsini Unit Metapelite)

The phase diagram for TLT1 (Fig. 2.20 A and B) predicts the observed assemblage Grt + Bt + Ms + Pl + ilm + Qtz + Liq in a small field directly on the water saturated solidus at 8.5 kbar and 680 °C and with a few degrees Celsius of the muscovite out reaction, consistent with <1% observed muscovite in the assemblage. The garnet in reaction is constrained to >640 °C and therefore provides a lower temperature bound. Consideration of garnet grossular (XCa) and pyrope (XMg) isopleths provides tight P–T constraints for garnet core growth (Prp = 0.02 and Grs = 0.19) at 7.7 kbar and 660 °C immediately after crossing the the garnet producing reaction, and garnet rims (Prp = 0.04 and Grs = 0.24) at 8.7 kbar, 680 °C in the phase field Grt + Bt + Pl +Ms + ilm + Hb + Liq. These results suggest garnet grew along a path of both increasing pressure and temperature over a very limited P–T range and explains the rare occurrence of garnet at outcrop. The occurrence of relict epidote, commonly breaking down to muscovite and plagioclase in the rock also strongly suggests the rock underwent a clockwise prograde P–T path. These P–T constraints are consistent with thermobarometry results and this pressure constraint provides the best estimate for

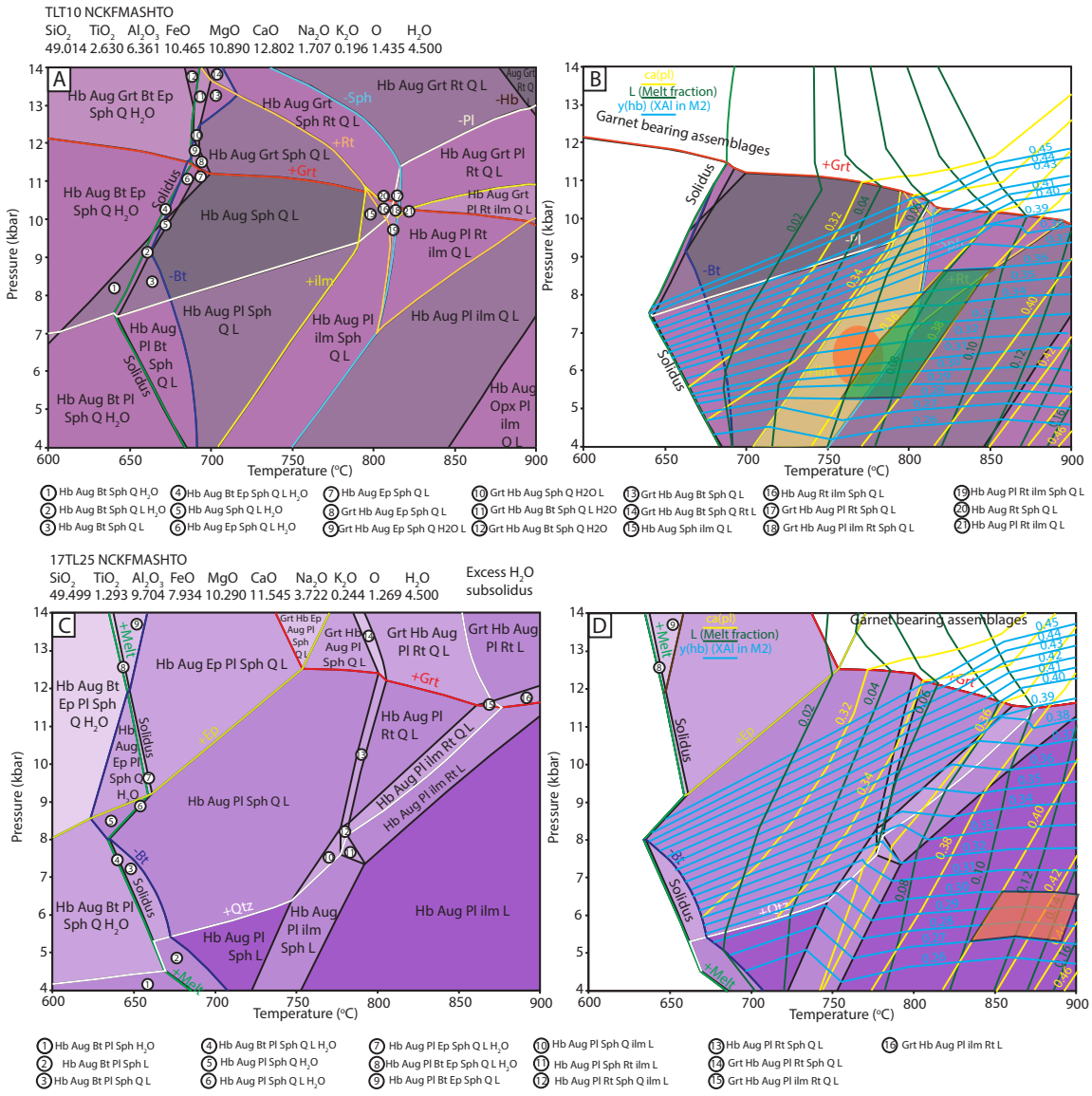


Figure 2.19: Equilibrium phase diagrams of anatectic amphibolite samples TLT10 and 17TL25: A) TLT10 phase relationsions, B) overlaid isopleths for y(hb), c(pl) and mode of melt for TLT10, C) 17TL25 phase relationsions, D) 17TL25 overlaid y(hb), c(pl) and mode of liquid (melt) isopleths.

the depth of metamorphism in the sole, and suggests at least under water saturated conditions, it started to melt. The presence of magnetite in the matrix, suggest its retrograde path involved decompression, whilst still at high temperature.

2.5.2.5 TLT13 (Mirsini Unit Meta-chert)

A phase diagram of this meta-chert (Fig. 2.20 E and F) predicts the peak assemblage Grt + Aug + Kfs + Pl + Hb + Bt + Qtz (+ Liq) occurs at <8.5 kbar at 680 to 750 °C and the occurrence of augite provides a minimum temperature constraint of 680–700 °C along a steep positive P–T slope Although garnets only show slight zoning associated with high Spessartine contents from core to rim, intersection of garnet rim grossular (Grs) and pyrope (Prp) isopleths of 0.26–0.28 and 0.06 respectively, provide further constraints on the conditions of peak metamorphism of ca. 7.0 ± 1.0 kbar and 715 ± 15 °C. These temperatures are in overall agreement with the Grt–Cpx and Hbl–Pl, and Ti in Biotite thermometry results. Unfortunately, due to the small and relatively un-zoned nature of the garnets, no additional prograde P–T information could be determined. Although lower pressure than TLT1 it is likely this pressure estimate does not represent peak pressures but was affected by re-equilibration during decompression owing to their small size (<0.3 mm; e.g. Caddick et al., 2010).

2.5.2.6 TLT15(Mirsini Unit Meta-chert)

The calculated pseudosectionfor TLT15 (Fig. 2.20 C and D) predicts garnet to be stable at all pressures and temperatures owing to the enriched Mn content associated with it being derived from a deep sea pelagic protolith. There are complicated phase relations at low temperatures associated with the appearance and breakdown of chlorite, epidote, muscovite, biotite and solid solutions between glaucophane and hornblende. However, at high temperatures the phase relations are simple, and the peak observed assemblage Grt + Hb + Bt + Pl + Qtz + Sph + Rt (+ Liq) plots over a wide range of P–T space between 5–12 kbar at >690 °C, which is in agreement with the independent thermometry results. Consideration of garnet outer rim isopleths of grossular (Grs) = 0.29–0.30 and pyrope (Prp) = 0.06, yields precise P–T constraints of ca. 8.7 ± 0.8 kbar and 705 ± 10 °C, and coincides with 8% volume garnet. This plots in the observed assemblage field, and therefore indicates peak metamorphic conditions was associated with the onset of water saturated melting, producing up to 3% melt volume. This

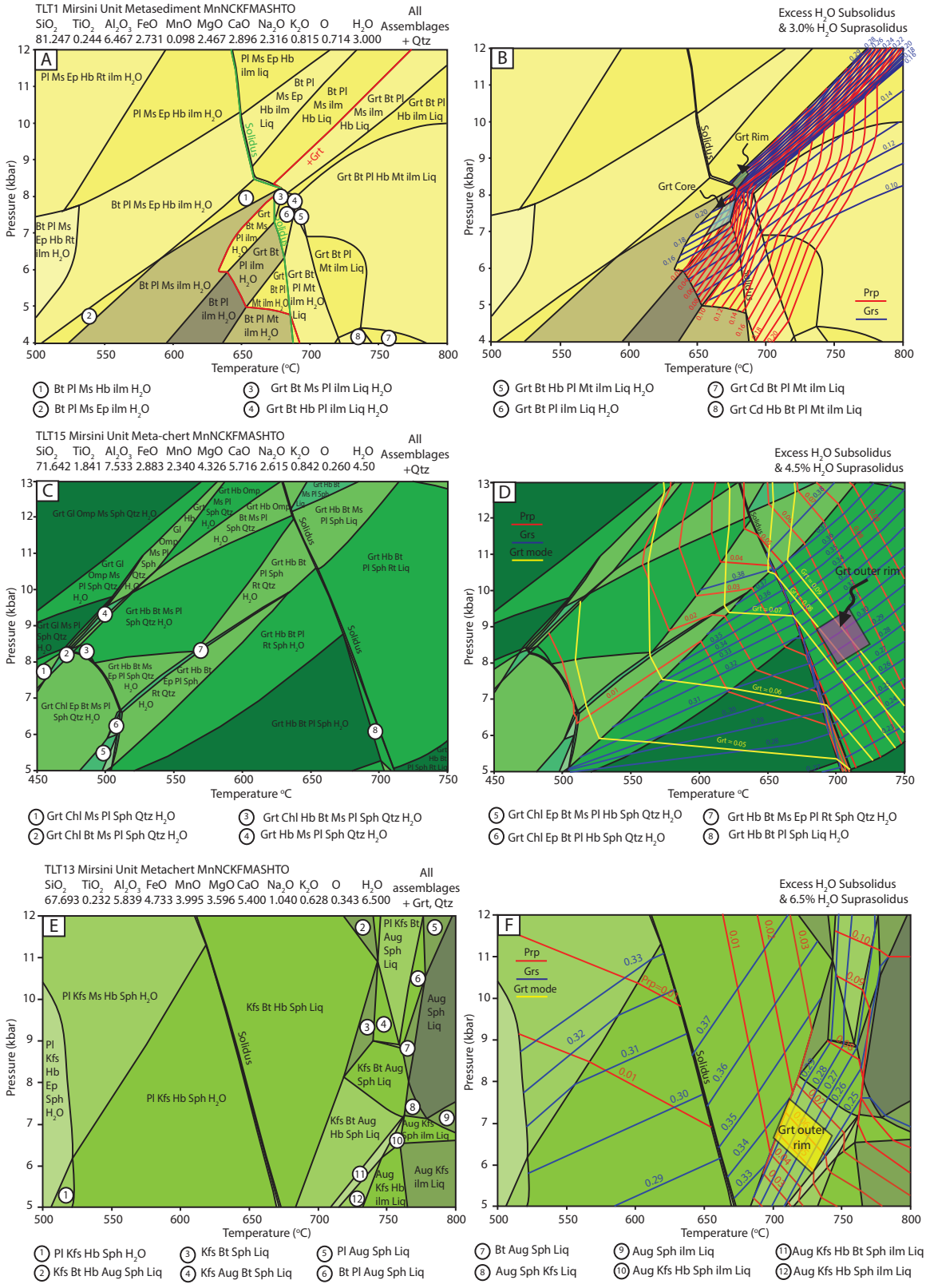


Figure 2.20: Mirsini Unit pseudosections (phase diagrams) for samples TLT1, TLT15 and TLT13: A) TLT1 phase relations with Grt in reaction (red line), B) Overlaid garnet pyrope and grossular composition isopleths, showing the garnet core and rim intersection (shaded polygons), C) TLT15 phase relations with D) Overlaid garnet grossular and pyrope isopleths, E) TLT13 phase relations with F) Overliad garnet composition isopleths

pressure estimate overlaps with TLT1 and therefore verifies that peak metamorphism in the Mirsini Meta-sediments occurred at 25 km depth, and therefore constrains the pressures of the amphibolites lying 50–150 m structurally above, assuming no considerable movement occurred between these rocks.

Tsiknias Gabbro Thermobarometry			Thermocalc Average P-T								Al in Amp Barometry	
Sample	GPS Location	Description	Endmembers	Temperature (°C)	S.D. (T)	Pressure (kbar)	S.D. (P)	Corr	sigfit	no. reactions	P max Schmidt, (1992)	P max Ross & Anderson, (1996)
17TL27	N37.61052, E25.24061	Hbl-Cpx-Pl-Sph-ilm-Qtz	tr-fact-ts-parg-an-ab-di-hed-cats-jd-ilm-sph-q-H2O	1059	125	7.5	1.9	0.22	1.24	6	9.14 ± 0.6	7.60 ± 0.6

Table 2.7: Tsiknias Gabbro thermobarometry results

2.5.2.7 Summary of *P–T* results

The integrated equilibrium phase diagram modelling and independent thermobarometry show that the gabbros and plagiogranite within the Tsiknias Ophiolite crystallized at 8.5 kbar pressure, equating to approximately 25 km depth in oceanic lithosphere. This is consistent with the occurrence of magmatic epidote and rutile within the plagiogranite, which constrains its emplacement depth to at least 8.5–9 kbar. This depth is much greater than any other exposed ophiolite plagiogranite globally which are typically emplaced at ca. 2 kbar equating to 7-8 km depth, however the field relations (and geochemistry) suggest it was emplaced along the Moho Transition zone adjacent to gabbros during the formation of oceanic crust and is discussed later. A resolvable temperature gradient of approximately 1000 °C/km also occurs throughout the metamorphic sole at approximately 8.5 kbar, although some slightly lower pressures are recorded possibly due to thermal re-equlibration. Anatectic amphibolites record temperatures of at least 850 °C directly under the Tsiknias thrust, and experienced at least 11–12% melting, and show a range of pressures from 9–6 kbar, implying they decompressed at high temperature. The Mirsini Unit metasediments also record high-temperatures of up 600–715 °C, also at 8.5 kbar although significantly lower temperature than the amphibolites 50–150 m directly above them. The, rocks, underwent a clockwise prograde *P–T* path as indicated by lower pressure phases overprinting

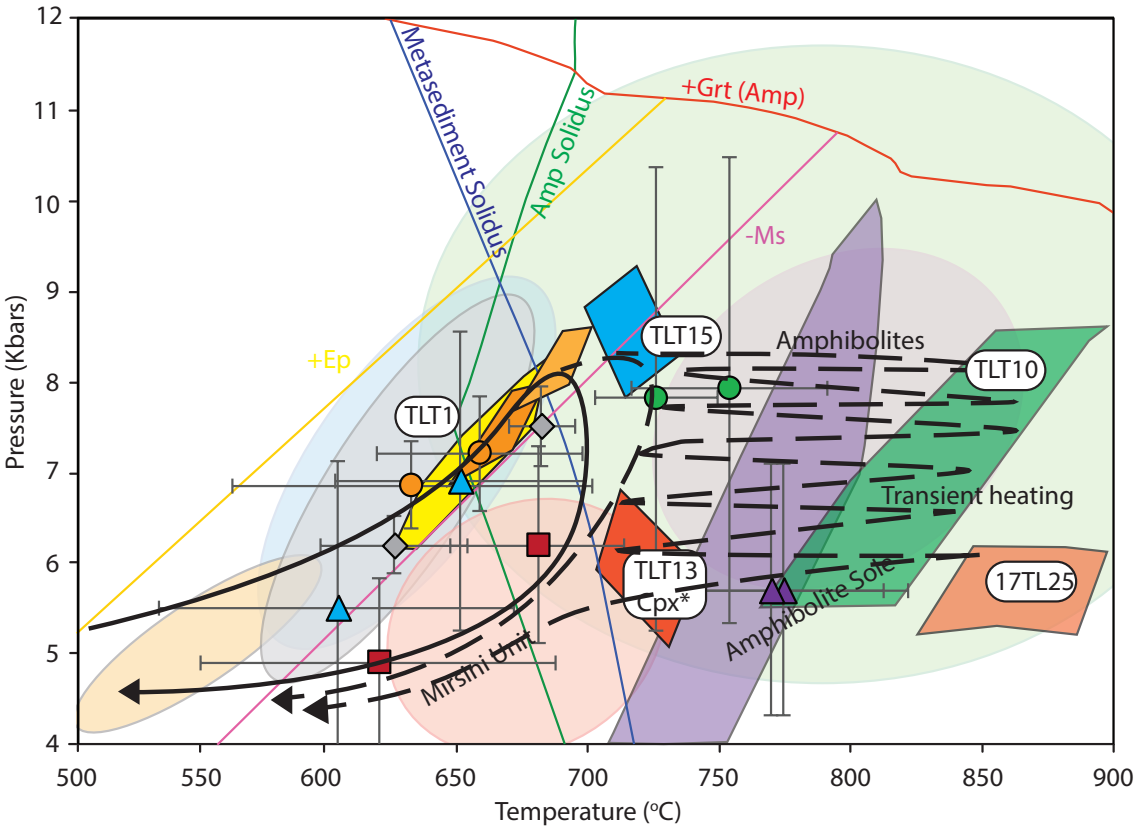


Figure 2.21: Summary P-T results overlaying thermobaromtery with pseudosection results. This clearly shows agreement between the results of the two methods and that although there are large pressure uncertainities, the temperatures systematically increase by ca. 300°C from the bottom to top of the expose sole, at around the same pressure of ca. 8.5 kbar (best constrained by TLT1)

higher pressure, peak metamorphic phases, and increases in pressure and temperature during garnet growth (TLT1). In summary the consistent pressures of ca. 8.5 kbar recorded in both the ophiolite and underlying metamorphic sole suggest the current exposed structural section of the Upper Unit represented a subduction zone interface at 25–28 km depth at the time of obduction.

Sample	Tsiklauss Sole Thermobarometry Results Unit	GPS Location	Description	Endmembers	Notes	Thermocalc Average P-T Temperature (°C)	S.D. (T)	Pressure (kbar)	S.D. (P)	Corr	Ti in Bt Temp Range (°C)	Temp (Edenite-Tremolite) (Ca underflow)	Temp (Edenite-Richterite) (Ca underflow)	Hb-Pl Thermometry Temp (Edenite-Tremolite) (No Ca underflow)	Temp (Edenite-Richterite) (No Ca underflow)	Grt-Cpx Thermometry T (Powell, 1985)	T (Krough Ravana, 2000)	Avg Pressure (from Temp) Temp (°C)	Pressure (kbar)	S.D (kbar)	Al in Amp Barometry P (Schmidt, 1992)	P Max (Anderson, 1996)	P Max Ross & Anderson, (1996)
TLT1	Mirsiui	N37.58585 E25.21225	Metasedimont/ Metavolcanic: Grt-Hb-Bt-Ms-Pl-Qtz-Sph-Ilm-Ep-CC	Prp-Alm-Fact-Ts-Parg-Phl-Anr-Mu-Pa-Au-Ab-Cz-Qtz-Sph-Ilm-H2O (CO2-CC)	with CO2 0.1	647	12	7.6	0.6	-0.628													
					with CO2 0.2	629	40	7.4	1.1	0.970								620	6.2	0.32			
					with CO2 0.3	617	40	6.7	1.1	0.968								640	6.7	0.36			
					pure H2O	652	37	6.5	0.8	0.958								660	7.1	0.4			
					Fluid absent	595	65	5.8	0.9	0.861								680	7.5	0.45			
					a(H2O)=0.9	626	42	6.8	1.7	0.836								700	7.9	0.31			
TLT13	Mirsiui	N37.58335 E25.20900	Metachert / Metavolcanic: Grt-Cpx-Hb-Bt-Pl-Qtz-Ms-Sph-Ilm-Ep-CC	Tr-Fact-Parg-Di-Hed-Jad-Co-Ep-Prp-And-Au-Ab-East-Ms-Feel-Pa-Qtz-H2O-Sph-Ilm-H2O (CC-CO2)	with CO2 0.1	582	22	8.1	0.9	0.947								580	4.2	0.85			
					with CO2 0.2	627	19	9.2	0.8	0.920	419-676	415-715 (595 ± 71)	496-636 (645 ± 40)	438-717 (610 ± 60)	545-723 (631 ± 32)	535 ± 30	655 ± 38	600	4.6	0.88	8.06 ± 0.6	8.38 ± 0.6	
					with CO2 0.3	656	19	10.0	0.8	0.900								620	5	0.92			
					pure H2O	634	54	9.2	1.5	0.953								640	5.4	0.97			
					a(H2O)=0.9	625	51	9.1	1.4	0.952								660	5.8	1.02			
					a(H2O)=0.7	604	44	8.9	1.2	0.951								680	6.2	1.09			
					with CO2 0.01	635	48	9.0	1.2	0.994								700	6.6	1.05			
					Pure H2O	609	31	8.3	0.9	0.937								720	6.9	1.23			
TLT15	Mirsiui	N37.58179 E25.21093	Metachert/ Metavolcanic: Grt-Hb-Bt-Qtz-Ep-Sph-Ilm-CC	Prp-Gr-Alm-Phl-Anr-Au-Ab-Tr-Fact-Ts-Sph-Ilm-Qtz-H2O (CC-CO2)	with CO2 0.1	466	30	5	0.9	0.964	289-617	484-709 (629 ± 66)	621-739 (680 ± 30)	484-697 (626 ± 64)	621-738 (667 ± 24)	-	-	600	5.9	0.42	10.11 ± 0.6	10.51 ± 0.6	
					with CO2 0.2	484	25	4.6	0.8	0.956								620	6.3	0.44			
					with CO2 0.01	380	45	5	1.6	0.970								640	7.1	0.56			
					with CO2 0.3	501	21	3.6	0.7	0.920								680	7.4	0.63			
					ure H2O	563	56	4	0.9	0.238								700	7.8	0.71			
					a(H2O) = 0.9	558	56	4.2	0.9	0.234								720	8.2	0.78			
TLT32	Amphibolite Sole	N37.57360 E25.23039	Metabasalt/ Metagabbro: Cpx-Hb-Pl-Qtz-Ep-CC-Sph-Ilm	Di-Hed-Jd-An-Ab-Tr-Fact-Ts-Parg-Gl-Ilm-Geik-Sph-Qtz-H2O (CC-CO2)	with CO2 0.1	592	35	7.5	1.5	0.987	-	431-678 (572 ± 74)	591-722 (655 ± 34)	455-681 (584± 63)	520-641 (600 ± 33)	-	-	600	5.5	1.63	4.8 ± 0.6	5.11 ± 0.6	
					with CO2 0.2	610	32	7.0	1.3	0.986								620	6.1	1.55			
					with CO2 0.3	619	33	6.7	1.4	0.985								640	6.7	1.6			
					pure H2O	628	47	7.1	1.7	0.676								660	7.2	1.65			
					X(H2O) 0.7	608	42	6.9	1.5	0.693								680	7.6	1.77			
TLT10	Amphibolite Sole	N37.60782 E25.23707	Metagabbro: Cpx-Pl-Qtz-Ep-Rhodngite-Sph-Ilm-Rt-Melt	Tr-Fact-Ts-Parg-Di-Hed-Jd-An-Ab-Sph-Ilm-Rt-Qtz-H2O	pure H2O	897	59	7.5	1.4	0.270	-	511-847 (709 ± 52)	655-866 (732 ± 47)	396-844 (701 ± 73)	467-739 (617 ± 66)	-	-	740	5.6	1.53	7.75 ± 0.6	5.01 ± 0.6	
					a(H2O)=0.7	844	54	7.6	1.3	0.241								760	5.7	1.38			
					a(H2O)=0.9	881	58	7.5	1.4	0.262								780	5.7	1.4			
					a(H2O)=0.5	798	59	7.6	1.5	0.208								800	5.8	1.41			
TL44	Amphibolite Sole	N37.60987 E25.23942	Metabalt: Hb-Pl-Sph-Sp-Ilm-Rt-Qtz-Melt	Tr-Fact-Ts-Parg-Ar-Ab-Sph-Qtz-Ilm-Ri-H2O	with CO2 0.1	590	56	10.5	2.8	0.995								700	7.7	2.31			
					with CO2 0.2	617	49	10.2	2.4	0.994	-	742 ± 89 (661-803)	704-799 (740 ± 23)	688-794 (741 ± 32)	623-758 (683 ± 30)	-	-	720	7.8	2.37	8.69 ± 0.6	5.8 ± 0.6	
					with CO2 0.3	655	46	9.9	2.3	0.993								740	7.9	2.45			
					pure H2O	802	132	7.9	2.8	0.019								760	7.9	2.55			
					a(H2O)=0.5	737	130	9.5	2.7	-0.018								780	8	2.68			
					a(H2O)=0.9	792	129	8.2	2.8	0.018								800	7.9	2.83			
17TL25	Amphibolite Sole	N37.60987 E25.23942	Mylonitized Metabasalt: Hb-Pl-Ilm-Sph-Melt-Mag	Tr-Fact-Parg-Di-Hed-Cz-Al-An-Qtz-H2O	pure H2O	671	44	8.2	1.2	0.857	-	522-832 (688 ± 74)	764-884 (834 ± 24)	741-840 (779 ± 23)	683-820 (759 ± 27)	-	-	600	6.6	0.74	8.22 ± 0.6	5.4 ± 0.6	
					a(H2O)=0.9	667	44	8.3	1.2	0.858								650	7.7	0.58			
					a(H2O)=0.7	658	43	8.5	1.2	0.859								700	8.9	0.62			
					a(H2O)=0.5	645	42	8.7	1.2	0.860								750	10	0.86			
17TL26	Amphibolite Sole	N37.60987 E25.23942	Mylonitized Metabasalt: Hb-Pl-Ilm-Sph-Melt-Mag	-	-	-	-	-	-	-	-	216-715 (535 ± 133)	604-736 (690 ± 34)	216-715 (536 ± 126)	476-714 (657 ± 56)	-	-	-	-	-	8.07 ± 0.6	5.28± 0.6	

Table 2.8: Sole thermobarometry results

2.6 Trace Element Geochemistry

Samples of amphibolite, gabbro and plagiogranite were crushed into a <80 μm powder at the Natural Environment Geosciences Laboratory (NIGL) at the British Geological Survey, Keyworth, and the Department of Earth Sciences, University of Oxford, using standard techniques, and a steel crucible. These were analysed by XRF at the Department of Earth and Environment, Franklin and Marshall College, Lancaster, Pennsylvania, USA, using the procedures described in the Appendix 3.

A spectrum of trace elements was collected on a Perkin Elmer 6100DRC Quadrupole inductively coupled plasma mass spectrometer (ICP-MS) with a dynamic reaction cell at the Department of Earth Sciences, University of Oxford. Samples were crushed using the same techniques, weighed, diluted and digested. Detailed sample handling and preparation procedures are described in Appendix 3. Reported precision is better than ± 5% (2.S.D), and the results are presented in Table 2.9, and as spider diagrams and discrimination plots in Figs. 2.22 to 2.24. The new geochemical data (n = 10) are combined with those presented by Stourati et al., (2017) and Katzir et al., (1996) (total n = 53).

2.6.1 Results

Samples were screened and plotted on the igneous rock classification diagram of Pearce (1996), based on the immobile element ratios of Zr/Ti and Nb/Y. Spiderdiagrams are used in Fig. 2.22 to illustrate the range in geochemical signatures normalized to normal mid-ocean ridge basalts (N-MORB) values from Sun and McDonough, (1989). In the Figs. 2.22a-b (N-MORB normalized) the full suite of elements are plotted including the large ion lithophile elements (Sr, K, Rb, Ba on the left-hand side of the diagrams). These are mobile in water to some extent, and their concentrations may have been affected by secondary alteration processes in the rocks. All samples have loss on ignition (L.O.I.) contents less than 2 wt.%, indicating they have not been altered. All the elements were plotted versus L.O.I. (of Table 2.9) and show no correlation that might

Rock type	Gabbro*	Gabbro*	Gabbro	Gabbro	Plagiogranite	Plagiogranite	Amp Sole	Amp sole	Amp Sole	Amp Sole
Specimen	TLT-26	17TL-23	17TL-24	17TL-27	TLT-63	17TL-35	TLTN-10	TLT-7	TLTN-12	17TL-26
XRF data (weight %)										
SiO2	50.36	48.69	56.41	49.24	74.89	73.04	55.14	56.13	49.25	61.03
TiO2	0.14	0.12	0.57	1.39	0.15	0.23	0.54	0.64	1.71	0.00
Al2O3	16.70	18.57	15.07	16.26	13.67	13.36	18.41	17.72	16.38	23.61
Fe2O3T	7.61	6.02	7.54	10.14	1.99	3.10	5.09	6.64	10.49	0.47
MnO	0.16	0.12	0.25	0.19	0.02	0.04	0.14	0.16	0.18	0.02
MgO	11.21	9.80	7.03	6.55	0.23	0.48	4.74	4.50	6.87	0.34
CaO	10.71	14.93	8.25	11.42	2.26	4.13	9.55	9.28	10.72	5.69
Na2O	3.01	1.38	4.11	3.56	6.67	5.67	5.51	4.53	3.82	8.51
K2O	0.19	0.09	0.32	0.53	0.08	0.06	0.40	0.53	0.38	0.66
P2O5	0.03	0.02	0.07	0.28	0.03	0.07	0.13	0.14	0.19	0.02
Total	100.12	99.74	99.62	99.56	99.99	100.18	99.65	100.27	99.99	100.35
LOI	3.77	1.49	1.70	1.39	0.76	0.82	2.36	1.51	2.37	1.10
FeO	5.03	3.95	5.39	6.81	0.41	0.48	3.06	2.57	6.42	0.19
Fe2O3	2.02	1.63	1.55	2.57	1.53	2.57	1.69	3.78	3.36	0.26
XRF data (ppm)										
Rb	4.1	1.6	6.8	3.9	1.0	1.0	16.1	25.6	24.4	25.6
Sr	59	118	135	763	113	156	229	245	237	267
Y	9.7	5.0	41.6	29.9	69.4	50.4	18.9	32.9	45.4	0.7
Zr	12	11	67	117	157	116	46	62	133	13
V	150	189	145	226	23	51	127	155	289	3
Ni	145	141	323	146	25	19	79	106	106	4
Cr	301	396	551	369	60	45	175	184	231	14
Nb	Below DL	Below DL	3.5	22.0	1.4	0.6	Below DL	10.7	0.7	Below DL
Ga	10.9	11.8	14.4	16.8	18.1	19.8	10.9	16.0	17.1	11.7
Cu	31	40	35	58	17	15	84	62	64	42
Zn	43	34	138	110	8	8	72	66	78	14
Co	43	50	51	60	Below DL	22	17	24	40	52
Ba	15	Below DL	92	77	19	29	20	44	23	13
La	9	11	19	18	17	18	10	13	7	13
Ce	8	9	45	36	25	21	15	16	11	8
U	Below DL	Below DL	Below DL	Below DL	1.2	0.5	Below DL	0.6	Below DL	Below DL
Th	Below DL	Below DL	6.6	Below DL	7.3	3.1	Below DL	4.7	Below DL	Below DL
Sc	36	41	19	34	6	8	19	22	35	Below DL
Pb	Below DL	Below DL	3	Below DL	Below DL	Below DL	5	Below DL	Below DL	5
K	1577	747	2656	4400	664	498	3321	4400	3155	5479
Ti	839	719	3417	8333	899	1379	3237	3837	10251	0
P	131	87	305	1222	131	305	567	611	829	87
ICP-MS data (ppm)										
V	157.6	186.3	128.5	213.0	18.7	42.7	115.1	149.3	262.0	2.5
Cr	320.4	546.1	528.8	385.3	6.9	33.8	169.6	173.5	234.3	6.4
Mn	1138.7	802.9	1725.9	1246.5	83.4	156.6	931.6	1115.6	1190.2	81.6
Co	41.3	55.7	45.3	59.4	1.0	23.6	21.9	25.8	36.0	58.8
Ni	130.7	126.2	278.7	152.2	15.2	12.6	63.4	89.2	97.9	3.1
Cu	16.2	29.7	14.1	41.2	3.4	2.2	63.2	39.6	45.9	23.7
Zn	35.7	26.9	121.7	105.1	3.0	3.2	67.7	63.1	73.3	8.2
Rb	3.6	0.7	7.1	2.5	1.1	1.0	13.7	24.6	26.3	15.3
Sr	62.7	105.4	119.8	715.0	90.0	136.6	221.7	258.9	243.4	270.7
Cd	0.2	0.1	0.1	0.2	0.0	0.1	0.3	0.2	0.2	0.1
In	0.1	0.1	0.1	0.1	0.1	0.1	0.1	0.1	0.1	0.1
Ba	15.6	6.9	85.6	69.1	15.0	10.1	30.0	34.8	20.4	18.3
Sc	31.0	31.2	18.2	33.6	15.9	15.5	17.2	24.1	36.4	0.2
Y	4.2	2.5	25.4	21.8	46.0	37.8	12.9	24.6	37.1	0.3
Cs	0.4	0.1	0.6	0.4	0.1	Below DL	3.3	4.2	3.5	0.6
La	0.5	0.1	20.3	17.9	7.7	7.0	1.4	6.7	4.6	Below DL
Ce	1.3	0.6	53.8	34.7	19.1	16.9	4.8	14.8	14.4	0.3
Pr	0.2	0.1	4.7	4.2	2.8	2.4	0.9	2.1	2.5	0.0
Nd	0.7	0.3	18.2	17.4	13.9	11.7	4.4	9.1	13.1	Below DL
Sm	0.3	0.2	4.1	3.9	4.7	3.9	1.6	2.8	4.3	0.1
Eu	0.2	0.2	1.1	1.5	1.3	1.4	0.6	0.9	1.6	0.0
Gd	0.6	0.4	4.1	4.3	6.2	5.1	2.1	3.6	5.8	0.1
Tb	0.1	0.1	0.7	0.7	1.2	1.0	0.4	0.7	1.1	0.0
Dy	0.8	0.5	4.4	4.3	7.9	6.6	2.3	4.3	6.8	0.1
Ho	0.2	0.1	0.9	0.8	1.7	1.4	0.5	0.9	1.4	0.0
Er	0.5	0.3	2.9	2.6	5.4	4.4	1.5	2.8	4.2	0.0
Tm	0.1	0.0	0.4	0.4	0.7	0.6	0.2	0.4	0.6	Below DL
Yb	0.5	0.3	2.7	2.3	4.5	3.9	1.2	2.6	3.6	0.0
Lu	0.1	0.1	0.4	0.3	0.7	0.6	0.2	0.4	0.5	0.0
Th	0.2	0.0	5.8	2.0	1.5	1.2	0.0	4.9	0.2	0.1
U	0.1	Below DL	1.0	0.5	0.5	0.4	0.1	1.4	0.2	0.0
Co	39.7	56.6	46.2	61.3	1.0	24.2	22.6	26.0	38.2	60.0
Ga	11.4	9.5	29.2	28.2	14.9	15.6	13.9	19.7	18.2	11.1
Ta	0.9	0.3	0.7	1.8	0.1	0.1	0.2	2.1	0.3	0.1
Nb	0.6	0.3	7.4	25.3	2.5	2.1	0.9	11.3	2.7	0.3
Mo	Below DL	0.0	Below DL	0.2	Below DL	0.2	0.4	0.2	0.2	0.0
Hf	0.8	0.2	0.3	0.7	0.3	0.4	0.4	0.5	0.9	0.3
W	0.1	185.5	70.7	141.7	0.3	166.9	1.3	0.9	0.8	473.5
Pb	3.7	0.6	7.2	4.6	1.0	0.8	15.4	20.3	5.4	15.0
Re	0.0	0.0	0.0	0.0	0.0	0.0	0.0	0.0	0.0	0.0

Table 2.9: Whole rock geochemistry results

indicate enrichment or depletion with variable L.O.I. Thus, alteration and metamorphism did not change original element concentrations in our samples to any significant extent. Sample 17TL-26 was plotted, but is excluded from the analysis as this represents a pure leucodiorite melt composition, a result of metamorphism rather than primary magmatic processes, and is significantly depleted in the rare earth elements (REEs). Fig. 2.22 shows only the immobile elements, ordered in terms of compatibility, and highlights significantly different patterns between gabbros, amphibolites and plagiogranites. The data is combined with whole rock XRF literature data of meta-basalts from Naxos, Paros and Samos, and gabbros and amphibolites from Tinos' "Upper Unit" (Katzir et al., 1996; Stourati et al., 2017) in Figs. 2.22c–h, and are plotted using a simplified range of incompatible elements with the inclusion of Va and Sc which are normalized to N-MORB values quoted in Klein, (2004), as these has been shown to be consumed by pyroxenes (Eby, 1973). At least two distinct gabbro chemistries can be identified using these plots. A subduction zone influenced gabbro (primary gabbro) (sample 17TL-24) that has significant large ion lithophile element (LILE) enrichment, with a negative Nb anomaly relative to Th, a subduction input proxy (Pearce, 2014), and a strong depletion in Hf. This gabbro displays flat high field strength (HFSE's) patterns relative to N-MORB and have slightly convex downward rare earth element (REE) patterns with relatively low REE abundances (10 times N-MORB) and have light rare earth element (LREE) patterns that indicate some enrichment relative to N-MORB.

Sample 17TL-27 shows similar REE patterns, although it lacks a depletion in Nb relative to Th, indicating it formed from a melt less influenced from subduction. The other gabbro population (17TL-23 and TLT26) shows some enrichment in LILEs but depletion in Th and Nb and strong depletion in the HFSs and REEs (0.1-0.9 times N-MORB). This HFSE depletion in these gabbros may be due to fractional crystallization, which changes the level but not the shape of the diagram (Pearce 1983). There is also a positive Y and Sc excursion relative to the rest of the REEs, suggesting the crystallization of pyroxene. This correlates with a depletion in these elements within

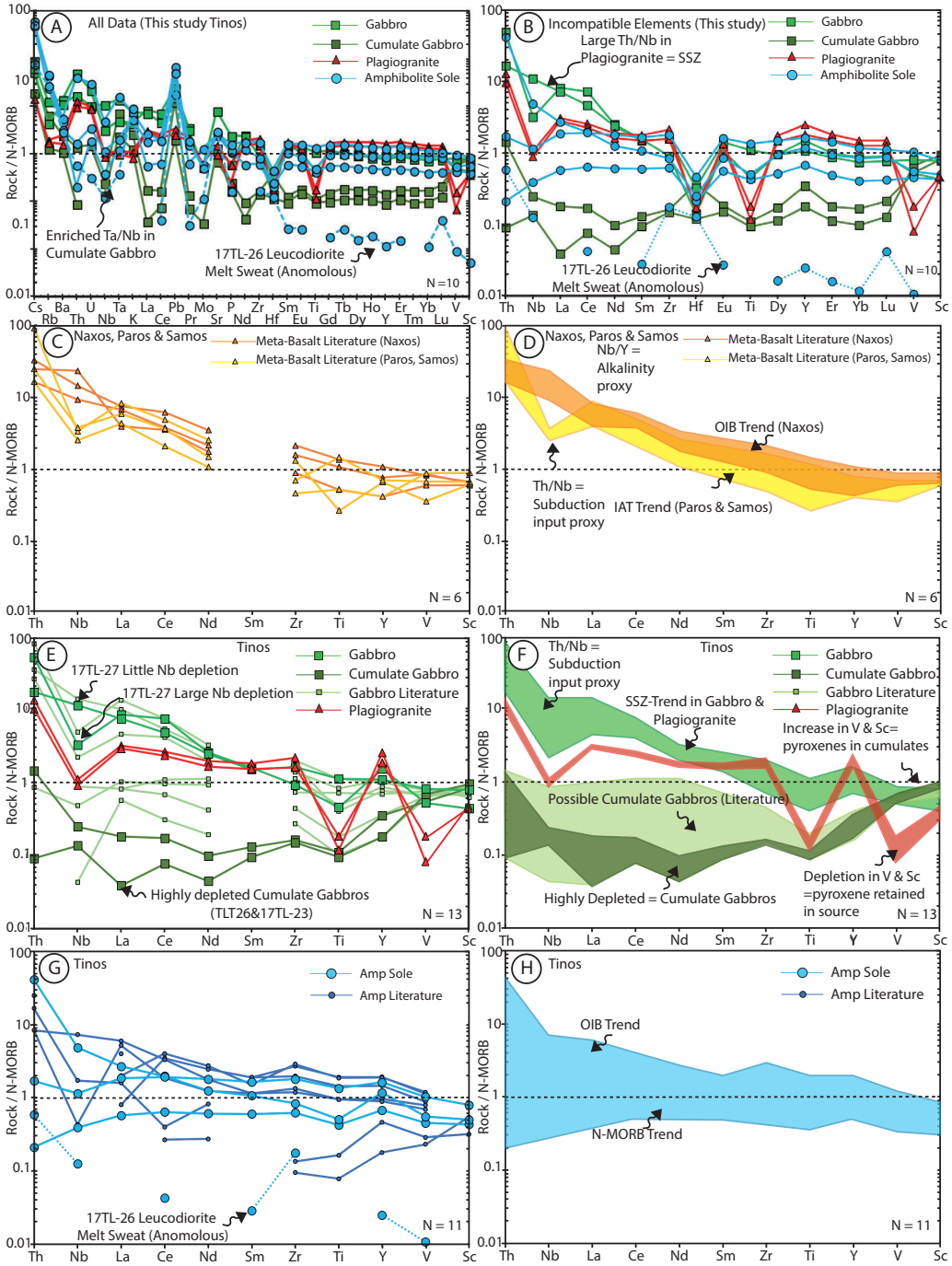


Figure 2.22: Spider diagrams of trace element data from the plagiogranite, gabbros and amphibolites from the sole, plotted with literature meta-basalt gabbro, and amphibolite data (from Stourati et al., 2017 and Katzir et al., 1996) normalized to N-MORB using the normalization of Sun and McDonough, (1989). C-H) Simplified spider diagrams normalized to N-MORB combined with literature data and plotted for rock type and summary trends. C and D) Cycladic Metabasalts. E and F) Intrusive ophiolitic rocks including primary gabbros and cumulate gabbros from this study, literature gabbros and plagiogranites from this study. G and H) Amphibolites including metamorphic sole rocks from this study and literature amphibolites, excluding 17TL-26 leucodiorite melt sweat.

the plagiogranites. These factors suggest that these gabbros are cumulates, and are therefore not primary mantle melts. This inverse correlation in trace elements between cumulates and the plagiogranite indicate the plagiogranite could be derived from the gabbros as a result of hydration and subsequent partial melting. The plagiogranite samples (TLT63 and 17TL-35) also show some enrichment in LILE, but remain relatively flat relative to MORB with significant depletion in Ti and Hf. A distinctive geochemical characteristic of many supra subduction zone magmas, is the depletion in HFSE, enrichment in LILE, and common enrichment in LREE relative to N-MORB. There is also strong evidence of Th enrichment relative to Nb, which is also typical for volcanic arc basalts (e.g. Pearce, 2014). These features are commonly explained as a two-stage melt extraction process because both HFSE and LILE behave incompatibly during partial melting of mantle (e.g. Woodhead et al., 1993). The first melt extraction event depletes the mantle source in both LILE and HFSE. A subsequent, hydrous LILE-enriched but HFSE-poor component, is added to the source before, or during, the second stage of melting. The source of this hydrated LILE-enriched, but HFSE-depleted component is primarily controlled by influx of H_2O and low ionic potential elements into the mantle wedge due to dehydration reactions in the subducting sediments, altered oceanic crust and mantle (e.g. Pearce, 1996; Dilek et al., 2008). These factors conclusively suggest that the ophiolite intrusive rocks have a supra-subduction zone signature.

In contrast, the sole amphibolites show significant enrichment of LILEs and convex upwards trends in REE with smaller degrees of enrichment in LREE's, relative to N-MORB and no obvious depletion in Nb relative to Th. In contrast, N-MORB samples invariably have LREE–depleted patterns (Saunders 1984), whereas flat to REE–enriched patterns with relatively low abundances are more characteristic of island arc tholeiites (IAT). (Cullers and Graf 1984). The metamorphic sole REE patterns therefore most closely match either enriched mid-ocean ridge basalt (E-MORB) or IAT trends.

The literature meta-basalts show two patterns. Naxos basalts display weak

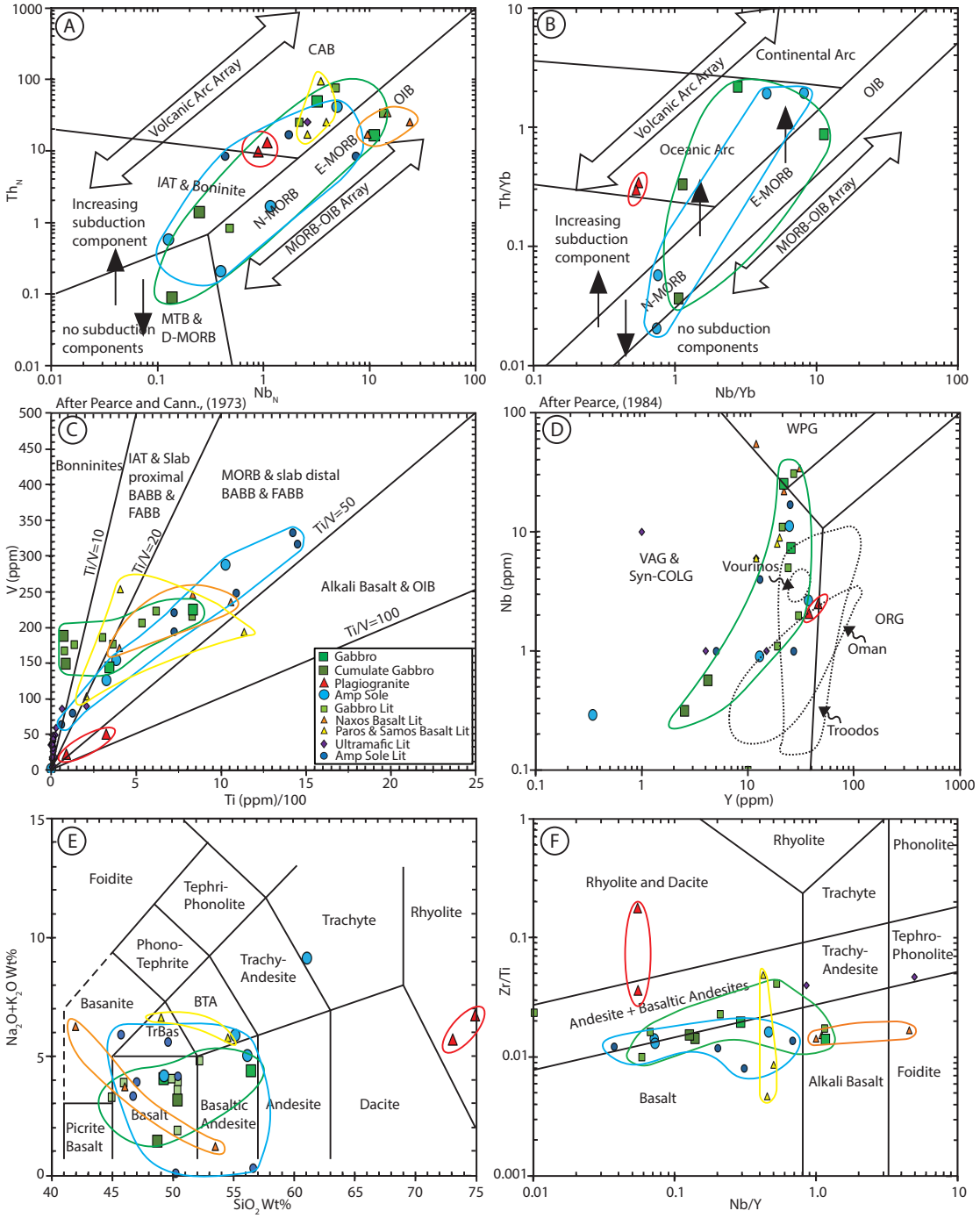


Figure 2.23: Tectonic discrimination diagrams showing trace element geochemistry of basaltic samples from the Tsiknias Ophiolite and metamorphic sole. A) Normalized Th-Nb to N-MORB after Sacanni,, 2015, B) Th/Yb-Nb/Yb diagram after Pearce, 2008, C) Ti vs V after Shervais (1982). D) Nb vs Y diagram for intrusive rocks VAG, volcanic arc granite, Syn-COLG, syn-collision granite, ORG, ocean ridge granite, WPG, within plate granite. E) The IUGS recommended Total alkali vs silica (TAS) discrimination diagram of Le Bas and Streckseisen, (1991). F) Immobile element-based TAS proxy diagram after Floyd and Winchester, (1975). Both diagrams show the meta-basalts span the basalt-alkali basalt fields whereas sole rocks are dominantly basalts.

depletion in Nb relative to Th, and positive and small REEs excursions relative to N-MORB, with a moderate Nb-Y variation, strongly suggesting an ocean island basalt (OIB) affinity (Stourati et al., 2017). Whereas on Paros and Samos, the basalts show some Nb depletion relative to Th, with mainly flat HFSE patterns and little variation between Nb and Y, indicative of an IAT affinity. Discrimination diagrams (Figs. 2.23 and 2.24) can help distinguish tectonic settings (Pearce, 1996) and include literature data from other Cycladic ophiolitic rocks where possible. In Fig. 2.23, the data is presented in the N-MORB normalized Th vs Nb diagram (Scannti et al., 2015) which accounts for samples where no Yb was not measured (i.e. XRF or literature data), and the Th/Yb vs Nb/Yb diagram of Pearce, (2008) that can distinguish subduction input due to enrichment in Th relative to Nb and deviation from the N-MORB to OIB array, and the V vs Ti/100 diagram, that can distinguish between different volcanic arc settings (Pearce and Cann, 1973). These plots re-enforce patterns observed in the spiderdiagrams and confirm the presence of cumulate gabbros as well as subduction influenced gabbros and non-subduction influenced gabbros (sample 17TL-27). Together with gabbros from the literature, the Tsiknias gabbros span the MORB-volcanic arc fields, suggesting a variable subduction influence. The plagiogranites definitively plot above the N-MORB / OIB array in the Th vs Nb diagrams and straddle the IAT to oceanic arc fields. These patterns are also observed in the other plots with the plagiogranites straddling the volcanic arc granite (VAG) and ocean ridge granite (ORG) in the Nb vs Y plot and overlapping with Oman and Troodos ophiolite plagiogranites. These samples also plot on the boundary between ocean ridge granite and volcanic arc affinities in the Rb vs (Y+Nb) and Rb vs (Yb+Ta) plots (Fig. 2.23), and strongly suggest a supra-subduction zone signature to the plagiogranites. The amphibolites mainly plot within the MORB / OIB array with some potential Th enrichment in samples TLT7 and TLTN12, and plot exclusively in the MORB and slab distal back arc basin fields in the V vs Ti/100 discrimination plot. Combination of the V-Ti/100, total alkali vs silica and Zr/Ti vs Nb/Y immobile element proxy plot (Pearce, 1996) suggests the sole rocks have basaltic protoliths, whereas the meta-basalts from other

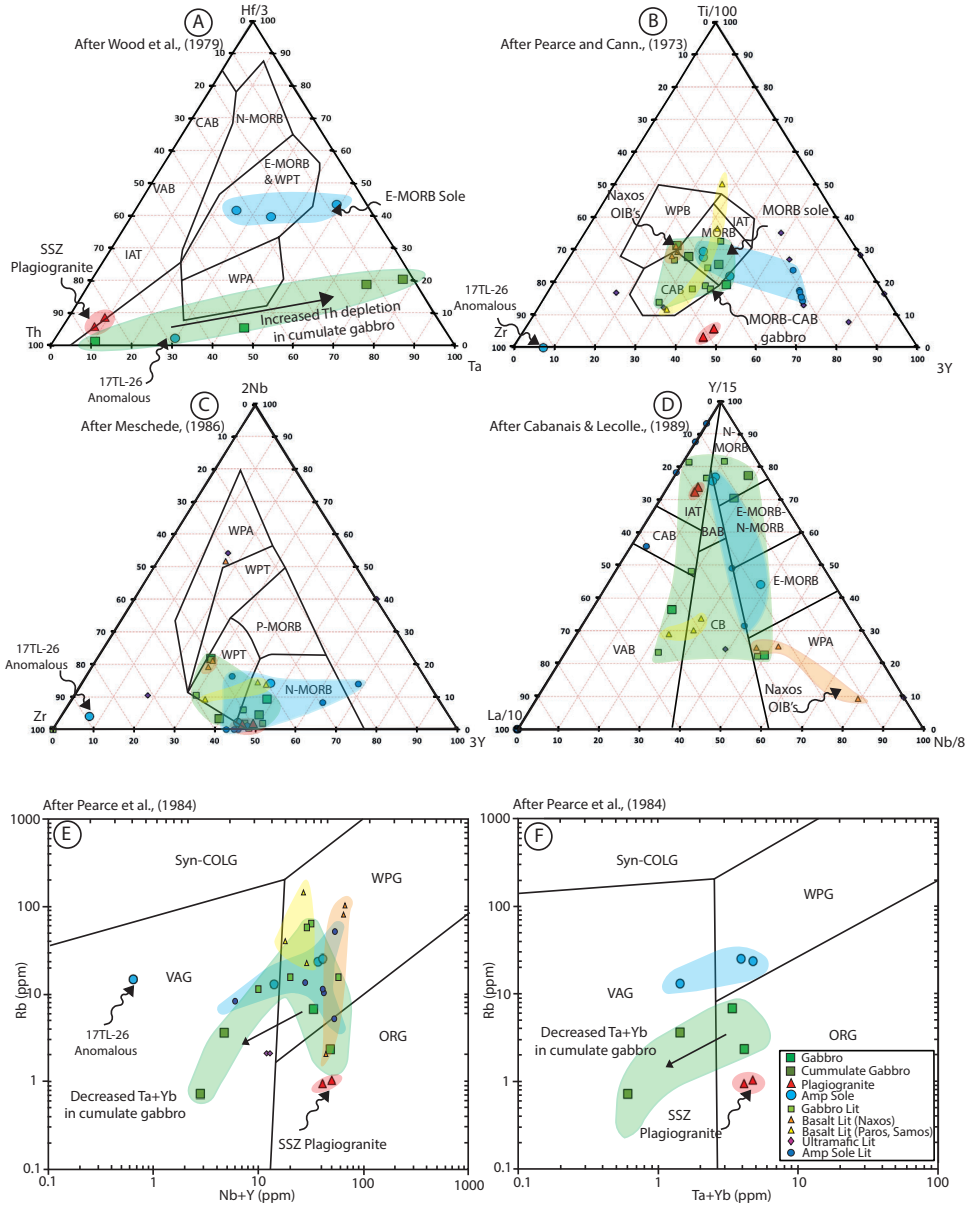


Figure 2.24: A) Hf/3-Th-Ta after Wood et al., (1979); E-MORB, oceanic basalt from an anomalous MOR segment (e.g., high-heat flow) B) Ti/100-Zr:3Y after Pearce and Cann (1973); WPB, within-plate basalt; OFB, ocean floor basalt; LKT, low-potassium tholeiite; CAB, calc-alkaline basalt. C) 2Nb-Zr-3Y after Meschede (1986); WPA, within-plate alkaline; WPT, within-plate tholeiite, N-type MORB, oceanic basalt from a normal MOR; P-type MORB, basalt from plume-influenced MOR; VAB, volcanic arc basalt. D) Y/15-La/10-Nb/8 after Cabanais and Lecolle, (1989).

islands span the basalt-alkali basalt and basaltic andesite fields. Two types of meta-basalts can be distinguished, an OIB affinity to the Naxos meta-basalts and a IAT trend in the Paros and Samos meta-basalts. In Fig. 2.24, the meta-basalts from Naxos plot mainly in the within plate alkali basalt and within plate tholeiite fields whereas Paros and Samos rocks plot in the within plate tholeiite to volcanic arc basalt fields (e.g. Ti/100-Zr-3Y, 2Nb-Zr-3Y and Y/15-La/10-Nb/3 ternary diagrams). The OIB trends from Naxos meta-basalts are distinctly different from the Tsiknias gabbros, which mainly plot across an array from IAT toto within plate basaltfields (e.g. Hf/3-Th-Ta and Y/15-La/10-Nb/8 ternary diagrams), and the sole rocks that span the N-MORB to E-MORB fields in all diagrams. However, it is possible that the Paros and Samos meta-basalts could be related to the Tsiknias ophiolite gabbros.

In summary, the most significant result from the geochemical data is that the Tsiknias Ophiolite gabbros and plagiogranites express a supra-subduction zone signature. There are both cumulate and ordinary gabbros with evidence to suggest that the plagiogranite was a highly fractionated product leaving behind a depleted residue which possibly represents the cumulate gabbros. This strongly implies the Tsiknias Ophiolite formed in a spreading environment above a subduction zone. However, there may have been a variable subduction influence during ophiolite formation, as sample 17TL-27 has an E-MORB affinity.

The meta-basalts reported by Stourati et al., (2017) show two contrasting trends: Ocean island and alkali basalts occur on Naxos within trench mélange (personal observations), whereas volcanic arc tholeiites on Paros and Samos with similar chemistry to the gabbros potentially suggesting that they could represent the upper crustal rocks. The sole amphibolites are slightly enriched in LILE's relative to N-MORB, and display flat-convex up LREE's patterns, signifying the basaltic and gabbroic protoliths to these rocks. These likely formed within the oceanic interior and can be best described as E-MORB with some hint of a distal subduction input.

2.7 Geochronology

2.7.1 U–Pb Geochronology

U–Pb zircon dating of a plagiogranite, gabbro and amphibolite melt sweat was carried out at the Natural Environmental Research Council (NERC) Isotope Geosciences Laboratory (NIGL), at the British Geological Survey, Keyworth, UK. Samples were crushed using standard techniques (Jaw-crushing, disc milling, sieving, Rogers table, heavy liquids, Frantz isodynamic magnetic separation). Approximately 40 zircons from each sample were then picked under alcohol, mounted in 1-inch epoxy resin mounts and polished until all grains were exposed. These were imaged by cathodoluminescence to distinguish zircon growth zoning and are presented with recorded spots and ages in Fig. 2.25. All U–Pb analyses were performed on a Nu Attom single collector inductively coupled mass spectrometer (SC-ICP-MS) coupled to a New Wave Research 193UC excimer laser ablation system fitted with a TV2 cell. Standard-sample bracketing using matrix-matched minerals was employed for all minerals, with full set-up and protocols described previously for zircon (Roberts et al., 2016) and full analytical data provided in the supplementary files. All data and ages are shown and quoted at 2-sigma, are $^{206}Pb/^{238}U$ ages unless stated otherwise, and follow uncertainty propagation guidelines of Horstwood et al., (2016). The data is presented as common-Pb weighted mean plots and Tera-Wasserburg plots using a regression through the data anchored at a $^{206}Pb/^{204}Pb$ value of 0.84 ± 0.02 (Stacey and Krammers, 1975) and is displayed in Table 2.11.

2.7.1.1 Results

2.7.1.1.1 17TL35 Plagiogranite: Zircons were small and un-zoned and dating both core and rims gave a single age population with mainly concordant data. A weighted mean of common-Pb-corrected data gives and age of 161.9 ± 3.5 Ma with an MSWD of 0.70 (Fig. 2.28), whereas a Tera-Wasserburg plot yields a regressed age of 161.9 ± 1.3 Ma with an MSWD of 0.68 (Fig. 2.26). This age is interpreted as

Table 2.10: SC-ICP-MS U–Pb zircon geochronology results for samples 17TL35 plagiogranite, 17TL27 gabbro and 17TL26 amphibolite samples

Analysis													Ratios								Ages						Disc. %	Corrected 206-238
Sample	Rock Type	Analysis	comments	204Pb cps	206Pb cps	207Pb cps	208Pb cps	232Th cps	238U cps	Th/U	Pb ppm	Th ppm	U ppm	238U/206Pb	ls %	207Pb/206Pb	ls %	206Pb/238U	ls %	Rho	207Pb/206Pb	2s abs	206Pb/238U	2s abs	207Pb/235U	2s abs	6-38/7-35	Age	2s [Ma]
17TL26	Amp Sole	17TL26.02		-210	4800	283	82	13200	3300	0.0	0.2	5.1	111.0	80.451	3.52	0.054	5.22	0.012	3.52	0.00	356.1	117.9	79.6	5.6	89.3	10.7	77.6	79.0	5.5
17TL26	Amp Sole	17TL26.03		70	1240	637	96	8260	8770	0.0	0.3	3.2	293.0	91.575	2.09	0.049	3.33	0.011	2.09	0.00	166.5	77.8	70.0	2.9	72.8	5.5	58.0	69.8	2.9
17TL26	Amp Sole	17TL26.05		-20	920	84	82	4110	5462	0.1	0.2	1.6	18.8	82.508	3.45	0.096	8.55	0.012	3.45	0.00	1550.8	160.6	77.7	5.3	151.2	25.6	95.0	72.9	5.2
17TL26	Amp Sole	17TL26.06		-100	2000	132	42	910	1120	0.0	0.1	0.4	37.4	75.358	3.86	0.065	8.72	0.013	3.86	0.00	767.1	1853.8	85.0	6.5	113.7	20.3	88.9	83.2	6.4
17TL26	Amp Sole	17TL26.07		0	600	60	-2	4380	360	0.1	0.1	1.7	12.1	81.301	5.38	0.102	16.90	0.012	5.38	0.00	1664.9	312.7	78.8	8.4	162.3	51.8	95.3	73.4	8.4
17TL26	Amp Sole	17TL26.09		220	1560	98	91	6100	1070	0.1	0.2	2.4	35.9	81.301	5.38	0.070	12.41	0.012	5.38	0.00	923.6	255.0	78.8	8.4	113.6	28.7	91.5	78.6	8.2
17TL26	Amp Sole	17TL26.10		0	1190	206	329	3080	730	0.0	0.1	1.2	24.5	79.114	3.85	0.173	5.97	0.013	3.85	0.00	2607.0	99.5	81.0	6.2	270.3	33.2	96.9	78.0	5.4
17TL26	Amp Sole	17TL26.11		-60	2950	75	80	2130	1760	0.1	0.2	4.1	25.1	84.507	7.46	0.070	14.27	0.012	7.46	0.00	929.5	1717.5	85.5	12.5	113.6	28.7	97.7	69.7	6.3
17TL26	Amp Sole	17TL26.13		-90	2270	130	126	15890	1630	0.1	0.4	6.1	55.0	84.746	6.02	0.094	12.27	0.013	6.02	0.00	518.1	271.6	75.6	9.0	91.1	23.7	85.4	74.7	8.9
17TL26	Amp Sole	17TL26.14		-90	2270	130	126	15890	1630	0.1	0.4	6.1	55.0	84.746	6.02	0.094	13.76	0.013	6.02	0.00	518.1	271.6	75.6	9.0	91.1	23.7	85.4	74.7	8.9
17TL26	Amp Sole	17TL26.20		155	600	60	56	6330	500	0.1	0.2	2.5	16.7	88.496	4.97	0.125	10.27	0.011	4.97	0.00	1196.0	177.3	72.4	7.2	119.2	22.8	93.9	69.5	6.9
17TL26	Amp Sole	17TL26.21		90	320	50	27	1700	182	0.1	0.1	0.7	6.1	68.493	9.98	0.130	13.75	0.015	9.98	0.00	2091.9	241.8	93.4	18.5	235.2	69.0	95.5	84.0	17.0
17TL26	Amp Sole	17TL26.22		110	574	61	102	2160	363	0.1	0.3	0.8	12.1	78.125	7.10	0.104	14.64	0.013	7.10	0.00	1701.1	269.7	82.0	11.6	171.4	50.1	95.2	76.0	11.0
17TL26	Amp Sole	17TL26.15	inherited	18	1030	181	138	870	1210	0.0	0.4	0.3	40.5	68.027	6.88	0.081	13.83	0.015	6.88	0.00	1220.8	271.9	94.1	12.8	154.2	43.3	92.3	90.0	12.0
17TL26	Amp Sole	17TL26.18	inherited	-110	1030	5200	10700	8020.00	2680	0.4	29.3	313.0	894.0	33.456	1.48	0.050	1.87	0.030	1.48	0.00	180.8	43.6	189.9	5.5	189.1	8.2	-5.0	189.9	5.5
17TL26	Amp Sole	17TL26.25	inherited	20	871.00	4530	11000	8500.00	2370	0.4	30.1	331.0	791.0	34.459	1.32	0.050	1.86	0.029	1.32	0.00	213.7	43.1	184.4	4.8	186.5	7.7	13.7	184.3	4.7
17TL26	Amp Sole	17TL26.26	inherited	90	4870.0	2420	4390	3680.00	1230.0	0.3	12.0	143.0	413.0	32.531	1.46	0.048	2.03	0.031	1.46	0.00	108.0	47.9	195.2	5.6	188.6	8.6	-80.7	195.6	5.6
17TL27	Gabbro	17TL 27.03a			401	69	75	630	1443.1	0.1	0.2	0.3	5.6	38.055	5.28	0.185	6.75	0.026	5.28	0.62	2697.0	222.8	167.2	17.4	520.4	67.5	67.9	138.9	12.4
17TL27	Gabbro	17TL 27.08			2226	54	bd	7826	153.07	0.0	0.1	0.0	3.0	34.946	5.97	0.296	7.19	0.029	5.97	0.64	3224.3	227.1	181.9	21.4	709.3	91.2	74.4	134.9	12.8
17TL27	Gabbro	17TL 27.14			368	56	bd	518	153.07	0.0	0.2	0.3	5.9	41.036	5.41	0.109	6.48	0.024	5.41	0.64	2333.3	221.8	155.2	16.6	411.7	55.6	62.3	135.9	12.9
17TL27	Gabbro	17TL 27.18c	inherited		5341	62	66	12738	1243	0.1	0.7	1.9	4.8	35.575	5.74	0.094	9.35	0.029	5.97	0.64	3036.2	211.4	181.9	21.4	709.3	91.2	74.4	134.9	12.8
17TL27	Gabbro	17TL 27.15	inherited		15753	3688	3967	241258	45259	0.1	0.2	1961.0	164.1	27.712	1.62	0.178	6.36	0.028	5.74	0.67	3536.2	211.4	179.7	20.3	535.4	68.9	66.4	174.2	14.7
17TL27	Gabbro	17TL 27.22			15145	135	bd	2.3E+05	691.32	0.5	0.6	1.2	24.5	41.986	2.27	0.056	5.80	0.024	2.27	0.36	1149.8	220.0	152.2	6.3	231.9	25.5	34.1	146.7	6.4
17TL27	Gabbro	17TL 27.30a	inherited		22974	1289	2256	90204	3382.61	0.3	8.7	47.3	149.9	17.131	1.46	0.056	1.29	0.058	1.46	0.75	447.9	57.4	365.7	10.3	377.0	12.2	3.0	364.8	10.3
17TL27	Gabbro	17TL 27.30b	inherited		17771	9346	8676	29884.81	2685.62	0.2	64.1	156.4	1042.0	15.431	1.15	0.055	0.65	0.490	1.32	0.96	407.0	29.0	404.8	9.0	405.0	8.8	0.0	404.8	9.0
17TL35	Plagiogranite	TIL17-35b.04			97224	4796	19524	17702.71	3682.65	0.6	41.4	954.7	1554.5	40.109	1.31	0.050	0.89	0.170	1.59	0.025	1.31	0.83	174.1	41.6	158.8	4.1	159.6	4.7	0.6	158.7	4.1
17TL35	Plagiogranite	TIL17-35b.09		106	163708	8243	49073	42966.20	61.071.27	0.9	75.3	2317.0	2577.8	39.787	1.20	0.050	1.06	0.172	1.60	0.025	1.20	0.75	174.1	49.4	160.0	3.8	160.8	4.7	0.5	160.0	3.8
17TL35	Plagiogranite	TIL17-35b.10		29	83459	4124	19477	18534.00	31.323.12	0.8	36.5	999.5	1322.3	39.549	1.61	0.048	1.45	0.167	2.17	0.025	1.61	0.74	88.7	68.8	161.0	5.1	156.4	6.3	-2.9	161.3	5.1
17TL35	Plagiogranite	TIL17-35b.03		160	86244	4355	17913	15946.60	32.001.70	0.6	37.0	860.0	1354.6	39.391	1.27	0.049	1.03	0.173	1.63	0.025	1.27	0.78	162.9	48.2	161.6	4.0	161.6	4.9	0.0	161.6	4.0
17TL35	Plagiogranite	TIL17-35b.01	bd		93372	4762	22413	19325.85	34.688.83	0.7	41.1	1042.2	1463.8	39.325	1.31	0.050	0.88	0.176	1.58	0.025	1.31	0.83	206.4	41.0	161.9	4.2	164.7	4.8	1.7	161.7	4.2
17TL35	Plagiogranite	TIL17-35b.02	bd		46174	2074	9328	7121.96	1770.76	0.5	19.9	384.1	747.5	36.607	1.37	0.062	1.49	0.222	2.02	0.026	1.37	0.68	686.2	63.5	164.5	4.5	203.6	7.4	19.2	161.8	4.3
17TL35	Plagiogranite	TIL17-35b.08	bd		69180	3456	12507	10596.21	2510.41	0.5	29.0	571.4	1061.1	39.037	1.27	0.051	1.13	0.179	1.70	0.026	1.27	0.75	223.7	52.3	163.1	4.1	167.0	5.2	2.3	162.8	4.1
17TL35	Plagiogranite	TIL17-35b.05	bd		81259	4117	17418	14160.64	2963.40	0.6	35.0	786.9	1230.6	38.869	1.22	0.050	1.07	0.177	1.62	0.026	1.22	0.75	195.9	49.9	163.8	3.9	165.8	5.0	1.2	163.6	3.9
17TL35	Plagiogranite	TIL17-35b.06	bd		122606	6268	34890	30539.98	4573.78	0.8	55.8	1636.1	1930.3	38.814	1.15	0.050	0.76	0.177	1.38	0.026	1.15	0.83	187.3	35.4	164.0	3.7	165.4	4.2	0.9	163.9	3.7
17TL35	Plagiogranite	TIL17-35b.11	bd	35	73522	3040	16903	14753.45	2739.93	0.7	32.0	794.5	1156.5	38.737	1.99	0.049	1.59	0.174	2.55	0.026	1.99	0.78	142.0	74.8	164.3	6.5	162.8	7.6	-0.9	164.4	6.5
17TL35	Plagiogranite	TIL17-35b.07	inherited	bd	242812	48671	100616	4.43E+04	4.27E+04	1.3	133.5	2.39E+03	1.80E+04	1.816	2.11	0.198	0.80	14.989	2.26	0.351	2.11	0.93	2805.8	26.3	2827.8	96.0	2814.5	42.1	-0.5	2857.8	96.7



Figure 2.25: Cathode luminescence images of zircon morphologies and zoning showing ablation spots with from reported ages of A) Plagiogranite (17-TL35), B) Leuco-diorite melt sweats from the metamorphic sole (17TL-26) and C) Gabbros (17TL-27)

an absolute minimum age of the formation of oceanic crust associated with ophiolite formation. Because the plagiogranite retains a strong SSZ signature, this confirms that spreading at ca. 162 Ma occurred above a subduction zone.

2.7.1.1.2 17TL27 Gabbro: Some zircon was successfully extracted from sample 17TL-27 a partially tectonized gabbro horizon belonging to the Moho Transition Zone (see Figs. 2.2, 2.2-2.4 and 2.6-2.8). Zircons were small (<30 μm) and display mild zoning. Successful data yielded a spectrum of ages from 160–140 Ma with variable amounts of common-Pb, and a mean U–Pb age of 144.4 ± 9.3 Ma with a MSWD of

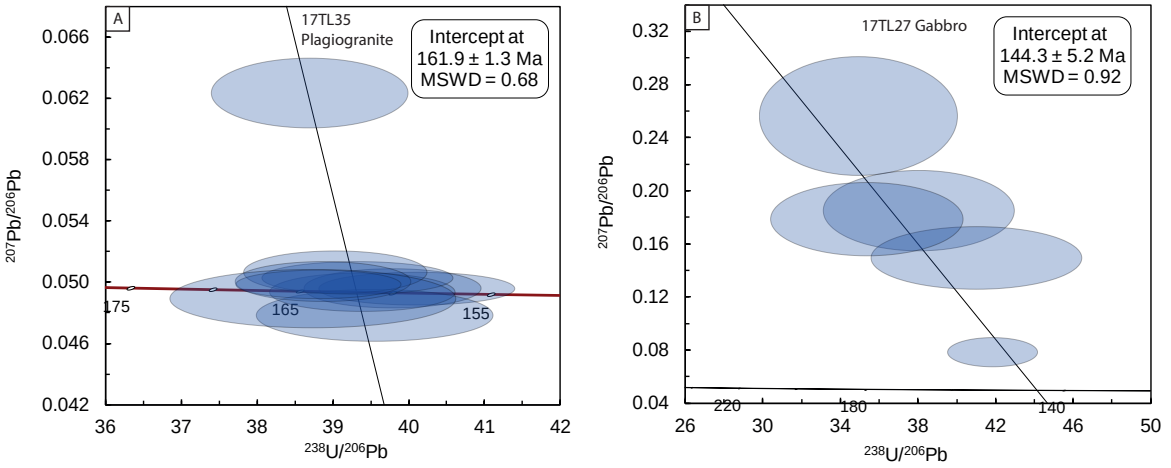


Figure 2.26: Plagiogranite and gabbro Tera-Wasserburg plots for Tsiknias ophiolite samples A) 17TL35, plagiogranite, B) 17TL27 a gabbro; see text for more discussion

1.30 (Fig. 2.28), whereas the Tera-Wasserburg plot (2.26) provides a regressed age of 144.3 ± 5.2 Ma with an MSWD of 0.92. Trace element data from this sample suggest an enriched signature relative to N-MORB, although the lack of Nb excursion relative to Th, suggests this sample didn't derive from a magma influenced by subduction. This rock is composed of over 40% hornblende, indicating strong amounts of magmatic hydration during crystallization. The range of ages, and ca. 9 Myr age discrepancy from the plagiogranite, which formed in an SSZ setting, suggests that gabbro formation, crystallization, and hydration occurred over a prolonged time interval with variable amounts of subduction interaction. Unfortunately, no other gabbro samples yielded zircon to test if gabbro crystallization occurred over a prolonged time interval.

2.7.1.1.3 17TL26 Leucodioritic Melt Sweats from Metamorphic Sole: Zircons extracted from the melt sweats hosted within amphibolites directly below the contact with the ophiolite are rare, small and have irregular morphologies and textures (see Fig. 2.25). They were unevenly zoned and characterized by low U concentrations. Thin rim overgrowth yields a minimum age of ca. 64 Ma (Fig. 2.25). However, due to the <5 μm rims and low U concentrations, extraction of uniquely rim ages was difficult. The youngest age population of 10 analyses, defined by the "TuffZirc" algorithm of Isoplot (Ludwig, 2003), gives a weighted mean of 69.8 +3.3/-2.0 Ma. Analysing just

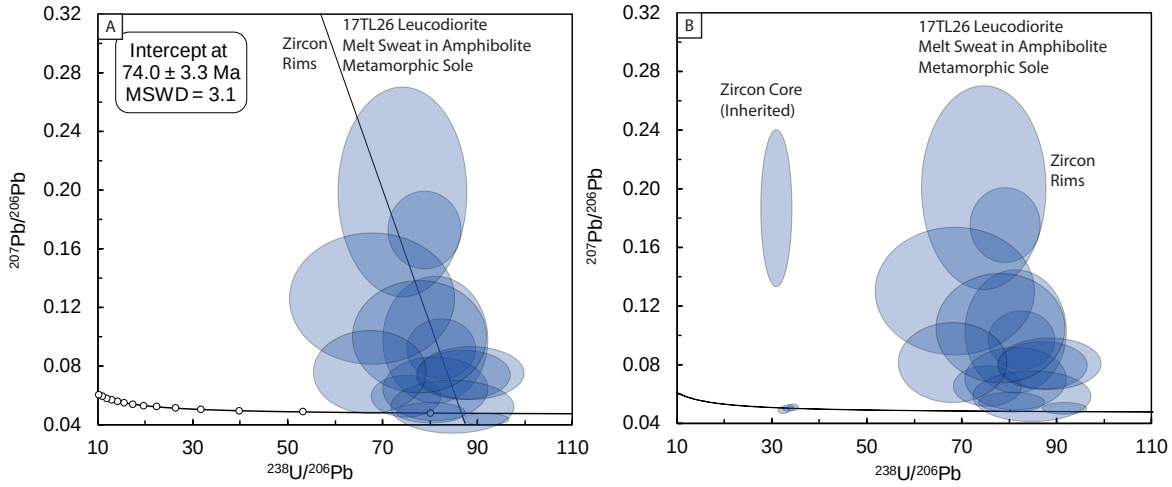


Figure 2.27: Tera-Wasserburg plots for sample 17TL26 A) Zircon rim age data with a lower intercept of 74.0 ± 3.3 Ma and B) Inhertited zircon core data with an approximate intercept of ca. 190 Ma

zircon rims, however and plotting on a Terra-Wasserburg diagram yields a regressed age of 74.0 ± 3.3 Ma (Fig. 2.27), which represents the best age estimate for crystallization of partial melt, following high grade metamorphism on the subduction interface during the obduction process. The U–Pb data are far from simple however, with a spread in ages between 120–70 Ma. This data could be interpretted as dominantly mixing across different zircon growth domains, due to the inaccuracy with measuring low-U contents and thin rims, smaller than the 20 μm ablation spot size. There is however an apparent age population of ca. 110 Ma, which complicates the data and its interpretation (see Fig. 2.28). It is unclear what this cryptic age represents, but of note, it is similar to that recorded by ^{40}K–^{39}Ar and ^{40}Ar–^{39}Ar dating of the Akrotiri Unit near Tinos Town (Patzak et al., 1994; Zeffren et al., 2005) and the Vari Unit on Syros (Tomascheck et al., 2003) both forming an integral part of the "Upper Unit". Therefore, there are several possibilities what this age recorded in the sole represents. It could be recording another phase of off-axis magmatism that remobilized previously grown magmatic zircon. Alternatively, it could represent metasomatism of ocean crust. However, it these ca. 110–90 Ma ages cannot represent the amphibolite partial melting event, and therefore do not represent the age of ophiolite obduction,because: 1) anatexis occurs exclusively within the uppermost five meters of the sole directly below the

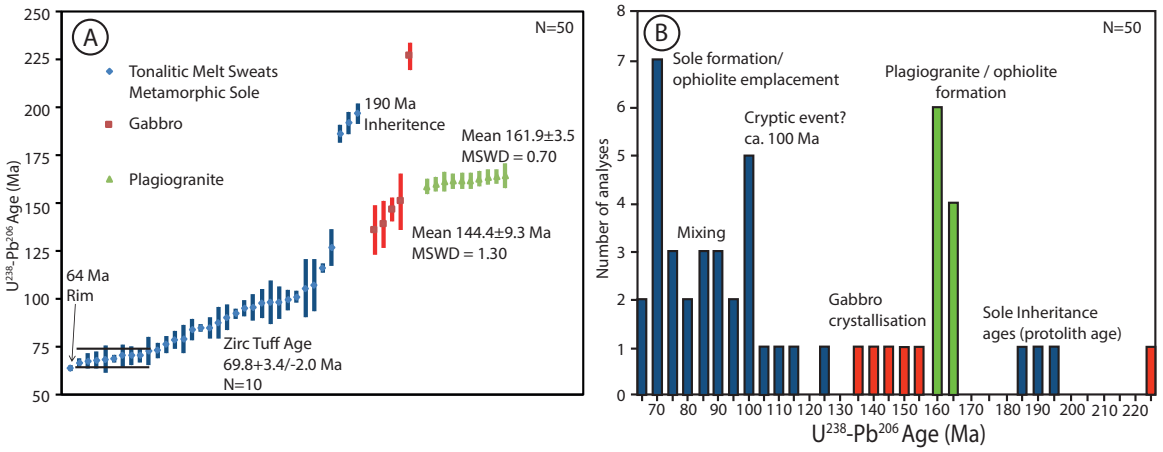


Figure 2.28: U-Pb age distributions A) Weighted mean U–Pb plot for all data reported in this study, with estimated uncertainties and quoted MSWD values. The quoted U–Pb age of the metamorphic sole is taken as the age plateau which is associated with purely rim ages this is taken to be 64–70 Ma, whereas the "Zirc-Tuff" statistical age is 69.8 +3.4-2.0 Ma based on 10 analyses. B) Age frequency histogram with binned age distributions. It is clear the youngest age population from the metamorphic sole is the largest, and there is a degree of mixing between this age population and older cores, due to the small irregular morphologies of zircons.

ophiolite contact, implying the heating was localized on that contact (Tsiknias Thrust); 2) leucosomes truncate the obduction related fabric (S_1 and S_2), and are evidently the last phase of deformation and metamorphism within the amphibolites, with no subsequent overprint. The youngest age population associated with zircon rims is therefore taken as the timing of metamorphism and yields an age of 74.0 ± 3.3 Ma as an absolute minimum constraint for the timing of ophiolite obduction, as there is no evidence for further deformation or metamorphism apart from granite intrusion (known at ca. 14.5 Ma) that post-dates anatexis. Cores of some zircons yield concordant data and constrain the protolith age of basalt or gabbro formation to ca. 190 Ma (Fig. 2.27). This age is significantly older than the formation age of the overriding ophiolite. This combined with differences in trace element data suggesting an E-MORB to back-arc basin basalt affinity, reveal that the metamorphic sole protolith belongs to a different fragment of oceanic crust to the overriding Tsiknias Ophiolite.

2.7.2 Lu–Hf Geochronology

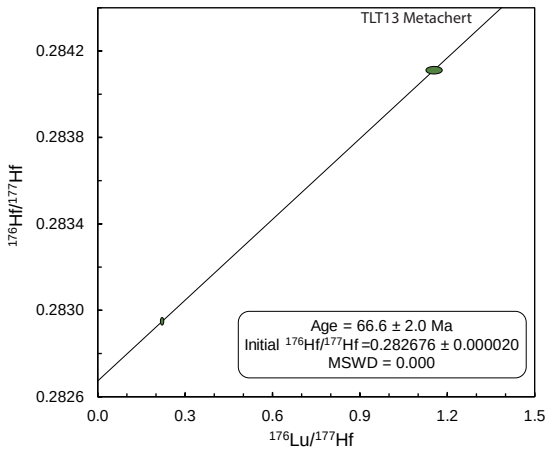


Figure 2.29: TLT13 two point Lu–Hf isochron

To verify the U–Pb age of metamorphism in the sole and to gain insight into the timing of metamorphism at different structural positions, Lu–Hf isotopic dating of garnets from meta-cherts (TLT13 and TLT15) within the Mirsini Unit at intermediate levels of the metamorphic sole, was undertaken at NIGL. Although allanite U–Pb geochronology was attempted in these samples, the U-Pb isotopic system had experienced open system behaviour and hence yield a meaningless age. Therefore Lu–Hf garnet geochronology was used as it is a powerful tool to directly constrain the timing of garnet growth and hence metamorphism and has been shown to have a high blocking temperature (100°C higher than Sm–Nd system at cooling rates <10°C/Myr; Scherer et al., 2000), hence enabling precise age determinations. The procedures for sample leaching, spiking and dissolution followed those described by Anczkiewicz and Thirlwall, (2003) and are extensively described in Appendix 2. Fortunately, >90% of garnets are well formed and inclusion free, albeit less than 100 μm in diameter and interpretted to have grown during a single period and therefore the largest garnet fractions were hand-picked under a binocular microscope. Although it is acknowledged that Lu–Hf age systematics are affected by zircon and rutile inclusions, with the former representing 1 wt.% Hf, or rutile, which can often be volumetrically significant and have a 50 times higher Hf concentration than coexisting garnet, no rutile occurred in the sample and negligible amount of zircon would have been included within garnets owing to their small size.

2.7.2.1 Results

2.7.2.1.1 TLT13 Meta-chert Due to the ongoing development of the technique at NIGL, Lu–Hf ages were only calculated by a two-point garnet–whole-rock ages at

Sample	Rock Type	Location	Analysis	Lu ppm	± 2SE	Hf ppm	± 2SE	176Lu/177Hf	± 2SE	176Hf/177Hf	± 2SE
TLT13	Meta-chert	Tinos Sole	TLT13 WR	0.29283	0.00004	0.18809	0.00001	0.22068895	-	0.28295	0.000008
TLT13	Meta-chert	Tinos Sole	TLT13 garnet	48.106	0.046	5.9008	0.0099	1.15587707	-	0.284113	0.000032
TLT15	Meta-chert	Tinos Sole	TLT15-1 garnet	5.945	0.01	2.5477	0.0005	0.33077011	-	0.282849	0.000002
TLT15	Meta-chert	Tinos Sole	TLT15-2 garnet	5.588	0.003	2.2994	0.0005	0.34447898	-	0.282826	0.000006
TLT15	Meta-chert	Tinos Sole	TLT15 WR	0.27487	0.00008	0.39786	0.00002	0.09792826	-	0.282702	0.000008
TLT1	Meta-Pelite	Tinos Sole	TLT1 WR	0.2792	0.0001	0.43846	0.000002	0.09025961	-	0.282665	0.000007

Table 2.11: Lu-Hf geochronology results

this time (Fig. 2.28). Although statistically less reliable, the two-point garnet–whole-rock ages have been shown to correspond closely with garnet growth defined either by the multiple point isochron where an MSWD can be derived, albeit with a large uncertainty (e.g. Bird et al., 2013). Another fraction of garnet will be subsequently analysed in the coming months, however for now the result is encouraging as garnet in sample TLT13 exhibits enrichment in $^{177}Lu/^{177}Hf$ which fixes the isochron age to 66.6 ± 2.0 Ma. This represents an average age of garnet growth, although it is likely this represents peak metamorphism as garnet had only just nucleated and grew during a single pulse, as reflected in the limited internal growth zoining.

This age is younger than the regressed zircon rim U-Pb age from the overlying partial melt sweats, albeit within error of the weighted mean zircon rim U-Pb ages, and indicates that metamorphism at stucturally high and intermediate levels of the sole occurred at around the same time, although the deeper parts may have experienced their peak metamorphic conditions at a slightly later time than high-grade amphibolites.

2.8 Discussion

2.8.1 Formation of the Tsiknias Ophiolite

2.8.1.1 Timing of ophiolite formation and comparisons to other ophiolites

U–Pb geochronology constrains the age of Tsiknias Ophilolite formation to 161.9 ± 1.3 Ma, within uncertainty of the reported U–Pb ages of 160 ± 1 Ma for the "East Vardar Ophiolites" on mainland Greece, particularly the Guevgueil Ophiolite (Froitzheim et al., 2014) and the Samothraki ophiolite sequence (Koglan, 2008). Although a similar

age is reported for the Mirdita Ophiolite (Dilek et al., 2007) (see Figs. 2.1, 2.30), its N-MORB geochemistry is incompatible with that of Tsiknias plagiogranites and gabbros. Geochemistry of gabbros and plagiogranite within the Tsiknias Ophiolite sequence show variable trace element patterns suggesting a complicated evolution. Plagiogranites and primary gabbros reveal an SSZ affinity, signifying that the ophiolite formed above a subduction zone. This is similar to many of the Dinaric Ophiolites, and the "East Vardar Ophiolites" but not the Mirdita, Vourinous or Orthis Ophiolites ("West Vardar Ophiolites") that display N-MORB / E-MORB geochemistries overprinted by SSZ signatures (e.g. Maffione and van Hinsbergen, 2018 and references therein; Roberson, 2002; Katzir et al., 1996; Stoureti et al., 2017). However, no further information on the geometry of the subduction zone responsible for the formation of the Tsiknias Ophiolite can be obtained from these data alone. One major difference the Tsiknias Ophiolite shows compared to these ophiolites, is a ca. 90 Myr discrepancy between the ophiolite and sole age, as these ophiolites were obducted shortly after they formed (e.g. Maffione and van Hinsbergen, 2018 and references therein).

Gabbro and plagiogranite petrography and chemistry suggest a complicated history of partial melting and crystallization within the Tsiknias Moho Transition Zone. In a simple fractional crystallization case, the observed volume of plagiogranite would require an exceptionally large initial volume of a low-K mantle melt what would have undergone extreme fractionation, much more than can be accounted for by the underlying gabbroic intrusions. The inverse correlation in REE's between highly depleted cumulate gabbros and the plagiogranites, strongly suggests the two could be derived from an original mafic source.

To further complicate matters, another type of gabbro with a composition lacking a subduction signature and of an E-MORB affinity forms part of the same sequence. U–Pb dating constrains the age of crystallization of this gabbro (17TL-27) to 144.3 ± 5.2 Ma, distinguishably younger than the SSZ plagiogranite. This suggests that spreading and formation of the Tsiknias Ophiolite occurred firstly in an SSZ proximal setting, followed by a transition to a distal subduction/ back arc

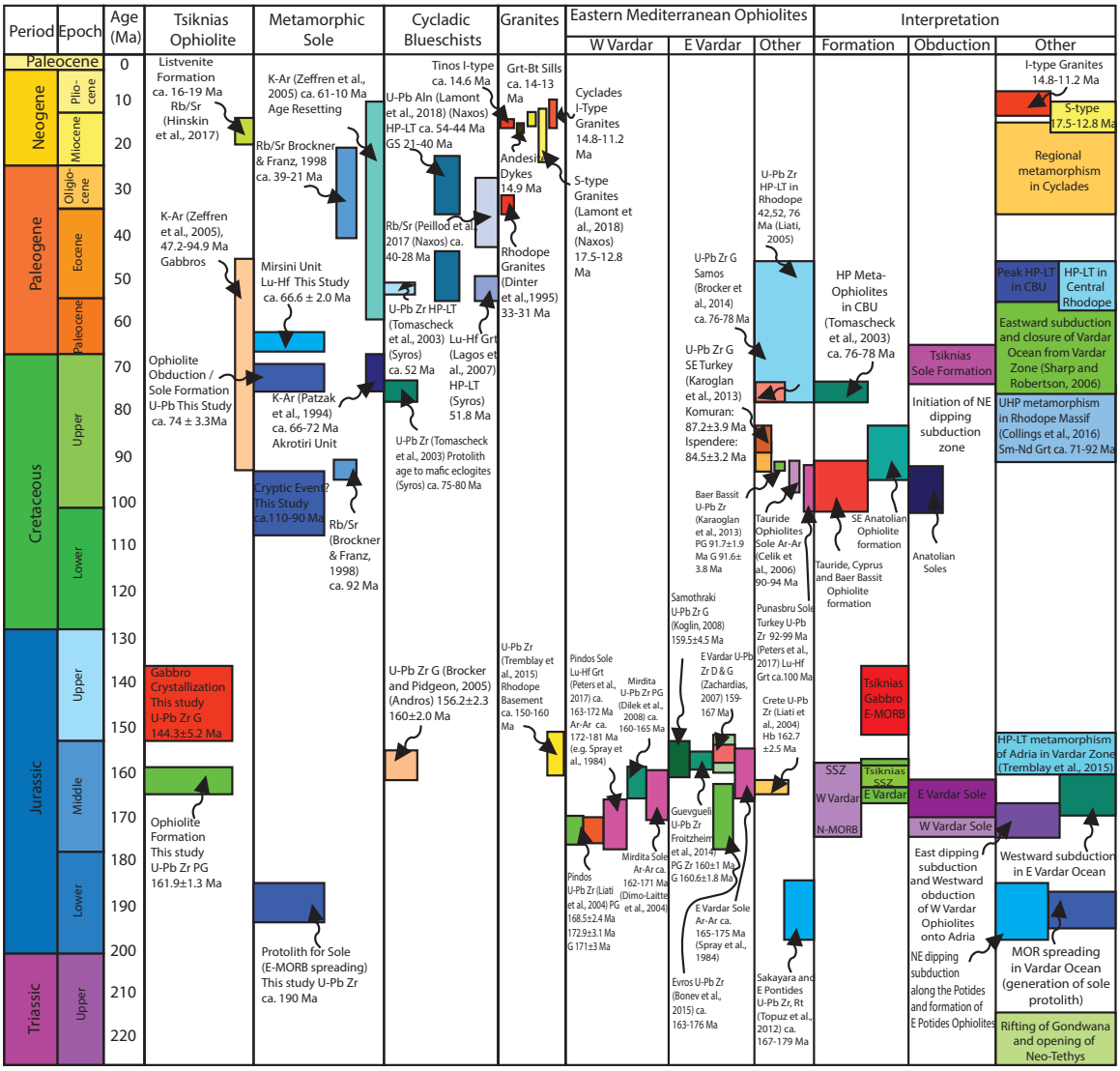


Figure 2.30: Weighted mean plots of U–Pb data of all samples with a summary time chart. Annotated time chart for the Tsiknias Ophiolite and metamorphic sole with a compilation of literature age data from U–Pb, ^{40}K–^{39}Ar, ^{40}Ar–^{39}Ar, Rb–Sr and Lu–Hf and Sm–Nd garnet ages. It includes data from granites, the Cycladic Blueschists and other Eastern Mediterranean Ophiolites to help correlate the reported ages in this study.

basin setting by ca. 145 Ma and/or seizure of subduction during the latter phases of spreading by ca. 144 Ma.

2.8.1.2 Mechanism of ophiolite formation

The stratigraphy of the Tsiknias Ophiolite is unusual with respect to conventional Penrose stratigraphy particularly the intrusion of such a large plagiogranite body (see

Fig. 2.10), the thick and highly tectonized gabbros of the Moho Transition Zone, and lack of exposure of upper-crustal rocks, all of which makes it difficult to fit this ophiolite into this traditional framework. Furthermore, a minimum emplacement depth of 25 km (ca. 8.5 kbar) for the plagiogranite (17TL35) suggests very deep crystallization, much greater than normal oceanic crust and deeper than any other recorded ophiolite plagiogranite. Gabbro P–T results, albeit with larger errors.

Additionally, petrographic, and major and trace element analyses suggest the entire ophiolite experienced extensive sea-floor alteration. Katzir et al., (1996) shown that δ^{18}O oxygen isotope values for gabbros, serpentinites and sole material range from 6-15‰, consistent with low temperature (50–200°C) alteration of parent rocks by sea-water at varying water/rock ratios. The early high-temperature alteration and amphibolitization of the gabbros, also require the circulation of δ^{18}O-enriched sea-water and this must have occurred during ophiolite formation close to the hot spreading center (Katzir et al., 1996). This also requires a mechanism to hydrate the Moho Transition Zone. One possibility is that a fault or shear zone enhanced permeability as the gabbros where crystallizing, or alternatively the gabbros crystallized at relatively shallow depths, much shallower than can be accounted for by a Penrose type stratigraphy. Additionally, Katzir et al., (1996) argue that the peridotites must have been exposed at the sea floor shortly after the ophiolite formed, due to the poor permeability in oceanic crust. The combination of these factors raises the possibility whether the Tsiknias Ophiolite may represent an Oceanic Core Complex.

Oceanic core complexes describe domes of serpentinized mantle and gabbros exposed on the seafloor, in the footwall of large normal faults (oceanic detachment faults) that accommodate lithospheric extension. They have been widely recognized along slow and ultraslow-spreading ridges, with over 200 known occurrences today (e.g. Ildefonse et al., 2007; Escartin et al., 2008; Smith et al., 2006; Cannat et al., 2006; Tucholke et al., 2008). It is suggested that they may comprise 50-60% of some ridge segments of the Mid-Atlantic Ridge (Smith et al., 2006), and are often located at the inside corner of ridge-transform intersection (Cannat et al., 2006; Ildefonse et

al., 2007; Escartin et al., 2008; Smith et al., 2006). Oceanic detachment faults dip towards the ridge axis and operate in some areas for several million years, resulting in the development of a series of topographic highs (commonly 1000 m) relative to the neighboring seafloor that are spread off-axis (e.g. Tucholke et al., 2008; Ildefonse et al., 2007).

An oceanic core complex model may potentially explain the lack of crustal ophiolitic rocks and high degree of tectonization in gabbros within the Moho Transition Zone. In this model, these would have crystallized below and within an active oceanic detachment surface and this would account for high-temperature shearing fabrics and hydration of seawater, and amphibolitization of gabbro. It may also be possible that the Elias Thrust (directly above the gabbro horizons), could actually represent a relict oceanic detachment fault that was reactivated during the obduction process. This could explain the preservation of high-temperature and magmatic top-to-NE S–C' fabrics in leuco-gabbros, the opposite to the SW directed thrusting direction during obduction. An oceanic core complex model may also explain the great emplacement depth of the plagiogranite and gabbros as in slow spreading environments, deep, low degree K-poor melts would be produced and could fractionate extensively during their ascent towards the surface. They would also be expected to crystalize at greater depths due to conductive cooling associated with amagmatic spreading.

An oceanic core complex model may also explain why the meta-basalts exposed on other islands do not acquire the same SSZ signature as the gabbros and plagiogranites on Tinos. This is because extrusive volcanic rocks are often in adjacent basins to oceanic core complexes, and not directly associated with them. However, the meta-basalts on Naxos are definitively not related to the Tsiknias Ophiolite, and probably represent alkali and ocean island basalts that formed on the subducting plate (lower plate) similar to the metamorphic sole protolith. Meta-basalts on Naxos are exposed today within trench mélange, pelagic sediments and limestone exotics (Lamont et al., in press), similar to the Haybi Complex beneath the Oman/UAE Ophiolite (Searle et al., 2004). Unfortunately, the lack of exposure and current erosion level of

the Tsiknias Ophiolite makes it difficult to conclusively prove this model and therefore it remains complete speculation.

In summary, unlike conventional supra-subduction zone ophiolites, the Tsiknias Ophiolite does not represent a standard Penrose-type ophiolite and remained as a stable and cooling piece of oceanic lithosphere for approximately 90 Myrs, before it was obducted.

2.8.2 Timing of Ophiolite Emplacement and Sole Formation

The timing of high-grade metamorphism and anatexis within the sole is constrained to ca. 74 ± 3.3 Ma, approximately 90 Myrs after the ophiolite formed. This is an unusual occurrence, as many ophiolites and their soles normally form at or around the same time (Wakabayashi and Dilek, 2000; van Hinsbergen et al., 2015). Examples include the Semail Ophiolite (Searle and Malpas, 1980; Searle and Cox, 1999; Gnos and Peters, 1993), the Bay of Islands Ophiolite in Newfoundland (Casey and Dewey, 1884; Dewey and Casey, 2011, 2013), the Vourinos-Pindos Ophiolite (e.g. Robertson, 2002) and Albanian ophiolites (Dilek et al., 2008). To explain subduction zone geochemical signatures within the ophiolitic crustal rocks, metamorphic sole formation in a subduction setting allows oceanic crust to be subducted simultaneous to forearc spreading and generation of SSZ crust in the overriding upper-plate. Importantly, the Tsiknias Ophiolite does not fit this pattern, as the ca. 90 Myr age difference between sole formation and ophiolite formation cannot be explained by a single subduction zone for both its origin and emplacement. Although different to most ophiolites, globally, no soles have been found that predate the ophiolites (Wakabashi and Dilek, 2003) which suggests that metamorphic soles form simultaneously with or following the first generation of oceanic crust. This led Wakabayashi and Dilek, (2003) to suggest that many ophiolites could have formed above an older subduction zone than the one responsible for the formation of their metamorphic sole. Under these circumstances, the ophiolite would be emplaced above a separate, younger, subduction zone than the one they formed above. The discrepancy in ages (ca. 162 Ma vs 190 Ma) and geochemistry (SSZ vs E-MORB)

between the Tsiknias Ophiolite and sole, are consistent with a model of separate subduction zones, thus requiring the formation of the sole to be completely unrelated to the subduction zone that formed the ophiolite. The Tsiknias Ophiolite likely formed over a time interval between ca. 162 Ma and 140 Ma. This is because 90 Myrs of continuous spreading equates to the formation of 1000's km of oceanic crust. If the ophiolite did form above the same subduction zone as the sole, it would require 1000's km of shortening to close a wide ocean basin, and is in disagreement with the present day regional structure, which rather argues for orders of magnitude less shortening.

It is unclear what the significance of the 110–70 Ma U–Pb age spectrum recorded within the sole represents, although it is similar to the reported ^{40}K –^{39}Ar, ^{40}Ar–^{39}Ar and Rb–Sr age ranges within the "Upper Unit" on Tinos and elsewhere in the Cyclades. These ages are interpretted as mixing between old cores and young rims as zircon rim analysis is consistent with the Lu–Hf garnet age. However, if these ages are not due to mixing, it is possible the earlier of these ages (ca. 110–100 Ma) could represent a phase of off–axis magmatism in old oceanic crust prior to subduction that may have remobilized and grown zircon in gabbroic and basaltic lithologies.

2.8.3 Sole Formation: Subduction Initiation in Old Cold Oceanic Lithosphere?

Partial melting within the uppermost five meters of the sole, directly under the Tsiknias Thrust and base of the ophiolite, occurred dominantly by water-saturated melting of amphibole during ductile shearing (Fig. 2.7-2.8 and 2.30). Burial, prograde metamorphism and subsequent dehydration of underlying metasediments within the sole and Mirsini Unit could have acted as a possible water source to drive partial melting due to fluid driven off during progressive underthrusting and dehydration reactions within subducted oceanic crust and sediments.

In many ophiolites worldwide (with coeval ophiolite and sole formation), the metamorphic sole has been proposed to represent the subduction zone interface with the heat causing metamorphism derived from the overlying mantle wedge. In these

settings, the mantle wedge is expected to be hot and would conductively heat the top of the subducting slab. Based on this reasoning, many argue that subduction initiation must occur immediately prior to sole formation (Hacker, 1990; Cowan et al., 2014), because if left any longer than a few Myrs, the mantle wedge would have cooled sufficiently (e.g. Gerya et al., 2006).

Although the processes governing the initiation of subduction zones remain highly debated, modelling studies of induced subduction initiation (Hall et al., 2003; Stern, 2004) suggest that subduction zones can form within a plate due to either: (i) far-field plate stresses that force convergence across a zone of weakness (e.g., the Maquarie-Puysegur-Fiordland system near New Zealand; Ruff et al., 1989), or (ii) the collision between an existing subduction zone and continental crust or unusually thick oceanic crust (e.g., Ontong Java Plateau collision with the Solomon Islands Trench; Cooper and Taylor, 1987). In contrast, "spontaneous" subduction initiation is thought to occur when stable ocean lithosphere, becomes gravitationally unstable and begins to sink back into the mantle, either adjacent to gravitationally stable oceanic lithosphere, or adjacent to buoyant continental crust (e.g. Karig, 1982; Casey and Dewey, 1984; Leitch, 1984; Stern and Bloomer, 1992; Stern, 2004; Dewey and Casey, 2011, 2013). Dewey and Casey (2011) suggest subduction initiation along a transform fault-fracture zone preserves a ridge at the leading edge of the overriding plate, perpendicular to the trench. With continued spreading at that ridge, it is expected that SSZ oceanic crust would be generated in the overriding plate. It is also proposed that in addition to transform faults, oceanic detachment faults at MORs may also play a role in subduction initiation (van Hinsbergen, 2015), and would produce a subduction zone parallel to a slow spreading center (Maffione et al., 2015). However, in this model an identical protolith age for both the sole and ophiolite is expected, as both would form at the same time. Although these scenarios maybe somewhat applicable to other ophiolites, none cannot explain subduction initiation in cold, old and stable oceanic lithosphere, as represented by the Tsiknias Ophiolite.

Many active subduction zones in the Western Pacific initiated away from mid

ocean ridge spreading centers on old cold Jurassic aged Pacific Oceanic Crust. The inconsistent ages between the ophiolite and the sole, strongly suggest the subduction zone forming the Tsiknias Metamorphic Sole must have also initiated away from a spreading ridge. Dymkova and Geyra, (2013) also propose that well-hydrated and deep oceanic fracture zones away from mid ocean ridges, could be potential zones for subduction initiation, as porous fluid-flow allows for percolation along faults which lubricate the subsequent subduction zone. This idea satisfies petrological, field and U–Pb data of the Tsiknias Ophiolite, as the gabbro, mantle and underlying amphibolites from the metamorphic sole records strong hydration.

Alternatively, the Gorringe Bank off the coast of Iberia could be a present-day analogy to subduction initiation in cold ca. 100 Myr old oceanic crust (Haywood et al., 1999; Munt et al., 2010 and references therein). This feature represents an intra-oceanic thrust, placing old oceanic crust and mantle over even older oceanic crust, strikes (NW–SE) oblique to the spreading direction, and could indeed represent similar processes in action to what is observed on the Tsiknias Thrust.

2.8.4 The Cause of Metamorphism in the Sole: Thermal Conduction vs Shear Heating

P–T conditions for metamorphism in the Tsiknias sole of ca. 8.5 kbar, 600–850 °C is significant, and correspond to an apparent metamorphic field gradient of ca. 1000°C/km. This is inconsistent with heating by exclusively thermal conduction due to the overriding mantle wedge. This is because if subduction initiated within cold and old oceanic lithosphere, conductive heating alone from an already cooled mantle of the upper plate would be insufficient to drive high-grade metamorphism at supra-solidus temperatures on the subduction interface of the down going slab (Tsiknias Thrust). Additional sources of heat are therefore necessary to form a metamorphic sole and an inverted temperature gradient.

It is possible that during subduction initiation, advection of hotter asthenospheric mantle would flow into the newly formed mantle wedge and would subsequently

act to heat the subduction interface, and this has been predicted in numerical models as the subducted slab starts to roll back (e.g. Stern, 2004).However,, shear heating on the subduction interface must be important in this case (Wada et al., 2008; Duarte et al., 2015; Edwards et al., 2015). It is shown that shear heating is required to explain the measured heat flow discrepancies in many active steady-state subduction zones (England, 2018), particularly if the mantle wedge had cooled over a long time-period. Field constraints of the Tsiknias Ophiolite suggest metamorphism of the sole could be due to a combination of both conductive heating and shearing. Although some argue shear heating would be localized along the particular fault plane and the addition of fluids would reduce the coefficient of friction and therefore substantially limit the degree of heating. The calculated temperature at 25 km depth for 90 Myr old oceanic lithosphere using the Parsons ans Schlater thermal plate cooling model is ca. 500 °C and thus clearly reveals that additional heat sources are required to cause heating and metamorphism in sole otherwise the temperature would be limited to 250°C from conduction alone. Although strain is localised on the Tsiknias Thrust representing the ophiolite contact and this is associated with the highest temperatures, high-strain is also distributed throughout the entire sole-section and underlying Mirsini Unit.

A potentially important mechanism for transient heating in shear-zone environments is seismicity. This could be particularly important in subduction zone settings, as seismicity can result in transient localized heating in rocks and is recorded over a range of depths, with variable magnitudes, frequencies and timescales (e.g. Rice, 2006; Dragert et al., 2001).

The Tsiknias Thrust exhibits bi-modal deformation styles, with plastic flow punctuated by episodic melting and brittle fracture consistent with episodic and transient heating during rapid slip. Although these types of behavior have been previously assumed to occur on different fault segments: one with stable, rate-strengthening friction and the other with rate-weakening friction that leads to stick-slip behaviour, the 2011 Tohoku-Oki earthquake shown this need not be the case as it accumulated its largest seismic slip in the area that had been assumed to be creeping (Noda and La-

pusta, 2013). Thus, stable, rate-strengthening behavior at low slip rates can be combined with co-seismic weakening due to rapid shear heating of pore fluids facilitating unstable slip on segments that can creep between events (Noda and Lapusta, 2013; Rice, 2006).

It has been shown that during rapid slip, weakening occurs due to: (1) thermal pressurization of pore fluid within and adjacent to the deforming fault core, which reduces the effective normal stress and therefore the shear strength for a given friction coefficient and (2) heating at highly stressed frictional asperities, which produces macroscopic melting, or gel in silica-rich lithologies, which act to reduce the coefficient of friction (Rice, 2006). Theoretical modelling, combined with lab-determined hydrologic and poro-elastic properties of fault core materials and lab friction studies at high slip rates reveals that during large degrees of slip, rocks are predicted to lose almost all strength and that melting should occur over much and, for small enough slip, all) of the seismically active zone (Rice, 2006). Brown and Fialako, (2011) also shown that initial weakening is associated with the formation of hotspots and macroscopic streaks of melt, which partially unload the rest of the slip interface. These workers shown that melt begins to form when the average rate of frictional heating exceeds 0.1–0.4 MWm^{-2} while the average temperature of the shear zone is sub-solidus. Furthermore, predicted shear fracture energies from such experients match seismically derived fracture energies by these heating mechanisms, over a range of slip magnitudes, and uncertainty of parameters (Rice, 2006), hence making seismicity a plausible mechanism for causing significant heating along major shear zones. Despite the potential for this process, it remains unclear whether the timescales for such transient heating would be recorded in mineral assemblages over 10's to 100's of meters. However, if it is indeed the cause of heating, temperatures of at least 850°C must have been achieved directly unde the Tsiknias Thrust.

Pressures of ca. 8–9 kbar equate to 25–28 km depth within oceanic lithosphere, which is well within the seismogenic zone recorded on subduction interfaces. It therefore seems plausible that the condensed and inverted thermal gradient across the

Tsikinas metamorphic sole is a combined result of thermal conduction but also importantly ductile shearing and transient heating during rapid slip. This latter mechanism provided the additional heating pulse required to induce melting that propagated into the surrounding rocks, and inducing high-grade metamorphism. The Tsiknias metamorphic sole thus possibly represents a record of intermediate depth (20–35 km) seismicity along a major subduction thrust and could be used as an analogue for present day subduction megathrust earthquakes. Other shear zones associated with highly condensed thermal gradients including other metamorphic soles should therefore be examined for such features in light of these observations.

2.8.5 Integrating the Tsiknias Ophiolite into the Tectonic Framework of Balkan Ophiolites

In order to successfully correlate the Tsiknias Ophiolite to other Aegean ophiolites, a thorough understanding of the regional ophiolite geology is necessary. Ophiolites are distributed across the Balkan Peninsular in two distinct belts striking NNW–SSE separated by the Pelagonian domain. There are three major tectonic models for ophiolite genesis and emplacement (see chapter 1) but the most favourable is the single ocean and far travelled nappe model (Papanikolaou, 1984) based on the following reasons. The Dinaric–Mirdita–Pindos–Vourinos–Orthis ophiolite belt to the west is also known as the "West Vardar Ophiolites" and sits above Adria continental rocks after Schmidt et al., (2008). The "West Vardar Ophiolites" show a distinct west to east change of geochemical composition and internal structure. The western part of the "West Vardar Ophiolites" is dominated by fertile lherzolites, locally exposed in fossil oceanic core complexes (e.g. Maffione et al., 2013; Tremblay et al., 2009), and a thin crust with high-Ti MOR affinity (Dilek et al., 2008; Saccani and Photiades, 2004). The high Ti/V ratios of these MOR-type ophiolites (e.g., Mirdita, Othris, and Pindos), ranging between 20 and 50, are incompatible with a subduction affinity (Reagan et al., 2010) and strongly suggest that these MOR-type ophiolites represent relics of Neo-Tethyan lithosphere formed prior to Jurassic subduction initiation (Maffione et

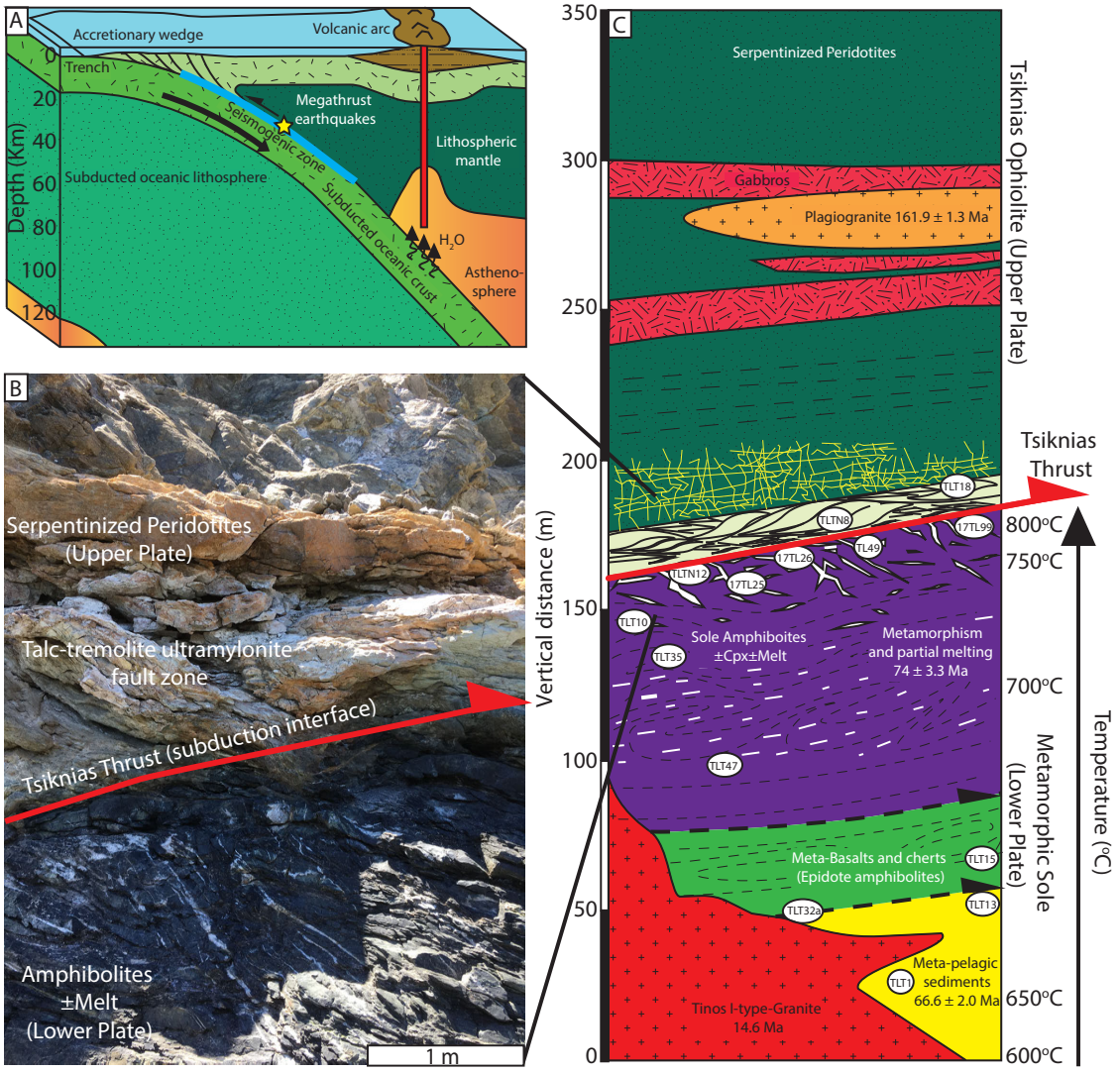


Figure 2.31: Summary temperature tectonic section through the metamorphic sole

al., 2015). The West Vardar Ophiolites contain a diverse range of mantle rocks, from fertile lherzolites to depleted harzburgites (e.g. Orthis Ophiolite), indicative of both anhydrous MOR-type and hydrous SSZ-type melting regimes (Barth et al., 2008). IAT and boninitic compositions have been reported (Barth and Gluhak, 2009; Jones and Robertson, 1991; Photiades et al., 2003; Saccani and Photiades, 2004). These variations were interpreted by Maffione et al. (2015) as the result of SSZ melts that during subduction initiation impregnated the pre-existing Neo-Tethyan lithosphere formed at a MOR. The eastern domain of the West Vardar Ophiolites is dominated by depleted

to extremely depleted harzburgites and a thick crustal sequence with an SSZ signature superimposed on it, indicating formation of oceanic lithosphere above an intraoceanic subduction zone (e.g., Pearce et al., 1984). Crustal ages of the West Vardar Ophiolites span the latest Bajocian-early Oxfordian (160–170 Ma) interval based on radiolarian cherts intercalated within the extrusive sequence of the Albanian Mirdita ophiolite (e.g. Chiari et al., 1994; Marcucci et al., 1994; Marcucci and Prela, 1996; Prela et al., 2000) and the Vourinos ophiolite of Greece (Chiari et al., 2003) (Figs. 2.1, 2.32). This age is comparable to zircon U–Pb ages of plagiogranites and gabbros from the Vourinos (172.9 ± 3.1 and 168.5 ± 2.4 Ma) and Pindos (171 ± 3 Ma) ophiolites (Liati et al., 2004) (Fig. 2.1, 2.30). Metamorphic soles are widespread below the West Vardar Ophiolites and show overall ^{40}Ar–^{39}Ar cooling ages of 170 Ma (Dimo-Lahitte et al., 2001; Roddick et al., 1979; Spray and Roddick, 1980; Spray et al., 1984; Sostarić et al., 2014) (Fig. 2.1, 2.32). These ages within the metamorphic soles probably slightly post-date the actual inception of the subduction (van Hinsbergen et al., 2015), indicating that subduction in the Vardar Ocean initiated in the Middle Jurassic, sometimes between 175 and 170 Ma (Maffionie and van Hinsbergen, 2018). Contrastingly to the east of the Pelagonian Domain, the Guevgueli-Demir-Kapija ophiolite belt collectively known as the "East Vardar Ophiolites" (Schmid et al., 2008), was emplaced above European-derived rocks (Schmid et al., 2008). The "East Vardar Ophiolites" were thrust towards the NE in Late Jurassic time upon units thought to belong to the former south eastern European margin of the Neo-Tethys, as suggested by Late Jurassic reef limestones uncomformably covering these ophiolites (e.g. Schmid et al., 2008). However, the tectonic history that led to the formation and emplacement of the "East Vardar Ophiolites" is still a source of debate. Schmid et al., (2008) suggested that they formed during SSZ spreading above a westward dipping, intraoceanic subduction zone in the Late Jurassic, followed by their obduction onto the Eurasian margin, whereas Robertson, (2002) argues they formed above a NE dipping subduction zone. In general, the "East Vardar Ophiolites" are thought to have formed close to or within the passive margin of Eurasia upon back-arc extension produced by an eastward (Europe) dipping subduction zone

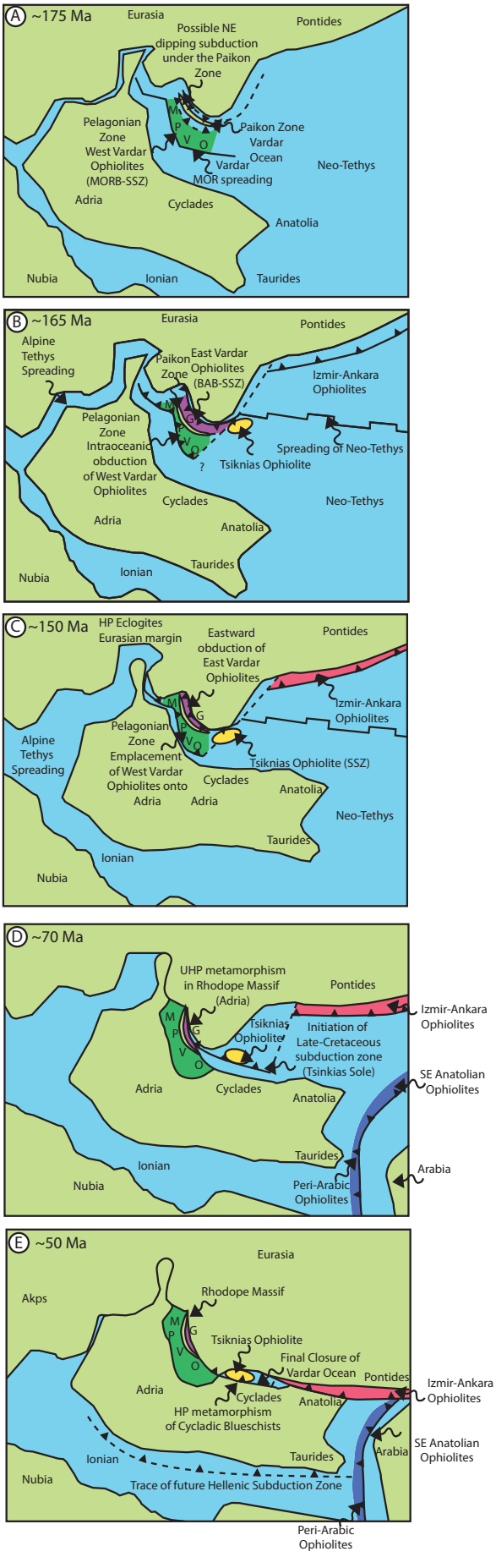


Figure 2.32: Cartoon paleogeographic reconstruction showing the position of the Tsiknias Ophiolite during the closure of the Vardar Ocean based on data from Maffione et al., (2018) and results from this study. A) Approximately 175 Ma, MOR spreading the the central Vardar Ocean forming MORB signature in the west Vardar Ophiolites, before initiation of eastward dipping subduction zone and obduction of the West Vardar Ophiolites. Possible NE dipping subduction at this time under the Paikon Zone to produce arc volcanism. B) Approximately 165 Ma showing the position of the Eurasian, Adriatic, and Nubian continents and the positions of westward dipping subduction zone (forming the East Vardar Ophiolites) to the west of Eurasia and an east dipping subduction zone to the east of Adria. The location of the MOR ophiolites derived from the Vardar Ocean is shown in stage (a), while these plus the SSZ and BAB ophiolites produced after subduction initiation are shown in stage (b). C) Approximately 150 Ma, obduction of the West Vardar Ophioites onto Adria and eastward obduction of East Vardar Ophiolites on to Eurasia, subsequent HP metamorphism of Eurasian margin (Tremblay et al., 2015). Position of Tsiknias to the SE of the East Vardar Ophiolites to the east of the zone of active subduction. D) Approximately 70 Ma, initiation of new NE dipping subduction zone, obduction of the Tsiknias Ophiolite, sole formation and UHP metamorphism of Adria rocks in the Rhodope massif (Collings et al., 2016). E) Approximately 50 Ma, final closure of the Vardar Ocean, HP metamorphism of Cycladic Blueschists and emplacement of the Tsiknias ophiolite onto the Cycladic (Adriatic) continental margin. Key: Spreading ridges (thick black lines), inferred transform faults (thin dashed black line), trenches (thin line with triangles) and inferred positions of future trenches (dashed lines with triangles) are shown. The ophiolite codes are as follows; M = Mirdita ophiolite; G = Guevgueli ophiolite; P = Pindos ophiolite, V = Vourinos ophiolite, and O = Othris ophiolite. The locations of the West Vardar Ophiolite belt (green), East Vardar Ophiolite belt (orange), Izmir-Ankara Ophiolite belt (purple), and Arabic-Tauride Ophiolites (dark blue) are indicated by the thick colored lines

(Bébien and Mercier, 1977; Bébien et al., 1987; Brown and Robertson, 2004; Robertson et al., 1996; Saccani et al., 2008). To explain the emplacement of these ophiolites onto the Eurasian margin, Gallhofer et al., (2017) invokes a reversal in subduction polarity (from Europe-ward to Adria-ward) occurring shortly after back-arc spreading of the Guevgueli basin. However there are no metamorphic soles identified below the "East Vardar Ophiolites". The geochemical composition of the "East Vardar Ophiolites" varies from back arc basin (BAB) affinity in the south (Guevueli ophiolite; Saccani et al., 2008), to a mix of MOR- and SSZ-geochemistries that also includes boninites in Serbia and Macedonia (Božović et al., 2013; Marroni et al., 2004; Resimić-Šarić et al., 2005, 2006; Šarić et al., 2009). In northern Greece (Guevgueli Ophiolite) the "East Vardar Ophiolites" occur between the deformed European margin (Rhodope Massif) and a continental fragment (i.e., Paikon arc; Brown and Robertson, 2004), which detached from either the continental margin Europe (Anders et al., 2005; Brown and Robertson, 2004) or Adria during rifting (Godfriaux and Ricou, 1991; Ricou and Godfriaux, 1991, 1995).

The origin and emplacement mechanisms of these two ophiolite belts has been a source of debate over the last three decades, particularly whether they represent closure of the same or separate ocean basins. Assuming the single ocean basin and far travelled nappe model of Maffione and van Hinsbergen, (2018). The "West Vardar Ophiolites" ophiolites are interpreted to have formed above an eastward dipping subduction zone off the eastern margin of Adria during the mid-Jurassic at ca. 170 Ma and were obducted to the SW onto the Adriatic margin in the latest Jurassic to Early Cretaceous (e.g., Schmid et al., 2008). Whereas, the "East Vardar Ophiolites" formed on the to the eastern side of the Vardar Ocean. They either formed first in a back-arc basin setting (e.g. Guevgeili Ophiolite) above above a NE dipping subduction zone between the Paikon Arc and the Eurasian Margin (Robertson, 2002), or above a westward dipping subduction zone a NE-dipping subduction zone at ca. 160 Ma, responsible for SSZ signatures and eastward emplacement of ophiolites onto the Eurasian Margin (Maffione and van Hinsbergen, 2018 and references therein). The latter is the

most likely as continued westward dipping subduction on the eastern side of the Vardar Ocean resulted in high-pressure metamorphism as the Eurasian Margin attempted to subduct at ca. 150 Ma (Tremblay et al., 2015).

Despite this Jurassic aged deformation and metamorphism, it remains debated when the "Eastern Vardar Ophiolites" were finally emplaced onto the Adriatic continental margin, associated with the final closure of the Vardar Ocean. Integration of U–Pb and trace element data with this tectonic framework, suggests that the Tsiknias Ophiolite must have also originated in an ocean to the north east of Tinos, and this seaway must have remained open until at least ca. 74 Ma. The age and SSZ geochemistry of the Tsiknias Ophiolite (ca. 162 Ma) matches "Eastern Vardar Ophiolites", thus potentially making it an along strike equivalent. In this scenario, the Tsiknias Ophiolite must have formed above an along strike equivalent to the Jurassic-age westward-dipping subduction zone to explain its SSZ chemistry, but unlike the mainland counterparts, this ophiolite was not obducted to the east at the same time it formed. One possibility is that the westward dipping Jurassic subduction zone responsible for its formation initiated at the mid-ocean ridge-transform intersection, and therefore that subduction was aligned perpendicular to the spreading axis (E–W). Under these circumstances, the southern portion of the spreading ridge may survive obduction if the oceanic crust had migrated further south beyond the zone of active subduction. The migration of the ophiolite away from subduction is consistent with the transition from SSZ to BAB and E-MORB gabbro chemistry, with the latter associated with younger ages (144.3 $\pm$ 5.2 Ma). Alternatively, these patterns could also be explained if subduction seized by ca. 150 Ma, whereas spreading continued for another 10 Myrs.

The obduction of the Tsiknias Ophiolite and formation of the metamorphic sole therefore must have occurred as the southern Vardar Ocean started to close during the Late Cretaceous times and this must have been associated with the development of a Late Cretaceous aged NE-dipping subduction system. This is further supported by evidence from along the Paikon and Axion zones which also suggests the Vardar Ocean remained open until the Late Cretaceous-Paleogene (Sharp and Robertson, 2006). Re-

cent Lu–Hf and Sm–Nd garnet dating of *(U)-HP* rocks within the Rhodope massif suggest that the Adriatic margin attempted to subduct towards the NE beneath Eurasia at ca. 92–71 Ma (Collings et al., 2016). This is interpreted to record the closure of the Northern Vardar Ocean and precisely correlates with the timing of sole formation on Tinos.

2.8.6 From Ophiolite Obduction to Attempted Subduction of the Cycladic Continental Margin

Following this intra-oceanic ophiolite obduction event at ca. 74–66 Ma (Fig. 2.32-2.33), the underlying high-pressure rocks of the Cycladic Blueschist Unit, record cold subduction of oceanic rocks and the Cycladic (Adriatic) continental margin at ca. 52–50 Ma (e.g. Lagos et al., 2007; Tomascheck et al., 2003), also down a NE-dipping subduction zone. It is suggested that this subduction signature recorded by the high pressure-low temperature (*HP-LT*) rocks is related to the same subduction zone that formed the Tsiknias Ophiolite metamorphic sole, albeit ca. 20 Myrs later. This implies that the NE-dipping subduction zone responsible for both the metamorphic sole and the underlying high-pressure rocks must have remained static and did not roll-back, as both rock types were subducted at different times (ca. 70 Ma and 52 Ma respectively), but are now preserved together within one km structural distance. In contrast, under a scenario of a retreating subduction zone, we would expect the younger *HP–LT* rocks to be located much further south than their current position.

This subduction-obduction process is similar to that recorded in the Oman-UAE, where the As-Sifah eclogites and blueschists within the Arabian continental margin attempted to subduct on the same subduction zone that formed the sole (e.g. Searle et al., 2004). This also occurred approximately 18 Myrs after the Semail Ophiolite formed and was obducted (Searle et al., 2004). As noted above, there is growing evidence for closure of the Northern Vardar Ocean as recent as the Late Cretaceous-Paleogene (Sharp and Robinson, 2006), and 71–92 Ma *(U)-HP* metamorphism associated with attempted NE-dipping continental subduction under Eurasia (Collings et

al., 2016). In this scenario, the same Late-Cretaceous to Eocene subduction zone to that recorded on Tinos must have continued along the entire western margin of the Vardar Ocean (striking NNE–SSW today) and was responsible for the collision with Eurasia and Adria.

2.8.7 Final Closure of Vardar Ocean

This Late Cretaceous-Eocene obduction-subduction event in the Cyclades marks the initial stages of closure of the Southern Vardar Ocean and precedes the collision between the Cycladic Massif (Adria) to the SE and the Eurasian plate to the NE during the Late Cretaceous - Eocene producing what has been termed the Aegean Orogeny. The Tsiknias Ophiolite, metamorphic sole, and structurally deeper high-pressure rocks, together with other (U)-HP rocks in the Rhodope Massif represents the only remaining evidence of a relict Cretaceous-Eocene subduction zone that was rooted to the NE of the Cyclades and continued northwards along the Vardar Zone. The Cycladic Blueschists could not have therefore been subducted on the current Hellenic subduction zone, but this earlier Cretaceous-Eocene subduction system that terminated following final closure of the Vardar Ocean at ca. 50 Ma and subsequent collision between Eurasia and Adria (Cyclades). Previous models of continuous slab roll-back and extension in the Aegean since 70 Ma (Jolivet et al., 2012) should therefore be re-examined in light of this new data.

2.8.8 Tectonic Model

The data presented and discussed above can be described in the following tectonic interpretation. A cartoon paleogeographic reconstruction of the closure of Vardar Ocean based on data from Maffione and van Hinsbergen, (2018) is presented in Fig. 2.32 and a simplified tectonic model of the Tsinkias Ophiolite in Fig. 2.33.

1. Formation of the Tsiknias Ophiolite at ca. 162 Ma above a westward dipping subduction zone to the NE of Tinos in present day co-ordinates (Fig. 2.33a).

This subduction zone was associated with SSZ spreading forming the "East Vardar Ophiolites" on the eastern side of the Vardar Ocean. The Tsiknias Ophiolite formed by either one of two mechanisms: i) Mid-ocean ridge magmatic spreading, that would predict the standard ophiolite stratigraphy and the eruptive SSZ to E-type MORB basaltic products being preserved on Paros or Samos. ii) Alternatively, an oceanic core complex mode of extension could have hydrated, exhumed and exposed deep gabbro and mantle on the seafloor, in accordance with oxygen isotope data. E-type MORB gabbros associated with younger ages of ca. 144 Ma suggest the later stages of spreading was not affiliated with subduction. The lower plate material in the metamorphic sole formed further westwards in the interior of the Vardar Ocean at ca. 190 Ma in an E-MORB to BAB setting as revealed by zircon core ages and trace element data.

2. Unlike the "East Vardar Ophiolites", the Tsiknias Ophiolite was not obducted at the time it formed, and remained as a piece of cooling oceanic crust for ca. 90 Myrs. At ca. 74 Ma, a new NE dipping intra-oceanic subduction zone initiated within old cold ca. 190 Ma oceanic crust (the metamorphic sole protolith), potentially in a similar fashion to the Gorringe Bank intra-oceanic thrust today (Fig. 2.33b). The metamorphic sole formed on the subduction interface of the leading edge of the down going (ca. 190 Ma) piece of oceanic crust. The metamorphic sole formed at ca. 74.0 ± 3.3 Ma attained upper amphibolite-facies anatectic conditions of ca. 8.5 kbar and 850°C. Thermal conduction from the mantle wedge alone is insuffcient to explain such temperatures and calls for other mechanisms. It is possible that shear heating provided an additional heating contribution to generate such high temperatures and a steep inverted metamorphic field gradient. Metamorphism propagated down structural level with time, due to the underplating of pelagic sediments as indicated by Lu–Hf garnet ages of 66.6 ± 2.0 Ma from the underlying meta-cherts.

3. During the initial stages of SW directed obduction, the metamorphic sole was

accreted to the base of the ophiolite, and subsequently stacked as a series of imbricate thrust sheets (Fig. 2.33c). The package was affected by out-of-sequence thrusts that structurally repeated the ophiolite sequence (e.g. the Elias Thrust) and thicken the metamorphic sole. The ophiolite and the sole were subsequently thrusted onto the Mirsini Unit pelagic metasediments, that attained amphibolite facies conditions of ca. 8.5 kbar, 660°C at 66.6 ± 2.0 Ma During this process the alkali and OIB basalts and marble 'exotics' preserved on Naxos, that represent off-shore seamounts in the subducting plate, attempted to subduct. This formed trench mélange that is exposed on Naxos, similar to the Haybi complex under the Oman/UAE ophiolite (Searle et al., 2004).

4. The Mirsini Unit, Metamorphic Sole, and Tsiknias Ophiolite together were accreted to become part of the upper plate, and the main subduction interface stepped back. Steady state NE-directed subduction continued between ca. 66–52 Ma, before the arrival of the leading edge of the Cycladic continental margin (representing the NE margin of Adria). Out of sequence thrusts such as the Elias Thrust structurally thickened the Tsiknias Ophiolite, Metamorphic Sole and Mirsini Unit during the later stages of obduction (Fig. 2.33d).

5. Attempted subduction of the Cycladic continental margin at ca. 52–45 Ma, was associated with eclogite- blueschist-facies metamorphism and is recorded within the Tinos "Lower Unit" and the Cycladic Blueschist Unit (Fig. 2.33e). These rocks reached P–T conditions of 24 kbars and 550 °C (Lauren et al., 2018), representing depths of up-to 80 km, before extruding to the SW bounded by passive roof normal sensed top-to-NE sense shear zones at the top (e.g. Vari Detachment) and top-to-SW thrusts at the base (e.g. Lauren et al., 2017). This represents the final closure of the Vardar Ocean and during this stage, the Tsiknias Ophiolite, Metamorphic Sole and Mirsini Unit would have been thrust to the SW onto the depressed and underthrusted Cycladic (Adriaic) continental margin. Following extrusion from 80 km depth and upon reaching mid-crustal depths later in the

orogenic history, these high-pressure rocks were then juxtaposed against the "Upper Unit" by the greenschist-facies top-to-NE shear zone (The Tinos Shear Zone) active during the Miocene, although it remains debated whether this structure was active during regional extension or during a phase syn-orogenic extrusion.

6. I-type granite intrusion occurred at ca. 14.6 Ma. A significant component of E–W shortening caused upright folding during the Miocene that affected all units and folded the detachments. Aplite sills emanating from the I-type pluton intrude the metamorphic sole at Livada Bay. Domino-style brittle normal faults associated with regional extension, clearly cut these sills, indicating the timing of extension must post-date intrusion at ca. 14 Ma.

2.9 Conclusions

The Tsiknias Ophiolite on Tinos, and its continuation onto other Aegean islands is a newly recognized and important ophiolite within the Aegean region. Its formation age, emplacement mechanism and structural relationships to the underlying and younger blueschist- eclogite-facies rocks has significant tectonic implications for our understanding of the Aegean geological evolution. This can be summarized by 11 key points:

1. The age of the Tsiknias ophiolite come from U–Pb zircon ages of a large plagiogranite and gabbros within the Moho Transition Zone section on Mt Tsiknias, from which constrains the plagiogranite and gabbro crystallization and therefore generation of oceanic crust at 161.9 ± 1.3 Ma and ca. 160–140 Ma respectively.

2. The best time constraints on amphibolite-facies metamorphism and localized anatexis within the uppermost five meters of the metamorphic sole are ca. 74.0 ± 3.3 Ma from U–Pb dating of zircon rims from in-situ leuco-diorite melt sweats directly under the Tsiknias Thrust (the main subduction thrust). Garnets from the meta-cherts at structurally deeper levels of the sole also yield a Lu–Hf garnet age of 66.6 ± 2.0 Ma age, indicating metamorphism in the sole occurred in the

Late Cretaceous and propagated down structural level with time. These ages post-date the age of crystallization of the ophiolite crustal sequence by almost 100 Myrs.

3. The Tsiknias Ophiolite can be correlated both geochronologically and geochemically with the "Eastern Vardar Ophiolites" of mainland Greece and Macedonia. Many of the gabbros and plagiogranites demonstrate an SSZ geochemical signature, and therefore indicate the ophiolite formed in a spreading environment above a subduction zone at ca. 162 Ma. This Jurassic subduction zone is proposed to be equivalent to the inferred westward dipping subduction zone off the western margin of Eurasia and therefore the ophiolite formed above and to the east of this subduction zone. However, some gabbros span a transition from BAB to E-MORB affinities and these post-date initial ophiolite formation, crystallizing between ca. 160–140 Ma, suggesting either the Tsiknias Ophiolite migrated away from a subduction environment or subduction seized by ca. 144 Ma.

4. The Tsiknias Ophiolite is dominantly composed of peridotites and sequence of highly tectonized gabbros in the Moho Transition Zone. Intrusive rocks include both primary and cumulate gabbros and a large plagiogranite body that possibly formed by extreme fractionation of deep formed low degree melts at ca. 162 Ma and were emplaced at ca. 8.5 kbar pressures. These pressures are highly unusual and not documented in any other ophiolite globally (where standard oceanic crust is 6-7 km thick; e.g. Searle, 1999). The lack of upper-crustal ophiolite stratigraphy (sheeted dykes, pillow lavas) in combination with the deep intrusive rocks and oxygen isotope data reported by Katzir et al., (1996) make this ophiolite highly unusual. Possible origins include a relict oceanic core complex that formed in a slow spreading environment and survived obduction at the time it formed, others possibilities include that it represents the mantle section of a volcanic arc that has subsequently been eroded, or hyperextended contiental margin. However these ideas are complete speculation and the lack of exposure

and subsequent orogenesis makes it difficult to conclusively test any of these ideas.

5. None of the metamorphic sole rocks can be correlated petrographically or geochemically with the Tsikinas Ophiolite crustal sequence, and therefore detachment and sole formation could not have occurred at a mid ocean ridge axis. The protolith of the metamorphic sole amphibolites are E-MORB basalts and gabbros and give inherited U–Pb ages of ca. 190 Ma. The meta-basalts on Naxos do not belong to the ophiolite sequence, and have ocean island basalt affinities, they formed on the lower plate prior to obduction. However, the meta-basalts on Paros and Samos could potentially represent the upper crust of the Tsiknias Ophiolite. Lower-grade metamorphic rocks in the sole and underlying Mirsini Unit are clearly the metamorphosed and tectonized equivalents of the pelagic and distal oceanic sediments, that overlaid the subducted oceanic crust. These were underthrust and accreted beneath the metamorphic sole and were subsequently metamorphosed to greenschist-facies conditions, as exhumation and thrusting progressed. Triassic exotic limestones and alkali basalts that possibly represented off-axis ocean island basalts or seamounts, form blocks with the tectonic mélanges, similar to those reported from Naxos.

6. Geochronology of the ophiolite crustal sequence and the amphibolite sole rocks suggests that the amphibolites were metamorphosed to upper amphibolite conditions beneath the ophiolite, on a new NE-dipping subduction zone almost 100 Myrs after the formation of the overriding ophiolite. The formation of the Tsinkias Ophiolite is therefore completely unrelated to the formation of its underlying metamorphic sole.

7. Metamorphism to form the sole must have occurred in an intra-oceanic subduction zone setting within old and cold oceanic lithosphere. Although it is unclear how this subduction zone initiated at ca. 74 Ma, it is likely to be analogous to an intra-oceanic thrust, similar to that seen in the Gorringe Bank today, off the

coast of Iberia.

8. The metamorphic sole formed beneath the Moho of the overriding ophiolite at ca. 8.5 kbar, 600–850°C, and is composed of old and therefore cold oceanic crust. Metamorphism along the subduction interface must have shortly followed subduction initiation, as the mantle wedge needs to remain sufficiently hot to drive conductive heating in the subducting slab interface. However, this was not the main heating mechanism. Possible heat sources to drive metamorphism are conductive heating from a newly developed mantle wedge (hotter mantle rocks than that preserved in the ophiolite), or however the most important is probably shear heating and seismicity along the subduction interface.

9. SW-directed thrusting during the subduction-obduction process occurred over a period of ca. 20 Myrs, and specifically between ca. 74–52 Ma. These time constraints record the evolution of a single subduction zone from subduction initiation to maturity, and termination upon continental collision. Obduction of the Tsiknias Ophiolite preceded *HP–LT* Eocene metamorphism of the Cycladic Blueschists from the same NE-dipping subduction zone responsible for the formation of the metamorphic sole.

10. The traditional ophiolite 'stratigraphy' is structurally repeated by out-of-sequence thrusts and reactivated by both high-angle and low-angle brittle-ductile faults that were active during the Miocene. The metamorphic sole and underlying meta-sediments is highly attenuated and truncated by a greenschist-facies extensional shear zone that juxtaposes it against footwall high-pressure rocks of the Cycladic Blueschist Unit.

11. This subduction-obduction process between ca. 74–52 Ma, marks the first stages of the Aegean Orogeny. This event records the final closure of the southern Vardar Ocean to the NE of the Cyclades during the Late Cretaceous-Eocene. This interpretation agrees with geological evidence from mainland Greece (Sharp and Robertson, 2006; Collings et al., 2016) where it is suggested the Northern

Vardar Ocean remained as an open seaway until at least the Late Cretaceous time before NE-directed subduction, subsequent *(U)-HP* metamorphism and finally continental collision.

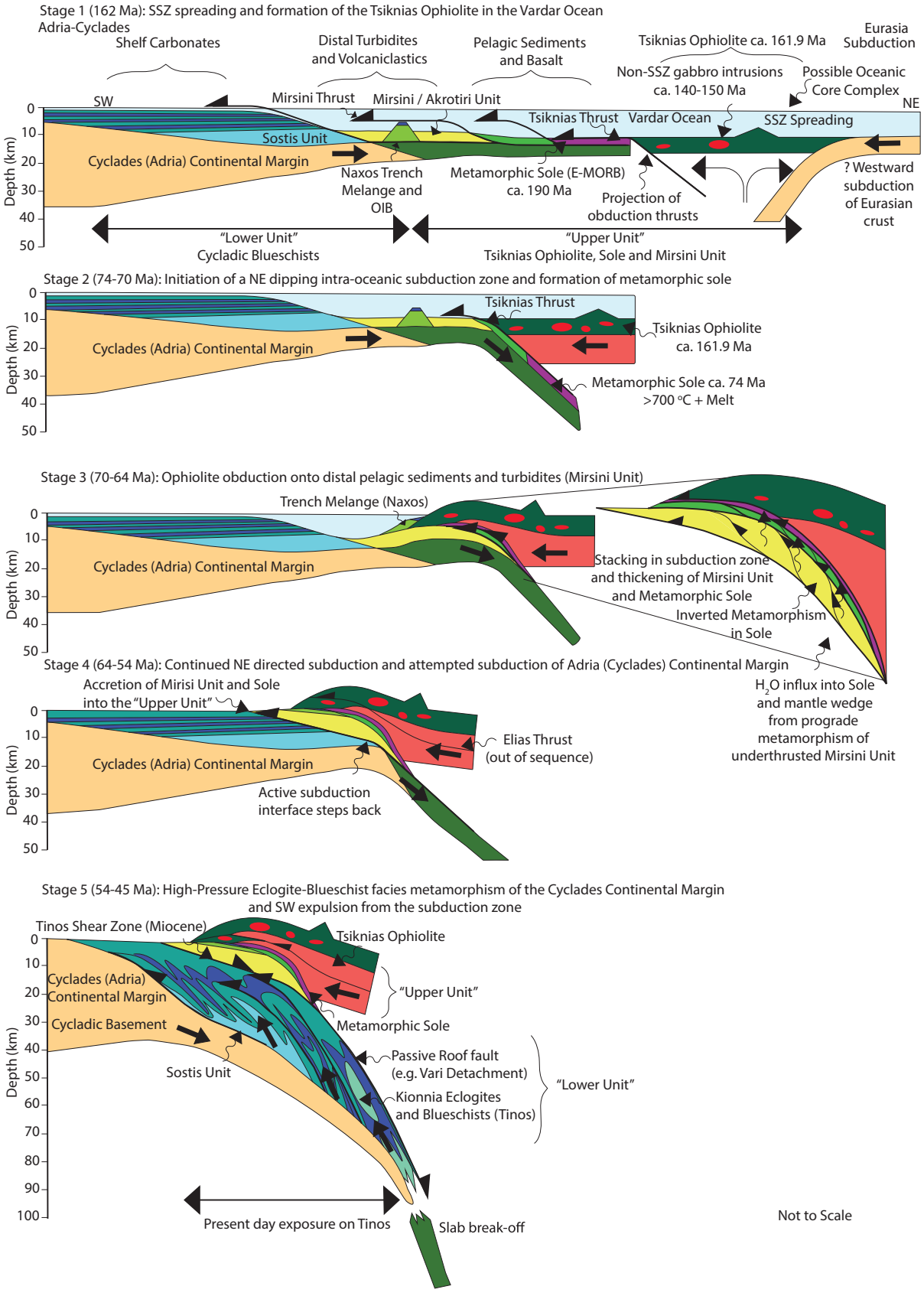


Figure 2.33: Continues on next page

Figure 2.33: Tectonic model for the formation and emplacement of the Tsiknias Ophiolite, metamorphic sole, and subduction of the NE Cycladic continental margin. Stage 1: 161.9 Ma Tsiknias Ophiolite formation above a westward dipping subduction zone, pre-existing ca. 190 Ma E-MORB crust to the SW which is the protolith to the metamorphic sole. Stage 2: ca. 74 Ma initiation of NE dipping subduction zone in ca. 90 Myr old oceanic crust and sole formation on the subduction interface due to conductive and shear heating. Stage 3: Ophiolite obduction and stacking of Mirsini Unit distal oceanic meta-sediments beneath the ophiolite. Stage 4: Detachment below the Mirsini Unit and main subduction thrust structurally steps backwards. Continued subduction for 20 Myrs before arrival of continental margin. Stage 5: Attempted subduction of the Cycladic continental margin at 52–50 Ma causing high-pressure eclogite and blueschist-facies metamorphism of the Cycladic Blueschists and SW directed extrusion of the Cycladic Blueschists and stacking of the nappe pile. Top-to-NE shear fabrics are preserved at the top of the extruding slab and top-to-SW fabrics record internal thrusting within and at the base of the Cycladic Blueschist Unit. The highest-pressure rocks are preserved at the highest structural level of the Cycladic Blueschists (see Fig. 2.2, 2.3 and chapter 3) and Lauren et al., (2016).

Chapter 3

Lawsonite eclogites and blueschists from Tinos, Greece

3.1 Introduction

High pressure-low temperature (*HP–LT*) metamorphism is a distinctive feature of subduction zone settings, and is characterized by rocks that have been buried along cool geothermal gradients (<10°C/km) (e.g. Miyrishmo, 1961; Oxburgh and Turcotte, 1971; Ernst, 1970, 1973, 1988; Goffé and Chopin, 1986; Okay, 1989; Maekawa et al., 1993; Maruyama and Lui., 1996; Fryer et al., 1999; Agard et al., 2009; St-Onge et al., 2013). In many locations, *HP–LT* metamorphism immediately pre-dates continent-continent collision and is normally associated with subduction of buoyant continental margin rocks (e.g. Searle et al., 1994; Parrish et al., 2007; St Onge et al., 2013). Thermobarometric and geochronological studies on many *HP–LT* terranes have yielded complex pressure (P), temperature (T), time (t) and deformational (D) histories (P–T–t–D) associated with rapid rates (cm/yr) of burial and exhumation (e.g. Parrish et al., 2006), and has provided crucial insight into deep subduction zone dynamics and the syn-collisional evolution of mountain belts (e.g. St-Onge et al., 2013; Palin et al., 2017). Despite this framework, there remains a limited understanding of the timescales and length-scales of subduction zone metamorphism and whether it represents a contin-

uous or transient process. Additionally, the role of conduction and advection within subduction zones, and their thermal evolution following initiation is poorly constrained.

Globally, in only a few localities, is the series of tectono-metamorphic events that pre-date *HP–LT* metamorphism preserved. The best examples include Oman and the Himalaya where high-pressure metamorphism post-dates ophiolite obduction by ca. 17 Myrs and ca. 25 Myrs respectively (e.g. Warren et al., 2003, 2005; Searle et al., 1994; 2004; St-Onge et al., 2013). This leaves several unanswered questions including: 1. does ophiolite obduction precede high-pressure metamorphism and by how long?; 2. do *HP–LT* metamorphic rocks record the same subduction zone that supra-subduction zone (SSZ) ophiolites are obducted onto earlier in the orogenic history?; 3. can ophiolite obduction trigger the exhumation of high-pressure continental rocks?.

The Cycladic Blueschists Unit (CBU) exposed on the island of Tinos, Greece, provides new insights into many of these questions. This is because on Tinos, continental margin rocks were deeply buried and exhumed beneath the over-riding Tsiknias Ophiolite (Chapter 1). Although lesser well known than neighboring Syros, Tinos also preserves fresh eclogite and blueschist-facies rocks which are juxtaposed directly against ophiolitic and pelagic metasedimentary rocks, which did not reach high-pressures and instead record subduction initiation during the earlier stages of orogenesis.

In this chapter the metamorphic history of Tinos is investigated to provide new constraints on timing of subduction and exhumation of the Cycladic Blueschists through new thermobarometry, equilibrium phase diagram modelling and Lu–Hf geochronology. The *P–T–t–D* histories of both blueschists and eclogites are integrated into a tectono-thermal model that a explains the structure of the island, the overlying Tsiknias Ophiolite and has wider tectonics implications for the regional Cycladic Blueschist Unit.

3.2 Geological setting

The Cyclades has experienced a complicated tectonic evolution, starting with Jurassic rifting and deposition of continental margin shelf carbonates (Andriessen, 1979), coeval with formation of oceanic crust to the north east associated with opening of the Neo-Tethys Ocean. During this rifting event, the Tsiknias Ophiolite formed at ca. 162 Ma (chapter 2) and is exposed at the highest structural levels within the Upper Unit on several Cycladic Islands including Tinos, Andros, Naxos, Ikirea, Mykonos and Paros. Subsequent closure of the Neo-Tethys during the Cretaceous times, eventually resulted in initiation of a new NE-dipping subduction zone and formed the metamorphic sole that underlies the Tsiknias Ophiolite on Tinos at ca. 74 ± 3.3 Ma (chapter 2).

Eclogite and blueschist-facies (M_1) metamorphic rocks form part of the Lower Unit which structurally underlies the Upper Unit and collectively belong to the Cycladic Blueschist Unit (CBU) (e.g. Papanikolaou, 2013; Jolivet et al., 2010) and include meta-pelites, calc-schists, psammites, marbles, and meta-volcanic lithologies forming the Cycladic Continental Margin sequence. The leading edge of the continental margin sequence experienced high-pressure metamorphism (M_1) (e.g. Papanikolaou, 2013; Keiter et al., 2004; Jolivet et al., 2010, 2013) during the Eocene, as a result of deep NE-dipping subduction (Tomaschek et al., 2003; Lagos et al., 2007; Dragovic et al., 2012). It is debated as to what followed this phase of subduction and accretion. Slab roll-back of the Hellenic subduction zone since the Eocene-present day (Jolivet and Brun, 2010; Jolivet et al., 2013, 2015) is a popular model to explain back-arc extension in the Cyclades. Many authors regard this model to have caused isobaric heating and Barrovian metamorphism (M_2) of previous *HP–LT* rocks, due to increased basal heating from the upwelling asthenosphere (e.g. Jolivet and Brun, 2010; Jolivet et al., 2013). In contrast, a model of crustal thickening is proposed by Lamont et al., (in press); (see chapter 4), who argue for compression as the cause of M_2 kyanite-sillimanite grade metamorphism on Naxos, based on the clockwise prograde *P–T–t* paths of kyanite grade gneisses and migmatites, and suggest compression continued until at least 17.5 Ma. These authors suggest a switch from compression to extension at ca. 15 Ma, co-

inciding with a decrease in the Nubia-Eurasia convergence rate (DeMets et al., 2015). This tectonic reversal may have occurred due to either gravitational collapse of over thickened crust, or removal of the lithospheric mantle, which resulted in the onset of normal faulting and causing rapid cooling at this time. Regardless of the timing of extension, it has definitively affected the area from the Miocene to present and resulted in thinning of the Aegean crust. Irrespective of this last phase of deformation, this contribution focusses on the earliest stages of orogenesis when the area represented a subduction-accretion complex.

3.2.1 Geology of Tinos

Tinos represents a NW–SE trending elongate dome, and comprises two distinct tectono-metamorphic units (Upper Unit and Lower Unit) which are separated by low angle normal sensed shear zone (The Tinos Shear Zone), which displays top-to-NE kinematics (Melodis, 1980; Avigad and Garfunkel, 1989; Katzir et al., 1996; Ring et al., 2003; Brichau et al., 2007; Jolivet et al., 2010). The Upper Unit, at the highest structural levels, comprises the Tsiknias Ophiolite and underlying metamorphic sole that have not experienced (M_1) high-pressure conditions. The Tsiknias Ophiolite represents the highest thrust sheet in the Cyclades comprising a fragmented piece of Jurassic oceanic crust and upper mantle dated at 161.8 ± 1.3 Ma by U–Pb zircon from a plagiogranite horizon within the Moho Transition Zone (see chapter 2). The ophiolite is largely incomplete and tectonically dismembered owing to intense deformation by both out of sequence thrusts and normal faults (Katzir et al., 1996; chapter 2). Structurally underlying the mantle section of the Tsiknias Ophiolite is a partially intact metamorphic sole which contains pelagic metasediments. Metamorphism and deformation occur during ophiolite emplacement at ca. 74.0 ± 3.3 Ma as revealed by U–Pb zircon from partial melt sweats, which emanate from the contact and by Lu–Hf garnet dating from meta-cherts in the sole (chapter 2). The metamorphic sole displays an inverted metamorphic gradient and attained upper amphibolite-facies conditions exceeding 800°C at the top, and ca. 600°C at the base at pressures of ca. 6–8 kbar. The age discrepancy

between the ophiolite and the sole suggest the heat to drive metamorphism must be derived from a combination of the overriding mantle wedge and shear heating on the subduction interface. The Akrotiri Unit is exposed on the SE coastline and comprises of amphibolites and paragneisses with K–Ar ages of ca. 66–76 Ma, similar to the metamorphic sole (Patzak et al., 1994).

The Lower Unit comprises of (M_1) high-pressure continental margin rocks of the CBU which are highly retrogressed to (M_2) greenschist-facies assemblages (Avigad and Garfunkel, 1989; Para, 2002; Ring et al., 2013). The best P–T estimates on Tinos come from chlorite–phengite thermobarometry in metapelites which indicate peak conditions of 18–15 kbar at 500°C (Parra et al. 2002). These workers also propose three stages of exhumation involving firstly decompression from peak conditions of 18–15 kbar at 500°C to 9–5 kbar at 400°C which was followed by a thermal overprint (400 to 550°C) and further decompression from 9 kbar at 550–570°C to 2 kbar at 420°C (Parra et al., 2002). A Basal Unit has been suggested to outcrop under the high-pressure rocks at Panormos bay due to the preservation of fossils within the marbles (Avigad and Garfunkel, 1989). However, this interpretation is debated owing to indistinguishable Rb–Sr ages and Si p.f.u in phengite contents (Brockner and Franz, 2005). If there is a distinct contrast in metamorphic grade between these two units, then the contact would have been a thrust, placing the Cycladic Blueschists over the Basal Unit which didn't experience as high pressures.

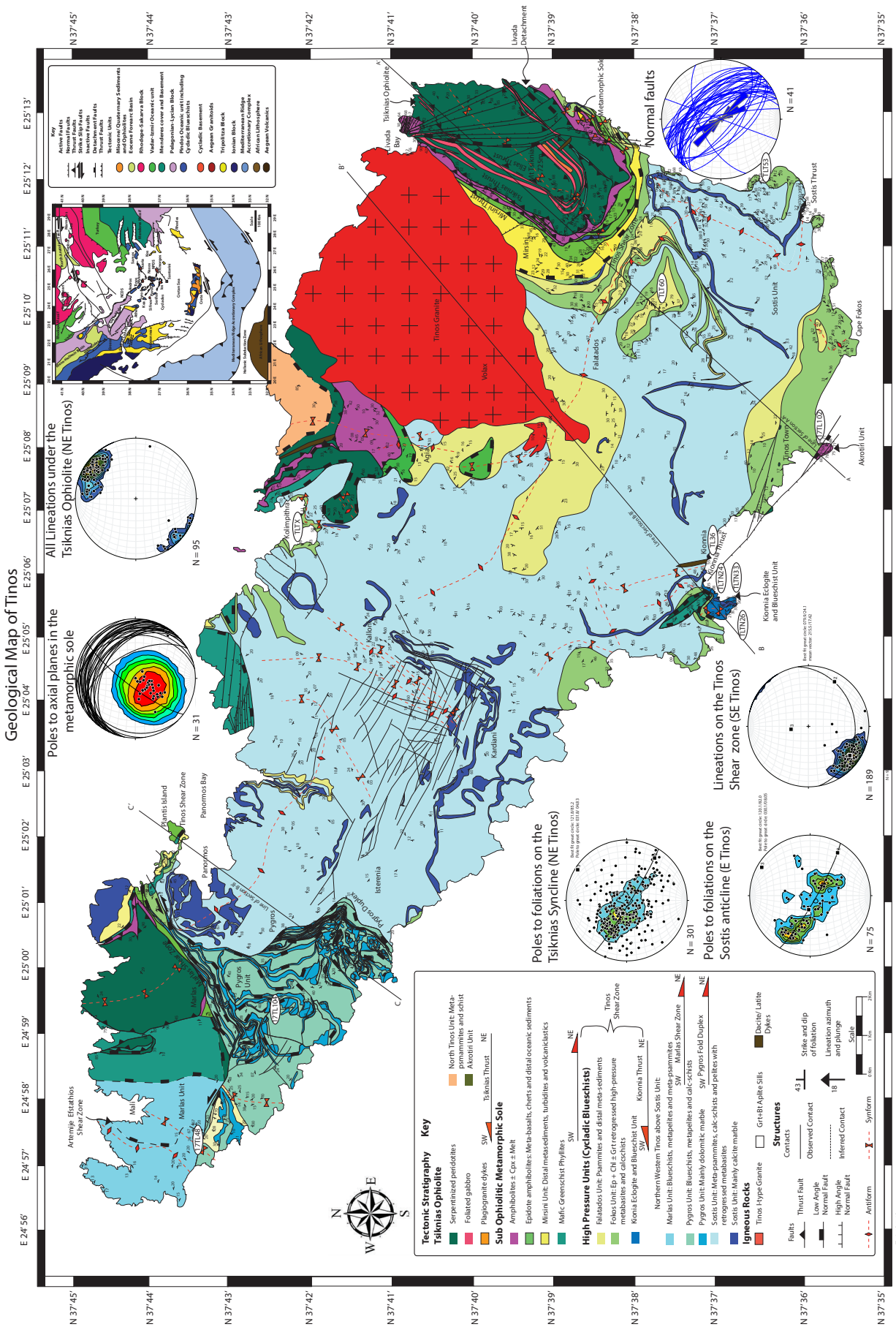


Figure 3.1: Continues on next page

Figure 3.1: New geological map of Tinos showing key structural units of the Lower Unit and samples locations used in this study. For cross sections A–A', B–B' and C–C' consult Fig. 3.2

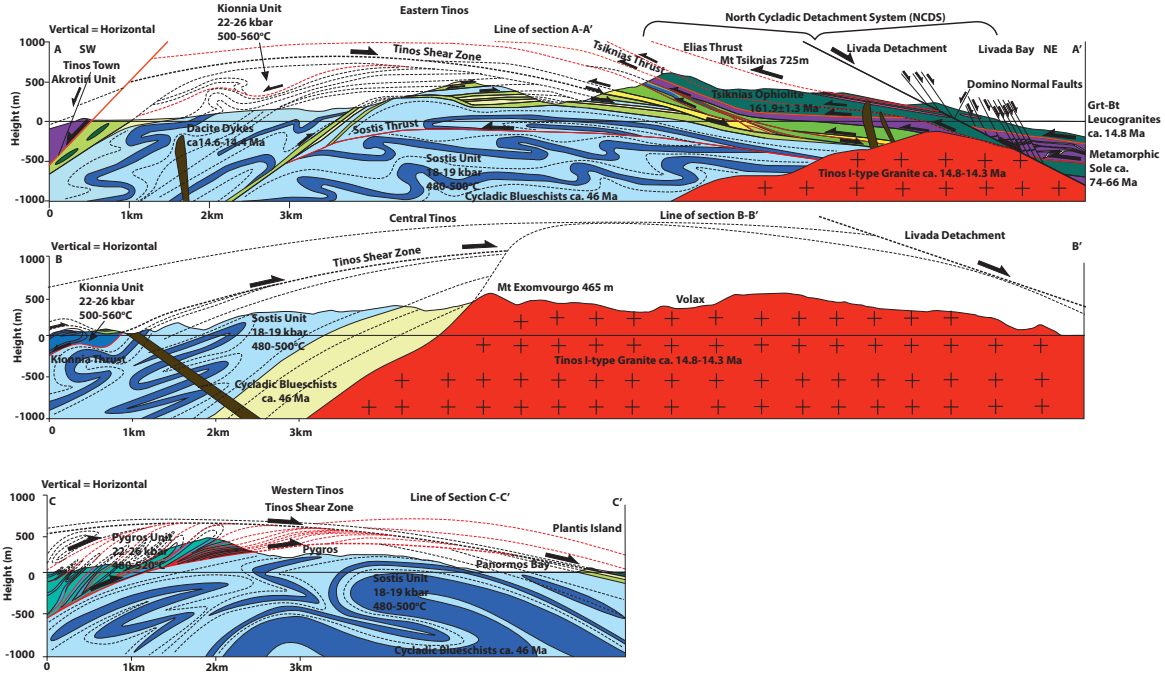


Figure 3.2: Cross sections through Tinos along the line of sections A–A', B–B', C–C'. For locations consult the geological map in Fig. 3.1, note the Kionnia Unit is projected at the highest structural level but only crops out on the Kionnia Penisular.

3.2.2 Overview of *P–T–t* data of the Cycladic Blueschists

Petrological studies from several Cycladic islands have yielded contrasting peak M_1 *P–T–*t estimates within the CBU. This ranges from 15–18 kbar and 500°C (Schliestedt et al., 1987; Okrusch and Bröcker, 1990; Avigad and Garfunkel, 1991; Parra et al., 2002; Schmädicke and Will, 2003; Schumacher et al., 2008) to 19–20 kbar and 525–550°C (Trotet et al., 2001b; Groppo et al., 2009; Dragovic et al., 2012; Ashley et al., 2014). Recently Lauren et al., (2018) suggested Syros eclogites reached peak conditions of 19–22 kbar at 550°C by phase equilibria modelling, and AMS thermometry, and proposed these rocks underwent isothermal decompression to 10 kbar by a syn-orogenic extrusion mechanism which was followed by reheating to 500–550°C upon reaching mid-crustal conditions. Contrastingly, Behr et al., (2018) obtain significantly lower pressures for eclogite facies metamorphism of 12.5–15.5 kbar at 450–550°C based

on quartz-in-garnet inclusion barometry using laser Raman spectroscopy (Kohn, 2014; Ashley et al., 2016), questioning whether the eclogites reached such high-pressures.

The timing and duration of this subduction-related P–T evolution have been reasonably constrained, using many isotopic dating systems including K–Ar, $^{40}Ar/^{39}Ar$, Rb–Sr, U–Pb, and Lu–Hf garnet dating (Altherr et al., 1979, 1982; Andriessen et al., 1979; Wijbrans and McDougall, 1986; Maluski et al., 1987; Wijbrans et al., 1990; Bröcker et al., 1993, 2013; Baldwin, 1996; Bröcker and Franz, 1998, 2006; Bröcker and Enders, 1999; Tomaschek et al., 2003; Putlitz et al., 2005; Lagos et al., 2007; Huet, 2010; Dragovic et al., 2012; Peillod et al., 2017; Lamont et al., under review). Lu–Hf garnet studies, which directly date the peak eclogite facies metamorphism, obtain ages of ca. 52.4–51.2 Ma (Lagos et al., 2007) of Syros eclogites and ca. 46.4 Ma (Dragovic et al., 2012, 2015) on Sifnos eclogites. In contrast, U–Pb data suggest peak metamorphic ages ranging from ca. 53–50 Ma (Tomaschek et al., 2003; Putlitz et al., 2005) on zircons from Syros eclogites, which overlap with Lu–Hf garnet ages, to ca. 49–46 Ma on allanites from Naxos blueschists (Lamont et al., under review) and a wide population from 64–40 Ma (Forster and Lister, 2004; Martin et al., 2006). In contrast, M_2 greenschist-facies retrogression has been dated between 40 and 15 Ma (Bröcker et al., 2013; Peillod et al., 2017; Lamont et al., under review), although it is debated what tectonic regime this represents. Final exhumation the CBU are constrained by low temperature thermochronology between 12 and 8 Ma (Ring et al., 2003; Soukis and Stöckli, 2013).

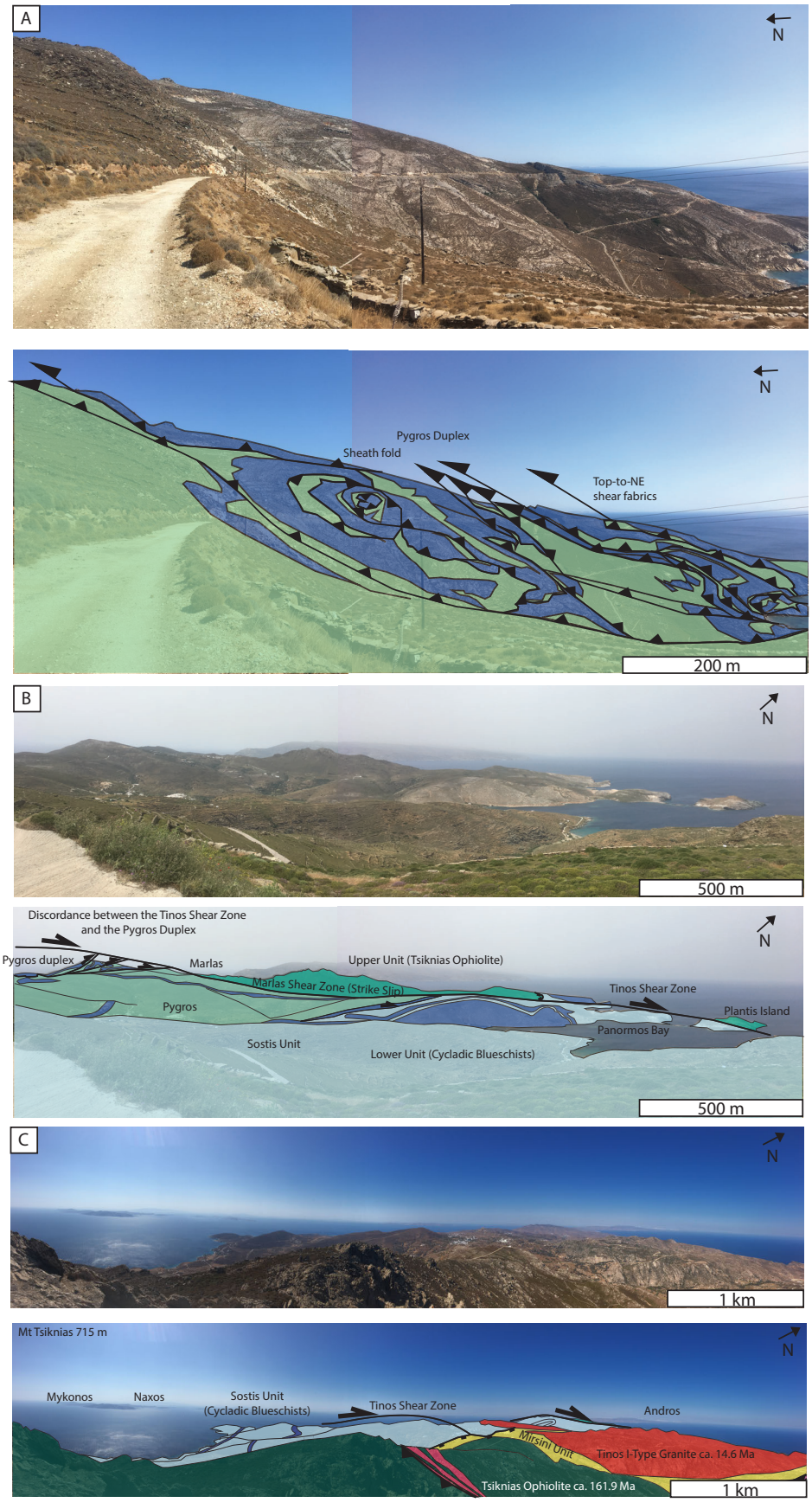


Figure 3.3: Continues on next page

Figure 3.3: Panormaic photographs of structures within the Lower Unit on Tinos: A) Cross section through marbles folds and shear zones of the Pygros Unit to the west of Isternia (N37.628200, E25.029618), the folds ar truncated by top-to-NE shearing structures (S_3). B) Overview of Panormos Bay (N37.635506, E25.058592) showing discordance of the high-pressure structures and the Tinos Shear Zone that is folded across the island. C) Overview of the large scale structures on Tinos from the top of Mt Tsiknias, (37.580569, 25.225505) showing the Upper and Lower Units that are cut by the Tinos pluton.

Although a reasonable framework exists for the tectonic evolution of the CBU, the subduction and exhumation processes and the regional tectonic significance of extensional top-to-NE/ENE and top-to-SW deformation fabrics recorded by *HP–LT* rocks remains controversial. Several schemes have been proposed to describe the ductile deformation history, mainly from studies on the island of Syros. (1) Trotet et al. (2001a), describes the main deformation phase as retrograde, and was acquired during exhumation of the CBU from eclogite- to greenschist-facies (D_1 to D_3). In their model, exhumation occurred during a continuum of top-to-E/NE shearing from the early Eocene (syn-orogenic exhumation) to the early Miocene. (2) Keiter et al. (2004, 2011) interpreted the main deformation event affecting the CBU as prograde, implying therefore a rigid body exhumation (D_1 to D_3), with no internal deformation and strain concentrated on the margins of each tectono-stratigraphic unit. (3) Philippon et al., (2011) describe two distinct ductile phases of deformation, i) Firstly top-to-SW prograde deformation (D_1) followed by, ii) an extensional top-to-NE penetrative shear (D_2) affecting the entire CBU. (4) Recently Lauren et al., (2017) demonstrates that on Syros, after the prograde (D_1) top-to-S/SW shearing, the CBU was exhumed by an overall top-to-E/NE shearing from the depth of the eclogite-facies all the way to greenschist-facies and finally, to the brittle crust (D_2–D_3). They suggested the exhumation process took place in a syn-orogenic phase (simultaneous subduction and exhumation within the subduction channel) during the Eocene and the latest stages of exhumation in a post-orogenic stage (regional Aegean extension). This model implies a major top-to-SW thrust fault at the base of the extruding channel. These authors also propose that once the rocks were exhumed to the greenschist-facies, top-to-NE deformation became progressively localized toward the base of the CBU, along large-

scale ductile shear zones, allowing the preservation of earlier *HP–LT* structures at the top of the sequence, that are cross-cut by greenschist-facies features. Due to the comparatively small amount of investigation of Tinos high-pressure rocks, the aim of this study is to: 1. quantify the *P–T* conditions and deformation history of Tinos across all structural levels; 2. constrain the timing of peak and retrograde metamorphism; and 3. test which burial and exhumation models best explain the *P–T–t–D* histories of Tinos *HP–LT* rocks.

3.3 Field Relationships of the Tinos High-Pressure Rocks

Detailed field mapping of Tinos was carried over three years (2015–2018), building on previous pioneering work (Melodis, 1980; Avigad and Garfunkel, 1989; Katzir et al., 1996; Brockner and Franz, 2001; Jolivet et al., 2010). A new structural and metamorphic map of Tinos is presented in Fig. 3.1 with accompanying cross sections in Fig. 3.2. In what follows, the key findings are systematically described from structurally high-low which have new and important implications for the evolution of high-pressure rocks on Tinos and the Cyclades.

3.3.1 The Kionnia Unit

Fresh eclogites and blueschists occur within an intensely folded meta-sedimentary sequence at Kionnia Peninsular on the south coast of Tinos (N37.548015, E25.125559), at the highest structural levels of the island. The Kionnia Unit is ca. 500 m thick and comprised of dolomitic marbles with intercalated meta-pelites, meta-tuffs and meta-basalts that have been recumbently folded (F_1 folds) and are boudinaged to various degrees. Eclogites and blueschists occur as discontinuous mafic boudins (forming granoblastic eclogites) and also as continuous horizons (forming foliated eclogites and blueschists), which have experienced the same deformation sequence as the meta-sediments as they

are coherent with the S_1–S_3 foliations. The unit is bounded at the top and bottom by shear zones that separate it from the rest of the Lower Unit. Along Kionnia Beach, at the base of this unit, top-to-SW kinematic indicators and S–C' fabrics (S_{2b}) are highly pervasive and affect peak M_1 assemblages suggesting they formed coeval with peak M_1 blueschist- eclogite-facies conditions. S_{2b} fabrics also affect retrograde minerals such as matrix clinozoisite, suggesting that top-to-SW shearing developed during the earliest stages of exhumation. Metamorphic grade increases up structural level throughout the unit, consistent with top-to-SW fabrics representing a high-pressure thrust, referred to herein as the Kionnia thrust, placing higher pressure rocks on top of lower pressure rocks. Near the the top of the unit, the shear direction reverses and highly penetrative top-to-NE extensional S–C' fabrics (S_3) in meta-pelites, meta-tuffs and meta-basalts which form the foliated blueschists and eclogites (e.g. TLTN26 and TLTN24). The most spectacular mafic eclogites occur within the interior of the unit as boudins in dilatational strain zones within a zone of intense folding structurally below the thick recumbently folded dolomitc marbles (N37.547909, E25.125488) (Fig. 3.4). Sheath folds (F_2) occur throughout the sequence, and display cats eye geometries (Fig. 3.4 and 3.7) with their noses trending WSW–SW parallel to the lineation, indicating they formed coeval with non-coaxial ductile shearing (Alsop, 2007). Mafic boudins forming the granoblastic eclogites (TLTN33) are not internally deformed by the S_3 shearing, whereas the adjacent meta-sediments deform around the bodies. This implies the meta-sedimentary hosts accommodated the bulk of the ductile-strain on the margins of the boudins, and therefore that the strong eclogite-facies assemblage had already formed prior to shearing.

Opposite kinematic indicators in blueschist to eclogite-facies rocks at the top and bottom of the Kionnia Unit, suggest this package of high-pressure rocks was extruded towards the SW over the underlying rocks (Sostis Unit). Several NE-trending upright and open folds (F_3) are superimposed on these recumbent (F_1) and sheath (F_2) folds. F_3 folds have a regular wavelength of 100–150 m with their hinge lines parallel to the NE–SW stretching lineation and re-fold both (S_{2a+b}) top-to-SW and

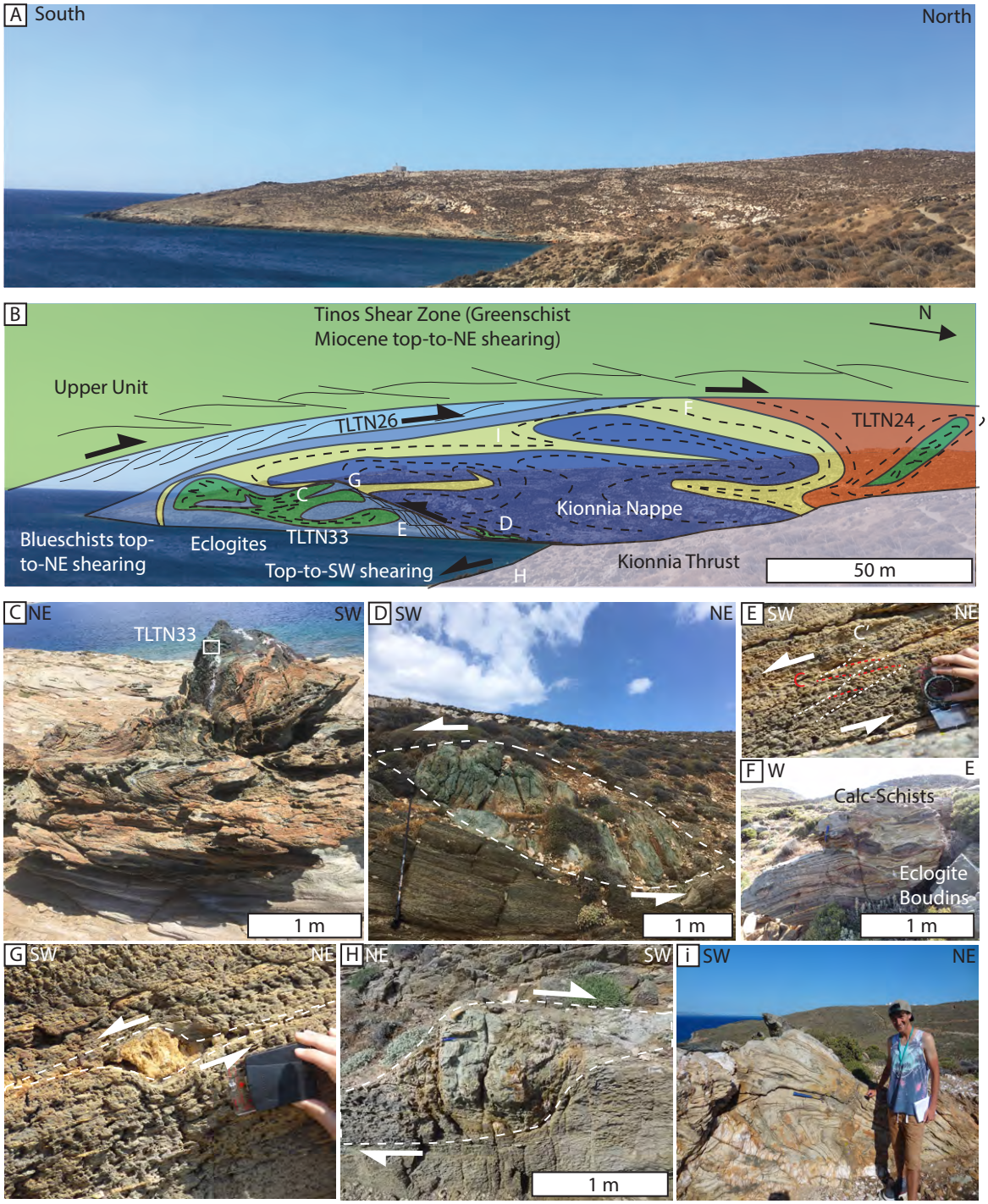


Figure 3.4: Annotated cross section of the Kionnia Unit A) Photograph of the Kionnia Penisular looking west with B) an overview of the key geological features and location of outcrop photographs below. C) F1 and F2 Isoclinally folded sediments with a relatively undeformed fresh eclogite boudin TLTN33 in a dilatent strain zone, D) S_{2b} top-to-SW retrogressed eclogite. E) Top-to-SW S-C' fabrics in meta-psammite. F)F_2 sheath folded calc schists with mafic retrogressed eclogite pods. Top-to-SW calcite sigma porphyroclast (S_{2b} fabric) on the Kionnia Thrust Zone. Retrogressed mafic boudin (now chl+pl+act) with meter scale top-to-SW asymmetry, i) F_1 SW verging isoclinal fold.

(S_3) top-to-NE shear fabrics. F_3 upright folds therefore formed during exhumation but post-date the intense F_1 isoclinal and recumbent folding. We therefore interpret F_3 folds to have formed due to a component of orthogonal shortening during exhumation.

Unfortunately, the Kionnia Unit is limited in its lateral extent and is truncated at the top by the Tinos Shear Zone which is associated with strong top-to-NE greenschist-facies ultra-mylonite fabrics, and places Upper Unit greenschists possibly derived from the metamorphic sole of the Tsiknias Ophiolite directly against eclogites (N37.552088, E25.124767). The Tinos Shear Zone must clearly post-date high-pressure deformation within the Kionnia Unit and has resulted in intense retrogression towards the structure. Although the very top of the Kionnia Unit is not exposed, it is acknowledged that (S_3) top-to-NE shearing would be expected to become more intense up structural section.

3.3.2 The Pygros Unit

In NW Tinos, a series of imbricated and isoclinally folded (F_1) dolomitic marbles are intercalated with meta-sedimentary and meta-volcaniclastic lithologies on the southern limb of the Tinos NW–SE trending dome, near the villages of Isternia and Pygros (Fig. 3.3a and Fig. 3.7c). The Pygros Unit sits at the highest structural level on Tinos, along strike and at a similar structural level to the Kionnia Unit and represents the structurally thickest succession of dolomitic marbles on Tinos. Up to twelve repeated dolomitic marble horizons crop-out, that are laterally discontinuous along strike and bounded by (S_3) top-to-NE mylonite zones that deform both (M_1) blueschist and (M_2) greenschist-facies assemblages. Isoclinal and recumbent folding in the marbles (F_1) is best seen across Vathi Bay (N37.628424, E25.028671) (Fig. 3.3a). F_1 folds, deform the S_1 foliation (which is defined by M_1 assemblages including glaucophane, phengite and rutile), verge towards the SW and are displaced and cross-cut by several shear zones with top-to-NE kinematics (S_3). Towards the top of the sequence, continuous horizons of fresh mafic garnet, glaucophane schists crop out with their peak S_{2a} foliation defined by sub-mm scale crenulations in glaucophane rich domains (e.g. 17TL104).

The S_{2a} fabric is cross-cut by clinozoisite grains which have subsequently been rotated by top-to-NE shearing (S_3), which is the dominant matrix foliation in these rocks. This foliation (S_3) deforms around and cross-cut the large-scale folds, suggesting the F_1 folding mainly pre-dates (S_3) top-to-NE shearing and formed at or near peak M_1 conditions, probably associated with the stacking and thickening of continental margin sediments at near their maximum pressures. In contrast, (S_3) top-to-NE shearing occurred during exhumation process explaining why it cross-cuts the folds and utilizes the interstitial schistose horizons for localizing strain.

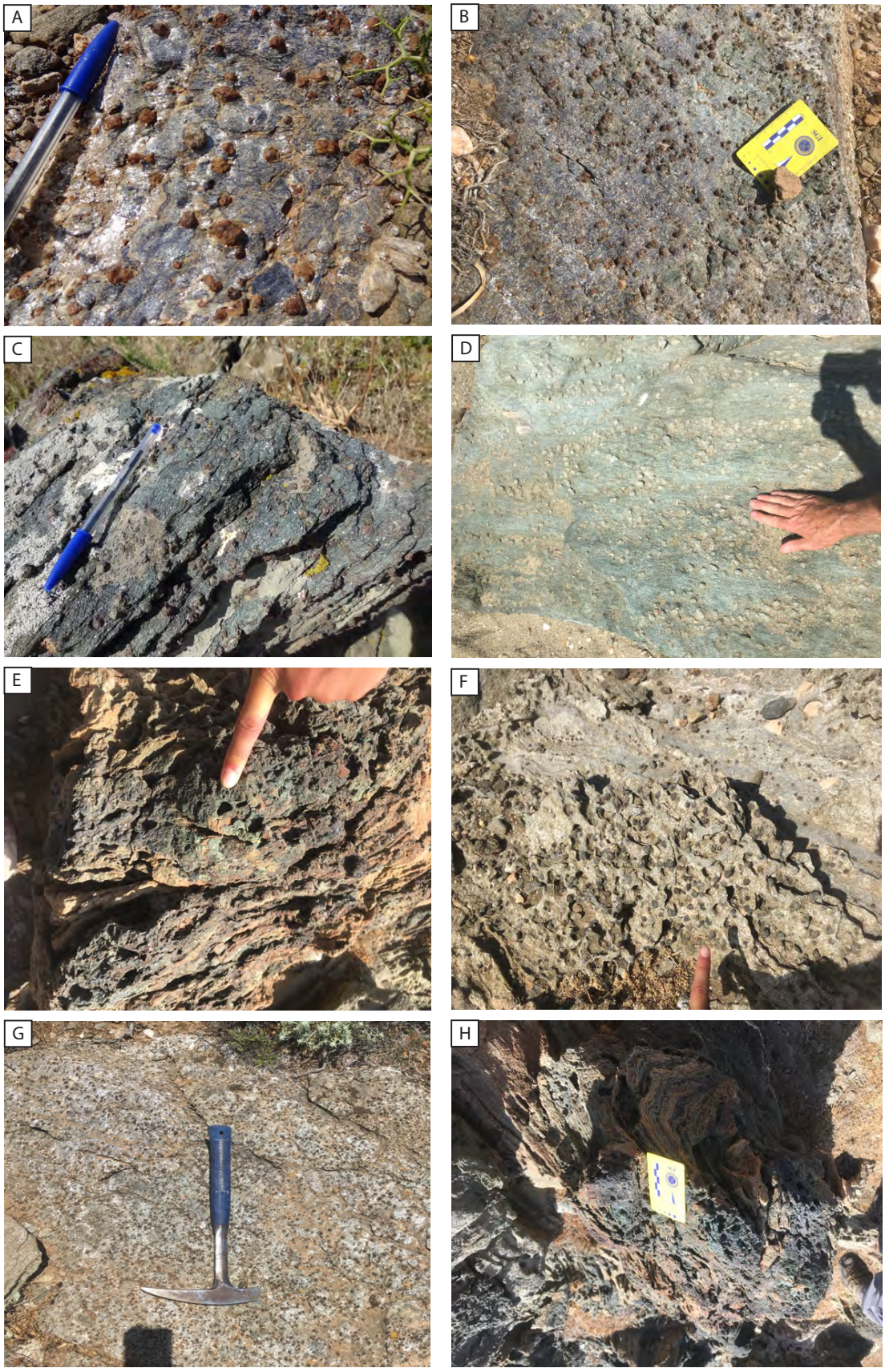


Figure 3.5: Continues on next page

Figure 3.5: Outcrop photographs of fresh blueschist and eclogite facies assemblages from the Kionnia and Pygros Units. A) Grt blueschist at the top of the Kionnia Unit (TLTN26) (N37.548336, E25.124193), B) Mafic blueschist with localised omphacite (green) indicating boarderline eclogite facies coditions, C) TLTN24 foliated eclogite (N37.550873, E25.124344), D) Lawsonite pseudomophs (now paragonite + amphibole+ plagioclase) in retrogressed calc shist (N37.553464, E25.129058) E) TLTN33 eclogite within folded calc-silicates. F) Pelitic eclogites with 2 cm sized garnets + phengite ± chloritoid. G) Grt Phengite schists interstitial with Kionnia eclogite, H) Another highly deformed mafic pod-similar to TLTN33.

Late M_2 greenschist-facies minerals such as epidote, actinolite, titanite and clinozoisites cross-cut the S_3 mylonite fabrics indicating a strain reduction once the rocks attained lower pressures (<10 kbars). Because the distributed top-to-NE shear zones affect both M_1 and M_2 assemblages, it suggests they were active during exhumation. These structures are gently folded about a WNW–ESE axis that defines the Tinos dome (F_4), indicating the doming is a much later feature and associated with greenschist conditions at mid-crustal depths.

3.3.3 Sostis Unit

The Sostis Unit makes up the majority of the interior of Tinos, and represents the deepest structural levels of the island. The unit dominantly comprises meta-psammites and meta-pelites which are intercalated with meta-volcaniclastic lithologies, with only a few marble bands which are recumbently folded on a km scale (F_1). Several mafic horizons can be found within this unit, however they are laterally discontinuous and extensively overprinted by strong M_2 greenschist-facies paragenesis. Several outcrops of mylonites that record (S_{2b}) top-to-SW or even top-to-SE movements are exposed throughout the unit. These structures oppose the dominant extensional (S_3) top-to-NE shear fabrics and therefore must represent thrusts. Several large recumbent folds also outcrop throughout this unit and can be best seen in central Tinos on the northeast face of Mt Exomvourgo (N37.612590, E25.111204), to the SW of Kalloni and Aetofolia villages in Central Tinos. These folds (see Fig. 3.7d, e), have a eastward vergence and are associated with N–S striking hinge lines. They form directly above high strain zones with intense (F_1) isoclinal and (F_2) sheath folding in marble bands

and are interpreted as hanging-wall anticlines above ductile thrust faults which were responsible for thickening and structurally repeating the metasedimentary sequence. The Sostis Thrust is the best exposed example of thrusting throughout the Sostis Unit. This structure crops out at Sostis Bay (N37.534477, E25.223566), and demonstrates intense top-to-WSW fabrics in mylonites, and clearly displaces the marble band in in its hanging-wall (Fig. 3.7a, b). It is also discordant to the greenschist-facies S_3 fabrics and the lineation of the Tinos Shear Zone structurally above, which truncates it.

3.3.4 Artemije and Efstathios Shear Zone (NW Tinos) (AESZ)

The Artemije and Efstathios Shear Zone (AESZ) in NW Tinos (N37.655951, E24.992683) is approximately 400 m thick and records both F_1 isoclinal folding overprinted by S_3 top-to-NE shearing. Intense F_1 SW verging parasitic folding affects both metasedimentary layering (S_0) and a spaced foliation (S_1), whereas S_{2a+b} develops axial planar to these folds and as a crenulation cleavage. Well-developed (S_3) top-to-NE S–C' fabric, cross-cut the limbs of these folds and is associated with a lineation parallel to the shear direction (230/30). Although this shear zone gently dips towards the SW, its original geometry would have dipped gently to the NE after restoring the late doming on Tinos, which folded the metamorphic stratigraphy. M_1 blueschist- M_2 greenschist-facies minerals are affected by the S_3 foliation, indicating the top-to-NE structure was active during exhumation from M_1 to M_2.The degree of (S_3) top-to-NE shearing intensifies up structural section and eventually discontinuous horizons of serpentinite and mafic greenschists crop-out on the northern coastline.

3.3.5 Tinos Shear Zone (TSZ)

The Tinos Shear zone (TSZ) is a normal sensed greenschist-facies structure that represents a major tectonic boundary, bounding the top of high-pressure rocks of the Cycladic Blueschist Unit. It is associated with top-to-NE kinematics in M_2 assemblages and is discordant to and truncates the M_1 blueschist and eclogite facies structures. The shear zone is domed around the island about a ENE–WSW axis. The gentle NNE-dip

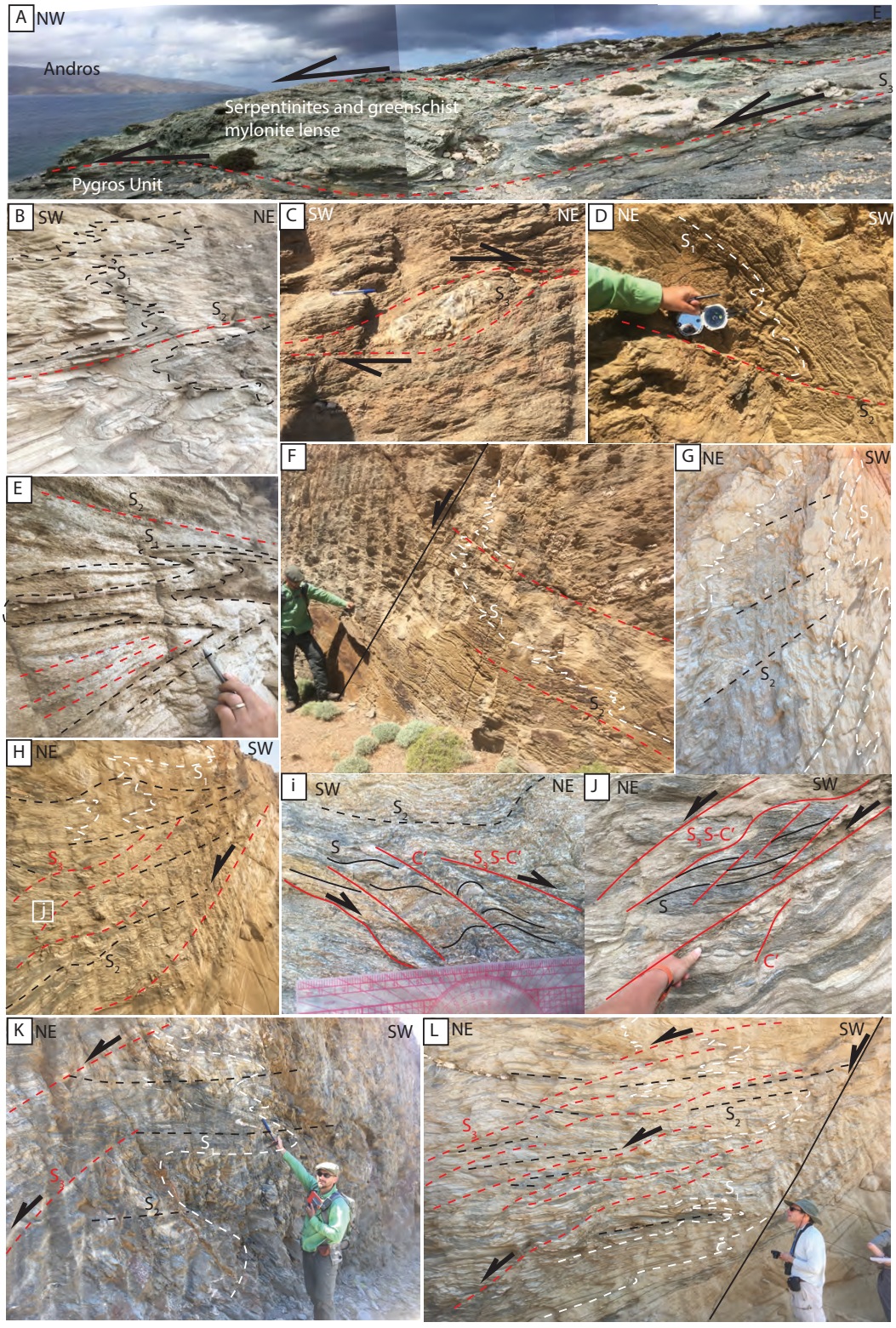


Figure 3.6: Deformation in NW Tinos: A) Top-to-NE extensional fabrics in greenschists and serpentinites at (N 37.672540, E24.976456), B-L) The AESZ at (N37.655769, E24.992651) with pervasive top-to-NE extensinal shearing Sit and brittle normal faulting overprinting inense isioclinal folding.

of this structure on the island's northern coastline is responsible for the exposure of the Upper Unit including the Tsiknias Ophiolite as klippe on structurally high topography such as Mt Tsiknias (N37.581047, E25.225637). The TSZ is cross-cut by the Tinos I-type granite, indicating it was active prior to intrusion (ca. 14.6 Ma).

Because the Kionnia Unit is not exposed elsewhere on Tinos, and sits at a structurally high level, the TSZ must cut it out along strike. The TSZ also cuts out the Pyrgros Unit in NW Tinos near the village of Marlas and at Panormos Bay places the Upper Unit directly against the deepest levels of the island (e.g. Avigad and Garfunkel, 1989; Brokner and Franz, 2001; Jolivet et al., 2010). It therefore must cut through all exposed M_1 high-pressure metamorphic stratigraphy. It is only on the south coast of Tinos where the thickest section of the CBU is preserved, which entrain the freshest high-pressure rocks (Kionnia and Pygros Units). The TSZ must therefore post-date M_1 high-pressure metamorphism and structures related to their exhumation. It must also post-date the stacking of high-pressure rocks within the interior of Tinos. It is however unclear if the Tinos Shear Zone is related to crustal extension, as extensional top-to-NE shear fabrics only record the relative ductile exhumation of material and cannot be used to characterize a specific tectonic regime. Although, it is acknowledged that extensive normal faulting occurs directly above and cross-cuts the structure, which is undoubtably related to regional extension.

3.3.6 Marlas Shear Zone (MSZ)

The Marlas shear zone crops out in NW Tinos nea Marlas (N37.654406, E25.032923) and steeply dips norward but displays dextral strike slip kinematics associated with sub-horizontal ENE–WSW trending lineations. This structure truncates through the Pygros Unit and places the Tsiknias Ophiolite, greenschists and serpentinites of the Upper Unit directly against *HP–LT* rocks. It is possible it represented the TSZ but has beeb folded from its original dip. Alternatively, it represents a late strike-slip fault that developed at greenschist facies conditions and displaces the TSZ and juxtaposes the Lower and Upper Units together.

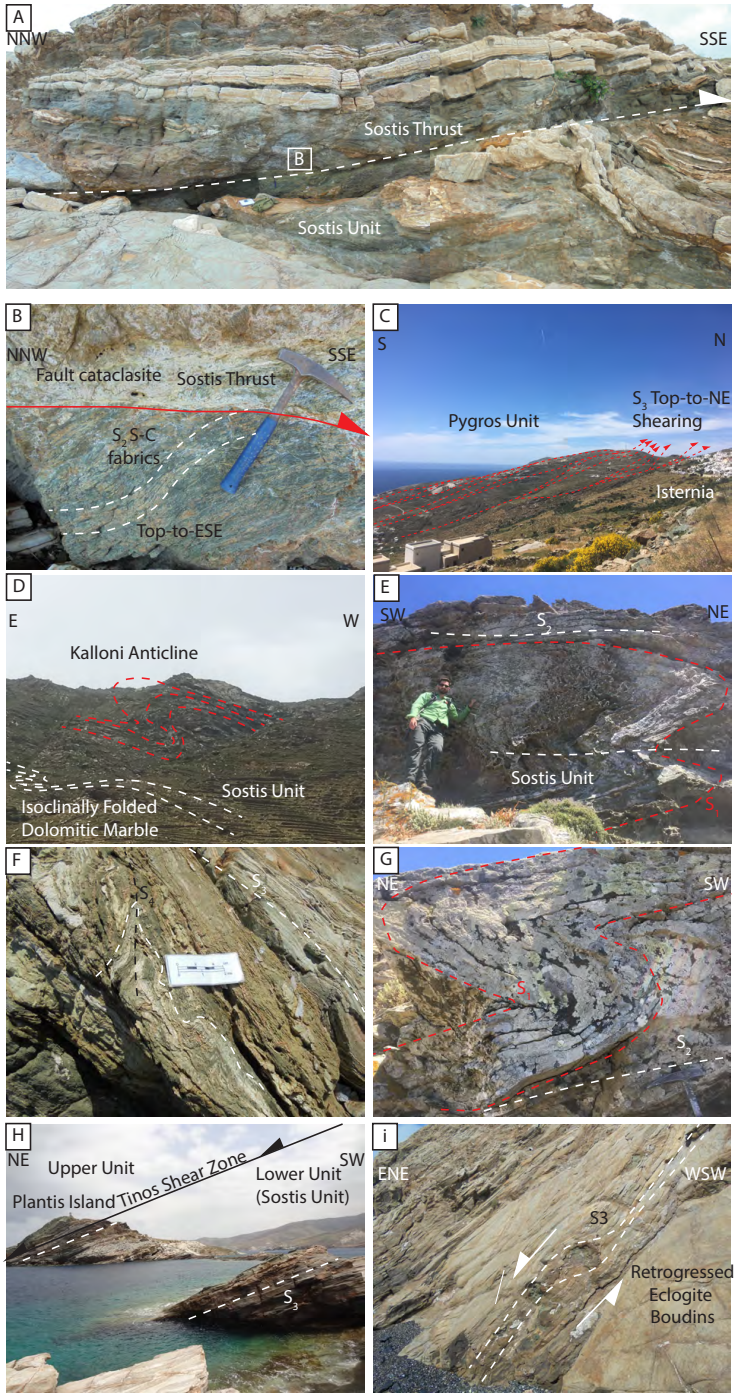


Figure 3.7: Meso-scale photographs of the Sostis Unit on Tinos: A and B) The Sostis Thrust (N37.534509, E25.223207), with clear brittle deformation overprinting ductile top-to-ESE shearing affecting glaucophane and phengite. C) Top-to-NE S_3 shearing in the pygros Unit, D) The Kalloni Anticline in central Tinos (N37.611719, E25.109457) that that verges towards the SE E) Hinge of a NE verging F_2 sheath fold within the Sostis Unit (N37.604766, E25.089470), F) Greenschist facies upright F_4 fold, G) F_1 fold in psammites from the Sostis Unit (37.604695, 25.090930), H) The Tinos Shear Zone at Panormos Bay (37.661674, 25.061793) i) retrogressed eclogite boudins in meta-pasmmite on the east coast of Tinos (37.542952, 25.229555), note the steep foliation.

3.4 Petrography and Mineral Chemistry

Blueschist, eclogite and greenschist samples used in this study were collected at various structural levels of Tinos to investigate spatial variations in the P–T conditions of prograde, peak, and retrograde metamorphism. The analytical techniques and procedures utilized to collect mineral composition data are outlined in Appendix 1. Mineral abbreviations follow the guidelines of Whitney and Evans (2010). Anhydrous phase compositions were calculated to standard numbers of oxygen per formula unit (Deer et al., 1992), micas were recalculated to 11 oxygens, and chlorite to 28 oxygens. Where present, H_2O content was assumed to occur in stoichiometric amounts. The proportion of Fe^{3+}/Fe_{total} was calculated using AX (Holland, 2009) and amphibole exchange vectors were calculated using the method of Holland and Blundy, (1994) and an inhouse spreadsheet see Appendix 1 for futher details. Representative photomicrographs are displayed in Figs. 3.8 and 3.9 and mineral compositions from all studied samples are presented in Figs. 3.10-3.12, and Tables 3.1-3.6.

3.4.1 Kionnia Unit

Fresh mafic and meta-sedimentary M_1 eclogite and blueschist-facies rocks outcrop on the Kionnia Peninsular (N37.548529, E25.125068). Although the mineral assemblage and chemistry of Syros eclogites have been well documented in numerous studies (e.g. Kieter et al., 2004; Schumacher et al., 2008; Lauren et al., 2018) Tinos eclogites have not yet been described in any detail. Two main types of mafic eclogites can be recognized within the Kionnia Unit: granoblastic and foliated. The granoblastic eclogites (e.g. TLTN33) occur as boudins unaffected by retrograde deformation (e.g., Fig. 3.4) and contain garnet, clinopyroxene and sodic amphibole, quartz, epidote and paragonite, phengite, rutile and titanite. They also contain pseudomorphed-lawsonite inclusions within garnet cores that defines the S_1 foliation. On the outcrop-scale, granoblastic eclogites are coarse-grained with garnets up to five cm in diameter. However, on the thin-section-scale, much of the matrix clinopyroxene is finely recrystallized and has only

a minor fabric preferred orientation that sometimes displays crenulations (S_{2a}). Within both types of eclogite, at four amphibole generations can be identified. 1) Fine matrix glaucophane that is prismatic and follows the S_{2a} and S_{2b} foliations with Na_B ranging between 1.96–1.75, 2) large amphibole laths which show a stepwise zoning from core to rim (generations 2–4). They display an inclusion rich glaucophane core (generation 2) which is overgrown by; 3) a a clean barroisite rim. 4) A forth amphibole composition occurs in TLTN33 on the outermost rims of the large laths and as fine grains in the matrix, and is magnesiohornblende in composition. Epidote also occurs as large zoned laths within the matrix which cross-cut the S_1 and S_2 deformation fabrics and produce a static decussate texture (S_2c). In contrast, the foliated eclogites (e.g. TLTN24; Fig. 3.5a and c) contain more sodic amphibole, phengite and quartz, and have a strong preferred fabric orientation formed by the alignment of phengite and blue amphibole (S_{2b}), but have experienced larger degrees of retrogression. In both types of eclogite, clinopyroxene is aegirine-omphacite in composition suggesting a highly oxidized redox state at peak M_1 conditions. Note that the sodic clinopyroxene classification scheme of Essene and Fyfe (1967) is used here in preference to the IMA-approved scheme (Marimoto, 1989), because many of the natural examples from Tinos lie on the 50:50 Fe^{3+}:Al boundary.

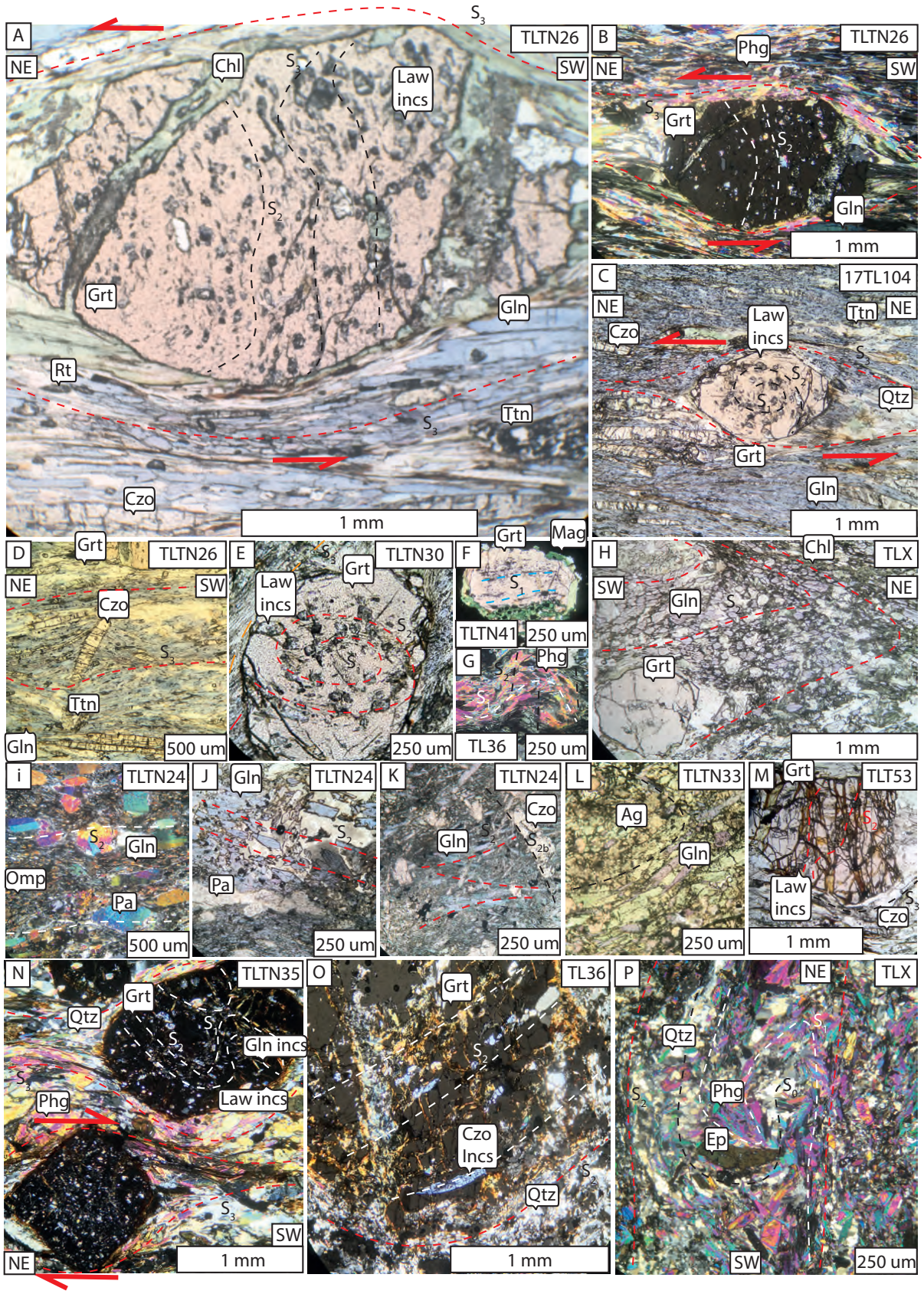


Figure 3.8: Continues on next page

Figure 3.8: Photomicrographs of prograde features: A and B) Discordance between S_2 internal garnet fabric and top-to-NE S_3 fabric. C and E) Rotatioal fabric defined by ex-lawsonite inclusions discordant to the external fabric. D) Rotated epidote porphyroclastsm that are oblique to the S_3, F, G, H) S_{2a} fabric within garnet porphyroclasts and affecteing matrix gln and phg. I) Coarse cross-cutting paragonite laths that appear late. J) Intergrown matrix Gln and prg defining thr S_{2a}. K) Cross-cutting Czo across fine accicular matrix glaucophane. M, N, O) folded pseudomorphed lawsonite-inclsions in garnet and affecting the matrix gln and Phg. Note TL36 rim contains a Czo inclusion and therefore grew under Czo stabillity (instead of lawsonite).

Structurally above the F_1 isoclinally folded anticline of dolomitic marbles, a layer of mafic garnet glaucophane schists crops out as a continuous horizon (TLTN26 Fig. 3.5b). In places, these blueschists lie adjacent to cm-scale eclogite-facies assemblages marked by the appearance of green clinopyroxene, suggesting that the transition from blueschist eclogite-facies is controlled by bulk composition. The blueschists are generally more foliated than the eclogites, with abundant phengite and blue amphibole being the main S_3 fabric-forming minerals, with cross cutting epidote-clinozoisite, but do not contain chloritoid or kyanite.

3.4.1.1 TLTN26 Garnet Glaucophane Blueschist

TLTN26 is a garnet glaucophane schist and was taken from a garnet-rich mafic horizon directly overlying the recumbently folded marbles (N37.548333, E25.124156) and records the most complete high-pressure deformation history. Within the cores of garnet porphyroblasts, a straight linear fabric (S_1) is defined by inclusions of glaucophane and rutile needles, and is associated with relict lawsonite crystals that are pseudomorphed to fine aggregates of paragonite, clinozoisite and chlorite that forms as prisms with lozenge cross-sections. Towards the garnet rims, the internal foliation rotates 180° into alignment with the external matrix fabric. This rotation recorded within garnets represents the S_{2a} fabric, and this can be seen as a ghost crenulation cleavage with relict microlithons (S_{2b}) defined by a glaucophane and phengite forming interlocking and herringbone structures and crenulation hinge zones, representing microlithons. These relationships suggest garnet grew syn-tectonic with respect to S_2 fabrics, and can be seen very clearly in the calcium electron microprobe map (Fig. 3.11), which

demonstrates the orientation of relict amphibole matrix phases during garnet growth, and the syn-tectonic rotation of the garnets with respect to the deforming matrix. Because the S_2 prograde fabric only affects the rim of garnet porphroblasts, and is preserved as relict features within lower strained domains, it is interpretted that this fabric formed during peak metamorphic conditions. Towards the most outer garnet rim, the S_2 fabric rotates very sharply with the external matrix S_3 fabrics. The external matrix is pervasively overprinted by a strong extensional top-to-NE shear fabric (S_3), forming S–C' features and a strong stretching lineation defined by rutile, chlorite and phengite, that is orthogonal-oblique to the S_1 fabric and lineation within the cores of garnets. Garnet also shows evidence for a degree of rotation due to S_3 with stair stepping features, also indicative of top-to-NE shearing and represent both alpha- and delta-type porhyroclasts. Clinozoisite grains are syn-tectonic with respect to this S_3 shearing fabric as the larger grains have experienced clockwise rotations of 30–60° , show stair-stepping asymmetries and must post-date garnet growth. Titanite occurs throughout the matrix, but cannot be found as inclusions within garnet rims, suggesting garnet rims grew outside the titanite stability field. In many cases, titanite occurs as a breakdown product of rutile and commonly pseudomorphs it. Rutile is trapped within matrix glaucophane and clinozoisite, suggesting both glaucophane and clinozoisite grew during rutile stability, whereas matrix rutile is commonly found breaking down to chlorite and titanite during M_2 retrogression. Based on these observationsm we interpret the S_3 top-to-NE microstructures to represent decompression and exhumation from peak M_1 blueschist-facies conditions to greenschist-facies conditions.

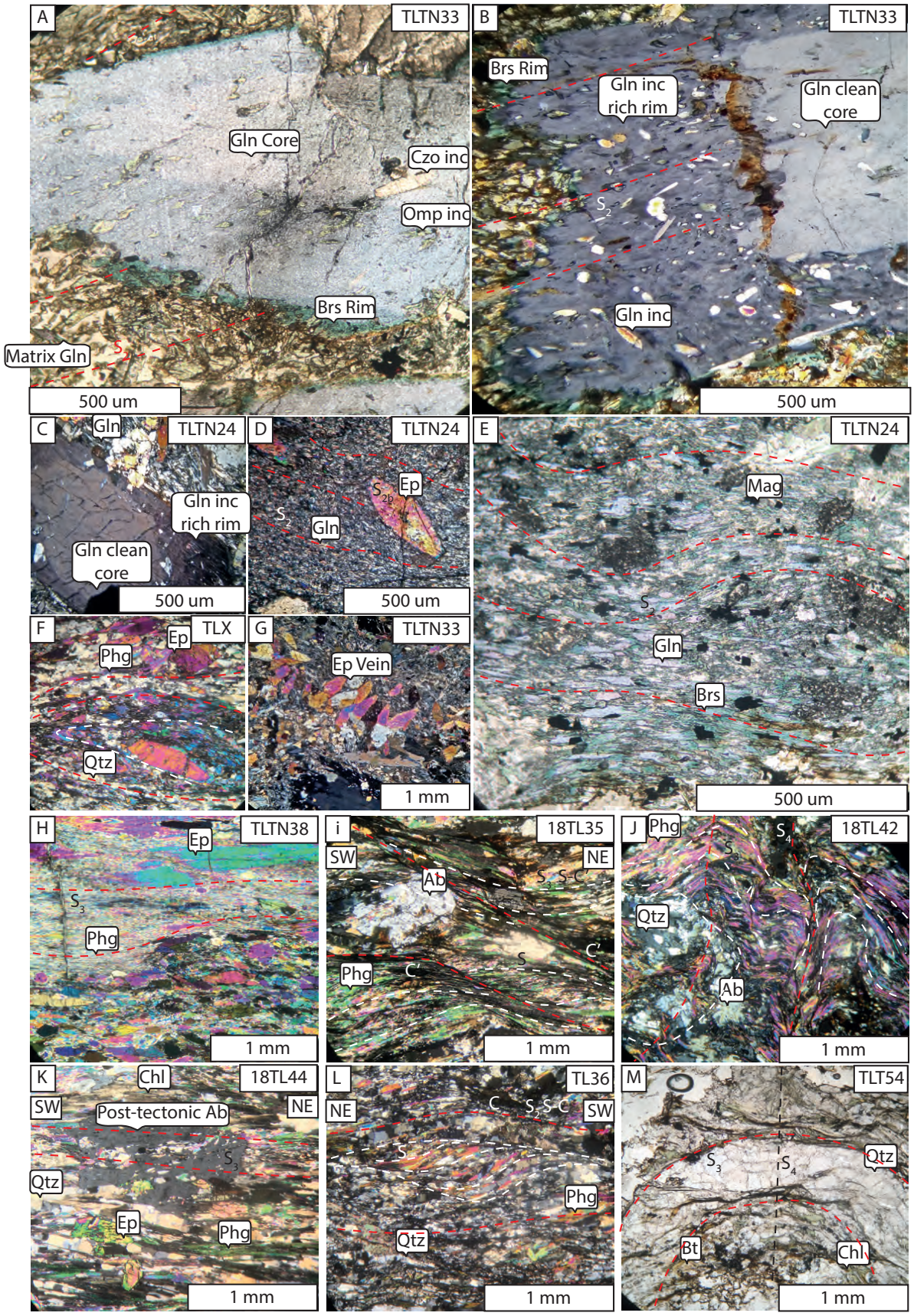


Figure 3.9: Continues on next page

Figure 3.9: Retrograde photomicrographs: A, B and C) TLTN33, coarse matrix ccross-cutting amphibole with a clean gln core and an inclusion dominated and green outer rim of Brs-MbH composition, D) Coarse cross-cutting epidote with fine matrix gln, E) S_{2b} fabric affecting matrix gln which is transforming to brs with interstial magneite. F) S_{2a} crenulation fabric and G) cross-cutting epidote vein. H) Cross-cutting epidote on fine grained phengite. I) Top to NE S-C' S_3fabric affecting greenschist assemblages. Upright F_4 folds in greenschists asssemblages. K) Post-tectonic Ab superimposed on S_3 fabric. L) S_{2b} top-to-SW fabric on Kionnia Thrust Zone. M) Upright F_4 fold in Sostis Unit greenschist.

Garnet X-ray maps and line profiles (Fig. 3.11) reveal significant chemical zonation. Mn displays a complex zonation pattern with concentric zonation from core to inner rim, followed by a step decrease in the outer rim, suggesting a two-stage garnet growth history. Similar patterns emerge in the grossular contents which remain fairly constant at 20% across the garnet cores but increase abruptly to 24% in the outer rim. Almandine displays a similar profile and increases from 54–62% from core to rim, whereas Pyrope only increases from 5–8% from core to rim. These features are indicative of prograde garnet growth under both increasing pressure, temperature under lawsonite stability and that S_1 and S_2 are prograde features whereas S_3 started to develop during the second phase of garnet growth producing the outermost rim. Matrix amphibolies are glaucophane composition, with B-site occupancy of Na (Na_B) = 2.0–1.75 pfu, Si = 8.0–7.7 pfu, A-site occupancy of Na + K ($(Na + K)_A$) = 0.0–0.05 pfu and XMg = $Mg/(Mg + Fe^{2+})$ = 0.57–0.69.

3.4.1.2 TLTN24 Garnet, Glaucophane Eclogite

This glaucophane-bearing foliated eclogite occurs within a mafic lens structurally overlying the recumbently folded dolomitic marbles (N37.550503, E25.124478). Although coarse-grained at the out-crop scale, under thin section it has a complex finely crystalline microstructure (see Fig. 3.8 and 3.9). Primary phases include: Garnet, paragonite, aegureine pyroxene, glaucophane, haematite, rutile, pseuodomorphed lawsonite, epidote and titanite, whereas secondary phases include chlorite biotite and minor plagioclase and actinolite. Garnet porphyroblasts are scattered throughout the rock sometimes up-to three cm in size, and are chemically zoned, with the concentric distribution

of Mn indicative of a single episode of prograde growth (Woodsworth, 1977), however Mn increases towards the outermost rim where it is associated with slightly elevated pyrope content (11%). Core to rim zonation is associated with increasing pyrope from 6–10%, increasing almandine from 60–64% and decreasing spessartine, whereas grossular remains relatively constant across the core at 28% but decreases to 24% in the inner rim. Many of the garnet grains are fractured, with an extensional direction subparallel to the NE–SW matrix foliation and an infill that includes chlorite, actinolite, hematite and quartz. Fracturing of the garnet is interpreted to have occurred at (M_2) greenschist facies conditions during exhumation of the sample. The cores are of glaucophane composition, with B-site occupancy of Na (Na_B) = 2.0–1.76 pfu, Si = 8.0–7.87 pfu, A-site occupancy of Na + K ($(Na + K)_A$) = 0.0–0.04 pfu and XMg = Mg/(Mg + Fe^{2+}) = 0.62–0.71. The inner rims are winchite-barroisite in composition, with Na_B = 1.51–0.59 pfu, Si = 7.51–7.69 pfu, $(Na + K)_A$ = 0.11–0.29 pfu and XMg = 0.62–0.69. Minor actinolite occurs as an interstitial matrix phase with Na_B = 0.32 pfu, Si = 7.845 pfu, $(Na + K)_A$ = 0.06 pfu and XMg = 0.69. Epidote is similarly zoned with pistacite content ($Fe^{3+}/(Fe^{3+} + Al)$) varying from 0.10 to 0.31.

Garnets have an internal fabric (S_1) defined by rutile needles, with composite inclusions of glaucophane and pseudomorphed lawsonite that have subsequently broken down to epidote and chlorite. This internal fabric (S_1), is discordant to the finely crystalline external matrix fabric. This is also true for large twinned paragonite porhyroblasts, that also show discordance between internal and external fabrics, and are retrogressed around the edges. S_2 is represented predominantly by strong and pervasive finely crystalline matrix Na pyroxene and glaucophane, and appears to have experienced dynamic recrystallization at eclogite-facies conditions. Paragonite appears to have grown pre-S_2 as this is generally aligned with the fabric. However, many of the porphyroblasts don't show obvious strain shadows associated with the development of the external matrix fabric (S_2). Indeed, most major phases including epidote, titanite and large glaucophanes appear to cross-cut the S_2 fabric, and rather define a static S_{2b} fabric. Many of these crystals show stepwise zoning from core to rim, suggesting

they were present during peak conditions, and overgrew the matrix during a hydration event or increase in temperature and were not subsequently overprinted by later deformation. Following this reasoning, we interpret S_1 and S_2 as prograde fabrics that developed leading up to peak conditions, and once at its highest-pressure, the rock annealed producing S_3. Due to the lack of deformation post-S_3, strain during exhumation must have become localized on the surrounding meta-sedimentary zones, creating foliated retrogressed blueschists.

3.4.1.3 TLTN33 Garnet, Aegirine, Glaucophane Eclogite

TLTN33 is a mafic eclogite that occurs as a boudin within the dilatational strain site (Fig. 3.5e) in the center of intensely deformed and isoclinally folded meta-sediments that structurally underlies a large recumbently folded dolomite band (37.547916, 25.125436). At outcrop scale, the occurrence of pyroxene is within very localized domains, almost certainly a result of the bulk compositional control on the mineral assemblages (Fig. 3.5) (e.g. Weller et al., 2015). Peak eclogite-facies assemblage is well preserved with a granoblastic texture, although it has experienced larger degrees of retrogression than eclogite sample TLTN24. The major phases include garnet, pyroxene, glaucophane, epidote, paragonite, rutile, titanite and quartz that are distributed between anhydrous pyroxene rich domains and hydrous glaucophane rich domains. The green pyroxene is length fast, has a high extinction angle with straight extinction along the cleavage, suggesting it is of aegerine composition (see Fig. 3.9), and indicating it grew in an oxidizing environment. The coarse microstructure suggests it has a porphritic origin and preserves relict igneous phenocrysts that are overprinted by M_1 paragenesis. Garnet forms large inclusion-rich porphroblasts that traps glaucophane, green aegirine pyroxene, epidote, rutile and titanite. In the garnet cores, pseudomorphed lawsonite inclusions occur and rutile is the only titanium bearing phase preserved, whereas a mixture of titantite and rutile is preserved elsewhere. These inclusion trails in the garnet core define a planar fabric (S_1) that occurred under lawsonite stability, whereas S_{2a}+b is defined by epidote inclusion trails formed oblique to this primary fabric and

formed under epidote stability. S_2 inclusion trails within garnet is concordant to the external fine grained matrix fabric including small glaucophanes and aegirine (Fig. 3.9). Coarse, optically and chemically zoned glaucophane and epidote porhyroblasts cross-cut this S_{2a}+b matrix fabric, and contain inclusions of aegirine pyroxene, glaucophane and rutile, and commonly display a clean core and textured rim. These grains form decussate textures defining the S_2c foliation and suggests these the sample was not affected by penetrative top-to-NE (S_3) shearing. The strong zoning in coarse amphiboles is reflected chemically with cores that are of glaucophane composition, with B-site occupancy of Na (Na_B) = 1.98–1.89 pfu, Si = 7.96–7.81 pfu, A-site occupancy of Na + K ($(Na + K)_A$) = 0.0-0.06 pfu and XMg = Mg/(Mg + Fe^{2+}) = 0.5-0.64. The inner rims are all barroisite in composition, with Na_B = 0.57–1.30 pfu, Si = 6.89–7.46 pfu, $(Na + K)_A$ = 0.17–0.49 pfu and XMg = 0.54–0.72 and the sharp outer green fibrous actinolite-magnesio-hornblende to magnesio-katophorite rims have compositions of Na_B = 0.41–0.85 pfu, Si = 6.83–7.27 pfu, $(Na + K)_A$ = 0.42–0.85 pfu and XMg = 0.46–0.62. Barrovsite and actinolite is also associated with fractured garnet grains and are interpreted to have formed during exhumation of the sample.

Epidote is similarly zoned with pistacite content (Fe^{3+}/(Fe^{3+} + Al)) varying from 0.09 to 0.70. In one domain, epidote grows as radiating crystals along a linear feature that post-dates the S_2 fabrics and probably represents a vein that was associated with hydration. Omphacite grains vary in size from matrix-aligned laths to small porphyroblasts up to 2 mm in length (Fig. 3.9), and exhibit minor zoning, with jadeite content (XJd = Na/(Na + Ca) increasing from the core to the rim (Table 3.2). Parogonite is the main white mica present as flakes in the matrix, although some minor phengite occurs and display minor chemical zoning, with Si increasing from 3.47 pfu in the core to 3.52 pfu in the rim (Table 3.2). All these features suggest TLTN33 provides the most complete insight into the prograde and hydration history and is consistent with the interpretation that of hydration shortly following peak eclogite-facies conditions.

3.4.1.4 TL36 Garnet, Phengite Retrogressed Whiteschist

TL36 is taken from Kionnia Beach within the top-to-SW Kionnia Thrust shear zone (N37.552989, E25.136092). This is a heavily retrogressed quartz mica-schist, with large (up-to five cm wide) garnet porphyroblasts that contain inclusions of high-pressure precursors including lawsonite pseudomorphs, rutile and phengite. Major phases include garnet, phengite, titanite, calcite, epidote, rutile, quartz, chlorite, and retrograde plagioclase. The rock has been affected by extensive retrogression associated with a greenschist-facies assemblage that has all but destroyed all evidence of high-pressure conditions within the matrix. Relict M_1 phases include matrix phengite, rutile and epidote which characterize a top-to-SW S–C' fabric (S_{2b}) that is deformed around the garnet porphyroblasts, indicating top-to-SW movements post-dates garnet growth. Due to the large amounts of inclusions within garnet, no obvious internal fabrics could be distinguished, although it is likely that it preserves similar prograde fabrics to other Kionnia Unit samples. Extensive metasomatism is apparent on both outcrop and thin-section scale with epidote/clinozoisite veins cross-cutting the (S_{2b}) top-to-SW fabrics and that grew epitaxially into an interlocking yet radiating pattern. These features suggest the top-to-SW movements (S_{2b}) were active at near peak conditions and continued during retrogression and terminated prior to the retrograde hydration event forming the veins. Amphibole is barrosite to actinolite in composition and interpretted to be retrograde.

3.4.2 Pygros Unit

Rocks from within the Pygros Unit show better preservation of M_1 assemblages than the Sostis Unit in the interior of Tinos. In a few localities fresh garnet glaucophane blueschists crop out, with similar assemblages to the garnet glaucophane schists within the Kionnia Unit, predominantly glaucophane, garnet, phengite, pseudomorphed lawsonite and rutile inclusions within garnet, whereas the matrix contains rutile, epidote, titanite, albite, chlorite and quartz. The degree of M_2 retrogression increases towards

Sample	TLTN26	TLTN26	TLTN26	TLTN26	TLTN26	TLTN26	TLTN26	TLTN26	TLTN26	TLTN26	TLTN26	TLTN26	TLTN26	TLTN24	TLTN24	TLTN24	TLTN24	TLTN24	TLTN24	TLTN24	TLTN24	TLTN24	TLTN24	TLTN24	TLTN24	TLTN24	TLTN24	TLTN24	TLTN24	TLTN24	TLTN24
Min	Czo	Czo	Grt	Grt	Grt	Grt	Gln	Gln	Gln	Chl	Plg	Plg	Sph	Grt	Grt	Grt	Grt	Grt	Omp	Omp	Gln	Gln	Brs	Act	Plg	Plg	Marg	Czo	Pl	Sph	Rt
Location	Matrix	Matrix	Core	Int	Rim	Rim	Matrix	Matrix	Matrix	Matrix	Matrix	Matrix	Matrix	Core	Core	Int	Inner Rim	Outer Rim	Matrix	Grt inc	Matrix	Core	Rim	Corona	Grt inc	Matrix	Matrix	Matrix	Matrix	Matrix	Matrix	Matrix
SiO2	37.89	38.09	37.10	36.70	37.17	37.75	57.61	57.98	57.89	27.38	55.47	54.72	30.97	38.50	38.47	38.90	38.66	39.04	56.89	56.87	57.75	57.23	53.44	55.61	52.61	55.14	44.61	38.69	65.69	31.53	0.06
TiO2	0.07	0.08	0.11	0.17	0.10	0.08	0.00	0.00	0.02	0.04	0.11	0.23	36.82	0.11	0.09	0.08	0.05	0.06	0.05	0.04	0.00	0.02	0.04	0.07	0.16	0.23	0.09	0.07	0.00	36.05	97.01
Al2O3	23.14	25.74	20.25	20.37	20.72	20.60	8.19	9.36	9.40	20.59	26.24	27.00	1.81	20.38	20.46	20.74	21.00	20.88	8.86	9.81	9.52	11.04	4.59	2.64	27.17	26.41	16.53	23.61	12.87	2.77	0.00
FeO	11.43	8.72	24.68	26.02	27.15	26.91	13.15	12.29	11.58	19.56	3.03	2.89	0.41	26.03	26.45	25.80	27.27	26.44	7.07	7.61	11.34	9.50	13.88	12.97	3.02	2.86	13.01	10.74	3.28	0.52	0.76
MnO	0.15	0.15	8.42	7.04	3.74	3.80	0.06	0.08	0.08	0.43	0.04	0.01	0.06	3.24	3.26	2.40	1.10	1.13	0.07	0.05	0.16	0.04	0.28	0.22	0.03	0.00	0.46	0.23	0.08	0.03	0.00
MgO	0.05	0.04	1.36	1.44	1.76	1.77	9.82	9.41	10.18	18.09	3.71	3.56	0.00	1.45	1.48	1.99	2.55	2.36	7.93	6.88	10.27	10.56	13.64	15.20	3.07	3.72	6.85	0.04	7.19	0.02	0.00
CaO	23.07	23.56	7.16	7.34	8.61	8.42	0.46	0.19	1.05	0.12	0.03	0.07	29.04	9.54	9.38	9.68	8.95	9.27	13.10	11.51	0.43	1.19	7.92	10.84	0.08	0.04	6.74	22.47	4.63	28.33	0.89
Na2O	0.02	0.00	0.02	0.03	0.02	0.02	7.10	7.21	6.69	0.03	0.18	0.31	0.04	0.02	0.02	0.02	0.02	0.03	6.94	7.80	7.09	6.73	3.08	1.29	0.38	0.29	3.44	0.00	6.80	0.05	0.00
K2O	0.01	0.00	0.01	0.01	0.00	0.00	0.01	0.00	0.02	0.21	10.13	9.98	0.00	0.00	0.00	0.00	0.00	0.00	0.00	0.00	0.02	0.02	0.12	0.14	10.38	10.21	0.94	0.00	0.03	0.00	0.02
Totals	95.83	96.38	99.11	99.12	99.28	99.35	96.41	96.53	96.90	86.45	98.94	98.77	99.15	99.29	99.60	99.60	99.60	99.21	100.91	100.58	96.57	96.32	96.99	98.98	96.89	98.88	92.66	95.85	100.57	99.29	98.75
Oxygens	12.5	12.5	12.0	12.0	12.0	12.0	23.0	23.0	23.0	14.0	11.0	11.0	5.0	12.0	12.0	12.0	12.0	12.0	6.0	6.0	23.0	23.0	23.0	23.0	11.0	11.0	11.0	12.5	8.0	5.0	2.0
Si	3.04	3.01	3.01	2.98	2.99	3.03	8.03	8.04	8.02	2.84	3.54	3.50	1.02	3.08	3.07	3.08	3.06	3.09	2.02	2.02	8.01	7.94	7.69	7.85	3.45	3.53	3.17	3.08	2.91	1.03	0.00
Ti	0.00	0.01	0.01	0.01	0.01	0.01	0.00	0.00	0.00	0.00	0.01	0.01	0.91	0.01	0.01	0.01	0.00	0.00	0.00	0.00	0.00	0.00	0.00	0.01	0.01	0.01	0.01	0.00	0.00	0.89	0.99
Al	2.19	2.40	1.94	1.95	1.97	1.95	1.35	1.53	1.54	2.51	1.98	2.04	0.07	1.92	1.93	1.94	1.96	1.95	0.37	0.41	1.56	1.81	0.78	0.44	2.10	1.99	1.38	2.22	0.67	0.11	0.00
Fe3+	0.76	0.57	0.03	0.09	0.05	0.00	0.62	0.48	0.29	0.00	0.00	0.00	0.00	0.00	0.00	0.00	0.00	0.00	0.06	0.08	0.36	0.07	0.33	0.11	0.00	0.00	0.54	0.71	0.12	0.00	0.00
Fe2+	0.01	0.01	1.64	1.68	1.78	1.81	0.91	0.95	1.05	1.69	0.16	0.16	0.01	1.74	1.77	1.71	1.80	1.75	0.15	0.14	0.96	1.03	1.34	1.42	0.17	0.15	0.23	0.01	0.00	0.01	0.01
Mn	0.01	0.01	0.58	0.48	0.26	0.26	0.01	0.01	0.01	0.04	0.00	0.00	0.00	0.22	0.22	0.16	0.07	0.08	0.00	0.00	0.02	0.01	0.03	0.03	0.00	0.00	0.03	0.02	0.00	0.00	0.00
Mg	0.01	0.00	0.17	0.17	0.21	0.21	2.04	1.94	2.10	2.79	0.35	0.34	0.00	0.17	0.18	0.23	0.30	0.28	0.42	0.36	2.12	2.18	2.92	3.19	0.30	0.35	0.72	0.01	0.47	0.00	0.00
Ca	1.98	2.00	0.62	0.64	0.74	0.72	0.07	0.03	0.16	0.01	0.00	0.01	1.02	0.82	0.80	0.82	0.76	0.79	0.50	0.44	0.06	0.18	1.22	1.64	0.01	0.00	0.51	1.92	0.22	0.99	0.01
Na	0.00	0.00	0.00	0.01	0.00	0.00	1.92	1.94	1.80	0.01	0.02	0.04	0.00	0.00	0.00	0.00	0.00	0.00	0.48	0.54	1.91	1.81	0.86	0.35	0.05	0.04	0.47	0.00	0.58	0.00	0.00
K	0.00	0.00	0.00	0.00	0.00	0.00	0.00	0.00	0.00	0.03	0.83	0.81	0.00	0.00	0.00	0.00	0.00	0.00	0.00	0.00	0.00	0.00	0.02	0.03	0.87	0.83	0.09	0.00	0.00	0.00	0.00
Sum	7.99	8.00	8.00	8.00	8.00	7.99	14.95	14.92	6.95	9.92	6.89	6.90	3.04	7.96	7.97	7.95	7.96	7.94	4.00	4.00	14.99	15.03	15.20	15.06	6.95	6.90	7.15	7.95	4.99	3.03	1.01
XMg	0.43	0.40	0.09	0.09	0.11	0.11	0.69	0.67	0.67	0.62	0.69	0.69	0.01	0.09	0.09	0.12	0.14	0.14	0.74	0.72	0.69	0.68	0.69	0.69	0.65	0.70	0.76	0.42	-	0.06	-
XCa	-	-	-	-	-	-	-	-	-	-	-	-	-	-	-	-	-	-	-	-	-	-	-	-	-	-	-	-	0.27	-	-
XMn	-	-	-	-	-	-	-	-	-	-	-	-	-	-	-	-	-	-	-	-	-	-	-	-	-	-	-	-	-	-	-
Al(iv)	-	-	-	-	-	-	-	-	-	-	0.46	0.50	-	-	-	-	-	-	-	-	-	-	-	-	0.55	0.48	0.84	-	-	-	-
Al(vi)	-	-	-	-	-	-	-	-	-	-	1.52	1.54	-	-	-	-	-	-	-	-	-	-	-	-	1.55	1.52	0.55	-	-	-	-
Alm	-	-	0.55	0.56	0.60	0.60	-	-	-	-	-	-	-	0.59	0.60	0.58	0.61	0.61	-	-	-	-	-	-	-	-	-	-	-	-	-
Prp	-	-	0.05	0.06	0.07	0.07	-	-	-	-	-	-	-	0.06	0.06	0.08	0.10	0.10	-	-	-	-	-	-	-	-	-	-	-	-	-
Grs	-	-	0.21	0.21	0.25	0.24	-	-	-	-	-	-	-	0.28	0.27	0.28	0.26	0.27	-	-	-	-	-	-	-	-	-	-	-	-	-
Spss	-	-	0.19	0.16	0.09	0.09	-	-	-	-	-	-	-	0.07	0.07	0.06	0.03	0.03	-	-	-	-	-	-	-	-	-	-	-	-	-
Jd	-	-	-	-	-	-	-	-	-	-	-	-	-	-	-	-	-	-	0.41	0.45	-	-	-	-	-	-	-	-	-	-	-
XFe3+	0.99	0.99	0.02	0.05	0.03	0.00	0.41	0.34	0.21	-	-	-	-	0.00	0.00	0.00	0.00	0.00	0.30	0.37	0.27	0.07	0.20	0.07	0.00	0.00	0.70	0.99	-	-	-
XPs	0.26	0.19	-	-	-	-	-	-	-	-	-	-	-	-	-	-	-	-	-	-	-	-	-	-	-	-	-	0.24	-	-	-

Table 3.1: Representative mineral compositions from the Kionnia Unit

Sample	TLTN33	TLTN33	TLTN33	TLTN33	TLTN33	TLTN33	TLTN33	TLTN33	TLTN33	TLTN33	TLTN33	TLTN33	TL36	TL36	TL36	TL36	TL36	TL36	TL36	TL36	TL36	TL36	TL36	TL36	TL36	TL36
Min	Grt	Grt	Grt	Grt	Omp	Omp	Gln	Gln	Bts	MBld	Mnz	Pz	Plag	Pl	Ep	Sph	Chl	Grt	Grt	Grt	Act	Act	Bt	Plag	Pz	Ms	Ep	Pl	Sph	Rt	Chl
Location	Core	Int	Inner Rim	Outer Rim	Matrix	Grt inc	Matrix	Core	Matrix	Outer Rim	Outer Rim	Matrix	Matrix	Matrix	Core	Rim	Matrix	Core	Int	Outer Rim	Inner Rim	Matrix	Matrix	Matrix	Grt inc	Matrix	Matrix	Matrix	Matrix	Matrix	Matrix	Matrix
SiO2	37.41	37.68	37.74	37.83	52.43	55.21	54.89	58.16	58.30	48.51	46.39	48.78	55.14	69.56	62.84	38.48	37.54	30.44	29.41	37.31	37.74	35.70	53.83	54.23	38.88	52.61	45.91	48.46	38.67	69.17	36.70	0.00	27.64
TiO2	0.12	0.08	0.07	0.06	0.03	0.03	0.04	0.01	0.00	0.03	0.08	0.05	0.23	0.00	0.01	0.08	0.07	35.91	0.00	0.08	0.05	0.10	0.12	0.03	0.22	0.43	0.03	0.40	0.12	0.02	36.82	84.83	0.05
Al2O3	20.94	21.24	21.30	21.46	3.33	10.06	8.75	9.77	10.25	4.44	8.77	38.72	26.41	17.69	13.69	28.65	21.74	2.67	20.73	21.18	21.20	20.60	4.12	1.34	17.90	22.47	39.18	28.47	27.40	19.46	2.76	0.00	19.17
FeO	26.50	25.67	27.44	28.05	13.61	7.67	9.24	11.08	11.89	14.80	16.67	17.31	2.86	0.61	5.52	6.89	10.59	0.61	18.56	27.78	28.14	28.32	12.87	13.33	21.02	2.57	0.44	2.30	7.09	0.00	0.26	14.18	29.89
MnO	3.38	2.56	0.96	0.98	0.07	0.08	0.06	0.02	0.13	0.10	0.13	0.00	0.00	0.01	0.03	0.18	0.14	0.04	0.57	1.15	0.54	0.66	0.39	0.17	0.44	0.20	0.21	0.04	0.00	0.14	0.10	0.00	0.33
MgO	1.49	2.29	2.72	2.64	7.12	6.76	6.91	9.29	9.38	11.50	11.71	10.03	0.18	0.00	0.06	0.06	0.07	0.00	19.56	1.21	1.77	2.04	2.31	14.31	15.67	10.29	3.40	0.00	2.65	0.00	0.23	0.30	11.04
CaO	9.73	10.00	8.99	9.03	12.64	11.53	12.06	0.06	0.25	6.95	8.86	7.09	0.15	0.00	3.38	23.40	22.92	28.58	0.10	10.77	11.36	10.37	0.57	12.37	0.13	0.06	0.17	0.27	23.93	0.20	28.82	0.52	0.21
Na2O	0.01	0.01	0.01	0.01	6.69	7.52	7.58	7.22	7.18	2.51	1.33	2.51	6.91	11.29	6.95	0.02	0.00	0.04	0.00	0.00	0.00	0.00	6.58	1.53	0.69	0.12	6.58	0.00	11.71	0.05	0.00	0.13	0.00
K2O	0.00	0.00	0.00	0.01	0.02	0.01	0.02	0.04	0.29	0.31	0.18	0.36	0.46	10.21	0.05	0.01	0.00	0.01	0.33	0.00	0.00	0.00	0.13	0.01	9.58	10.93	0.90	10.10	0.03	0.03	0.00	0.03	0.76
Totals	99.58	99.54	99.23	100.13	95.65	99.18	99.54	97.29	96.60	95.81	96.18	93.79	94.39	95.88	98.88	100.17	99.58	97.77	96.07	98.28	89.27	99.48	100.80	100.35	99.11	97.71	97.74	98.22	93.09	93.09	93.05	92.97	96.77	100.70	99.81	100.65	89.08
Oxygens	12.0	12.0	12.0	12.0	6.0	6.0	6.0	23.0	23.0	23.0	23.0	23.0	23.0	11.0	11.0	8.0	8.0	12.5	12.5	5.0	14.0	12.0	12.0	2.9	12.0	23.0	23.0	23.0	11.0	11.0	11.0	11.0	12.5	8.0	5.0	2.0	14.0
Si	3.00	3.00	3.01	2.99	2.01	1.99	1.98	8.03	8.03	7.56	7.34	7.41	7.05	3.08	3.52	3.03	2.84	2.98	2.99	1.01	2.92	2.99	2.97	0.01	2.88	7.71	7.80	2.87	3.61	3.00	3.32	2.99	3.00	1.00	0.99	0.00	2.94
Ti	0.01	0.01	0.00	0.00	0.00	0.00	0.00	0.00	0.00	0.01	0.00	0.00	0.01	0.00	0.01	0.00	0.00	0.00	0.00	0.00	0.00	0.01	0.00	0.00	0.01	0.01	0.00	0.01	0.02	0.00	0.02	0.01	0.00	0.00	0.00	0.00	0.00
Al	1.98	1.99	2.00	2.00	0.15	0.43	0.37	1.59	1.67	1.65	1.18	0.80	1.57	2.89	1.99	0.91	0.73	2.62	2.33	0.10	2.43	1.98	1.97	0.00	1.95	0.70	0.23	1.56	1.82	3.02	2.30	2.53	1.00	0.11	0.00	2.40	0.00
Fe3+	0.02	0.01	0.00	0.01	0.31	0.15	0.20	0.39	0.31	0.23	0.44	0.44	0.43	0.00	0.00	0.02	0.21	0.38	0.67	0.00	0.00	0.03	0.08	0.00	0.29	0.10	0.16	0.00	0.00	0.00	0.00	0.46	0.00	0.00	0.00	0.00	0.00
Fe2+	1.76	1.70	1.83	1.84	0.13	0.00	0.00	0.00	1.07	1.57	1.62	1.79	0.02	0.00	0.00	0.00	0.00	0.00	0.04	1.54	1.86	1.77	0.04	1.79	1.78	1.44	1.44	1.30	0.17	0.02	0.13	0.01	0.00	0.00	0.01	0.17	2.66
Mn	0.23	0.17	0.07	0.07	0.00	0.00	0.00	0.00	0.02	0.02	0.01	0.02	0.00	0.00	0.00	0.00	0.00	0.00	0.00	0.00	0.00	0.07	0.04	0.03	0.03	0.02	0.05	0.01	0.01	0.00	0.00	0.01	0.00	0.00	0.00	0.01	0.03
Mg	0.35	0.42	0.35	0.34	1.58	1.49	1.53	2.07	2.35	2.63	2.67	2.67	0.02	0.00	0.00	0.00	0.00	0.00	0.02	0.65	0.69	0.51	0.00	3.56	3.55	0.02	0.05	0.01	0.01	0.00	0.00	0.00	0.00	0.00	0.00	0.00	0.00
Ca	0.84	0.85	0.77	0.77	1.91	1.64	1.77	0.01	0.01	0.03	0.03	0.10	1.45	0.01	0.17	1.94	1.96	1.02	0.01	1.93	1.94	1.96	0.08	0.84	0.77	1.91	1.91	0.01	0.01	0.00	0.55	0.00	0.01	0.01	0.01	0.01	0.02
Na	0.00	0.00	0.00	0.00	0.48	0.55	0.53	1.92	0.00	1.65	1.18	0.74	1.24	0.85	0.03	0.85	0.74	0.00	0.00	0.00	0.00	0.00	0.00	0.01	0.54	0.09	0.00	0.02	0.81	0.04	0.00	0.00	0.00	0.99	0.01	0.00	0.00
K	0.00	0.00	0.00	0.00	0.00	0.00	0.00	0.00	0.00	0.01	0.00	0.00	0.04	0.04	0.00	0.00	0.00	0.00	0.00	0.04	0.00	0.01	0.00	0.00	0.00	0.02	0.00	0.00	0.96	0.08	0.88	0.00	0.00	0.00	0.00	0.00	0.10
Sum	8.00	8.00	7.99	8.00	4.00	4.00	4.00	14.95	14.95	15.35	15.47	15.36	15.60	6.92	6.90	4.92	5.06	8.02	8.00	3.04	9.89	8.00	8.00	5.06	8.00	15.16	15.05	7.79	6.95	6.94	6.98	8.01	5.00	3.05	1.10	9.91
XMg	0.09	0.14	0.15	0.14	0.76	0.81	0.82	0.64	0.70	0.56	0.61	0.60	0.56	0.33	0.70	0.06	0.19	0.00	0.18	0.00	0.65	0.07	0.11	0.12	0.13	0.68	0.70	0.47	0.68	0.00	0.67	0.00	0.01	0.62	0.04	0.04	0.40
XCa	0.28	0.28	0.26	0.26	0.02	0.33	0.20	0.01	0.00	0.01	0.01	0.01	0.01	0.00	0.00	0.00	0.00	0.00	0.00	0.00	0.00	0.00	0.00	0.00	0.00	0.00	0.00	0.00	0.00	0.00	0.00	0.00	0.00	0.00	0.00	0.00	0.00
XMn	0.08	0.06	0.02	0.02	0.17	0.49	0.33	0.00	0.00	0.00	0.00	0.00	0.00	0.00	0.00	0.00	0.00	0.00	0.00	0.00	0.00	0.00	0.00	0.00	0.00	0.00	0.00	0.00	0.00	0.00	0.00	0.00	0.00	0.00	0.00	0.00	0.00
Al(vi)	0.01	0.00	0.00	0.01	0.70	0.63	0.72	0.22	0.30	0.13	0.21	0.20	0.04	0.00	0.00	0.00	0.00	0.85	0.95	0.00	0.00	0.02	0.04	0.00	0.14	0.07	0.10	0.00	0.00	0.00	0.00	0.99	0.00	0.00	0.00	0.00	0.00
Al(vi)	-	-	-	-	-	-	-	-	-	-	-	-	-	-	-	-	-	0.13	0.22	-	-	-	-	-	-	-	-	-	-	-	-	0.15	-	-	-	-	-
Prp	-	-	-	-	-	-	-	-	-	-	-	-	-	-	-	-	-	-	-	-	-	-	-	-	-	-	-	-	-	-	-	-	-	-	-	-	-
Alm	0.59	0.57	0.61	0.62	-	-	-	-	-	-	-	-	-	0.92	0.48	-	-	-	-	-	-	0.62	0.60	0.61	0.62	-	-	1.13	0.39	1.00	0.69	-	-	-	-	-	-
Grs	0.28	0.28	0.26	0.26	-	-	-	-	-	-	-	-	-	-	-	-	-	-	-	-	-	0.31	0.32	0.30	0.27	-	-	0.43	1.43	2.01	1.61	-	-	-	-	-	-
Sps	0.08	0.06	0.02	0.02	-	-	-	-	-	-	-	-	-	-	-	-	-	-	-	-	-	0.02	0.01	0.01	0.01	-	-	-	-	-	-	-	-	-	-	-	-
Jd	-	-	-	-	-	-	-	-	-	-	-	-	-	-	-	-	-	-	-	-	-	-	-	-	-	-	-	-	-	-	-	-	-	-	-	-	-
XMg	0.09	0.14	0.15	0.14	0.76	0.81	0.82	0.64	0.70	0.56	0.61	0.60	0.56	0.33	0.70	0.06	0.19	0.00	0.18	0.00	0.65	0.07	0.11	0.12	0.13	0.68	0.70	0.47	0.68	0.00	0.67	0.00	0.01	0.62	0.04	0.04	0.40
XCa	-	-	-	-	-	-	-	-	-	-	-	-	-	-	-	-	-	-	-	-	-	-	-	-	-	-	-	-	-	-	-	-	-	-	-	-	-
XMn	-	-	-	-	-	-	-	-	-	-	-	-	-	-	-	-	-	-	-	-	-	-	-	-	-	-	-	-	-	-	-	-	-	-	-	-	-
Al(vi)	-	-	-	-	-	-	-	-	-	-	-	-	-	-	-	-	-	-	-	-	-	-	-	-	-	-	-	-	-	-	-	-	-	-	-	-	-
Alm	0.59	0.57	0.61	0.62	-	-	-	-	-	-	-	-	-	0.92	0.48	-	-	-	-	-	-	0.62	0.60	0.61	0.62	-	-	1.13	0.39	1.00	0.69	-	-	-	-	-	-
Prp	0.06	0.09	0.11	0.10	-	-	-	-	-	-	-	-	-	1.97	1.51	-	-	-	-	-	-	0.05	0.07	0.08	0.10	-	-	0.43	1.43	2.01	1.61	-	-	-	-	-	-
Grs	0.28	0.28	0.26	0.26	-	-	-	-	-	-	-	-	-	-	-	-	-	-	-	-	-	0.31	0.32	0.30	0.27	-	-	-	-	-	-	-	-	-	-	-	-
Sps	0.08	0.06	0.02	0.02	-	-	-	-	-	-	-	-	-	-	-	-	-	-	-	-	-	0.02	0.01	0.01	0.01	-	-	-	-	-	-	-	-	-	-	-	-
Jd	-	-	-	-	0.17	0.49	0.33	-	-	-	-	-	-	-	-	-	-	-	-	-	-	-	-	-	-	-	-	-	-	-	-	-	-	-	-	-	-
XKs	0.01	0.00	0.00	0.01	0.70	0.63	0.72	0.22	0.30	0.13	0.21	0.20	0.04	0.00	0.00	0.00	0.00	0.85	0.95	0.00	0.00	0.02	0.04	0.00	0.14	0.07	0.10	0.00	0.00	0.00	0.00	0.99	0.00	0.00	0.00	0.00	0.00
XPs	-	-	-	-	-	-	-	-	-	-	-	-	-	-	-	-	-	0.13	0.22	-	-	-	-	-	-	-	-	-	-	-	-	0.15	-	-	-	-	-

Table 3.2: Representative mineral compositions from the Kionnia Unit

the top of the unit, where the S_3 top-to-NE fabrics intensify.

3.4.2.1 17TL104 Garnet Glaucophane Blueschist

17TL104 crops out in a 100 m thick mafic band of garnet glaucophane schists intercalated between calc-schists and meta-psammite lithologies at the higher structural levels of the Pygros Unit (N37.639889, E25.025361). In thin section, this rock is strikingly similar to TLTN26, with garnet, glaucophane, phengite, titanite, pseudomorphed lawsonite inclusions, rutile, and epidote, as its major phases, and chlorite, minor albite, actinolite and ankorite as its retrograde greenschist-facies assemblage; four fabrics can be identified. Garnet grains are chemically zoned, with the bell-shaped distribution of Mn indicative of a single episode of growth (Fig. 3.11; Woodsworth, 1977). Core to rim zonation is characterized by increasing pyrope and almandine, and decreasing spessartine and grossular content (Fig. 3.11). The concentric and bell-shaped distribution of Mn suggests that diffusion has not significantly affected the original growth zonation, such that the rim composition is interpreted to preserve the composition formed during peak metamorphism. All amphibole is glaucophane-winchite in composition, with Na_B = 1.59–1.95 pfu, Si = 7.48–8.00 pfu, $(Na + K)_A$ = 0.00–0.35 pfu and XMg = 0.60–0.70. Epidote is present as elongate grains and in very fine-grained clusters, with pistacite content varying from 0.24 to 0.29. Phengite is present as small matrix-aligned flakes, with Si = 3.40–3.51 pfu. Garnets are chemically zoned with a sharp concentric distribution of Mn from 15% in core to 1% in the rim, indicative of a single episode of prograde growth (Woodsworth, 1977). Core to rim zonation is associated with increasing pyrope from 3–7%, increasing almandine from 60–64%, whereas grossular remains relatively constant across the core at 28% but decreases to 22–24% in the outer rim.

Within the garnet cores, a rotational fabric (S_1) is defined by inclusions of pseudomorphed lawsonite and rutile, indicating garnet grew simultaneous to prograde shearing deformation. Within the garnet rims, a second fabric (S_2), defined by the same inclusions forms oblique to S_1 as a truncation plane. Both S_1 and S_2 are discordant to the external planar matrix foliation (S_3), the major foliation at outcrop and thin

section scale defined top-to-NE shearing in glaucophane, phengite and rutile needles. In the outermost rims of some garnets, particularly in strain shadows, deflection of inclusion trails indicate rotation of the S_2 fabric into alignment with the S_3 foliation, whereas elsewhere the S_3 fabrics wrap around the garnets suggesting, garnet growth finished during the initial stages of S_3. Epidotes are commonly zoned, and contain inclusions of pseudomorphed lawsonite, and glaucophane and are also aligned with the S_3 foliation, suggesting they either grew during top-to-NE shearing or they slightly pre-date it. The lack of epidote within garnet rims, however, suggests that epidote was not stable during garnet rim growth, that is associated with the highest pyrope content (6%). A gentle crenulation cleavage (S_4) is sometimes superimposed orthogonally onto these to the main fabrics (S_2 and S_3), rotating and buckling grains of glaucophane, epidote, phengite and titanite, suggesting a component of E–W pure shear during the later stages of exhumation at M_2 conditions.

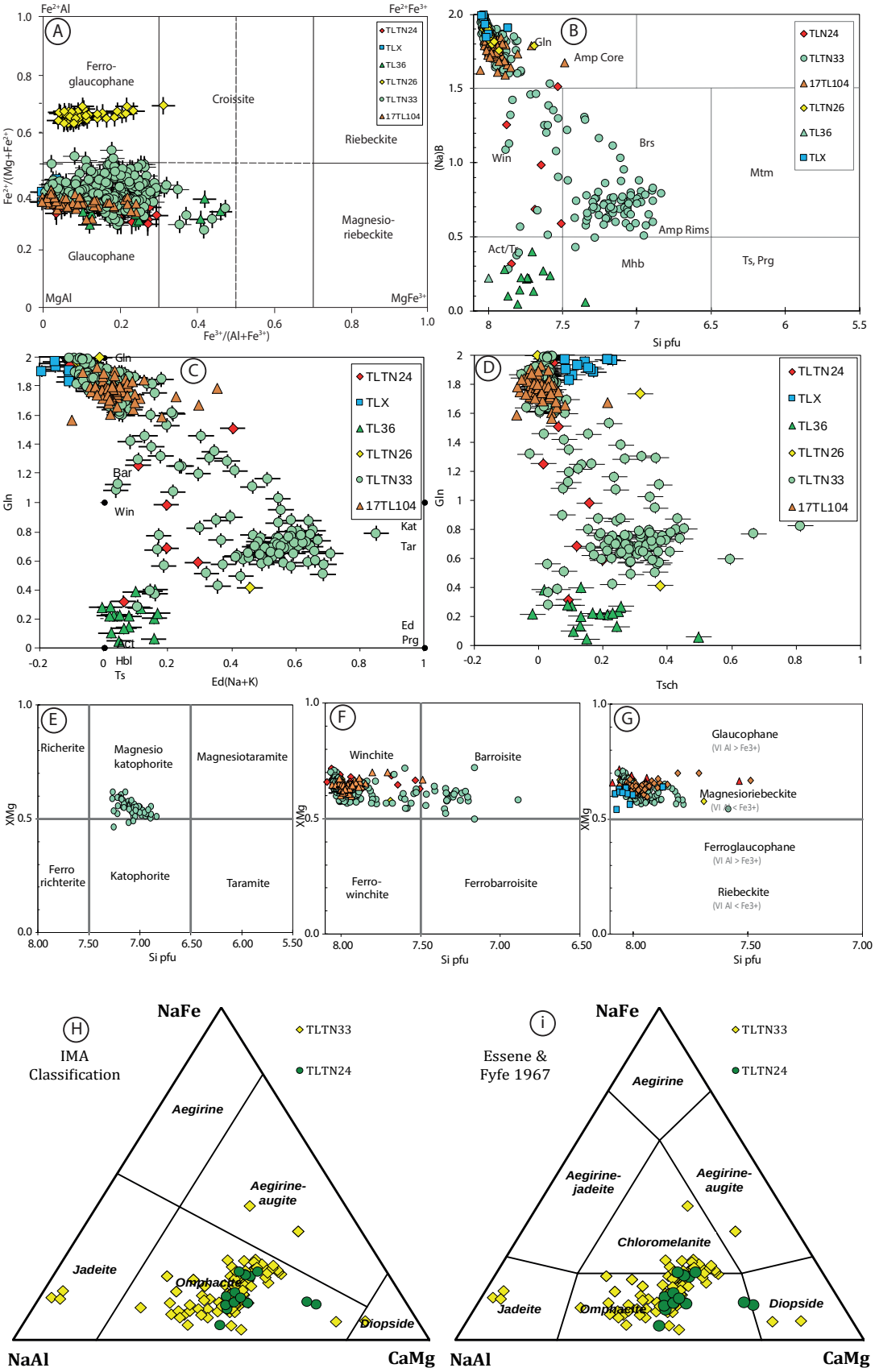


Figure 3.10: Continues on next page

Figure 3.10: Mineral chemistry of amphiboles and pyroxene. A) Sodic amphibole discrimination diagram, showing most are glaucophane (TLTN26 is ferro-glaucophane in composition)., B)Na in the B-site vs Si p.f.u showing most amphiboles are sodic and glaucophane comoition, but TLTN33 has Barrovsite rims on coarse matrix amphibole. C) amphibole vector plots, total edenite vs glaucophane and D) Glaucophane versus tschermakite showing similar trends to above. E, F and G) XMg vs Si p.f.u for group 3 sodic-calcic amphiboles with E) (Na+K) in A site >0.5, F) (Na+K) in A site <0.5 and G) group 4 sodic amphiboles with (Na+K) in A site <0.5, with fairly constant XMg. H) IMA classification pyroxene ternary plot, showoing a a range of cpx but mostly ophacite, i) Essen anf Fyfe, 1967 ternary plot showing most cpx is omphacite-chloromelenite.

3.4.3 Sostis Unit

The Sostis Unit compromises meta-sedimentary semi-pelites and psammites with several dolomitic marble bands which were probably derived from a shelf-slope-setting and are intercalated with meta-volcanic mafic lithologies. Unlike, the overlying units which preserve fresh M_1 assemblages, this thick package of rocks is affected by very strong M_2 overprint, and metasomatism, although rare garnet bearing rocks can be found which preserve its some of its M_1 history.

3.4.3.1 TLX Garnet, Glaucophane, Clinozosite, Mica Schist

TLX is a meta-pelite taken from Kolimpithra bay in northern Tinos (N37.633225, E25.145059). Only limited M_2 greenschist-facies retrogression affects this sample, allowing peak M_1 fabrics and features to be preserved. Major M_1 phases include garnet, Na-amphibole (glaucophane-winchite), clinozoisite, phengite, rutile, titanite, chlorite, quartz and M_2 phases include albite, biotite and small grains of tourmaline. Pseudomorphs of lawsonite occur as inclusions within garnet cores, but have been broken down into dominantly paragonite, phengite and chlorite. Garnets are mildly zoned with a distribution of Mn from 5% in core to 1% in the rim. Core to rim zonation shows slight increases in pyrope from 4–6%, increasing almandine from 60–64%, whereas grossular remains relatively constant across the core at 27–29%. All amphibole is glaucophane-winchite in composition, with Na_B = 1.84–2.0 pfu, Si = 7.87–8.00 pfu, $(Na + K)_A$ = 0.00–0.10 pfu and XMg = 0.54–0.61. Epidote is present as elongate grains and in very fine-grained clusters, with pistacite content varying from 0.24 to 0.29. Phengite

is present as small matrix-aligned flakes, with Si = 3.40–3.51 pfu. Pseudomorphed lawsonite and rutile inclusions within garnet cores define a planar fabric (S_1), which rotates towards the rim (S_{2a}), but is still discordant to the external (S_3) top-to-NE matrix foliation that deforms around the garnet. S_{2a} crenulations are preserved within low-strain matrix domains represented by interlocking grains of phengite that form herringbone structures, and developed under conditions of lawsonite stability and were likely present during peak M_1 conditions. All peak M_1 metamorphic assemblages (Grt + Gln + Phg + Law + Chl + Rt + Qtz) show pre-tectonic relationships with respect to S_3 top-to-NE shearing. Garnet outer rims contain inclusions of rutile and are affected by rotation with respect to the surrounding S_3 fabric, creating alpha and delta-style porphyroclasts. In contrast, S_3 occurred coeval with M_2 mineral growth. Clinozoisite forms large lath-like porphyroblasts with their long axes parallel to the S_3 foliation, suggesting they grew syn-tectonic with respect to S_3. S_3 also deforms around large plagioclase grains, producing sigma-type porhyroclasts with definitive top-to-NE kinematics. These plagioclase porphyroclasts trap epidote and rutile inclusions, signifying they post-date high-pressure M_1 conditions and grew at much lower pressures. Top-to-NE shearing (S_3) must have thus initiated prior to plagioclase growth and continued way into the greenschist facies. A mildly developed upright crenulation cleavage (S_4) produces cm-mm scale (F_4) folds trending NE–SW. This is superimposed on S_3 and causes kinking and folding of phengites and muscovite within the main foliation, and therefore indicates a component of E–W shortening during exhumation.

3.4.3.2 TLT60 Garnet Mica Epidote Schist (Retrogressed Blueschist)

TLT60 is a meta-pelite collected from central Tinos (N37.563955, E25.19662) at the deepest exposed structural levels of the Sostis Unit. It is characterized by repeated layers of quartz rich and epidote, chlorite and micaceous rich domains, which are aligned parallel with the S_3 top-to-NE shear fabric. Garnet is partially broken down within the micaceous rich domains and is shows very little zoning, possibly indicating it has been modified by diffusion. Mn slightly decreasing from 3–2% from core to rim, whereas

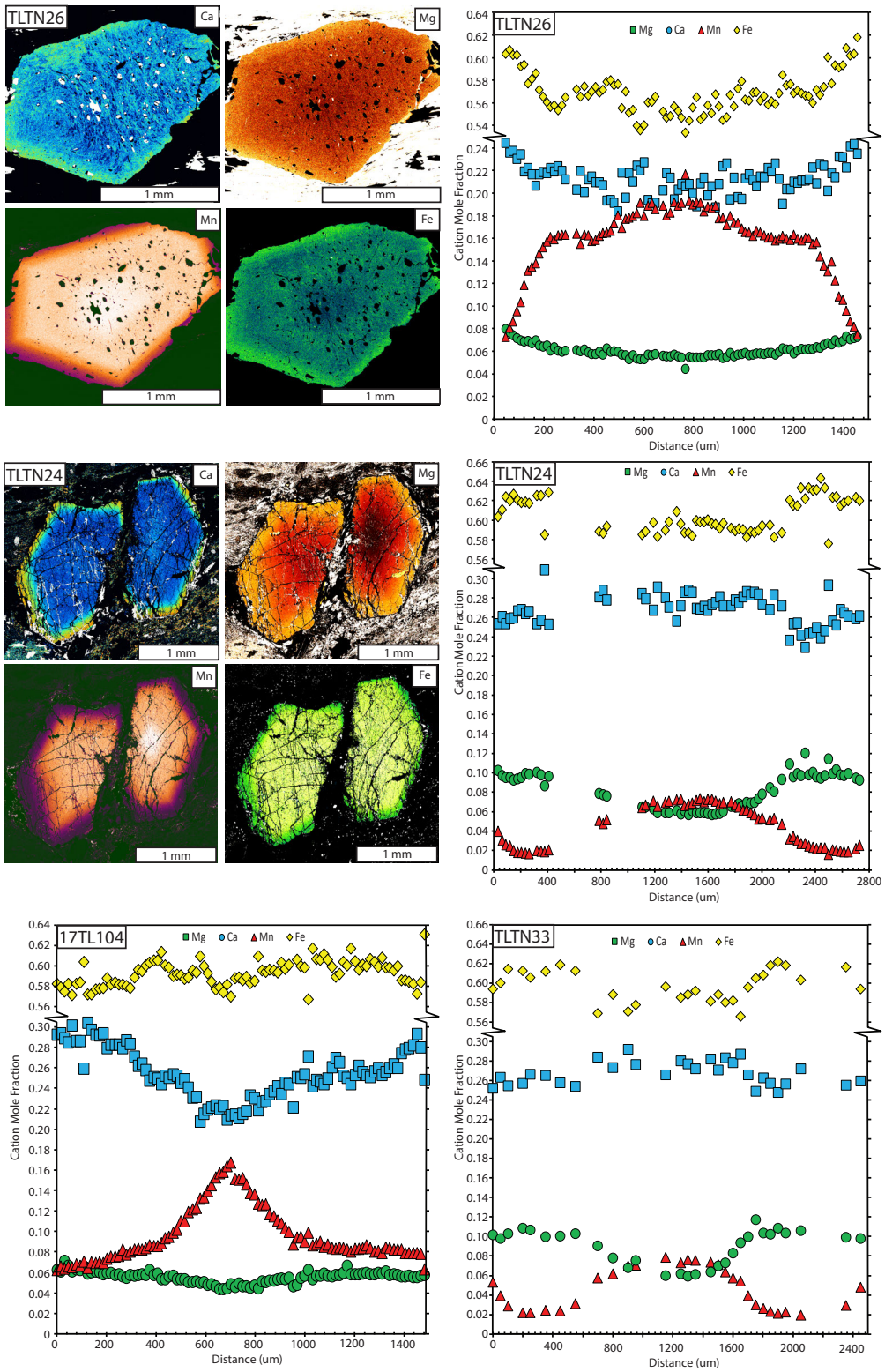


Figure 3.11: Prograde garnet maps and profiles for Kionnia and Pygros Unit samples. showing TLTN26 with rotation textures in the calcium map, indicating it grew syn-tectonic with glaucophane in the matrix and strong spessartine zoning from core to rim, with increasing grossular,pyrope and almandine. Eclogite TLTN24 garnets showing strong grossular and pyrope increases from core to rim with a small inflexion in spessartine and almandine affecting the outer most rim. Sharp prograde and symmetrical zoning in blueschist 17TL104 with increasing grossular towards the rim, interpretted as a single growth history. TLTN33, showing similartrends to TLTN24 but heavily affected by fractures (missing data).

Sample	17TL104	17TL104	17TL104	17TL104	17TL104	17TL104	17TL104	17TL104	17TL104	17TL104	17TL104	17TL104	17TL104	17TL104	17TL104	17TL104	17TL104	TLX	TLX	TLX	TLX	TLX	TLX	TLX	TLX	TLX	TLX	17TL48	17TL48	17TL48	17TL48	17TL48	17TL48
Min	Grt	Grt	Grt	Grt	Grt	Gln	Gln	Cpx	Pa	Phg	Chl	Pl	Pl	Rt	Sph	Ep	Grt	Grt	Grt	Grt	Gln	Phg	Phg	Czo	Czo	Sph	Ep	Chl	Ms	Phg	Pa	Pl
Location	Core	Core	Int	Inner Rim	Outer Rim	Matrix	Matrix	Grt inc	Matrix	Matrix	Matrix	Matrix	Matrix	Grt inc	Matrix	Matrix	Core	Int	Inner Rim	Rim	Matrix	Matrix	Matrix	Matrix	Matrix	Matrix	Matrix	Matrix	Matrix	Matrix	Matrix	Matrix	Matrix
SiO2	36.91	37.07	37.28	37.36	37.38	Grt inc	57.30	52.55	41.95	52.77	28.29	62.37	67.40	0.06	30.14	37.77	37.24	37.07	36.93	37.84	57.55	49.87	49.42	37.27	38.65	29.80	37.92	28.32	49.77	52.71	48.16	68.77
TiO2	0.12	0.11	0.08	0.10	0.09	0.31	0.02	0.05	0.02	0.09	0.02	0.00	0.00	98.31	38.84	0.09	0.11	0.08	0.13	0.07	0.08	0.26	0.14	0.15	0.12	37.41	0.13	0.03	0.15	0.24	0.04	0.00
Al2O3	20.56	20.70	20.62	20.69	20.97	9.17	10.50	1.15	28.17	27.15	20.60	24.30	21.16	0.00	1.19	25.26	20.91	20.73	20.82	21.33	9.54	25.04	34.06	30.81	27.63	2.64	27.69	19.45	31.78	27.92	41.98	20.18
FeO	25.46	26.35	27.26	25.99	26.22	11.92	10.99	10.00	9.31	3.27	18.18	0.12	0.53	1.46	0.59	10.43	30.09	0.00	29.18	28.59	14.86	2.95	1.91	0.09	0.04	1.48	6.72	19.01	1.95	2.52	0.40	0.39
MnO	8.55	7.20	3.62	2.85	3.04	0.09	0.07	0.41	0.10	0.06	0.31	0.00	0.00	0.18	0.02	0.11	1.72	29.32	0.81	0.77	0.10	0.02	0.00	6.31	7.19	0.06	0.14	0.14	0.00	0.01	0.00	0.01
MgO	0.99	1.10	1.45	1.48	1.46	10.26	10.67	11.67	5.90	4.26	20.12	0.00	0.26	0.00	0.00	0.06	1.12	1.07	1.58	1.68	7.66	3.01	1.36	0.06	0.18	0.10	0.04	19.04	2.88	3.76	0.16	0.02
CaO	7.27	7.26	9.20	10.59	10.45	1.17	0.36	23.64	0.59	0.01	0.05	4.89	0.38	0.39	28.82	23.11	9.15	1.36	9.85	10.50	0.13	0.03	0.04	18.55	0.00	28.00	23.01	0.30	0.04	0.01	0.08	0.07
Na2O	0.01	0.00	0.03	0.02	0.02	6.39	7.33	0.41	4.51	0.12	0.00	8.07	9.64	0.00	0.02	0.03	0.04	9.86	0.00	0.00	6.66	0.00	0.08	0.75	23.96	0.20	0.00	0.04	0.26	0.18	5.65	10.99
K2O	0.00	0.00	0.00	0.02	0.00	0.03	0.02	0.01	0.03	8.81	0.00	0.15	0.07	0.01	0.01	0.01	0.00	0.01	0.00	0.01	0.05	10.99	10.05	1.03	0.00	0.29	0.01	0.17	8.05	8.05	0.39	0.04
Totals	99.86	99.79	99.54	99.10	99.63	39.35	97.27	99.89	90.58	96.53	87.58	99.91	99.44	100.41	99.63	96.86	100.39	99.50	99.31	100.80	96.63	92.17	97.08	95.02	97.78	100.02	95.66	86.50	94.87	95.39	96.87	100.47
Oxygens	12.00	12.00	12.00	12.00	12.00	23.00	23.00	6.00	11.00	11.00	14.00	8.00	8.00	2.00	5.00	12.50	12.00	12.00	12.00	12.00	23.00	11.00	11.00	12.50	12.50	5.00	12.50	14.00	11.00	11.00	11.00	8.00
Si	2.98	2.99	2.99	3.00	2.96	8.03	7.92	1.98	2.92	3.42	2.86	2.65	2.95	0.00	0.99	2.99	2.98	2.98	2.97	2.97	8.07	3.46	3.20	2.98	3.00	0.98	3.00	2.92	3.26	3.43	2.99	2.98
Ti	0.01	0.01	0.01	0.01	0.01	0.03	0.00	0.00	0.00	0.00	0.00	0.00	0.00	0.99	0.96	0.01	0.01	0.01	0.01	0.01	0.01	0.01	0.01	0.01	0.01	0.92	0.01	0.00	0.01	0.01	0.00	0.00
Al	1.96	1.97	1.95	1.96	1.98	1.50	1.71	0.05	2.31	2.08	2.45	1.36	1.09	0.00	0.05	2.36	1.97	1.96	1.97	1.98	1.58	2.05	2.60	2.90	2.53	0.10	2.58	2.36	2.46	2.14	3.07	1.03
Fe3+	0.07	0.03	0.05	0.03	0.09	0.19	0.17	0.02	0.38	0.12	0.00	0.01	0.02	0.00	0.00	0.64	0.07	0.07	0.08	0.07	0.39	0.00	0.03	0.08	0.46	0.00	0.41	0.00	0.08	0.10	0.02	0.01
Fe2+	1.65	1.75	1.78	1.72	1.64	1.19	1.10	0.30	0.16	0.05	1.54	0.00	0.00	0.02	0.02	0.05	1.94	1.90	1.88	1.84	1.35	0.17	0.08	0.34	0.01	0.04	0.03	1.64	0.03	0.04	0.01	0.00
Mn	0.59	0.49	0.25	0.19	0.20	0.01	0.01	0.01	0.01	0.00	0.03	0.00	0.00	0.00	0.00	0.01	0.12	0.07	0.06	0.04	0.01	0.00	0.00	0.00	0.01	0.00	0.01	0.01	0.00	0.00	0.00	0.00
Mg	0.12	0.13	0.17	0.18	0.18	2.12	2.20	0.66	0.61	0.41	3.03	0.00	0.02	0.00	0.00	0.01	0.13	0.16	0.19	0.19	1.60	0.31	0.13	0.00	0.00	0.00	0.00	2.92	0.28	0.37	0.02	0.00
Ca	0.63	0.63	0.79	0.91	0.95	0.17	0.05	0.95	0.04	0.00	0.01	0.34	0.02	0.01	1.01	1.96	0.78	0.85	0.85	0.89	0.02	0.00	0.00	1.59	1.99	0.98	1.95	0.03	0.00	0.00	0.01	0.00
Na	0.00	0.00	0.00	0.00	0.00	1.72	1.96	0.03	0.61	0.02	0.00	0.66	0.82	0.00	0.00	0.01	0.00	0.00	0.00	0.00	0.00	1.81	0.00	0.01	0.12	0.00	0.01	0.03	0.02	0.68	0.92
K	0.00	0.00	0.00	0.00	0.00	0.01	0.00	0.00	0.00	0.73	0.00	0.01	0.00	0.00	0.00	0.00	0.00	0.00	0.00	0.00	0.01	0.97	0.83	0.11	0.00	0.01	0.00	0.02	0.67	0.67	0.03	0.00
Sum	8.00	8.00	8.00	8.00	8.00	14.96	15.13	4.00	7.04	6.84	9.91	5.01	4.91	1.01	3.03	8.02	8.00	8.00	8.00	8.00	14.85	6.99	6.89	8.12	8.00	3.06	8.00	9.92	6.82	6.78	6.82	4.96
XMg	0.07	0.07	0.09	0.09	0.10	0.64	0.67	0.69	0.79	0.89	0.66	-	-	-	-	0.12	0.06	0.08	0.09	0.09	0.54	0.65	0.63	-	-	0.11	0.11	0.64	0.90	0.90	0.71	-
XCa	-	-	-	-	-	-	-	-	-	-	-	0.34	0.02	-	-	-	-	-	-	-	-	-	-	-	-	-	-	-	-	-	-	0.00
XMn	-	-	-	-	-	-	-	-	-	-	-	-	-	-	-	-	-	-	-	-	-	-	-	-	-	-	-	-	-	-	-	-
Al(iv)	-	-	-	-	-	-	-	-	1.08	0.58	-	-	-	-	-	-	-	-	-	-	-	0.54	0.80	-	-	-	-	-	-	-	-	-
Al(vi)	-	-	-	-	-	-	-	-	1.23	1.50	-	-	-	-	-	-	-	-	-	-	-	1.51	1.81	-	-	-	-	-	-	-	-	-
Alm	0.55	0.58	0.59	0.57	0.55	-	-	-	-	-	-	-	-	-	-	-	-	-	-	-	-	-	-	-	-	-	-	-	-	-	-	-
Prp	0.04	0.04	0.06	0.06	0.06	-	-	-	-	-	-	-	-	-	-	-	-	-	-	-	-	-	-	-	-	-	-	-	-	-	-	-
Grs	0.21	0.21	0.26	0.30	0.32	-	-	-	-	-	-	-	-	-	-	-	-	-	-	-	-	-	-	-	-	-	-	-	-	-	-	-
Spss	0.20	0.16	0.08	0.06	0.07	-	-	-	-	-	-	-	-	-	-	-	-	-	-	-	-	-	-	-	-	-	-	-	-	-	-	-
Jd	-	-	-	-	-	-	-	0.01	-	-	-	-	-	-	-	-	-	-	-	-	-	-	-	-	-	-	-	-	-	-	-	-
XFe3+	0.04	0.02	0.03	0.02	0.05	0.14	0.13	0.05	0.70	0.70	-	-	-	-	-	0.93	0.03	0.04	0.04	0.04	0.22	0.00	0.26	0.20	0.99	-	0.92	-	0.70	0.70	0.71	-
XPs	-	-	-	-	-	-	-	-	-	-	-	-	-	-	-	0.21	-	-	-	-	-	-	-	0.03	0.15	-	0.14	-	-	-	-	-

Table 3.3: Pygros Unit representative mineral compositions

pyrope, almandine and grossular remain constant at 4%, 66% and 28% respectively. However, towards the outermost rim, grossular increases to 30% associated with a decrease in almandine content to 64%. Cloudy albite porphyroclasts overgrow the S_3 fabric, as revealed by continuous inclusion trails between the interior and exterior of the grains, indicating S_3 developed prior to albite growth on the initial stages of decompression. The S_3 fabric deforms around the garnet porphyoblasts that also contain inclusions of pseudomorphed lawsonite and rutile in the core, with a relatively inclusion free rim. However, no earlier prograde fabrics could be distinguished due to abundance of inclusions in garnet and the extensive alteration. Phengite within the matrix gives a range of compositions with Si pfu = 3.27-3.46, and epidote has pistacite content ($Fe^{3+}/(Fe^{3+} + Al)$) varying from 0.19 to 0.29. Quartz grains exhibit incipient recrystallization by grain boundary migration, which suggests deformation temperatures in excess of 500°C (Stipp et al., 2002).

3.4.3.3 TLT53 Garnet Clinozoisite Mica Schist

TLT53 was taken from Lifatani Beach on the eastern coastline of Tinos (N37.542787, E25.229480) directly under the TSZ. It comprises of garnet, clinozoisite, epidote, phengite, pseudomorphed lawsonite inclusions, quartz, calcite, rutile, titanite, and is highly retrogressed with abundant biotite, plagioclase and chlorite. Within the garnets, relict lawsonite pseudomorph inclusions define a planar fabric (S_1) within the core which rotate anticlockwise towards the rim to form the S_2 fabric, and suggest that garnet grew syn-tectonically with respect to the development of the S_2 fabric. Garnets reveal minor chemical zoning with a concentric distribution of Mn from core to rim, although almandine, pyrope and grossular contents remain constant at 65%, 2–3% and 25% respectively. This suggests that garnet grew within a single episode under lawsonite stability and post-dated the S_1 and S_2 prograde fabrics. These fabrics are discordant to the external top-to-NE matrix fabric (S_3), which deforms around the garnets producing stair-stepping and sigma-style porphyroclasts. Epidote and clinozoisite within the matrix, with pistacite content ($Fe^{3+}/(Fe^{3+} + Al)$) varying from , and also contain inclu-

sions of pseudomorphed lawsonite, rutile that are oblique to the main external foliation (S_3). Epidote therefore grew at high-pressure following S_2 and prior to or during S_3 top-to-NE shearing. The S_3 matrix fabric is defined by alignment of anchorite, phengite and also retrograde chlorite and plagioclase. These features suggest that S_3 is purely a retrograde feature, that developed following the highest-pressure conditions but not under lawsonite stability, which had previously transformed to epidote/clinozoisite and paragonite.

Sample	TLIT60	TLIT60	TLIT60	TLIT60	TLIT60	TLIT60	TLIT60	TLIT60	TLIT53	TLIT53	TLIT53	TLIT53	TLIT53	TLIT53	TLIT53	TLIT53	TLIT59	TLIT59	TLIT59	TLIT59	TLIT59	TLIT59	TLIT59	TLIT59
Min	Grt	Grt	Grt	Grt	Chl	Ms	Plg	Sph	Pl	Grt	Grt	Grt	Ms	Plg	Ms	ilm	Rt	Sph	Bt	Bt	Bt	Ep	Marg	Plg	Hem	Pl	Chl
Location	Core	Int	Inner Rim	Outer Rim						Core	Core	Int	Rim	Grt inc	Matrix	Matrix	Matrix	Grt inc	Matrix	Matrix	Matrix	Matrix	Matrix	Matrix	Matrix	Matrix	Matrix
SiO2	37.30	37.13	37.53	37.40	38.09	26.42	45.51	52.67	30.28	68.88	38.46	36.31	36.71	36.78	44.80	52.87	45.08	8.35	0.04	30.26	36.48	37.13	36.71	37.21	46.63	49.08	0.21	68.16	28.15
TiO2	0.06	0.12	0.15	0.10	0.14	0.05	0.11	0.32	38.07	0.00	0.33	0.12	0.07	0.05	0.37	0.14	0.35	49.15	98.60	36.90	1.57	2.23	1.60	0.04	0.03	0.15	0.02	0.01	0.18
Al2O3	21.05	20.93	20.97	21.00	27.21	20.50	32.36	24.98	1.83	19.90	21.79	20.50	20.71	20.80	31.64	25.66	31.87	0.41	0.00	2.64	14.89	15.61	16.16	22.39	13.87	26.11	0.06	19.82	16.02
FeO	30.67	29.98	30.76	29.47	6.93	26.90	1.83	3.88	0.46	0.15	29.66	30.26	31.11	30.76	5.01	2.87	4.77	31.73	0.65	0.28	23.26	22.63	23.56	13.34	17.02	7.31	94.73	0.13	35.42
MnO	1.32	1.09	0.89	0.74	0.18	0.26	0.02	0.00	0.00	0.01	2.47	2.86	1.70	0.90	0.10	0.02	0.06	1.83	0.02	0.04	0.16	0.08	0.25	0.42	0.19	0.06	0.05	0.01	0.23
MgO	0.89	0.85	1.04	0.96	0.00	12.61	1.37	3.80	0.00	0.00	0.32	0.47	0.58	0.79	1.03	2.12	1.01	0.03	0.00	0.00	7.46	6.94	6.78	0.00	0.43	2.27	0.00	0.01	5.44
CaO	9.13	9.80	9.41	10.86	24.45	0.02	0.00	0.00	29.45	0.08	7.61	8.03	8.03	8.90	0.04	0.00	0.05	8.36	0.14	28.87	0.03	0.08	0.00	22.40	10.21	0.00	0.00	0.06	0.21
Na2O	0.02	0.02	0.02	0.02	0.01	0.02	0.23	0.01	0.02	11.57	0.02	0.01	0.13	0.02	0.22	0.25	0.21	0.03	0.00	0.03	0.05	0.17	0.05	0.00	8.54	0.16	0.00	11.78	0.13
K2O	0.00	0.00	0.00	0.00	0.01	0.01	9.62	9.24	0.01	0.12	0.00	0.00	0.10	0.01	10.97	9.79	11.02	0.03	0.00	0.06	8.36	8.25	8.50	0.03	0.01	10.54	0.01	0.06	4.58
Totals	100.44	99.92	100.77	100.55	97.02	86.79	91.05	94.90	100.12	100.71	100.87	98.56	99.14	99.01	94.18	93.73	94.41	99.93	99.46	99.09	92.27	93.12	93.61	95.84	96.93	95.69	95.08	100.05	90.37
Oxygens	12	12	12	12	12.5	14	11	11	5	8	12	12	12	12	11	11	11	3	2	5	11	11	11	12.5	11	11	3	8	14
Si	2.98	2.98	2.99	2.97	2.98	2.83	3.15	3.49	0.99	2.99	3.04	2.98	2.98	2.98	3.07	3.56	3.08	0.20	0.00	1.00	2.91	2.92	2.89	3.00	3.37	3.32	0.01	2.98	3.08
Ti	0.00	0.01	0.01	0.01	0.01	0.00	0.01	0.02	0.94	0.00	0.02	0.01	0.00	0.00	0.02	0.01	0.02	0.86	1.00	0.91	0.09	0.13	0.10	0.00	0.00	0.01	0.00	0.00	0.02
Al	1.98	1.98	1.97	1.97	2.51	2.59	2.64	1.95	0.07	1.02	2.03	1.98	1.98	1.99	2.56	2.04	2.57	0.01	0.00	0.10	1.40	1.45	1.50	2.13	1.18	2.08	0.00	1.02	2.07
Fe3++	0.05	0.05	0.04	0.08	0.45	0.00	0.06	0.15	0.00	0.01	0.00	0.06	0.08	0.04	0.16	0.00	0.13	0.00	0.00	0.00	0.00	0.00	0.00	0.87	0.00	0.24	1.98	0.01	0.41
Fe2+	2.00	1.96	2.00	1.89	0.01	2.41	0.05	0.07	0.01	0.00	1.96	2.02	2.04	2.05	0.13	0.16	0.14	0.62	0.01	0.01	1.55	1.49	1.55	0.03	1.03	0.17	0.02	0.00	2.83
Mn	0.09	0.07	0.06	0.05	0.01	0.02	0.00	0.00	0.00	0.00	0.17	0.20	0.12	0.06	0.01	0.00	0.00	0.04	0.00	0.00	0.01	0.01	0.02	0.03	0.01	0.00	0.00	0.00	0.02
Mg	0.11	0.10	0.12	0.11	0.00	2.01	0.14	0.38	0.00	0.00	0.06	0.06	0.07	0.10	0.11	0.21	0.10	0.00	0.00	0.00	0.89	0.81	0.80	0.00	0.05	0.23	0.00	0.00	0.89
Ca	0.78	0.84	0.80	0.93	2.05	0.00	0.00	0.00	1.03	0.00	0.65	0.71	0.70	0.77	0.00	0.00	0.00	0.21	0.00	1.02	0.00	0.01	0.00	1.94	0.79	0.00	0.00	0.00	0.03
Na	0.00	0.00	0.00	0.00	0.00	0.00	0.03	0.00	0.00	0.97	0.00	0.00	0.02	0.00	0.03	0.03	0.03	0.00	0.00	0.00	0.01	0.03	0.01	0.00	1.20	0.02	0.00	1.00	0.03
K	0.00	0.00	0.00	0.00	0.00	0.00	0.85	0.78	0.00	0.01	0.00	0.00	0.01	0.00	0.96	0.84	0.96	0.00	0.00	0.00	0.85	0.83	0.85	0.00	0.00	0.91	0.00	0.00	0.64
Sum	8.00	8.00	8.00	8.00	8.03	9.87	6.93	6.83	3.04	4.99	7.93	8.00	8.00	8.00	7.04	6.85	7.04	1.94	1.00	3.05	7.72	7.66	7.70	8.00	7.63	6.98	2.01	5.01	10.00
XMg	0.05	0.05	0.06	0.06	0.00	0.46	0.75	0.85	-	-	0.03	0.03	0.03	0.04	0.45	0.57	0.42	0.00	-	-	0.36	0.35	0.34	0.00	0.04	0.57	-	-	0.24
XCa	-	-	-	-	-	-	-	-	-	0.00	-	-	-	-	-	-	-	0.04	-	-	-	-	-	-	-	-	-	0.00	-
XMn	-	-	-	-	-	-	-	-	-	-	-	-	-	-	0.03	0.44	0.92	-	-	-	1.09	1.08	0.36	0.39	-	0.68	-	-	-
Al(iv)	-	-	-	-	-	-	0.85	0.51	-	-	-	-	-	-	1.63	1.60	1.65	-	-	-	0.32	0.36	0.39	-	0.56	1.40	-	-	-
Al(vi)	-	-	-	-	-	-	1.80	1.44	-	-	-	-	-	-	-	-	-	-	-	-	-	-	-	-	-	-	-	-	-
Alm	-	-	-	-	-	-	-	-	-	-	0.19	0.21	0.13	0.07	-	-	-	-	-	-	-	-	-	-	-	-	-	-	-
Prp	0.09	0.07	0.06	0.05	-	-	-	-	-	-	0.74	0.73	0.77	0.83	-	-	-	-	-	-	-	-	-	-	-	-	-	-	-
Grs	0.80	0.82	0.81	0.85	-	-	-	-	-	-	0.00	0.00	0.02	0.00	-	-	-	-	-	-	-	-	-	-	-	-	-	-	-
Spss	0.00	0.00	0.00	0.00	-	-	-	-	-	-	0.00	0.00	0.02	0.00	-	-	-	-	-	-	-	-	-	-	-	-	-	-	-
Jd	0.11	0.10	0.12	0.10	-	-	-	-	-	-	0.07	0.06	0.08	0.10	-	-	-	-	-	-	-	-	-	-	-	-	-	-	-
XFe3+	0.02	0.02	0.02	0.04	0.99	-	0.56	0.70	-	-	0.00	0.03	0.04	0.02	0.56	0.00	0.48	0.00	-	-	0.00	0.00	0.00	0.97	0.00	0.58	0.99	-	0.13
XPs	-	-	-	-	0.15	-	-	-	-	-	-	-	-	-	-	-	-	-	-	-	-	-	-	0.29	-	-	-	-	-

Table 3.4: Pygros Unit representative mineral compositions

3.5 Pressure-Temperature (P–T) Conditions of Metamorphism

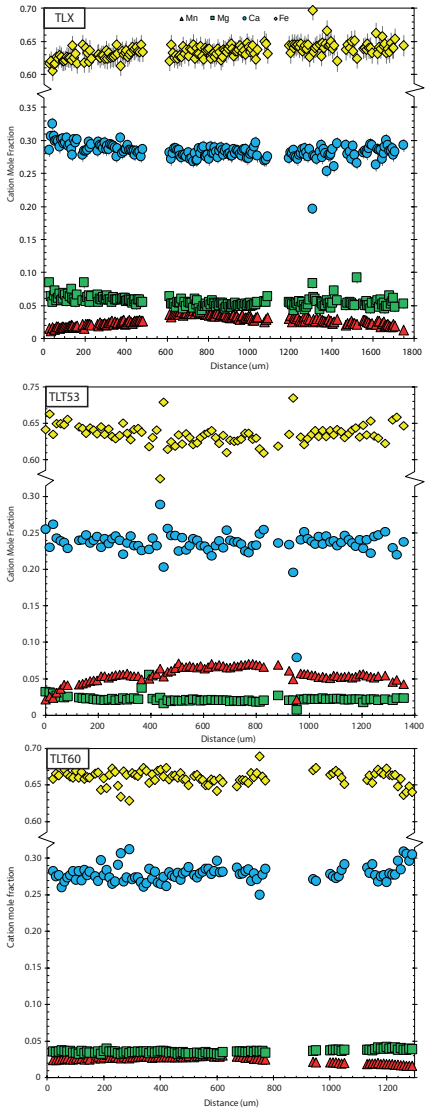


Figure 3.12: Sostis garnet line profiles, showing spessartine, almandine, grossular and pyrope endmembers, missing data corresponds to inclusins or fractures

Several forms of thermobarometry were employed in this work to constrain the P–T evolution of Tinos high-pressure rocks. The garnet, clinopyroxene, phengite barometer (Waters and Martin, 1993; Krough Ravna and Terry, 2004) was used on eclogite samples TLTN24 and TLTN33, and where possible, this was combined with the Grt–Cpx thermometer using the calibration of both Powell (1995) and Krough Ravna (2000) and a Monte-Carlo method to estimate the statistical uncertainty to a 1 S.D. level using 100 perturbed analyses. Retrograde M_2 conditions were estimated using Ti in biotite thermometry (Henry et al., 2005) combined with the amphibole–plagioclase thermometer of Holland and Blundy (1994). THERMOCALC mode 2, average P–T (Av-PT) (Powell and Holland, 1998) using version 3.40i, was utilized for all samples across all structural levels of Tinos to estimate both M_1 and M_2 conditions. Activities of solid-solution end members for each coexisting mineral were calculated using AX (Holland, 2009), and a series of predicted reactions using these end members intersect about a

single point in P–T space. The result are displayed in Fig. 3.13 and Table 3.5 and discussed below.

3.5.1 Thermobarometry

3.5.1.1 Peak M_1 conditions

For eclogite samples from the Kionnia Unit, he Grt–Cpx thermometer (Schmidt, 1993; Krough Ravana, 2000) and Grt–Cpx–Phg barometer was utilized using the program Ecbar (Waters, personal communication) which uses a Monte Carlo approach to perturb mineral compositions and activity solutions to a 1 S.D. uncertainity (Waters and Martin, 1993; Krough Ravna and Terry, 2004). Core conditions where calculated using garnet core compositions with omphacite and phengite inclusions, whereas peak conditions were calculated by using analysed garnet outer rim compositions, combined with matrix omphacite and phengite. End member activities were calculated using the garnet model of Ganguly et al., (1989). Sample TLTN24 yielded a garnet core P–T condition of 18.08 ± 2.77 kbar and 497 ± 17 °C and a garnet rim condition of 22.58 ± 2.91 kbar and 560 ± 16 °C. Sample TLTN33 also yielded garnet core P-T results of 18.01 ± 2.88 kbar and 428 ± 15 °C and a very similar garnet rim result of 22.40 ± 2.92 kbar and 547 ± 17°C. The Av-PT function of THERMOCALC was used to constrain garnet core and outer rim P–T conditions of all samples, using inclusions not otherwise mentioned above. Considered phases with solid solutions include Grt + (Omp) + Phg + Amp + (Chl) + (Ep) and pure phases include Law + Rt + Ttn + Qtz + H_2O. An X(H_2O) = 1.0 was used for all calculations in samples that did not have calcite and X(H_2O) = 0.9 when calcite was present.

Calculated P–T results demonstrate that there are at least two distinct peak M_1 P–T populations on Tinos. M_1 P–T conditions of the Sostis Units (Fig. 13 TLT60, TLT53 and TLX) give typical P–T results of 18.5 ± 0.6 kbar, 498 ± 10 °C (TLT60). TLX similarly predicts peak conditions of 18.6 ± 1.2 kbar and 510 ± 18°C within error of TLT60 result (See Table 3.5). Contrastingly, the Kionnia Unit reached slightly

higher pressure M_1 blueschist-facies conditions of 20–22 kbar, 500–520 °C. TLTN26 garnet cores grew at 17.7 ± 0.8 kbar 487 ± 11°C and rims at 19.7 ± 1.4 kbar and 499 ± 19°C. In contrast, eclogite facies samples TLTN24 and TLTN33 yield elevated P–T conditions with TLTN33 garnet cores giving 19.1 ± 1.1 kbar and 493 ± 14 °C ,and garnet rims suggesting 22 ± 2 kbar and 526 ± 26 °C using the set of independent reactions. Whereas TLTN24 yields similar P–T conditions of 18.5 ± 0.8 kbar and 501 ± 16°C for garnet core growth and 19.0 ± 1.0 kbar and 509 ± 20°C for garnet rims.

These result overlap to some degree with the large uncertainties associated with the Grt–Cpx–Phg barometer and Grt–Cpx thermometer on eclogite facies samples, except that Av-PT systematically predicts slightly lower temperatures and pressures owing to inclusion of epidote. Despite this, the data still show that all rocks within the Lower Unit on Tinos experienced high-pressure, although the Kionnia Unit did reach slightly higher pressures (ca. 22 kbar) during M_1 in agreement with Grt-Cpx-Phg thermobarometery.

3.5.1.2 Retrograde M_2 Conditions

Estimates of retrograde conditions were achieved by equilibria involving exclusively lower pressure M_2 assemblages using where possible the Av-PT function in THERMOCALC. Although no symplectites occur in Tinos eclogites and blueschists, presumably as they are too low temperature (D. J. Waters pers comms, 2017), many of the large amphibole laths in eclogite sample TLTN33 exhibit thin magnesio-hornblende rims in contact with retrograde matrix albite, pyroxene and titanite and rutile. Thin coronas associated with garnet breakdown also contain fine plagioclase, green amphibole, epidote, are in contact with pyroxene which cross-cut the S_{2b} matrix fabric, and were also used by this method. M_2 retrograde pressures were also determined using average pressure calculations in Av-PT using the coexisting activities of amphibole, plagioclase, pyroxene, titanite, epidote and H_2O. Temperatures were derived independently using the amphibole–plagioclase thermometer of Holland and Blundy (1994), and is advantageous as it is not reliant on fluid composition or activity and only considers

anhydrous phases using the following reactions:

$$edenite + 4quartz \rightarrow tremolite + albite \tag{3.1}$$

$$edenite + albite \rightarrow richerite + anorthite \tag{3.2}$$

Although Holland and Blundy (1994) calibrations allow for portioning of Ca onto the M_1 and M3 sites in amphibole structure, in some scenarios this can result in negative cummingtonite when calculating end-member proportions (D.J. Waters pers comms, 2014). This is because the IMA stoichiometric criterion requires <13 cations (excluding K+Na+Ca) and therefore restricts Ca to the M4 site (e.g. Leake et al., 1997), whereas a limit of 12.9 is utilized by Holland and Blundy (1994), allowing Ca on the M_1 or M3 sites. To prevent this problem, formula recalculation was performed using spreadsheet HBPL94 (D.J. Waters pers comms, 2014) which prevents Ca underflow onto the M_1 or M3 sites and the cation total is reset to 13.

Because these reactions exhibit very small dT/dP 2–4°C/kbar, pressure does not control the result significantly. Thus, a reference pressure of 13 kbar was chosen for final calculations based on Av-PT derived average pressure results (see below), yielding temperatures ranging between 485–560°C (Ca underflow) and 485–570°C (no Ca underflow). Pressures for amphibole rim growth were determined using five independent barometers within THERMOCALC and include:

$$jd + q \rightarrow ab \tag{3.3}$$

$$tr + 3sph \rightarrow 5di + q + H_2O + 3ru \tag{3.4}$$

$$di + parg + 4ab \rightarrow 5jd + tr + an \tag{3.5}$$

$$5hed + 2parg + 6ab \rightarrow 5di + 8jd + fact + ts \tag{3.6}$$

$$hed + parg + 4ab \rightarrow 4di + 5jd + fact + an \tag{3.7}$$

Pressures obtained by reactions 3.3–3.5 give overlapping results of 11.9–14.6 kbar between 500 and 600°C, however reaction 3.7 consistently predict higher pressures by two kilobars (15–16 kbar), whereas reaction 3.4 gives lower pressure by two kilobars (10.9–12.1 kbar) over the same temperature interval. However, treating all reactions together and finding their statistical average, yields pressures between 12.6 and 13.7 kbar (± 0.8 kbar) between 500 and 600°C . Results were combined with previously calculated temperatures to produce a P–T array for amphibole rim growth between 520 and 570°C and 12.6–13.7 kbar. THERMOCALC Average P–T mode was also carried out for sample TLT53 using M_2 phases Grt + Ep + Chl + Ttn + Ms + Plag + H_2O + CO_2, and an XH_2O of 0.9 (minor matrix carbonate present) and yielded a P–T result of 7.3 ± 0.7 kbar and 536 ± 16°C. These conditions are also consistent with the Ti in Bt thermometer (Henry et al., 2005) on adjacent sample TLT59 which yields temperatures between 480–560°C, and implies that the Sostis Unit decompressed whilst remaining at high temperature through the lower amphibolite facies field during M_2. Despite these well-behaved P–T estimates for M_1 and M_2 on Tinos, the nature of the prograde and retrograde path leading up-to and during peak M_1 conditions is poorly constrained using this method. This is because conventional therombarometry is largely ineffective at constraining peak P–T conditions in high-pressure rocks (e.g. Stipsaka and Powell, 2005), owing to large uncertainties concerning the calculation of Fe^{3+} in garnet and pyroxene. This is due to an assumption that all iron in omphacite is Fe^{2+}, which biases estimates up temperature, and generally has large associated uncertainties (typically, > ± 50°C and ± 1 kbar at 1 S.D.; Powell and Holland, 2008; Palin et al., 2016). It is also possible that phase compositions used in thermobaromertry are not representative of peak conditions. Hence, phase diagram modelling (pseudosection

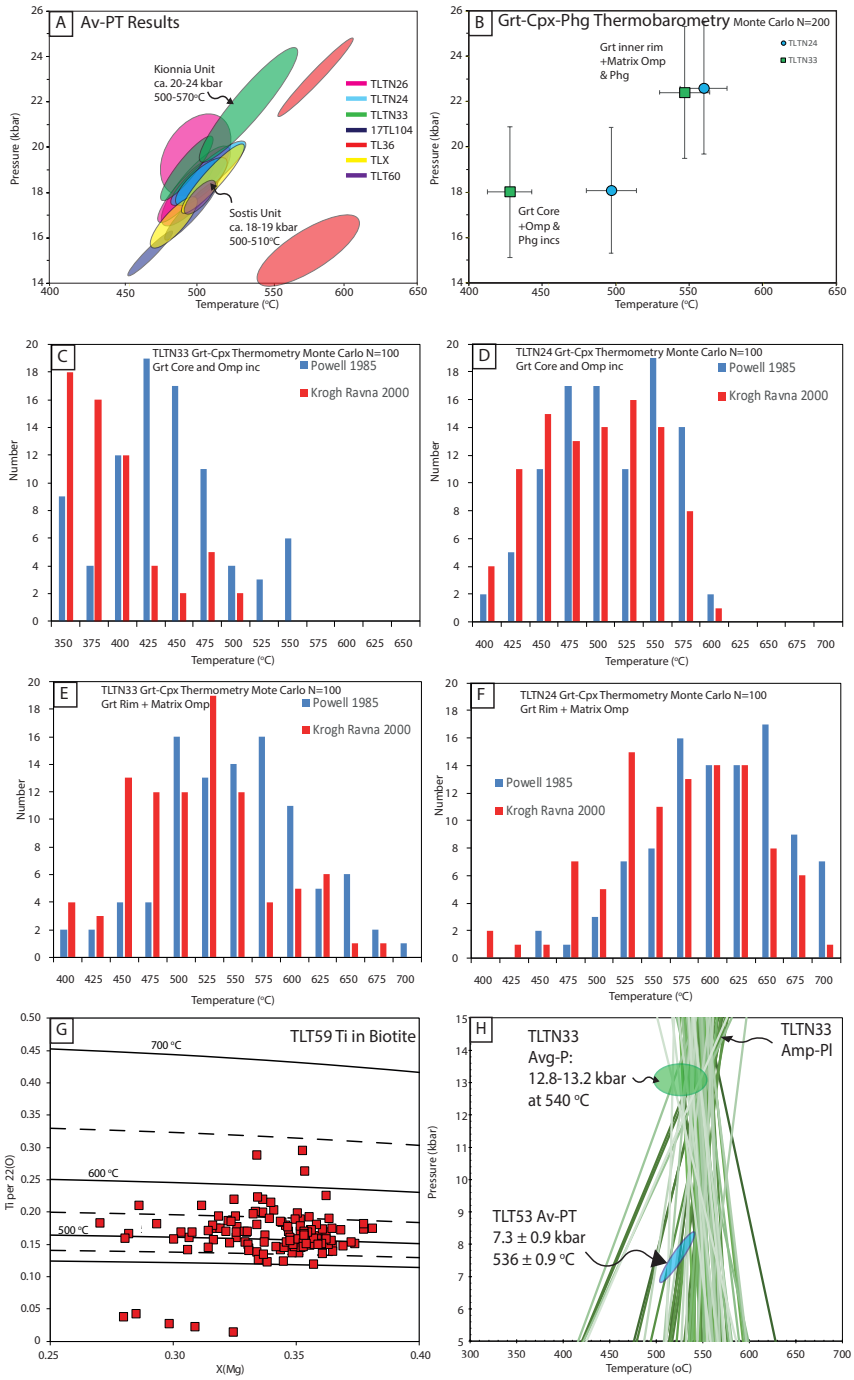


Figure 3.13: Summary results of conventional thermobarometry: A) THERMOCALC mode 2 Av-PT results of all key samples. A range of pressures are calculated from 18-24 kbar, over a temperature range of 480-560°C eclogites of the Kionnia Unit (TLTN24 and TLTN33) yield the highest pressures and temperatures and blueschists of the Sostis Unit the lowest P-T conditions, B) Grt-Cpx-Phg thermobarometry results for samples TLTN33 and TLTN24 peak Grt rims plotting at ca. 22.5 kbar, 550 °C, see text for further discussion. C-D) Grt-Cpx thermometry (Krogh Ravna , 2000 and Powell, 1985) temperature distributions for samples TLTN24 and TLTN33 Grt cores showing variable lower temperature conditions due to large uncertainty calculating Fe^{3+} in low temperature Cpx. E-F) Grt-Cpx thermotery for Grt rims giving fairly consistent results but with a wide temperature distribution. G) TLT59, Ti in Biotite thermometry of Henry et al., (2005) giving retrograde temperatures in the Sostis Unit as high as 570°C, H) Hb-Pl for TLTN33 coshowing the reaction lines associated with indivual amphibole compositions for the Ed-Tr and Ed-Ri thermometers, overlaid with pressure estimate from THERMOCALC and TLT53 retrograde M_2 P-T estimate

construction) was employed herein as the major tool to harness prograde, peak and retrograde P–T information.

3.5.2 Equilibrium Phase Diagram Modelling

Equilibrium phase diagrams (pseudosections) were constructed over a wide range of pressure, temperature, bulk rock H_2O content and redox conditions, using THERMOCALC version 3.40i and internally consistent thermodynamic dataset ds-62 (Powell and Holland, 1988; Holland and Powell, 2011; White et al., 2014a, 2014b). Due to reasonably high spessartine contents in garnets and low temperature assemblages, modelling of metasediments and mafic rocks was performed in the MnO–Na_2O–CaO–K_2O–FeO–MgO–Al_2O_3–SiO_2–H_2O–TiO_2–O (MnNCKFMASHTO) system using the following activity–composition relations: White et al., (2014a), White et al., (2014b) and use of the omphacitic clinopyroxene and amphibole activity–composition relations of Green et al., (2016) modified to swtch off the Ti and K end mebers due to their negligible effect at low temperatures. The pure phases andalusite, kyanite, sillimanite, rutile, quartz, and H_2O were considered in all cases. Although it is acknowledged the lack of Mn-bearing activity models of other eclogite and blueschist bearing phases (amphibole, clinopyroxene white mica) prevents examination of partitioning between these phases (St-Onge et al., 2013). MnO was included in all cases due to moderate concentrations within garnet, particularly in their cores. Inclusion of MnO is thus crucial for accurate prediction of garnet stability, especially at low temperatures during garnet nucleation, although it is acknowledged that there will be a limited portioning of Mn between the other high-pressure low temperature phases. All samples were modelled with excess H_2O due to them containing hydrous phases including lawsonite at peak M_1 conditions.

Detailed investigation into the prograde evolution and P–T conditions leading up to peak metamorphism was achieved by investigation of compositional isopleths for pyrope and grossular content in garnet. As these isopleths vary to first order with changes in pressure and temperature and commonly intersect at high angles, they provide unique intersection points for tracking garnet composition evolution in P–T

Sample Description					THERMOCALC Average P-T							Grt-Cpx-Phg Waters and Martin. (1993)	Barometry	Grt Cpx Thermometery						Hbl-Pl Holland and Blundy. (1994)	Thermometry	Ti in Bt Thermometry Henry et al. (2005)	
Unit	Sample	Rock-type	location	End members included	X(H2O)	Temp (°C)	S.D. (°C)	Pressure (kbar)	S.D. (kbar)	corr	fit	no. reactions	Pressure (kbar)	S.D. (kbar)	Powell. (1985) Temp (°C)	S.D. (°C)	Krogh Ravna. (2000) Temp (°C)	S.D. (°C)	Eld-Tr Temp (°C)	Eld-Ri Temp (°C)	Temp (°C)	S.D. (°C)
Kiomnia Unit	TLTN26	Mafic Blueschist	Grt rim	py-gr-ahn-gl-fgl-mu-cel-fcel-clin-daph-ames-law-q-H2O	1.00	499	19	19.7	1.4	0.382	1.67	6	-	-	-	-	-	-	-	-	-	-
			Grt Core	py-gr-ahn-gl-fgl-mu-cel-fcel-daph-law-q-H2O	1.00	492	16	19.3	1.3	0.607	1.21	4	-	-	-	-	-	-	-	-	-	-
			Grt Core	py-gr-ahn-cz-fgl-mu-cel-fcel-pa-daph-law-ru-sph-ta-q-H2O	1.00	487	11	17.7	0.8	0.908	0.89	7	-	-	-	-	-	-	-	-	-	-
	TLTN33	Mafic Eclogite	Grt Core	py-gr-ahn-di-hed-jd-gl-fgl-mu-cel-fcel-pa-law-q-	1.00	493	14	19.1	1.1	0.893	1.16	5	18.012	2.884	428	15	400	112	-	-	-	-
			Grt RimA	py-gr-ahn-di-gl-cz-gl-H2O	1.00	536	26	22.0	2.0	0.919	1.39	4	22.4	2.918	547	17	500	86	-	-	-	-
			Grt RimB	py-gr-ahn-di-hed-jd-acm-cz-gl-fgl-fcel-law-ru-sph-q-cc-H2O-CO2	0.99	557	34	21.9	3.4	0.969	3.04	9								-	-	-	-
			Retrograde Matrix	di-hed-jd-fact-ts-parg-an-ab-sph-ru-H2O	1.00	540	20	13.0	0.4	-	0.92	5	-	-	-	-	-	-	-	517-588 (546 ± 12)	485-645 (589 ± 27)	-	-
	TLTN24	Mafic Eclogite	Grt Rim	py-gr-ahn-di-hed-jd-mu-cel-fcel-pa-law-q-H2O	1.00	509	20	19.0	1.0	0.866	0.93	5	22.582	2.912	560	16	574	65	-	-	-	-
			Grt Core	py-gr-ahn-di-hed-jd-gl-fgl-mu-cel-fcel-pa-law-q-H2O	1.00	501	16	18.5	0.8	0.840	1.01	7	18.077	2.772	497	17	467	67	-	-	-	-
			Retrograde Matrix	-	-	-	-	-	-	-	-	-	-	-	-	-	-	-	323-579 (446 ± 69)	423-500 (460 ± 69)	-	-
	TL36	Retrogressed Eclogite	Grt Rim	py-ahn-tr-fact-ts-mu-cel-fcel-cz-law-q-H2O	1.00	583	21	23.1	1.4	0.977	0.87	5	-	-	-	-	-	-	-	-	-	-
			Retrograde Matrix	an-ab-mu-cel-fcel-pa-amp-tr-fact-ts-parg-clin-daph-q-sph-ru-H2O	1.00	576	28	15.4	1.3	0.773	1.46	8	-	-	-	-	-	-	-	-	-	-	-
Pygros Unit	17TL104	Mafic Blueschist	Grt Core	py-ahn-cz-ep-mu-cel-clin-gl-fgl-rieb-law-ru-q-sph-H2O	1.00	468	12	15.3	0.8	0.953	0.34	5	-	-	-	-	-	-	-	-	-	-
			Grt Rim	py-gr-ahn-cz-ep-mu-cel-clin-daph-gl-fgl-rieb-law-ru-sph-q-H2O	1.00	496	15	17.2	1.1	0.931	1.49	7	-	-	-	-	-	-	-	-	-	-	-
	17TL48	Retrogressed Blueschist	Matrix	daph-ames-mu-cel-fcel-cz-law-ru-q-sph-H2O	1.00	488	29	17.0	1.9	0.908	1.88	3	-	-	-	-	-	-	-	-	-	-
Sestis Unit	TLX	Peltic Blueschist	Grt Core	py-gr-ahn-gl-fgl-mu-cel-fcel-cz-clin-daph-ames-q-ru-sph-law-H2O	1.00	493	20	17.3	1.4	0.914	2.2	8	-	-	-	-	-	-	-	-	-	-
			Grt rim	py-gr-ahn-gl-fgl-mu-cel-fcel-cz-clin-daph-q-law-H2O	1.00	510	18	18.6	1.2	0.918	1.69	6	-	-	-	-	-	-	-	-	-	-
	TLT53	Retrogressed schist	Grt Rim + Matrix	py-gr-ahn-cz-mu-cel-clin-daph-law-sph-ru-q-cc-H2O-CO2	0.90	536	14	7.5	0.6	0.959	0.99	5	-	-	-	-	-	-	-	-	-	-
	TLT60	Retrogressed Blueschist	Grt Rim+ Matrix	py-gr-ahn-cz-mu-cel-clin-daph-law-sph-ru-q-H2O	1.00	502	10	18.2	0.7	0.920	1.01	5	-	-	-	-	-	-	-	-	-	-
	TLT59	Retrogressed mite	Bt	-	-	-	-	-	-	-	-	-	-	-	-	-	-	-	-	-	408-617	13-26

Table 3.5: Thermobaroetry results of Tinos HP rocks

space with low levels of uncertainty. Isopleths of amphibole were used to constrain the retrograde P–T evolution, as decreasing pressure and temperature results in garnet breakdown. The intersections of isopleths representing measured compositions are represented by shaded boxes indicating uncertainties at the 1 S.D. level calculated by THERMOCALC. Retrograde M_2 greenschist-facies conditions were further determined by modal proportions of characteristic minerals and amphibole and plagioclase thermobarometry that form coronas around some garnets and rims on coarse blue amphibole representing breakdown products of garnet and omphacite during decompression.

The effective bulk composition used to construct all equilibrium phase diagrams are presented in Appendix 1 and on the diagrams themselves. The bulk compositions of samples TLTN26, TLTN33, TLX, TLT60 and 17TL104 where calculated from point counted volume estimates combined with average chemical analysis of the minerals. Zoning within minerals was accounted for by spherical averaging techniques. The composition of sample TLTN24 was accounted for by whole-rock XRF analysis, following the method of Weller et al. (2015). XRF was the preferred choice for sample TLTN24 as it accounts for larger equilibration volumes, and removes uncertainty from point counting the finely recrystallized matrix.

The hydration and redox state during peak M_1 conditions and exhumation was investigated for all Kionnia Unit samples. This was achieved treating H_2O and oxygen as extensive variables. The H_2O content of the bulk rock is designated M(H_2O) to avoid confusion with X(H_2O) used to describe fluid composition. Values for M range from 0 (anhydrous assemblage) to 1 (the molar H_2O content required to make peak lawsonite bearing conditions hydrous) (Palin et al, 2014). In THERMOCALC, the oxygen content appears in the bulk composition as the proportion of O, with Fe represented as total iron as FeO allowing the actual FeO and Fe_2O_3 to be calculated. Oxygen content, M(O), extends from completely reduced (zero O), to M(O) = 1, corresponding to a value were all Fe occurs as Fe_2O_3 (equal to total iron as FeO divided by 2) (Rebay et al., 2010).

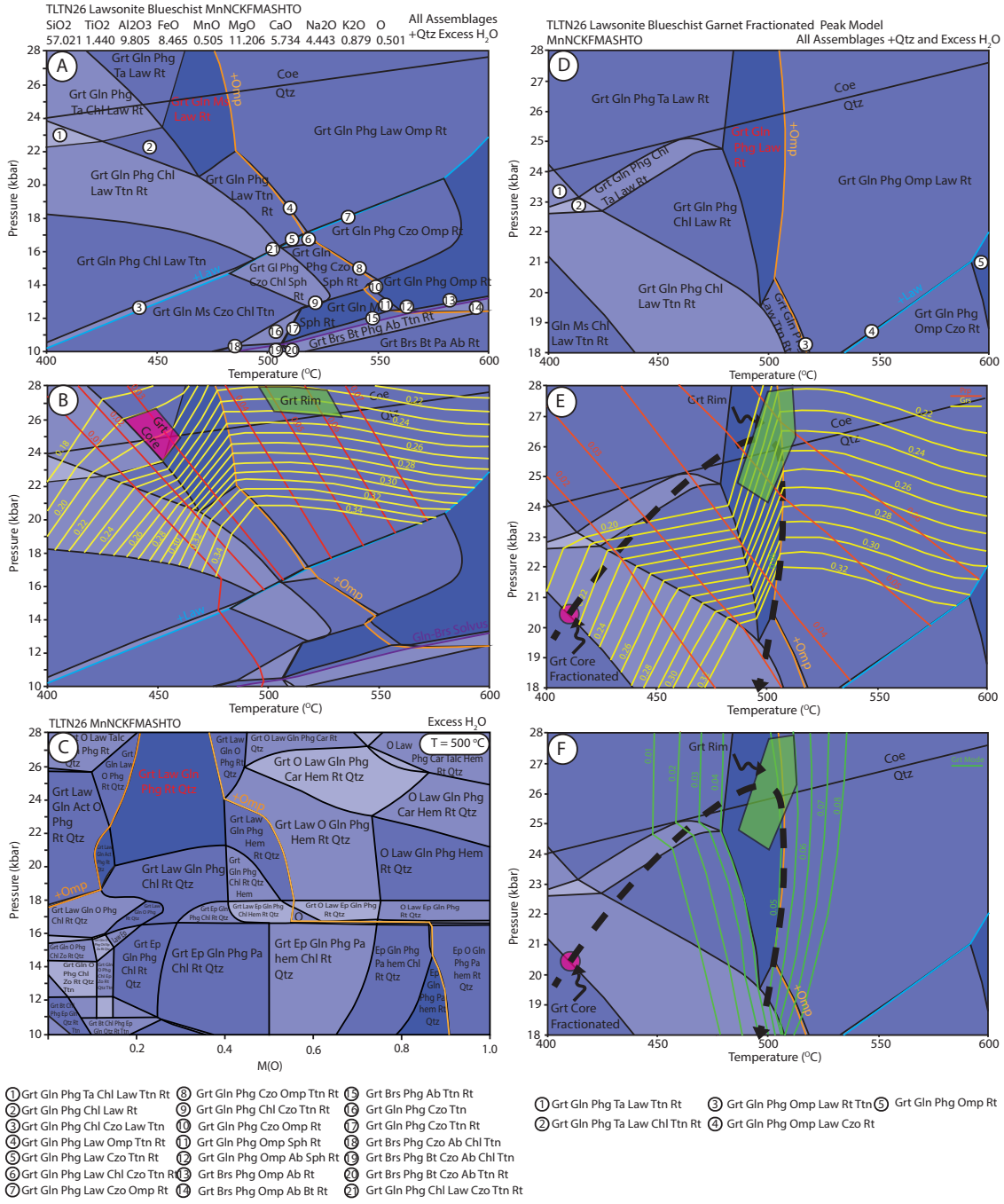


Figure 3.14: Equilibrium phase diagrams for TLTN26 A) topology showing the major reactions (Law in; omp in; kyanite in and rutile and titanite, B) overalid isopleths for grossular (grs) and prypope (prp) and garnet modal proportions. C) M(O) pseudosection to investigate theoxidation state on the assemblage field, red text indicates the obseved field. D) Fractionated out garnet core at a hypothetical point on its predicted prograde path (20 kbar 420°C, E) Overlaid pyrope and grossular isopleths for the fractioned garnet model which intersect in the observed assemblage field F) Garnet modes, which are mainly temperature sentisive.

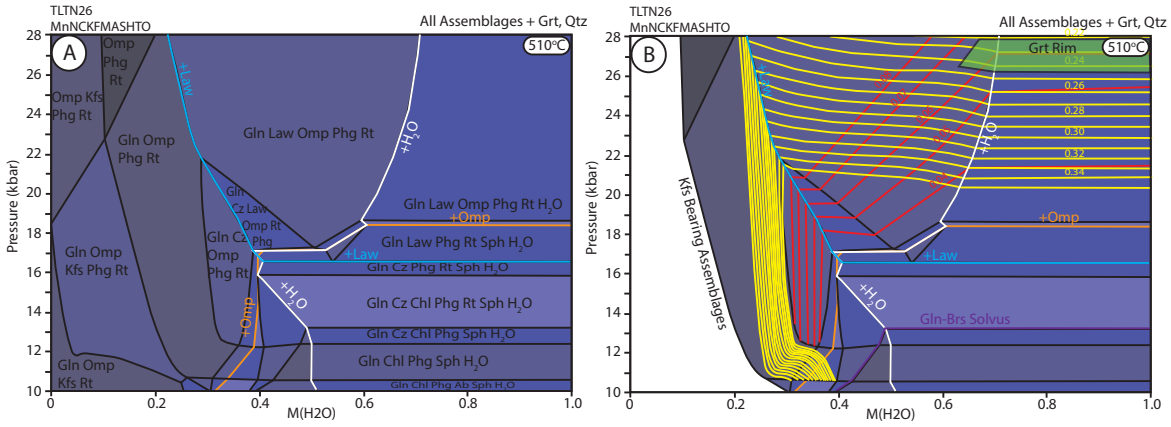
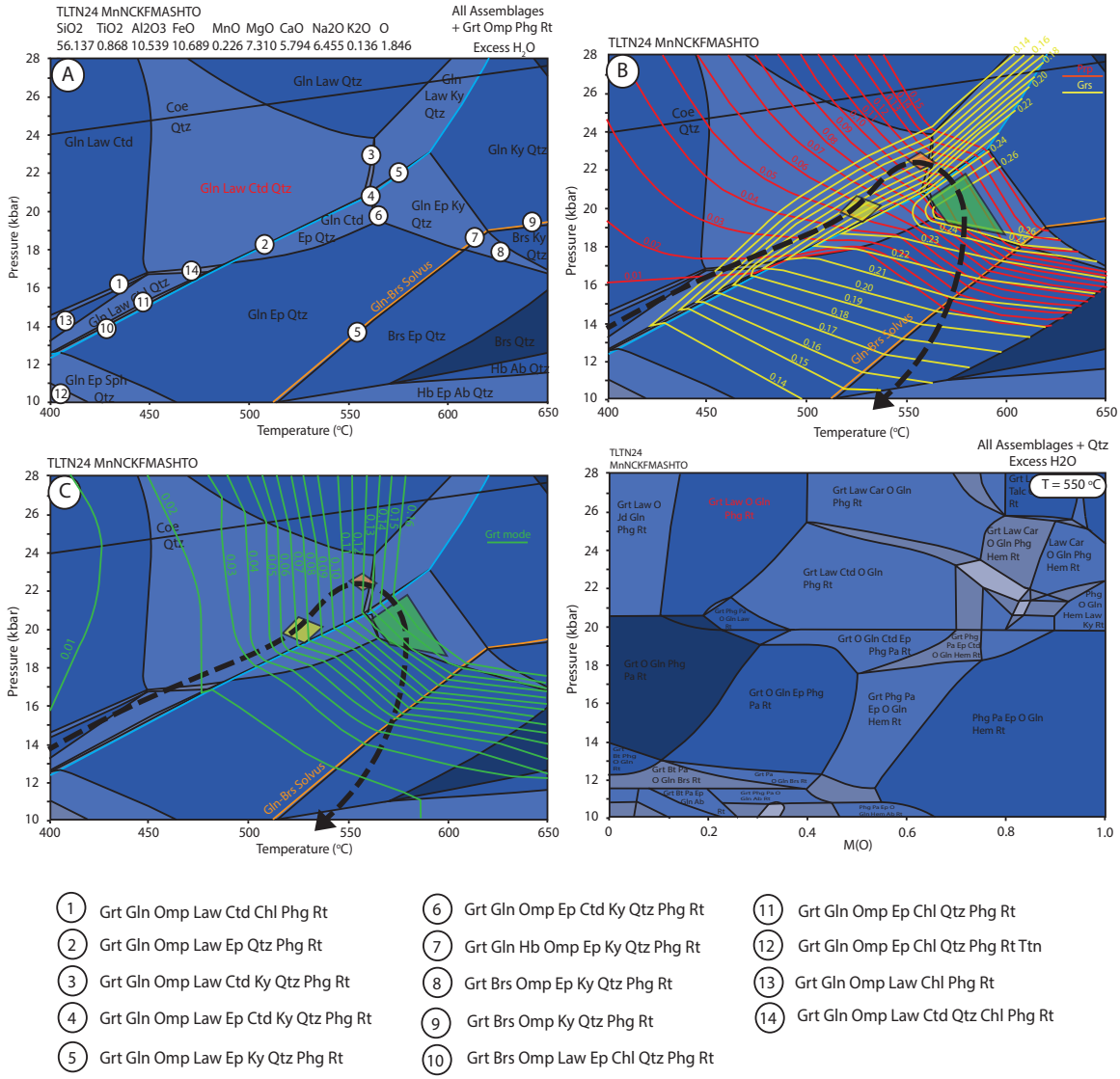


Figure 3.15: An M(H_2O) pseudosection for TLTN26 showing that the peak assemblage ould only occur under the presence of abundant H_2O

3.5.2.1 TLTN26: Garnet, Glaucophane, Lawsonite Blueschist (Kionnia Unit)

A calculated P–T equilibrium phase diagram reveals that the observed assemblage Grt + Gln + Law + Phg + Rt + Qtz (red text) is stable over a relatively narrow field at 20–24 kbar and 490–500°C. Across the peak field, the amphibole Na_B content ranges between 1.90 and 1.96 pfu, in good agreement with measured compositions (Fig. 3.14). Consideration of garnet core (4–5% pyrope, 20–22% grossular) and rim chemistry (6–7% pyrope, 22–24% grossular; Fig. 3.14b) provides further constraints on the prograde evolution of the sample (pink shading, Fig.), and suggests peak P–T conditions of 24–27 kbar and 520–540°C (pink polygon) but plotting inside the omphacite stability phase field, in disagreement with lack of observed omphacite. Due to the predicted presence of omphacite in the peak assemblage, a one-step garnet fractionation was carried out, with fractionation of garnet applied along the proposed P–T path on Fig. 3.14 at 20 kbar and 450°C. The same trends are observed on the resultant fractionated equilibrium phase diagram (Fig. 14d-f), with H_2O-saturated topologies, however the omphacite producing reaction is shifted to higher temperatures by this procedure. Pyrope and grossular isopleths also shift to lower temperatures and intersect at 22–26 kbar at 500–510°C in the Grt + Gln + Law + Phg + Rt + Qtz phase field (red text), in good agreement with observations.



1. Grt Gln Omp Law Ctd Chl Phg Rt
2. Grt Gln Omp Law Ep Qtz Phg Rt
3. Grt Gln Omp Law Ctd Ky Qtz Phg Rt
4. Grt Gln Omp Law Ep Ctd Ky Qtz Phg Rt
5. Grt Gln Omp Law Ep Ky Qtz Phg Rt
6. Grt Gln Omp Ep Ctd Ky Qtz Phg Rt
7. Grt Gln Hb Omp Ep Ky Qtz Phg Rt
8. Grt Brs Omp Ep Ky Qtz Phg Rt
9. Grt Brs Omp Ky Qtz Phg Rt
10. Grt Brs Omp Law Ep Chl Qtz Phg Rt
11. Grt Gln Omp Ep Chl Qtz Phg Rt
12. Grt Gln Omp Ep Chl Qtz Phg Rt Ttn
13. Grt Gln Omp Law Chl Phg Rt
14. Grt Gln Omp Law Ctd Qtz Chl Phg Rt

Figure 3.16: TLTN24 pseudosections using the XRF derived bulk comosition showing A) phase relations and the position of the lawsonite and Brs-Gln solvus, B) isopleths of grossulat and pyrope that match obseved compositions at ca. 22kbar and 560 °C C) Garnet modes, which steadily increase up temperature and D) A P-M(O) pseudosection to evaluate the oxidation state at high-pressures, the red text highlights the observed field.

3.5.2.2 TLTN24: Garnet, Augerine, Glaucophane, Paragonite Eclogite (Kionnia Unit)

The calculated P–T equilibrium phase diagram for TLTN24 reveals that the observed assemblage Grt + Law + Gln + Omp + Phg + Rt + Qtz is stable at >21 kbar, with temperatures between 510–560°C. The calculated assemblage does however predict 1%

chloritoid, which is not observed. However, owing to the very low abundance, it can be volumetrically ignored and could possibly be related to too much aluminum in the modelled bulk composition. The measured range in matrix amphibole ($Na_B = 0.84$–0.99 pfu, Fig. 3.10) constrains this field further, indicating that the peak assemblage is stable at 540–560°C (green shading), with minor chloritoid predicted. Consideration of garnet core (5–6% pyrope, 26–28% grossular) and rim chemistry (11–12% pyrope, 22–24% grossular) further constrains the prograde evolution of the sample (red shading, Fig. 3.16), and indicates that garnet cores grew already at high pressure at 19 kbar, 510°C, whereas peak P–T conditions of 22 kbar and 540–560°C (green polygon) are calculated from garnet rims. Following the methodology above, fractionation of 50% of the garnet does not affect the peak estimate (Fig. 3.16). The various constraints imply a gentle prograde P–T path (dotted black line, Fig. 3.16), which is also compatible with the composition of amphibole observed as inclusions in garnet (Fig. 3.16). The only phase that does not show a reasonable model fit is phengite, with the calculated Si range of pfu in the peak assemblage field everywhere less than the measured value of 3.50-3.52 pfu.

3.5.2.3 TLTN33: Garnet, Augerine, Galucophane, Epidote, Phengite Eclogite (Kionnia Unit)

A P–T equilibrium phase diagram for TLTN33 reveals that the observed assemblage Grt + Gln + Omp + Law/Ep + Rt (red text) is stable over a relatively large field, from 18 to 28 kbar, and 480 to 600°C, with this upper temperature boundary representing the appearance of kyanite. At 20 kbar, lawsonite (blue line) is predicted to replace epidote in the assemblage, and at higher temperatures, glaucophane is lost from the assemblage and is replaced by kyanite. Contours of Na_B (dashed purple lines) reveal that glaucophane becomes less sodic with decreasing pressure until the glaucophane–barroisite solvus extension is met, across which Na_B rapidly decreases from 1.60 to 1.10 pfu. Two areas are highlighted by shading on Fig. 3.17, which correspond to the range in Na_B of the glaucophane cores and barroisite–magnesiohornblende rims with

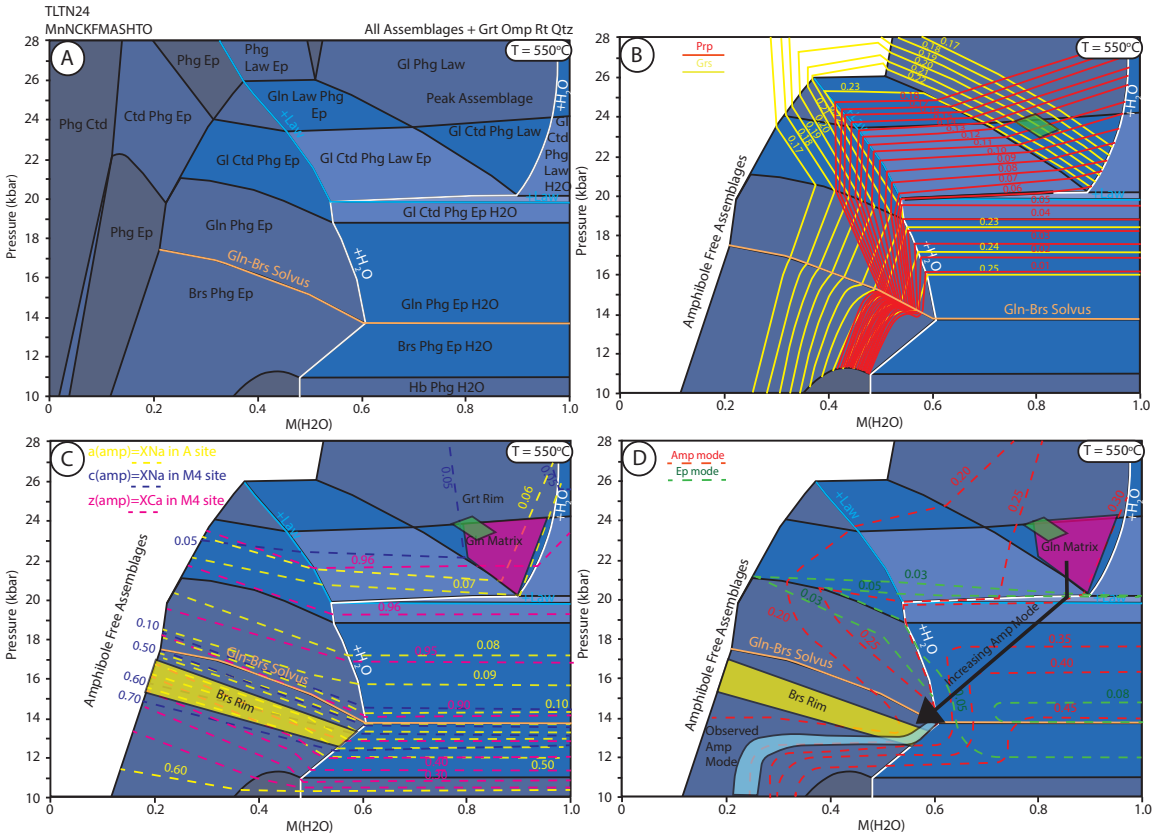


Figure 3.17: TLTN24 M(H_2O) pseudosections showing A) Phase relatins with varing H_2O, B) Garnet isopleths, which only intersect under hydrous conditions, C) amphibole isopleths for a(amp), c(amp) and z(amp) D) Epidote and amphibole modes

the former only present at high-pressure within the peak field or within the epidote stability region. With these constraints, the composition zoning in large amphibole matrix laths must be retrogressive in origin. Further constraints on the prograde evolution of the sample are provided by consideration of the garnet pyrope and grossular content, which vary from 6–7% pyrope and 28–32% grossular in the garnet core, whereas garnet rims contain 12–13% pyrope and 25–27% grossular (Fig. 3.18). The coloured shaded regions on Fig. 3.18 correspond to where these constraints are met with cores growing at 22–23 kbar 540–550°C, whereas rims correspond to 24 kbar 570–575°C in the observed peak field. All phases show a good model fit with the exception of white mica. In this case, the model does not recreate paragonite found within the matrix and instead paragonite is not predicted until much lower pressures (>13 kbar).

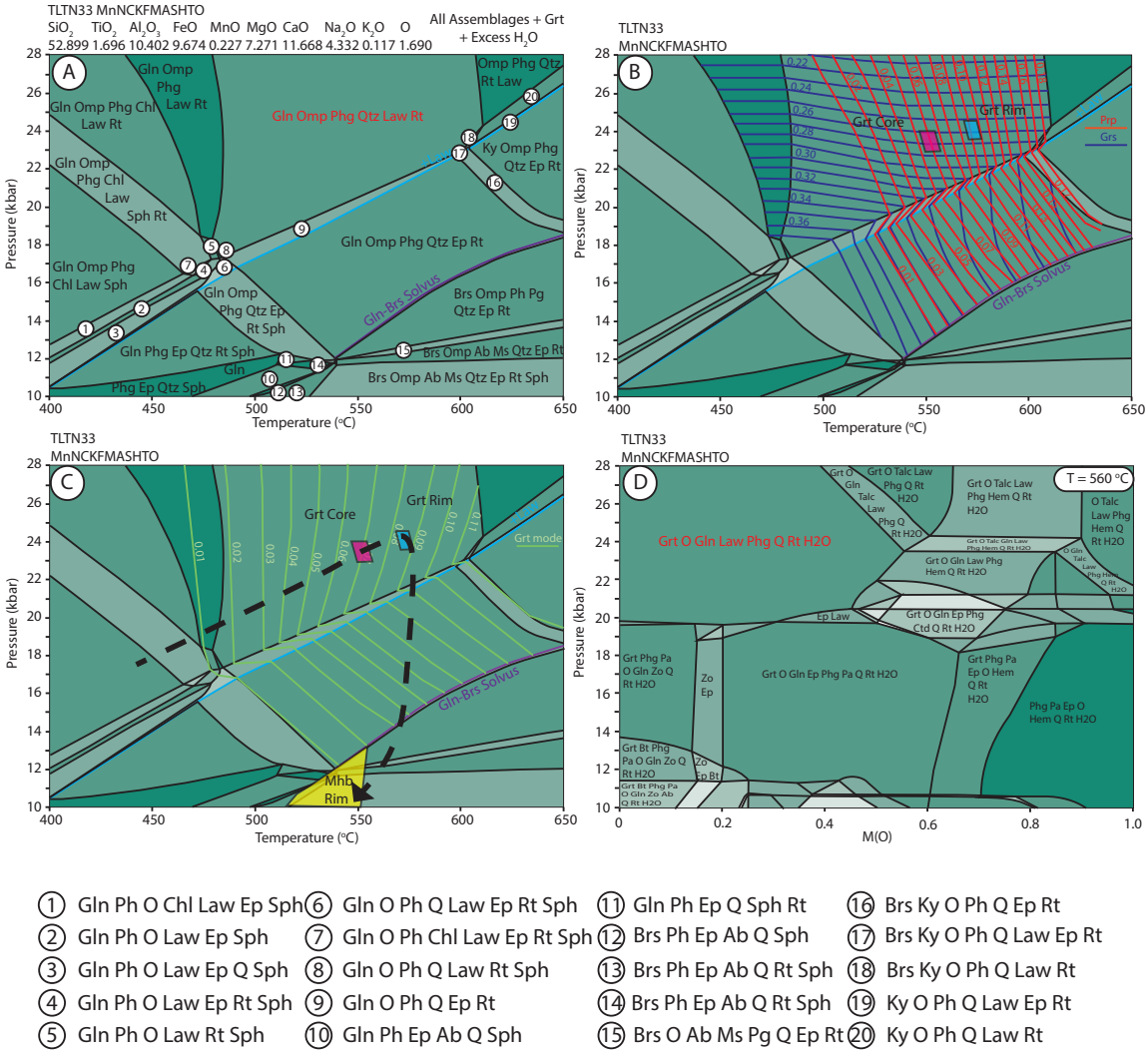


Figure 3.18: Equilbrium phase diagram TLTN33, A) showing the major phase reltions, B) Pyrope and grossular isopleths showing garnet core and rim intersections, C) Garnet modes, increasing up temperature and pressure, D) P-M(O) phase diagram to investigate the role of oxidation state on the phase relations.

3.5.2.4 17TL104: Garnet, Glaucophane, Lawsonite, Phengite Schist (Pygros Unit)

An equilibrium phase diagram for 17TL104 reveals that the peak assemblage Grt + Gln + Law + Phg + Rt + Qtz (red text) is stable over a relatively narrow field at 20–28 kbar and 470–510°C. Across the peak field, the amphibole Na_B content ranges between 1.85 and 1.96 pfu, consistent with measured compositions (Fig. 3.10). Garnet core (4% pyrope, 20–22% grossular) and rim chemistry (6–7% pyrope, 30–32%

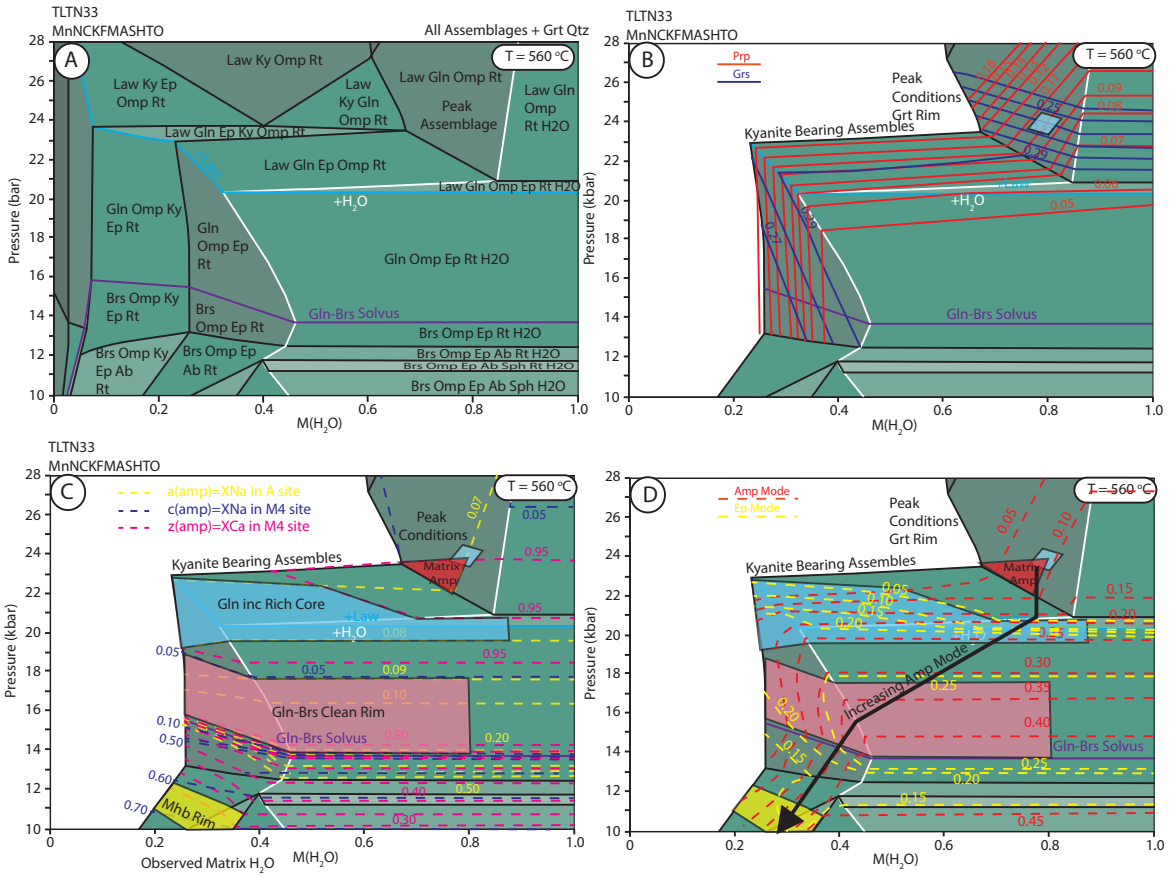


Figure 3.19: TLTN33 calculated M(H_2O) pseudosections showing A)Phase relations with water saturation given by the white line, lawsonite in (light blue line) and Gln-Brs solvus (purple), B) Comositional isopleths for pyrope and grossular showing peak conditions only satisfied at high water contents, C) isopleths for a(amp), c(amp) and z(amp) showing the magnesio-hornblende rim is intersected at 12 kbar at <0.4 M(H_2O)

grossular; Fig. 3.20) further constrain the prograde evolution of the sample (pink shading, Fig. 3.20). Intersection of garnet core isopleths indicate garnet nucleation occurred at 27 kbar 490°C in the peak assemblage field. In contrast the grossular rich rims intersect at 22 kbar, 510°C (pink polygon) but just plotting inside the omphacite stability phase field, in disagreement with lack of observed omphacite in the sample, although minimal omphacite is predicted (<0.02 mode). These results imply 17TL104 experienced decompression during garnet growth from ca. 27–22 kbar whilst temperatures increased by only 20°C, and is consistent with an increase in garnet mode from 0.06 to 0.10 between core and rim intersections.

If the *P*–*T* result from the garnet core of ca. 27 kbar is indeed correct, this

indicates that the Pygros Unit experienced conditions of coesite stability. Although, no relict coesite inclusions were observed in garnet cores, which raises ambiguity as to whether ca. 27 kbar was achieved during garnet core growth. A minimum P–T of 22 kbars can be rectified on the basis of the predicted assemblage, lack of titanite inclusions in garnet and glaucophane chemistry as revealed by contours of Na_B (dashed purple lines) between 1.96 and 1.90. This decompression path during garnet growth also suggests S_{2a} and S_{2b} rotational fabrics where associated with the earliest stages of exhumation, thus implying top-to-SW shearing was active during decompression. Further constraints can be placed on the retrograde history associated with growth of matrix epidote, chlorite and titanite. These join the assemblage and coexist together between 470 and 525°C at less than 17 kbar and coexist until ca. 12 kbar when the sample crosses the glaucophane-barroisite solvus and plagioclase becomes stable.

3.5.2.5 TLX: Garnet Glaucophane Clinozoisite Schist (Sostis Unit)

A calculated P–T equilibrium phase diagram (Fig. 3.21a-b) reveals the peak metamorphic assemblage Grt + Gln + Law + Phg + Chl + Rt + Qtz (red text) is stable between 18–26 kbar and 460–540°C. Across the peak field, the amphibole Na_B content ranges between 1.90 and 1.96 pfu, in good agreement with measured compositions (Fig. 3.10). Intersection of garnet core (4% pyrope, 27–29% grossular) and rim (6% pyrope, 27–29% grossular; Fig. 3.21) isopleths provides further constraints on the prograde evolution of the sample (pink shading, Fig. 21), and suggest garnet cores grew at P–T conditions of 21 kbar and 480°C (pink polygon) whereas rims grew at 22 kbar 510–520°C in the same field. This implies TLX underwent a dominantly heating P–T trajectory during garnet growth, consistent with increases in garnet mode. Although garnet rim isopleths also intersect at ca. 12 kbars, the predicted assemblage of garnet, barroisite, chlorite biotite, epidote, rutile and titanite is not consistent with observations of pseudomorphed lawsonites in the garnet cores or Na_B compositions of amphibole. Constraints on the retrograde history can be determined by the lack of biotite in the matrix, implying the rock decompressed through the garnet, glauco-

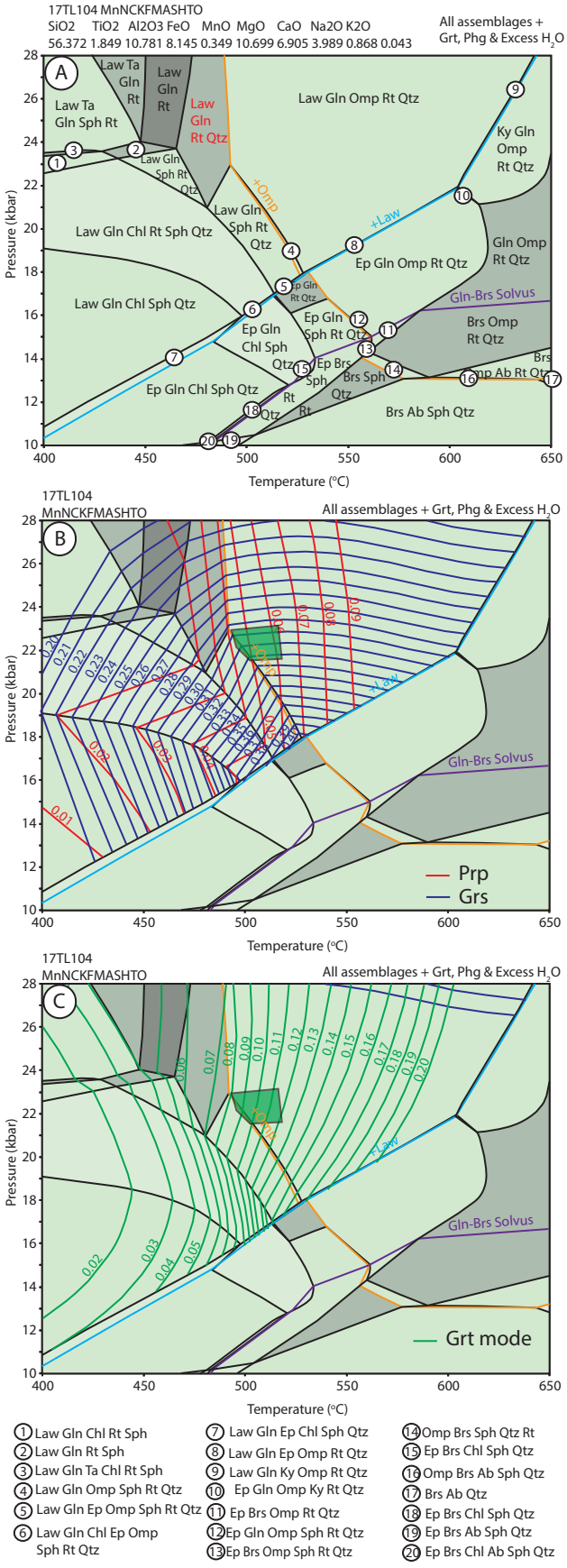


Figure 3.20: Calculated equilibrium phase diagrams for 17TL104 showing A) the phase relations, omphacite in reaction (orange) and observed assemblage in red text, B) garnet pyrope and grosular comositional isopleths, C) garnet modal prortions.

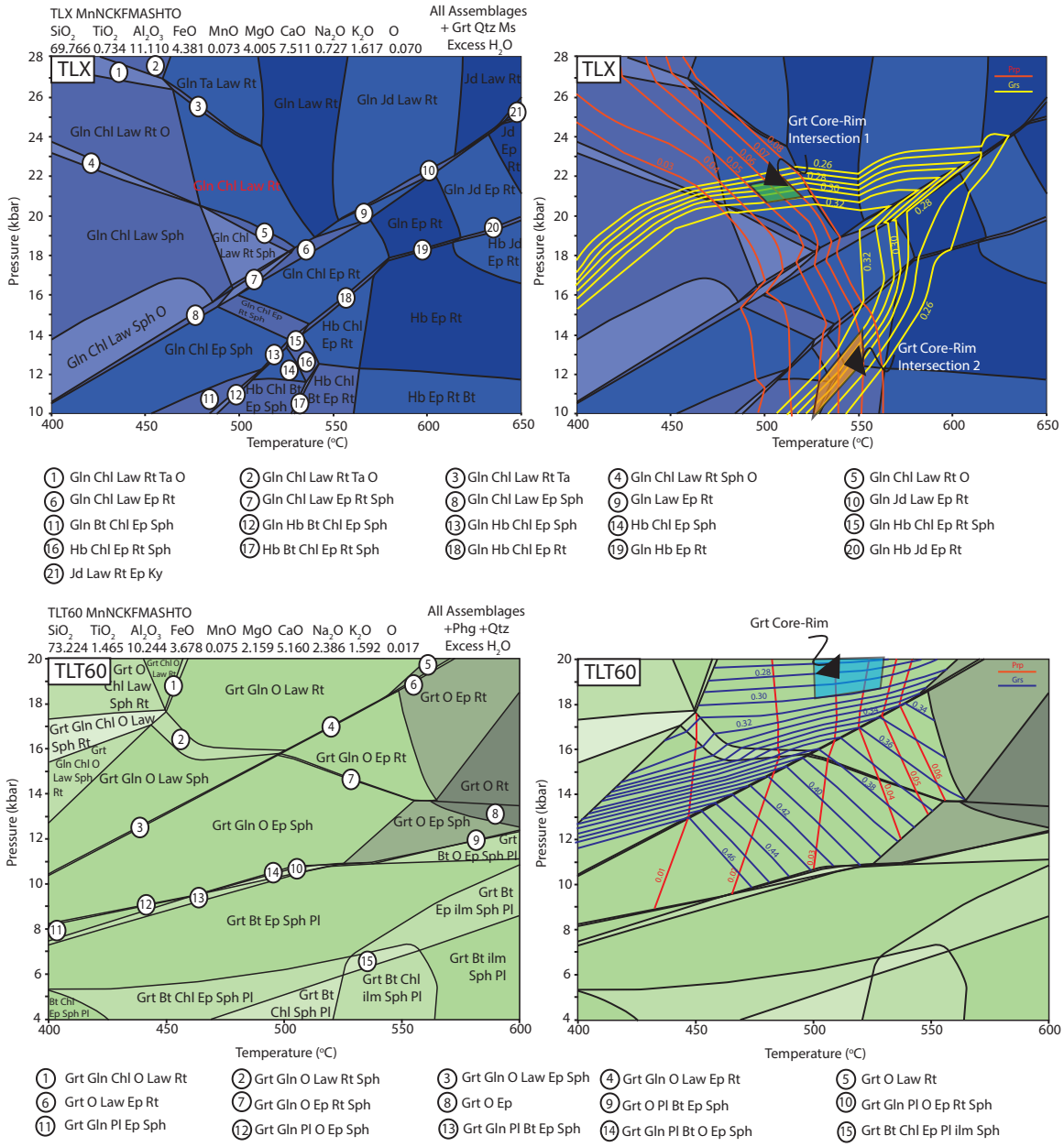


Figure 3.21: Equilbrium phase diagrams of samples TLX and TLT60 from the Sostis Unit, showing the phase relations (left) with isopleths of garnet pyrope and grossular (right) which show unique points of intersection, red text is the observed phase field for TLX)

phane, epidote, chlorite, titanite phase field between 400–510°C and 10–15 kbar, and remained cool during exhumation.

3.5.2.6 TLT60: Garnet Mica Epidote Schist (Sostis Unit)

A pseudosection of TLT60 (Fig. 3.21 c-d), reveals relatively simple phase relations, with large fields without a change in variance. Although the sample is highly retrogressed intersection of un-zoned garnet core and rim isopleths of pyrope (3–4%) and grossular (28–30%) at ca. 18 kbar 510–520°C, reveal peak (M_1) conditions were achieved in the Grt + Gln + Phg + Law + Omp + Rt + Qtz phase field. The presence of lawsonite is consistent with relict pseudomorphed inclusions within garnet cores, further the observed phengite Si pfu of 3.51 is also predicted at this P–T conditions, although no omphacite or glaucophane have survived into the current assemblage. This peak P–T result for M_1 is in good agreement with an Av–PT result of 18.5 ± 0.8 kbar 498 ± 10°C. Upon reaching its peak pressures, the rock decompressed to the M_2 matrix assemblage of Grt + Bt + Pl + Ep + Chl + Ms + Ttn + Qtz, stable between 400–520°C at less than 5.5–6 kbar. The upper bound of this wide M_2 P–T estimate is similar to 7.3 ± 0.9 kbar and 536 ± 19°C calculated for sample TLT53, at a similar structural level to TLT60.

3.5.2.7 M(H_2O) Evolution During Retrogression

The formation of zoned amphibole in mafic eclogites has been suggested to be a direct consequence of fluid addition during exhumation (Massone, 2012) which results in the breakdown of omphacite and garnet through the proposed hydration reaction (Zhang et al., 2003):

$$omphacite + garnet \rightarrow plagioclase + Na\text{-}Ca\ amphibole \pm clinopyroxene \qquad (3.8)$$

Pseudosection analysis, combined with petrological observations suggests that peak M_1 conditions in all samples occurred under lawsonite stability and that the rocks at peak conditions were more hydrated than the current matrix assemblage suggests. This implies that the rocks dehydrated during exhumation and released water into

the surrounding matrix and it may have infiltrated into surrounding rocks. Although the exact fluid loss cannot be quantified without isotopic evidence to trace the bulk rock fluid content, a composition calculated from the observed phases is the most realistic estimate of bulk rock fluid content during exhumation. The range of amphibole compositions is shown in Fig. 3.10 and can also be characterized as common amphibole exchange vectors. Transformation of glaucophane to edenite involves addition of both Na+K to the A site, whereas transformation to tremolite involves subtraction of Na to the B site.

Amphibole exchange vectors used by THERMOCALC activity-composition relationships include x(amp) = Fe/(Fe+Mg), z(amp) = mole fraction of Na in M4 site, a(amp) = Na on the A site, and c(amp) = mole fraction of Ca on M4 site (Diener et al., 2007). Intersection of these isopleths is used to track amphibole growth in P–M(H_2O) space. Within any individual assemblage field across a range of P–M(H_2O) space, the calculated equilibrium composition of the amphibole can vary considerably such as Na on the M4 site. For example an amphibole could be classed as a barroisite at one P–M(H_2O) point, and a magnesiohornblende at another P–M(H_2O) point within the same field, with no change in variance between. A vertical trajectory in P–M(H_2O) space represents exhumation under closed-system conditions with no change in the effective bulk composition, whereas any other trajectory involving a changing M(H_2O) represents the loss or gain of fluid in an open-system environment. The results for each sample are presented separately below.

3.5.2.7.1 TLTN26 Because peak conditions are constrained to no more than 510°C, P–M(H_2O) pseudosections were produced between 0–12% bulk rock molar H_2O using the unfractionated bulk composition (Fig. 3.15). These diagrams reveal that although garnet rim isopleths intersect at ca. 27 kbar in the garnet + omphacite + lawsonite + phengite + glaucophane + rutile + quartz + H_2O phase field, omphacite is in low abundance (<3%) and its stability is strongly dependent on bulk rock water content. This is seen as at low M(H_2O) (<0.40) omphacite is stable at all pressures >12 kbar,

whereas in water saturated fields omphacite is only stable at >19 kbar and the omphacite producing reaction is invariant with both pressure and temperature. Amphibole compositions and modal abundances vary significantly across P–M(H_2O) space with significant amphibole growth shown by increases in amphibole mode following omphacite and lawsonite breakdown at 17.5–19 kbar. THERMOCALC compositional parameters were obtained from prismatic matrix amphiboles which are glaucophane-winchite in composition with parameters as follows: z(amp) = 1.0–0.89 a(amp) = 0–0.04 c(amp) = 0–0.07. These intersect together with amphibole mode of 0.45 at pressures >19 kbar and thus implies water was lost from the rock immediately in order to preserve peak pressure amphiboles, without subsequent resorbtion or overgrowth of barroisite compositions.

3.5.2.7.2 TLTN24 P–M(H_2O) pseudosections were produced between 0–12% at 550°C (Fig. 3.17), to simulate the maximum temperature during M_1. Amphibole composition varies over P–M(H_2O) space, particularly when the rock is under saturated in H_2O whereas elsewhere it is mainly pressure dependent. The proportion of Na in M4 site (parameter z(amp) ranges from 0.25–0.95 between 23 and 13 kbar and M(H_2O) of 0.4 and 1.0. Garnet rim isopleths intersect at 23 kbar at reasonably high M(H_2O)>0.75 in the phengite, lawsonite, garnet, omphacite, glaucophane, rutile and minor chloritoid and quartz field, which is taken as a minimum H_2O content during the initiation of exhumation. At M(H_2O) > 0.45, lawsonite breakdown occurs at ca. 21 kbar invariantly with M(H_2O) in the presence of chloritoid. Across this reaction the assemblage becomes saturated in H_2O and modal proportions of amphibole significantly increase over a very short decrease in pressure, and an amphibole mode of 0.30. Amphibole mode increases steadily with decreasing pressure in H_2O saturated assemblages, whereas in water undersaturated assemblages, amphibole growth is insensitive to pressure, and varies only with increasing M(H_2O). THERMOCALC compositional parameters were obtained from several zoned matrix amphiboles, and are as follows: amphibole cores: z(amp) = 1.0–0.89 a(amp) = 0–0.03 c(amp)= 0.02–0.03, and barroisite rims z(amp)

= 0.29–0.75 a(amp) = 0.05–0.25 c(amp) = 0.08–0.82. These ranges for core and rim compositions are shown in P–M(H_2O) space in Fig. 3.10.

All composition parameters for glaucophane cores intersect at ca. 21 kbar and M(H_2O) > 0.4, whereas barroisite rims intersect over a range of pressures; its most extreme composition plots between 12.5–14 kbar and M(H_2O)>0.35, corresponding to an amphibole mode of 0.30 in the rims. This rock must have remained saturated during decompression in order for amphibole to continue growing (corresponding to increasing amphibole mode), and an observed molar H_2O value of 4% corresponds to M(H_2O) values of 0.33, implying the rock lost at least 60% of its peak H_2O content during its exhumation.

3.5.2.7.3 TLTN33 P–M(H_2O) phase diagrams were produced at 560°C between 0–12% H_2O (Fig. 3.19), interpreted to represent the maximum temperature during M_1. Large variations in calculated amphibole composition occur over P–M(H_2O) space when the rock is under saturated in H_2O; such as the proportion of Na in M4 site (parameter z(amp) ranges from 0.25–0.95 between 23 and 11 kbar and M(H_2O) of 0.4 and 1.0. The inferred peak assemblage of phengite, lawsonite, garnet, omphacite, glaucophane, rutile and minor quartz occurs at 23 kbar and a M(H_2O) >0.7 which is taken as a minimum H_2O content during the initiation of exhumation. Upon lawsonite breakdown at ca. 21 kbar, modal proportions of amphibole significantly increase over a very short decrease in pressure, and an amphibole mode of 0.35 in the presence of H_2O is predicted immediately upon crossing this reaction, although amphibole mode increases steadily with decreasing pressure in H_2O saturated assemblages, whereas elsewhere amphibole growth is insensitive to pressure, and varies with only with increasing M(H_2O). To interpret these pseudosections, THERMOCALC compositional parameters were obtained from several large zoned matrix amphibole laths, and measured compositions are as follows: glaucophane cores: z(amp) = 0.97–0.94 a(amp) = 0–0.04 c(amp)= 0.02–0.04 , and barroisite rims z(amp) = 0.30–0.65 a(amp) = 0.40–0.30 c(amp) = 0.25–0.65 with a magnesiohornblende outermost rim of z(amp) = 0.21–0.24

a(amp) = 0.41–0.43 c(amp)= 0.69–0.72 compositions. These ranges for core and rim compositions are shown in P–M(H_2O) space in Fig. 3.20.

All composition parameters for glaucophane cores intersect at 21 kbar and M(H_2O) > 0.4 whereas magnesiohornblende rims intersect at pressures between 11–13 kbar and M(H_2O)>0.35, which correspond to amphibole comprising of a mode of 0.25 in core regions and 0.45 in the rims. Matrix amphibole in TLTN33 constitutes 25% volume of the rock and garnet comprises of 8% total rock volume. Only 1% garnet is predicted to have contributed to the assemblage and therefore can be ignored. Re-normalizing the calculated modes to remove garnet (multiplied by 0.91; assuming the modal proportion is approximately equal to volume conversion for simplicity), predicts amphibole cores and rims would have modes of 10% and 15% respectively, in good agreement with the observed volume proportions and compositions. If fluid was retained by the rock during lawsonite breakdown and the M(H_2O) remained >0.5, initial amphibole growth could be highly sodic composition (e.g. glaucophane) which would match amphibole cores (Figs. 3.9 (a and b) and 3.10) The increasing amphibole modes during decompression in water saturated fields implies, the rock sequentially lost water during exhumation until it reached attained its current observed molar water content of 4.76% corresponding to an M(H_2O) = 0.40, implying the rock at least half its water. Water was not lost during a single extraction event, as amphibole would not have grown to a sufficient volume, and therefore required to remain water saturated.

3.5.2.8 M(O) Redox State During Peak M_1 Conditions

3.5.2.8.1 TLTN26 TLTN26 in outcrop showed variations between omphacite present and omphacite absent domains. However, Fig. 3.15 indicates that minor variations in M(O) through the outcrop could explain this behavior and further shows that the oxidation state of sample TLTN26 is near the omphacite stability field, such that relatively minor increases and decreases in oxidation state could account for omphacite occurrence. The observed assemblage field (red text) places tight constraints for the redox state (M(O)) between 0.2–0.3 at between 22–26 kbar.

3.5.2.8.2 TLTN24 An XRF titration value of $XFe^{3+}(Fe^{3+}/Fe_{total}) = 0.35$ was applied for TLTN24, as well as using the observed mineral assemblage as a guide to oxidation state. The effect of this value is analysed using a *P–T* equilibrium phase diagram (Fig. 3.16). At the suggested peak pressure of 22–24 kbar, the observed assemblage is stable between 0.20 to 0.20. At lower oxidation states, chloritoid is lost from the assemblage (Fig. 3.17d), and at higher oxidation states, hematite joins the assemblage followed by destabilization of glaucophane and eventually garnet. The same trends and limits apply in temperature space (see supplementary material). As the oxidation state is increased, epidote and hematite join the assemblage. The presence of epidote implies the sample must have been reasoNa$_B$ly oxidized (>15%). The glaucophane–barroisite solvus is invariant of oxidation state, as the top of the solvus (purple line) is met consistently at 12 kbar.

3.5.2.8.3 TLTN33 An effective bulk composition for sample TLTN33 was derived using the observed mineral assemblage as a guide to oxidation state (see Appendix 1), a value of $XFe^{3+} = 0.31$ was derived. The effect of redox state is investigated using a *P–T* equilibrium phase diagram (Fig. 3.18d). At the suggested peak pressure of ca. 23 kbar, the observed assemblage is stable between 0 to 0.42, implying a good fit with observations. With increasing redox state, chloritoid becomes stable at lower pressures (18–21 kbar) with hematite, whereas at higher pressure talc becomes stable at M(O)>0.4, shortly followed by the loss of glaucophane from the assemblage.

3.6 Geochronology

3.6.1 Lu-Hf Garnet Geochronology

Dating peak high-pressure metamorphism presents one of the major problems in geochronology, due to the wide range of *P–T* conditions that datable minerals such as allanite, rutile, titanite, white mica and amphibole can crystallise or be altered under (e.g. Smye et al., 2014). However, the Lu–Hf dating system on garnet provides a tool to di-

rectly constrain the timing of garnet growth during peak eclogite and blueschist-facies conditions. Garnet strongly fractionates Lu^{3+} from HF^{4+} (e.g., Green et al., 2000, van Westrenen et al., 2000), and therefore bulk garnet fractions generally have higher Lu/Hf and over time a much more radiogenic Hf signature than the whole rock. The Lu–Hf system is also relatively insensitive to the presence of LREE-rich, Hf-poor inclusions in garnet (Scherer et al., 2000) and is associated with a high closure temperature (e.g. 540–700°C for garnets 0.48 mm to 8 cm in diameter and is greater than the Sm–Nd system at cooling rates <10°C/Myr; Scherer et al., 2000), hence enabling precise age determinations. A thorough overview of the method and analytical procedure is provided in Appendix 2.

A further limitation of this method is that garnet growth occurred over a period of time as highlighted by growth zoning with distinctly different cores and rims. Because garnet core and rims are optically undistinguishable, they could not be separated and therefore the calculated garnet ages represent an average age of garnet growth. However, because the rates of burial and metamorphism on subduction zones is rapid, it is unlikely this method will capture the resolution of different core and rim ages taking into account statistical uncertainty. Phase equilibrium modelling also suggests >80% of garnet grew at high-pressures near peak conditions, much beyond the garnet stability limit at low P–T, as indicated by low calculated garnet modes during prograde metamorphism. The calculated ages therefore represent an absolute minimum age of peak M_1 conditions. Hence the data is presented as a grouped population (n = 8) which give a smaller age uncertainty and overlaps with the larger uncertainties on the individual samples.

3.6.2 Results

Lu-Hf concentrations in garnets from samples TLTN26 and TLTN24 are low and invariable to whole rock concentrations, and therefore 2 point isochrons were not constructed for individual samples. However blueschist samples 17TL102 and 17TL104 exhibit a range in ^{177}Lu between garnet and whole rock of 26.97-0.57 ppm and 11.48-0.42 ppm

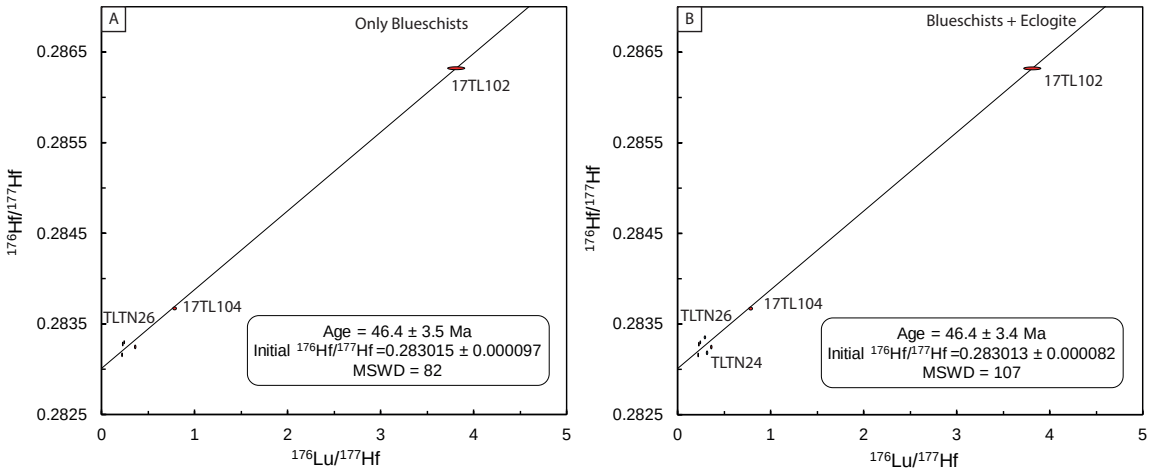


Figure 3.22: Lu-Hf isochrons for Tinos high-pressure rocks; A) Isochron using only blueschist samples, B) Isochron using both eclogites and blueschists

respectively, which together fall on the same isochron line that is pinned by the high Lu concentrations in garnet. Although low in Lu concentration, samples TLTN26 and TLTN24 garnet and whole rock analyses, also plot on or very close to this isochron line. Inclusion of blueschist TLTN26 with 17TL102 and 17TL104 defines an ischron age of 46.4 Ma ± 3.5 Ma with an MSWD of 82, whereas addition of eclogite sample TLTN24 gives 46.4 ± 3.4 Ma with an MSWD of 107. However, the large MSWD associated with the ages indicates this does not represent a single age population. It is therefore likely the garnets from samples TLTN26 and TLTN24 of the Kionnia Unit grew at slightly different times than in the underlying Sostis and Pygros Unit samples. Due to ongoing development of the technique at NIGL, this data is prelimary and further garnet fractions are going to analysed in the coming months.

Sample	Rock Type	Unit	Analysis	Lu ppm	± 2SE	Hf ppm	± 2SE	176Lu/177Hf	± 2SE	176Hf/177Hf	± 2SE
17TL102	Metapelite	Sostis	17TL102 garnet	26.966	0.08	1.0028	0.0001	3.81418504	-	0.286328	0.000007
17TL102	Metapelite	Sostis	17TL102 WR	0.5688	0.0002	0.33394	0.00001	0.24146252	-	0.2833	0.000011
17TL104	Mafic Blueschist	Pygros	17TL104B15 garnet	11.4786	0.0085	2.0719	0.0003	0.78543167	-	0.283673	0.000007
17TL104	Mafic Blueschist	Pygros	17TL104 WR	0.4164	0.0002	0.16457	0.00001	0.35868606	-	0.283248	0.00001
TLTN26	Mafic Blueschist	Kionnia	TLTN26 WR	0.541	0.0001	0.34997	0.00001	0.21913604	-	0.283159	0.00001
TLTN26	Mafic Blueschist	Kionnia	TLTN26 garnet	2.0392	0.0016	1.2759	0.0004	0.22656876	-	0.283278	0.000003
TLTN24	Mafic Eclogite	Kionnia	TLTN24 WR	0.38685	0.00008	0.18599	0.00001	0.29486013	-	0.283356	0.000011
TLTN24	Mafic Eclogite	Kionnia	TLTN24 garnet	1.513	0.001	0.6853	0.0001	0.31297343	-	0.283183	0.000008

Table 3.6: Lu-Hf geochronology results

3.7 Discussion

3.7.1 Petrography

3.7.1.1 The Role of Bulk Composition and Oxidation State on deciphering Blueschist to Eclogite-Facies

Equilibrium phase diagram modelling demonstrates that bulk composition and oxidation state are the key controls on deciphering whether the rocks of the Kionnia Unit record blueschist or eclogite-facies assemblages. The overlap between the peak assemblage fields of blueschist TLTN26 and eclogite TLTN24 shows that variable bulk composition can account for the different facies assemblages at similar P–T conditions. Several studies have also documented the control of bulk composition in juxtaposing blueschist and eclogite facies assemblages at the same grade (e.g. Weller et al., 2015; Tian and Wei, 2014, and references therein), revealing a wide transition zone between what are traditionally considered distinct metamorphic facies defined using mineralogy alone. Equilibrium phase diagram modelling, investigating the bulk composition and redox state, is the most effective way to interpret such rocks, as the competing effects of pressure and temperature, bulk composition, hydration and redox state on the predicted assemblage can be resolved. In all cases, bulk composition of mafic rocks is the major control on the presence of omphacite, with preferred growth under Al_2O_3, Na_2O and FeO enrichment. Blueschists typically have less Al_2O_3, Na_2O and FeO contents fixing the omphacite generating reaction to lower temperatures, ca. 500°C, due to increased stability of glaucophane and phengite. More reducing conditions also destabilizes pyroxene at lower temperatures in the preference of glaucophane, but has a somewhat limited control over the transition from blueschist to eclogite as pyroxene becomes stable again at M(O)<0.2. Redox state influences the presence of hematite, chloritoid or talc as these become stabilized under increasing Fe^{3+} at the expense of glaucophane and eventually garnet. Most rocks in this study where moderately oxidized (XFe^{3+} = 0.3–0.35), which verifies the assumption of water-saturation during peak conditions.

3.7.1.2 Lawsonite Breakdown and Hydration During Exhumation

Lawsonite was predicted in all models to be stable at peak water-saturated conditions, and is a pertinent mineral for water behavior within the crust as it acts as a sponge, soaking up available water released during prograde metamorphic dehydration reactions. The presence of lawsonite pseudomorphs preserved as inclusions within garnet, but not the external matrix, suggests complete breakdown to clinozoisite and paragonite during decompression, and therefore that the preserved total assemblage records a lower hydration state compared to when at peak conditions. Pseudosections from all rocks consistently show that between 3–6% molar H_2O became available upon crossing the lawsonite-out reaction during the initial stages of exhumation following peak M_1 pressures. This water must have escaped the rock, and in doing so, hydrated the matrix resulting in growth of secondary zoned amphiboles and epidotes associated with lower values of Na_B and increasing barroisite composition from core to rim, which is indicative of decompression. The observed assemblages do not record water saturation during M_2 retrograde metamorphism, and therefore 3–6% volume water must have escaped the rock during exhumation. Hydration of the adjacent shear zones would be expected to have increased weakening, thereby facilitating exhumation, and resulting in extreme retrogression. The P–T conditions of water loss due to lawsonite breakdown immediately following peak pressures, implies that water escaped the rocks at between ca. 15–21 kbars, equating to approximately 48–73 km depth. Water released during lawsonite breakdown into the overlying mantle wedge may represent a significant hydration event, and could potentially act as a key contributor to hydration of the mantle wedge in mature subduction settings, and thereby facilitating strain localization into such zones.

3.7.1.3 Garnet Growth History In The CBU

Modelled prograde garnet growth P–T trajectories in Tinos eclogites and blueschists imply garnet grew over a very limited range in P–T, with cores growing at much higher pressures than the predicted garnet stability limit. This possible delayed garnet

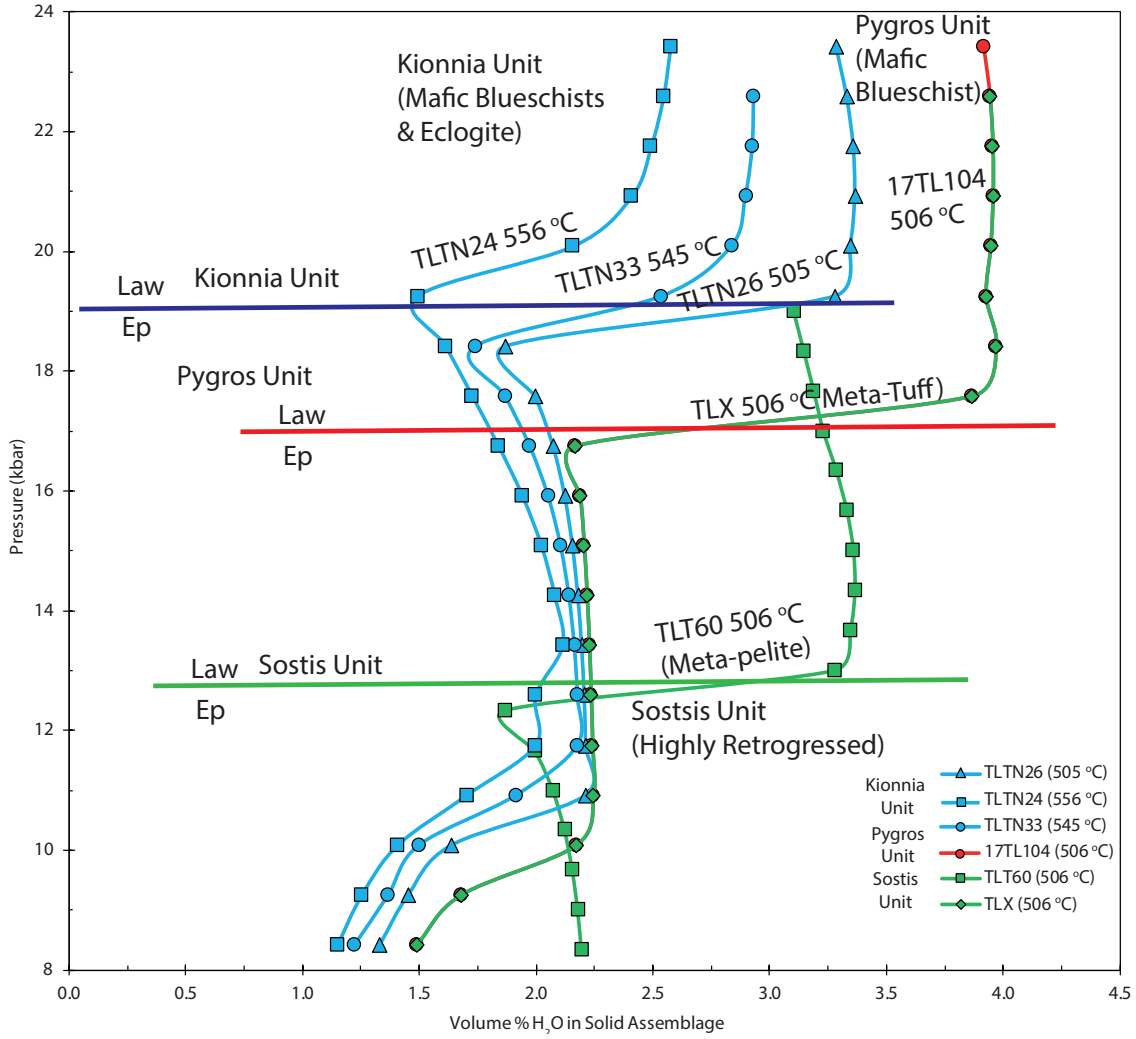


Figure 3.23: Plot of H_2O released during isothermal decompression from peak M_1 conditions due to primarily lawsonite breakdown. The Kionnia Unit samples crossed the lawsonite out reaction at higher pressures causing the rock in question to loose fluid and the surrounding rocks to become hydrated. This devolatization reaction promoting is likely to enhace retrogresssion, and the formation of secondary amphiboles and epidote. In contrast, the Sostis Unit crossed the lawsonite stability limit at lower pressures, possibly explaining why they have a stronger greenschist retrogression.

nucleation phenomenon is also documented in eclogites from Sifnos (Dragovic et al., 2012, 2015), with cores growing at ca. 20 kbar 450–500°C and rims at 22–24 kbar 530–560°C; almost identical to the P–T results of this study. The Sifnos eclogites also yield an identical Lu–Hf age (ca. 46.4 Ma) as the Tinos eclogites documented here, and the geochronology demonstrates that garnet growth must have occurred in <1 Myrs by dating both cores and rims (Dragovic et al., 2012). Unfortunately, core and

rim ages could not be distinguished in this study, but it seems likely that garnet growth rates in the Tinos eclogites would have been similar to Sifnos, given the similar ages and predicted P–T conditions of garnet growth.

Several possibilities have been suggested to explain the apparent mismatch between the predicted garnet stability and the predicted P–T data from garnet compositions: 1. rapid overstepping (in P and/or T) of closely spaced garnet-in reaction isopleths (e.g. Waters and Lovegrove, 2001; Pattison et al., 2011; Spear et al., 2014); 2. the influence of a kinetic catalyst via infiltration of externally derived fluids (e.g. Baxter, 2003); and 3. apparent observed garnet compositions not representing true garnet core and rim compositions during growth due to sampling bias and heterogeneity within garnet growth zoning, (e.g. George et al., 2017). The first possibility (a rapid P–T shift) seems likely within this study, given the evidence for rapid heating from 460°C to 560°C in less than one Myrs from Syros (Dragovic et al., 2012, 2015). However, it is also clear from the phase diagrams that garnet-mode isopleths do not significantly increase >1% until ca. 20 kbar at temperatures < 500°C (Figs. 3.14-3.21), implying very limited garnet prograde growth, whereas 1–2% garnet mode corresponds closely to observed core compositions. These modelling predictions increase the likelihood of sampling bias when investigating garnet growth zoning and would result in only a partial P–T path being recorded, not representing the true and complete garnet growth history. To conclusively test whether delayed garnet nucleation did indeed occur would require 3D X-ray tomographic garnet characterization to discriminate garnet cores and true growth zoning, which is beyond the scope of this study.

3.7.2 Tectonics

3.7.2.1 Fabric Development within Tinos Eclogites and Blueschists

Nearly all samples used in this study consistently show that the dominant deformation preserved on Tinos is (S_3) top-to-NE shearing that is retrogressive and developed over a wide range of P–T conditions from M_1 eclogite to M_2 greenschist-facies conditions.

This shearing overprints relict prograde fabrics that provide insight into the prograde and peak metamorphic evolution of Tinos.

At least two prograde fabrics (S_1 and S_2) occur within the freshest blueschists and eclogites samples at outcrop scale, as inclusions within prograde garnets or within rigid eclogite boudins that are unaffected by retrograde (S_3) top-to-NE deformation, owing to their increased competency compared to the surrounding host rocks. Both prograde fabrics formed in the presence of lawsonite, and can mainly be found within the Kionnia Unnit. S_1 consistently forms a planar fabric, and occurred whilst rocks were already at high-pressure as defined by relict lawsonite, glaucophane and rutile needles in the core of garnets, and is folded and outcrop scale by recumbent F_1 folds. S_2 occurred during garnet growth, creating rotational snowball type inclusion trails and formed a crenulation cleavage (S_{2a}) of glaucophane and rutile that are sometimes still preserved in lower strain domains within the external matrix. S_2 is the peak metamorphic fabric as it is preserved within garnet rims, which record the highest pressures and temperatures. S_2 was a compressive fabric that developed during latest stages of burial and is axial planar to the meso-scale F_1 isoclinal folds. S_2 is also associated top-to-SW shear fabrics (S_{2b}) that utilize the cleavage domains of (S_{2a}) crenulations e.g. Kionnia Thrust, and is well developed on Sostis Thrust within the Sostis Unit (Figs. 3.6 and 3.7). Because S_{2b} also deforms around garnet and affects retrograde assemblages, it must have developed over a range of P–T conditions associated with exhumation. These two major thrusts combined with several other minor structures provide substantial evidence that top-to-SW S_{2b} fabrics continued to develop along discrete shear zones during exhumation coeval with S_3 top-to-NE fabrics at structurally higher levels.

Upon reaching the maximum pressures, the rocks began to decompress associated with lawsonite breakdown. This involved transformation of lawsonite to epidote/-clinzoisite and paragonite, with zoned epidote or clinozoisite which demonstrate pre or syn-tectonic relationships with respect to S_3 top-to-NE shearing. In zones unaffected by S_3 top-to-NE shearing, a further static fabric (S_{2b}) is preserved (e.g. TLTN33),

which is represented by planar alignment of aegerine pyroxene, glaucophane and epidote within both garnet core and rim (S_{2b}), that is later statically overprinted by cross-cutting coarse-zoned glaucophanes and epidote (S_{2c}).

S_3 top-to-NE extensional fabrics occurred at different conditions and presumably at different times across the various units on Tinos. In the Kionnia Unit (at the structurally highest level), S_3 only developed within the blueschist meta-sediments that are distributed along the uppermost margins, and is associated with (F_2) sheath folds. S_3 initiated during the very final stages of garnet growth, as indicated by rotation of inclusions in its outermost rim into alignment with the matrix, and continued during decompression associated with clinozoisite growth (e.g. TLTN26). In the Pygros Unit, (S_3) top-to-NE shear zones deform around the margins of F_1 isoclinally folded marbles and schist, indicating it post-dates these large-scale structures. Epidote and clinozoisite commonly grows syn-tectonic with respect to top-to-NE shearing as it is often rotated at an angle to or aligned with the shearing. In the lowest strained rocks some epidote sometimes cross-cuts the S_3 fabric, indicating extensional strain became localized onto discrete shear zones as deformation proceeded. In contrast, within the Sostis Unit, S_3 top-to-NE extensional shearing firstly developed after garnet had finished growing, but prior to retrograde plagioclase growth, which displays a continuity of inclusions suggesting syn- post-kinematic growth in some samples. Top-to-NE shearing must have also continued extensively into the greenschist-facies, as it aligns all epidote and chlorite grains along its lineation, and also deforms around retrograde plagioclase porphyroclasts. Together these features suggest that S_3 top-to-NE shearing was highly penetrative throughout the entire Cycladic Blueschist Unit, and propagated downwards with time.

S_4 is an upright mildly developed crenulation fabric, that refolds the S_3 top-to-NE fabrics and affects M_1 blueschist and M_2 greesnschist-facies assemblages. It is associated with the series of larger scale NE–SW trending upright and open folds that traverse across Tinos parallel with the NE-trending stretching lineation. These folds deform the Tinos Shear Zone, and Upper Unit and therefore developed at mid-

crustal conditions during the final stages of exhumation. The presence of S_4 and F_4 upright folds suggests a component of shortening orthogonal to the top-to-NE shearing direction, creating a non-ideal pure-shear scenario during exhumation.

3.7.2.2 *P–T–t–D* paths on Tinos

Although only spatially covering 150 km^2, the diverse *P–T–t–D* paths recorded from various structural levels on Tinos, indicate that the Cycladic Blueschists Unit does not represent a homogeneous package of rocks. Instead, we interpret the Tinos Lower Unit as representing a series of tectono-metamorphic slices. Each tectono-metamorphically distinct package of rocks experienced different *P–T* histories and were subsequently juxtaposed against each other during exhumation, by a series of top-to-NE extensional shear zones at the top of the packages and top-to-SW directed thrusts along their base. The exhumation mechanism of the Tinos high-pressure rocks is thus consistent with a model of syn-orogenic extrusion, whereby buoyant continental margin derived rocks return from subduction depths via return ductile flow in a channel or extruding wedge (Chaminda, 1995; England and Holland, 1978; Agard et al., 2009; Hacker, 2011). An inverted metamorphic gradient is recorded across Tinos with structural depth, indicative of progressive stacking of high-pressure nappes within the subduction channel or wedge. The describe the evolution of each unit from structurally high-to-low:

3.7.2.2.1 The Kionnia Unit Rocks that sit at the highest structural level in the present day, within the upper levels of the Kionnia Unit, reached boarder-line ultra-high-pressure blueschist-facies conditions of ca. 22–24 kbars, 490–520°C during its peak pressure stage (M_1) at 46.4 Ma. In contrast, eclogites that sit 200 m structurally below, record slightly lower pressures of 20–23 kbar but higher temperatures of 530–570°C. The transition of blueschist to eclogite-facies is dependent on the first appearance of clinopyroxene, and this is strongly dependent on the bulk composition and fluid availability, thus allowing the two metamorphic facies to be present within the same rock

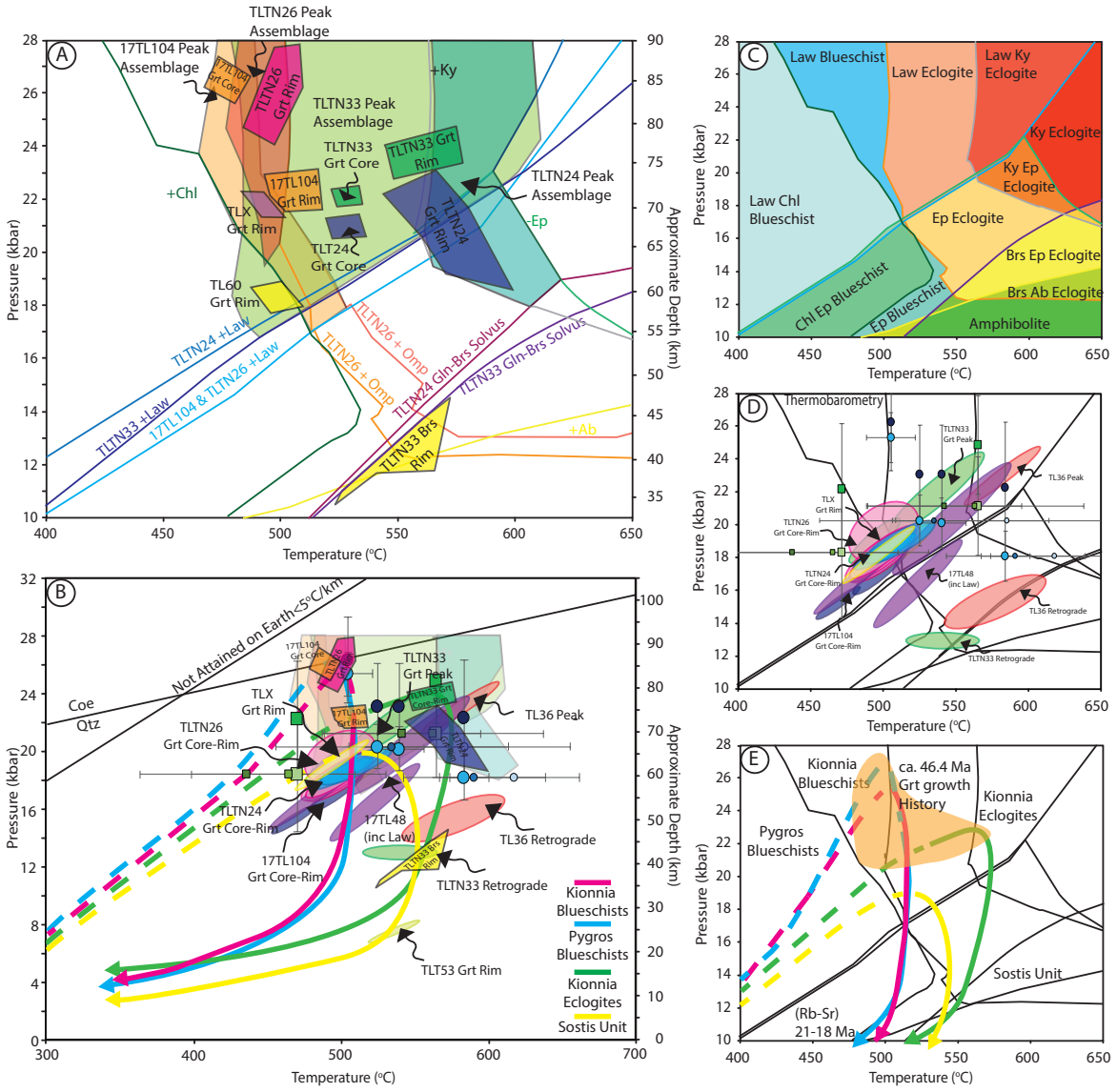


Figure 3.24: Summary of *P-T* results A) Pseudosection constrains of peak metamorphism with overlaid reactions for omphacite, lawsonite albite and the Gln-Brs solvus. B) All *P-T* constrains with the oberlaid coesite-Qtz transition from Byod, 1960, C) Approximate metamorphic facies based on a mafic bulk composition (from samples TLTN26 and 17TL104), explaining such high-pressures in blueschists before the omphacite in reaction. D) Thermobarometry of all samples showing variable pressures between the different units. E) Interpretted *P -T-t* paths for the Kionnia, Pygros, and Sostis Units showing possible *P-T* conditions of garnet growth predicted from pseudosection analysis that is constained at ca. 46.4 Ma by mean Lu-Hf dating. The ca. 21-18 Ma Rb-Sr age is from Brocker and Franz, (1998) dating greenschist facies deformation.

volume as documented at outcrop scale (e.g. Fig 3.5b). Prograde fabrics within these rocks include a planar S_1 fabric within the cores of garnet, followed by an S_2 crenulation cleavage that can be identified by rotational inclusion trails and microlithons within the matrix. S_1 and S_{2a} prograde fabrics are consistent with the larger-scale F_1 folding and S_{2b} top-to-SW shearing persistently preserved throughout the middle-lower part of this sequence, associated with thrusting. One possibility to explain this apparent pressure jump is that the upper levels of the Kionnia Unit were buried deeper (2–4 kbar equating to ca. 6–12 km), and were juxtaposed against the underlying eclogites by a top-to-SW thrust, which is consistent with top-to-SW fabrics throughout the lower part of the Kionnia section. This is difficult to prove, as these blueschists are affected by extensive top-to-NE fabrics. Another possibility is that both packages of rocks were buried to similar pressures of ca. 22–26 kbars at temperatures of ca. 500°C, and at this point during their evolution, detachment from the down going slab occurred and was followed by buoyancy driven exhumation. The rocks at the upper levels of the Kionnia Nappe, (the garnet blueschists) would have been affected by localized top-to-NE extensional shearing (S_3), and kept sufficiently cool to maintain their peak high-pressure M_1 blueschist assemblages. Contrastingly, the eclogites within the interior of the Kionnia Unit had a conductive boundary layer and increased in temperature during the early stages of exhumation, allowing for breakdown of lawsonite to epidote and growth of coarse and zoned epidote and glaucophane due to re-equilibration along a hotter geotherm at slightly lower than its peak pressures. This increase in temperature may also explain the smoother garnet zoning profiles from core-to-rim as the composition corresponding to their maximum pressures may have been affected by diffusion and therefore give an apparent prograde P–T trajectory. This interpretation is also consistent with the eclogite microstructures, that reflect post-peak mineral growth, with respect to shearing top-to-SW deformation (TLTN24) and others that show no pervasive post-eclogite facies shearing whatsoever (e.g. TLTN33).

Irrespective of these scenarios, the eclogites within the interior of the Kionnia Unit were passively exhumed by a combination of (S_3) top-to-NE normal sensed

shearing concentrated on the exterior upper zones, and top-to-SW thrust sensed shearing at the base which show a continuum of deformation from M_1 blueschist to M_2 greenschist-grade. The exhumation history of this unit therefore follows an extrusion type mechanism and combines simultaneous top-to-SW thrusting at the base and top-to-NE normal faulting at the top. This exhumation was associated with the development of F_2 folds and isothermal decompression to conditions of ca. 13 kbar 520–540°C (e.g. TLTN33), as represented by retrograde matrix phase relations including coexisting titanite and plagioclase and growth of barrosite cross-cutting amphibole rims. Upright open folds (F_3), with their axes trending parallel to the shear direction developed during exhumation and were probably related to constriction within the extruding channel, owing to along strike variations in channel thickness. If there was no variation in along strike exhumation rates, zones of restriction would produce a component of convergent flow orthogonal to the main transport direction (e.g. Levy and Jaupart, 2011) in between the restrictive zones.

3.7.2.2.2 Pygros Unit The Pygros Unit, that also sits at a high structural level on Tinos, records the stacking and folding of the proximal shelf carbonates under blueschist-facies conditions. This unit records peak M_1 blueschist facies conditions of ca. 22 kbars, 510°C also at 46.4 Ma. However, this represents a minimum pressure as garnet cores yield pressures of ca. 27 kbar, 480 – 490°C. These P–T conditions are comparable to that recorded by blueschists of the Kionnia Unit (TLTN26) that sits at a similar structural level, although no eclogites can be found in the Pygros Unit. Deformation followed a similar style to the Kionnia Unit along strike, with prograde features related to top-to-SW deformation (S_1 and S_{2a+b}) producing (F_1) isoclinal folds during burial of the continental margin. This was later overprinted by top-to-NE kinematics (S_3) that developed during ductile extrusion towards the SW, followed by a M_2 greenschist-facies pervasive S_3 top-to-NE shearing that overprints all previous potential prograde structures.

3.7.2.2.3 Sostis Unit In contrast to the eclogites and blueschist-facies rocks at higher structural levels, the interior of Tinos, (Sostis Unit), achieved slightly lower peak pressures and temperatures of ca. 18–19 kbar, 490–500 °C during M_1 and was affected by extensive retrogression through the greenschist to amphibolite-facies. Rocks from this unit underwent a similar prograde style to the overlying blueschists and eclogites, and display lawsonite pseudomorphs as inclusions within garnet and >3.5 Si p.f.u. of phengites, before also experiencing decompression through the lower amphibolite-greenschist facies. Ti in biotite thermometry (Henry et al., 2005) together with amphibole-plagioclase thermometry (Holland and Blundey, 1994) and Thermocalc Av-PT (Holland and Powell, 1998) yields retrograde amphibolite facies P–T conditions of ca. 7.3 kbar, 500–540°C, indicating a component of heating once the rocks reached mid-crustal conditions. Kilometer-scale (F_1) recumbent eastward verging folds e.g. near the village of Kalloni in central Tinos are related to this burial process and the stalling of relatively buoyant meta-sedimentary material as the Cycladic continental margin attempted to subduct. This presumably occurred upon reaching the point of neutral buoyancy due to entrainment of sufficient continental derived material to overcome subduction forces. F_2 NE-trending sheath folds within all units are associated with the (S_3) top-to-NE fabrics and presumably also developed during its exhumation from subduction depths.

Mean Lu–Hf garnet dating reveals metamorphism in this unit also occurred at ca. 46 Ma, which overlaps with Lu–Hf garnet ages from the overlying Kionnia and Pyrgros Units . However due to the (top-to-SW) thrusting contact separating this lower structural unit from the overlying (and higher pressure) Kionnia Unit, combined with a ca. 4 kbar pressure jump (12 km). It is likely the Sostis Unit was underplated beneath the Kionnia Unit and achieved its peak pressures (equating to 65 km depth) at the same time as the eclogites and blueschists of the Kionnia and Pygros Units were experiencing their return journey back towards the surface. This is because we should expect the higher pressures in the underlying Sostis Unit if both units were buried at exactly the same time without any differential exhumation. A ca. 4 kbar

pressure difference between the units also implies a minimum vertical displacement on the top-to-SW Sostis Thrust of 12 km. This *P–T–t–D* data also suggest that prograde and retrograde deformation progressed down structural level with time similar to the deformation models proposed for Syros by Lauren et al., (2018), as the rocks were sequentially buried and extruded towards the SW from the subduction zone.

In summary, the current geometry of the Tinos high-pressure rocks does not represent the architecture of the subduction channel or wedge at peak metamorphic conditions, but rather a snapshot of the subduction-accretion architecture during the exhumation pathway. Upon reaching mid-crustal greenschist-facies conditions, the Tinos Shear Zone (associated with top-to-NE kinematics), completely truncates the high-pressure structures preserved within these nappes, as seen at Panormos Bay in NW Tinos. Deformation on this feature solely occurred from greenschist-facies to brittle conditions (On the Livada Detachment and was responsible for SW directed exhumation of rocks from mid-crustal depths much later in the orogenic history. Juxtaposing the Upper Unit containing the Tsiknias Ophiolite, metamorphic sole, Mirsini Unit (pelagic meta-sediments) and Akrotiri Units in the hangingwall against the *HP–LT* of the CBU in its footwall.

3.7.2.3 Relationship between the Tsiknias Ophiolite Metamorphic Sole and High-Pressure Rocks

The timing of peak high-pressure metamorphism on Tinos is particularly interesting, due to the relationship with the structurally overlying Tsiknias Ophiolite. U–Pb and Lu–Hf age constraints suggest the metamorphic sole immediately beneath the Tsiknias Ophiolite formed at ca. 74–66 Ma (Chapter 2), and calls for a process of subduction initiation combined with shear heating to generate supra-solidus conditions within amphibolites from the uppermost few meters of the metamorphic sole (chapter 2). In this model, the metamorphic sole amphibolites and underlying pelagic meta-sediments and turbidites record the initial stages of subduction and accretion as the Vardar Ocean began to close. In this scenario, the same subduction zone would be responsible for both

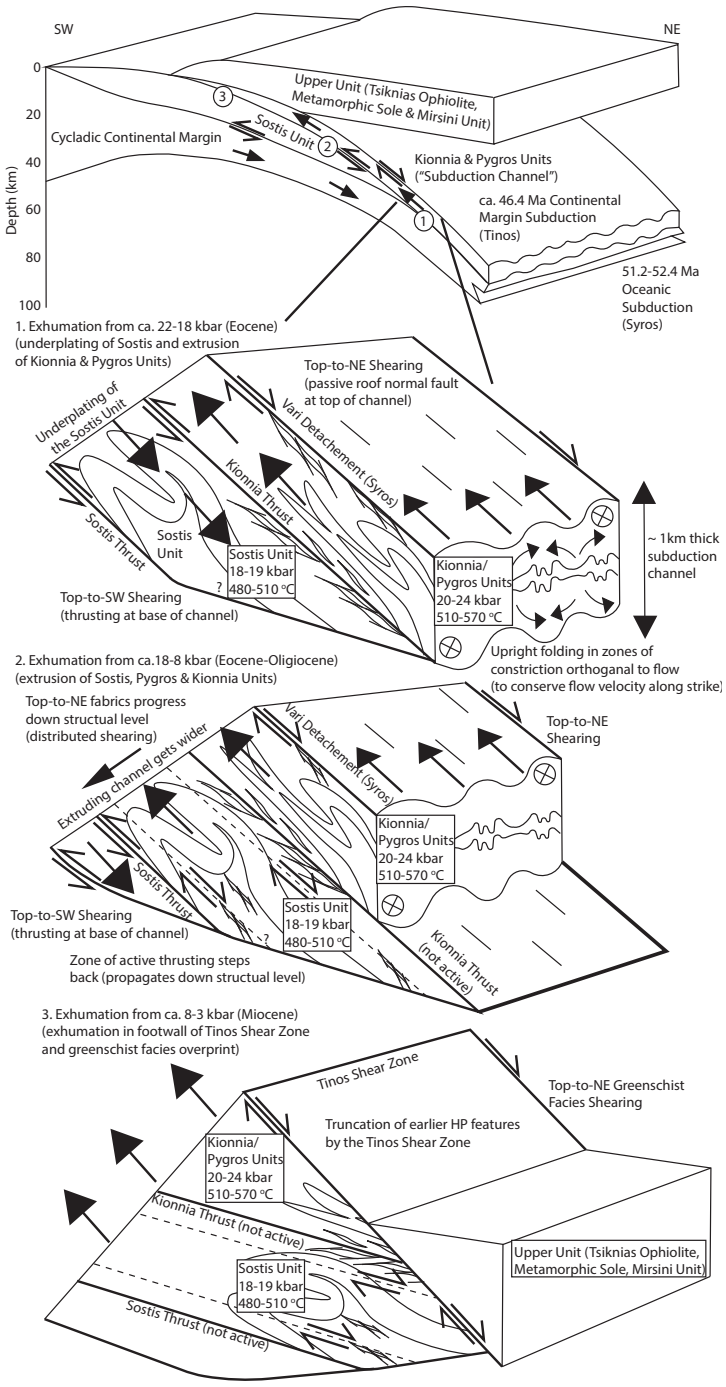


Figure 3.25: Extrusion model for exhumation of Tinos HP rocks: A) Schematic sketch of a subduction zone with the location of the subduction channel, B) Extrusion of high-pressure rocks by top-to-SW thrusting at the base and normal sensed motion at the top, placing higher pressure rocks ontop of lower pressure rocks. C) Migration of the thrust zone down structural section, causing an overprint of extensional fabrics at the top of the channel. Note lateral variation in channel width can cause localized construction and open folding orthoganal to the transport direction. D) All high-pressure fabrics are truncated by the Tinos Shear Zone at mid crustal greenschist-facies conditions.

ophiolite obduction, metamorphic sole formation and eventual high-pressure metamorphism as the Cycladic continental margin incepted the subduction zone some ca. 20 Myrs later. This model also implies the subduction zone must have sufficiently cooled to preserve a low geothermal gradient within the blueschists and eclogites documented in this study. Lu–Hf garnet geochronology indicates that eclogite facies garnet grew at ca. 46.4 Ma. If the *HP–LT* rocks within the CBU did indeed form on the same subduction zone, then NE-dipping subduction must have continued for at least ca. 20 Myrs to the north of the Cycladic continental margin and cooled into a steady-state subduction system. During this time, the Upper Unit, including the Tsiknias Ophiolite, metamorphic sole and Mirsini Unit, must have been accreted in an upper-plate position with the active subduction front stepping back beneath these features as shown in Fig. 3.26.

3.7.2.4 Cold Subduction and High-Pressure Blueschist Facies Metamorphism

The conditions recorded in Tinos *HP–LT* rocks and particularly the high-pressure blueschists (e.g. TLTN26, 17TL104) are extreme - 24–26 kbars and 490–510°C, which suggests the rocks reached near ultra-high-pressure conditions associated with the stability of coesite (Boyd and England, 1960). These pressures equate to subduction of the continental margin to ca. 80–90 km depth, and implies a minimum geothermal gradient of approximately 5.6°C/km, representing one of the coolest geotherms ever globally ever recorded.

Thermal modelling of subduction zones shows that considerable conductive cooling occurs in the mantle wedge within the first few million years following initiation, eventually converging on a steady-state system (e.g. Molnar and England, 1990, 1995; Peacock et al., 1992, 1994; Kincaid and Sacks, 1997; Warren et al., 2007). Immediately following subduction initiation, temperatures have been shown to reach 800–900 °C at ca. 70 km depth, enough to trigger melting of the sediments under water-saturated conditions (Kincaid and Sacks, 1997). Once reaching an early thermal

maximum, the slab surface temperatures gradually decrease with time, converging on steady-state within a few Myrs due to conductive cooling of the mantle wedge by the cold subducting slab (Molnar and England, 1990, 1995; Peacock et al., 1992, 1994; Kincaid and Sacks, 1997). It is shown that the thermal evolution of the slab surface following subduction initiation and therefore the subducted sediments, is strongly influenced by a variety of factors including: 1) the subduction rate; 2) the age of the subducting plate; and 3) factors controlling the flux of hot material into the wedge to oppose the cooling effects of the slab (Molnar and England, 1990, 1995; Peacock et al., 1992; 1994; England and Wilkins, 2004). However, the two most important factors are the age or thickness of the overriding plate and the slab dip angle (e.g. Molnar and England, 1990, 1995 Peacock et al., 1994). For a fixed dip angle, rapid subduction beneath a thicker overriding plate results in increased cooling of the mantle wedge and generates the coolest slab surface temperatures (Molnar and England, 1990, 1995; England, 2018). In contrast, the maximum slab surface temperatures are recorded in slow subduction zones, where both the subducting and overriding plates are young and thin (Molnar and England, 1990, 1995; England, 2018). A further consideration is dissipative heating (Turcotte and Schubert, 1973; England, 2018). Although some authors regard dissipation as playing a negligible role in metamorphism and melting at subduction zones (e.g., Abers et al., 2017; Syracuse et al., 2010), it is demonstrated that shear stresses of order 10–100 MPa are required to explain addition heat flow observations of 40 mWm^{-2} (England, 2018),corresponding to a coefficient of friction on subduction zone interfaces as 0.05–0.07 (England, 2018). Shear heating would therefore act to increase temperatures near subduction zone interfaces in subduction zones with faster convergence rates. The calculated P–T conditions on Tinos suggest minimum geothermal gradients during peak M_1 conditions of approximately 5.6–6.5 °C/km. This contrasts from the geothermal gradients of approximately 32 °C/km recorded by the metamorphic sole under the Tsiknias Ophiolite, associated with subduction initiation. The age of the subducted oceanic plate has been shown to be early Jurassic (ca. 190 Ma) (chapter 2) similar to the age of the continental margin (Altherr,

1981). These would have been >120 Myrs old at the timing of subduction/ M_1 high-pressure metamorphism and therefore would have been cold. Using these ages, and the shortest possible time between sole formation (subduction initiation) and *HP–LT* metamorphism of approximately ca. 20 Myrs, the average geothermal cooling rate on the subduction zone is approximately 1.5 °C/km/Myr assuming cooling occurred at a constant rate. Because Molnar and England, (1990) demonstrated that most cooling occurs in the first few Myrs following subduction initiation, this cooling rate represents an absolute minimum.

A final consideration to explain such low recorded temperatures is whether the Tinos high-pressure rocks remained within the interior of the subducting slab, and therefore had a conductive boundary layer separating them from the hotter slab surface. This mechanism may be sufficient to preserve such cool temperatures within the slab interior (e.g. England, 2018) whereas higher temperatures would occur on the interface due to both shear heating and conduction from the overlying mantle wedge (England et al., 2018). Following these arguments, fast subduction maybe responsible for an overall cool temperature regime on this Cretaceous-Eocene subduction system, although the first order control was most probably the cold and old subducting lithosphere as well as the exhumed rocks located away from the slab interface (ca. 190 Ma oceanic lithosphere and the ca. 162 MaThe Tsiknias Ophiolite).

3.7.3 Implications for High-Pressure Metamorphism in the Cyclades

3.7.3.1 Timing of M_1 Eclogite and Blueschist-Facies Conditions

The timing of peak M_1 conditions on Tinos at ca. 46 Ma is interesting as it is the same age derived from Lu–Hf garnet dating of eclogites of Sifnos (hosted in continental margin rocks; Dragovic et al., 2012) and overlaps with Naxos blueschist U–Pb allanite ages (Lamont et al., in review), but post-dates by at least 4 Ma the Lu–Hf garnet (52.2–51.4 Ma; Lagos et al., 2007) and U–Pb zircon ages (ca. 52 Ma; Tomaschek

et al., 2003) from Syros that are interpreted to represent peak (M_1) eclogite facies conditions. These latter ca. 52–51 Ma ages are derived from rocks within the Kampos Unit at the highest structural levels of Syros, which comprises a complete range of mafic and ultramafic lithologies interpreted to represent a meta-ophiolite sequence, including meta-chert, meta-gabbro, meta-plagiogranite and peridotites deformed in a mélange (Keitier et al., 2001; 2004; 2011); this is completely different to the continental margin hosted eclogites within the Kionnia Unit on Tinos. If the Kampos Unit rocks indeed represent a relict slice of subducted oceanic lithosphere, then we would expect them to have been subducted and experiencing (M_1) high-pressure metamorphism at an earlier time than when the attached continental margin attempted to subduct (see Fig. 3.25). Upon reaching their maximum depths (ca. 20–23 kbar; Laurent et al., 2018), these oceanic derived eclogites would have started their exhumation, prior to the subduction of the Cycladic continental margin (e.g. Agard et al., 2009), as a consequence of the slight positive density and rheological contrast of the serpentinites compared the surrounding mantle (Agard et al., 2011). NE-dipping subduction must have continued until the arrival of the leading edge of the Cycladic Continental Margin between 51–46 Ma, which achieved maximum depths of burial of 22–26 kbar (ca. 70–80 km depth) at ca. 46 Ma. Therefore, we predict that continental margin hosted eclogites or blueschists on Syros also yield a similar ca. 46 Ma age for peak metamorphism.

Due to the positive buoyancy of continental margin rocks compared to the surrounding mantle, subduction would have seized at this point and the subducted continental margin high-pressure rocks would have begun their exhumation by a sequential extrusion mechanism as part of a channel. Field observations of high-pressure S_{2b} top-to-SW shear fabrics on the Kionnia thrust and top-to-NE S_3 fabrics on the top of the Kionnia and Pygros Units are consistent with coeval top-to-SW thrusting at the base and top-to-NE normal sensed movements at the top of the extruding channel. The zone of active top-to-SW thrusting must have propagated down structural level with time, developing thrusts within the Sostis Unit (e.g. the Sostis Thrust) and causing the highest pressure and earliest subducted and extruded rocks to be preserved at the

top of the sequence.

3.7.3.2 Possible Comparisons to High-Pressure Rocks under Other Ophiolites

The occurrence of high-pressure rocks directly underneath ophiolite complexes in the geological record are somewhat common, however are rarely well preserved and usually structurally dismembered. The best-known example is the As-Sifah eclogites and blueschists in Oman, which crop out at deepest levels of the Arabian continental margin sequence, approximately six structural km under the Semail Ophiolite and metamorphic sole (Searle et al., 2004; Warren and Waters, 2006, Cornish et al., 2017). Eclogites in As-Sifah occur as mafic boudins that represented sills which intruded the Arabian shelf carbonates (Searle et al., 2004) similar to the eclogites and blueschists within the Kionnia Unit on Tinos. These high-pressure rocks also reached 20–22 kbar, 530–570 °C at ca. 78 Ma (Warren et al., 2004; Warren and Waters, 2006) as the Arabian continental margin attempted to subduct. They are also associated with extensive top-to-ENE extensional shear fabrics that formed during extrusion of buoyant continental margin back up the subduction channel during the final stages of immediately following ophiolite obduction, similar to what is proposed for Tinos (Searle et al., 2004; Warren et al., 2004). However, in As-Sifah the highest pressure rocks are at the deepest levels and each tectono-metamorphic unit is separated by normal sensed shear zones associated with large P–T jumps. As-Sifah thus represents the top of the extruding channel, whereas on Tinos, we are observing the base of the extruding channel and hence have inverted metamorphism associated with thrusting. The subduction-extrusion event also occurred some ca. 17 Myrs following subduction initiation and obduction of the Semail Ophiolite (Warren et al., 2004; Searle et al., 2004), although recent Lu–Hf work has shown it could be as much as 25 Myrs (Guillmette et al., 2018). The timing, occurrence and P–T–D constraints of high-pressure metamorphism following ophiolite obduction in Oman are almost identical to that recorded on Tinos. The only difference is that on Tinos, the high-pressure sequence is cut by the later greenschist facies Tinos

Shear Zone, which places the Tsiknias Ophiolite and Metamorphic Sole directly against the CBU which was subducted some ca. 20 Myrs later.

3.7.4 Tectonic Model

Integrating the *P–T–t–D* data presented in this study, the tectono-thermal evolution of the Tinos blueschists and eclogites involves the following stages:

1. Initiation of a NE-dipping subduction zone at 74–66 Ma, and southwest obduction of the ca. 162 Ma Tsiknias Ophiolite, coeval with the formation of the metamorphic sole (74–67 Ma; chapter 2). Distal pelagic meta-sediments and basalts of the metamorphic sole were subducted to shallow depths (ca. 8 kbar) and experienced high-grade metamorphism and partial melting directly under the Tsiknias Thrust due to conductive heating on the subduction interface combined with shear heating on the Tsiknias Thrust (see chapter 2). These rocks were accreted to the base of the ophiolite and became part of the upper plate during the obduction process. These rocks are today exposed in the "Upper Unit" on Tinos that did not reach high-pressure conditions (M_1). During obduction, the main subduction interface must have stepped back, allowing steady-state subduction of oceanic lithosphere under the Upper Unit (in the upper plate) for ca. 20 Myrs .

2. Steady-state NE-dipping subduction of old ca. 190 Ma oceanic lithosphere continued for ca. 20 Myrs and during this period, the subduction zone rapidly cooled, owing to fast plate motions and advection of cold oceanic crust down the subduction zone. Oceanic crust was subducted to ca. 70 km depth and was metamorphosed to M_1 eclogite-facies conditions at ca. 52.4–51.2 Ma (Lagos et al., 2007), and is exposed today within the Kampos Unit on Syros. The arrival of the leading edge of the Cycladic Continental Margin at the trench resulted in the subduction of continental crust. These rocks were buried under a cold geothermal gradient of 5.6–6.5°C/km and underwent prograde metamorphism through the

lawsonite stability field to peak (M_1) blueschist- eclogite-facies conditions at ca. 46.4 Ma (ca. 4 Myrs later than the oceanic high-pressure rocks on Syros) forming S_1 and S_2 prograde fabrics. This burial and underplating process produced (S_{2b}) top-to-SW thrusts and intense isoclinal (F_1) folding as rocks were continuously underplated, causing the subduction wedge to thicken. The mafic eclogites exposed on the Kionnia peninsular achieved P–T conditions of ca. 21–26 kbar 500–570°C, which equates to burial to depths of ca. 80–90 km. Such burial depths were only achieved due to the slab-pull force from already subducted and eclogitized dense oceanic crust at greater depths (e.g. Kampos Unit on Syros) (ref to this mechanism).

3. Upon reaching peak pressures, the Kionnia and Pygros Units detached from the subducting slab, and were buoyantly extruded back up an over-riding channel producing top-to-NE (S_3) extensional fabrics on its roof, top-to-SW fabrics (S_{2b}) on its base, and (F_2) sheath folds due to non-coaxial ductile flow. During this exhumation process, deformation was localized at the margins, allowing the preservation of slightly colder garnet-bearing blueschists on the exterior shear zones, whilst internally, slightly hotter and more competent eclogites were passively exhumed. Eclogites within the interior of the Kionnia Unit remained unaffected by the decompression related deformation, due to strain localization at the margins of the boudins owing to the competency difference with the host meta-sediments. Lawsonite breakdown as a result of decompression, hydrated the matrix of these rocks at ca. 18–20 kbar and produced cross-cutting coarse and zoned epidotes and glaucophane that grew continually during decompression. During the early stages of exhumation, upright open folds (F_3) with their fold axes parallel to the shear direction developed within the extruding channel due to lateral constriction conserving flow, likely owing to the channel having a variable thickness across strike - localised constriction would have occurred in the narrowest parts of the channel due to converging ductile flow in response to the obstruction at the margins.

4. During extrusion from their peak M_1 pressures, eclogite-facies rocks of the Kionnia Unit were overthrust onto the Sostis Unit, which did not reach as great depths as the overlying Kionnia Unit. This implies it achieved its peak pressures at a slightly later time than the Kionnia Unit, although it did experience a similar prograde evolution, through the lawsonite stability field but reaching less extreme P–T conditions of ca. 18.5 kbar and 490–500 °C. Upon reaching its peak pressures, this unit also underwent isothermal decompression associated with extensive (S_3) top-to-NE shearing from M_1 blueschist- M_2 greenschist-facies conditions. This extensional shearing was highly pervasive through this lower unit, causing intense M_2 retrogression that overprints nearly all relict prograde fabrics. Top-to-SW thrusting also occurred throughout this unit, simultaneous with top-to-NE movements. The Sostis Thrust is the best exposure of a high-pressure thrust that developed during this extrusion stage. The sequential movement and juxtaposition of material during ductile extrusion was when the architecture of Tinos was aggregated.

5. Upon reaching crustal depths (<12 kbar), top-to-NE (S_3) greenschist-facies (M_2) deformation was localized on the Tinos shear zone, which was responsible for juxtaposing M_1 high-pressure rocks of the Lower Unit against the lower pressure and ophiolitic "Upper Unit". Across this shear zone, 20 Myrs of subduction history is recorded. This shear zone is discordant to, and truncates all fabrics and folds associated with (M_1) high-pressure metamorphism and therefore post-dates syn-orogenic extrusion of high-pressure rocks from subduction depths. Top-to-NE (S_3) greenschist-facies deformation was also penetrative throughout the entire nappe pile, although to varying degrees.

6. During M_2 greenschist- amphibolite-facies retrogression, (S_4) gentle upright crenulation cleavages and open upright folds formed across all units on Tinos with NE–SW axes parallel to the (S_3) top-to-NE extensional lineation. A component of E–W shortening must therefore have occurred at a late stage during exhuma-

tion at greenschist facies conditions.

7. The Tinos Shear Zone is domed, as with all structures within the CBU on Tinos, and is cut by the I-type granite pluton, suggesting deformation on this structure ceased by ca. 14.6 Ma (Brichau et al., 2007). The doming of Tinos is therefore a late feature, and occurred during the Late Miocene at mid-upper crustal conditions. The final exhumation to the surface occurred via brittle normal faulting passively exhuming the island to its present-day geometry.

3.8 Conclusions

Several key conclusions from this study include:

1. The Cycladic Blueschist Unit on Tinos is not a homogenous body of rocks that experienced the same subduction history, but represents a series of tectonically bound slices that each experienced their own distinct deformation and tectono-thermal histories, and that are separated by discrete normal and thrust sensed shear zones that were responsible for their exhumation and juxtaposition against each other. These rocks record processes of crustal deformation with a subduction-extrusion channel.

2. Peak P–T conditions within the Kionnia Unit were ca. 22–26 kbars at 490–510°C for blueschists, and ca. 22–23 kbars at 540–570°C for eclogites; although the latter record slightly lower pressures and higher temperatures, this could be due to thermal equilibration. The local transition to eclogite-facies is based entirely on the effective bulk composition and oxidation state. These rocks record near isothermal decompression to ca. 13 kbar 520–540°C, associated with an M_2 epidote amphibolite facies overprint. Contrastingly, the Sostis Unit within the interior of Tinos Island reached slightly lower peak pressures of ca. 18–19 kbar, 480–510°C, but has been affected by strong greenschist to amphibolite-facies retrogression. This unit may have experienced reheating at mid-crustal conditions

of ca. 7.3 kbar, 536°C, during exhumation.

3. The timing of *HP–LT* metamorphism on Tinos is recorded at ca. 46.4 ± 3.4 Ma by garnet Lu–Hf geochronology, and post-dates obduction of the Tsiknias Ophiolite by ca. 20 Myrs. This implies that ca. 20-25 Myrs of subduction zone history is record on Tinos over less than three structural kilometers.

4. The timing of M_1 conditions on Tinos post-dates Lu–Hf and U–Pb ages derived from oceanic-derived eclogites on Syros by ca. 4 Myrs, but is the same as ages derived from continental margin hosted eclogites on Sifnos. Eclogites on Tinos represent the leading edge of the Cycladic Continental Margin which is expected to have been subducted at a later time than oceanic material on Syros. The timing of high-pressure metamorphism on Tinos provides a constraint for the end of subduction in the Cyclades, caused by the arrival of the buoyant Cycladic Continental Margin.

5. Deformation associated with extrusion of the high-pressure rocks propagated down structural level with time. During exhumation from subduction depths, top-to-NE shearing was localized on discrete shear zones and progressed down structural level, with the highest-pressure nappes being exhumed the earliest. This extensional shearing took place in a syn-orogenic setting, and relates to passive roof faulting on the upper boundary of the subduction channel. Upon reaching mid-crustal levels, the Tinos Shear Zone truncated and overprinted all earlier high-pressure deformation. This structure was responsible for the last stages of exhumation from mid-crustal depths, and juxtaposed the "Upper Unit", (comprising the Tsiknias Ophiolite, metamorphic sole, Mirisi Unit, Akrotiri Unit and Vari Unit) that did not experience high-pressure conditions, against *HP–LT* rocks of the Cycladic Blueschists in the footwall.

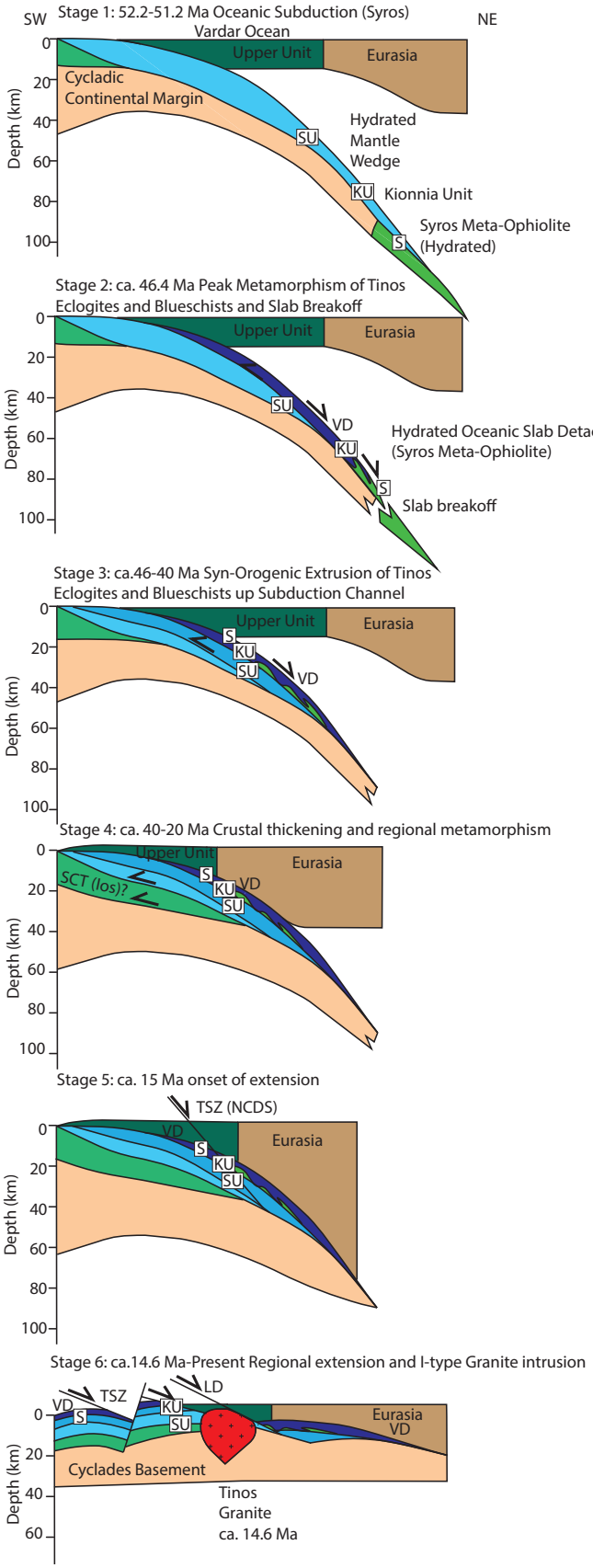


Figure 3.26: Tectonic Model for the formation of Tinos *HP* rocks, S=Syros, KU=Kionnia Unit, SU=Sostis Unit, VD=Vari Detachment TSZ=Tinos Shear Zone, SCT = South Cycladic Thrust (exposed on Ios) and LD=Livada Detachment; see text for discussion of tectonics during each stage

Chapter 4

Compressional origin to the Naxos metamorphic core complex: Structure and Metamorphism

4.1 Introduction

Metamorphic core complexes (MCCs) are generally believed to form during lithospheric extension (e.g. Lister et al., 1984; Teyssier and Whitney, 2002). However, the pre-extensional histories of many such examples worldwide are poorly understood, including those on the Cycladic islands, Greece. Metamorphic core complexes occur in a variety of tectonic settings, ranging from wholly extensional (e.g. Basin and Range Province; Coney, 1980; Armstrong, 1982; Wernicke, 1985; Yin, 1991) to purely compressional (e.g. North Himalayan Gneiss Domes; e.g., Burg et al., 1984; Lee et al., 2004, 2006) regimes, making it unlikely that they share a common mechanism of formation (Platt et al., 2014). Although the exhumation of deep-crustal metamorphic rocks by footwall unroofing beneath an extensional detachment fault is now largely accepted (Wernicke, 1981; Axen, 2007), there remains a limited understanding of the relationship between the timing of metamorphism and the onset of extensional motion (Platt et al., 2014). Furthermore, the processes driving the initiation of detachment faulting,

and whether this is associated with lithospheric-scale faulting or localized extension in a compressional environment (e.g. Searle, 2010) are debated (Fig. 4.1).

The transition from compression to extension is commonly recorded by the development of characteristic extensional structures and metamorphic assemblages that overprint older collisional features (Platt, 1986; Vanderhaeghe and Teyssier, 2001). Examples include overprinting of suture zones by low-angle extensional detachments, and the replacement of high-pressure–low-temperature metamorphic mineral assemblages by high-temperature–medium-pressure assemblages, often due to an increased basal heat flow associated with crustal thinning, e.g. Betics Rif, Spain (e.g. Platt et al., 2013). Nevertheless, Barrovian metamorphic overprints and metamorphic core complexes are characteristic features in many active orogens such as the Lepontine Dome and Tauern Window in the Alps (e.g. Smye et al., 2011 and references therein) and the Greater Himalayan Series in the Himalayan Range (e.g. Jessup et al., 2006; Searle et al., 2006). Notably, a thickened crust that formed in response to continental collision would also equilibrate along a hotter geothermal gradient, resulting in widespread regional metamorphism driven largely by the conductive relaxation of perturbed isotherms (Bickle et al., 1975; England and Richardson, 1977; England and Thompson, 1984). Although normal-sense extensional shear fabrics indeed record localized extension on their associated shear zone, they occur in zones of both overall crustal shortening and extension, and record the relative uplift and exhumation of material, rather than a specific tectonic stress regime. Extensional microstructures typically form via one of three geodynamic mechanisms: 1. buoyancy-driven extrusion of crustal material transported to depth within a subduction zone, which occurs under a passive-roof normal fault on the interface between the subducting slab and overlying mantle wedge, responsible for creating extensional fabrics in blueschists and eclogites (e.g. England and Holland, 1979; Hacker et al., 2013); 2. exhumation and extrusion of high-grade migmatites and gneisses from a deep crustal root by coeval movement of a thrust at the base and an extensional syn-orogenic normal fault at the top (e.g. the top of the Greater Himalayan Series beneath the South Tibetan Detachment system;

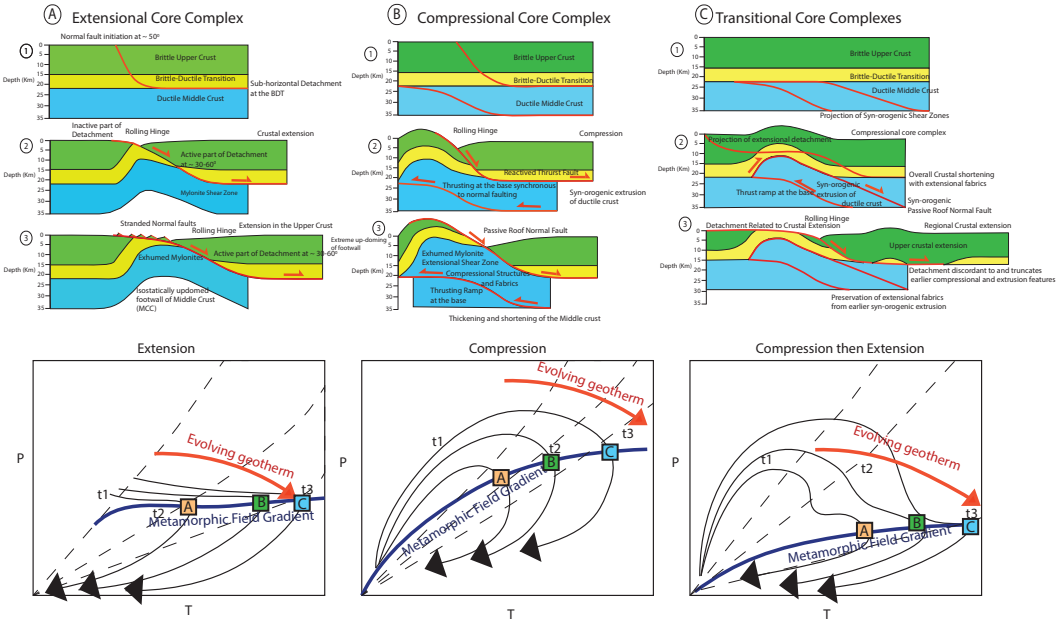


Figure 4.1: Schematic cartoon illustrating various tectonic models and P–T–t paths associated with the formation of metamorphic core complexes (after Weller et al., 2013). A cogenetic suite of P–T–t paths for three samples (A, B and C), the P–T loci of their respective T-max positions define the metamorphic field gradient, which is typically concave to the T-axis, polychronic and at a steep angle to the P–T paths of an individual sample (England and Richardson, 1977; England and Thompson, 1984; Spear, 1993): A) Classical Cordilleran style metamorphic core complex formed by simple shear extension of the entire continental lithosphere and unroofing under a low-angle normal fault (e.g. Basin and Range). Predicted P–T–t path dominantly follows an isobaric heating excursion at lower pressure due to increased basal heating. B) Compressional type metamorphic core complexes formed by doming above a thrust ramp at depth coeval with exhumation under a passive roof normal fault (e.g. North Himalayan Gneiss Domes). These record a classical Barrovian type P–T–t path with heating to peak temperatures due to radiogenic heating. C) Transitional metamorphic core complex, where compression and crustal thickening causes metamorphism and early syn-orogenic extrusion followed by the switch to regional extension responsible for the last phase of heating and exhumation. A classical Barrovian type clockwise P–T–t path followed by an isobaric heating excursion upon the onset of extension.

Law et al., 2006; Searle et al., 2006); or 3. normal faulting during crustal extension and rifting (e.g. Lister, 1984; Jolivet et al., 2010; Teyssier and Whitney, 2002; Wernicke, 1985). Mechanisms 1 and 2 occur in compressional tectonic settings, whilst mechanism 3 occurs in crustal or lithospheric extensional settings. All three processes are reported herein to have occurred on Naxos.

The Cycladic Islands in the Aegean Sea and in particular, the island of Naxos

(Fig. 4.2), expose a range of geological features that document the transition from a compressional to an extensional tectonic regime (Jansen, 1976; Jansen and Schuiling, 1976; Buick and Holland, 1989; Urai et al., 1990). Naxos also exposes the deepest structural levels of the Attic–Cycladic Massif, which experienced high-grade metamorphism, anataxis, and leucogranite formation during the Miocene. This study documents the pre-extensional, prograde, and retrograde history of the Naxos core complex, and links the timing of kyanite- and sillimanite-grade Barrovian-type metamorphism to the prevailing tectonic regime. A companion paper to this work presents the absolute ages of both compressional and extensional microstructures, which have been constrained via in-situ U–Th–Pb isotope geochronology performed on zircon, monazite, allanite, xenotime, and rutile. Finally, we assess various tectonic scenarios to explain the history of Naxos prior to extension, and conclude that the core complex formed due to prolonged compression, crustal thickening and heating prior to the switch to extension in the late Miocene.

4.2 Geology of Naxos

Naxos is the largest island in the Cyclades and shows evidence for having experienced multiple tectono-metamorphic events (see Figs. 4.2 and 4.3). It comprises a NNE–SSW elongated dome in the exhumed footwall of a major low-angle normal fault, the NPDS that developed in response to regional Aegean extension (Cao et al., 2013, 2017). The hanging wall comprises mainly ophiolitic rocks with a mélange of disrupted Miocene–Pliocene sediments (Jansen, 1973), which are possibly syn-extensional (Urai et al., 1990; Gautier and Brun., 1994a, b). Upper Pliocene conglomerates containing pebbles of footwall material have been deposited on the flanks of the dome during unroofing (Lister et al., 1984; Buick, 1991; Gautier and Brun, 1994a, b). The lower unit represents a Barrovian-type metamorphic sequence that developed during M_2 (Jansen, 1973; Jansen and Schuiling, 1976; Buick and Holland, 1989; Buick., 1991; Urai et al., 1990) reaching upper-greenschist facies in the east, (biotite zone: 5 kbar and 400°C)

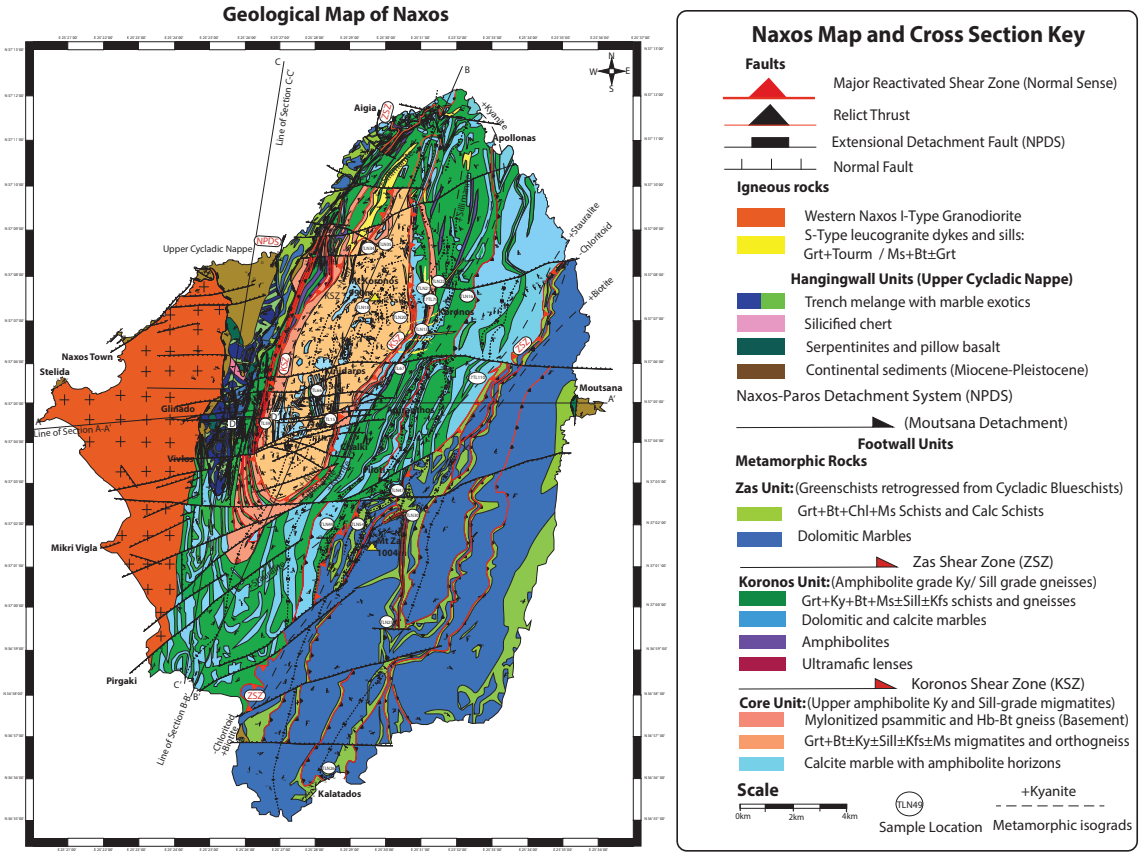


Figure 4.2: New geological map of Naxos metamorphic core complex, following previous mapping after Jansen (1973), Jansen and Schuiling (1976), Buick (1991), Urai (1991), Vanderhaugue (2001) and Kruckenberg et al., (2011). Major tectonic units within the metamorphic footwall include the Zas Unit (retrogressed Cycladic Blueschists), Koronos Unit (amphibolite facies shelf carbonates) and Core Unit (upper amphibolite facies gneisses and migmatites). See text for more discussion and interpretation. Line of section A–A' B–B' C–C' and D–D' are presented in Figs. 4.3 and 4.6.

that overprints relict (M_1) blueschist assemblages along the southeast coastline (Avigad, 1998; Peillod et al., 2017), to upper-amphibolite (M_3) anatectic conditions in the core (sillimanite zone: 7 kbar and 700°C;). In the west, an I-type granodiorite pluton with a U–Pb age of ca. 12.2 Ma intrudes the metamorphic sequence and developed a narrow metamorphic aureole (M_4) (Keay et al., 2001; Koukouvelas and Kokkalas, 2003; Jansen and Schuiling, 1976). The core region comprises highly strained M_3 sillimanite-bearing migmatites and gneisses, with intercalated marbles and leucogranites, which are separated from a lower-grade deformed sequence of Mesozoic shelf carbonates by a

major ductile shear zone, forming the carapace (the attenuated metamorphic sequence structurally above the migmatite core) to the migmatite dome. Top-to-NNE kinematic indicators are associated with this ductile shear zone that formed during exhumation of the core complex. Due to this complex deformation and metamorphic history, the development of most of the footwall structures and fabrics are poorly understood, and there is confusion as to whether they formed during crustal extension or pre-date the extensional movements and are reactivated by them (Ring et al., 2007b). Recent work has shown that the blueschist rocks on southeast Naxos experienced a contrasting metamorphic history to the underlying higher-grade rocks (Peillod et al., 2017), and there has been confusion about whether the entire island experienced (M_1) blueschist facies conditions or whether there are discrete tectono-stratigraphic units. Furthermore, the cause of regional $M_(2)$ and M_3 kyanite-sillimanite-grade metamorphism, the pre-extensional, prograde evolution of the core complex and the relative timing of peak metamorphism in relation to the onset of extension has remained controversial. Two contrasting models have been proposed for the initiation of extension. Wijbrans et al., (1993) and Parra et al., (2002) argue that extension commenced at 30 Ma (see also Jolivet et al., 2003) due to slab roll-back, followed by M_2 heating of the Cycladic blueschists (Bröcker and Franz, 1998). Alternatively, others argue for the concept of syn-orogenic extension, during underthrusting and compression in the Cyclades until 21 Ma, followed by post-orogenic extension and crustal thinning (Peillod et al., 2017; Ring and Lawyer, 2003; Ring et al., 2007a, 2007b, 2010).

Competing models have been proposed to explain the decompression of migmatites and the formation of the doubly plunging migmatite dome making up the core of Naxos. These include diapirism (Jansen and Schuiling, 1976; Vanderhaeghe, 2004), exhumation during regional extension (Gautier and Brun, 1994b), and superimposed folding from E–W shortening followed by top-to-NNE shearing (Urai et al., 1990; Buick, 1991), as well as a combination of buoyancy and isostasy-driven flow during crustal extension (Kruckenberg et al., 2011). This study presents a systematic characterization of the tectonic and metamorphic evolution of the Naxos that addresses the role of compres-

sional and extensional tectonics in formation of the core complex.

4.3 Field Relationships

Geological mapping was carried out (Figs. 4.2 and 4.3), building on previous detailed work (e.g. Jansen and Schuiling; Buick, 1991; Buick and Holland 1989; Urai et al., 1990; Vanderhauge, 2004; Kruckenberg et al., 2011), but with new and important structural interpretations (Figs. 4.3–4.9). In this section we describe each tectono-stratigraphic unit in descending structural order and discuss the major fabrics, folds and mineral growth (Figs. 4.3–4.9) in relation to the deformation.

4.3.1 Tectono-Stratigraphy

4.3.1.1 Zas Unit (Retrogressed Cycladic Blueschists)

Retrogressed blueschists exposed in the SE corner of the island (Avigad, 1998) represent the highest structural level of the metamorphic carapace. These are comprised of (M_1) blueschist and (M_2) greenschist-facies rocks derived from proximal-distal shelf and slope meta-sediments including turbidites, dolomitic marbles, pelites, meta-conglomerates and meta-volcanics. The existence of deeper sea clays is indicated by piemontite-bearing schists, which together have similarities to the Cycladic Blueschist Unit exposed on Syros, Ios, Andros and Tinos. Additional exposures of blueschist-facies assemblages can be found towards the top of the sequence, spanning the entire eastern coastline (see Figs. 4.2 and 4.3). Within this unit, there are two types of top-to-NNE extensional shear fabrics. S_1 is defined by blueschist facies assemblages including glaucophane, phengitic mica and paragonite that are preserved within only partially retrogressed high-pressure boudins, bearing many similarities to the fabric seen throughout the Cycladic Blueschists. This extensional fabric is belived to be associated with extrusion of rocks from a NE-dipping subduction zone during the Eocene and developed under passive roof normal faults such as the Vari Detachment on Syros and Sifnos (e.g. Roche et al., 2016; Laurent et al., 2016). Pelitic horizons have highly strained contacts with

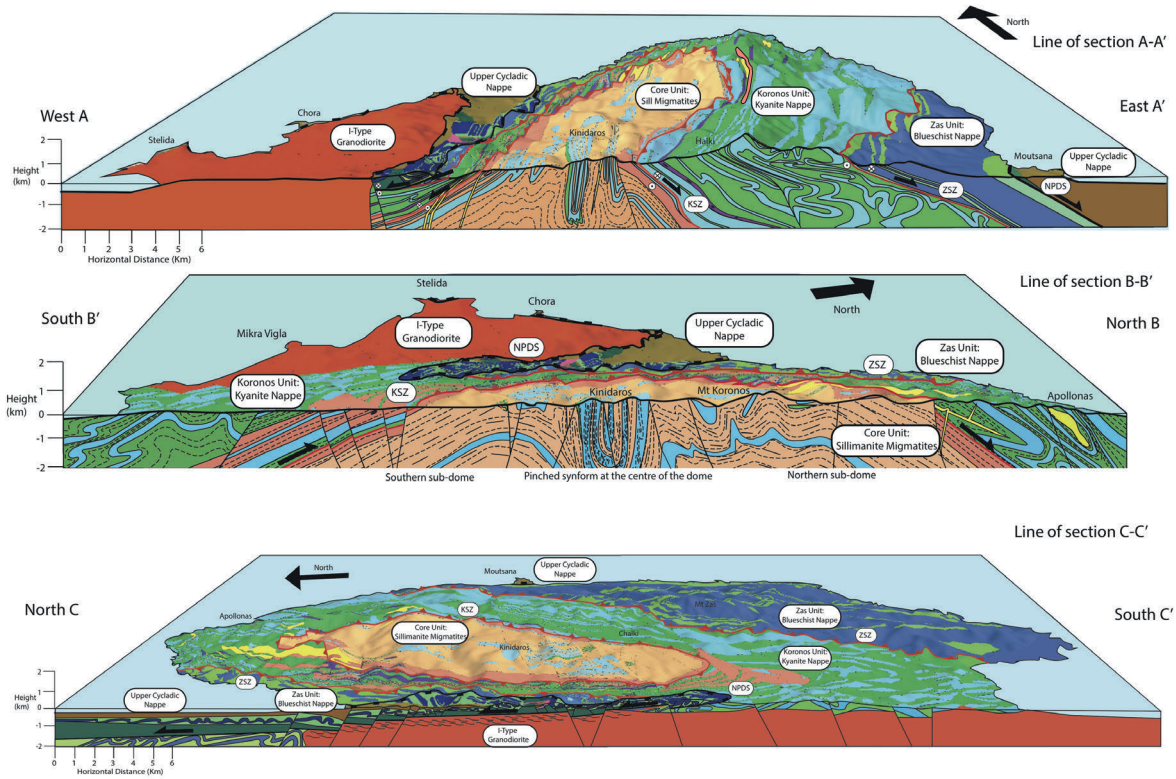


Figure 4.3: Three-dimensional models of the Naxos metamorphic core complex to illustrate structural and cross-cutting relationships, produced using the QGIS plugin 2threejs with superimposed cross-section, scale 1:1, using same color scheme for geological units as in Fig. 4.2.

dolomitic marbles that preserve internal folding and cm-scale crenulation cleavage (S_{2a}). These are overprinted and truncated by a sub-parallel highly-localized extensional S–C' shearing fabric (S_3), exclusively defined by greenshist facies assemblages. The intensity of shearing increases towards the boundaries of the unit, where major normal-sense shear-zones, the Moutsana Detachment and Zas Shear Zone, (Fig. 4.6) have developed. Along these shear zones, some discontinuous horizons of serpentinite enclaves crop out (Katzir et al., 1999, 2002), that are also affected by the (S_3) extensional foliation. These are interpreted as fragments of serpentinized mantle, from the overlying ophiolitic thrust sheet that where incorporated at low temperature during extensional shearing (S_3).

4.3.1.2 Koronos Unit (Kyanite-Grade Mesozoic Shelf Carbonates)

The Koronos Unit is a 4 km-thick metasedimentary sequence of intercalated marble and schists that represents a proximal Mesozoic shelf carbonate cover to the Cycladic Basement (Durr et al., 1978). This unit is characterized by M_2 amphibolite facies Barrovian metamorphic rocks in contrast to the overlying Zas Unit. In coarse-grained dolomitic marbles at the top of the unit, corundum (emery) and magnetite horizons represent paleosols that formed during sedimentation and sub-aerial exposure of the continental margin during the Jurassic (Altherr et al., 1979). Within the succession, meter-scale amphibolite bodies trend parallel to the regional foliation and represent doleritic sills that intruded along bedding prior to burial and metamorphism. M_2 kyanite gneisses, marbles and schists crop out at the deepest levels and the metamorphic grade dramatically decreases up structural section to staurolite and garnet-grade. At the base of this unit, slices of continental basement are exposed and are structurally repeated overlying semi pelitic schists and marbles of the shelf carbonate sequence. This indicates structural repetition of the shelf sequence, which could only be achieved by thick-skinned thrusting of the shelf and basement over more proximal continental shelf meta-sediments. Garnet and clinopyroxene-bearing amphibolites outcrop 100 m below this horizon, within the metasedimentary sequence as a semi continuous layer along strike. These enclose partially serpentinized peridotite lenses, (Katzir et al., 1998; 2002) that remained stronger during deformation as the amphibolites flow and deform around them during top-to-NNE ductile shearing (see Fig. 4.6). The intensity of top-to-NNE shearing within the unit increases towards the base, where the Koronos Shear Zone separates this unit from the underlying migmatites.

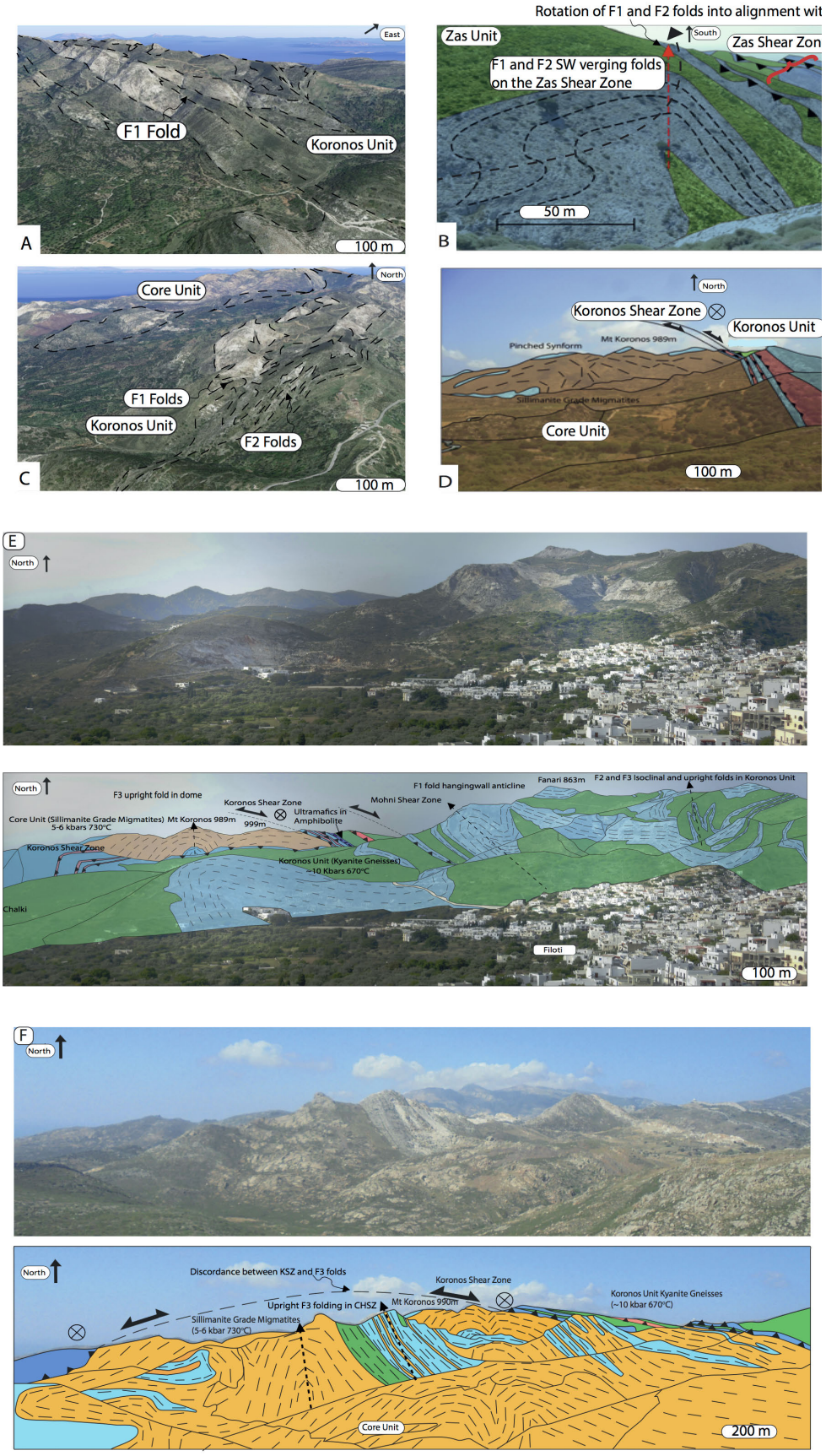


Figure 4.4: Continues on next page

Figure 4.4: Panoramic photos of folding styles on Naxos (color scheme: Green – schist, Blue – Marble, pink – Gneiss, Tan – Migmatite, Purple – Amphibolite). A) Google Earth imagery using 3D view mode to show an F_1 NE-SW verging recumbent isoclinal fold within the Koronos Unit north of the town of Filoti (N37.066816, E25.507647). B) F_1 and F_2 isoclinal and sheath folding on the Zas Shear Zone under the western flank of Mt Zas (N37.031232, E25.497227). C) Google Earth 3D view of intense F_1 and F_2 folding to the east of Filoti illustrating the F_2 isoclinal sheath type folds superimposed on early F_1 NE-SW trending isoclinal recumbent folds (N37.057519, E25.504086). D) Annotated and overlaid field sketch of the interior of the migmatite dome and the mantling Koronos Shear Zone on the eastern margin of the migmatite dome, showing the repetition of marble bands due to intense shearing (N37.092747, E25.493531). E) Panoramic annotated photograph of the folding styles within the Koronos Unit and how it contrasts to the underlying F_3 folds within the Core Unit looking north (N37.042451, E25.498678). F) Annotated panoramic photograph from the top of Apano Kastro (N37.066894, E25.459924) showing the interior structure of the migmatite dome including the Core High Strain Zone (CHSZ) marked by vertically dipping marble bands representing a tight upright F_3 folds at the center of the migmatite dome.

4.3.1.3 Core Unit (Kyanite to Sillimanite-Grade Migmatites)

The Core Unit is composed of M_2 kyanite to M_3 sillimanite-grade migmatites, gneisses and leucogranites, which make up the deepest levels of the core complex. The first-order dome structure contains second-order sub-domes (Kruckenberg et al., 2011) which are separated by a high strain zone (Core High Strain Zone) of tight upright and isoclinally folded marbles, amphibolite and migmatites that have been subsequently boudinaged. The Core Unit is separated from the overlying carapace by the Koronos Shear Zone along the dome margins (see below) (Figs. 4.3 and 4.4). Within the anatectic core, the extent of partial melting varies with bulk composition, as well as with increasing metamorphic grade. There is lithological variation throughout the migmatite zone, with banded leucocratic gneisses representing continental basement, commonly interleaved between pelitic and semi-pelitic protoliths and marbles of the shelf carbonate cover sequence. This structural repetition in lithology again provides further evidence for thick-skinned ductile thrusting and imbrication of the shelf-basement contact, during crustal thickening. Stromatic migmatites (Fig. 4.8), representing the first appearance of melt, outcrop along the perimeter of the dome or adjacent to metasedimentary rafts and are characterized by a continuous foliation marked by alternating quartzo-feldspathic and biotite layers with distinct leucosomes and melanosomes (see also Kruckenberg et

al., 2011). Leucosomes occur along the foliation marked by biotite, muscovite, and kyanite in aluminium-rich domains and increase in abundance with depth and become concentrated in fold hinges where they display magmatic textures. Leucosomes also occur in boudin necks and in shear bands that cross-cut compositional layering (S_0). At deeper structural levels, both coarse quartzo-feldspathic horizons and pockets of melt are ptygmatically folded, with melt distributed along fold hinges indicating it accumulated in dilatant structural sites during compression (Brown, 2002; Sawyer, 2001; Holness, 2008). Where evidence of melting becomes locally more extensive, particularly in pelitic horizons, diatexites are characterized by magmatic textures containing enclaves of the host rocks and are heterogeneous at outcrop and thin section scale. They include schollen, and schlieren-structured varieties (Fig. 4.8) with a magmatic foliation defined by schlieren of biotite or alignment of schollen (see also Kruckenberg et al., 2011). Although these features can be locally extensive, our observations and data reveal they are not as widespread as these authors imply. It is therefore suggested that most of the gneisses previously described as diatexites are instead granitic basement with Variscan metamorphic ages (see chapter 5). Although some diatexites do locally occur, they are confined to fertile lithologies upon crossing the K-feldspar isograd at the deepest levels of the migmatite dome.

4.3.2 Structures within the Metamorphic Core Complex

The large-scale structure of Naxos consists of a complex superimposition of three generations of km-to meter-scale isoclinal and sheath folds, overprinted and truncated by a series of normal sensed shear zones (Jansen, 1973; Buick and Holland, 1989; Urai et al., 1990; Buick, 1991). Three-dimensional models, panoramic sketches and accompanying interpretations are presented in Figs. 4.2–4.4, while structural analyses of these folds and shear zones are displayed in Figs. 4.5 and 4.6.

4.3.2.1 F_1 and F_2 Folds

Isoclinal, recumbent and non-cylindrical (F_1) folds occur mainly within the metamorphic carapace (Zas and Koronos Units) up to km-scale and trend along NNE–SSW fold axes. They are characterized by sub-horizontal hinge lines that strike parallel with the fold axes and display a SW vergence direction and hanging wall anticline geometries above discrete detachments (e.g. on the western flank of Mt Zas Fig. 4.4 and 4.5). The limbs of these folds are refolded by smaller tight to isoclinal, also NNE–SSW trending (F_2) folds and sometimes produce an overall sheath fold type geometry with their noses trending NNE–SSW, parallel to the lineation and shear direction, and are particularly well developed along the Zas Shear Zone (Fig. 4.4, 4.5 and 4.7a). Sheath folds form by progressive rotation of fold hinges and are defined by curvilinear fold axes with more than 90° of curvature (Ramsay and Huber, 1987). They initially form as isoclinal folds with axes aligned orthogonal to shear and rotate towards the transport direction under progressive non-coaxial, high strain, deformation (e.g. Cobbold and Quinquis, 1980; Ramsay and Huber, 1987; Alsop and Holdsworth, 2006;). Sheath fold formation involves: 1. initial buckling of layers, largely controlled by lithological contrasts such as between marble and schist; and 2. amplification and rotation of fold axes as shear strain increases (Alsop and Holdsworth, 2006). It has been shown that sheath folds can form under both constrictional (e.g. Ez, 2000) and 'non-constrictional' regimes (e.g. Cobbold and Quinquis, 1980; Alsop and Holdsworth, 2006). Under constriction, a bull's eye sheath fold pattern is predicted with ellipticity of the innermost ring less than that of the outermost ring, whereas under general shear, a cat's eye geometry with innermost ring ellipticity greater than that of the outer ring. During simple shear, innermost and outermost rings have similar ellipticities producing an analogous eye pattern. F_2 tight to isoclinal fold closures commonly do not show eye patterns. However, along the Zas Shear Zone, cat's eyes geometries occur indicative of general shear (a combination of simple shear and pure shear flattening). Along the perimeter of migmatite dome, these folds strongly rotate into alignment with the strong (S_3) top-to-NNE shearing fabric in the Koronos Shear Zone, indicating the structures formed during top-to-NNE

shearing (Alsop and Holdsworth, 2006). These folds preserve S_2 crenulation cleavages in their limbs with axial planar kyanite, indicating that these structures formed during M_2 conditions. Kyanite is also aligned with the pervasive S_3 NNE–SSW stretching lineation, and therefore we interpret the folds formed in two stages: 1) F_1 isoclinal folds developed during prograde burial and thickening. 2) This was followed by non-coaxial top-to-NNE general shear during exhumation, synchronous with (M_2) Barrovian conditions forming F_2 folds that produce the sheath-type geometries as shown in Fig. 4.5e.

4.3.2.2 F_3 Folds

Upright isoclinal folds (F_3) (Figs. 4.3–4.8) also occur along NNE–SSW axes parallel to the NNE–SSW lineation and have been noted by several workers on Naxos (Urai et al., 1990; Buick, 1991) and other Aegean islands including Tinos, Andros, Syros, Paros and Mykonos (e.g. Virgo et al., 2018 and references therein). These folds outcrop across all units despite spatially contrasting in style. Within the migmatitic core, an earlier generation of upright isoclinal E–W trending isoclinal folds are refolded by orthogonal to NNE–SSW trending upright structures and are defined by vertically dipping marble bands and pelitic horizons that sometimes enclose boudinaged amphibolites which have experienced polyphase micro- and macroscale folding. Although meter-scale folds in the migmatites do occur, they do not have a consistent axial trend and were probably formed by flow of partial melts (Jansen and Schuiling, 1976). Within the migmatite dome, our observations suggest that F_3 folds are completely discordant to the overlying structures and are truncated by normal faults and the Naxos Paros Detachment System that bounds the metamorphic footwall. Within migmatite, the leucosomes and kyanite blades are folded with the foliation (Figs. 4.7, Fig. 4.12b, c) by F_3 folds. This differs from the overlying carapace, where these structures range from open to tight and refold the limbs of F_1 and F_2 folds, but also have their fold axes trending parallel to the lineation (NNE–SSW) (Fig. 4.5h). Therefore, F_3 folds must post-date peak M_2 kyanite-grade conditions and F_1 and F_2 folding, yet must form in the presence of melt

and simultaneous to doming as they wrap around the core (Buick, 1991).

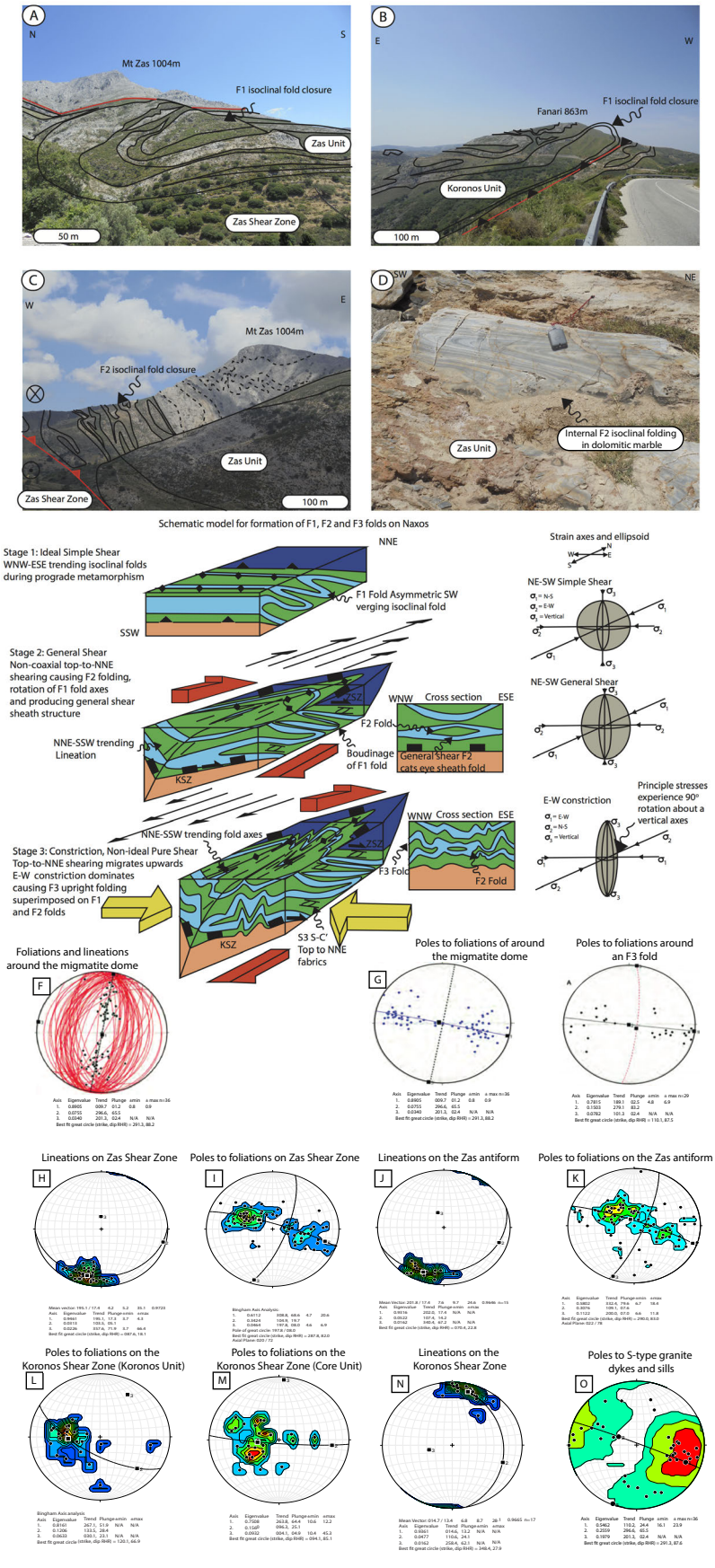


Figure 4.5: Continues on next page

Figure 4.5: Mesoscale annotated photographs of the folding geometries within the metamorphic carapace and schematic model to explain their structural relationships. A) Boundinaged F_1 isoclinal fold closures of marble bands within the Zas Shear Zone under the western flank of Mt Zas (N37.035727, E25.495403). B) Overview of folding geometries cross-cutting Fanari (863m) (N37.107506, E25.527892) showing late upright F_3 folds superimposed on early recumbent and isoclinal folds. C) Panorama looking north along strike with the Zas Shear Zone, showing tight F_2 isoclinal folds overprinting the limbs of F_1 folds, with the western face of Mt Zas to the right of the image (N37.013864, E25.480907). D) Internal isoclinal folding within dolomitic marble of the Zas Unit near Kalatados Bay (N36.935074, E25.468323), the limbs of which are detached following ductile shearing. E) Schematic cartoon showing the development of F_1, F_2 and F_3 folds on Naxos. Stage 1) NE–SW verging isoclinal folds form during the prograde evolution. 2) Non-coaxial top-to-NNE general shearing initiates and produces F_2 folds that overprint the limbs of F_1 folds and sheath type structures develop with "cats eyes". 3) Rotation of principal stress axes causes late stage E–W constriction to produce E–W trending open to tight folds. (See text for more discussion). Below: Lower hemisphere equal area stereonets of structural data from the Zas, Koronos and Core Units. F) Foliations of the migmatite southern sub-dome demonstrating a symmetric morphology to the dome. G) Poles to foliations of the migmatite dome southern subdome, demonstrating its upright symmetrical and doubling plunging nature along a NNE–SSW axes. H) Foliations and poles to foliations of an F_3 fold within the Koronos Unit highlighting its upright and isoclinal nature with a fold axes trending: 189° , 83° . I) Lineations on the Zas Shear Zone mean lineation: 195.4° , plunge 17.4° . J) Poles to foliations on Zas Shear Zone, best fit great circle: 020° , 78° . K) Lineations on the Zas Anticline on the western flank of Mt Zas, mean lineation: 201.8° , 17.4° . L) Poles to foliations on the Zas anticline, best fit axial plane: 022° , 78° . M) Koronos Unit poles to foliation, best fit great circle: 120.1° , 66.9° . N) Koronos Shear Zone poles to foliations: best fit great circle: 094.1° , 84.1° . O) Lineations on the northern segment of the Koronos shear Zone, mean lineation: 014.7° , 13.4° plunge. P) Poles to S-type granite dykes and sills emanating from the migmatite dome. On the eastern side of the Core Unit, granite dykes dip to the west and cross-cut the KSZ shear fabric, in the center of Core Unit, dykes dip vertically, whereas on the western side of the dome, they rotate into alignment with the NPDS foliation and strike sub-parallel with the lineation.

The origin of these folds has been the subject of considerable debate. Some workers have suggested that F_3 folds formed during E–W compression responsible for island-scale gentle post metamorphic E–W doming of the isograds (Buick and Holland., 1989; Urai et al., 1990; Buick 1991), whilst other studies inferred their origin to be a result of extensional shearing, as similar features are present in other extensional terrains (Hodges et al., 1987). Rey et al., (2011, 2017) and Kruckenberg et al., (2011) argue that folds in the migmatite dome developed during convergent flow and the viscous collision of two weak channels of the lower crust during regional NE–SW crustal extension. However, this mechanism cannot explain the earlier isoclinal folding, top-

to-NNE related sheath folding and upright F_3 fold geometries within the metamorphic carapace. Alternatively, Buick (1991) proposed F_3 folds within the carapace originated in their current orientation under greenschist-facies conditions, as rotation into alignment with top-to-NNE shearing would cause flattening. Based on the observation that F_3 structures fold ductile mylonite fabrics, have NNE–SSW boudinaged limbs (see Fig. 4.9) and have upright fold axes that are truncated by the NPDS, it is interpretted that they form due to significant E–W shortening that pre-dates NNE–SSW crustal extension.

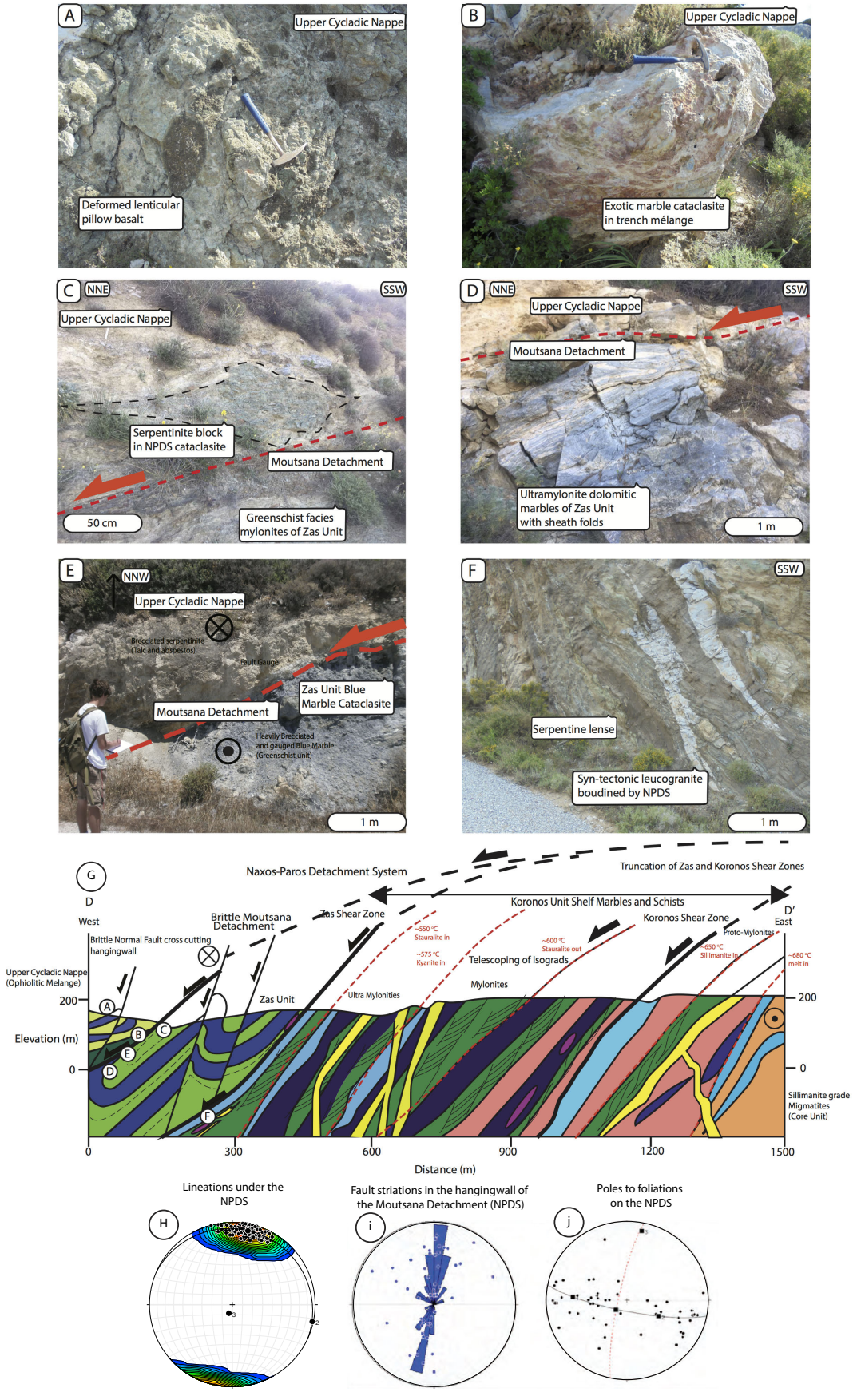


Figure 4.6: Continues on next page

Figure 4.6: Representative outcrop photographs of key features from the Upper Cycladic Nappe and Naxos-Paros-Detachment System, with small scale cross-section through the NPDS. A) Silicified and altered pillow basalt from the Trench Melange within the Upper Cycladic Nappe (N37.075998 E25. 416638). B) Exotic marble cataclasite with the trench mélange, marked by pink coloring, diagnostic of piemotite (manganese epidote) representing interlayered distal oceanic oozes (N37.077357, E25.420516). C) Outcrop of serpentine cataclasite and fault breccia and blocks from the brittle Moutsana Detachment of the NPDS (N37.071605, E25.416424). D) Ultramylonitized dolomitic marble of the Zas Unit directly under the Moutsana Detachment on west Naxos (N37.070526, E25.415716) 50 m from photo C. E) Brittle cataclasite and fault gauge of dolomitic marble from the Zas Unit against brecciated serpentinites of the Upper Cycladic Nappe, separated by the Moutsana Detachment (N37.079374, E25.428907). F) S-type leucogranite sills intruding syn-tectonically into the NPDS ductile shear zone on NW Naxos (N37.183128, E25.506907). G) Simplified cross section through the NPDS on western Naxos representing extreme telescoped isograds with metamorphic field gradients of up to 700°C/km outcrop photos are projected into the line of section. H) Lineations on mylonities from the Moutsana Detachment, mean lineation: 011.4° , 10.1° plunge. I) Rose diagram of slickenslides along normal faults in the hanging wall of the Moutsana Detachment, most faults slipping on ESE–WNW, ENE–WSW trending planes. J) Poles to Foliations of mylonities from the Moutsana Detachment Western Naxos, with best with great circle, representing a synform with its hinge line striking 012° and plunging at 14degr to the NNE, which formed due to late stage E–W shortening.

4.3.2.3 Core High-Strain Zone (CHSZ)

Three dimensional relationships of polyphase folding can be spectacularly observed in amphibolite bands within marble in the Core High-Strain Zone (CHSZ) of the Boulibas and Kinidaros Quarries, where ductile pinching and boudinage of tight upright F_3 antiforms and synforms crop out (Figs. 4.8 and 4.9). These amphibolite horizons act as strain markers and show evidence for superimposition of multiple F_3 fold geometries, vertical boudinage (i.e. boudinage with subhorizontal neck lines), horizontal NNE–SSW boudinage (i.e. boudinage with neck-lines orientated subvertically), flattening, S–C shear fabrics with opposing shear senses on opposite limbs of folds and brittle fracture. Boudinage and shear bands with opposing shear senses are orientated in the vertical and NNE–SSW horizontal planes, symmetrically arranged on the limbs of F_3 folds and aligned with their axial surfaces (Fig. 4.8 and 4.9). These indicate directions of maximum extension in the vertical and NNE–SSW horizontal planes. F_3 fold interference patterns suggest E–W trending upright isoclinal folds are refolded by tight to isoclinal NNE–SSW trending folds with vertically plunging hinge-

lines and are refolded by several scales of upright parasitic folds with N–S trending hinge lines. Intersection of these three-fold axes about a vertical point (Fig. 4.9e) suggests this structure is a Ramsay type-2 fold interference feature. Vertical boudinage affects the limbs of these folds and vertically intruded pegmatites and indicates the minimum principal stress (σ_3) was vertically orientated and much less than the horizontal stresses. These observations suggests the maximum and intermediate principal compressive stresses (σ_1 and σ_2) must have been almost equal and orientated in the horizontal plane at the time of F_3 folding and shortly following it. This indicates that bulk horizontal shortening and constriction coincided with sillimanite-grade partial melting. During this constrictional regime, the maximum principal stress σ_1 must have firstly oriented N–S to produce E–W trending folds and was subsequently rotated about a vertical axis into an E–W orientation to produce NNE–SSW trending fold axes. Finally, NNW–SSE horizontal stretching lineations, horizontal boudinage and fracture, indicative of a horizontal NNE–SSW oriented σ_3, post-dates the folding and vertical boudinage and occurred whilst the amphibolite was starting to behave in a brittle manner during cooling. These NNE–SSW horizontally boudinaged amphibolites indicate NNE–SSW extensional strains of ca. 50% by dominantly pure shear (Fig. 4.8f) with a component of simple shear as demonstrated by domino boudins (Fig. 4.8d), that show opposing shear senses on opposite limbs of F_3 folds, suggesting the shearing post-dates folding (Fig. 4.8g) (Virgo et al., 2018). Based on this evidence, NNE–SSW stretching, which is definitively related to horizontal crustal extension, must post-date upright F_3 folding and horizontal constriction, but commenced whilst the rocks were still hot enough to deform in a plastic manner shortly following peak anatectic conditions, but at temperatures when amphibolite starts to deform in a brittle manner (e.g. <640°C at 6.5 kbar; Cao et al., 2017).

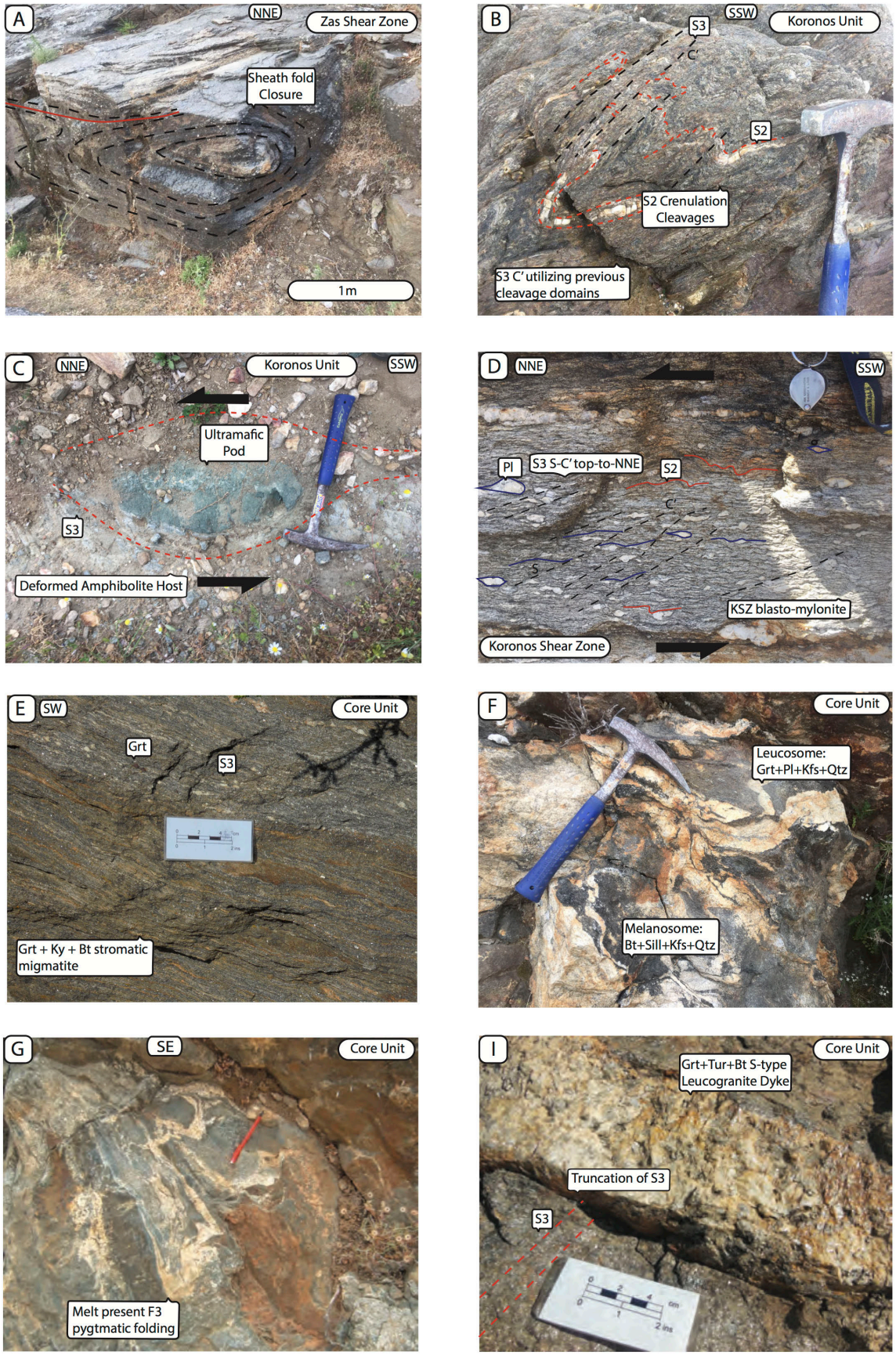


Figure 4.7: Continues on next page

Figure 4.7: Representative field outcrop photographs from intermediate levels of the Naxos metamorphic core complex. A) Cat's eye sheath fold within the Zas Shear Zone (N37.037370, E25.492597) indicative of non-coaxial general shear with fold hinge plunging to the NNE. B) S_2 Crenulation cleavages within micaceous schist from the Koronos Unit with S_3 C' planes overprinting S_2 cleavage domains (N36.932450, E25.429476). C) Ultramafic partially serpentinized pod within host foliated amphibolite from the Main Ultramafic Horizon (Katzir et al., 1999; 2002) directly structurally above the Koronos Shear Zone also characterized by top-to-NNE shear fabrics (N37.104116, E25.510806). D) Blastomylonite basement gneiss from the Koronos Shear Zone (N37.047572 E25.455538) displaying diagnostically S–C and S–C' top-to-NNE kinematic indicators and quartz rods that form σ and δ porphyroclasts with consistent shear senses. E) Foliated kyanite-grade stromatic migmatite from the perimeter of the migmatite dome (N37.060807, E25.452099) showing coarsening textures and representing the first appearance of partial melt. F) Diatexite migmatite marked by extensive melting destroying all previous fabrics, characteristic of fertile lithologies and locally extensive anatexis (N37.090701, E25.460878). G) Ptygmatically folded partial melt indicative of contractional deformation in the presence of extensive melting (N37.091540, E25.459035). H) Garnet + tourmaline + biotite leucogranite sill cross-cutting the extensional top-to-NNE S_3 shear fabric at the perimeter of the migmatite dome (N37.067065, E25.447091).

These interpretations agree with Virgo et al., (2018) and Von Hagke et al., (2018), who demonstrated that there are five generations of boudinage and that vertical boudins formed first which are overprinted by later NNE–SSW horizontal boudins. Vertical boudinage includes two generations of pinch and-swell boudins, the first with a longer and the second with a shorter wavelength. These features are followed by NNE–SSW horizontal domino boudins, torn boudins and hairline veins reflecting embrittlement of the amphibolite layers associated with retrograde cooling and exhumation. These studies also demonstrated that outcrop-scale parasitic asymmetric folds predate torn boudins and hairline veins, whereas domino boudins indicate locally deviating shear sense on opposite limbs of F_3 folds (Fig. 4.8g). Virgo et al., (2018) and Von Hagke et al., (2018) conclude that long-wavelength pinch-and swell boudins (i.e. vertically orientated boudinage) are consistent with syn-migmatic flow and F_3 folding in the surrounding rocks and note that static recrystallization in the amphibolite must post-date vertical boudinage. Based on the above reasoning and the synchronicity between upright F_3 folding, vertical boudinage and migmatization, we also agree that static recrystallization must post-date upright F_3 folding and horizontal constriction at the centre of the migmatite dome, but annealing was due to high-temperatures outlasting

contractional deformation during M_2, and prior to NNE–SSW extensional deformation. We therefore propose that the CHSZ documents a major rotation in principal stress axes from bulk horizontal shortening and constriction to NNE–SSW extension during the close of the M_3 event in the presence of partial melt.

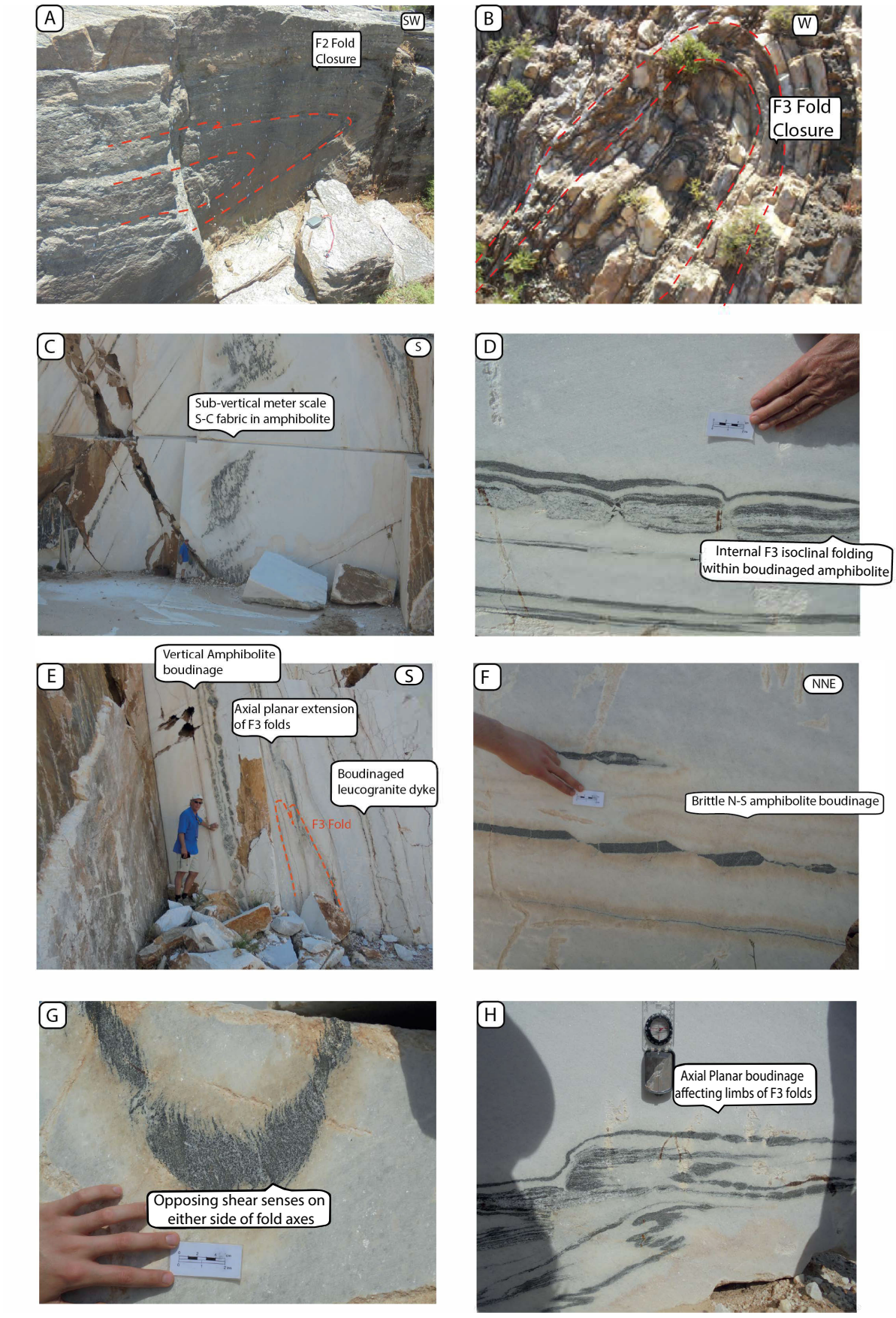


Figure 4.8: Continues on next page

Figure 4.8: Outcrop photographs of characteristic deformation from deep levels of the core complex. A) F_2 fold closure within graphitic schist of the Koronos Unit looking NNE (N37.100354, E25.517359). B) F_3 upright isoclinal fold closure trending NNE–SSW within the migmatite dome (N37.095943, E25.468734). C) Deformation within the Core High Strain Zone (CHSZ) (N37.106237, E25.482500), subvertical meter scale S–C fabrics in amphibolites that have been later boudinaged both vertically and horizontally N–S. D) Horizontally boudinaged amphibolites and leucogranites from the Core High Strain Zone (N37.107807, E25.482510), that shows internal cm scale isoclinal folds. E) Upright folded amphibolites along NNE–SSW axes, with vertically boudinaged amphibolites and also a leucogranite dyke diagnostic of horizontal constriction (N37.108102, E25.483013), within the center of the Naxos migmatite dome. F) Horizontal extension and boudinage indicated by amphibolites show 50% pure shear and brittle simple shear in the amphibolites, with anticlockwise rotation. G) S–C extensional fabrics overprinting F_3 folds of amphibolites, aligned axial planar with the vertical fold. H) Extensional axial planar boudinage and shearing fabrics overprinting F_3 intensely and isoclinally folded amphibolites (N37.107807, E25.482510).

4.3.3 Extensional Shear Zones

Although extensional (S_3) top-to-NNE shearing is penetrative throughout the entire metamorphic carapace (Zas and Koronos Units), there is petrological and geochronological evidence that the fabrics formed at different times and at different conditions across Naxos. Discrete shear zones represented by ultramylonites, separate each tectonostratigraphic unit and are truncated by the geometry of the Naxos Paros Detachment System (NPDS). These are now described in chronological order from structurally deep to shallow.

4.3.3.1 Koronos Shear Zone (KSZ)

The Koronos Shear Zone (KSZ) is a normal sensed NNE–SSW trending shear zone that wraps around and is folded by the underlying migmatite dome. It represents the basal contact of the highly strained metamorphic carapace mantling the migmatite dome and places the kyanite-grade Koronos Unit against relatively less sheared migmatites of the Core Unit. Immediately around the dome margins, the migmatitic foliation is concordant with the overlying carapace; however, over less than 100 m down structural section, this foliation becomes highly discordant, where F_3 upright folds and km-scale sub-domes can be traced along the migmatitic foliation (Kruckenberg et al. 2011). This abrupt truncation in foliation and its gradual rotation into alignment with the

enveloping Koronos Unit suggests the presence of a major tectonic boundary along the migmatite–gneiss contact, characterized by extreme grain size reduction. High-temperature blastomylonites, feldspar plasticity, grain boundary migration and chess-board extinction of quartz indicate deformation temperatures exceeding 600°C (Figs. 4.7 and 4.11). Strain analysis of kinematic indicators implies overall general shear (a combination of NNE–SSW simple shear and E–W pure shear) suggesting a large component of flattening perpendicular to this shear zone coeval with definitively top-to-NNE kinematics on all dome margins in both northern and southern Naxos. This strongly indicates this shear zone is folded by the doming migmatites and therefore its movement pre-dates migmatite dome formation.

Along the east and west margins of the migmatite dome, leucogranitic sills and dykes increase in abundance and emanate from the underlying migmatites (Vanderhauge, 2004). These sills and dykes commonly truncate the S_3 mylonite foliation, suggesting they intruded synchronously with or post-date high-temperature shearing on the KSZ, whereas on Western Naxos they rotate about a NNE–SSW horizontal axis into alignment with the NPDS (see below and Fig. 4.5p). These dykes appear to have been rotated by ca. 45° due to later doming of all fabrics. Domains of less strained material unaffected by penetrative (S_3) S–C' fabrics reveal earlier folding, (S_{2a}) crenulation cleavages and (S_{2b}) cleavage domains that display top-to sigma porphyroclasts with opposing top-to-SW shear senses (see Fig. 4.7), signifying structural reactivation at high-grade conditions. Structural imbrication and preservation of relict thrust features are inferred from thin marble bands along the KSZ that display tight to isoclinal internal folding bounded by highly strained intercalated schists that has localized the deformation due to the competency contrast with the stronger marbles (see Fig. 4.7). Imbricated slices of the same marble horizon can be identified by abrupt change in foliation across strike and splay off the main detachment horizon.

Slices of orthogneisses basement underlying the shelf-sequence are structurally repeated and overlie metasediments and amphibolites at the upper levels of the shear zone. This, combined with microstructural evidence, suggests the Koronos Shear Zone

possibly represents a relict SW verging thick-skinned thrust that was one of presumably many thrusts responsible for thickening of the continental margin. These structures imply crustal shortening and thickening was extensive across Naxos and possibly lead to regional Barrovian metamorphism. The compressional features and thrusts were then reactivated as a normal sensed shear zones during the exhumation of the migmatites from (M_2) kyanite to (M_3) sillimanite-grade conditions in the footwall.

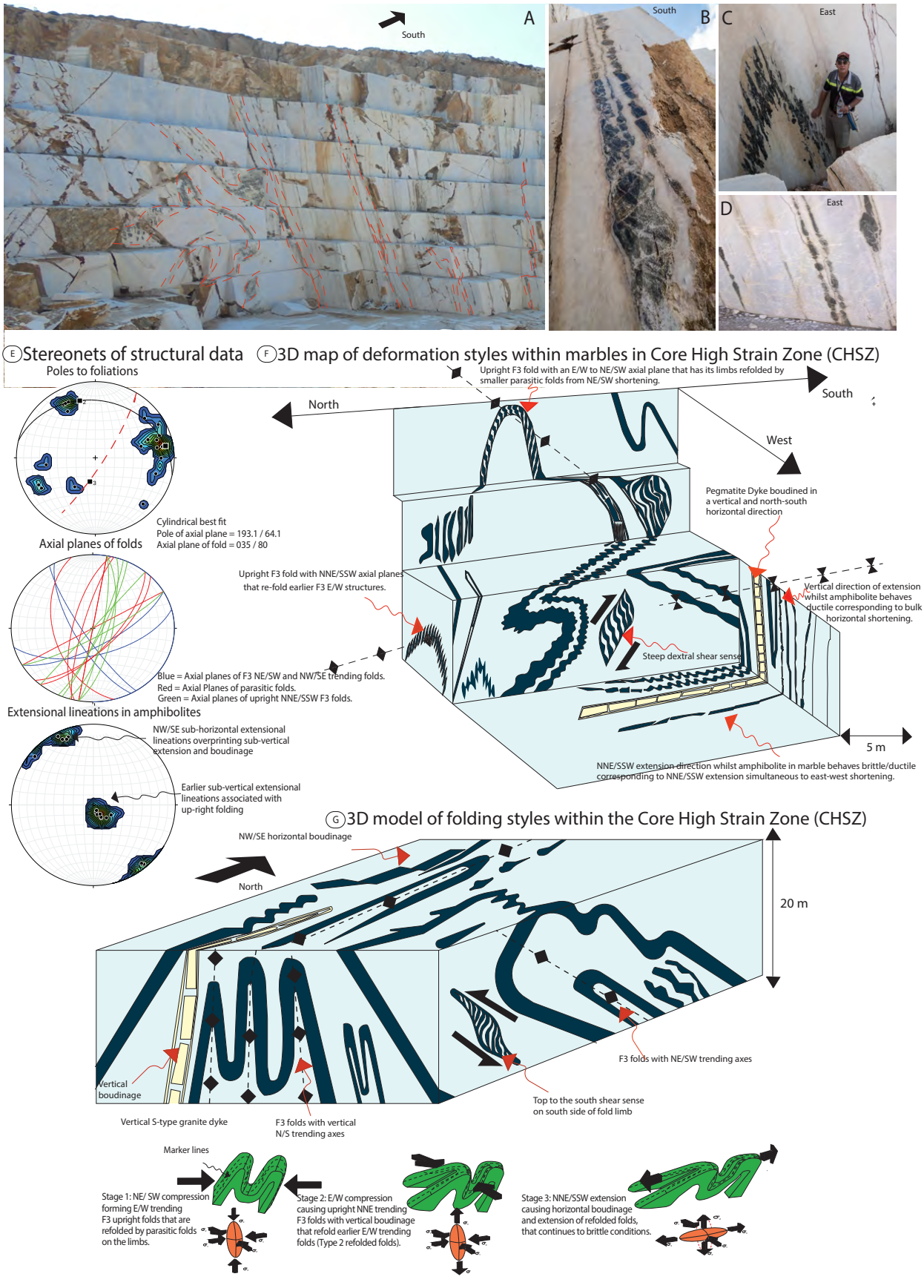


Figure 4.9: Continues on next page

Figure 4.9: Core High Strain Zone at the center of the migmatite dome (N37.108102 E25.483013), with overview photograph, and outcrop photographs of the boudinage, stereonets and three-dimensional outcrop map and model to show the key deformation and structural features. A) Overview photograph showing the three-dimensional exposure of the Kinidaros Quarry and deformation the CHSZ. B) Vertical ductile boudinage of amphibolites, with a domino style more brittle overprint C) Upright E–W trending F_3 fold with vertical boudinage overprinting its limbs. D) Pinch and swell boudinage affecting limbs of an E–W trending F_3 fold. E) Stereonets of structural data displaying poles to foliations, axial planes of folds and extensional lineations. Note the intersection of axial planes of folds represent an overall vertically orientated sheath fold with bimodal vertically and NNW–SSE orientated stretching lineations and boudinage. C) Three-dimensional map of deformation within the CHSZ, highlighting the structural superposition of three fold generations in relation to the intrusion of a leucogranite dyke and vertical and horizontal stretching. Note that dyke intrusion post-dates all folding and pre-dates shearing and vertical and horizontal boudinage. D) Three-dimensional block model of deformation structures within the CHSZ, F_1 and F_2 isoclinal folding overprinted by F_3 tight-isoclinal upright folds along NNE–SSW trending axes.

4.3.3.2 Zas Shear Zone (ZSZ)

A NE–SW trending greenschist-facies shear zone cuts through the flank of Mt Zas juxtaposing the greenschist-facies (relict blueschists) Zas Unit against the underlying kyanite-grade Koronos Unit and can be traced over 20 km along strike (Figs. 4.2 and 4.3). This structure is associated with an increase in mylonitization over a 500 m zone overprinting and truncating F_1 and F_2 structures. These folds rotate into alignment with the shear zone, producing sheath folds with their noses pointing parallel to the lineation (NE–SW) in agreement with Buick, (1991). This structure could represent a re-activated thrust originally placing the Cycladic Blueschist Unit onto the underlying more proximal sedimentary cover (Koronos Unit), as relict (F_1) hanging wall anticlines, S_2 crenulation cleavages and relict top-to-SW S–C fabrics are preserved in micaceous domains and in within greenschist facies porphroblasts (see Figs. 4.5 and 4.12). S–C' mylonites are associated with top-to-NNE (S_3) shearing and exclusively affect greenschist-facies assemblages. These structures signify extensional reactivation during the close of regional (M_2) conditions at temperatures of 280–450°C as demonstrated by subgrain rotation and bulging of quartz grain microstructures (Stipp et al., 2002b).

4.3.3.3 Naxos-Paros-Detachment System (NPDS)

The NPDS records the evolution of a ductile shear zone from solely brittle deformation at the top to completely ductile deformation beneath a few hundred meters (Buick, 1991). This detachment horizon truncates all compressional structures (Fig. 4.2) and is gently folded along a NNE–SSW axis, and potentially bounds the entire island if the the outcrop at Moutsana Peninsular represents the same structure. The brittle fault (Moutsana Detachment; Cao et al., 2013, 2017) and its associated deformation is best exposed in the NW and central Naxos (near the towns of Melanes and Galanado; Fig. 4.2) and on the eastern coastline at Moutsana peninsular. Numerous brittle high-angle faults root into the fault horizon, which is associated with a 20 m cataclasite and fault breccia zone including pseudotachylites and grades into ductile mylonites. The fault surface is commonly steeply dipping at ca. 40° perpendicular to the transport direction and is associated with a NNE shallowly plunging lineation which is oblique to the foliation, consistent with a lateral ramp geometry. In central Naxos, the detachment is folded into a gently northerly plunging synform (see Fig. 4.6g), causing the non-metamorphic hanging wall to be exposed in a graben type structure that is bounded by steep late cross-cutting E–W trending normal and NE–SW and NW–SE trending strike slip faults (see Fig. 4.2), juxtaposing the granodiorite to the west and the metamorphic sequence to the east (see Fig. 4.2 and Fig. 4.3). This doming also affects the Pliocene-Pleistocene sedimentary successions within the hanging wall of the NPDS and requires a component of E–W shortening during and after movement on this structure, that was also responsible for folding the isograds and development of minor brittle thrust faults.

Beneath this low-angle normal fault, right way-up regional metamorphic isograds are telescoped and affected by flattening, indicating the fault cut through metamorphic stratigraphy (Fig. 4.6g). On West Naxos, brittle deformed cataclasites and sediments are juxtaposed against upper amphibolite-grade migmatites, a transition of 700°C within 1000 m across strike, revealing frozen-in metamorphic field gradients of up to ca. 700°C/km. Although S–C' fabrics (S_3) affect all structural levels of the

footwall, there is a larger intensity of shearing fabric development on this structure. Quartz microstructures indicate dynamic recrystallization occurred via a spectrum of deformation mechanisms from subgrain rotation, bulging to brittle deformation indicative of deformation temperatures less than ca. 500°C (Stipp et al., 2002a). Over 95% of samples demonstrate top-to-NNE kinematic indicators by asymmetrical alpha and delta porphyroclasts of biotite, kyanite, plagioclase and garnet, in agreement with Urai et al., (1990) and Buick (1991). We interpret this brittle-ductile shear zone to be related to crustal extension and exhumation, as brittle normal faults root into it and it clearly post-dates, is discordant to, and truncates all compressional and metamorphic features. The west Naxos I-type-granodiorite is mylonitized on its eastern margin indicating the fault was active during crystallization at ca. 12.2 Ma (Keay et al., 2001). The NPDS presumably represents a similar structure to the North Cycladic Detachment System on Mykonos, Tinos and Andros (e.g. Jolivet et al., 2010, 2012) in accommodating regional crustal extension by top-to-NNE shearing along a localized zone on the brittle–ductile transition.

In contrast to the NPDS, the extensional fabrics in the ZSZ and the KSZ and condensation of right way up high-grade metamorphic isograds, are purely ductile features that are concordant to the island scale foliation. The structural discordance between these internal shear zones and the brittle-ductile NPDS (Fig. 4.2 and 4.3) suggests movement on the KSZ and ZSZ pre-date movement on the NPDS and therefore record the early stages of exhumation in the mid-lower crust prior to migmatite doming and regional NNE–SSW Aegean extension.

4.3.4 Structures outside the Metamorphic Core Complex:

4.3.4.1 Upper Cycladic Nappe (Trench Melange)

In western central Naxos, a largely dismembered sequence of ophiolitic material comprising hydrothermally altered pillow basalts, serpentinites and oceanic sediments including cherts with manganese-nodules outcrops in the hanging-wall of the NPDS that

transects central Naxos (Jansen and Schuiling., 1976; Vanderhaugue, 2004). Structurally above this a disturbed sequence of Nummulite-bearing dolomitic limestones / marbles, chloritized-schists and randomly orientated exotic-blocks of marble and volcanic debris (Fig. 4.6). These field relations have been previously attributed to a "km-scale gravity slide" derived from the footwall of this detachment system (Vanderhaeghe, 2004; Kruckenberg et al., 2011). Although this could explain the wide variety of rock types, randomly orientated metamorphic boulders and evidence for paleo-karstification, the extreme folding and entrainment of a variety of ophiolitic and distal oceanic material as blocks within a serpentine matrix bears many similarities to the ophiolitic mélanges of the Oman-UAE ophiolite (Searle and Cox, 1999; 2002). We tentatively suggest that this sequence represents a tectonic mélange formed in a trench environment and was deformed during SW obduction of an ophiolite prior to Eocene subduction of the continental margin. Although scattered remains of upper ophiolitic material is distributed across the Cyclades at high structural levels (Katzir et al., 1996; Hinskin et al., 2017), ophiolite stratigraphy including mantle peridotite, gabbro, plagiogranite and metamorphic sole are exposed on Tinos island (chapter 2)), implying that the ophiolite may have been widespread as the highest structural nappe across the entire Cyclades. The Miocene to Pleistocene sedimentary successions are un-conformably laid on top of this mélange, and are composed of fluvial conglomerates, in some cases with boulders and clasts of a variety of ophiolitic and metamorphic material derived from the footwall. The sedimentary rocks dip at 30° away from the core complex, which is inconsistent with the dip predicted by normal faulting. Clearly these sediments must have been rotated by gentle doming of the island during the Pliocene-Pleistocene and therefore calls for a significant component of E–W shortening after the core complex was exhumed. The I-type granodiorite has aplitic sills that are folded along an N–S trending axis also suggesting significant E–W shortening during and following crystallization at ca. 12.2 Ma.

Stage	Lithology	Location	Unit	P-T conditions	Associated uncertainty	Method	Study
Peak M2	Metapelite	Migmatite dome	Core	6-7 kbar, 670	± 2 kbar, ± 50	Conventional thermobarometry	Jansen and Schuiling., (1976)
Peak M2	Metapelite	Carapace	Koronos-Zas	5-7 kbar, 400-670	± 2 kbar, ± 50	Conventional thermobarometry	Jansen and Schuiling., (1976)
Prograde M2	Metapelite	Migmatite dome	Core	8.0-9.7 kbar, 600	± 2 kbar, ± 50	Holland and Powell, (1988)	Buick and Holland., (1989)
Peak M2	Metapelite	Migmatite dome	Core	6-8 kbar, 690	± 2 kbar, ± 50	Holland and Powell, (1988)	Buick and Holland., (1989)
Prograde M2	Metapelite	Carapace	Koronos-Zas	10 kbar, 500	± 1-2 kbar, ± 50	Grt-Bt, GASP	Deuchene et al., (2006)
Peak M2	Metapelite	Migmatite dome	Core	6-7 kbar, 700	± 1-2 kbar, ± 50	Grt-Bt, GASP	Deuchene et al., (2006)
Peak M2	Ultramafic	Carapace	Koronos	700-800	± 50	Opx-Cpx thermometry	Katzir et al., (1999)
Peak M1	Metabasite	SE Naxos	Zas	12 kbar, 470	± 2 kbar, ± 50	THERMOCALC Average P-T	Avigad, (1998)
Peak M1	Diaspore	East Naxos	Zas	¿12kbar, 450	± 2 kbar, ± 50	Diaspore-Corrundum	Feenstra, (1985)
Peak M1	Metabaite	SE Naxos	Zas	15.5 kbar, 576	±0.5 kbar, ± 16	THERMOCALC Average P-T	Peillod et al., (2017)
Peak M2	Metabaite	SE Naxos	Zas	16.5 kbar, 619	±0.9 kbar, ± 32	THERMOCALC Average P-T	Peillod et al., (2017)
Retrograde M2	Metabaite	SE Naxos	Zas	3.8 kbar, 384	±1.1 kbar, ± 30	THERMOCALC Average P-T	Peillod et al., (2017)

Table 4.1: Compilation of previous *P-T* estimates for various stages of deformation and metamorphism on Naxos

4.4 Petrography and mineral chemistry

Blueschist, gneiss, and migmatite samples used in this study were collected at various structural levels of the Naxos MCC to investigate spatial variations in the *P–T* conditions of peak metamorphism. The analytical techniques and procedures utilized to collect mineral composition data are outlined in Appendix 1 Mineral abbreviations follow the guidelines of Whitney and Evans (2010) and migmatite terminology is after Ashworth (1985). Anhydrous phase compositions were calculated to standard numbers of oxygen per formula unit (Deer et al., 1992), micas were recalculated to 11 oxygens, and chlorite to 28 oxygens. Where present, H_2O content was assumed to occur in stoichiometric amounts. The proportion of Fe^{3+}/Fetotal was calculated using AX (Holland, 2009) and amphibole exchange vectors were calculated using the method of Holland and Blundy, (1994). Representative photomicrographs, backscattered electron images and mineral compositions are shown for the Zas Unit in Fig. 11, the Koronos Unit in Fig. 4.11, and the Core Unit in Fig. 4.12. A summary of the relative timings of fabric development is displayed in Fig. 14, and garnet maps and line profiles from samples TL67, TL15 and TL66 are presented in Fig. 4.14, Tables 4.2–4.4, and the further analysis in Appendix 1.

4.4.1 Petrography of the Zas Unit

All samples in this unit display microstructural evidence for M_2 greenschist facies overprinting of older M_1 blueschist facies mineral assemblages and fabrics, with replacement

spatially concentrated along zones of fluid alteration. M_1 high-pressure precursors occur as prograde inclusions or as relict matrix phases that have been pseudomorphed or trapped inside late lower-grade minerals. Glaucophane is unzoned and is preserved within the cores of epidote grains, with phengitic and paragonitic white mica, clinozoisite and no plagioclase and also along unaltered microstructural domains and foliations (Fig. 4.10a, c, g, i).

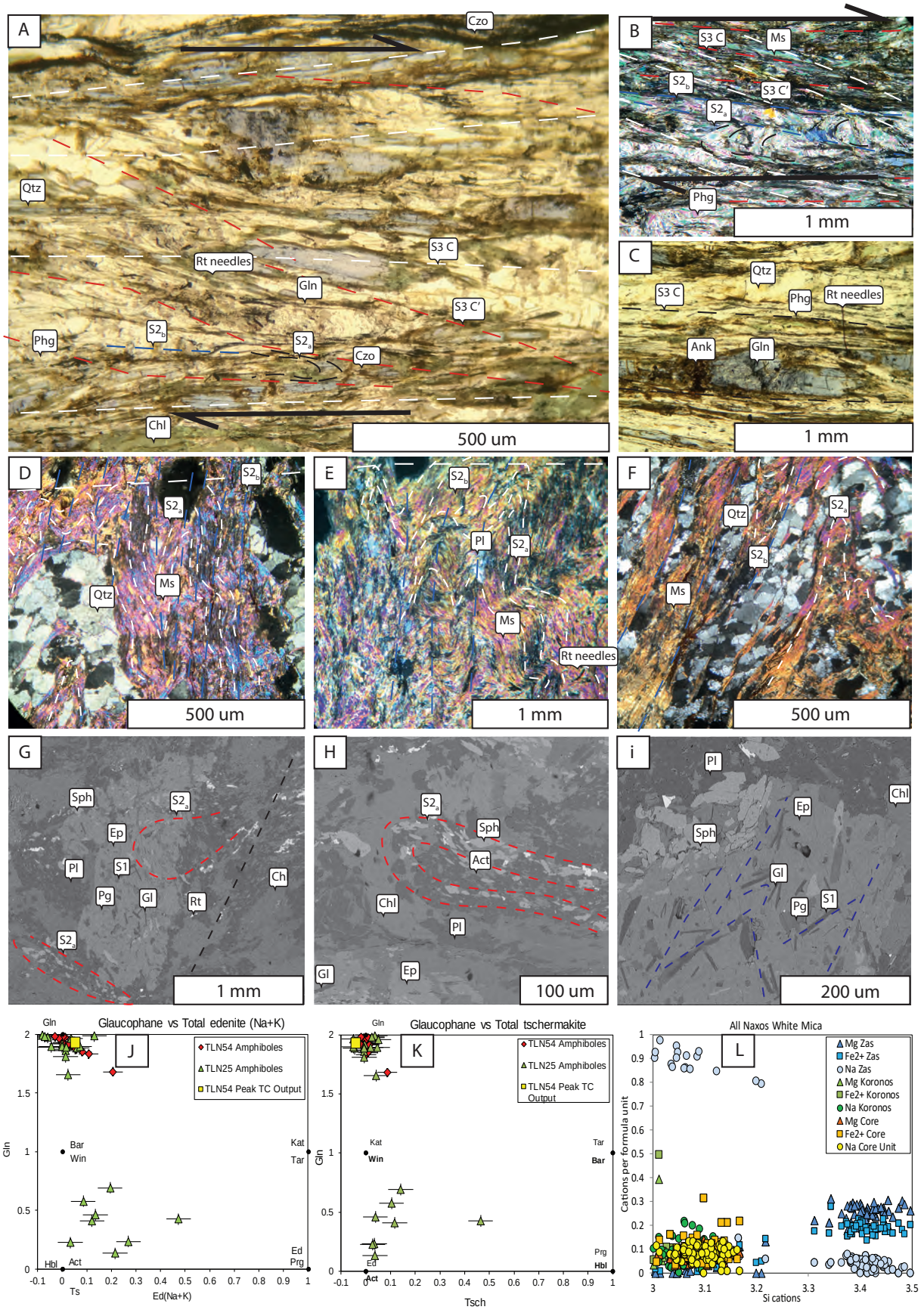


Figure 4.10: Continues on next page

Figure 4.10: Representative photomicrographs, backscattered electron images of Zas Unit microstructures and mineral chemistry. A, B and C) TLN54 (meta-tuff) glaucophane phengite schist displaying well preserved glaucophanes aligned with S_1 top-to-NNE shearing fabrics, but also affected by S_3 top-to-NNE S–C' fabrics that affect both M_1 and M_2 assemblages. In lower strained domains S_{2a} and S_{2b} crenulation cleavages can be identified by folded bands of rutile needles, titanite phengite and plagioclase suggesting S_2 post-dates high-pressure conditions. D, E and F) A quartz mica schist displaying well developed S_2 microstructures including mm-scale isoclinal folds and S_{2a} crenulation cleavages, with no evidence for S_3. This greenschist assemblages implies that S_2 fabrics also developed during M_2. G) TLN25 (Zas Unit) calcshist, epidote traps earlier S_{2a} fabric and microfolding defined by phengitic mica, actinolite and titanite. Inclusions of glaucophane and paragonite in epidote represent M_1 conditions and outline S_1 fabrics. S_3 top-to-NNE extensional S–C' fabrics affect matrix assemblages including actinolite, chlorite and plagioclase. H) TLN25, backscattered image showing S_2 microfolded fabric that is defined by grains of titanite, formed after peak M_1 conditions and predating greenschist facies shearing. This implies that S_2 crenulation cleavages formed at upper greenschist facies conditions on the retrograde part of the P–T loop. H) TLN25, zoomed in backscattered image of M_1 inclusions in epidote defined by glaucophane and paragonite, which preserve S_1 S–C shear fabric, small inclusions of sphene are also included in epidote, although coarse sphene grows externally. J) Glaucophane vs Total Edenite for Zas Unit samples plotting solely in the bottom left hand corner diagnostic of low temperature high pressure amphibole. K) Glaucophane vs Total Tschermakite for Zas Unit Samples TLN54 and TLN25 showing the range from actinolite to glaucophane compositions, with TLN54 modelled glaucophane composition for comparison. L) All Naxos white mica, note the distinctive tri-modal population of data, with high Si>3.4 pfu represents high pressure phengite solely within the Zas Unit, high Na>0.9 pfu is characteristic of paragonite again only within the Zas Unit, whereas Koronos and Core Units represent one mica population characteristic of Barrovian M_2 conditions.

All mineral compositional trends are displayed in Fig. 4.10j, k, l, and highlight the high Na and low Al content of primary amphibole, high Si pfu of mica, indicative of phengitic compositions, and paragonite that is characteristic of blueschist facies conditions. A subsidiary population of actinolite is confined to the matrix, and characterizes the M_2 greenschist facies overprint. Late cross-cutting greenschist-facies minerals are well developed in lesser-strained domains within the pre-existing foliation, presumably from the breakdown of large porphyroblasts such as garnet to form epidote, plagioclase, chlorite, tremolite and actinolite (Fig. 4.10g, h). Sodic amphiboles occur mainly as small prismatic inclusions in epidote and commonly display decussate-shear textures that could be associated with top-to-NE shearing during exhumation from blueschist facies (S_1) (Fig. 4.10a, c, g, i). This is aligned sub-parallel to the pervasive greenschist facies top-to-NNE extensional fabric (S_3) that solely affects the surrounding quartz-

mica rich matrix. In low-strain domains, blueschist- to greenschist-facies assemblages containing phengitic muscovite, paragonite, biotite, plagioclase, green amphibole and cloudy plagioclase are deformed in crenulation cleavages (S_2) that forms a continuous fabric as inclusions throughout epidotes, with preserved microlithons (S_{2a}) and cleavage domains (S_{2b}) (Fig. 4.10b, d, e, f, g, h). These grains are rimmed by retrograde plagioclase and chlorite, indicating they are most likely associated with decompression from high-pressure conditions. S_{2a} is also associated with cm-scale isoclinal folding, with well-developed microlithons that act as parasitic folds on the limbs of larger scale folds (see Fig. 4.10f). S_{2a} and S_{2b} presumably formed by shortening along two orthogonal axes at upper greenschist facies conditions but predates the characteristic lower pressure retrograde M_2 greenschist assemblage. We therefore relate S_2 fabrics to overthrusting and ductile stacking of high-pressure nappes at crustal depths that post-dates high-pressure conditions.

S_2 fabrics contrasts to the more localized top-to-NNE S–C' shearing fabric (S_3) that purely affects greenschist facies assemblages including quartz, mica, plagioclase and chlorite rich domains. S_3 mylonite fabrics are heterogeneous and localized along discrete shear zones. It is particularly developed in samples taken from the ZSZ, in a parallel orientation to the fold axial planes, and appears to utilize S_{2b} cleavage domains. Microstructurally, S_3 deforms the quartz, fine grained mica rich matrix around pre-tectonic greenschist-facies porphyroclasts including clinozoisite, epidote and late cross-cutting muscovites, creating strain shadows, asymmetrical boundinage and rotation of the porphyroclasts (Fig. 4.10a, b, c). Dynamic recrystallization via subgrain rotation and bulging, is persistent within quartz rich domains indicating deformation temperatures must have not have exceeded 450°C (Stipp et al., 2002a, b). Due to these relationships, we interpret S_3 as a purely retrograde feature post-dating (M_1) high-pressure and (M_2) greenschist facies conditions and related to exhumation of the core complex through the brittle-ductile transition (Buick 1989, Urai et al., 1990, Avigad, 1998).

Sample	TLN25	TLN25	TLN25	TLN25	TLN25	TLN25	TLN25	TLN25	TLN25	TLN25	TLN25	TLN25	TLN54	TLN54	TLN54	TLN54	TLN54	TLN54	TLN54	TLN54	TLN26	TLN26	TLN26	TLN26	TLN26	TLN26
Mineral	Prg	Prg	Ms	Ms	Ep	Pl	Bt	Ta	Ta	Amp	Amp	Amp	Amp	Amp	Amp	Chl	Ph	Ph	Prg	Pl	Chl	Ph	Ph	Ms	Prg	Pl
SiO2	49.12	47.82	49.4	48.01	38.53	62.3	40.82	62.68	63.05	58.66	59.65	56.89	55.94	57.04	56.66	25.63	50.10	49.01	48.22	68.59	24.84	50.64	50.96	49.12	47.20	68.08
TiO2	0.28	0.25	0.32	0.17	0	0	0.78	0.07	0.2	0.07	0.08	0.03	0.13	0.08	0.11	0.07	0.52	0.27	0.1	0.07	0.23	0.15	0	0.63	0.28	0.00
Al2O3	38.6	39.79	25.81	26.6	25.34	20.73	15.8	0.7	0.25	9.77	8.48	1.51	10.71	10.89	10.92	19.50	26.49	27.02	37.73	18.8	20.27	25.39	25.21	26.66	33.35	19.59
FeO	0.66	0.62	3.63	3.98	8.53	2.43	14.42	7.02	6.83	12.87	13.23	10.64	15.48	14.51	14.67	29.91	3.53	3.41	0.14	0.45	28.2	3.64	3.56	2.86	1.31	0.00
MnO	0.03	0	0	0	0.28	0.09	0.18	0	0	0.17	0.00	0.00	0.07	0.00	0.06	0.32	0.00	0	0.06	0	0	0	0.14	0.15	0.06	0.05
MgO	0.56	0.08	2.98	2.72	0.25	0.45	16.28	26.73	26.5	8.91	10.26	17.23	6.65	6.85	6.98	11.43	1.89	1.86	0.63	0.17	12.4	2.69	2.55	2.67	1.13	0.33
CaO	0.21	0.31	0	0.22	23.48	5.65	0.34	0.18	0.14	0.31	0.38	11.75	0.24	0.19	0.22	0.00	0.14	0.01	0.07	0.18	0.01	0.11	0	0	0.15	0.18
Na2O	7.1	7.41	0.7	0.36	0.09	8.06	0.2	0.12	0.32	7.99	7.05	0.96	7.03	7.25	7.06	0.03	0.36	0.46	7.33	11.27	0.11	0.01	0	0.5	1.13	11.20
K2O	1.69	0.86	10.02	10.17	0.07	0.1	8.82	0.43	0	0.07	0.00	0.00	0.03	0.05	0.00	0.06	10.29	10.37	0.4	0.05	0.01	10.53	10.77	9.84	9.56	0.07
Totals	98.25	97.14	92.86	92.23	96.57	99.81	97.64	97.93	97.29	98.81	99.13	99.01	96.27	96.85	96.70	86.95	93.32	92.41	94.68	99.58	86.07	93.16	93.19	92.43	94.17	99.50
Oxygens	11	11	11	11	12.5	8	11	11	11	23	23	23.00	23.00	23.00	23.00	14	11	11	11	8	14	11	11	11	22	8
Si	2.898	2.843	3.208	3.149	2.922	2.653	2.749	3.769	3.802	8.039	8.061	7.939	7.975	8.018	7.998	2.776	3.408	3.464	3.027	2.993	2.716	3.475	3.498	3.386	3.089	2.98
Ti	0.012	0.011	0.016	0.008	0	0	0.04	0.003	0.009	0.007	0.008	0.004	0.014	0.008	0.012	0.006	0.027	0.004	0	0.002	0.019	0.008	0	0.033	0.014	0
Al	2.685	2.789	1.976	2.057	2.266	1.041	1.254	0.05	0.018	1.578	1.352	0.249	1.800	1.805	1.817	2.49	2.124	2.045	2.911	0.967	2.613	2.054	2.04	2.166	2.573	1.011
Fe3+	0.39	0.393	0.43	0.434	0.502	0.282	0.446	0.398	0.399	0.229	0.583	0.059	0.096	0.159	0.090	0.075	0.047	0.048	0.046	0.03	0	0	0	0	0.179	0.01
Fe2+	0.033	0.031	0.197	0.218	0.541	0.087	0.812	0.353	0.344	1.246	0.912	1.183	1.750	1.547	1.642	2.709	0.201	0.165	0.03	0.016	2.578	0.209	0.204	0.165	0.072	0
Mn	0.001	0	0	0	0.018	0.003	0.01	0	0	0.019	0.000	0.000	0.008	0.000	0.008	0.029	0	0.003	0	0	0	0	0.008	0.009	0.003	0.002
Mg	0.049	0.007	0.288	0.266	0.028	0.029	1.634	2.396	2.381	1.819	2.068	3.584	1.412	1.435	1.469	1.845	0.192	0.287	0	0.011	2.02	0.275	0.261	0.274	0.11	0.022
Ca	0.013	0.02	0	0.015	1.908	0.258	0.025	0.012	0.009	0.045	0.055	1.758	0.037	0.028	0.034	0	0.01	0.008	0.008	0.008	0.001	0.008	0	0	0.011	0.008
Na	0.812	0.854	0.088	0.046	0.013	0.665	0.026	0.014	0.037	2.124	1.847	0.259	1.942	1.977	1.933	0.006	0.047	0.027	0.897	0.953	0.023	0.001	0	0.067	0.143	0.951
K	0.127	0.065	0.83	0.851	0.007	0.005	0.758	0.033	0	0.013	0.000	0.000	0.005	0.009	0.000	0.008	0.893	0.898	0.047	0.003	0.001	0.922	0.943	0.865	0.798	0.004
Sum	7.02	7.013	7.033	7.044	8.205	5.023	7.754	7.028	6.999	15.119	14.886	15.033	15.038	14.985	15.003	9.944	6.949	6.949	6.966	4.983	9.971	6.952	6.954	6.965	6.992	4.988
XMg	0.598	0.184	0.594	0.550	0.049		0.668	0.872	0.874	0.593	0.694	0.752	0.447	0.481	0.472	0.405	0.489	0.635	0.000		0.439	0.568	0.561	0.624	0.604	
Fe3+ %	92.2	92.7	68.6	66.6	48.1		35.5	53.0	53.7	15.5	39.0	4.7	5.2	9.3	5.2	2.7	19.0	22.5	60.5		0.0	0.0	0.0	0.0	71.3	
Alm%																										
Sps%																										
Prp%																										
Grs%																										
XCa						0.278														0.008						0.008
Pl Al/Si						0.059														-0.034						0.011

Table 4.2: Representative quatative mineral analysis of samples from the Zas Unit derived by electron microprobe

4.4.2 Petrography of the Koronos Unit (Kyanite-Grade Gneisses)

M_2 kyanite-grade schists reveal this unit attained a contrasting metamorphic history to the overlying Zas Unit, with no petrographic evidence for (M1) blueschist facies conditions (Figs. 4.11 and 4.14). High-grade deformational textures are present throughout this unit, with evidence for both prograde, peak and retrograde microstructural fabrics that developed over a large temperature range from lower to upper amphibolite facies conditions (Buick and Holland., 1989; Urai et al., 1990). In metapelitic lithologies, major phases include quartz, plagioclase, Ti-rich biotite, muscovite, garnet aluminosilicate and minor K-feldspar (Fig. 4.12a-j) and accessory minerals include tourmaline, apatite, chlorite, rutile, ilmenite, magnetite, monazite, and zircon. In aluminum-rich bands, up to cm-scale kyanite blades and euhedral garnet grains occur in close proximity, with the matrix separated into quartzo-felspathic domains and biotite and muscovite folia (see Fig. 4.11a, b, c, d). The rare occurrence of staurolite is attributed to the semi-pelitic nature of the protoliths, with only relic fragments remaining following breakdown to produce garnet and kyanite:

$$staurolite + muscovite + quartz \rightarrow biotite + kyanite + garnet + H_2O \qquad (4.1)$$

This unit also shows contrasting microstructural fabrics to the overlying Zas Unit. S_1 is aligned parallel to bedding and is preserved as inclusions within kyanite and garnet cores, whereas crenulation cleavages (S_{2a} and S_{2b}) can be found in less strained enclaves and as inclusions in garnet. Isoclinal folding occurs on a mm-scale and is associated with microlithons (S_{2a}) and utilizes compositional layering between quartzo-feldspathic and pelitic domains (see Fig. 4.11a, b, c, e). Cleavage domains (S_{2b}), are superimposed on S_{2a} and in places completely overprint the microlithons to produce a strong spaced foliation defined by biotite-muscovite foliation (Fig. 4.11d, e). Large kyanite porphyroblasts are aligned co-axial with the foliation (S_{2a} and S_{2b}) and sometimes cross-cut them, indicating these are prograde features. In numerous samples (e.g. TL67), euhe-

dral garnets overgrow kyanite bearing S_{2b} fabrics preserved in aluminum-rich domains whereas in other samples (e.g. TLN22), garnets are enclosed by large kyanite porphyroblasts suggesting simultaneous prograde growth of kyanite at peak M_2 conditions. In sample TLN21, garnets are up to several mm in diameter and distributed uniquely along tightly isoclinally folded pelitic layers (S_{2a}), whereas in TL67, euhedral garnet porphyroblasts show straight faces truncating both S_{2a} and S_{2b} foliations and show, indicating garnet in this sample postdates initial thrusting and folding (Fig. 4.11d). Within some of these garnet porphyroblasts, dark fluid inclusions indicate garnet growth in a mixed saline CO_2 / H_2O fluid, as noted previously (Baker and Matthews., 1994; Baker et al., 1989; Bickle and Baker, 1990; Kruelen, 1980). Kyanite has commonly broken down to biotite and is confined to pelitic domains with garnet. These domains form enclaves that are partially recrystallized as an extensional blastomylonitic top-to-NNE shear fabric (S_3) affecting the matrix and deforming around stronger Ky–Bt–Ms–Pl–Grt rich enclaves, indicating these M_2 kyanite-grade assemblages are pre-tectonic with-respect to S_3 (Fig. 4.11d, g, h). S3 was accommodated via grain boundary migration of quartz and ductile deformation of plagioclase associated with temperatures exceeding 600°C (Stipp and Kunz, 2008). This was followed by coarsening and Ostwald ripening of grain boundaries, revealing static recrystallization and annealing postdates deformation at close to peak conditions (Fig. 4.12j).

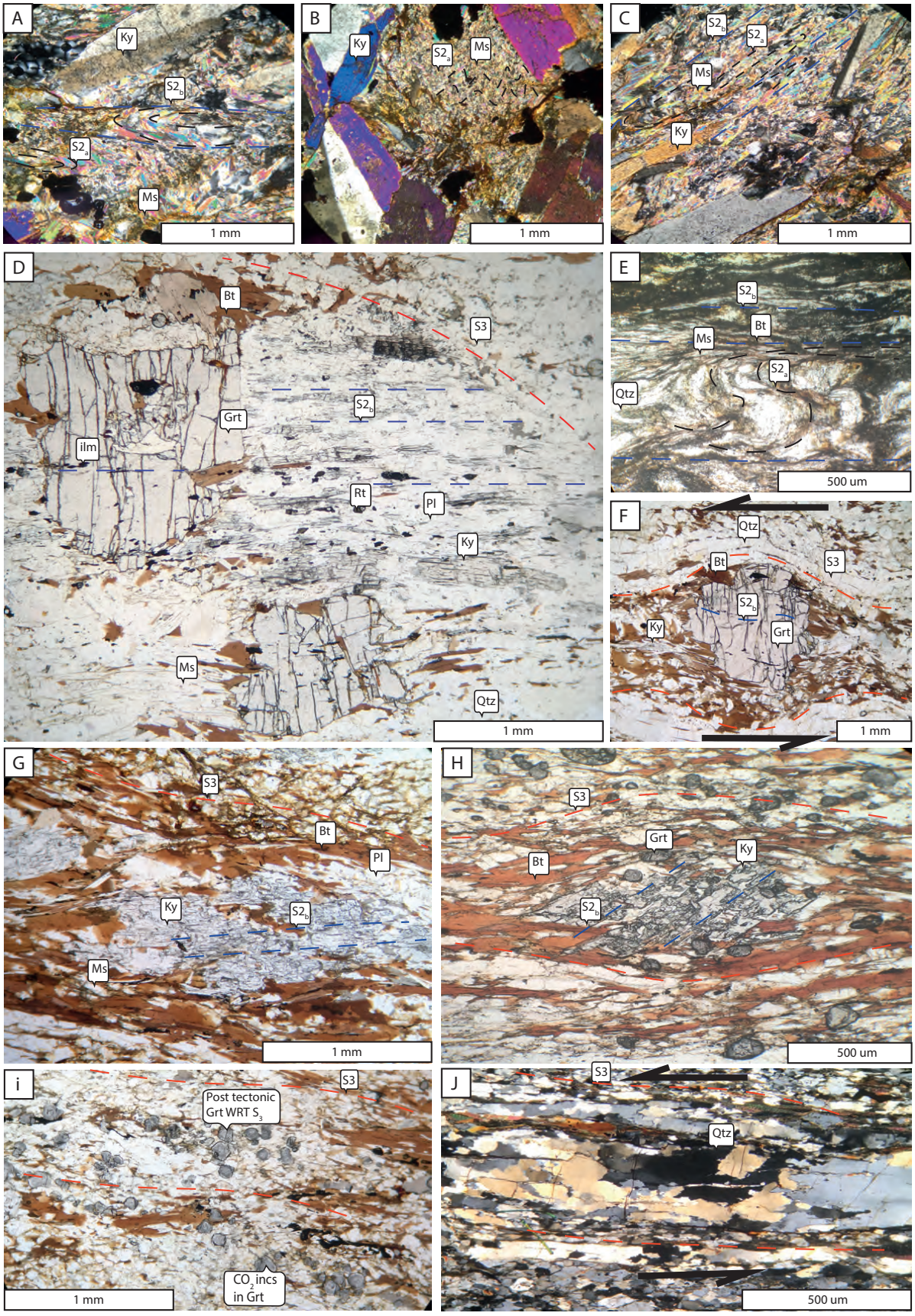


Figure 4.11: Continues on next page

Figure 4.11: Collection of photomicrographs from the Koronos Unit to demonstrate key microstructures and fabrics during prograde and peak M_2 conditions. A, B and C) 17TL110, a kyanite muscovite schist with coarse millimeter-sized kyanite blades that overgrow the S_{2a} crenulation cleavages defined by muscovite and are aligned sub-parallel to the subsequent S_{2b} foliation. D) TL67 (Koronos Unit) Peak M_2 Grt–Ky–Rt–Ilm–Ms–Pl enclave that is pre-tectonic with respect to S_3, which deforms around it. Garnet is post-tectonic to S_{2b} that developed along cleavage domains of previous S_{2a} crenulations, seen as inclusion trains through garnet. Ky and Rt grew simultaneously with S_{2b} as they are aligned parallel to the fabric, but discordant to the external S_3 fabric. E) TLN47, a Ky mica schist well preserving S_{2a} crenulations. G) TLN13 (Koronos Unit), PPL image showing enclaves of pre-tectonic Ky + Ms breaking down to Bt which is affected by S_3 S–C' fabric. Small garnets (<100 mm) are found as inclusions within kyanite, preserving peak assemblage Grt–Ky–Bt–Ms–Plag–Qtz. H) TLN22 (Koronos Unit) showing early kyanite enclaves that preserve S_1 and S_2, that have been rotated anticlockwise associated with development of S_3. Small post-tectonic garnets have idioblastic faces and cross-cut the S_3 fabric, and show fluid inclusion bubbles, many of which are dark indicating a mixed CO_2 – H_2O fluid during garnet growth after shearing top-to-NNE shearing. I) TLN22 clearly showing small post-kinematic garnets that cross-cut the S_3 fabrics implying high temperatures outlasted deformation and possibly associated with hydration at M_3 sillimanite-grade conditions. J) TL67 blastomylonite quartz microstructures showing sweeping subgrain boundaries consistent with grain boundary migration followed by static recrystallization and coarsening.

Towards the base of this unit along the KSZ, many samples display evidence for a thermal and static, lower pressure overprint on a blasto-mylonitic S_3 fabric. This is demonstrated by post-tectonic growth of (M_3) sillimanite and garnet (e.g. TLN21 and TLN22), which truncate the top-to-NNE S_3 fabric, indicating that high-temperatures outlasted deformation. Peak (M_2) kyanite-bearing assemblages are overprinted by (M_3) sillimanite, biotite intergrowths with plagioclase and quartz in dilational strain zones, demonstrating the transition from kyanite to sillimanite occurred via a Carmicheal-type reaction scheme (Carmicheal,1969) that post-dates shearing (Fig. 4.11h, i).

Within metapelitic samples, garnet shows a variety of compositional profiles that correlates directly with their microstructural relationships (Fig. 4.14l). Garnet in TL67 preserves prograde growth zoning associated with a smooth transition from core to rim, increasing in pyrope content and homogenous to slightly decreasing grossular content as shown in Fig. 4.14b. An inflection in the spessartine content on the outermost rim is indicative of some garnet resorption following peak conditions. Contrastingly TLN22 has small garnets that cross-cut the S_3 fabric and in places are

engulfed by kyanite. These garnets show either a general decrease in the grossular component from core to rim whereas the pyrope content slightly increases towards the inner rim followed by a decrease towards the outer rim indicative of late garnet growth at lower pressure and temperature or homogenous garnet profiles due to re-equilibration at lower pressures.

Along the KSZ, there is a band of ultramafic rock that is enclosed within foliated garnet-bearing amphibolites that are semi continuous along strike and wrap around the dome. The meta-peridotite enclaves enclosed within the amphibolites show partial serpentinization to anthopyllite, talc and actinolite, but preserves in situ olivine and orthopyroxene. Katzir et al., (1999) gives a detailed description of the petrography and geochemistry of these lenses and notes bimodal temperatures of ca. 700°C and 1200°C from pyroxene thermometry, suggesting they remained hot as they were emplaced into the shelf carbonate sequence. Within these amphibolites, there is some degree of hydrous M_2 migmatization but no petrographic evidence whatsoever to suggest they attained M_1 blueschist facies conditions.

4.4.3 Petrography of the Core Unit

Samples from the migmatite dome preserve a petrologic record of kyanite-sillimanite-grade (M_2–M_3) partial melting, and display no evidence for having experienced Eocene M_1 conditions. Careful textural examination reveals that hydrous melting was the dominant melting process occurring within the Naxos dome, capable of producing between 1% and 7% volume melt based on reaction stoichiometry. Whereas at the deepest levels in pelitic lithologies, incongruent muscovite dehydration melting is the major melting process associated with growth of peritectic K-feldspar, removal of muscovite and melt segregation from larger melt fractions (>20% melt), which eventually pooled to form S-type leucogranites which cross-cut and intrude into the mantling carapace.

There is evidence for a heterogeneous degree of melting throughout the Core Unit, due to lithological and bulk compositional control because of repetition of infertile ortho-gneissic basement, with more fertile meta-sedimentary horizons, due to

Sample Min	TL67 Grt Inner Rim	TL67 Grt Core	TL67 Grt Int	TL67 Bt Matrix	TL67 Bt with Ky	TL67 Ms Matrix	TL67 Ms with Ky	TL67 Pl Matrix	TL67 Kfs with Grt	TL67 Kyanite Matrix	TLN21 Grt Int	TLN21 Grt Core	TLN21 Grt Inner Rim	TLN21 Grt Outer Rim	TLN21 Bt Matrix	TLN21 Bt Matrix	TLN21 Ms Matrix	TLN21 Pl Matrix	TLN22 Grt Core	TLN22 Grt Inner Rim	TLN22 Grt Outer Rim	TLN22 Grt Int	TLN22 Ms Matrix	TLN22 Ms Matrix	TLN22 Bt Matrix	TLN22 Pl Matrix	TLN22 Pl Matrix
SiO2	37.97	37.51	37.20	36.29	35.07	46.30	46.88	61.41	65.34	36.03	37.72	36.90	37.70	36.82	36.11	35.56	46.75	61.23	38.57	37.46	38.94	37.97	46.06	47.45	36.52	60.95	61.94
TiO2	0.10	0.08	0.20	3.27	3.40	1.05	1.29	0.00	0.18	0.09	0.28	0.00	0.32	0.13	3.74	3.99	1.28	0.08	0.00	0.05	0.18	0.00	1.07	1.30	1.95	0.02	0.00
Al2O3	20.75	21.29	20.24	19.54	18.36	34.79	34.44	24.33	18.64	62.45	20.37	20.84	20.67	20.73	19.10	18.23	34.11	23.69	21.03	20.46	19.56	20.69	35.45	35.35	19.50	24.19	23.77
FeO	31.11	28.77	31.66	19.13	21.08	1.85	1.65	0.03	0.01	0.77	31.17	33.56	32.60	30.93	19.98	19.64	1.52	0.30	29.98	31.53	31.83	31.03	0.72	0.95	17.60	0.54	0.45
MnO	2.22	4.73	2.10	0.23	0.16	0.00	0.00	0.01	0.00	0.02	1.78	3.27	2.20	6.12	0.00	0.22	0.00	0.06	2.76	4.14	6.28	3.16	0.44	0.00	0.17	0.17	0.00
MgO	3.57	2.71	3.28	9.70	8.09	0.60	0.61	0.00	0.00	0.00	4.16	2.98	3.47	2.57	8.09	8.13	1.19	0.00	3.32	3.83	2.02	4.25	1.09	0.61	11.16	0.13	0.00
CaO	4.83	5.72	5.07	0.00	0.05	0.06	0.00	5.58	0.00	0.01	3.43	2.59	3.37	2.08	0.24	0.00	0.08	5.23	4.27	2.80	1.50	3.60	0.00	0.00	0.55	4.86	5.04
Na2O	0.01	0.00	0.07	0.05	0.31	0.85	0.60	8.34	0.40	0.00	0.13	0.24	0.07	0.59	0.07	0.19	0.75	8.96	0.00	0.26	0.01	0.20	1.13	1.12	0.00	8.61	8.68
K2O	0.00	0.03	0.00	9.84	9.64	10.54	10.23	0.22	16.71	0.14	0.00	0.01	0.00	0.07	8.32	9.75	10.89	0.14	0.01	0.00	0.02	0.00	9.37	9.81	8.89	0.20	0.00
Totals	100.56	100.85	99.82	98.05	96.17	96.03	95.70	99.91	101.28	99.51	99.05	100.41	100.38	100.05	95.65	95.70	96.58	99.71	99.94	100.54	100.34	100.90	95.33	96.60	96.33	99.67	99.87
Oxygens	12	12	12	11	11	11	11	8	8	5	12	12	12	12	11	11	11		12	12	12	12	11	11	11	8	8
Si	3.01	2.973	2.978	2.679	2.678	3.073	3.107	2.728	2.987	0.982	3.028	2.952	3.005	2.954	2.72	2.707	3.106	2.734	3.06	2.976	3.129	2.991	3.091	3.079	2.71	2.718	2.748
Ti	0.006	0.005	0.012	0.182	0.195	0.052	0.064	0	0.006	0.002	0.017	0	0.019	0.008	0.212	0.228	0.039	0.003	0	0.003	0.011	0	0.045	0.058	0.109	0.001	0.000
Al	1.939	1.989	1.91	1.7	1.653	2.722	2.691	1.274	1.005	2.007	1.928	1.966	1.943	1.961	1.696	1.636	2.741	1.247	1.967	1.916	1.853	1.921	2.737	2.717	1.706	1.272	1.243
Fe3+	0.031	0.059	0.12	0	0	0	0	0.001	0	0	0.002	0.169	0.019	0.213	0	0	0	0	0	0.166	0	0.128	0	0	0	0.020	0.017
Fe2+	2.032	1.848	2	1.181	1.346	0.103	0.091	0	0	0.018	2.091	2.077	2.154	1.862	1.259	1.25	0.059	0.011	1.989	1.928	2.139	1.916	0.078	0.074	1.092	0	0
Mn	0.149	0.318	0.142	0.014	0.01	0	0	0	0	0	0.121	0.222	0.149	0.416	0	0.014	0	0.002	0.185	0.279	0.427	0.211	0.021	0.008	0.011	0.006	0
Mg	0.422	0.32	0.391	1.067	0.921	0.059	0.06	0	0	0	0.498	0.355	0.412	0.307	0.908	0.922	0.06	0	0.393	0.453	0.242	0.499	0.048	0.074	1.234	0.009	0
Ca	0.41	0.486	0.435	0	0.004	0.004	0	0.266	0	0	0.295	0.222	0.288	0.179	0.019	0	0	0.250	0.363	0.238	0.129	0.304	0	0.009	0.044	0.232	0.240
Na	0.002	0	0.011	0.007	0.046	0.109	0.077	0.718	0.035	0	0.02	0.037	0.011	0.092	0.01	0.028	0.098	0.776	0	0.04	0.002	0.031	0.186	0.132	0	0.744	0.747
K	0	0.003	0	0.927	0.939	0.892	0.865	0.012	0.975	0.005	0	0.001	0	0.007	0.8	0.947	0.859	0.008	0.001	0	0.002	0	0.767	0.838	0.842	0.011	0.000
Sum	8.001	8.001	7.999	7.757	7.792	7.014	6.955	4.999	5.008	3.015	8.000	8.001	8.000	7.999	7.624	7.732	6.962	5.032	7.958	7.999	7.934	8.001	6.973	6.989	7.748	5.013	4.995
XMg	0.172	0.148	0.164	0.475	0.406	0.364	0.397				0.192	0.146	0.161	0.142	0.419	0.424	0.504		0.165	0.190	0.102	0.207	0.381	0.500	0.531		
Fe3+ %	0	0	0.1	0	0	0	0				0	0.1	0	0.1	0	0	0		0	0.1	0	0.1	0	0	0		
Alm%	67.3	62.5	67.7								69.5	73.4	71.7	69.9					68.6	67.7	73.4	66.2					
Sps%	5.0	10.6	4.7								4.0	7.4	5.0	13.9					6.2	9.3	14.2	7.0					
Prp%	14.1	10.7	13.0								16.6	11.8	13.7	10.2					13.1	15.1	8.1	16.6					
Grs%	13.7	16.2	14.5								9.8	7.4	9.6	6.0					12.1	7.9	4.3	10.1					
XCa								0.267	0.000									0.242								0.235	0.243
Pl Al/Si								0.273	0.005									0.252								0.275	0.245

Table 4.3: Representative quatative mineral analysis of samples from the Koronos UNit derived by electron microprobe

prograde thrusting. Samples TL66 and TL15 outcrop as stromatic migmatites with cm-scale folded leucosome and melanosome banding, whereas TLN18 and TLN20A represent diatexites. Melanosome foliations are defined mostly by muscovite, biotite, fibrolite (fibrous sillimanite), relict kyanite and in some samples peritectic K-feldspar (Fig. 4.12g–i). Leucosome segregations contain around equal proportions of quartz and plagioclase with lesser amounts of biotite, muscovite, fibrolite, garnet, and ilmenite, whilst K-feldspar occurs in other samples (e.g. TL59, TLN18, TLN34, TLN35). Accessory minerals include tourmaline, apatite, magnetite, pyrite, zircon, and monazite. Leucosome segregations comprise approximately 10–20% of the migmatite sequence in outcrop. Whilst diatextite only occurs at the deepest levels and has foliations defined by schollen of biotite and some relict muscovite with leucosomes characterizing larger volumes of the rock (>20%).

Garnet occurs in both the leucosome and melanosomes as small idioblastic porphyroblasts <1 mm in diameter, displaying subhedral to anhedral faces (Fig. 4.12a, e, f). In sample TL15, leucosome garnet preserves rotational inclusion trails that define the S_{2a} fabric that rotate into alignment with the external matrix S_{2b} fabric towards its rims (Fig. 4.13a and j) indicating garnet grew syn-kinematically with the development of these prograde features. However, many of these porphyroblasts in sillimanite-grade samples are fractured and filled by biotite and muscovite intergrowths (Fig. 4.13f). In samples TLN34 and TL66, garnet is almost compositionally homogeneous (Fig. 4.14f and supplementary material). Muscovite in sample TL59 and TL66 occur similarly as laths with associated fibrolite or as symplectic intergrowths with quartz (Fig. 4.12e–h). These intergrowths are often associated with either biotite–quartz symplectite or myrmekite (plagioclase–quartz intergrowths). Secondary muscovite in leucosomes are oriented randomly relative to the foliation and fibrolitic sillimanite in the matrix and on the margins of leucosomes is typically surrounded by coarse-grained, cross-cutting muscovite (Spear et al., 1990) (Fig. 4.13e–f). Biotite occurs as individual crystals in the leucosome, as part of the melanosome foliation and also forms symplectic intergrowths with quartz, but shows no significant compositional variation between

these petrographic positions with Mg/(Mg + Fe). In kyanite-grade migmatites (e.g. TL15), kyanite is associated with the S_2 foliation, which is folded by F_3 folds (Fig. 4.13b–d), indicating upright F_3 folding post-dates kyanite growth and occurred after the rocks attained their peak pressures.

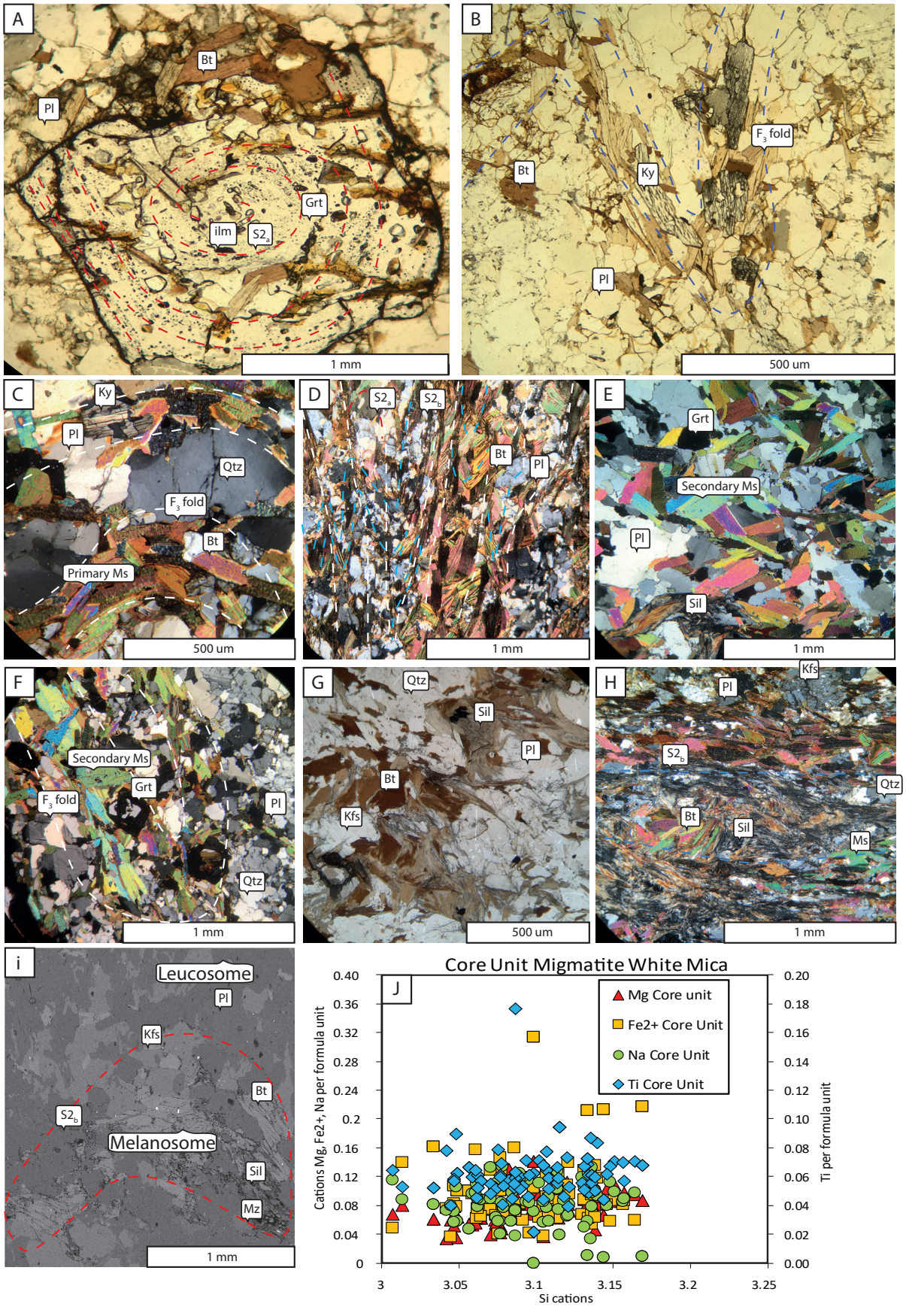


Figure 4.12: Continues on next page

Figure 4.12: Representative photomicrographs and back-scattered electron images and mineral data from Core Unit samples. A) TL15 garnet, kyanite migmatite showing prograde garnet with a rotational inclusion trail that rotates into alignment with the external S_{2b} matrix fabric, indicating that garnet formed coeval with S_{2a} and S_{2b}. B) TL15, kyanite folded with the S_{2b} foliation by an upright F_3 fold, clearly implying that kyanite pre-dates F_3 folding. C) TL15 showing another example of an F_3 fold closure affecting biotite kyanite muscovite folia, with some primary prismatic muscovite preserved. D) TLN34 showing well developed S_{2b} foliations with S_{2a} crenulations preserved by the interlocking habit of biotite. E and F) TL66 garnet, sillimanite migmatite showing coarse cross-cutting secondary muscovite in both leucosome and melanosomes, with atoll garnets. Sillimanite-biotite intergrowths show decussate textures diagnositic of kyanite to sillimanite transformation and coarse cross-cutting secondary muscovite indicative of re-equilibration and back reaction through the muscovite-dehydration melting reaction. G) TLN34 sillimanite garnet, k-feldspar migmatite with peritectic K-feldspar adjacent to biotite and sillimanite, indicative of incongruent melting. It also shows a range of deformation microstructures from brittle fracture to dynamic recrystallization and extensive grain size reduction with chess board extinction in quartz following anatexis, indicative of deformation temperatures from 700–350°C. H) TLN20A biotite, sillimanite migmatite with peritectic K-feldspar and well developed S_{2b} fabrics, there is a very small amount of primary muscovite preserved. I) TLN34 showing inclusions of monazite within biotite, sillimanite quartz intergrowths within melanosomes, which were dated in chapter 5. J) Core Unit white mica data, showing the spectrum of muscovite compositions where Si<3.10 pfu and Ti>0.06 pfu is diagnostic of secondary muscovite.

4.4.4 Textures of Sillimanite-Grade Migmatites

At mid-crustal pressures in the upper amphibolite-facies, the first appearance of anatectic melt is usually triggered by the intersection of the wet granite or pelite solidus and destabilization of prograde muscovite through the following hydrous melting reactions (Petö, 1976; St-Onge, 1984; Patiño Douce and Harris, 1998):

$$muscovite + quartz + plagioclase + K - feldspar + H_2O \rightarrow melt \qquad (4.2)$$

$$muscovite + quartz + plagioclase + H_2O \rightarrow aluminosilicate + melt \qquad (4.3)$$

However, these reactions produce very small volumes of melt, unless a substantial external supply of fluid is available (Thompson, 1982; Pattison and Tracy, 1991). Nevertheless, volumetrically significant melting can occur with continued prograde meta-

morphism above the wet solidus via the fluid-absent muscovite dehydration melting reaction (4). Due to the positive$P$–T slope of this reaction, at lower temperatures and pressures, K-feldspar is also produced by its vapour present equivalent reaction (5) at subsolidus temperatures. In the field, these reactions are often referred to as the 'upper sillimanite' or 'second sillimanite isograd' (Evans and Guidotti, 1966) due to the formation of a K-rich neosome (García-Casco et al., 2003):

$$muscovite + quartz \rightarrow K - feldspar + aluminosilicate + melt \tag{4.4}$$

$$muscovite + quartz \rightarrow K - feldspar + aluminosilicate + H_2O \tag{4.5}$$

Several authors have observed that K-feldspar is commonly absent from sillimanite-grade migmatites despite being present at peak conditions, due to replacement by secondary muscovite in the back reaction during cooling (Ashworth, 1975 and Tippet, 1980). By identifying different generations of muscovite through various petrographic characteristics, secondary muscovite can be distinguished. Tyler and Ashworth (1982) suggested that prograde (primary) muscovite that survives the partial melting process often occurs as flakes orientated in the melanosome foliation. Retrograde muscovite occurs as large lath-like porphyroblasts containing sillimanite, or as symplectic intergrowths with quartz (Fig. 4.12e–h) (Ashworth, 1975, 1979; Tippet, 1980). Textural features in samples TL66 include muscovite laths containing numerous fibrolite inclusions and muscovite–quartz symplectite and intergrowths of sillimanite–quartz "faserkiesel", which are typical of retrograde replacement of K-feldspar at sillimanite-grade conditions (Fig. 4.12e–g) (Evans and Guidotti, 1966; Ashworth, 1975; Tippet 1980; Brown, 2002), the reversal of the muscovite dehydration melting reaction.

Although peritectic K-feldspar is commonly lacking in the Naxos migmatites due to hydrous melting textures and retrograde replacement by secondary muscovite, leucosomes in migmatites from deep levels are volumetrically abundant in outcrop rep-

resenting 15–25% volume proportion of rock. This volume of melt greatly exceeds the proposed melt connectivity threshold of 7–10% that allows melt extraction in such lithologies (Rosenberg and Handy, 2005). However, it has been shown that the observed leucocratic component of migmatites does not directly correlate with actual quantities of melting. At shallow dome levels rocks that have been described as leucosomes, leucogneiss and diatexites we interpret as orthogneiss basement that coarsened upon experiencing small degrees of partial melting (B. Dyck, personal communication). This has major implications for the proposed mechanisms that drove migmatite doming, as the weakening effect depending on the extent of partial melting may have been extremely overestimated. At structurally high levels of the dome, the stability of primary muscovite within the melanosomes supports this interpretation, as they did not experience muscovite de-hydration melting - the first major melt producing reaction. Although diatexites occur on Naxos, they are confined to fertile lithologies at deeper levels upon crossing the K-feldspar isograd. Some inference into the temperature of mineral growth can be made with compositional characteristics of different mineral generations. Prograde muscovite commonly contains higher paragonite content than retrograde muscovite that has replaced K-feldspar (Evans and Guidotti, 1966; Ashworth, 1975). Generally, low Si content (<3.10 pfu per 11-oxygens) combined with high Ti content (up to 0.08 pfu) is characteristic of high-grade and magmatic muscovite (Miller et al., 1981; Guidotti, 1984). In all analyzed samples, leucosome muscovite is low in Si and contains a moderate-high Ti content (0.04–0.10) (Fig. 4.15), indicating that they formed during melt crystallization or retrogressively while still at high-temperature. Compositional zoning profiles in garnet give further support of high-grade metamorphic conditions, as inferred from compositional and textural characteristics in muscovite. Several authors have demonstrated that garnet compositional zoning profiles form principally as a function of changes in pressure and temperature conditions during growth (e.g. Tracy et al., 1976; Spear and Selverstone, 1983; St-Onge, 1987). During prograde metamorphism in a pelitic bulk composition, garnet preferentially fractionates Mn into core regions and therefore spessartine content de-

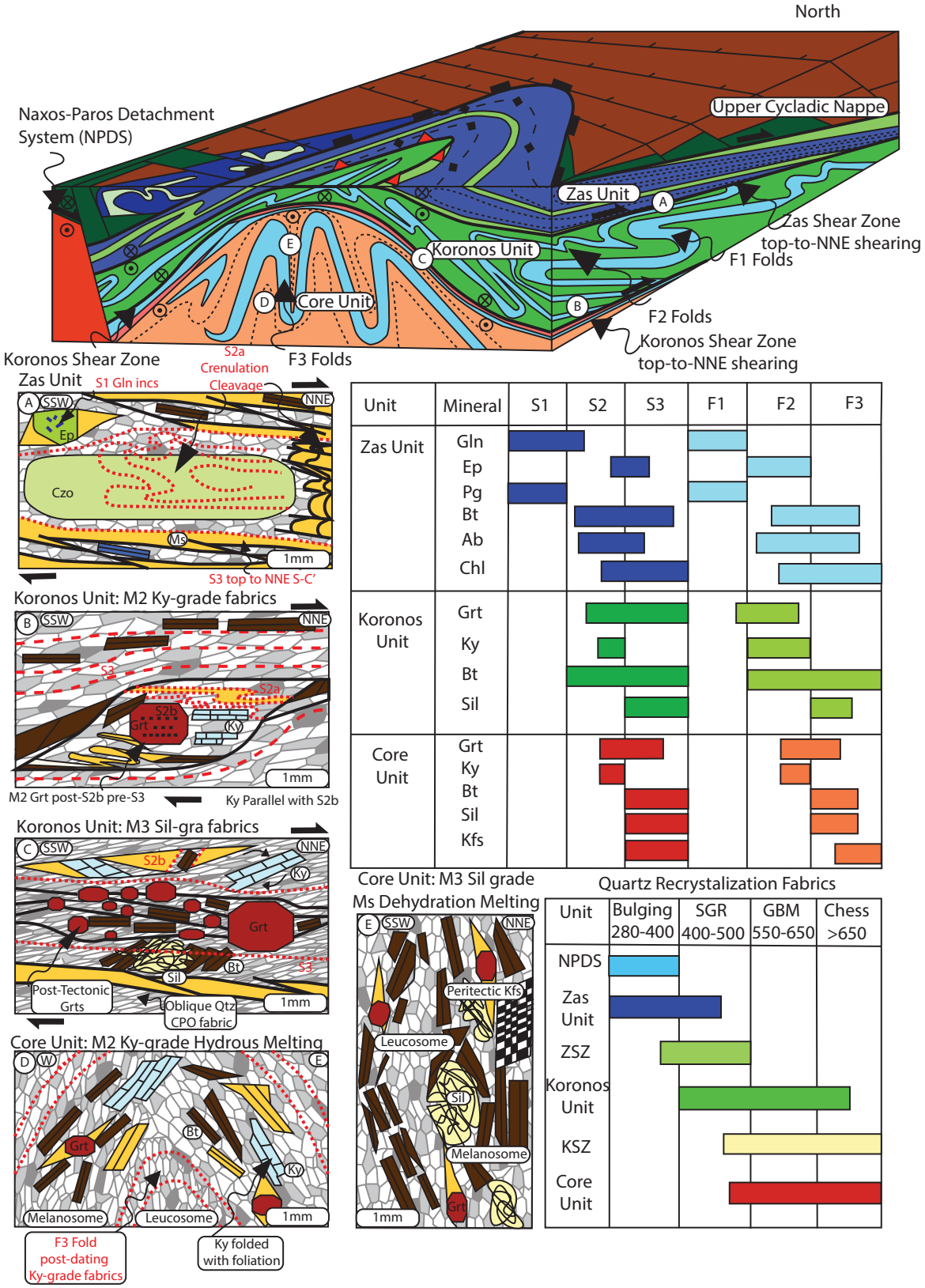


Figure 4.13: Schematic illustration of the deformation macro- and microstructures on Naxos, showing fabrics, order of mineral growth, deformation temperatures and sequence of shearing and simplified sketches of microstructures. Grain boundary migration (GBM), Grain boundary rotation (GBR), see text for discussion.

creases towards rims as a result of progressive Mn-depletion in the reacting matrix (Hollister, 1966). However, in the Naxos migmatites, garnet contains spessartine profiles that are homogenous or concave upwards with increasing Mn content from core to rim. The length scale of Mn (and Mg, Fe and Ca) zonation within the garnets is less than the diffusional length scale (up to 3 mm) suggested by >5 Myrs residence time at peak temperatures >650°C (Caddick et al., 2010). These factors indicate that preservation of the prograde growth history will be modified somewhat by diffusion, whereas peak conditions will be preserved by thermal re-equilibration (Woodsworth, 1977; Spear, 1993). Nevertheless, the shape and trends of garnet profiles will be somewhat preserved if peak conditions were attained for only a geologically brief time and therefore insight into the prograde metamorphic history Core Unit may be obtained. Due to these reasons in what follows, we take peak pressure estimates as a minimum depth of burial.

4.4.5 Textures of Kyanite-Grade Migmatites

Kyanite-grade migmatites (e.g. TL15) occur at higher structural levels of the dome and record the earlier prograde history. Texturally these are stromatic migmatites with distinct leucosomes highlighting cm-scale ptygmatic flow folding during anatectic conditions. In these samples, melanosomes preserve the S_{2a} crenulation cleavages and S_{2b} spaced foliations along cleavage domains similar to the overlying Koronos Unit (Fig. 4.12c, d, h). Kyanite is bladed and lies in the folded S_2 foliation, indicating that it grew in Al-rich bands prior to anatectic deformation associated with upright F_3 folding (Fig. 4.12b–c). Contrastingly, some biotite and secondary muscovite in the melanosome are orientated axial planar to and cross-cut the folding, indicating they post-date deformation and are mainly retrogressive features associated with hydration contemptuous to regional NNE–SSW extensional exhumation. This specimen does not exhibit any of the K-feldspar replacement features described above, suggesting that its leucosomes were never of a granitic composition and consequently their formation must be a result of a K-feldspar-absent melting reaction. When H_2O is in excess, K-feldspar-absent

Sample	TL15	TL15	TL15	TL15	TL15	TL15	TL66	TL66	TL66	TL66	TL66	TLN34	TLN34	TLN34	TLN34	TLN34	TLN34
Mineral	Grt	Grt	Grt	Bt	Ms	Pl	Grt	Grt	Ms	Bt	Pl	Pl	Grt	Grt	Kfs	Ms	Pl	Sill
	Core	Inner Rim	Outer Rim	Int	Melanosome	Primary	Matrix	Rim	Core	Int	Secondary	Melanosome	Leucosome	Rim	Core	Matrix	Secondary	Matrix	Melanosome
SiO2	37.08	38.64	37.55	37.67	36.31	47.07	62.45	37.12	37.27	37.12	45.95	35.07	56.95	61.66	37.10	37.23	65.12	46.34	65.79	36.16
TiO2	0.00	0.00	0.03	0.07	3.29	1.37	0.00	0.00	0.20	0.00	1.20	3.40	0.00	0.10	0.00	0.13	0.47	1.57	0.00	0.00
Al2O3	20.60	20.07	20.27	20.60	18.80	33.67	23.45	20.58	20.33	20.63	34.62	18.36	29.84	24.87	20.73	20.71	19.01	34.86	20.94	62.16
FeO	31.56	31.12	33.73	32.56	20.28	1.54	0.26	32.92	33.90	32.68	1.78	21.08	0.07	0.04	28.07	30.00	0.00	0.73	0.00	0.62
MnO	1.85	1.27	2.48	1.68	0.08	0.06	0.00	4.03	1.77	4.22	0.01	0.16	0.00	0.00	10.78	7.41	0.00	0.00	0.19	0.27
MgO	2.60	4.49	3.45	3.47	8.49	0.88	0.00	2.94	3.78	3.02	0.51	8.09	0.00	0.00	3.07	4.58	0.00	0.66	0.00	0.00
CaO	6.09	3.55	2.48	3.83	0.10	0.00	5.08	2.25	2.24	2.31	0.02	0.05	6.64	6.23	0.55	0.45	0.00	0.00	2.20	0.13
Na2O	0.00	0.31	0.00	0.00	0.32	0.44	8.72	0.13	0.00	0.00	0.44	0.31	6.80	7.66	0.00	0.00	1.40	0.44	10.03	0.00
K2O	0.14	0.23	0.00	0.02	9.12	10.06	0.08	0.10	0.00	0.02	10.46	9.64	0.36	0.18	0.00	0.02	14.59	11.03	0.14	0.24
Totals	99.910	99.677	99.991	99.901	96.777	95.096	100.040	100.06	99.49	100.00	95.00	96.17	100.66	100.73	100.30	100.53	100.59	95.63	99.29	99.58
Oxygens	12	12	12	12	11	11	8	12	12	12	11	11	8	8	12	12	8	11	8	5
Si	2.969	3.067	3.017	3.015	2.722	3.134	2.766	2.985	3.003	2.989	3.076	2.678	2.521	2.715	2.989	2.965	2.973	3.075	2.909	0.986
Ti	0	0	0.002	0.004	0.185	0.069	0	0	0.012	0	0.06	0.195	0	0.003	0	0.008	0.016	0.078	0	0
Al	1.945	1.878	1.92	1.944	1.662	2.643	1.224	1.951	1.931	1.958	2.732	1.653	1.558	1.291	1.969	1.945	1.023	2.728	1.091	1.999
Fe3+	0.131	0.059	0.043	0.021	0	0	0.01	0.111	0.037	0.065	0	0	0.003	0.001	0.054	0.111	0	0	0	0
Fe2+	1.982	2.006	2.223	2.159	1.271	0.086	0	2.103	2.247	2.135	0.1	1.346	0	0	1.837	1.887	0	0.041	0	0.014
Mn	0.125	0.085	0.169	0.114	0.005	0.003	0	0.274	0.121	0.288	0.001	0.01	0	0	0.736	0.5	0	0	0.007	0.006
Mg	0.31	0.531	0.413	0.414	0.949	0.087	0	0.352	0.454	0.362	0.051	0.921	0	0	0.369	0.544	0	0.065	0	0
Ca	0.523	0.302	0.213	0.328	0.008	0	0.241	0.194	0.193	0.199	0.001	0.004	0.315	0.294	0.047	0.038	0	0	0.104	0.004
Na	0	0.048	0	0	0.047	0.057	0.749	0.02	0	0	0.057	0.046	0.584	0.654	0	0	0.124	0.057	0.86	0
K	0.014	0.023	0	0.002	0.872	0.854	0.005	0.01	0	0.002	0.893	0.939	0.02	0.01	0	0.002	0.85	0.934	0.008	0.008
Sum	7.999	7.999	8	8.001	7.721	6.933	4.995	8.000	7.998	7.998	6.971	7.792	5.001	4.968	8.001	8.000	4.986	6.978	4.979	3.018
XMg	0.135	0.209	0.157	0.161	0.427	0.503		0.143	0.168	0.145	0.338	0.406			0.167	0.224		0.613		
Fe3+ %	0.1	0	0	0	0	0		0.1	0	0	0	0			0	0.1		0		0
Alm%	68.1	69.4	73.5	71.5				72.7	74.4	71.7					61.6	63.9				
Sps%	4.2	2.8	5.6	3.8				9.1	4.0	9.6					24.5	16.7				
Prp%	10.3	17.7	13.8	13.8				11.7	15.1	12.1					12.3	18.1				
Grs%	17.4	10.1	7.1	10.9				6.5	6.4	6.6					1.6	1.3				
XCa							0.242						0.343	0.307			0		0.107	
Pl Al/Si							0.226						0.517	0.289			0.023		0.091	

Table 4.4: Representative quatative mineral analysis from the Core Unit samples

reactions extend to lower temperatures (García-Casco et al., 2001, 2003; Cruciani et al., 2008), and increasing pressure also favors fluid-saturated melting reactions before reaching conditions that favor dehydration melting during typical prograde metamorphism (Cruciani et al., 2008). Due to an inverse correlation between pressure and plagioclase stability, an increase in the plagioclase/muscovite ratio consumed in melting reactions with increasing pressure (Patiño Douce and Harris, 1998), and increasing H_2O activity leads to preferential solution of plagioclase components by lowering the Pl + Qtz solidus (Conrad et al., 1988). These factors result in a significant shift of products of H_2O-fluxed melting towards tonalitic/trondhjemitic compositions and are typical of fluid-rich environments at high-pressure and low-temperature conditions.

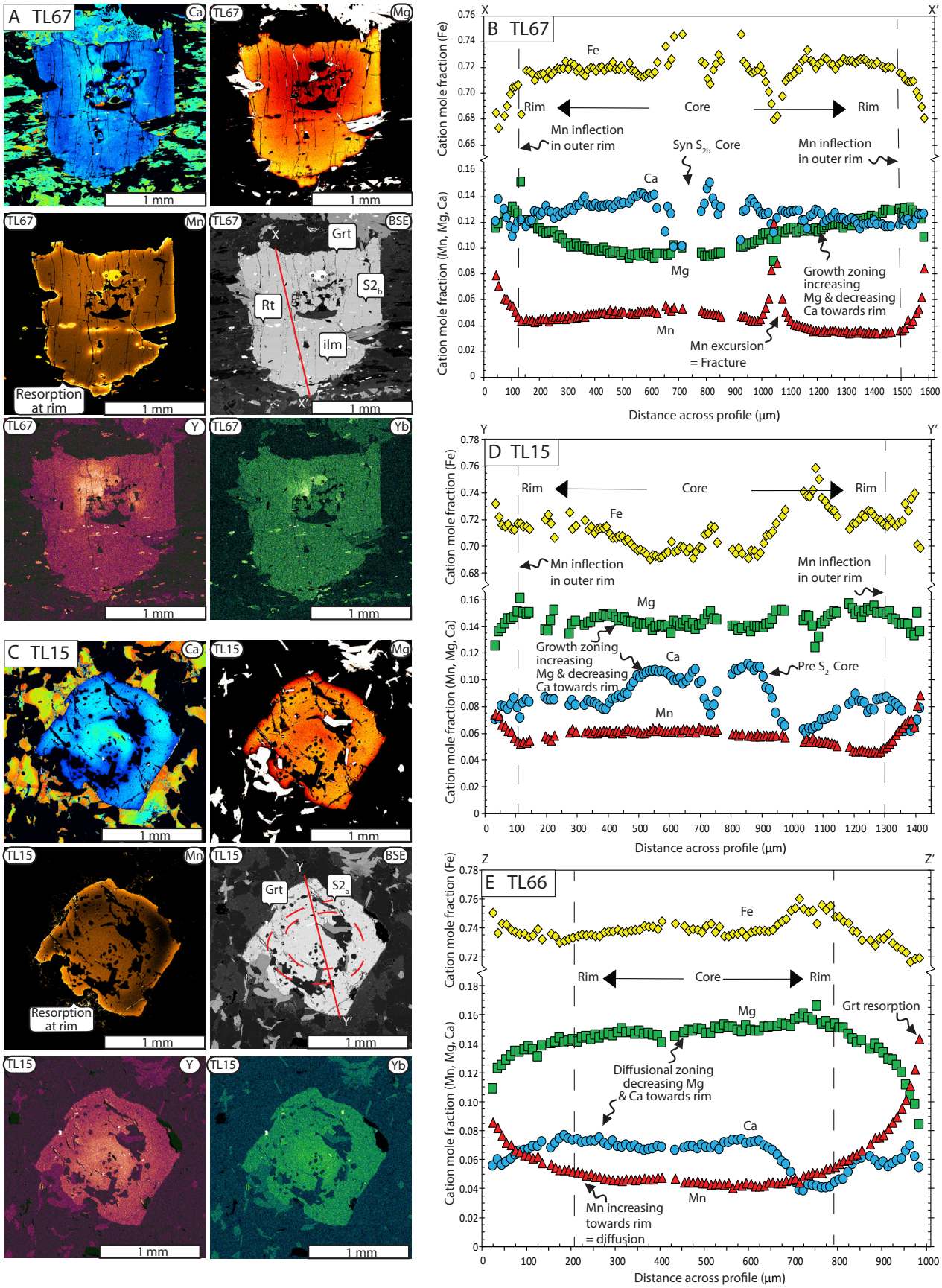


Figure 4.14: Continues on next page

Figure 4.14: Representative fully quantitative electron microprobe maps and line profiles of garnet for samples TL15, TL67 and TL66 showing cation mole fractions of Grossular, Almandine, Pyrope and Spessartine, see text and supplementary material for discussion. Gaps in the profiles exist from crossing fractures and inclusions. A) TL67, maps of Ca, Mg, Mn, Y and Yb showing prograde growth zoning and a backscattered electron image showing line profile X–X' across the internal S_{2b} fabric. Note brighter color correspond to larger element abundances. B) TL67 profile X–X' showing prograde growth zoning with increasing Mg from core to rim and decreasing Ca. An Mn inflection 120 mum from the garnet rim is indicative of partial modification of the outer rim by diffusion. C) TL15 maps and backscattered electron images of a garnet with line Y–Y' cross-cutting the S_{2a} rotational inclusion trails. D) TL15 profile Y–Y' showing a slight increase in Mg and an abrupt stepwise decrease in Ca from core to rim indicative of a two-stage garnet growth history. An inflection in Mn indicates only the outermost 100 mum rim is somewhat modified by diffusion. E) TL66 Z–Z' showing diffusional zoning with a decrease in Mg from core to rim and generally decreasing Ca with an enrichment in Mn towards the rim see supplementary material for trace of line profile.

Garnet within leucosome segregations in sample TL15 often demonstrates idioblastic faces (Fig. 4.12j), which as a microstructural feature in migmatites is usually interpreted to represent growth in the presence of melt (Whitney and Irving, 1994; Guilmette et al., 2011). This inference is further supported by different core and rim compositions in large porphyroblasts, and evidence for prograde growth zoning during development of S_2 (Fig. 4.12a, Fig. 4.14c and d), suggesting that garnet growth occurred in two stages, each at different P–T conditions (Spear, 1993). In the case of almandine and grossular content in the measured profile, rim compositions are separated from core compositions by an abrupt step and only sometimes show a smooth transition (Fig. 4.14c and d), with the latter interpreted as a diffusion profile that formed between two initially distinct compositional domains (e.g. Caddick et al., 2010). This two-stage growth scenario is further supported by zonation in both Y and Yb (Fig. 4.14c), which show a stepwise decrease from core to rim and small leucosome garnet grains that have similar compositions to rims of large porphyroblasts, indicating growth in the presence of melt. Diffusion has only modified the outermost 100 mum of the rim, as demonstrated by an inflection in spessartine content, suggesting core-inner rim zoning is prograde (e.g. Caddick, 2010). For these reasons, we conclude that sample TL15 best records the prograde evolution of the Core Unit and the initial stages of partial melting at higher-pressure M_2 conditions, through the following K-

feldspar-absent hydrous reaction that has been proposed by García-Casco et al., (2001) for similar kyanite-bearing pelitic migmatites:

$$biotite + muscovite + plagioclase + quartz + H_2O \rightarrow garnet + kyanite + melt \quad (4.6)$$

4.5 Pressure-Temperature Evolution of Metamorphism

Several forms of thermobarometry were used in this work to constrain the P–T conditions of metamorphism on Naxos. The Ti-in-biotite thermometer of Henry et al. (2005) was used alongside the GASP (Grt–Als–Pl–Qtz) barometer and the Grt–Bt thermobarometer (Spear, 1993; Bhattacharya et al., 1992), and Av-PT (Powell and Holland, 1998) using THERMOCALC version 3.40i was employed using characteristic end members for each sample and the results are displayed in Fig. 4.15. Activities of solid-solution end members were calculated using AX (Holland, 2009) (Table 4.5). The results systematically demonstrate that there are two distinct P–T populations on Naxos. M_1 blueschist facies P–T conditions are exclusively confined to the Zas Unit (Fig. 4.15a blue circles) and gives typical P–T results of 12.3 ± 0.8 kbar, 483 ± 13°C (TLN54). In contrast an upper amphibolite facies M_2-M_3 population is recorded within the Koronos and Core Units (green and red circles, respectively; Fig. 4.15a). These rocks typically record increasing pressure and temperature conditions from garnet core to rim. Kyanite bearing M_2 assemblages record higher pressures, up to 11.4 ± 1.0 kbar, 682 ± 38°C (TL67). Whereas sillimanite bearing M_3 assemblages record re-equilibration at lower pressure conditions such as of 7.5 ± 1.2 kbar, 742 ± 39°C (TL66). Within these units, prograde garnets compositions show increases in both pressure and temperature from core to rim diagnostic of crustal thickening and do not represent isobaric heating as previously inferred (Buick, 1991). However, the nature of the P–T path leading up-to and during peak anatectic conditions is poorly constrained using this method. This is because conventional thermobarometry

is largely ineffective at constraining peak P–T conditions in high-grade and/or partially melted rocks (e.g. Halpin et al., 2007; Indares et al., 2008; Palin et al., 2013) owing to changing mineral compositions due to retrograde diffusion (Kohn and Spear, 2000; Pattison et al., 1994; Pattison et al., 2003) and has large associated uncertainties (typically, ± 50°C and ±1 kbar at 1 S.D.; Powell and Holland, 2008; Palin et al., 2016). As such, phase diagram modelling (pseudosection construction) was employed herein as the main investigative tool to harness P–T information, which has significantly smaller uncertainties. Pseudosections were constructed using THERMOCALC version 3.40i and internally consistent thermodynamic dataset ds-62 (Powell and Holland, 1988; Holland and Powell, 2011). Modeling of metasediments TL67, TL15, and TL66 was performed in the MnO–Na_2O–CaO–K_2O–FeO–MgO–Al_2O_3–SiO_2–H_2O–TiO_2–O (Mn-NCKFMASHTO) system using the following activity–composition relations: silicate melt (White et al., 2007), cordierite (Mahar et al., 1997; Holland and Powell, 1998), garnet and ilmenite (White et al., 2005), orthopyroxene (White et al., 2002), chlorite (Mahar et al., 1997; Holland et al., 1998), Ti-bearing biotite (White et al., 2007), muscovite (Coggon and Holland, 2002), K-feldspar and plagioclase (Holland and Powell, 2003) and magnetite (White et al., 2002). Modeling of metabasic lithologies TLN54 was performed in the MnO-absent NCKFMASHTO system, with the additional usage of the omphacitic clinopyroxene and amphibole activity–composition relations of Green et al., (2016). The pure phases andalusite, kyanite, sillimanite, rutile, quartz, and H_2O were considered in all cases. The bulk-rock supra-solidus water content of migmatitic units was fixed on an individual basis in order to allow minimal fluid saturation at the wet solidus; here defined as 1 mol% free H_2O.

Detailed investigation into the prograde evolution and P–T conditions leading up to peak metamorphism was achieved by investigating compositional isopleths for pyrope and grossular content in garnet. Since these isopleths vary to first order with changes in pressure and temperature and commonly intersect at high angles, they specify unique intersection points with a high degree of confidence for tracking garnet composition evolution in P–T space. The intersections of isopleths representing

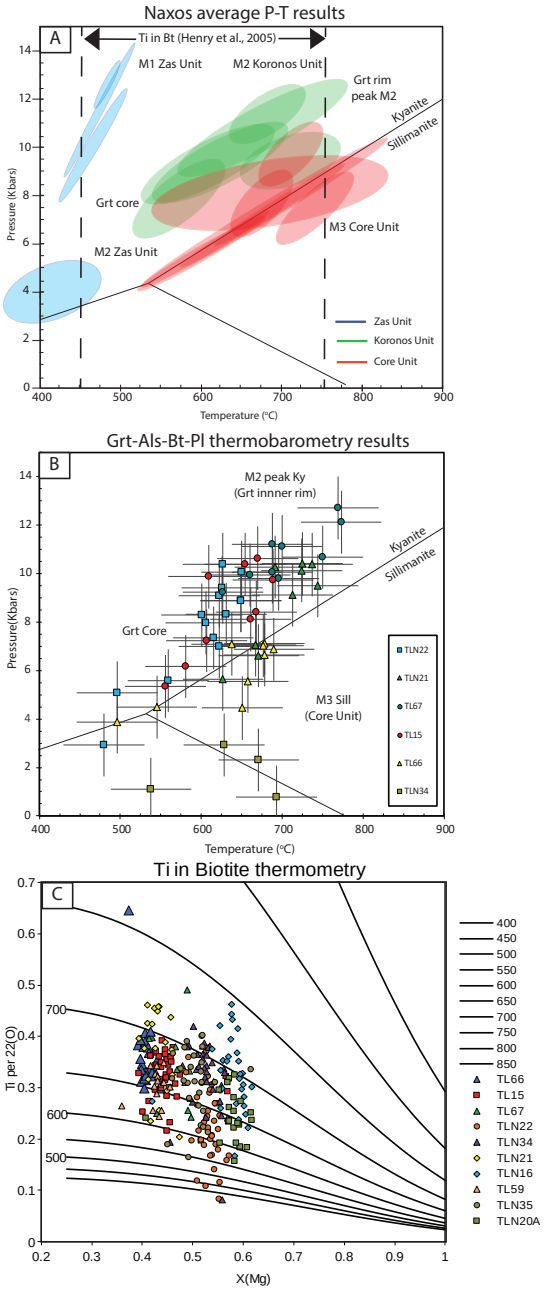


Figure 4.15: Thermobarometry results of Naxos samples. A) Av-PT results using THERMOCALC version 3.40i for all samples with overlaid Ti-in-biotite thermometry results (see Table 4.5 and Appendix 1 for more discussion). B) Results from Grt–Ky/Sill–Plag–Qtz geobarometry (Spear et al., 1993) combined with Grt–Bt Fe/Mg exchange thermometry (Bhattacharya et al., 1992) showing an increase in both pressure and temperature from garnet core to rim, TLN34 and TL66 record lower pressures due to diffusional homogenization of garnet compositions. C) Ti-in-biotite thermometry (Henry et al., 2005) results for Naxos high-grade samples (Koronos and Core Unit), note the range in temperatures due to thermal re-equilibration of particularly high-grade rocks during retrogression.

measured compositions are represented by shaded boxes indicating uncertainties at the 1-sigma level calculated by THERMOCALC.

4.5.1 TLN54: Retrogressed Blueschist (M_1 Zas Unit)

Fig. 4.16 shows the calculated P–T pseudosection for blueschist-facies sample TLN54. Using the methods described in the supplementary material, and the absence of carbonate phases for the modelled area, the fluid was assumed to be pure H_2O in excess. The observed peak M_1 assemblage Gl–Ms–Chl–Rt–Sph–Qtz was calculated to be stable at 11–15 kbar 400–520°C. Glaucophane isopleths of z(gl) = 0.96, f(gl) = 0.02-0.03 and a(gl) = 0.05-0.06 suggest that peak M_1 P–T conditions reached at least 14.5 ± 0.5 kbar, 470 ± 20°C. Model amphibole compositions match well with observed sodic amphibole analytical data from both samples TLN54 and TLN25 (Fig. 4.15). A range of Av-PT results from samples TLN54, TLN25 and TLN26 from the Zas Unit record minimum P–T conditions of around 12 kbar, 450°C, a similar result to peak metamorphic conditions of 13 kbar and 450°C suggested by Avigad (1998) for a jadeite-bearing blueschist within the Zas Unit and comparable to the recently published results of 15.5 kbar, 576°C by Peillod et al. (2017).

4.5.2 TL67: Kyanite Gneiss (M_2 Koronos Unit)

TL67 reveals the prograde and peak P–T conditions for the Koronos Unit and is shown in Fig. 4.17. Using a pure H_2O aqueous fluid, the predicted assemblages are incompatible with observed textures and assemblages, particularly the lack of evidence for melting and sub-solidus K-feldspar. Upon careful observation, the existence of graphite and dark CO_2 fluid inclusions in garnet and quartz indicate circulation of CO_2 fluids during peak metamorphism. A reduction in water activity, a(H_2O), causes the dehydration equilibria that underlie prograde processes in metasedimentary rocks to be displaced down-temperature. Although estimating the actual value of water activity in a rock system is difficult, some constraints can be placed if the rock contains graphite. The coexistence of solid carbon with a C-H-O fluid has a variance of three, so that one

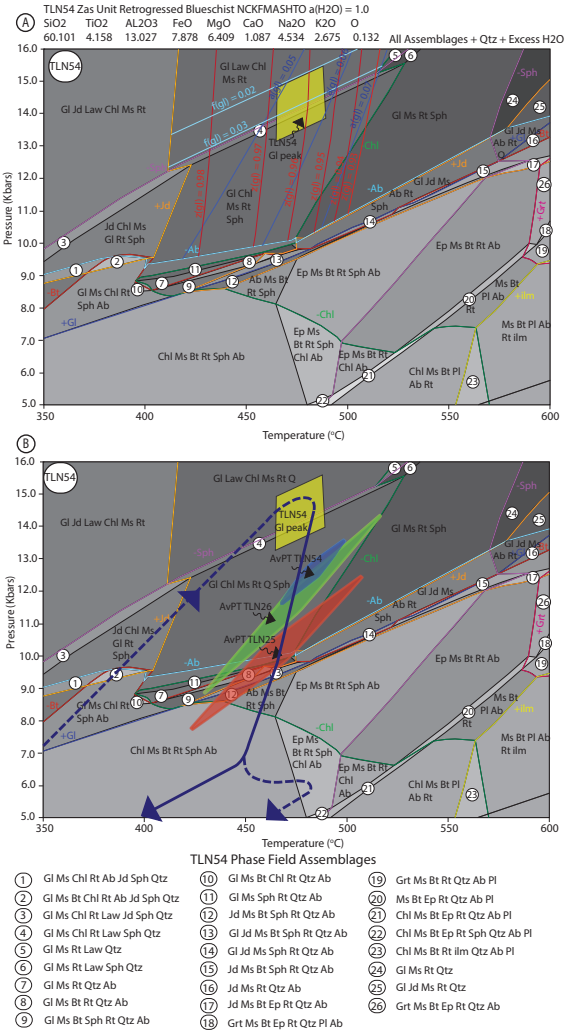


Figure 4.16: *P–T* pseudosection for sample TLN54 from the Zas Unit, using the observed bulk composition, blue arrows and dashed lines present suggested *P–T* paths taken by this rock. A) Glaucophane compositional isopleths of f(gl), z(gl) and a(gl) intersect at peak conditions of ca. 14.5 kbar and 470°C. B) Overlain Av-PT results from this and other samples from the Zas Unit.

further constraint, such as oxygen fugacity, potentially allows the concentration of all C-H-O fluid species to be calculated at any given P and T. Therefore, investigation of the effect of water activity on the calculated phase relations was performed (Fig. 4.17b). Using this method, a reduced a(H_2O) = 0.5 was chosen to represent fluids during peak metamorphism and corresponds to the findings of previous studies of metamorphic fluids on the island (Kruelen, 1980; Barker et al., 1989). This has been shown to shift the solidus to higher temperatures (Peto, 1976; Peterson and Newton,

1989; Stevens and Clemens, 1993; Weinburg and Hasalova, 2015), stabilizing K-feldspar at sub-solidus temperatures as shown in Fig. 4.17b and c.

For a localized Al-rich domain, compositional isopleths representative of garnet core domains (10% pyrope and 11% grossular) intersect at 6.5 kbar and 550°C in the assemblage field Grt–Ms–St–Bt–Pl–Ilm–Qtz–H2O, and those representative of the inner rim (14–15% pyrope and 13% grossular) intersect at 10.5 kbar and 675°C in the assemblage field Grt–Ms–Bt–Pl–Ilm–Rt–Qtz–H_2O. This is consistent with temperature estimates of 630–710°C calculated from the Ti concentration of biotite (Henry et al., 2005), therefore we take these estimates to represent peak M_2 P–T conditions. Garnet outermost rims (13–14% pyrope and 10% grossular) have isopleth intersections at 7.5 kbar, 655°C and crosses the muscovite dehydration reaction to produce K-feldspar. This is associated with an increase in garnet mode that is consistent with garnet rims cross-cutting the S_2 kyanite-grade fabric. Garnet-rim upward inflections in Fe/(Fe+Mg) and spessartine content, are also characteristic features of retrograde replacement by biotite (Kohn and Spear, 2000), and suggest some garnet was resorbed during retrogression.

4.5.3 TL15: Kyanite Migmatite (Core Unit): Peak (M_2) Kyanite-Grade Conditions

This sample records the prograde evolution of the Naxos migmatites and the corresponding pseudosection is shown in Fig. 4.19. Isopleths for garnet core compositions (10% pyrope and 13–16% grossular) indicate prograde metamorphism through the Grt–Ms–Bt–Pl–Ilm–Chl–Qtz–H_2O assemblage field at 6 kbar and 550°C. During prograde metamorphism, significant garnet is predicted to have formed via staurolite breakdown (e.g. reaction 4.1). Garnet compositions just within the inner diffusion-affected porphyroblast rims provide minimum constraints on the conditions of peak metamorphism (Caddick et al., 2010). Isopleths for 17% pyrope and 9–10% grossular intersect at 9.5 kbar and 700°C in the Grt–Ms–Bt–Pl–Ilm–Qtz–Liq–H_2O–Ky assemblage field, indicating that prograde metamorphism occurred along a heating path that

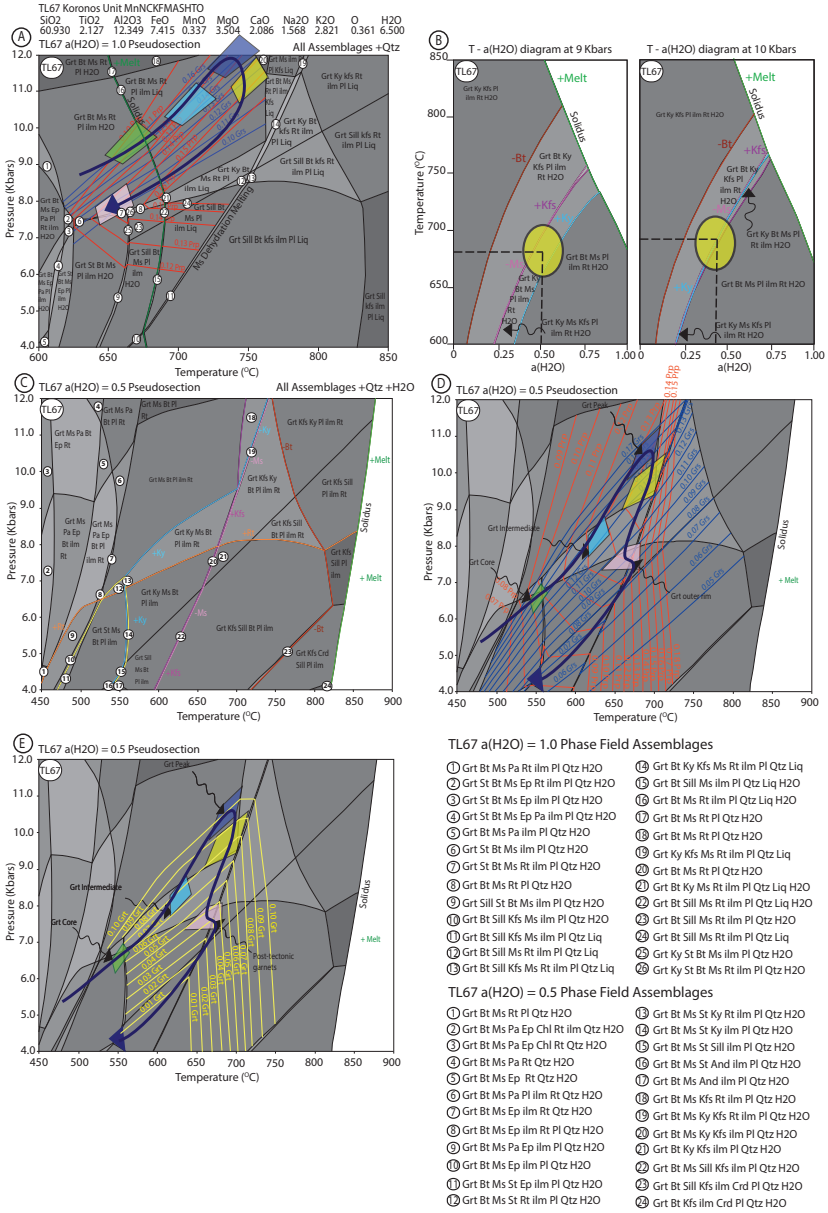


Figure 4.17: Calculated P–T pseudosections for sample TL67 from the Koronos Unit, using the observed bulk compositions, compositional isopleths of grossular (Grs) and pyrope (Prp) for garnet are blue and red respectively. A) Calculated pseudosection for TL67 in the presence of pure water, predicting peak conditions supra-solidus. B) Temperature vs water activity plots at 9 and 10 kbars to show the predicted change in assemblages in response to water activity, water activity of 0.5 relates to the occurrence of Ms + Ky + Kfs at reasonable temperatures from independent Ti in biotite thermometry. C) P–T pseudosection of TL67 for a water activity of 0.5 showing key phase fields. D) Compositional isopleths for garnet showing core compositions intersecting at ca. 6 kbar and 560°C, whereas inner rim compositions representing peak conditions intersect at ca. 10 kbar and 680°C. E) Garnet mode isopleths showing garnet growth with both increasing pressure and temperature, but upon crossing the muscovite dehydration reaction garnet mode isopleths are almost isothermal indicating garnet growth by isobaric heating proposed for small post-tectonic garnets e.g. TLTN22.

crossed the water-saturated solidus (reaction 4.6) at a minimum of 8 kbar, 680°C. High pressure melting is in agreement with the presence of prograde muscovite, bladed kyanites and small proportions (1–4%) of melt distributed along rounded grain boundaries, although peak pressures may have been higher due to diffusional re-equilibration (Caddick et al., 2010). As this rock lies within the same unit as sillimanite-grade migmatites, it is likely that this rock experienced the same prograde path the underlying sillimanite bearing migmatites experienced before obtaining higher temperatures. Due to the lack of sillimanite in this rock, but within 10's - 100's meters of the sillimanite isograd, this rock may have crossed the kyanite/sillimanite transition at peak conditions, via an indirect Carmichael reaction scheme, but preserves no textural evidence owing to its sluggish reaction kinetics. Overall, peak P–T conditions of 730 ± 20°C and 9.5 ± 0.8 kbar obtained from sample TL15 are consistent with peak conditions for sample TL59 (see supplementary material). Therefore, burial of the Core Unit occurred under kyanite-grade (M_2) conditions of 680–730°C and minimum pressures of 8–10 kbar, similar to 670 ± 31°C and 10 ± 0.5 kbar of the overlying Koronos Unit. This should be taken as a minimum pressure and this apparent pressure inversion between the Core Unit and the Koronos Unit could be explained by diffusional homogenization between two contrasting garnet compositions at high-grade conditions. Textural relationships of kyanite aligned and within the uprightly folded migmatitic foliation suggest upright (F_3) folding along a N–S axis occurred immediately following peak M_2 kyanite-bearing conditions. Therefore, E–W-directed compressional deformation that produced these folds took place at lower pressures in the sillimanite-stability field (M_3), the P–T conditions of which have been constrained using garnet rim compositions affected by retrograde equilibration. These compositions (13% pyrope and 6% grossular) suggest P–T conditions of 7 kbar and 710°C (Fig. 4.17), signifying an almost isothermal decompression P–T path during exhumation, cooling at 3°C /km.

4.5.4 TL66: Sillimanite Migmatite (Core Unit): Peak (M_3) Sillimanite-Grade Conditions

TL66 was collected from the deepest parts of the dome across the K-feldspar isograd and bulk compositions were calculated from the observed mineral proportions combining both leucosome and melanosome. Leucocratic networks within and radiating from the Naxos high-grade core combined with the partial preservation of garnet suggests that some melt has been lost from the rock system during its P–T evolution (White and Powell, 2002). Therefore, this bulk composition is appropriate for modeling P–T conditions after the loss of that melt fraction (i.e. it is valid for assessment of peak/near-peak and supra-solidus retrograde metamorphism, but not the prograde sub-solidus evolution prior to melt loss). The resulting pseudosections are presented in Fig. 19d–f, revealing complex sub-solidus topologies whilst supra-solidus the phase relationships are simple with large areas of P–T space without a change in variance. Phase equilibria with excess H_2O was calculated for sub and supra-solidus conditions, representing an external flux of water to produce maximum melting. A closed system model, more realistic of melting, was calculated from analyzing the water content at the hydrous solidus. It was determined that 7.6% H_2O was required to ensure all H_2O enters melt at the solidus, leaving water under-saturated at supra-solidus conditions. The calculated bulk compositions are shown in the supplementary material with associated pseudosections. At sub-solidus conditions, both models predict the low proportions of garnet consistent with the sample and a garnet core composition (14% pyrope, 9% grossular) plotting within the Grt–Ms–Bt–Ky–Ilm–Pl–Qtz–H_2O field at 6.0 kbar and 610°C. This is within 0.3 kbar of the garnet producing reaction, probably reflecting delayed garnet nucleation. The model predicts a prograde P–T path through the kyanite stability field, accounting for kyanite inclusions in muscovite. Supra-solidus, the externally open-system H_2O model predicts K-feldspar absence in the presence of high melt fractions, consistent with faiserkaisel textures and diatexites. Garnet rim compositions (15% pyrope, 6% grossular) plot at 4.9 kbar and 705°C with 33%

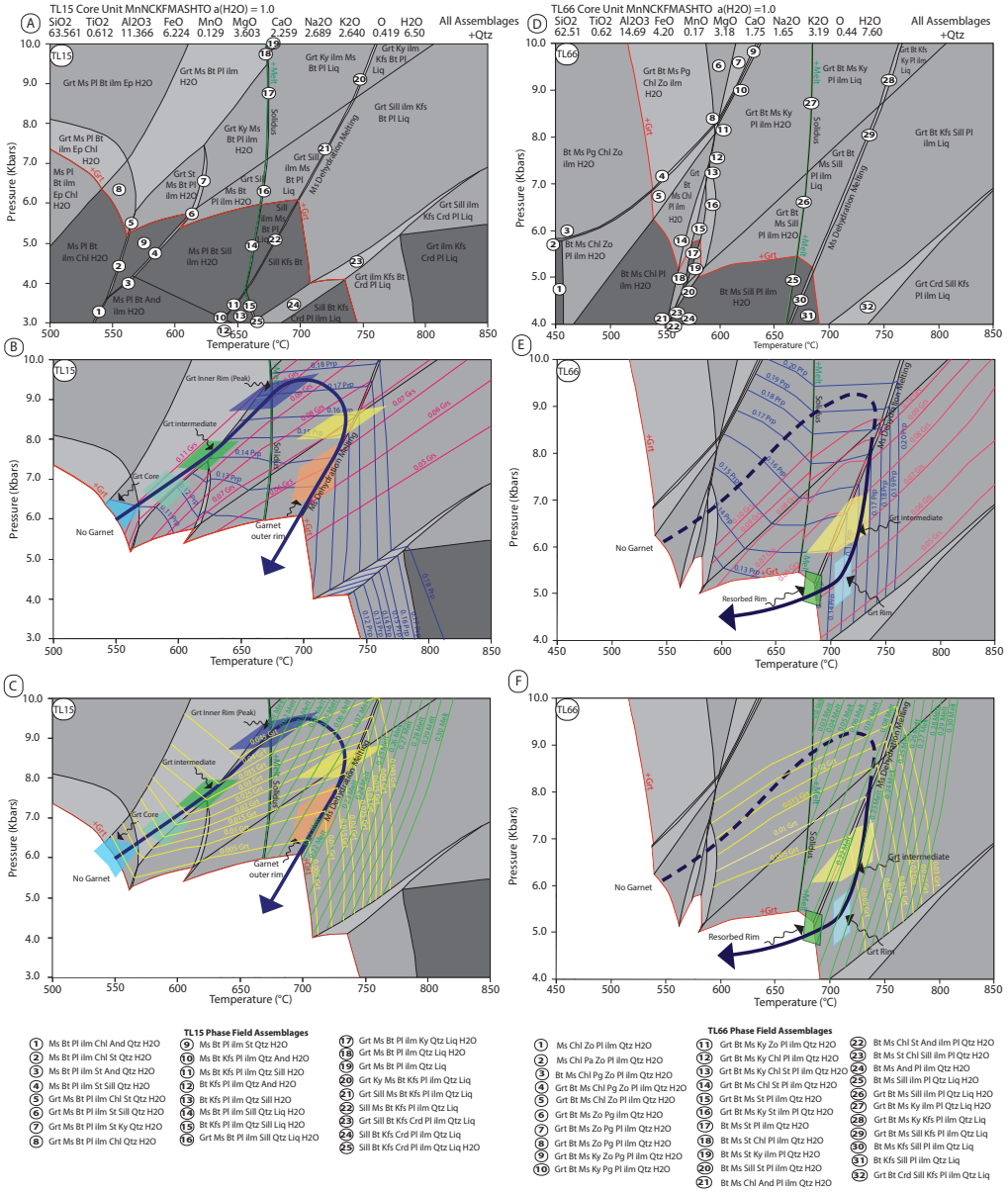


Figure 4.18: Calculated P–T pseudosections for samples TL15 and TL66 from the Core Unit, with garnet compositional isopleths pyrope (Prp) blue and grossular (Grs) Pink and modal proportion of garnet is plotted in yellow. A) TL15 pseudosection using the observed assemblage and pure water activity showing key phase fields, B) Isopleths for garnet compositions show a clockwise P–T loop and suggest the P–T path never crossed the muscovite-dehydration melting reaction. C) Isopleths for garnet mode and proportions of melt, note the rapid increase in partial melt upon crossing the muscovite dehydration melting reaction. D) TL66 pseudosection using the observed assemblage and pure water activity showing phase relations and E) TL66 isopleths for garnet compositions only showing the retrograde part of the P–T path through the sillimanite stability field due to garnet homogenization and resorption. F) Garnet mode and melt fraction isopleths for TL66, note isothermal decompression through the muscovite dehydration melting reaction is expected to decrease garnet mode and cause resorption.

melt. It is unlikely this rock experienced such extensive melting and the presence of kyanite preserved as inclusions within muscovite suggests little fluid infiltration above the solidus.

For the closed system case, less melt is predicted (20%) and the garnet rim compositions plot at higher pressure and temperature (6.0 kbar, 720°C), in the stability field: Grt–Kfs–Bt–Sil–Pl–Ilm–Qtz–Liq beyond the muscovite dehydration melting reaction. This is consistent with the abundance of secondary muscovite produced through the back reaction by eliminating all K-feldspar (shown in reaction 4.4). Assuming a molar 1:1 ratio between K-feldspar and muscovite, it was calculated that 18% volume K-feldspar was required to produce all secondary-muscovite (24% volume). However, only 11% K-feldspar is predicted to coincide with garnet rim compositions, suggesting secondary-muscovite formed by a more complicated process. Release of fluids during crystallization through the solidus re-hydrates the rock associated with the assemblage Grt–Bt–Ms–Pl–Qtz–Ilm and may account for more muscovite production through retrograde water-conserving reactions such as:

$$biotite + sillimanite + quartz + plagioclase \rightarrow garnet + muscovite \tag{4.7}$$

In this case, 11% volume K-feldspar could be attained with just 14% volume muscovite in a simple 1:1 molar ratio. Production of secondary-muscovite through this reaction would also account for less sillimanite and biotite observed than predicted (8% observed compared to 10% predicted) by production of secondary garnet and muscovite. However due to diffusional equilibration at high temperature it is unlikely that garnet rim compositions represent peak temperatures. Ti-in-biotite thermometry also predicts most biotite homogenized at temperatures of 650–700°C which is unlikely to represent peak temperatures. However, Av-PT predicts garnet innermost rims with representative matrix minerals compositions of 7.5±1.2 kbar, 742±39°C (Table 4.5) in agreement with predicted garnet modal proportions. Based on these lines of reasoning, suggest

these results represent peak M_3 sillimanite-grade conditions.

4.5.5 Melt re-integration (prograde evolution)

To account for leucogranites that emanate from and throughout the Core Unit, it is likely that the Naxos migmatites have experienced some degree of melt-loss. This occurs because once melt accumulation reaches a critical threshold, a portion may be lost, creating an open-system environment (Vanderhaege, 2001). This melt composition is dependent on the *P–T* conditions of formation (White and Powell, 2002), and melt extraction events may occur in an interrupted or continuous process (Sawyer, 1996). This open-system behavior, combined with the uncertainty concerning the proportion and composition of melt lost, makes recovering a bulk composition of the protolith very unlikely (Palin et al., 2013). However, White and Powell (2002) showed that various melt-loss scenarios do not change the major sub-solidus and supra-solidus topologies or compositions of peritectic phases. It is therefore possible to calculate an approximate bulk composition suitable for prograde modeling. To reduce uncertainty, the melt-loss was modeled as a single extraction event, representing a simple end-member case. A melt-reintegrated bulk composition was therefore calculated by the addition of a proportion of melt to the observed bulk composition to displace the solidus down-temperature to H_2O-saturated conditions maximizing the amount of mica present prior to melting following the method of White et al., (2004). The composition of reintegrated melt was calculated at 7.75 kbar and 680°C by using the solidus of the original bulk composition in the presence of kyanite. Although higher-pressure than final melt crystallization, this P–T value was chosen because it accounts for the presence of kyanite-bearing migmatites and inclusions in secondary muscovite at higher structural levels (TL15), allowing for a clockwise *P–T* evolution. It was determined that 10% melt should be added to make the solidus water-saturated.

Contours for modal proportion of silicate melt are presented in the supplementary material, and show that melt production across the wet solidus in garnet-bearing assemblages are negligible (1%). It is not until fluid-absent muscovite dehydration oc-

curs that melt generation reaches significant volumes, increasing from 4% to 12% over a very small temperature interval. Contours for calculated modal proportion of garnet allow interpretation of probable conditions of garnet core growth with respect to the melting history. Although garnet cores lack prograde compositional zoning, making the early stages of the P–T evolution poorly constrained, certain inferences can be made. The presence of muscovite inclusions within garnet suggest garnet nucleated prior to the muscovite dehydration melting reaction in a muscovite present field. The presence of kyanite relicts within secondary muscovite suggests that garnet grew when kyanite was stable. A possible interpretation involves a P–T evolution along an initial continental geotherm of 25–30°C/km. This allows initial garnet growth to occur at 600°C and 6 kbar in an assemblage containing Bt–Ms–Pl–Ilm–Qtz–H2O. Contours for modal proportion of garnet reveals that growth in muscovite-bearing assemblages was minor and significant growth of garnet was delayed until K-feldspar is produced as a result of muscovite dehydration along the effective solidus where the proportion of garnet increases significantly with increasing temperature (see supplementary material). However, due to the presence of only 1.5% garnet, we conclude temperatures did not increase significantly upon passing this melting reaction, and thus it is likely that crossing the effective solidus is largely related to de-compression at peak metamorphic conditions.

4.5.6 Post-peak supra-solidus evolution

Crystallization of the final melt fraction upon crossing the solidus is thought to mark the final retrograde textural evolution of an anatectic rock, if no further episodes of deformation or fluid influx occur (e.g. White and Powell, 2002; Indares et al., 2008; Palin et al., 2013). Nonetheless, post-peak compositional changes may still occur via intracrystalline diffusion, as seen in garnet porphyroblast outer rims in contact with matrix biotite, which have grossular and pyrope contents of 6% and 15%, respectively. These are lower than the concentrations recorded in core regions consistent with equilibration down-temperature and pressure (Spear, 1993). Isopleths for the cal-

culated modal proportions of garnet and melt are presented in Fig. 4.18, and show that both phases are produced up-temperature due to the breakdown of muscovite. However, retrograde decompression from our calculated peak *P–T* conditions to the solidus would have involved a reduction in the modal proportion of garnet to form biotite and sillimanite, consistent with observed textures. Taking these factors into consideration reveals that the Naxos migmatites remained supra-solidus during deep crustal exhumation and crystalized through the water saturated solidus at ca. 4.9 kbar, 690°C.

4.5.7 Summary of *P–T* Results

The above data clearly demonstrates that two distinct and contrasting clockwise *P–T* loops are recorded within the Naxos core complex (Figs. 4.15 and 4.21). At high structural levels, the Zas Unit records M_1 conditions of ca. 14.5 kbar, 470°C followed only by retrograde greenschist-facies conditions at < 450°C. In contrast, at deeper structural levels (Koronos and Core Units), (M_1) *HP–LT* conditions are not recorded and instead the rocks experience a clockwise textitP–T path involving (M_2) prograde burial and heating along a Barrovian metamorphic thermal gradient 25°C/km to peak (M_2) *P–T* conditions of ca. 10 kbar, 600–730°C (TL15, TLN22, TL67). At the deepest levels (Core Unit) the rocks cross the water-saturated solidus and then experience hydrous (M_2) kyanite-grade melting (reaction 4.6) (TL15). They then record near isothermal decompression to (M_3) sillimanite-grade conditions of 5–6 kbar, 700–730°C (TL66, TLN34, TLN20A). During this process, the hottest and deepest rocks crossed the muscovite dehydration melting reaction to produce larger melt volumes and peritectic K-feldspar. Textural evidence suggests most melt remained in communication with the rock, and therefore crystallization through the solidus at ca. 5 kbar, 690°C released fluids, causing metasomatism and growth of secondary muscovite cross-cutting the earlier extensional fabric (S_3). Juxtaposition of the hot migmatites against the overlying Koronos Unit causes a thermal (M_3) sillimanite-grade overprint and post-tectonic garnet growth that truncates the S_3 top-to-shear fabrics and earlier (M_2) kyanite-grade

Summary P-T Results Table							Thermocalc AvPT				Ti-in Bt	Pseudosection	
Unit	Sample	Rock type	Mineralogy	Location	Notes	XH2O	End members included	avT ± 1 S.D.	avP ± 1 S.D.	corr	P-T interpretation	Temp-Range	P ± 1 S.D.	T ± 1 S.D.
Zas	TLN54	Glaucophane Rutile Schist	Gln, Czo, Qtz, Ms, Phg, Pg, Chl, Cal, Rt, Sph, Pl	N37.036781 E25.493024	with ab	0.99	gln-fgln-ms-cel-fcel-pa-clin-ab-q-H2O-CO2-cc-rt-sph	483 ± 13	12.6 ± 0.8	0.951	Post-peak M1 albite in	-	14.5 ± 0.5	470 ± 30
Zas	TLN25	Epidote-calc-schist	Gln, Act, Tc, Czo, Qtz, Ms, Pg, Ep, Chl, Cal, Rt, Sph, Bt, Pl	N36.999229 E25.486564	with ab	0.99	gln-fgln-rieb-tr-ts-daph-ames-ep-ta-fta-tats-clin-ab-q-H2O-CO2-cc-rt-sph	465 ± 34	10.1 ± 1.9	0.979	Retrograde M1 albite in	-	-	-
Zas	TLN26	Mica-calc-schist	Act, Czo, Ms, Phg, Ep, Bt, Chl, Cal, Rt, Sph, Qtz, Pl	N36.935434 E25.475521	with ab	0.99	mu-cel-fcel-pa-phl-ab-ilm-sph-rt-cc-CO2-H2O	473 ± 35	11.6 ± 2.2	0.988	Post-peak M1 albite in	-	-	-
Koronos	TL67	Kyanite gneiss	Grt, Ky, Bt, Ms, Kfs, Pl, Rt, Qtz, Tur, ilm	N37.08808 E25.49797	Grt rim	0.50	prp-grs-alm-mu-cel-fcel-phl-ann-east-an-ky-q	682 ± 38	11.4 ± 1.0	0.686	Peak M2	616-731	10.0 ± 0.5	670 ± 20
					Grt int	0.90	prp-alm-phl-ann-east-mu-ky-sill-q-rt-ilm	622 ± 68	9.4 ± 1.3	0.778	Prograde M2	616-732	6.1 ± 0.5	600 ± 15
					Grt rim	1.00	prp-grs-phl-ms-cel-an-q-ky	675 ± 83	10.8 ± 1.6	0.854	Peak M2	616-733	10.0 ± 0.5	670 ± 20
Koronos	TLN22	Kyanite schist	Grt, Ky, Bt, Ms, Kfs, Pl, Rt, Qtz, Tur, ilm	N37.127084 E25.524576	Grt rim	1.00	prp-grs-alm-mu-cel-fcel-phl-ann-an-ky-q	607 ± 67	9.3 ± 1.3	0.770	Prograde-peak M2	458-699	-	-
Koronos	TLN16	Biotite-Schist	Grt, Bt, Kfs, Pl, Qtz, Rt, Ilm	N37.100794 E25.515643	Grt rim	0.50 - 1.00	prp-grs-alm-phl-ann-east-mu-cel-fcel-an-ky-ilm-rt	534 ± 134	7.2 ± 2.1	0.61	Prograde M2	578-740	-	-
					Grt rim	0.50- 1.00	prp-grs-alm-phl-ann-east-mu-cel-fcel-an-ky-sill-ilm-rt	678 ± 122	7.3 ± 2.5	0.986	Post-peak M2-high temp (M3)	578-740	-	-
Koronos	TLN21	Kyanite-Sillimanite-gneiss	Grt, Ky, Sill, Bt, Ms, Kfs, Pl, Rt, Qtz, Tur, ilm, Ap, Chl	N37.125787 E25.518516	Grt rim	1.00	prp-alm-phl-ann-east-mu-cel-fcel-ky-sill-q-rt-ilm	695 ± 67	7.6 ± 1.4	0.984	Post-peak M2-high temp (M3)	586-713	-	-
					Grt rim	1.00	prp-alm-phl-ann-east-mu-ky-sill-q-rt-ilm	625 ± 48	6.1 ± 1.0	0.985	Post-peak M2 re-equilibration (M3)	586-713	-	-
Koronos	17TL75	Garnet Amphibolite	Grt, Hb, Pl, ilm, Qtz, Chl, Rt	N37.125993 E25.517824	Grt int	1.00	prp-alm-grs-tr-fact-ts-parg-rt-q-an-ab	703 ± 69	8.9 ± 1.1	0.819	Peak M2	-	-	-
Core	TL66	Sillimanite-migmatite	Grt, Sill, Bt, Ms(secondary), Pl, ilm, Qtz, Kfs	N37.08880 E25.47022	Grt rim	1.00	prp-grs-alm-phl-ann-east-mu-cel-fcel-an-ky-sill-ilm-rt	742 ± 39	7.5 ± 1.2	0.812	Peak M3 sillimanite-grade melting	651-751	5.5 ± 0.6	720 ± 25
					Grt core	1.00	prp-grs-alm-phl-ann-east-mu-cel-fcel-an-ky-sill-ilm-rt	726 ± 37	7.8 ± 1.1	0.774	M2 kyanite-grade melting	651-751	6.0 ± 0.6	725 ± 25
Core	TL15	Kyanite-migmatite	Grt, Ky, Bt, Ms, Pl, ilm, Qtz	N37.08022 E25.47802	Grt rim	1.00	prp-alm-phl-ann-east-ms-cel-q-ky-rt-ilm	710 ± 31	9.7 ± 1.1	0.693	Peak M2 kyanite-grade melting	589-690	8.0 ± 0.4	690 ± 15
					Grt int	1.00	prp-grs-alm-phl-ann-east-ms-cel-fcel-an-q-ky-rt-ilm	684 ± 118	8.1 ± 1.3	0.517	Prograde M2 onset of melting	589-690	7.5 ± 0.3	710 ± 20
Core	TL59	Garnet-Biotite gneiss	Grt, Bt, Pl, Ms, ilm, Qtz, Tur	N37.06824 E25.44170	Grt rim	1.00	prp-grs-alm-phl-ann-east-ms-cel-fcel-an-q-rt-ilm	675 ± 32	7.7 ± 1.1	0.673	Peak M2 onset of melting	612-674	7.7 ± 0.5	690 ± 25
Core	TLN35	Ms-dehydration migmatite	Grt, Bt, Kfs, Pl, Qtz, ilm, Ap, minor secondary Ms	N37.16228 E25.50452	Grt int	1.00	prp-grs-alm-phl-ann-east-ms-cel-fcel-an-q-ky-sill-rt-ilm	629 ± 47	6.2 ± 1.0	0.983	Post-peak M3 retrograde re-equilibration	615-709	-	-
Core	TLN34	Sillimanite-migmatite	Grt, Sill, Bt, Kfs, Pl, Qtz, ilm, Ap, minor secondary Ms	N37.16236 E25.50238	Grt int	1.00	prp-grs-alm-phl-ann-east-ms-cel-fcel-an-q-ky-sill-rt-ilm	598 ± 66	5.5 ± 1.3	0.98	Post-peak M3 retrograde re-equilibration	570-712	-	-

Table 4.5: Summary of *P-T* results from thermobarometry and THERMOCALC DS-62 Av-PT and pseudosection calculation for all

assemblage (e.g. TLN13, TLN21, TLN22). The rocks then experience a kink in the P–T path associated with cooling at <5 kbar pressure causing resorption of garnet and cooling along a thermal gradient of ca. 40°C/km.

4.6 Palinspatic restoration of the Naxos Core Complex

Although balanced and restored cross-sections cannot be applied to intensely deformed rocks under ductile conditions, we attempted a palinspastic restoration of the metasedimentary and basement units to place minimum constraints on crustal shortening. A simple restoration of Naxos metamorphic core complex was performed to estimate minimum amounts of shortening during the lead up to peak M_3 conditions and post-metamorphic doming, by considering all structural, petrographic, P–T–D, and U–Th–Pb data presented above and in chapter 5. A simple two-dimensional area- and line-balance restoration along section A–A' provides insight into how the metamorphic core complex formed, and how nappes of differing lithologies attained different P–T conditions at different times were juxtaposed against each other. The restoration assumes that in general deformation propagated down-structural section with time, in agreement with structural, petrographic and P–T–D data. The restoration process involves the following steps:

1. The late stage E–W doming and normal faulting has been restored prior to pre-Miocene extension and granodiorite intrusion using the Galanado normal fault as a pinning point (pinning point 5) (Fig. 4.19 stage 1).

2. Three units (Zas Unit, Koronos Unit and Core Unit) are identified within the metamorphic footwall and treated separately; each unit is separated by a major extensional shear zone that cannot be restored due to lack of suitable pinning points (see text for more discussion).

3. Zas Unit (Cycladic Blueschists) is assumed to behave in a brittle-ductile manner

dominantly by thrusting and was restored first (Fig. 4.19, stage 2).

4. Koronos Unit thrusts were restored to align the F_1 and F_2 folds. These folds were then restored using area and line length balancing and assuming there are only 3 bands of marble structurally repeated. Basement-cover repetitions are assumed to represent thick-skinned thrusts and were restored to their original geometry.

5. The Core Unit deformation was restored in two steps. The KSZ was restored by line length balancing of the imbricate stack that utilizes basement material as a relict thick-skinned thrust. Ductile deformation and isoclinal folding is restored using line length and area balancing as above (Fig. 4.19, stage 2). This represents a minimum amount of shortening as the thick-skinned thrusts structurally repeating the basement over shelf are laterally discontinuous and overprinted and reworked by upright folding and ductile flow.

6. Finally a restoration of the continental margin was attempted in stage 3, based on structural mapping in this study. This suggests that Naxos records a thrusted and thickened continental margin sequence in a similar style to the Helvetic Nappes in the Alps and Greater Himalayan Series (Fig. 4.19, stage 3). The results show the restored continental margin was intruded by numerous basaltic and doleritic sills, with intercalated tuffaceous, siliciclastic and carbonate.

A section 13 km wide today restores to a minimum of 60 km. Approximately 400% ENE–WSW shortening across the Naxos MCC is required to explain the folding and thickening during its prograde evolution. Although accurate section balancing is precluded in terrains of ductile deformation such as Naxos metamorphic core complex, an absolute minimum shortening of 47 km cannot be rectified. Although several assumptions were applied, which may be over simplistic and violated in ductile environments, however, this exercise illustrates that the folding of high-grade rocks forming the core complex could not have formed by purely extensional mechanisms. This magnitude of shortening within a continental margin sequence is commonly seen across many recent mountain ranges that experienced shortening and underthrusting of rocks to

kyanite-grade conditions over timescales of tens of millions of years, such as the Himalaya (Corfield and Searle., 2001, 2006) and accretionary wedges including Oman (Searle et al., 2004). Therefore, we believe most of the structures (F_1 and F_2 folding), prograde and peak (M_2) Barrovian conditions of Naxos metamorphic core complex occurred under a compressional tectonic regime, and not under crustal extension. Upright (F_3) folding within migmatites occurred at M_3 sillimanite-grade conditions and invokes a horizontal contractional stress regime. Whatever the cause for this constriction, it highlights a significant space problem requiring lateral displacement of material from the sides, and therefore must have formed when the maximum principal stresses (σ_1) were orientated in a horizontal plane. Deformation as a result of this contraction must have become localized within the rheologically weaker migmatites upon experiencing muscovite dehydration melting causing them to intensely fold, thicken and dome the overlying units. A significant component of E–W shortening is necessary to form the structures on Naxos, and it is suggested that some E–W shortening is occurring throughout the Aegean today (McClusky et al., 2000) accommodated on active conjugate ENE–WSW and WNW–ESE trending strike slip faults like those that cross cut Naxos (see Fig. 4.1). This could be possibly related to a 20° counter clockwise rotation of Naxos about a vertical axis since the mid-Miocene (Kissel and Laj, 1988; Avigad, 1998; Malandri et al., 2016) and explain the late stage gentle folding of the NPDS, the sedimentary units in the upper Cycladic Nappe and the metamorphic sequence. Although the origin of Miocene E–W shortening remains unclear, there are several possible mechanisms that are discussed below. Due to extreme attenuation, missing metamorphic stratigraphy and many unknowns, such as original dip of the NPDS, restoration of the extensional features and therefore the full amount of extension cannot be accurately determined. However, NNE–SSW crustal extension is the last phase of deformation, is pervasive, overprinting and truncating all shortening structures and frozen in metamorphic stratigraphy and the migmatite dome. Assuming the doming occurred at ca. 5 kbar (17.5 km depth), and the NPDS maintained its original dip of ca. 10°C to the north and was responsible for the entire exhumation of Naxos, the throw

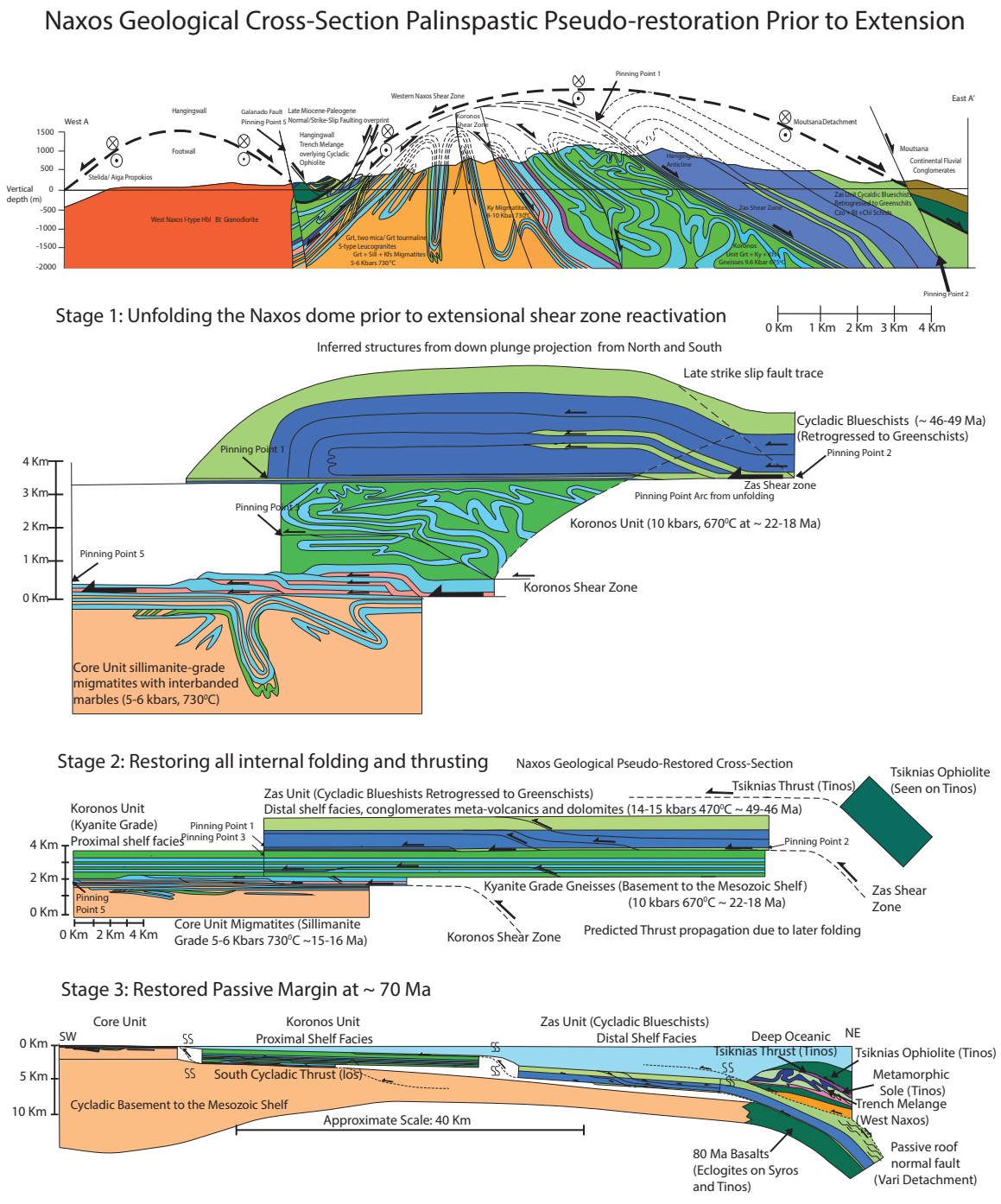


Figure 4.19: Palinspastic pseudo-restoration of the Naxos metamorphic core complex, using the same color scheme as the maps and cross-sections along line of section A–A'. Deformation was restored to that prior to late doming and I-type intrusion at 12.2 Ma, then each unit was restored individually with deformation propagating down structural section with time, finally to the un-deformed restored continental margin at ca. 70 Ma. See text for more discussion and details on each stage of the restoration.

on this single fault is > 100 km. This fault must have been active in its present-day shallow geometry and could not have been rotated from steeper to shallower angles, as the migmatite dome and metamorphic footwall cannot be rotated by over 40°C. It seems likely, however, that the NPDS was not responsible for the entire exhumation on Naxos but rather represents the brittle-ductile transition, mechanically uncoupling the upper and mid crust and was exhumed in its present-day geometry by uplift on several younger cross-cutting brittle normal-faults. The simplistic relationships and restoration for the geometry of the Naxos-Paros Detachment and earlier peak M_2 and M_1 geometries based on field relations, and *P–T–D* data is presented in Fig. 4.20.

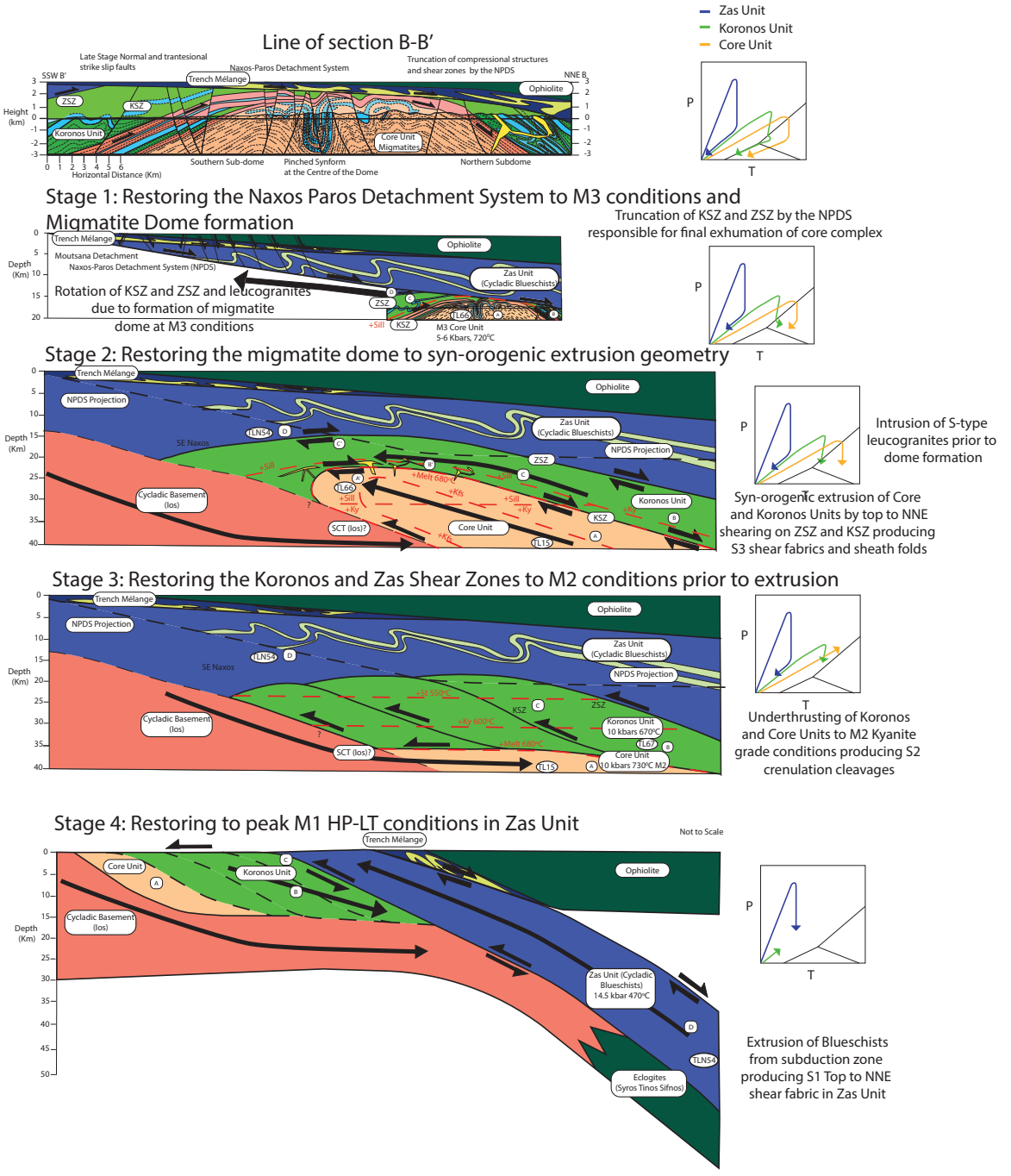


Figure 4.20: Schematic restoration of the Naxos metamorphic core complex along line of section B–B', highlighting that the NPDS must truncate and post-date movement on the ZSZ and KSZ. Schematic predicted P–T–t paths for each unit are displayed on the right. Stage 1, Restoration prior to extension, placing the core complex at 18-20 km depth during migmatite formation. Stage 2, Restoration of the migmatites prior to dome formation. Stage 3, Restoration of the core complex prior to extrusion at peak M_2 kyanite-grade conditions representing 35 km depth. Stage 4, Restoration prior to prograde burial of the Koronos and Core Units during peak M_1 conditions in the Zas Unit. See text for more discussion.

4.7 Discussion

4.7.1 Integration of Structural, Petrographic and *P–T–D* Data

4.7.1.1 Crustal Thickening, Prograde and Peak Metamorphism

The field, petrological and *P–T–D* data from this study imply a complicated tectonic evolution that cannot be explained by extension alone, with juxtaposition of several nappes that experienced differing metamorphic histories, as summarized by Figure 4.21. Previous models of Naxos, whereby all rocks experienced M_1 high-pressure conditions, followed by isobaric heating and Barrovian metamorphism during crustal extension, (e.g. Buick and Holland, 1989; Buick, 1991; Urai, 1991; Avigad, 1998; Vanderhauge, 2001; Kruckenberg et al., 2010), cannot explain the clockwise Barrovian *P–T–D–(t)* paths that involve prograde increasing pressure and temperature of the Koronos and Core Units.

The rocks of south east Naxos (Zas Unit or Cycladic Blueschists) underwent a completely different metamorphic evolution to the underlying higher-grade units. Contrary to previous suggestions that the whole island experienced (M_1) high-pressure conditions (Avigad, 1998, Martin et al., 2006), we find no evidence in the petrography or geochronology (discussed in chapter 5) to suggest that either the Koronos or the Core Units experienced this event. Although it is poorly understood how meta-peridotites occur as enclaves within meta-gabbro (amphibolites) and are associated with both the Koronos and the Zas Shear Zones (Katzir et al., 1999, 2002), several mechanisms have been proposed: 1. Katzir et al., (1999) suggested that the ultramafics were emplaced during Eocene subduction of the continental margin. 2. They could have also been emplaced by thrusting of lithospheric mantle and meta-gabbros into the Naxos shelf carbonate sequence. 3. They were doleritic or gabbroic sills that intruded the continental margin prior to deformation and the ultramafic component represents cumulates that formed during fractional crystallization. 4. They are slithers of serpentinite that were incorporated from a structurally higher ophiolitic thrust sheet, although this requires over several structural km of movement. To explain the

thermometry data of Katzir et al., (2002), minor compositional layering within the host amphibolites and the absence of high-pressure relicts (see 17TL75 in Appendix 1), they are therefore interpretted to represent doleritic-gabbroic sills that intruded the continental margin prior to deformation. This is because the host garnet-bearing meta-gabbros show no evidence of a high-pressure history, and this is the most likely rock composition to preserve evidence for blueschist- or eclogite facies metamorphism (Heinrich, 1982). Furthermore, the mantle wedge in a subduction setting is cold and this disagrees with two-pyroxene thermometry temperatures exceeding 1000°C (Katzir et al., 2002) and this is more likely to be associated with hot intrusion. If the Koronos and Core Units did experience M_1 conditions, they must have been re-incorporated into another prograde burial Barrovian tectono-metamorphic cycle that obliterated all trace of this previous metamorphic event.

Eocene zircon ages of ca. 40 Ma have been reported from amphibolites from northern Naxos and within the Koronos Unit (Martin et al., 2006; Bolhar et al., 2016), and these could represent two possibilities: 1. The ages represent zircon growth during (M_1) *HP–LT* conditions but not in the presence of garnet (Martin et al., 2006), and the unit was extruded to the mid crust before being re-buried and incorporated as part of a separate metamorphic cycle. In this scenario, prograde and peak M_2 conditions would occur ca. 25 Ma after experiencing high-pressure conditions, like the Lepontine metamorphism in the central Alps (e.g. Wiederkehr et al., 2008). 2. Alternatively, the ages do not represent M_1 conditions, which occurred on Naxos between 49–46 Ma (see chapter 5) and regionally at 54–45 Ma (Tomaschek et al., 2003; Lagos et al., 2007; Dragovich et al., 2012). In the absence of high-pressure relicts, the ca. 40 Ma zircon ages could be interpreted to represent the earliest M_2 Barrovian-type age due to overthrusting of the blueschists (Zas Unit). The latter of these two suggestions is our preferred choice and agrees with the petrological record on Naxos and new U–Pb data presented in chapter 5.

To account for contrasting *P–T–D* paths recorded at different structural levels on Naxos, our model features subduction of the distal continental margin (Zas

Unit) down a NE dipping subduction zone, to (M_1) *HP–LT* conditions that reached blueschist facies conditions on Naxos but also eclogite facies conditions as seen on the islands of Syros, Tinos and Sifnos. This was followed by SW expulsion of high-pressure rocks under a passive roof normal fault (Vari Detachment on Syros; Roche et al., 2016; Laurent et al., 2016) at the top of the subduction channel and a thrust at the base. Although this thrust is not convincingly exposed on Naxos due to extensional reworking, there is a strong record of thrust related fabrics (S_{2a} and S_{2b}) and it is possible that the South Cycladic Thrust on Ios (Huet et al., 2009; Mizera and Behrmann, 2015) could be this structure or a related structure. This would produce S_1 top-to-NE shear fabrics in the Zas Unit and the rest of the Cycladic Blueschists and would adequately explain S_2 crenulation cleavages and thrust fabrics under M_2 greenschist facies conditions. Overthrusting of this high-pressure unit onto the more proximal Cycladic continental margin with continued crustal shortening would have led to the generation of a nappe pile (Robertson and Dixon 1984). The proximal sedimentary cover of the continental margin (Koronos Unit) would have subsequently experienced burial, polyphase folding and thick-skinned thrusting as exemplified by structural repetition of basement material overlying metasedimentary protoliths during M_2 kyanite-grade conditions. This would have led to crustal thickening and (M_2) regional metamorphism during the Oligocene to Miocene (40–15 Ma). A crustal shortening mechanism would explain isoclinal F_1 folding during prograde (M_2) Barrovian metamorphism and development of the (S_{2a}) crenulation cleavages (S_{2b}) top-to-SW thrust fabrics under amphibolite facies conditions, preserved in domains unaffected by late cross-cutting S_3 extensional fabrics. Burial of the continental margin to (M_2) kyanite-grade pressures of ca. 10 kbar (ca. 35 km depth) was associated with the development of these shortening structures. Growth of garnet porphyroblasts occurred syn to post-tectonically with localized (S_{2b}) thrust fabrics along cleavage domains at the base of the Koronos Unit, indicating a synchronicity between peak (M_2) kyanite-grade conditions and thick-skinned thrusting. Contrasting peak *P–T* conditions between the Koronos and Core Units, indicate these packages equilibrated along an evolving geotherm at slightly dif-

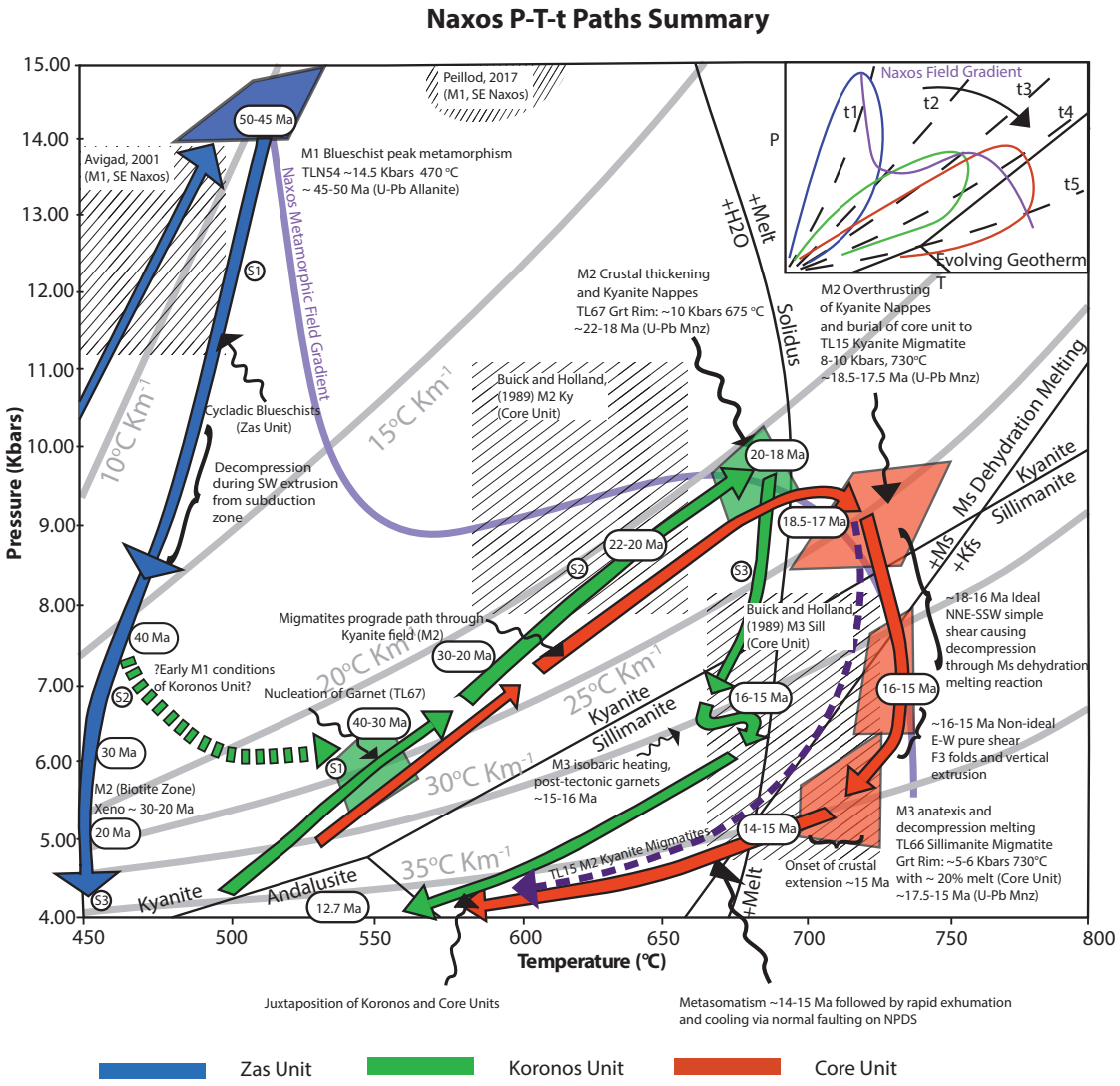


Figure 4.21: Summary P–T–t–D paths for all units from the Naxos metamorphic core complex based on the results of this study. Shaded black hashed boxes represent previous estimated P–T conditions by Buick and Holland (1989), Avigad (1998) and Peillod et al. (2017). Colored polygons represent estimated peak metamorphic conditions presented in this study, with labelled colored arrows that represent suggested P–T paths discussed in the text, with U–Pb ages from geochronology presented in chapter 5.

ferent times (see chapter 5). The most likely explanation in accordance with field evidence is that thick-skinned thrusting was responsible for burying the Core Unit under the Koronos Unit. Repetition of basement rocks interleaved with meta-sedimentary schists and marbles along the base of the Koronos Unit and within the Core Unit are

consistent with this idea. Further evidence for a southwestward verging thrust also occurs on the island of Ios as the South Cycladic Thrust, and places a thin package of amphibolite-grade meta-sedimentary cover over Cycladic basement (Huet et al., 2009; Mizera and Behrmann, 2015).

Following thick-skinned thrusting, conductive relaxation of the footwall geotherm would have heated and driven partial melting over a time span of several million years (England and Thompson, 1984). Footwall rocks firstly underwent prograde hydrous melting in the kyanite field, producing kyanite and garnet bearing microstructural domains and leucosomes (reaction 4.6). Upon experiencing melt weakening, the rocks then record decompression through the muscovite-dehydration melting reaction to sillimanite-grade-conditions. This decompression was associated with non-coaxial (S_3) top-to-NNE shearing, flattening and the development of F_2 sheath folds on the Koronos Shear Zone and Zas Shear Zones. This reaction is the first major melt producing reaction and would allow deformation to become localized along weakened zones of melt segregation and facilitate the development of upright folding. Kyanite-grade fabrics are folded with this foliation, placing tight constraints on the timing of upright (F_3) folding after (M_2) kyanite-grade conditions and following decompression to (M_3) sillimanite-grade conditions.

4.7.1.2 Partial Melting, Decompression and Formation of the Migmatite Dome

Several models for isothermal decompression and migmatite dome formation have been suggested, but many fail to explain all structural, petrological and *P–T–D* constraints. In chapter 5, it is found that decompression of migmatites from ca. 10–5 kbar occurred in less than 2.5 Myrs, a timescale much shorter than previously thought. From the structural and petrological features described in this paper, a relative chronology and framework for sequence of deformation events leading to doming can be firmly established, and therefore the various dome forming mechanisms can be assessed.

Cross-cutting relationships on the Koronos Shear Zone bounding the migmatites,

demonstrate that (S_3) top-to-NNE shearing pre-dates doming and leucogranite intrusion. This is because the shear zones are folded around the dome with consistent top-to-NNE kinematics on all margins. This normal sensed shearing must be associated with SW-directed exhumation of the footwall Core Unit relative to the overlying Koronos Unit. S-type leucogranite dykes and sills clearly post-date shearing as they cross-cut the (S_3) mylonite fabrics on the KSZ (refer to Figs. 4.6–4.7 and supplementary material) and show emanating geometries from the migmatite core (see Figs. 4.5o and 4.7h). The cross-cutting dykes dip at ca. 45°C towards the center of the dome and intrude perpendicular to the S_3 foliation, particularly on the eastern margin. Because these dykes and the shearing foliation are tilted around the dome, it is inferred that both the dykes and shear zones have experienced rotations of ca. 45°C about a NNE–SSW horizontal axis from their original subhorizontal orientation. The leucogranites dykes probably intruded vertically when the KSZ and migmatites where subhorizontal and were passively rotated as the dome formed. Because leucogranites are the product of melt extraction and this only occurs upon reaching the critical melt threshold (7–10%; Rosenberg and Hardy, 2007). This volume of melting only occurred upon decompression through the muscovite dehydration melting reaction (reaction 4.4), at lower pressure (M_3) sillimanite-grade conditions, also coeval with the timing of up-right folding. Upright F_3 folds in the CHSZ have three-fold axes populations that intersect around a vertical point, a type-2 Ramsey fold interference pattern. Vertical boudinage of folds and leucogranite dykes (see Figs. 4.7–4.9), suggests overall horizontal constriction whilst also at M_3 sillimanite-grade conditions. The intense upright E–W and N–S trending isoclinal folds in the center of the dome require the maximum and intermediate principal stresses σ_1 and σ_2 must be almost equal and orientated E–W and N–S in the horizontal planes, whereas the minimum principal stress σ_3, must be orientated vertically. This horizontal contraction scenario can be easily explained to have formed under overall shortening of the crust, and although diapirism would predict similar features (Ramberg, 1980), the low overall melt fractions in migmatites (see Fig. 4.18) are inconsistent with diapirism being the dominant

doming process. Similar features have been documented in Archean granite greenstone terrains such as the Pilbara North Pole Dome in Australia (e.g. Nijman et al., 2017). Although diapirism or crustal turn over has been proposed as a mechanism to form these tonalite-trondhjemite-granodiorite (TTG) cored domes (e.g. Collins et al., 1998), which are associated with larger melt fractions than Naxos migmatites. The pattern of dome and basins with other observed shortening phenomena have indicated the importance of regional compression during the formation of these domes, which may have caused a first Raleigh instability leading to an egg-box pattern of sinking greenstones around the TTG domes (Nijman et al., 2017). N–S horizontal boudinage, and a range of brittle deformation features overprints these folds, suggesting the principal stress axes rotated to an NNE–SSW orientated σ_3 and E–W oriented σ_1 shortly after these folds formed.

Migmatite doming must have therefore occurred as a late feature at low-pressure (M_3) (ca. 5–6 kbar 700–730°C) after top-to-NNE shearing on the KSZ, and upon crossing the muscovite dehydration melting reaction. Although lower crustal isostasy-driven flow during crustal extension has been suggested as a mechanism to produce such upright contractional features at the center of migmatite domes (Kruckenberg et al., 2011; Rey et al., 2011, 2017), the predicted sequence of deformation is inconsistent with our observations. Isostasy-driven flow predicts that decompression is caused by convergent flow of a partially molten lower crust under a horizontally extending upper crust. In this scenario, we would expect high overall melt fractions and doming to occur simultaneously with shearing and opposing and divergent shear senses on all margins of the dome due to a mechanical decoupling of the migmatites with the overlying rocks. In contrast the observations and data presented above suggest the doming, upright folding, vertical boudinage and constriction is a late feature that formed under compression and post-dates decompression and top-to-NNE shearing from peak M_2 pressures. The migmatite dome folds the isograds, intruding S-type granite dykes and the entire overlying metamorphic sequence including the top-to-NNE shear zones (KSZ and ZSZ) and was therefore not mechanically decoupled from the

overlying rocks at the time it formed. Doming therefore represents a separate process to the decompression of rocks from kyanite-sillimanite-grade conditions. To explain the high temperature N–S boudinage overprinting the upright folds and vertical boudinage, it is probable the early stages of doming resulted from constrictional strain localization in the mid crust associated with the rheological weakening upon crossing the muscovite dehydration melting, whereas the latter stages of doming coincided with a change in boundary conditions, most notably a decrease in the N–S principal stress, presumably associated the transition from overall compressional to extensional tectonics (see Fig. 4.22).

4.7.1.3 Origin of top-to-NNE fabrics: Syn-orogenic Extrusion vs Crustal Extension

Isothermal decompression of migmatites and gneisses from 10–5 kbar (ca. 35–17.5 km depth) was rapid and associated with S_3 top-to-NNE shearing on the normal sensed Koronos and Zas Shear Zones. If this normal sensed shearing occurred synchronously with SW directed thrusting within or under the migmatites, it would result in syn-orogenic ductile extrusion in an overall compressional setting (Law et al., 2006; Searle et al., 2006, 2010; Searle, 2010). Ductile extrusion can explain the decompression P–T path and extensional fabrics recoded in several other Barrovian metamorphic terrains in compression, including the Greater Himalayan Series, the Lepontine dome and the Tauern Window in the Alps. There is an abundance of evidence for SSW verging thick-skinned thrusting and compression across Naxos and it seems likely more thick-skinned thrusts are preserved at depth under the migmatites. It is proposed that normal sensed shearing on the Koronos and Zas shear zones occurred due to extrusion in an overall crustal thickening scenario based on five key reasons: 1. If the crust was extending, we would not expect horizontal constrictional strains associated with doming. NNE–SSW crustal extension clearly produced NNE–SSW pure shear boudinage under M_3 conditions that post-dates upright F_3 folding in the migmatite dome. Because F_3 folding pre-dates NNE–SSW extension but post-dates movement on the KSZ, extrusion and

top-to-NNE shearing on the KSZ and ZSZ must also pre-date extension. 2. The KSZ and ZSZ records only top-to-NNE kinematics on all margins of the dome and were therefore active prior to doming, they are not a multi divergent shear zones as predicted by extensional dome models (Kruckenberg et al., 2010; 2011; Rey et al., 2011, 2017). 3. The KSZ and ZSZ are completely discordant to the NPDS at a higher structural level, which truncates them (see Fig. 4.2, 4.3) and the S_3 foliation associated with the ZSZ and KSZ is refolded by F_3 folds which are cut by the NPDS. Therefore, these shear zones formed earlier and are separate structures to the NPDS which exhibits both brittle and ductile deformation features. 4. If movement on the KSZ represents the deep lower crustal signature of a detachment fault associated with crustal extension, then we would expect rapid cooling and migration of the brittle-ductile transition (England and Bickle, 1987). There is no evidence to suggest this occurred. Instead isothermal decompression of migmatites to ca. 5 kbar cooled by ¡30°C upon their exhumation to the mid-crust. This isothermal decompression P–T path would be predicted if the KSZ and ZSZ represent stretching faults or ductile shear zones that progressed up-structural section with time (Means, 1989). 5. Hydrous melting is the major anatectic process for the Naxos migmatites and is responsible for initial melting and weakening at M_2 kyanite-grade conditions. This hydration reaction acts as a large sink of water. To balance the net water budget of the deep crust, requires a large external supply of water. A potential water source to drive partial melting process could be the result of prograde dehydration reactions from underthrusted crust. Underthrusted rocks would have been experiencing prograde metamorphism and dehydration reactions at the time of migmitization in the overlying units. This could alleviate this conundrum as liberated water will migrate into the overlying migmatites and act as a source to drive anatexis. Contrastingly during crustal extension, underthrusting of hydrated rocks would not occur and we would expect dry granulite facies rocks to underlie Naxos migmatites which would be strong and less likely to flow or act as a source of water to drive anatexis.

If indeed the Koronos and Zas Shear Zones represent passive roof stretching normal faults in an overall compressive and E–W horizontal constrictional regime.

These faults would form at the top of the SW extruding wedge, as material was returned via ductile flow towards the foreland and possible erosion front due to melt weakening and the buoyancy and viscosity contrast of migmatites. Together these shear zones preserve a sequence of right way up metamorphic isograds, similar to the South Tibetan Detachment in the Himalaya by a process of general shear (simple shear plus pure shear flattening) which telescoped the isograds (Jessup et al., 2006; Cottle et al., 2007; Law et al., 2004; Searle et al., 2006, 2010). Top-to-NNE shearing (S_3) (Fig. 4.22, stage 1), firstly developed along the rheological boundary marking the solidus. Deformation temperatures on the KSZ exceed 650°C and it is therefore responsible for the earliest and deepest stages of exhumation. With subsequent ductile flow, sheath folds developed under general shear due to high non-coaxial shear strain followed by E–W constriction (Fig. 4.22, stage 2).

Emplacement of hot migmatites at mid-crustal levels would have provided the thermal perturbation in the hangingwall of the KSZ to nucleate post-tectonic garnets that cross-cut S_2 kyanite-grade and S_3 top-to-NNE shearing fabrics and M_3 sillimanite-biotite intergrowths with strong annealing textures (Fig. 4.22, Stage 2). This thermal pulse would also explain the intrusion of S-type leucogranites into the Koronos Unit, that cross-cut the S_3 blasto-mylonite fabric. All structures were then gently domed about a N–S axis that resulted in the frozen in bulls-eye isograd pattern. Following extrusion of migmatites to shallower crustal levels and F_3 upright folding, initiation of NNE–SSW regional extension produced retrograde greenschist facies, top-to-NNE (S_3) mylonite fabrics associated with the NPDS that truncates, reactivate and utilize sub-parallel (S_{2a}) crenulation cleavages and top-to-SW (S_{2b}) fabrics. NNE–SSW boudinage of amphibolites in the CHSZ, indicate a rapid switch from crustal thickening to NNE–SSW regional extension during the closure of the M_3 event.

4.7.1.4 Exhumation of the Core Complex and Regional Extension

Regional extension from 15 Ma (See chapter 5) (Fig. 4.22, stage 3), was accommodated by normal faulting and horizontal NNE–SSW directed pure shear ductile boudinage.

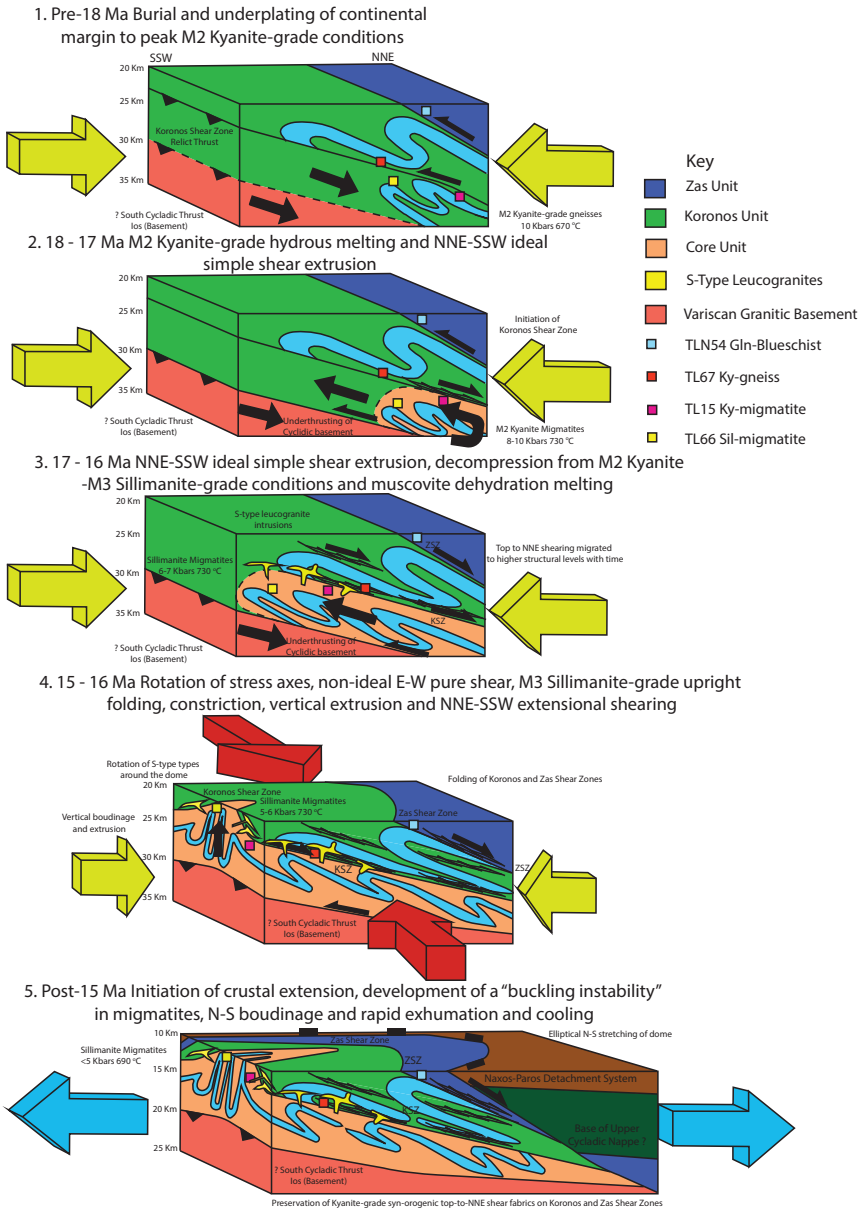


Figure 4.22: An extrusion model to explain and visualize the sequence of deformation events that created S*3* top-to-NNE shear fabrics on the KSZ and ZSZ and the decompression of high-grade rocks on Naxos from 10-5 kbars followed by migmatite doming. Inclusion of U–Pb age data presented in chapter 5 is shown to avoid confusion and samples TL15, TL66, TL67 and TLN54 are approximately located and their spatial evolution is illustrated as the model progresses. Stage 1: pre-18 Ma, Prograde burial and metamorphism of the Koronos and Core Units forming F_1 isoclinal folds. Stage 2: Peak M_2 kyanite-grade metamorphism and partial melting of the Core Unit. Stage 3: Syn-orogenic extrusion of the Koronos and Core Units under passive roof normal faults. Stage 4, rotation of principal stress axes causing constriction at M_3 sillimanite-grade conditions. Stage 3, Onset of extensional tectonics and initiation of NPDS that truncates and is discordant to all earlier structures.

In the upper crust, normal faults sole into and cross-cut a low-angle detachment horizon (NPDS). This structure is discordant to, and truncates the folding, migmatite dome and metamorphic stratigraphy within the core complex, caused extreme telescoping of previously frozen in isograds beneath it, and rapid footwall cooling at rates of 60–90°C/Myr along a peak thermal gradient of 40°C/km (see chapter 5). The onset of extension is recorded by the kink in the P–T path whilst the migmatites were at the close of the M_3 event at ca. 5 kbar, 690°C (Fig. 4.21). The Naxos I-type granodiorite intruded into the metamorphic sequence at ca. 12.2 Ma, and is cut by the NPDS, with brittle-ductile deformation features including pseudotachylites suggesting the arrival of the core complex to the brittle-ductile transition at this time. Contrastingly, in the ductile crust, extensional strain during the latter stages of the sillimanite-grade event was accommodated by mainly NNE–SSW directed pure shear with extensional strains of up to ca. 50%, resulting in horizontal boudinage and stretching that overprints earlier compressional features (e.g. Figs. 4.8 and 4.9) and forms the elliptical dome structure.

4.7.2 Significance of E–W Shortening

This study and several others highlight a significant component of E–W shortening on Naxos (e.g. Virgo et al., 2018). This shortening occurred during migmatite dome formation, F_3 folding and occurred prior to and synchronous with regional NNE–SSW extension. All structures including the NPDS, aplite sills within the 12.2 Ma granodiorite and even Pliocene-Pleistocene sediments are folded or tilted around the island, that cannot be explained by isostatic footwall rebound alone. It is unclear what the origin of this shortening was during the Miocene, as it would pre-date movement on the North Anatolian Fault that commenced at ca. 11 Ma (e.g. Menant et al., 2013). Convergent E–W lower crustal flow during NNE–SSW extension (Kruckenberg et al., 2011) could possibly explain E–W shortening in the middle of the migmatite dome, but this should be simultaneous with NNE–SSW extensional boudinage and would exclusively affect migmatites, in disagreement with our observations of F_3 folding also affecting

the entire carapace. Furthermore, many islands in the Cyclades document a significant component of E–W shortening (e.g. Virgo et al., 2018 and references therein) indicating it was a regional compressive stress and not related to ductile convergent flow of migmatites under crustal extension (Kruckenberg et al., 2011). It is possible that Miocene E–W shortening relates to the westward escape of Anatolia into the Cyclades (e.g. Phillipon et al., 2014). This would be accommodated via dextral strike slip reactivation of the eastward Vardar Suture Zone to the north of the Cyclades and possibly related to strike slip movement on the Mid-Cycladic Linement (e,g. Malindri et al., 2016), prior to rollback on the Hellenic subduction zone. This scenario may possibly produce horizontal constriction type conditions due to shortening in all directions like those recorded in the Naxos migmatite dome. This would be followed by NNE–SSW extension following a change in boundary stresses, either due to the onset of slab roll back on the Hellenic subduction zone or removal of lithospheric mantle during the mid-Miocene. Doming of Pleistocene sediments on the margins of Naxos is probably related to a component of recent E–W transpression, which possibly resulted in a 20° anti-clockwise rotation about a vertical axis (Kissel and Laj, 1988) and the series of conjugate NNE–SSW NNW–SSE trending strike slip faults that cross-cut the island.

4.7.3 Possible Comparisons to Other Mountain Belts

Naxos records the entire evolution of an orogeny, from ophiolite obduction to post-orogenic collapse and displays similarities to many well studied geological areas including:

1. Oman / UAE: The relatively unmetamorphosed hangingwall of the NPDS displays an ophiolitic mélange similar to the Haybi Oceanic Unit, directly underlying the sole of the Oman / UAE Ophiolite (Searle and Cox, 2001). This unit is interpreted to represent off-axis alkali seamounts with carbonate caps that formed on the lower plate and were scraped off into a mélange during the subduction/obduction process. Oman also records blueschist-eclogite facies rocks that are bounded by normal sensed extensional shear zones within the continental margin sequence

under the ophiolite. These formed ca. 15 Myrs after the initiation of obduction as the leading edge of the Arabian continental margin attempted to subduct. A comparable ophiolite obduction scenario could also have taken place in the Cyclades prior to high-pressure metamorphism of the Cycladic Blueschists, that also represent the leading edge of the Cycladic Continental Margin.

2. The Tauern Window, Austrian Alps: The metamorphic footwall of the Naxos MCC records Barrovian metamorphism due to the stacking of various tectonic slices. Many comparisons can be drawn to the Tauern Window in the Austrian Alps, one of the most intensely studied overthrust terrains on the planet (e.g. Schmidt, 2013; Smye et al., 2011 and references therein), composed of an amphibolite facies metamorphic core that underlies discrete slices of eclogite and blueschist facies thrust sheets. Barrovian metamorphism was a result of overthrusting Austroalpine nappes derived from the Adriatic continental margin (upper plate), in some respects like the Upper Cycladic Nappe (Jolivet et al., 2013) and Cycladic Blueschists.

3. The Greater Himalayan Series (GHS) in the Himalaya: The metamorphic core of the Himalaya records an almost identical P–T–D path to what we observe on Naxos. Kyanite-grade conditions followed by isothermal decompression through the muscovite dehydration melting reaction to lower-pressure sillimanite-grade conditions and S-type leucogranite formation. Decompression occurred during SW-directed extrusion of the GHS in an overall compressional setting, bounded by the Main Central Thrust at the base and the South Tibetan Detachment System (STDS) at the top, that were active at the same time. The extensional top-to-NE shear fabrics on the STDS formed due to exhumation of footwall material beneath a fixed hanging wall in an overall compressional setting and preserve a sequence of right way up metamorphic isograds, strikingly similar to the Koronos and Zas Shear Zones on Naxos. Naxos has gone one stage further than the Himalaya and represents a collapsed orogen that beautifully documents the tran-

sition from an overall compressional to extensional environment that coincided with the latter stages of migmatite dome formation.

4. Betic-Rif, Spain: Records the transition from overall compressional to extensional tectonics. Eocene to Oligocene south directed subduction was associated with high-pressure metamorphism of the Iberian continental margin and was followed by significant crustal thinning and coeval heating during the early stages of arc formation (e.g. Platt et al., 2013). It is debated what caused extension within the hinterland of this orogen, but removal of lithospheric mantle, seems the most likely scenario and would result in upwelling of the asthenosphere causing heating, a rise in topography, crustal extension, and rapid westward rollback on the West Mediterranean subduction zone (Platt et al., 2013 and references therein). Comparable processes could have caused extension within the Aegean during the late Miocene. An important difference between Naxos and the Betics, is that there is substantial kyanite-grade metamorphism and no sub-continental lithospheric mantle exhumed in the Cyclades, as the Moho lies at approximately 25 km depth and deepens to the north (Cossete et al., 2016).

4.8 Conclusions

The tectonothermal evolution of Naxos MCC is more complicated than can be explained purely by crustal extension. The data presented in this study demonstrate that Naxos records a prolonged history of compression, resulting in crustal thickening and regional metamorphism followed by extension. Eight key points can be made:

1. The footwall of Naxos metamorphic core complex represents three tectono-metamorphic units that each record contrasting *P–T–D–(t)* paths and represents a series of nappes that were stacked due to prolonged crustal thickening. During this process, rocks were buried and metamorphosed diachronously as the geothermal gradient conductively increased over time, and eventually resulted in Barrovian metamorphism and partial melting. The sequence records M_1 blueschist facies

conditions at the top to M_2–M_3 upper amphibolite facies migmatites at the base.

2. These nappes are juxtaposed against one another by top-to-NNE normal sense ductile extensional shear zones that coincides with peak M_2–M_3 Barrovian conditions at the deepest levels. This resulted in telescoping of previously frozen-in isograds during extrusion of footwall rocks, similar to the normal sense shear zone of the South Tibetan Detachment bounding the top of the Greater Himalayan Sequence. Deformation migrated from deep to shallow structural levels with time and was associated with general shear. These shear zones pre-date doming and are discordant to, and pre-date normal faulting related to crustal extension. In contrast, the low-angle normal faults truncate all structures and metamorphic stratigraphy in their footwall.

3. The hanging wall of the NPDS dominantly comprises of trench mélange formed along the base of the obducting ophiolite. This may record further evidence for a relict ophiolite obduction event, as seen on Tinos (see chapter 2), that preceded M1 high-pressure metamorphism in the Cyclades. Ophiolitic rocks are exposed at the highest structural level across the Cyclades. Miocene-Pliocene fluvial sediments and conglomerates are unconformable on top of this, suggesting that topography was much higher during the Miocene.

4. At the deepest levels, M_2 kyanite-grade hydrous melting (reaction 4.6) was the dominant melting process and was followed by isothermal decompression from ca. 10 kbars 680–750°C to 5–6 kbars 700–730°C. With small degrees of partial melting the migmatites weakened and decompressed under a passive roof normal fault (Koronos Shear Zone). The hottest and most deeply buried rocks decompressed through the muscovite dehydration melting reaction (reaction 4.4), locally producing up to 20–25% melt. This advective process may act as substantial source of heat applicable to many Barrovian metamorphic terrains.

5. The migmatite dome is a late feature and formed in a constrictive stress regime at lower pressure M_3 sillimanite-grade conditions. This post-dates top-to-NNE

shearing on the Koronos and Zas Shear Zones and folds the entire metamorphic sequence. Structural analysis of polyphase deformation within the center of the dome indicates a major change in stress regime from NNE–SSW compression to dominantly E–W contraction and later NNE–SSW extension, coinciding with doming.

6. Naxos records the transition from compression to extension in the Cyclades. The formation of the sillimanite-grade migmatites marks the climax of high-grade metamorphism in the Cyclades, and no evidence for crustal thickening post-dates this event. Within the dome, N–S pure shear horizontal extensional boudinage occurred during ending of the M_3 sillimanite-grade event and overprints earlier upright F_3 isoclinal folds and vertical boudinage. This corresponds to the final stage of migmatite dome formation and marks the transition from regional compression to extension in the Cyclades.

7. Regional extension and crustal thinning was accommodated by brittle-ductile normal faulting that cross-cuts and is discordant to all footwall structures. It attenuates and telescopes the frozen in metamorphic isograds to produce metamorphic field gradients of up to 700°C/km, particularly in west Naxos. Whereas in the ductile crust, horizontal N–S pure shear boudinage accommodates extensional strains of up to 50%. These structures post-date all earlier collisional features and brittle-ductile normal faulting was responsible for the final stage of exhumation from 5 kbar (approximately 17.5 km depth) to the surface along an apparent geothermal gradient of 40°C/km.

8. Three types of extensional fabrics are recorded on Naxos: i) SW extrusion from the subduction zone as recorded in the Zas Unit with top-to-NE fabrics, ii) Syn-orogenic SSW extrusion of migmatites and high-grade gneisses under a passive roof fault (Koronos and Zas Shear Zones) with top-to-NNE kinematic indicators, and iii) Top-to-NNE extensional fabrics due to late brittle-ductile cross-cutting normal faults related to crustal extension and cooling (NPDS) that is superim-

posed on earlier fabrics along the western side of the core complex. In particular, extensional fabrics on the Koronos and Zas Shear Zones within the metamorphic footwall are responsible for syn-orogenic extrusion of kyanite to sillimanite-grade gneisses and migmatites that pre-date extension. These are truncated and cross-cut by later S-type granite dykes and lower-grade fabrics and structures related to crustal extension.

Because the timing constraints and rates of deformation, metamorphism and partial melting are crucial in resolving the complete *P–T–D–(t)* history of Naxos to a high resolution. In chapter 5 new U–Th–Pb age data is presented and a fully integrated tectonic model for the development and exhumation of Naxos metamorphic core complex and show that Naxos documents the entire evolution of what we term the "Aegean Orogeny". This mountain belt records a full orogenic cycle from ophiolite obduction, high-pressure metamorphism, subduction-related exhumation, crustal thickening and regional metamorphism to post-orogenic extension. We demonstrate that the transition from compression to extension on Naxos coincided with the latter stages of migmatite formation at ca. 15 Ma, corresponding with the timing of a major slow-down in the convergence rate between Nubia and Eurasia (DeMets et al., 2015). This new structural and metamorphic framework is built upon and show that crustal extension was associated with rapid cooling, brittle-ductile normal faulting and was responsible for the final stages of core complex exhumation that post-dates peak metamorphism, partial melting and syn-orogenic extrusion.

Chapter 5

Compressional origin of the Naxos metamorphic core complex: U-Th-Pb geochronology

5.1 Introduction

The time-scales of metamorphism and the thermal budget of mountain belts has remained a fundamental conundrum in our understanding of metamorphic processes and the transfer of heat through the continental crust. In particular, there is much to learn about how the crust responds to crustal thickening followed by extensional tectonics, and the timescales and structural and metamorphic signatures associated with this switch. Furthermore, the thermal evolution of metamorphic core complexes and rates at which they form, and the causes of partial melting and migmatite dome formation in orogenic belts are poorly understood (Platt et al., 2014).

Metamorphic core complexes (MCCs) occur in both compressional and extensional tectonic environments, and deciphering their thermal evolution and the relative roles and timing of compression and extension is often difficult, as earlier collisional features have been completely or extensively overprinted by features associated with either syn-orogenic or regional crustal extension. Normal sensed extensional fabrics do

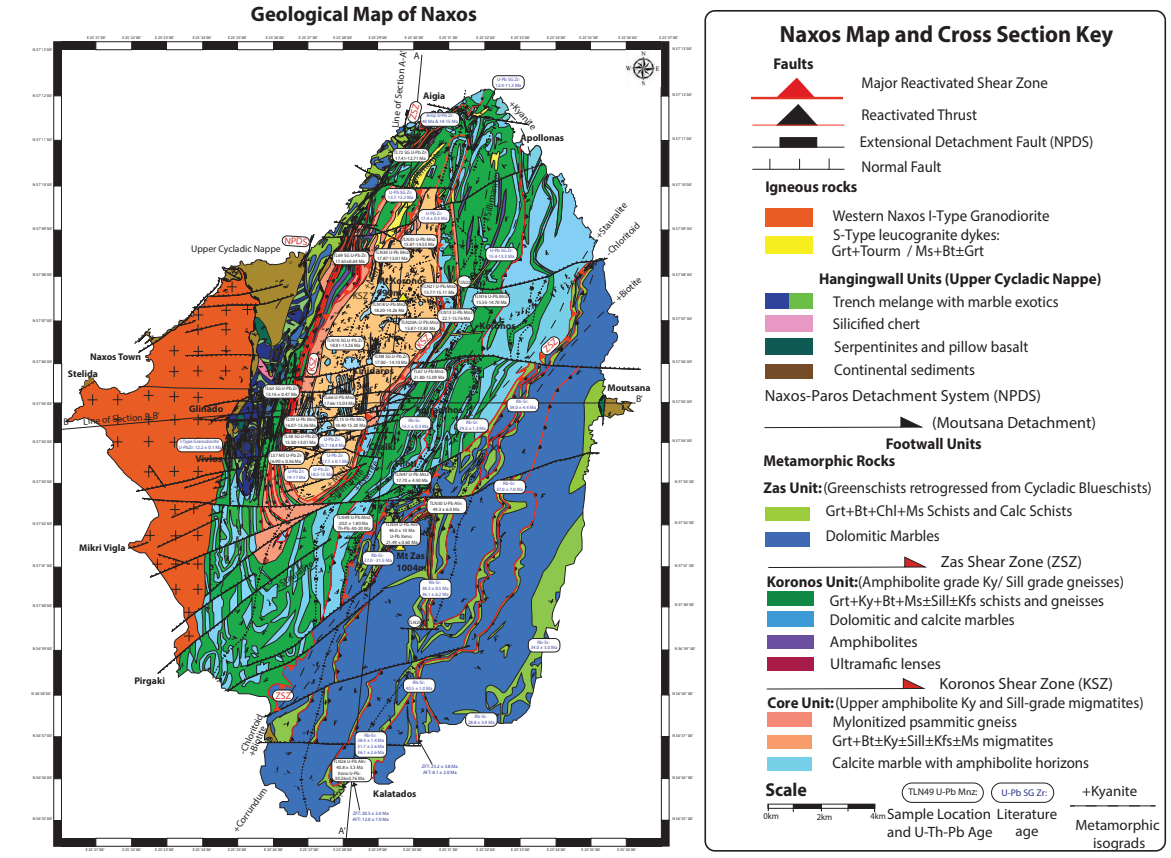


Figure 5.1: New geological map of Naxos described in chapter 4 with new key tectonic implications: Three tectono-stratigraphic units include the Zas Unit (blueschist-facies M_1 conditions), Koronos Unit (kyanite-grade M_2 conditions) and Core Unit (kyanite and sillimanite-grade anatexis M_2-M_3). Sample locations with U–Pb ages are presented on the map with errors reported to 2 sigma level (Mnz = Monazite, Zr = Zircon, Aln = Allanite).

not exclusively decipher the tectonic regime, but rather record the relative movement and exhumation of material. Extensional shear fabrics are abundant in many metamorphic core complexes and cannot be exclusively used as indicators for crustal extension as they also occur in many compressional environments, such as at the top of an extruding subduction channel, e.g. Oman (Searle et al., 2004) and the top of the Greater Himalayan Series under the South Tibetan Detachment System (e.g. Law et al., 2006; Searle et al., 2006, 2010; Searle, 2010). For this reason, the detailed tectono-thermal histories of metamorphic core complexes can only be successfully interpreted by examining the nature and style of P–T–t–D paths in relation to the larger scale structures. Naxos in the central Aegean Sea provides a natural laboratory for gaining insight into

such an enigma, as there is evidence for a whole sequence of deformation leading up to peak Barrovian metamorphism and partial melting (presented in chapter 4) that was followed by the onset of extensional tectonism. Detailed structural and textural relationships and *P–T–D* conditions of metamorphism from all levels of the Naxos metamorphic core complex was presented in chapter 4. Previous zircon U–Pb dating of granites, gneisses and amphibolites has been undertaken from deep levels of the core complex (Keay et al., 2001, Martin et al., 2006, Bolhar et al., 2017), however, this has not been combined with detailed petrographic and textural observations, cross-cutting field relationships or satisfactorily linked to the *P–T* paths, making the interpretation of the reported ages uncertain. In this contribution, we focus on monazite, zircon, allanite, xenotime and rutile U–(Th)–Pb geochronology across all structural levels of Naxos to obtain a high-resolution chronology of metamorphism, anatexis and cooling of the core complex. We integrate the new geochronological dataset with pre-existing published ages and the established*P–T–D* paths of each tectonostratigraphic unit (described in chapter 4), to obtain insight into the nature and rates of the processes involved with metamorphic core complex formation and exhumation. Key questions we aim to address include the timescales associated with overthrusting, prograde metamorphism, decompression melting, migmatite dome development and the timing and onset of extensional tectonics.



Figure 5.2: Continues on next page

Figure 5.2: A) Summary annotated N-S cross-section (A-A') across Naxos with outcrop photographs highlighting key structural relationships. Sample locations are projected onto the line of cross-section. B) Upright vertical boudinaged leucogranite dyke (TLN8) intruding uprightly folded marble within the central high strain zone (CHSZ) at the center of the migmatite dome (N37.106308, E25.482335), indicating horizontal constriction during dome formation. C) Outcrop photograph of TLN49 showing crenulation cleavages (S_{2a})affecting lower amphibolite facies assemblages (N37.04549 E25.50794). D) TL72 representing a deformed leucogranitite dyke with a U-Pb age of 12.71 ± 0.81 Ma that is sheared into alignment with the Naxos-Paros Detachment System (NPDS) (N37.182468, E25.506512) with small ultramafic lenses along the foliation plane, constraining the age of extensional shearing to post ca. 12.7 Ma. E) Mylonitites from the Koronos Shear Zone (N37.048169, E25.455655) with top-to-NNE kinematic indicators but preservation of earlier compressional features and isoclinal folds along zones of lower strain. F) Cross-cutting leucogranite dyke (N37.094469, E25.443173) on the western side of the dome, sample TL63 yields 13.16 ± 0.47 Ma providing an upper limit of shearing on the KSZ. G) Upright vertical boudinage within the central high strain zone (CHSZ) at the center of the migmatite dome (N37.106308, E25.482335), with a minimum principal stress orientated vertically. H) Outcrop photo of high melt fraction migmatite (diatexite) (N37.089809, E25.462043) with clear selvages of melt and pathways of melt extraction. I) Cross-cutting leucogranite dyke across the Koronos Shear Zone (N37.117168, E25.529470), TL58 yield ages of 14.43 ± 0.90 Ma suggesting the timing of top-to-NE shearing and foliation development on the KSZ to pre 14.4 Ma. J) Pure shear N-S boudinage of amphibolites in marbles that overprint tight isoclinal folds from the CHSZ (N37.106017, E25.482672), indicating N-S extension after high-grade compression, see text for more discussion. K) Upright E-W trending F_3 folds in amphibolites within marble from the CHSZ that have been vertically boudinaged.

5.2 Overview of Existing Geochronology

Current understanding of the timing of metamorphism within the Naxos metamorphic core complex is based on ^{40}K–^{40}Ar and ^{40}Ar–^{39}Ar thermochronology, and Rb–Sr and U–Pb geochronology of granitoid, migmatite and amphibolite samples (Andriessen et al., 1979; Wijbrans and McDougall, 1986, 1988; Keay et al., 2001; Martin et al., 2006; Duechene et al., 2009; Bolhar et al., 2017; Peillod et al., 2017). These studies have highlighted that the island experienced a prolonged period of metamorphism prior to peak conditions spanning ca. 40–15 Ma. Various workers have presented a thorough ^{40}K–^{40}Ar and ^{40}Ar–^{39}Ar study of micas and hornblende across all structural levels of the metamorphic core complex, finding that ages get younger towards the migmatite core (Andriessen, 1979; Andriessen et al., 1987; Wijbrans and McDougall, 1986, 1988), as presented in Fig. 5.3.

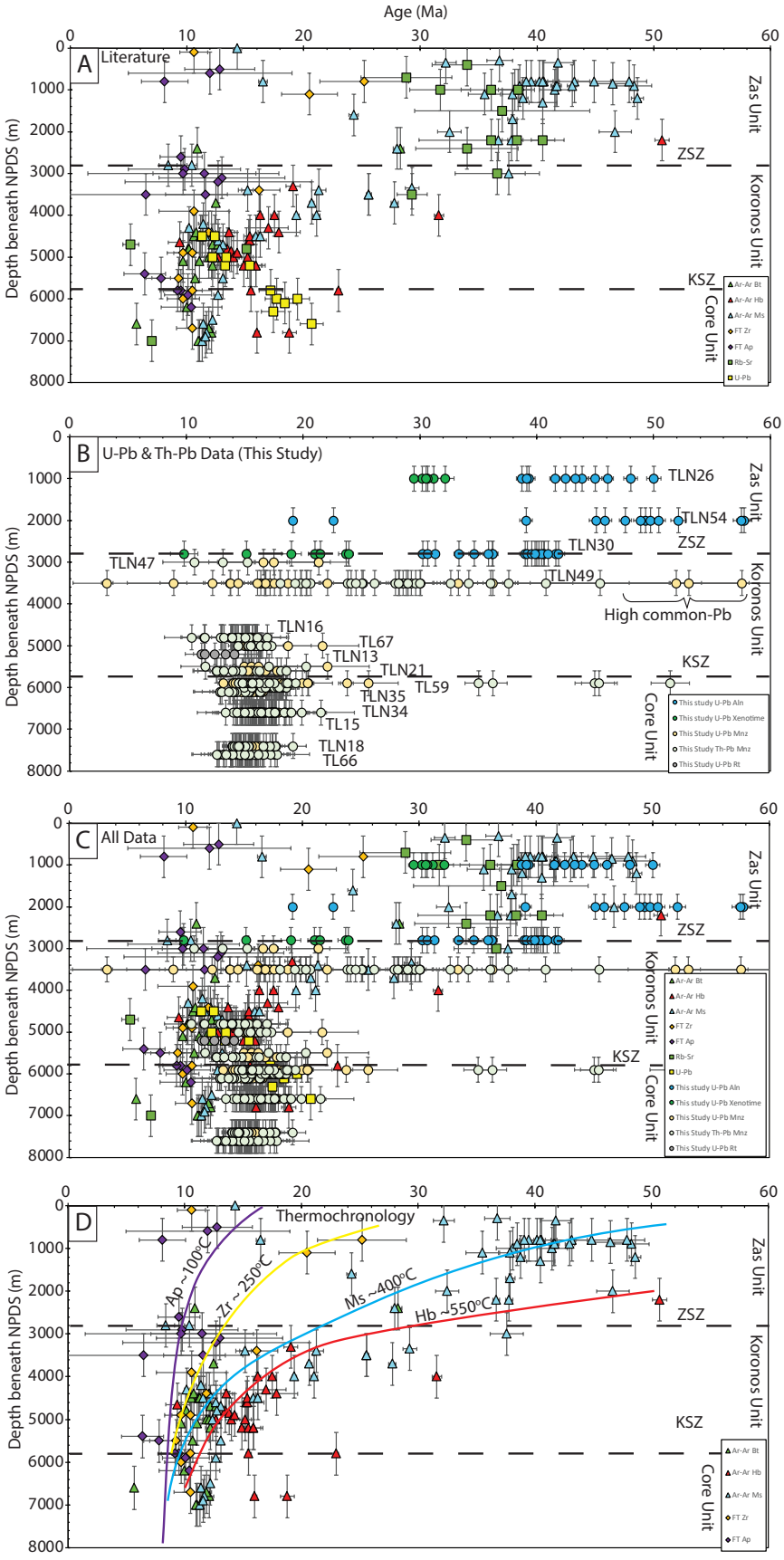


Figure 5.3: Continues on next page

Figure 5.3: Age vs depth plots of literature and U-Pb ages from this study, and predictions from crustal thickening and crustal extension, ages get younger with increasing structural depth. Published literature geochronology vs structural depth for U–Pb (Keay et al., 2001; Martin et al., 2006; Bolhar et al., 2017), ^{40}Ar–^{39}Ar and ^{40}K–^{39}Ar from Hb, Ms and Bt (Andriensen, 1979; Wijbrans and Mcdougall, 1988; Andriensen et al., 1987, Cao et al., 2017), Rb–Sr ages (Deuchene et al., 2006; Peillod et al., 2017), and zircon and appatite fission track ages (Brichau et al., 2006; Seward et al., 2009). Ages taken from map view and projected onto line of section from which, depth beneath the NPDS was calculated. Approximate closure temperatures of ca. 550°C for Hb, 400°C for Ms, 250°C for zircon and 100°C for appatite fission track data has been overlaid onto the graph. Where there is large age scatter in data, reasonable youngest ages where taken as closure through these isotherms due to inherent problems with Ar-loss and excess Ar. Grain size and cooling rate can affect these isotherm values, but unfortunately no description of grain size was documented in these studies. Data shows that metamorphism gets younger with structural depth, with cooling through the isotherms earlier at high structural levels coeval with metamorphism at depth.

5.2.1 Zas Unit:

The highest levels of the metamorphic footwall records muscovite ^{40}Ar–^{39}Ar cooling ages and Rb–Sr ages of ca. 40.5 ± 1.0 Ma representing (M_1) Eocene blueschist facies metamorphism, that corresponds to the occurrence of glaucophane in the south east of the island which correlates with the Zas Unit noted (Avigad, 1998; Peillod et al., 2017). The same rocks experienced a greenschist-facies overprint dated at 32–27 Ma by Rb–Sr (Peillod et al., 2017) indicating they were incorporated into the mid crust by this time. Fission-track and (U–Th)/He ages constrain the arrival of the Zas Unit in the brittle crust at ca. 25 Ma (see Fig. 5.3) (Brichau et al., 2006; Seward et al., 2009), which contrasts with prograde Barrovian (M_2) metamorphism in the structurally deeper units.

5.2.2 Koronos Unit:

Within the Barrovian metamorphic rocks at intermediate levels of the core complex, ^{40}Ar–^{39}Ar ages progressively get younger to 30–20 Ma at deeper levels beyond the biotite and chloritoid out isograds, the equivalent to the Koronos Unit in this study. Martin et al., (2006), report three stages of metamorphic zircon growth that were dated at 55, 45, and 16 Ma from samples taken within this unit, although the 55 Ma age

likely results from mixing across zircon domains (Bolhar et al., 2017). They suggested that the ca. 45 Ma age reflects zircon growth not in the presence of garnet, whilst the younger age reflects peak Barrovian conditions in the presence of garnet characterized by circulation of low δ18O (<10‰) fluids. Bolhar et al. (2017) also report zircon growth stages of ca. 700–550 Ma (up to 2046 Ma), ca. 262–220 Ma, ca. 47–38 Ma and c. 15–14 Ma. The oldest ages represent inherited cores, the 262–220 Ma ages represent magmatic zircon that did not crystalize in situ and therefore does not date intrusion but rather dates assimilation of the host gneisses during emplacement. Whereas the two rim overgrowths at ca. 40 and 15–14 Ma are likely metamorphic in origin, although it is unclear what the 40 Ma age represents. This age could either represent the M_1 blueschistfacies conditions affecting the Koronos Unit, or could represent the initial stages of collision and Barrovian metamorphic conditions prior to garnet growth and is something we aim to address. Whatever the Eocene history of this Unit, if it did experience M_1 high-pressure conditions, then it must have been extruded and reincorporated into another tectono-metamorphic cycle along a Barrovian type clockwise P–T path as revealed in chapter 4. Rb–Sr whole rock isotopic dating was presented by Deuchene et al., (2006) for the equivalent of the Koronos Unit, who shown a span of four ages from 29.3 Ma to 5.2 Ma. Although the two young ages are meaningless due to retrograde resetting, ages of 29.3 ± 1.2 Ma and 15.2 ± 0.7 Ma from the equivalent of the structurally highest and deepest part of the Koronos Unit within the carapace of the dome. Therefore, suggesting Barrovian conditions continued over at least a 15 Myr period, and preceeded partial melting as inferred from zircon ages in the Core Unit (Keay et al., 2001).

5.2.3 Core Unit:

Zircon U–Pb dating by Keay et al., 2001 show that partial melting occurred between 20.7 Ma to 16.8 Ma, whereas Ring et al., 2018 presented Rb-Sr ages spanning from ca. 14.3-11 Ma. These workers proposed that crustal extension must have initiated prior to 20.7 Ma, and infer the migmatite dome formed during crustal extension, over this period

of time period. They also note that older ages could reflect mixed ages from analytical error induced by measuring across <10 μm thin metamorphic zircon rims growing on inherited cores commonly yielding Varsiscan ages in rocks representative of continental basement (Andriessen et al., 1987; Keay et al., 2001). Although the previous U–Pb ages from within the migmatite dome provide a timeframe over which anatexis occurred on Naxos, they provide little insight as to whether prograde or retrograde metamorphism was prevailing during zircon crystallization, and thus the prevailing tectonic regime occurring over the timeframe of partial melting and gneiss dome formation cannot be accurately asserted on these data alone.

^{40}Ar–^{39}Ar ages of ca. 11 Ma in the core migmatites at the deepest structural level (Core Unit) show that rapid cooling occurred following peak Barrovian conditions. Due to the inherent problems of the ^{40}Ar–^{39}Ar system with excess Ar, yielding ages that are too oldand Ar loss due to deformation, fluid flow or weathering yields ages that are too young. These factors, combined with its low closure temperature, make these ages unlikely to represent peak metamorphic ages but rather represent cooling through the 300–550°C isotherms (Kelley, 2002). Fig. 5.3 shows an overview of the ages plotted against projected distance below the Naxos-Paros Detachment System. Ages show a step like function with younger ages at increasing structural depth into the core complex and below 5000 m depth the ^{40}Ar–^{39}Ar ages become constant within error at ca. 11 Ma indicating the deepest levels of the core complex cooled at this time.

However, the poor resolution of age data, large uncertainties combined with the known susceptibility of and Rb–Sr isotopic resetting during deformation and retrograde metamorphism (Thoni and Jagoutz, 1992), and the inability of ^{40}Ar–^{39}Ar to record peak conditions means confirmation of the timing of Barrovian conditions requires a more robust dating system. The U–Pb system is the preferred choice given its high closure temperature (>600°C), and the potential to demonstrably link ages with P–T conditions. Constraining this age trend is crucial to deciphering where the heat to drive metamorphism was derived from.

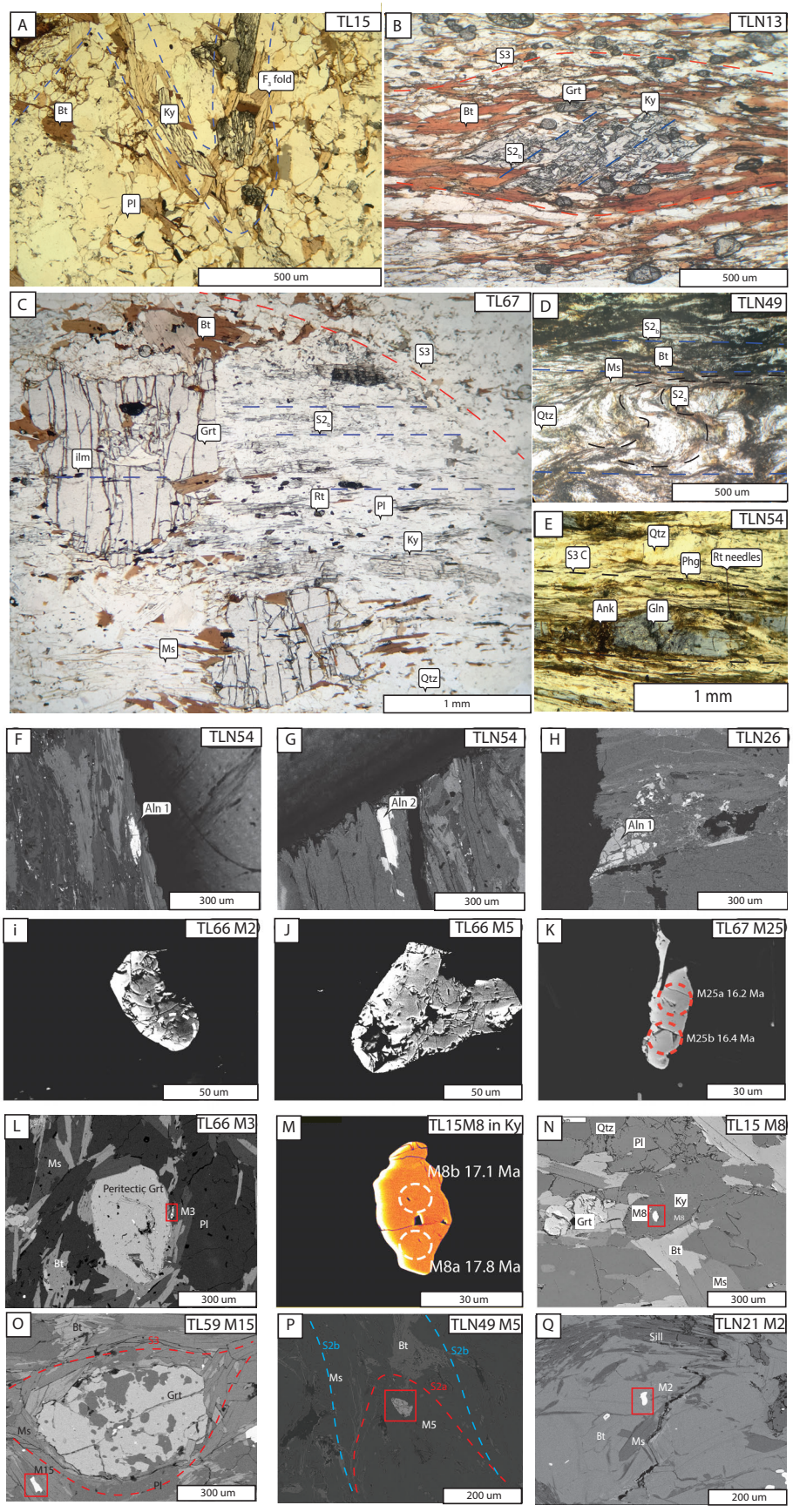


Figure 5.4: Continues on next page

Figure 5.4: Representative backscatter electron (BSE) images and electron microprobe maps of allanite and monazite. A) Upright folding of S_{2b} kyanite grade foliation in TL15, B) Grt-kyanite enclave in TLN13 that preserves the S_{2b} fabric that is discordant (and pre-tectonic) with the S_3 top-to-NNE extensional fabric. C) Kyanite, Grt, Rt enclave in TL67 that is pre-tectonic with respect to S_3, kyanite aligned with the S_{2b} fabric but is overgrown by garnet. D) Microlithon of S_{2a} crenulation cleavage defined by Ms, Bt and plagioclase in TLN49. E) M_1 Gln, Phg, Rt assemblage in TLN54 with grains aligned with the pervasive top-to-NNE fabric. F and G) Allanites 1 and 2 from TLN54 aligned with the blueschist-facies foliation. H) Allanite 1 from TLN26, aligned and partially broken down by greenschist-facies retrogression. I and J) TL66 monazites M3 and M7 showing larger and well formed morphologies and irregular zonation interpreted as growth in the presence of melt. K) TL67 monazite M25, a matrix hosted monazite with smaller and irregular morphology yielding sillimanite grade ages. L) Monazite TL66 M3 located along a resorbed garnet rim and H and I) False coloured BSE images of monazite TL15 M8 and BSE image from TL15 kyanite migmatite, M8 was an inclusion within a kyanite grain constraining a minimum age of M_2.

5.3 U–Th–Pb Geochronology

Geochronology was carried out at the Natural Environment Research Council (NERC) Isotope Geoscience Laboratories (NIGL), Keyworth, Nottingham. Leucogranite samples were crushed using standard techniques (jaw-crushing, disc milling, sieving, Rogers table, heavy liquids, Frantz magnetic separation). Approximately 40 zircons from each sample were then picked under alcohol, mounted in 1-inch epoxy resin mounts and polished until all grains were exposed. All monazite, allanite, xenotime and rutile analyses were performed in-situ in polished thin sections to provide textural context of resultant U–(Th)–Pb ages. Chemical and textural analysis of all zircon, monazite and allanite grains was performed using a FEI quanta 650 Scanning Electron Microscope (SEM) operated in backscatter detection mode, and/or a Cameca SX5-FE electron microprobe equipped with a field emission gun at the Department of Earth Sciences. Complexities in zircon growth patterns were identified prior to U–Pb analysis by cathodoluminescence (CL) imaging of zircon grains. Energy dispersive X-ray spectrometry (EDS) and wavelength dispersive X-ray spectrometry (WDS) element maps were collected for selected in-situ monazite grains to investigate zonation of heavy rare earth element's (HREE's) and domains with variations in Y or Yb content, which typically correlates to growth or resorption of garnet (Gibson et al., 2004; Yang and Pattison., 2006). This is because when garnet is present in significant quantities, it acquires the bulk of

a rock's Y and HREE budget. Therefore, significant Y or Yb depletion in monazite can indicate crystallization towards the end of, or after, garnet growth (Foster et al., 2000). Full electron microprobe garnet maps were collected on the Cameca SX5-FE and are presented in chapter 4 and shown in Figs. 5.4 and 5.5. Locations of ablation spots for geochronological work were chosen to ensure separate domains could be analysed, therefore minimizing the potential mixing of different ages. Analyzed monazite grains existed both within the rock matrix and as inclusions within biotite, muscovite, garnet and kyanite porphyroblasts; whereas allanite occurred within the matrix or cores of clinozoisite. Within these porphyroblasts, monazite and allanite can become isolated from the reacting matrix, allowing evidence of former metamorphic events to be preserved intact, even if matrix crystals are partially reset during subsequent metamorphism (Montel et al., 2000). Although it is possible for fluid infiltration along penetrative fractures to allow young monazite to crystallize as inclusions (e.g. Carson et al., 2004), this rarely occurs. A maximum age for porphyroblast growth can therefore be obtained from inclusions away from such features.

All U–Th–Pb analyses were performed on a Nu Attom single collector inductively coupled mass spectrometer (SC-ICP-MS) coupled to a New Wave Research 193UC excimer laser ablation system fitted with a TV2 cell. Standard-sample bracketing using matrix-matched minerals was employed for all minerals, with full set-up and protocols described previously for zircon (Spencer et al., 2015); monazite and xenotime (Cooper et al., 2015); allanite (Smye et al., 2014); and rutile (Roberts et al., 2016), and full analytical data provided in the supplementary files. All data and ages are shown and quoted at 2-sigma, are $^{206}Pb/^{238}U$ ages unless stated otherwise, and follow uncertainty propagation guidelines of Horstwood et al. (2016). Tera–Wasserburg (T–W) plots are used for interpretation of U–Pb sample data. Common lead bearing data are regressed to a lower intercept age using a free regression if the data allows or anchored to a $^{207}Pb/^{206}Pb$ ratio of 0.84 ± 0.02 (based on Stacey and Kramers, 1975), if the data do not. Where U–Pb data do not allow interpretation of coherent populations, durations of crystallization are shown between generalized age limits; absolute uncertainties are

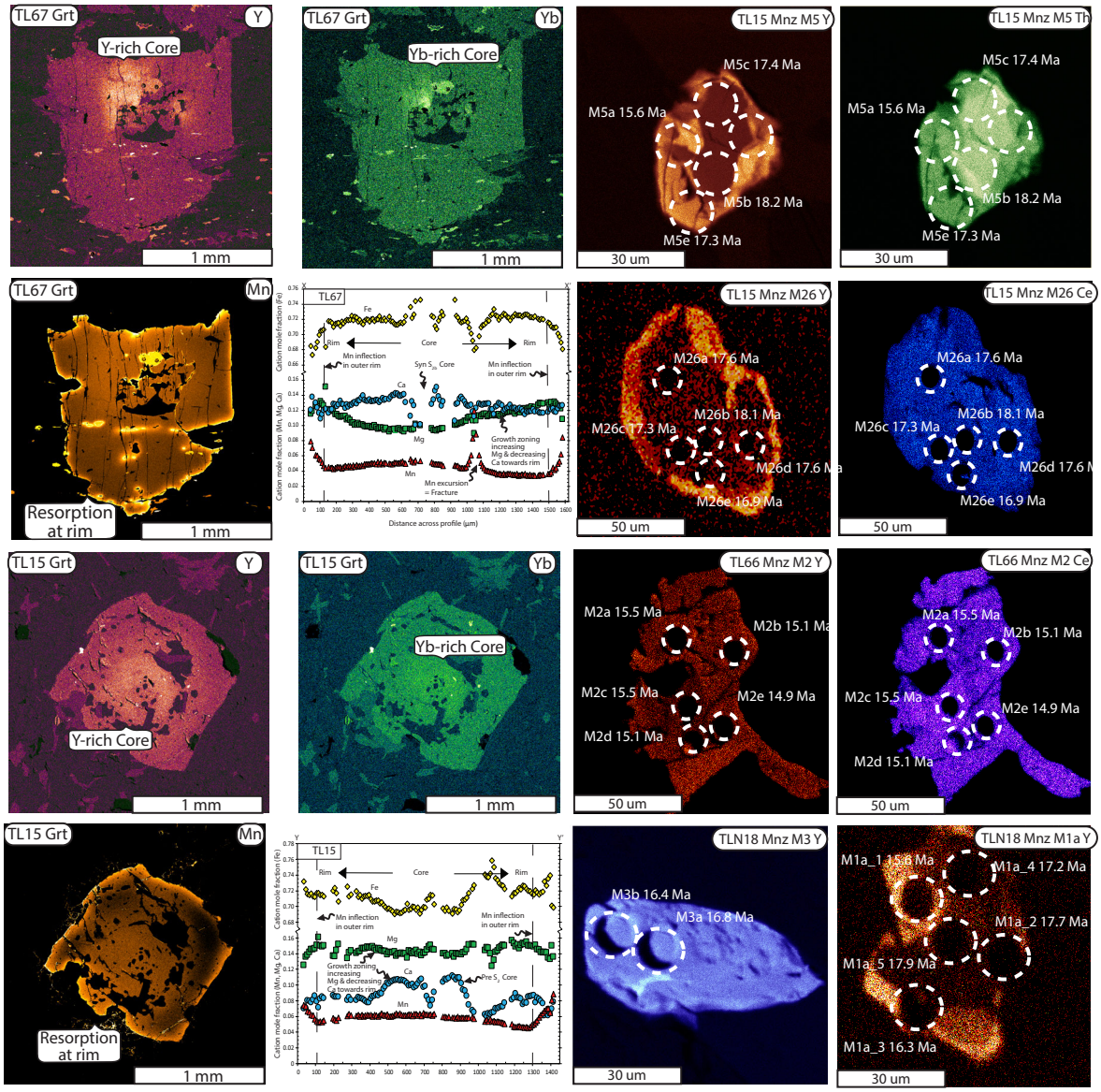


Figure 5.5: X-Ray maps of monazite and garnet illustrating the Y and HREE poor cores and enriched rims with an inverse correlation to garnet. Note the garnet outer rims show an inflection of spessartine associated with garnet resorption. Electron microprobe maps for Y and Th for TL15 M5, brighter colours correspond to higher concentrations. TLN18 M3 Y microprobe map, with only slight and irregular zonation. SEM WDS Y map for monazites TL15 M26, showing Y rich rims corresponding to ablation spots yielding younger ages. TL66 M2 Y and Ce WDS SEM maps showing uniform Y corresponding to young ages, with subtle variations in Y.

provided only for regressed populations with a calculated MSWD value. For monazite and allanite, U–Pb and Th–Pb data were collected for all samples. The preferential incorporation of Th in place of U can result in significant amounts of radiogenic ^{230}Th

being incorporated during crystallization (Scharer, 1984). Consequently, the resultant excess daughter ^{206}Pb causes calculated ^{238}U/^{206}Pb apparent ages to be older than the true crystallization age, and becomes increasingly significant in Cenozoic monazite (Scharer, 1984; Parrish, 1990). Because the Th–Pb system is unaffected by this initial disequilibrium, ^{232}Th/^{208}Pb ages are the most reliable estimates of the timing of monazite growth in these samples. The interpreted ages for all samples are discussed with reference to both common-lead corrected (using a ^{207}Pb-based correction and assuming concordance) ^{238}U/^{206}Pb ages and ^{232}Th/^{208}Pb ages. For a complete description of set up parameters and standards please consult Appendix 2.

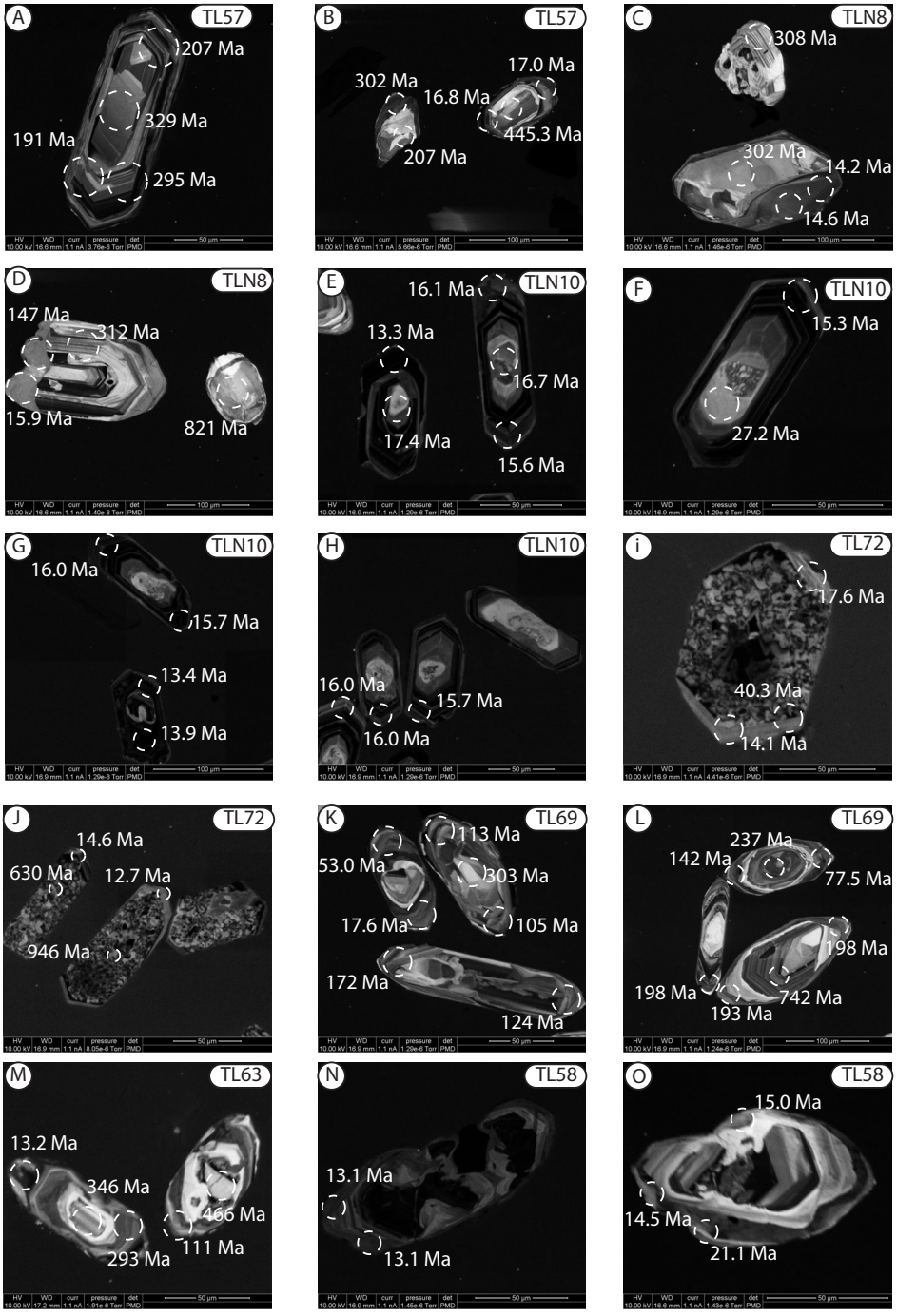


Figure 5.6: Representative cathodoluminescence (CL) images of zircons from Naxos S-type leucogranites, A and B) TL57, zircons have inherited cores with Variscan ages, with younger thin rim overgrowths (<10 μm rims) related to anatexis on Naxos. C and D) TLN8 zircons showing irregular internal zoning morphologies, inherited cores with rim overgrowths associated with Miocene ages. E, F, G and H) Zircons from TLN10 showing euhedral shapes and younger inherited cores up to 27.2 Ma and thin rim overgrowths as young as 13.3 Ma. I and J) Zircons from TL72 showing irregular and thin (<10 μm) rim overgrowths associated with anatexis and dyke emplacement and mottled and altered internal inherited cores. K and L) Zircons from TL69 showing a range of ages and mixing due to ablation spot position between growth domains of different ages, the youngest age of 17.6 Ma is associated with an irregular overgrowth. M) TL63 zircon showing young 13.3 Ma age related to rim overgrowth, over inherited core recoding growth at 466, 346 and 293 Ma. N and O) Zircons from TL58 with young rim ages of 15.0-13.1 Ma and also mixing to give an age of 21.1 Ma.

Table 5.1: Allanite and xenotime U-Th-Pb SC-ICP-MS geochroological results for the Zas Unit

| | | |

Table 5.3: Monazite U-Th-Pb SC-ICP-MS geochrooligical results for the Core Unit part 1

Mineral	Sample	Spot no.	Unit	Comments	Cps 204Pb	f206c	Cps 206Pb	Cps 207Pb	Cps 208Pb	Cps 232Th	Cps 238U	Th/U	P1ppm	T1ppm	U1ppm	Cps Dy	Cps Yb	Ratio Dy/Yb	Ratios: Data for Tera-Wasserburg plot 238U/206Pb	1s %	207Pb/206Pb	1s %	Ratios: Data for Wetherill plot 207Pb/235U	1s %	206Pb/238U	1s %	Rho	Ages: 207Pb/206Pb Age	2s abs	Ages: 206Pb/238U Age	2s abs	Ages: Calculated 207Pb/235U Age	2s abs	Ages: 208Pb/232U Age	2s abs	Discordance % 6-38/7-6	6-38/7-35	Corrected Ages: Cor.Th-Pb Age	2s [Ma]	Cor.206/238-Pb Age	2s [Ma]	230 Th Cor. 206/238 age	2s [Ma]
Monazite	TL15	M3a	Core		37	6.5	7743	1451	19990	18869990	2601964	5.8	23	18804	3221	-	-	-	311.18	1.8	0.184	1.6	0.081	2.4	0.003	1.8	0.733	2689	27	21	1	80	4	21	1	99.2	74.0	18.52	*1.0*	17.1	0.5	17.0	*0.5*
Monazite	TL15	M3b	Core		20	3.6	9392	669	16333	18842380	4034842	3.8	21	18777	4995	-	-	-	387.32	1.7	0.073	1.9	0.026	2.5	0.003	1.7	0.672	1018	38	17	1	26	1	17	1	98.4	36.3	16.48	*1.0*	16.1	0.5	16.0	*0.5*
Monazite	TL15	M4a	Core		70	10.9	8922	1538	23497	23083360	2909820	6.4	27	23003	3602	-	-	-	303.90	1.7	0.172	1.6	0.078	2.3	0.003	1.7	0.738	2580	26	21	1	76	3	20	1	99.2	72.3	17.73	*1.0*	17.8	0.5	17.7	*0.5*
Monazite	TL15	M4b	Core		40	6.3	8532	1606	21215	19972010	2758370	5.8	25	19902	3415	-	-	-	292.06	1.7	0.186	1.6	0.088	2.3	0.003	1.7	0.732	2711	26	22	1	86	4	21	1	99.2	74.3	18.20	*1.0*	18.1	0.5	18.0	*0.5*
Monazite	TL15	M4c	Core	rim	56	10.5	7660	1261	20095	19493470	2629092	6.0	23	19426	3255	-	-	-	306.14	1.9	0.154	1.6	0.069	2.4	0.003	1.9	0.758	2393	27	21	1	68	3	20	1	99.1	69.1	18.13	*1.0*	18.2	0.6	18.1	*0.6*
Monazite	TL15	M4d	Core	rim	34	6.3	8758	878	17135	18937820	3492181	4.4	21	18872	4323	-	-	-	366.76	1.8	0.097	3.4	0.036	3.9	0.003	1.8	0.470	1569	64	18	1	36	3	18	1	98.9	51.8	17.09	*1.0*	16.4	0.6	16.4	*0.6*
Monazite	TL15	M2a	Core	small	-30	-8.6	6528	304	353	439357	2973594	0.1	6	438	3681	-	-	-	422.66	1.8	0.048	2.4	0.016	3.0	0.002	1.8	0.601	115	57	15	1	16	1	16	2	86.7	4.0	14.97	*1.4*	15.2	0.6	15.3	*0.6*
Monazite	TL15	M5a	Core	rim	12	2.5	8521	540	13566	16683020	3856234	3.5	18	16625	4774	-	-	-	401.79	1.8	0.065	2.0	0.022	2.7	0.002	1.8	0.671	763	41	16	1	14	1	16	1	97.9	28.0	15.60	*1.0*	15.7	0.5	15.6	*0.5*
Monazite	TL15	M5b	Core		13	3.5	5361	858	16126	16192850	1760301	7.4	18	16136	2190	-	-	-	300.21	2.0	0.159	2.4	0.073	3.1	0.003	2.0	0.636	2442	40	21	1	71	4	20	1	99.1	70.0	17.99	*1.1*	18.4	0.6	18.2	*0.6*
Monazite	TL15	M5c	Core	rim	20	2.8	10573	1371	21290	21810140	3887512	4.5	26	21734	4812	-	-	-	331.69	1.8	0.128	1.6	0.053	2.4	0.003	1.8	0.744	2065	28	19	1	52	2	19	1	99.1	63.0	17.50	*1.0*	17.4	0.6	17.4	*0.6*
Monazite	TL15	M5d	Core	rim	27	4.3	9238	1238	18574	19033440	3325867	4.6	23	18967	4117	-	-	-	329.09	1.7	0.135	1.3	0.057	2.2	0.003	1.7	0.793	2166	23	20	1	56	2	20	1	99.1	65.0	17.36	*1.0*	17.4	0.5	17.3	*0.5*
Monazite	TL15	M5e	Core	rim	31	4.8	9832	1261	16956	16695110	3613640	3.7	22	16637	4473	-	-	-	333.58	1.8	0.126	1.4	0.052	2.3	0.003	1.8	0.783	2049	25	19	1	52	2	20	1	99.1	62.7	17.97	*1.0*	17.3	0.6	17.3	*0.6*
Monazite	TL15	M7a	Core		16	2.9	8017	1267	21338	20886190	2822837	5.9	24	20734	3495	-	-	-	319.72	1.7	0.156	1.4	0.067	2.2	0.003	1.7	0.781	2415	23	20	1	66	3	20	1	99.2	69.6	18.02	*1.0*	17.3	0.5	17.2	*0.5*
Monazite	TL15	M8a	Core	inc Ky	76	14.7	7387	1145	19199	18561870	2473329	6.0	22	18497	3062	-	-	-	310.69	1.8	0.156	1.4	0.069	2.3	0.003	1.8	0.783	2409	24	21	1	68	3	20	1	99.1	69.4	18.29	*1.0*	17.9	0.6	17.7	*0.6*
Monazite	TL15	M8b	Core	inc Ky	-5	-1.2	8096	526	14106	16425010	3310709	4.0	18	16368	4098	-	-	-	367.12	1.8	0.065	1.6	0.024	2.4	0.003	1.8	0.745	781	33	18	1	25	1	17	1	97.8	28.6	16.87	*1.1*	17.1	0.6	17.1	*0.6*
Monazite	TL15	M9a	Core		111	14.5	11755	1439	20001	19214120	4269183	3.6	26	19147	5285	-	-	-	333.85	1.7	0.119	2.0	0.049	2.6	0.003	1.7	0.635	1944	36	19	1	49	3	20	1	99.0	60.5	18.19	*1.0*	17.5	0.5	17.5	*0.5*
Monazite	TL15	M10a	Core		76	11.2	9720	1475	22655	22049060	3362719	5.3	27	21969	4163	-	-	-	306.62	1.9	0.151	1.6	0.068	2.5	0.003	1.9	0.763	2361	27	21	1	67	3	20	1	99.1	68.6	18.21	*1.0*	18.2	0.6	18.1	*0.6*
Monazite	TL15	M26a	Core		68	10.9	9136	1334	21338	20947470	3118954	5.4	25	20874	3861	-	-	-	317.32	1.7	0.146	1.3	0.064	2.1	0.003	1.7	0.806	2305	22	20	1	63	3	20	1	99.1	67.6	17.93	*1.0*	17.7	0.5	17.6	*0.5*
Monazite	TL15	M26b	Core	rim	49	6.4	10905	1651	23878	23195710	3641020	5.1	29	23115	4507	-	-	-	305.46	1.8	0.154	1.3	0.069	2.2	0.003	1.8	0.812	2390	22	21	1	68	3	20	1	99.1	69.1	17.92	*1.0*	18.2	0.6	18.1	*0.6*
Monazite	TL15	M26c	Core	rim	14	3.1	6732	920	17774	18152410	2380598	6.1	20	18089	2946	-	-	-	326.65	1.9	0.138	1.9	0.058	2.7	0.003	1.9	0.705	2197	33	20	1	57	3	19	1	99.1	65.6	17.55	*1.0*	17.4	0.6	17.3	*0.6*
Monazite	TL15	M26d	Core		55	11.1	7050	1160	20254	19493530	2439404	6.4	22	19426	3020	-	-	-	310.57	1.9	0.160	1.6	0.071	2.5	0.003	1.9	0.765	2457	27	21	1	70	3	21	1	99.2	70.3	18.51	*1.0*	17.7	0.6	17.6	*0.6*
Monazite	TL15	M26e	Core		25	5.4	6661	977	18552	18749410	2362757	6.4	21	18684	2925	-	-	-	331.68	2.0	0.145	1.9	0.060	2.8	0.003	2.0	0.717	2285	34	19	1	59	3	20	1	99.2	67.3	17.81	*1.0*	17.0	0.6	16.9	*0.6*
Monazite	TL15	M22	Core		15	3.0	7802	738	17088	18810210	3126107	4.8	20	18745	3870	-	-	-	362.01	1.9	0.097	2.9	0.037	3.5	0.003	1.9	0.550	1562	55	18	1	37	3	18	1	98.9	51.6	16.78	*1.0*	16.7	0.6	16.6	*0.6*
Monazite	TL15	M35a	Core		60	16.5	5416	718	19039	19156660	1829777	8.4	20	19090	2265	-	-	-	312.03	1.9	0.133	1.8	0.059	2.6	0.003	1.9	0.722	2135	31	21	1	58	3	20	1	99.0	64.3	18.59	*1.1*	18.4	0.6	18.2	*0.6*
Monazite	TL15	M35b	Core		27	7.0	5579	792	19230	20255970	1896644	8.6	20	20185	2348	-	-	-	312.00	1.9	0.139	1.9	0.061	2.7	0.003	1.9	0.719	2217	32	21	1	61	3	19	1	99.1	66.0	17.96	*1.1*	18.2	0.6	18.0	*0.6*
Monazite	TL66	M2a	Core		25	2.8	15251	1093	44933	44859260	6962086	7.1	17	20326	2861	-	-	-	399.47	1.6	0.072	1.3	0.025	2.1	0.003	1.6	0.773	976	27	16	1	25	1	15	1	98.3	35.0	14.24	*0.9*	15.6	0.5	15.5	*0.5*
Monazite	TL66	M2b	Core	rim	78	14.1	8966	871	27808	26778040	4182329	7.1	11	12133	1719	-	-	-	397.40	1.7	0.094	1.6	0.032	2.3	0.003	1.7	0.746	1502	29	16	1	32	1	15	1	98.9	50.1	14.70	*0.9*	15.2	0.5	15.1	*0.5*
Monazite	TL66	M2c	Core		-29	-4.2	11904	1004	40021	39471010	5365596	8.1	15	17885	2205	-	-	-	395.24	1.7	0.075	1.5	0.026	2.3	0.003	1.7	0.745	1069	30	16	1	26	1	15	1	98.5	37.9	14.64	*0.9*	15.7	0.5	15.5	*0.5*
Monazite	TL66	M2d	Core		-48	-6.1	13402	1019	40594	41550630	6265194	7.3	15	18827	2575	-	-	-	409.17	1.6	0.073	1.4	0.025	2.2	0.002	1.6	0.741	1009	29	16	1	25	1	15	1	98.4	36.0	14.27	*0.9*	15.2	0.5	15.1	*0.5*
Monazite	TL66	M2e	Core	rim	21	2.9	12033	932	39349	40642230	5684722	7.9	15	18415	2336	-	-	-	413.00	1.8	0.075	1.7	0.025	2.4	0.002	1.8	0.728	1060	34	16	1	25	1	14	1	98.5	37.6	13.92	*0.8*	15.0	0.5	14.9	*0.5*
Monazite	TL66	M2f	Core		76	10.6	12194	907	38999	40339390	5584184	8.0	15	18278	2294	-	-	-	402.34	1.8	0.073	1.6	0.025	2.4	0.002	1.8	0.737	1021	33	16	1	25	1	14	1	98.4	36.4	14.00	*0.9*	15.5	0.5	15.3	*0.5*
Monazite	TL66	M3a	Core		2	0.2	11753	868	39438	36167530	5106739	7.8	15	16388	2099	-	-	-	379.91	1.8	0.073	1.6	0.027	2.4	0.003	1.8	0.736	1023	33	17	1	27	1	16	1	98.3	36.4	15.39	*0.9*	16.4	0.6	16.2	*0.6*
Monazite	TL66	M3b	Core		36	3.5	17606	1297	59614	56745910	7793172	8.0	22	25712	3203	-	-	-	383.23	1.6	0.072	1.2	0.026	2.0	0.003	1.6	0.793	1000	25	17	1	26	1	16	1	98.3	35.7	15.36	*0.9*	16.2	0.5	16.1	*0.5*
Monazite	TL66	M5a	Core		154	16.2	13992	2088	46011	42598260	5697888	8.2	17	19302	2341	-	-	-	353.96	3.4	0.137	9.6	0.053	10.2	0.003	3.4	0.332	2189	167	18	1	53	10	16	1	99.2	65.5	14.63	*1.0*	16.1	1.0	15.9	*1.0*
Monazite	TL66	M5b	Core		140	12.5	15573	2796	51847	45150020	5987145	8.3	20	20458	2460	-	-	-	339.08	1.9	0.174	2.5	0.071	3.1	0.003	1.9	0.618	2597	41	19	1	69	4	17	1	99.3	72.7	15.06	*0.9*	15.9	0.5	15.7	*0.5*
Monazite	TL66	M5c	Core		197	17.1	15467	3035	48742	43676500	5784713	8.3	19	19790	2377	-	-	-	319.97	2.7	0.197	5.8	0.085	6.4	0.003	2.7	0.417	2798	95	20	1	83	10	17	1	99.3	75.6	14.57	*0.9*	16.3	0.8	16.1	*0.8*
Monazite	TL66	M5d	Core	rim	55	5.1	16990	1558	53429	51504690	7456406	7.6	20	23337	3064	-	-	-	385.09	1.9	0.101	5.2	0.036	5.6	0.003	1.9	0.347	1651	97	17	1	36	4	15	1	99.0	53.8	14.26	*0.9*	15.6	0.6	15.4	*0.6*
Monazite	TL66	M6a	Core		-35	-6.3	9182	795	50599	51921680	3967585	14.4	17	23526	1630	-	-	-	385.04	1.7	0.086	1.8	0.031	2.5	0.003	1.7	0.700	1348	34	17	1	31	2	14	1	98.8	45.9	14.15	*0.9*	15.9	0.5	15.5	*0.5*
Monazite	TL66	M6b	Core	rim	17	2.7	10468	804	38741	39324210	5045741	8.6	14	17818	2073	-	-	-	411.46	1.7	0.073	1.4	0.025	2.2	0.002	1.7	0.762	1018	29	16	1	25	1	15	1	98.5	36.3	14.35	*0.9*	15.1	0.5	14.9	*0.5*
Monazite	TL66	M6c	Core		-46	-8.4	8762	931	48551	48152170	3753702	14.1	16	21818	1543	-	-	-	363.88	1.7	0.102	1.8	0.039	2.5	0.003	1.7	0.705	1656	32	18	1	38	2	15	1	98.9	53.9	14.56	*0.9*	16.5	0.5	16.1	*0.5*
Monazite	TL66	M6d	Core		23	3.8	9391	1135	50099	49752470	3802848	14.4	17	22543	1563	-	-	-	355.21	1.8	0.116	1.9	0.045	2.6	0.003	1.8	0.697	1896	34	18	1	45	2	15	1	99.0	59.5	14.50	*0.9*	16.5	0.6	16.1	*0.6*
Monazite	TL66	M8a	Core		29	2.9	15578	1612	48634	46939130	7221356	6.3	18	18550	2968	-	-	-	372.00	2.2	0.107	6.6	0.040	7.0	0.003	2.2	0.312	1743	121	17	1	39	5	18	1	99.0	56.0	17.38	*1.1*	16.0	0.7	15.9	*0.7*
Monazite	TL66	M8b	Core	rim	112	12.1	13699	1669	42059	34795190	5919743	6.5	16	15766	2433	-	-	-	364.17	2.0	0.136	5.1	0.051	5.5	0.003	2.0	0.370	2171	90	18	1	51	5	18	1	99.2	65.2	16.87	*1.0*	15.7	0.6	15.6	*0.6*
Monazite	TL66	M9a	Core		-18	-2.0	15430	1245	46805	38363150	6979608	6.1	18	17383	2868	-	-	-	383.05	1.7	0.078	1.5	0.028	2.3	0.003	1.7	0.737	1155	31	17	1	28	1	18	1	98.5	40.4	17.68	*1.1*	16.1	0.5	16.0	*0.5*
Monazite	TL66	M9b	Core		96	12.3	11750	1493	50999	38288930	4464128	9.5	18	17349	1834	-	-	-	327.39	1.7	0.127	1.3	0.054	2.2	0.003	1.7	0.791	2061	23	20	1	53	2	20	1	99.0	62.9	19.14	*1.1*	17.7	0.5	17.4	*0.5*
Monazite	TL66	M9c	Core		-11	-0.9	19596	1726	62111	50967310	8645440	6.5	23	23094	3553	-	-	-	372.21	1.6	0.087	3.0	0.032	3.4	0.003	1.6	0.485	1365	57	17	1	32	2	18	1	98.7	46.4	17.66	*1.1*	16.4	0.5	16.3	*0.5*
Monazite	TL66	M9d	Core		54	4.7	19499	1529	53707	45633410	8819519	5.7	21	20677	3624	-	-	-	386.45	1.6	0.076	1.5	0.027	2.2	0.003	1.6	0.720	1101	31	17	1	27	1	18	1	98.5	38.8	17.16	*1.0*	16.0	0.5	15.9	*0.5*
Monazite	TL66	M10a	Core		37	5.0	12626	931	36610	31625290	5919259	5.9	14	14330	2432	-	-	-	396.23	1.6	0.072	1.6	0.025	2.3	0.003	1.6	0.722	973	32	16	1	25	1	17	1	98.3	34.9	16.63	*1.0*	15.7	0.5	15.6	*0.5*
Monazite	TL59	M1a	Core		50	7.3	9956	1436	50699	41895200	4215200	11.2	23	25896	2290	-	-	-	365.43	1.8	0.147	2.1	0.056	2.8	0.003	1.8	0.652	2314	36	18	1	55	3	18	1	99.2	67.9	16.75	*1.0*	15.4	0.5	15.1	*0.5*
Monazite	TL59	M1c	Core		235	19.4	15803	3436	52789	35050480	5180638	7.6	27	21489	2814	-	-	-	291.04	1.6	0.216	1.1	0.102	2.0	0.003	1.6	0.818	2951	18	22	1	99	4	22	1	99.3	77.6	18.85	*1.0*	17.4	0.4	17.2	*0.4*
Monazite	TL59	M2a	Core	rim	10	1.4	11304	1184	26118	22082870	5210140	4.8	14	13539	2830	-	-	-	407.15	1.8	0.097	3.4	0.033	3.8	0.002	1.8	0.461	1562	64	16	1	33	2	17	1	99.0	51.7	15.91	*1.0*	14.8	0.5	14.7	*0.5*
Monazite	TL59	M6-2b	Core	rim	10	1.6	10211	1146	49318	43857010	4587324	10.8	23	26876	2492	-	-	-	381.68	1.9	0.114	4.9	0.041	5.3	0.003	1.9	0.357	1865	89	17	1	41	4	16	1	99.1	58.8	15.68	*1.0*	15.4	0.5	15.1	*0.5*
Monazite	TL59	M7a	Core		-1	-0.2	10994	724	31322	28244620	5204867	6.1	16	17317	2827	-	-	-	423.56	1.8	0.065	1.8	0.021	2.5	0.002	1.8	0.710	781	37	15	1	21	1	16	1	98.1	28.7	15.66	*1.0*	14.8	0.5	14.7	*0.5*
Monazite	TL59	M7b	Core		37	6.3	9982	757	30589	27553710	4739745	6.6	16	16893	2574	-	-	-	424.60	1.7	0.075	1.8	0.024	2.5	0.002	1.7	0.697	1079	36	15	1	25	1	16	1	98.6	38.2	15.95	*1.0*	14.6	0.5	14.5	*0.5*
Monazite	TL59	M8-2a	Core		3	0.3	18187	996	24247	21577320	8946005	2.7	16	13229	4860	-	-	-	426.91	1.8	0.054	1.4	0.018	2.2	0.002	1.8	0.783	384	31	15	1	18	1	16	1	96.1	14.5	16.00	*1.0*	14.9	0.5	14.9	*0.5*
Monazite	TL59	M8-3a	Core	rim	21	3.5	10742	650	25039	22451810	5365930	4.7	14	13761	2915	-	-	-	437.54	1.7	0.060	1.9	0.019	2.6	0.002	1.7	0.670	599	42	15	1	19	1	16	1	97.5	22.4	16.06	*1.0*	14.5	0.5	14.4	*0.5*
Monazite	TL59	M8-3b	Core	rim	98	15.5	11061	712	31575	28386600	5417763	5.9	16	17404	2939	-	-	-	433.20	1.8	0.064	1.7	0.021	2.5	0.002	1.8	0.720	757	37	15	1	21	1	16	1	98.0	27.9	15.43	*0.9*	14.5	0.5	14.4	*0.5*
Monazite	TL59	M11	Core		65	10.4	9680	1138	54850	50353520	4315951	13.2	25	30871	2344	-	-	-	391.97	1.9	0.111	5.3	0.039	5.7	0.003	1.9	0.341	1808	97	16	1	39	4	16	1	99.1	57.6	15.31	*0.9*	15.1	0.6	14.7	*0.6*
Monazite	TL59	M13b	Core		-54	-9.2	10097	663	33770	31442930	4756076	7.5	17	19277	2584	-	-	-	428.03	1.8	0.067	1.8	0.022	2.6	0.002	1.8	0.716	840	37	15	1	22	1	16	1	98.2	30.7	15.29	*0.9*	14.6	0.5	14.5	*0.5*
Monazite	TL59	M15a	Core	rim	-8	-2.0	7379	476	28332	27775530	3935897	8.0	14	17029	2138	-	-	-	471.50	1.8	0.064	1.7	0.019	2.5	0.002	1.8	0.728	734	37	14	0	19	1	15	1	98.1	27.2	14.48	*0.9*	13.4	0.5	13.2	*0.5*
Monazite	TL59	M15b	Core	rim	39	8.1	6677	1076	23117	19060300	2826033	7.8	12	12017	1535	-	-	-	365.82	4.0	0.170	9.6	0.064	10.4	0.003	4.0	0.383	2554	161	18	1	63	13	16	1	99.3	72.0	14.83	*1.0*	14.9	1.1	14.7	*1.1*
Monazite	TL59	M15c	Core		366	30.8	10658	6405	28047	13160070	1872394	7.9	17	8068	1017	-	-	-	130.86	5.9	0.581	1.7	0.612	6.2	0.008	5.9	0.962	4461	24	49	6	485	46	36	4	98.9	89.9	17.57	*1.1*	15.9	0.7	15.8	*0.7*
Monazite	TL59	M15d	Core	high cm-ph	29	8.8	5747	380	18027	16493130	2813268	6.6	9	10112	1528	-	-	-	443.44	2.1	0.063	2.1	0.020	3.0	0.002	2.1	0.716	710	44	15	1	20	1	15	1	98.0	26.3	14.98	*1.0*	14.2	0.6	14.1	*0.6*
Monazite	TL59	M15e	Core	high cm-ph	-35	-10.1	6020	385	17438	16262840	2962494	6.2	9	9971	1600	-	-	-	445.99	2.1	0.063	2.1	0.019	2.9	0.002	2.1	0.700	699	45	14	1	19	1	15	1	97.9	25.9	14.84	*0.9*	14.1	0.6	14.0	*0.6*
Monazite	TL59	M15f	Core	high cm-ph	183	21.9	9363	3404	27360	18131000	2908558	7.0	15	11116	1580	-	-	-	234.80	8.2	0.344	6.9	0.202	10.8	0.004	8.2	0.764	3680	106	27	4	187	36	22	2	99.3	85.3	15.95	*1.3*	17.1	2.0	17.0	*2.0*
Monazite	TL59	M16a	Core	high cm-ph	504	27.1	18667	8500	36463	14870570	4683366	3.6	24	9117	2547	-	-	-	212.49	2.1	0.455	1.2	0.295	2.5	0.005	2.1	0.866	4102	18	30	1	263	11	35	2	99.3	88.5	16.22	*0.6*	14.6	0.4	14.6	*0.4*
Monazite	TL59	M16b	Core	high cm-ph	-39	-7.5	9383	571	16594	14952410	2597833	3.5	10	9167	2606	-	-	-	443.83	1.8	0.059	1.7	0.018	2.5	0.002	1.8	0.728	562	37	14	1	18	1	16	1	97.4	21.1	15.55	*1.0*	14.2	0.5	14.2	*0.5*
Monazite	TL59	M18a	Core		68	10.1	10281	1041	19319	15882210	4622131	3.9	11	9737	2511	-	-	-	359.03	5.0	0.118	10.5	0.045	11.6	0.003	5.0	0.432	1923	188	18	2	45	10	17	1	99.1	60.1	15.59	*1.2*	16.3	1.5	16.3	*1.5*
Monazite	TL59	M18b	Core		26	4.4	10316	615	23513	20780830	5042730	4.7	13	12741	2739	-	-	-	435.48	1.7	0.059	1.7	0.019	2.4	0.002	1.7	0.701	578	37	15	0	19	1	16	1	97.4	21.7	15.69	*1.0*	14.5	0.5	14.5	*0.5*
Monazite	TL59	M5-2	Core		437	19.3	27808	7538	58432	32336560	8158260	4.5	35	19825	4431	-	-	-	257.20	1.7	0.266	1.2	0.142	2.0	0.004	1.7	0.820	3280	18	25	1	135	5	26	2	99.2	81.5	19.36	*0.9*	18.1	0.4	18.0	*0.4*
Monazite	TL59	M6-1a	Core		432	24.0	17437	7667	43457	22259450	3886203	6.5	26	13647	2101	-	-	-	108.63	10.5	0.494	3.5	0.626	11.0	0.009	10.5

5.4 Results

The LA-ICP-MS and U–Th–Pb data are presented in Tables 5.1-5.8. Allanite and xenotime results from the Zas Unit are presented in Table 5.1, monazite results from the Koronos and Core Units are presented in Table 5.2-5.5, and U–Pb zircon data from cross cutting granites are shown in Table 5.6-5.8. The relevant features of each U–Th–Pb dataset are summarized below and integrated with microstructural evidence and a series of equilibrium phase diagrams including garnet mode isopleths for relevant samples which are discussed and presented in Part 1 to decipher the *P–T–t–D* histories of the various levels of Naxos MCC. For a full discussion of phase diagram modelling please refer to chapter 4 and Appendix 1.

5.4.1 Zas Unit (Blueschists)

5.4.1.1 TLN26: Phengite-Clinozoisite Schist

Sample TLN26 is reasonably unaltered and preserves S_2 relict fabric elements defined by inclusion trails within epidote and crenulation cleavage domains and is commonly defined by phengite, chlorite, biotite and albite and titanite, indicating it developed at upper greenschist-facies conditions. Allanite is aligned with this S_2 crenulated fabric, has a high common/initial lead component and gives a lower intercept age of 40.8 ± 3.3 Ma (MSWD = 2.4) (Fig. 5.7). Due to the lack of high-pressure index minerals in this sampled as well as apparent coeval growth of epidote and allanite, we interpret this age as representing an upper greenschist-facies metamorphic overprint of earlier blueschist facies conditions following exhumation from the subduction zone. Xenotime in this sample was large and associated with veining fractures and is aligned sub-parallel to them. The xenotime data give a lower intercept age of 30.26 ± 0.76 Ma (MSWD = 2.5) (Fig. 5.7), which we interpret as a retrograde greenschist-facies metamorphic age. Growth of xenotime is probably due to metasomatism and hydration related to higher grade metamorphism and dehydration reactions occurring at deeper levels. Yttrium remobilization during greenschist-facies conditions could occur due to the breakdown of

allanite or garnet and concentration of yttrium rich fluids in fractures would facilitate growth of xenotime.

5.4.1.2 TLN54: Glaucophane-Rutile-Phengite Schist

Allanite was euhedral and showed pristine preservation under backscattered electron imaging (Fig. 5.4). However, analysis of these grains indicates uniformly high amounts of common/initial Pb. Regression of the data gives a lower intercept age of 46.0 ± 10.0 Ma (MSWD = 0.65) (Fig. 5.7), which we interpret to represent peak high-pressure metamorphism (M_1). Although the data have a large uncertainty, inherent from the lack of radiogenic lead, the age overlaps with Lu–Hf garnet ages of 52.2 ± 1.2 Ma from Syros that represent peak eclogite-facies conditions (Lagos et al., 2007).

Xenotime from this sample occurred along healed fluid fractures along domain boundaries, including a large magnetite crystal, which we interpret to be a secondary retrograde phase associated with metasomatism. Xenotime has variable amounts of common/initial Pb, with a retrogression of the data providing a lower intercept age of 21.49 ± 0.60 Ma (MSWD = 0.92), which we interpret as associated with the greenschist-facies overprint (M_2).

5.4.1.3 TLN30: Clinozoisite-Phengite Schist

Allanite from sample TLN30 is characterized by domains within the cores of clinozoisite, that itself makes up 50% of the rock. The grains are subhedral and associated with alteration zones that define its presence with an overgrown fairly uniform rim of clinozoisite. The grains are characterized by high amounts of common/initial Pb. Regression of the data provides a lower intercept age of 49.3 ± 6.0 Ma (MSWD = 0.20) (Fig. 5.7). The lack of radiogenic lead precludes a robust and precise age determination. However, due to the textural relationships we can be confident that this age is representative of high pressure M_1 blueschist-facies conditions, as clinozoisite would be expected to grow at peak conditions or shortly after during retrogression. We therefore interpret this age as an absolute minimum for high-pressure M_1 conditions. This age

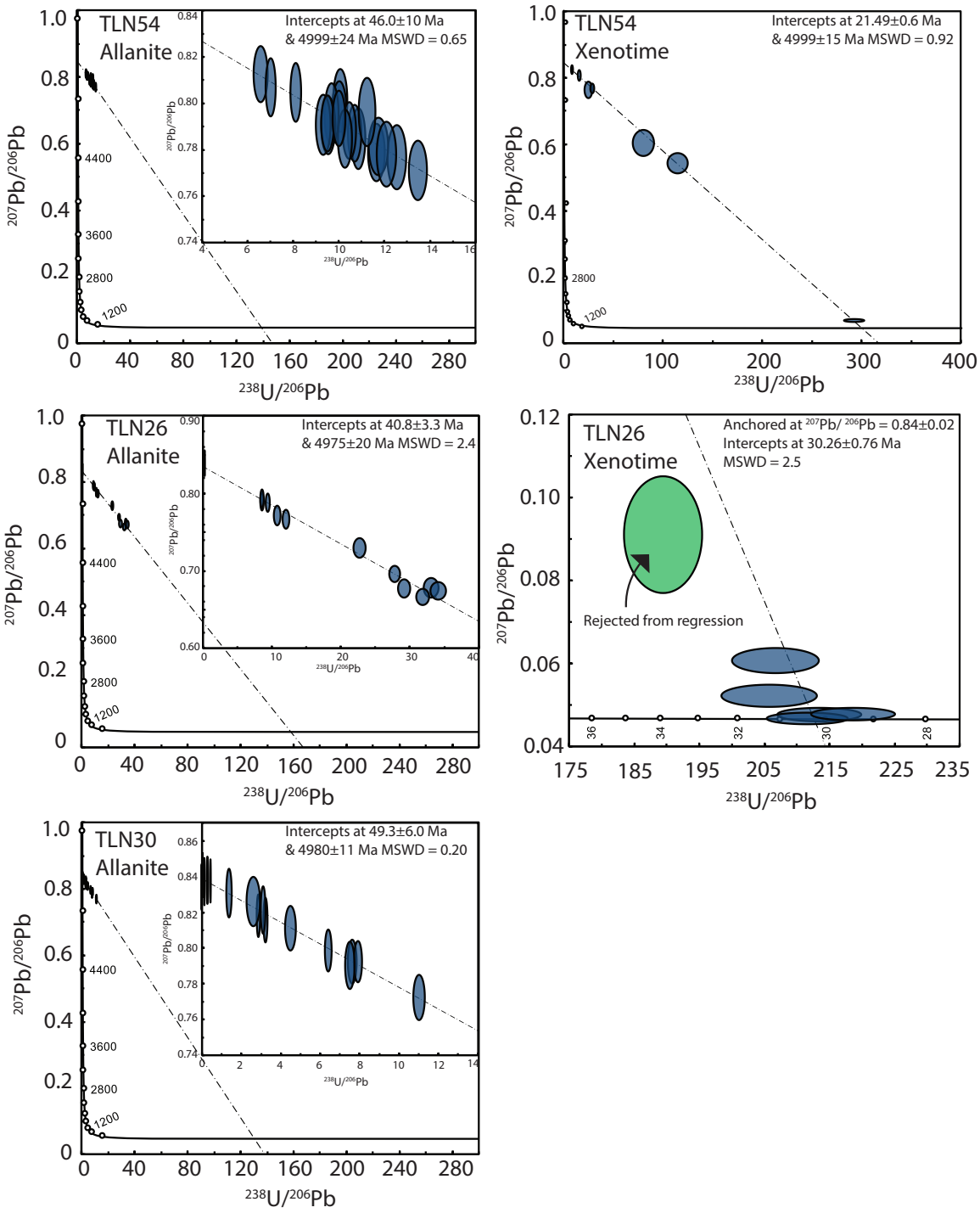


Figure 5.7: Tera-Wasserburg concordia plots for Zas Unit samples using LA-ICP-MS analysis of allanite and xenotime. A) TLN54 allanite Tera-Wasserburg plot illustrates the length of extrapolation required to generate an intercept age. Inset plot shows zoomed in view of data for goodness of fit. B) TLN54 xenotime reflecting younger ages with a range of common Pb-radiogenic Pb giving a good age of greenschist-facies metasomatism. C) TLN26 allanite Tera-Wasserburg plot illustrating the length of extrapolation associated the intercept age of 40.8 ± 3.3 Ma, inset shows zoomed in goodness of fit of the data. D) TLN26 xenotime Tera-Wasserburg plot showing a concordant age of 30.26 ± 0.76 Ma, with a discordant analysis rejected from the data. E) TLN30 Tera-Wasserberg allanite plot with inset showing zoomed in trend of the data. All ages were calculated using Isoplot v. 3.00 (Ludwig, 2003).

also lies within analytical uncertainty of sample TLN54, as well as other independent ages from Syros (Lagos et al., 2007; Tomaschek et al., 2003), defining an Eocene age range for M_1 high-pressure metamorphism of the Cycladic Blueschists from 54–45 Ma.

5.4.2 Koronos Unit

5.4.2.1 TLN49: Kyanite, Biotite Schist

TLN49 was taken from the higher structural levels of the Koronos Unit and has in-situ kyanite that forms axial planar to the S_2a crenulation cleavage fabric and mm-scale isoclinal folds. These features deform amphibolite-facies minerals, indicating they developed during its prograde burial history. Monazites from this sample were located within muscovite and biotite folia, <40 μm in size and characterized by irregular morphologies. Due to the small size, imaging combined with multiple spot analyses was not attempted and single analyses for individual grains was obtained. The U–Pb data provide a large range of lower intercept ages with variable amounts of common-Pb (Fig. 5.8). An upper bound is defined by a monazite crystallization age of 55 ± 22 Ma, and a lower bound at 12.9 ± 1.8 Ma. However, a reliable population of U–Pb and well correlated Th–Pb ages suggest a prolonged period of metamorphism between ca. 39.2–14 Ma. A mean regression through the data gives a lower intercept age of 20.0 ± 1.8 Ma with an MSWD of 5.0. In U–Pb and Th–Pb space contoured for Dy/Yb concentrations, the data plots off the 1:1 correlation line with a systematic shift to older Th–Pb ages by 5–10 Myrs. There is no distinct pattern to the Dy/Yb ratios with time, possibly owing to the lack of garnet in the sample. The distribution of both U–Pb and Th–Pb ages between ca. 39–18 Ma presumably represent the M_2 Barrovian event, whereas the potentially younger U–Pb age population of 17–13 Ma may be recording the M_3 sillimanite grade overprint, although this younger age population is not robust due to the lack of correlation with Th–Pb ages.

Because monazite participates in metamorphic reactions involving major alu-

minosilicate minerals (Foster et al., 2002; Kohn and Malloy, 2004; Fitzsimons et al., 2005) or form directly from the prograde breakdown of lower temperature REE-bearing minerals including allanite (Simpson et al., 2000; Yang and Pattison, 2006; Janots et al., 2008), it is possible to link these older ages to the prevailing P–T conditions. Thermodynamic modelling of Ce-bearing systems reveals that in the middle amphibolite facies, predicts a prograde transition between allanite-monazite for a typical metapelite composition (Janots et al., 2007; Spear, 2010; Spear and Pyle, 2010). Janots et al., (2008) has shown that the temperature of this transition is strongly dependent on CaO and Al bulk rock content, with a high CaO concentration delaying the breakdown of allanite and inhibiting monazite formation. However, because average metapelites are low in CaO (Shaw, 1956), they are not expected to contain allanite at temperatures above the middle-amphibolite facies (Janots et al., 2008). All studied samples lack any textural evidence to discriminate the reactions responsible for the formation of monazite, therefore microstructural relationships of monazite deformed with the S_2a crenulated fabric and microfolds thus provide a minimum constraint of prograde deformation and M_2 Barrovian metamorphism.

5.4.2.2 TLN47: Biotite, Clinzoisite Schist

TLN47 lies directly beneath the Zas Shear Zone (ZSZ) and is a heavily altered and metasomatised rock. Monazite analyses from this sample do not provide a precise age estimate due to the high levels of common Pb and small population size, but regression of successful data gives a lower intercept age of 17.7 ± 4.5 Ma (MSWD = 4.0) (Fig. 5.8), lying within error of other M_2 age data from this unit.

5.4.2.3 TLN13: Kyanite Schist

Monazite in TLN13 was extremely small and un-zoned, and dominantly within the matrix. The data is presented in Fig. 5.8 and it provides a lower intercept U–Pb age of 15.71 ± 0.51 Ma (MSWD = 0.83), based on 3 spots. However, a single analysis from a small monazite located within kyanite (M_2), gives an age of 22.1 ± 3.8 Ma, and provides

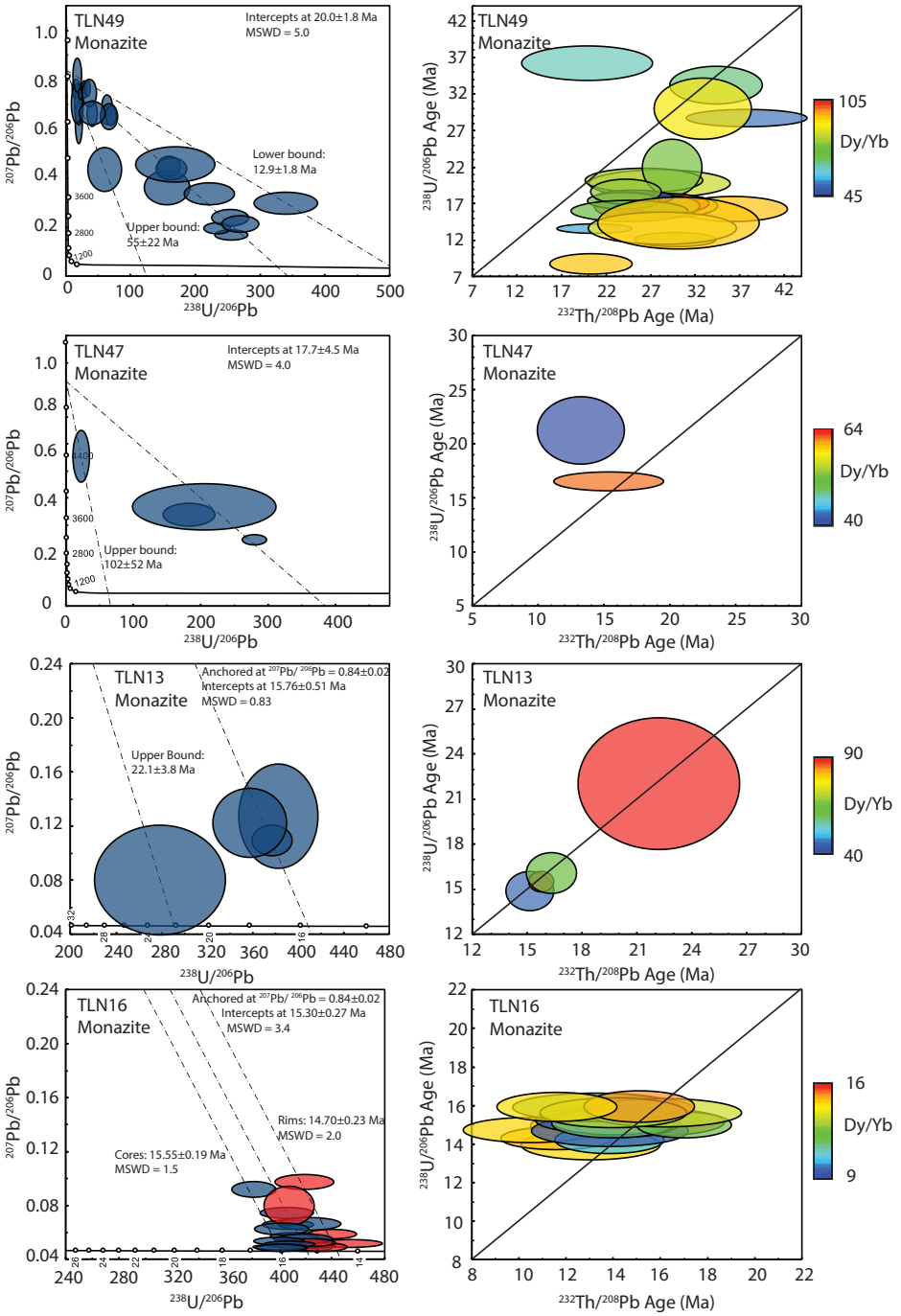


Figure 5.8: Tera-Wasserburg concordia plots for Koronos Unit samples using LA-ICPMS analysis of monazite, upper intercepts where calculated using a $^{207}Pb/^{206}Pb$ value of 0.84 using Stacey and Krammers, 1975 for young monazite and U–Pb vs Th–Pb age plots, with coloured circles representing the measured ratio of Dy/Yb. A and B) TLN49 monazites showing a range of ages with the main population between 40 and 17 Ma. C and D) TLN47 monazites with ages between 22 and 16 Ma but lack of data. E and F) TLN13 monazites with 2 age populations, a concordant 22.1 ± 3.8 Ma age and 15.76 ± 0.51 Ma, with good fit between U–Pb and Th–Pb ages. G and H) TLN16 monazite Tera-Wasserburg plot with blue circles representing monazite cores and red circles monazite rims with regressed ages of 15.55 ± 0.19 Ma and 14.70 ± 0.23 Ma, with a large amount of data falling on the 1:1 line for U–Pb vs Th–Pb ages.

an upper bound of the prograde growth of kyanite between 26 and 18 Ma. This age is associated with high Dy/Yb values (90), indicating monazite growth in the presence of garnet. The Th–Pb ages correlate directly with U–Pb ages and show a systematic decrease in Dy/Yb with younger ages, indicative of monazite growth during garnet breakdown, which would act to release Yb into the surrounding matrix. Pseudosection analysis, of a similar sample (TLN22), reveal that garnet cores grew during prograde metamorphism and burial to peak M_2 conditions, garnets were then partially resorbed during decompression which resulted in decreasing garnet proportions. Small thermally nucleated post-tectonic garnets grew after top-to-NNE shearing which must post-date young monazites.

5.4.2.4 TLN16: Biotite, Garnet Schist

This sample lies close to the Koronos Shear Zone at the base of the Koronos Unit and is characterized by small matrix monazites associated with small <300 μm garnets. These garnets cross-cut the S_3 fabric and are therefore post-tectonic with respect to the S_3 top-to-NNE shearing and are associated with thermal metamorphic textures developed during M_3. In chapter 4, these textures are interpretted to be related to juxposition of the hot migmatites adjacent to the cooler Koronos Unit at higher structural levels. Monazite data reveal consistently young U–Pb and Th–Pb ages (Fig. 5.8). Monazite core and rims were able to be distinguished in some grains and gave respective lower intercept ages of 15.55 ± 0.19 Ma for the cores (MSWD =1.5) and a rim age of 14.7 ± 0.23 Ma (MSWD = 2.0). Trace element data show a weak trend to smaller Dy/Yb values for younger ages, which we interpret to be related to growth of monazite during garnet breakdown, increasing the available Yb budget of the rock. This data suggests that garnet grew until 15.5 Ma due to heating from the exhuming Core Unit but then rapidly started to breakdown during decompression.

5.4.2.5 TL67: Kyanite Gneiss

This rock records the prograde metamorphic evolution of the lower levels of the Koronos Unit and is associated with peak metamorphic M_2 kyanite grade conditions of ca. 10 kbar and 670°C. Microstructurally, this rock has S_2 kyanite-grade fabrics preserved in garnet, kyanite and rutile rich enclaves which are overprinted by S_3 top-to-NNE extensional fabrics related to shearing on the KSZ along the margins of the migmatite dome. These blasto-mylonite top-to-NNE fabrics are strongly annealed at M_3 sillimanite-grade conditions, also indicative of high-temperatures outlasting deformation. A total of 35 monazite grains were identified using the backscattered electron imaging and are typically anhedral, very small (up to 30 μm diameter) and located mainly within the matrix or sometimes as tiny inclusions within kyanite, but is rarely trapped within the cores and rims of garnet porphyroblasts. U–Pb ages span from 21.8 ± 3.1 Ma to 15.09 ± 0.48 Ma. The oldest age is from M4b which is trapped as an inclusion within kyanite and therefore constrains kyanite growth during prograde M_2. However, the large error associated with this age, combined with the contrasting corresponding Th–Pb age of 16.9 ± 1.9 Ma suggests this analysis is not robust. Nevertheless, the oldest Th–Pb age from sample TLN13 at a similar metamorphic grade of 20.3 ± 1.9 Ma confirms this older population of monazite. A regression of all but the two older analyses gives a lower intercept age of 15.93 ± 0.56 Ma (MSWD = 5.3) (Fig. 5.9). The large MSWD value indicates this is not a single population and instead represents monazite growth over a period from ca. 16.5–15 Ma and corresponds to a mean Th–Pb age of 15.89 Ma. Matrix monazites analyzed show relatively high Y contents, indicating most monazite grew during garnet breakdown. in agreement with garnet compositional profiles which show an increasing spessartine content towards the outermost rims due to resorption. The subsequent matrix ages of ca. 16.5–15 Ma therefore represent syn- post-peak metamorphic conditions on the retrograde part of the P–T path and is supported by comparison with pseudosection analysis that demonstrate a decrease in garnet mode with decreasing pressure. These younger ages also coincide with monazite rim ages within the Core Unit that represents (M_3) sillimanite-grade conditions. This data sug-

gests that the rocks within the Koronos Unit began to decompress prior to 16–15 Ma and therefore shearing on the Koronos and Zas Shear Zones initiated prior to 16–15 Ma at (M_2) kyanite-grade conditions. The younger age population must represent heating and fluid infiltration at lower pressure (M_3) sillimanite-grade conditions following juxtaposition of the hot Core Unit.

Rutile is distributed as 30 μm grains within enclaves containing garnet and kyanite and gives a lower intercept age of 12.7 ± 1.3 Ma (MSWD = 0.56) (Fig. 5.9). This represents a cooling age through approximately the 520 °C isotherm accounting for grain sizes and cooling rate using the calculation of Cherniak (2000), indicating the rock cooled by ca. 150 °C over 2–3 Myrs. Alignment of rutile long axis with the top-to-NNE shear fabrics which show subsequent annealling suggest this cooling age post-dates shearing on the Koronos Shear Zone and is related to cooling of the whole core complex.

5.4.2.6 TLN21: Kyanite, Sillimanite Gneiss

TLN21 was taken from the base of the Koronos Unit within the Koronos Shear Zone. In thin section, it displays earlier (M_2) kyanite grade fabrics overprinted by (S_3) extensional shearing and lower pressure (M_3) silliamite-biotite intergrowths. Monazite from this sample was small and uniformly zoned, with the core region giving a lower intercept age of 15.77 ± 0.29 Ma (MSWD = 2.1) (Fig. 5.9), and the rims giving ages of 15.11 ± 0.65 (MSWD = 2.5), with an overall lower intercept age of 15.43 ± 0.42 (MSWD = 3.1). Dy/Yb ratios provide no obvious pattern within the small timeframe of monazite crystallization.

5.4.3 Core Unit

5.4.3.1 TL15: Kyanite-grade Migmatite

Monazite from sample TL15 is found within the matrix and as inclusions within garnet and kyanite porphyroblasts. Due to the variation in textural relationships, different

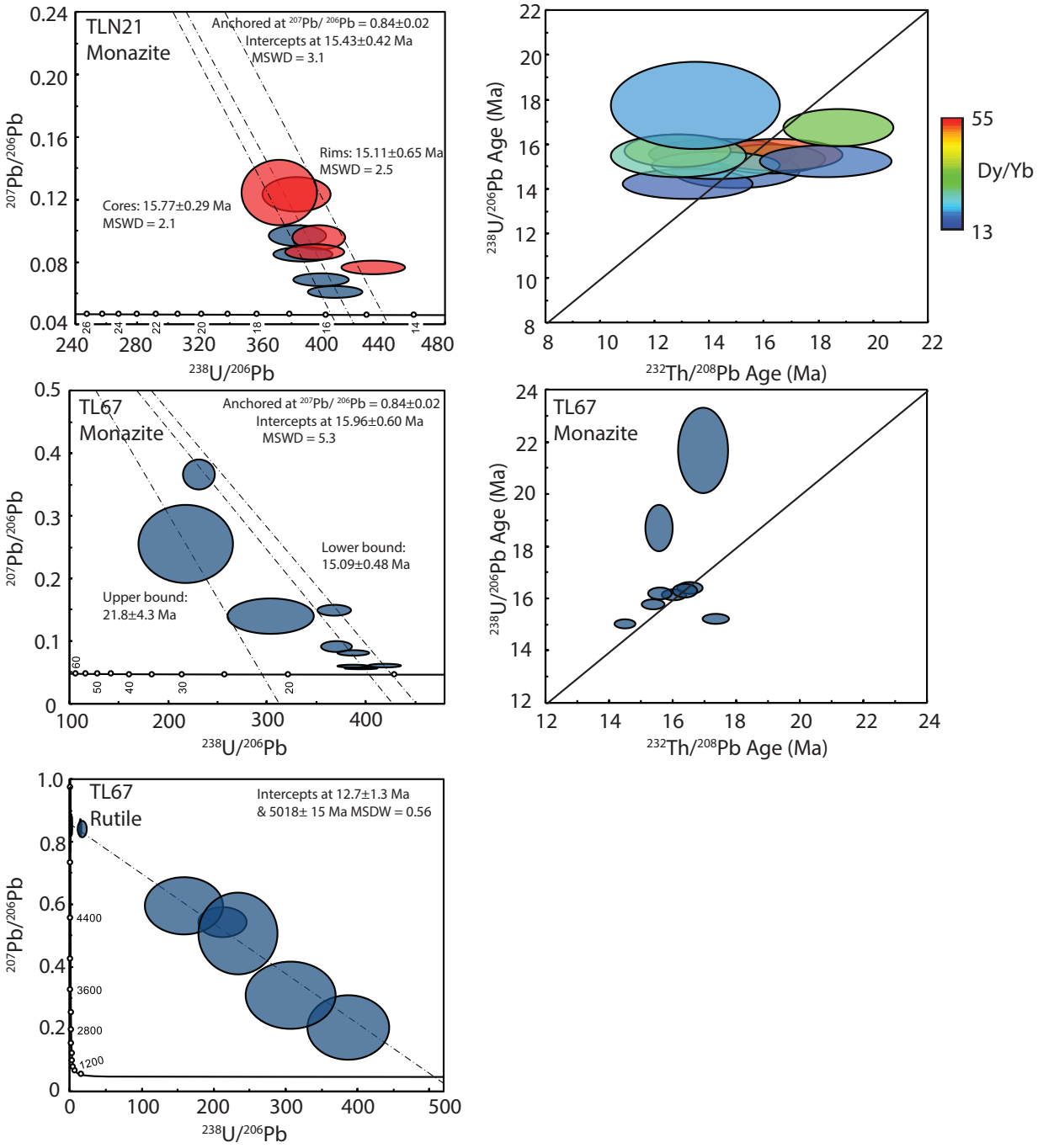


Figure 5.9: Tera-Wasserburg concordia plots for Koronos Unit samples using LA-ICPMS analysis of monazite, upper intercepts where calculated using a $^{207}Pb/^{206}Pb$ value of 0.84 using Stacey and Krammers, 1975 for young monazite, blue circles represent cores and red circles represent rims. U–Pb vs Th–Pb age plots, with coloured circles representing the measured ratio of Dy/Yb. A and B) TLN21 data with cores giving regressed ages of 15.77 ± 0.29 Ma and rims giving 15.11 ± 0.65 Ma, with reasonable correlation between U–Pb and Th–Pb ages. C and D) TL67 monazite with data falling between 21.8 ± 4.3 Ma and 15.09 ± 0.48 Ma, with some scatter between U–Pb and Th–Pb ages. E) TL67 rutile Tera-Wasserburg concordia plot showing a range in analyses from high common Pb to mainly radiogenic Pb giving a retresseged age of 12.7 ± 1.3 Ma.

monazite grains could potentially provide maximum age constraints on the timing of different stages of metamorphism. A total of nine grains were analysed with U–Pb ages ranging from 18.41 ± 0.75 Ma to 15.20 ± 0.55 Ma, with a similar Th–Pb age distribution (Fig. 5.9). Except for two slightly younger analyses, most data fall between 18 and 16 Ma. Older ages (17–18 Ma) correspond to Y poor monazite cores or monazites trapped as inclusions within kyanite porphyroblasts. These observations suggest initial monazite growth due to muscovite-breakdown during hydrous melting at kyanite-grade conditions of ca. 8–10 kbars, 730 °C (reaction 5.1), and that monazites were subsequently included within the peritectic products such as garnet rims and kyanite porphyroblasts by the reaction proposed by García-Casco et al., (2001):

$$biotite + muscovite + plagioclase + quartz + H_2O \rightarrow kyanite + garnet + melt \quad (5.1)$$

Textural relationships of monazite enclosed within kyanite in grains 4 and 8 thus constrain the minimum age of (M_2) kyanite-grade metamorphism and partial melting to between 18–17 Ma. The regressed age of 17.58 ± 0.33 Ma (MSWD = 6.4), (Fig. 5.9) is therefore interpreted to provide a minimum age constraint for kyanite-grade anatectic conditions for Naxos migmatites. Because kyanite is folded with the foliation in this sample (Fig. 5.4a), which is in turn associated with km-scale upright F_3 isoclinal folding. This age constrains the timing of F_3 NNE–SSW upright folding to post-17 Ma, presumably following decompression to M_3 conditions.

Monazites M5 and $M_2$6, show a range of ages from 18.2–15.2 Ma, and display internal zoning in LREE's and Y content with a distinguishable core and rim domains (Fig. 5.5). Y content increases abruptly along the rim, which correlates to the younger ages <16 Ma. The replacement of garnet by biotite during melt crystallization during retrogression can liberate Y back into the reacting matrix and allow for the growth of Y (+ HREE)-rich monazite (Pyle and Spear, 1999; Kohn et al., 2005). This is supported by evidence for garnet resorption with an increasing Mn content towards the rim and

garnet breakdown into biotite at post-peak conditions (Fig. 5.15).

For this scenario to occur, decompression of this rock to lower pressures beyond the garnet stability field (see Fig. 5.15) must have occurred between ca. 17 Ma and 15.2 Ma. This is consistent with textural features, such as sillimanite intergrowing with biotite-quartz nodules after kyanite in a different domain of the rock, as suggested by Carmichael (1969). Furthermore, estimated P–T conditions from pseudosection analysis on sillimanite grade migmatites reveals garnet rim compositional isopleths intercept at lower pressures of 4.9–5.5 kbars at 690 °C, (e.g. TL66, TLN34) adjacent to the zone of garnet instability, at lower temperatures than the anhydrous solidus. This is coherent with post-peak (M_3) metamorphic conditions and the production of secondary muscovites that formed in the back reaction from water release during melt crystallization.

5.4.3.2 TL66: Sillimanite-Migmatite

Monazite from sample TL66 is typically anhedral and 40–100 μm in diameter (Fig. 5.5). Eight monazite grains were analysed, which were much larger in size and fewer in abundance in comparison to the other migmatite samples. We suggest these relationships are indicative of the presence of larger degrees of melt, which enhances chemical diffusion, increasing the ability of resorption and redistribution of monazite to more numerous grains with more favorable compositions. For melt to excessively lubricate grain boundaries, and substantially increase the diffusional length scales and transport of HREE, melt volumes must exceed 7–10%, the critical melt threshold (Rosenburg and Hardey, 2007). The most effective way to achieve this is the muscovite dehydration melting (reaction 5.2) (Evans and Guidotti, 1966; García-Casco et al., 2003; Patiño Douce and Harris, 1998), which has a moderately dipping positive P–T slope, and would be expected to be crossed upon decompression from kyanite-grade conditions.

$$muscovite + quartz + plagioclase \rightarrow K - feldspar + aluminosilicate + melt \quad (5.2)$$

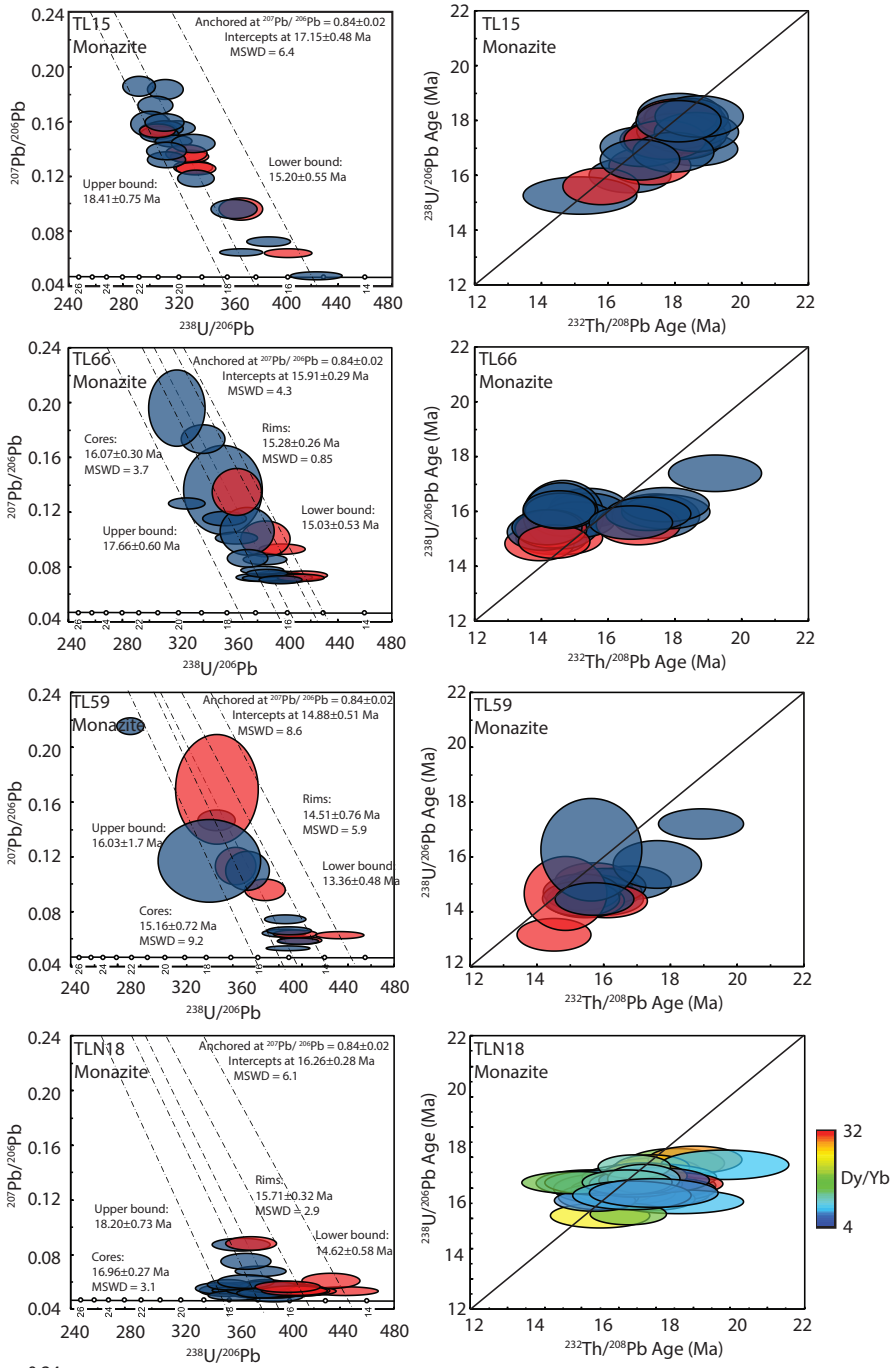


Figure 5.10: Tera-Wasserburg concordia plots for Core Unit samples using LA-ICPMS analysis of monazite, upper intercepts where calculated using a $^{207}Pb/^{206}Pb$ value of 0.84 using Stacey and Krammers, 1975 for young monazite, blue circles represent cores and red circles represent rims. U–Pb vs Th–Pb age plots, with coloured circles representing the measured ratio of Dy/Yb. A and B) TL15 monazite data with a range in ages between 18.41 ± 0.75 and 15.20 ± 0.55 Ma with good correlation between U–Pb and Th–Pb ages. C and D) TL66 data with ages falling between 17.66 ± 0.60 Ma and 15.03 ± 0.53 Ma and overall reasonable correlation between U–Pb and Th–Pb ages. E and F) TL59 age data with U–Pb data falling between 16.03 ± 1.7 Ma and 13.36 ± 0.48 Ma with a reasonable fit between U–Pb and Th–Pb ages, the Th–Pb system gives slightly older ages for two of the analyses. G and H) TLN18 monazite data with a definitive core and rim distribution in ages with regressed ages of 16.96 ± 0.27 Ma and 15.71 ± 0.32 Ma respectively, and good overall fit between U–Pb and Th–Pb ages.

25 analyses were obtained from eight different grains and are shown in Fig. 5.9. Five analyses were rejected due to high common lead counts. Despite variable amounts of common lead between grains, all analyses of monazite form a regression with a lower intercept age of 15.90 ± 0.29 Ma (MSWD = 4.3). However, ages derived from grain 5 indicate an age of 17.64 Ma, which is most probably representing the M_2 kyanite grade event earlier in the rock's metamorphic evolution. This gives an almost identical age as TL15, whilst ages from grains 3 and 6 give an age of 15.03 ± 0.53 Ma, probably indicating monazite growth after the metamorphic peak whilst still in the presence of and or during the crystallization of melt. The monazite cores give a regressed age of 16.07 ± 0.30 Ma (MSWD = 3.7) indicating these do not fall in a single population whereas the rims give a lower intercept age of 15.28 ± 0.26 (MSWD = 0.85). These data suggest monazite grew continuously between ca. 17.6–15.0 Ma. However, the Th–Pb data show a larger range of ages which are distributed into two major age populations with mean ages of 17.50 Ma and 14.52 Ma respectively. The older age population has a maximum age of 19.14 Ma, which we associate with M_2 kyanite grade partial melting, and the youngest age is 14.0 Ma presumably recording the closure of partial melting at lower pressure (M_3) sillimanite grade conditions.

5.4.3.3 TLN18: Diatexite Migmatite

TLN18 is a diatexite and was taken from the deepest structural levels of the migmatite dome. Monazite in this sample are typically found within the leucosomes but also as incluions within biotite-sillimanite intergrowths and are typically larger and have irregular Y zoning (Fig. 5.10), although still have a distinct core low in Y and an Y rich rim (Fig. 5.5), which can be interpreted as growth during garnet breakdown (Pyle and Spear, 1999; Kohn, 2005). Monazite ages represent a continuous population, spanning from 18.20 ± 0.73 Ma to 14.62 ± 0.58 Ma (Fig. 5.10), which represents the most complete record for the evolution of partial melting on Naxos. Treating cores and rims separately, cores give regressed U–Pb ages of 16.96 ± 0.27 Ma with an MSWD of 3.1, whereas rims associated with higher Y content give regressed ages of 15.71 ± 0.32

Ma with a corresponding MSWD of 2.9. Due to the lack of garnet in this sample there is little correlation between Dy/Yb, and the spread in Th–Pb ages overlaps within uncertainty of the U–Pb ages.

5.4.3.4 TL59: Metasomatized Gneiss

Sample TL59 was taken from the western boundary of the migmatite dome and is affected by shearing on the Naxos-Paros Detachment system that overprints the Koronos shear zone. In this sample, monazite is located within the matrix, and as inclusions within secondary muscovite and garnet rims, however, no monazite was observed within inclusion-rich garnet core regions. All grains exhibit subedral morphologies and lack obvious compositional domains (Fig. 5.10). A total of 18 spot analyses were obtained from 7 grains and give regressed U–Pb lower intercept age of 14.88 ± 0.51 Ma (MSWD = 5.9), whilst an absolute minimum age from spot $M_1$5a has an intercept of 13.36 ± 0.48 Ma. This age falls within error of young ages from other sillimanite-grade migmatites (TLN34 and TLN20A) and either represents the final stages of sillimanite grade partial melting (M_3) or retrogression and metasomatism whilst still at high-temperatures. The later of these possibilities could be related to back reaction through the muscovite dehydration melting reaction (reaction 5.2) upon melt crystallization, which would act to hydrate the surrounding rock and produce the large cross-cutting secondary muscovites. The Y contents of the monazites are surprisingly low, possibly signifying these monazites grew in the presence of garnet, and therefore possibly represent a minimum age of final garnet growth. Because this sample was taken from the western margin of the migmatite dome immediately adjacent to the cross-cutting Naxos-Paros Detachment System, the resultant ages constrain the timing of top-to-NNE shearing on the NPDS. Microstructural evidence suggests most of the garnets are pre-tectonic with respect to the development of S_3 top-to-NNE extensional fabrics, that deforms secondary muscovites. Textural considerations of monazite within secondary muscovites thus constrains the timing of melt crystallization and sub-solidus shearing related to the NPDS to post 15 Ma.

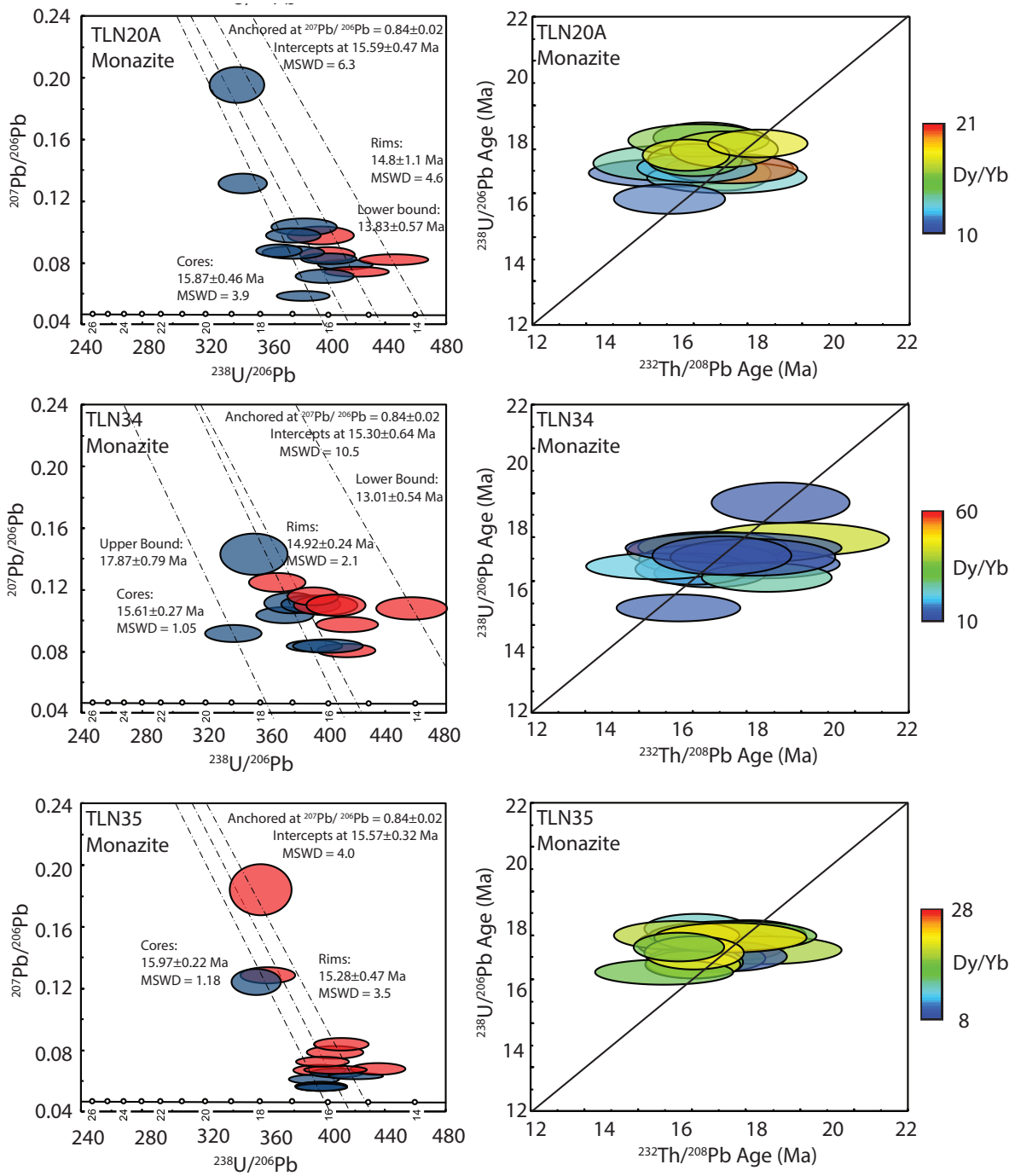


Figure 5.11: Tera-Wasserburg concordia plots for Core Unit samples using LA-ICPMS analysis of monazite, upper intercepts where calculated using a $^{207}Pb/^{206}Pb$ value of 0.84 using Stacey and Krammers, 1975 for young monazite, blue circles represent cores and red circles represent rims. U–Pb vs Th–Pb age plots, with coloured circles representing the measured ratio of Dy/Yb. A and B) TLN20A monazite with definitive core and rim age distributions with ages of 15.87 ± 0.46 Ma and 14.80 ± 1.10 Ma respectively and good overall fit between U–Pb and Th–Pb ages. C and D) TLN34 monazite data with discrete core and rim age populations, cores give an age of 15.61 ± 0.27 Ma and rims 14.92 ± 0.24 Ma with data falling between 17.87 ± 0.79 Ma and 13.01 ± 0.54 Ma with good overall fit between U–Pb and Th–Pb ages. E and F) TLN35 monazites show core and rim populations which are 15.97 ± 0.22 Ma and 15.27 ± 0.47 Ma respectively and good fit between U–Pb and Th–Pb ages.

5.4.3.5 TLN20A: Stromatic Migmatite

Taken from the perimeter of the dome, this migmatite records muscovite dehydration melting textures with peritectic K-feldspar. The corresponding monazites are surprisingly small, (<40 μm in diameter) and appear compositionally homogeneous under backscattered electon imagaing. Taken as one population, regression to the lower intercept corresponds to 15.59 ± 0.47 Ma with an MSWD of 6.3 (Fig. 5.11), suggesting this is not one population. Treating cores and rims separately, monazite cores give regressed ages of 15.87 ± 0.46 Ma with MSWD of 3.9 and rims give younger ages of 14.80 ± 1.10 Ma with an MSWD of 4.6. We interpret these ages as representing sillimanite grade conditions at temperatures above the anhydrous solidus. The youngest age of 13.83 ± 0.57 Ma lies within the uncertainty of Th–Pb ages and presumably represents the final stages of partial melting on Naxos or retrograde monazite growth in the presence of fluids released following crystallization. There is good correlation between U–Pb and Th–Pb ages and a general trend to lower values of Dy/Yb with younger ages, which we interpret as monazite growth during garnet breakdown at supra-solidus conditions, associated with decompression to <5 kbars at ca. 15 Ma.

5.4.3.6 TLN34: Sillimanite, K-feldspar Migmatite

TLT34 is a sillimanite grade stromatic migmatite that experienced muscovite dehydration melting producing peritectic k-feldspar, the U–Pb and Th–Pb age data is presented in Fig. 5.11. The oldest monazite U–Pb age is 17.87 ± 0.79 Ma that records the early stages of partial melting, presumably at kyanite-grade pressures, whereas the youngest monazites give ages of 13.01 ± 0.54 Ma. This age represents an absolute minimum age for partial melting at the deep levels of the migmatite dome and must either represent the final stage of monazite growth in the presence of melt or high-grade retrograde metasomatism due to release of fluids from melt crystallization. Regression of cores and rims (excluding two outliers) gives U–Pb intercept ages of 15.61 ± 0.27 Ma (MSWD = 1.05) for cores, and 14.92 ± 0.24 Ma (MSWD = 2.1) for rims. U–Pb and Th–Pb data gives consistent ages, however there is no systematic pattern to the trace element

ratios, presumably due to the lack of garnet present during monazite growth.

5.4.3.7 TLN35: Garnet, Sillimanite Migmatite

Monazite in TLN35 gives a narrow spread of ages (Fig. 5.11) from 16 to 14.5 Ma, regressing to a single age of 15.57 ± 0.32 Ma (MSWD = 4.0). Treating monazite cores separately gives an age of 15.97 ± 0.22 and an MSWD of 1.18, making it likely this represents a single population, whereas rims gives ages of 15.28 ± 0.47 Ma with an MSWD of 3.5. There is little to no pattern in the trace element ratios and there appears to be a spatial control to the HREE distributions in the rock as each monazite grain records different but rather uniform values of Dy/Yb possibly indicating a spatially inhomogeneous HREE distribution. The U–Pb and Th–Pb ages fall on the 1:1 line demonstrating consistency between the two decay systems in this sample.

5.4.4 S-Type Leucogranites and Gneisses

TL57: Cycladic Basement Orthogneiss This sample is a banded acid gneiss and was collected from the SW edge of the migmatite dome near the village of Ano-Potamia. We interpret it to represent a slice of the basement to the metamorphosed shelf carbonates. It has a range of ages, but regression through rim data only give a lower intercept age of 16.36 ± 0.36 Ma with an MSWD of 0.06 (Fig. 5.12). Older ages represent inherited ages with a major cluster at ca. 300 Ma, which we interpret as an older Variscan event, verifying it indeed represents the basement to the metasedimentary cover.

5.4.4.1 TL58: Garnet Tourmaline Leucogranite

TL58 is a garnet–tourmaline leucogranite dyke that intruded through the migmatites south of the village of Ano Potamia. It has a range of ages from 17–13 Ma with a major age population around ca. 14 Ma (Fig. 5.12), similar to the monazite ages from adjacent sample TL59, associated with secondary muscovites. This age is therefore interpreted to represent late-stage S-type intrusion into migmatites with only very small degrees of melt, releasing fluids upon crystallization causing metasomatism in

Table 5.5: Zircon U-Pb SC-ICP-MS geochroological results for leucogranites part 1

Mineral	Rock Type	Location	Sample	Spot number	comment	204Pb	f206c	206Pb	Cps	208Pb	Cps	232Th	Cps	235U	Th / U	Pbppm	Thppm	Uppm	Ratios								Ages								Discordance %	Common-Pb corrected ages		
																			Data for Tera-Wasserburg plot				Data for Wetherill plot				Ages												
																			238U/206Pb	1s %	207Pb/206Pb	1s %	207Pb/235U	1s %	Rho	Age	206Pb/238U	2s abs	Age	207Pb/235U	2s abs	Age	206Pb/238U	2s abs	6-8/7-6	6-8/7-535	Cor.206/238-Pb Age	2s [Ma]
Zircon	Orthogneiss	Core	TL57	1		-5	0.0	2234162	134552	142260	4010698	20848	#####	2680	1954408	1064	988	11.80	2.1	0.05358		0.68069	2.46	0.09847	2.14	####	561	524	22	531	20	6.6	6.6	1.3	522.6	
Zircon	Orthogneiss	Core	TL57	2		90	1.0	1582305	110069	1077	2401388	19359	83.4	1902	823350	988	9	14.08	4.2	0.0651	1.34	0.64373	4.38	0.07107	4.17	####	777	442	36	501	34	43.1	11.6	437.5	34.7	
Zircon	Orthogneiss	Core	TL57	3		-26	0.3	1155783	81137	1285	3041511	18577	12.2	1246	312148	950	76	19.39	2.4	0.05862	1.57	0.47960	2.71	0.05929	2.54	####	941	378	17	392	17	37.9	10.1	376.3	17.6	
Zircon	Orthogneiss	Core	TL57	4		-7	0.1	1230312	66991	4906	2804146	21263	86.4	1503	93709	1085	9	19.61	2.1	0.05536	1.42	0.3765	2.55	0.0510	2.11	####	353	321	13	324	13	9.1	1.2	320.4	13.2	
Zircon	Orthogneiss	Core	TL57	5		49	0.7	1311302	7730	20111	5985334	13782	####	1694	2001143	703	145	13.06	4.3	0.05187	4.48	0.04108	4.48	0.0766	4.27	####	557	476	60	490	34	14.6	2.9	474.4	38.8	
Zircon	Orthogneiss	Core	TL57	6		7	0.1	1130982	6991	6694	2804146	21263	86.4	1503	93709	1085	9	19.61	2.1	0.05536	1.42	0.3765	2.55	0.0510	2.11	####	353	321	13	324	13	9.1	1.2	320.4	13.2	
Zircon	Orthogneiss	Core	TL57	7		34	0.3	2085310	129005	42127	6173966	12366	####	2011	2067710	641	60	6.70	6.9	0.05924	2.72	0.1693	7.44	0.1693	6.92	####	1476	1003	897	1082	94	393	17.1	872.3	108.7	
Zircon	Orthogneiss	Core	TL57	8		18	0.2	1096545	10016	10019	3237746	20338	####	2011	2022038	1657	169	19.33	1.7	0.05540	1.30	0.38857	2.12	0.0517	1.67	####	969	325	11	330	12	11.9	1.6	329.7	10.6	
Zircon	Orthogneiss	Core	TL57	9		11	0.4	1353986	6566	5300	3240960	22035	96.4	1472	1088988	1125	105	20.88	1.6	0.05323	1.29	0.3454	2.06	0.0479	1.61	####	906	302	9	307	11	4.7	1.9	301.6	9.5	
Zircon	Orthogneiss	Core	TL57	10		31	0.4	1358361	6567	5300	3240960	22035	96.4	1472	1088988	1125	105	20.88	1.6	0.05323	1.29	0.3454	2.06	0.0479	1.61	####	906	302	9	307	11	4.7	1.9	301.6	9.5	
Zircon	Orthogneiss	Core	TL57	11		-21	-6.4	5879	314	2	10135	66	####	2	3390	825	63	373.37	2.3	0.05334	3.63	0.0196	4.29	0.0027	2.29	####	347	17	1	20	2	90.1	13.0	17.0	0.8	
Zircon	Orthogneiss	Core	TL57	12		-59	-0.3	6199	320	29	19453	992	####	70	6941	992	64	14.89	2.1	0.05503	2.67	0.0182	3.37	0.0026	2.06	####	207	17	1	18	1	91.9	7.7	16.8	0.7	
Zircon	Orthogneiss	Core	TL57	13		-16	-0.6	49983	3058	6211	1765385	7486	####	630	59068	379	32	13.89	8.5	0.0610	8.67	0.0720	8.92	####	639	69	64	69	30	29.8	9.7	454.3	145.3	
Zircon	Orthogneiss	Core	TL57	14		-7	0.1	1105838	6911	1437	3931742	21263	86.4	1503	93709	1085	9	19.61	2.1	0.05536	1.42	0.3765	2.55	0.0510	2.11	####	353	321	13	324	13	9.1	1.2	320.4	13.2	
Zircon	Orthogneiss	Core	TL57	15		-54	-1.1	86321	4999	10319	2510370	21670	####	1081	839883	1254	117	30.38	7.0	0.0571	7.17	0.2261	7.67	0.0229	6.96	####	496	146	75	200	29	29.1	10.8	207.0	28.1	
Zircon	Orthogneiss	Core	TL57	16		-12	-0.4	59136	3270	811	625732	9279	18.2	673	8614	474	41	19.02	2.1	0.05973	3.00	0.0526	2.05	####	####	405	98	330	13	340	17	18.6	2.8	329.5	13.1	
Zircon	Orthogneiss	Core	TL57	17		57	1.6	64608	3525	1844	1245454	19212	4.2	727	4106	980	86	33.02	8.2	0.0545	1.89	0.2277	8.37	0.0303	8.16	####	393	192	31	208	31	51.1	7.6	191.3	30.5	
Zircon	Orthogneiss	Core	TL57	18		223	7.0	55109	3941	3934	325261	21633	9.9	670	10880	10974	1.5	475.04	1.5	0.0703	1.52	0.0467	3.60	0.0467	3.29	####	253	294	19	269	18	18.9	5.4	294.5	18.9	
Zircon	Orthogneiss	Core	TL57	19		-45	-0.6	141983	1233	1500	252544	9407	1.9	1500	14388	1288	53	21.42	3.3	0.05213	1.46	0.3259	3.29	####	####	253	67	284	19	287	17	1.6	1.6	284.1	9.2	
Zircon	Orthogneiss	Core	TL57	20		404	14.6	30721	7784	1583	1253259	5764	1.9	642	5238	1036	23	33.40	2.3	0.06854	4.88	0.0029	2.33	####	####	2870	159	19	1	18	1	99.3	76.7	18.9	0.6	
Zircon	Orthogneiss	Core	TL57	21		-51	-2.6	33702	1905	690	1029310	13283	9.5	408	64228	6792	1.5	440.72	1.5	0.0162	2.21	0.0022	1.47	####	####	322	75	14	0	0	0	99.6	12.2	14.2	0.4	
Zircon	Orthogneiss	Core	TL57	22		209	5.1	61756	10263	2127	1722121	19917	7.8	978	76120	9815	3.7	382.74	3.7	0.0636	3.74	####	####	0.0022	####	2082	129	14	17	1	1	99.2	63.5	15.1	0.4	
Zircon	Orthogneiss	Core	TL57	23		842	9.7	130899	38222	18622	3441651	68690	####	6420	535570	19066	2.6	339.29	2.6	0.1415	5.36	0.0543	5.97	0.0028	2.62	####	2246	185	18	448	18	99.2	66.6	15.8	0.8	
Zircon	Orthogneiss	Core	TL57	24		-16	-0.6	49983	3058	6211	1765385	7486	####	630	59068	379	32	13.89	8.5	0.0610	8.67	0.0720	8.92	####	639	69	64	69	30	29.8	9.7	454.3	145.3	
Zircon	Orthogneiss	Core	TL57	25		304	9.4	47079	2742	1798	1566048	9.3	1.3	714	74236	7982	1.8	0.1432	4.4	0.0464	4.78	0.0025	1.58	####	####	2366	153	14	16	1	1	99.3	67.1	14.3	0.5	
Zircon	Orthogneiss	Core	TL57	26		164	4.3	66454	4778	4635	2645212	22261.7	7.8	807	88479	11361	2.4	4.20	0.0681	4.20	0.0225	4.86	0.0024	2.44	####	872	174	15	23	2	98.2	31.7	15.0	0.7	
Zircon	Orthogneiss	Core	TL57	27		223	7.0	55109	3941	3934	325261	21633	9.9	670	10880	10974	1.5	475.04	1.5	0.0703	1.52	0.0467	3.60	0.0467	3.29	####	253	294	19	269	18	18.9	5.4	294.5	18.9	
Zircon	Orthogneiss	Core	TL57	28		###	2.4	37976	#####	#####	958027	5277.9	3.5	1.03	330061	7.1	3.8	389.41	3.8	0.2097	1.9	0.1501	4.1	0.0712	####	2903	85	17	1	16	1	73.3	99.4	77.3	1.1	
Zircon	Orthogneiss	Core	TL57	29		###	3.1	99615	12455	88941	12644	24921	9.5	1.03	87462	23247	2.4	407.47	2.4	0.0511	1.9	0.1504	2.7	0.0711	####	2347	161	14	14	1	1	99.4	68.5	14.1	0.4	
Zircon	Orthogneiss	Core	TL57	30		699	12.5	98615	8050	8050	1266545	5555.7	23.6	1251	290151	13379	4.7	45.57	4.7	0.0526	5.45	0.0227	2.73	####	####	1456	93	17	1	17	1	99.7	68.5	11.6	0.4	
Zircon	Orthogneiss	Core	TL57	31		242	6.5	57909	6935	10753	2284308	55583	7.8	805	76403	9762	3.7	409.65	1.9	0.1083	6.64	0.0364	6.91	0.0024	1.90	####	1770	242	16	36	1	99.1	56.7	14.5	0.5	
Zircon	Orthogneiss	Core	TL57	32		-55	-1.2	69329	8235	4944	3509042	13767	####	1762	1702	1762	1.1	29.01	1.1	0.0543	1.35	0.2733	1.96	0.0365	1.35	####	1715	232	12	247	10	10.4	2.2	246.5	10.2	
Zircon	Orthogneiss	Core	TL57	33		103	0.3	3920701	11853	9407	5766869	21959	0.1	74	127	2130	1.7	1.78	1.7	0.0274	1.15	0.2753	1.92	0.0274	1.15	####	1757	175	10	247	10	29.1	0.5	175.2	2.9	
Zircon	Orthogneiss	Core	TL57	34		33	0.2	202390	17758	9297	2842243	10.10	0.41	9	192	675	0.2	0.0200	0.2	0.0427	1.99	0.0221	1.42	####	####	384	10	0	0	0	0	0	0	0	0	
Zircon	Orthogneiss	Core	TL57	35		18	0.2	175740	11786	4724	1013307	17475	0.05	32	22	433	0.2	0.0668	0.2	0.0532	1.04	0.0793	1.95	0.0793	1.65	####	832	482	16	492	16	40.8	11.6	486	15.3	
Zircon	Orthogneiss	Core	TL57	36		6	0.1	39528	2206	1445	1010453	7737	0.10	31	70	1335	0.4	0.2200	0.4	0.0427	1.99	0.0221	1.42	####	####	384	10	0	0	0	0	0	0	0	0	
Zircon	Orthogneiss	Core	TL57	37		9	0.1	49105	2744	1965	1257147	9815	0.17	32	70	1335	0.4	0.2200	0.4	0.0427	1.99	0.0221	1.42	####	####	384	10	0	0	0	0	0	0	0	0	
Zircon	Orthogneiss	Core	TL57	38		31	0.4	154850	8107	10872	3509042	13767	####	1762	1702	1762	1.1	29.01	1.1	0.0543	1.35	0.2733	1.96	0.0365	1.35	####	1715	232	12	247	10	10.4	2.2	246.5	10.2	
Zircon	Orthogneiss	Core	TL57	39		35	0.3	193847	10073	2316	587086	27098	0.03	34	19	671	0.2	0.0570	0.2	0.0532	1.04	0.0793	1.95	0.0793	1.65	####	832	482	16	492	16	40.8	11.6	486	15.3	
Zircon	Orthogneiss	Core	TL57	40		20	0.1	312076	21852	910	367730	84	0.86	74	127	2130	1.7	1.78	1.7	0.0274	1.15	0.2753	1.92	0.0274	1.15	####	1757	175	10	247	10	29.1	0.5	175.2	2.9	
Zircon	Orthogneiss	Core	TL57	41		33	0.2	202390	17758	9297	2842243	10.10	0.41	9	192	675	0.2	0.0200	0.2	0.0427	1.99	0.0221	1.42	####	####	384	10	0	0	0	0	0	0	0	0	
Zircon	Orthogneiss	Core	TL57	42		18	0.2	175740	11786	4724	1013307	17475	0.05	32	22	433	0.2	0.0668	0.2	0.0532	1.04	0.0793	1.95	0.0793	1.65	####	832	482	16	492	16	40.8	11.6	486	15.3	
Zircon	Orthogneiss	Core	TL57	43		6	0.1	39528	2206	1445	1010453	7737	0.10	31	70	1335	0.4	0.2200	0.4	0.0427	1.99	0.0221	1.42	####	####	384	10	0	0	0	0	0	0	0	0	
Zircon	Orthogneiss	Core	TL57	44		9	0.1	49105	2744	1965	1257147	9815	0.17	32	70	1335	0.4	0.2200	0.4	0.0427	1.99	0.0221	1.42	####	####	384	10	0	0	0	0	0	0	0	0	
Zircon	Orthogneiss	Core	TL57	45		31	0.4	154850	8107	10872	3509042	13767	####	1762	1702	1762	1.1	29.01	1.1	0.0543	1.35	0.2733	1.96	0.0365	1.35	####	1715	232	12	247	10	10.4	2.2	246.5	10.2	
Zircon	Orthogneiss	Core	TL57	46		35	0.3	193847	10073	2316	587086	27098	0.03	34	19	671	0.2	0.0570	0.2	0.0532	1.04	0.0793	1.95	0.0793	1.65	####	832	482	16	492	16	40.8	11.6	486	15.3	
Zircon	Orthogneiss	Core	TL57	47		20	0.1	312076	21852	910	367730	84	0.86	74	127	2130	1.7	1.78	1.7	0.0274	1.15	0.2753	1.92	0.0274	1.15	####	1757	175	10	247	10	29.1	0.5	175.2	2.9	
Zircon	Orthogneiss	Core	TL57	48		33	0.2	202390	17758	9297	2842243	10.10	0.41	9	192	675	0.2	0.0200	0.2	0.0427	1.99	0.0221	1.42	####	####	384	10	0	0	0	0	0	0	0	0	
Zircon	Orthogneiss	Core	TL57	49		18	0.2	175740	11786	4724	1013307	17475	0.05	32	22	433	0.2	0.0668	0.2	0.0532	1.04	0.0793	1.95	0.0793	1.65	####	832	482	16	492	16	40.8	11.6	486	15.3	
Zircon	Orthogneiss	Core	TL57	50		6	0.1	39528	2206	1445	1010453	7737	0.10	31	70	1335	0.4	0.2200	0.4	0.0427	1.99	0.0221	1.42	####	####	384	10	0	0	0	0	0	0	0	0	
Zircon	Orthogneiss	Core	TL57	51		9	0.1	49105	2744	1965	1257147	9815	0.17	32	70	1335	0.4	0.2200	0.4	0.0427	1.99	0.0221	1.42	####	####	384	10	0	0	0	0	0	0	0	0	
Zircon	Orthogneiss	Core	TL57	52		31	0.4	154850	8107	10872	3509042	13767	####	1762	1702	1762	1.1	29.01	1.1	0.0543	1.35	0.2733	1.96	0.0365	1.35	####	1715	232	12	247	10	10.4	2.2	246.5	10.2	
Zircon	Orthogneiss	Core	TL57	53		35	0.3	193847	10073	2316	587086	27098	0.03	34	19	671	0.2	0.0570	0.2	0.0532	1.04	0.0793	1.95	0.0793	1.65	####	832	482	16	492	16	40.8	11.6	486	15.3	
Zircon	Orthogneiss	Core	TL57	54		20	0.1	312076	21852	910	367730	84	0.86	74	127	2130	1.7	1.78	1.7	0.0274	1.15	0.2753	1.92	0.0274	1.15	####	1757	175	10	247	10	29.1	0.5	175.2	2.9	
Zircon	Orthogneiss	Core	TL57	55		33	0.2	202390	17758	9297	2842243	10.10	0.41	9	192	675	0.2	0.0200	0.2	0.0427	1.99	0.0221	1.42	####	####	384	10	0	0	0	0	0	0	0	0	
Zircon	Orthogneiss	Core	TL57	56		18	0.2	175740	11786	4724	1013307	17475	0.05	32	22	433	0.2	0.0668	0.2	0.0532	1.04	0.0793	1.95	0.0793	1.65	####	832	482	16	492	16	40.8	11.6	486	15.3	
Zircon	Orthogneiss	Core	TL57	57		6	0.1	39528	2206	1445	1010453	7737	0.10	31	70	1335	0.4	0.2200	0.4	0.0427	1.99	0.0221	1.42	####	####	384	10	0	0	0	0	0	0	0	0	
Zircon	Orthogneiss	Core	TL57	58		9	0.1	49105	2744	1965	1257147	9815	0.17	32	70	1335	0.4	0.2200	0.4	0.0427	1.99	0.0221	1.42	####	####	384	10	0	0	0	0	0	0	0	0	
Zircon	Orthogneiss	Core	TL57	59		31	0.4	154850	8107	10872	3509042	13767	####	1762	1702	1762	1.1	29.01	1.1	0.0543	1.35	0.2733	1.96	0.0365	1.35	####	1715	232	12	247	10	10.4	2.2	246.5	10.2	
Zircon	Orthogneiss	Core	TL57	60		35	0.3	193847	10073	2316	587086	27098	0.03	34	19	671	0.2	0.0570	0.2	0.0532	1.04	0.0793	1.95	0.0793	1.65	####	832	482	16	492	16	40.8	11.6	486	15.3	
Zircon	Orthogneiss	Core	TL57	61		20	0.1	312076	21852	910	367730	84	0.86	74	127	2130	1.7	1.78	1.7	0.0274	1.15	0.2753	1.92	0.0274	1.15	####	1757	175	10	247	10	29.1	0.5	175.2	2.9	
Zircon	Orthogneiss	Core	TL57	62		33	0.2	202390	17758	9297	2842243	10.10	0.41	9	192	675	0.2	0.0200	0.2	0.0427	1.99	0.0221	1.42	####	####	384	10	0	0	0	0	0	0	0	0	
Zircon	Orthogneiss	Core	TL57	63		18	0.2	175740	11786	4724	1013307	17475	0.05	32	22	433	0.2	0.0668	0.2	0.0532	1.04	0.0793	1.95	0.0793	1.65	####	832	482	16	492	16	40.8	11.6	486	15.3	
Zircon	Orthogneiss	Core	TL57	64		6	0.1	39528	2206	1445	1010453	7737	0.10	31	70	1335	0.4	0.2200	0.4	0.0427	1.99	0.0221	1.42	####	####	384	10	0	0	0	0	0	0	0	0	
Zircon	Orthogneiss	Core	TL57	65		9	0.1	49105	2744	1965	1257147	9815	0.17	32	70	1335	0.4	0.2200	0.4	0.0427	1.99	0.0221	1.42	####	####	384	10	0	0	0	0	0	0	0	0	
Zircon	Orthogneiss	Core	TL57	66		31	0.4	154850	8107	10872	3509042	13767	####	1762	1702	1762	1.1	29.01	1.1	0.0543	1.35	0.2733	1.96	0.0365	1.35	####	1715	232	12	247	10	10.4	2.2	246.5	10.2	
Zircon	Orthogneiss	Core	TL57	67		35	0.3	193847	10073	2316	587086	27098	0.03	34	19	671	0.2	0.0570	0.2	0.0532	1.04	0.0793	1.95	0.0793	1.65	####	832	482	16	492	16	40.8	11.6	486	15.3	
Zircon	Orthogneiss	Core	TL57	68		20	0.1	312076	21852	910	367730	84	0.86	74	127	2130	1.7	1.78	1.7	0.0274	1.15	0.2753	1.92	0.0274	1.15	####	1757	175	10	247	10	29.1	0.5	175.2	2.9	
Zircon	Orthogneiss	Core	TL57	69		33	0.2	202390	17758	9297	2842243	10.10	0.41	9	192	675	0.2	0.0200	0.2	0.0427	1.99	0.0221	1.42	####	####	384	10	0	0	0	0	0	0	0	0	
Zircon	Orthogneiss	Core	TL57	70		18	0.2	175740	11786	4724	1013307	17475	0.05	32	22	433	0.2	0.0668	0.2	0.0532	1.04	0.0793	1.95	0.0793	1.65	####	832	482	16	492	16	40.8	11.6	486	15.3	
Zircon	Orthogneiss	Core	TL57	71		6	0.1	39528	2206	1445	1010453	7737	0.10	31	70	1335	0.4	0.2200	0.4	0.0427	1.99	0.0221	1.42	####	####	384	10	0	0	0	0	0	0	0	0	
Zircon	Orthogneiss	Core	TL57	72		9	0.1	49105	2744	1965	1257147	9815	0.17	32	70	1335	0.4	0.2200	0.4	0.0427	1.99	0.0221	1.42	####	####	384	10	0	0	0	0	0	0	0	0	
Zircon	Orthogneiss	Core	TL57	73		31	0.4	154850	8107	10872	3509042	13767	####	1762	1702	1762	1.1	29.01	1.1	0.0543	1.35	0.2733	1.96	0.0365	1.35	####	1715	232	12	247	10	10.4	2.2	246.5	10.2	
Zircon	Orthogneiss	Core	TL57	74		35	0.3	193847	10073	2316	587086	27098	0.03	34	19	671	0.2	0.0570	0.2	0.0532	1.04	0.0793	1.95	0.0793	1.65	####	832	482	16	492	16	40.8	11.6	486	15.3	
Zircon	Orthogneiss	Core	TL57	75		20	0.1	312076	21852	910	367730	84	0.86	74	127	2130	1.7	1.78	1.7	0.0274	1.15	0.2753	1.92	0.0274	1.15	####	1757	175	10	247	10	29.1	0.5	175.2	2.9	
Zircon	Orthogneiss	Core	TL57	76		33	0.2	202390	17758	9297	2842243	10.10	0.41	9	192	675	0.2	0.0200	0.2	0.0427	1.99	0.0221	1.42	####	####	384	10	0	0	0	0	0	0	0	0	
Zircon	Orthogneiss	Core	TL57	77		18	0.2	175740	11786	4724	1013307	17475	0.05	32	22	433	0.2	0.0668	0.2	0.0532	1.04	0.0793	1.95	0.0793	1.65	####	832	482	16	492	16	40.8	11.6	486	15.3	
Zircon	Orthogneiss	Core	TL57	78		6	0.1	39528	2206	1445	1010453	7737	0.10	31	70	1335	0.4	0.2200	0.4	0.0427	1.99	0.0221	1.42	####	####	384	10	0	0	0	0	0	0	0	0	
Zircon	Orthogneiss	Core	TL57	79		9	0.1	49105	2744	1965	1257147	9815	0.17	32	70	1335	0.4	0.2200	0.4	0.0427	1.99	0.0221	1.42	####	####	384	10	0	0	0	0	0	0	0	0	
Zircon	Orthogneiss	Core	TL57	80		31	0.4	154850	8107	10872	3509042	13767	####	1762	1702	1762	1.1	29.01	1.1	0.0543	1.35	0.2733	1.96	0.0365	1.35	####	1715	232	12	247	10	10.4	2.2	246.5	10.2	
Zircon	Orthogneiss	Core	TL57	81		35	0.3	193847	10073	2316	587086	27098	0.03	34	19	671	0.2	0.0570	0.2	0.0532	1.04	0.0793	1.95	0.0793	1.65	####	832	482	16	492	16	40.8	11.6	486	15.3	
Zircon	Orthogneiss	Core	TL57	82		20	0.1	312076	21852	910	367730	84	0.86	74	127	2130	1.7	1.78	1.7	0.0274	1.15	0.2753	1.92	0.0274	1.15	####	1757	175	10	247	10	29.1	0.5	175.2	2.9	
Zircon	Orthogneiss	Core	TL57	83		33	0.2	202390	17758	9297	2842243	10.10	0.41	9	192	675	0.2	0.0200	0.2	0.0427	1.99	0.0221	1.42	####	####	384	10	0	0	0	0	0	0	0	0	
Zircon	Orthogneiss	Core	TL57	84		18	0.2	175740	11786	4724	1013307	17475	0.05	32	22	433	0.2	0.0668	0.2	0.0532	1.04	0.0793	1.95	0.0793	1.65	####	832	482	16	492	16	40.8	11.6	486	15.3	
Zircon	Orthogneiss	Core	TL57	85		6	0.1	39528	2206	1445

																Ratios										Ages						Discordance %		Common-Pb corrected ages	
						Cps		Cps	Cps	Cps	Cps	Cps					Data for Tera-Wasserburg plot				Data for Wetherill plot					Age		Age		Age					
Mineral	Rock Type	Location	Sample	Spot number	comment	204Pb	f206c	206Pb	207Pb	208Pb	232Th	235U	Th/U	Pbppm	Thppm	Uppm	238U/206Pb	1s %	207Pb/206Pb	1s %	207Pb/235U	1s %	206Pb/238U	1s %	Rho	207Pb/206Pb	2s abs	206Pb/238U	2s abs	207Pb/235U	2s abs	6-38/7-6	6-38/7-35	Cor.206/238-Pb Age	2s [Ma]
Zircon	Leucogranite	KSZ	TL69	1		-31	-0.4	152712	8020	145	9462	40358	0.00	27	2	1000	33.2808	1.64	0.0522	1.03	0.2161	1.94	0.0300	1.64	0.85	293	47	191	6	199	7	34.9	3.9	190	6.1
Zircon	Leucogranite	KSZ	TL69	2		54	0.2	561912	35368	32720	902666	44176	0.18	106	198	1095	9.8443	1.62	0.0623	0.95	0.8725	1.87	0.1016	1.62	0.86	685	41	624	19	637	18	9.0	2.1	622	19.1
Zircon	Leucogranite	KSZ	TL69	3		-63	-0.9	124136	6587	157	10063	35597	0.00	22	2	882	31.7533	5.90	0.0528	0.99	0.2293	5.99	0.0315	5.90	0.99	322	45	200	23	210	22	37.9	4.7	199	23.0
Zircon	Leucogranite	KSZ	TL69	4		-16	-0.2	150929	8227	6859	286494	25662	0.10	28	63	636	21.5709	2.08	0.0541	1.21	0.3458	2.41	0.0464	2.08	0.86	376	55	292	12	302	13	22.3	3.1	291	11.8
Zircon	Leucogranite	KSZ	TL69	5		-17	-0.4	80773	4573	8396	367138	12036	0.27	16	81	298	18.7604	2.11	0.0559	1.10	0.4106	2.38	0.0533	2.11	0.89	448	49	335	14	349	14	25.3	4.2	334	13.7
Zircon	Leucogranite	KSZ	TL69	6		88	1.8	92143	4906	247	19492	33575	0.01	16	4	832	45.2423	3.90	0.0526	1.03	0.1601	4.03	0.0221	3.90	0.97	310	47	141	11	151	11	54.5	6.5	140	10.8
Zircon	Leucogranite	KSZ	TL69	7		38	0.7	98082	5250	542	32674	26249	0.01	18	7	651	34.3459	1.48	0.0527	1.24	0.2113	1.93	0.0291	1.48	0.77	314	57	185	5	195	7	41.0	4.9	184	5.4
Zircon	Leucogranite	KSZ	TL69	8		33	0.8	60496	6998	13030	119130	1530	0.69	14	26	38	3.2029	1.90	0.1147	1.11	4.9339	2.20	0.3122	1.90	0.86	1875	40	1752	58	1808	36	6.6	3.1	1737	57.0
Zircon	Leucogranite	KSZ	TL69	9		22	0.2	188297	10074	493	18413	41728	0.00	34	4	1034	28.0251	1.55	0.0539	1.14	0.2651	1.92	0.0357	1.55	0.81	367	51	226	7	239	8	38.4	5.3	225	6.8
Zircon	Leucogranite	KSZ	TL69	10		3	0.0	136808	7473	2417	33526	32760	0.01	25	7	812	29.6871	2.36	0.0541	1.05	0.2512	2.58	0.0337	2.36	0.91	376	47	214	10	228	10	43.2	6.2	213	9.8
Zircon	Leucogranite	KSZ	TL69	11		86	1.0	162363	8544	116	12282	50010	0.00	29	3	1239	39.2686	1.57	0.0519	1.21	0.1823	1.99	0.0255	1.57	0.79	283	56	162	5	170	6	42.7	4.7	162	5.0
Zircon	Leucogranite	KSZ	TL69	12		-28	-0.7	73594	5039	26586	592876	4641	1.13	18	130	115	7.9886	1.47	0.0675	1.18	1.1644	1.89	0.1252	1.47	0.78	853	49	760	21	784	20	10.9	3.0	758	20.9
Zircon	Leucogranite	KSZ	TL69	13		11	1.9	10644	545	75	16245	30454	0.00	2	4	755	363.5676	1.81	0.0498	2.41	0.0189	3.02	0.0028	1.81	0.60	186	112	18	1	19	1	90.5	6.8	18	0.6
Zircon	Leucogranite	KSZ	TL69	14		-23	-1.3	31640	2013	1151	24835	30146	0.01	6	5	747	118.7538	3.56	0.0628	1.34	0.0729	3.80	0.0084	3.56	0.94	703	57	54	4	71	5	92.3	24.4	53	3.7
Zircon	Leucogranite	KSZ	TL69	15		41	0.9	88236	4696	4513	280039	38522	0.06	16	61	955	56.2980	2.52	0.0528	1.15	0.1292	2.77	0.0178	2.52	0.91	319	52	114	6	123	6	64.4	8.0	113	5.6
Zircon	Leucogranite	KSZ	TL69	16		67	1.0	117625	6339	17643	978395	18766	0.46	24	215	465	20.7123	1.52	0.0540	1.23	0.3595	1.96	0.0483	1.52	0.78	372	56	304	9	312	10	18.4	2.5	303	9.0
Zircon	Leucogranite	KSZ	TL69	17		107	2.1	91178	4800	6780	405558	41777	0.09	17	89	1035	60.3470	2.00	0.0516	1.09	0.1177	2.28	0.0166	2.00	0.88	266	50	106	4	113	5	60.2	6.3	105	4.2
Zircon	Leucogranite	KSZ	TL69	18		20	0.4	87145	4653	9056	548496	25269	0.19	17	120	626	36.9137	1.91	0.0531	1.02	0.1982	2.16	0.0271	1.91	0.88	333	46	172	6	184	7	48.2	6.2	172	6.4
Zircon	Leucogranite	KSZ	TL69	19		19	0.3	124873	6776	16908	1202376	49178	0.22	25	264	1219	51.1269	2.79	0.0537	1.10	0.1449	3.00	0.0196	2.79	0.93	360	50	125	7	137	8	65.3	9.1	124	6.8
Zircon	Leucogranite	KSZ	TL69	20		-41	-0.7	112094	5946	237	13258	18791	0.01	20	3	466	21.1582	1.74	0.0527	1.23	0.3432	2.13	0.0473	1.74	0.82	315	56	298	10	300	11	5.5	0.6	298	10.1
Zircon	Leucogranite	KSZ	TL69	21		32	0.3	163982	12419	6986	149440	26836	0.05	31	33	665	20.6541	3.53	0.0747	1.07	0.4982	3.69	0.0484	3.53	0.96	1059	43	305	21	410	25	71.2	25.7	296	19.8
Zircon	Leucogranite	KSZ	TL69	22		9	0.1	165977	8689	260	12871	42659	0.00	30	3	1057	32.6898	1.47	0.0517	1.15	0.2179	1.87	0.0306	1.47	0.79	272	53	194	6	200	7	28.5	3.0	194	5.6
Zircon	Leucogranite	KSZ	TL69	23		13	0.1	164590	8683	571	35663	42361	0.01	29	8	1050	32.1670	2.75	0.0531	1.12	0.2274	2.97	0.0311	2.75	0.93	332	51	197	11	208	11	40.6	5.1	197	10.6
Zircon	Leucogranite	KSZ	TL69	24		45	1.7	45013	3450	12516	198815	2173	0.81	10	44	54	6.3174	1.95	0.0759	1.27	1.6563	2.33	0.1583	1.95	0.84	1093	51	947	34	992	29	13.3	4.5	942	33.9
Zircon	Leucogranite	KSZ	TL69	25		33	1.8	32463	1677	165	37668	38107	0.01	6	8	944	154.0906	3.42	0.0522	1.52	0.0467	3.74	0.0065	3.42	0.91	296	70	42	3	46	3	85.9	10.1	41	2.8
Zircon	Leucogranite	KSZ	TL69	26		-40	-1.6	44506	2448	808	70063	57455	0.01	8	15	1424	162.5965	1.67	0.0545	1.40	0.0462	2.18	0.0062	1.67	0.77	390	63	40	1	46	2	89.9	13.8	39	1.3
Zircon	Leucogranite	KSZ	TL69	27		65	1.9	61466	4007	20817	486995	13260	0.33	15	107	329	27.3606	1.94	0.0641	1.24	0.3230	2.30	0.0365	1.94	0.84	746	53	231	9	284	11	69.0	18.6	228	8.5
Zircon	Leucogranite	KSZ	TL69	28		-58	-5.7	17735	1158	609	14688	29732	0.00	3	3	737	213.5286	1.68	0.0632	2.81	0.0408	3.27	0.0047	1.68	0.51	716	119	30	1	41	3	95.8	25.8	29	1.0
Zircon	Leucogranite	KSZ	TL69	29		-11	-0.1	382290	20575	356	21714	69474	0.00	68	5	1722	23.6997	2.16	0.0526	1.07	0.3059	2.41	0.0422	2.16	0.90	312	49	266	11	271	11	14.6	1.7	266	11.2
Zircon	Leucogranite	KSZ	TL69	30		-37	-0.1	500095	82890	25140	198119	9698	0.18	103	43	240	2.7260	1.77	0.1634	0.99	8.2606	2.03	0.3668	1.77	0.87	2491	33	2015	61	2260	36	19.1	10.9	1926	55.7
Zircon	Leucogranite	KSZ	TL69	31		27	0.4	123182	6643	142	7907	20774	0.00	22	2	515	21.7846	1.44	0.0536	1.10	0.3389	1.81	0.0459	1.44	0.79	353	50	289	8	296	9	18.0	2.4	289	8.1
Zircon	Leucogranite	KSZ	TL69	32		50	0.7	126547	7112	5513	100731	20235	0.04	24	22	502	20.0597	3.66	0.0551	1.13	0.3784	3.83	0.0499	3.66	0.96	416	50	314	22	326	21	24.5	3.8	313	22.2
Zircon	Leucogranite	KSZ	TL69	33		15	0.1	306022	20211	58606	1279238	19712	0.57	65	281	489	8.1996	1.43	0.0649	1.11	1.0911	1.81	0.1220	1.43	0.79	772	47	742	20	749	19	3.9	1.0	741	19.9
Zircon	Leucogranite	KSZ	TL69	34		-22	-0.4	108001	5782	1004	25168	17471	0.01	19	6	433	20.7951	1.69	0.0537	1.07	0.3556	2.00	0.0481	1.69	0.84	356	48	303	10	309	11	15.1	2.0	302	9.9
Zircon	Leucogranite	KSZ	TL69	35		28	0.7	77404	4135	109	8357	19465	0.00	14	2	482	31.8916	1.81	0.0524	1.37	0.2266	2.27	0.0314	1.81	0.80	305	62	199	7	207	8	34.7	4.0	198	7.1
Zircon	Leucogranite	KSZ	TL69	36		-27	-0.6	78203	4170	155	8433	20102	0.00	14	2	498	32.7194	1.93	0.0527	1.33	0.2219	2.34	0.0306	1.93	0.82	315	61	194	7	203	9	38.4	4.6	193	7.3
Zircon	Leucogranite	KSZ	TL69	37		24	0.2	218912	14560	45050	1015148	14018	0.64	47	223	347	8.1804	1.55	0.0661	1.06	1.1132	1.88	0.1222	1.55	0.82	809	44	743	22	760	20	8.1	2.1	742	21.6
Zircon	Leucogranite	KSZ	TL69	38		80	1.9	78064	4221	371	24183	44274	0.00	14	5	1097	81.9832	8.17	0.0544	1.20	0.0914	8.26	0.0122	8.17	0.99	386	54	78	13	89	14	79.8	12.0	77	12.5
Zircon	Leucogranite	KSZ	TL69	39		-28	-0.5	94269	5010	120	15164	33538	0.00	17	3	831	44.6836	1.64	0.0521	1.07	0.1608	1.96	0.0224	1.64	0.84	291	49	143	5	151	6	51.0	5.7	142	4.6
Zircon	Leucogranite	KSZ	TL69	40		-22	-0.2	174566	17932	4805	57351	33771	0.02	33	13	837	25.1515	3.95	0.0990	2.01	0.5423	4.43	0.0398	3.95	0.89	1605	75	251	19	440	31	84.3	42.9	237	17.2
Zircon	Leucogranite	KSZ	TL69	41		52	0.0	1513596	308234	158959	1027696	24865	0.37	335	225	616	2.0820	1.43	0.1985	1.06	13.1406	1.78	0.4803	1.43	0.80	2814	35	2529	60	2690	33	10.1	6.0	2437	55.3
Zircon	Leucogranite	KSZ	TL69	42		72	4.8	26654	1595	580	17670	26929	0.01	5	4	667	129.3125	1.61	0.0591	1.35	0.0630	2.10	0.0077	1.61	0.77	571	59	50	2	62	3	91.3	19.9	49	1.5
Zircon	Leucogranite	KSZ	TL69	43		-16	-0.3	90610	4996	7384	306427	21175	0.13	17	67	525	29.5414	1.51	0.0545	1.29	0.2540	1.99	0.0339	1.51	0.76	390	58	215	6	230	8	45.0	6.6	214	6.3
Zircon	Leucogranite	KSZ	TL69	44		8	0.1	170409	10563	13320	284705	26001	0.10	33	62	644	19.7304	1.46	0.0620	1.11	0.4330	1.83	0.0507	1.46	0.80	674	47	319	9	365	11	52.7	12.8	315	8.8
Zircon	Leucogranite	KSZ	TL69	45		-1	0.0	176727	9222	205	18399	58190	0.00	31	4	1442	38.3029	6.58	0.0519	1.06	0.1866	6.66	0.0261	6.58	0.99	279	49	166	22	174	21	40.5	4.4	166	21.4
Zircon	Leucogranite	KSZ	TL69	46		15	0.1	266046	14276	2421	88535	46352	0.02	48	19	1149	22.5896	1.55	0.0531	1.11	0.3240	1.91	0.0443	1.55	0.81	333	50	279	8	285	9	16.3	2.0	279	8.4
Zircon	Leucogranite	KSZ	TL69	47		94	0.6	276452	15505	2123	31501	49940	0.01	50	7	1238	23.2603	1.58	0.0553	1.18	0.3279	1.97	0.0430	1.58	0.80	426	52	271	8	288	10	36.3	5.8	270	8.3
Zircon	Leucogranite	KSZ	TL69	48		23	0.5	76773	4477	6480	154543	11577	0.12	15	34	287	19.1817	2.58	0.0575	1.05	0.4130	2.79	0.0521	2.58	0.93	510	46	328	16	351	16	35.8	6.7	326	16.3
Zircon	Leucogranite	KSZ	TL69	49		15	0.1	290518	16002	6166	446118	149111	0.03	53	98	3696	67.0420	2.01	0.0546	1.09	0.1122	2.28	0.0149	2.01	0.88	396	49	95	4	108	5	75.9	11.6	95	3.7
Zircon	Leucogranite	KSZ	TL69	50		57	0.1	710000	37809	49654	2684062	135088	0.18	135	589	3348	24.3571	1.43	0.0528	1.02	0.2990	1.76	0.0411	1.43	0.81	322	46	259	7	266	8	19.4	2.3	259	7.2
Zircon	Leucogranite	KSZ	TL69	51		51	0.1	650487	121888	53294	485953	23252	0.19	139	107	576	4.6336	1.99	0.1848	1.46	5.4972	2.47	0.2158	1.99	0.81	2697	48	1260	45	1900	42	53.3	33.7	1111	35.6
Zircon	Leucogranite	KSZ	TL69	52		9	0.1	143776	7823	404	27435	32306	0.01	26	6	801	28.6409	3.08	0.0536	1.05	0.2582	3.25	0.0349	3.08	0.95	356	47	221	13	233	13	37.9	5.1	220	13.3
Zircon	Leucogranite	KSZ	TL69	53		17	0.5	69389	3648	101	12141	25017	0.00	12	3	620	46.8711	2.26	0.0527	1.25	0.1550	2.58	0.0213	2.26	0.87	317	57	136	6	146	7	57.0	7.0	135	6.0
Zircon	Leucogranite	KSZ	TL69	54		23	0.4	94176	5109	4897	289755	18904	0.14	18	64	469	26.1148	1.62	0.0534	1.17	0.2818	2.00	0.0383	1.62	0.81	346	53	242	8	252	9	30.0	3.9	242	7.6
Zircon	Leucogranite	KSZ	TL69	55		59	1.5	69451	4878	14261	140424	12883	0.10	15	31	319	22.5064	2.94	0.0704	1.43	0.4313	3.27	0.0444	2.94	0.90	941	59	280	16	364	20	70.2	23.0	274	15.4
Zircon	Leucogranite	KSZ	TL69	56		-29	-0.1	385466	58786	14791	120991	15275	0.07	78	27	379	5.0838	1.63	0.1523	0.96	4.1290	1.89	0.1967	1.63	0.86	2372	33	1158	34	1660	30	51.2	30.3	1059	28.8
Zircon	Leucogranite	KSZ	TL69	57		55	0.7	135094	7470	4233	129022	20895	0.05	25	28	518	19.6388	1.84	0.0554	0.98	0.3884	2.09	0.0509	1.84	0.88	427	44	320	12	333	12	24.9	3.9	319	11.4
Zircon	Leucogranite	KSZ	TL69	58		-47	-0.6	143722	9261	513	16806	17192	0.01	26	4	426	15.2319	3.44	0.0631	2.25	0.5708	4.11	0.0657	3.44	0.84	711	96	410	27	459	30	42.3	10.6	406	26.7
Zircon	Leucogranite	KSZ	TL69	59		-64	-0.2	532190	80489	50473	420017	20113	0.18	112	92	498	4.7261	2.71	0.1485	1.06	4.3308	2.91	0.2116	2.71	0.93	2329	36	1237	61	1699	47	46.9	27.2	1143	51.8
Zircon	Leucogranite	KSZ	TL69	60		20	0.7	49352	2926	32349	770494	29358	0.23	14	169	728	74.9620	2.10	0.0584	1.25	0.1074	2.45	0.0133	2.10	0.86	545	55	85	4	104	5	84.3	17.5	84	3.5
Zircon	Leucogranite	KSZ	TL69	61		46	0.6	144889	7460	18400	1320100	95037	0.12	29	290	2355	83.0888	2.31	0.0505	1.22	0.0837	2.61	0.0120	2.31	0.88	217	56	77	4	82	4	64.4	5.5	77	3.5
Zircon	Leucogranite	KSZ	TL69	62		-46	-3.1	27011	1372	396	26180	16030	0.01	5	6	397	76.1995	3.29	0.0516	1.71	0.0934	3.71	0.0131	3.29	0.89	268	78	84	5	91	6	68.7	7.3	84	5.4
Zircon	Leucogranite	KSZ	TL69	63		42	0.2	383609	20234	13882	724710	68836	0.09	71	159	1706	23.3516	1.58	0.0525	1.16	0.3099	1.96	0.0428	1.58	0.81	307	53	270	8	274	9	12.1	1.4	270	8.3

Table 5.6: Zircon U-Pb SC-ICP-MS geochroological results for leucogranites part 2

Table 5.7: Zircon U-Pb SC-ICP-MS geochronological results for leucogranites part 3

															Data for Tera-Wasserburg plot			Ratios			Ages								
Mineral	Rock Type	Location	Sample	Spot number	comment	Cps 204Pb	Cps 206Pb	Cps 207Pb	Cps 208Pb	Cps 232Th	Cps 235U	Th/U	Pb$_{pm}$/Th	Th$_{pm}$/U	^{238}U/^{206}Pb	1s %	^{207}Pb/^{206}Pb	1s %	Data for Wetherill plot ^{207}Pb/^{235}U	1s %	Rho	Age ^{207}Pb/^{206}Pb	2s abs	Age ^{206}Pb/^{238}U	2s abs	Age ^{207}Pb/^{235}U	2s abs	Discordance %	Common-Pb corrected ages
Zircon	Leucogranite	CHSZ	TLN8	44		12	0.6	39131	2072	6305	2970?2	6258	5435	0.4	7	59	122	19.2792	1.35	0.0526	1.46	0.3761	1.99	0.0519	1.35	0.68	312	33	3226	9	328	8	324	11	-4.4	-0.6	326
Zircon	Leucogranite	CHSZ	TLN8	43		109	5.9	33847	1804	4947	2282?5	5435	0.4	7	6	46	106	19.1449	1.18	0.0524	1.30	0.3772	1.76	0.0522	1.18	0.67	3003	30	3328	8	325	10	-8.5	-1.0	328
Zircon	Leucogranite	CHSZ	TLN8	42		27	2.2	21858	1186	3165	1487?5	3661	0.4	4	4	30	71	20.0777	1.32	0.0534	1.76	0.3668	2.20	0.0498	1.32	0.60	3147	40	3313	8	317	12	9.8	1.2	313
Zircon	Leucogranite	CHSZ	TLN8	41		6	0.3	39447	2087	7568	3526?1	6597	0.5	7	7	71	128	19.8574	1.24	0.0532	1.51	0.3692	1.80	0.0504	1.24	0.69	3317	30	3317	8	319	10	6.0	0.7	317
Zircon	Leucogranite	CHSZ	TLN8	40		94	1.6	21858	1186	3165	1487?5	3661	0.4	4	2	30	71	20.0777	1.32	0.0534	1.76	0.3668	2.20	0.0498	1.32	0.60	3147	40	3313	8	317	12	9.8	1.2	313
Zircon	Leucogranite	CHSZ	TLN8	39		27	2.2	21858	1186	3165	1487?5	3661	0.4	4	7	30	71	20.0777	1.32	0.0534	1.76	0.3668	2.20	0.0498	1.32	0.60	3147	40	3313	8	317	12	9.8	1.2	313
Zircon	Leucogranite	CHSZ	TLN8	38		5	0.2	23349	1111	1980?3	1990?7	1	0.4	1	47	387	1486	19.9137	1.40	0.0600	1.58	0.5109	1.71	0.0581	1.40	0.82	5413	40	3636	9	463	13	357.1	35.7	463
Zircon	Leucogranite	CHSZ	TLN8	37		-30	-0.2	23349	1111	1980?3	1990?7	1	0.4	1	47	398	1486	19.9137	1.40	0.0600	1.58	0.5109	1.71	0.0581	1.40	0.82	5413	40	3636	9	463	13	357.1	35.7	463
Zircon	Leucogranite	CHSZ	TLN8	36		80	4.8	30197	1735	5469	2443?7	5600	0.4	5	4	49	109	21.9303	1.69	0.0561	1.82	0.3526	2.48	0.0456	1.69	0.68	4566	40	3636	9	456	15	287.1	30.7	456
Zircon	Leucogranite	CHSZ	TLN8	35		130	9.8	24315	1218	115	2407?7	76366	0.0	4	4	66	301	378.0290	1.25	0.0496	1.66	0.0181	2.07	0.0926	1.25	0.60	177	39	3112	7	90.4	2.2	18	1	90.4	0.4	90.4
Zircon	Leucogranite	CHSZ	TLN8	34		-20	-0.8	48017	2684	6672	3286?9	15468	0.2	8	8	6	33	37.3000	1.13	0.0547	1.17	0.2020	1.63	0.0268	1.13	0.69	3999	26	3171	4	327	8	57.2	0.7	57.2
Zircon	Leucogranite	CHSZ	TLN8	33		48	0.2	450752	25834	72221	1628960	35233	0.5	78	78	326	685	9.1642	1.21	0.0623	0.99	0.9382	1.56	0.1091	1.21	0.77	6683	21	6624	15	671	15	2.2	0.5	667
Zircon	Leucogranite	CHSZ	TLN8	32		44	0.2	330252	20030	32770	852511	51180	0.2	37	54	171	996	15.9220	2.97	0.0625	0.88	0.4550	3.10	0.0328	2.97	0.96	6911	19	3324	19	332	19	30.4	0.7	328
Zircon	Leucogranite	CHSZ	TLN8	31		35	0.3	225605	13715	21539	510854	26265	0.2	37	102	511	1410	14.3439	1.10	0.0606	1.02	0.5821	1.50	0.0697	1.10	0.73	4334	22	3204	9	434	9	30.4	0.7	432
Zircon	Leucogranite	CHSZ	TLN8	30		36	1.4	149317	7815	16274	782457	25590	0.3	24	156	498	1176	9.2290	1.23	0.0638	1.13	0.5828	1.67	0.1084	1.23	0.74	7335	24	3255	9	663	16	680	15	9.8	2.4	662
Zircon	Leucogranite	CHSZ	TLN8	29		109	1.4	114917	7815	16274	782457	25590	0.3	24	156	498	1176	9.2290	1.23	0.0638	1.13	0.5828	1.67	0.1084	1.23	0.74	7335	24	3255	9	663	16	680	15	9.8	2.4	662
Zircon	Leucogranite	CHSZ	TLN8	28		36	125.2	410	72	46	985	1222	0.0	0	0	24	344.5734	3.91	0.0629	9.51	0.0233	14.02	0.0320	13.81	0.99	3398	108	3255	55	3011	54	219	5	49.1	7.4	201.6
Zircon	Leucogranite	CHSZ	TLN8	27		67	272	4305	287	961	34548	1529	0.2	1	0	30	42.3059	2.52	0.0675	3.29	0.2198	4.15	0.0226	2.52	0.61	8852	68	3255	16	3231	15	69	5	91.6	22.3	53
Zircon	Leucogranite	CHSZ	TLN8	26		-81	-0.4	37004	2245	4815	187927	3313	0.0	0	56	28	645	10.4827	1.13	0.0599	1.23	0.7870	1.67	0.0954	1.13	0.68	5999	27	3255	16	587	13	589	15	1.9	0.4	587
Zircon	Leucogranite	CHSZ	TLN8	25		-15	-0.1	88802	5272	4260	335022	69715	0.1	12	72	1356	119.4486	3.57	0.0611	1.72	0.0705	3.96	0.0884	3.57	0.90	6942	37	3834	54	3317	54	5	4	91.6	22.3	53
Zircon	Leucogranite	CHSZ	TLN8	24		54	1.0	98502	5272	4260	335022	69715	0.1	12	72	1356	119.4486	3.57	0.0611	1.72	0.3067	3.96	0.0884	3.57	0.90	6942	37	3834	54	3317	54	5	4	91.6	22.3	53
Zircon	Leucogranite	CHSZ	TLN8	23		0	0.0	22092	1070	37	22089	82229	0.0	3	4	1600	439.9114	1.22	0.0484	1.69	0.0152	2.08	0.0823	1.22	0.58	1119	24	3255	16	1015	15	15	1	87.7	4.2	15
Zircon	Leucogranite	CHSZ	TLN8	22		43	0.4	179411	11582	18854	293351	13099	0.2	29	59	272	0.1894	1.23	0.0638	1.13	0.5828	1.67	0.1084	1.23	0.74	7335	24	3255	16	663	16	680	15	9.8	2.4	662
Zircon	Leucogranite	CHSZ	TLN8	21		-13	-0.1	37600	2456	4443	187927	3313	0.0	0	56	28	645	10.4827	1.13	0.0599	1.23	0.7870	1.67	0.0954	1.13	0.68	5999	27	3255	16	587	13	589	15	1.9	0.4	587
Zircon	Leucogranite	CHSZ	TLN8	20		54	1.0	98502	5272	4260	335022	69715	0.1	12	72	1356	119.4486	3.57	0.0611	1.72	0.3067	3.96	0.0884	3.57	0.90	6942	37	3834	54	3317	54	5	4	91.6	22.3	53
Zircon	Leucogranite	CHSZ	TLN8	19		0	0.0	22092	1070	37	22089	82229	0.0	3	4	1600	439.9114	1.22	0.0484	1.69	0.0152	2.08	0.0823	1.22	0.58	1119	24	3255	16	1015	15	15	1	87.7	4.2	15
Zircon	Leucogranite	CHSZ	TLN8	18		122	3.0	72061	4260	7773	335022	69715	0.1	12	72	1356	119.4486	3.57	0.0611	1.72	0.3067	3.96	0.0884	3.57	0.90	6942	37	3834	54	3317	54	5	4	91.6	22.3	53
Zircon	Leucogranite	CHSZ	TLN8	17		78	3.7	37600	2178	1910	67955	23048	19.3	444	1176	22731	31.30	13.8	0.0547	2.40	0.2407	14.02	0.0320	13.81	0.99	3398	108	3255	55	3011	54	219	5	49.1	7.4	201.6
Zircon	Leucogranite	CHSZ	TLN8	16		55	0.8	128203	6994	1321	66604	21330	20.5	1453	22270	1089	20.42	1.4	0.0532	1.26	0.3588	1.92	0.0490	1.44	0.75	3346	57	3308	9	311	10	8.3	1.0	307.9
Zircon	Leucogranite	CHSZ	TLN8	15		19	0.2	169285	9114	15383	921753	28402	210.6	2062	4556	3265?2	20.83	1.4	0.0527	1.28	0.3490	1.87	0.0489	1.57	0.73	3118	58	3022	8	304	10	4.8	0.5	302.2
Zircon	Leucogranite	CHSZ	TLN8	14		54	0.3	389940	20959	17256	976267	65496	97.7	4556	3265?2	3354?2	19.83	1.7	0.0530	1.13	0.3681	2.04	0.0504	1.70	0.83	3328	51	3317	11	318	11	3.2	0.4	317.0
Zircon	Leucogranite	CHSZ	TLN8	13		68	0.7	176454	10136	15862	917270	36910	169.1	2155	3065?8	1575	20.75	1.5	0.0526	1.12	0.3760	2.15	0.0519	1.69	0.80	3274	40	3255	16	326	12	4.5	0.5	315.9
Zircon	Leucogranite	CHSZ	TLN8	12		-54	0.2	76957	5158	7111	511501	51915	0.0	14	16	1576	38.21	1.7	0.0492	1.41	0.1774	2.51	0.0261	1.70	0.68	1710	29	3255	16	1015	15	15	1	87.7	4.2	15
Zircon	Leucogranite	CHSZ	TLN8	11		14	0.3	38598	2284	1519	102181	13099	0.0	4	6	99	1571	20.83	1.4	0.0527	1.28	0.3490	1.87	0.0489	1.57	0.73	3118	58	3022	8	304	10	4.8	0.5	302.2
Zircon	Leucogranite	CHSZ	TLN8	10		68	0.7	176454	10136	15862	917270	36910	169.1	2155	3065?8	1575	20.75	1.5	0.0526	1.12	0.3760	2.15	0.0519	1.69	0.80	3274	40	3255	16	326	12	4.5	0.5	315.9
Zircon	Leucogranite	CHSZ	TLN8	9		-40	-1.4	53371	2889	4061	225185	8571	172.2	642	788	75325	437	19.90	1.5	0.0530	1.51	0.3674	2.09	0.0503	1.45	0.69	331	68	3255	16	316	12	4.5	0.5	315.9
Zircon	Leucogranite	CHSZ	TLN8	8		-67	-1.4	85459	4598	2888	257693	8726?3	3065?4	788	1154?2	586	21.94	1.6	0.0526	1.51	0.3508	2.19	0.0456	1.39	0.73	314	69	3255	16	287	9	290	8	287.2	15	287.2
Zircon	Leucogranite	CHSZ	TLN8	7		-41	-5.5	13730	662	29	18937	2.6	153	1167	17326	2396	410.36	1.7	0.0475	2.44	0.0160	3.00	0.0424	1.74	0.58	77	116	3255	16	16	1	79.6	2.5	15.7
Zircon	Leucogranite	CHSZ	TLN8	6		18	0.7	46807	2504	5749	21131?7	8224	169.9	565	712?8	420	20.75	1.8	0.0523	1.48	0.3475	2.31	0.0482	1.78	0.77	900	67	3255	16	3003	12	79.6	2.5	303.4
Zircon	Leucogranite	CHSZ	TLN8	5		-54	0.3	90044	5083	5010	51784?3	17396	192.9	1167	1732?9	598	38.21	12.1	0.0092	6.33	0.2133	13.66	0.0261	12.11	0.89	5714	166	3255	16	1066	196	71.0	15.3	164.1
Zircon	Leucogranite	CHSZ	TLN8	4		64	0.7	176454	10136	15862	917270	36910	169.1	2155	3065?8	1575	20.75	1.5	0.0526	1.12	0.3760	2.15	0.0519	1.69	0.80	3274	40	3255	16	326	12	4.5	0.5	315.9
Zircon	Leucogranite	CHSZ	TLN8	3		54	0.3	389940	20959	17256	976267	65496	97.7	4556	3265?2	3354?2	19.83	1.7	0.0530	1.13	0.3681	2.04	0.0504	1.70	0.83	3328	51	3317	11	318	11	3.2	0.4	317.0
Zircon	Leucogranite	CHSZ	TLN8	2		261	4.4	101968	9591	8924	1308776	54207?	0.0	17	282	1054?6	9.08	1.5	0.0659	2.06	0.0184	3.85	0.0920	3.26	0.85	804	43	570	13	570	19	98.4	29.6	13
Zircon	Leucogranite	NPDS	TLT2	1		19	0.2	184825	13175	10777	212307	1024?6	136.2	2221	5234?0	523	6.33	2.2	0.0704	1.26	0.1580	2.56	0.1330	2.23	0.87	941	52	946	39	944	31	946.1	-0.6	939.1
Zircon	Leucogranite	NPDS	TLT2	3		11	0.1	126038	8429	9608	113673	10358?	71.4	1492	3892?4	5240	9.08	1.5	0.0593	1.15	0.1333	3.56	0.1630	3.56	0.95	796	79	634	9	670	19	670	5	670.4	0.0	669.6
Zircon	Leucogranite	NPDS	TLT2	4		56	1.1	337557	20132	9611	1021477	10238?	2.7	377	1399?8	3225?	0.0	1.5	0.0517	1.67	0.0177	1.67	0.0249	0.0	0.00	276	0	159	2	159	5	159.1	0.0	159.1
Zircon	Leucogranite	NPDS	TLT2	5		2955	7.5	53661	6191	9822	54078?	1889?	0.0	10	3677	3676	413.4426	1.63	0.0403	4.62	0.0241	4.62	0.0403	1.63	0.33	1960	83	159	1	46	1	46	1	46.0	0.1	46.0
Zircon	Leucogranite	NPDS	TLT2	6		42	1.6	46898	2922	471	49427	6258?	5.2	535	1654?	3194	156.70	3.2	0.0614	1.69	0.0450	3.64	0.0604	3.22	0.89	652	72	41	3	53	4	53.2	2.5	43.6
Zircon	Leucogranite	NPDS	TLT2	7		372	0.4	1162266	216244	127102	1887156	23183	0.8	213	377	451	2.4110	1.29	0.1877	1.02	10.7311	1.64	0.4148	1.29	0.79	2722	17	2237	49	2500	30	17.8	10.5	43.6
Zircon	Leucogranite	NPDS	TLT2	8		50	0.1	704589	130827	153229	851741	10911?	0.8	140	170	212	1.8237	1.25	0.0547	0.99	13.8057	1.60	0.5483	1.25	0.78	2677	16	2818	57	2736	30	-5.3	-3.0	2873
Zircon	Leucogranite	NPDS	TLT2	9		-67	-1.4	85459	4598	2888	257693	8726?3	3065?4	788	1154?2	586	21.94	1.6	0.0526	1.51	0.3508	2.19	0.0456	1.39	0.73	314	69	3255	16	287	9	290	8	287.2	15	287.2
Zircon	Leucogranite	NPDS	TLT2	10		-40	-1.4	53371	2889	4061	225185	8571	172.2	642	788	75325	437	19.90	1.5	0.0530	1.51	0.3674	2.09	0.0503	1.45	0.69	331	68	3255	16	316	12	4.5	0.5	315.9
Zircon	Leucogranite	NPDS	TLT2	11		-27	0.8	62706	3346	7073	463145	11482	264.4	788	1549?2	586	21.94	1.6	0.0526	1.51	0.3508	2.19	0.0456	1.39	0.73	314	69	3255	16	287	9	290	8	287.2	15	287.2
Zircon	Leucogranite	NPDS	TLT2	12		-12	-0.2	64941	3624	7727	484107	11037?	69.1	969	1606?8	716	22.48	1.5	0.0519	1.51	0.3393	1.98	0.0474	1.51	0.76	3118	78	3255	16	3255	16	3255	16	3255.0	0.0	3255.0
Zircon	Leucogranite	CHSZ	TLN8	1		-10	-0.7	28837	1235	632	67389	6294?	7.0	306	2254?	3212	315.61	10.8	0.0471	2.60	0.0294	10.98	0.0441	10.80	0.98	95	26	2818	57	26	6	51.1	1.1	26.2
Zircon	Leucogranite	CHSZ	TLN8	2		34	3.3	18749	1047	214	169985	33966	3.3	219	5683	1733	136.94	19.0	0.0470	2.38	0.0343	19.11	0.0479	18.96	0.99	1941	111	51	54	54	54	20	73.9	5.7	18.9
Zircon	Leucogranite	CHSZ	TLN8	3		-23	-0.9	47971	2843	7826	241940	5875	269.9	6924	8092?	300	15.18	7.1	0.0580	1.77	0.5271	7.36	0.0659	7.14	0.97	5312	78	411	57	430	50	22.6	4.3	409.8
Zircon	Leucogranite	CHSZ	TLN8	4		-19	-0.7	28837	1235	632	67389	6294?	7.0	306	2254?	3212	315.61	10.8	0.0471	2.60	0.0294	10.98	0.0441	10.80	0.98	95	26	2818	57	26	6	51.1	1.1	26.2
Zircon	Leucogranite	CHSZ	TLN8	5		34	3.3	18749	1047	214	169985	33966	3.3	219	5683	1733	136.94	19.0	0.0470	2.38	0.0343	19.11	0.0479	18.96	0.99	1941	111	51	54	54	54	20	73.9	5.7	18.9
Zircon	Leucogranite	CHSZ	TLN8	6		372	0.4	1162266	216244	127102	1887156	23183	0.8	213	377	451	2.4110	1.29	0.1877	1.02	10.7311	1.64	0.4148	1.29	0.79	2722	17	2237	49	2500	30	17.8	10.5	43.6
Zircon	Leucogranite	CHSZ	TLN8	7		42	1.6	46898	2922	471	49427	6258?	5.2	535	1654?	3194	156.70	3.2	0.0614	1.69	0.0450	3.64	0.0604	3.22	0.89	652	72	41	3	53	4	53.2	2.5	43.6
Zircon	Leucogranite	CHSZ	TLN8	8		2955	7.5	53661	6191	9822	54078?	1889?	0.0	10	3677	3676	413.4426	1.63	0.0403	4.62	0.0241	4.62	0.0403	1.63	0.33	1960	83	159	1	46	1	46	1	46.0	0.1	46.0
Zircon	Leucogranite	CHSZ	TLN8	9		-67	-1.4	85459	4598	2888	257693	8726?3	3065?4	788	1154?2	586	21.94	1.6	0.0526	1.51	0.3508	2.19	0.0456	1.39	0.73	314	69	3255	16	287	9	290	8	287.2	15	287.2
Zircon	Leucogranite	CHSZ	TLN8	10		-81	-0.4	37004	2245	4815	187927	3313	0.0	0	56	28	645	10.4827	1.13	0.0599	1.23	0.7870	1.67	0.0954	1.13	0.68	5999	27	3255	16	587	13	589	15	1.9	0.4	587
Zircon	Leucogranite	CHSZ	TLN8	11		14	0.3	38598	2284	1519	102181	13099	0.0	4	6	99	1571	20.83	1.4	0.0527	1.28	0.3490	1.87	0.0489	1.57	0.73	3118	58	3022	8	304	10	4.8	0.5	302.2
Zircon	Leucogranite	CHSZ	TLN8	12		-54	0.2	76957	5158	7111	511501	51915	0.0	14	16	1576	38.21	1.7	0.0492	1.41	0.1774	2.51	0.0261	1.70	0.68	1710	29	3255	16	1015	15	15	1	87.7	4.2	15
Zircon	Leucogranite	CHSZ	TLN8	13		68	0.7	176454	10136	15862	917270	36910	169.1	2155	3065?8	1575	20.75	1.5	0.0526	1.12	0.3760	2.15	0.0519	1.69	0.80	3274	40	3255	16	326	12	4.5	0.5	315.9
Zircon	Leucogranite	CHSZ	TLN8	14		54	0.3	389940	20959	17256	976267	65496	97.7	4556	3265?2	3354?2	19.83	1.7	0.0530	1.13	0.3681	2.04	0.0504	1.70	0.83	3328	51	3317	11	318	11	3.2	0.4	317.0
Zircon	Leucogranite	CHSZ	TLN8	15		19	0.2	169285	9114	15383	921753	28402	210.6	2062	4556	3265?2	20.83	1.4	0.0527	1.28	0.3490	1.87	0.0489	1.57	0.73	3118	58	3022	8	304	10	4.8	0.5	302.2
Zircon	Leucogranite	CHSZ	TLN8	16		55	0.8	128203	6994	1321	66604	21330	20.5	1453	22270	1089	20.42	1.4	0.0532	1.26	0.3588	1.92	0.0490	1.44	0.75	3346	57	3308	9	311	10	8.3	1.0	307.9
Zircon	Leucogranite	CHSZ	TLN8	17		78	3.7	37600	2178	1910	67955	23048	19.3	444	1176	22731	31.30	13.8	0.0547	2.40	0.2407	14.02	0.0320	13.81	0.99	3398	108	3255	55	3011	54	219	5	49.1	7.4	201.6
Zircon	Leucogranite	CHSZ	TLN8	18		122	3.0	72061	4260	7773	335022	69715	0.1	12	72	1356	119.4486	3.57	0.0611	1.72	0.3067	3.96	0.0884	3.57	0.90	6942	37	3834	54	3317	54	5	4	91.6	22.3	53
Zircon	Leucogranite	CHSZ	TLN8	19		-81	-0.4	37004	2245	4815	187927	3313	0.0	0	56	28	645	10.4827	1.13	0.0599	1.23	0.7870	1.67	0.0954	1.13	0.68	5999	27	3255	16	587	13	589	15	1.9	0.4	587
Zircon	Leucogranite	CHSZ	TLN8	20		54	1.0	98502	5272	4260	335022	69715	0.1	12	72	1356	119.4486	3.57	0.0611	1.72	0.3067	3.96	0.0884	3.57	0.90	6942	37	3834	54	3317	54	5	4	91.6	22.3	53
Zircon	Leucogranite	CHSZ	TLN8	21		-15	-0.1	37600	2456	4443	187927	3313	0.0	0	56	28	645	10.4827	1.13	0.0599	1.23	0.7870	1.67	0.0954	1.13	0.68	5999	27	3255	16	587	13	589	15	1.9	0.4	587
Zircon	Leucogranite	CHSZ	TLN8	22		43	0.4	179411	11582	18854	293351	13099	0.2	29	59	272	0.1894	1.23	0.0638	1.13	0.5828	1.67	0.1084	1.23	0.74	7335	24	3255	16	663	16	680	15	9.8	2.4	662
Zircon	Leucogranite	CHSZ	TLN8	23		0	0.0	22092	1070	37	22089	82229	0.0	3	4	1600	439.9114	1.22	0.0484	1.69	0.0152	2.08	0.0823	1.22	0.58	1119	24	3255	16	1015	15	15	1	87.7	4.2	15
Zircon	Leucogranite	CHSZ	TLN8	24		109	1.4	114917	7815	16274	782457	25590	0.3	24	156	498	1176	9.2290	1.23	0.0638	1.13	0.5828	1.67	0.1084	1.23	0.74	7335	24	3255	16	663	16	680	15	9.8	2.4	662
Zircon	Leucogranite	CHSZ	TLN8	25		36	125.2	410	72	46	985	1222	0.0	0	0	24	344.5734	3.91	0.0629	9.51	0.0233	14.02	0.0320	13.81	0.99	3398	108	3255	55	3011	54	219	5	49.1	7.4	201.6
Zircon	Leucogranite	CHSZ	TLN8	26		67	272	4305	287	961	34548	1529	0.2	1	0	30	42.3059	2.52	0.0675	3.29	0.2198	4.15	0.0226	2.52	0.61	8852	68	3255	16	3231	15	69	5	91.6	22.3	53
Zircon	Leucogranite	CHSZ	TLN8	27		27	2.2	21858	1186	3165	1487?5	3661	0.4	4	4	30	71	20.0777	1.32	0.0534	1.76	0.3668	2.20	0.0

															Ratios									Ages						Discordance %		Common-Pb corrected ages	
						Cps		Cps	Cps	Cps	Cps	Cps					Data for Tera-Wasserberg plot				Data for Wetherill plot					Age		Age		Age					
Mineral	Rock Type	Location	Sample	Spot number	comment	204Pb	f206c	206Pb	207Pb	208Pb	232Th	235U	Th/U	Pbppm	Thppm	Uppm	238U/206Pb	1s %	207Pb/206Pb	1s %	207Pb/235U	1s %	206Pb/238U	1s %	Rho	207Pb/206Pb	2s abs	206Pb/238U	2s abs	207Pb/235U	2s abs	6-38/7-6	6-38/7-35	Cor.206/238-Pb Age	2s [Ma]
Zircon	Leucogranite	CHSZ	TLN10	1		19	0.5	65923	3173	201	116693	207689	0.00	12	26	5147	404.7846	1.70	0.0472	1.59	0.0161	2.33	0.0025	1.70	0.73	57	76	16	1	16	1	72.1	1.6	16	0.5
Zircon	Leucogranite	CHSZ	TLN10	2		110	3.3	61065	2927	181	153047	195633	0.01	11	34	4849	413.4505	1.44	0.0475	1.15	0.0158	1.84	0.0024	1.44	0.78	74	55	16	0	16	1	79.0	2.4	16	0.4
Zircon	Leucogranite	CHSZ	TLN10	3		56	1.8	59060	2897	267	175236	192519	0.01	11	38	4771	413.7720	1.56	0.0487	1.60	0.0162	2.24	0.0024	1.56	0.70	134	75	16	0	16	1	88.4	4.8	16	0.5
Zircon	Leucogranite	CHSZ	TLN10	4		24	2.3	18988	1142	5669	507727	40367	0.11	4	111	1000	260.3713	3.85	0.0577	2.39	0.0306	4.53	0.0038	3.85	0.85	520	105	25	2	31	3	95.2	19.2	24	1.8
Zircon	Leucogranite	CHSZ	TLN10	5		29	1.9	28352	1411	68	50186	90934	0.00	5	11	2254	412.9695	1.51	0.0483	1.80	0.0161	2.35	0.0024	1.51	0.64	114	85	16	0	16	1	86.4	4.0	16	0.5
Zircon	Leucogranite	CHSZ	TLN10	6		62	1.7	67842	3893	1716	194151	221170	0.01	12	43	5481	414.9278	1.59	0.0563	1.31	0.0187	2.06	0.0024	1.59	0.77	462	58	16	0	19	1	96.6	17.4	15	0.5
Zircon	Leucogranite	CHSZ	TLN10	7		59	5.4	17425	1773	13504	1273386	16304	0.69	6	279	404	121.8133	2.55	0.1000	2.28	0.1132	3.42	0.0082	2.55	0.75	1625	85	53	3	109	7	96.8	51.6	49	2.3
Zircon	Leucogranite	CHSZ	TLN10	8		79	0.4	361600	17401	5111	3665055	1210826	0.03	65	804	30009	440.0793	1.54	0.0488	1.04	0.0153	1.86	0.0023	1.54	0.83	139	49	15	0	15	1	89.5	5.0	15	0.4
Zircon	Leucogranite	CHSZ	TLN10	9		-79	-3.4	43182	2101	206	121630	135750	0.01	8	27	3364	400.9187	1.69	0.0485	1.58	0.0167	2.31	0.0025	1.69	0.73	122	74	16	1	17	1	86.8	4.3	16	0.5
Zircon	Leucogranite	CHSZ	TLN10	10		-5	-0.1	81479	4023	342	272460	268539	0.01	14	60	6655	423.2053	1.46	0.0480	1.17	0.0156	1.88	0.0024	1.46	0.78	101	55	15	0	16	1	84.9	3.4	15	0.4
Zircon	Leucogranite	CHSZ	TLN10	11		27	0.7	67474	3234	294	206447	214018	0.01	12	45	5304	401.1789	1.48	0.0474	1.11	0.0163	1.85	0.0025	1.48	0.80	70	53	16	0	16	1	77.0	2.2	16	0.5
Zircon	Leucogranite	CHSZ	TLN10	12		14	0.6	45089	2217	297	100272	140381	0.01	8	22	3479	401.2870	1.30	0.0494	1.23	0.0170	1.79	0.0025	1.30	0.73	168	57	16	0	17	1	90.5	6.1	16	0.4
Zircon	Leucogranite	CHSZ	TLN10	13		5	0.1	67024	3284	303	189658	212775	0.01	12	42	5273	408.6444	1.40	0.0486	1.30	0.0164	1.91	0.0024	1.40	0.73	130	61	16	0	17	1	87.9	4.6	16	0.4
Zircon	Leucogranite	CHSZ	TLN10	14		34	2.7	22599	1311	3269	376502	58692	0.06	5	83	1455	337.1052	1.67	0.0584	1.80	0.0239	2.46	0.0030	1.67	0.68	546	79	19	1	24	1	96.5	20.3	19	0.6
Zircon	Leucogranite	CHSZ	TLN10	15		78	1.2	116918	5971	964	435955	314008	0.01	21	96	7782	361.0343	2.63	0.0493	1.24	0.0188	2.91	0.0028	2.63	0.90	161	58	18	1	19	1	88.9	5.8	18	0.9
Zircon	Leucogranite	CHSZ	TLN10	16		30	0.4	126396	5994	593	219908	249890	0.01	22	48	6193	279.4176	4.71	0.0474	1.24	0.0234	4.87	0.0036	4.71	0.97	68	59	23	2	23	2	65.9	1.8	23	2.2
Zircon	Leucogranite	CHSZ	TLN10	17		-8	-0.3	47934	2307	144	92942	148456	0.01	9	20	3679	400.5487	1.49	0.0475	1.49	0.0163	2.11	0.0025	1.49	0.71	75	71	16	0	16	1	78.5	2.4	16	0.5
Zircon	Leucogranite	CHSZ	TLN10	18		52	3.4	27195	1555	4666	718065	15099	0.42	6	158	374	72.0386	1.54	0.0579	2.19	0.1108	2.67	0.0139	1.54	0.58	526	96	89	3	107	5	83.1	16.7	88	2.6
Zircon	Leucogranite	CHSZ	TLN10	19		45	1.7	48284	2354	173	93066	160607	0.01	9	20	3980	428.4740	1.70	0.0482	1.89	0.0155	2.54	0.0023	1.70	0.67	109	89	15	1	16	1	86.2	3.8	15	0.5
Zircon	Leucogranite	CHSZ	TLN10	20		-65	-1.8	65503	3178	759	549255	231442	0.02	12	121	5736	449.3746	1.35	0.0476	1.27	0.0146	1.86	0.0022	1.35	0.73	81	60	14	0	15	1	82.2	2.7	14	0.4
Zircon	Leucogranite	CHSZ	TLN10	21		22	0.1	330684	20062	59684	1662510	36057	0.41	69	365	894	1.41053	1.49	0.0595	1.07	0.5817	1.84	0.0709	1.49	0.81	587	47	442	13	466	14	24.7	5.2	440	12.6
Zircon	Leucogranite	CHSZ	TLN10	22		21	0.1	417173	25323	55588	1355828	39816	0.30	84	297	987	12.0750	1.84	0.0595	1.32	0.6796	2.26	0.0828	1.84	0.81	587	57	513	18	527	18	12.6	2.6	512	18.0
Zircon	Leucogranite	CHSZ	TLN10	23		26	0.4	126133	6059	517	300380	395413	0.01	22	66	9800	402.7834	1.52	0.0472	1.33	0.0162	2.02	0.0025	1.52	0.75	59	63	16	0	16	1	73.1	1.7	16	0.5
Zircon	Leucogranite	CHSZ	TLN10	24		41	0.8	95621	4669	528	254383	310602	0.01	17	56	7698	408.2162	1.41	0.0482	1.14	0.0163	1.81	0.0024	1.41	0.78	111	54	16	0	16	1	85.8	3.9	16	0.4
Zircon	Leucogranite	CHSZ	TLN10	25		53	1.0	93681	4394	3499	4021666	334718	0.11	17	882	8296	477.9532	1.52	0.0479	1.32	0.0138	2.02	0.0021	1.52	0.75	96	63	13	0	14	1	86.0	3.3	13	0.4
Zircon	Leucogranite	CHSZ	TLN10	26		-45	-1.1	72807	3483	803	759661	259900	0.03	13	167	6441	462.5208	1.48	0.0476	1.39	0.0142	2.03	0.0022	1.48	0.73	77	66	14	0	14	1	82.0	2.5	14	0.4
Zircon	Leucogranite	CHSZ	TLN10	27		-21	-3.7	10103	654	8048	674638	18139	0.33	3	148	450	232.6683	3.22	0.0598	3.16	0.0354	4.51	0.0043	3.22	0.71	596	137	28	2	35	3	95.4	21.8	27	1.7
Zircon	Leucogranite	CHSZ	TLN10	28		19	0.4	100060	4866	329	202188	325458	0.01	18	44	8066	419.2376	1.56	0.0474	1.18	0.0156	1.96	0.0024	1.56	0.80	71	56	15	0	16	1	78.5	2.3	15	0.5
Zircon	Leucogranite	CHSZ	TLN10	29		35	3.7	16421	1100	5527	654530	21763	0.27	4	144	539	170.0246	1.84	0.0658	1.94	0.0534	2.67	0.0059	1.84	0.69	801	81	38	1	53	3	95.3	28.4	37	1.3
Zircon	Leucogranite	CHSZ	TLN10	30		64	5.6	21403	1032	115	48514	63867	0.01	4	11	1583	369.3086	1.92	0.0475	1.88	0.0177	2.69	0.0027	1.92	0.71	75	89	17	1	18	1	76.7	2.3	17	0.7
Zircon	Leucogranite	CHSZ	TLN10	31		9	0.3	46723	2313	216	73274	146551	0.00	8	16	3632	398.6188	1.47	0.0499	1.69	0.0173	2.24	0.0025	1.47	0.65	191	79	16	0	17	1	91.5	7.0	16	0.5
Zircon	Leucogranite	CHSZ	TLN10	32		6	0.1	99248	4816	486	279996	318704	0.01	18	61	7899	411.8116	1.46	0.0480	1.22	0.0160	1.90	0.0024	1.46	0.77	97	58	16	0	16	1	83.9	3.3	16	0.5
Zircon	Leucogranite	CHSZ	TLN10	33		41	2.4	31186	1557	120	63801	91340	0.01	6	14	2264	385.1116	1.76	0.0479	1.53	0.0171	2.33	0.0026	1.76	0.75	95	73	17	1	17	1	82.5	3.2	17	0.6
Zircon	Leucogranite	CHSZ	TLN10	34		-49	-1.0	88582	4376	944	855066	333190	0.02	16	188	8258	484.0016	1.49	0.0486	1.23	0.0138	1.93	0.0021	1.49	0.77	129	58	13	0	14	1	89.7	4.7	13	0.4
Zircon	Leucogranite	CHSZ	TLN10	35		-8	-0.4	37262	1818	354	87387	106080	0.01	7	19	2629	369.9037	1.79	0.0475	1.73	0.0177	2.49	0.0027	1.79	0.72	77	82	17	1	18	1	77.3	2.4	17	0.6
Zircon	Leucogranite	CHSZ	TLN10	36		42	2.5	31099	1602	1621	212872	86964	0.02	6	47	2155	361.6600	1.82	0.0505	1.96	0.0193	2.68	0.0028	1.82	0.68	220	91	18	1	19	1	91.9	8.1	18	0.6
Zircon	Leucogranite	CHSZ	TLN10	37		34	0.7	91696	4266	279	180559	271275	0.01	16	40	6723	385.3961	1.70	0.0464	1.62	0.0166	2.35	0.0026	1.70	0.72	19	78	17	1	17	1	13.2	0.1	17	0.6
Zircon	Leucogranite	CHSZ	TLN10	38		54	1.2	80631	3877	301	204997	236129	0.01	14	45	5852	361.0336	1.85	0.0467	1.61	0.0178	2.45	0.0028	1.85	0.75	33	77	18	1	18	1	45.1	0.6	18	0.7
Zircon	Leucogranite	CHSZ	TLN10	39		21	0.7	53883	2572	291	197247	189488	0.01	10	43	4696	455.1546	1.64	0.0475	1.54	0.0144	2.25	0.0022	1.64	0.73	72	73	14	0	14	1	80.4	2.3	14	0.5
Zircon	Leucogranite	CHSZ	TLN10	40		63	2.5	47973	2309	149	95447	151665	0.01	9	21	3759	415.5703	1.58	0.0481	1.37	0.0159	2.09	0.0024	1.58	0.75	103	65	15	0	16	1	84.9	3.5	15	0.5

Table 5.8: Zircon U-Pb SC-ICP-MS geochroological results for leucogranites part 4

the surrounding rocks and secondary muscovite growth.

5.4.4.2 TL63: Garnet Tourmaline Leucogranite

This leucogranite dyke intrudes through the Koronos Shear Zone on the Western Side of Naxos near the village of Koucharchi, and clearly is post-tectonic with respect to the shearing deformation in the country rock. Ignoring inherited ages, it shows one zircon rim age of 13.16 ± 0.47 Ma (Fig. 11), which we interpret as representing intrusion through the Koronos Shear Zone post-dating shearing. This age provides an upper age constraint for movement on the Koronos Shear zone to at least pre-13.16 Ma.

5.4.4.3 TL69: Garnet Biotite Leucogranite (Aligned with KSZ)

TL69 intruded prior to or synchronous to deformation along the Western side of the dome and is aligned with the foliation of the Koronos Shear Zone. A single rim age of 17.63 ± 0.64 Ma (Fig. 5.12) and provides an approximate upper bound for movement on the Koronos Shear Zone associated with decompression from kyanite-sillimanite grade conditions.

5.4.4.4 TL72: Garnet Tourmaline Leucogranite (Sheared with NPDS)

This garnet tourmaline leucogranite intrudes into the overlying carapace through a serpentine lense along the Koronos Shear Zone, along the north coast of Naxos near the village of Agia and is clearly post-tectonic with respect to deformation. This sample gives a range of ages from 17.41 ± 0.41 to 12.71 ± 0.81 Ma (Fig. 5.12), indicating a prolonged period of partial melting and anatexis on Naxos, and clearly intruded prior to movement on the NPDS which deforms it. The youngest age of 12.71 ± 0.81 Ma provides an upper age constraint for movement on the NPDS associated with regional extension, and deformation migrated up to higher structural levels with time.

5.4.4.5 TLN8: Biotite-Muscovite Leucogranite (Boudinaged Vertically and Horizontally)

TLN8 is from a leucogranite dyke that intruded vertically through marble bands in the Core High Strain Zone (CSHZ) at the center of the Naxos migmatite dome, and provides structural context and constraints on the interpreted ages. This dyke is aligned vertically, parallel to the (F_3) fold axes of the uprightly folded marble bands. It is also vertically boudinaged with lobate boundaries indicating it intruded and crystallized under constructional strains when the minimum principal stress (σ_3) was vertically orientated and must have intruded after upright F_3 folding, and is later boudinaged horizontally N–S due to a N–S extensional strains (see Fig. 5.2). Ages span between 17.0–14.2 Ma (Fig. 5.12). The major age population lies between 16 and 14 Ma, whereas the older analysis could represent the earliest stage of melting and not dyke emplacement. Using this major age population as the timing of crystallization, we infer upright folding occurred immediately prior to crystallization, vertical boudinage occurred during crystallization of the granite, whereas N–S pure shear extension post-dates crystallization. Therefore, N–S extensional deformation must post-date 14.2 Ma, while constriction must have occurred between ca. 16–14.5 Ma, thus providing approximate age constraints for horizontal shortening and migmatite doming.

5.4.4.6 TLN10: Biotite-Muscovite Leucogranite (Boudinaged Vertically And Horizontally N–S)

TLN10 is from a deformed vertical dyke within the CHSZ at the center of the Naxos migmatite dome, that strikes N–S and is boudinaged both vertically and horizontally, providing additional constraints on the timing of E–W contraction, constriction and the onset N–S extension. It the largest spread of U-Pb ages relating to anataxis, with a continuous age population between 18.81 ± 0.62 Ma and 13.27 ± 0.39 Ma (Fig. 5.12). Unfortunately, there is no way to discriminate these ages, and it is possible that mixing with older inherited cores has occurred. It is likely however that the younger age population represents dyke intrusion and crystallization. Post crystallization, the dyke

was subsequently boundinaged vertically, and then horizontally associated with the onset of crustal extension. The youngest zircon age indicates suprasolidus conditions continued in the center of Naxos dome to at least ca. 13.3 Ma and therefore provides an approximate age for the onset of crustal extension at ca. 13.3 Ma.

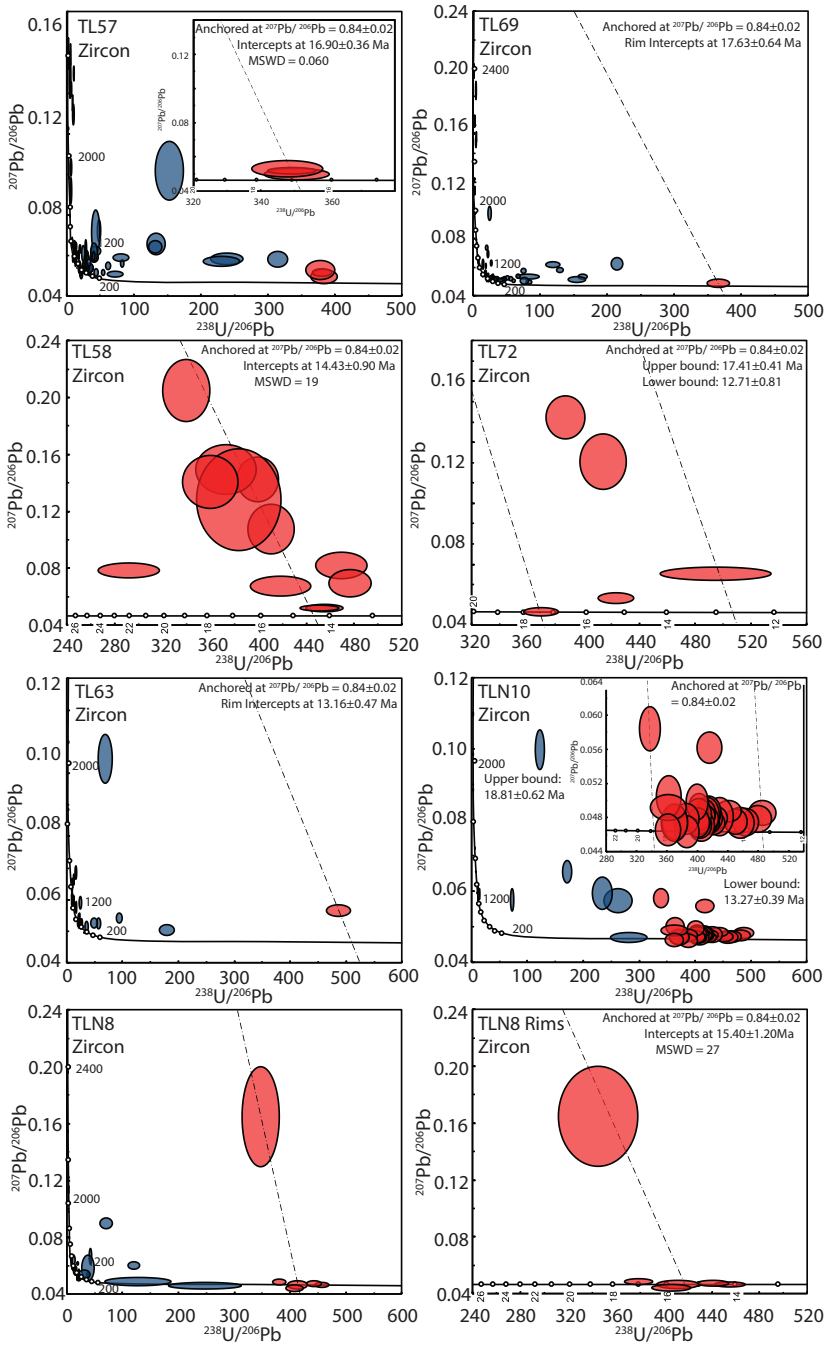


Figure 5.12: Tera-Wasserburg concordia plots for leucogranite samples using LA-ICPMS analysis ofzircon, upper intercepts where calculated using a $^{207}Pb/^{206}Pb$ value of 0.84 ± 0.02 using Stacey and Krammers, 1975 for young zircon, blue circles represent old inhered cores and red circles represent young rims. A) TL57 Tera-Wasserberg plot showing a range in ages for inheritance and young concordant rims, inset zoomed view of rim data with regressed age of 16.90 ± 0.36 Ma. B) TL69 Tera-Wasserburg plot showing concordant rim age of 17.63 ± 0.64 Ma. C) TL58 Tera-Wasserburg plot showing young rim ages spanning between 15.7 and 13.1 Ma. D) TL72 Tera-Wasserburg plot showing young rims spanning 17.41 ± 0.41 Ma concordant age and 12.71 ± 0.81 Ma. E) TL63 Tera-Wasserburg plot showing a single young age of 13.16 ± 0.47 Ma. F) TLN10 Tera-Wasserburg plot with inset showing distribution of young ages between 18.81 ± 0.61 Ma and 13.27 ± 0.39 Ma. G and H) TLN8 zircon Tera-Wasserburg plots showing young concordant ages between 17.0 and 14.1 Ma.

5.5 Discussion

5.5.1 Interpreting Zircon Growth and Ages in S-Type Leucogranites

New zircon growth in leucogranites and gneisses commonly forms thin < 20 m rims or terminations on pre-existing grains and invariably occurs as homogeneous to faintly zoned overgrowths with low luminescence and low Th/U ratios, in agreement with Keay et al., 2001. Zircon rims in leucogranite samples can be identified as precipitating from melt by analysis of zircon domains using CL-zoning patterns, from the zircon rim morphology, Th/U chemistry and age.

Metamorphic zircon has been shown to grow by (1) net-transfer reactions (e.g. Vavra et al., 1996; Fraser et al., 1997), (2) hydrothermal precipitation (e.g. Mumpton and Roy, 1961; Marshall, 1969; Rubin et al., 1993; Williams et al., 1996), (3) solid-state recrystallization (Pidgeon, 1992), and (4) precipitation from melts (Davis et al., 1968; Watson and Harrison, 1983). In Naxos gneisses and leucogranites, the later of these mechanisms is most important. This is because; net-transfer reactions involve limited volumes of zircon growth by solid-state nucleation and crystallization due to the breakdown of Zr- and Si-bearing phases. The lack in other Zr-bearing phases in migmatites and leucogranites, discern this as a major process in zircon growth. We can also discount the possibility of new zircon growth by precipitation from fluids, due to the lack of hydrothermal veining, and most zircon rims clearly truncate earlier zircon structures, rather than replacing them and are therefore unlikely to be the products of recrystallization. Growth of new zircon grains or overgrowths nucleated on pre-existing grains during melt crystallization and may have involved resorption of existing zircon during partial melting (Davis et al., 1968; Watson and Harrison, 1983). CL-imaging shows zircon morphologies with dissolution embayments infilled and overgrown by younger zircon zones, with only small volumes of new zircon grown during metamorphism and partial melting. Although zircon overgrowths show a large age range, the youngest population of zircon overgrowths at 19–13 Ma represents the

overgrowth population constraining the timing of the M_2-M_3 partial melting process and dyke emplacement due to the thin nature of the rims and much older inherited cores. Integration with monazite ages confirms that high-grade metamorphism and partial melting was occurring on Naxos between ca. 18.5–13 Ma, coinciding with zircon growth during anatexis.

5.5.2 Linking Ages to Metamorphic Histories and *P–T–D* Paths

The data presented above provides high resolution timing constraints on the rates of metamorphism and deformation within the Naxos MCC, with a complex array of ages associated with early M_1 high-pressure metamorphism of the Zas Unit followed by a prolonged period of metamorphism leading to peak M_2–M_3 Barrovian conditions in the deeper structural levels. A detailed discussion of the ages coupled with P–T constraints for each unit is discussed below in chronological order.

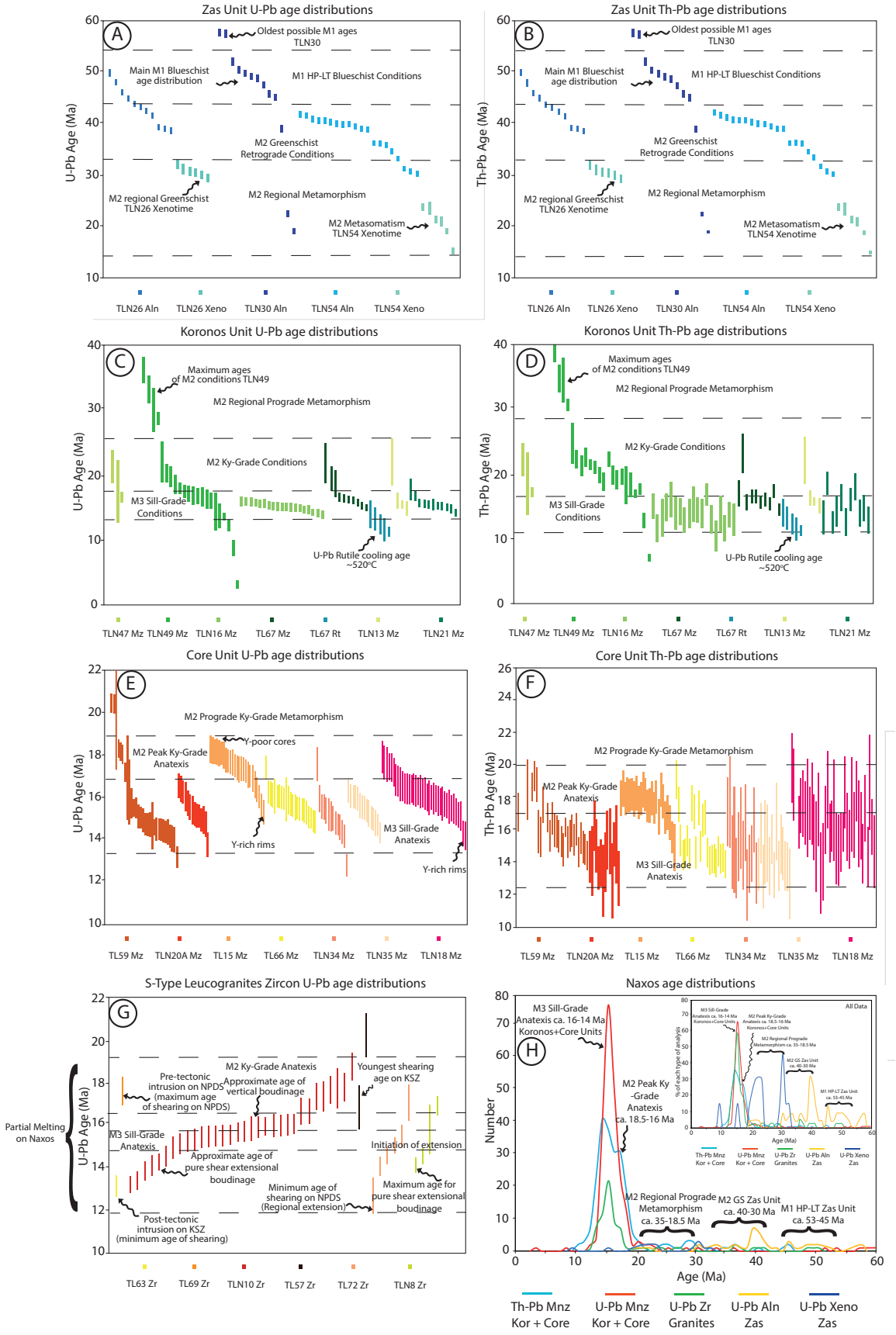


Figure 5.13: Continues on next page

Figure 5.13: Age distributions of all U–Pb and Th–Pb data aligned in chronological order for U–Pb with corresponding Th–Pb ages. A and B) Zas Unit allanite and xenotime U–Pb age data (A) and Th–Pb age data (B) showing the variation of ages for M_1 conditions between samples and between grains, with main age population ca. 54–45 Ma and Xenotime M_2 ages between 20-31 Ma with good correlation to Th-Pb ages. C and D) Koronos Unit U–Pb and Th–Pb monazite and rutile ages showing M_2 conditions spanning 36–18 Ma with reasonable correlation although more scattered Th–Pb ages, with M_3 cluster at 16–15 Ma recorded by both Th–Pb and U–Pb. E and F) Core Unit U–Pb and Th–Pb monazite ages showing good correlation between the 2 systems and a spectrum of ages from 18.5–13 Ma recorded by both systems recording M_2 kyanite grade partial melting and decompression to M_3 sillimanite grade conditions. G) Leucogranite U-Pb zircon age spectrum with annotations giving an interpretation of each age with respect to deformation. H) Compiled and binned age data from the entire island coloured for each unit accordingly with number of analyses recording specific ages. This shows that metamorphism on Naxos was diachronous spatially and occurred over a prolonged time period. Inset shows frequency of each age with respect to the total number of analyses for each unit dataset.

5.5.2.1 Zas Unit:

In chapter 4 it was shown that this unit experienced M_1 blueschist-facies HP-LT conditions of ca. 14.5 kbars 470 °C during NE-directed attempted subduction of the Cycladic continental margin. To get a meaningful metamorphic age, allanite was chosen for U–Pb dating as it is the dominant carrier of LREEs in subducted crust, and the progressive metamorphic sequence to constrain accessory phase relationships is well understood (Janots et al., 2007, 2008, 2009; Rasmussen et al., 2006; Tomkins and Pattison, 2007; Smye et al., 2014), making it is best suited for dating blueschist-eclogite facies metamorphic events. In rocks of sufficient CaO and LREE, allanite forms at the expense of metamorphic or detrital monazite under low-temperature (350–450 °C) conditions (Wing et al., 2003; Janots et al., 2008, 2009) and breaks down at conditions close to the staurolite isograd (Janots et al., 2008, 2009), like what is observed on Naxos. Textural consideration of allanite trapped within the cores of retrograde clinozoisite (TLN30) and as pristine allanite aligned with the S_1 top-to-NE blueschist fabric (TLN54) suggests U–Pb ages from these samples represent peak M_1 *HP-LT* conditions and have not been thermally reset. Because metamorphic allanite has been shown to grow prior to garnet during prograde Alpine subduction and retained its radiogenic Pb to temperatures >600 °C (Smye et al., 2014), allanite U–Pb ages bracket peak (M_1)

blueschist facies conditions to between ca. 46–49 Ma whereas retrograde allanite from sample TLN26 records a distinctly different age of ca. 40 Ma (Fig. 5.13). Intriguingly this age is consistent with Rb–Sr and ^{40}Ar–^{39}Ar cooling ages from high-pressure rocks on Naxos (Peillod et al., 2017), and could represent hydration during retrogression. Other U–Pb and Lu–Hf and Sm–Nd garnet geochronological studies of the Cycladic Blueschists systematically shows that peak M_1 conditions occurred between ca. 54–45 Ma (Tomascheck, 2003; Lagos et al., 2007; Dragovic et al., 2012) with a greenschist-facies overprint from ca. 40–20 Ma (Peillod et al., 2017).

Xenotime records ages between ca. 30–20 Ma (Fig. 5.13). Because xenotime has an irregular habit and is distributed along fractures and veins, we interpret this age to represent metasomatism under greenschist-facies conditions overprinting the earlier M_1 high-pressure event, that resulted in breakdown of allanite or garnet liberating Y into the surrounding rock. The range of xenotime ages therefore does not represent individual metamorphic events, but a prolonged period of regional metamorphism and fluid infiltration that was diachronous in time and lateral extent. Xenotime ages generally pre-date peak M_2 Barrovian ages from structurally deeper levels of the core complex by 15–5 Myrs and presumably represent the initial stages of M_2 conditions during the Oligiocene to mid-Miocene, whilst the structurally deeper rocks (Koronos and Core Units) where getting underthrusted and experiencing prograde dehydration reactions that would hydrate the overlying units. This data agrees with recent work by Peillod et al., (2017), who shown that the greenschist-facies overprint yields Rb–Sr ages between 32–27 Ma.

5.5.2.2 Koronos Unit:

Koronos Unit samples exhibit a range of monazite U–Pb ages from ca. 39.2–14.5 Ma with a main population between 26–14.5 Ma, which postdates M_1 conditions of the Zas unit by ca. 20–30 Myrs. Moreover, there is no evidence of the M_1 event or the Oligocene greenschist-facies overprint recorded in the petrology, mineral chemistry or monazites geochronology (Figs. 5.13 and 5.14). Bolhar et al. (2017) provide evidence

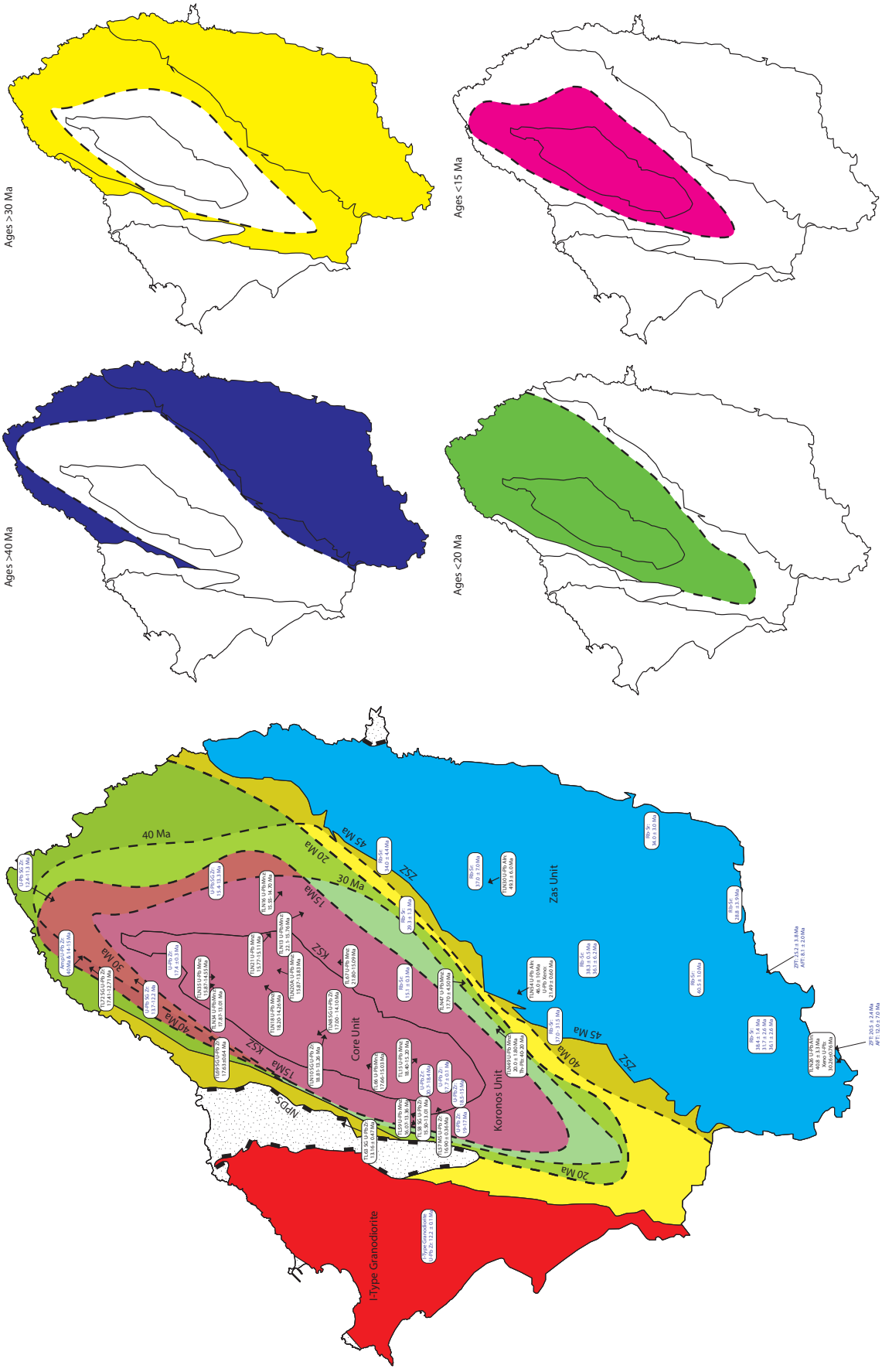


Figure 5.14: Summary geochronological maps of Naxos left; contoured for U-Pb ages, showing the spatial distribution of ages which systematically get younger with structural depth and correlate with the major shear zones. Right; regions of Naxos where metaorphic ages of pre 40 Ma, pre 30 Ma, younger than 20 Ma and younger than 15 Ma ae recorded

for a ca. 40 Ma zircon growth ages from amphibolites on northern Naxos with a 15–14 Ma rim. This 40 Ma age could be interpreted as one of two options: i) It represents the burial of the continental margin in a subduction setting (M_1), which has been completely overgrown by a separate crustal thickening prograde orogenic cycle to explain a clockwise P–T loop (shown in Part 1) and peak M_2 Barrovian conditions approximately 25 Myrs after collision, like the Lepontine metamorphism in the central Alps (e.g. Wiederkehr et al., 2008). ii) Ca. 40 Ma ages represents the initial stages of collision between the Cyclades (Adria) and Euarsia and is associated with the overthrusting of the Cycladic Blueschists (Zas Unit). This is because these ages are different enough from the Zas Unit M_1 ages and the established peak regional M_1 age of ca. 54–45 Ma (Tomaschek et al., 2003; Lagos et al., 2007; Dragovic et al., 2012) and are associated with a continuous spectrum of ages from ca. 40 to 15 Ma. Sample TLN49 is associated with M_2 kyanite-grade conditions and is relatively unaffected by late M_3 heating with a main M_2 monazite population between 26–16 Ma, with a maximum reliable U–Pb age of 39.2 ± 1.9 Ma ($TLN49_M7_2$) (Fig. 5.13). The continuous spectrum of M_2 ages spanning >20 Myrs implies that older ages represent prograde amphibolite facies metamorphism, as monazite has been shown to form following allanite breakdown in the mid-amphibolite facies in rocks with sufficient CaO (Jannots et al., 2008). These older monazite ages also provide a maximum age constraint for the development of kyanite-grade S_2a crenulation cleavage and F_1 isoclinal folding within the Koronos Unit.

Peak M_2 kyanite-grade monazite ages in samples TL67, TLN13 and TLN49 are distributed between ca. 22–18 Ma and this occurs exactly 25–30 Myrs following M_1 conditions in the Zas Unit. This time window to obtain peak Barrovian conditions is consistent with the timescales predicted by thermal models of overthrust terrains (England and Richardson, 1977; England and Thompson, 1984). This combined with independent structural evidence presented in chapter 4, strongly supports an overthrusting mechanism as the driver of metamorphism on Naxos. In this scenario, burial and thickening of the continental shelf to ca. 35 km depth, would increase the geotherm

over several tens of million years due to an increase in radiogenic heating and would likely invoke M_2 kyanite-grade conditions and partial melting at the deepest levels. In samples from deeper levels of the Koronos Unit, only a single generation of small <30 μm matrix unzoned monazites were found and record a homogeneous age of ca. 16.5–14.5 Ma (TL67, TLN21 and TLN16) (Fig. 12). Textural, petrological and P–T constrains determined in chapter 4, suggest this age almost certainly does not date the age of peak pressures kyanite-grade pressures (M_2). Instead, we relate this age with (M_3) sillimanite-grade thermal metamorphism at the base of the Koronos Unit at lower pressures than peak M_2 conditions of ca. 5–6 kbars, 650°C vs ca. 10 kbars, 670°C. This younger age correlates with petrographic observations of lower pressure (M_3) sillimanite-grade fabrics that overprint earlier M_2 kyanite-grade assemblages, such as small post-tectonic garnets that post-date the S_3 shear fabrics of the Koronos Shear Zone, sillimanite biotite sheaths from breakdown from kyanite following a Carmichael reaction scheme (Carmichael, 1969), and high degrees of static recrystallization and annealing which indicate high temperatures outlasted deformation. The 16.5–14.5 Ma age therefore represents (M_3) sillimanite-grade conditions that post-dates decompression and shearing movement on the Koronos Shear Zone, responsible for juxtaposing the Koronos Unit adjacent to the hotter migmatite Core Unit. Small 35 μm rutile that formed during (M_2) kyanite-grade conditions provide a U–Pb age of 12.7 ± 1.2 Ma, demonstrating that the carapace of the migmatite dome was exhumed through the ca. 520 °C isotherm at around this time (based on the Dodson diffusion equation; Cherniak, 2000; Dodson, 1973 and cooling rate suggested by other thermochronometers). This implies the core complex cooled by ca. 180 °C in less than 2–3 Myrs following peak conditions (ca. 15.5 Ma) at a rate of 60–90 °C/Myr. This magnitude of cooling requires advective processes such as tectonic denudation and normal faulting during the onset of crustal extension. Juxtaposition of cooler rocks at higher levels combined with rapid exhumation is consistent with normal faulting during crustal extension.

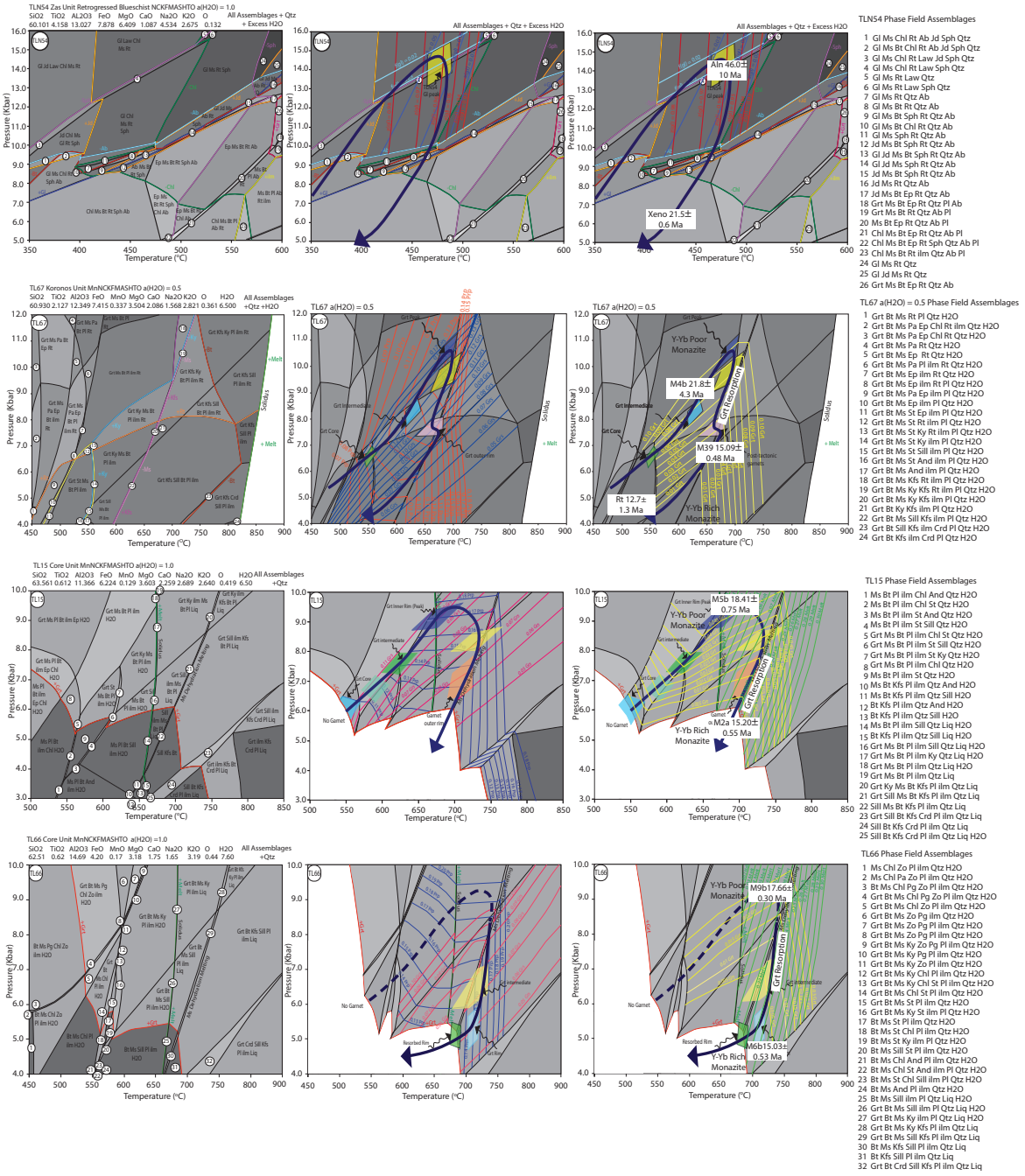


Figure 5.15: Petrochronology of Naxos samples with a compilation of pseudosections for samples TLN54 (blueschist), TL67 (kyanite gneiss), TL15 (kyanite migmatite) and TL66 (sillimanite migmatite) presented in chapter 4 with overlaid U-Pb ages related to the *P-T* conditions, constrained by garnet isopleths pyrope and grossular and y(hb) (TLN54). Younger monazite ages in samples TL15 and TL66 correspond with Y rich monazite rims, interpretted to formed during garnet resorbtion during decompression associated with decreasing garnet modes.

5.5.2.3 Core Unit:

Monazite and zircon data reveals a complete story for the timing of anatexis and the rates of decompression melting. P–T conditions from rocks modelled in chapter 4 demonstrate that Naxos migmatites attained peak M_2 conditions during the onset of hydrous melting at ca. 8–10 kbars, 690–750 °C, which was followed by decompression through the muscovite dehydration melting reaction to sillimanite-Kfs present (M_3) conditions of ca. 5–6 kbars 700–730 °C. Monazite data from the Core Unit demonstrate a U–Pb monazite age range from 18.5–13.5 Ma (Fig. 5.13), with most ages clustering as a continuous population around 17.5–15 Ma. Older ages are almost entirely associated with monazites trapped as inclusions within kyanite or in the cores of large monazites and are typically Y-poor, assumed to be due to monazite growth in the presence of garnet (see Fig. 5.4). This older spectrum of ages is thus interpreted to represent the onset of hydrous melting at M_2 kyanite grade pressures. Whereas younger ages (15.5–13 Ma) are distributed along the rims of larger monazite grains or as small-moderate sized matrix grains (30-50 μm) that are Y-rich. Y rich monazite (rims) relates to monazite growth during or after garnet breakdown during decompression at ca. 5 kbars, 690 °C (see chapter 4 and Fig. 5.13 and 5.15) as garnet is the main consumer of Y and LREE budget of high-grade metapelites. This decompression event is consistent with garnet breakdown and correlates with garnet compositional profiles in high-grade migmatites, which all show an increase in Mn towards the rim representative of resorption. Ages younger than ca. 15.5 Ma therefore represents growth of monazite during M_3 and exhumation and ages younger than ca. 15 Ma are associated with secondary muscovites that grew during hydration following melt crystallization at sub-solidus M_3 conditions. The monazite age range therefore reflects monazite growth firstly during supra-solidus decompression from 35 to 17.5 km depth through the muscovite dehydration melting reaction producing larger melt volumes and therefore larger monazite grains (Samples TL66, TLN18, TLN20A, TLN34) and subsequent metasomatism associated with melt crystallization.

5.5.3 Relating Age Distributions to Tectonics Regime

A scenario of purely crustal extension following M_1 high-pressure metamorphism cannot reproduce many aspects of the *P–T–t–D* paths recorded on Naxos. In particular, it cannot explain the range of Oligocene-Miocene metamorphic ages or the prograde clockwise *P–T–t* loop recorded by the Koronos and Core Units, which involves increasing both pressure and temperature to peak M_2 pressures of ca. 10 kbars, 730 °C, and the lack of M_1 precursors. Under crustal extension, the peak pressure of metamorphism is expected to also increase with structural depth and the U–Pb or Th–Pb age of peak metamorphism should be consistent across all units and associated with a contemporaneous isobaric heating pulse due to increased basal heatflow from the asthenosphere (Sandiford et al., 1986; Bohlen, 1987 and Ruppel et al., 1988). This heating should be associated with either a single generation of metamorphic ages across all units or delayed cooling during exhumation and should not involve rocks increasing in both pressure and temperature to peak kyanite-grade conditions or rapid cooling immediately following 15 Ma (Figs. 5.16 and 5.17).

Contrastingly during crustal thickening metamorphism is predicted to be diachronous in space and time, and involve a clockwise *P–T–t* path as a result of continuous burial and stacking of nappes. Peak M_2–M_3 Barrovian metamorphic ages get younger with both increasing metamorphic grade and structural depth across Naxos, and this is diagnostic of a prolonged period of crustal thickening following extrusion of high-pressure rocks from a northward dipping subduction zone. Crustal thickening would cause an increase in radiogenic heating allowing the geotherm to evolve over time due to thermal relaxation of isotherms following overthrusting of firstly the Cycladic Blueschists (Zas Unit) followed by thick–skinned thrusting and thickening of the un-subducted shelf carbonates and basement (Koronos and Core Units). The rocks on Naxos recorded their peak metamorphic conditions at different times along this evolving geotherm (See Fig. 5.16), and have been later juxtaposed against each other by normal sensed movements on ductile shear zones producing a condensed series of frozen in isograds. The most deeply buried rocks reached the highest temperatures but

took the longest to do so, and thermally equilibrated at their maximum temperature that occurs after attaining their peak pressures. Peak metamorphic conditions were obtained approximately 25–30 Myrs following M_1 and overthrusting of the Cycladic Blueschist Unit, and is consistent with simple thermal models (England and Richardson, 1977; England and Thompson, 1984). Crustal thickening can thus account for the burial, the prograde evolution, the distribution and range of U–Pb ages and increasing metamorphic grade with depth into the core complex.

Integration of these U–Pb and Th–Pb ages with pre-existing thermochronological ^{40}Ar–^{39}Ar hornblende, muscovite and biotite data (representing 550°C, 450°C and 300°C isotherms respectively, taking into account grain size and cooling rate; Harrison et al., 1985; Wijbrans and McDougall,., 1986; Harrison et al., 2009; Warren et al., 2012) with zircon and apatite fission track data (representing a proxy for the 250 °C and 100 °C isotherms respectively; Kumar et al., 1995; Ravenhurst and Donelick, 1992), provides insight into the thermal and cooling history of the core complex (Fig. 5.16). Assuming the youngest age cluster as the most reliable due to inherent problems of Ar loss and excess Ar (Kelley, 2002; Warren et al., 2012), a clear trend can be established. The highest structural levels on Naxos (Zas Unit or Cycladic Blueschists) experienced cooling through these isotherms between 40 and 15 Ma following burial to peak pressures. Cooling between 40–15 Ma occurred at rates of 3 °C/Myr, and must have been dominantly erosion driven. This cooling within the Zas Unit overlaps with M_2 prograde and peak monazite ages of the underlying units (Koronos and Core Units) between 39–22 Ma. The older ages are associated with low (Dy/Yb ratios) reflecting conditions prior to garnet growth, whereas higher pressure and temperature peak M_2 conditions within migmatites of ca. 10 kbar 730 °C occurred later at ca. 18.5–17.5 Ma and are associated with larger monazite Dy/Yb ratios suggesting monazite growth during or following garnet breadown. Due to these reasons, we believe that crustal thickening must be the cause of (M_2-M_3) regional metamorphism on Naxos, as there is no mechanism to invoke burial of sedimentary rocks to ca. 35 km depth along an evolving geothermal gradient in an extensional tectonic setting.

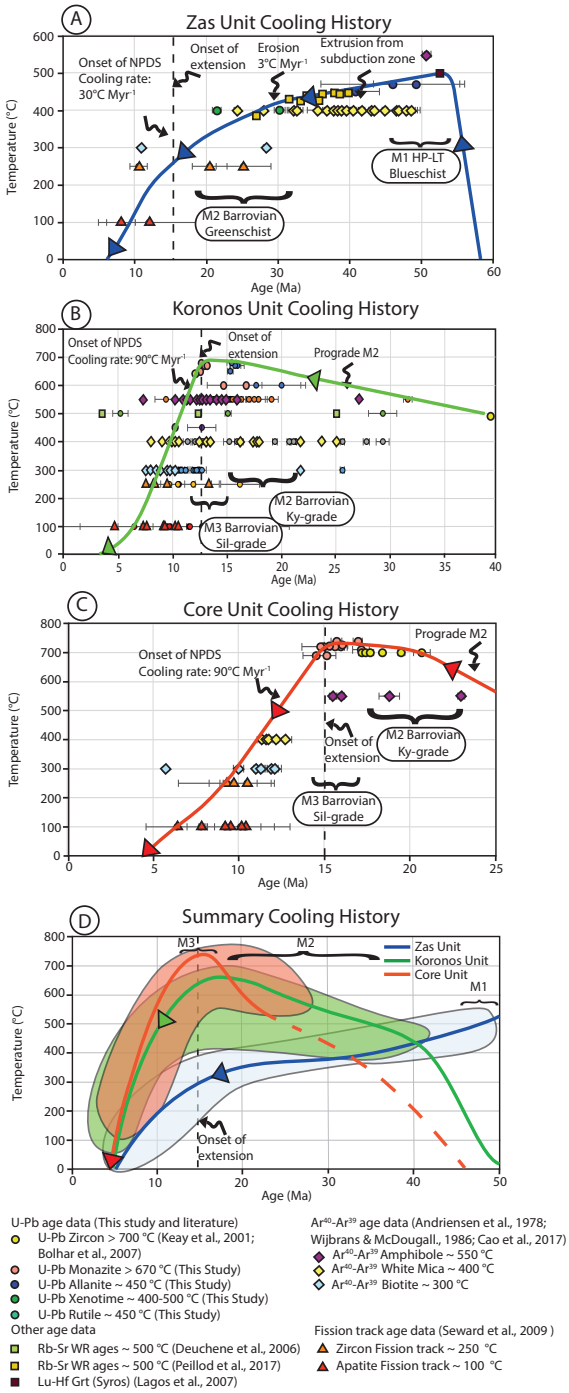


Figure 5.16: Cooling paths of each unit incorporating all geochronological data from Naxos. Youngest reasonable ^{40}Ar–^{39}Ar ages for a specific mineral are taken as the age of cooling through the approximate closure temperature. U–Pb monazite and zircon are interpreted as representing >600-650°C. A) Zas Unit cooling path from M_1 blueschist-facies conditions of ca. 14.5 kbar 470°C at ca. 49–46 Ma at a slow rate of ca. 3°C/Myr followed by rapid cooling of ca. 30°C/Myr post 20–15 Ma inferred from zircon and apatite fission track ages. B) Koronos Unit cooling path following prograde heating from 40 Ma to 20-15 Ma followed by rapid cooling of ca. 60-90°C/Myr after 15 Ma. C) Core Unit cooling path following prograde heating until 18-15 Ma, again associated with rapid cooling post 15 Ma at rates of ca. 60-90°C Myr. D) Summary cooling path of each unit, with blue representing the Zas Unit which cooled at the same time prograde metamorphism of the Koronos and Core Units was taking place at structurally deeper levels until 15 Ma, at which point the 3 units cool rapidly and converge associated with the onset of the Naxos-Paros Detachment System.

5.5.4 Timing of Partial Melting, Top-to-NNE Shearing and Exhumation

Tight timing constraints can be established on the decompression melting process, migmatite dome formation, and the initiation of extensional tectonics in the central Aegean, all of which occurs between 18–13 Ma. An overview of the age data is presented in Fig. 5.18 with a time chart relating the ages to deformation and metamorphism in Fig. 5.19. M_2 kyanite-grade migmatites attained 8–10 kbars, 700–730°C and are associated with monazite ages as young as ca. 18–17 Ma. These data alone place an absolute maximum age constraint for compressional tectonics on Naxos, and implies the burial of rocks to 35 km depth occurred to at least this time. Following peak burial, leucogranites constrain the timing and nature of deformation at deep levels of the core complex, due to cross cutting relationships with shear zones, folds and boudinage. Several cross-cutting leucogranites dykes (TL63, TL64, TL69, TL72) on the Koronos Shear Zone constrain the timing of top-to-NNE shearing to between 18 and 15.5 Ma. Integration with monazite geochronology suggest the Core Unit rapidly decompressed from ca. 35–17.5 km depth over <2.5 Myrs (18–15.5 Ma), a rate of ca. 6 km/Myr. Top-to-NNE movements on the normal sensed Koronos and Zas Shear Zones bounding the migmatites was responsible for this rapid decompression to (M_3) sillimanite-grade conditions. Vertically upright folding within the migmatite dome that folds kyanite blades and post-dates (M_2) kyanite-grade fabrics, definitively occurred at lower pressure M_3 sillimanite-grade conditions in the presence of larger degrees of ductile flow. Zircon crystallization ages from vertically boudinaged dykes (TLN8) from the center of the dome indicate vertical boudinage and horizontal constriction (associated with a vertically orientated σ_3) must have occurred between 15.5–14 Ma whereas horizontally boudinaged leucogranites constrain the onset of horizontal N–S extension to be between 15–13.3 Ma (TLN10) (N–S orientated σ_3). The young Y and Yb rich monazite population in both the Koronos and Core Units is associated with garnet breakdown because of the decompression from ca. 10–5 kbar. These petrochronological relations

combined with post-tectonic M_3 assemblages that overgrow M_2 assemblages suggest that the migmatites were juxtaposed against the colder kyanite-grade rocks of the Koronos Unit structurally above by 16–15.5 Ma. This caused the Koronos Unit rocks to remain hot during the initial stages of exhumation. Therefore, movement on the bounding normal sense shear zones (Koronos and Zas Shear Zones), associated with top-to-NNE shearing, must have occurred prior to 15.5 Ma and was specifically active between ca. 18–15.5 Ma and was responsible for decompression from peak (M_2) kyanite-grade pressures. Textures from KSZ samples suggest that high-temperatures outlasted deformation. This presumably facilitated the growth of post-tectonic garnets and caused static recrystallization, sillimanite-grade paragenesis and young (16–15 Ma) matrix monazite ages which suggest deformation seized by ca. 15.5–15 Ma. The higher level Zas Shear Zone is a top-to-NNE greenschist-facies structure responsible for localizing later exhumation and accommodated the SW extrusion of the Koronos and Core Units against relict blueschists (Zas Unit) at a higher structural level that were relatively cool. Sheath folds developed under the Zas Shear Zone and within the Koronos Unit during this episode of distributed top-to-NNE non-coaxial shear strain between ca. 18–15 Ma. The juxtaposition of these two distinct units resulted in a large jump in frozen in peak P–T conditions that were obtained at different times, whereby relict (M_1) blueschist-facies rocks of the Zas Unit are juxtaposed against (M_2) kyanite-grade gneisses of the Koronos Unit. Shearing on this structure occurred at greenschist-facies conditions whilst the rocks were around 300–400 °C at between 17.5–15 Ma (Figs. 5.16 and 5.18). Because the Zas Shear Zone is truncated and discordant to the Naxos-Paros Detachment System, it must pre-date movement on the brittle-ductile NPDS and regional extension. A maximum age bracket of <15 Ma can thus be inferred for movement on the NPDS. This interpretation is consistent with work by Cao et al. (2017) who present ^{40}Ar–^{39}Ar white mica cooling ages of ca. 16.52 ± 0.39 Ma from the equivalent of the Zas Shear Zone and an age of ca. 12.6 ± 0.28 Ma from the highest structural levels of the Zas Unit affected by deformation under the NPDS. These authors interpret these ages as dating the ductile movement on these structures, through

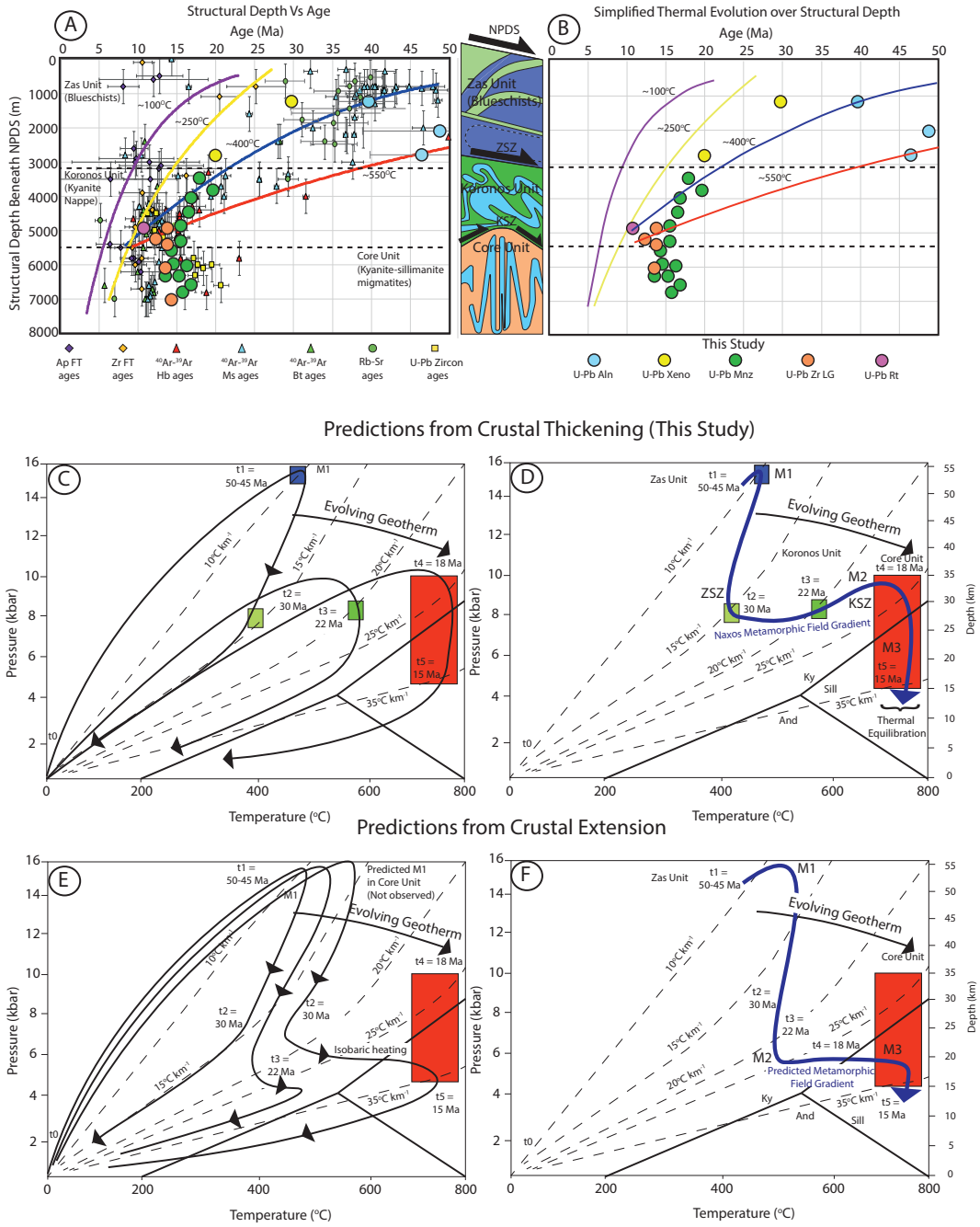


Figure 5.17: A) summary of geochronolgical data with depth with superimposed U–Pb results from this study, B) U–Pb results alone for clarity showing metamorphism propagates to deeper levels with time. Schematic showing simplified *P–T–t* paths for a compressional vs extensional model for the Naxos core complex. C and D) During compression, 3 different *P-T-t* paths are recorded at different times associated with an evolving geotherm as a result of radiogenic heating from crustal thickening. The observed metamorphic field gradient would record frozen in peak *P-T* conditions of each unit that would each be recorded at different times. Firstly, high-pressure M_1 conditions in the Zas Unit at 50–45 Ma, M_2 amphibolite-facies kyanite-grade conditions in the Koronos Unit between 26–18 Ma. M_2 Kyanite to M_3 sillimanite grade anatectic conditions within the Core Unit at the deepest structural levels followed by partial re-equilibration. E and F) Under crustal extension, all units are perceived to have experienced M_1 conditions and that following exhumation from the subduction zone there was a thermal pulse associated with the onset of crustal extension. In this scenario, the M_2-M_3 amphibolite facies overprint would occur at the same time across each unit and at lower pressure conditions, and predict a single population of ages Barrovian ages inconsistent with our data.

the 350 °C isotherm (Fig. 5.16).

Leucogranites with U–Pb ages of 15.5–12.8 Ma cross-cut the mylonite fabrics of the Koronos Shear Zone (Figs. 5.2, 5.12, 5.13, 5.18), and clearly post-date movement on this structure. These dykes have emanating and rotated geometries from the migmatites, indicating they intruded prior to migmatite doming, that gently folds the entire metamorphic carapace. The continuity of structural relationships between the dome and its margins, folding of the Koronos and Zas Shear Zones with consistent top-to-NNE shear fabrics on all margins of the dome, and upright folding that post-dates M_2 kyanite-grade fabrics. The timing of migmatite dome formation and (F_3) NNE–SWW trending upright folding and vertical boudinage within the center of the migmatite dome also must have also occurred at lower pressure (M_3) conditions of 5–6 kbars, 700–730 °C at ca. 15 Ma. Because F_3 upright folds have experienced pure-shear N–S boudinage superimposed on vertical boudinage, we infer the latter stages of dome formation records the transition from compressional to extensional tectonics and places the timing of extension at ca. 15 Ma (Fig. 5.18 and 5.19).

5.5.5 Transition From Compression To Extension And Migmatite Doming

The migmatite dome is the last metamorphic feature to develop on Naxos, occurred at low pressure M_3 sillimanite-grade conditions, refolds the entire metamorphic sequence, and post-dates the decompression of rocks from their peak pressures (10 kbars), which was associated with top-to-NNE shearing. In chapter 4, it was shown that within the migmatite dome, vertical and horizontal boudinage indicate that the dome formed by processes that conform to a switch in stress regime, from prolonged compression and horizontal constriction followed by N–S extension. Although the mechanisms by which gneiss domes form are highly debated (Whitney et al., 2004), the above data can assess the applicability of the various doming mechanisms.

Diapirism, due to the buoyancy contrast between migmatites and the overlying rocks, may contribute to doming and could cause constriction at the center of

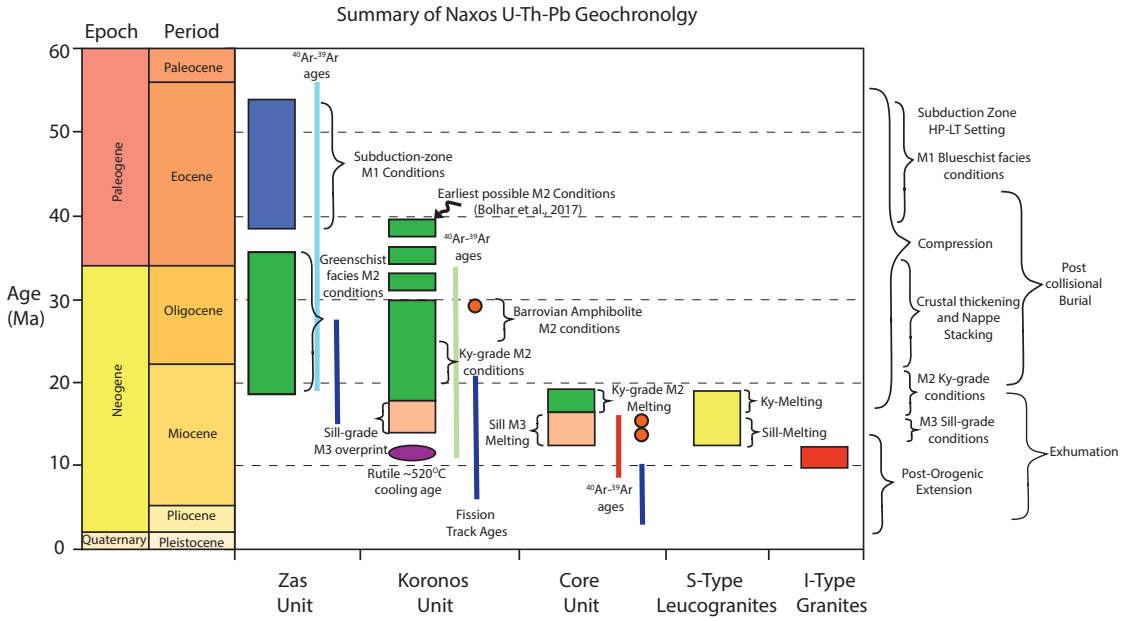


Figure 5.18: Summary of Naxos geochronology with U–Pb data from this study, Keay et al., 2001, Martin et al., 2006 and Bolhar et al., 2017; separated into structural units and granites with compilation of ^{40}Ar–^{39}Ar ages and fission track ages (Seward et al., 2009; Birchau et al., 2006). Zas Unit experienced M_1 conditions 54–45 Ma, with greenschist overprint ca. 40-20 Ma. Koronos Unit experienced M2 conditions ca. 40–18 Ma with M_3 overprint at 16–15 Ma followed by rapid cooling through the 520°C isotherm by 12.7 ± 1.3 Ma. Core Unit experienced anatexis from ca. 18.5–13 Ma with early melting at M_2 kyanite grade conditions and ages younger than 16 Ma at sillimanite-grade M_3 conditions followed by rapid cooling to the surface by 6–10 Ma. S-type leucogranites span ages similar to Core Unit, between 19–12.7 Ma and the Naxos I-type granite intruded at ca. 12.2 Ma (Keay et al., 2001), whilst the metamorphic units were rapidly cooling.

the dome (Ramberg, 1980). However, this cannot be the dominant doming mechanism due to the low overall melt fractions across Naxos migmatites (discussed in chapter 4). Isostasy driven flow of migmatites (Kruckenberg et al., 2011; Rey et al., 2009, 2011, 2017) due to gravitational potential energy gradients under crustal extension, could possibly explain contractional deformation in the center of the migmatite dome, but cannot adequately explain the decompression of migmatites and doming, for several reasons. Firstly, this model is predicted to produce opposing and divergent shear senses on all dome margins in a radial pattern. This is inconsistent with field and microstructural data, that conclusively show all dome margins are associated with consistent top-to-NNE kinematics on a series of ductile shear zones (Koronos Shear and Zas Shear

Zones), that have been later folded by the doming process. For isostasy driven flow to occur under this short timescale (2.5 Ma), it requires excessively large melt fractions and temperatures as predicted by numerical modelling studies (Rey et al., 2011; Rey et al., 2017). The melt fractions required to make this mechanism feasible (>40%) must be much more than can be accounted for based on field and petrological observations in chapter 4, were it was demonstrated that only the deepest levels of the Core Unit experienced muscovite dehydration melting associated locally with up to 20% melt. Finally, upright fold interference and vertical boudinage in the center of the migmatite dome argues for a vertically orientated minimum principal stress (σ_3). This can be easily explained by horizontal constrictional strains as a result shortening in two orthogonal directions creating a Ramsay type-2 fold interference pattern, and not localized compression in a zone of overall extension. Similar features of horizontal constriction are found in other compressional core complexes including Naga Parbat, on the western Himalayan syntaxis (Whipp et al., 2014). To explain the supra-solidus N–S boudinage in leucogranites and amphibolites that overprints the vertical boudinage and upright folding however, requires a rapid switch from constrictional to horizontal extensional strains at around ca. 15 Ma as documented by zircon U–Pb ages from these deformed granites.

There is evidence for a two-fold decrease in the convergence rate between Nubia and Eurasia during the period 18–13 Ma (DeMets et al., 2015). It has been shown that the transition from compression to extension in a regime of overall convergence requires a change with time in at least one of the following: horizontal normal stress applied to the belt by its surroundings; the distribution of shear traction on the base of the belt; the constitutive relation between stress and strain rate of material in the belt itself; the surface height of the belt (Dalmayrac and Molnar, 1981; England and Molnar, 1993; Platt et al., 1986). In a scenario where NE–SW compressional forces start to wane during this transition, some of these mechanisms will become important particularly in the hinterland of an orogenic belt associated with the thickest, hottest and weakest crust. During this window, body forces within the orogeny are expected to dominate.

This may act to rotate the principal stress axes, causing an apparent switch from constructional to NNE–SSW extensional strains. The onset of lithospheric extension would therefore be due to either gravitational potential energy gradients induced due to variations in crustal thicknesses from the Hellenic Trench associated with thin crust, to thicker orogenic crust in the absence of horizontal stresses for a narrow mountain belt (Dalmayrac and Molnar, 1981; England and Houseman, 1989; England et al., 1985; England and Molnar, 1993; Houseman and England, 1986). Alternatively, removal of the lithospheric mantle (e.g. Houseman and England, 1986; Platt and England, 1994) would result in a rapid rise in topography due to inflow of warmer asthenospheric mantle followed by extension (e.g. Garzione et al., 2007).

Following exhumation of migmatites from 10–5 kbars and decompression through the muscovite dehydration melting reaction, larger degrees of ductile flow would be predicted. If the stress regime had switched to NNE–SSW extension in the presence of melt bounded by two stronger layers, a "buckling instability" may have been induced within the rheologically weaker migmatites (Martinod and Davy, 1992; Ismail-Zadeh et al., 2001, 2002; Fletcher and Hallet, 1983). This is predicted to produce a dome with a wavelength on the order of three times the thickness of the overlying stronger layer (Martinod and Davy, 1992). For a 25 km thick stronger layer overlying a weaker partially melted layer, we would expect a dome to form with a half wavelength of 35 km (Martinod and Davy, 1992). This is largely in agreement with the approximate size of the migmatite dome and the distance separating many of the metamorphic domes representing other Cycladic islands. If the migmatites remained supra-solidus during the onset of crustal extension, this mechanism could also be coupled with small degrees of ductile flow derived from gradients in gravitational potential energy due to upper crustal normal faulting (Kruckenberg et al., 2011; Rey et al., 2011, 2017). These models may explain supra-solidus N–S boudinage superimposed on intense contractional features, folded limbs, and the elliptical dome architecture that refolds the earlier top-to-NNE shear zones responsible for the isothermal decompression process. Contrastingly, this two-stage dome forming mechanism, with firstly SSW-directed duc-

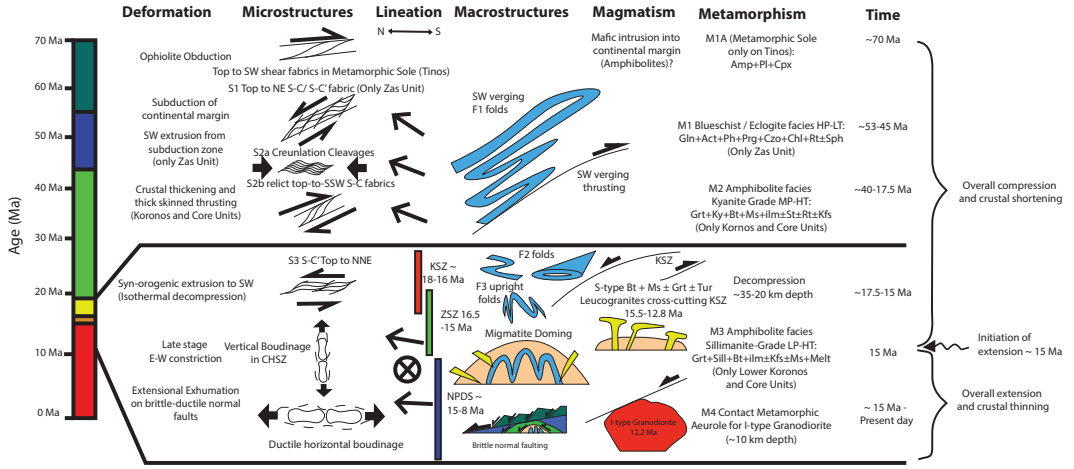


Figure 5.19: Annotated timeline showing the interpreted timing of deformation and metamorphism on Naxos. It summarizes the timing of folding, fabric development, shearing, doming and intrusion.

tile extrusion followed by doming would have a minimal contribution to the isothermal decompression P–T path recorded in migmatites, as doming only occurred once the migmatites obtained 5–6 kbars after their peak pressures.

5.5.6 Post Peak Cooling and Exhumation

Rutile thermochronometry, combined with published ^{40}Ar–^{39}Ar, zircon and apatite fission track cooling ages, reveal the rates and timing of exhumation during retrogression. Rutile ages of 12.7 ± 1.2 Ma of small grains from the base of the Koronos Unit indicate approximate cooling through the 520°C isotherm accounting for grain sizes of 30 μm using the calculation of Cherniak (2000). This 180–200 °C cooling from peak conditions over 2.5 Myrs suggests cooling rates of ca. 60–90 °C/Myr. Assuming a peak geothermal gradient of 40 °C/km, this indicates exhumation rates of at least 3–4.5 km/Myr, a rate only possible by tectonic dendudation (see Fig. 5.16). Although rapid, this is like the initial exhumation rates recorded by the decompression of the migmatite dome which records relative uplift rates of at least ca. 4 km/Myr between 18–15.5 Ma, while the hanging wall remained static. After 15 Ma, integration of ^{40}Ar–^{39}Ar and

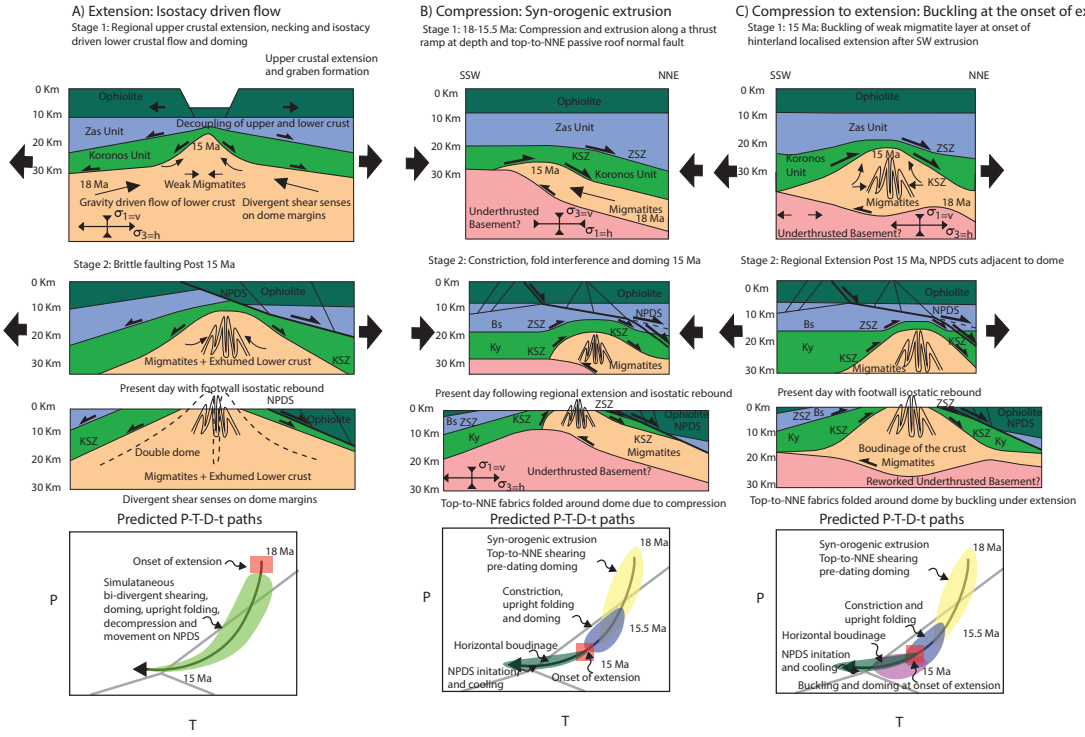


Figure 5.20: Simplified cartoons to illustrate the setup and physics of different extrusion and dome forming models with overlaid conceptual velocity vectors as a thought experiment to compare and contrast the different models. A) Isostasy driven flow during crustal extension. There is a rheological discontinuity between the upper and weak ductile hot crust, with upper crustal extension inducing a gradient in gravitational potential energy and horizontal pressure gradient in the lower crust which converges to remove any horizontal pressure gradients, with the rheological discontinuity acting as a shear zone with opposing shear senses. B) Syn-orogenic extrusion during crustal shortening whereby rocks are continually underthrusted hydrating and therefore partially melting and weakening the overlying wedge that extrudes due to a horizontal pressure gradient from the buoyancy contrast of migmatites and variations in crustal thickness. In this scenario the top of the extruding wedge acts as a passive roof normal fault. C) Buckling instability during the onset of extension. In this setup the migmatites act as a weak layer bounded by 2 stronger layers above and below. During the onset of extension when the overlying stronger layer is approximately three times the thickness of the weaker layer, the weaker layer will buckle producing a dome whereas the stronger layers will neck as predicted by Martinod and Davy, (1992). See text for more discussion.

fission track cooling ages from both the Koronos and Core Units overlaps with or very closely post-dates U–Pb monazite ages by 2–5 Myrs, with an age cluster between 13 and 11 Ma.

The Zas Unit which sat at a structurally higher level was already relatively

close to the surface during this time and also records a kink in its cooling path at ca. 15 Ma, with a jump to accelerated cooling rates. Because this abrupt increase in cooling rate is observed across all levels of Naxos it indicates the whole island rapidly cooled from ca. 15 Ma, presumably due the initiation of the Naxos-Paros Detachment System, responsible for un-roofing the island from mid crustal conditions. This extensional normal fault must have only been active post ca. 15 Ma as it cross-cuts the earlier shear zones and would have acted as the major structure to conductively cool and exhume these rocks at rapid rates. Thermal models of low angle normal faults also predict rapid cooling and migration of the brittle-ductile transition upon extension (e.g. England and Jackson, 1987) in agreement with this data. Normal faulting must not have occurred prior to 15 Ma due to persistence of high temperatures until this time. Therefore 15 Ma represents the maximum age for normal faulting along the Naxos-Paros-Detachment System, as suggested by Cao et al., (2017) and Ryb et al., (2017).

It is unlikely the NPDS was active at a low angle like its present-day dip (15°) throughout its entire history, as minimum vertical uplift rates of 3 mm/yr (corresponding to cooling rates of 60 °C/Myr) (England and Jackson, 1989) would invoke N–S horizontal displacement rates of >10.5 mm/yr (10.5 km/Myr) and >60 km of extension on this single structure integrated over its entire history. This magnitude of localized horizontal extensional motion is not seen in the rock structures within the core complex which adhere to predominantly vertical rather than horizontal motions. Furthermore, the NPDS on west Naxos truncates and telescopes frozen in metamorphic stratigraphy, indicating it must have cross-cut several metamorphic nappes when it was active. The migmatite dome, however, must have formed in its current orientation as it cannot have rotated to shallower angles upon un-roofing. Due to this reasoning, the NPDS must have been active at relatively shallow angles in the ductile crust, cross-cutting metamorphic stratigraphy, but could not be the sole structure responsible for exhumation of the core complex. One possibility was that the NPDS was passively exhumed from the brittle-ductile transition to the surface, as strain became localized

on a series of cross-cutting high-angle normal faults, that are observed to cross cut the island (Fig. 1).

Irrespective of whether the NPDS was active at low angles or not, these calculations conclusively demonstrate that extension and exhumation of the core complex was well under way by ca. 13 Ma, only 2–3 Myrs following peak (M_3) sillimanite grade conditions. The west Naxos I-type granodiorite intruded at ca. 12.2 Ma (Keay et al., 2001), and has sheared margins indicating it intruded syn-tectonically with movement on the NPDS. The country rock at this time would have been recording upper greenschist-facies conditions of 450 °C at ca. 10–12 km depth. The Naxos-Paros Detachment System therefore must have been active between ca. 15–8 Ma and was responsible for exhuming the core complex from ca. 17.5 km at ca. 15 Ma to about 10 km depth by 12 Ma and cooling the footwall at a rate of 60–90 °C/Myr as inferred by comparing U–Pb monazite to rutile ages, in agreement with similar cooling rates calculated from clumped isotope data from Ryb et al., (2017).

5.5.7 Mechanisms For The Switch From Compression to Extension:

Kyanite-grade metamorphism could not have been a local phenomenon, and must have been a regional feature associated with crustal thickening to ca. 50–60 km depth. Kyanite grade rocks and S-type leucogranites are also exposed on the island of Paros, Ios and Delos, indicating this series of Barrovian metamorphic rocks regionally underlie the Cycladic Blueschists. The Cycladic Blueschists also yield a greenschist-facies cooling of 25–20 Ma that we suggest also represents delayed cooling due to ongoing regional Barrovian metamorphism because of thickening and not crustal extension. Thickening the crust by a factor of two is unlikely to occur during continuous slab roll-back, as this is predicted to cause extension from the Eocene to present day. Instead, our data argues for a switch from compressional to extensional tectonics during the middle-late Miocene, specifically at ca. 15 Ma, in agreement with original ideas by Angilier, (1982). Although slab roll-back is a popular model to explain present day extension and core

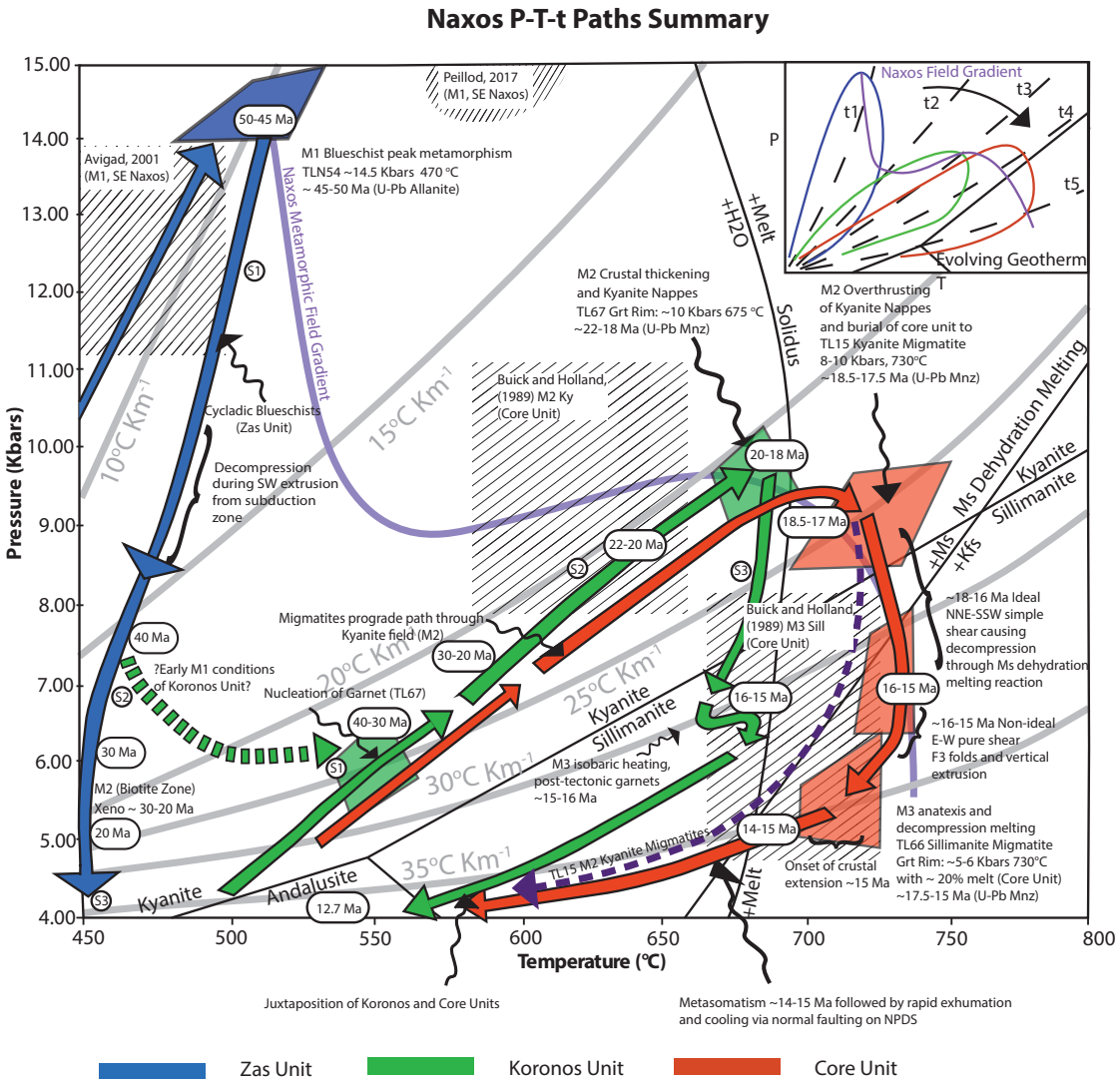


Figure 5.21: *P-T-t* paths of the Naxos metamorphic core complex showing 2 distinct clockwise *P-T-t* loops; firstly a *HP-LT* loop that is associated with subduction of the leading edge of the continental margin and affects soley the Zas Unit. Secodly, a Barrovian type clockwise *P-T* loop that requires crustal thickening to cause peak M_2 conditions at 17.5 Ma, followed by near isothermal decompression to M_3 sillimanite grade conditions and migmatite dome formation.

complex formation, there is growing evidence to suggest it need not be the cause of extension either today or throughout the Tertiary. Although gradients in gravitational potential energy between thick crust in Eurasia and Anatolia and thin crust along the Hellenic trench could be a result of back arc extension and slab roll-back, England et al., (2016) suggest the gravitational potential energy differences between thick and thin

crust are actually the driver of extension. They show that both the magnitudes and spatial variation of the observed GPS velocity field, can be explained by only stresses associated with lateral variations in internal density structure of the lithosphere and argue that tractions caused by flow in the upper mantle exert only a minor influence on the deformation of the lithosphere in this region, thereby making slab-retreat unnecessary for extension. The lack of migration of the present day volcanic arc relative to the Hellenic subduction zone also supports this idea of a static slab, as this has remained in the same position for at least the past 4 Ma (e.g. Pe-Piper and Piper, 2005). In a continuous slab roll-back scenario, a distinct southward trail of volcanism, across the Cyclades would be expected. This is not observed and only a suite of Miocene I-type granites is observed spanning between 14.6 and 12.2 Ma (Tinos at 14.6 Ma, Mykonos at 13.3 Ma and Naxos at 12.2 Ma) (Brichau et al., 2007; Keay et al., 2001). Slab roll-back also predicts extension to occur immediately following peak burial of blueschist-facies rocks, as the locus of subduction migrates further south towards the foreland. Therefore, the entire continental crust to the south of the Cyclades (>300 km) would be expected to have experienced a subduction zone signature and is not supported by this study. Extrapolation of present day extension rates of 12mm/yr back to the Eocene would predict over 1000 km of crustal extension, which is far from being plausible.

The switch from compression to extension during the mid-Miocene could be explained by a two-fold decrease in convergence rate between Nubia and Eurasia between 18–13 Ma (DeMets et al., 2015). In thickened crust, the onset of NNE–SSW regional extension is expected to occur when gradients in gravitational potential energy, induced from variations in crustal thicknesses (between the Hellenic Trench associated with thin crust to thicker orogenic crust under Anatolia), are greater than the horizontal stresses for a narrow mountain belt (Dalmayrac and Molnar., 1981; England et al., 1985; Houseman and England., 1986; England et al., 2016). Alternatively, potassic and ultra-potassic alkali magmatism in Western Turkey has been shown to have migrated southwards from ca. 15 Ma to present day, indicating melting of a lithospheric mantle

source (Soder et al., 2016; Caran et al., 2016). This could either be a result of i) a slab tear at ca. 15 Ma and roll-back on the current Hellenic Trench (Jolivet et al., 2013, 2015) or ii) removal of the lithospheric mantle at ca. 15 Ma, which would cause an increase in elevation due to replacement of warmer asthenosphere (England and Houseman, 1989; Molnar and Houseman, 1997). Both these mechanisms are predicted to trigger regional extension and normal faulting, and could potentially explain why the convergence rate between Africa and Eurasia decreased at around this time.

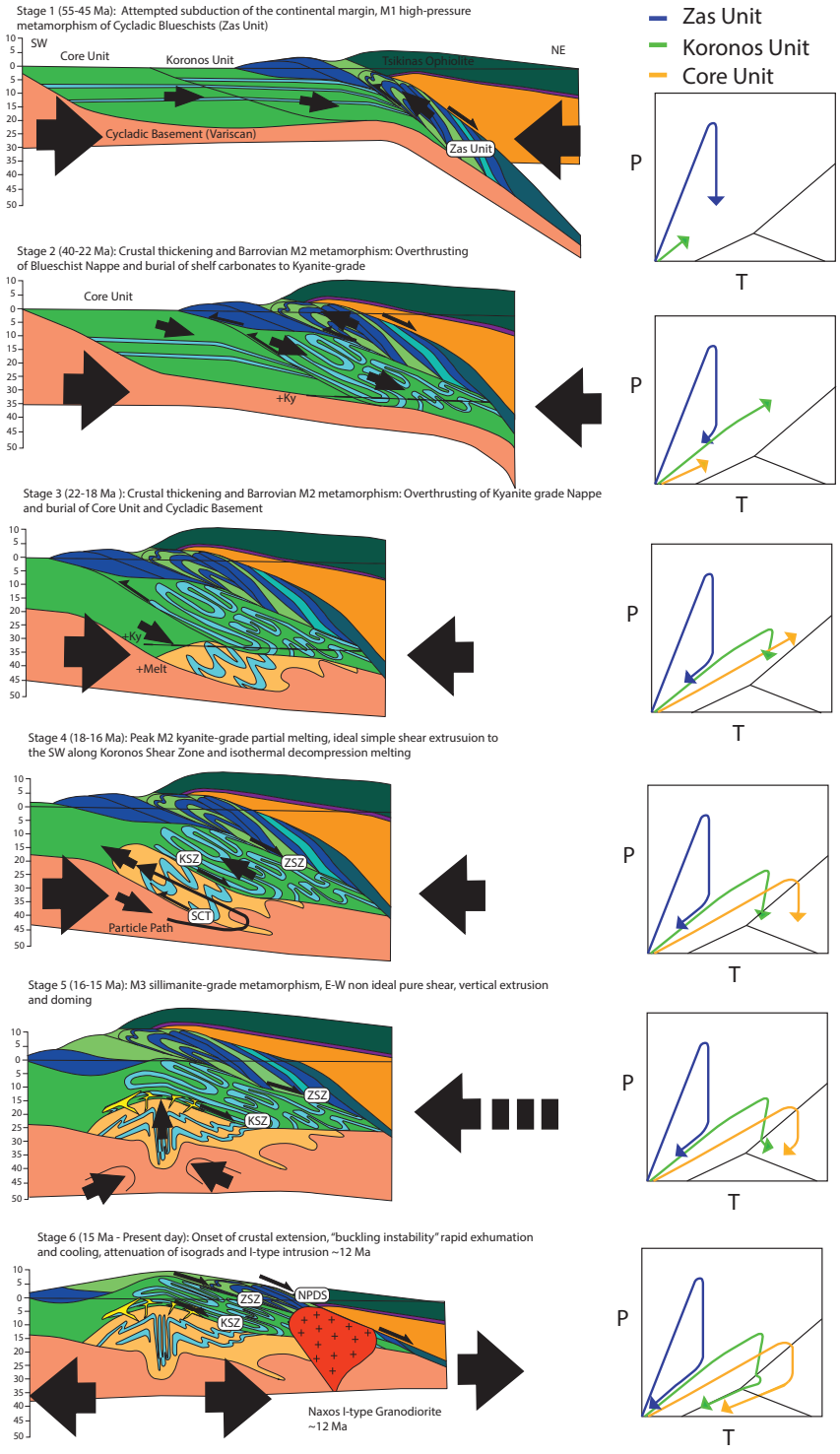


Figure 5.22: Tectonic synthesis for Naxos and the Cyclades based on the data from this study. 1) Ophiolite obduction and high pressure metamorphism of the Cycladic Blueschists (Zas Unit). 2) Crustal thickening and underthrusting of the continental shelf carbonates (Koronos Unit). 3) Continued crustal thickening causing kyanite grade metamorphism in the Koronos and Core Units and eventual partial melting. 4) Syn-orogenic extrusion of the Core Unit under the KSZ and later ZSZ. 5) Transition from compression to extension, formation of the migmatite dome at mid crustal levels. 6) Onset of extension, cooling, initiation of NPDS and I-type granite intrusion.

5.6 Tectonic Model

The data presented in these two chapters highlight that prograde and peak metamorphism on Naxos was diachronous and occurred due to crustal shortening and thickening over a time-scale from ca. 54–15 Ma. Due to the disparity in P–T–D–t paths between each structural level, and the clockwise nature of the P–T paths, we conclude that thrusting and metamorphism during crustal thickening is the simplest explanation of juxtaposition of units with varying tectonic histories, deformation structures and metamorphic grades. In particular, peak metamorphism gets younger and higher grade with increasing structural depth and can be explained by a series of rocks whose peak metamorphic conditions were frozen in at different times, consistent with conductive relaxation of the isotherms following thrusting and thickening. A six-stage scenario presented in Fig. 5.22 and show that Naxos records all stages of what we term the Aegean Orogeny:

1. Ophiolite obduction: Ophiolitic rocks and trench mélange found in the hanging wall of the Naxos-Paros Detachment System represent a remnant dismembered ophiolite that lies at the highest structural level of the Cyclades (Brockner and enders, 1989; Katzir et al., 1996; Stouraiti et al., 2017). This ophiolite must have been obducted during the first stage of compression, during closure of a basin to the NE of the Cyclades (Fig. 5.22a).

2. Subduction and extrusion of the continental margin (54–45 Ma): Northeastward subduction of the leading edge of the continental margin during the Eocene resulted in M_1 high-pressure metamorphism of the widespread Cycladic Blueschists (Zas Unit). Eclogite facies rocks associated with this stage occur on the islands of Syros, Sifnos and Tinos. P–T conditions reached at least ca. 14.5 kbar, 470 °C at 49–46 Ma on Naxos, in agreement with results from Avigad, (1998) and Peillod et al., (2017). During this process, high-pressure rocks were exhumed from beneath lower pressure rocks by buoyancy-driven extrusion along a subduction channel, associated with top-to-NE extensional fabrics formed between 54–45

Ma (Fig. 5.22a). This lies as the highest structural level of the metamorphic sequence and was cooling as the underlying rocks where being underthrusted and metamorphosed along a Barrovian-type prograde P–T path.

3. Crustal thickening, Barrovian metamorphism and partial melting (40–15 Ma): Subduction-zone metamorphism was followed by a phase of post-collisional crustal shortening and thickening, resulting in M_2 regional Barrovian metamorphism 40–15 Ma). Peak M_2 kyanite and M_3 sillimanite-grade metamorphism accompanied partial melting, ductile flow and extrusion of 10–5 kbar kyanite and sillimanite-grade rocks from depths of ca. 35-17.5 km. Thick-skinned thrusting and nappe-stacking would have caused continuous burial and underplating of rocks. At the deepest structural levels, kyanite grade conditions of 10 kbar 670-750 °C prevailed between 22–17.5 Ma and conductive relaxation of the isotherms eventually raised temperatures through the water-saturated solidus at depths of ca. 35-30 km at 18.5–17.5 Ma in the kyanite field whilst under compressional tectonics (Fig. 5.22b).

4. Syn-orogenic Extrusion (18–15.5 Ma): Upon burial to peak-pressures, decompression of migmatites and high-grade gneisses occurred between 18–15.5 Ma and was associated with rapid exhumation from ca. 35-17.5 km depth and development of top-to-NNE extensional fabrics. Although previous interpretations relate this to extension, we suggest it must have occurred due to extrusion tectonics. During crustal shortening, the presence of melt would have weakened the mid-lower crust and may have resulted in ideal simple shear extrusion scenario at (M_2) kyanite-grade conditions, causing the initial decompression of migmatites and gneisses from ca. 10-5 kbar and forming passive roof stretching faults (Koronos Shear Zone and Zas Shear Zones) with top-to-NNE shearing fabrics that were active between 18–15.5 Ma. Ductile flow of material to the SSW resulted in general shear (simple shear plus pure shear) and constriction and produced (F_2) sheath folds (Fig. 5.22c). Top-to-NNE movement across the ductile shear-

zones resulted in large jumps in P–T conditions and condensed a sequence of right way-up isograds by the process of general shear. These structures resemble the South Tibetan Detachment normal sense shear zones in the Himalaya that also preserve earlier thrust related fabrics (Law et al., 2006; Jessup et al., 2006; Searle et al., 2006, 2010). This mechanism explains the decompression history of migmatites to mid-crustal depths, that pre-dates deformation related to regional extension and all structural, petrological phenomenon.

5. Migmatite Dome Formation (15.5–15 Ma): Following decompression to (M_3) sillimanite-grade conditions, constriction occurred in the mid-crust at 5–6 kbars, 700–730 °C , resulting in intense upright NNE-SSW trending F_3 folding and vertical boudinage within migmatites and formation of the migmatite dome, that folds the earlier shear zones and rotates emanating leucogranite dykes (Fig. 5.22d). This doming process would have become amplified upon crossing the muscovite-dehydration melting reaction, allowing constrictional strains to become localized on pre-existing weakened zones affected by larger melt fractions. We attribute doming to the combined effects of N–S and E–W shortening followed by a rotation of the principal stress axes coinciding with the timing of peak M_3 conditions. This occurred as a result in changes in far field stresses and resulted in the onset of N–S extension. Relative juxtaposition of hot migmatites against colder, higher level kyanite-grade rocks caused a sillimanite-grade (M_3) metamorphic overprint in the carapace, that outlasted deformation and resulted in growth of post-tectonic garnet and sillimanite.

6. Crustal Extension (15 Ma–Present Day): The formation of the sillimanite-grade migmatites on Naxos marks the climax of high-grade metamorphism in the Aegean, and no evidence for crustal thickening post-dates this event. Within the migmatite dome, N–S horizontal extensional boudinage in high-grade gneisses overprints earlier isoclinal folds. This corresponds to the final stage of migmatite dome formation and marks the transition from regional compression to extension

in the Cyclades (Fig. 5.22e). DeMets et al., (2015) document a 2-fold decrease in convergence rate between Nubia and Eurasia coinciding with the timing of doming. A waning of far-field compressional forces may have caused a change in the deformation styles and strain distribution within the orogeny. We would expect NNE–SSW regional extension to initiate following thickening due to either three possibilities. 1) Roll-back on the current Hellenic trench. 2) Gradients in gravitational potential energy induced by variations in crustal thickness in the absence of substantial horizontal stresses. 3) Alternatively, removal of the lithospheric mantle could initiate regional extension due to a rapid increase in topography that is gravitationally unsupported (England and Houseman, 1997). Upon the switch to regional Aegean extension at ca. 15 Ma coinciding with the end of (M_3) sillimanite-grade conditions, it has been proposed that ductile flow in the presence of melt may drive extensional dome mechanisms. Upon this switch, a buckling instability may have developed in high melt fraction migmatites amplifying the internal dome structures or alternatively, small degrees of isostasy driven flow may have occurred (Kruckenberg et al., 2011; Rey et al., 2009, 2011, 2017). The onset of extension was associated with rapid cooling rates (60-90°C/Myr) due to upper crustal normal faulting combined with ductile pure-shear boudinage and thinning of the mid-lower crust. This post-dates the extrusion of migmatites, truncates and is discordant to all shortening features and shear zones and telescopes the previously frozen in metamorphic stratigraphy producing a metamorphic field gradient of 700 °C/km on west Naxos. Extension must only contribute to the final stage of the exhumation from mid-crustal depths to the surface.

5.7 Conclusions

Six major conclusions can be emphasized from this study:

1. The Naxos metamorphic core complex represents a cross section through a folded and thickened continental margin sequence with evidence for three distinct tectono-

stratigraphic units which each experienced different tectonic and metamorphic histories over a 50 Myr time period.

2. Naxos records a complete orogenic cycle, from ophiolite obduction, high-pressure metamorphism, crustal thickening and regional metamorphism to extensional exhumation. The hanging-wall of the core complex represents an ophiolite mélange associated with the obduction of an ophiolite that sits as the highest structural level across-the Cyclades. Structurally beneath this lies the Zas Unit that attained M_1 high-pressure conditions of ca. 14.5 kbars 470 °C, recording the attempted subduction of the continental margin at between ca. 49–47 Ma. These are associated with top-to-NNE extensional fabrics that pre-date crustal extension and are related to extrusion from the subduction zone.

3. The Koronos and Core Units at deeper levels did not get subducted and instead record a clockwise P–T loop characteristic of Barrovian metamorphism between 40–15 Ma as a result of overthrusting of the Cycladic Blueschists and thick-skinned thrusting of the basement over sedimentary cover. The Koronos Unit records peak M_2 kyanite grade conditions of 10 kbar 600–670°C at between 22–17 Ma. The structurally deeper Core Unit obtained peak M_2 kyanite grade anatectic conditions of 8–10 kbars 670–750°C between 18.5–17 Ma and records a sillimanite grade lower pressure overprint of 5–6 kbars, 700–730°C between 16–14 Ma. Metamorphism propagated down-structural section with time. Peak metamorphic conditions approximately 25–30 Myrs following overthrusting, consistent with the predictions of simple thermal models.

4. The decompression of gneisses and migmatites from 10–5 kbars occurred by SW directed syn-orogenic extrusion on a series of passive roof normal faults associated with top-to-NNE shearing between 18–15.5 Ma. These shear zones pre-date doming and are folded around the dome with consistent top-to-NNE kinematics on all dome margins. The exhumation of migmatites is a completely separate process to migmatite doming. Extrusion of migmatites from ca. 35–17.5 km depth

must act as fundamental process in the advection of heat and fluids through the continental crust.

5. The migmatite dome is a late feature that refolds all frozen in metamorphic stratigraphy. It post-dates isothermal decompression of migmatites through the muscovite dehydration melting reaction to 5–6 kbars at ca. 15.5–15 Ma. Dome formation firstly occurred by horizontal constriction under deep-seated compression resulting in vertical boudinage and upright isoclinal folding between ca. 15.5–15 Ma. This was followed N–S pure shear extensional boudinage due to rotation of the stress axes associated with the transition from compression to extension at ca. 15 Ma. The late stages of dome formation could have been facilitated by the development of a buckling instability following the switch from compression to extension.

6. The initiation of crustal extension at ca. 15 Ma was associated with 2-fold slowdown in convergence rate between Nubia and Eurasia. On Naxos, it was associated with rapid cooling at rates of 60–90°C/Myr and migration of the brittle-ductile transition. The Naxos-Paros Detachment System initiated after 15 Ma and cross-cuts all metamorphic stratigraphy, internal shortening features, shear zones and leucogranites. The 12.2 Ma Naxos I-type granodiorite has sheared margins indicating it intruded coeval with movement on the fault.

This new data support a compressional origin to the Barrovian metamorphism and anatexis within the Naxos metamorphic core complex. The switch from compression to regional Aegean extension at ca. 15 Ma was associated with rapid cooling, upper crustal normal faulting, combined with horizontal N–S pure shear in the ductile crust. After ca. 15 Ma, low angle normal faults were responsible for the final stages of core complex exhumation from the brittle-ductile transition to the surface. These cross-cut all earlier frozen in metamorphic stratigraphy and fabrics that formed in a compressional setting over a 50–15 Ma time period.

Chapter 6

Coeval I and S-type granitoids on Tinos and Delos, Grecce

6.1 Introduction

Since the first description of I- and S-type granites by Chappell and White (1974), who differentiated between granites formed by igneous-sourced melt as "I-type", and those formed from sedimentary sourced melt as "S-type", the I and S-type granite classification scheme has been applied to many granitic terranes around the world (Beckinsale, 1979; Grosse et al., 2011; Ng et al., 2015). I-type granites typically contain hornblende and titanite, whereas S-type granites typically contain muscovite, andalusite, cordierite, and garnet (Chappell and White, 1974). I- and S-type granites can also be discriminated from each other by their different geochemical and isotopic behaviour, such as the aluminium saturation index, proportion of potassic to sodic oxides, trace element patterns and Sr-Nd isotopic compositions.

Rarely in the geological record do both I and S-type granites form in the same location at almost the same time. One such location where this phenomenon occurs is within the Cycladic metamorphic core complexes in the Central Aegean Sea, Greece. The relationship between I and S-type granitoids is interesting, as they intrude the footwalls of several metamorphic core complexes, and are closely associated with

normal faulting and normal sensed ductile shearing responsible for their exhumation. The emplacement of the I-type granites also coincides with peak (M_3) sillimanite-grade metamorphism and partial melting at the deepest levels of the Cyclades (Buick, 1991; Keay et al., 2001; Lamont et al., under review) and overlaps with the onset of rapid cooling and exhumation during the middle-late Miocene, which has been previously interpreted to be a result of the regional Aegean extension (e.g. Lister et al., 1984).

The island of Tinos is particularly important as the oldest "I-type" monzogranite in the Cyclades crops out (Brichau et al., 2007), and it displays the most complete magmatic evolution. Subsidiary dacite dykes and smaller garnet-bearing leucogranite intrusions crop out which together display key cross-cutting relationships to low-angle normal faults and structures related to regional extension (Brichau et al., 2007; 2010). A key question is deciphering whether the leucogranites can be derived from the same source as the "I-type" hornblende-biotite plutons or vice versa. Determining the origin and exact age of granitoid crystallization is therefore crucial to constraining the magmatic evolution of the Cyclades as well as the timing and rates of deformation, exhumation and crustal extension on Tinos and the central Aegean. The island of Delos is also important as leucogranites occur in-situ with sillimanite grade gneiss, and crop out immediately adjacent to a larger I-Type pluton, the Mykonos monzogranite (Denele et al., 2011).

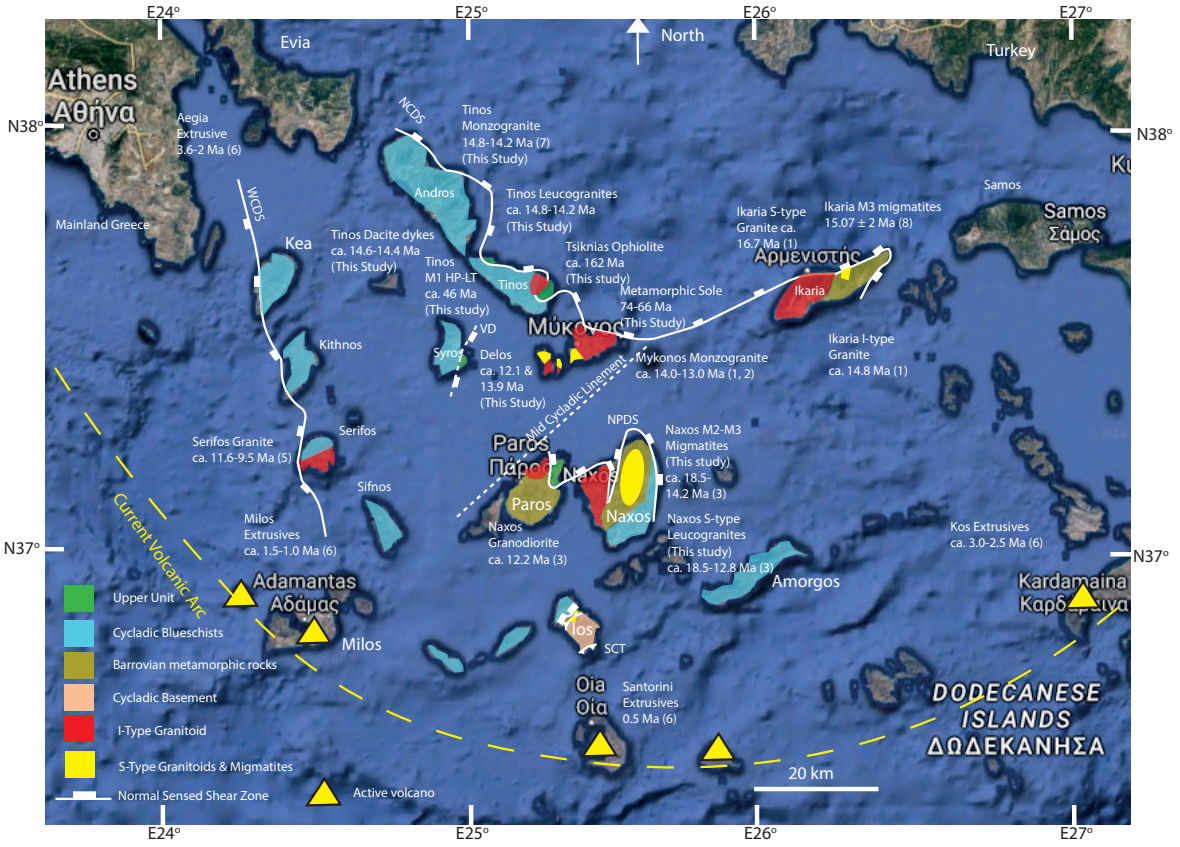
In this contribution, new U–Pb zircon geochronology is presented and integrated with whole-rock geochemistry from both I- and S-type granitoids to gain insight into their origin. This is tied into a sequence of intrusion, fabric development, deformation and exhumation of Tinos, and linked into the evolution of the "Aegean Orogeny".

6.2 I-Type And S-Type Magmatism in The Cyclades

I-type magmatism has episodically occurred throughout the Aegean throughout the Cenozoic (Pe-Piper, 2002), and is associated with several types of igneous rocks. Calc-

alkaline arc-related I-type granitoids form large plutons of granodiorite or monzogranite composition. The origin of these granitoids has been the subject of considerable debate. Some authors propose they are derived from crustal melts that mixed with mantle-derived mafic magma (Altherr et al., 1982, 1988, 1992; Pe-Piper et al., 2005, 2006) as they show a strong crustal influence (Pe-piper and Piper, 2002). However, the popular interpretation involves them being derived from a hydrated mantle wedge and emplaced above the Hellenic subduction zone (Fytikas et al., 1984). Fytikas et al., (1984) showed that the calc-alkaline volcanism episodically shifted southward across the Aegean throughout the Cenozoic and interpreted this trend to represent migration of the volcanic arc due to slab roll-back which resulted in regional extension (Lister et al., 1984; Pe-piper and Piper, 1989; Block and Royden, 1993). In the middle to late-Miocene, it is suggested the magmatic arc reached the Cyclades producing arc related volcanic rocks between 12–5 Ma (Fytikas et al., 1984; Weidmann et al., 1984) and I-type batholiths spanning from ca. 14.6–11 Ma (Keay, 1998, Brichau et al., 2007, 2010; Iglseder et al., 2009). In the Cyclades, the largest I-type plutons outcrop on the islands of Tinos, Mykonos, Ikaria, Paros, Naxos and Serifos, with published U–Pb ages spanning between ca. 14.6 Ma on Tinos (Brichau et al., 2007) to ca. 12.2 Ma on Naxos (Keay et al., 2001) and ca. 11 Ma on Serifos (Iglseder et al., 2009). Regional extension has undoubtably occurred during the last ca. 15–10 Ma, and has led to the development of a series of bivergent low-angle normal fault systems and ductile shear zones. These include the North Cycladic Detachment System (NCDS) exposed on Andros, Tinos and Mykonos with top-to-NE kinematics (Jolivet et al., 2010), the Naxos-Paros Detachment System (NPDS) on Naxos and Paros with top-to-NNE shearing, the West Cycladic Detachment on Kos, Serifos and Sifnos with top-to-SW motion (Grasemann et al., 2012), and the Messari Detachment on Ikaria also with top-to-NW displacement (e.g. Beaudoin et al., 2015; Lauren et al., 2015). However, the timing of initiation of regional extension remains controversial.

With the exception of the current volcanic arc, which has been in its present position during the last 4 Ma (e.g. Matsuda et al., 1998; Pe-Piper and Piper, 2005,



.

Figure 6.1: Location map summarising the reported U-Pb ages of Cycladic granitoids with new ages from this study; NCDS=North Cycladic Detachment System, NPDS=Naxos-Paros Detachment System and WCDS=West Cycladic Detachment System. References: (1) Bolhar et al., (2010); (2) Brichau et al., (2010); (3) Keay et al., (2001); (4) Brichau et al., (2007); (5) Igelseder et al., (2009); (6) Matsuda et al., 1999 (Ar-Ar volcanics), (7) Beauodin et al., 2015

Stourati et al., 2010), volumetrically smaller yet distinct I-type magmas formed between the Middle-Miocene to Pleistocene and include: (1) Arc calc-alkaline volcanism with minor tholeiitic components characterising the Pliocene-Quaternary Aegean arc and some volcanic rocks. In the recent volcanic arc, the erupted products have greater contributions from the lithospheric mantle and crust in the western part of the arc than in the central and eastern part (Pe-piper, 2008). (2) Early-Mid Miocene shoshonitic volcanic rocks in the Northern Aegean and Western Anatolia which were derived from a subcontinental lithospheric mantle enriched by past subducted material. (3) Small volume back-arc basalt, rhyolite and trachyte volcanic rocks, which are associated

with sub-alkaline rocks and display characteristics of shoshonites, the source of which is interpreted to be enriched sub-continental lithospheric mantle. Back-arc basalts were erupted in the eastern Aegean and western Anatolia from the Mid-Miocene to the Quaternary, while Late Miocene trachytes are also present in the western Aegean and western Rhodope. (4) High-Mg basalts exposed in Evia, Skyros and Chios show geochemistry of adakite affinities (Pe-Piper and Piper, 1994. Back-arc basalts are thus interpreted as the result of local mantle melting during crustal thinning in the back-arc region. (5) Alkali volcanic rocks including potassic and ultra-potassic volcanism in Western Anatolia were erupted during the Plio-Quaternary (Soder et al., 2015; Caran et al., 2016). There is a southward trail of ultra-potassic volcanism between 15 Ma to present day, interpreted to be a result of influx of hot asthenospheric mantle into the mantle wedge due to slab rollback or a slab tear (e.g. Jolivet et al., 2015). Despite this framework, the origin and emplacement mechanisms of Cycladic I-type granitoids remains controversial, as their emplacement ages occur over such a short duration (ca. 14.6–11 Ma) and overlap with, or slightly post-date, adjacent S-type leucogranite dykes and sills, which formed as a product of regional metamorphism and partial melting at deep structural levels of the Cyclades between 18.5 and 13.5 Ma (Pe-piper and Piper, 1997; Keay et al., 2001; Lamont et al., under review). The S-type granitoids are similar to the collisional S-type leucogranites found in the Himalayan region (Searle et al., 2010), as they are not voluminous plutons, but are associated with widespread exposure of regions characterized by Barrovian metamorphism and migmatisation. These relationships are best exposed on Naxos but also occur on several other islands including Delos, Tinos, Paros and Ios (Pe-Piper, 1997, 2000; Keay et al., 2001; Lamont et al., under review; personal observation).

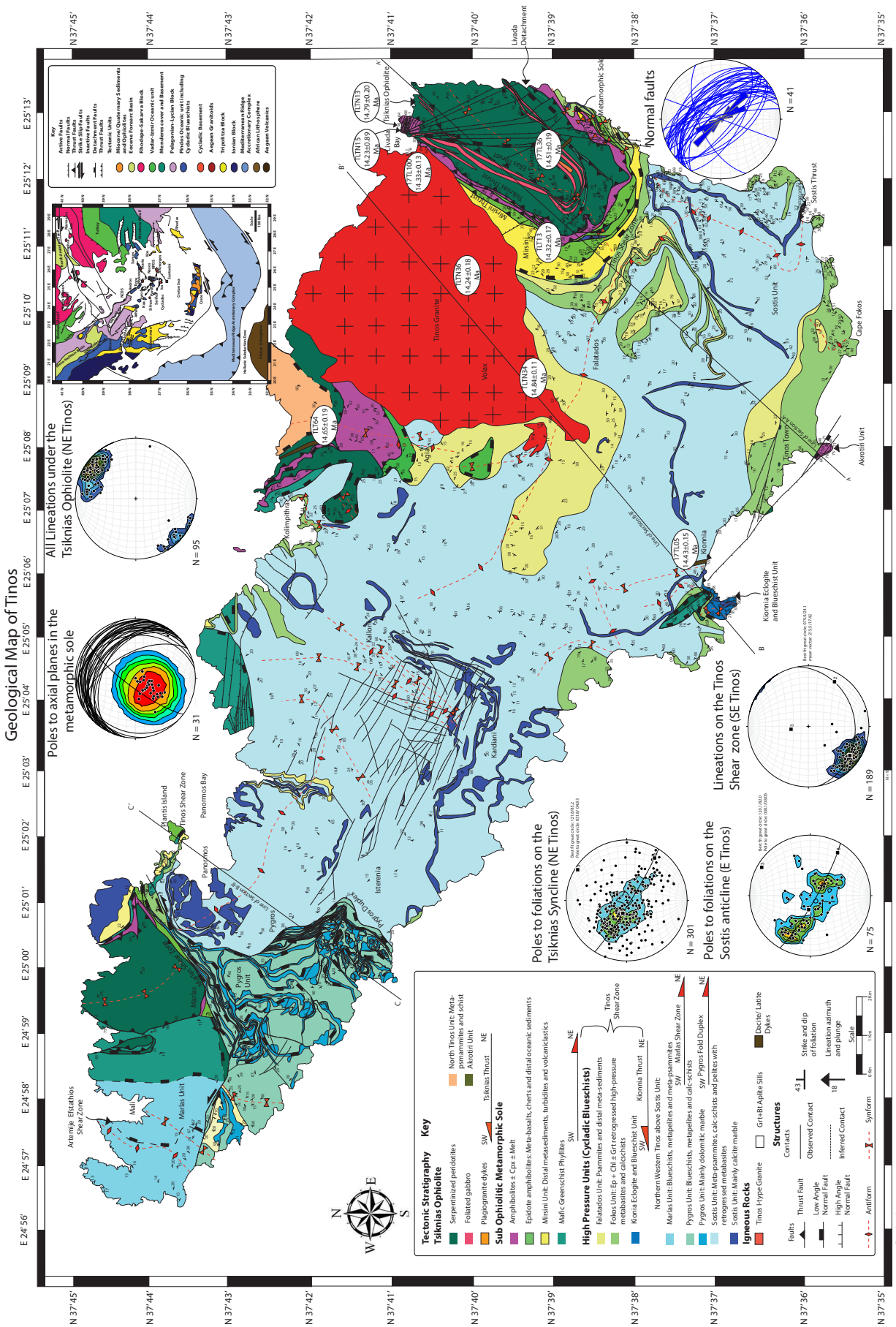


Figure 6.2: Geological map of Tinos with sample locations and U-Pb ages

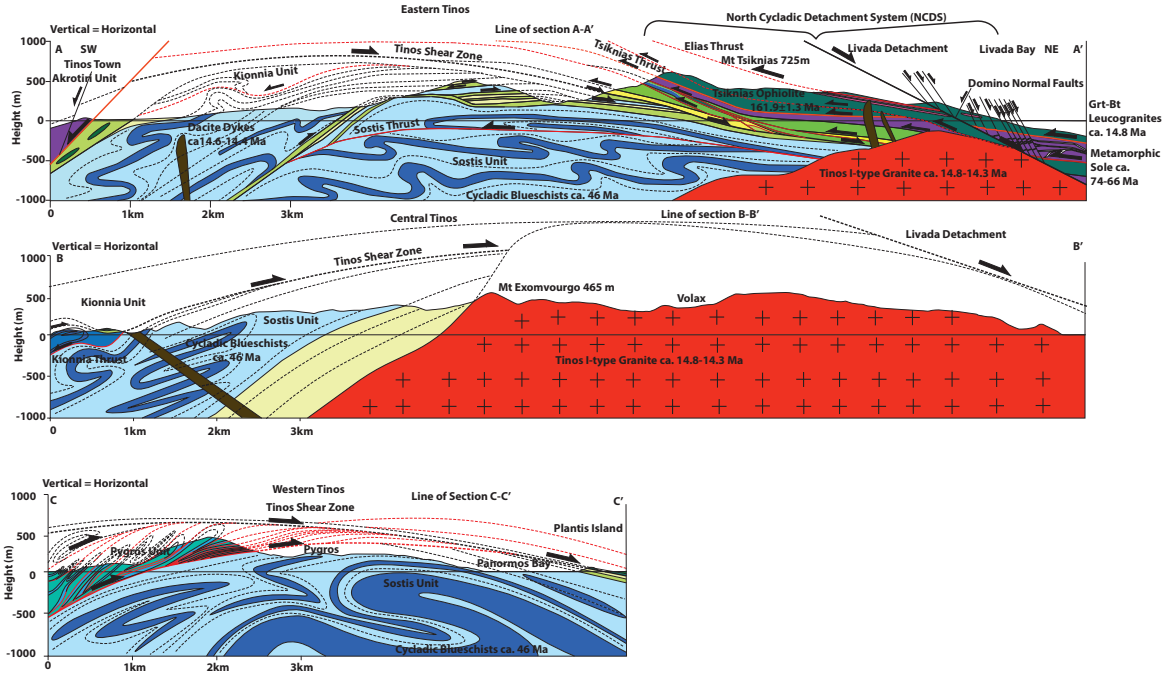


Figure 6.3: Cross-sections showing the cross-cutting relationships of the granites and the NCDS on Tinos

6.3 Field Relations and Petrography

6.3.1 The North Cycladic Detachment System and Extensional Deformation on Tinos

The tectonostratigraphic framework of Tinos comprises two major tectonic units: i) The Upper Unit comprising the ca. 162 Ma Tsiknias Ophiolite and ca. 74 Ma metamorphic sole with a 190 Ma protolith (see chapter 2); and ii) The Lower Unit comprising high-pressure blueschist and eclogite facies metamorphic rocks of the Cycladic Blueschist Unit that obtained peak conditions at ca. 46 Ma (Fig. 6.2-6.3) (chapter 4). The Tinos Shear Zone is a top-to-NE normal sense ductile shear zone that separates the two distinct units, and is folded about the main NW-SE trending dome axis running down the centre of the island. Top-to-NE shearing on this structure occurred concomitantly with (M_2) greenschist-facies conditions dated at ca. 21–18 Ma by Rb–Sr (Bröcker and Franz, 1998; Zeffren et al., 2005) (Fig. 6.3). This greenschist-facies tectono-metamorphic event has not been detected in the Akrotiri Unit (Patzak

et al., 1994) or the rest of the Upper Unit, which originated at much higher structural levels.

A series of brittle normal faults cross-cut the Upper Unit, above the Tinos Shear Zone, particularly on the northern coastline. Together, the Tinos Shear Zone and the series of normal faults make up the North Cycladic Detachment System (NCDS) (Jolivet et al., 2010) which also outcrops along strike on the north coast of Mykonos to the east, and Andros to the west. The NCDS is interpreted to represent a crustal scale low-angle normal fault that accommodated up to 100 km of extension during the Miocene (Jolivet et al., 2010; Jolivet et al., 2002; Jolivet and Partot, 1994). The Tinos granites intrude this sequence of normal sense shear zones during the Miocene and therefore place tight time constraints on the sequence of deformation.

6.3.2 Tinos Hornblende Biotite Monzogranite

The large hornblende, biotite and titanite-bearing monzogranite pluton intrudes both the Upper and Lower Units and the Tinos Shear Zone in Northern and Central Tinos and has a U–Pb age of ca. 14.6 Ma (Brichau et al., 2007). Its mineralogy comprises (35%) plagioclase, (31%) quartz, (17%) K-feldspar (16%) biotite, (3%) hornblende and (2%) titanite. It is largely undeformed and exhibits magmatic textures (Faure et al., 1991) with a magmatic foliation defined by weakly aligned euhedral K-feldspar, plagioclase, biotite and hornblende and quartz; the latter is associated with little or no signs of deformation or recrystallization. However, near the structurally highest exposed parts of the monzogranite, the dip of the magmatic foliation is moderate to sub-horizontal and the long axes of prismatic K-feldspars define a weak NE stretching lineation. Along the southwestern margin, Brichau et al., (2007), noted the monzogranite locally displays a very weakly formed sub-horizontal tectonic foliation associated with weak NE trending stretching lineations defined by recrystallized, flattened and elongated quartz grains and aligned biotite (Fig. 6.5). Here, quartz forms polycrystalline ribbons, shows undulose extinction, dynamic recrystallization and grain boundary migration (Brichau et al., 2007) indicating solid-state deformation occurred immediately following crystal-

lization. In discrete localities in contact with the host meta-psammites of the Lower Unit it locally displays a well-developed solid-state foliation. Brittle deformation structures overprint these features over a range of scales, from km-scale normal faults to microscale-normal faults through K-feldspar and hornblende grains at moderate to high angles to the magmatic and tectonic foliation. A metamorphic aureole around the Tinos granite has been described by Brockner and Franz, (2000), who note kinked metamorphic biotites which yielded a Rb-Sr age of 10–8 Ma. However, detailed field mapping and petrographic study of what was described as a contact aureole rocks to the eastern side of the pluton by Lamont et al., (under review) found that the rocks previously described as part of a large metamorphic aureole and Tinos Shear Zone mylonites actually represent the metamorphic sole to the Tsiknias Ophiolite associated with top-to-SW fabrics that formed at ca. 74–66 Ma (rather than Miocene ages associated with top-to-NE with the Tinos shear zone interpretation). It is only within 50 m of the granite contact where contact metamorphic textures are found, including diopside-hornblende rims on pre-existing amphibole, and coarse titanite that cross-cuts the earlier obduction related S_{2b} fabrics. Because the pluton cross-cuts the Tinos Shear Zone and mostly exhibits post-kinematic relationships, the age of the undeformed granite provides a minimum constraint on the timing of pervasive shearing on the Tinos Shear Zone, whereas sample TLTN34 taken from a deformed margin places an absolute maximum lower age limit on ductile deformation on the Tinos Shear Zone.

6.3.3 Garnet Muscovite Leucogranite Sills

Garnet bearing leucogranites (Fig. 6.4-6.5) intrude through the monzogranite pluton and emanate into the Upper Unit, intruding through the metamorphic sole to the Tsiknias Ophiolite in Livada Bay in NE Tinos. They are characterized by dominantly plagioclase (45%), quartz (35%), and K-feldspar (7%) with <300 µm diameter garnets (4%), muscovite (5%) and biotite (3%). The leucogranites typically occur as a branching network of sills, typically between 10's cm to several meters wide (Fig. 6.4-6.5). These sills intrude parallel to the amphibolite sole mylonite foliation (S_{2b} obduction



Figure 6.4: Outcrop phographs of the Tinos granitoids: A and B) Domino normal faults at Livada Bay that cross-cut the Grt leucogranite sills(N37.612165, E25.242085) C) Tinos Monzogranite intruding into the amphibolites of the metamorphic sole (N37.609699, E25.238379), D) Western edge of the Tinos Hb-Bt pluton (N37.577060, E25.167255), E) 17TL36 undeformed dacite dyke intruding the Tsiknias Ophiolite (N37.580870, E25.234811). F) 17TL05 dacite dyke intruding Kionnia Bay (37.553493, 25.134870), G) Dacite dyke weakly deformed east of Kolimpritha Bay N37.628227, E25.164213

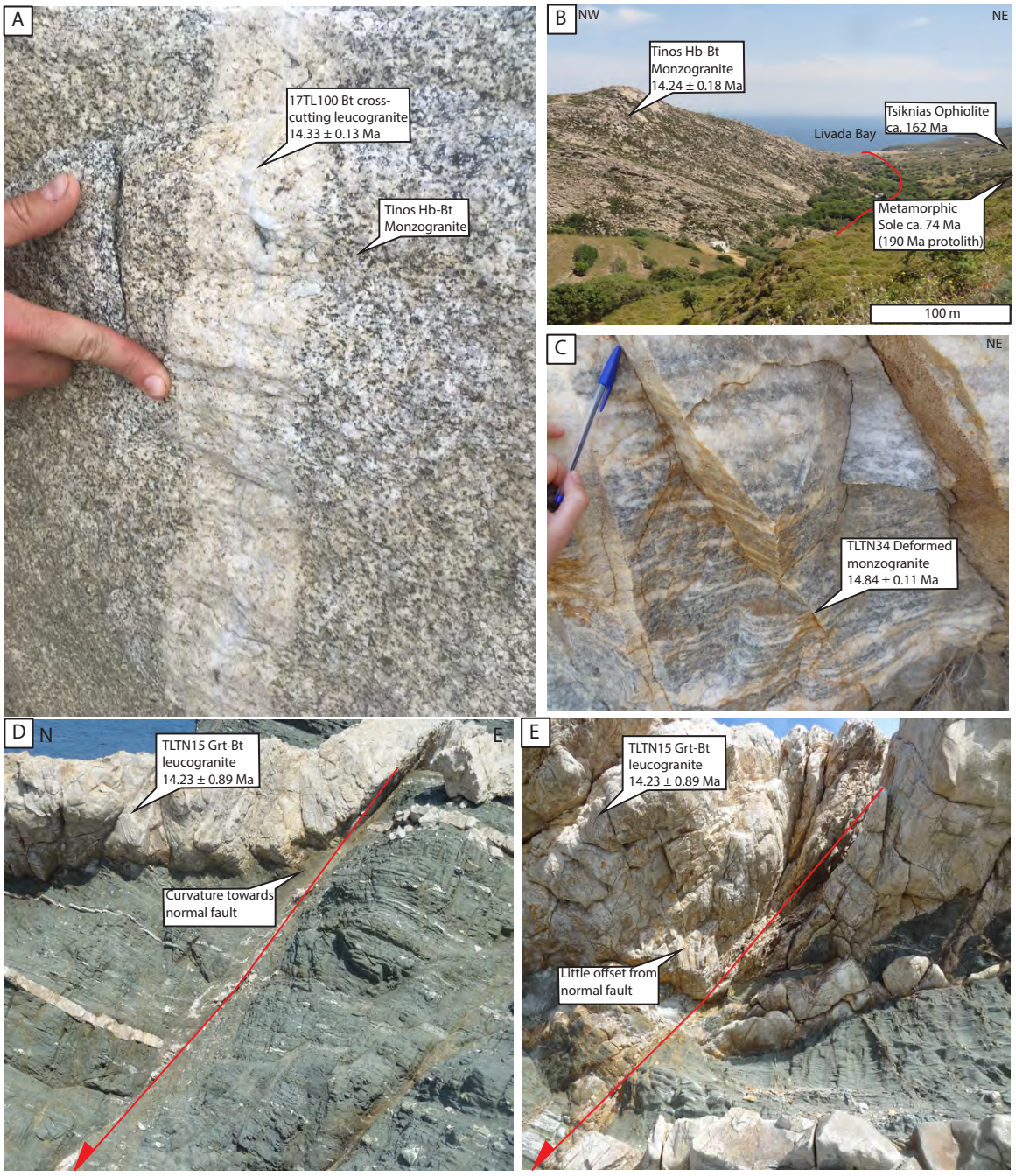


Figure 6.5: Cross-cutting relations of Tinos Granitoids: A) 17TL100 cross-cutting leucogranite through the Tinos pluton (N37.610454, E25.236740), B) Livada Bay showing the Tinos pluton intruding into the Upper Unit (N37.587249, E25.210244), C) TLTN34 deformed monzogranite (N37.582920, E25.175475, D and E) Livada Bay normal faults showing possible faulting during granite crystallization (N37.613040, E25.244052)

fabric) and are clearly cut by a spectacular series of domino style normal faults that cross-cut the poorly exposed Livada Detachment at Livada Bay (Fig. 6.3-6.4), each with an offset of between 1–10 m.

Although many of the sills are clearly cut by the brittle normal faults, some smaller subsidiary smaller sills show curvature into alignment with the faults, indicating that they had just crystallized as normal faulting took place, (Jolivet et al., 2010). Within the leucogranites, a tectonic foliation is defined by flattened and elongated quartz and biotite and a NE-directed stretching lineation is expressed by stretched quartz aggregates and aligned muscovite. Quartz forms polycrystalline ribbons and displays undulose extinction, dynamic recrystallization and grain boundary migration, suggesting NE–SW directed ductile deformation occurred immediately following crystallization whilst still reasonably hot. Keay, (1998) reported a U–Pb zircon age of ca. 14 Ma; however no structural context or geochemistry was provided with this age. The subsequent age of leucogranite crystallization therefore constrains an upper limit on the timing of brittle normal faulting that post-dates the major phase of ductile deformation on Tinos.

6.3.4 Dacite-Andesite Dykes

Several dacite dykes intrude both the Upper and Lower Units on Tinos (Fig. 6.4) (Avigad et al., 1998). Their mineralogy comprises plagioclase (61%) phenocrysts, biotite (18%), and hornblende (10%), in a fine-grained groundmass with quartz (<10%) and titanite (3%). These dykes occur in several locations across Tinos (Fig. 6.2) including: i) Kionnia Bay, where a dyke cross-cuts high-pressure (S_{2b}) top-to-SW fabrics associated with the Kionnia Thrust; ii) to the NE of Kolimpritha Bay within the metamorphic sole amphibolites and Tsiknias Ophiolite; and iii) across the Tsiknias Ophiolite Moho Transition Zone sequence of alternating gabbros and peridotites on the eastern side of Mt Tsinkias. Most of these dykes are undeformed and because they intrude both Upper and Lower Units they also cross-cut the Tinos Shear Zone and post-date pervasive ductile top-to-NE shearing on the Tinos Shear Zone. However, sample 17TL-36

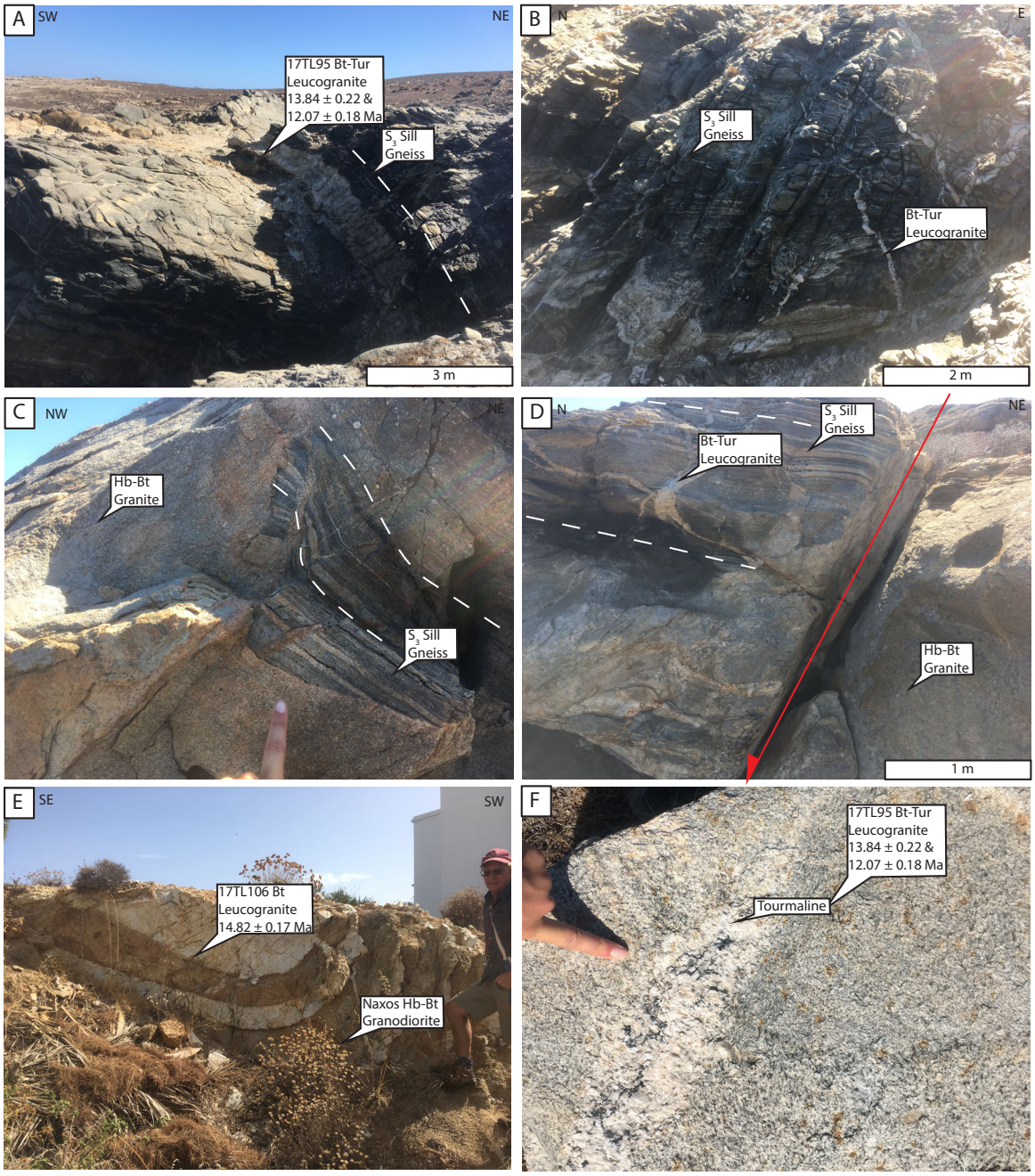


Figure 6.6: Delos and Naxos Granites: A-D (N37.406667, E25.267651) The Delos Hb-Bt monzogranite which cross-cuts a Bt-Tourm leucogranite sills, both granitoids cross-cut the M_3 foliation, E) Deformed leucogranite within the Naxos granodiorite (N37.073962, E25.399889, E) Close up photograph of 17TL95 with cm sized tourmaline and biotite

represents a mildly deformed dyke on the north east side of Kolimpritha Bay that intrudes the Upper Unit adjacent to a highly localized deformed zone within the Upper Unit above the Tinos Shear Zone. Its age therefore represents the timing of localized top-to-NE shearing.

All dykes are up to 10 m wide, are orientated at moderate dips and display consistent emanating geometries from the interior of the island (the centre of the fold axis), possibly indicating they have experienced gentle folding post-emplacement. The best available age constraint for these dykes is an Ar–Ar age of ca. 12–11 Ma (Avigad et al., 1998), although this is unlikely to represent the true age of crystallization and is more likely to represent a cooling age. The subsequent U–Pb ages therefore place constraints on the seizure of pervasive and distributed shearing on the Tinos Shear Zone.

6.3.5 Delos Biotite-Tourmaline Leucogranites

Leucogranite sills crop out on Delos along the top-to-NE regional foliation in M_3 sillimanite-grade gneisses and migmatites, directly adjacent to the I-type Hbl–Bt I-type pluton (Mykonos monzogranite) (Fig. 6.6). The leucogranites cross-cut the foliation and are mainly two-mica leucogranites, but biotite + tourmaline leucogranites also locally crop out (Sample 17TL95). Their occurrence is very similar to the leucogranites exposed on Naxos, where they formed as a result of muscovite dehydration melting at M_3 sillimanite-grade conditions. There is no reported U–Pb age on granitoids from Delos, and therefore their age will place constraints on the timing of regional M_3 sillimanite-grade metamorphism. Further, because the leucogranites are deformed with the top-to-NE foliation, their age will constrain the timing of ductile shearing on Delos.

6.3.6 Naxos Granodiorite

Towards the eastern margin of the Naxos Granodiorite pluton (dated at ca. 12.2 Ma; Keay et al., 2001), a series of leucocratic dykes cross-cut the host-granodiorite. Near the

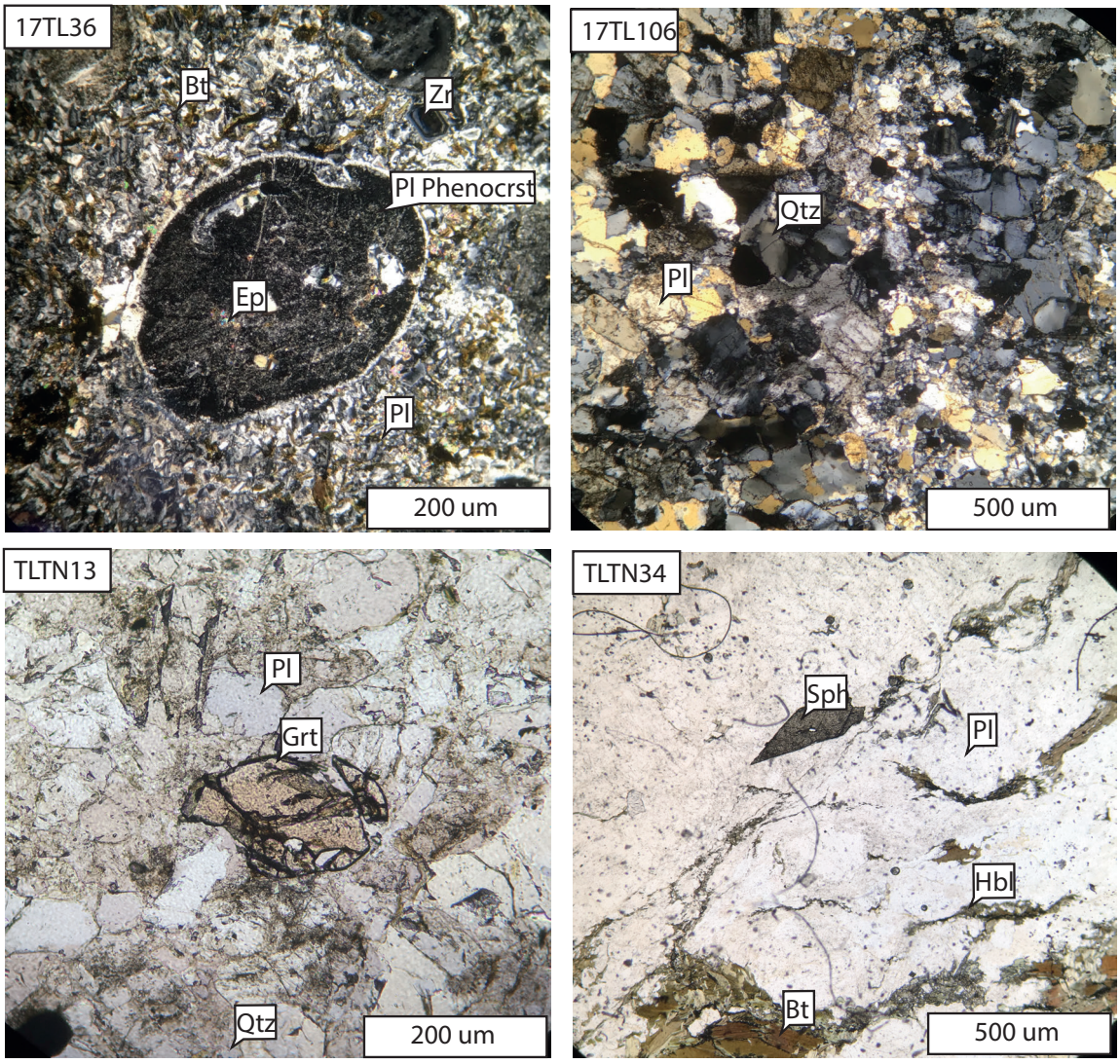


Figure 6.7: Photomicrigraphs of deformation textures and mineralogy of the granitoids: 17TL36 Dacite dke with finely crystalline matrix of plagioclase and dominantly biotite with lobate phagioclase phenocrysts, TLTN34 Tinos deformed Hb-Bt granite with solid state deformation textures with subgrain rotation in quartz and slight undulose extinction in plagioclase suggesting deformation temperatures between 400-550 °C. TLTN13 Grt bearing leucogranite with garnets that are 100-200 μ in diameter, and significantly less deformed than TLTN34. 17TL106 Titanite bearing Hb-Bt leucogranite from a vein within the Naxos granodiorite.

village of Glinado (Fig. 6.1), one of these leucogranites is gently folded about an NNE–SSW axis, (17TL106) and therefore possibly constrains the timing of E–W deformation on Naxos assuming it was emplaced in-situ and planar. The Naxos Granodiorite has sheared margins with the Naxos-Paros Detachment System and therefore intruded immediately prior to or during top-to-NE shearing at ca. 12.2 Ma.

6.4 Geochemistry

Major and trace element geochemistry was used to examine the differences between the various granitoids on Tinos and also to compare and contrast the characteristics of Tinos granites with classic I- and S-type examples. The sample locations used in this study are presented in Fig. 6.2. All samples were crushed into a <80 µm powder at the Natural Environment Geosciences Laboratory (NIGL) at the British Geological Survey, Keyworth, and the Department of Earth Sciences, University of Oxford, using standard techniques, and a steel crucible. These were analysed by X-ray Fluorescence (XRF) at the Department of Earth and Environment, Franklin and Marshall College, Lancaster, Pennsylvania, USA, using the procedures described in the supplementary material; the data is presented in Table 6.1.

A complete suite of trace elements was collected on a Perkin Elmer 6100DRC Quadrupole inductively coupled plasma mass spectrometer (ICP-MS) with a dynamic reaction cell at the Department of Earth Sciences, University of Oxford. Samples were crushed using the same techniques, weighed, diluted and digested. Detailed sample handling and preparation procedures are described in the supplementary material. Reported precision is less than ± 1% for major elements and ± 5% (2.S.D) for trace elements, and the results are presented in Tables 1, and as spider diagrams and discrimination plots in Figs.6.8–6.12.

6.4.1 Results

6.4.1.1 Aluminum Saturation Index (A/CNK)

Granitoids can be geochemically discriminated by their aluminum saturation index (A/CNK which comes from the abbreviation of its formula Al_2O_3/ [(CaO - 1.67 P_2O_5) + Na_2O + K_2O]) using the I- and S-type classification scheme. The division is drawn where A/CNK = 1.1, such that I-type granitoids are essentially metaluminous and gradually become weakly peraluminous with increasing silica contents, while S-type granitoids are typically peraluminous (Chappell and White, 1974, 1992). The Tinos

Location	Tinos	Tinos	Tinos	Tinos	Tinos	Tinos	Tinos	Tinos	Tinos	Naxos	Naxos	Naxos	Naxos	Naxos	Naxos	Naxos	Delos
Description	Dacite Dyke	Dacite Dyke	Dacite Dyke	Grt Leucogran-ite	Grt Leucogran-ite	Grt Leucogran-ite	Late Cross-Cutting Dyke	Hb-Bt Monzo-granite	Hb-Bt Monzo-granite	Leucogranit sill in granodi-orite	S-type leucogran-ite in-truding marble	S-type leucogran-ite	S-type leucogran-ite	S-type leucogran-ite	S-type leucogran-ite	S-type leucogran-ite	Bt-Tourm leucogran-ite
Sample	TLT-64	17TL-36	17TL-05	TLTN-13	TLTN-14	TLTN-15	17TL-100	TLTN-34	TLTN-36	17TL-106	TLN-8	TLN-37	TL-58	TL-63	TL-64	TL-72	17TL-95
SiO2	67.82	67.66	70.32	76.73	77.03	76.45	76.53	70.88	71.37	74.78	67.46	73.58	75.29	75.14	74.98	74.39	64.86
TiO2	0.48	0.49	0.51	0.01	0	0	0.01	0.34	0.34	0.02	0.46	0	0	0	0	0.01	1
Al2O3	16.07	16.04	15.93	13.63	13.41	13.81	13.37	15.44	14.98	14.33	16.28	16.16	15.02	14.49	14.38	15.06	14.97
Fe2O3	1.24	1.50	3.17	0.26	0.32	0.29	0.50	0.87	1.11	0.72	0.77	0.28	0.75	0.30	0.37	0.21	1.44
FeO	2.32	2.08	1.09	0.26	0.19	0.16	0.29	1.49	1.51	0.12	3.15	0.15	0.21	0.36	0.25	0.4	3.52
MnO	0.09	0.09	0.09	0.16	0.2	0.12	0.02	0.07	0.07	0.02	0.07	0.02	0.05	0.09	0.07	0.11	0.1
MgO	2.26	2.35	1.58	0.11	0.08	0.08	0.07	1.07	1.09	0.14	1.72	0.25	0.18	0.07	0.07	0.26	1.51
CaO	2.98	2.77	0.57	1.11	0.73	0.77	0.74	2.83	2.79	1	1.76	3.3	0.42	0.56	0.48	0.91	5.25
Na2O	3.85	3.85	3.16	4.99	5.19	5.92	3.69	3.57	3.54	3.84	3.62	5.84	2.93	5.43	4.95	5.15	3.04
K2O	2.63	2.62	3.24	2.66	2.98	2.13	4.78	3.28	3.1	4.97	4.19	0.35	4.97	3.25	4.03	3.23	3.56
P2O5	0.12	0.12	0.14	0.02	0.03	0.02	0.02	0.1	0.1	0.03	0.17	0.02	0.06	0.06	0.05	0.05	0.19
Total	100.12	99.8	99.92	99.97	100.18	99.77	100.05	100.11	100.17	99.98	100	99.97	99.9	99.79	99.66	99.82	99.83
LOI	1.68	1.85	2.86	0.38	0.41	0.48	0.51	1.09	1.04	0.79	1.8	1.09	1.06	0.38	0.35	0.52	1.18
Fe2O3T	3.82	3.81	4.38	0.55	0.53	0.47	0.82	2.53	2.79	0.85	4.27	0.45	0.98	0.7	0.65	0.65	5.35
XRF																	
Rb	139.5	130.8	153.3	251.5	271.6	213.8	347.7	190.6	183.4	344.4	164	26.3	303.1	372.6	458.8	521.9	117.4
Sr	603	578	301	18	16	18	35	288	280	81	179	520	24	5	5	24	465
Y	17.8	18.1	20.8	61.2	50.1	72.1	1.1	13.8	13.7	6.3	26.4	16.3	BD	BD	BD	37.6	4.8
Zr	172	178	212	90	102	100	63	184	187	88	144	41	21	22	18	33	392
V	93	85	67	8	13	7	6	43	41	8	91	6	7	8	3	8	53
Ni	154	187	25	25	8	8	6	7	7	3	35	16	5	4	4	12	9
Cr	97	57	32	54	10	29	22	21	22	15	66	9	19	11	8	18	35
Nb	12.8	14.2	14.4	61.3	78.8	81.2	23.8	15.8	16.8	36.9	9.6	28.6	22.4	37.9	35.7	39.3	48.3
Ga	21.4	20.9	20.1	26	27.9	27.1	24.6	21.3	21.2	28.5	19.6	23.9	25.7	30.2	29.2	38.7	22.9
Cu	23	21	46	17	19	16	13	14	8	42	51	23	13	13	15	12	25
Zn	45	52	351	14	9	13	32	39	39	12	74	17	18	26	26	36	72
Co	5	31	42	BD	BD	BD	13	BD	BD	27	7	BD	BD	BD	BD	BD	58
Ba	673	711	616	28	8	16	33	442	400	43	1297	198	45	4	3	22	629
La	29	30	35	16	15	19	17	25	21	18	23	18	13	12	13	17	36
Ce	58	59	70	19	20	17	15	46	38	26	43	17	12	13	14	25	73
U	4.2	2.5	1.5	5.2	5.7	6.4	BD	3.2	2.5	4.3	1.1	6.5	0.9	BD	BD	4.3	4.6
Th	18.9	20.2	81	43.8	37.45	36.7	25.1	20.7	17.5	43.4	11.7	5.1	3.6	7.7	7	17.8	17.1
Sc	8	5	4	3	BD	1	BD	5	5	BD	10	1	BD	BD	BD	BD	5
Pb	30	36	254	80	70	90	72	31	49	95	27	23	7	5	13	36	25
Ti	28768	29367	30566	599	0	0	599	20377	20377	1199	27569	BD	BD	BD	BD	599	59933
K	21833	21750	26897	22082	24738	17682	39681	27229	25734	6558	14943	9049	8800	3155	2905	4317	9796
ICP-MS																	
Sc 45	11.29	12.32	10.56	-	6.14	7.11	32.00	6.63	6.37	2.03	-	2.42	4.38	3.66	3.38	5.88	10.48
V 51	74.06	74.91	55.12	-	6.39	4.01	148.36	30.59	29.04	3.75	-	1.06	1.86	2.27	73.67	0.62	34.57
Cr 52	23.02	27.33	34.17	-	21.55	62.46	500.17	11.28	9.36	32.83	-	3.33	4.37	4.47	22.25	24.37	24.59
Mn 55	531.00	552.63	537.34	-	1197.63	755.73	739.34	407.64	385.09	29.14	-	32.07	247.52	554.27	522.13	611.94	629.62
Co 59	9.09	34.03	44.15	-	0.30	0.60	453.40	4.79	4.64	34.67	-	1.05	0.92	BD	9.12	0.55	59.50
Ni 60	113.68	140.50	17.09	-	3.53	3.80	58.93	4.40	4.13	1.83	-	10.02	2.17	1.22	112.15	8.64	8.32
Cu 65	6.36	9.26	47.35	-	7.60	4.18	40.58	2.61	2.36	22.54	-	1.29	2.07	2.25	6.20	1.39	9.61
Zn 66	44.12	43.69	300.26	-	4.64	5.52	493.52	39.60	38.11	6.82	-	8.43	11.72	16.85	43.08	22.93	77.58
Ga 69	182.40	202.39	175.14	-	18.89	17.19	465.40	120.31	127.43	26.39	-	63.37	29.85	18.82	183.64	28.90	181.06
Rb 85	124.73	120.91	133.43	-	208.88	168.90	6064.57	165.17	165.25	281.67	-	18.92	233.08	295.01	123.05	414.00	117.87
Sr 88	579.63	568.95	304.87	-	12.18	14.02	496.21	284.43	285.71	66.34	-	483.09	20.15	2.94	579.76	19.43	475.73
Y 89	16.04	17.43	20.08	-	42.60	57.53	186.01	17.08	17.52	13.98	-	13.95	3.87	5.75	16.12	22.92	39.94
Zr 90	69.20	77.71	100.27	-	10.59	6.19	301.05	4.56	5.52	9.30	-	2.15	2.32	1.58	70.29	6.44	22.01
Nb 93	12.46	13.56	13.10	-	58.90	62.05	372.83	14.89	14.79	27.33	-	25.25	16.32	27.45	12.35	30.53	44.53
Mo 98	BD	0.13	0.40	-	0.37	0.63	6.27	0.13	0.13	0.35	-	BD	0.18	0.13	0.15	0.24	0.93
Cd 111	0.05	0.10	3.98	-	0.09	0.10	1.71	0.10	0.07	0.08	-	0.05	0.19	0.25	0.08	0.13	0.12
In 115	0.10	0.09	0.08	-	0.08	0.10	2.06	0.10	0.08	0.10	-	0.10	0.10	0.10	0.09	0.11	0.09
Cs 133	15.45	15.65	4.37	-	4.06	5.48	142.77	12.84	12.44	15.29	-	0.38	5.76	5.46	6.37	22.99	2.81
Ba 138	651.49	735.34	633.22	-	10.44	5.64	512.91	410.43	448.49	31.07	-	181.84	52.55	2.74	654.14	18.98	638.47
La 139	32.61	35.58	35.28	-	6.56	5.41	82.70	34.43	27.73	9.76	-	4.55	2.26	2.96	32.74	10.62	53.60
Ce 140	60.89	66.56	68.26	-	15.47	11.77	132.43	64.03	52.64	19.74	-	8.72	4.35	6.37	61.06	20.69	129.01
Pr 141	6.25	6.95	7.26	-	2.08	1.58	21.02	6.50	5.51	2.19	-	0.96	0.53	0.82	6.39	2.27	15.32
Nd 143	23.06	25.50	27.00	-	8.59	6.72	75.07	23.22	20.21	7.66	-	3.11	1.72	2.64	23.06	7.66	58.57
Sm 147	4.25	4.37	4.96	-	3.07	2.93	20.53	4.05	3.85	1.73	-	1.23	0.58	1.18	4.20	2.51	10.89
Eu 153	1.00	1.03	0.88	-	0.10	0.11	3.57	0.80	0.81	0.26	-	0.32	0.10	0.02	0.02	0.06	1.74
Gd 157	3.53	4.00	4.23	-	3.73	4.59	18.81	3.52	3.48	1.48	-	1.42	0.52	0.98	3.54	2.42	9.22
Tb 159	0.56	0.59	0.65	-	0.85	1.13	4.17	0.55	0.57	0.27	-	0.38	0.14	0.23	0.57	0.55	1.35
Dy 163	3.19	3.50	3.86	-	5.97	8.45	27.25	3.14	3.23	1.64	-	2.49	0.77	1.20	3.20	3.76	7.45
Ho 165	0.65	0.69	0.80	-	1.33	1.90	6.42	0.65	0.65	0.40	-	0.47	0.17	0.22	0.66	0.80	1.48
Er 166	1.80	1.94	2.44	-	4.50	6.60	24.48	1.88	1.98	1.39	-	1.42	0.45	0.58	1.80	2.78	4.51
Tm 169	0.28	0.30	0.38	-	0.77	1.13	4.83	0.30	0.30	0.32	-	0.29	0.12	0.14	0.28	0.56	0.67
Yb 173	1.56	1.76	2.28	-	5.30	8.13	34.86	1.77	1.78	2.61	-	1.95	0.69	0.92	1.57	4.33	4.31
Lu 175	0.25	0.28	0.38	-	0.85	1.26	6.85	0.31	0.29	0.57	-	0.32	0.15	0.19	0.26	0.74	0.70
Hf 178	2.21	2.42	0.54	-	0.84	0.46	22.21	0.37	0.38	0.59	-	0.26	0.21	0.18	2.34	0.62	1.67
Ta 181	1.25	1.33	0.14	-	20.61	11.73	75.89	1.55	1.67	3.71	-	14.21	2.26	4.48	1.24	7.61	3.44
W 182	1.60	179.10	33.23	-	2.53	2.88	2349.60	3.70	2.15	224.63	-	1.88	23.90	2.71	1.54	3.90	384.50
Re 185	0.04	0.04	0.03	-	0.03	0.04	0.83	0.04	0.03	0.04	-	0.04	0.04	0.04	0.03	0.04	0.04
Pb 208	35.62	35.68	35.80	-	76.20	78.70	1493.91	42.02	42.28	80.37	-	27.08	32.27	32.58	35.03	64.42	32.80
Bi 209	0.10	0.09	0.52	-	0.08	0.09	1.98	0.10	0.07	0.11	-	0.10	0.09	0.09	0.09	0.10	0.09
Th 232	14.36	15.36	2.28	-	22.95	22.99	328.49	23.10	21.09	28.68	-	4.70	1.17	4.12	14.29	12.43	16.26
U 238	4.62	5.07	0.79	-	6.88	7.97	87.27	7.83	6.57	7.66	-	8.40	3.29	3.17	4.62	7.22	3.91

Table 6.1: XRF and ICP-MS results for Tinos, Naxos and Delos granitoids

Hbl–Bt pluton and dacite dykes follow variable trends spanning the I-S type divide (Fig. 6.8b), whereas the leucogranites are more variable but are essentially peraluminous. Because the garnet-bearing leucogranites are more enriched in silica (more highly fractionated), the A/CNK plot for the Tinos granites does not discriminate the

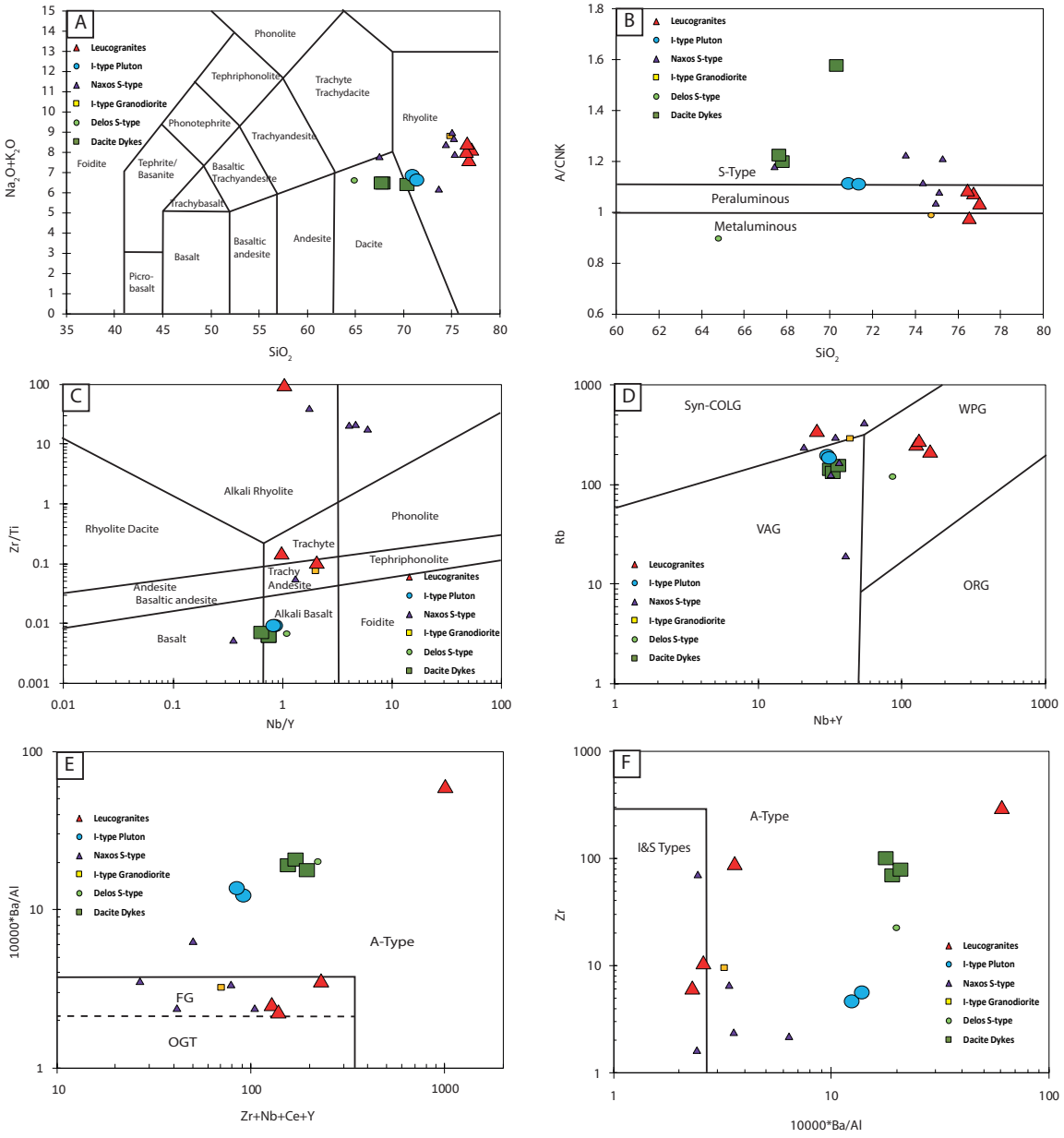


Figure 6.8: Discrimination diagrams

two granites effectively as there is some overlap between these populations.

6.4.1.2 Alkali Oxides

Another geochemical scheme used for I- and S-type discrimination is the proportion of alkali oxides, namely K_2O and Na_2O, reflecting the K-feldspar–to–plagioclase ratio. I-type granites generally become more sodic in composition with increasing SiO_2, whereas

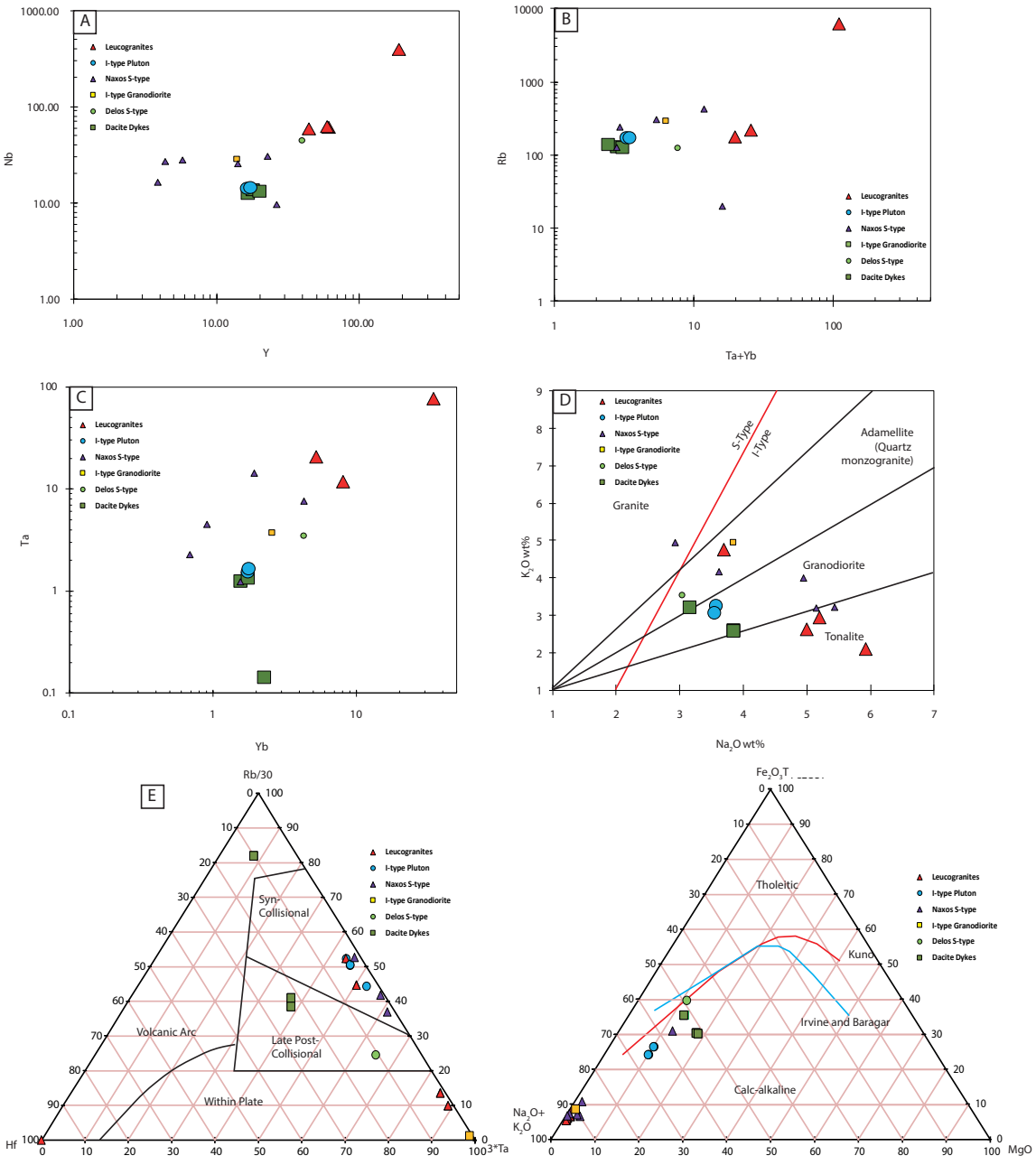


Figure 6.9: Discrimination diagrams

S-type granites are more potassic (Chappell and White, 1974, 1992; Clarke, 1992; Cobbing et al., 1992; Pitcher, 1997; Ghani et al., 2013b), as shown by the I–S division line in Fig.6.9d. The Tinos I-type pluton and dacite dykes plot in the I-type field while the leucogranites from Tinos, Naxos and Delos have enriched but highly variable Na_2O plotting across the I-type field. Therefore, on the basis of major elements the granites

show too much variation to make a meaningful interpretation.

6.4.1.3 Trace Elements

An indication of tectonic setting in which the magmas were formed can be inferred by the trace element ratios of incompatible elements (Pearce et al., 1984; Harris et al., 1986). In the ternary Rb/30–Hf–3*Ta ternary plot (Harris et al.,1984) (Fig. 6.9), Tinos Hb–Bt monzogranite and dacite samples fall within the syn-collisional granite field, but in the Rb vs Y+Nb discrimination diagram (Pearce et al., 1984) (Fig. 6.8), the monzogranite and dacite dykes plot within the volcanic arc granite field and straddle the collisional- and within plate granite fields (Fig. 6.9), which reflects an enrichment of high field strength elements (HFSEs) such as Y and Nb. The monzogranite and dacite dykes are also characterized by high-Rb contents. The elevated HFSE's of the I-type granitoids suggests they were derived HFSE bearing source and the high Rb in monzogranite and dacite dykes could reflect the incorporation of more evolved (crustal) source material into the parental magma, or to Rayleigh fractional crystallization of the magma (Halliday et al., 1991). Contrastingly, the leucogranites consistently plot within the within plate granite and syn-collisional granite fields (Figs. 6.8d and 6.9e) due having lower Rb, although one sample one (17TL100 which cross-cuts the monzogranite) shows syn-collisional features in both diagrams owing to lower concentrations of Nb, Yb and Ta relative to Rb. These features suggest the leucogranites are distinct from the other plutonic rocks on Tinos and were likely sourced from magmas generated within the continental crust to cause reduced lare ion lithophile elements (LILE) and high field strength elements (HFSE)s compared to the adjacent monzogranite pluton and dacite dykes.

6.4.1.4 Fractionation Processes

Harker diagrams (Fig. 6.10) show that the Tinos granitoids have fairly consistent trends in major element chemistry with variable SiO_2. These trends are interpreted to represent the granitoids have experienced various degrees of fractionation. It is,

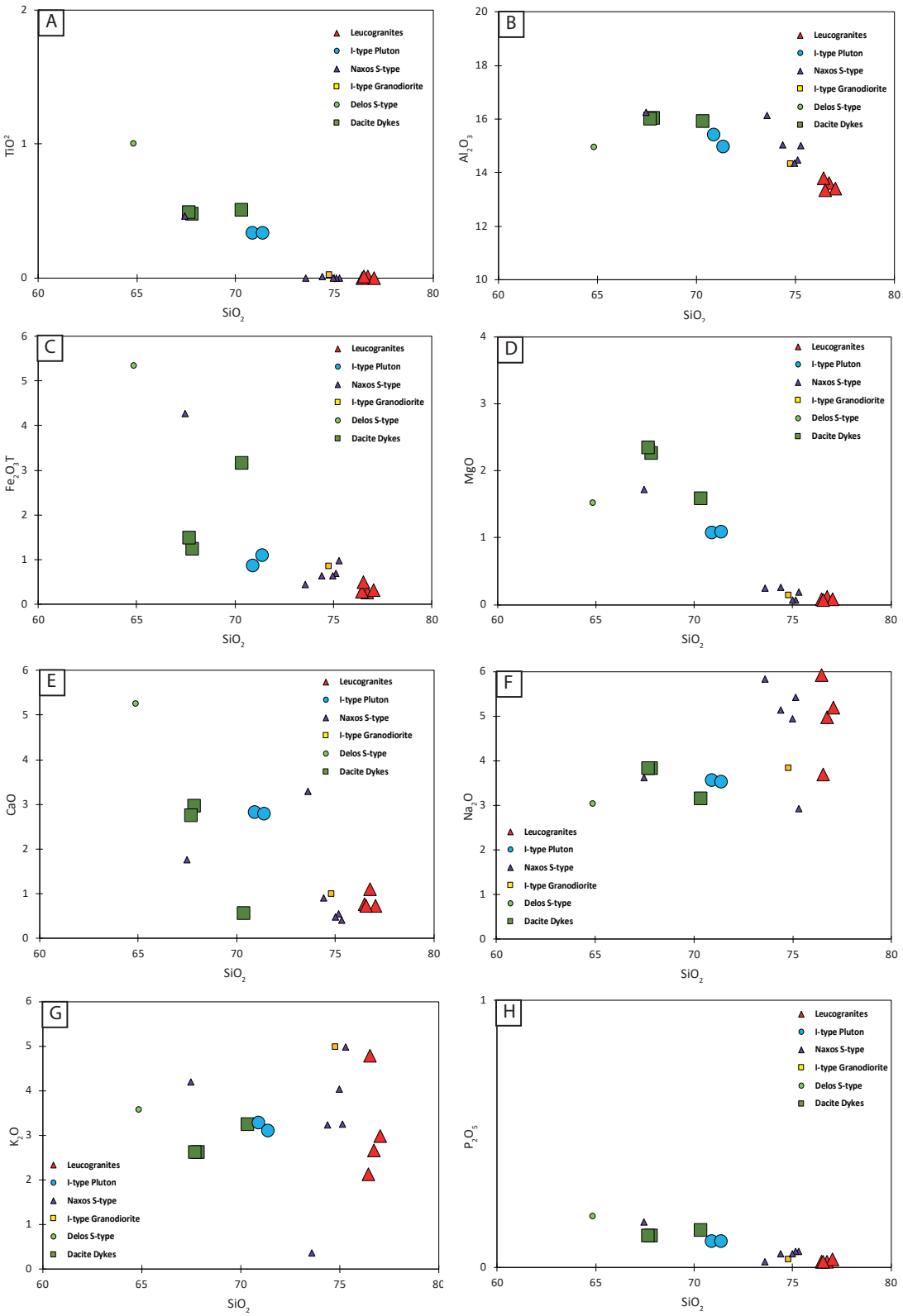


Figure 6.10: Harker diagrams

however, clear that the Tinos leucogranites exhibit higher SiO_2 than the Tinos monzogranite and dacitic dykes and display similar major element geochemistry to the Naxos S-type granites. In general, as the silica contents increase, the TiO_2, Al_2O_3, FeO, MgO, CaO, and P_2O_5 decrease, while K_2O shows a weak positive correlation with increasing silica in all separate granitoid types. In contrast Na_2O shows a weak inverse correlation and is in higher concentrations in the leucogranites but lower concentrations in the dacite dykes and monzogranite pluton. Compatible trace elements Ba, Sr, and Fe were chosen to compare with Rb (an incompatible element) in various bivariate diagrams in Fig 6.11. The Ba, Sr, and Fe contents decrease by up to two orders of magnitude with increasing Rb contents, indicating that fractionation of feldspars (decrease in Sr and Ba) and biotite and hornblende (decrease in Fe) were likely to have played a role in the evolving magmatic systems. Bulk liquid lines of descent (LLODs) are plotted in each diagram to demonstrate the combined effect of K-feldspar, plagioclase, biotite, and hornblende fractionation. Each increment on a LLOD represents 20% crystallization. The bulk LLOD for the Tinos monzogranite and dacite dykes was constructed for fractionation of 10% hornblende, 1% biotite, 50% plagioclase, and 39% K-feldspar, based upon the proportion of observed phases in the monzogranite excluding quartz and using the major element trends from Harker diagrams as a guide. Despite the small sample number, plots demonstrate that the LLODs between the I-type Tinos pluton and dykes generally intersect, with zirconium being the exception, indicating they were likely derived from the same parent magma, with the dykes experiencing lower degrees of fractionation than the I-type pluton. However, it is also clear that this LLODs does not generally intersect the Tinos leucogranites, signifying the garnet bearing leucogranites have different hypothetical starting compositions and therefore were derived from different source materials. Thus, fractionation alone from the I-type granitoids cannot not explain their major element chemistry. Moreover, the larger Rb/Sr ratios in the leucogranites (Figs. 6.11) suggest that they have experienced larger degrees of fractionation than the I-type pluton and dacite dykes.

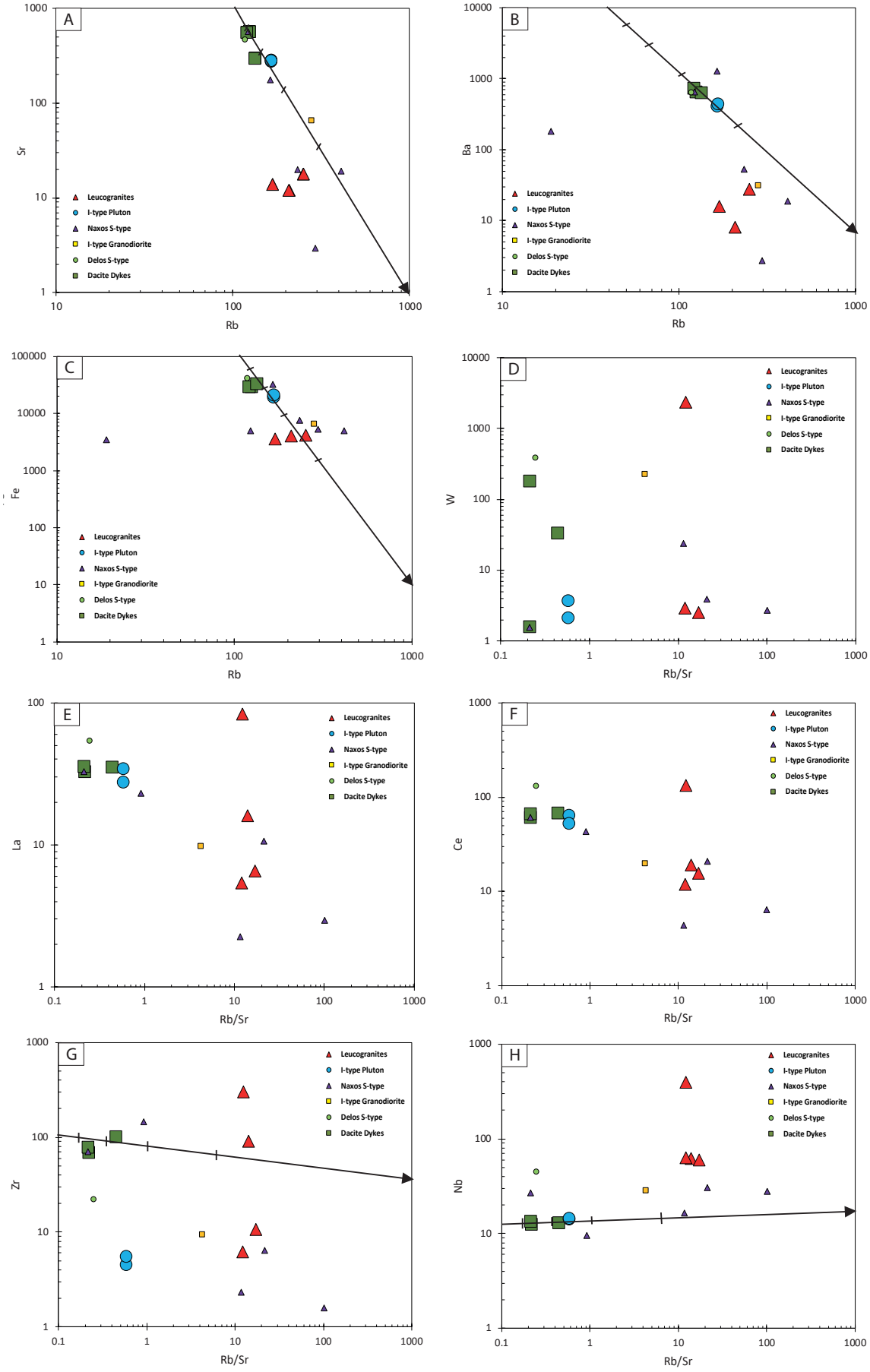


Figure 6.11: Trace element bivariate diagrams

6.4.1.5 Spider diagrams

'Spider diagrams' of all trace elements arranged in order of compatibility (Fig. 6.12 a and c), reveal that all Tinos granites exhibit convex down patterns with increasing incompatibility relative to primitive mantle (Sun and McDonough, 1989). The dacite dykes (17TL05, 17TL36 and TLT64) show the least enrichment, and this is consistent with them experiencing lower degrees of fractionation, with the Tinos monzogranite (TLTN34 and TLTN36) showing the most enrichment. All granites are also highly enriched in tungsten, which has been shown to be incompatible in crystallizing fractions and therefore enriched in highly fractionated felsic magmas, that reach secondary boiling implying all granitoids represent late fractionates in the magmatic system. All granitoids also show variable Nb depletion relative to Th possibly indicating a subduction source to the magmas or a possible protolith that has inherited a subduction signature.

Incompatible heavy rare earth element (HREE) patterns (Fig. 6.12b and d), reveal two distinct trends. The dacite dykes and I-type monzogranite show convex down patterns relative to chondrite (Sun and McDonough, 1989), whereas the garnet-bearing leucogranites (TLTN13, TLTN15 and 17TL100) show convex-up patterns with significant depletion in Eu, indicating crystallization of plagioclase. The garnet-bearing leucogranites also show similar trace element patterns to the Naxos S-type granites (Lamont et al., under review), with a depletion in Eu indicating retention of plagioclase in the source. Sample 17TL95 from Delos and sample 17TL106 from Naxos, display an intermediate trace element pattern possibly indicating they represents a mixture of both S-type and I-type magmas, which is consistent with U–Pb results presented below. In summary, the trace element patterns strongly suggest that the garnet-bearing leucogranites on Tinos were derived from a completely different source to the adjacent monzogranite pluton, and exhibit similar patterns to the Naxos S-type garnet and tourmaline bearing leucogranites. In contrast, the dacite dykes appear to be derived from the same parent magma as the I-type Tinos monzogranite, albeit less fractionated.

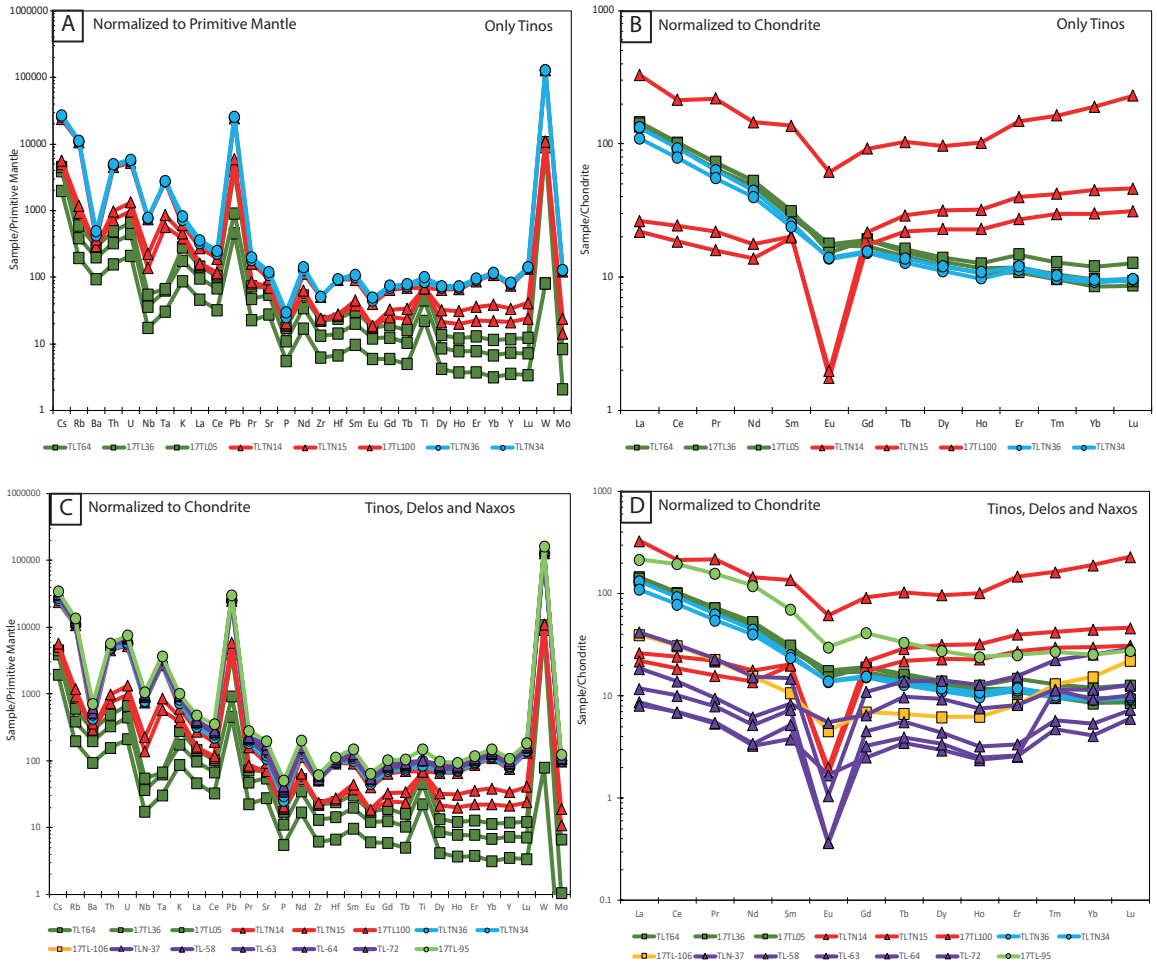


Figure 6.12: Spiderdiagrams

6.5 U–PB Geochronology

U–Pb zircon dating of dacite dykes (TLT64, 17TL36 and 17TL05), Plutonic rocks (TLTN34 and TLTN36) and garnet-bearing leucogranites (TLTN13, TLTN15, 17TL100) was carried out at the Natural Environmental Research Council (NERC) Isotope Geosciences Laboratory (NIGL), at the British Geological Survey, Keyworth, UK. Samples were crushed using standard techniques (Jaw-crushing, disc milling, sieving, Rogers table, heavy liquids, Frantz isodynamic magnetic separation). Approximately 30 zircons from each sample were then picked under alcohol, mounted in 1-inch epoxy resin mounts and polished until all grains were exposed. These were imaged by cathodoluminescence to distinguish zircon growth zoning and are presented with recorded spots and ages in

Fig. 6.13. All U–Pb analyses were performed on a Nu Attom single collector inductively coupled mass spectrometer (SC-ICP-MS) coupled to a New Wave Research 193UC excimer laser ablation system fitted with a TV2 cell. Standard-sample bracketing using matrix-matched minerals was employed for all minerals, with full set-up and protocols described previously for zircon (Roberts et al., 2016) and full analytical data provided in Appendix 2. All data and ages are shown and quoted at 2-sigma, are $^{206}Pb/^{238}U$ ages unless stated otherwise, and follow uncertainty propagation guidelines of Horstwood et al., (2016). Many samples exhibit a range of ages that is outside of uncertainty of a single population, which is common for crustally-derived granites due to the common occurrence of protracted melting and inclusion of antecrysts and xenocrysts (e.g. Lederer et al., 2013), therefore outlying data points from the main population, particularly if plotting off Concordia are rejected from weighted mean common-Pb corrected ages. A summary of the U–Pb data from the Tinos granites is presented in Fig. 6.18 and Tables 6.2–6.5.

6.5.1 Results

6.5.1.1 TLT64-Dacite Dyke (NE of Kolimpratha)

Sample TLT64 is taken from a partially deformed dacite dyke that intrudes amphibolites of the metamorphic sole in the Upper Unit to the NE of Kolimpritha Bay (N37.628196, E25.164215) and dips towards the southeast. Zircons are well formed (6.13) and interpreted to have a magmatic origin. Ablation of zircon rims constrains dyke emplacement and yields a weighted mean U–Pb common-Pb corrected age of 14.65 ± 0.19 Ma and an MSWD of 1.7 with the data lying between 14.2 ± 0.4 Ma and 15.0 ± 0.5 Ma (6.14). This age is interpreted to give a lower age bracket for movement on the Tinos Shear Zone as the dyke intrudes across it. However, because it shows slight solid-state ductile deformation, indicated by partial recrystallization of plagioclase and quartz, it suggests some localised deformation was still occurring at least at this structural level of the Upper Unit. Ablation of zircon cores gives an inherited



Figure 6.13: Zircon cathodeluminescence images

Table 6.2: SC-ICP-MS Zircon U-Pb results for Dacite Dykes on Tinos

			Analysis							Ratios						Ages							
Rock type	Sample	Analysis	comments	204Pb cps	206Pb cps	207Pb cps	208Pb cps	232Th cps	238U cps	Th/U	Pb ppm	Th ppm	U ppm	238U/206Pb%	207Pb/206Pb%	206Pb/238U%	Rho	207Pb/206Pb abs Age	206Pb/238U abs Age	207Pb/235Ub abs Age	Disc. % 6-38/7-35	Common-Pb corrected Age	Cor-rection
																						Cor.206/238b [Ma]	Pb Age
	TLT64J02	TLT64J02		bd	39655	200	259		238341	0.20	1.4	128.5	628.2	4133.41	1.90	0.0023	3.55	0.0023	0.0178	4.03	0.47	449.0	157.9	14.9	0.6	17.9	1.4		
	TLT64J03a	TLT64J03a		bd	27793	153	337		312891	0.35	1.1	168.7	475.7	4224.55	1.86	0.0543	4.08	0.0024	0.0176	4.08	0.46	384.9	163.2	15.2	0.6	17.8	1.4	17.0	
	TLT64J03b	TLT64J03b		bd	111324	576	1573		1558895	0.43	4.5	580.7	1973.4	4443.86	1.42	0.0012	2.36	0.0023	0.0159	2.75	0.82	108.4	145.5	14.5	0.4	16.0	0.9	14.6	
	TLT64J05	TLT64J05		bd	1011719	1035	2833		3850491	0.30	7.9	722.6	2662.5	4117.07	1.66	0.0024	1.58	0.0022	0.0157	1.66	0.60	91.8	142.3	14.3	0.4	15.9	0.7	14.5	
	TLT64J06	TLT64J06		bd	36859	60	161		154041	0.31	1.0	66.2	264.2	4117.07	2.26	0.0024	5.09	0.0022	0.0157	5.09	0.44	91.8	142.3	14.3	0.4	15.9	0.7	14.5	
	TLT64J07a	TLT64J07a		bd	19834	979	1310		1227949	0.19	7.5	663.2	3437.2	4122.22	1.23	0.0023	1.25	0.0023	0.0157	2.27	0.54	12.6	142.6	14.2	0.4	15.9	0.7	14.5	
	TLT64J07b	TLT64J07b		bd	7034	356	851		654615	0.30	2.8	353.0	1179.4	4126.25	1.51	0.0023	3.50	0.0023	0.0155	3.50	0.46	24.8	135.2	15.1	0.5	16.6	1.1	15.0	
	TLT64J08	TLT64J08		bd	22076	1158	1569		1375148	0.19	8.4	741.6	3919.1	4149.13	1.47	0.0059	1.95	0.0059	0.0155	2.44	0.60	282.9	80.1	14.3	0.4	16.1	0.8	14.2	
	TLT64J13	TLT64J13		bd	22843	1109	1545		1385696	0.19	8.7	747.3	3837.8	4130.34	1.39	0.0480	1.53	0.0154	0.0154	2.07	0.67	99.8	72.5	15.0	0.4	15.5	0.6	14.9	
	TLT64J14	TLT64J14		bd	8119	401	866		785700	0.31	3.2	423.7	1372.0	4129.15	1.61	0.0487	3.21	0.0146	0.0153	3.21	0.30	133.1	130.7	15.0	0.5	15.8	1.0	15.0	
Dacite Dyke	TLT64	TLT64J16		bd	7285	315	1057		1117023	0.30	3.2	402.4	1198.7	4121.44	1.76	0.0720	2.20	0.0235	0.0153	3.49	0.64	986.0	211.8	15.3	0.5	23.6	2.6	14.8	
	TLT64J17	TLT64J17	inherited	bd	77855	3858	11567		12251715	0.17	71.2	2313.5	13417.1	4127.35	1.76	0.0024	1.76	0.0024	0.0153	3.53	0.50	1.7	153.1	15.3	0.5	15.7	0.6	15.3	
	TLT64J01	TLT64J01	inherited	bd	10599	530	3144		2402231	0.88	4.9	129.5	147.5	35.21	1.60	0.0508	2.29	0.0284	0.1989	2.79	0.51	2232.8	105.6	180.5	5.7	184.2	9.4	180.3	
	TLT64J04a	TLT64J04a	inherited	bd	64306	3306	9569		734370	0.45	26.3	396.0	887.4	34.25	1.48	0.0510	1.21	0.0292	0.2052	1.91	0.77	240.9	55.7	185.5	5.4	189.5	6.6	185.2	
	TLT64J04b	TLT64J04b	inherited	bd	10599	530	3144		2402231	0.88	4.9	129.5	147.5	35.21	1.60	0.0508	2.29	0.0284	0.1989	2.79	0.51	2232.8	105.6	180.5	5.7	184.2	9.4	180.3	
	TLT64J09	TLT64J09	inherited	bd	38389	1895	14716		1174713	1.25	18.7	633.5	568.8	33.86	1.33	0.0497	1.44	0.0295	0.2023	1.96	0.68	181.0	67.3	187.6	4.9	187.1	6.7	187.7	
	TLT64J10b	TLT64J10b	inherited	bd	19520	1017	3899		290438	0.59	8.3	156.6	268.7	33.89	1.57	0.0506	2.26	0.0295	0.2057	2.26	0.49	222.5	75.2	187.4	5.8	190.0	7.8	187.3	
	TLT64J11	TLT64J11	inherited	bd	95056	4739	8270		618708	0.26	36.8	333.7	1299.8	34.43	1.27	0.0494	1.00	0.0290	0.1977	1.61	0.79	166.0	40.6	184.6	5.4	183.2	-0.8	184.7	
	TLT64J12	TLT64J12	inherited	bd	95056	4739	8270		618708	0.26	36.8	333.7	1299.8	34.43	1.27	0.0494	1.00	0.0290	0.1977	1.61	0.79	166.0	40.6	184.6	5.4	183.2	-0.8	184.7	
	TLT64J15	TLT64J15	inherited	bd	19520	1017	3899		290438	0.59	8.3	156.6	268.7	33.89	1.57	0.0506	2.26	0.0295	0.2057	2.26	0.49	222.5	75.2	187.4	5.8	190.0	7.8	187.3	
	TLT64J18	TLT64J18	inherited	bd	94349	4666	14226		1070150	0.46	38.6	882.0	1235.5	33.73	1.20	0.0490	1.04	0.0296	0.2006	1.59	0.76	153.1	48.7	188.3	4.5	185.7	-1.4	186.5	
	TLT64J10a	TLT64J10a	high cps-pb	2742007	412220	293446		6712058	1199882	0.71	1143.5	5064.2	4464	1223	0.1445	0.74	4.2885	1.44	0.2153	1.23	0.86	2281.9	25.4	1257.2	28.1	1691.2	223.4	25.7	24.3
	1TTL-36J01	1TTL-36J01		bd	5890	300	1116		941565	0.40	2.5	307.8	1040.6	4143.87	1.71	0.0509	2.53	0.0158	0.0158	3.05	0.60	237.2	116.6	14.5	0.5	15.9	1.0	14.4	0.5
	1TTL-36J02	1TTL-36J02		bd	4654	243	660		606698	0.41	1.9	323.9	788.2	4306.92	1.83	0.0498	2.99	0.0157	0.0157	3.50	0.52	183.7	139.3	14.7	0.5	15.8	1.1	14.7	0.5
	1TTL-36J03	1TTL-36J03		bd	4737	300	511		509096	0.33	1.9	271.6	834.2	4152.93	1.75	0.0614	3.54	0.0157	0.0157	3.95	0.44	651.9	151.8	14.2	0.5	15.8	1.5	13.9	0.5
	1TTL-36J04	1TTL-36J04		bd	16658	830	1593		1565597	0.29	6.5	810.8	2837.8	4130.76	1.43	0.0492	1.69	0.0158	0.0152	2.21	0.64	158.7	79.1	14.9	0.4	15.3	0.6	14.8	0.4
	1TTL-36J05	1TTL-36J05		bd	61105	2918	4613		4198797	0.22	23.4	2264.3	10356.1	4133.36	1.27	0.0478	1.29	0.0152	0.0152	1.81	0.70	88.0	61.4	14.9	0.4	15.3	0.6	14.8	0.4
	1TTL-36J06	1TTL-36J06		bd	1016	75	111		89073	0.25	0.4	43.2	173.8	4130.76	1.43	0.0492	1.69	0.0158	0.0158	2.21	0.64	158.7	79.1	14.9	0.4	15.9	0.7	14.9	0.4
	1TTL-36J07	1TTL-36J07		bd	11405	1016	2222	1062	1010708	0.19	6.2	351.6	1864.5	4134.15	1.76	0.0502	2.17	0.0153	0.0153	3.35	0.42	196.9	94.5	14.3	0.4	15.7	0.7	14.4	0.4
Dacite Dyke	1TTL36	1TTL-36J08		bd	15668	107	98		651176	0.11	0.6	351.1	254.3	4134.09	2.94	0.0671	3.01	0.0153	0.0153	3.50	0.58	841.5	223.9	14.5	0.4	15.7	0.7	14.5	0.4
		1TTL-36J09		bd	5817	284	623		606619	2.3	2.3	323.9	988.0	4131.81	1.79	0.0480	3.01	0.0153	0.0153	3.50	0.51	98.7	142.3	14.9	0.5	15.4	1.1	14.9	0.5
		1TTL-36J10		bd	6678	576	950		248337	0.12	2.8	133.9	1119.5	4127.95	1.68	0.0855	3.54	0.0275	0.0275	3.91	0.68	1327.2	136.9	15.0	0.5	27.6	2.1	13.9	0.5
		1TTL-36J11		bd	2403	109	309		997273	0.9	0.9	53.5	420.9	4144.80	2.03	0.0565	3.99	0.0175	0.0175	4.38	0.43	473.5	176.7	14.5	0.4	17.6	1.6	14.5	0.5
		1TTL-36J12		bd	8369	461	805		777408	0.29	3.3	419.3	1462.6	4142.48	1.52	0.0542	3.24	0.0169	0.0169	3.57	0.42	381.4	145.5	14.6	0.4	17.0	1.2	14.4	0.4
		1TTL-36J13		bd	8513	427	927		846421	0.32	3.4	456.5	1433.1	4129.58	1.43	0.0510	2.70	0.0023	0.0153	3.50	0.53	173.0	106.7	15.0	0.4	16.0	0.9	14.9	0.4
		1TTL-36J14		bd	8842	256	477		496506	0.28	1.9	246.3	874.6	4139.36	1.66	0.0507	3.07	0.0022	0.0152	3.49	0.47	227.9	142.0	15.0	0.5	15.3	1.1	13.9	0.5
		1TTL05J01		bd	32924	1532	2115		1703876	0.20	8.9	838.2	4152.9	4148.50	1.21	0.0461	1.70	0.0022	0.0142	1.70	0.71	2.9	57.3	14.4	0.3	14.3	0.5		
		1TTL05J02a		bd	4717	434	1530		832702	0.71	1.6	410.1	557.3	4106.46	2.49	0.1139	10.69	0.0024	0.0384	10.97	0.23	1863.0	385.8	15.8	0.8	38.3	8.2	14.4	0.7
		1TTL05J02b		bd	15552	1015	1122		5611704	0.71	5.7	2425.7	3382.5	4106.46	2.49	0.0490	2.49	0.0022	0.0147	2.49	0.58	194.8	68.3	14.8	0.4	14.8	0.6	14.4	0.4
		1TTL05J04		bd	3226	191	1215		988710	0.11	7.0	889.4	3372.5	4109.04	1.47	0.0477	1.73	0.0022	0.0147	1.73	0.51	74.9	141.3	14.8	0.4	14.8	0.6	14.4	0.4
		1TTL05J05		bd	32302	1876	3192		1393745	0.23	9.1	931.5	3988.2	4106.42	1.32	0.0574	4.69	0.0023	0.0181	4.87	0.27	508.2	206.2	14.8	0.4	18.3	1.8	14.5	0.4
		1TTL05J07		bd	2483	159	275		191775	0.32	0.7	94.3	297.9	4142.28	1.99	0.0622	3.90	0.0104	0.0104	4.38	0.45	681.5	166.7	14.6	0.6	19.5	1.7	14.3	0.6
		1TTL05J08		bd	27805	1354	1322		1023256	0.15	7.4	503.4	3358.9	4139.89	1.28	0.0484	1.68	0.0152	0.0146	2.11	0.60	117.2	79.4	14.6	0.4	15.3	0.6	14.6	0.4
Dacite Dyke	1TTL05	1TTL05J09		bd	3970	426	916		207714	0.31	1.3	146.5	470.1	4123.77	2.24	0.0882	6.90	0.0024	0.0287	7.26	0.31	1387.3	265.0	15.2	0.7	28.7	4.1	14.4	0.6
		1TTL05J10		bd	11943	1573	1573		1260064	0.20	5.3	603.9	2539.4	4128.69	1.31	0.0484	1.48	0.0023	0.0156	1.58	0.66	121.1	101.6	15.0	0.4	15.7	0.6	14.7	0.4
		1TTL05J12		bd	35855	1967	1967		2461569	0.20	10.1	1189.6	4444.3	4131.76	1.33	0.0485	1.67	0.0023	0.0152	1.83	0.62	123.1	145.9	14.8	0.4	15.2	0.6	14.7	0.4
		1TTL05J13		bd	37534	2001	348		2481093	0.27	1.0	1211.1	444.3	4115.42	1.77	0.0513	3.42	0.0024	0.0170	3.85	0.46	255.0	157.2	15.54	0.5	17.1	1.3	14.6	0.4
		1TTL05J14		bd	15668	896	2818		2413020	0.51	5.5	1189.6	2314.6	4149.69	1.33	0.0485	1.67	0.0149	0.0149	2.13	1.63	78.5	121.8	14.3	0.5	15.0	0.6	14.3	0.4
		1TTL05J15		bd	2572	145	217		1751507	0.27	0.7	85.9	313.0	4132.07	2.28	0.0582	4.51	0.0023	0.0186	5.06	0.45	537.2	197.5	14.9	0.7	18.7	1.9	14.2	0.7
		1TTL05J16		bd	10747	544	1237		963428	0.36	3.0	474.0	1304.0	4136.48	1.45	0.0507	2.08	0.0023	0.0160	2.53	0.57	228.1	95.9	14.8	0.4	16.1	0.8	14.7	0.4
		1TTL05J03		bd	120173	6510	5604		2290554	0.18	32.2	127.4	713.9	4121.45	3.19	0.0530	0.89	0.0421	0.1851	3.31	0.96	330.2	40.5	265.9	15.7	272.4	15.7	265.4	16.5
		1TTL05J11	inherited	bd	101108	5191	15068		7686040	0.34	29.6	378.1	1101.8	37.98	3.33	0.0510	0.89	0.0263	0.2077	3.45	0.0263	3.33	0.97	241.7	40.9	167.5	11.0	172.5	10.9	167.2	11.0

Analysis													Ratios									Ages							Disc. % 6-38/7-35	Common-Pb Corrected Age	
Rock type	Sample	Analysis	comments	204Pb cps	206Pb cps	207Pb cps	208Pb cps	232Th cps	238U cps	Th/U	Pb ppm	Th ppm	U ppm	238U/206Pb abs	%	207Pb/206Pb abs	%	207Pb/235U abs	%	206Pb/238U abs	%	Rho	207Pb/206Pb abs Age		206Pb/238U abs Age		207Pb/235U abs Age				Cor.206/238 Pb Age	[Ma]
		TLTN34_01		12	26512	1360	1873	1433024	92543	0.19	6.6	589.2	3054.0	449.12	1.89	0.0511	1.73	0.0157	2.57	0.0022	1.89	0.74	245.9	79.8	14.3	0.5	15.8	0.8	9.3	14.3	0.5
		TLTN34_02		5	17876	882	994	831012	60337	0.17	4.4	341.7	1991.2	443.62	1.90	0.0491	2.16	0.0153	2.88	0.0023	1.90	0.66	153.0	101.3	14.5	0.6	15.4	0.9	5.6	14.5	0.5
		TLTN34_03		117	4631	259	703	440176	15228	0.36	1.2	181.0	502.5	416.66	2.47	0.0548	3.45	0.0181	4.24	0.0024	2.47	0.58	405.1	154.4	15.5	0.8	18.2	1.5	15.3	15.3	0.7
		TLTN34_04		-85	10495	528	773	614601	34634	0.22	2.6	252.7	1142.9	432.03	2.10	0.0494	2.24	0.0158	3.07	0.0023	2.10	0.68	167.0	104.7	14.9	0.6	15.9	1.0	6.1	14.8	0.6
		TLTN34_05	rej from age cal	-47	2170	136	156	117133	7401	0.20	0.5	48.2	244.2	447.83	2.71	0.0612	4.07	0.0188	4.89	0.0022	2.71	0.55	647.7	174.7	14.4	0.8	19.0	1.8	24.2	14.1	0.7
		TLTN34_06	rej from age cal	74	16445	819	1196	792264	51480	0.19	4.1	325.8	1698.9	405.53	1.96	0.0488	2.22	0.0166	2.96	0.0025	1.96	0.66	138.0	104.4	15.9	0.6	16.7	1.0	4.9	15.8	0.6
		TLTN34_07		-7	21545	1550	6065	3654734	70147	0.65	6.4	1502.7	2314.9	426.92	1.57	0.0711	2.25	0.0229	2.74	0.0023	1.57	0.57	959.7	91.8	15.1	0.5	23.0	1.2	34.5	14.6	0.4
		TLTN34_08		82	23763	1182	1292	978505	78100	0.16	5.8	402.3	2577.3	426.57	1.78	0.0491	1.98	0.0159	2.67	0.0023	1.78	0.67	152.0	92.9	15.1	0.5	16.0	0.8	5.5	15.0	0.5
		TLTN34_09		159	22251	1128	1444	1003795	74035	0.17	5.5	412.7	2443.2	431.47	1.92	0.0492	2.16	0.0157	2.89	0.0023	1.92	0.67	157.7	101.0	14.9	0.6	15.8	0.9	5.8	14.9	0.6
		TLTN34_10		142	4999	289	724	455731	15919	0.36	1.3	187.4	525.3	410.38	2.01	0.0563	3.09	0.0189	3.69	0.0024	2.01	0.55	463.7	137.2	15.7	0.6	19.0	1.4	17.5	15.5	0.6
		TLTN34_11		128	23739	1213	1485	1062875	79537	0.17	5.8	437.0	2624.8	438.43	1.70	0.0507	1.73	0.0159	2.42	0.0023	1.70	0.70	227.2	79.8	14.7	0.5	16.1	0.8	8.5	14.6	0.5
		TLTN34_13		49	33336	1723	3755	3040080	113637	0.33	8.6	1250.0	3750.1	435.92	1.45	0.0499	1.49	0.0158	2.08	0.0023	1.45	0.70	191.6	69.1	14.8	0.4	15.9	0.7	7.1	14.7	0.4
		TLTN34_14		77	24382	1219	1399	1025741	82154	0.16	6.0	421.8	2711.1	429.83	1.57	0.0492	1.74	0.0158	2.34	0.0023	1.57	0.67	156.7	81.2	15.0	0.5	15.9	0.7	5.7	14.9	0.5
		TLTN34_15		199	23975	1207	2204	1658831	77887	0.27	6.0	682.1	2570.3	424.09	1.64	0.0501	1.86	0.0163	2.48	0.0024	1.64	0.66	198.6	86.5	15.2	0.5	16.4	0.8	7.4	15.1	0.5
		TLTN34_16		152	7550	411	830	653189	24532	0.33	1.9	268.6	809.6	425.63	1.98	0.0570	3.03	0.0184	3.62	0.0023	1.98	0.55	490.2	133.5	15.1	0.6	18.6	1.3	18.5	14.9	0.6
		TLTN34_17		-72	10495	562	916	704903	33376	0.26	2.6	289.8	1101.4	413.29	1.72	0.0531	2.12	0.0177	2.73	0.0024	1.72	0.63	332.4	95.9	15.6	0.5	17.8	1.0	12.6	15.4	0.5
		TLTN34_18		-2	13595	726	792	445453	44613	0.12	3.3	183.2	1472.3	428.83	1.63	0.0527	2.22	0.0169	2.75	0.0023	1.63	0.59	314.7	100.9	15.0	0.5	17.0	0.9	11.9	14.9	0.5
Hb-Bt Monzogranite	TLTN34	TLTN34_19		138	7002	481	726	455479	23030	0.25	1.8	187.3	760.0	424.61	1.92	0.0646	3.17	0.0210	3.71	0.0024	1.92	0.52	760.3	133.5	15.2	0.6	21.1	1.5	28.0	14.8	0.6
		TLTN34_20		-12	165580	8254	11104	9103157	557067	0.20	40.8	3742.9	18383.5	431.23	1.37	0.0483	0.85	0.0154	1.61	0.0023	1.37	0.85	115.4	40.1	14.9	0.4	15.6	0.5	4.1	14.9	0.4
		TLTN34_21		33	17472	865	3149	2906826	59341	0.61	4.7	1195.2	1958.3	441.80	1.42	0.0489	1.79	0.0153	2.28	0.0023	1.42	0.62	144.7	83.9	14.6	0.4	15.4	0.7	5.3	14.5	0.4
		TLTN34_22		35	9959	521	1509	1155439	34465	0.42	2.6	475.1	1137.4	439.28	1.94	0.0516	2.70	0.0162	3.32	0.0023	1.94	0.58	267.7	123.8	14.7	0.6	16.3	1.1	10.1	14.6	0.6
		TLTN34_23		-28	4764	244	519	444299	16007	0.35	1.2	182.7	528.2	434.37	2.10	0.0512	3.48	0.0162	4.06	0.0023	2.10	0.52	249.5	160.1	14.8	0.6	16.4	1.3	9.4	14.7	0.6
		TLTN34_24		-83	2630	147	309	248284	8652	0.36	0.7	102.1	285.5	435.23	2.12	0.0544	4.76	0.0172	5.21	0.0023	2.12	0.41	389.4	213.5	14.8	0.6	17.4	1.8	14.8	14.6	0.6
		TLTN34_25		-4	7124	355	948	761920	23731	0.40	1.9	313.3	783.1	429.95	1.87	0.0496	2.45	0.0159	3.08	0.0023	1.87	0.61	177.8	114.4	15.0	0.6	16.0	1.0	6.6	14.9	0.6
		TLTN34_26		-91	23449	1157	2231	2014022	78953	0.32	5.9	828.1	2605.5	433.03	1.68	0.0489	1.46	0.0156	2.23	0.0023	1.68	0.75	143.5	68.7	14.9	0.5	15.7	0.7	5.2	14.8	0.5
		TLTN34_27		31	21759	1127	2671	2225959	74108	0.37	5.6	915.2	2445.6	431.99	1.46	0.0498	1.48	0.0159	2.08	0.0023	1.46	0.70	184.5	68.9	14.9	0.4	16.0	0.7	6.8	14.8	0.4
		TLTN34_28		-5	3401	184	144	95751	11115	0.11	0.8	39.4	366.8	417.32	2.18	0.0530	3.61	0.0175	4.22	0.0024	2.18	0.52	330.3	163.6	15.4	0.7	17.6	1.5	12.5	15.3	0.7
		TLTN34_30		-14	27192	1314	751	555533	88836	0.08	6.5	228.4	2931.6	418.87	1.73	0.0496	1.54	0.0163	2.32	0.0024	1.73	0.75	175.6	71.8	15.4	0.5	16.4	0.8	6.5	15.3	0.5
		TLTN34_31		80	18950	917	1912	1697461	64450	0.33	4.8	697.9	2126.9	442.46	1.54	0.0501	1.92	0.0156	2.46	0.0023	1.54	0.63	200.1	89.1	14.6	0.4	15.7	0.8	7.5	14.5	0.4
		TLTN34_32		131	16974	816	823	684657	57070	0.15	4.1	281.5	1883.3	435.57	1.61	0.0478	1.90	0.0151	2.49	0.0023	1.61	0.65	91.6	90.0	14.8	0.5	15.3	0.8	3.1	14.8	0.5
		TLTN34_33		22	5500	290	695	555117	17996	0.38	1.4	228.2	593.9	425.95	1.85	0.0523	2.79	0.0169	3.35	0.0023	1.85	0.55	299.1	127.4	15.1	0.6	17.0	1.1	11.3	15.0	0.6
		TLTN34_34		50	4257	218	517	467536	14048	0.41	1.1	192.2	463.6	421.02	2.13	0.0489	3.64	0.0160	4.22	0.0024	2.13	0.51	142.2	171.0	15.3	0.7	16.1	1.3	5.1	15.2	0.6
		TLTN34_12	high cm-Pb	80	5211	992	2258	259167	12801	0.25	1.9	106.6	422.4	308.57	6.05	0.1526	13.12	0.0681	14.45	0.0032	6.05	0.42	2375.1	447.4	20.9	2.5	66.9	18.6	68.8	18.1	2.0
		TLTN34_29	high cm-Pb	132	44876	4505	6996	1520237	139857	0.14	12.4	625.1	4615.4	282.82	6.08	0.2747	11.41	0.1339	12.92	0.0035	6.08	0.47	3333.3	357.0	22.8	2.8	127.6	30.5	82.2	16.2	1.8
		TLTN36_01	rej from age cal	78	15266	789	845	509637	48161	0.13	3.7	209.5	1589.3	421.75	2.35	0.0489	2.23	0.0160	3.24	0.0024	2.35	0.72	143.1	104.6	15.3	0.7	16.1	1.0	5.2	15.2	0.7
		TLTN36_02		-74	10371	538	1106	687786	33692	0.25	2.6	282.8	1111.9	432.49	2.03	0.0504	3.24	0.0161	3.83	0.0023	2.03	0.53	213.8	150.2	14.9	0.6	16.2	1.2	8.0	14.8	0.6
		TLTN36_03	rej from age cal	83	16200	1131	2639	1140341	50921	0.28	4.4	468.9	1680.4	406.71	2.21	0.0705	4.07	0.0230	4.63	0.0025	2.21	0.48	944.1	166.7	15.8	0.7	24.0	2.2	34.0	15.3	0.7
		TLTN36_04	rej from age cal	94	11158	555	408	222170	34088	0.08	2.7	91.3	1124.9	413.95	2.13	0.0517	3.07	0.0172	3.74	0.0024	2.13	0.57	271.8	140.8	15.6	0.7	17.3	1.3	10.2	15.4	0.7
		TLTN36_05		10	2139	117	220	131645	6905	0.24	0.5	54.1	227.9	438.27	2.67	0.0547	5.33	0.0172	5.96	0.0023	2.67	0.45	399.4	239.0	14.7	0.8	17.3	2.0	15.1	14.5	0.8
		TLTN36_08		-90	20902	997	1032	760867	70137	0.14	5.1	312.8	2314.5	447.16	1.93	0.0468	2.04	0.0144	2.81	0.0022	1.93	0.69	39.9	97.7	14.4	0.6	14.5	0.8	1.0	14.4	0.6
		TLTN36_09		-3	8979	459	1197	921375	30738	0.37	2.3	378.8	1014.4	450.42	1.99	0.0494	2.26	0.0151	3.01	0.0022	1.99	0.66	166.4	105.4	14.3	0.6	15.2	0.9	6.1	14.2	0.6
		TLTN36_10		-6	5089	273	463	321612	17486	0.23	1.3	132.2	577.0	458.76	2.27	0.0525	2.78	0.0158	3.59	0.0022	2.27	0.63	306.6	126.9	14.0	0.6	15.9	1.1	11.6	13.9	0.6
		TLTN36_11		18	9892	473	1367	964383	33558	0.36	2.6	396.5	1107.4	447.09	2.62	0.0468	2.55	0.0144	3.65	0.0022	2.62	0.72	40.5	121.8	14.4	0.8	14.6	1.1	1.0	14.4	0.8
		TLTN36_12		53	7748	432	523	349672	26088	0.17	1.9	143.8	860.9	451.08	2.35	0.0693	6.86	0.0212	7.25	0.0022	2.35	0.32	906.4	282.6	14.3	0.7	21.3	3.0	32.9	13.9	0.6
		TLTN36_13		-49	16419	990	2103	1129479	54408	0.26	4.3	464.4	1795.5	438.23	2.14	0.0600	2.55	0.0189	3.33	0.0023	2.14	0.64	605.1	110.4	14.7	0.6	19.0	1.3	22.6	14.4	0.6
		TLTN36_15		72	10546	530	2866	1922606	38163	0.63	3.1	790.5	1259.4	473.12	2.04	0.0486	2.32	0.0141	3.09	0.0021	2.04	0.66	127.2	109.3	13.6	0.6	14.3	0.9	4.6	13.6	0.6
		TLTN36_17	rej from age cal	62	26159	1292	884	543042	81133	0.08	6.2	223.3	2677.4	406.43	2.19	0.0474	2.00	0.0161	2.97	0.0025	2.19	0.74	71.7	95.0	15.8	0.7	16.2	1.0	2.2	15.8	0.7
Hb-Bt Monzogranite		TLTN36_18	rej from age cal	-52	2964	149	201	146296	9522	0.19	0.7	60.2	314.2	425.23	2.57	0.0504	4.44	0.0163	5.13	0.0024	2.57	0.50	213.0	205.8	15.1	0.8	16.4	1.7	7.9	15.1	0.8
		TLTN36_19	rej from age cal	46	9231	478	681	447432	29665	0.19	2.3	184.0	979.0	425.02	2.13	0.0511	3.04	0.0166	3.71	0.0024	2.13	0.57	245.6	140.0	15.1	0.6	16.7	1.2	9.2	15.1	0.6
		TLTN36_20		79	16282	946	1011	577445	55158	0.13	4.0	237.4	1820.2	446.52	1.98	0.0566	3.13	0.0175	3.70	0.0022	1.98	0.54	477.2	138.2	14.4	0.6	17.6	1.3	18.0	14.2	0.6
		TLTN36_21		29	1787	96	151	106823	6197	0.21	0.4	43.9	204.5	457.42	2.74	0.0538	4.68	0.0162	5.42	0.0022	2.74	0.51	362.1	211.1	14.1	0.8	16.3	1.8	13.8	13.9	0.8
		TLTN36_22		9	18423	925	1221	826382	65288	0.16	4.5	339.8	2154.5	459.43	1.78	0.0486	2.30	0.0146	2.91	0.0022	1.78	0.61	129.2	108.5	14.0	0.5	14.7	0.8	4.7	14.0	0.5
		TLTN36_23		-11	21836	1082	3380	2733407	76026	0.45	5.8	1123.9	2508.9	442.50	1.93	0.0490	1.75	0.0153	2.60	0.0023	1.93	0.74	148.6	82.1	14.6	0.6	15.4	0.8	5.4	14.5	0.6
		TLTN36_24		-64	8639	426	508	392680	29242	0.17	2.1	161.5	965.0	440.40	2.12	0.0475	2.83	0.0149	3.54	0.0023	2.12	0.60	76.3	134.3	14.6	0.6	15.0	1.1	2.5	14.6	0.6
		TLTN36_25		-38	4545	219	741	552702	15275	0.45	1.2	227.3	504.1	439.79	2.75	0.0477	3.23	0.0149	4.24	0.0023	2.75	0.65	83.9	153.3	14.6	0.8	15.1	1.3	2.8	14.6	0.8
		TLTN36_26		-4	6325	312	734	540356	21362	0.32	1.6	222.2	705.0	433.33	2.17	0.0470	2.96	0.0149	3.67	0.0023	2.17	0.59	49.3	141.2	14.9	0.6	15.1	1.1	1.4	14.8	0.6
		TLTN36_27		-77	29720	1440	1740	1339238	108630	0.15	7.3	550.7	3584.8	462.69	1.74	0.0503	2.30	0.0150	2.88	0.0022	1.74	0.60	207.2	106.5	13.9	0.5	15.1	0.9	7.8	13.8	0.5
		TLTN36_28	rej from age cal	66	7447	351	370	296143	23254	0.16	1.8	121.8	767.4	417.99	2.33	0.0478	2.77	0.0158	3.62	0.0024	2.33	0.64	90.2	131.4	15.4	0.7	15.9	1.1	3.0	15.4	0.7
		TLTN36_29		79	28694	1411	1932	1288885	98644	0.16	7.1	530.0	3255.3	447.87	2.03	0.0492	2.16	0.0151	2.97	0.0022	2.03	0.68	158.4	101.2	14.4	0.6	15.3	0.9	5.8	14.3	0.6
		TLTN36_06	inherited	-26	15354	905	2780	104839	3045	0.43	4.2	43.1	100.5	26.02	2.09	0.0579	2.42	0.3065	3.20	0.0384	2.09	0.65	525.3	106.3	243.1	10.0	271.5	15.1	10.5	241.0	9.8
		TLTN36_14	high cm-pb	42	7830	1120	2173	307452	21625	0.18	2.5	126.4	713.6	391.74	3.67	0.1156	12.79	0.0407	13.31	0.0026	3.67	0.28	1889.8	460.5	16.4	1.2	40.5	10.5	59.4	15.0	1.1

Table 6.3: SC-ICP-MS Zircon U-Pb results for the Hb-Bt monzogranite on Tinos

Analysis													Ratios								Ages							Disc. % 6-38/7-35	Common-Pb Corrected Age	
Rock type	Sample	Analysis	comments	204Pb cps	206Pb cps	207Pb cps	208Pb cps	232Th cps	238U cps	Th/U	Pb ppm	Th ppm	U ppm	238U/206Pb a %		207Pb/206Pb a %		207Pb/235U a %		206Pb/238U a %		Rho	207Pb/206Pb abs Age		206Pb/238U abs Age		207Pb/235U abs Age			Cor.206/238a [Ma] Pb Age	
Granite Vein	TLT13	TLT13_01		80	29210	1607	2963	1991769	97294	0.26	7.4	819.0	3210.7	443.30	1.45	0.0554	2.34	0.0172	2.75	0.0023	1.45	0.53	427.9	104.4	14.5	0.4	17.3	0.9	16.2	14.4	0.4
		TLT13_02		-16	3907	216	321	294547	13452	0.27	1.0	121.1	443.9	453.52	2.17	0.0567	4.18	0.0172	4.71	0.0022	2.17	0.46	478.0	184.9	14.2	0.6	17.3	1.6	18.1	14.0	0.6
		TLT13_03a		78	5511	320	546	431023	17963	0.30	1.4	177.2	592.8	432.17	1.84	0.0556	2.85	0.0177	3.39	0.0023	1.84	0.54	438.3	126.7	14.9	0.5	17.9	1.2	16.6	14.7	0.5
		TLT13_03b		30	34470	1634	5752	5560168	116532	0.59	9.2	2286.2	3845.6	446.92	1.40	0.0464	1.28	0.0143	1.90	0.0022	1.40	0.74	20.2	61.6	14.4	0.4	14.4	0.5	0.2	14.4	0.4
		TLT13_04		12	11830	583	2332	2195692	40047	0.68	3.3	902.8	1321.6	454.94	1.58	0.0499	2.25	0.0151	2.75	0.0022	1.58	0.57	191.6	104.5	14.2	0.4	15.2	0.8	7.1	14.1	0.4
		TLT13_05		43	14779	787	972	684066	50019	0.17	3.6	281.3	1650.6	451.63	1.47	0.0529	3.02	0.0162	3.36	0.0022	1.47	0.44	325.8	137.0	14.3	0.4	16.3	1.1	12.4	14.1	0.4
		TLT13_06		8	52377	2543	943	930245	184280	0.06	12.3	382.5	6081.3	460.97	1.36	0.0474	1.24	0.0142	1.84	0.0022	1.36	0.74	68.6	59.1	14.0	0.4	14.3	0.5	2.2	14.0	0.4
		TLT13_07b		-77	15878	753	612	529519	46837	0.14	3.8	217.7	1545.6	395.26	2.25	0.0466	1.79	0.0163	2.87	0.0025	2.25	0.78	30.4	85.8	16.3	0.7	16.4	0.9	0.5	16.3	0.7
		TLT13_08		-126	14053	642	1231	1171512	46909	0.31	3.5	481.7	1538.1	442.38	1.47	0.0447	2.14	0.0139	2.59	0.0023	1.47	0.57	-72.9	104.5	14.6	0.4	14.0	0.7	-3.7	14.6	0.4
		TLT13_09		49	19171	910	1144	1226698	66851	0.23	4.7	504.4	2206.1	462.57	1.46	0.0473	2.16	0.0141	2.60	0.0022	1.46	0.56	64.4	102.7	13.9	0.4	14.2	0.7	2.0	13.9	0.4
		TLT13_10		46	15836	754	1512	1335894	52829	0.32	4.0	549.3	1743.4	435.70	1.59	0.0478	2.05	0.0151	2.59	0.0023	1.59	0.61	90.7	97.1	14.8	0.5	15.2	0.8	3.1	14.8	0.5
		TLT13_11		-36	20989	978	2920	2678632	70162	0.48	5.5	1101.4	2315.4	440.52	1.47	0.0463	1.75	0.0145	2.29	0.0023	1.47	0.64	11.7	84.2	14.6	0.4	14.6	0.7	-0.2	14.6	0.4
		TLT13_12		21	2505	123	91	113840	8584	0.17	0.6	46.8	283.3	455.30	2.18	0.0487	6.06	0.0147	6.44	0.0022	2.18	0.34	131.7	284.9	14.1	0.6	14.8	1.9	4.7	14.1	0.6
		TLT13_14		171	19380	1018	1095	832247	65905	0.16	4.7	342.2	2174.9	423.11	2.44	0.0607	5.64	0.0198	6.14	0.0024	2.44	0.40	629.6	242.8	15.2	0.7	19.9	2.4	23.5	14.9	0.7
		TLT13_15		7	4248	179	435	487692	14285	0.43	1.1	200.5	471.4	444.13	1.95	0.0415	5.16	0.0129	5.52	0.0023	1.95	0.35	-254.5	261.5	14.5	0.6	13.0	1.4	-11.5	14.6	0.6
		TLT13_16		66	6742	312	762	677234	23398	0.36	1.7	278.5	772.1	454.02	1.88	0.0452	2.76	0.0137	3.34	0.0022	1.88	0.56	-44.4	134.2	14.2	0.5	13.8	0.9	-2.5	14.2	0.5
		TLT13_07a	inherited	35	152436	8114	38424	1803509	31438	0.71	43.9	741.5	1037.5	27.11	1.39	0.0523	0.89	0.2660	1.65	0.0369	1.39	0.84	299.4	40.5	233.5	6.4	239.5	7.0	2.5	233.1	6.3
		TLT13_13	inherited	-27	82732	6319	8033	1014324	3342	0.38	21.4	41.7	110.3	5.36	1.56	0.0750	0.87	1.9290	1.78	0.1866	1.56	0.87	1068.8	35.0	1102.9	31.5	1091.2	23.6	-1.1	1104.5	31.6
Grt Leucogranite	TLTN13	TLTN13_02	rej from age cal	402	71599	9310	19723	6625422	221636	195.93	1070.8	2216207.2	1131.1	373.74	3.40	0.1360	10.89	0.0501	11.41	0.0027	3.40	0.30	2176.3	379.2	17.2	1.2	49.7	11.0	65.3	15.3	1.0
		TLTN13_03		269	108599	7679	13091	7402274	371143	132.33	1376.5	2306504.1	1894.2	415.03	1.34	0.0748	6.54	0.0249	6.67	0.0024	1.34	0.20	1064.4	262.9	15.5	0.4	24.9	3.3	37.8	15.0	0.4
		TLTN13_04		113	131957	7561	11055	10100080	471338	140.45	1602.2	3378482.1	2354.6	428.13	1.35	0.0573	1.95	0.0187	2.37	0.0024	1.35	0.57	503.4	85.8	15.2	0.4	18.8	0.9	19.0	15.0	0.4
		TLTN13_05		366	115720	10454	23758	11426230	3911140	191.47	1595.3	3822080.0	1996.1.7	413.20	1.59	0.0892	4.91	0.0298	5.16	0.0024	1.59	0.31	1409.0	187.9	15.6	0.5	29.8	3.0	47.7	14.7	0.5
		TLTN13_09	rej from age cal	246	64627	5664	9114	2740480	207583	86.53	844.9	916692.0	10594.0	396.38	1.74	0.0859	4.61	0.0299	4.93	0.0025	1.74	0.35	1336.9	178.2	16.2	0.6	29.9	2.9	45.7	15.4	0.5
		TLTN13_10		473	155238	13614	23818	9946093	523834	124.45	2050.1	3326973.4	26733.8	408.22	1.42	0.0849	2.90	0.0287	3.23	0.0024	1.42	0.44	1312.4	112.4	15.8	0.4	28.7	1.8	45.0	15.0	0.4
		TLTN13_11		340	149764	11329	17548	9105758	519389	114.93	1900.8	3046483.0	26506.9	438.35	1.49	0.0747	2.96	0.0236	3.32	0.0024	1.49	0.45	1061.5	139.3	15.4	0.5	24.7	1.6	37.7	14.8	0.4
		TLTN13_12		363	169268	13314	25798	12028060	596628	132.14	2217.3	4023392.5	30448.8	427.63	1.65	0.0805	5.70	0.0259	5.94	0.0023	1.65	0.28	1208.5	224.6	15.1	0.5	26.0	3.0	42.1	14.4	0.5
		TLTN13_16		326	129339	10493	16135	7417416	440378	110.40	1659.6	2481129.6	2247.4.6	413.88	1.35	0.0787	5.43	0.0262	5.60	0.0024	1.35	0.24	1165.5	215.3	15.6	0.4	26.3	2.9	40.8	14.9	0.4
		TLTN13_01		215	347419	20490	29386	24903250	1289562	0.20	56.2	4980.7	25089.4	427.18	1.19	0.0582	1.79	0.0188	2.15	0.0023	1.19	0.56	536.7	39.1	15.1	0.4	18.9	0.8	20.2	14.8	0.3
		TLTN13_05	rej from age cal	423	451347	26379	35655	24046150	1520762	0.16	72.6	4809.3	29587.5	396.14	1.15	0.0575	1.35	0.0200	1.77	0.0025	1.15	0.65	509.5	29.6	16.3	0.4	20.1	0.7	19.1	16.0	0.4
		TLTN13_07	rej from age cal	576	205678	18853	37608	22409320	739002	198.51	2789.3	7495920.5	37760.7	435.70	1.33	0.0872	7.54	0.0276	7.66	0.0023	1.33	0.17	1365.1	290.6	14.8	0.4	27.6	4.2	46.5	14.0	0.4
		TLTN13_14		168	137391	8946	12066	8295601	498959	108.97	1685.5	2774882.9	25464.3	440.67	1.43	0.0637	2.09	0.0199	2.54	0.0023	1.43	0.57	731.3	88.7	14.6	0.4	20.0	1.0	27.0	14.3	0.4
		TLTN13_01	high cm-Pb	2075	68266	33607	82090	3535187	105212	220.23	1957.4	1182521.9	5369.4	183.84	2.44	0.4832	1.59	0.3622	2.91	0.0054	2.44	0.84	4190.7	47.0	35.0	1.7	313.9	15.6	88.9	15.7	0.4
		TLTN13_06	high cm-Pb	1066	140452	23818	51715	9055346	431494	137.55	2298.2	3029018.1	22021.2	385.07	2.10	0.1577	5.85	0.0565	6.21	0.0026	2.10	0.34	2431.6	198.3	16.7	0.7	55.8	6.7	70.0	14.4	0.6
		TLTN13_08	high cm-Pb	1083	166414	23107	56351	17413350	524904	217.44	2637.5	5824774.8	26788.4	388.31	2.13	0.1452	5.90	0.0515	6.28	0.0026	2.13	0.34	2290.5	203.1	16.6	0.7	51.0	6.2	67.5	14.5	0.6
		TLTN13_02	high cm-Pb	1407	3827939	197818	2756426	1565398000	121410620	1.33	9709.3	313083.5	230224.0	373.30	0.96	0.0516	2.38	0.0191	2.57	0.0027	0.96	0.37	267.9	54.6	17.2	0.3	19.2	1.0	10.0	17.1	0.3
		TLTN13_03	high cm-Pb	2411	3954873	210951	2911982	-9	12667960	0.00	1001.1	0.0	246464.4	375.23	1.07	0.0542	2.56	0.0199	2.77	0.0027	1.07	0.39	378.9	57.5	17.2	0.4	20.0	1.1	14.3	17.0	0.4
		TLTN13_06	high cm-Pb	2583	206890	48045	115700	46804870	627507	0.77	52.4	9361.1	12208.6	359.55	2.02	0.2245	4.67	0.0861	5.09	0.0028	2.02	0.40	3013.3	74.9	17.9	0.7	83.8	8.2	78.6	13.9	0.5
Grt Leucogranite	TLTN15	TLTN15_01		-17	12777	1361	2459	427453	39403	0.14	3.7	175.8	1300.3	410.54	2.43	0.0962	10.22	0.0323	10.51	0.0024	2.43	0.23	1552.1	383.8	15.7	0.8	32.3	6.7	51.4	14.7	0.7
		TLTN15_02		65	11442	631	544	373584	39345	0.12	2.8	153.6	1298.4	457.40	1.82	0.0539	2.05	0.0162	2.74	0.0022	1.82	0.67	366.1	92.2	14.1	0.5	16.4	0.9	13.9	13.9	0.5
		TLTN15_03		-108	5375	435	918	399247	17313	0.29	1.5	164.2	571.3	431.66	2.06	0.0799	3.24	0.0255	3.84	0.0023	2.06	0.54	1195.2	127.7	14.9	0.6	25.6	1.9	41.7	14.3	0.6
Delos Bt-Tourm Leucogranite	17TL95	17TL95_01a		64	3411	240	444	431035	1669372	37.6	1.3	140.0	3.7	444.9	1.76	0.0702	3.21	0.0218	3.66	0.0022	1.76	0.48	935	132	14.5	0.5	21.9	1.6	98.5	14.0	0.5
		17TL95_01b		73	3166	182	700	1067635	1605799	96.9	1.3	346.9	3.6	459.3	1.56	0.0580	3.78	0.0174	4.09	0.0022	1.56	0.38	531	166	14.0	0.4	17.5	1.4	97.4	13.8	0.4
		17TL95_01c		-11	2256	134	253	352357	1157563	44.3	0.8	114.5	2.6	467.6	1.84	0.0609	5.00	0.0180	5.33	0.0021	1.84	0.34	636	215	13.8	0.5	18.1	1.9	97.8	13.5	0.5
		17TL95_02		44	6134	354	751	1149171	3584045	46.7	2.2	373.3	8.0	527.1	1.41	0.0562	4.12	0.0147	4.35	0.0019	1.41	0.32	459	183	12.2	0.3	14.8	1.3	97.3	12.1	0.3
		17TL95_03a		100	9339	641	1004	926260	5334297	25.3	3.4	300.9	11.9	521.2	1.44	0.0678	1.80	0.0179	2.30	0.0019	1.44	0.62	864	75	12.4	0.4	18.1	0.8	98.6	12.0	0.3
		17TL95_03b		55	2683	156	837	1466306	15679.47	136.2	1.1	476.4	3.5	527.7	1.81	0.0617	4.37	0.0161	4.73	0.0019	1.81	0.38	663	187	12.2	0.4	16.2	1.5	98.2	12.0	0.4
		17TL95_04		11	6733	351	437	668056	3407451	28.6	2.3	217.0	7.6	458.5	1.44	0.0520	2.72	0.0156	3.08	0.0022	1.44	0.47	283	124	14.0	0.4	15.7	1.0	95.0	13.9	0.4
		17TL95_05		82	67742	350	906	1483216	3912448	15.2	2.5	481.9	8.7	523.3	1.51	0.0520	2.25	0.0137	2.71	0.0019	1.51	0.56	287	103	12.3	0.4	13.8	0.7	95.7	12.2	0.4
Cross-cutting leucogranite through Tinos pluton	17TL100	17TL100_01		-10	6764	413	547	536498	3302231	23.7	2.4	174.3	7.4	448.9	1.73	0.0598	3.12	0.0184	3.57	0.0022	1.73	0.48	597	135	14.3	0.5	18.5	1.3	97.6	14.1	0.5
		17TL100_02a		20	855	67	143	161134	403264	58.2	0.3	52.4	0.9	426.1	3.00	0.0725	8.67	0.0234	9.18	0.0023	3.00	0.33	1000	352	15.1	0.9	23.5	4.3	98.5	14.6	0.8
		17TL100_02b		50	3061	182	300	367795	1489922	36.0	1.1	119.5	3.3	447.9	1.83	0.0596	4.12	0.0183	4.51	0.0022	1.83	0.41	589	179	14.4	0.5	18.4	1.6	92.7	14.1	0.5
		17TL100_02b		50	14843	745	2954	4071587	6987721	84.9	5.7	1322.8	15.6	436.5	1.33	0.0501	1.89	0.0158	2.31	0.0023	1.33	0.58	201	88	14.8	0.4	15.9	0.7	97.6	14.7	0.4
		17TL100_03		79	5175	257	862	1184084	2549259	67.7	1.9	385.0	5.7	449.1	1.75	0.0484	2.74	0.0148	3.25	0.0022	1.75	0.54	117	129	14.3	0.5	15.0	1.0	87.8	14.3	0.5
		17TL100_03b		71	4714	252	752	1163117	2256092	75.1	1.8	377.9	5.0	441.5	1.83	0.0521	2.86	0.0163	3.39	0.0023	1.83	0.54	292	130	14.6	0.5	16.4	1.1	95.0	14.5	0.5
		17TL100_04		78	6321	313	367	502417	3075558	23.8	2.2	163.2	6.9	450.0	1.90	0.0493	2.90	0.0151	3.47	0.0022	1.90	0.55	163	136	14.3	0.5	15.2	1.0	91.2	14.3	0.5
		17TL100_05		66	5797	307	345	388182	2771940	20.4	2.0	126.1	6.2	438.8	1.94	0.0534	3.14	0.0168	3.69	0.0023	1.94	0.53	347	142	14.7	0.6	16.9	1.2	95.8	14.5	0.6
		17TL100_06		45	4277	253	405	463423	2090016	32.2	1.5	150.6	4.7	448.3	2.06	0.0588	2.70	0.0181	3.40	0.0022	2.06	0.61	558	118	14.4	0.6	18.2	1.2	97.4	14.1	0.6
		17TL100_07		69	3454	186	260	324262	1728954	27.3	1.2	105.3	3.9	461.5	1.68	0.0533	3.21	0.0159	3.62	0.0022	1.68	0.46	340	145	14.0	0.5	16.0	1.2	95.9	13.8	0.5
		17TL100_08		62	2863	174	316	388246	1202525	47.0	1.0	126.1	2.7	377.4	2.14	0.0569	3.32	0.0208	3.95	0.0020	2.14	0.54	488	147	17.1	0.7	20.9	1.6	96.5	16.8	0.7
		17TL100_09		67	2227	126	285	315865	1069576	43.0	0.8	102.6	2.4	440.7	2.02	0.0536	5.10	0.0168	5.48	0.0023	2.02	0.37	355	230	14.6	0.6	16.9	1.8	95.9	14.5	0.6
		17TL100_10		75	3768	188	298	321692	1820861	25.7	1.3	104.5	4.1	443.7	1.93	0.0494	3.17	0.0154	3.71	0.0023	1.93	0.52	168	148	14.5	0.6	15.5	1.1	91.4	14.5	0.6
		17TL100_11		-1	6047	307	422	470203	2969088	23.1	2.1	152.8	6.6	455.6	1.79	0.0496	2.79	0.0150	3.32	0.0022	1.79	0.54	177	130	14.1	0.5	15.1	1.0	92.0	14.1	0.5
		17TL100_13		28	4135	211	319	399741	1969337	29.6	1.4	129.9	4.4	440.8	1.90	0.0495	3.37	0.0155	3.87	0.0023	1.90	0.49	172	158	14.6	0.6	15.6	1.2	91.5	14.5	0.6
		17TL100_14		43	4933	262	416	533665	2403189	32.3	1.7	173.4	5.4	443.5	1.80	0.0522	3.68	0.0162	4.10	0.0023	1.80	0.44	293	168	14.5	0.5	16.3	1.3	95.0	14.4	0.5
		17TL100_15		16	1258	86	188	203277	590934	50.1	0.5	66.0	1.3	428.6	2.98	0.0637	5.75	0.0205	6.48	0.0023	2.98	0.46	733	243	15.0	0.9	20.6	2.6	98.0	14.7	0.9
		17TL100_16		47	5582	280	382	467890	2693100	25.3	1.9	152.0	6.0	447.0	1.91	0.0498	2.71	0.0153	3.31	0.0022	1.91	0.58	183	126	14.4	0.5	15.5	1.0	92.1	14.3	0.5
		17TL100_12	inherited	32	149187	7788	10579	6466021	3154506	29.9	51.8	210.1	7.0	19.45	1.67	0.0519	1.28	0.3674	2.10	0.0514	1.67	0.79	279	59	323	11	318	11	-15.7	323.6	10.6
Naxos leucogranites in granodiorite	17TL106	17TL106_01		48	7306	383	922	1182218	3459773	49.8	2.7	384.1	7.7	435.3	1.52	0.0516	2.58	0.0163	2.99	0.0023	1.52	0.51	267	118	14.8	0.4	16.5	1.0	94.5	14.7	0.4
		17TL106_02a		77	10681	549	1420	1935881	5074336	55.6	3.9	628.9	11.3	440.4	1.44	0.0496	1.87	0.0155	2.36	0.0023	1.44	0.61	177	87	14.6	0.4	15.6	0.7	91.7	14.6	0.4
		17TL106_03a		18	6614	358	865	1259414	3096815	59.3	2.4	409.2	6.9	430.1	1.62	0.0529	2.39	0.0170	2.88	0.0023	1.62	0.56	325	108	15.0	0.5	17.1	1.0	95.4	14.8	0.5
		17TL106_04a		12	8883	445	972	1350894	3959604	49.7	3.2	438.9	8.8	418.0	1.58	0.0495	2.31	0.0163	2.80	0.0024	1.58	0.56	171	108	15.4	0.5	16.4	0.9	91.0	15.3	0.5
		17TL106_04b		17	8100	418	1434	1985789	3771391	76.7	3.1	645.2	8.4	435.5	1.40	0.0513	2.33	0.0162	2.72	0.0023	1.40	0.51	255	107	14.8	0.4	16.4	0.9	94.2	14.7	0.4
		17TL106_05a		88	3595	210	319	410376	1655009	36.1	1.3	133.3	3.7	428.4	1.66	0.0577	3.05	0.0186	3.47	0.0023	1.66	0.48	519	134	15.0	0.5	18.7	1.3	97.1	14.8	0.5
		17TL106_05b		57	3158	180	400	484137	1445266	48.8	1.2	157.3	3.2	425.8	1.73	0.0564	3.83	0.0183	4.21	0.0023	1.73	0.41	468	170	15.1	0.5	18.4	1.5	96.8	14.9	0.5

Table 6.4: SC-ICP-MS Zircon U-Pb results for garnet bearing leucogranites and granitic veins on Tinos and cross-cutting leucogranites on Tinos, Delos and Naxos

age of ca. 185 Ma which is the same age as the protolith age to the amphibolites of the metamorphic sole under the Tsiknias Ophiolite, indicating incorporation of some country rock during dyke emplacement.

6.5.1.2 17TL36-Dactite Dyke (East of Mt Tsiknias)

Sample 17TL36 is a coarse-grained dacite dyke that intrudes through the Moho Transition Zone sequence of alternating serpentinites and gabbros of the Tsiknias Ophioite on the eastern flank of Mt Tsiknias (N37.580526, E25.23496). U–Pb common-Pb corrected ages of 12 data points span between 13.9 ± 0.5 Ma and 14.9 ± 0.5 Ma, with a weighted mean of 14.51 ± 0.19 Ma and a MSWD of 2.0 Ma (Fig. 6.14), which is interpreted to represent the timing of dyke emplacement. Because this dyke is completely undeformed, this age provides a minimum age for ductile deformation along the Tinos Shear Zone.

6.5.1.3 17TL05-Dacite Dyke (Kionnia Bay)

Sample 17TL05 is taken from a more evolved dacite dyke that intrudes eclogite and blueschist facies rocks of the Kionnia Thrust Zone (in the Lower Unit) at Kionnia Bay (N37.553558, E25.134661). The dyke dips towards the NE and cross-cuts prograde top-to-SW fabrics, and retrograde greenschist facies top-to-NE fabrics (Lamont et al., in prep). Common-Pb corrected U–Pb ages range between 14.0 ± 0.3 Ma and 15.0 ± 0.4 Ma, with successful data (14/15 analyses) yielding a weighted mean age of 14.43 ± 0.15 Ma with a MSWD of 1.5 Ma (Fig. 6.14). This weighted mean age is slightly younger than less evolved dykes, although it lies within error of the ages of the other dykes. Some zircon cores give inheritance ages of ca. 167 Ma and 265 Ma, the first of which is similar to the protolith age of the Cycladic Blueschist metasediments, and the older age is similar to an inheritance age also recorded in basement rocks on Naxos (6.18).

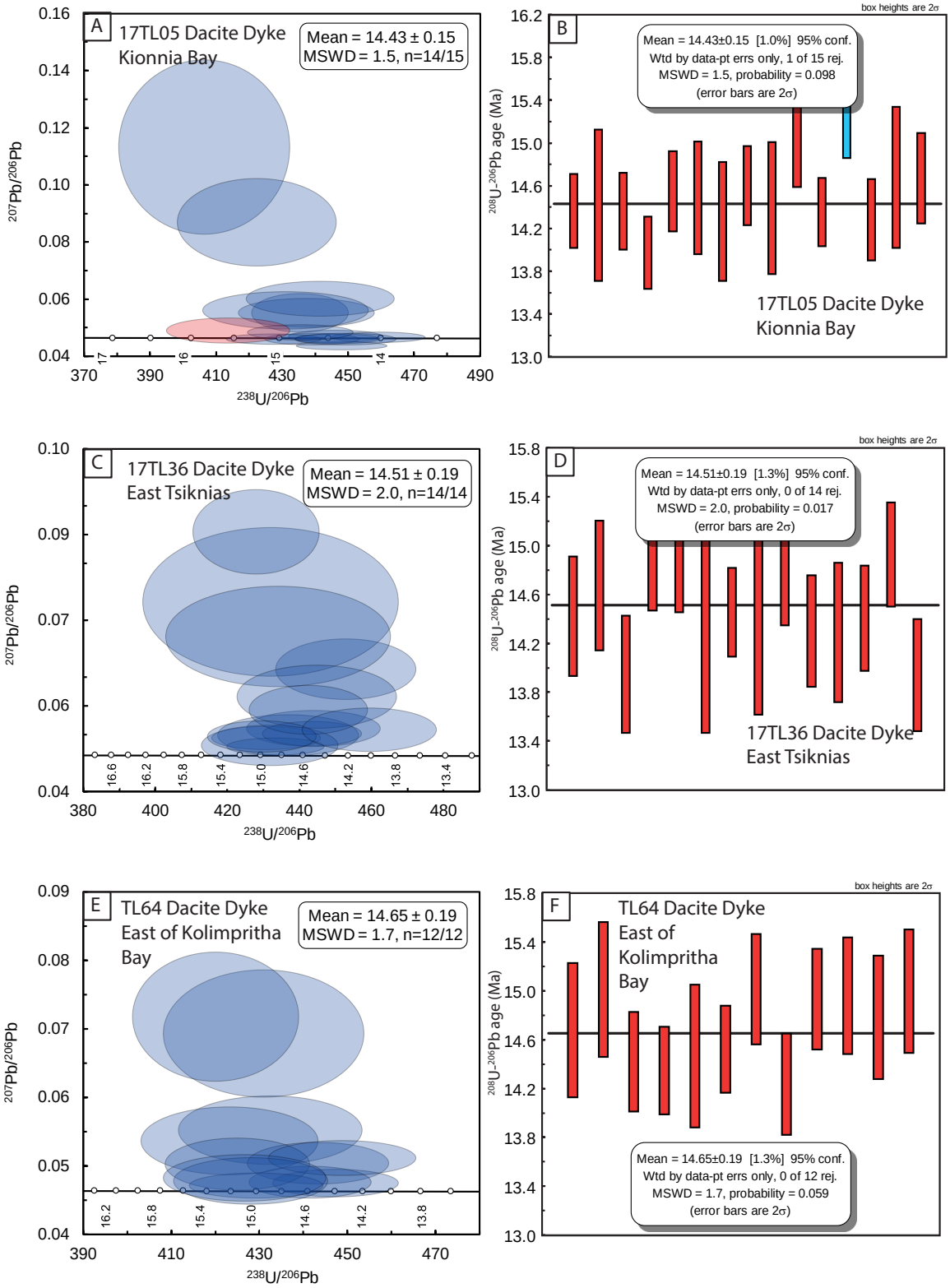


Figure 6.14: Dacite dyke Tera-Wasserburg diagrams and weighted mean box plots

6.5.1.4 TLTN36-Undeformed Hb-Bt Monzogranite (Centre of the batholith)

Sample TLTN36 is taken from the centre of the Hbl-Bt monzongranite pluton (37.596171, 25.197489), and is undeformed, with no preferred alignment of hornblende and biotite, K-feldspar and plagioclase phenocrysts. Zircons are well formed and interpreted as having a magmatic origin. Ablation of zircon cores and rims gives a range of ages between 15.7 ± 0.7 Ma and 13.6 ± 0.6 Ma, however because zircon growth can occur over a time period in the magmatic system prior to granite crystallization, the youngest data population (18/25 data points) were used to calculate a weighted mean of 14.24 ± 0.18 Ma with a MSWD of 1.4 Ma (Fig. 6.15). This age is therefore interpreted to constrain the timing of pluton emplacement that must cross-cut the Tinos Shear Zone and no deformation occurred after this time.

6.5.1.5 TLTN34-Foliated Hb-Bt Monzogranite (western margin of the batholith)

Sample TLTN34 was taken from the south western margin of the monzogranite pluton (N37.582732, E25.175706) and is highly foliated, with recrystallization of quartz and plagioclase that form mildly elongation towards the NE. Zircons show magmatic textures and ablation of cores and rims gives a spectrum of common-Pb corrected ages between 14.1 ± 0.7 and 18.1 ± 2.0 Ma, however these end members were rejected from the weighted mean calculated age of 14.84 ± 0.11 with an MSWD of 1.2 Ma based on 30/32 data points (Fig. 6.15). This age agrees with field observations as it is older than the ages of undeformed granitoids and dykes, and signifies the monzogranite firstly intruded from its southwestern margin coeval with top-to-NE shearing on the Tinos Shear Zone.

6.5.1.6 TLT13-Granite Vein intruding Mirsini Unit

Sample TLT13 is a few centimetre-wide granite vein that intrudes a meta-chert from the Mirsini Unit (37.583181, 25.20910). The appears to emanate from the monzogranite pluton (300 m away). Zircons from this vein are magmatic and ablation of cores and rims give a range of ages between 13.9 ± 0.4 Ma and 16.3 ± 0.7 Ma and provides

a weighted mean common-Pb corrected age of 14.31 ± 0.17 with an MSWD of 1.8 based on 15/16 analyses (Fig. 6.15). This age is almost identical to the age of sample TLTN36 (undeformed monzogranite) and thus constrains the latter stages of pluton emplacement. An inherited age of ca. 233 Ma is derived from a zircon core, and is similar to that reported in sample 17TL05, possibly representing inheritance from Cycladic basement rocks (Lamont et al, under review).

6.5.1.7 TLTN13-Garnet Muscovite Leucogranite Sill (Livada Bay)

This garnet-bearing leucogranite crops out at Livada Bay (N37.612741, E25.242176), where it intrudes parallel to the (S_{2b}) foliation of amphibolites within the metamorphic sole of the Tsiknias ophiolite and is clearly cross-cut by brittle high angle normal faults. Zircon in these granites shows complicated morphologies and therefore only zircon rims were analysed in order to constrain the emplacement age of the sill. Common-Pb corrected ages range from 13.9 ± 0.5 Ma to 17.1 ± 0.3 Ma, although selection of the most concordant data (9/14 data points) provide a weighted mean age of 14.79 ± 0.20 Ma with an MSWD of 1.6 (Fig. 6.16). This age constrains the timing of sill emplacement and therefore provides a maximum age for the timing of brittle normal faulting.

6.5.1.8 TLTN15-Garnet Muscovite Leucogranite Sill (Livada Bay)

This leucogranite sill (N37.613210, E25.244438) is smaller than the major meter wide sills (TLTN13). It appears to be a second-generation sill that also intrudes the sole amphibolites and is cross-cut by normal faults, although it displays minor curvature into alignment with the normal faults, suggesting it intruded immediately before normal faulting and was sitting close to the solidus when normal faulting initiated. Only a few zircons were successfully extracted and they display complicated morphologies. Extraction of zircon rim data prove a common-Pb corrected ages between 13.9 ± 0.5 and 14.7 ± 0.3 Ma, with a weighted mean age of 14.23 ± 0.89 Ma with an MSWD of 1.6 (Fig. 6.16), which constrains the onset of brittle normal faulting, although it has a

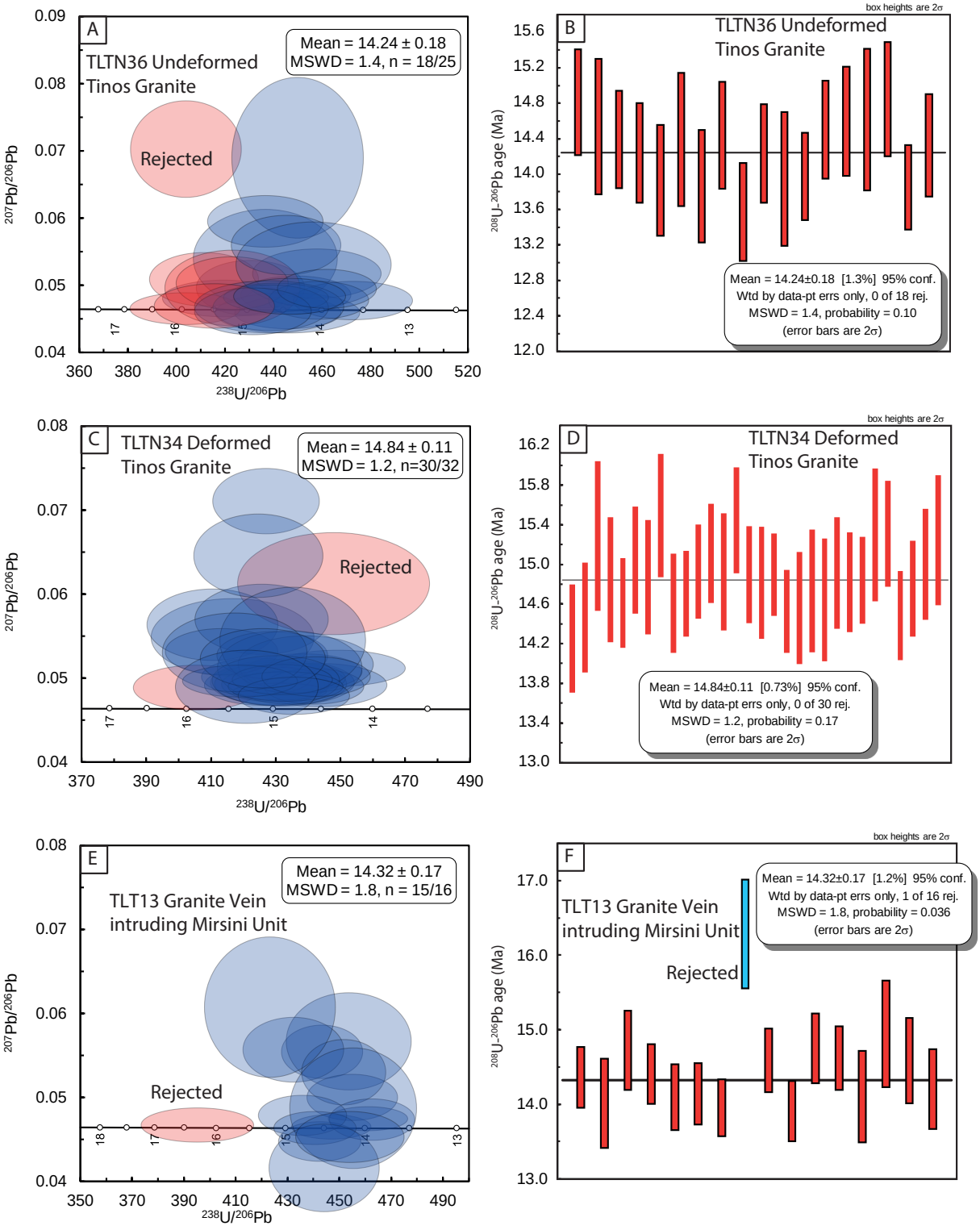


Figure 6.15: Tinos monzogranite Tera-Wasserburg diagrams and weighted mean box plots: A) All U-Pb granitoid ages, B) Inheritance U-Pb age distributions

larger error owing to fewer data points. Zircon cores give an inherited age of ca. 174 Ma, which presumably represents the protolith age of the sole amphibolites, suggesting some incorporation of the host amphibolites during intrusion.

6.5.1.9 17TL100 – Cross-Cutting Leucogranite Dyke within the Hbl-Bt Monzogranite

Sample 17TL100 is from a late cross-cutting leucogranitic dyke through the Tinos monzogranite at Livada Bay (N37.610512, E25.236602). Zircons exhibit magmatic crystal habits and common-Pb corrected U–Pb ages of core and rims range between 13.8 ± 0.5 Ma and 16.8 ± 0.7 Ma, although this oldest age is rejected from a weighted mean age of 14.33 ± 0.13 Ma with an MSWD of 0.89 (Fig. 6.16). This age places an absolute lower bound for the crystallization of the monzogranite at Livada Bay, as this dyke cross-cuts it, and therefore the monzogranite must have been in a solid-state during dyke intrusion. The age of sample 17TL100 is within error of the 14.24 ± 0.18 Ma age of undeformed monzogranite sample TLTN36, and therefore granite crystallization must have occurred between ca. 14.4 and 14.3 Ma, and the cross-cutting dyke must have intruded immediately after.

6.5.1.10 17TL95 – Delos Biotite Tourmaline Leucogranite

This biotite-tourmaline bearing leucogranite was taken from a sill that intrudes parallel to the sillimanite grade foliation on the eastern coast of Delos (N37.406523, E25.266933). The sill and the surrounding rocks locally exhibit complex relationships with Hbl-Bt bearing granitoids that cross-cut the foliation and the biotite-tourmaline leucogranites (Fig. 6.17), indicating the leucogranites must pre-date the larger volume Hbl-Bt granitoids. Zircons from sample 17TL95 display complex morphologies, but ablation of zircon rims yielded two distinct age populations. An older population yielded a weighted mean common-Pb corrected age of 13.84 ± 0.22 Ma with an MSWD of 0.90, whereas a younger age population gave a weighted mean age 12.07 ± 0.18 Ma with an MSWD of 0.33. This bimodal age distribution is interpreted as two

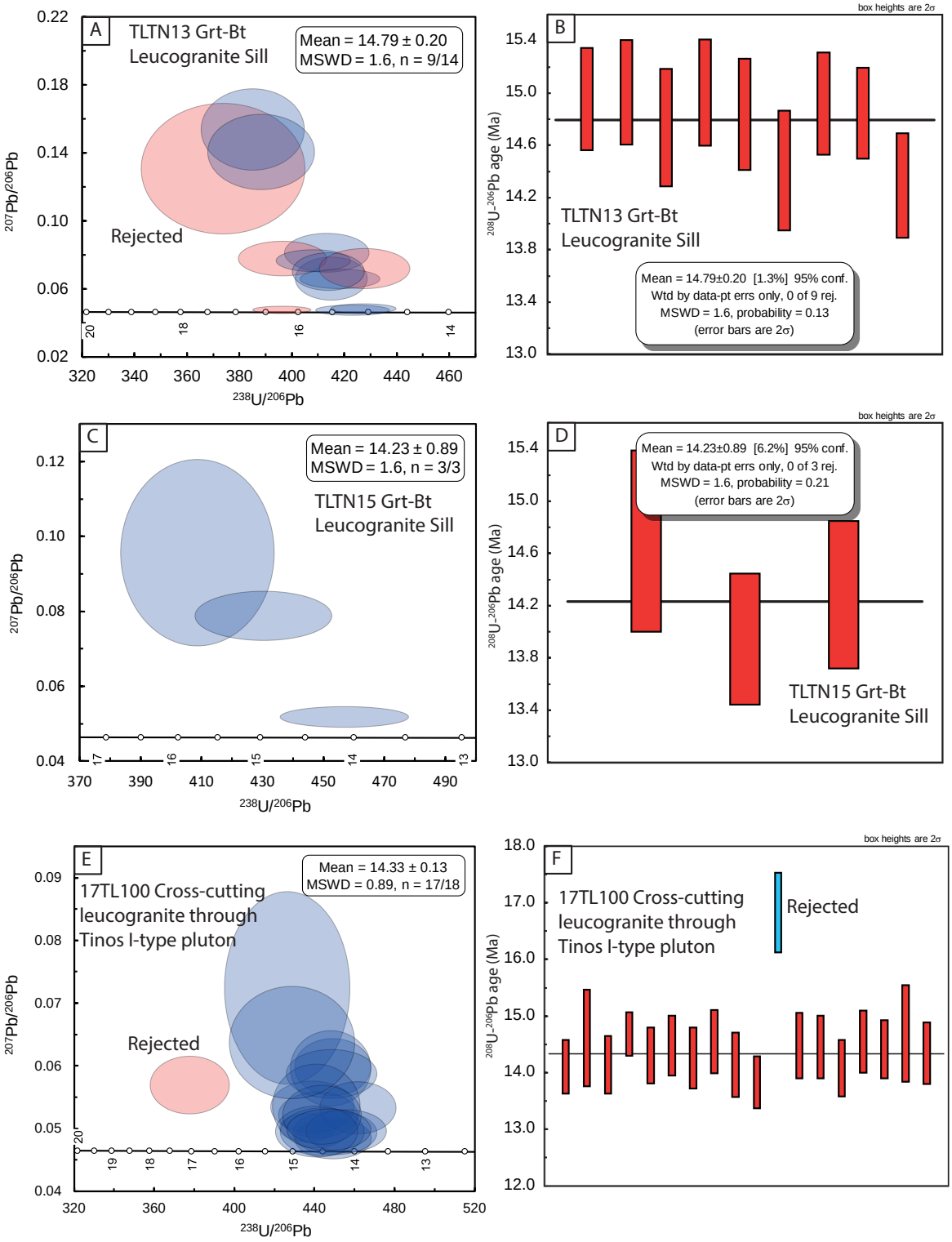


Figure 6.16: Tinos leucogranite Tera-Wasserburg diagrams and weighted mean box plots

distinct periods of zircon rim growth. Based on field relationships, the older age must represent partial melting of the host sillimanite-grade gneisses, whereas the younger ca. 12 Ma presumably represents the intrusion of the adjacent Hbl–Bt granites and possibly remobilization and incorporation of the later magma (that could potentially be interpreted from the geochemistry). The Hbl-Bt granites are probably related to the adjacent Mykonos monzogranite which has a U–Pb age of ca. 13.3 Ma (1 Myrs older) suggesting I-type magmatism occurred over a prolonged period of time

6.5.1.11 17TL106–Folded Leucocratic Enclave in the Naxos Granodiorite

This sample is from a folded biotite bearing leucogranite near the village of Glinado within the interior of the Naxos I-type granodiorite (N37.074694, E25.399604). The sill is folded about a NE-SW trending axis with the host granodiorite. Zircons display magmatic well-developed euhedral growth zoning, and ablation of zircon rims yields common-Pb corrected data between 14.6 ± 0.4 Ma and 15.3 ± 0.5 Ma, and yields a weighted mean age of 14.82 ± 0.17 Ma with an MSWD of 1.19 (6.17). This age is intriguing as it pre-dates the reported U–Pb age of the host granodioirite by ca. 2.5 Ma (12.2 Ma; Keay et al., 2001). It therefore cannot represent a late stage fractionate melt of the granodiorite. Alternatively, it could represent an enclave or xenolith of an earlier melt or a leucogranite derived from the adjacent metamorphic core complex, that was incorporated into the granodiorite during emplacement. With this latter explanation, the folding could be a result of either magmatic flow during granodiorite emplacement or from regional E–W shortening.

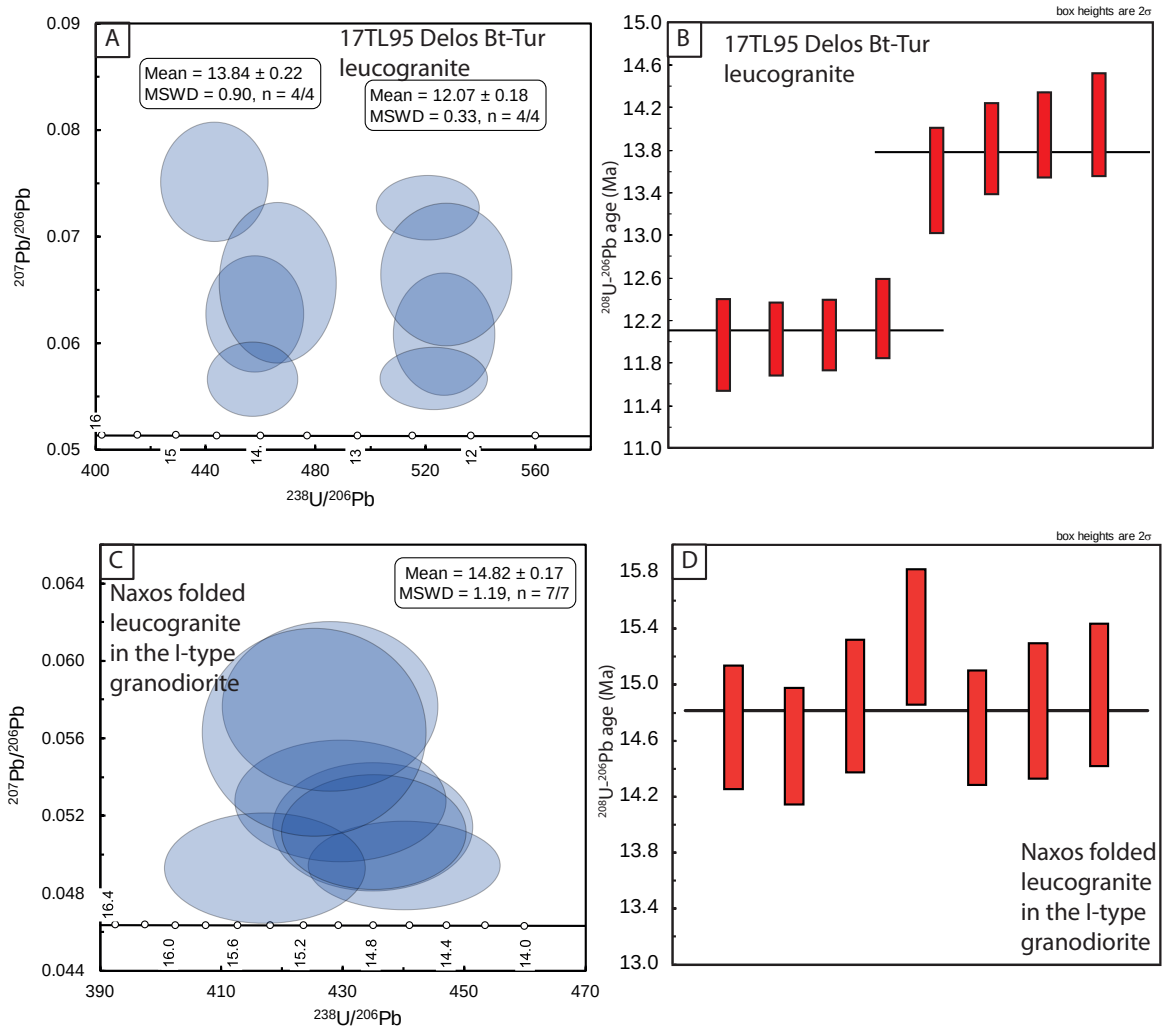


Figure 6.17: Delos and Naxos leucogranite Tera-Wasserburg diagrams and weighted mean box plots

6.6 Discussion

6.6.1 Relative Timing of Granite Intrusion

U–Pb geochronology can successfully distinguish that the dacite dykes on Tinos intruded at ca. 14.6–14.4 Ma, immediately prior to, or coeval with, the I-type pluton (ca. 14.8–14.2 Ma) (Fig. 6.18). Both were sourced from the same parent magma as revealed by Harker and bivariate diagrams and also trace element spider diagrams. However, U–Pb geochronology constrains the Tinos S-type garnet-bearing leucogranites intruded at ca. 14.8 Ma within the analytical uncertainty of the adjacent I-type

pluton, despite geochemistry discriminating them as being derived from completely different sources. Phase diagrams (Fig. 6.19) reveal that the water saturated granite solidus has a negative dP/dT slope which occurs at low pressures (ca. 2 kbar) at high temperature (>750 °C) but gets steeper at lower temperature, and is crossed at higher pressures at <700 °C. The water saturated solidus is intersected by the muscovite, biotite and hornblende dehydration melting reactions with a positive P–T slope (Hyndmann, 1981) (Fig. 6.19). S-type garnet, biotite and muscovite bearing leucogranite magmas are enriched in fluids, and would intersect the water saturated solidus at lower temperature, but at higher pressures (e.g. 680 °C, at ca. 4–5 kbar) (Fig. 6.19) due to the presence of these low temperature phases crystallizing from the magma. These granites probably did not migrate far from their source before crystallizing and therefore only form low volume sills that intrude along the foliation (e.g. Livada Bay; Fig. 6.4). In contrast, the I-type monzogranite and dacite dykes contain smaller proportions of hydrous phases and would therefore contain less water during crystallization and characteristically have hotter intrusion temperatures associated with crystallizing hornblende and biotite. These are predicted to intersect the water saturated solidus at lower pressures but higher-temperatures (ca. 2–3 kbar at 750–800 °C) (Fig. 6.19). Based on this reasoning, the relative sequence of intrusion involved S-types granite crystallization at higher pressures shortly followed by I-type crystallization at slightly lower pressures, although the absolute U–Pb weighted mean ages are indistinguishable. As both granite types are separated by only 50 m without any cross-cutting structures implies the region must have been exhumed by ca. 1–2 kbars from ca. 4–5 kbar to 2–3 kbar within the analytical uncertainty of the U–Pb analyses (approximately 100,000–500,000 years). If this is indeed true, this decompression equates to approximately 3.5–7 km of vertical displacement, and would correspond to vertical uplift rates of 7–70 mm/yr. However, without conclusive thermobarometry this model is somewhat speculative. Alternatively both type of granites formed at around the same time, with one coming from a deeper source, and one coming from a more proximal shallow source - and intruded at the same crustal level, to be exposed in the same outcrops

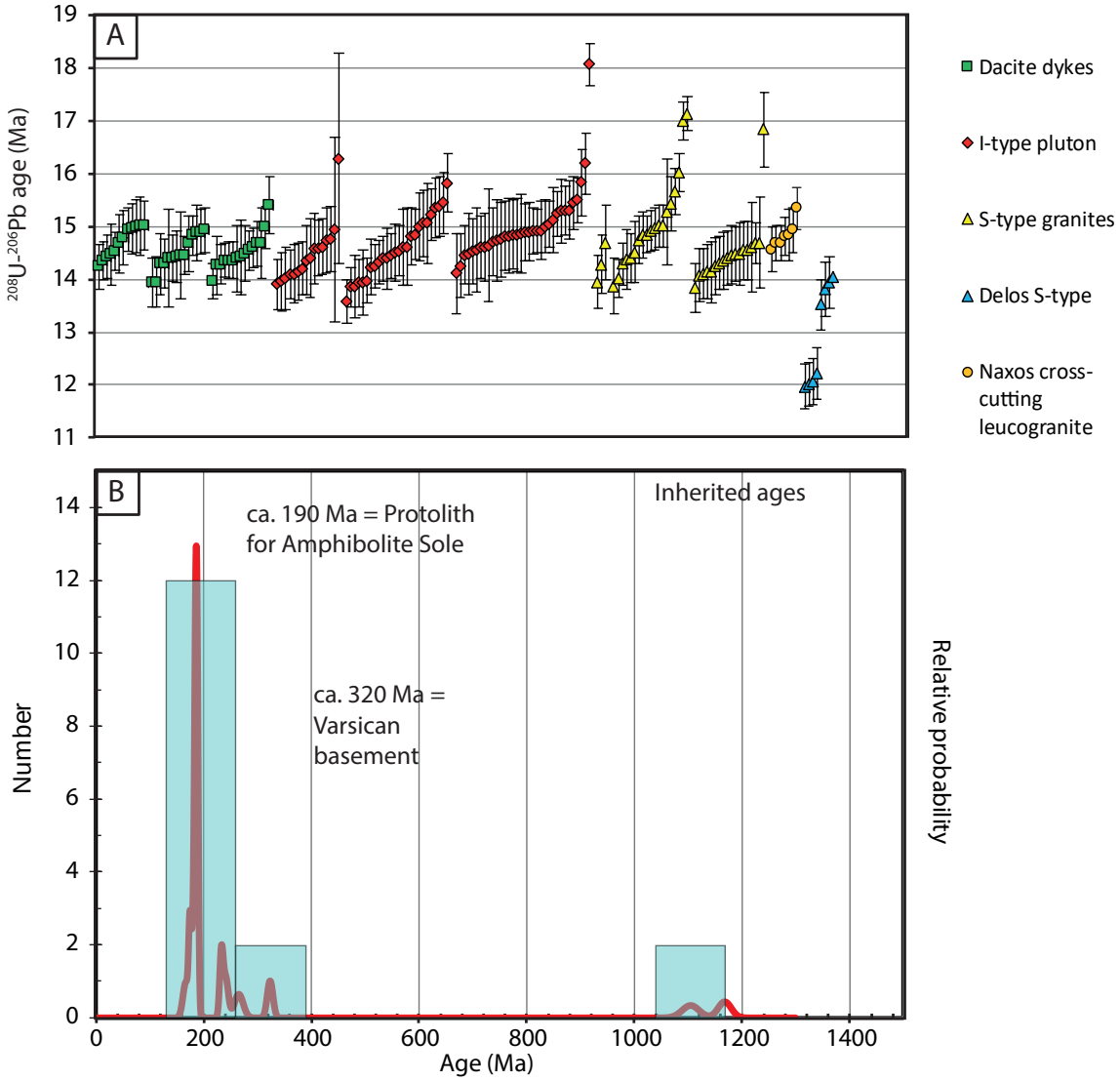


Figure 6.18: U-Pb geochronolgy of all granitoids and inhertitence age frequency plot

today (with no exhumation needed). During crystallization of the I-type granites, another magma source, similar to that of the S-type garnet-bearing leucogranites forms late leucocratic dykes which cross-cut the I-type pluton at ca. 14.3–14.2 Ma, and provide constrains on a lower bound of the crystallization age of the I-type monzogranite and ending of ductile deformation on the TSZ.

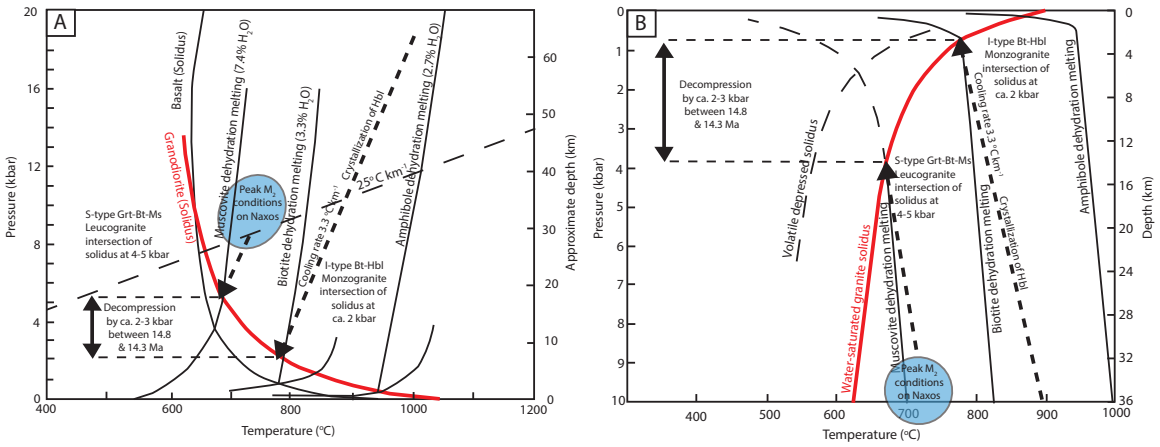


Figure 6.19: Phase diagrams showing the position of the water saturated granite solidus and the muscovite, biotite and hornblende dehydration melting reactions showing that the garnet biotite S-type leucogranites intersect the solidus at higher pressure and lower temperture than the Hbl-Bt monzogranite

6.6.2 Timing of Deformation on Tinos

Tight constraints of ca. 18–14.6 Ma can be placed for movement on the NCDS on Tinos by integrating the U–Pb data with Rb–Sr ages of Brockner and Franz (1998). Deformation on this structure must have evolved from purely ductile to brittle conditions over this time period. The crystallization of the Tinos dacite dykes by ca. 14.6 Ma and the undeformed interior of the large I-type batholith at ca. 14.3 Ma which intrudes both the Upper and Lower Units, implies these two tectono-stratigraphic units where juxtaposed against each other by at least this time. Furthermore, the pervasive and distributed ductile greenschist facies to-to-NE movements along the Tinos Shear Zone must pre-date this age but localized deformation was still occurring at ca. 14.8 Ma as demonstrated by localized shearing fabrics on the margin of the pluton (sample TLTN34). However, this deformation was probably very localised and could not have resulted in significant displacements as there is no offset on the I-type pluton across the deformed zone. Highly localised brittle normal faulting became the dominant mode of extensional deformation post-ca. 14.8 Ma, affecting rocks structurally above the Tinos Shear Zone. The S-type granites constrain the onset of brittle normal faulting to after ca. 14.8 Ma and possibly as young as 14.2 Ma. This suggests that extensional

deformation migrated up structural section with time. The timing of brittle normal faulting at around ca. 14.8 Ma implies the normal fault responsible for the potential rapid footwall uplift rates of ca. 7–70 mm/yr and cooling occurs off the north Coast of Tinos. Therefore, the Tinos Shear Zone and the poorly exposed Livada Detachment on Tinos cannot be responsible for the final stages of exhumation of the northern Cyclades. These shear zones were responsible for the early stages of exhumation in the ductile mid-crust coeval with greenschist facies conditions prior to 14.6 Ma and they are presumably cut by a higher angle fault offshore post-14.8 Ma.

These age constraints also indicate the timing of shearing on NCDS structures varies along strike. The 13.3 Ma Mykonos monzogranite, is definitively cut by a ductile shear zone that Jolivet et al., (2010) refer to as the Livada Detachment. However, on Tinos, this clearly cannot be the same structure as the Tinos Shear Zone or the poorly exposed "Livada Detachment" that cross-cuts the Tsinkias ophiolite, as pervasive shearing on the TSZ must have ceased by at least ca. 14.6 Ma associated with dyke intrusion, thus questioning whether they represent the same mappable structure.

One possibility to explain this discrepancy is that the "Livada Detachment" on Tinos was cross-cut by a higher angle faults accommodating exhumation post 14.6 Ma, whereas further east there was still ductile movement where it cuts the Mykonos Granite over 1 Myrs later. The Mykonos Detachment, another low-angle normal fault, overlies the Livada Detachment on Mykonos and places silicified sediments against the meta-basalts, of the Tsiknias Ophiolite or metamorphic sole or the Mykonos Granite. Cross-cutting barite veins derived from hydrothermal alteration on the margins of the granite The Mykonos Detachment therefore accommodated deformation and exhumation during the cooling of the granite post ca. 13.3 Ma on Mykonos (Brichau et al., 2008; Denele et al., 2011; Rabillard et al., 2018), whereas on Tinos this structure is not exposed although it could well be the fault associated with the rapid uplift rates offshore as suggested above.

Additionally, because the ca. 14.6–14.4 Ma dacite dykes are also oriented at steep-moderate angles with dips converging towards the large-scale NW–SE fold axis

running down the centre of Tinos. It suggests they may have been rotated slightly from their original geometry (assumed vertical). Because the Tinos Shear zone is also folded about this axis like the dykes, it implies the timing of doming on Tinos must post-date dacite dyke intrusion and hence be younger than approximately 14.4 Ma. The gentle doming on Tinos must have therefore occurred concomitantly with, or after, I-type granite intrusion. However, the doming could not have been related to isostatic rebound associated with regional extension as the metamorphic foliation often dips away from the island at up to ca. 50° along the eastern and western coastlines, thus indicating a phase of E–W shortening that post-dates movement on the Tinos Shear Zone.

6.6.3 Origin of Cycladic I and S-Type Granitoids and Implications for Regional Tectonics

The generation of the voluminous I-type plutons coeval with, or immediately post-dating S-type granites is rarely observed in the geological record. S-type granitoids are geochemically distinct and derived from partial melting of a presumably metasedimentary source material. On Naxos, it is shown that leucogranites formed as the melt products of (M_3) sillimanite-grade muscovite dehydration melting of meta-pelites, following M_2 kyanite-grade metamorphism and crustal thickening (Lamont et al., in press). We interpret the leucogranites on Tinos as forming by the same mechanism, because they display similar mineralogy, major element and trace element geochemistries, are depleted in HFSE's and have similar ages (14.2–14.8 Ma) Thus, the occurrence of S-type granites on Tinos and Delos is regionally significant as it implies the entire deep levels of the Cyclades experienced a sillimanite-grade metamorphic event that resulted in partial melting. This implies that the previously interpreted "thermal anomalies" of the Naxos and Ios metamorphic core complexes (e.g. Ring et al., 2010), are not anomalies, but are just tectonic windows that expose the deepest levels of the Cyclades. In contrast, it is proposed that a series of high-grade metamorphic rocks, migmatites and leucogranites underlie the entire Cyclades, as a result of regional metamorphism

following crustal thickening (i.e. the Aegean Orogeny).

Post-collision crustal thickening could have resulted in the formation of I-type magmas if an igneous protolith melted during high-grade metamorphism, and this has been used to explain the post-collisional I-type granites in the Variscan belt of NW Iberia (e.g. Orejana et al., 2012 and references therein). The possible interpretation of crustal derived melting to produce an I-type magma is further supported by I-type granites in Attica, from which ca. 11.2 Ma zircons display textures interpreted to be a result of deep crustal granulite-facies metamorphism, due to possible underplating during the onset of crustal extension (Liati et al., 2009). Furthermore, Variscan orthogneisses dominate the Cycladic basement, as exposed on Naxos (Lamont et al, under review; Keay et al., 2001) and would be a likely protolith, in agreement with Variscan inherited U–Pb ages in this study (Fig. 6.18).

Despite the possible arguments for a crustal derived origin of I-type magmas, previous interpretations of the I-type Cycladic granitoids relate them to subduction processes rather than from purely Barrovian metamorphism and partial melting (e.g Pe-Piper and Piper, 2006; Stourati et al., 2010; Jolivet and Brun, 2010; Jolivet et al., 2012; Rallibard et al., 2018). Subduction on the current Hellenic trench could easily explain trace element patterns displayed within the I-type granites, which are common of global arc magmas, with a distinct Th–Nb depletion. However, the geochemistry could also be satisfactorily explained by inheriting a subduction signature from melting a previous arc-derived protolith (e.g. Variscan orthogneiss).

The I-type granitoids can thus be derived from melting orthogneiss basement during regional metamorphism based on this data. Because the age of I-type magmatism (ca. 14.8–12 Ma) occurs during the closure of, or shortly post-dates, the climax of regional metamorphism (ca. 17–14 Ma) and occurs coeval with extensional deformation, it is possible that magmatic underplating could be important. Magmatic underplating following either a slab tear or removal of lithospheric mantle during the onset of extension would thus seem to be a logical process to generate both extra heat and the fluid-induced melting to make the I-type Cycladic granites in contrast to just

regional metamorphism alone. Partial melting at upper-amphibolite to granulite facies in the middle and lower crust could be achieved with or without the presence of water by the fluid-present or fluid-absent melting reactions. Therefore, the Tinos I-type monzogranite and its dacite dykes are the first I-type granitoids in the Cyclades, and either possibly constrain the age of subduction on the current Hellenic subduction zone to ca. 14.8–14.6 Ma, or partial melting of the lower crust during the onset of regional Aegean extension that pre-dates the current volcanic arc. This latter possibility would also explain why the I-type granites are so localized across the Cyclades.

6.6.4 The Influence of Magmatism on Normal Faulting

I- and S-type intrusions were emplaced alongside active and inactive normal faults during the late stages of exhumation on Tinos, Delos, and Naxos (Bolhar et al., 2010; Brichau et al., 2008, 2007; Iglseder et al., 2009; Keay, 1998; Keay et al., 2001; Lamont et al., under review), indicating the two processes maybe inter-related. It has been shown that magmas may influence the style and pattern of faulting such as the upward arching of pre-existing ductile shear zones or localize several generatios of faults (Daniel and Jolivet, 1995; Davis et al., 1993; Lister and Baldwin, 1993; Rallibard et al., 2018). Despite this, the mechanisms responsible for the observed field and geochronological relations between the Cycladic plutons and the adjacent normal fault systems remain debated. Several studies have suggested that I-type magmatism does not trigger the development of ductile shear zones and does not contribute to localizing strain along flanking normal fault systems (Bolhar et al., 2010; Brichau et al., 2008, 2007). According to this argument, extensional deformation would have influenced preferential pathways for magma transport through the crust, while the location of pluton emplacement would be controlled by active detachments (Bolhar et al., 2010). In contrast, other field-based studies have suggested a more fundamental role of magmatism in influencing localization of extensional deformation by promoting the development of new normal sensed shear zones (Bessière et al., 2017; Denèle et al., 2011; Jolivet et al., 2010; Laurent et al., 2015; Rabillard et al., 2018). Alternatively, a few studies have

proposed the importance of transtensional or transpressional strike-slip faults for both the emplacement of those granitoids (Boronkay and Doutsos, 1994; Koukouvelas and Kokkalas, 2003). Based on the results of this study, the location of extensional shearing possibly influenced the initial intrusion of the Tinos monzogranite (as indicated by syn-kinematic intrusion of sample TLTN34 at ca. 14.8 Ma). However, this first generation purely ductile normal sensed shear zone that then became inactivate with further magmatism (dacite dykes and undeformed monzogranite; sample TLTN36) which cross-cuts it and was replaced by a new zone of strain localization along the upper contact of the intrusion (possibly the Livada Detachment). A ductile shear zone developed on the margins of the granitoid with a strain gradient toward the new active normal fault or shear zone that causes cooling, rapid uplift and evolves toward purely brittle behaviour. This structure was then replaced by a major brittle fault forming higher up in the crust, that may truncate the earlier ductile fabrics and was responsible for the final stages of exhumation.

6.6.5 Comparisons to Other I and S-Type Granite Terranes

The relationship between I-type and S-type granites in the Cyclades is unusual and one of only a few locations where I-type magmatism immediately post-dates S-type magmatism that is a product of regional metamorphism. The closest comparison is the I and S-type granites that intruded the Variscan of NW Iberia (e.g. Orejana et al., 2012 and references therein) where I-type magmas post-date S-type magmas by 1–2 Myrs. In this setting, the I-type granitoids are interpreted to have formed as a product of lower crustal granulite facies metamorphism and partial melting of igneous protoliths, which could be applicable in the Cyclades.

Comparisons can also be drawn between the "collision-related" S-type leucogranites exposed across the Cyclades and the Greater Himalayan tourmaline two-mica leucogranites. The Himalayan leucogranites are entirely of sedimentary origin (e.g. Searle et al., 2010; Hopkinson et al., 2016), have garnet, sillimanite, cordierite and rarely andalusite in the melt phase, have abundant magmatic tourmaline from boron-

rich fluids, occur as in situ melts within sillimanite-grade migmatites. They are spatially and temporally associated with widespread regional Barrovian metamorphism and partial melting at pressures varying from 10–4 kbar (e.g. Searle et al., 2010), very similar to peak metamorphic conditions observed in the Naxos gneisses and migmatites (Lamont et al., in press). The Himalayan leucogranites and their migmatitic host rocks occur along a mid-crustal channel, bounded by a crustal scale thrust fault along the base (Main Central thrust) and by a crustal-scale low-angle normal fault (the South Tibetan Detachment System; STDS) along the top. The Himalayan leucogranites are all within the footwall of the South Tibetan detachment normal fault but some sills intrude through the ductile shear zone beneath (Searle et al., 2010). The STD in the Himalaya is very similar to the North Cycladic Detachment System on Tinos and top-to-NNE normal sense Koronos and Zas shear zones within the interior of the Naxos metamorphic core complex that were responsible for the early stages exhumation of the gneisses from ca. 10–5 kbar (Lamont et al., in press). Furthermore, the deepest ductile structures are truncated and overprinted by deformation related to regional extension. Thus, a possible analogy could be drawn between the STDS and ductile shearing in the Cyclades between ca. 21–14.6 Ma on Tinos, and ca. 18.5–15 Ma on Naxos, prior to the onset of extension.

Finally, the S-type leucogranites generally form as low volume melts that intrude parallel to the foliation and freeze upon crossing the hydrous solidus at ca. 4–5 kbar in contrast to the I-type magmas which form larger plutonic bodies and are predicted to crystallize at shallower crustal levels due to having lower degrees of water and higher intrusive temperatures.

6.6.6 Tectonic Model

The timing and nature of kinematics on the North Cycladic Detachment System on Tinos and can be summarised as follows:

1. 18–14.8 Ma: During this period peak kyanite and sillimanite grade metamorphism and partial melting occurred in the rocks at depths of ca. 35–17.5 km.

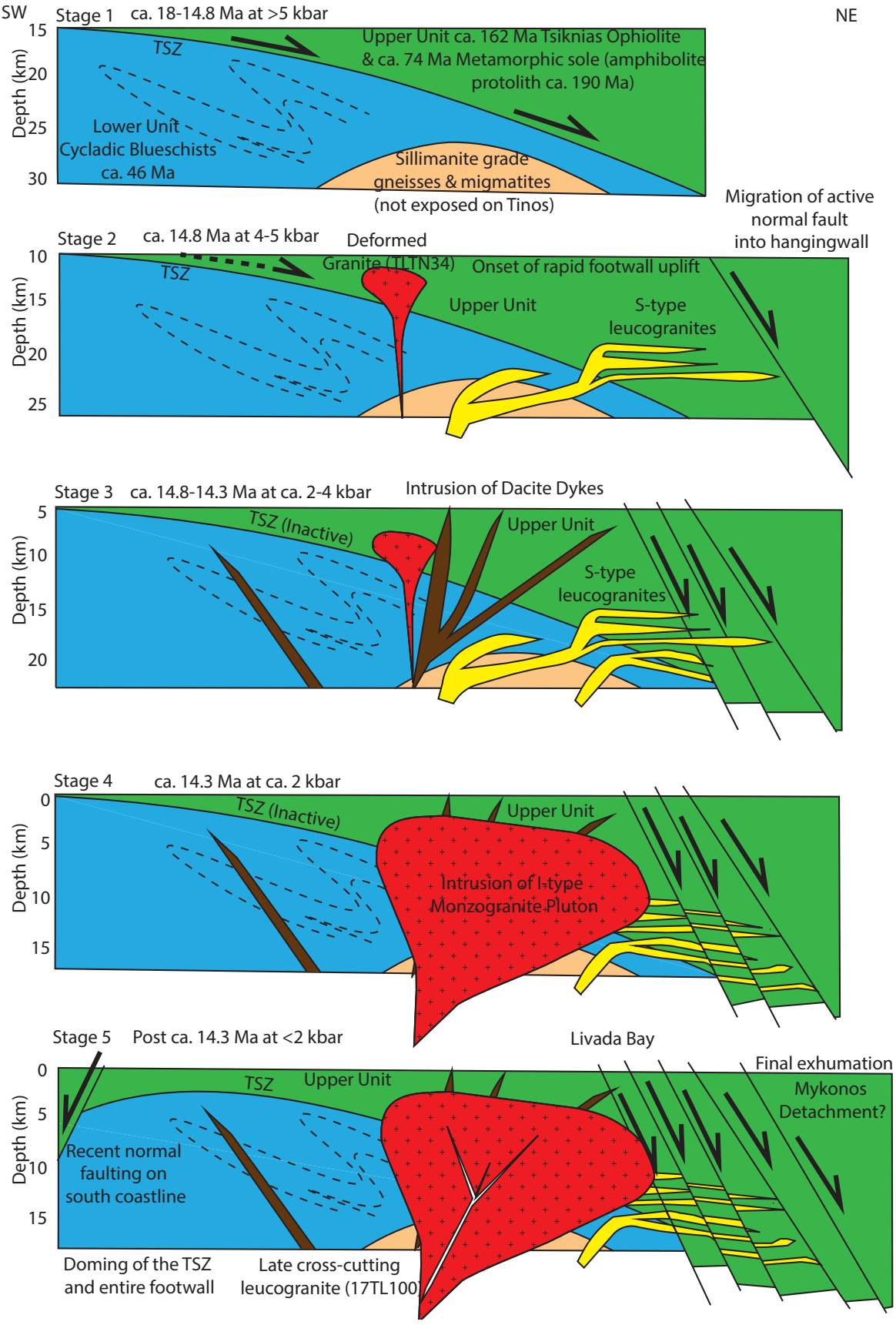


Figure 6.20: Tectonic model of the magmatism and the evolution of the NCDS, see text for discussion

This presumably affected the rocks structurally beneath the high-pressure rocks currently exposed in the Lower Unit on Tinos and are exposed on Naxos, Delos and Ikaria. During this time, pervasive top-to-NE ductile shearing occurred on the Tinos Shear Zone under greenschist facies conditions (ca. 25–31 Myrs, following the exhumation of the high-pressure rocks from subduction depths).

2. 14.8 Ma: Timing of intrusion of the S-type Grt–Bt leucogranite sills into the sole amphibolites and intrusion of the southwestern part of the monzogranite, with highly localized ductile to-to-NE shearing. At this time, assuming the phase relations of the Hyndman diagrams are correct, the structural section was probably at 4 kbar pressure.

3. 14.8–14.3 Ma: Ending of movement on the Tinos Shear Zone, intrusion of dacite dykes and the I-type monzogranite. During this time, the exposed section on Tinos decompressed from ca. 4–2 kbar associated with the formation of a proposed new major normal fault to the NE of Tinos in the hangingwall of the Tinos Shear Zone, causing footwall uplift at rates between 7–70 mm/yr. This new strain localization caused the onset of brittle normal faulting at Livada Bay at ca. 14.3–14.2 Ma.

4. 14.3–14.2 Ma: Timing of intrusion of another leucogranite that cross-cuts the Tinos monzogranite and is undeformed, suggesting that extensional strain migrated up structural section further towards the NE.

5. 14.2 Ma – present: Final stages of exhumation of Tinos by brittle normal faulting. All rocks within the metamorphic footwall including the Tinos Shear Zone are domed, suggesting that folding post-dates top-to-NE normal fault movements, and therefore be younger than ca. 14.6 Ma. This doming is too steep to be solely accounted for by isostatic rebound and thus calls for other mechanisms. On Naxos, the sediments are also dipping away from the island implying the doming is a recent feature, and must involve another phase of shortening during the Pliocene or Pleistocene.

6.7 Conclusions

Several key conclusions can be summarised as follows:

1. The Tinos I-type monzogranite intruded at ca. 14.8–14.3 Ma, with dacite dykes intruding at ca. 14.6–14.4 Ma, and constrain the timing of pervasive top-to-NE shearing on the Tinos Shear Zone to between ca. 18–14.6 Ma.

2. Garnet-bearing S-type leucogranite sills intruded at ca. 14.8–14.2 Ma and constrain the onset of brittle normal faulting associated with regional extension in the Cyclades to post ca. 14.8 Ma, and possibly post 14.2 Ma.

3. The Delos biotite-tourmaline bearing leucogranites show some degree of mixing between sedimentary and igneous and I-type sources and give two distinct age populations at ca. 13.8 Ma (which represents anatexis during sillimanite grade metamorphism) and ca, 12.1 Ma possibly associated with I-type plutonism.

4. The almost coeval intrusion of Tinos I and S-type granitoids can only be explained by being derived from two distinct sources and parent magmas. Geochemical analyses suggest that the I-type Hbl–Bt plutons and dacite dykes formed from the same magma source which yield trace element patterns characteristic of arc-related magmas. In contrast, the S-type garnet-bearing leucogranite sills could not have formed during fractionation of the same parent magma source and are more enriched in HFSEs. Such enrichment is independent of the fractionation and is more likely to be the result of melting of a fertile meta-pelitic protolith which underlies the current exposure on Tinos, similar to the sillimanite-grade metapelites which form migmatites and leucogranites on Naxos. The incorporation of sedimentary sourced melts possibly increased the peraluminous nature of the melt.

5. The intrusion of S and I-type granitoids on Tinos occurred within the uncertainty of U–Pb geochronology between 14.8 and 14.3 Ma. It is speculated that this corresponds to rapid footwall uplift at rates between ca. 7–70 mm/yr, associated

with strain localization and the initiation of another major normal fault structurally above the Tinos Shear Zone, although it is unclear whether this relates to the Mykonos Detachment.

6. The regional occurrence of S-type granites implies the deepest levels of the Cyclades is affected by sillimanite-grade metamorphism and underwent anatexis. Although no such rocks are currently exposed on Tinos, the intrusion of S-type garnet bearing leucogranites at a similar time to that on Naxos and Delos (ca. 15–14 Ma) implies a regional scale partial melting event occurred immediately prior to the onset of regional extension that resulted in rapid exhumation and cooling. This regional sillimanite grade metamorphic event coinciding with a switch from compressional to extensional tectonics could be compatible with regional heating following a prolonged period of crustal thickening.

Chapter 7

Regional Synthesis, Conclusions and Further Work

The results from this thesis demonstrate the Cyclades have experienced an entire cycle of mountain building that is termed the "Aegean Orogeny". This was associated with the closure of the Vardar Ocean and the proposed collision between the Eurasia to the NE and the Cyclades (Adria) to the SW spanning from the Late Cretaceous to Mid-Miocene ad involved several key stages each associated with distinct tectonic and metamorphic episodes which includes:

1. Formation of the Tsikinias Ophiolite at 161.9 ± 1.3 Ma during the opening of the Vardar Ocean. This ophiolite exposed on Tinos and has the same age as the Guivegueli ophiolite exposed in the Vardar Zone in northern Greece (referred to as the East Vardar Ophiolites) (ca. 161 Ma) and also possesses a supra-subduction zone geochemistry with depleted Nb relative to Th. A large plagiogranite sill within the Moho Transition Zone contains magmatic epidote, which constrains the depth of crystallization to >8.5 kbar in agreement with Al in amphibole barometry of gabbros. It is thus proposed that during ophiolite formation, the spreading centre was cool and associated with deep low degree melts that highly fractionated upon decompressing and crystallized at deep levels. This could be consistent with an oceanic core complex model, and could explain the lack of

upper crustal rocks in the exposed section. However, there is no feasible way to conclusively test this hypothesis due to lack of exposure at current erosion levels on Tinos.

2. Initiation of a NE-dipping subduction zone in old ca. 190 Ma oceanic crust in the Vardar Ocean occurred at ca. 74–66 Ma. This event induced high-grade metamorphism on the subducting ca. 190 Ma oceanic lithospheric plate producing a metamorphic sole directly under the Tsinkaias Ophiolite in the upper plate. This displays a highly condensed temperature gradient of >1000°C/km and resulted in partial melting in amphibolites directly under the Tsiknias Thrust (inferred to be the relict subduction interface). The timing of anatexis directly below the Tsiknias Thrust is constrained to 74.0 ± 3.3 Ma by U–Pb dating of zircon rims and occurred at P–Tconditions of ca. 6–8.5 kbar and 850°C. This overlaps in age with the underlying pelagic meta-sediments which yielded a Lu–Hf garnet age of 66.6 ± 2.0 Ma, which can be directly related to garnet growth at P–Tconditions of ca. 8–8.5 kbar and 690°C. This age coincides with the age that Nubia begins to move northwards (DeMets et al., 2015). The cause of metamorphism in the sole represents a thermal conundrum as heat from the overlying ca. 90 Myr old ophiolite would be insufficient to induce temperatures >250°C from thermal conduction alone. An additional source of heat is therefore neccessary. One possibility is shear heating or potentially transient rapid slip events on the Tsiknias Thrust fault zone. This is in agreement with field and microstructural observations and may have caused the adjacent rocks to experiance high temperatures and may have caused a steep and inverted metamorphic field gradient in the underlying rocks.

3. The main subduction thrust stepped back causing the metamorphic sole to be accreted to the upper plate (in the hangingwall of the subduction zone). Alkali basalts and island arc tholeiites with distinctively different geochemistry to the Tsinkaias Ophiolite and pelagic limestones were then underthrusted and formed

a melange, which is exposed in the hangingwall of the Naxos-Paros Detachment System.

4. Continued NE-directed subduction of oceanic crust, resulted in high-pressure eclogite-facies metamorphism of meta-ophiolite rocks within the Kampos Unit on Syros, constrained to ca. 51.2–52.4 Ma (Lagos et al., 2007; Tomaschek et al., 2003). This must have detached from the down-going plate and been entrained in serpentinites to provide the positive buoyancy for return ductile flow.

5. Arrival of the leading-edge Cycladic continental margin at the subduction zone, resulted in burial of continental margin sediments under a cold geothermal gradient of 5.6–6.5°C/km and underwent prograde metamorphism through the lawsonite stability field to peak blueschist- eclogite-facies conditions at ca. 46.4 Ma (ca. 4 Myrs later than the oceanic high-pressure rocks on Syros). This burial process produced top-to-SW thrusts and intense isoclinal folding as rocks were continuously underplated causing the subduction wedge to thicken. The mafic eclogites exposed on the Kionnia peninsular, achieved P–Tconditions of ca. 21–26 kbar 500–570°C, which equates to burial to depths of ca. 70–90 km. Such burial depths were only achieved due to the slab pull force from already subducted and dense eclogitized oceanic crust at greater depths (e.g. Kampos Unit on Syros). Upon reaching peak pressures, the Kionnia and Pygros Units at the highest structural levels on Tinos, detached from the subducting slab, and were buoyantly extruded in an over-riding channel producing top-to-NE extensional fabrics on the roof and top-to-SW fabrics on the base of the channel. During this exhumation process, deformation was localized at the margins of the channel, allowing the preservation of slightly colder garnet bearing blueschists on the exterior shear zones whilst internal slightly hotter and more competent eclogites were passively exhumed. Eclogites within the interior of the Kionnia Unit remained unaffected by the decompression related deformation, due to strain localization at the margins of the boudins owing to the competency difference with

the host meta-sediments. Lawsonite breakdown during decompression, hydrated the matrix of these rocks at ca. 18–20 kbar and produced cross-cutting, coarse and zoned epidotes and glaucophane. During the early stages of exhumation, upright open folds with their fold axes parallel to the shear direction developed within the extruding channel due to lateral constriction, owing to the channel having a variable across strike thickness. Localised constriction would have occurred in the narrowest parts of the channel due to converging ductile flow in response to the lateral along strike obstruction at the margins.

6. During SW-directed extrusion, the highest pressure eclogite and blueschist-facies rocks were overthrusted towards the SW over rocks which did not reach as great depths. The Sostis Unit on Tinos reached ca. 18.5 kbar and 490–500°C, whereas the Zas Unit exposed in in SE Naxos, records even lower pressures and temperatures of ca. 14.5 kbar 470°C between ca. 46–49 Ma and represents proximal continental margin sediments including thick sequences of dolomitic limestones. These units also underwent isothermal decompression associated with top-to-NE shearing from blueschist to greenschist-facies conditions. This extensional shearing was highly pervasive, causing intense retrogression that overprints nearly all relict prograde fabrics. Top-to-SW thrusting occurred simultaneously with top-to-NE movements above and propagated down structural levels with time associated with the sequential underplating of rocks during continued convergence.

7. Upon extruding to crustal levels, the rocks remained hot as suggested by P–Tconditions of ca. 13 kbar and 540°C in eclogite sample TLTN33, ca. 7.3 kbar and 536°C in TLT53 and Ti-in-biotite thermometry (TLT59). The rocks therefore retrogressed through the lower amphibolite to greenschist facies. During this retrograde phase, top-to-NE shearing was highly distributed throughout the Cycladic Blueschist Unit and lasted during the Oligocene–Miocene, dated by U–Pb xenotime on Naxos as 31.6 ± 1.1 Ma and 20.7 Ma.

8. Continued shortening and underplating of the very proximal Cycladic continen-

tal margin resulted in regional metamorphism. During this process, rocks were buried and metamorphosed diachronously as the geothermal gradient conductively increased over time. At the deepest structural levels on Naxos, prograde garnets (from samples TL67 and TL15) demonstrate the rocks experienced a clockwise prograde P–Tevolution associated with both increasing pressure and temperature to peak kyanite-grade conditions of ca. 10 kbars 680–750°C. This was associated with water saturated melting and occurred at ca. 18.5–16 Ma, constrained by U–Pb Y-poor monazite that is also trapped as inclusions in kyanite.

9. Upon reaching their maximum pressures, the migmatites on Naxos then experienced near isothermal decompression from ca. 10 kbars 680–750°C at 18.5–16 Ma to 5–6 kbars 700–730°C at 15.5–14 Ma, implying exhumation rates of up to ca. 6 km/ Myrs. Younger ages are associated with Y-rich monazite rims implying they grew during garnet breakdown. With small degrees of partial melting in the kyanite-grade field, the migmatites weakened and decompressed under a passive roof normal fault (Koronos Shear Zone) associated with top-to-NNE shearing. The hottest and most deeply buried rocks decompressed through the muscovite dehydration melting reaction locally producing up to 20–25% melt, which would have locally facilitated the decompression process.

10. The timing of top-to-NNE shearing on the Koronos and Zas Shear zones that overlie the Naxos migmatites, is constrained by U–Pb zircon dating of cross-cutting leucogranites. The Koronos Shear Zone was active during the earliest stages of exhumation between 18.5–16 Ma, but seized by 15.5 Ma and deformation migrated up structural section with time, juxtaposing a series of distinct tectono-metamorphic units with different P–T–t–D histories over just seven structural km. The migmatite dome did not form by gravity driven flow of migmatites during regional extension as this is expected to produce radial and divergent shear fabrics on all dome margins and is inconsistent with solely top-to-NE fabrics on

all margins of the dome.

11. The migmatite dome formed in a constrictive stress regime at lower pressure sillimanite-grade conditions at 15.5–14 Ma. It post-dates top-to-NNE shearing on the Koronos and Zas Shear Zones and folds the entire overlying metamorphic sequence. Structural analysis of polyphase deformation within the centre of the dome indicates a major change in regional stress regime from NNE–SSW compression to dominantly E–W contraction and later NNE–SSW extensional as demonstrated by horizontal boudinage, constrained to ca. 15 Ma.

12. The onset of regional extension and crustal thinning was accommodated by brittle-ductile normal faulting that cross-cuts and is discordant to all footwall structures on Tinos and Naxos. It attenuates and telescopes the frozen in metamorphic isograds to produce apparent metamorphic field gradients of up to 700°C/km, particularly in west Naxos. Whereas in the ductile crust, horizontal N–S pure shear boudinage accommodates extensional strains of up to 50%. These structures post-date all earlier collisional features and brittle-ductile normal faulting was responsible for the final stage of exhumation from 5 kbar (17.5 km) to the surface along an apparent geothermal gradient of 40°C/km on Naxos. The onset of normal faulting was associated with rapid cooling of the footwall rocks at rates of 60°C/Myr demostrated by a U–Pb rutile age of 12.8 ± 1.3 Ma representing cooling through the 520°C isotherm.

13. I-type magmatism occurred coeval with S-type leucogranites across the Cyclades. On Tinos distinct I and S-type granites intrude adjacent to each other with the same age span of ca. 14.8–14.3 Ma within geological uncertainty. The S-type magmas were derived from a different source to the I-type granitoids and most likely sillimanite grade gneisses and migmatites like that exposedon Naxos and Delos, which must structurally underlie current exposed levels on Tinos, and the granites must have emanated through the overlying Cycladic Blueschists. These garnet bearing S-type leucogranites are also cut by brittle normal faults and thus

place an upper limit for upper crustal normal faulting on Tinos to ca. 14.8 Ma. These age constraints also imply that the leucogranites must have crystallized first at ca. 4 kbars due to being more hydrated before being rapidly exhumed by ca. 2 kbar within uncertainty of U–Pb analysis (100,000-500,000 years) in order for the I-type granite (associated with lower water content) to crystallize at lower pressures. This rapid exhumation implies extensional strain localized on a new normal fault, structurally above exposed levels on Tinos and probably off the northern coastline to induce rapid footwall uplift. It is also suggested that the I-type granitoids intruded over a prolonged time-period, possibly supporting them to be derived from partial melting of orthogneisses of the lower crust, rather than the volcanic arc.

14. Leucogranites related to crustal melting as result of sillimanite grade metamorphism also occur adjacent to I-type granitoids on Delos. A single S-type leucogranite from Delos yields two distinct U–Pb age populations of 12.2 and 14.4 Ma, in comparison to the I-type Mykonos granite which is constrained as ca. 13.3 Ma. This indicates regional-scale partial melting of the lower crust occurred during the onset of extension. This may have formed the I-types magmas by melting an igneous protolith. Alternatively, it was contemporaneous with the formation of the volcanic arc, and hence constrain the onset of subduction on the Hellenic Trench.

15. Finally, all metamorphic foliation, ductile shear zones and Pliocene–Pleistocene hangingwall sediments on all the Cycladic Islands are steeply dip away from the island centres towards the coastlines in a radial pattern, suggesting a recent component of doming. This doming cannot be adequately explained by isostatic rebound of the crust alone as dips commonly exceed 50° , and therefore requires another mechanism. A component of post-exhumation E–W shortening seems the most plausible mechanism, that would also explain the NE–SW trending upright F_3 folds on Naxos and Tinos, that refold the metamorphic stratigraphy.

Although the origin of this shortening is poorly understood, it possibly relates to gradients in graviational potential energy between thicker crust on the east and west of the Cyclades.

16. The continental margin rocks of the Cycladic-Attic Massif probably relate to the Gavrovo-Tripolitza shelf carbonates on mainland Greece, due to the similar lithologies and occurrence of bauxite horizons on Mt Olympus, similar to those recorded in the Koronos Unit on Naxos. However, in the Cyclades the underlying sequence is more condensed and the underlying basement is comparable to the Variscan basement of the Pelagonian Zone. However on the mainland no metamorphism is recorded in these rocks, whereas in the Cyclades, these rocks were subjected to depths exceeding 35 km. This implies that the Aegean Orogeny did not laterally continue for 1000's km along strike, and was probably associated with the oblique convergence between Adria (Cyclades) and Eurasia that initiated during the Late Cretaceous and continued until the Mid-Miocene.

7.1 Future Work

The results of this thesis have highlighted several future research directions. From a regional perspective continued investigation of the ophiolitic rocks in the Aegean is crucial in completing our understanding of the Late Cretaceous – Eocene closure of the Vardar Ocean. The Tsiknias Ophiolite albeit fairly substantial, is only exposed as a 700 m thick thrust sheet on Tinos and is likely to continue along strike to the NW on the islands of Andros and onto Evia. Further investigation must also be carried out to identify more outcrops of metamorphic sole rocks that structurally underlie the ophiolite. This is required to verify that the Tsiknias Thrust at the base of the ophiolite sequence does indeed represent a relict subduction interface active between 74–66 Ma. A possible outcrop occurs on the island of Skyros to the north of Evia, which must be re-visited to verify this model.

Lu–Hf geochronology for an additional garnet fraction from sample TLT13 is

due to be analysed during October–November 2018. This is essential as the current isochron is derived on two points, one of which is enriched in Lu, which pins the age. Thus, adding a third point should significantly improve the statistical error as an MSWD can be derived without largely affecting the age. Ar–Ar geochronology on amphiboles from the metamorphic sole on Tinos would also add further cooling age constraints for the timescale of metamorphism in the metamorphic sole. Although this current work has not added further P–T–t constraints on the Akrotiri Unit in SE Tinos, several samples contain xenotime which will be dated by in-situ laser ablation at NIGL in the coming months.

Throughout the exposed ophiolite sequence, additional work is required to determine the origin of such a large plagiogranite sill. This could be achieved using a combined thermodynamic approach of THERMOCALC utilizing the new universal melt model of Holland, (2016) combined with calculating fractionation paths along liquid lines of decent using MELTS software. This method should be able to constrain the depth of plagiogranite crystallization and whether it formed due to deep and low degree partial melting as expected for a slow spreading centre as alluded to in chapter 2.

The origin of the inverted temperature gradient in the Tsiknias Metamorphic Sole is also a topic for further investigation. In chapter 2 it is demonstrated that shear heating is fundamentally required to cause high-grade metamorphism in the metamorphic sole due to the ca. 90 Myr age discrepancy between the overlying ophiolite and sole formation. This combined with evidence for episodic partial melting which emanates from the Tsiknias Thrust also suggests seismicity could provide an important heating contribution and be the origin of melting. The Tsiknias Thrust fault zone is composed of talc-tremolite ultramylonite and further microstructural characterization of samples across a transect using EBSD must be performed to identify any micron-scale vorticities diagnostic rapid slip. It is possible this two-meter wide mylonite zone was originally an amphibolite that lost melt upon rapid heating producing a hydrated ultramafic composition.

Although U–Pb dating titanite and allanites from Tinos HP rocks was unsuccessful due to high common-Pb, more promising samples collected during September 2017 and June 2018 may prove to be more useful. U–Pb titanite ages will constrain the retrograde part of the P–Tpath on Tinos, and thus tightly constrain the rates of exhumation from the subduction zone.

Further work must also be carried out on the Ios metamorphic core complex. This is because on Ios, amphibolite facies garnet mica schists crop out as a thin slice just above basement orthogneisses. It is highly probable these rocks are comparable to the kyanite grade gneisses of the Koronos Unit on Naxos, and their P–T–t paths must be determined. An eclogite locality was also found on the NW coast during a brief visit in June 2018, and its P–T–t history needs to be unravelled by a combined and detailed structural, phase diagram modelling and Lu–Hf garnet or U–Pb allanite geochronological approach. This work would greatly improve our geospatial understanding of the Eocene subduction zone dynamics as the Cycladic Continental margin was buried. Finally, a series of undescribed biotite-tourmaline bearing leucogranite sills cross-cut the basement orthogneisses and are deformed with the South Cycladic Thrust top-to-SW S–C fabrics structurally above the basement (personal observations, June 2018). These rocks are essential for constraining the timing of top-to-SW thrusting in the Cyclades. U–Pb zircon dating the time of crystallization would therefore directly place an absolute minimum age for shortening related deformation. It would also improve our understanding of a largely undescribed regional scale high-grade metamorphism and partial melting event that affected the deepest structural levels of the Cyclades. This work should hopefully be completed within the next 12 months with Nick Roberts at NIGL due our recent successful NIGFSC proposal.

Finally, thermal and mechanical modelling of various shortening or extensional scenarios building on simple models that were developed during the D.Phil is neccessary as a tool to assess the applicability of different tectonic models for the region. The idea of a buckling instability during the onset of extension is an exciting mechanism that may explain the late stage doming of all the Cycladic Islands and is

directly applicable to the Naxos metamorphic core complexes.

Bibliography

Abers, G. A., Van Keken, P. E., and Hacker, B. R., 2017. The cold and relatively dry nature of mantle forearcs in subduction zones. Nature Geoscience, v. 40, p. 1–5.

Agard, P., Yamato, P., Jolivet, L. and Burov, E., 2009. Exhumation of oceanic blueschists and eclogites in subduction zones: timing and mechanisms. Earth-Science Reviews, v. 92(1-2), p. 53–79.

Aktuğ, B., J. Nocquet, M., Cingöz, A., Parsons, B., Erkan, Y., England, P., Lenk, O., Gürdal, M.A., Kilicoglu, A., Akdeniz, H. and Tekgül, A. 2009. Deformation of western Turkey from a combination of permanent and campaign GPS data: Limits to block-like behavior. Journal of Geophysical Research: Solid Earth, 114(B10).

Allègre, C.J., Manhes, G., Göpel, C., 1995. The age of the Earth. Geochimica et Cosmochimica Acta, v. 59, p. 1445–1456.

Alsop, G.I., Holdsworth, R.E., 2006. Sheath folds as discriminators of bulk strain type. Journal of Structural Geology. v. 28, p. 1588–1606.

Altherr, R., Henjes-Kunst, F., Mathews, A., Friedrichsen, H., Hansen, B.T. 1988: O-Sr isotopic variations in Miocene granitoids from the Aegean: evidence for an origin by combined assimilation and fractional crystallization. Contributions to Mineral. Petrology. v. 100, p. 528–541

Altherr, R., Kreuzer, H., Wendt, I., Lenz, H., Wagner, G.A., Keller, J., Harre, W., Hohndorf, A. 1982: A late Oligocene/early Miocene high temperature belt in the Attic-Cycladic Crystalline Complex (SE Pelagonian, Greece). Geolog. Jb , E23, p. 97–164.

Altherr, R., and Siebel, W. 2002. I-type plutonism in a continental back-arc setting: Miocene granitoids and monzonites from the central Aegean Sea, Greece. Contributions to Mineralogy and Petrology, v. 143(4), p. 397–415. doi: https://doi.org/10.1007/s00410 -002-0352-y

Anczkiewicz, R., and Thirlwall, M. F., 2003. Improving precision of Sm-Nd garnet dating by H_2SO_4 leaching: a simple solution to the phosphate inclusion problem, Geological Society, London, Special Publications, v. 220, p. 83–91.

Anders, B., Reischmann, T., Poller, U., and Kostopoulos, D., 2005. Age and origin of granitic rocks of the eastern Vardar Zone, Greece: Newconstraints on the evolution of the Internal Hellenides. Journal of the Geological Society of London, v. 162(5), p. 857–870. https://doi.org/10.1144/0016-764904-077

Andriessen, P.A.M., Banga, G. and Hebeda, E.H., 1987, Isotopic age study of pre-Alpine rocks in the basal units on Naxos, Sikinos and Ios, Greek Cyclades. Geologie en Mijnbouw, v. 66, p. 3–14

Andriessen, P. A. M., Boelrijk N. A. I. M, E. H., Hebeda, H. N. A., Priem, E. A. T., Verdurmen and Verschure, R. H., 1979, Dating the events of metamorphism and granitic magmatism in the Alpine Orogen of Naxos (Cyclades, Greece), Contributions to Mineral Petrology, v. 69, p. 215–225

Armijo, R., Meyer, B., Hubert, A., and Barka, A., 1999, Westward propagation of the North Anatolian fault into the northern Aegean: Timing and kinematics., Geology, v. 27(3), p. 267–270

Armijo, R., Meyer, B., King, G., Rigo, A., and Papanastassiou, D., 1996, Quaternary evolution of the Corinth rift and its implications for the late Cenozoic evolution of the Aegean, Geophysical Journal International., v. 126 (1), p. 11–53.

Armstrong, R. L. 1982. Cordilleran metamorphic core complexes from Arizona to southern Canada. Annual Review of Earth and Planetary Sciences, v. 10, p. 129–154.

Ashworth, J. R., 1975, The sillimanite zones of the Huntly Portsoy area in the north-east Dalradian, Scotland, Geological Magazine, v. 112, p. 113–136.

Aubouin, J., Bonneau, M., Celet, P., 1970. Contribution à la géologie des héllenides: Le gavrovo, le pinde et la zone ophiolitique subpélagonian, Annales de la Société Géologique du Nord, v. 90, p. 277–306

Avigad, D., 1998, High-pressure metamorphism and cooling on SE Naxos (Cyclades, Greece), European Journal of Mineralogy, v. 10, p. 1309–1319.

Avigad, D., Baer, G., and Heimann, A., 1998, Block rotations and continental extension in the central Aegean Sea: palaeomagnetic and structural evidence from Tinos and Mykonos, Earth and Planetary Science Letters, v. 157, p. 23–40.

Avigad, D. and Garfunkel, Z. 1989. Low-angle faults above and below a blueschist belt—Tinos Island, Cyclades, Greece. Terra Nova, v. 1, p. 182–187.

Avigad, D. and Garfunkel, Z. 1991. Uplift and exhumation of high-pressure metamorphic terrains: the example of the Cycladic blueschist belt (Aegean Sea). Tectonophysics, v. 188, p. 357–372.

Axen, G. J., 2007, Research Focus: Significance of large-displacement, low-angle normal faults. Geology, v. 35, p. 287–288.

Baker, J., Bickle, M. J., Buick, I. S., Holland, T. J. B., and Matthews, A., 1989. Isotopic and petrological evidence for the infiltration of water-rich fluids during the Miocene M2 metamorphism on Naxos, Greece. Geochimica et Cosmochimica Acta, v. 53, p. 2037–2050.

Baker, J., and Matthews, A., 1994. Textural and isotopic development of marble assemblages during the Barrovian-style M2 metamorphic event, Naxos, Greece. Contributions to Mineralogy and Petrology, v. 116, p. 130-144.

Barth, M. G., and Gluhak, T. M., 2009. Geochemistry and tectonic setting of Mafic rocks from the Orthis Ophiolite, Greece. Contributions to Mineralogy and Petrology, v. 157 (1), p. 23–40. https://doi.org/10.1007/s00410-008-0318-9

Barth, M. G., Mason, P. R. D., Davies, G. R., and Drury, M. R., 2008. The Othris Ophiolite, Greece: A snapshot of subduction initiation at amid-ocean ridge. Lithos, v. 100 (1-4), p. 234–254. https://doi.org/10.1016/j.lithos.2007.06.018.

Baxter, E.F., 2003. Natural constraints on metamorphic rates. In: Vance, D., Müller,

W., Villa, I.M. (Eds.), Geochronology: Linking the Isotopic Record with Petrology and Textures: Geol. Soc. Special Publication, v. 220, p. 183–202.

Beaudoin, A., Augier, R., Laurent, V., Jolivet, L., Lahfid, A., Bosse, V., et al. 2015. The Ikaria high-temperature metamorphic core complex (Cyclades, Greece): Geometry, kinematics and thermal structure. Journal of Geodynamics, 92, 18–41. https://doi.org/10.1016/j. jog.2015.1009.1004

Bébien, J., 1977. Mafic and ultraMafic rocks associated with granites in the Vardar zone. Nature, v. 270 (5634), p. 232–234. https://doi.org/10.1038/270232a0.

Bébien, J., and Mercier, J. L., 1977. Le cadre structural de l9association ophiolites-migmatites-granites de Guevgueli (Macedoine, Grece); une croute de bassin interarc? Bulletin de la Société géologique de France, v. 7 (4), p. 927–934.

Beckinsale, R.D., 1979, Granite magmatism in the tin belt of Southeast Asia, in Atherton, M.P., and Tarney, J., eds., Origin of Granite Batholiths: Geochemical Evidence: Orpington, UK, Shiva Publishing, p. 34–44.

Becquerel, H., 1896, Sur les radiations emises par phosphorescence. Comptes Rendus, v. 122, p. 420-421.

Bessière, E., Rabillard, A., Précigout, J., Arbaret, L., Jolivet, L., Augier, R., et al. 2017. Strain localization within a syn-tectonic intrusion in a backarc extensional context: The Naxos monzogranite (Greece). Tectonics, 37, 558–587. https://doi.org/10.1002/2017TC004801

Bhattacharya, L., Mohanty,L., Maji, A., Sen, S. K., and Raith, M., 1992, Non-ideal mixing in the phlogopite-annite binary: Constraints from experimental data on Mg-Fe partitioning and a reformulation of the biotite-garnet geothermometer, Contributions to Mineral Petrology, v. 111, p. 87–98.

Bickle, M. J., and Baker, J., 1990. Advective-diffusive transport of isotopic fronts: an example from Naxos, Greece. Earth and Planetary Science Letters, v. 97, p. 78–93.

Bickle, M., Hawkesworth, C., England, P. C, Athey, D., 1975. A preliminary thermal model for regional metamorphism in the Eastern Alps. Earth and Planetary

Science Letters, v. 26, p. 13.

Bird, A.F., Thirlwall, M.F., Strachan, R.A. and Manning, C.J., 2013. Lu–Hf and Sm–Nd dating of metamorphic garnet: evidence for multiple accretion events during the Caledonian orogeny in Scotland. Journal of the Geological Society, v. 170(2), p. 301–317.

Bohlen, S.R., 1987, Pressure-temperature-time paths and a tectonic model for the evolution of granulites. Journal of Geology, v.95, p.617–632.

Bolhar, R., Ring, U., and Allen, C. M. 2010. An integrated zircon geochronological and geochemical investigation into the Miocene plutonic evolution of the Cyclades, Aegean Sea, Greece: Part 1: Geochronology. Contributions to Mineralogy and Petrology, v. 160, p. 719–742. https:// doi.org/10.1007/s00410–00010–00504-00414

Bolhar, R., Ring, U. and Ireland, T. R., 2017, Zircon in amphibolites from Naxos, Aegean Sea, Greece: origin, significance and tectonic setting. Journal of Metamorphic Geology, v. 35, p. 413–434. doi:10.1111/jmg.12238

Bolhar, R., Ring, U., Kemp, A. I. S., Whitehouse, M. J., Weaver, S. D., Woodhead, J. D., et al. 2012. An integrated zircon geochronological and geochemical investigation into the Miocene plutonic evolution of the Cyclades, Aegean Sea, Greece: Part 2: Geochemistry. Contributions to Mineralogy and Petrology, v. 164(6), p. 915–933. https://doi.org/10.1007/s00410-012-0759-z

Bonev, N., Marchev, P., Moritz, R., Collings, D., 2015, Jurassic subduction zone tectonics of the Rhodope Massif in the Thrace region (NE Greece) as revealed by new U–Pb and $^{40}Ar/^{39}Ar$ geochronology of the Evros ophiolite and high-grade basement rocks, Gondwana Research, v. 27, p. 760–775, doi.org/10.1016/j.gr.2014.08.008.

Boronkay, K., and Doutsos, T. 1994. Transpression and transtension in different structural levels in the Central Aegean region. Journal of Structural Geology, v. 16, p. 1555–1573. https://doi.org/10.1016/0191–8141(1594)90033–90037

Bortolotti, V., Chiari, M., Marcucci, M., Photiades, A., Principi, G., and Saccani, E., 2008. New geochemical and age data on the ophiolites fromthe Othrys area

(Greece): Implication for the Triassic evolution of the Vardar ocean. Ofioliti, v. 33, p. 135–151.

Bortolotti, V., Chiari, M., Marroni, M., Pandolfi, L., Principi, G., and Saccani, E. 2013. Geodynamic evolution of ophiolites from Albania and Greece (Dinaric-Hellenic belt): One, two, or more oceanic basins? International Journal of Earth Sciences, v. 102 (3), p. 783–811. https://doi.org/10.1007/s00531-012-0835-7

Bortolotti, V., Marroni, M., Pandolfi, L., and Principi, G., 2005. Mesozoic to tertiary tectonic history of the Mirdita ophiolites, northern Albania Island Arc, v. 14, p. 471–493. https://doi.org/10.1111/j.1440-1738.2005.00479.x

Boudier, F., Bouchez, J.L., Nicolas, A., Cannat, M., Ceuleneer, G., Misseri, M. and Montigny, R., 1985, Kinematics of oceanic thrusting in the Oman ophiolite: model of plate convergence. Earth and Planetary Science Letters, v. 75, p. 215–222.

Boyd, F. R., and J. L. England, 1960. The quartz-coesite transition, J. Geophys. Res., v. 65(2), p. 749–756, doi: 10.1029/JZ065i002p00749.

Božović, M., Prelević, D., Romer, R. L., Barth, M., van Den Bogaard, P., and Boev, B., 2013. The demir kapija ophiolite, Macedonia (FYROM): A Snapshot of subduction initiation within a back-arc. Journal of Petrology, v. 54, p. 1399–1425. https://doi.org/10.1093/petrology/egt016

Bracciali, L., Parrish, R. R., Horstwood, M. S. A., Condon, D. J., Najman, Yani. 2013 U-Pb LA-(MC)-ICP-MS dating of rutile: new reference materials and applications to sedimentary provenance. Chemical Geology, v. 347. P. 82–101.

Brichau, S., Ring, U., Carter, A., Bolhar, R., Monié, P., Stockli, D., and Brunel, M. 2008. Timing, slip rate, displacement and cooling history of the Mykonos detachment footwall, Cyclades, Greece, and implications for the opening of the Aegean Sea basin. Journal of the Geological Society of London, 165, 263–277. https://doi.org/10.1144/0016–76492006-76492145

Brichau, S., Ring, U., Carter, A., Monie, P., Bolhar, R., Stockli, D., and Brunel, M. 2007. Extensional faulting on Tinos Island, Aegean Sea, Greece: How many

detachments? Tectonics, 26, TC4009. https://doi.org/10.1029/2006TC001969

Brichau, S. Ring, U., Ketcham, R.A., and Carter, A., 2006, Constraining the long-term evolution of the slip rate for a major extensional fault system in the central Aegean, Greece, using thermochronology. Earth and Planetary Science Letters, v. 241, p. 293–306. ISSN 0012-821X.

Brichau, S., Thomson, S., and Ring, U. 2010. Thermochronometric constraints on the tectonic evolution of the Serifos detachment, Aegean Sea, Greece. International Journal of Earth Sciences (Geol Rundsch), 99, 379–393. https://doi.org/10.1007/s00531 –00008 –00386 -00530

Bröcker, M., and Enders, M., 1999, U–Pb zircon geochronology of unusual eclogite-facies rocks from Syros and Tinos (Cyclades, Greece). Geology Magazine, v.136, p. 111–118.

Bröcker, M., and Franz, L. 1994. The contact aureole on Tinos (Cyclades, Greece). Part I: field relationships, petrography and P-T conditions. Chemie der Erde, v. 54, p. 262–280.

Brocker, M., and Franz, L. 1998. Rb–Sr isotope studies on Tinos Island (Cyclades, Greece): Additional time constraints for meta-morphism, extent of infiltration-controlled overprinting and deformational activity. Geological Magazine, v. 135, p. 369–382.

Brocker, M., and Franz, L. 2005. The base of the Cycladic blueschist unit on Tinos Island (Greece) re-visited: Field relationships, phengite chemistry and Rb–Sr geochronology. Journal of Mineralogy and Geochemistry, v. 181, p. 81– 93.

Brocker, M., Bieling, D., Hacker, B., and Gans, P. 2004. High-Si phengite records the time of greenschist facies overprinting: Implications for models suggesting mega-detachments in the Aegean Sea. Journal of Metamorphic Geology, v. 22, p. 427–442.

Bröcker, M., Franz, L., 2000. Contact metamorphism on Tinos (Cyclades, Greece): the importance of tourmaline, timing of the thermal overprint and Sr isotope characteristics. Mineralogy and Petrology v. 70, p. 257–283.

Bröcker, M., Kreuzer, A., Matthews, A. and Okrusch, M., 1993,^{40}Ar/^{39}Ar and oxygen isotope studies of poly-metamorphism from Tinos Island, Cycladic blueschist belt, Greece. Journal of Metamorphic Geology, v. 11, p. 223– 240.

Bröcker, M., Löwen, K., Rodionov, N., 2014, Unraveling protolith ages of meta-gabbros from Samos and the Attic–Cycladic Crystalline Belt, Greece: Results of a U–Pb zircon and Sr–Nd whole rock study, Lithos, v. 198, p. 234–248 doi.org/10.1016/j.lithos.2014.03.029.

Brown, M., 2002, Retrograde processes in migmatites and granulites revisited. Journal of Metamorphic Geology, 20: 25–40. doi:10.1046/j.0263-4929.2001.00362.x

Brown, K.M. and Fialko, Y., 2012. 'Melt welt' mechanism of extreme weakening of gabbro at seismic slip rates. Nature, v. 488(7413), p.638.

Brown, S.A. and Robertson, A.H., 2004. Evidence for Neotethys rooted within the Vardar suture zone from the Voras Massif, northernmost Greece. Tectonophysics, v. 381(1-4), p.143–173.

Brun, J. P., and Faccenna, C., 2008. Exhumation of high-pressure rocks driven by slab rollback. Earth and Planetary Science Letters, v. 272, p. 1–7.

Buick, I. S., 1991a, Mylonite fabric development on Naxos, Greece, Journal of Structural Geology, v. 13, p. 643–655.

Buick, I. S., 1991b, The late Alpine evolution of an extensional shear zone, Naxos, Greece, Journal of the Geological Society of London, v. 148, p. 93–103.

Buick, I. S., and Holland, T. J. B., 1989, The P-T-t path associated with crustal extension, in Evolution of Metamorphic Belts, edited by J. S. Daly et al., Geological Society Special Publication, v. 43, p. 365–369.

Buick, I. S., and Holland, T. J. B., 1991, The nature and distribution of fluids during amphibolite-facies metamorphism, Naxos (Greece). Journal of Metamorphic Geology, v. 9, p. 301–314.

Burg, J. P. and Gerya, T. V., 2005, The role of viscous heating in Barrovian metamorphism of collisional orogens: thermomechanical models and application to the Lepontine Dome in the Central Alps. Journal of Metamorphic Geology, v. 23, p.

75–95. doi:10.1111/j.1525-1314.2005.00563.x

Burg, J.P., Guiraud, M., Chen, G.M., and Li, G.C., 1984, Himalayan metamorphism and deformations in the North Himalayan Belt (southern Tibet, China): Earth and Planetary Science Letters, v. 69, p. 391–400, doi:10.1016/0012-821X(84)90197-3.

Bürgmann, R. and Dresen, G., 2008, Rheology of the Lower Crust and Upper Mantle: Evidence from Rock Mechanics, Geodesy, and Field Observations, Annual Review of Earth and Planetary Sciences, v. 36, p. 531–567.

Cabanis, B., and Lecolle, M., 1989. The La/10-Y/15-Nb/ 8 diagram: a tool for discriminating volcanic series and evidencing continental crust magmatic mixtures and/ or contamination. C. R. Academic Science Series II, v. 309, p. 2023–2029.

Caddick. M. J., Konopásek, J., Thompson, A. B., 2010, Preservation of Garnet Growth Zoning and the Duration of Prograde Metamorphism. J Petrology 2010; v. 51 p. 2327–2347. doi: 10.1093/petrology/egq059

Cannat, M., Sauter, D., Mendel, V., Ruellan, E., Okino, K., Escartin, J., ... and Baala, M. 2006. Modes of seafloor generation at a melt-poor ultraslow-spreading ridge. Geology, v. 34(7), p. 605-608.

Cao, S., Neubauer, F., Bernroider, M., Genser, J., Liu, J., Friedl, G., 2017, Low-grade retrogression of a high-temperature metamorphic core complex: Naxos, Cyclades, Greece. Geological Society of America Bulletin, v. 129, p. 93–117.

Cao, S., Neubauer, F., Bernroider, M., Liu, J., 2013, The lateral boundary of a metamorphic core complex: The Moutsounas shear zone on Naxos, Cyclades, Greece, Journal of Structural Geology, v. 54, p. 103–128

Caran. S., 2016, Mineralogy and petrology of leucite ankaratrites with affinities to kamafugites and carbonatites from the Kayıköy area, Isparta, SW Anatolia, Turkey: Implications for the influences of carbonatite metasomatism into the parental mantle sources of silica-undersaturated potassic magmas, Lithosphere, v. 256–257, p. 13–25, doi.org/10.1016/j.lithos.2016.03.024.

Carosi, R., Cortesogno, L., Gaggero, L., and Marroni, M., 1996. Geological and petro-

logical features of the metamorphic sole from the Mirdita nappe, northern Albania. Ofioliti , v. 21 (1).

Carson, C. J., Berman, R. G., Stern, R. A. et al., 2004. Age constraints on the Palaeoproterozoic tectonometamorphic history of the Committee Bay region, western Churchill Province, Canada: evidence from zircon and in-situ monazite SHRIMP geochronology. Canadian Journal of Earth Sciences, v. 41, p. 1049–1076.

Casey, J.F. and Dewey, J.F., 1984. Initiation of subduction zones along transform and accreting plate boundaries, triple-junction evolution, and forearc spreading centers— implications for ophiolitic geology and obduction. Geological Society, London, Special Publications, v. 13, p. 269–290.

Castro, A. E., and Spear, F. S. 2017. Reaction overstepping and re-evaluation of peak P–T conditions of the blueschist unit on Sifnos, Greece: Implications for the Cyclades subduction zone. International Geology Review, 59(5–6), 548–562.

Çelik, Ö. F., Delaloye, M., and Feraud, G., 2006. Precise^{40}Ar–^{39}Ar ages from the metamorphic sole rocks of the Tauride Belt Ophiolites, southern Turkey: Implications for the rapid cooling history. Geological Magazine, v. 143 (02), p. 213. https://doi.org/10.1017/S0016756805001524

Chappell, B.W., and White, A.J.R., 1974, Two contrasting granite types: Pacific Geology, v. 8, p. 173–174.

Chappell, B.W., and White, A.J.R., 1992, I- and S-type granites in the Lachlan Fold Belt: Transactions of the Royal Society of Edinburgh: Earth Sciences, v. 83, p. 1–26, doi:10.1017/S0263593300007720.

Cherniak. D.J, Pyle. J and Rakovan.J, 2004, Synthesis of REE and Y phosphates by Pb-free flux methods and their utilization as standards for electron microprobe analysis and in design of monazite chemical U-Th-Pb dating protocol, American Mineralogist, v. 89, p. 1533–1539.

Chester, F.M., and Chester, J.S., 1998, Ultracataclasite structure and friction processes on the Punchbowl fault, San Andreas system, California: Tectonophysics, v. 295, p. 199–221, doi:10.1016/S0040-1951(98)00121-8.

Chiari, M., Bortolotti, V., Marcucci, M., Photiades, A., and Principi, G., 2003. The middle Jurassic siliceous sedimentary cover at the top of the vourinos ophiolite (Greece). Ofioliti, v. 28 (2), p. 95– 103.

Chiari, M., Marcucci, M., and Prela, M., 1994. Mirdita ophiolites project: 2 radiolarian assemblages in the cherts at Fushe Arrez and Shebaj (Mirdita area, Albania). Ofioliti, v. 19 (2)

Clarke, D.B., 1992, Granitoid Rocks: London, Chapman and Hall, Topics in the Earth Sciences, v. 283

Clarke, G.L., Powell, R. and Fitzherbert, J.A., 2006. The lawsonite paradox: a comparison of field evidence and mineral equilibria modelling. Journal of Metamorphic Geology, v. 24, p. 715–725.

Cobbing, E.J., Pitfield, P.E.J., Darbyshire, D.P.F., and Mallick, D.I.J., 1992, The Granites of the South-East Asian Tin Belt: London, British Geological Survey, Overseas Memoir, v. 369

Cobbold, P.R., Quinquis, H., 1980. Development of sheath folds in shear regimes. Journal of Structural Geology, v. 2, p. 119–126.

Coggon, R. and Holland, T. J. B., 2002, Mixing properties of phengitic micas and revised garnet-phengite thermobarometers. Journal of Metamorphic Geology, v. 20, p. 683–696. doi:10.1046/j.1525-1314.2002.00395.x

Coleman, R.G. and Donato, M.M., 1979. Oceanic plagiogranite revisited. Developments in petrology v. 6, p. 149–168

Coleman, R. G., and Peterman, Z. E., (19750, Oceanic plagiogranite, Journal of Geophysical Research, v. 80 (8), p. 1099–1108, doi: 10.1029/JB080i008p01099.

Collings, D., Savov, I., Maneiro, K., Baxter, E., Harvey, J., Dimitrov, I., 2016, Late Cretaceous UHP metamorphism recorded in kyanite–garnet schists from the Central Rhodope Mountains, Bulgaria, Lithos, v. 246–247, p. 165–181, doi.org/ 10.1016/j. lithos.2016.01.002.

Collins, W.J., Van Kranendonk, M.J. and Teyssier, C. 1998. Partial convective overturn of Archaean crust in the east Pilbara Craton, Western Australia: driving

mechanisms and tectonic implications. Journal of Structural Geology, v. 20, p. 1405–1424.

Coney, P.J., 1980, Cordilleran metamorphic core complexes. In: Crittenden, M.D.,

Conrad, W.K., Nicholls, L.A. and Wall, V.J., 1988, Water-saturated and-under saturated melting of metaluminous and peraluminous crustal compositions at 10 kb: evidence for the origin of silicic magmas in the Taupo V. canic Zone, New Zealand, and other occurrences. Journal of Petrology, v. 29, p. 765–803.

Cooper, P., and Taylor, B., 1987, Seismotectonics of New Guinea: A model for arc reversal following arc-continent collision, Tectonics, v. 6, p. 53–67, doi:10.1029/TC006i001p00053.

Corfield. R. I and Searle. M. P., 2001, Crustal shortening estimates across the north Indian continental margin, Ladakh, NW India, Geological Society, London, Special Publications 2000, v. 170, p. 395–410. doi: 10.1144/GSL.SP.2000.170.01.21

Corfield, R. I., Searle, M. P., and Pedersen, R. B., 2001, Tectonic Setting, Origin, and Obduction History of the Spontang Ophiolite, Ladakh Himalaya, NW India, The Journal of Geology, v. 109, p. 715–736.

Corfu, F., 2007. Comment to short-communication 'Comment: Hf isotope heterogeneity in zircon 91500' by W.L. Griffin, N.J. Pearson, E.A. Belousova and A. Saeed (Chemical Geology, v. 233, p. 358–363). Chemical Geology, v. 244, p. 350–353

Cossette, É., Audet, P., Schneider, D., and Grasemann, B., 2016, Structure and anisotropy of the crust in the Cyclades, Greece, using receiver functions constrained by in situ rock textural data, Journal of Geophysical Research Solid Earth, v.121, p. 2661–2678, doi:10.1002/2015JB012460

Cottle, J. M., Jessup, M. J., Newell, D. J., Searle, M. P., Law, R. D., and Horstwood, M. S. A., 2007, Structural insights into the early stages of exhumation along an orogen-scale detachment: The South Tibetan Detachment System, Dzakaa Chu section, Eastern Himalaya, Journal of Structural Geology, v. 29, p. 1781–1797, http://dx.doi.org/10.1016/j.jsg.2007.08.007.

Cowan, R.J., Searle, M.P. and Waters, D.J., 2014. Structure of the metamorphic sole

to the Oman Ophiolite, Sumeini Window and Wadi Tayyin: Implications for ophiolite obduction processes. Geological Society, London, Special Publications, v. 392, p. 155–175.

Cruciani, G., Franceschelli, M., Elter, F.M., Puxeddu, M. and Utzeri, D., 2008. Petrogenesis of Al–silicate-bearing trondhjemitic migmatites from NE Sardinia, Italy. Lithos, v. 102, p. 554–574.

D'Agostino, N., England, P. C., Hunstad, I et al., 2014, Gravitational potential energy and active deformation in the Apennines. Earth and Planetary Science Letters, v. 397, p. 121–132. doi.org/10.1016/j.epsl.2014.04.013

Dalmayrac, B., and Molnar, P.,1981, Parallel thrust and normal faulting in Peru and constraints on the state of stress, Earth and Planetary Science Letters, v. 55, p. 473–481.

Danelian, T., Robertson, A. H. F., and Dimitriadis, S., 1996. Age and significance of radiolarian sediments within basic extrusives of the marginal basin Guevgueli Ophiolite (northern Greece). Geological Magazine, v. 133, p. 127–136. https://doi.org /10.1017/ S0016756800008645

Davis, G.L., Hart, S.R., and Tilton, G.R., 1968. Some effects of contact metamorphism on zircon ages, Earth and Planetary Science Letters. v. 5, p. 27–34.

Deer, W. A., Howie, R. A. and Zussman, J., 1992. An Introduction to the Rock Forming Minerals, 2nd edition. Longman Scientific and Technical, Harlow, Essex, UK.

Degnan, P. J., and Robertson, A. H. F., 1998. Mesozoic-early Tertiary passive margin evolution of the Pindos ocean (NW Peloponnese, Greece), Sedimentary Geology, v. 117(1), p. 33–70.

DeMets. C, Iaffaldano. G., and Merkouriev, S., 2015, High-resolution Neogene and Quaternary estimates of Nubia-Eurasia-North America Plate motion. Geophysical Journal International, v. 203 416–427. doi: 10.1093/gji/ggv277

Denèle, Y., Lecomte, E., Jolivet, L., Lacombe, O., Labrousse, L., Huet, B., and Le Pourhiet, L. 2011. Granite intrusion in a metamorphic core complex: The example of the Mykonos laccolith (Cyclades, Greece). Tectonophysics, 501(1-4),

52–70. https://doi.org /10.1016/j. tecto.2011.1001.1013

Dercourt, J., Zonenshain, L.P., Ricou, L.C., 1985. Présentation des 9 cartes paléogéographiques au 1/20 000 000 s'étendant de l'Atlantique au Pamir pour la période du Lias à l'Actuel. Bulletin de la Societe Geologique de France. V. 8, p. 637–652.

Dewey, J.F. and Casey, J.F., 2011. The origin of obducted large-slab ophiolite complexes. In Arc-Continent Collision, p. 431–444. Springer Berlin Heidelberg.

Dewey, J.F. and Casey, J.F., 2013. The sole of an ophiolite: the Ordovician Bay of Islands Complex, Newfoundland. Journal of the Geological Society, v. 170, p. 715–722.

Dewey, J. F. and Şengör, C., 1979. Aegean and surrounding regions: complex multiplate and continuum tectonics in a convergent zone, Geological Society of America Bulletin, v. 90, p. 84–92.

Di Toro, G., Goldsby, D.L. and Tullis, T.E., 2004. Friction falls towards zero in quartz rock as slip velocity approaches seismic rates. Nature, 427(6973), p.436.

Di Toro, G., Han, R., Hirose, T., De Paola, N., Nielsen, S., Mizoguchi, K., Ferri, F., Cocco, M. and Shimamoto, T., 2011. Fault lubrication during earthquakes. Nature, v. 471(7339), p. 494.

Dilek, Y. and Furnes, H., 2011. Ophiolite genesis and global tectonics: Geochemical and tectonic fingerprinting of ancient oceanic lithosphere. Bulletin, 123(3-4), p.387-411.

Dilek, Y., H. Furnes, and M. Shallo, 2007, Suprasubduction zone ophiolite formation along the periphery of Mesozoic Gondwana, Gondwana Research., v. 11, p. 453–475.

Dilek, Y., Furnes, H. and Shallo, M., 2008. Geochemistry of the Jurassic Mirdita Ophiolite (Albania) and the MORB to SSZ evolution of a marginal basin oceanic crust. Lithos, v. 100 (1–4), p.174–209.

Dilek, Y., and Thy, P., 2009. Island arc tholeiite to boninitic melt evolution of the Cretaceous Kizildag (Turkey) ophiolite: Model for multi-stage early arc-forearc

magmatism in Tethyan subduction factories. Lithos, v. 113, p. 68–87.

Dimo-Lahitte, A., Monié, P., and Vergély, P., 2001. Metamorphic soles from the Albanian ophiolites: Petrology,40Ar/39Ar geochronology, and geodynamic evolution. Tectonics, v. 20 (1), p. 78–96. https://doi.org/10.1029/2000TC900024

Dinter, D. A., Macfarlane, A., Hames, W., Isachsen, C., Bowring, S., and Royden, L., 1995. U-Pb and^{40}Ar/39Ar geochronology of the Symv. on granodiorite: Implications for the thermal and structural evolution of the Rhodope metamorphic core complex, northeastern Greece, Tectonics, v. 14 (4), p. 886–908, doi: 10.1029/95TC00926.

Dinter, D. A., Royden, L., 1993. Late Cenozoic extension in northeastern Greece: Strymon Valley detachment system and Rhodope metamorphic core complex. Geology v. 21 (1) p. 45–48. doi:10.1130/0091-76131993021¡0045:LCEING¿2.3.CO;2

Dixon, S. and Rutherford, M.J., 1979. Plagiogranites as late-stage immiscible liquids in ophiolite and mid-ocean ridge suites: an experimental study. Earth and Planetary Science Letters, v. 45, p. 45–60.

Dragert, H., Wang, K., and James, T. S., 2001. A silent slip event on the deeper Cascadia subduction interface. Science, v. 292 (5521), p. 1525–1528.

Dragovic, B., Baxter, E. F., Caddick, M. J., 2015. Pulsed dehydration and garnet growth during subduction revealed by zoned garnet geochronology and thermodynamic modeling, Sifnos, Greece, Earth and Planetary Science Letters, v. 413, p. 111–122, ISSN 0012-821X, https://doi.org/10.1016/j.epsl.2014.12.024.

Dragovic, B., Samanta, L.M., Baxter, E.F. and Selverstone, J., 2012. Using garnet to constrain the duration and rate of water-releasing metamorphic reactions during subduction: An example from Sifnos, Greece. Chemical Geology, v. 314, p. 9–22.

Duarte, J. C., W. P. Schellart, and A. R. Cruden, 2015, How weak is the subduction zone interface? Geophysical Research Letters., v. 42, p. 2664–2673, doi: 10.1002/2014 GL062876.

Duchêne, S., Aïssa. R., and Vanderhaeghe. O., 2006, Pressure–temperature time evolution of metamorphic rocks from Naxos (Cyclades, Greece): Constraints from

thermobarometry and Rb/Sr dating, Geodinamica Acta, v. 19, 299–319.

Dürr, S., Altherr, R., Keller, J., Okrusch, M., Seidel, E., 1978, The median Aegean crystalline belt: stratigraphy, structure, metamorphism, magmatism H. Closs, D. Roeder, K. Schmidt (Eds.), Alps, Appenines and Hellenides, Schweizerbart, Stuttgart, p. 455–476

Dymkova, D., and Gerya, T, 2013, Porous fluid flow enables oceanic subduction initiation on Earth, Geophysical Research Letters. v. 40, p. 5671–5676 doi: 10.1002/2013GL057798.

Edwards, S. J., Schellart, W. P., and Duarte, J. C., 2015. Geodynamic models of continental subduction and obduction of overriding plate forearc oceanic lithosphere on top of continental crust. Tectonics, v. 34, p. 1494–1515. doi: 10.1002/2015TC003884.

Elitok, Ö. and Drüppel, K., 2008. Geochemistry and tectonic significance of metamorphic sole rocks beneath the Beysehir–Hoyran ophiolite (SW-Turkey). Lithosphere, v. 100, p. 322–353.

England, P. C, 1978. Some thermal considerations of the Alpine metamorphism, past, present and future. Tectonophysics, v. 46, p. 21–40.

England, P. C., 1993, Convective removal of thermal boundary layer of thickened continental lithosphere: A brief summary of causes and consequences with special reference to the Cenozoic tectonics of the Tibetan Plateau and surrounding regions, Tectonophysics, v. 223, p. 67–73.

England, P., 2018. On shear stresses, temperatures, and the maximum magnitudes of earthquakes at convergent plate boundaries. Journal of Geophysical Research: Solid Earth, 123. https://doi.org/10.1029/2018JB015907

England, P.C., and Holland, T.J.B., 1979, Archimedes and the Tauern eclogites: the role of buoyancy in the preservation of exotic eclogite blocks, Earth and Planetary Science Letters, v. 44, p. 287–294, http://dx.doi.org/10.1016/0012-821X(79)90177-8.

England, P. and Houseman, G., 1986. Finite strain calculations of continental deforma-

tion: 2. Comparison with the India-Asia collision zone. Journal of Geophysical Research: Solid Earth, v. 91(B3), p. 3664–3676.

England, P. C. and Houseman, G., 1989, Extension during continental convergence, with application to the Tibetan Plateau, J. Geophysical Research., v. 94(B12), p. 17,561–17,579, doi:10.1029/JB094iB12p17561.

England, P.C., Houseman, G. and Nocquet. J. M., 2016, Constraints from GPS measurements on the dynamics of deformation in Anatolia and the Aegean, Journal of Geophysical Research, Solid Earth, v. 121, p. 8888–8916, doi:10.1002/2016JB013382.

England, P., Houseman, G. and Sonder, L., 1985. Length scales for continental deformation in convergent, divergent, and strike-slip environments: Analytical and approximate solutions for a thin viscous sheet model. Journal of Geophysical Research: Solid Earth, v. 90(B5), p.3551–3557.

England, P. C. and Jackson. J., 1987, Migration of the seismic-aseismic transition during uniform and non-uniform extension of the continental lithosphere, Geology, v, 15, p. 291–294.

England, P. and Molnar, P., 1993. The interpretation of inverted metamorphic isograds using simple physical calculations. Tectonics, v. 12, p.145–157.

England, P. C. and Molnar, P., 1993, Cause and effect among thrust and normal faulting, anatectic melting and exhumation in the Himalaya, Geological Society, London, Special Publications, v. 74, p. 401–411.

England, P. C. and Richardson, S. W., 1977, The influence of erosion upon the mineral facies of rocks from different metamorphic environments. Journal of the Geological Society, London, v. 134, p. 201–213.

England, P.C. and Thompson, A. B., 1984, Pressure– temperature–time paths of regional metamorphismI. Heat transfer during the evolution of regions of thickened continental crust. Journal of Petrology, v. 25, p. 894–928.

England, P., and Wilkins, C., 2004. A simple analytical approximation to the temperature structure in subduction zones, Geophysical Journal International, v. 159, p. 1138–1154, https://doi.org/10.1111/j.1365-246X.2004.02419.x

Ernst, W. G., 1970.Tectonic contact between the Franciscan Mélange and the Great Valley Sequence—Crustal expression of a Late Mesozoic Benioff Zone, J. Geophys. Res., v. 75(5), p. 886–901, doi: 10.1029/JB075i005p00886.

Ernst, W. G., 1973. Blueschist metamorphism and P-T regimes in active subduction zones, Tectonophysics, v. 17 (3), p. 255–272, doi: 10.1016/0040-1951(73)90006-1.

Ernst, W. G., 1988; Tectonic history of subduction zones inferred from retrograde blueschist P-T paths. Geology; v. 16 (12): p. 1081–1084. doi:10.1130/0091-76131988016¡1081:THOSZI¿2.3.CO;2

Escartín, J., Smith, D. K., Cann, J., Schouten, H., Langmuir, C. H., and Escrig, S. 2008. Central role of detachment faults in accretion of slow-spreading oceanic lithosphere. Nature, v. 455(7214), p. 790.

Essen, E. J. and Fyfe, W. S., 1967. Omphacite in Californian rocks. Contributions to Mineral Petrology., v. 15, p. 1-23.

Essene, E.J., 1989. The current status of thermobarometry in metamorphic rocks. In: Evolution of Metamorphic Belts (eds Daly, J.S., Cliff, R.A. and Yardley, B.W.D.). Geological Society, London, Special Publications, v. 43, p. 1–44.

Evans, B. W. and Guidotti, C. V., 1966, The sillimanite-potash feldspar isograd in western Maine, U.S.A. Contributions to Mineralogy and Petrology, v. 12, p. 25–62

Ez, V., 2000. When shearing is a cause of folding. Earth Science Reviews v. 51, p. 155–172. http://dx.doi.org/10.1016/S0012-8252(00)00020-9.

Fagereng, A. and Sibson, R. H., 2010. Mélange rheology and seismic style. Geology; v. 38 (8), p. 751–754.

Faure, M., Bonneau, M., and Pons, J. 1991. Ductile deformation and syntectonic granite emplacement during the late Miocene extension of the Aegean (Greece). Bulletin de la Societe Geologique de France, v. 162, p. 3–12.

Ferriére, J., 1982. Paléogéographie et tectonique superpose oes dans les Hellenides internes: Les massifs de l'Othrys et du Pélion (Gréce septentrionale). Société de la Géologie du Nord, v. 8, p. 1–970.

Fitzsimons, I., Kinny, P., Wetherley, S. and Hollingsworth, D., 2005, Bulk chemical control on metamorphic monazite growth in pelitic schists and implications for U–Pb age data. Journal of Metamorphic Geology. V. 23, p. 261–277.

Fletcher, R. C., and B. Hallet, 1983, Unstable extension of the lithosphere: A mechanical model for Basin-and-Range structure, Journal of Geophysical Research, v. 88, p. 7457–7466, doi:10.1029/JB088iB09p07457

Floyd, M. A., et al., 2010. A new velocity field for Greece: Implications for the kinematics and dynamics of the Aegean, Journal of Geophysical Research., v. 115, B10403.Goldsworthy, M., Jackson, J., Haines, J., 2001. The continuity of active fault systems in Greece, Geophysical Journal International, v. 48, Issue 3, p. 596–618.

Floyd, P.A., Göncüoğlu, M.C., Winchester, J.A. and Yaliniz, M.K., 2000. Geochemical character and tectonic environment of Neotethyan ophiolitic fragments and metabasites in the Central Anatolian Crystalline Complex, Turkey. Geological Society, London, Special Publications, v. 173 (1), p. 183–202.

Floyd, P. A., and Winchester, J. A., 1975. Magma type and tectonic setting discrimination using immobile elements, Earth and Planetary Science Letters, v. 27 (2), p. 211-218, ISSN 0012-821X, https://doi.org/10.1016/0012-821X(75)90031-X.

Forster, M. A., and Lister, G. S. 2005. Several distinct tectono-meta-morphic slices in the Cycladic eclogite–blueschist belt, Greece. Contributions to Mineralogy and Petrology, v. 150, p. 523–545.

Fraser, G., Ellis, D., Eggins, S., 1997. Zirconium abundance in granulite-facies minerals, with implications for zircon geochronology in high-grade rocks, Geology v. 25, p. 607–610.

Fryer, P., Wheat, C. G., and Mottl, M. J., 1999. Mariana blueschist mud v. canism: Implications for conditions within the subduction zone. Geology ; v. 27 (2), p. 103–106. doi: 10.1130/0091-76131999027¡0103:MBMVIF¿2.3.CO;2

Fytikas, M., Innocenti, F., Piero, M., Peccerillo, A., Mazzuoli, R., and Villari, L, 1984. Tertiary to Quaternary evolution of volcanism in the Aegean region. Geological

Society, London, Special Publications. v. 17. p. 687-699. 10.1144/GSL.SP.1984.017.01.55.

Gaggero, L., Marroni, M., Pandolfi, L., and Buzzi, L., 2009. Modeling the oceanic lithosphere obduction: Constraints from the metamorphic sole of Mirdita ophiolites (northern Albania). Ofioliti, v. 34 (1), p. 17–42.

Gallhofer, D., Von Quadt, A., Schmid, S. M., Guillong, M., Peytcheva, I., and Seghedi, I., 2017. Magmatic and tectonic history of Jurassic ophiolitesand associated granitoids from the South Apuseni Mountains (Romania). Swiss Journal of Geosciences, v. 110 (2), p. 699–719. https://doi.org/10.1007/s00015-016-0231-6

Ganguly, J., Cheng, W. and Tirone, M., 1996. Thermodynamics of aluminosilicate garnet solid solution: new experimental data, an optimized model, and thermometric applications. Contributions to Mineralogy and Petrology, v. 126(1-2), p. 137–151.

García-Casco, A., Haissen, F., Castro, A., El-Hmidi, H., Torres-Roldán, R. L., and Millán, G., 2003, Synthesis of Staurolite in Melting Experiments of a Natural Metapelite: Consequences for the Phase Relations in Low-Temperature Pelitic Migmatites. Journal of Petrology, v. 44, p. 1727–1757. doi: 10.1093/petrology/egg056

García-Casco, A., Torres-Roldán, R. L., Millán, G., Monié, P. and Haissen, F., 2001, High-grade metamorphism and hydrous melting of metapelites in the Pinos terrane (W Cuba): Evidence for crustal thickening and extension in the northern Caribbean collisional belt. Journal of Metamorphic Geology, v. 19, p.699–715.

Garzione, C. N., P. Molnar, J. C. Libarkin, and B. J. MacFadden, 2006, Rapid Late Miocene rise of the Bolivian Altiplano: Evidence for removal of mantle lithosphere, Earth and Planetary Science Letters, v. 241, p. 543–556.

Gautier, P., and Brun, J.P., 1994a, Crustal-scale geometry and kinematics of late-orogenic extension in the central Aegean (Cyclades and Evvia island), Tectonophysics, v. 238, p. 399–424.

Gautier, P., and Brun, J.P., 1994b, Ductile crust exhumation and extensional detach-

ments in the central Aegean (Cyclades and Evvia islands), Geodinamica Acta, v. 7, p. 57–85.

George, F.R. and Gaidies, F., 2017. Characterisation of a garnet population from the Sikkim Himalaya: insights into the rates and mechanisms of porphyroblast crystallisation Contributions to Mineral Petrology v. 172 p. 57. https://doi.org/10.1007/s00410-017-1372-y

Gerlach, D.C., Leeman, W.P. and Lallemant, H.G.A., 1981. Petrology and geochemistry of plagiogranite in the Canyon Mountain Ophiolite, Oregon. Contributions to Mineralogy and Petrology, v. 77 (1), p. 82–92.

Ghani, A.A., Searle, M.P., Robb, L.J., and Chung, S.-L., 2013b, Transitional I-S type characteristic in the Main Range Granite, Peninsular Malaysia: Journal of Asian Earth Sciences, v. 76, p. 225–240, doi:10.1016/j.jseaes .2013.05.013

Gibson, D. H., Carr, S. D., Brown, R. L. and Hamilton, M. A., 2004. Correlations between chemical and age domains in monazite, and metamorphic reactions inv. ving major pelitic phases: an integration of ID-TIMS and SHRIMP geochronology with Y-Th–U X-ray mapping. Chemical Geology, v. 211, p. 237–260.

Gnos, E., 1998. Peak metamorphic conditions of garnet amphibolites beneath the Semail ophiolite: implications for an inverted pressure gradient. International Geology Review, v. 40, p. 281–304.

Gnos. E., Peters T., 1993, K-Ar ages of the metamorphic sole of the Semail Ophiolite: implications for ophiolite cooling history. Contributions to Mineralogy and Petrology, v. 113 p. 325–332.

Godfriaux, I., and Ricou, L.E., 1991. The Paikon, a tectonic window within the Internal Hellenides, Macedonia, Greece — Le Paikon, une fenetretectonique dans les Hellenides Internes (Macedoine, Grece). Comptes Rendus - Academie des Sciences Series II, v. 313 (12).

Goffé, B., and Chopin, C., 1986. High-pressure metamorphism in the Western Alps: zoneography of metapelites, chronology and consequences. Schweiz. mineral. petrogr. Mitt. v. 66. p. 41–52.

Govindaraju, K., 1994. Compilation of Working Values and Sample Description for 383 Geostandards: Geostandards Newsletter, v. 18, Special Issue, p. 1-158

Grasemann, B., Schneider, D. A., Stockli, D. F., and Iglseder, C., 2012, Miocene bivergent crustal extension in the Aegean: Evidence from the western Cyclades (Greece), Lithos, doi:10.1130/L1164.1131.

Green, E., Powell, R., and White, R. 2013. Exploring uncertainties in phase diagram calculations via a Monte Carlo method. Goldschmidt Conference 2013.

Green, E.C.R., White, R.W., Diener, J.F.A., Powell, R., Holland, T.J.B. and Palin, R.M., 2016. Activity–composition relations for the calculation of partial melting equilibria in metabasic rocks. Journal of Metamorphic Geology, v. 34, p. 845–869.

Green, T.H., Blundy, J.D., Adam, J. and Yaxley, G.M., 2000. SIMS determination of trace element partition coefficients between garnet, clinopyroxene and hydrous basaltic liquids at 2–7.5 GPa and 1080–1200 C. Lithos, v. 53, p. 165-187.

Griffin, W.L., Pearson, N.J., Belousova, E.A. and Saeed, A., 2006. Comment: Hf-isotope heterogeneity in zircon 91500. Chemical Geology, v. 233, p.358–363.

Gromet L. and Silver L. T., 1983, Rare earth element distributions among minerals in a granodiorite and their petrogenetic implications. Geochim. Cosmochim. Acta v. 47, p. 925–939.

Groppo, C., Forster, M., Lister, G., and Compagnoni, R. 2009. Glaucophane schists and associated rocks from Sifnos (Cyclades, Greece): New constraints on the P-T evolution from oxidized systems. Lithos, v. 109, p. 254–273.

Grosse, P., Bellos, L.I., de los Hoyos, C.R., Larrovere, M.A., Rossi, J.N., and Toselli, A.J., 2011, Across-arc variation of the Famatinian magmatic arc (NW Argentina) exemplified by I-, S- and transitional I/S-type Early Ordovician granitoids of the Sierra de Velasco: Journal of South American Earth Sciences, v. 32, p. 110–126, doi:10.1016/j.jsames.2011.03.014.

Guidotti, C. V., 1984, Micas in metamorphic rocks. In S.W. Bailey, Ed., Micas, v. 13, p. 357–467. Reviews in Mineralogy, Mineralogical Society of America, Washing-

ton, D.C.

Guilmette, C., Indares, A., Hébert, R., 2011. High-pressure anatectic paragneisses from the Namche Barwa, Eastern Himalayan Syntaxis: textural evidence for partial melting, phase equilibria modeling and tectonic implications. Lithos, v. 124, p. 66–81.

Gürdal, A. Kılıçoğlu, H. Akdeniz, and A. Tekgül, 2009. Deformation of western Turkey from a combination of permanent and campaign GPS data: Limits to block-like behavior, J. Geophys. Research, v. 114 (B10), p. 1–22.

Hacker, B.R., 1990. Simulation of the metamorphic and deformational history of the metamorphic sole of the Oman ophiolite. Journal of Geophysical Research, v. 95, p. 4895–4907.

Hacker, B.R. and Gnos, E., 1997. The conundrum of Samail: explaining the metamorphic history. Tectonophysics, v. 279, p. 215–226.

Hacker, B. R., Gerya, T. V., and Gilotti, J. A., 2013. Formation and Exhumation of Ultrahigh-Pressure Terranes. Elements, v. 9, p. 289–293.

Hacker, B.R., Mosenfelder, J.L. and Gnos, E., 1996. Rapid emplacement of the Oman ophiolite: thermal and geochronologic constraints. Tectonics, v. 15, p. 1230–1247.

Hall, C. H., Gurnis, M., Sdrolias, M., Lavier, L. L., Müller, R. D., 2003, Catastrophic initiation of subduction following forced convergence across fracture zones, Earth and Planetary Science Letters, v. 212, p. 15–30, https://doi.org/10.1016/S0012-821X(03)00242-5.

Halliday, A.N., Davidson, J.P., Hidreth, W., and Holden, P., 1991, Modelling the petrogenesis of high Rb/Sr silicic magmas: Chemical Geology, v. 92, p. 107–114, doi:10 .1016/0009-2541(91)90051-R

Harris, N. B., Kelley, S., and Okay, A. I., 1994. Post-collision magmatism and tectonics in northwest Anatolia. Contribution to Mineralogy and Petrology, v. 117, p. 241–252.

Harris, N.B.W., Pearce, P.A., and Tindle, A.G., 1986, Geochemical characteristics of

collision-zone magmatism, in Coward, M.P., and Ries, A.C., eds., Collision Tectonics: Geological Society of London Special Publication 19, p. 67–81, doi:10.1144 /GSL.SP.1986.019 .01.04.

Harrison, T.M., Célérier, J., Aikman, A.B., Hermann, J., Heizler, M.T., 2009. Diffusion of^{40}Ar in muscovite. Geochimica et Cosmochimica Acta, v. 73, p. 1039–1051. doi:10.1016/j.gca.2008.09.038.

Harrison, T.M., Duncan, I. and McDougall, I., 1985. Diffusion of^{40}Ar in biotite: temperature, pressure and compositional effects. Geochimica et Cosmochimica Acta, v. 49, p. 2461–2468.

Henry, D. J., Guidotti, C. V. and Thomson, J. A., 2005, The Ti-saturation surface for low-to-medium pressure metapelitic biotite: Implications for Geothermometry and Ti-substitution Mechanisms: American Mineralogist, v. 90, p. 316–328.

Hess, H. H., 1962. History of Ocean Basins, Petrologic Studies, A. E. J. Engel, Harold L. James, B. F. Leonard

Hiess, J., Condon, D. J., McLean, N., and Noble, S. R., 2012. 238U/235U systematics in terrestrial uranium-bearing minerals. Science, v. 335(6076), p.1610-1614.

Holdaway, M. J., 2000. Application of new experimental and garnet Margules data to the garnet–biotite geothermometer: American Mineralogist, v. 85, p. 881–892.

Holland, T. J. B., 2009, AX: a program to calculate activities of mineral end-members from chemical analyses. Available at: http://www.esc.cam.ac.uk/research/research-groups/ holland/ax.

Holland, T. J. B., Baker, J. M., and Powell, R., 1998, Mixing properties and activity–composition relationships of chlorites in the system MgO–FeO– Al2O3–SiO2–H2O. European Journal of Mineralogy, v. 10, p. 395–406.

Holland, T. J. B, and Blundy, J., 1994. Non-ideal interactions in Calcic amphiboles and their bearing on Amphibole-Plagioclase Thermometry: Contributions to Mineralogy and Petrology, v. 116, p. 433–447.

Holland, T. J. B., and Powell, R., 1998, An internally-consistent thermodynamic dataset for phases of petrological interest. Journal of Metamorphic Geology,

v. 16, p. 309–344.

Holland, T. J. B., and Powell, R., 2003, Activity–composition relations for phases in petrological calculations: an asymmetric multicomponent formulation. Contributions to Mineralogy and Petrology, v. 145, p. 492–501.

Holland, T. J. B. and Powell, R., 2011. An improved and extended internally consistent thermodynamic dataset for phases of petrological interest, inv. ving a new equation of state for solids. Journal of Metamorphic Geology, v. 29 p. 333–383.

Holness, M., 2008, Decoding migmatite microstructures, in Working With Migmatites, Short Course Ser., v. . 38, edited by E. W. Sawyer and M. Brown, p. 57–76, Mineralogical Association of Canada., Quebec, Que., Canada.

Horstwood, M. S. A., 2008. Data reduction strategies, uncertainty assessment and interpretation of LA-(MC-)ICP-MS isotope data. In: Laser Ablation ICP-MS in the Earth Sciences: Current Practices and Outstanding Issues (ed. Sylvester, P.), Mineralogical Association of Canada: Short Course Series, v. 40, p. 283–303.

Horstwood, M. S. A., Košler, J., Gehrels, G., Jackson, S. E., McLean, N. M., Paton, C., Pearson, N. J., Sircombe, K., Sylvester, P., Vermeesch, P., Bowring, J. F., Condon, D. J. and Schoene, B., 2016. Community-Derived Standards for LA-ICP-MS U-(Th-)Pb Geochronology – Uncertainty Propagation, Age Interpretation and Data Reporting. Geostandard Geoanalytical Research, v. 40 p. 311–332. doi:10.1111/j.1751-908X.2016.00379.x

Houseman, G. and England, P., 1986, A dynamical model of lithosphere extension and sedimentary basin formation., Journal of Geophysical Research, v. 91, p. 719–729.

Houseman, G. and England, P., 1986. Finite strain calculations of continental deformation: 1. Method and general results for convergent zones. Journal of Geophysical Research: Solid Earth, v. 91(B3), p. 3651–3663.

Houseman, G. A. and Molnar, P., 1997, Gravitational (Rayleigh–Taylor) instability of a layer with non-linear viscosity and convective thinning of continental lithosphere, Geophysical Journal International, v. 1, p. 125–150

Huet, B., Labrousse, L. and Jolivet, L., 2009, Thrust or detachment? Exhumation processes in the Aegean: Insight from a field study on Ios (Cyclades, Greece), Tectonics, v. 28, TC3007, doi:10.1029/2008TC002397.

Huet, B., Labrousse, L., Monie, P., Malvoisin, B., and Jolivet, L. 2015. Coupled phengite^{40}Ar–^{39}Ar geochronology and thermo-barometry: P-T-t evolution of Andros Island (Cyclades, Greece). Geological Magazine, v. 152, p. 711–727.

Hyndman, D.W, 1981. Controls on source and depth of emplacement of granitic magma. Geology ; v. 9 (6): p. 244–249. doi: https://doi.org/10.1130/0091-761319819¡244:COSADO¿2.0.CO;2

Iglseder, C., Grasemann, B., Rice, A. H. N., Petrakakis, K., and Schneider, D. A. 2011. Miocene south directed low-angle normal fault evolution on Kea (West Cycladic Detachment System, Greece). Tectonics, v. 30, TC4013. https://doi.org/10.1029/2010TC002802

Iglseder, C., Grasemann, B., Schneider, D. A., Petrakakis, K., Miller, C., Klötzli, U. S., et al. 2009. I and S-type plutonism on Serifos (W-Cyclades, Greece). Tectonophysics, v. 473(1-2), p. 69–83. https://doi.org/10.1016/j.tecto.2008.1009.1021

Ildefonse, B., Blackman, D. K., John, B. E., Ohara, Y., Miller, D. J., and MacLeod, C. J. 2007. Oceanic core complexes and crustal accretion at slow-spreading ridges. Geology, v. 35(7), p. 623-626.

Indares, A., White, R. W. and Powell, R., 2008, Phase equilibria modelling of kyanite-bearing anatectic paragneiss from the central Grenville Province. Journal of Metamorphic Geology, v. 26, p. 815–836.

Ishizuka, O., Tani, K., Reagan, M.K., Kanayama, K., Umino, S., Harigane, Y., Sakamoto, I., Miyajima, Y., Yuasa, M. and Dunkley, D.J., 2011. The timescales of subduction initiation and subsequent evolution of an oceanic island arc. Earth and Planetary Science Letters, v. 306, p. 229–240.

Ismail-Zade, A.T., Korotkii, A.I., Naimark, B.M., and Tsepelev, I.A., 2001, Numerical simulation of three-dimensional viscous flows with gravitational and thermal effects, Computational mathematics and mathematical physics, v. 41 p.

1331–1345.

Ismail-Zadeh, A. T., Huppert, H. E., and Lister, J. R., 2002, Gravitational and buckling instabilities of a rheologically layered structure: implications for salt diapirism, Geophysical Journal, v. 148, p. 288–302.

Jackson, J., 1994. Active tectonics of the Aegean region, Annu. Rev. Earth Planet. Sci., v. 22,

Jackson, J., and McKenzie, D. P., 1988. The relationship between plate motions and seismic moment tensors and the rate of active deformation in the Mediterranean and Middle East, Geophys. J. R. Astr. Soc., v. 93, p. 45–73.

Janots, E., Brunet, F., Goffé, B., Poinssot, C., Burchard, M., Cemič, L., 2007, Thermochemistry of monazite-(La) and dissakisite-(La): implications for monazite and allanite stability in metapelites Contributions to Mineral Petrology., v. 154, p. 1–14.

Janots, E., Engi, M., Berger, A., Allaz, J., Schwarz, J.O., and Spandler, C., 2008, Prograde metamorphic sequence of REE minerals in pelitic rocks of the Central Alps: implications for allanite–monazite–xenotime phase relations from 250 to 610 °C, Journal of Metamorphic Geology, v. 26, p. 509–526.

Janots, E, Engi, M., Rubatto, D., Berger, A., Gregory, C., Rahn, M., 2009, Metamorphic rates in collisional orogeny from in situ allanite and monazite dating Geology, v. 37, p. 11–14.

Jansen, J. B. H., 1973, Geological Map of Greece, Island of Naxos, Institute for Geology and Mineral Resources, Athens.

Jansen, J. B. H., and Schuiling, R. D., 1976, Metamorphism on Naxos: Petrology and geothermal gradients, American Journal of Science, v. 276, p. 1225–1253, doi: 10.2475 /ajs.276.10.1225.

John, B.E., and Howard, K.A., 1995, Rapid extension recorded by cooling age pattern and brittle deformation, Naxos, Greece. Journal of Geophysical Research, v. 100, p. 9969–997.

Jolivet, L., 2001, A comparison of geodetic and finite strain pattern in the Aegean,

geodynamic implications, Earth and Planetary Science. Letters., v. 5793, p. 1–10.

Jolivet, L., Faccenna, C., Goffé, B., Burov, E., and Agard, P., 2003, Subduction tectonics and exhumation of high-pressure metamorphic rocks in the Mediterranean orogens, Am. J. Sci., 303, 353–409.

Jolivet, L., Famin, V., Mehl, C., Parra, T., Aubourg, C., Hébert, R. and Philippot, P., 2004, Strain localization during crustal-scale boudinage to form extensional metamorphic domes in the Aegean Sea, Special Paper. Geological Society of America., v. 380, p. 185–210.

Jolivet, L. and Brun, J. P., 2010, Cenozoic geodynamic evolution of the Aegean region, International Journal of Earth Sciences, v. 99, p. 109–138, doi:10.1007/s00531-008-0366-4.

Jolivet, L., Lecomte, E., Huet, B., Denèle, Y., Lacombe, O., Labrousse, L., Le Pourhiet, L. and Mehl, C., 2010, The north cycladic detachment system, Earth and Planetary Science Letters, v. 289, p. 87–104, doi:10.1016/j.epsl.2009.1010.1032.

Jolivet, L., Faccenna. C., Huet. B, Labrousse. L., Le Pourhiet. L., Lacombe. O, Lecomte. E., et al., 2013, Aegean tectonics: Strain localisation, slab tearing and trench retreat, Tectonophysics, v. 597–598, p. 1–33, doi.org/10.1016/j.tecto.2012.06.011.

Jolivet, L., Menant. A., Sternai. P., Rabillard. A., Arbaret. A., et al., 2015, The geological signature of a slab tear below the Aegean. Tectonophysics, v. 659, p. 166–182.

Jones, G., and Robertson, A. H., 1991. Tectono-stratigraphy and evolution of the Mesozoic Pindos ophiolite and related units, northwestern Greece. Journal of the Geological Society of London, v. 148 (2), p. 267–288. https://doi.org/10.1144/gsjgs.148.2 .0267

Karaoğlan, F., Parlak, O., Kloetzli, U., Thöni, M., and Koller, F., 2013. U–Pb and Sm–Nd geochronology of the Kızıldağ (Hatay, Turkey) ophiolite: Implications for the timing and duration of suprasubduction zone type oceanic crust formation in

southern Neotethys. Geological Magazine, v. 150, p. 283–299.

Karaoğlan, F., Parlak, O., Robertson, A. H. F., Thöni, M., Klötzli, U., Koller, F., and Okay, A. I., 2013. Eocene HT/ HP metamorphism of ophiolitic rocks and Eocene crosscutting granitoid intrusions (Doğanşehir, area SE Anatolia) related to late-stage Neotethyan subduction processes. In A. H. F. Robertson, O. Parlak, and U. C. Ünlügenç (Eds.), Geological development of Anatolia and the Easternmost Mediterranean Region v. 372, p. 249–272. Geological Society: London. Special Publication.

Karig, D.E., 1982. Initiation of subduction zones: implications for arc evolution and ophiolite development. Geological Society, London, Special Publications, v. 10, p. 563–576.

Katzir, Y., Garfunkel, Z., Avigad, D. and Matthews, A., 2007, The geodynamic evolution of the Alpine orogen in the Cyclades (Aegean Sea, Greece): Insights from diverse origins and modes of emplacement of ultramafic rocks. In: The Geodynamics of the Aegean and Anatolia (eds Taymaz T., Yilmaz Y. Dilek Y.). Geological Society, London, Special Publications v. 291, p. 17–40.

Katzir, Y., John, E., Valley, W., Matthews, A. and Spicuzza, M.J., 2002, Tracking fluid flow during deep crustal anatexis: metasomatism of peridotites (Naxos, Greece), Contributions to Mineral Petrology, v. 142, p. 700–713, DOI:10.1007/s00410-001-0319-4

Katzir, Y., Matthews, A., Garfunkel, Z., Schliestedt, M., Avigad, D., 1996, The tectono-metamorphic evolution of a dismembered ophiolite (Tinos, Cyclades, Greece), Geological Magazine v. 133, p. 237–254. DOI:10.1017/S0016756800008992

Keay, S., Lister, G. and Buick. I., 2001, The timing of partial melting, Barrovian metamorphism and granite intrusion in the Naxos metamorphic core complex, Cyclades, Aegean Sea, Greece, Tectonophysics, v. 342, p. 275–312, doi:10.1016/S0040-1951(01)00168-8.

Keiter, M., Ballhaus, C., and Tomaschek, F. 2011. A new geological map of the Island of Syros (Aegean Sea, Greece): Implications for lithostratigraphy and structural

history of the Cycladic Blueschist Unit. Geological Society of America Special Papers, v. 481, p. 1–43.

Keiter, M., Piepjohn, K., Ballhaus, C., Lagos, M., and Bode, M. 2004. Structural development of high-pressure metamorphic rocks on Syros island (Cyclades, Greece). Journal of Structural Geology, v. 26, p. 1433–1445.

Kellet, D. A., Grujic, D., Warren, C., Cottle, J., Jamieson, R., Tenzin, T., 2010. Metamorphic history of a syn convergent orogen parallel detachment: the South Tibetan detachment system, Bhutan Himalaya, Journal of Metamorphic Geology, v. 28, p. 785–808.

Kelley, S., 2002. Excess argon in K–Ar and Ar–Ar geochronology. Chemical Geology, v. 188, p. 1–22.

Kelsey, D. E., Clark, C., and Hand, M., 2008. Thermobarometric modelling of zircon and monazite growth in melt-bearing systems: examples using model metapelitic and metapsammitic granulites. Journal of Metamorphic Geology, v. 26, p. 199–212. doi:10.1111/j.1525-1314.2007.00757.x

Kelsey, D. E., White, R.W., Holland, T.J.B. and Powell, R., 2004: Calculated phase equilibria in K2O–FeO–MgO–Al2O3–SiO2–H2O for sapphirine–quartz-bearing mineral assemblages. Journal of metamorphic Geology, v. 22, p. 559–578.

Kelvin, W. T.., 1863. On the secular cooling of the earth. Transcripts of Royal Society of Edinburgh, v. 23, 157-170.

Kincaid, C., and Sacks, I. S., 1997. Thermal and dynamical evolution of the upper mantle in subduction zones, J. Geophys. Res., v. 102(B6), p. 12295–12315, doi: 10.1029/96JB03553.

Kissel, C. and Laj, C., 1988, The Tertiary geodynamical evolution of the Aegean arc: a paleomagnetic reconstruction, Tectonophysics, v. 146, p. 183–201.

Klein, E.M., 2004. Geochemistry of the Igneous Oceanic Crust. In: Holland, H.D., Turekian, K.K. (Eds.), Treatise on Geochemistry. Elsevier, Amsterdam. v. 3, p. 433–463.

Koglin, N., 2008. Geochemistry, petrogenesis and tectonic setting of Ophiolites and

Mafic-ultraMafic complexes in the Northeastern Aegean Region: New trace-element, isotopic and age constraints (PhD thesis). Mainz, Germany . Koglin, N., Kostopoulos, D., and Reichmann, T., 2009. Reichmann, Geochemistry, petrogenesis and tectonic setting of the Samothraki Mafic suite, NE Greece: Trace-element, isotopic and zircon age constraints. Tectonophysics, v. 473, p. 53–68. doi:10.1016/j.tecto.2008.10.028

Kohlstedt, D.L. and Holtzman, B.K., 2009. Shearing melt out of the Earth: An experimentalist's perspective on the influence of deformation on melt extraction. Annual Review of Earth and Planetary Sciences, v. 37, p. 561-593.

Kohn, M. J., 2009. Models of garnet differential geochronology. Geochimica et Cosmochimica Acta, v. 73, p. 170–182.

Kohn, M. J. and Spear, F. S., 2000. Retrograde net transfer reaction insurance for pressure–temperature estimates. Geology, v. 28, p. 1127–1130.

Kohn, M. J., Wieland, M. S., Parkinson, C. D. and Upreti, B. N., 2005, Five generations of monazite in Langtang gneisses: implications for chronology of the Himalayan metamorphic core. Journal of Metamorphic Geology, v. 23, p. 399–406. doi: 10.1111/j.1525-1314.2005.00584.x

Konstantinou, A., Wirth, K. R., and Vervoort, J., 2007. U–Pb ısotopic dating of troodos plagiogranite, Cyprus by LAICP-MS/. GSA Denver Annual Meeting, Denver, CO

Koukouvelas, I. K., and Aydin, A., 2002. Fault structure and related basins of the North Aegean Sea and its surroundings, Tectonics, v. 21(5), p. 1046, doi: 10.1029/2001TC901037

Koukouvelas, I.K. and Kokkalas, S., 2003, Emplacement of the Miocene west Naxos pluton (Aegean Sea, Greece): a structural study. Geological Magazine, v. 140, p. 45–61, doi: 10.1017/S0016756802007094

Krogh Ravna, E. J., 2000. The garnet–clinopyroxene Fe 2 –Mg geothermometer: An updated calibration. Journal of Metamorphic Geology, v. 18(2), p.211-219.

Krogh Ravna, E. J. and Terry, M. P., 2004. Geothermobarometry of UHP and HP

eclogites and schists – an evaluation of equilibria among garnet–clinopyroxene–kyanite–phengite–coesite/quartz. Journal of Metamorphic Geology, v. 22, p. 579–592.

Kruckenberg, S.C., Ferré, E.C., Teyssier, C., Vanderhaeghe, O., Whitney, D.L., Seaton, N.C.A., and Skord, J.A., 2010, Viscoplastic flow in migmatites deduced from fabric anisotropy: an example from the Naxos dome, Greece, Journal of Geophysical Research – Solid Earth, v. 115, B09401, doi: 10.1029/2009JB007012.

Kruckenberg, S.C., Vanderhaeghe, O., Ferré, E.C., Teyssier, C., and Whitney, D.L., 2011, Flow of partially molten crust and the internal dynamics of a migmatite dome, Naxos, Greece, Tectonics, v. 30, TC3001, 24 p., doi: 10.1029/2010TC002751.

Kukoč, D., Goričan, Š., Košir, A., Belak, M., Halamić, J., and Hrvatović, H., 2015. Middle Jurassic age of basalts and the post-obduction sedimentary sequence in the Guevgueli Ophiolite Complex (Republic of Macedonia). International Journal of Earth Sciences, v. 104 (2), p. 435–447.

Kumar, A., Lal, N., Jain, A. K., and Sorkhabi, R. B., 1995. Late Cenozoic-Quarternary thermo-tectonic history of Higher Himalaya Crystalline (HHC) in Kishtwar-Padar-Zanskar region, NW Himalaya: evidence from fission track ages. Journal of Geological Sociecty India, v. 45, p. 375–391.

Lagos, M., Scherer, E. E., Tomaschek, F., Munker, C., Keiter, M., et al., 2007. High precision Lu–Hf geochronology of Eocene eclogite-facies rocks from Syros, Cyclades, Greece. Chemical Geology, v. 243, p. 16–35.

Lapen, T. J., Johnson, C. M., Baumgartner, L. P., Mahlen, N. J., Beard, B. L., and Amato, J. M.,2003. Burial rates during prograde metamorphism of an ultra-high-pressure terrane: an example from Lago di Cignana, western Alps, Italy. Earth and Planetary Science Letters, v. 2003, p. 57–72.

Lapen, T.J., Mahlen, N.J., Johnson, C.M. and Beard, B.L., 2004, High Precision Lu and Hf isotope analysis of both spiked and unspiked samples: a new approach. Geochemistry, Geophysics, Geosystems, v. 5(1), p. 1-17. doi:10.1029/2003GC000582.

Laurent, V., Beaudoin, A., Jolivet, L., Arbaret, L., Augier, R., and Rabillard, A., 2015. Interrelations between extensional shear zones and synkinematic intrusions: The example of Ikaria Island (NE Cyclades, Greece). Tectonophysics, 651-652, 152–171. https://doi.org/10.1016/j.tecto.2015.1003.1020

Laurent. V., Jolivet. L., Roche. R., Augier. R., Scaillet. R., et al., 2016, Strain localization in a fossilized subduction channel: Insights from the Cycladic Blueschist Unit (Syros, Greece). Tectonophysics, v. 672–673, p.150–169.

Laurent V, Lanari P, Naïr I, Augier R, Lahfid A, Jolivet L, 2018. Exhumation of eclogite and blueschist (Cyclades, Greece): Pressure–temperature evolution determined by thermobarometry and garnet equilibrium modelling. Journal of Metamorphic Geology, v.36 p. 769–798. https://doi.org/10.1111/jmg.12309

Law, R. D., Searle, M. P., and Godin, L., 2006, Channel flow, ductile extrusion and exhumation in continental collision zones, Geological Society, London, Special Publications v. 268 https://doi.org/10.1144/GSL.SP.2006.268.01.28

Le Bas, M. J., and Streckeisen, A. L., 1991. The IUGS systematics of igneous rocks. Journal of the Geological Society; v. 148 (5), p. 825–833. doi: https://doi.org /10.1144 /gsjgs.148.5.0825

Le Pichon, X., 1982. Land-locked oceanic basins and continental collision; the Eastern Mediterranean as a case example, in Mountain Building Processes, edited by K. Hsü, p. 129–146, Academic Press, London

Le Pichon, X., and Angelier, J., 1979, The Hellenic arc and trench system: A key to the neotectonic evolution of the eastern Mediterranean area, Tectonophysics, v. 60, p. 1–42.

Le Pichon, X., and Angelier, J., 1981. The Aegean Sea. Philosophical Transcript Royal Society of London, v. 300, 357–372.

Le Pichon, X., and Kreemer, C., 2010. The Miocene-to-Present kinematic evolution of the Eastern Mediterranean and Middle East and its implications for dynamics, Annu. Rev. Earth Planet. Sci., v. 38(1), p. 323–351.

Leake, B., Woolley, A., Arps, C., Birch, W., Gilbert, M., Grice, J., . . . Youzhi, G.,

1997. Nomenclature of Amphiboles; Report of the Subcommittee on Amphiboles of the International Mineralogical Association Commission on New Minerals and Mineral Names. Mineralogical Magazine, v. 61(405), p. 295–310. doi:10.1180 /minmag.1997.061.405.13

Lederer, G.W., Cottle, J.M., Jessup, M.J., Langille, J.M. and Ahmad, T., 2013. Timescales of partial melting in the Himalayan middle crust: insight from the Leo Pargil dome, northwest India. Contributions to Mineralogy and Petrology, v. 166(5), p.1415–1441.

Lee, J., Hacker, B., and Wang, Y., 2004, Evolution of North Himalayan gneiss domes: Structural and metamorphic studies in Mabja Dome, southern Tibet: Journal of Structural Geology, v. 26, p. 2297–2316.

Lee, J., McClelland, W., Wang, Y., Blythe, A., and McWilliams, M., 2006, Oligocene –Miocene middle crustal flow in southern Tibet: Geochronology of Mabja Dome, in Law, R.D., and Searle, M.P., eds., Channel flow, ductile extrusion and exhumation in continental collision zones: Geological Society of London Special Publication, v. 268, p. 445–469.

Lévy, F., Jaupart, C., 2011. Folding in regions of extension, Geophysical Journal International, v. 185, Issue 3, 1, p. 1120–1134, https://doi.org/10.1111/j.1365-246X.2011.05013.x

Li, X., Tang, G., Gong, B., Yang, Y., Hou, K., Hu, Z., Li, Q., Liu, Y. and Li, W., 2013. Qinghu zircon: A working reference for microbeam analysis of U-Pb age and Hf and O isotopes. Chinese Science Bulletin, v. 58, p. 4647–4654.

Liati, A., 2005. Identification of repeated Alpine (ultra) high-pressure metamorphic events by U–Pb SHRIMP geochronology and REE geochemistry of zircon: the Rhodope zone of Northern Greece. Contributions to Mineralogy and Petrology, v. 150, p. 608–630.

Liati, A., Gebauer, D., Fanning, C. M., 2004, The age of ophiolitic rocks of the Hellenides (Vourinos, Pindos, Crete): first U–Pb ion microprobe (SHRIMP) zircon ages, Chemical Geology, v. 207, p. 171–188, doi.org/10.1016/j.chemgeo.2004.02.010.

Liati, A., Skarpelis, N. and Pe-Piper, G., 2009. Late Miocene magmatic activity in the Attic-Cycladic Belt of the Aegean (Lavrion, SE Attica, Greece): implications for the geodynamic evolution and timing of ore deposition. Geological Magazine, v. 146(5), p.732-742.

Lister, G. S., Banga, G., and Feenstra, A., 1984, Metamorphic core complexes of cordilleran type in the Cyclades, Aegean Sea, Greece, Geology, v. 12, p. 221–225.

Lister, G. S., and Forster, M. A., 2016. White mica^{40}Ar/^{39}Ar age spectra and the timing of multiple episodes of high-P metamorphic mineral growth in the Cycladic eclogite–blueschist belt, Syros, Aegean Sea, Greece. Journal of Metamorphic Geology, v. 34, p. 401–421.

Ludwig, K.R., 2003. User's Manual for Isoplot 3.00: A Geochronological Toolkit for Microsoft Excel. Berkeley Geochronology Center Special Publication, Berkeley, CA.

Ludwig, K., 2003b, Isoplot/Ex Version 3.00: a geological toolkit for Microsoft Excel, Berkeley Geochronology Center Special Publication, v. 4, p. 70

Lyell, C., 1833. Principles of geology, being an attempt to explain the former changes of the Earth's surface by reference to causes now in operation. V. 3. London, John Murray.

Lyell, C., Elements of Geology. London, John Murray.

Maekawa, H., Shozul, M., Ishll, T., Fryer, P., and Pearce, J.,1993. Blueschist Metamorphism in an Active Subduction Zone. Nature. v. 364. p. 520-523. 10.1038/364520a0.

Maffione, M., Thieulot, C., van Hinsbergen, D.J., Morris, A., Plümper, O. and Spakman, W., 2015. Dynamics of intraoceanic subduction initiation: 1. Oceanic detachment fault inversion and the formation of supra-subduction zone ophiolites. Geochemistry, Geophysics, Geosystems, v. 16, p. 1753–1770.

Maffione, M., and van Hinsbergen, D. J. J., 2018. Reconstructing plate boundaries in the Jurassic Neo-Tethys from the East and West Vardar Ophiolites (Greece and Serbia). Tectonics, v. 37, p. 858–887. https://doi.org/10.1002/2017TC004790

Mahar, E. M., Baker, J. M., Powell, R., Holland, T. J. B. and Howell, N. 1997, The

effect of Mn on mineral stability in metapelites. Journal of Metamorphic Geology, v. 15, p. 223–238. doi:10.1111/j.1525-1314.1997.00011.x

Malandri, C., Soukis, K., Maffione, M., Özkaptan, M., Vassilakis, E., Lozios, S. and van Hinsbergen, D.J., 2016. Vertical-axis rotations accommodated along the Mid-Cycladic lineament on Paros Island in the extensional heart of the Aegean orocline (Greece). Lithos, p. 575-601.

Marcucci, M., Kodra, A., Pirdeni, A., and Gjata, T., 1994. Radiolarian assemblages in the Triassic and Jurassic cherts of Albania. Ofioliti, v. 19.

Marcucci, M., and Prela, M., 1996. The Lumi i Zi (Puke) section of the Kalur Cherts: Radiolarian assemblages and comparison with other sectionsin northern Albania. Ofioliti, v. 21(1), p. 71–76.

Marshall, B., 1969. Zircon behavior during extreme metamorphism. Special Publication of Geological Sociecy Australia v. 2, p. 349–351.

Martin, L., Duchêne. S., Deloule, E. and Vanderhaeghe. O., 2006, The isotopic composition of zircon and garnet: A record of the metamorphic history of Naxos, Greece, Lithos, v. 87, p. 174–192, doi:10.1016/j.lithos.2005.06.016.

Martinod, J. and Davy, P., 1992, Periodic instabilities during compression or extension of the lithosphere 1. Deformation modes from an analytical perturbation method, Journal of Geophysical Research, v. 97 (B2), doi:10.1029/91JB02715.

Maruyama, S. and Liou, J., 1996. Blueschists and Eclogites of the World and Their Exhumation. International Geology ldots. v. 38. p. 485–594. doi: 10 .10 80/ 0020681 9709465347.

Massonne, H.-J., 2012. Formation of amphibole and clinozoisite-epidote in eclogite owing to fluid infiltration during exhumation in a subduction channel. Journal of Petrology, 53, 1969–1998.

Matsuda, Jun-ichi and Senoh, Kenji and Maruoka, Teruyuki and Sato, Hiroki and Mitropoulos, Panagiotis. 1999. K-Ar ages of the Aegean volcanic rocks and their implication for the arc-trench system. GEOCHEMICAL JOURNAL. v. 33. p. 369-377. 10.2343/geochemj.33.369.

McClusky, S., Balassanian, S., Barka, A., Demir, C., Ergintav, S., Georgiev, I., Gurkan, O., Hamburger, M., Hurst, K., Kahle, H. and Kastens, K., 2000, Global Positioning System constraints on plate kinematics and dynamics in the eastern Mediterranean and Caucasus, Journal of Geophysical Research: Solid Earth, v. 105(B3), p. 5695–5719.

Mcfarlane, C.R.M. and McCulloch M.T., 2007, Coupling of in-situ Sm-Nd systematics and U-Pb dating of monazite and allanite with applications to crustal evolution studies, Chemical Geology, v. 245, p. 45–60.

McKenzie, D. P., 1969. Speculations on the consequences and causes of plate motions. Geophysical Journal of the Royal Astronomical Society, v. 18, p. 1–32.

McKenzie, D., 1972. Active tectonics of the Mediterranean region, Geophys. J. Royal Astron.

McKenzie, D. P, 1978. Active tectonics of the Alpine—Himalayan belt: the Aegean Sea and surrounding regions, Geophysical Journal International, v. 55 (1), p. 217–254, doi:0.1111/j.1365-246X.1978.tb04759.x

Means, W.D., 1989, Stretching faults, Geology, v. 17, p. 893–896, doi: 10.1130/0091-761319890172.3.CO;2.

Menant, A., Jolivet, L., Augier, R., and Skarpelis, N., 2013. The North Cycladic Detachment System and associated mineralization, Mykonos, Greece: Insights on the evolution of the Aegean domain, Tectonics, v. 32, p. 433–452, doi: 10.1002/tect.20037.

Mehl, C., Jolivet, L., and Lacombe, O. 2005. From ductile to brittle: Evolution and localization of deformation below a crustal detachment (Tinos, Cyclades, Greece). Tectonics, v. 24(4), TC4017.

Melidonis, N. G., 1980, The geological structure and mineral deposits of Tinos island (Cyclades, Greece), Geol. Greece, v. 13, p. 1–80.

Meschede, M., 1986, A method of discriminating between different types of mid-ocean ridge basalts and continental tholeiites with the Nb-Zr-Y diagram: Chemical Geology, v. 56, p. 207–218.

Miller, C.F., Stoddard, E.F., Bradfish, L.J. and Dollase, W.A., 1981. Composition of plutonic muscovite; genetic implications. The Canadian Mineralogist, v. 19, p. 25-34.

Miyashiro, A., 1961. Evolution of Metamorphic Belts, Journal of Petrology, v. 2 (3,1), p. 277–311, doi: https://doi.org/10.1093/petrology/2.3.277

Mizera. M. and Behrmann. J.H, 2015, Strain and flow in the metamorphic core complex of Ios Island (Cyclades, Greece), International Journal of Earth Science (Geol Rundsch), p. 1–14. doi:10.1007/s00531-015-1259-y

Münker, C., Weyer, S., Scherer, E., Mezger, K., 2001. Separation of high field strength elements (Nb, Ta, Zr, Hf) and Lu from rock samples for MC-ICPMS measurements. Geochemistry Geophysics and Geosystems. v. 2. doi:10.1029/2001GC000183.

Molnar, P., and England, P., 1990. Temperatures, heat flux, and frictional stress near major thrust faults. Journal of Geophysical Research, v. 95, p. 4833–4856.

Molnar, P., England, P., and Martinod, J. 1993. Mantle dynamics, uplift of the Tibetan Plateau, and the Indian Monsoon. Reviews of Geophysics. v. 31. p. 357-396. doi:10.1029/93RG02030.

Molnar, P., and England, P., 1995. Temperatures in zones of steady-state underthrusting of young oceanic lithosphere. Earth and Planetary Science Letters, v. 131, p. 57–70.

Mottram, C., Warren, C., Regis, D., Roberts, N., Harris, N., Argles, T. and Parrish, R. 2014 Developing an inverted Barrovian sequence; insights from monazite petrochronology. Earth and Planetary Science Letters, v. 403, p. 418–43.

Mukasa, S. B., and Ludden, J. N., 1987. Uranium-lead ages of plagiogranites from the Troodos ophiolite, Cyprus, and their tectonic significance. Geology, v. 5, p. 825–828.

Mumpton, F.A., Roy, R., 1961. Hydrothermal stability studies of the zircon-thorite group. Geochimica Cosmochimica. Acta v. 21, p. 217 – 238. Newton, R.C. 1989. Metamorphic fluids in the deep crust. Annual review of Earth and Planetary Sciences, v. 17, p. 385–412.

Ng, S. W., Chung, S. L., Robb, L. J., Searle, M. P., Ghani, A. A., Whitehouse, M. J., Oliver, G. J. H., Sone, M., Gardiner, N. J., Roselee, M. H., 2014. Petrogenesis of Malaysian granitoids in the Southeast Asian tin belt: Part 1. Geochemical and Sr-Nd isotopic characteristics. GSA Bulletin; v. 127 (9-10): p. 1209–1237. doi: https://doi.org/10.1130/B31213.1

Nijman, W., Kloppenburg, A. and de Vries, S.T., 2017. Archaean basin margin geology and crustal evolution: an East Pilbara traverse. Journal of the Geological Society, p. 2016-2027.

Nocquet, J.-M., 2012, Present-day kinematics of the Mediterranean: A comprehensive overview of GPS results, Tectonophysics, p. 1–23, doi:10.1016/ j.tecto.2012.03.037

Noda, H. and Lapusta, N., 2013. Stable creeping fault segments can become destructive as a result of dynamic weakening. Nature, v. 493(7433), p. 518.

Nowell, G.M. and Parrish, R.R., 2001. Simultaneous acquisition of isotope compositions and parent/daughter ratios by non-isotope dilution-mode plasma ionisation multi-collector mass spectrometry (PIMMS). In Plasma Source Mass Spectrometry: The New Millenium (Holland, G. and Tanner, S.D. eds) Royal Society Chemisty. Special. Publication. v. 267, p. 298–310.

Nyst, M., and Thatcher. W., 2004. New constraints on the active tectonic deformation of the Aegean, Journal. Geophysical. Research., v. 109 (B11), B11406. Okay, A. I., 1989. Alpine Himalayan Blueschists, Annual reviews of Earth and Planetary Sciences, v. 17, p. 55–87.

Okrusch, M., Seidel, E., Kreuzer, H. and Harre, W., 1978. Jurassic age of metamorphism at the base of the Brezovica peridotite (Yugoslavia). Earth and Planetary Science Letters, v. 39(2), p. 291–297.

Orejana, D., Villaseca, C., Armstrong, R. A., Jeffries, T. E., 2011. Geochronology and trace element chemistry of zircon and garnet from granulite xenoliths: Constraints on the tectonothermal evolution of the lower crust under central Spain, Lithos, v. 124, p. 103-116. doi:doi.org/10.1016/j.lithos.2010.10.011.

Oxburgh, E. R., and Turcotte, D. L., 1971. Origin of paired metamorphic belts and

crustal dilation in island arc regions, J. Geophys. Res., v. 76(5), p. 1315–1327, doi: 10.1029/JB076i005p01315 p. 239–271.

Palin, R. M., Reuber, G. S., White, R. W., Kaus, B. J. P., and Weller. O. M., 2017. Subduction metamorphism in the Himalayan ultrahigh-pressure Tso Morari massif: An integrated geodynamic and petrological modelling approach. Earth and Planetary Science Letters, v. 467, p. 108–119.

Palin R. M., Searle, M. P., Waters, D. J., Parrish, R. R., Roberts, N. M. W., Horstwood, M. S. A., Yeh, M.-W., Chung, S.L., and Anh, T.T., 2013. A geochronological and petrological study of anatectic paragneiss and associated granite dykes from the Day Nui Con Voi metamorphic core complex, North Vietnam: constraints on the timing of metamorphism within the Red River shear zone, Journal of Metamorphic Geology, v. 31, p. 359–387. doi: 10.1111/ jmg.2013.31.

Palin, R.M., Weller, O.M., Waters, D.J. and Dyck, B., 2016. Quantifying geological uncertainty in metamorphic phase equilibria modelling; a Monte Carlo assessment and implications for tectonic interpretations. Geoscience Frontiers, v. 7, p.591–607.

Palin, R. M., White, R. W., Green, E. C. R., Diener, J. F. A., Powell, R. and Holland, T. J. B. 2016, High-grade metamorphism and partial melting of basic and intermediate rocks. Journal of Metamorphic Geology. v. 34, p. 871–892. doi:10.1111/jmg.12212

Pallister, J.S. and Knight, R.J., 1981. Rare-earth element geochemistry of the Samail Ophiolite near Ibra, Oman. Journal of Geophysical Research: Solid Earth, v. 86 (B4), p. 2673–2697.

Papanikolaou D., 1984. The three metamorphic belts of the Hellenides: a review and a kinematic interpretation, Geological Society of London, Special Publication, v. 17, p. 551–561.

Papanikolaou, D., 2013, Tectonostratigraphic models of the Alpine terranes and subduction history of the Hellenides: Tectonophysics, v. 595–596, p. 1–24, doi: doi.org/10.1016/j.tecto.2012.08.008.

Parlak, O., Çolakoğlu, A., Dönmez, C., Sayak, H., Yildirim, N., Türkel, A., and Odabaşi, İ., 2013. Geochemistry and tectonic significance of ophiolites along the İzmir–Ankara–Erzincan Suture Zone in northeastern Anatolia. Geological Society, London, Special Publications, v. 372 (1), p. 75–105.

Parlak, O., and Delaloye, M., 1999, Precise^{40}Ar/^{39}Ar ages from the metamorphic sole of the Mersin ophiolite (southern Turkey), Tectonophysics, v. 301, p. 145–158, https://doi.org/10.1016/S0040-1951(98)00222-4.

Parrish, R. R., 1990, U–Pb dating of monazite and its application to geological problems. Canadian Journal of Earth Sciences, v. 27, p. 1431–1450.

Parrish, R. R., Gough, S. J., Searle, M. P. and Waters, D. J., 2006. Plate velocity exhumation of ultrahigh-pressure eclogites in the Pakistan Himalaya. Geology, v. 34, p. 989–992.

Parsons, B. and Sclater, J.G., 1977. An analysis of the variation of ocean floor bathymetry and heat flow with age, Journal of geophysical Research, v. 82, p. 803–827

Patterson, C., 1956. Age of meteorites and the earth. Geochimica et Cosmochimica Acta, v. 10, Issue 4, p. 230–237.

Patiño Douce, A. E. and Harris, N. 1998, Experimental Constraints on Himalayan Anatexis. Journal of Petrology, v. 39, p. 689–710. doi: 10.1093/petroj/39.4.689

Patriat, M., and Jolivet, L. 1998. Post-orogenic extension and shallow-dipping shear zones, study of a brecciated decollement horizon in Tinos (Cyclades, Greece). Comptes Rendus Mathematique Academie des Sciences, Paris, 326, 355–362. https://doi.org/10.1016/S1251– 8050(1098)80306–80306

Pattison, D. R. M. and Begin, N. J., 1994, Hierarchy of closure temperatures in granulites and the importance of an intergranular exchange medium (melt?) in controlling maximum Fe–Mg exchange temperatures. Mineralogical Magazine, v. 58A, p. 694–695.

Pattison, D. R. M., Chacko, T., Farquhar, J., and Mcfarlane C. R. M., 2003, Temperatures of granulite-facies metamorphism: constraints from experimental phase

equilibria and thermobarometry corrected for retrograde exchange. Journal of petrology, v. 44 p. 867–900. doi: 10.1093/petrology/44.5.867

Pattison, D.R., De Capitani, C. And Gaidies, F., 2011. Petrological consequences of variations in metamorphic reaction affinity. Journal of Metamorphic Geology, v. 29(9), p. 953–977.

Pattison, D. R. M., and Tracy, R. J., 1991, Phase equilibria and themobarometry of metapelites. Mineralogy Society of America Reviews Mineral v. 26 p. 105–206.

Patzak, M., Okrusch, M. and Kreuzer, H. 1994. The Akrotiri Unit on the island of Tinos, Cyclades, Greece: witness to a lost terrane of Late Cretaceous age. Neues Jahrbuch fu¨r Geologie und Pala¨ontologie, Abhandlungen, v. 194, p. 211–252.

Pearce, J. A. 1983. Role of the subcontinental lithosphere in magma genesis at active continental margins. In Hawkesworth, C. J., and Norry, M. J., eds. Continental basalts and mantle xenoliths. Nantwich, Shiva, p. 230–249.

Pearce, J. A. 1996. A users guide to basalt discrimination diagrams. In Wyman, D. A., ed. Trace element geochemistry of v. canic rocks: applications for massive sulphide exploration. Geological Association of Canada Short Course Notes v. 12, p. 79–113.

Pearce, J.A., 2003. Supra-subduction zone ophiolites: the search for modern analogues. Special Papers-Geological Society of America, p. 269–294.

Pearce, J. A., Alabaster, T., Shelton, A. W., and Searle, M. P. 1981. The Oman ophiolite as a Cretaceous arc basin complex: evidence and implications. Philosphical Transcripts of the Royal Society of London. v. 300, p. 299–317.

Pearce, J. A., and Cann, J. R., 1971. Ophiolite origin investigated by discriminant analysis using Ti, Zr and Y. Earth and Planetary Science Letters, v. 12 p. 339–349.

Pearce, J. A., and Cann, J. R., 1973. Tectonic setting of basic v. canic rocks determined using trace element analyses. Earth and Planetary Science Letters, v. 19, p. 290–300.

Pearce, J. A., and Deng, W. 1988. The ophiolites of the Tibet Geotraverses, Lhasa to

Golmud 1985 and Lhasa to Kathmandu 1986. Philosophical Transcripts of the Royal Society of America v. 327

Pearce, P.A., Harris, N.B.W., and Tindle, A.G., 1984, Trace element discrimination diagrams for the tectonic interpretation of granitic rocks: Journal of Petrology, v. 25, p. 956–983, doi:10.1093/petrology/25.4.956.

Pedersen, R. B., Searle, M. P., and Corfield, R. I., 2001, U–Pb zircon ages from the Spontang Ophiolite, Ladakh Himalaya, Journal of the Geological Society, v. 158, p. 513–520, https://doi.org/10.1144/jgs.158.3.513

Peillod, A., Ring, U., Glodny, J. and Skelton, A. 2017, An Eocene/Oligocene blueschist-/greenschist-facies P–T loop from the Cycladic blueschist unit on Naxos Island, Greece: Deformation-related reequilibration vs thermal relaxation. Journal of Metamorphic Geology, v. 35, p. 805–830 doi:10.1111/jmg.12256

Pe-Piper, G. 2000. Origin of S-type granites coeval with I-type granites in the Hellenic subduction system, Miocene of Naxos, Greece. European Journal of Mineralogy, v. 12(4), p. 859–875. https://doi.org/10.1127 /ejm/1112/1124/0859

Pe-Piper, G., and Piper, 1994. Miocene magnesian andesites and dacites, Evia, Greece: adakites associated with subducting slab detachment and extension, Lithos, v. 31 (3–4), p. 125–140 , doi:https://doi.org/10.1016 /0024-4937(94)90004-3.

Pe-Piper, G., and Piper, D., 2005, The South Aegean active volcanic arc: Relationships between magmatism and tectonics, Dev. V. canol., v. 7, p. 113–133.

Pe-Piper, G., and Piper, D. J. W. 2006. Unique features of the Cenozoic igneous rocks of Greece. In Y. Dilek and S. Pavlides (Eds.), Postcollisional tectonics and magmatism in the Mediterranean region and Asia (pp. 259–282). Boulder, CO: Geological Society of America. https://doi.org/ 10.1130/2006.2409(1114)

Pe-Piper, G., NKotopouli, C., and Piper, D. J. W. 1997. Granitoid rocks of Naxos, Greece: regional geology and petrology. Geological Journal, v. 32(2), p. 153–171. https://doi.org/10.1002/(SICI)1099–1034(199706)1997 32:199702 ¡199153:: AID-GJ199737¿199703.199700.CO;199702–199701

Pe-Piper, G., Piper, D. J. W., and Matarangas, D. 2002. Regional implications of

geochemistry and style of emplacement of Miocene I-type diorite and granite, Delos, Cyclades, Greece. Lithos, 60(1–2), 47–66. https://doi.org/10.1016/S0024-4937(1001)00068-00068

Perkins, R, Cooper, F, Condon, D, Tattitch, B and Naden, J, 2018. Post-collisional Cenozoic extension in the northern Aegean: The high-K to shoshonitic intrusive rocks of the Maronia Magmatic Corridor, northeastern Greece. Lithosphere.

Perry, J. 1895a. On the age of the Earth. Nature, v. 51, p. 224–227.

Perry, J. 1895b. On the age of the Earth. Nature, v. 51, p. 341–342.

Perry, J. 1895c. The age of the Earth. Nature, v. 51, p. 582–585.

Peters, K., Smit, M., van Hinsbergen, D., van Roermund, H., Brouwer, F., 2017. The longevity of Neotethyan metamorphic soles from Lu-Hf garnet chronology. Geophysical Research Abstracts, v. 19, EGU2017-15673, 2017, EGU General Assembly 2017

Peterson, J.W., Newton, R.C., 1989. Reversed experiments on biotite–quartz–feldspar melting in the system KMASH: implications for crustal anatexis. Journal of Geology v. 97, p. 465–485.

Pëto, P., 1976. An experimental investigation of melting reactions inv. ving muscovite and paragonite in the silica-saturated portion of the system K2O–Na2O–Al2O3–SiO2–H2O to 15 kbar total pressure: United Kingdom Natural Environment Research Council.

Philippon, M., Brun, J. P., and Gueydan, F., 2011. Tectonics of the Syros blueschists (Cyclades, Greece): From subduction to Aegean extension. Tectonics, v. 30(4), TC4001.

Philpotts A. R., 1976. Silicate liquid immiscibility: Its probable extent and petrogenetic significance. American Journal of Science., v. 276, p. 1147–1177.

Photiades, A., Saccani, E., and Tassinari, R., 2003. Petrogenesis and tectonic setting of v. canic rocks from the subpelagonian ophiolitic mélange in the Agoriani area (Othrys, Greece). Ofioliti, v. 28 (2), p. 121–135.

Pidgeon, R.T., 1992. Recrystallisation of oscillatory zoned zircon: some geochronolog-

ical and petrological implications. Contributions to Mineral Petrology. v. 110, p. 463– 472.

Pitcher, W.S., 1997, The Nature and Origin of Granite: London, Chapman and Hall, v. 387

Platt, J. P. 1986. Dynamics of orogenic wedges and the uplift of high-pressure metamorphic rocks. Geological Society of America Bulleitein, v. 97 p. 1037–1053.

Platt, J. P, Behr, W., and Cooper, F. J., 2014. Metamorphic core complexes: windows into the mechanics and rheology of the crust. Journal of the Geological Society. v. 172, p. 9–27, doi: 10.1144/jgs2014-036

Platt, J. P., Behr, W. M., Johanesen, K., and Williams, J. R., 2013. The Betic-Rif arc and its orogenic hinterland: A review. Annual Review of Earth and Planetary Sciences, v. 41, p. 313–357.

Platt, J. P., and England, P. C. 1994. Convective removal of lithosphere beneath mountain belts: thermal and mechanical consequences. American Journal Science. V. 294 p. 307–336.

Powell, R., 1978. Equilibrium thermodynamics in petrology, an introduction. Harper and Row publishers.

Powell, R, 1985. Regression diagnostics and robust regression in geothermometer/geobarometer calibration; the garnet-clinopyroxene geothermometer revisited. Journal of Metamorphic Geology. v. 3, p. 231-243

Powell, R., and Holland, T. J. B., 1988, An internally consistent thermodynamic dataset with uncertainties and correlations: 3. Application to geobarometry, worked examples and a computer program. Journal of Metamorphic Geology, v. 6, p. 173–204.

Powell, R., and Holland, T. J. B., 1994. Optimal geothermobarometry and geobarometry. American mineralogist, v. 79, p. 120–133.

Powell, R., Holland, T.J.B., and Worley, B, 1998, Calculating phase diagrams involving solid solutions via non-linear equations, with examples using THERMOCALC Journal of Metamorphic Geology, v. 16, p. 577–588.

Prela, M., Chiari, M., and Marcucci, M., 2000. Jurassic radiolarian biostratigraphy of the sedimentary cover of ophiolites in the Mirdita area, Albania: New data. Ofioliti, v. 25 (1), p. 55–62.

Pyle, J. M. and Spear, F. S., 1999, Yttrium zoning in garnet: coupling of major and accessory phases during metamorphic reactions. Geological Materials Research, v. 1, p. 1–49.

Rabillard, A., Jolivet, L., Arbaret, L., Bessière, E., Laurent, V., Menant, A., et al. 2018. Synextensional granitoids and detachment systems within Cycladic metamorphic core complexes (Aegean Sea, Greece): Toward a regional tectonomagmatic model. Tectonics, 37, 2328–2362. https://doi.org/10.1029/ 2017TC004697

Ramberg, H., 1980, Diapirism and gravity collapse in the Scandinavian Caledonides, Journal of the Geological Society, v. 137, DOI: 10.1144/gsjgs.137.3.0261

Rapp, R.P., Ryerson, F. and Miller, C.F. 1987. Experimental evidence bearing on the stability of monazite during crustal anatexis. Geophysical Research Letters, v. 14, p. 307–310.

Rasmussen B., Muhling J. R., Fletcher I. R. and Wingate M. T., 2006, In situ SHRIMP U–Pb dating of monazite integrated with petrology and textures: does bulk composition control whether monazite forms in low-Ca pelitic rocks during amphibolite facies metamorphism? Geochimica et Cosmochimica Acta v. 70, p. 3040–3058.

Rassios, A., Grivas, E., Konstantopoulou, G., and Vacondios, I., 1994, The geometry of structures forming around the ductile–brittle transition in the Vourinos–Pindos–Othris oceanic slab. Bulletin of the Geological Society of Greece. 2.

Ravenhurst, C. E. and Donelick, R. A., 1992. Fission Track Thermochronology. in Short Course Handbook on Low Temperature Thermochronology, ed. M. Zentilli and P. H. Reynolds. P. 21–42. Nepean, Ontario: Mineralogical Society of Canada.

Reagan, M. K., Ishizuka, O., Stern, R. J., Kelley, K. A., Ohara, Y., Blichert-Toft, J., et al., 2010. Fore-arc basalts and subduction initiation in the zu-Bonin-Mariana sys-

tem. Geochemistry, Geophysics, Geosystems, v. 11, Q03X12. https:// doi.org/10.1029 /2009GC002871

Rebay, G., Powell, R., Diener, J., 2010. Calculated phase equilibria for a MORB composition in a P T window, 450–650°C and 18–28 kbar: the stability of eclogite.. Journal of Metamorphic Geology. v. 28. p. 635-645.

Reichen, L.E. and Fahey, J.J., 1962. An improved method for the determination of FeO in rocks and minerals including garnet. U.S. Geological Survey Bulletin. v. 1144B, pp. 1-5.

Reilinger, R., et al., 2006. GPS constraints on continental deformation in the Africa-Arabia-Eurasia continental collision zone and implications for the dynamics of plate interactions, J. Geophys. Res., v. 111, B05411, doi: 10.1029/2005JB004051.

Resimić-Šarić, K., Cvetković, V., and Balogh, K., 2005. Radiometric K/Ar data as an evidence of the geodynamic evolution of the Ždraljicaophiolitic complex (central Serbia). Annales Géologiques de la Péninsule Balkanique, v. 66, p. 73–79.

Resimić-Šarić, K., Cvetković, V., Balogh, K., and Koroneos, A., 2006. Main characteristics of ophiolitic complexes within the eastern branch of the Vardar Zone Composite Terrane in Serbia. In International Symposium on the Mesozoic ophiolite belts of the northern part of the Balkan Peninsula, Belgrade (Serbia) and Banja Luka (Bosnia and Herzegovina), p. 112–115.

Rey. P.F., Mondy. L., Duclaux. G., Teyssier. C., Whitney. D.L., Bocher. M., and Prigent. C., 2017, The origin of contractional structures in extensional gneiss domes. Geology v. 45 p. 263–266. doi: 10.1130/G38595.1

Rey, P.F., Teyssier, C., Kruckenberg, S.C., and Whitney, D.L. 2011, Viscous collision in channel explains double domes in metamorphic core complexes:, Geology, v. 39, p. 387–390, DOI: https://doi.org/10.1130/G31587.1

Rey, P., C. Teyssier, and Whitney, D.L., 2009, The role of partial melting and extensional strain rates in the development of metamorphic core complexes, Tectonophysics, v. 477, p. 135–144, doi:10.1016/j.tecto.2009. 03.010.

Rice, J. R., 2006. Heating and weakening of faults during earthquake slip. Journal of

Geophysical Research: Solid Earth, v. 111(B5).

Ricou, L.E., and Godfriaux, I., 1991. A cross-section through allochthonous ophiolites and gneiss between the Pelagonian massif and the Paikon window, northern Greece — Une coupe a travers les ophiolites et gneiss allochtones entre le massif Pelagonien et la fenetre du Paikon (Grece du Nord). Comptes Rendus - Academie des Sciences Series II, v. 313 (13).

Ricou, L.E., and Godfriaux, I., 1995. Review on the Paikon multiple window and the structure of the Vardar in Greece French with abridged English — Mise au point sur la fenetre multiple du Paikon et la structure du Vardar en Grece. Comptes Rendus - Academie des Sciences Ser. II Sci. la Terre des Planetes, v. 321 (7).

Ring, U.,Glodny, J., Peillod, A., Skelton, A., 2018. The timing of high-temperature conditions and ductile shearing in the footwall of the Naxos extensional fault system, Aegean Sea, Greece. Tectonophysics. 745. 10.1016/j.tecto.2018.09.001

Ring, U., Glodny, J., Will, T., Thomson, S., 2007a. An Oligocene extrusion wedge of blueschists-facies nappes on Evia, Aegean Sea, Greece: implications for the early exhumation of high-pressure rocks. J. Geological Society of London v. 164, p. 637–652.

Ring, U., Glodny, J., Will, T. and Thomson, S., 2010, The Hellenic subduction system: High-pressure metamorphism, exhumation, normal faulting, and large-scale extension, Annual Reviews of Earth and Planetary Science, v. 38, p. 45–76.

Ring, U., and Layer, P.W., 2003, High-pressure metamorphism in the Aegean, eastern Mediterranean: underplating and exhumation from the Late Cretaceous until the Miocene to Recent above the retreating Hellenic subduction zone. Tectonics v. 22.

Ring, U., Thomson, S.N., Bröcker, M., 2003, Fast extension but little exhumation: The Vari detachment in the Cyclades, Greece. Geological Magazine, v. 140, p. 245–252.

Ring, U., Will, T., Glodny, J., Kumerics, C., Gessner, K., Thomson, S., Güngör, T., Monie, P., Okrusch, M., Drüppel, K., 2007b. Early exhumation of high-pressure

rocks in extrusion wedges: cycladic blueschist unit in the eastern Aegean, Greece, and Turkey. Tectonics v. 26, TC2001. doi:10.1029/2005TC001872.

Roberts, N. M. W., Parrish, R. R., Horstwood, M. S. A. and Brewer, T. S., 2011. The 1.23 Ga Fjellhovdane rhyolite, Grøssæ-Totak; a new age within the Telemark supracrustals, southern Norway. Norwegian Journal of Geology, v. 91, p. 239–246.

Roberts, N. M. W., Thomas, R. J., and Jacobs, J., 2016, Geochronological constraints on the metamorphic sole of the Semail ophiolite in the United Arab Emirates, Geoscience Frontiers, v. 7, p. 609–619.

Robertson, A. H. F., 2002, Overview of the genesis and emplacement of Mesozoic ophiolites in the eastern Mediterranean Tethyan region, Lithos, v. 65, p. 1–67.

Robertson, A.H.F., 2006. Contrasting modes of ophiolite emplacement in the Eastern Mediterranean region. In: Robertson, A.H.F., Mountrakis, D. (Eds.), Tectonic Development of the Eastern Mediterranean Region. Geological Society of London Special Publication, v. 260, p. 235–261.

Robertson, A. H. F., and Dixon, J. E., 1984, Introduction: aspects of the geological evolution of the Eastern Mediterranean in J. E. Dixon, A. H. F. Robertson (Eds.), The Geological Evolution of the Mediterranean, Oxford university press, p. 551–561

Robertson, A. H. F., Karamata, S., and Sarie, K., 2009, Overview of ophiolites and related units in the Late Palaeozoic-Early Cenozoic magmatic and tectonic development of Tethys in the northern part of the Balkan region, Lithoshere, v. 108, p. 1–36.

Robertson, A. H. F., and Shallo, M., 2000. Mesozoic-Tertiary evolution of Albania in its regional eastern Mediterranean context, Tectonophysics, v. 316, p. 197–254.

Robertson, A. H. F., Trivic, B., Deric, N., and Bucur, I., 2013, Tectonic development of the Vardar ocean and its margin: Evidence from the Republic of Macedonia and Greek Macedonia, Tectonophysics, v. 596, p. 25–54.

Roche. V., Laurent. V., Cardello. G.L., L. Jolivet, Scaillet. S., 2016, Anatomy

of the Cycladic Blueschist Unit on Sifnos Island (Cyclades, Greece), Journal of Geodynamics, v. 97, p. 62–87 http://dx.doi.org/10.1016/j.jog.2016.03.008.

Roddick, J. C., Cameron, W. E., and Smith, A. G., 1979. Permo-Triassic and Jurassic^{40}Ar-39Ar ages from Greek ophiolites and associated rocks. Nature, v. 279 (5716), p. 788–790. https://doi.org/10.1038/279788a0.

Royden, L., 1996, Coupling and decoupling of crust and mantle in convergent orogens: Implications for strain partitioning in the crust, Journal Geophysical. Research, v. 101(B8), p. 17679–17705, doi:10.1029/96JB00951.

Rubatto, D., Williams, I.S., and Buick, I.S., 2001. Zircon and monazite response to prograde metamorphism in the Reynolds Range, central Australia. Contributions to Mineralogy and Petrology, v. 140, p. 458–468.

Rubin, J.N., Henry, C.D., and Price, J.G., 1993. The mobility of zirconium and other "immobile" elements during hydrothermal alteration. Chemical Geology, v. 110, p. 29–47.

Ruff, I. J., Given, J. W., Sanders, C. O., and Sperber, C. M., 1989, Large earthquakes in Macquarie Ridge Complex: transitional tectonics and subduction initiation. Pure and Applied Geophysics, v. 128, p. 72–129.

Ruppel, C., Royden, L., and Hodges, K. V., 1988. Thermal modeling of extensional tectonics: Application to pressure-temperature-time histories of metamorphic rocks, Tectonics, v. 7, p. 947–957, doi:10.1029/TC007i005p00947.

Ryb, U., Lloyd, M. K., Stolper, D. A. and Eiler, J. M., 2017, The clumped-isotope geochemistry of exhumed marbles from Naxos, Greece, Earth and Planetary Science Letters, v. 470, p. 1–12, doi:10.1016/j.epsl.2017.04.026

Saccani, E., 2015. A new method of discriminating different types of post-Archean ophiolitic basalts and their tectonic significance using Th-Nb and Ce-Dy-Yb systematics. Geoscience Frontiers, v. 6 (4), p. 481–501.

Saccani, E., Bortolotti, V., Marroni, M., Pandolfi, L., Photiades, A., and Principi, G., 2008. The Jurassic ass ociation of back arc basin ophiolites and calc-alkaline v. canics in the Guevgueli complex (northern Greece): Implication for the evolution

of the Vardar zone. Ofioliti, v. 33 (2), p. 209–227.

Saccani, E., and Photiades, A., 2004, Mid-ocean ridge and supra-subduction affinities in the Pindos ophiolites (Greece): Implications for magmagenesis in a forearc setting. Lithos, v. 73 (3–4), p. 229–253. https://doi.org/10.1016/j.lithos.2003.12.002

Sandiford, M. and Powell, R., 1986, Deep crustal metamorphism during continental extension: modern and ancient examples. Earth and Planetary Science Letters, v. 79, p.151–158.

Šarić, K., Cvetković, V., Romer, R. L., ChristOfides, G., and Koroneos, A., 2009. Granitoids associated with East Vardar ophiolites (Serbia, F.Y.R. of Macedonia and northern Greece): Origin, evolution and geodynamic significance inferred from major and trace element data and Sr-Nd-Pb isotopes. Lithos, v. 108 (1-4), p. 131–150. https://doi.org/10.1016/j.lithos.2008.06.001

Sarıfakıoğlu, E., Dilek, Y., Uysal, I., 2012. The Petrogenesis and Geodynamic Significance of Bahçe (Osmaniye) Ophıolite. 5th Geochemistry Symposium, p. 112–113.

Saunders, A. D. 1984. The rare earth element characteristics of igneous rocks from the ocean basins. In Henderson, P., ed. Rare earth element geochemistry. Amsterdam, Elsevier, p. 205–236.

Sawyer, E. W., 1996, Melt segregation and magma flow in migmatites: Implications for the generation of granite magmas, Special Paper Geological Society of America, v. 315, p. 85–94, doi:10.1130/0-8137-2315-9.85.

Sawyer, E. W., 2001, Melt segregation in the continental crust: Distribution and movement of melt in anatectic rocks, Journal of Metamorphic Geology, v. 19, p. 291–309, doi:10.1046/j.0263-4929.2000.00312.x.

Scharer U, 1984.The effect of initial^{230}Th disequilibrium on young U–Pb ages: The Makalu case, Himalaya. Earth and Planetary Science Letters, v. 67, p. 191–204.

Scherer, E. E., Cameron, K. L., Blichert-Toft, J., 2000. Lu–hf garnet geochronology: closure temperature relative to the Sm–Nd system and the effects of trace mineral inclusions, Geochimica et Cosmochimica Acta, v. 64, p. 3413–3432, doi: /doi.org/10.1016/S0016-7037(00)00440-3. Scherer, E., Münker, C., Mezger, K.,

2001. Calibration of the Lutetium–Hafnium clock, Science, v. 293, p. 683–686.

Schmidt, M. W., 1993, Phase relations and compositions in tonalite as a function of pressure; an experimental study at 650°C. American Journal of Science, v. 293, p. 1011–1060.

Schmid, S. M., Bernoulli, D., Fügenschuh, B., Matenco, L., Schefer, S., Schuster, R., et al., 2008. The Alpine-Carpathian-Dinaridic orogenic system: Correlation and evolution of tectonic units. Swiss Journal of Geosciences, v. 101, p. 139–183. https://doi.org/10.1007/s00015-008-1247-3.

Schmid, S. M., Scharf, A., Handy, M. R., Rosenberg, C. L., 2013, The Tauern Window (Eastern Alps. Austria): a new tectonic map, with cross-sections and a tectonometamorphic synthesis. Swiss Journal of Geosciences v. 106 p. 1–32

Schumacher, J. C., Brady, J. B., Cheney, J. T., and Tonnsen, R. R. 2008. Glaucophane-bearing marbles on Syros, Greece. Journal of Petrology, v. 49, p. 1667–1686.

Searle, M.P., 2010, Low-angle normal faults in the compressional Himalayan orogen; Evidence from the Annapurna–Dhaulagiri Himalaya, Nepal, Geosphere, v. 6, p. 296–315 doi: 10.1130/GES00549.1

Searle, M.P., Cottle, J.M., Streule, M.J., and Waters, D.J., 2010, Crustal melt granites and migmatites along the Himalaya: melt source, segregation, transport and granite emplacement mechanisms, Earth and Environmental Science Transactions of the Royal Society of Edinburgh. p. 219–233 doi: 10.1017/S175569100901617X

Searle, M. P., and Cox, J., 1999, Tectonic setting, origin, and obduction of the Oman ophiolite, Geological Society of America Bulletin, v. 111, p. 104–122.

Searle, M.P. and Cox, J., 2002, Subduction zone metamorphism during formation and emplacement of the Semail ophiolite in the Oman Mountains, Geological Magazine. p. 241–255 doi: 10.1017/S0016756802006532

Searle, M.P., Law, R.D., and Jessup, M.J., 2006, Crustal structure, restoration and evolution of the Greater Himalaya in Nepal-South Tibet: implications for channel flow and ductile extrusion of the middle crust, Geology Society of London Special Publications, v. 268, p. 355-378

Searle, M.P. and Malpas, J., 1982. Petrochemistry and origin of sub-ophiolitic metamorphic and related rocks in the Oman Mountains. Journal of the Geological Society, v. 139, p. 235–248.

Searle, M. P., Warren, C. J., Waters, D. J., and Parrish, R. R., 2004. Structural evolution, metamorphism and restoration of the Arabian continental margin, Saih Hatat region, Oman Mountains. Journal of Structural Geology, v. 26, p. 451–473.

Searle, M.P., Waters, D.J., Martin, H.N. and Rex, D.C., 1994. Structure and metamorphism of blueschist–eclogite facies rocks from the northeastern Oman Mountains. Journal of the Geological Society, v. 151(3), p. 555–576.

Şengʹor, A.M.C., 1979, Mid-Mesozoic closure of Permo-Triassic Tethys and its implications. Nature, v. 279, p. 590–593

Şengʹor, A.M.C., 1984, The Cimmeride orogenic system and the tectonics of Eurasia, Geological Society of America Special Papers, v. 195, p. 74

Seward, D., Vanderhaeghe, O., Siebenaller, L., Thomson, S., Hibsch, C., Zingg, A., Holzner, P., Ring, U. and Duchêne, S., 2009, Cenozoic tectonic evolution of Naxos Island through a multi-faceted approach of fission track analysis, Geological Society Special Publication, v. 321, p. 179–196.

Shaw, B., and Jackson. J., 2010, Earthquake mechanisms and active tectonics of the Hellenic subduction zone, Geophysical Journal International, v. 181, p. 966–984.

Shervais, J. W., 1982, Ti-V plots and the petrogenesis of modern ophiolitic lavas: Earth and Planetary Science Letters, v. 59, p. 101–118.

Shimon, W., O'Connell, R. J., and England, P., 1989. A continuum model of continental deformation above subduction zones: Application to the Andes and the Aegean. Journal of Geophysical Research: Solid Earth v. 94, no. B8, p. 10331–10346.

Skora, S., Baumgartner, L. P., Mahlen, N. J., Johnson, C. M., Pilet, S., and Hellebrand, E., 2006. Diffusion-limited REE uptake by eclogite garnets and its consequences for Lu–Hf and Sm–Nd geochronology. Contributions to Mineralogy and Petrology, v. 152, p. 703–720.

Skourlis, K., and Doutsos, T., 2003. The Pindos Fold-and-thrust belt (Greece): Inversion kinematics of a passive continental margin. International Journal of Earth Sciences, v. 92, p. 891–903. doi:10.1007/s00531-003-0365-4.

Sláma, J., Kosler, J., Condon, D.J., Crowley, J.L., Gerdes, A., Hanchar, J.M., Horstwood, M.S.A., Morris, G.A., Nasdala, L., Norberg, N., Schaltegger, U., Schoene, B., Tubrett, M.N., Whitehouse, M.J., 2008. Plesovice zircon: A new natural reference material for U-Pb and Hf isotopic microanalysis. Chemical Geology v. 249, p. 1–35.

Smith, A. G., Spray, 1984, A half-ridge transform model for the Hellenic-Dinaric ophiolites in Dixon, E., and Robertson, A.H.F. (Eds.), The Geological Evolution of the Eastern Mediterranean, Geol. Soc. London, Spec. Publ., v. 17, p. 629–644.

Smith, D. K., Cann, J. R., and Escartín, J. 2006. Widespread active detachment faulting and core complex formation near 13 N on the Mid-Atlantic Ridge. Nature, v. 442(7101), p. 440.

Smye, A.J., Bickle, M.J., Holland, T.J.B., Parrish, R.R. and Condon, D.J., 2011. Rapid formation and exhumation of the youngest Alpine eclogites: A thermal conundrum to Barrovian metamorphism; Earth and Planetary Science Letters, v. 306, p. 193–204.

Smye. A. J, Roberts, N. M. W., D. J. Condon, M.S.A. Horstwood, R.R. Parrish, 2014. Characterising the U–Th–Pb systematics of allanite by ID and LA-ICPMS: Implications for geochronology. Geochimica et Cosmochimica Acta, v. 135, p. 1–28.

Soder. C, Altherr, R., and Romer, R. L., 2016, Mantle Metasomatism at the Edge of a Retreating Subduction Zone: Late Neogene Lamprophyres from the Island of Kos, Greece. Journal of Petrology, 57, p. 1705–1728. doi: 10.1093/petrology/egw054

Sostarić, B. S., Palinkaš, A. L., Neubauer, F., Cvetković, V., Bernroider, M., and Genser, J., 2014. The origin and age of the metamorphic sole from the Rogozna Mts., Western Vardar Belt: New evidence for the one-ocean model for the Balkan ophiolites. Lithos, v. 192–195, p. 39–55 https:// doi.org/10.1016/j.lithos

.2014.01.011

Soukis, K., and Stockli, D. F., 2013. Structural and thermochronometric evidence for multi-stage exhumation of southern Syros, Cycladic islands, Greece. Tectonophysics, v. 595, p. 148–164.

Spear, F. S., 1993, Metamorphic Phase Equilibria and Pressure–Temperature–Time Paths. Mineralogical Society of America, Monograph Series, Washington, DC.

Spear, F. S., Hickmott, D. D. and Selverstone, J., 1990, Metamorphic consequences of thrust emplacement, Fall Mountain, New Hampshire, Geological Society of America Bulletin v. 102, p. 1344–1360.

Spear, F. S, Pyle, J. M, 2010, Theoretical modeling of monazite growth in a low-Ca metapelite, Chemical Geology, v. 273, p. 111–119

Spear, F. S. and Selverstone, J., 1983. Quantitative P–T paths from zoned minerals: theory and tectonic applications. Contributions to Mineralogy and Petrology v. 83, p. 348–357.

Spear, F. S., Thomas, J. B., and Hallett, B. W., 2014. Overstepping the garnet isograd: A comparison of QuiG barometry and thermodynamic modeling. Contributions to Mineralogy and Petrology, v. 168(3), p. 1059.

Spencer, C. J, Cawood, P. A, Hawkesworth, C. J., Prave, A. J., Roberts, N. M. W., Horstwood, M. S. A., Whitehouse, M. J., 2015, Generation and preservation of continental crust in the Grenville Orogeny, Geoscience Frontiers, v. 6, p. 357–372.

Spray, J. G., Bébien, J., Rex, D. C., and Roddick, J. C., 1984. Age constraints on the igneous and metamorphic evolution of the Hellenic-Dinaric ophiolites. Geological Society London, Special Publications, v. 17, p. 619–627. https://doi.org/10.1144/GSL.SP.1984.017.01.48

Spray, J. G., and Roddick, J. C., 1980. Petrology and $^{40}Ar/^{39}Ar$ geochronology of some Hellenic sub-ophiolite metamorphic rocks. Contributions to Mineralogy and Petrology, v. 72(1), p. 43–55. https://doi.org/10.1 007/BF00375567

Spulber, S.D. and Rutherford, M.J., 1983. The origin of rhyolite and plagiogranite in oceanic crust: an experimental study. Journal of Petrology, v. 24(1), p. 1–25.

Stacey J. S. and Kramers J. D., 1975, Approximation of terrestrial lead isotope evolution by a two-stage model. Earth and Planetary Science. Letters v. 26, p. 207–221.

Stepanov, A.S., Hermann, J., Rubatto, D. and Rapp, R.P. 2012, Experimental study of monazite/melt partitioning with implications for the Ree, Th and U geochemistry of crustal rocks. Chemical Geology, v. 300, p. 200–220.

Stern, R. J., 2004, Subduction initiation: spontaneous and induced, Earth and Planetary Science Letters, v. 226, p. 275–292.

Stern, R.J. and Bloomer, S.H., 1992, Subduction zone infancy: examples from the Eocene Izu-Bonin-Mariana and Jurassic California arcs. Geological Society of America Bulletin, v. 104, p. 1621–1636.

Stern, R. J. and Geyra, T., In Press, Subduction initiation, past and present a review. Tectonophysics.

Stern, R.J., Reagan, M., Ishizuka, O., Ohara, Y. and Whattam, S., 2012. To understand subduction initiation, study forearc crust: To understand forearc crust, study ophiolites. Lithosphere, v. 4, p. 469–483.

Stipp, M. and Kunze, K., 2008, Dynamic recrystallization near the brittle–plastic transition in naturally and experimentally deformed quartz aggregates. Tectonophysics, v. 448, p.77–97.

Stipp, M., StuÈnitz, H., Heilbronner, R. and Schmid, S.M., 2002b, The eastern Tonale fault zone: a 'natural laboratory' for crystal plastic deformation of quartz over a temperature range from 250 to 700 °C. Journal of Structural Geology, v. 24, p.1861–1884.

Stipp, M., Stünitz, H., Heilbronner, R. and Schmid, S.M., 2002a. Dynamic recrystallization of quartz: correlation between natural and experimental conditions. Geological Society, London, Special Publications, v. 200 (1), p.171–190.

St-Onge, M. R., 1984, The muscovite-melt bathograd and low-P isograd suites in north-central Wopmay Orogen, Northwest Territories, Canada. Journal of Metamorphic Geology, v. 2, p. 315–326. doi:10.1111/j.1525-1314.1984.tb00592.x

St-Onge, M.R., 1987, Zoned poikiloblastic garnets: PT paths and syn-metamorphic uplift through 30 km of structural depth, Wopmay Orogen, Canada. Journal of Petrology, v. 28, p. 1–21.

St-Onge, M. R., Rayner, N., Palin, R. M., Searle, M. P. and Waters, D. J., 2013, Integrated pressure–temperature–time constraints for the Tso Morari dome (Northwest India): implications for the burial and exhumation path of UHP units in the western Himalaya. J. Meta. Geol., v. 3, p. 469–504. doi:10.1111/jmg.12030

Stouraiti, C., Mitropoulos, P., Tarney, J., Barreiro, B., McGrath, A. M., and Baltatzis, E. (2010). Geochemistry and petrogenesis of late Miocene granitoids, Cyclades, southern Aegean: Nature of Sourcesource components. Lithos, v. 114, p. 337–352. doi: https://doi.org/10.1016/j. Lithoslithos.2009.1009.1010

Stouraiti, C., Pantziris, I., Vasilatos, C., Kanellopoulos, C., P Mitropoulos, P., Pomonis, P., Moritz, R., and Chiaradia, M., 2017. Ophiolitic Remnants from the Upper and Intermediate Structural Unit of the Attic-Cycladic Crystalline Belt (Aegean, Greece): Fingerprinting Geochemical Affinities of Magmatic Precursors, Geosciences, v. 7, p. 14; doi:10.3390/geosciences7010014

Sun, S. S. and McDonough, W. F. 1989. Chemical and isotopic systematics of oceanic basalts: implications for mantle composition and process. In: Saunders, A. D. and Norry, J. M. (eds) Magmatism in the Ocean Basins. Geological Society, London, Special Publications, v. 42, p. 313 –345.

Syracuse, E. M., Keken, P. E. V., and Abers, G. A., 2010. The global range of subduction zone thermal models. Physics of the Earth and Planetary Interiors, v. 183, p. 73–90.

Taymaz, T., Jackson, J., and McKenzie, D., 1991, Active tectonics of the north and central Aegean Sea, Geophys. J. Int., v. 106 (2), p. 433–490

Teyssier, C., and Whitney D.L., 2002, Gneiss domes and orogeny, Geology, v. 30, p. 1139–1142, doi:10.1130/0091-76132002030¡1139: GDAO¿2.0.CO;2.

Thirlwall, M.F. and Anczkiewicz, R., 2004. Multidynamic isotope ratio analysis using MC–ICP–MS and the causes of secular drift in Hf, Nd and Pb isotope ratios.

International Journal of Mass Spectrometry, v. 235, p. 59–81.

Thuizat, R., Whitechurch, H., Montigny, R., Juteau, T., 1981. K-Ar dating of some infra-ophiolitic metamorphic soles from the Eastern Mediterranean: New evidence for oceanic thrustings before obduction. Earth and Planetary Science Letters, v. 52 (2), p. 302–310, ISSN 0012-821X, https://doi.org/10.1016/0012-821X(81)90185-0.

Tippett, C.R. 1980, A geological cross-section through the southern margin of the Foxe Fold Belt, Baffin Island, Arctic Canada, and its relevance to the tectonic evolution of the northeastern Churchill Province; Ph.D. thesis, Queen's University, Kingston, Ontario, Canada

Tomaschek, F., Kennedy, A. K., Villa, I. M., Lagos, M., Ballhaus, C., 2003, Zircons from Syros, Cyclades, Greece—Recrystallization and Mobilization of Zircon During High-Pressure Metamorphism. Journal of Petrology, v. 44 p. 1977–2002. doi: 10.1093/petrology/egg067

Tomkins H. and Pattison D., 2007, Accessory phase petrogenesis in relation to major phase assemblages in pelites from the Nelson contact aureole, southern British Columbia. Journal of Metamorphic Geology, 25, 401–421.

Topuz, G., Göçmengil, G., Rolland, Y., Çelik, Ö. F., Zack, T., and Schmitt, A. K., 2012. Jurassic accretionary and ophiolite from northeast Turkey: No evidence for the Cimmerian continental ribbon. Geology, v. 41, p. 255–258. doi:10.1130/G33577.1

Tracy, R. J., Robinson, P. and Thompson, A. B., 1976, Garnet composition and zoning in the determination of temperature and pressure of metamorphism, central Massachusetts. American, Mineralogist, v. 6, p. 762–775.

Tremblay, A., Meshi, A., and Bédard, J. H., 2009. Oceanic core complexes and ancient oceanic lithosphere: Insights from Iapetan and Tethyanophiolites (Canada and Albania). Tectonophysics, v. 473 (1–2), p. 36–52. https:// doi.org/10. 1016/j.tecto.2008.08.

Tremblay, A., Meshi, A., Deschamps, T., Goulet, F. and Goulet, N., 2015, The Vardar

zone as a suture for the Mirdita ophiolites, Albania: Constraints from the structural analysis of the Korabi-Pelagonia zone. Tectonics, v. 34, p. 352–375. doi: 10. 1002 /2014 TC003807

Trotet, F., Jolivet, L., and Vidal, O., 2001. Tectono-metamorphic evolution of Syros and Sifnos islands (Cyclades, Greece). Tectono-physics, v. 338, p. 179–206.

Trotet, F., Vidal, O., and Jolivet, L., 2001. Exhumation of Syros and Sifnos metamorphic rocks (Cyclades, Greece). New constraints on the PT paths. European Journal of Mineralogy, v. 13, p. 901–902.

Tucholke, B. E., Behn, M. D., Buck, W. R., and Lin, J. 2008. Role of melt supply in oceanic detachment faulting and formation of megamullions. Geology, v. 36(6), p. 455-458.

Turcotte, D. L., and Schubert, G., 1973. Frictional heating of descending lithosphere. Journal of Geophysical Research, v. 78, p. 5876–5886.

Tyler, I. M. and Ashworth, J. R., 1982, Sillimanite potash feldspar assemblages in graphitic pelites, Stronian area, Scotland, Contributions to Mineral Petrology, v. 81, p. 18–29.

Urai, J. L., Schuiling, R.D. and Jansen, J. B. H., 1990, Alpine deformation on Naxos (Greece), in Deformation Mechanisms, Rheology and Tectonics, edited by R. J. Knipe and E. H. Rutter, Geol. Soc. Spec. Publ., v. 54, p. 509–522.

Van Hinsbergen, D.J., Peters, K., Maffione, M., Spakman, W., Guilmette, C., Thieulot, C., Plümper, O., Gürer, D., Brouwer, F.M., Aldanmaz, E. and Kaymakcl, N., 2015. Dynamics of intraoceanic subduction initiation: 2. Suprasubduction zone ophiolite formation and metamorphic sole exhumation in context of absolute plate motions. Geochemistry, Geophysics, Geosystems, v. 16, p. 1771–1785.

Van Hinsbergen, D. J. J., Zachariasse, W. J. M., Wortel, J. R. and Meulenkamp, J. E., 2005, Underthrusting and exhumation: A comparison between the external Hellenides and the “hot” Cycladic and “cold” South Aegean core complexes (Greece), Tectonics, v. 24, TC2011, doi:10.1029/ 2004TC001692.

Van Westrenen, W. Blundy, J. and Wood, B., 2000. Effect of Fe^{2+} on garnet-melt

trace element partitioning: Experiments in FCMAS and quantification of crystal-chemical controls in natural systems. Lithos. v. 53. p. 189-201. doi: 10.1016/S0024-4937(00)00024-4.

Vanderhaeghe, O., 2004, Structural development of the Naxos migmatite dome, Special Paper, Geological Society of America, v. 380, p. 211–227.

Vanderhaeghe, O., and Teyssier, C., 2001, Partial melting and flow of orogens, Tectonophysics, v. 342, p. 451–472, doi:10.1016/S0040-1951(01)

Vavra, G., Gebauer, D., Schmid, R., and Compston, W., 1996. Multiple zircon growth and recrystallisation during polyphase Late carboniferous to triassic metamorphism in granulites of the Ivrea zone (Southern Alps): an ion microprobe (SHRIMP) study. Contributions to Mineral Petrology v. 122, p. 337–358.

Vervoot. J. D., 2014, Lu-Hf Dating: The Lu-Hf Isotope System, In book: Encyclopedia of Scientific Dating Methods doi: 10.1007/978-94-007-6326-5-46-1

Vine, F. J., Matthews, D. H., 1963. Magnetic Anomalies Over Oceanic Ridges. Nature, v. 199 (4897), p. 947–949. doi:10.1038/199947a0.

Virgo, S., von Hagke, C., and Urai, J. L., 2018, Multiphase boudinage: a case study of amphibolites in marble in the Naxos migmatite core, Solid Earth, v. 9, p. 91–113, https://doi.org/10.5194/se-9-91-2018, 2018.

Von-Blankenberg, F., 1992. Combined high-precision chronometry and geochemical tracing using accessory minerals: applied to the Central-Alpine Bergell intrusion (central Europe), Chemical geology, v. 100, p. 19–40.

Von Hagke, C., Bamberg, B., Virgo, S., Urai, J. L., In Press, Outcrop-scale tomography: insights into the 3D structure of multiphase boudins. Journal of Structural Geology.

Wada, I., K. Wang, J. He, and Hyndman, R. D., 2008. Weakening of the subduction interface and its effects on surface heat flow, slab dehydration, and mantle wedge serpentinization, Journal of Geophysical Research., v. 113, B04402, doi:10.1029/2007JB005190

Wakabayashi, J. and Dilek, Y., 2000. Spatial and temporal relationships between

ophiolites and their metamorphic soles: a test of models of forearc ophiolite genesis. Geological Society of America, Special Papers, p. 53–64.

Warren, C. J., Beaumont, C., and Jamieson, R. A., Modelling tectonic styles and ultra-high pressure (UHP) rock exhumation during the transition from oceanic subduction to continental collision, Earth and Planetary Science Letters, v. 267, p. 129–145

Warren, C.J., Hanke, F. and Kelley, S.P., 2012. When can muscovite^{40}Ar/^{39}Ar dating constrain the timing of metamorphic exhumation? Chemical Geology, v. 291, p. 79–86.

Warren, C. J., Parrish, R. R., Searle, M. P., and Waters, D. J., 2003. Dating the subduction of the Arabian continental margin beneath the Semail ophiolite, Oman. Geology, v. 31, no. 10, p. 889–892. doi: 10.1130/G19666.1

Warren, C.J., Parrish, R.R., Waters, D.J. and Searle, 2005. Dating the geologic history of Oman's Semail ophiolite: insights from U-Pb geochronology, Contrib Mineral Petrol v. 150, p. 403, doi:https://doi.org/10.1007/s00410-005-0028-5

Warren, R.G. and Stewart, A.J., 1988: Isobaric cooling of Proterozoic high-temperature metamorphites in the northern Arunta Block, Central Australia: implications for tectonic evolution. Precambrian Research, v. 40–41, 175-198.

Warren, C. J., and Waters, D. J. 2006. Oxidized eclogites and garnet-blueschists from Oman: P-T path modeling in the NCFMASHO system. Journal of Metamorphic Geology, v. 24, p. 783–802.

Waters, D.J., 1990, Thermal history and tectonic setting of the Namaqualand granulites, southern Africa: clues to Proterozoic crustal development. in: Granulites and Crustal Evolution, NATO-ASI series C-311, Vielzeuf, D., Vidal, P., Eds., Amsterdam, Kluwer, p. 243–256.

Waters, D.J. and Lovegrove, D.P., 2002. Assessing the extent of disequilibrium and overstepping of prograde metamorphic reactions in metapelites from the Bushveld Complex aureole, South Africa. Journal of Metamorphic Geology, v. 20(1), p. 135–149.

Waters, D. J., and Martin, H. N., 1996. The garnet-Cpx-phengite barometer. Recommended Calibration and Calculation Method, 1.

Watson, E.B. and Harrison, T.M. 1983. Zircon saturation revisited: Temperature and composition effects in a variety of crustal magma types. Earth and Planetary Science Letters, v. 64, p. 295–304.

Weidmann, M., Solounias, N., Drake, R. H., Curtis, G. H., 1984. Neogene stratigraphy of the eastern basin, Samos island, Greece, Geobios, v. 17 1984, p. 477–490

Weinberg. R, and Hasalová, P., 2015, Water-fluxed melting of the continental crust: A review, Lithos, v. 212–215 p. 158–188.

Weller, O. M., St-Onge, M. R., Waters, D. J., Rayner, N., Searle, M. P., Chung, S.-L., Palin, R. M., Lee, Y.-H. and Xu, X., 2013, Quantifying Barrovian metamorphism in the Danba Structural Culmination of eastern Tibet. Journal of Metamorphic Geology., v. 31, p. 909–935. doi:10.1111/jmg.12050

Weller, O. M., Wallis, S. R., Aoya, M. and Nagaya, T., 2015. Phase equilibria modelling of blueschist and eclogite from the Sanbagawa metamorphic belt of southwest Japan reveals along-strike consistency in tectonothermal architecture. J. Metamorph. Geol., v. 33, p. 579–596. doi:10.1111/jmg.12134

Wells, P.R.A., 1980, Thermal models for the magmatic accretion and subsequent metamorphism of continental crust. Earth and Planetary Science Letters, v. 46, p. 253–265.

Wetherill, G. W., 1956b. Discordant uranium-lead ages, I. Transcripts of American Geophysical Union, v. 37, p. 320–327.

Whipp, D. M., Beaumont, C., and J. Braun, 2014, Feeding the “aneurysm”: Orogen-parallel mass transport into Nanga Parbat and the western Himalayan syntaxis, Journal of Geophysical Research Solid Earth, v. 119, p. 5077–5096, doi:10.1002/2013JB010929.

White, R. W., Pomroy, N. E. and Powell, R., 2005. An in-situ metatexite–diatexite transition in upper amphibolite-facies rocks from Broken Hill, Australia, Journal of Metamorphic Geology, v. 23, p. 579–602.

White, R. W. and Powell, R., 2002, Melt loss and the preservation of granulite-facies mineral assemblages. Journal of Metamorphic Geology, v. 20, p. 621–632.

White, R. W., Powell, R. and Baldwin, J. A., 2008, Calculated phase equilibria involving chemical potentials to investigate the textural evolution of metamorphic rocks. Journal of Metamorphic Geology, v. 26, p. 181–198.

White, R. W., Powell, R. and Clarke, G. L., 2002, The interpretation of reaction textures in Fe-rich metapelitic granulites of the Musgrave Block, central Australia: constraints from mineral equilibria calculations in the system K2O–FeO–MgO–Al2O3–SiO2 –H2O–TiO2–Fe2O3. Journal of Metamorphic Geology, v. 20, p. 41–55.

White, R. W., Powell, R. and Halpin, J. A., 2004, Spatially focused melt formation in aluminous metapelites from Broken Hill, Australia. Journal of Metamorphic Geology, v. 22, p. 825–845.

White, R. W., Powell, R. and Holland, T. J. B., 2007, Progress relating to calculation of partial melting equilibria for metapelites. Journal of Metamorphic Geology, v. 25, p. 511–527.

White, R.W., Powell, R., Holland, T.J.B., Johnson, T., Green, E.C.R., 2014a. New mineral activity-composition relations for thermodynamic calculations in metapelitic systems. Journal of Metamorphic Geology v. 32, 261e286.

White, R.W., Powell, R., Johnson, T., 2014b. The effect of Mn on mineral stability in metapelites revisited: new a-x relations for manganese-bearing minerals. Journal of Metamorphic Geology, v. 32, 809e828.

Whitney, D. L. and Evans, B. W., 2010, Abbreviations for names of rock-forming minerals. American Mineralogist, v. 95, p. 185–187.

Whitney, D. L., and Irving, A. J., 1994, Origin of K-poor leucosomes in a metasedimentary migmatite complex by ultrametamorphism, syn-metamorphic magmatism and subsolidus processes, Lithos, v. 32, p. 173–192

Whitney, D. L, Teyssier, C., and Vanderhaeghe, O., 2004, Gneiss domes and crustal flow, Geological Society of America Special Papers, v. 380, p. 15–33

Wiedenbeck, M., Allé, P., Corfu, F., Griffin, W.L., Meier, M., Oberli, F., Quadt, A.V.O.N., Roddick, J.C., Spiegel, W., 1995. Three natural zircon standards for U-Th-Pb, Lu-Hf, trace element and REE analysis. Geostandards and Geoanalytical Research v. 19, p. 1– 23.

Wijbrans. J. R, van Wees. J. D, Stephenson. R. A., and Cloetingh. S.A.P.L., 1993, Pressure–temperature–time evolution of the high-pressure, metamorphic complex of Sifnos, Greece, Geology, v. 21, p. 443–446

Williams, N. Tetley, W. Compston, I. McDougall, 1982. A comparison of K–Ar and Rb–Sr ages of rapidly cooled igneous rocks: two points in the Palaeozoic time scale re-evaluated Journal of Geology Society, v. 139, p. 557–568

Williams, I.S., Buick, I.S., and Cartwright, I., 1996. An extended episode of early Mesoproterozoic metamorphic fluid flow in the Reynolds Range, central Australia. Journal of Metamorphic Geology, v.14, p. 29–47.

Wilson, J. T., 1965. A New Class of Faults and their Bearing on Continental Drift, Nature, v. 207, (4995), p. 343–347. doi:10.1038/207343a0

Wing B. A., Ferry J. M. and Harrison T. M., 2003, Prograde destruction and formation of monazite and allanite during contact and regional metamorphism of pelites: petrology and geochronology, Contributions to Mineral Petrology, v. 145, p. 228–250.

Wood, D. A., Joron, J. L., and Treuil, M. 1979. A reappraisal of the use of trace elements to classify and discriminate between magma series erupted in different tectonic settings. Earth and Planetary Science Letters, v. 45, p. 326–336.

Woodhead, J. Eggins, S., and Gamble, J., 1993. High field strength and transition element systematics in island arc and back-arc basin basalts: Evidence for multi-phase melt extraction and a depleted mantle wedge. Earth and Planetary Science Letters. v. 114, p. 491–504. doi:10.1016/0012-821X(93)90078-N.

Woodsworth, G. J., 1977, Homogenization of zoned garnets from pelitic schists, Canadian Mineralogist, v. 15, p. 230–242.

Wortel M. J. R. and Spakman, W., 2000. Subduction and slab detachment in the

Mediterranean-Carpathian region, Science, v. 290, p. 1910–1917.

Yakymchuk, C. J. A., and Brown, M., 2014, Behaviour of zircon and monazite during crustal melting, Journal of the Geological Society, London, v. 171, p. 465–479.

Yang, P. and Pattison, D., 2006. Genesis of monazite and Y zoning in garnet from the Black Hills, South Dakota. Lithos, v. 88, p. 233–253.

Yeats, C.J., McNaughton, N.J., and Groves, D.I., 1996. SHRIMP U–Pb geochronological constraints on Archean v. canichosted massive sulfide and lode gold mineralization at Mount Gibson, Yilgarn Craton, Western Australia. Economic Geology, v. 91, p. 1354–1371.

Yin, A. 1991. Mechanisms for the formation of domal and basinal detachment faults: a three-dimensional analysis, Journal of Geophysical Research, v. 96, p. 14,577–14,594.

Zhang, R. Y., Zhai, S. M., Fei, Y. W. and Liou, J. G., 2003. Titanium solubility in coexisting garnet and clinopyroxene at very high pressure: the significance of exsolved rutile in garnet. Earth and Planetary Science Letters, v. 216, p. 591-601.

Zeffren, S., Avigad, D., Heimann, A., and Gvirtzman, Z., 2005, Age resetting of hanging wall rocks above a low-angle detachment fault: Tinos Island (Aegean Sea), Tectonophysics, v. 400, p. 1–25.

Appendices

Appendix 1: Metamorphic petrology, thermodynamics and electron microprobe analysis

1.1 Metamorphic Petrology

The term "metamorphic" originates from Charles Lyell's 19th Century visit to Norway where he described Paleozoic sediments that had been "changed by heat" due to the intrusion of Permian granite-syenite intrusions (Lyell, 1833, 1838). Since then, metamorphism has become regarded as the process by which a rock responds to changes in physical and or chemical conditions. During mountain building, rocks are buried and experiences changes in pressure (P), temperature (T) and composition (X) which induce physiochemical reactions between solid and fluid phases which form new mineral assemblages and/or microstructures. Therefore, minerals and microstructures observed in rocks collected from the Earth's surface today record the rock's P–T–X and strain history. The main aim of metamorphic petrology is therefore to quantify the relative or absolute changes in P–T–X and strain over time and therefore gain insight into the tectonic processes responsible.

Metamorphism acts to minimize a rock's internal free energy. This can be achieved through several mechanisms such as growth of new minerals via chemical reactions or recrystallization of minerals into a new fabric following a change in strain conditions. Eventually a rock attempts to reach a state of chemical and textural equi-

librium with a characteristic mineral assemblage with certain proportions and compositions of the constituent phases that are unique to that P–T–X conditions. Equilibrium thermodynamics can be used to predict the stable mineral assemblage (with the lowest total free energy) in a rock under chemical equilibrium at a given P–T–X condition. Utilizing petrological techniques on metamorphic rocks thus represents a reverse modelling problem, whereby the P–T–X conditions are the desired result from which the stable mineral assemblage is found.

Although metamorphic rocks attempt to reach a state of minimum free energy, in the real world a state of true chemical equilibrium may never be fully achieved, and rocks may preserve their previous stable mineral assemblages at an earlier P–T–X condition, in a state of disequilibrium. This situation is often preferable as a rock's earlier history can be unravelled and numerous points along a P–T path can be determined by such features. In fact, a rock representing true chemical equilibrium is of limited use to a geologist for making any tectonic interpretation as although peak metamorphic P–T–X conditions may be readily obtained, no information about how the rock got to those conditions is revealed. In order to calculate P–T conditions, a thorough understanding of the underlying thermodynamic principles is required with the following discussion after Spear, (1993).

1.2 Thermodynamics

In a multiphase system, the thermodynamic potential to do work governs the thermodynamic state of the system. Considering the state variables P, T and number of moles (n_i) of components, the thermodynamic potential becomes the Gibbs free energy (G). For a rock of a given bulk composition, several different phase assemblages could theoretically exist at any given$_{P–T}$ condition and each assemblage would have a different Gibbs free energy (G_{syst}). The assemblage that has the lowest Gibbs free energy would be the stable assemblage at a given P-T condition and would occur in a state of heterogeneous equilibrium, whereas all other assemblages with higher values

of G_{syst} will be metastable. If G_{syst} is not minimized then the phases in the system will undergo heterogeneous reaction to reduce the thermodynamic potentional. As a rock moves through *P–T–X* space during metamorphism, it will thus experience a series of continuous and discontinuous reactions to approach equilibrium at those given *P–T–X* conditions.

When a rock is composed of three phases (X, Y and Z) at heterogeneous equilibrium all phases will be experiencing the same pressure and temperature and the free energy of the system will be minimised as Gsyst has no potential to change, hence:

$$dG_{syst} = 0 \tag{1}$$

Because G_{syst} is the total sum of all free energies within the system, therefore:

$$dG_{syst} = 0 = dGX + dGY + dGZ \tag{2}$$

Upon changing ambient *P–T* conditions, the rock is momentarily no longer in heterogeneous equilibrium, therefore chemical reactions between the constuent ph ases act to drive the system to a new equilibrium condition, at which point the free energy for further reaction (dG_R) = 0. In a closed system, total mass and therefore chemical potentials (μ) of the phase components is conserved during the total course of the reaction such that the sum of the chemical potentials of products is equal to the sum of the chemical potentials of the reactants.

$$\sum_{j=1}^{m} v_j.\mu_j = \Delta G_R \tag{3}$$

Where v_j represents the stoichiometric coefficient for each phase component (j) in a reaction where there are m phase components. If a phase has solid solution between multiple end members (i.e. is impure), the chemical potential of each phase component

is reduced from its pure state due to the entropy of mixing:

$$\mu_j = \mu_j^o + RT\ \ln(a_j) \tag{4}$$

Where μ_j^o is the chemical potential of phase component j at standard state conditions (pure j at the defined P–T conditions), R is the gas constant (8.314 $JK^{-1}mol^{-1}$), T is the temperature in Kelvin and aj is the activity of a component in a given phase.

Combing equations 3 and 4 gives:

$$\Delta G_R = 0 = \Delta Go + RT\ln(K_{eq}) \tag{5}$$

Where K_{eq} is the equilibrium constant that relates the activities of the reactants and products. The full relationship between pressure, temperature and phase composition at equilibrium can be defined as follows (Spear, 1993):

$$\begin{aligned}\Delta G_R = 0 = &\Delta H_{298K,1\text{bar}} + \int_{298}^{T} CpdT + \int_{1}^{P} \Delta V dP \\ &- T\Big(\Delta S_{298K,1\text{bar}} + \int_{298}^{T} \frac{\Delta Cp}{T} dT\Big) + RT\ln(K_{eq})\end{aligned} \tag{6}$$

Where H, S, V and Cp are the enthalpy, entropy, volume and heat capacity respectively and these thermodynamic properties are give at standard state conditions of 298 K and 1 bar. When there are no volatiles involved, such as at subsolidus conditions, this relationship can be simplified. Despite Cp being a function of temperature, the ΔCp of the reaction can often be neglectcted. If all phases have a similar compressibility, then ΔV can be assumed constant leading to the expression:

$$\Delta G_R = 0 = \Delta H + P\Delta V - T\Delta S + RT\ln(K_{eq}) \tag{7}$$

Which can be arranged to give ln K_{eq} as follows:

$$lnK_{eq} = T\Delta S - \Delta H - P\Delta V RT \tag{8}$$

And can be expressed as a thermometer:

$$T = P\Delta V + \Delta H \Delta S - R\ln(K_{eq}) \tag{9}$$

Or a barometer:

$$P = T\Delta S - RTlnK_{eq} - \Delta H \Delta V \tag{10}$$

At equilibrium, the values of ΔH, ΔS and ΔV can be calculated from experimentally determined values for specific phases and the ln Keq may be calculated from the measured or assumed compositions of reactants and products. Therefore, a univariant reaction line representing a particular equilibrium can be located in P–T space with a slope defined by the Clausius-Clapeyron equation when considering pure phases as:

$$\frac{dP}{dT} = \frac{\Delta S}{\Delta V} \tag{11}$$

Or with phases with solid solutions as:

$$\frac{dP}{dT} = \Delta S - R\ln(K_{eq})\Delta V \tag{12}$$

Because thermodynamic data for most common mineral end members widely accessible, the equilibrium constant K_{eq} can be determined. The equilibrium constant is defined as the multiplicative product of the concentrations of products (raised to the first power of their coeffcients) divided by the multiplicative power of the reactants (raised to the power of their coefficient):

$$aA + bB \rightarrow cC + dD \tag{13}$$

Where the equilibrium constant is defined as:

$$K_{eq} = \frac{(a_C)^c (a_d)^d}{(a_a)^a (a_a)^a} \tag{14}$$

The compositions of minerals in solid solutions are reported in mole proportions of end members. This is not the same as activity unless mixing is ideal. For example

almuniosilcate garnet ($X_3Al_2Si_3O_{12}$) is a solid solution between 4 major end members, where X represents a divalent cation: (Fe) almandine, (Mg) pyrope, (Ca) grossular and (Mn) spessartine. Because this is not ideal mixing, end member activities of garnet are determined by an ionic model describing the mixing of cations over the crystallographic sites. For ideal mixing of n cations on a single site the activity of each component is calculated by:

$$a_i = (X_j)^n \tag{15}$$

Where the activity of component I is the mole fraction of cation j raised to the number of sites over the mixing occurs over. For aluminosilicate garnet, if it was assumed the divalent cations mix ideally over a single site the activity of pyrope garnet for explale is given by:

$$a_{py} = (X_{py})^3 = \left(\frac{Mg}{Fe + Mg + Ca + Mn}\right)^3 \tag{16}$$

End member activities become complex where cation mixing takes place over several sites, where mixing is non-ideal or involves coupled substitutions (e.g. Tschermak's exchange)

1.2.1 Thermobarometry

The P–T conditions of equilibration maybe calculated from the observed mineral assemblages assuming they represent a frozen in equilibrium. However, the time available for equilibrium to be reached at a particular P–T condition and the scale at which equilibrium forms are the two most important factors to decipher whether equilibrium is achieved (Powell, 1978). These two factors are inter-related as the longer a rock remains at a given P–T condition, the larger the volume of rock that should reach equilibrium. For small volumes of rock, only geologically short amounts of time are required to reach equilibrium, even if the system as a whole is out of equilibrium. This is termed local or mosaic equilibrium. When this occurs, careful petrographic analysis must be used to determine the state of the assemblage under investigation. The two main methods used in this thesis to determine the changing P–T–X conditions of rocks in question are:

conventional thermobarometry and phase equilibria modelling. Deciphering which to choose depends on many factors, most importantly the extent of equilibrium observed for the sample under investigation.

1.2.1.1 Conventional thermobarometry

Although phase equilibrium phase diagrams has been shown to be the most powerful tool in harnessing P–T–X information from metamorphic rocks, it cannot be applied in all situations such as large scale mosaic equilibrium or investigating rocks where the bulk composition has changed considerably throughout its history. In these circumstances conventional thermobarometry is the preferred method to extract P–T conditions of equilibration for a given mineral assemblage, by analysing the distribution of elements between various phases.

Good geothermometers have steep P–T slopes and a relatively large ΔS and small ΔV and are usually cation exchange reactions e.g. Grt-Cpx Mg-Fe exchange reaction. In contrast good geobarometers have shallow slopes in P–T space, a relatively large ΔV and small ΔS and are typically net transfer reactions. Thermobarometry involves utilizing equation 8. Parameters occurring on the righ hand side of the equation can be used to produce a linear relationship between P and T. The equilibrium constant on the left-hand side of the equation gives a compositional constraint that determines the position of this relationship in P–T space. Using a single reaction gives an equilibrium along a calculated line, however simultaneous application of multiple reactions (thermometers and barometers) yields a P–T point where these intersect, this methodology is utilized with THERMOCALC v. 340i using mode 2 average P–T in DS62(Powell and Holland, 1988; Holand and Powell, 2011). This is advantageous as greater confidence can be placed in the result of multiple independent reactions than single P or T conditions using individual thermometers or barometers. Average P–T (Av-PT) function, provides detailed statistical information on the confidence level and reliability of the calculated result, allowing exclusion of data that are suspected to be of poor quality (i.e. a phase not in chemical equilibrium with the rest of the assem-

blage). In this thesis, when the fit parameter exceeded the maximum allowance for 95% confidence, the end member with the most suspicious input activity (largest e*) was removed from the calculation and the calculation re-run until all the indices where satisfied (the chi^2 test; Powell and Holland, 1994). Furthermore, Av-PT allows calculations with varying fluid composition and content (XH_2O-XCO_2) or activity which is particularly useful when the rock contains carbonate or graphite, or in fluid absent conditions.

1.2.1.2 Equilibrium phase diagram modelling

This method utilizes the observed mineral compositions and proportions in rocks to calculated equilibrium assemblages from a self consistent thermodynamic dataset 62 using THERMOCALC v.3.40i (Powell and Holland, 1988; Holland and Powell, 2011). THERMOCALC constructs phase diagrams (pseudosections) by solving sets of non-linear equations that relate to an assemblage that undergoes balanced chemical reactions between end-members of phases that are in equilibrium (assuming they satisfy equation 3). Each phase in the system has a solid solution and contains e_n end-members, therefore making e_{n-1} compositional variables. Thus, for P phases in an equilibrium assemblage, the number of end-members of phases (S) and compositional variables can be calculated by:

$$\sum_{n=1}^{P} e_n = S \tag{17}$$

And:

$$\sum_{n=1}^{P} (e_n - 1) = S - P \tag{18}$$

Therefore the number of independent reactions between phases is independent and is equal to the number of components subtracted from the number of end members (S - C). This is also equal to the number of unknowns that can be solved for (Powell and Holland, 2011) There are a total of S – P + 2 variables at equilibrium. This is equal to the number of compositional variables (equation 12) plus pressure and temperature. Hence the total number of degrees of freedom (F) is equal to the number of variables

(S – P + 2) minus the number of solveable unknowns (S – C), and is given by the Gibbs phase rule:

$$F = C - P + 2 \tag{19}$$

For a given chemical system, the various equilibria between those phases maybe graphically presented in several ways. A total phase diagram contains all the phase equilibria within a specific system and defines all possible stable assemblages at all P–T–X conditions. However, for graphical presentation, a 2-dimensional slice is taken through this 3-dimensional system and projected onto an appropriate plane, such as projection of all compositional variables onto P–T space to produce a 'P–T projection' or 'petrogenetic grid'. If a total phase diagram is sectioned with respect to an extensive variable (S, V, n_i) compositions ofphases in the system do not lie on a sigle sectioned plane and the phase diagram is referred to as a pseudosection. If a total phase diagram is sectioned with respect to an intensive variable (textitP, T or ui) the calculated assemblage will lie on the plane of section because the value of any intensive variable is equal in all places.

Pseudosections are extremely useful, especially when the sectioning variable specifies the systems composition (X) and the two remaining variables are P and T. Because pseudosection construction involves solving sets of non-linear equations for equilibrium relations that require simultaneous equations for mass-balance constraints. It requires phase proportions and compositions to sum to the total bulk rock composition. Therefore, the equilibrium state of the system can be defined by two intensive variables (P and T) which is also known as Dunhems Theorem.

In this thesis, model chemical systems for a given area of rocks (bulk compositions) were determined by either point counting to determine volume estimates of phases in equilibrium which was then integrated to calculate the effective bulk composition using average mineral compositions derived from electron microprobe analysis or X-ray fluorescence of representative rock volumes are shown in Table 1.

The effective bulk composition used for modeling was initially calculated following the method of Carson et al., (1999). Bulk rock compositions were calculated by

Calculated Bulk Rock Molar Compositions	SiO2	TiO2	Al2O3	FeO	MnO	MgO	CaO	Na2O	K2O	O	H2O
TLN54											
From mineral data	48.903	3.383	10.599	6.410	-	5.214	0.884	3.689	2.177	0.107	18.633
TL67											
From mineral data	62.359	2.177	12.639	7.589	0.345	3.586	2.135	1.605	2.887	0.369	4.652
6.5% H2O	60.930	2.127	12.349	7.415	0.337	3.504	2.086	1.568	2.821	0.361	6.500
TL66											
From mineral data	62.625	0.751	14.894	4.273	0.174	3.468	1.750	1.655	3.216	0.459	6.908
7.6% H2O	62.043	0.744	14.756	4.234	0.173	3.436	1.734	1.640	3.186	0.454	7.600
TL59											
From mineral data	66.589	0.571	11.469	5.727	0.162	2.166	1.920	1.912	3.041	0.537	6.069
6.5% H2O	66.169	0.567	11.396	5.691	0.161	2.153	1.908	1.900	3.021	0.533	6.500
TL15											
From mineral data	64.301	0.619	11.498	6.296	0.130	3.645	2.285	2.720	2.671	0.424	5.541
6.5% H2O	63.561	0.612	11.366	6.224	0.129	3.603	2.259	2.689	2.640	0.419	6.500
TLT1											
From XRF	81.247	0.244	6.467	2.731	0.098	2.467	2.896	2.316	0.815	0.714	3.000
TLT13											
From Mineral data	67.693	0.232	5.839	4.733	3.995	3.596	5.400	1.040	0.628	0.343	6.500
TLT15											
From mineral data	71.642	1.841	7.533	2.883	2.340	4.326	5.716	2.615	0.842	0.260	4.500
TLT10											
From mineral data with 4% H2O	49.014	2.630	6.361	10.465	-	10.890	12.802	1.707	0.196	1.435	4.500
17TL25											
XRF +4.5% H2O	49.499	1.293	9.704	7.934	-	10.290	11.545	3.722	0.244	1.269	4.500
TLT63											
XRF with 4.5% H2O	75.889	0.114	8.165	1.518	-	0.347	2.454	6.553	0.052	0.585	4.500
TLTN26											
From mineral data + Excess H2O	57.021	1.440	9.805	8.465	0.505	11.206	5.734	4.443	0.879	0.501	Excess
TLTN24											
XRF + water saturated	56.127	0.868	10.539	10.689	0.226	7.310	5.794	6.455	0.136	1.846	Excess
TLTN33											
From mineral data + water saturated	52.899	1.696	10.402	9.674	0.227	7.271	11.668	4.332	0.117	1.690	Excess
17TL104											
From mineral data +water saturated	56.372	1.849	10.781	8.145	0.349	10.699	6.905	3.989	0.868	0.043	Excess
TLT60											
From mineral data +water saturated	69.766	0.734	11.110	4.381	0.073	4.005	7.511	0.727	1.617	0.070	Excess
TLX											
From mineral data +water saturated	73.224	1.465	10.244	3.678	0.075	2.159	5.160	2.386	1.592	0.017	Excess

Table 1.1: Calculated molar bulk compositions used in on samples in this thesis

point counting various phases within a representative area of the thin section that is envisaged to be in equilibrium at a certain set of P-T conditions. Areas were targeted within the thin section that were believed to represent peak metamorphic conditions in the rock and a well equilibrated area. Full slide scans combined with representative SEM images were used to discriminate between optically similar minerals quartz, plagioclase and K-feldspar using J-microvision imaging software. These proportions were then combined with their representative average compositions using mineral geometrical data for un-zoned minerals. Garnet was the only phase to have internal compositional zoning; therefore, a compositional contribution was produced by the integration of concentric shells, assuming spherical geometry in order to obtain an average chemical composition. Where relevant, the Fe content of individual minerals was calculated using the software AX (Holland, 2009). Because THERMOCALC utilizes molar proportions of oxides, an in house spreadsheet recalculates averaged data from individual minerals into overall molar proportions, suitable for THERMOCALC. Note that in thermocalc Fe_2O_3 is treated as $2 * FeO + O$, hence FeO is the molar sum of total Fe and O is defined separately.

1.2.2 Limitations and uncertainities with using THERMOCALC and paractical thermobarometry

There are numerous sources of uncertainty associated with thermobarometry. The most important are probably the following:

1. Uncertainty on the thermobarometer calibration, e.g. uncertainty in the position of an end member equilibrium determined by bracketed phase equilibrium experiments. If the calibration has been derived from an optimised, self-consistent thermodynamic data set, it should be possible to provide a reasonable estimate of this uncertainty. A calculation using THERMOCALC will quote for you an uncertainty based on the correlated uncertainties of the enthalpies of end members in the Holland and Powell data set.

2. Analytical uncertainty on the mineral analyses. This is derived from counting statistics, standardisation and correction procedures in the electron microprobe. This type of error will be made up of a mixture of random errors (e.g. those deriving from counting statistics) and systematic errors. The contribution from random errors can be estimated quite readily and is predicted to be normally distributed and can be calculated from X-ray counting statistics.

3. Uncertainty in activity-composition relationships. This source of error is difficult to quantify the most appropriate formulation for the thermodynamic mole fraction maynot be known. For example ideal behaviour for a phase maybe assumed which actually behaves in a non-ideal manner. If a non-ideal actvity model is used, it may also not extrapolate correctly to the P, T or composition range of interest, and is particularly problematic at high-pressure were order dis-odeing in pyroxenes occurrs.

4. "Geological" error. This involves the systematic, non-statistical errors introduced by petrologists, in selecting phase compositions which may not be in chemical equilibrium at theparicular point of interest in the rock's history. On the other hand that rock can be to blame for not equilibrating properly.

Furthermore overall uncertainty, which is the sum of all the above errors, should be distinguished from comparison uncertainty, which reduces the ability to resolve two pressures or temperatures determined using the same calibration of a particular thermobarometer. The comparison uncertainty depends largely on the analytical imprecision, and may be a much smaller than the overall uncertainty.

THERMOCALC can be an extremly useful petrological tool as it can calculate univariant reactions between mineral endmembers (Mode 2 Average P-T) and also phase diagrams (calculated in Mode 1 and are also known as pseuosections). Because most geologists are interested in specific mineral assemblages in the rocks that they are studying, a pseudosection approach has numerous advantages. Firstly this type of diagram portrays only the reactions we as geologists are interested in by examining a

compositional slice through the full multi-component chemical system of interest and therefore directly relates analysed compositions and modal abundances of minerals in real rocks to that predicted by equilibrium thermodynamics at a given P-T position. Pseudosections can also be used to investigate volumes of fluid released during various metamorphic reactions, modal abundances of phases and the effect of varying oxidation state during metamorphism. One major caveat of the pseudosection approach however is the choice of bulk composition which has been shown to potentially have a large impact on the topology of the pseudosection. Calculation of the bulk composition ca be achieved via a whole rock geochemical (XRF) analysis if equilibrium is achieved on the 'rock' scale. However, many metamorphic rocks preserve chemical zoning of porphyroblasts and therefore a calculation using an 'effective' bulk composition is more appropriate. This is acheived by combining mineral chemistry data with modal proportions (e.g. by only including garnet cores and excluding the rims). Of the several factors that can affect the accuracy and precision of pseudosections, "geological" uncertainty related to natural petrographic variation at the hand sample- and/or thin section-scale is rarely considered and influences the sample's bulk composition (Palin et al., 2016). This is the primary control on its equilibrium phase relationships and thus the interpreted pressure–temperature (P–T) conditions of formation. Palin et al., (2016) demonstrated that absolute displacements of equilibria can approach ± 1 kbar for only a moderate degree of modal proportion uncertainty, therefore being essentially similar to the magnitudes reported for analytical uncertainties in conventional thermobarometry. Bulk compositions determined from multiple thin sections of a heterogeneous sample may demonstrate a wide range in major-element oxides, due to variation in mineral proportions. Palin et al., (2016) also shown that the main discrepancies between choosing large or small equilibration volumes relate to varying proportions of matrix phases (e.g. mica) relative to porphyroblasts (e.g. garnet), and suggest that point counting preserves small-scale petrographic features that are otherwise averaged out in XRF analysis of a larger sample. Therefore before undertaking equilibrium phase diagram modelling, careful consideration of the size of the equili-

bration volume and the constituents of which comprise the effective bulk composition should be carried out. The best technique to determine this is dependant on rock type and petrographic characteritics and is essential in order to produce trustworthy data from pseudosection analysis.

Furthermore, uncertainities in the activity composition relations (A-X relations) must be considered before using THERMOCALC to extract a meaningful result. The usefulness of the calculated diagrams cannot exceed the accuracy of the thermodynamic parameterisations for phases, and these parameterisations are under-constrained by the available data. Phase diagrams calculated with currently available sets of thermodynamic models typically reproduce the broad patterns of field observations quite well (Green et al., 2013); however, one should avoid taking the details of modelling results too literally. For example, Green et al., (2013) shown that uncertainties in the parameterisation of a set of activity-composition relations can be examined by a Monte Carlo technique. This can be used to explore the sensitivity of calculated phase diagrams to these uncertainties, via a new facility in THERMOCALC. Monte Carlo in THERMOCALC (MCTC) repeatedly calculates a set of equilibria using values for poorly-constrained model parameters drawn at random from a gaussian distribution. It has been demonstrated that some features of the resulting phase diagrams vary greatly with the values of one or more parameters (Green et al., 2013). Fortunately however, Green et al., (2013) demonstrate that key equilibria typically vary in a correlated fashion thanks to the systematic changes in mineral assemblage across a calculated phase diagram, from which the overall topology of any given phase diagram can be infered to be stable with respect to a reasonable range of parameter values. This is consistent with the observation that phase diagrams calculations do generally produce plausible results over a wide range of P–T and composition space and generally give consistent results with indenpendant thermobarometers and brometers. The uncertainities in activity composition relations maybe particularly problematic at high pressure and low temperature, partly due to the lack of experimental data, but also the potential violation of the equilibrium assumption. Although the uncertainities were not fully ex-

plored in this thesis due to tight time constraints, further work will be carried out in the comming months and years to properly address the uncertainities of THERMOCALC results under high-pressure and temperature.

An alternative and more classical method to estimate P-T conditions of metamorphism is by using univariant reactions in a petrogenetic grid and this can be extremely useful in providing bounding constraints on the stability of mineral assemblages. However, petrogenetic grids can become extremly complex with lots of reactions, and can be difficult to interpret and they show assemblages in all possible rocks in the system under question. Furthermore most mineral assemblages in real rocks are higher variance than just considering reactions between end members. Moreover, for specific rock compositions, many of these reactions are not 'seen' by a particular bulk composition (i.e. the reaction is not favorouble for a the given bulk composition at a given P-T condition). For example, in mafic rocks, pseudosections for a given bulk rock composition predict that there are large areas of P-T space that have high variance assemblages stable, and these are not partaking in metamorphic reaction between specific end-members. In this scenario, a petrogenetic grid can give an erroneous result as it considers only discontinuous reactions, assumes fixed mineral compositions in rocks and it cannot deal well with phases of variable compositions.

If time permits, the best solution to the above problems maybe to investigate the effect of bulk composition with regard to phase relations in THERMOCALC, perform Average P-T and other univariant conventional thermobarometers, and possibly explore other methods such as raman spectroscopy as an independant check on calculated P-T results, particularly at high pressure and low temperature.

1.3 Electron microprobe analysis (EPMA) and operating conditions

The compositions of phases in rocks under investigation were derived from electron microrobe analysis (EMPA) using a at the Department of Earth Sciences, University

of Oxford and the Bristish Geological Survey. Compositional analyses were performed on a Cameca SX5-Fe electron microprobe with a tungsten tipped field emission gun at the Department of Earth Sciences, University of Oxford. Operating conditions involved an accelerating voltage of 15.0 keV corresponding to a current of 9 nA, a range of primary and secondary standards were used including andradite (Fe, Mg, Ca) TiO_2, Mn metal, labradorite (Na, Al, Si) and sanidine (K) for major elements and synthetic standards for REE's. Garnet line profiles were collected using a consistent 10-micron step size across all garnets corresponding to between 100 and 200 analyses. High resolution garnet maps were acquired using a setup with a 15 keV accelerating voltage with a step size of 2 microns and a dwell time of 60 s for Naxos garnets. For Tinos garnets line profiles, a 10 micron spotsize was also used for eclogites in chapter 3 and 4 microns for the metamorphic sole rocks in chapter 2.

Additional analyses were collected on a JEOL JS-840A scanning electron microscope (SEM) equipped with an Oxford Instruments Isis 300 energy-dispersive analytical system, and a LEO 535VP SEM equipped with an Oxford instruments Inca EDS system. Operating conditions comprised of a working distance of 15 mm on the JEOL and 19 mm on the LEO, an acceleration voltage of 20.0 kV and a corresponding current of 6.00 nA. Calibrations were performed every 120 min using a cobalt standard and a ZAF correction procedure provided by the JEOL and Inca software was applied. Compositional analyses were taken for 60 s, with multiple point analyses acquired to determine if any chemical heterogeneity occurred within or between grains. Anhydrous phase compositions were calculated to standard numbers of oxygen per formula unit (Deer et al., 1992), micas were recalculated to 11 oxygens, and chlorite to 28 oxygens. For hydrous mineral species, H_2O content was assumed to be present in stoichiometric amounts and, where relevant, the proportion of Fe_{3+}/Fe_{total} was calculated using AX (Holland, 2009) and amphibole vectors were calculated using the method of Holland and Blundy, 1994 using an in house excel spreadsheet.

A number of polished thin sections were analyzed for major elements and x-ray mapping was performed on a variety of scales; from entire thin section to major and

accessory phase maps. Compositional profiles across garnets were determined on the JEOL by accumulating counts along a 256- channel line scan for approximately (25-30) minutes. The profiles were background-corrected and calibrated against up to six full point analyses taken at known positions along the profile in order to calculate mole fractions of garnet end members. On the LEO, garnet profiles were taken as equally spaced individual point analyses along a line traversing the garnets. Backscattered electron images of characteristic mineral associations, textures, compositional maps and line profiles are shown below for each sample.

Uncertainties on reported major elements were <1%. Scanning Electron Microscope imaging was also undertaken at the British Geological Survey UK, using a FEI Quanta 500 SEM. The SEM detectors were used to make element X-ray maps of whole thin sections (Al, Ca, Fe, K, Mg, Mn, Na, P, Si) Operating conditions were 15mm working distance and 0.6nA and 20kV beam conditions and the WDS spectrometer was used to collect maps of Y, Th, Ce, U, Yb zonation of monazites. X-ray maps were obtained for a range of major and trace elements using 15kV and 20nA beam conditions.

Full analytical data for extra Naxos samples including ferric iron re-calculations are presented below in the following tables:

Unit	Zas Unit																									
Sample	TLN25											TLN26							TLN54							
Mineral	Actinolite	Barrosite	Glaucophane	Biotite	Chlorite	Epidote	Muscovite	Paragonite	Albite	Plagioclase	Talc	Chlorite	Phengite	Muscovite	Paragonite	Albite	Glaucophane	Rutile	Glaucophane	Biotite	Chlorite	ilhem	Phengite	Muscovite	Paragonite	Albite
Location	Matrix	Matrix	Inc in Ep	Matrix	Matrix	Matrix	Matrix	Inc in Ep	Matrix	Matrix	Matrix	Matrix	Matrix	Matrix	Matrix	Matrix	Matrix	Matrix	Matrix	Matrix	Matrix	Matrix	Matrix	Matrix	Matrix	Matrix
SiO2	55.54	52.14	60.42	40.91	26.55	39.73	48.01	47.86	67.60	62.30	63.05	24.84	50.55	49.36	47.20	68.08	54.19	0.00	55.94	45.18	25.74	0.28	50.10	50.53	48.22	68.59
TiO2	0.05	0.00	0.15	0.37	0.05	0.37	0.17	0.05	0.05	0.00	0.20	0.23	0.13	0.40	0.28	0.00	0.00	98.74	0.13	0.13	0.00	52.71	0.52	0.28	0.1	0.07
Al2O3	1.11	17.53	9.05	13.87	20.35	23.66	26.60	41.32	18.52	20.73	0.25	20.27	26.28	26.70	33.35	19.59	39.04	0.32	10.71	15.10	19.39	0.06	26.49	27.68	37.73	18.8
FeO	10.58	10.47	12.92	13.88	19.21	10.36	3.98	0.58	0.26	2.43	6.83	28.20	3.25	3.92	1.31	0.00	0.33	0.69	15.48	16.12	28.89	43.02	3.53	2.96	0.14	0.45
MnO	0.37	0.10	0.14	0.09	0.04	0.00	0.00	0.28	0.00	0.09	0.00	0.00	0.00	0.00	0.06	0.05	0.15	0.03	0.07	0.05	0.27	1.74	0.00	0.00	0.06	0
MgO	17.68	6.40	10.00	17.81	19.52	0.15	2.72	0.00	0.00	0.45	26.50	12.40	2.69	2.07	1.13	0.33	0.12	0.03	6.65	9.98	12.37	0.15	1.89	2.85	0.63	0.17
CaO	12.47	9.00	0.32	0.50	0.00	22.98	0.22	0.25	0.08	5.65	0.14	0.01	0.32	0.06	0.15	0.18	0.22	0.00	0.24	0.24	0.00	0.03	0.14	0.27	0.07	0.18
Na2O	0.98	4.17	7.40	0.03	0.00	0.00	0.36	7.91	11.94	8.06	0.32	0.11	0.42	0.44	1.13	11.20	7.56	0.15	7.03	0.00	0.00	0.20	0.36	0.39	7.33	11.27
K2O	0.00	0.00	0.07	9.02	0.00	0.06	10.17	0.67	0.10	0.10	0.00	0.01	10.43	10.06	9.56	0.07	0.53	0.01	0.03	7.43	0.00	0.18	10.29	10.28	0.4	0.05
Total	98.78	99.81	100.47	96.48	85.72	97.31	92.23	98.92	98.55	99.81	97.29	86.07	94.07	93.01	94.17	99.50	102.14	99.98	96.28	94.23	86.66	98.37	93.32	95.24	94.68	99.58
Si	7.76	7.10	8.08	2.94	2.58	3.00	3.15	2.80	2.85	2.65	3.80	2.72	3.44	3.40	3.09	2.98	6.69	0.00	7.97	3.28	2.78	0.01	3.41	3.36	3.027	2.993
Ti	0.01	0.00	0.02	0.02	0.00	0.02	0.01	0.00	0.00	0.00	0.01	0.02	0.01	0.02	0.01	0.00	0.00	0.99	0.01	0.01	0.00	1.00	0.03	0.01	0	0.002
Al	0.18	2.81	1.43	1.18	2.33	2.11	2.06	2.85	0.92	1.04	0.02	2.61	2.11	2.17	2.57	1.01	5.68	0.01	1.80	1.29	2.47	0.00	2.12	2.17	2.911	0.967
Fe3+	0.15	0.15	0.15	0.08	0.64	0.50	0.43	0.39	0.28	0.28	0.40	0.00	0.00	0.00	0.18	0.01	0.03	0.00	0.10	0.05	0.08	0.02	0.05	0.05	0.046	0.03
Fe2+	1.24	1.19	1.44	0.83	1.56	0.66	0.22	0.03	0.01	0.09	0.34	2.58	0.19	0.23	0.07	0.00	0.03	0.01	1.75	0.98	2.61	0.91	0.20	0.17	0.03	0.016
Mn	0.04	0.01	0.02	0.01	0.00	0.00	0.00	0.01	0.00	0.00	0.00	0.00	0.00	0.00	0.00	0.00	0.02	0.00	0.01	0.00	0.03	0.04	0.00	0.00	0	0
Mg	3.68	1.30	1.99	1.91	2.82	0.02	0.27	0.00	0.00	0.03	2.38	2.02	0.27	0.21	0.11	0.02	0.02	0.00	1.41	1.08	1.99	0.01	0.19	0.28	0	0.011
Ca	1.87	1.31	0.05	0.04	0.00	1.86	0.02	0.02	0.00	0.26	0.01	0.00	0.02	0.00	0.01	0.01	0.03	0.00	0.04	0.02	0.00	0.00	0.01	0.02	0.008	0.008
Na	0.27	1.10	1.92	0.00	0.00	0.00	0.05	0.90	0.98	0.67	0.04	0.02	0.06	0.06	0.14	0.95	1.81	0.00	1.94	0.00	0.00	0.01	0.05	0.05	0.897	0.953
K	0.00	0.00	0.01	0.83	0.00	0.01	0.85	0.05	0.01	0.01	0.00	0.00	0.90	0.88	0.80	0.00	0.08	0.00	0.01	0.69	0.00	0.01	0.89	0.87	0.047	0.003
Sum	15.20	14.98	15.09	7.83	9.94	8.17	7.04	7.05	5.04	5.02	7.00	9.97	6.99	6.97	6.99	4.99	14.40	1.01	15.04	7.39	9.95	1.99	6.95	6.98	6.966	4.983
Oxygen	23.00	23.00	23.00	11.00	14.00	12.50	11.00	11.00	8.00	8.00	11.00	14.00	11.00	11.00	22.00	8.00	23.00	2.00	23.00	11.00	14.00	3.00	11.00	11.00	11.00	8.00

Table 1.2: Zas Unit additional EMPA

Unit	Koronos Unit																			
Sample	TL67																			
Mineral	Biotite	Biotite	Biotite	Muscovite	Muscovite	Muscovite	Plagioclase	Garnet	Garnet	Garnet	Garnet	Garnet	Garnet	Garnet	Garnet	K-feldspar	Chlorite	Kyanite	Sphene	Plagioclase
Location	Matrix	with Ms	with Ky	with Grt	Matrix	with Grt	Matrix	Core	Core	Core	Inner Rim	Inner Rim	Rim	Rim	Outer Rim	with Grt	Matrix	Enclave	Matrix	Matrix
SiO2	35.99	36.32	34.85	45.13	45.67	45.13	61.41	37.31	37.14	36.80	37.35	37.85	37.65	38.00	37.95	65.34	30.13	36.03	31.23	58.62
TiO2	4.36	3.75	3.43	0.58	1.33	0.58	0.00	0.17	0.00	0.23	0.07	0.12	0.13	0.20	0.15	0.18	1.86	0.09	31.64	0.00
Al2O3	18.08	19.42	19.04	35.11	33.29	35.11	24.33	20.46	20.56	20.73	20.67	20.26	20.69	20.80	20.73	18.64	36.57	62.45	6.62	25.68
FeO	18.03	19.62	18.88	1.89	1.71	1.15	0.03	31.97	30.45	31.43	30.94	28.59	31.18	30.27	30.85	0.01	11.83	0.77	0.48	0.13
MnO	0.23	0.19	0.14	0.00	0.00	0.03	0.01	2.45	2.00	2.03	2.29	3.20	2.14	2.12	3.42	0.00	0.12	0.02	0.00	0.00
MgO	9.69	9.40	7.54	0.68	1.19	0.68	0.00	2.12	2.52	2.74	3.52	3.50	3.48	3.22	3.38	0.00	4.11	0.00	0.00	0.00
CaO	0.04	0.01	0.00	0.08	0.01	0.00	5.58	5.26	6.25	5.79	5.01	5.60	5.69	5.58	3.90	0.00	0.08	0.01	28.90	7.32
Na2O	0.09	0.07	0.15	0.74	0.11	0.26	8.34	0.22	0.18	0.04	0.00	0.15	0.19	0.05	0.11	0.40	0.03	0.00	0.04	7.99
K2O	10.25	10.75	9.39	10.59	10.61	10.60	0.22	0.05	0.00	0.00	0.04	0.00	0.02	0.04	0.02	16.71	5.12	0.14	0.37	0.11
Total	96.76	99.53	93.43	94.80	93.91	93.54	99.91	100.01	99.10	99.78	99.88	99.25	101.20	100.28	100.52	101.28	89.84	99.51	99.28	99.85
Si	2.70	2.66	2.70	3.04	3.10	3.06	2.73	3.00	2.99	2.95	2.98	3.03	2.96	3.02	3.02	2.99	2.87	0.98	1.02	2.63
Ti	0.25	0.21	0.20	0.03	0.07	0.03	0.00	0.01	0.00	0.01	0.00	0.01	0.01	0.01	0.01	0.01	0.13	0.00	0.78	0.00
Al	1.60	1.68	1.74	2.79	2.66	2.81	1.27	1.94	1.95	1.96	1.95	1.91	1.92	1.95	1.94	1.01	4.10	2.01	0.25	1.36
Fe3+	0.00	0.00	0.00	0.00	0.00	0.00	0.00	0.09	0.09	0.12	0.09	0.04	0.17	0.00	0.03	0.00	0.00	0.00	0.00	0.01
Fe2+	1.13	1.20	1.23	0.11	0.10	0.07	0.00	2.05	1.96	1.99	1.98	1.88	1.88	2.01	2.03	0.00	0.94	0.02	0.01	0.00
Mn	0.02	0.01	0.01	0.00	0.00	0.00	0.00	0.17	0.14	0.14	0.16	0.22	0.14	0.14	0.23	0.00	0.01	0.00	0.00	0.00
Mg	1.08	1.03	0.87	0.07	0.12	0.07	0.00	0.25	0.30	0.33	0.42	0.42	0.41	0.38	0.40	0.00	0.58	0.00	0.00	0.00
Ca	0.00	0.00	0.00	0.01	0.00	0.00	0.27	0.45	0.54	0.50	0.43	0.48	0.48	0.48	0.33	0.00	0.01	0.00	1.01	0.35
Na	0.01	0.01	0.02	0.10	0.01	0.03	0.72	0.03	0.03	0.01	0.00	0.02	0.03	0.01	0.02	0.04	0.01	0.00	0.00	0.69
K	0.98	1.01	0.93	0.91	0.92	0.92	0.01	0.01	0.00	0.00	0.00	0.00	0.00	0.00	0.00	0.98	0.62	0.00	0.02	0.01
Sum	7.76	7.80	7.70	7.04	6.97	6.98	5.00	8.00	8.00	8.00	8.00	8.00	8.00	8.00	8.00	5.01	9.27	3.01	3.09	5.04
Oxygen	11.00	11.00	11.00	11.00	11.00	11.00	8.00	12.00	12.00	12.00	12.00	12.00	12.00	12.00	12.00	8.00	14.00	5.00	5.00	8.00

Unit	Koronos Unit															
Sample	TLN21															
Mineral	Biotite	Biotite	Chlorite	Garnet	Garnet	Garnet	Garnet	Garnet	Garnet	Garnet	Garnet	Garnet	Muscovite	Muscovite	Plagioclase	Albite
Location	Matrix	Matrix	Matrix	Outer Rim	Inner Rim	Intermediate	Core	Core	Intermediate	Rim	Rim	Core	Matrix	in Grt	Matrix	Matrix
SiO2	35.56	35.19	27.04	36.82	38.15	37.91	37.63	36.73	37.72	38.21	37.80	36.90	45.33	45.14	61.98	69.32
TiO2	3.99	3.99	0.23	0.13	0.17	0.00	0.18	0.08	0.28	0.02	0.07	0.00	1.48	0.95	0.28	0.00
Al2O3	18.23	18.06	19.82	20.73	20.67	20.90	20.39	20.97	20.37	20.88	20.63	20.84	34.65	34.22	22.73	19.67
FeO	19.64	19.13	28.30	30.93	32.57	32.10	33.01	32.02	31.17	31.91	32.18	33.56	1.31	1.14	0.27	0.22
MnO	0.22	0.50	0.54	6.12	3.55	1.91	1.83	3.18	1.78	3.05	3.63	3.27	0.05	0.00	0.22	0.00
MgO	8.13	8.18	11.69	2.57	3.62	4.20	3.78	3.60	4.16	3.57	3.65	2.98	0.75	0.73	0.03	0.05
CaO	0.00	0.18	0.03	2.08	2.11	3.89	3.19	2.55	3.43	2.21	1.82	2.59	0.13	0.00	5.79	0.71
Na2O	0.19	0.32	0.00	0.59	0.08	0.00	0.08	0.00	0.13	0.27	0.00	0.24	0.03	0.62	8.63	11.58
K2O	9.75	9.46	0.02	0.07	0.00	0.06	0.14	0.10	0.00	0.00	0.00	0.01	10.76	10.65	0.18	0.02
Total	95.70	95.02	87.68	100.05	100.92	100.96	100.24	99.23	99.05	100.10	99.77	100.41	94.49	93.45	100.12	101.57
Si	2.71	2.70	2.89	2.95	3.03	2.99	3.00	2.96	3.03	3.05	3.03	2.95	3.06	3.12	2.76	2.99
Ti	0.23	0.23	0.02	0.01	0.01	0.00	0.01	0.01	0.02	0.00	0.00	0.00	0.09	0.09	0.01	0.00
Al	1.64	1.63	2.50	1.96	1.94	1.94	1.92	1.99	1.93	1.96	1.95	1.97	2.72	2.62	1.19	1.00
Fe3+	0.00	0.00	0.00	0.21	0.00	0.09	0.09	0.08	0.00	0.00	0.00	0.17	0.00	0.00	0.00	0.00
Fe2+	1.25	1.23	2.53	1.86	2.16	2.03	2.11	2.08	2.09	2.13	2.16	2.08	0.08	0.07	0.01	0.01
Mn	0.01	0.03	0.05	0.42	0.24	0.13	0.12	0.22	0.12	0.21	0.25	0.22	0.01	0.00	0.01	0.00
Mg	0.92	0.94	1.86	0.31	0.43	0.49	0.45	0.43	0.50	0.42	0.44	0.36	0.05	0.11	0.00	0.00
Ca	0.00	0.02	0.00	0.18	0.18	0.33	0.27	0.22	0.30	0.19	0.16	0.22	0.00	0.00	0.28	0.03
Na	0.03	0.05	0.00	0.09	0.01	0.00	0.01	0.00	0.02	0.04	0.00	0.04	0.05	0.06	0.74	0.97
K	0.95	0.93	0.00	0.01	0.00	0.01	0.01	0.01	0.00	0.00	0.00	0.00	0.91	0.92	0.01	0.00
Sum	7.73	7.74	9.85	8.00	8.00	8.00	8.00	8.00	8.00	8.00	7.99	8.00	6.97	6.97	5.01	5.00
Oxygen	11.00	11.00	14.00	12.00	12.00	12.00	12.00	12.00	12.00	12.00	12.00	12.00	11.00	11.00	8.00	8.00

Table 1.3: Koronos Unit additional EMPA Part 1

Unit	Koronos Unit																
Sample	TLN16						17TL75										
Mineral	Biotite	Biotite	Garnet	Garnet	Garnet	Plagioclase	Garnet	Garnet	Garnet	Garnet	Hornblende	Hornblende	Hornblende	Hornblende	Plagioclase	Plagioclase	ilhem
Location	Matrix	Matrix	Rim	Inner Rim	Core	Matrix	Inner Rim	Inner Rim	Intermediate	Core	Matrix	With Grt	Matrix	with Grt	Matrix	Matrix	Matrix
SiO2	35.69	35.45	38.02	38.27	38.30	59.82	37.87	37.87	37.78	37.64	44.04	43.24	45.26	42.94	59.41	60.55	0.07
TiO2	3.45	4.05	0.03	0.22	0.00	0.00	0.02	0.04	0.03	0.02	0.84	0.68	0.62	0.82	0.00	0.00	51.24
Al2O3	18.10	18.52	21.67	20.78	20.73	24.81	21.49	21.35	21.45	21.46	13.59	13.41	12.22	13.62	25.81	25.08	0.09
FeO	15.10	14.25	25.77	25.91	25.91	0.17	28.04	27.99	27.51	27.20	15.95	16.87	15.60	14.99	0.16	0.07	42.64
MnO	0.09	0.01	6.26	5.32	5.51	0.00	2.62	2.66	3.07	3.19	0.31	0.29	0.23	0.25	0.00	0.00	3.25
MgO	11.48	10.93	3.68	4.15	3.66	0.08	4.84	4.79	4.54	4.52	10.21	9.99	11.08	10.86	0.00	0.01	0.10
CaO	0.10	0.00	5.36	6.16	5.68	7.08	5.30	5.23	5.71	5.81	10.83	10.69	11.08	10.96	7.23	6.42	0.06
Na2O	0.40	0.38	0.00	0.19	0.34	7.98	0.02	0.00	0.01	0.02	1.54	1.37	1.25	1.46	7.47	7.83	0.04
K2O	9.20	9.48	0.04	0.00	0.00	0.17	0.00	0.00	0.00	0.00	0.33	0.35	0.25	0.38	0.04	0.09	0.03
Total	93.62	93.07	100.83	101.00	100.13	100.11	100.20	99.92	100.08	99.87	97.63	96.88	97.58	96.29	100.13	100.05	97.52
Si	2.71	2.70	2.99	2.99	3.03	2.67	2.98	2.99	2.98	2.98	6.46	6.40	6.61	6.36	2.65	2.69	0.00
Ti	0.20	0.23	0.00	0.01	0.00	0.00	0.00	0.00	0.00	0.00	0.09	0.08	0.07	0.09	0.00	0.00	1.00
Al	1.62	1.66	2.01	1.92	1.93	1.31	1.99	1.98	1.98	1.98	2.35	2.34	2.10	2.38	1.36	1.31	0.00
Fe3+	0.00	0.00	0.01	0.10	0.07	0.01	0.06	0.04	0.06	0.06	0.42	0.58	0.43	0.50	0.01	0.00	0.01
Fe2+	0.96	0.91	1.68	1.60	1.64	0.00	1.78	1.80	1.76	1.73	1.54	1.51	1.48	1.36	0.00	0.00	0.91
Mn	0.01	0.00	0.42	0.35	0.37	0.00	0.17	0.18	0.21	0.21	0.04	0.04	0.03	0.03	0.00	0.00	0.07
Mg	1.30	1.24	0.43	0.48	0.43	0.01	0.57	0.56	0.55	0.54	2.23	2.20	2.41	2.40	0.00	0.00	0.00
Ca	0.01	0.00	0.45	0.52	0.48	0.34	0.45	0.44	0.46	0.51	1.70	1.70	1.73	1.74	0.35	0.31	0.00
Na	0.06	0.06	0.00	0.03	0.05	0.69	0.00	0.00	0.00	0.00	0.44	0.39	0.36	0.42	0.65	0.67	0.00
K	0.89	0.92	0.00	0.00	0.00	0.01	0.00	0.00	0.00	0.00	0.06	0.07	0.05	0.07	0.00	0.01	0.00
Sum	7.76	7.72	8.00	8.00	8.00	5.02	8.00	8.00	8.00	8.00	15.32	15.30	15.26	15.35	5.00	4.99	2.00
Oxygen	11.00	11.00	12.00	12.00	12.00	8.00	12.00	12.00	12.00	12.00	23.00	23.00	23.00	23.00	8.00	8.00	3.00

Unit	Koronos Unit													
Sample	TLN22													
Mineral	Biotite	Biotite	Biotite	Garnet	Garnet	Garnet	Garnet	Garnet	Garnet	ilhem	Muscovite	Muscovite	Plagioclase	Plagioclase
Location	Matrix	with Ky	with Grt	Inner Rim	Intermediate	Outer Rim	Intermediate	Core	Outer Rim	Matrix	with Ky	Matrix	Matrix	Matrix
SiO2	36.73	36.11	36.11	38.40	36.90	36.73	36.58	38.57	38.94	36.46	46.02	46.57	62.75	61.79
TiO2	2.72	2.87	2.87	0.00	0.00	0.02	0.00	0.00	0.18	0.00	1.12	0.73	0.00	0.06
Al2O3	17.91	19.37	19.37	20.60	19.84	20.48	20.80	21.03	19.56	61.90	34.20	35.69	22.92	23.66
FeO	17.46	16.63	16.63	31.04	30.88	32.45	30.89	29.98	31.83	0.33	0.93	1.56	0.17	0.33
MnO	0.40	0.00	0.00	4.11	3.40	5.37	3.16	2.76	6.28	0.37	0.00	0.00	0.00	0.10
MgO	11.41	10.58	10.58	4.00	4.13	2.98	4.03	3.32	2.02	0.00	0.68	0.76	0.00	0.07
CaO	0.10	0.00	0.00	2.92	3.83	2.32	3.62	4.27	1.50	0.00	0.27	0.00	4.58	5.24
Na2O	0.00	0.00	0.00	0.13	0.13	0.13	0.00	0.00	0.01	0.00	1.01	0.82	9.31	8.54
K2O	8.76	9.35	9.35	0.00	0.00	0.00	0.00	0.01	0.02	0.00	10.01	9.48	0.12	0.14
Total	95.49	94.91	94.91	101.20	99.11	100.49	99.09	99.94	100.34	99.06	94.23	95.62	99.85	99.92
Si	2.75	2.71	2.71	3.03	2.97	2.95	2.94	3.06	3.13	0.01	3.12	3.04	2.79	2.75
Ti	0.15	0.16	0.16	0.00	0.00	0.00	0.00	0.00	0.01	1.02	0.04	0.04	0.00	0.00
Al	1.58	1.72	1.72	1.92	1.88	1.94	1.97	1.97	1.85	0.00	2.67	2.80	1.20	1.24
Fe3+	0.00	0.00	0.00	0.05	0.21	0.19	0.15	0.00	0.00	0.00	0.00	0.00	0.01	0.01
Fe2+	1.09	1.05	1.05	2.00	1.87	1.99	1.93	1.99	2.14	0.91	0.06	0.07	0.00	0.00
Mn	0.03	0.00	0.00	0.27	0.23	0.37	0.22	0.19	0.43	0.04	0.01	0.02	0.00	0.00
Mg	1.27	1.18	1.18	0.47	0.50	0.36	0.48	0.39	0.24	0.00	0.11	0.05	0.00	0.01
Ca	0.01	0.00	0.00	0.25	0.33	0.20	0.31	0.36	0.13	0.00	0.01	0.00	0.22	0.25
Na	0.00	0.00	0.00	0.02	0.02	0.02	0.00	0.00	0.00	0.00	0.11	0.16	0.80	0.74
K	0.84	0.90	0.90	0.00	0.00	0.00	0.00	0.00	0.00	0.00	0.87	0.85	0.01	0.01
Sum	7.72	7.72	7.72	8.00	8.00	8.00	8.00	7.96	7.93	1.98	7.00	7.02	5.02	5.00
Oxygen	11.00	11.00	11.00	12.00	12.00	12.00	12.00	12.00	12.00	3.00	11.00	11.00	8.00	8.00

Table 1.4: Koronos Unit additional EMPA part 2

Unit	Core Unit																	
Sample	TL15																	
Mineral Location	Biotite Leucosoome	Biotite Melanosome	Biotite Melanosome	Garnet Outer Rim	Garnet Intermediate	Garnet Core	Garnet Outer Rim	Garnet Inner Rim	Garnet Core	Garnet Core	Garnet Inner Rim	Garnet Outer Rim	Muscovite With Bt	Muscovite Primary	Muscovite Secondary	Muscovite Primary	Plagioclase Leucosome	Plagioclase Melanosome
SiO2	35.86	35.43	35.00	36.64	37.89	37.08	37.42	37.20	37.33	37.72	38.64	37.70	45.98	47.07	45.80	47.56	62.49	59.48
TiO2	3.08	3.34	3.44	0.03	0.02	0.00	0.12	0.08	0.00	0.00	0.00	0.00	1.17	1.37	0.80	1.40	0.00	0.00
Al2O3	18.67	18.74	18.84	20.67	21.26	20.60	20.84	20.75	21.05	20.78	20.07	20.77	34.17	33.67	34.48	33.22	22.96	25.02
FeO	19.34	19.16	20.08	33.39	31.69	31.56	33.51	32.38	33.23	33.64	31.12	33.44	1.30	1.54	1.38	1.45	0.09	0.00
MnO	0.08	0.23	0.10	3.03	1.76	1.85	2.18	1.59	1.47	2.32	1.27	2.12	0.05	0.06	0.06	0.14	0.32	0.00
MgO	9.20	9.19	8.82	3.21	3.83	2.60	3.63	3.81	3.35	3.32	4.49	4.16	0.93	0.88	0.83	0.91	0.12	0.12
CaO	0.02	0.01	0.15	2.13	4.18	6.09	2.43	3.71	3.11	2.74	3.55	2.77	0.02	0.00	0.00	0.00	4.60	6.98
Na2O	0.07	0.47	0.49	0.00	0.18	0.00	0.00	0.00	0.12	0.00	0.31	0.00	0.57	0.44	1.02	0.66	9.50	7.70
K2O	9.58	9.37	9.07	0.00	0.08	0.14	0.01	0.01	0.10	0.00	0.23	0.00	10.42	10.06	10.17	10.14	0.12	0.07
Total	95.89	95.94	95.99	99.10	100.88	99.91	100.15	99.54	99.76	100.53	99.68	100.95	94.61	95.10	94.55	95.49	100.21	99.36
Si	2.71	2.68	2.66	2.97	2.98	2.97	2.99	2.98	2.99	3.01	3.07	2.98	3.09	3.13	3.08	3.16	2.77	2.67
Ti	0.18	0.19	0.20	0.00	0.00	0.00	0.01	0.01	0.00	0.00	0.00	0.00	0.06	0.07	0.04	0.07	0.00	0.00
Al	1.66	1.67	1.69	1.98	1.97	1.95	1.97	1.96	1.99	1.96	1.88	1.94	2.70	2.64	2.73	2.60	1.20	1.32
Fe3+	0.00	0.00	0.00	0.07	0.09	0.13	0.03	0.07	0.06	0.02	0.06	0.10	0.00	0.00	0.00	0.00	0.00	0.00
Fe2+	1.22	1.21	1.28	2.19	1.99	1.98	2.21	2.10	2.17	2.23	2.01	2.12	0.07	0.09	0.08	0.08	0.00	0.00
Mn	0.01	0.02	0.01	0.21	0.12	0.13	0.15	0.11	0.10	0.16	0.09	0.14	0.00	0.00	0.00	0.01	0.01	0.00
Mg	1.04	1.04	1.00	0.39	0.45	0.31	0.43	0.46	0.40	0.40	0.53	0.49	0.09	0.09	0.08	0.09	0.01	0.01
Ca	0.00	0.00	0.01	0.19	0.35	0.52	0.21	0.32	0.27	0.23	0.30	0.24	0.00	0.00	0.00	0.00	0.22	0.34
Na	0.01	0.07	0.07	0.00	0.03	0.00	0.00	0.00	0.02	0.00	0.05	0.00	0.07	0.06	0.13	0.09	0.82	0.67
K	0.92	0.90	0.88	0.00	0.01	0.01	0.00	0.00	0.01	0.00	0.02	0.00	0.89	0.85	0.87	0.86	0.01	0.00
Sum	7.75	7.78	7.78	8.00	8.00	8.00	8.00	8.00	8.00	8.00	8.00	8.00	6.99	6.93	7.02	6.95	5.04	5.01
Oxygen	11.00	11.00	11.00	12.00	12.00	12.00	12.00	12.00	12.00	12.00	12.00	12.00	11.00	11.00	11.00	11.00	8.00	8.00

Unit	Core Unit																	
Sample	TL59																	
Mineral Location	Biotite Matrix	Biotite Matrix	Biotite Matrix	Chlorite Matrix	Garnet Core	Garnet Inner Rim	Garnet Inner Rim	Garnet Intermediate	Garnet Outer Rim	Garnet Outer Core	Garnet Core	ilhem Matrix	Muscovite Matrix	Muscovite Matrix	Muscovite Inc in grt	Muscovite matrix	Plagioclase Matrix	Plagioclase Matrix
SiO2	37.31	37.65	37.74	34.68	38.23	38.51	38.12	38.30	37.59	38.27	37.42	0.19	46.42	46.85	47.67	45.14	64.87	62.98
TiO2	3.05	3.00	2.82	2.00	0.17	0.00	0.02	0.00	0.18	0.02	0.00	47.69	0.70	1.15	1.07	0.45	0.08	0.05
Al2O3	17.31	17.82	17.06	18.54	20.84	21.35	21.09	20.95	20.65	20.52	20.92	0.17	32.61	31.40	30.72	32.91	22.41	23.51
FeO	19.12	18.96	19.89	14.74	29.86	32.54	32.23	32.29	30.72	31.57	31.38	49.71	3.49	3.65	3.37	3.80	0.04	0.03
MnO	0.26	0.43	0.21	0.35	2.38	1.78	2.57	2.03	5.20	2.60	2.45	1.56	0.00	0.08	0.00	0.03	0.00	0.04
MgO	8.52	7.58	8.41	6.43	2.97	3.37	3.08	2.92	2.40	2.42	1.64	0.05	0.63	0.99	1.19	0.61	0.00	0.00
CaO	0.20	0.06	0.24	0.00	6.11	4.18	3.72	4.10	3.22	5.21	5.92	0.00	0.01	0.01	0.00	0.00	3.29	4.95
Na2O	0.38	0.19	0.53	0.39	0.13	0.15	0.00	0.18	0.20	0.04	0.08	0.00	0.62	0.54	0.50	0.67	9.98	9.13
K2O	9.01	8.35	7.95	8.26	0.02	0.00	0.00	0.00	0.08	0.00	0.02	0.08	10.54	10.52	10.34	10.28	0.19	0.24
Total	95.16	94.04	94.85	85.39	100.73	101.92	100.83	100.77	100.29	100.65	99.84	100.40	95.02	95.19	94.86	93.95	100.86	100.93
Si	2.83	2.87	2.86	3.65	3.02	3.02	3.02	3.04	3.02	3.05	3.01	0.01	3.14	3.17	3.22	3.09	2.84	2.77
Ti	0.17	0.17	0.16	0.16	0.01	0.00	0.00	0.00	0.01	0.00	0.00	0.90	0.04	0.06	0.05	0.02	0.00	0.00
Al	1.55	1.60	1.53	2.30	1.94	1.97	1.97	1.96	1.95	1.93	1.99	0.01	2.60	2.50	2.45	2.66	1.16	1.22
Fe3+	0.00	0.00	0.00	0.00	0.01	0.02	0.00	0.00	0.03	0.00	0.00	0.18	0.00	0.00	0.00	0.03	0.00	0.00
Fe2+	1.21	1.21	1.26	1.30	1.96	2.11	2.14	2.14	2.03	2.10	2.11	0.87	0.20	0.21	0.19	0.19	0.00	0.00
Mn	0.02	0.03	0.01	0.03	0.16	0.12	0.17	0.14	0.35	0.18	0.17	0.03	0.00	0.01	0.00	0.00	0.00	0.00
Mg	0.96	0.86	0.95	1.01	0.35	0.39	0.36	0.35	0.29	0.29	0.20	0.00	0.06	0.10	0.12	0.06	0.00	0.00
Ca	0.02	0.01	0.02	0.00	0.52	0.35	0.32	0.35	0.28	0.45	0.51	0.00	0.00	0.00	0.00	0.00	0.15	0.23
Na	0.06	0.03	0.08	0.08	0.02	0.02	0.00	0.03	0.03	0.01	0.01	0.00	0.08	0.07	0.07	0.09	0.85	0.78
K	0.87	0.81	0.77	1.11	0.00	0.00	0.00	0.00	0.01	0.00	0.00	0.00	0.91	0.91	0.89	0.90	0.01	0.01
Sum	7.69	7.58	7.64	9.64	8.00	8.00	7.99	8.00	8.00	7.99	8.00	2.00	7.02	7.02	6.98	7.04	5.01	5.01
Oxygen	11.00	11.00	11.00	14.00	12.00	12.00	12.00	12.00	12.00	12.00	12.00	3.00	11.00	11.00	11.00	11.00	8.00	8.00

Table 1.5: Core Unit additional EMPA Part 1

Unit	Core Unit																	
Sample	TL15																	
Mineral Location	Biotite Leucosoome	Biotite Melanosome	Biotite Melanosome	Garnet Outer Rim	Garnet Intermediate	Garnet Core	Garnet Outer Rim	Garnet Inner Rim	Garnet Core	Garnet Core	Garnet Inner Rim	Garnet Outer Rim	Muscovite With Bt	Muscovite Primary	Muscovite Secondary	Muscovite Primary	Plagioclase Leucosome	Plagioclase Melanosome
SiO2	35.86	35.43	35.00	36.64	37.89	37.08	37.42	37.20	37.33	37.72	38.64	37.70	45.98	47.07	45.80	47.56	62.49	59.48
TiO2	3.08	3.34	3.44	0.03	0.02	0.00	0.12	0.08	0.00	0.00	0.00	0.00	1.17	1.37	0.80	1.40	0.00	0.00
Al2O3	18.67	18.74	18.84	20.67	21.26	20.60	20.84	20.75	21.05	20.78	20.07	20.77	34.17	33.67	34.48	33.22	22.96	25.02
FeO	19.34	19.16	20.08	33.39	31.69	31.56	33.51	32.38	33.23	33.64	31.12	33.44	1.30	1.54	1.38	1.45	0.09	0.00
MnO	0.08	0.23	0.10	3.03	1.76	1.85	2.18	1.59	1.47	2.32	1.27	2.12	0.05	0.06	0.06	0.14	0.32	0.00
MgO	9.20	9.19	8.82	3.21	3.83	2.60	3.63	3.81	3.35	3.32	4.49	4.16	0.93	0.88	0.83	0.91	0.12	0.12
CaO	0.02	0.01	0.15	2.13	4.18	6.09	2.43	3.71	3.11	2.74	3.55	2.77	0.02	0.00	0.00	0.00	4.60	6.98
Na2O	0.07	0.47	0.49	0.00	0.18	0.00	0.00	0.00	0.12	0.00	0.31	0.00	0.57	0.44	1.02	0.66	9.50	7.70
K2O	9.58	9.37	9.07	0.00	0.08	0.14	0.01	0.01	0.10	0.00	0.23	0.00	10.42	10.06	10.17	10.14	0.12	0.07
Total	95.89	95.94	95.99	99.10	100.88	99.91	100.15	99.54	99.76	100.53	99.68	100.95	94.61	95.10	94.55	95.49	100.21	99.36
Si	2.71	2.68	2.66	2.97	2.98	2.97	2.99	2.98	2.99	3.01	3.07	2.98	3.09	3.13	3.08	3.16	2.77	2.67
Ti	0.18	0.19	0.20	0.00	0.00	0.00	0.01	0.01	0.00	0.00	0.00	0.00	0.06	0.07	0.04	0.07	0.00	0.00
Al	1.66	1.67	1.69	1.98	1.97	1.95	1.97	1.96	1.99	1.96	1.88	1.94	2.70	2.64	2.73	2.60	1.20	1.32
Fe3+	0.00	0.00	0.00	0.07	0.09	0.13	0.03	0.07	0.06	0.02	0.06	0.10	0.00	0.00	0.00	0.00	0.00	0.00
Fe2+	1.22	1.21	1.28	2.19	1.99	1.98	2.21	2.10	2.17	2.23	2.01	2.12	0.07	0.09	0.08	0.08	0.00	0.00
Mn	0.01	0.02	0.01	0.21	0.12	0.13	0.15	0.11	0.10	0.16	0.09	0.14	0.00	0.00	0.00	0.01	0.01	0.00
Mg	1.04	1.04	1.00	0.39	0.45	0.31	0.43	0.46	0.40	0.40	0.53	0.49	0.09	0.09	0.08	0.09	0.01	0.01
Ca	0.00	0.00	0.01	0.19	0.35	0.52	0.21	0.32	0.27	0.23	0.30	0.24	0.00	0.00	0.00	0.00	0.22	0.34
Na	0.01	0.07	0.07	0.00	0.03	0.00	0.00	0.00	0.02	0.00	0.05	0.00	0.07	0.06	0.13	0.09	0.82	0.67
K	0.92	0.90	0.88	0.00	0.01	0.01	0.00	0.00	0.01	0.00	0.02	0.00	0.89	0.85	0.87	0.86	0.01	0.00
Sum	7.75	7.78	7.78	8.00	8.00	8.00	8.00	8.00	8.00	8.00	8.00	8.00	6.99	6.93	7.02	6.95	5.04	5.01
Oxygen	11.00	11.00	11.00	12.00	12.00	12.00	12.00	12.00	12.00	12.00	12.00	12.00	11.00	11.00	11.00	11.00	8.00	8.00

Unit	Core Unit																	
Sample	TL59																	
Mineral Location	Biotite Matrix	Biotite Matrix	Biotite Matrix	Chlorite Matrix	Garnet Core	Garnet Inner Rim	Garnet Inner Rim	Garnet Intermediate	Garnet Outer Rim	Garnet Outer Core	Garnet Core	ilhem Matrix	Muscovite Matrix	Muscovite Matrix	Muscovite Inc in grt	Muscovite matrix	Plagioclase Matrix	Plagioclase Matrix
SiO2	37.31	37.65	37.74	34.68	38.23	38.51	38.12	38.30	37.59	38.27	37.42	0.19	46.42	46.85	47.67	45.14	64.87	62.98
TiO2	3.05	3.00	2.82	2.00	0.17	0.00	0.02	0.00	0.18	0.02	0.00	47.69	0.70	1.15	1.07	0.45	0.08	0.05
Al2O3	17.31	17.82	17.06	18.54	20.84	21.35	21.09	20.95	20.65	20.52	20.92	0.17	32.61	31.40	30.72	32.91	22.41	23.51
FeO	19.12	18.96	19.89	14.74	29.86	32.54	32.23	32.29	30.72	31.57	31.38	49.71	3.49	3.65	3.37	3.80	0.04	0.03
MnO	0.26	0.43	0.21	0.35	2.38	1.78	2.57	2.03	5.20	2.60	2.45	1.56	0.00	0.08	0.00	0.03	0.00	0.04
MgO	8.52	7.58	8.41	6.43	2.97	3.37	3.08	2.92	2.40	2.42	1.64	0.05	0.63	0.99	1.19	0.61	0.00	0.00
CaO	0.20	0.06	0.24	0.00	6.11	4.18	3.72	4.10	3.22	5.21	5.92	0.00	0.01	0.01	0.00	0.00	3.29	4.95
Na2O	0.38	0.19	0.53	0.39	0.13	0.15	0.00	0.18	0.20	0.04	0.08	0.00	0.62	0.54	0.50	0.67	9.98	9.13
K2O	9.01	8.35	7.95	8.26	0.02	0.00	0.00	0.00	0.08	0.00	0.02	0.08	10.54	10.52	10.34	10.28	0.19	0.24
Total	95.16	94.04	94.85	85.39	100.73	101.92	100.83	100.77	100.29	100.65	99.84	100.40	95.02	95.19	94.86	93.95	100.86	100.93
Si	2.83	2.87	2.86	3.65	3.02	3.02	3.02	3.04	3.02	3.05	3.01	0.01	3.14	3.17	3.22	3.09	2.84	2.77
Ti	0.17	0.17	0.16	0.16	0.01	0.00	0.00	0.00	0.01	0.00	0.00	0.90	0.04	0.06	0.05	0.02	0.00	0.00
Al	1.55	1.60	1.53	2.30	1.94	1.97	1.97	1.96	1.95	1.93	1.99	0.01	2.60	2.50	2.45	2.66	1.16	1.22
Fe3+	0.00	0.00	0.00	0.00	0.01	0.02	0.00	0.00	0.03	0.00	0.00	0.18	0.00	0.00	0.00	0.03	0.00	0.00
Fe2+	1.21	1.21	1.26	1.30	1.96	2.11	2.14	2.14	2.03	2.10	2.11	0.87	0.20	0.21	0.19	0.19	0.00	0.00
Mn	0.02	0.03	0.01	0.03	0.16	0.12	0.17	0.14	0.35	0.18	0.17	0.03	0.00	0.01	0.00	0.00	0.00	0.00
Mg	0.96	0.86	0.95	1.01	0.35	0.39	0.36	0.35	0.29	0.29	0.20	0.00	0.06	0.10	0.12	0.06	0.00	0.00
Ca	0.02	0.01	0.02	0.00	0.52	0.35	0.32	0.35	0.28	0.45	0.51	0.00	0.00	0.00	0.00	0.00	0.15	0.23
Na	0.06	0.03	0.08	0.08	0.02	0.02	0.00	0.03	0.03	0.01	0.01	0.00	0.08	0.07	0.07	0.09	0.85	0.78
K	0.87	0.81	0.77	1.11	0.00	0.00	0.00	0.00	0.01	0.00	0.00	0.00	0.91	0.91	0.89	0.90	0.01	0.01
Sum	7.69	7.58	7.64	9.64	8.00	8.00	7.99	8.00	8.00	7.99	8.00	2.00	7.02	7.02	6.98	7.04	5.01	5.01
Oxygen	11.00	11.00	11.00	14.00	12.00	12.00	12.00	12.00	12.00	12.00	12.00	3.00	11.00	11.00	11.00	11.00	8.00	8.00

Table 1.6: Core Unit additional EMPA Part 1

Unit	Core																
Sample	TL66																
Mineral Location	Biotite with Sill	Biotite Paleosome	Biotite Melanosome	Muscovite Secondary	Muscovite Primary	Muscovite Secondary	Plagioclase Leucosome	Plagioclase with Grt	Garnet Outer Rim	Garnet Inner Rim	Garnet Inner Rim	Garnet Intermediate	Garnet Core	Garnet Core	Garnet Inner Rim	Sillimanite with Bt	Chlorite Matrix
SiO2	34.85	35.07	35.98	46.87	46.75	45.74	56.95	61.66	37.12	37.48	37.27	37.72	37.61	37.95	36.66	36.03	30.13
TiO2	3.43	3.40	3.42	1.43	1.45	1.22	0.00	0.10	0.00	0.02	0.20	0.07	0.00	0.00	0.06	0.09	1.86
Al2O3	19.04	18.36	17.97	34.18	33.12	33.34	29.84	24.87	20.58	20.73	20.33	20.58	20.90	20.78	20.84	62.45	36.57
FeO	18.88	21.08	20.74	2.15	1.93	1.83	0.07	0.04	32.92	32.19	33.90	33.14	32.16	32.97	32.38	0.77	11.83
MnO	0.14	0.16	0.06	0.00	0.00	0.00	0.00	0.00	4.03	4.82	1.77	1.67	3.78	3.00	4.16	0.02	0.12
MgO	7.54	8.09	7.64	0.88	1.13	0.95	0.00	0.00	2.94	3.23	3.78	3.50	2.98	3.60	3.05	0.00	4.11
CaO	0.00	0.05	0.01	0.00	0.00	0.00	6.64	6.23	2.25	2.55	2.24	2.46	3.06	2.22	2.29	0.01	0.08
Na2O	0.15	0.31	0.42	0.66	0.50	0.54	6.80	7.66	0.13	0.04	0.00	0.09	0.09	0.11	0.04	0.00	0.03
K2O	9.39	9.64	9.13	10.35	10.62	10.41	0.36	0.18	0.10	0.00	0.00	0.00	0.00	0.04	0.03	0.14	5.12
Total	93.43	96.17	95.38	96.53	95.50	94.03	100.66	100.73	100.06	101.05	99.49	99.22	100.60	100.67	99.51	99.51	89.84
Si	2.70	2.68	2.75	3.09	3.12	3.10	2.52	2.72	2.99	2.98	3.00	3.04	3.00	3.02	2.96	0.98	2.87
Ti	0.20	0.20	0.20	0.07	0.07	0.06	0.00	0.00	0.00	0.00	0.01	0.00	0.00	0.00	0.00	0.00	0.13
Al	1.74	1.65	1.62	2.66	2.61	2.66	1.56	1.29	1.95	1.94	1.93	1.95	1.97	1.95	1.99	2.01	4.10
Fe3+	0.00	0.00	0.00	0.00	0.00	0.00	0.00	0.00	0.11	0.10	0.04	0.00	0.04	0.04	0.09	0.00	0.00
Fe2+	1.23	1.35	1.33	0.12	0.11	0.10	0.00	0.00	2.10	2.05	2.25	2.23	2.10	2.16	2.10	0.02	0.94
Mn	0.01	0.01	0.00	0.00	0.00	0.00	0.00	0.00	0.27	0.33	0.12	0.11	0.26	0.20	0.29	0.00	0.01
Mg	0.87	0.92	0.87	0.09	0.11	0.10	0.00	0.00	0.35	0.38	0.45	0.42	0.35	0.43	0.37	0.00	0.58
Ca	0.00	0.00	0.00	0.00	0.00	0.00	0.32	0.29	0.19	0.22	0.19	0.21	0.26	0.19	0.20	0.00	0.01
Na	0.02	0.05	0.06	0.08	0.07	0.07	0.58	0.65	0.02	0.01	0.00	0.01	0.01	0.02	0.01	0.00	0.01
K	0.93	0.94	0.89	0.87	0.90	0.90	0.02	0.01	0.01	0.00	0.00	0.00	0.00	0.00	0.00	0.00	0.62
Sum	7.70	7.79	7.72	6.98	6.99	6.99	5.00	4.97	8.00	8.00	8.00	7.99	8.00	8.00	8.00	3.01	9.27
Oxygen	11.00	11.00	11.00	11.00	11.00	11.00	8.00	8.00	12.00	12.00	12.00	12.00	12.00	12.00	12.00	5.00	14.00

Unit	**Core Unit**													
Sample	TLN18										TLN20A			
Mineral Location	Biotite Leucosome	Biotite Leucosome	Biotite Melanosome	Biotite Melanosome	K-feldspar Leucosome	K-feldspar Leucosome	Muscovite Primary	Muscovite Secondary	Muscovite Secondary	Plagioclase Leucosome	Biotite Melanosome	Biotite Melanosome	Biotite Melanosome	Biotite Melanosome
SiO2	34.83	34.64	35.02	35.34	65.44	64.93	45.91	45.10	45.59	64.16	37.63	38.49	35.81	47.43
TiO2	3.50	3.57	4.02	3.80	0.18	0.60	0.98	1.35	3.47	0.18	2.52	2.32	2.64	2.29
Al2O3	17.27	18.52	18.16	16.70	18.01	18.33	32.67	33.29	31.89	22.98	19.37	19.71	19.92	18.80
FeO	0.00	0.00	0.00	0.00	0.00	0.00	0.00	0.00	0.00	0.00	14.23	13.56	15.70	13.03
MnO	20.79	20.08	19.88	19.28	0.00	0.26	2.25	2.15	2.03	0.00	0.26	0.54	0.89	0.31
MgO	0.03	0.41	0.00	0.44	0.05	0.26	0.00	0.08	0.15	0.05	11.08	12.16	10.88	5.01
CaO	8.18	7.96	8.16	8.11	0.00	0.03	0.86	0.46	0.68	0.00	0.36	1.69	0.00	0.24
Na2O	0.23	0.40	0.32	0.32	1.90	0.51	0.38	0.63	0.28	9.64	0.18	0.04	0.42	0.27
K2O	9.73	9.96	9.58	9.42	14.23	15.46	10.23	10.24	9.94	0.19	9.36	8.17	8.95	8.50
Total	94.56	95.55	95.14	93.43	99.81	100.38	93.28	93.31	94.04	97.20	94.98	96.67	95.20	95.88
Si	2.70	2.66	2.68	2.76	3.01	2.98	3.13	3.08	3.09	2.81	2.79	2.78	2.68	3.34
Ti	0.20	0.21	0.23	0.22	0.01	0.02	0.05	0.07	0.18	0.01	0.14	0.13	0.15	0.12
Al	1.58	1.68	1.64	1.54	0.98	0.99	2.63	2.68	2.55	1.19	1.69	1.68	1.76	1.56
Fe3+	0.00	0.00	0.00	0.00	0.00	0.01	0.00	0.00	0.00	0.00	0.00	0.00	0.00	0.00
Fe2+	1.35	1.29	1.27	1.26	0.00	0.00	0.13	0.12	0.12	0.00	0.88	0.82	0.98	0.77
Mn	0.00	0.03	0.00	0.03	0.00	0.01	0.00	0.01	0.01	0.00	0.02	0.03	0.06	0.02
Mg	0.95	0.91	0.93	0.94	0.00	0.00	0.09	0.05	0.07	0.00	1.22	1.31	1.21	0.53
Ca	0.04	0.00	0.02	0.01	0.00	0.01	0.01	0.03	0.02	0.19	0.03	0.13	0.00	0.02
Na	0.04	0.06	0.05	0.05	0.17	0.05	0.05	0.08	0.04	0.82	0.03	0.01	0.06	0.04
K	0.96	0.98	0.94	0.94	0.84	0.91	0.89	0.89	0.86	0.01	0.89	0.75	0.85	0.76
Sum	7.81	7.81	7.76	7.74	5.00	4.98	6.97	7.00	6.91	5.01	7.68	7.64	7.75	7.16
Oxygen	11.00	11.00	11.00	11.00	8.00	8.00	11.00	11.00	11.00	8.00	11.00	11.00	11.00	11.00

Table 1.7: Core Unit additional EMPA Part 2

Unit	**Core Unit**																	
Sample	TLN34																	
Mineral	Biotite	Biotite	Biotite	Biotite	Garnet	Garnet	Garnet	Garnet	Garnet	Garnet	Garnet	K-feldspar	K-feldspar	Muscovite	Muscovite	Plagioclase	Plagioclase	Sillimanite
Location	With Sill	Melanosome	Melanosome	Leucosome	Outer Rim	Core	Intermediate	Inner Rim	Inner Rim	Core	Rim	Leucosome	Melanosome	Secondary	Secondary	Leucosome	With Sill	Melanosome
SiO2	37.18	38.38	36.07	36.26	36.52	37.25	37.87	37.05	38.10	36.90	37.29	64.89	63.69	46.34	45.68	65.21	65.55	36.16
TiO2	3.34	3.25	3.72	3.24	0.00	0.00	0.00	0.07	0.00	0.00	0.00	0.42	0.33	1.57	1.30	0.33	0.23	0.00
Al2O3	18.21	19.20	19.73	19.06	20.88	20.54	20.46	20.43	19.56	20.77	20.63	17.52	19.42	34.86	36.30	21.67	20.69	62.16
FeO	16.48	14.79	16.30	16.42	28.29	28.84	27.65	28.19	28.35	29.85	28.28	0.00	0.12	0.73	0.89	0.03	0.58	0.62
MnO	0.25	0.00	0.13	0.49	9.25	8.08	9.13	10.24	8.07	7.21	8.92	0.00	0.00	0.00	0.08	0.34	0.06	0.27
MgO	8.87	9.27	9.17	9.54	3.32	4.43	3.98	3.63	4.63	4.89	4.06	0.22	0.13	0.66	0.68	0.00	0.02	0.00
CaO	0.07	0.00	0.00	0.43	0.62	0.71	0.49	0.60	0.70	0.66	0.69	0.20	0.11	0.00	0.01	2.70	2.45	0.13
Na2O	0.20	0.36	0.51	0.28	0.43	0.05	0.00	0.30	0.05	0.19	0.01	1.64	1.43	0.44	0.90	10.08	10.60	0.00
K2O	9.49	9.07	8.70	9.00	0.13	0.05	0.00	0.08	0.05	0.00	0.00	14.12	15.20	11.03	10.78	0.30	0.33	0.24
Total	94.09	94.32	94.33	94.72	99.44	99.95	99.58	100.59	99.51	100.47	99.88	99.01	100.43	95.63	96.62	100.66	100.51	99.58
Si	2.82	2.85	2.72	2.73	2.94	2.98	3.05	2.96	3.06	2.93	2.99	3.01	2.93	3.08	3.01	2.86	2.88	0.99
Ti	0.19	0.18	0.21	0.18	0.00	0.00	0.00	0.00	0.00	0.00	0.00	0.02	0.01	0.08	0.06	0.01	0.01	0.00
Al	1.63	1.68	1.75	1.69	1.98	1.94	1.94	1.92	1.85	1.94	1.95	0.96	1.05	2.73	2.82	1.12	1.07	2.00
Fe3+	0.00	0.00	0.00	0.00	0.21	0.11	0.00	0.21	0.03	0.23	0.06	0.00	0.01	0.00	0.00	0.00	0.02	0.00
Fe2+	1.05	0.92	1.03	1.04	1.70	1.82	1.86	1.68	1.87	1.75	1.84	0.00	0.00	0.04	0.05	0.00	0.00	0.01
Mn	0.02	0.00	0.01	0.03	0.63	0.55	0.62	0.69	0.55	0.49	0.61	0.00	0.00	0.00	0.00	0.01	0.00	0.01
Mg	1.00	1.03	1.03	1.07	0.40	0.53	0.48	0.43	0.56	0.58	0.49	0.02	0.01	0.07	0.07	0.00	0.00	0.00
Ca	0.01	0.00	0.00	0.04	0.05	0.06	0.04	0.05	0.06	0.06	0.06	0.01	0.01	0.00	0.00	0.13	0.12	0.00
Na	0.03	0.05	0.07	0.04	0.07	0.01	0.00	0.05	0.01	0.03	0.00	0.15	0.13	0.06	0.12	0.86	0.90	0.00
K	0.92	0.86	0.84	0.87	0.01	0.01	0.00	0.01	0.01	0.00	0.00	0.84	0.89	0.93	0.91	0.02	0.02	0.01
Sum	7.65	7.58	7.65	7.69	8.00	8.00	7.99	8.00	8.00	8.00	8.00	4.99	5.04	6.98	7.03	5.01	5.02	3.02
Oxygen	11.00	11.00	11.00	11.00	12.00	12.00	12.00	12.00	12.00	12.00	12.00	8.00	8.00	11.00	11.00	8.00	8.00	5.00

Unit	Core Unit														
Sample	TLN35														
Mineral	Biotite	Biotite	Biotite	Garnet	Garnet	Garnet	Garnet	Garnet	Garnet	Garnet	Muscovite	Muscovite	Plagioclase	Plagioclase	Plagioclase
Location	with Sill	with Grt	Matrix	Outer Rim	Inner Rim	Inner Rim	Intermediate	Core	Outer Rim	Core	Secondary	Secondary	Leucosome	Leucosome	Melanosome
SiO2	35.09	35.88	36.65	36.61	37.33	37.20	36.63	38.17	37.76	37.65	45.85	44.18	60.12	60.25	56.87
TiO2	3.29	3.60	3.59	0.05	0.00	0.00	0.00	0.00	0.40	0.00	1.62	3.25	0.07	0.08	0.00
Al2O3	18.57	19.75	18.76	21.94	20.73	20.88	21.20	21.29	20.41	21.11	34.09	32.67	25.05	25.05	27.10
FeO	17.87	17.15	16.40	29.71	31.88	30.67	31.04	29.85	29.58	29.94	0.73	0.81	0.08	0.08	0.01
MnO	0.03	0.04	0.37	7.66	4.02	4.52	4.02	3.27	6.92	2.88	0.05	0.00	0.10	0.00	0.08
MgO	9.39	10.33	9.98	3.12	4.64	4.36	4.58	4.25	3.52	4.13	0.40	0.73	0.00	0.00	0.00
CaO	0.25	0.18	0.07	1.85	1.85	2.11	2.07	2.90	1.41	3.39	0.04	0.14	6.25	6.27	9.04
Na2O	0.09	0.13	0.07	0.00	0.04	0.26	0.42	0.00	0.00	0.26	0.54	0.51	8.28	7.95	6.75
K2O	9.93	9.83	9.50	0.00	0.00	0.05	0.10	0.05	0.00	0.01	10.61	10.19	0.20	0.35	0.06
Total	94.50	96.89	95.40	100.92	100.49	100.05	100.05	99.76	99.99	99.36	93.93	92.48	100.15	100.03	99.90
Si	2.69	2.66	2.74	2.92	2.96	2.96	2.90	3.03	3.03	3.00	3.09	3.04	2.68	2.68	2.56
Ti	0.19	0.20	0.20	0.00	0.00	0.00	0.00	0.00	0.02	0.00	0.08	0.17	0.00	0.00	0.00
Al	1.68	1.73	1.66	2.06	1.94	1.96	1.98	1.99	1.93	1.99	2.71	2.65	1.32	1.32	1.44
Fe3+	0.00	0.00	0.00	0.11	0.14	0.17	0.29	0.00	0.00	0.05	0.00	0.00	0.00	0.00	0.00
Fe2+	1.15	1.06	1.03	1.87	1.97	1.87	1.77	1.98	1.99	1.95	0.04	0.05	0.00	0.00	0.00
Mn	0.00	0.00	0.02	0.52	0.27	0.30	0.27	0.22	0.47	0.20	0.00	0.00	0.00	0.00	0.00
Mg	1.07	1.14	1.11	0.37	0.55	0.52	0.54	0.50	0.42	0.49	0.04	0.08	0.00	0.00	0.00
Ca	0.02	0.01	0.01	0.16	0.16	0.18	0.18	0.25	0.12	0.29	0.00	0.01	0.30	0.30	0.44
Na	0.01	0.02	0.01	0.00	0.01	0.04	0.07	0.00	0.00	0.04	0.07	0.07	0.72	0.69	0.59
K	0.97	0.93	0.91	0.00	0.00	0.01	0.01	0.01	0.00	0.00	0.91	0.89	0.01	0.02	0.00
Sum	7.78	7.75	7.69	8.00	8.00	8.00	8.00	7.98	7.98	8.00	6.96	6.95	5.03	5.01	5.02
Oxygen	11.00	11.00	11.00	12.00	12.00	12.00	12.00	12.00	12.00	12.00	11.00	11.00	8.00	8.00	8.00

Table 1.8: Core Unit additional EMPA Part 3

Unit	Sample	Notes	Temp (℃)	Pressure (Kbar)
Koronos	TLN22	Inner Rim	650	10.05
Koronos	TLN22	Core	627	10.37
Koronos	TLN22	Outer rim	496	5.09
Koronos	TLN22	Mid rim	601	8.3
Koronos	TLN22	Int	626	9.42
Koronos	TLN22	Core	649	8.89
Koronos	TLN22	Rim	615	7.34
Koronos	TLN22	Rim	480	2.94
Koronos	TLN22	Int	649	8.89
Koronos	TLN22	Core	606	7.97
Koronos	TLN22	Rim	622	6.98
Koronos	TLN22	Rim	631	8.32
Koronos	TLN22	Core Int	622	9.09
Koronos	TLN22	Rim	559	5.59
Koronos	TLN21	Inner Rim	744	9.5
Koronos	TLN21	Inner Rim	724	10.13
Koronos	TLN21	Inner Rim	725	10.4
Koronos	TLN21	Inner Rim	691	10.27
Koronos	TLN21	Inner Rim	737	10.37
Koronos	TLN21	Outer Rim	667	7.05
Koronos	TLN21	Inner Rim	713	9.12
Koronos	TLN21	Core	627	5.63
Koronos	TLN21	Outer Rim	671	6.62
Koronos	TL67	Inner Rim	773	12.12
Koronos	TL67	Core	700	11.12
Koronos	TL67	Int	688	10.07
Koronos	TL67	Core	660	9.93
Koronos	TL67	Outer Rim	750	10.67
Koronos	TL67	Inner Rim	696	9.78
Koronos	TL67	Grt Core	627	9.24
Koronos	TL67	Grt Core-Int	688	11.2
Koronos	TL67	Grt Rim	769	12.7
Core	TL15	Core	609	9.87
Core	TL15	Int	689	9.73
Core	TL15	Inner Rim	654	10.38
Core	TL15	Core	668	8.4
Core	TL15	Outer Rim	556	5.34
Core	TL15	Outer Rim	607	7.22
Core	TL15	Outer Rim	661	8.1
Core	TL15	Inner Rim	670	10.63
Core	TL15	Outer Rim	581	6.18
Core	TL66	Inner Rim	690	6.88
Core	TL66	Inner Rim	638	7.08
Core	TL66	Inner Rim	678	6.65
Core	TL66	Outer Rim	545	4.49
Core	TL66	Core	678	7.12
Core	TL66	Core	677	7.02
Core	TL66	Outer Rim	658	5.56
Core	TL66	Outer Rim	496	3.87
Core	TL66	Outer Rim	651	4.45
Core	TLN34	Core	671	2.31
Core	TLN34	Int	693	0.77
Core	TLN34	Core	628	2.94
Core	TLN34	Rim	538	1.09

Table 1.9: Naxos GASP thermobarometry results

Appendix 2: Geochronology

2.1 Geochronology

The field of geochronology has immensely evolved in the last 150 years since physicist William Thompson's (who later become known as Lord Kelvin) landmark paper suggesting the age of the earth was between 24 and 400 Ma, based upon the time scale required to cool a homogeneous molten Earth to its surrounding temperature (Kelvin, 1863). Although a breakthrough at the time, crucially what Kelvin did not consider was convection in a layered earth, nor did he contemplate any additional heat sources in his calculation. Therefore, even the oldest possible age he derived was still an order of magnitude too small to account for many observed geological phenomena as summarised by James Hutton's famous quote "No vestige of a beginning, no prospect of an end.". It was only some 30 years later, that radioactive decay was discovered accidently by French chemist Henri Becquerel, whilst investigating phosphorescence in uranium salts (Becquerel, 1896). Although the "young earth" problem was eventually solved by John Perry, who took into account mantle convection (Perry, 1895a, b, c); if radiogenic heating was added to his calculations it would have given an even better result. Radioactive decay has subsequently had a major impact on the field of geology as it provides a means by which the age of the Earth or individual rocks sampled from it can be determined absolutely. It therefore represents a tool that allows us to determine the rates of tectonic processes to an extremely high level of accuracy and was used extensively in this thesis.

2.1.1 The principles of radioactive decay

Radioactive decay describes the probability that a constituent particle of the nucleus of an atom will overcome the potential energy barrier binding it to the nucleus, thus escaping the atom and creating a new nuclide. The rate of radioactive decay is exponential and is independent of varying physical or chemical conditions that may occur in the earth (Rutherford and Soddy, 1902). A radioactive atom at the start of a decay chain is called the "parent" and ultimately produces a stable "daughter" atom at the end of the decay chain, with several intermediate radioactive nuclides in between, The decay rate of a parent atom is directly proportional to the number of those atoms (N) present in the system at any time (t) through the relationship:

$$-\frac{dN}{dt} \propto N \tag{1}$$

The variation in decay rate of various elements is associated with a decay constant (λ), which is assumed to be constant over all of geological time:

$$-\frac{dN}{dt} = \lambda N \tag{2}$$

Rearrangement of the equation to relate to the number of parent atoms present at any time since the decay started to the initial number of parent atoms (N_0) yields:

$$\frac{N}{N_0} = e^{-\lambda t} \tag{3}$$

If there is no radiogenic daughter present at the start of the decay (at t = 0) then the total number of atoms produced by the decay (D*) at any time can be related to (N_0) through the expression:

$$D^* = N_0(1 - e^{-\lambda t}) \tag{4}$$

Alternatively, if the original number of parent atoms is unknown, D* can be related to simply N by re-arranging and substituting equation (known as 'the age equation):

$$D^* = N(e^{\lambda t} - 1) \tag{5}$$

This latter case is relevant to most geological problems, and the total number of atoms present in the system (D_{tot}) is simply the addition of the atoms initially present at the start of the decay chain (N_0) and those that have been produced by the decay process:

$$D_{tot} = D_0 + N(e^{\lambda t} - 1) \tag{6}$$

The analysis of a sample by mass spectrometry allows the measurement of Dtot and N, whereas D_0 can be assumed or calculated based on the behaviour of the individual metamorphic minerals. Because the decay constant for a particular radioactive isotope is known, this equation may then be resolved for t, thereby allowing the calculation of the time since decay was initiated using the rearranged equation:

$$t = \frac{1}{\lambda} ln(\frac{D_{tot} - D_0}{N} + 1) \tag{7}$$

2.2 U–Th–Pb Geochronology

Uranium has three naturally occurring radioactive isotopes ^{238}U, ^{235}U and ^{234}U; only ^{238}U and ^{235}U have slow enough decay to be useful to geochronology on the million-year time scale. Ultimately these two parent isotopes produce daughter isotopes ^{206}Pb and ^{207}Pb through the 'uranium Series' and 'actinium series' decay chains respectively, whereas ^{234}U exists as solely an intermediate nuclide in the uranium series. Thorium exists in nature almost exclusively as ^{232}Th and produces the stable daughter nuclide ^{208}Pb through the 'thorium series' decay chain. The total decay chains for these radioactive nuclides involves the emission of α and β radiation with energies shown in

the reactions below:

$$^{238}U \rightarrow^{206} Pb + 8\alpha + 6\beta^{-} + 47.4\text{MeV/atom} \tag{8}$$

$$^{235}U \rightarrow^{207} Pb + 7\alpha + 4\beta^{-} + 45.2\text{MeV/atom} \tag{9}$$

$$^{232}Th \rightarrow^{208} Pb + 6\alpha + 4\beta^{-} + 39.8\text{MeV/atom} \tag{10}$$

Although intermediate daughter nuclide exists in these decay schemes, the half lives of the parent U and Th isotopes are several orders of magnitude greater than these intermediate products (Faure, 1986). Therefore, the production rate of each stable Pb isotope is limited by the decay of each parent, thus U and Th are effectively considered to decay directly to Pb over timescales >600,000 years in a state of secular equilibrium.

The production of each Pb isotope is defined by the governing equations presented below where concentrations are normalised to ^{204}Pb, the only non-radiogenic lead isotope (Faure, 1986):

$$\frac{^{206}Pb}{^{204}Pb_t} = \frac{^{206}Pb}{^{204}Pb_0} + \frac{^{238}Pb}{^{204}Pb_t}(e^{-\lambda_{238}t} - 1) \tag{11}$$

$$\frac{^{207}Pb}{^{204}Pb_t} = \frac{^{207}Pb}{^{204}Pb_0} + \frac{^{235}Pb}{^{204}Pb_t}(e^{-\lambda_{235}t} - 1) \tag{12}$$

$$\frac{^{208}Pb}{^{204}Pb_t} = \frac{^{208}Pb}{^{204}Pb_0} + \frac{^{232}Pb}{^{204}Pb_t}(e^{-\lambda_{232}t} - 1) \tag{13}$$

Using these equations and solving for time, three independent ages maybe obtained. If a sample yields ages from all three that overlap within the uncertainty of the measurement, they are referred to as concordant. Where these ages don not agree they are termed discordant, and the processes leading to this discordance could be due to several factors discussed below.

2.2.1 Sample preparation

All U–Pb analytical work in this thesis was carried out at the Natural Environment Research Council (NERC) Isotope Geosciences Laboratory (NIGL), Keyworth, Nottingham. Granite, gneiss, amphibolite, gabbro and plagiogranite samples were crushed using standard techniques (Jaw-crushing, disc milling, sieving, Rogers table, heavy liquids, Frantz magnetic separation). Approximately 40 zircons from each sample were then picked under alcohol and mounted in 1-inch epoxy resin mounts and polished until all grains were exposed. All monazite, allanite, xenotime and rutile analyses were performed in-situ from polished thin sections to provide textural context of resultant U–Pb ages.

Chemical and textural analysis of all zircon, monazite and allanite grains was performed on a LEO (Zeiss) 435VP Variable Pressure Digital Scanning Electron Microscope (SEM) operated in backscatter detection mode (20 kV accelerating voltage, 3.6–3.7 nA beam current at 19 mm working distance). Backscatter images reflect variations in the relative concentrations of high-atomic number elements (REEs + U and Th) between individual micro-domains. Element maps and further imaging was performed on a FEI Quanta 600 ESEM and a Cameca microprobe, by using the same techniques and working conditions as described in Appendix 1 but running under high current (>150 nA at 15 KV) and small step size (0.2 μm). Enhanced contrast backscattered electron (BSE) images, which primarily highlight variations in Th content (Gibson et al., 2004) were produced to aid identification of internal compositional domains where present. Complexities in zircon growth patterns were identified prior to analysis by careful cathodoluminescence (CL) imaging of zircon grains, and element maps (using EDS +/- WDS) were collected for selected in-situ monazite and allanite grains from thin section highlighting zoning of REEs and domains with variations in Y content. Locations of ablation spots for geochronological work were chosen to ensure separate domains could be analysed, therefore minimizing the potential mixing of different ages.

2.2.2 Tinos samples analytical procedures

U–Pb geochronology was performed in three separate sessions the Tsiknias ophiolite rocks and metamorphic sole in one session during August 2017 whereas the granites where analysed during August 2017 and August 2018. Due to the rare occurrence of zircon in ophiolitic rocks, approximately 10-20 kg of each sample was crushed to ensure sufficient extraction of enough zircon. Zircons from each successful sample were then picked under alcohol and mounted in 1-inch epoxy resin mounts and polished until all grains were exposed. All imaging was performed on a FEI Quanta 600 ESEM. Complexities in zircon growth patterns were identified prior to analysis by careful cathodoluminescence CL imaging of zircon grains. Locations of ablation spots for geochronological work were chosen to ensure separate domains could be analysed, therefore minimizing the potential mixing of different ages. Some zircon grains were analysed by placing the grains on double-sided tape, after rinsing with weak nitric acid, and ablating directly on the surface of the grains.

Zircon grains were successfully extracted from three key samples within the ophiolite suit and underlying metamorphic sole and include a plagiogranite intrusion (17TL-35), a gabbro (17TL-27) and a leucodiorite melt sweat from amphibolites at the highest-grade part of the metamorphic sole (17TL-26). Whereas zircon was abundant in the granites with the exception of the Grt bearing leucogranites at Livada Bay.

U–Pb geochronology was conducted using a Nu Instruments Attom HR sector-field single-collector inductively coupled plasma mass spectrometer (SC-ICP-MS). Laser ablation was performed with a New Wave Research 193UC laser ablation system, using a New Wave Research TV2 cell; this features a moveable cup with an ablation volume of ca. 1 cm^3. The analytical protocol is previously described for zircon (Spencer et al., 2015). A standard-sample-bracketing technique was used to normalise the data, this involved calculation of normalisation factors based on the of the measured/accepted value for the $^{207}Pb/^{206}Pb$ and $^{206}Pb/^{238}U$ ratios of the reference material, analysed at regular intervals during each session. The Nu Attom ICP-MS was used in peak-jumping mode with measurement on a MassCom secondary electron multiplier (SEM). The fol-

lowing masses were measured in each sweep: ^{202}Hg, ^{204}Pb+Hg, ^{206}Pb, ^{207}Pb, ^{208}Pb, ^{232}Th, and ^{235}U. Each data integration records 80 sweeps of the measured masses, which roughly equates to 0.3 seconds. Because ^{235}U is measured, ^{238}U is calculated from ^{235}U *137.818 (Hiess et al., 2012).

Laser ablation parameters were 15 μm or 25 μm (depending on the session) static spots, a fluence of 2.0–2.5 J/ cm^2, an ablation time of 20 s, a repetition rate of 5 Hz, and a 5 s washout between ablations. A 60 s on-peak gas blank is taken before every set of standard and sample ablations. U–Pb data were normalized to the average 'normalization factor', i.e. drift-corrected measured/accepted value, for zircon reference materials 91500, GJ-1 and Plešovice.

A ^{207}Pb based common lead correction utilises the measured ^{207}Pb/^{206}Pb ratios, and an assumed ^{207}Pb/^{206}Pb ratio of common lead to calculate the proportion of common ^{206}Pb was used. This correction assumes that the U-Pb data are concordant and is useful in young grains where accurate knowledge of the $^{206Pb}/^{238}$U is required. The Stacey and Kramers (1975) model composition is used in calculating these common lead corrections and an initial age estimate is based on regression in a Tera-Wasserburg diagram. Another correction is made to the common-lead corrected ages to account for any excess ^{206}Pb that is derived from ^{230}Th, an intermediate daughter nuclide of the ^{238}U decay series. This correction involves estimation of the whole-rock Th/U ratio. For full analytical conditions please consult the table below.

Data processing used the time-resolved analysis on the Nu Instuments' software, an in-house Excel spreadsheet for data reduction and uncertainty propagation (after Horstwood et al., 2016), and Isoplot (Ludwig, 2003) for data presentation. All data are plotted at the 2σ confidence interval.

Reproducibility of standards

2.2.3 Naxos sampes analytical procedures

In Chapter 5, Zircon grains from cross-cutting granites were analyzed during November 2016 from 8 samples at various levels of the core complex that show variable relation-

Laboratory Name	NERC Isotope Geosciences Laboratory
Minerals analysed	Zircon, monazite, allanite, rutile
Sample preparation	In situ/ polished thin sections (Monazite, Allanite, Rutile). Heavy liquid and magnetic separation (Zircon)
Imaging	X-ray mapping using Electron Microprobe Analysis (Oxford University, Oxford) or SEM with WDS capability (BGS, Keyworth)
Laser ablation system	
Make model and type	ESI/ New Wave Research 193UC
Ablation and cell volume	NWR TV2; washout time < 1sec.
Laser wavelength (nm)	193 nm
Pulse width (ns)	3-4 ns
Fluence (J cm-2)	2.5 J cm-2
Repetition rate (Hz)	5 Hz
Ablation duration (Sec)	Variable, see text
Ablation pit depth/ ablation rate	12 μm on standard zircon ablation (30 s)
Spot size	
Zircon	15-25 mm
Monazite	10-15 mm
Allanite	30 mm
Rutile	35 mm
Sampling mode/ pattern	Static spot ablation
Carrier gas	100% He, Ar make-up gas combined ca.50% along sample line.
Cell carrier gas flow (l/min) 0.7l/min	0.6l/min
ICPMS Instrument	
Make model and type	Nu Instruments Attom SC-SF-ICP-MS
Sample introduction	Free air aspiration of desolvator
RF power (W)	1300W
Make-up gas flow (l/min)	0.8l/min Ar
Detection system	Discrete dynode MassCom ion counter
Masses measured	202, 204, 206, 207, 208, 232, 235
Integration time per peak	200μs (202, 204, 206), 400μs (232, 208), 1000μs (207, 235) 80 sweeps per integration
Total integration time per reading (secs)	0.30 seconds
Sensitivity / Efficiency (%, element)	0.2% for Uranium
IC Dead time (ns)	15ns
Data Processing	In-house spreadsheet, Nu TRA software
Gas blank	60 second on-peak zero subtracted
Calibration strategy	
Monazite	Stern, Manangotry, Moacyr (Palin et al. 2013). Stern used as primary reference material for normalization others for check on accuracy.
Zircon	91500 (Wiedenbeck et al., 1995) used as primary reference material, GJ-1 (Jackson et al., 2004) and Plešovice (Sláma et al., 2008) used as secondary references materials.
Xenotime	FC-1 (55 Ma, in-house data)
Allanite	40010, Siss, Bona and Tara (Smye et al., 2014), Diabosatu
Rutile	Sugluck-4, PCA-S207 (Bracciali et al., 2013)
Data processing package used / Correction for LIEF	Nu Instruments TRA acquisition software, in-house spreadsheet data processing
Mass discrimination	207Pb/206Pb, 206Pb/238U and 208Pb/232Th normalised to reference material
Common-Pb correction, composition and uncertainty	Stacey & Kramers (1975) model composition, based on f206c, using estimated age derived from 206Pb/238U and f208c using measured 208Pb/206Pb.
Uncertainty level & propagation	Ages in the data table are quoted at 2sigma absolute, propagation is by quadratic addition. Excess variance of reference material is propagated.
Quality control / Validation	See below for validation results of standards. Reproducibility and accuracy on standards for all sessions 3% or under.

Table 2.10: Full Laboratory and analytical procedures for Tinos samples

Mineral	*Ref Mat.*	*206Pb/238U*	*2s*	*MSWD*	*n*
Zircon	91500	1055.6	4.4	2	40/40
Zircon	Ples	337.9	1.2	1.3	45/45
Zircon	GJ-1	603.8	2.2	0.91	40/40

Table 2.11: Reproducibility of standards for U-Pb zircon on Tinos

ships with the host rocks. These included; TL57, TL58, TL63, TL64, TL72, TLN8, TLN10. A 10 μm diameter spot size was used in order to target the thin zircon rims associated with dyke emplacement. Monazite grains were analyzed during three sessions from March 2015 to January 2017. Samples TL15, TL59, TL66 and TL67 were analyzed during session 1, samples TLN16 TLN18 TLN 20 TLN21 TLN34 TLN35 during session 2 and samples TLN13, TLN47 and TLN49 during session 3. Allanites were analyzed during a single session in January 2017 for 3 samples from the Zas Unit that attained blueschist-facies conditions. These included; TLN26, TLN30 and TLN54, for sample locations please consult Fig. 5.1. Rutile data was also collected from samples TL67 in the same session, in order to place constraints on the cooling and exhumation history of the core complex.

Data processing used the time-resolved analysis on the Nu Instuments' software, an in-house Excel spreadsheet for data reduction and uncertainty propagation, and Isoplot (Ludwig, 2003) for data presentation. All data are plotted at the 2σ confidence interval.

The Nu Attom ICP-MS was used in peak-jumping mode with measurement on a MassCom secondary electron multiplier (SEM). The following masses were measured in each sweep: ^{202}Hg, ^{204}Pb+Hg, ^{206}Pb, ^{207}Pb, ^{208}Pb, ^{232}Th, and ^{235}U (^{238}U for rutile analysis). Each data integration records 80 sweeps of the measured masses, which roughly equates to 0.3 seconds. Because ^{235}U is measured (except for rutile), ^{238}U is calculated from ^{235}U *137.818 (Hiess et al., 2012). For allanite and monazite, measurement of the larger signals (^{208}Pb and ^{232}Th) uses the Attom's attenuation mechanism so that these could be measured on the SEM. For samples with low Pb concentra-

tion, this leads to increased uncertainty on the 208Pb measurement, and thus worse precision on the Th–Pb ages.

Methods for zircon follow those described previously in Spencer et al. (2015). Laser ablation parameters were 15 μm or 25 μm (depending on the session) spots for zircon, a fluence of 2.0–2.5 J/ cm^2, an ablation time of 20 s, a repetition rate of 5 Hz, and a 5 s washout between ablations. A 60 s on-peak gas blank is taken before every set of standard and sample ablations. U–Pb data were normalized to the average 'normalization factor', i.e. drift-corrected measured/accepted value, for zircon reference materials 91500, GJ-1 and Plešovice.

For monazite, the ablation parameters were a 10μm or 15μm diameter spot, a repetition rate of 5 Hz, a fluence of 2.5 J/cm^2, a 5 s washout period between analyses, and a 15 s ablation time. Tuning was adopted that gave a ThO of <0.4% and UO of <0.1%. The monazite 'Stern' was used as a primary reference material with 'Manangotry' and 'Moacyr' (Palin et al., 2013; Mottram et al., 2014) used as the secondary reference materials in order to validate the precision and accuracy of each analytical session.

In-situ thin-section allanite geochronology was achieved following the methods and descriptions of Smye et al., (2014). Optimal signal strengths were attained using the following ablation parameters: 30 μm spot diameter; 5 Hz; 2.5 J/cm^2; 5 s wait between ablations to ensure sample washout and a 30 s ablation time. Oxide production was minimized by tuning the gas flows such that ThO <0.4%, and UO <0.1%. The primary reference material used was 40010, and Siss, Bona, Tara and Diabosatsu were used as secondary standards for validation.

Xenotime was analyzed using 15 μm spot sizes using the same methods as described for monazite. The reference materials used was FC-1.

For Rutile, 35 μm spot sizes were used due to low quantities of uranium and large inherent common-Pb and, methods are identical for zircon, except that ^{238}U is measured instead of ^{235}U, and sweep and dwell times are adjusted. Sugluk-4 was as a primary reference material, with a secondary reference material PCA-S207.

A ^{207}Pb based common lead correction utilises the measured ^{207}Pb/^{206}Pb ratios, and an assumed ^{207}Pb/^{206}Pb ratio of common lead to calculate the proportion of common ^{206}Pb was used. This correction assumes that the U-Pb data are concordant and is useful in young grains where accurate knowledge of the ^{206}Pb/^{238}U is required. The common Pb corrected ^{208}Pb/^{232}Th ages are calculated again assuming concordance and in a similar fashion. The Stacey and Kramers (1975) model composition is used in calculating these common lead corrections and an initial age estimate is based on regression in a Tera-Wasserburg diagram. Another correction is made to the common-lead corrected ages to account for any excess ^{206}Pb that is derived from ^{230}Th, an intermediate daughter nuclide of the ^{238}U decay series.

Both U–Pb and Th–Pb decay schemes can be used to date monazites (both common-Pb ages shown in full data tables). As excess ^{206}Pb can be incorporated into the monazite during crystallisation, this can cause the ^{238}U/^{206}Pb ages to appear older than the true crystallisation age, which is thought to be particularly significant in Cenozoic monazites (Parrish, 1990). The common-Pb-corrected ^{232}Th- ^{208}Pb ages have therefore been regarded as more accurate in some previous studies. Where U–Pb data do not allow interpretation of coherent populations, durations of crystallization are shown between generalized age limits; absolute uncertainties are provided only for regressed populations with a calculated MSWD value.

For monazite, U–Pb and Th–Pb data were collected for all samples. The preferential incorporation of Th in place of U can result in significant amounts of radiogenic ^{230}Th being incorporated during crystallization (Scharer, 1984). Consequently, the resultant excess daughter 206Pb causes calculated ^{238}U/^{206}Pb apparent ages to be older than the true crystallization age, and becomes increasingly significant in Cenozoic monazite (Scharer, 1984; Parrish, 1990). Because the Th–Pb system is unaffected by this initial disequilibrium, ^{232}Th/^{208}Pb ages are the most reliable estimates of the timing of monazite growth in these samples. We therefore discuss the interpreted ages for all samples with reference to both common-lead corrected (using a ^{207}Pb-based correction and assuming concordance) ^{238}U/^{206}Pb ages and ^{232}Th/^{208}Pb ages.

Full laboratory and analytical procedures Laboratory and Sample Preparation Table	
Laboratory Name	NERC Isotope Geosciences Laboratory
Minerals analysed	Zircon
Sample preparation	Whole rock, heavy liquid and magnetic separation (Zircon)
Imaging	Cameca 600 FEI Quanta SEM with WDS capability (BGS, Keyworth)
Laser ablation system	
Make model and type	ESI/ New Wave Research 193UC
Ablation and cell volume	NWR TV2; washout time < 1sec.
Laser wavelength (nm)	193 nm
Pulse width (ns)	3-4 ns
Fluence (J cm-2)	2.5 J cm-2
Repetition rate (Hz)	5 Hz
Ablation duration (Sec)	Variable, see text
Ablation pit depth/ ablation rate	12 μm on standard zircon ablation (30 s)
Spot size	
Zircon	15-25 mm
Sampling mode/ pattern	Static spot ablation
Carrier gas	100% He, Ar make-up gas combined ca.50% along sample line.
Cell carrier gas flow (l/min) 0.7l/min	0.6l/min
ICPMS Instrument	
Make model and type	Nu Instruments Attom SC-SF-ICP-MS
Sample introduction	Free air aspiration of desolvator
RF power (W)	1300W
Make-up gas flow (l/min)	0.8l/min Ar
Detection system	Discrete dynode MassCom ion counter
Masses measured	202, 204, 206, 207, 208, 232, 235
Integration time per peak	200μs (202, 204, 206), 400μs (232, 208), 1000μs (207, 235) 80 sweeps per integration
Total integration time per reading (secs)	0.30 seconds
Sensitivity / Efficiency (%, element)	0.2% for Uranium
IC Dead time (ns)	15ns
Data Processing	In-house spreadsheet, Nu TRA software
Gas blank	60 second on-peak zero subtracted
Calibration strategy	
Zircon	91500 (Wiedenbeck et al., 1995) used as primary reference material, GJ-1 (Jackson et al., 2004) and Plešovice (Sláma et al., 2008) used as secondary references materials.
Data processing package used / Correction for LIEF	Nu Instruments TRA acquisition software, in-house spreadsheet data processing
Mass discrimination	207Pb/206Pb and 206Pb/238U normalised to reference material
Common-Pb correction, composition and uncertainty	Stacey & Kramers (1975) model composition, based on f206c, using estimated age derived from 206Pb/238U
Uncertainty level & propagation	Ages in the data table are quoted at 2sigma absolute, propagation is by quadratic addition. Excess variance of reference material is propagated.
Quality control / Validation	See below for validation results of standards. Reproducibility and accuracy on standards for all sessions 3% or under.

Table 2.12: Laboratory and Sample Preparation Table for Naxos Samples

Uncertainty propagation followed the method of Horstwood (2008) and Horstwood et al., (2016), which includes a contribution from the external reproducibility of a reference material for the ratios $^{206}Pb/^{238}U$ and $^{208}Pb/^{232}Th$. This includes the internal uncertainty, i.e. the reproducibility of the measured ratios during an ablation, and addition of an excess variance uncertainty, which is based on the reproducibility of the bracketing reference material during each session; these were added in quadrature.

Mineral	*Ref Mat.*	*208Pb/232Th*	*2s*	*MSWD*	*n*	*206Pb/238U*	*2s*	*MSWD*	*n*
Monazite	FC-1	55.09	0.56	2.3	93/97	57.33	0.24	1.7	94.97
Monazite	Man	548.2	2.4	1	102/107	555	2	1.4	104/107
Monazite	Moacyr	506.8	2.4	1.4	110/117	498.9	2.4	2.4	115/117
Monazite	Stern	509.3	2.1	2.1	122/126	509.7	2.1	2	121/126
Allanite	40010	2715*	16	2.2	34/38	2758.4*	9.6	0.7	38/38
Allanite	Diabasotsu	12.52	0.2	14	33/34	12.32	0.2	15	33/34
Allanite	Tara	418	3.4	3	33/34	417	3.4	3.1	33/34
Xenotime	FC-1					53.8	0.3	0.6	16/16

Mineral	*Ref Mat.*	*207Pb/206Pb*	*2s*	*MSWD*	*n*	*206Pb/238U*	*2s*	*MSWD*	*n*
Zircon	91500	1066.2	4.5	1.6	65/68	1053.7	3.5	1.1	68/68
Zircon	Ples	343.7	5.1	1.6	62/67	339.2	1	0.9	67/67
Zircon	Qinghu	187.5#	9.4	1.7	38/41	160	0.8	1.1	37/41
Rutile	PCA	1991#	62	117	10-Nov	1888	49	6	11-Nov
Rutile	Sugluk-4	1738	4.9	1	09-Sep	1736	20	1	09-Sep
Rutile	R10	1118#	39	10	06-Jun	1086	28	3	06-Jun

Table 2.13: Reproducibility of standards for U-Th-Pb geochronology

2.3 Lu-Hf geochronology

The following summary of Lu–Hf geochronology is based largely after Vervoort, (2014). The Lu–Hf isotopic system takes advantage of variations in 176Hf due to radioactive decay of parent nuclide ^{176}Lu to daughter nuclide ^{176}Hf by beta decay with a half-life of 37.12 Ga defined by the following equation:

$$^{176}Lu \rightarrow ^{176}\ Hf + \beta^{-} \tag{14}$$

Only 1 % of ^{176}Hf in rocks and minerals is radiogenic and produced by the decay of Lu, thus the majority of ^{176}Hf is "common-Hf", produced mainly during nucleosynthesis. The radiogenic decay equation below describes the temporal evolution of radiogenic ^{176}Hf in a rock or mineral will due to the decay of ^{176}Lu:

$$^{176}Hf_{pres} = ^{176}\ Hf_{tot} + ^{176}\ Lu_{pres} * (e^{\lambda t} - 1) \tag{15}$$

This equation shows that the ^{176}Hf present in a sample today is a function of (i) the ^{176}Hf in that sample at some time, t, in the past; (ii) the amount of radiogenic ^{176}Lu in that material; (iii) the amount of time elapsed since formation; and (iv) the decay constant. In practice, we reference these isotopes to ^{177}Hf, a stable isotope of Hf. Therefore, the equation becomes:

$$\frac{^{176}Hf}{^{177}Hf}_{pres} = \frac{^{176}Hf}{^{177}Hf}_{tot} + \frac{^{176}Lu}{^{177}Lu}_{pres} (e^{-\lambda_{176} t} - 1) \tag{16}$$

Therefore, a material with high Lu/Hf ratios, such as garnet (see below), will generate proportionally more ^{176}Hf over time and evolve to higher^{176}Hf/^{177}Hf ratios. Conversely, the material with low Lu/Hf ratios, such as zircon, will produce less ^{176}Hf with time and so its ^{176}Hf/^{177}Hf ratio will increase only very slowly.

2.3.1 Lu–Hf garnet geochronology

Lutetium is the heaviest of the rare-earth elements (REEs), has a +3 valence and is partitioned into garnet most strongly of all the REEs. In contrast the daughter element Hf, is not a REE, but a high-field-strength element (HFSE) with a +4 valence and is only weakly incorporated into garnet. This different geochemical behaviour between Lu and Hf, causes strong fractionation in the Lu/Hf ratios in garnet, but also commonly results in Lu–Hf zoning in garnet. High Lu/Hf ratios usually occur in garnet cores, due to the strong incorporation of Lu during early garnet growth, and lower Lu/Hf ratios occur towards the rim due to the depletion of Lu. The high Lu/Hf in the garnet cores exert a strong control on the slope of the regression, and therefore it has been suggested that Lu/Hf ages will be biased toward the early stages of garnet growth (Lapen et al. 2003; Skora et al. 2006). Lu–Hf garnet ages are therefore expected to be slightly older compared with Sm–Nd ages in a slowly growing garnet (Lapen et al. 2003; Skora et al. 2006). The Lu–Hf isotopic system in garnet is also useful due to it having a high closure temperature (significantly higher than the Sm–Nd system), which makes the Lu–Hf garnet geochronology extremely useful.

2.3.2 Lu–Hf isochron method

Lu–Hf geochronology uses an "isochron" method to calculate absolute ages. Unlike U–Pb systematics in e.g. zircon where there is little, if any, daughter isotope at the time of mineral growth, in the Lu–Hf system, some daughter isotopes are always present (i.e., "common Hf"). It is therefore impossible to determine the age of a single mineral sample by measuring the accumulation of daughter isotopes in the sample. Therefore Lu–Hf geochronology uses an isochron approach, which utilizes coexisting rocks and minerals to determine an age.

Several important assumptions are used in this approach. These include: (1) All the minerals formed at the same time (i.e., have the same age); (2) all samples are cogenetic i.e. have the same isotopic composition at the time of formation; (3) the

sample has been in a closed system since the time of mineral growth. The systematics of the Lu–Hf isochron method in garnet also requires (1) Prior to mineral formation, whether in a magma or metamorphic protolith, the bulk rock has a low Lu/Hf ratio and (at least approximately) a uniform Hf isotopic composition at the hand sample scale. (2) During crystallization, or, in this example, metamorphism, different phases form with different Lu/Hf ratios, but all with the same initial $^{176}Hf/^{177}Hf$. (3) Over time, the Hf isotopic compositions of the different components evolve as a function of their Lu/Hf concentrations. High ratios of Lu/Hf evolve more quickly than $^{176}Hf/^{177}Hf$ and low Lu/Hf ratios evolve more slowly. (4) At some later time, if the rock has been a closed system with respect to Lu and Hf, all components will have compositions that plot along a line that is a function of time.

Regression of a line through these points yields a slope from which an age can be calculated using the formula:

$$Age = \frac{1}{\lambda_{Lu}^{176}} ln(\text{slope} + 1) \tag{17}$$

And for a special case where there are only two points (i.e. sample TLT13 in chapter 2) this reduces to:

$$Age = \frac{1}{\lambda_{Lu}^{176}} ln((\frac{(\frac{^{176}Hf}{^{177}Hf}_2) - (\frac{^{176}Hf}{^{177}Hf}_1)}{(\frac{^{176}Lu}{^{177}Hf}_2) - (\frac{^{176}Lu}{^{177}Hf}_1)} + 1) \tag{18}$$

Although a very powerful tool, unfortunately many of the assumptions of the garnet isochron method are not strictly met. In most cases the rock is certainly not in perfect isotopic equilibrium (i.e., homogeneous $^{176}Hf/^{177}Hf$) prior to metamorphism. In addition, the time different phases in the rock form may not be precisely the same, especially in the case of prolonged garnet growth (e.g., Kohn 2009). These can be serious obstacles if there is a small range of Lu/Hf and $^{176}Hf/^{177}Hf$ variations in samples but are often overcome in isochrons with high Lu/Hf phases and large amounts of radiogenic Hf ingrowth.

2.3.3 Methodology

All preparation and analyses were undertaken at the Natural Environment Research Council Isotope Geosciences Laboratory (NIGL) and the Department of Earth Sciences, University of Oxford under the supervision of Dr Ian Millar and Dr Nick Roberts. Whole-rock powders were crushed using a steel jaw crusher and further ground using a disk mill. An aliquot of crushed material was used to determine a whole-rock isotopic composition. The remaining crushed material was split into various grain-size fractions depending on the garnet size within the sample by sieving, then the garnets were separated using a Frantz Isodynamic magnetic separator and heavy liquid (di-iodomethane; S.G. = 3.3) density separation. The cleanest and most inclusion-free garnet fragments were then hand-picked under a binocular microscope.

Garnet fractions were crushed using an agate mortar and pestle under acetone, then pipetted into pre-weighed Savillex teflon beakers, and dried. Whole-rock fractions were weighed directly into cleaned Savillex beakers. All laboratory Teflon-ware was precleaned in concentrated hydrochloric and nitric acids for several days at 170°C prior to use. 2 ml of concentrated nitric acid was added to the garnet samples and heated at 160°C for 40 minutes to leach any REE-rich phosphate inclusions. After centrifuging and rinsing to remove the nitric acid, the garnet samples were dried and re-weighed. Mixed ^{176}Lu-^{180}Hf spikes with appropriate elemental ratios were added to garnet and whole-rock samples.

Spiked samples were dissolved in 2 ml of 16 M HNOtextsubscript3 and 6 ml of 29 M HF for 48 hours at 170°C. 1.5ml of 16m HNO_3 followed by 1 ml of distilled HClO4 were added to the samples to remove any fluorides and dried at 150°C. Finally, 5 mls of 8 M HCl was added to convert the samples to chloride form. All evaporations were carried out in an Analab Evapoclean system.

Primary ion exchange columns consisting of 2 mls of Dowex AG50-X8 ion exchange resin were used to separate high field strength element (HFSE), light rare earth element (LREE) and heavy rare earth element (HREE) fractions. LREE fractions were reserved for future Sm-Nd analysis if required. Hf was separated from the HFSE

fraction using 1ml LN-SPEC columns, broadly following the method of Münker et al. (2001). After elution of matrix elements using 6M HCl, Ti was quantitatively removed by repeated elution in a citric acid-nitric acid-peroxide mixture. Zr was eluted using 6M HCl-0.06M HF, and finally, Hf was collected by elution with 6M HCl – 2M HF. Lu was separated from the HREE fraction using 2 ml LN-SPEC columns. Lu fractions were dissolved in 1 ml of 2% HNO_3 prior to analysis on a Thermo-Electron Neptune mass spectrometer, using a Cetac Aridus II desolvating nebuliser. 0.006 l/min of nitrogen were introduced via the nebulizer in addition to Ar in order to minimise oxide formation. The instrument was operated in static multicollection mode, with cups set to monitor ^{176}Er, ^{177}Er, ^{172}Yb, ^{173}Yb, ^{175}Lu, ^{176}Lu+Hf+Yb, ^{177}Hf and ^{179}Hf. Jet sample cones and X-skimmer cones were used, giving a typical signal of c. 600 V/ppm Lu. 1% dilutions of each sample were tested prior to analysis, and samples diluted to c. 20ppb prior to the addition of c. 20ppb of Er. Data reduction followed Lapen et al. 2004, using a ratio of 0.6841 for ^{167}Er/^{166}Er to correct ^{176}Lu/^{175}Lu for mass fractionation using an exponential law. ^{176}Yb and ^{176}Hf interferences on ^{176}Lu were monitored using ^{173}Yb and ^{177}Hf respectively; ^{176}Yb/^{173}Yb and ^{176}Hf/^{177}Hf were corrected for mass bias using ^{167}Er/^{166}Er = 0.6841 before interference corrections were made.

Hf fractions were dissolved in 1 ml of 2% HNO_3 + 0.1M HF, prior to analysis on a Thermo-Electron Neptune mass spectrometer, using A Cetac Aridus II desolvating nebuliser. 0.006 l/min of nitrogen were introduced via the nebulizer in addition to Ar in order to minimise oxide formation. The instrument was operated in static multicollection mode, with cups set to monitor ^{172}Yb, ^{173}Yb, ^{175}Lu, ^{176}Lu+Hf+Yb, ^{177}Hf, ^{178}Hf, ^{179}Hf and ^{180}Hf. 1% dilutions of each sample were tested prior to analysis, and samples diluted to c. 20ppb. Jet sample cones and X-skimmer cones were used, giving a typical signal of c. 800-1000 V/ppm Hf. Correction for ^{176}Yb on the ^{176}Hf peak was made using reverse-mass-bias correction of the ^{176}Yb/^{173}Yb ratio empirically derived using Hf mass-bias corrected Yb-doped JMC475 solutions (Nowell and Parrish, 2001). ^{176}Lu interference on the ^{176}Hf peak was corrected by using the measured ^{175}Lu and assuming ^{176}Lu/^{175}Lu = 0.02653. The column procedure used to separate Hf effectively

removes most Yb and Lu, so these corrections are minimal. Spike-stripping was carried out using an iterative algorithm. Data are reported relative to $^{179}Hf/^{177}Hf = 0.7325$.

The Hf standard solution JMC475 was analyzed during each analytical session and sample $^{176}Hf/^{177}Hf$ ratios are reported relative to a value of 0.282160 for this standard (Nowell and Parrish, 2001). Eleven analyses of JMC475 gave a mean $^{176}Hf/^{177}Hf$ value of 0.282143 ± 0.000005 (1-sigma). Isochron ages and uncertainties were calculated using Isoplot version 4.15(Ludwig 2011) with the decay constant of 1.865×10^{-11} a^{-1} for ^{176}Lu (Scherer et al. 2001).

Although every care was taken to remove inclusions, unfortunately the total dissolution of garnet naturally incorporates some inclusions, which can affect Lu–Hf analyses (e.g. Scherer et al. 2000; Anczkiewicz and Thirlwall 2003). Lu–Hf age systematics are affected by zircon and rutile inclusions, with the former representing

1 wt.% Hf, or rutile, which can often be volumetrically significant and have a

50 times higher Hf concentration than coexisting garnet. Establishing the Hf ratios of the zircon inclusions within the garnets was not a part of this work, but the effect is likely to be low owing to the minimal observed zircon in thin section due to the mafic composition of the dated rocks.

2.3.4 Additional U-Pb analysis

Rock type	Sampl	Analysis	comments	204Pb cps	206Pb cps	207Pb cps	208Pb cps	232Th cps	238U cps	Th/U	Pb ppm	Th ppm	U ppm	238U/206Pb	1s %	207Pb/206Pb	1s %	207Pb/235U	1s %	206Pb/238U	1s %	Rho	207Pb/206Pb Age	2s abs	206Pb/238U Age	2s abs	207Pb/235U Age	2s abs	Disc. % 6-38/7-35	Cor.206/238-Pb Age	2s [Ma]
North Tinos psammite	17TL43	17TL 43.01		bd	184101	20515	51977	331590	756220	0.65	67.0	163.5	250.9	4.49	1.93	0.1103	0.64	3.3896	2.03	0.2230	1.93	0.95	1804.6	23.2	1297.5	45.3	1502.0	31.4	13.6	1258.9	42.6
North Tinos psammite	17TL43	17TL 43.02		bd	280364	15252	8348	293361	4861728	0.09	79.4	144.6	1613.0	19.07	1.12	0.0532	0.76	0.3846	1.35	0.0524	1.12	0.83	337.5	34.4	329.5	7.2	330.4	7.6	0.3	329.4	7.2
North Tinos psammite	17TL43	17TL 43.03		bd	122145	6991	14554	357669	1458730	0.36	37.5	176.3	484.0	13.04	1.22	0.0562	1.00	0.5942	1.58	0.0767	1.22	0.77	461.4	44.5	476.2	11.2	473.5	11.9	-0.6	476.5	11.2
North Tinos psammite	17TL43	17TL 43.04		bd	437884	23478	34649	1319199	8267805	0.24	129.5	650.4	2743.0	20.75	1.19	0.0524	0.77	0.3478	1.42	0.0482	1.19	0.84	301.2	35.2	303.4	7.0	303.0	7.4	-0.1	303.4	7.0
North Tinos psammite	17TL43	17TL 43.05		bd	321827	17196	29935	1103346	5961869	0.28	96.4	544.0	1978.0	20.42	1.18	0.0530	0.88	0.3576	1.47	0.0490	1.18	0.80	327.5	40.1	308.3	7.1	310.4	7.9	0.7	308.1	7.1
North Tinos psammite	17TL43	17TL 43.06		bd	177095	9495	18135	676975	3288490	0.31	53.5	333.8	1091.0	20.28	1.14	0.0524	0.96	0.3561	1.49	0.0493	1.14	0.77	302.8	43.6	310.3	6.9	309.3	7.9	-0.3	310.4	6.9
North Tinos psammite	17TL43	17TL 43.07		bd	17470	973	2917	95266	286760	0.49	5.6	47.0	95.1	17.80	1.47	0.0552	1.43	0.4275	2.05	0.0562	1.47	0.71	420.5	64.0	352.4	10.0	361.4	12.4	2.5	351.7	10.0
North Tinos psammite	17TL43	17TL 43.08		bd	222782	25336	54037	453249	925446	0.73	78.9	223.5	307.0	4.58	2.38	0.1128	0.80	3.3970	2.51	0.2185	2.38	0.95	1845.1	29.1	1274.0	54.8	1503.7	38.7	15.3	1231.0	51.2
North Tinos psammite	17TL43	17TL 43.09		bd	157533	10895	57234	630665	1114358	0.84	58.9	310.9	369.7	7.62	2.53	0.0699	1.14	1.2643	2.77	0.1313	2.53	0.91	925.2	46.9	795.0	37.7	829.8	31.0	4.2	791.1	37.3
North Tinos psammite	17TL43	17TL 43.10		bd	225077	12755	18087	443845	2863881	0.23	66.8	218.8	950.1	13.87	1.14	0.0556	0.82	0.5527	1.40	0.0721	1.14	0.81	437.5	36.3	448.8	9.9	446.8	10.1	-0.4	448.9	9.9
North Tinos psammite	17TL43	17TL 43.11		bd	62483	3698	5240	151583	1092022	0.21	18.7	74.7	362.3	19.08	1.16	0.0558	1.29	0.4033	1.74	0.0524	1.16	0.67	446.0	57.4	329.3	7.5	344.0	10.1	4.3	328.1	7.4
North Tinos psammite	17TL43	17TL 43.12		bd	113718	7169	26354	481542	1007734	0.71	38.5	237.4	334.3	9.65	1.23	0.0621	0.92	0.8876	1.54	0.1036	1.23	0.80	678.8	39.5	635.7	14.8	645.1	14.6	1.4	634.8	14.8
North Tinos psammite	17TL43	17TL 43.13		bd	73308	4183	4293	107952	901020	0.18	21.4	53.2	298.9	13.37	1.25	0.0561	1.28	0.5782	1.79	0.0748	1.25	0.70	456.2	56.6	464.9	11.2	463.3	13.2	-0.4	465.0	11.2
North Tinos psammite	17TL43	17TL 43.14		bd	38155	2261	5284	125120	499064	0.37	11.9	61.7	165.6	14.22	1.60	0.0579	1.16	0.5609	1.98	0.0703	1.60	0.81	525.8	50.7	438.0	13.6	452.1	14.3	3.1	436.8	13.5
North Tinos psammite	17TL43	17TL 43.15		bd	71840	4039	756	19960	1163238	0.03	20.0	9.8	385.9	17.69	1.33	0.0557	0.99	0.4338	1.66	0.0565	1.33	0.80	440.0	44.0	354.4	9.2	365.9	10.1	3.1	353.5	9.1
North Tinos psammite	17TL43	17TL 43.16		bd	128701	7489	4891	114915	1459101	0.12	36.8	56.7	484.1	12.38	1.11	0.0571	0.80	0.6353	1.37	0.0808	1.11	0.81	494.1	35.1	500.8	10.7	499.4	10.7	-0.3	500.9	10.7
North Tinos psammite	17TL43	17TL 43.17		bd	264200	15922	78157	1631818	2738658	0.89	93.6	804.5	908.6	11.24	1.34	0.0583	0.89	0.7150	1.61	0.0890	1.34	0.83	541.6	39.0	549.4	14.1	547.7	13.5	-0.3	549.5	14.1
North Tinos psammite	17TL43	17TL 43.18		bd	461798	24789	42153	1636011	8586092	0.28	138.1	806.6	2846.8	20.42	1.14	0.0527	0.77	0.3558	1.37	0.0490	1.14	0.83	316.8	35.0	308.2	6.9	309.1	7.3	0.3	308.2	6.9
North Tinos psammite	17TL43	17TL 43.19		bd	179316	10352	3729	92320	2170941	0.06	50.5	45.8	720.1	13.18	1.13	0.0564	0.75	0.5898	1.36	0.0758	1.13	0.83	469.1	33.1	471.3	10.3	470.7	10.2	-0.1	471.3	10.3
North Tinos psammite	17TL43	17TL 43.20		bd	167483	13449	30379	269192	1341423	0.30	55.2	132.7	445.0	8.70	1.27	0.0775	0.82	1.2285	1.51	0.1150	1.27	0.84	1134.6	32.8	701.7	16.8	813.7	16.8	13.8	689.5	16.2
North Tinos psammite	17TL43	17TL 43.21		bd	109743	6418	23286	598696	1349693	0.66	36.4	295.2	447.8	13.24	1.12	0.0568	0.78	0.5912	1.37	0.0755	1.12	0.82	483.0	34.3	469.5	10.2	471.6	10.2	0.5	469.3	10.2
North Tinos psammite	17TL43	17TL 43.22		bd	228605	12746	5776	142990	2546684	0.08	64.5	70.5	844.9	12.33	1.17	0.0560	0.70	0.6259	1.36	0.0811	1.17	0.86	451.5	31.2	502.9	11.3	493.5	10.6	-1.9	503.7	11.3
North Tinos psammite	17TL43	17TL 43.23		bd	331634	22248	39556	505988	2654522	0.28	102.8	249.5	880.7	8.71	1.05	0.0658	0.57	1.0410	1.19	0.1148	1.05	0.88	800.5	23.9	700.4	13.9	724.4	12.3	3.3	697.9	13.8
North Tinos psammite	17TL43	17TL 43.24		bd	226264	12184	68046	2705767	4394178	0.92	80.0	1334.0	1457.9	20.94	1.11	0.0526	0.79	0.3461	1.36	0.0477	1.11	0.82	311.4	35.8	300.7	6.5	301.8	7.1	0.4	300.6	6.5
North Tinos psammite	17TL43	17TL 43.25		bd	60338	3292	12307	473078	1123765	0.63	19.8	233.2	372.8	20.08	1.17	0.0532	1.04	0.3654	1.56	0.0498	1.17	0.75	338.8	47.0	313.3	7.1	316.2	8.5	0.9	313.1	7.1
North Tinos psammite	17TL43	17TL 43.26		bd	116884	6446	24660	868177	2141745	0.60	38.7	428.0	710.6	20.05	1.40	0.0550	1.17	0.3781	1.82	0.0498	1.40	0.77	412.6	52.2	313.8	8.5	325.7	10.1	3.7	312.8	8.5
North Tinos psammite	17TL43	17TL 43.27		bd	267883	15893	5089	92768	3849691	0.04	75.4	45.7	1277.2	15.67	1.08	0.0577	0.76	0.5070	1.32	0.0638	1.08	0.82	516.7	33.4	398.7	8.4	416.4	9.0	4.3	397.3	8.3
North Tinos psammite	17TL43	17TL 43.28		bd	123114	7615	7513	112926	1592682	0.11	36.1	55.7	528.4	13.72	2.08	0.0603	0.82	0.6051	2.24	0.0729	2.08	0.93	612.6	35.4	453.4	18.2	480.4	17.0	5.6	451.1	18.0
North Tinos psammite	17TL43	17TL 43.29		bd	452162	25946	3161	72507	5637466	0.02	125.7	35.7	1870.3	13.45	1.01	0.0565	0.65	0.5791	1.20	0.0743	1.01	0.84	473.1	28.6	462.2	9.0	463.9	8.9	0.4	462.0	9.0
North Tinos psammite	17TL43	17TL 43.30		bd	344119	20821	16121	315809	3341706	0.14	99.5	155.7	1108.7	10.55	1.04	0.0598	0.62	0.7814	1.21	0.0948	1.04	0.86	597.0	26.8	583.8	11.6	586.3	10.8	0.4	583.5	11.6
North Tinos psammite	17TL43	17TL 43.31		bd	657133	35075	21343	843382	######	0.10	186.4	415.8	4100.1	20.23	1.07	0.0525	0.61	0.3575	1.23	0.0494	1.07	0.87	306.2	28.0	311.1	6.5	310.4	6.6	-0.2	311.1	6.5
North Tinos psammite	17TL43	17TL 43.32		bd	116628	6659	4409	105205	1413372	0.11	33.4	51.9	468.9	12.99	1.16	0.0566	0.69	0.6002	1.35	0.0770	1.16	0.86	474.0	30.4	478.2	10.7	477.3	10.2	-0.2	478.3	10.7
North Tinos psammite	17TL43	17TL 43.33		bd	124669	6629	24067	954196	2325071	0.61	40.6	470.4	771.4	20.09	1.09	0.0529	0.92	0.3628	1.43	0.0498	1.09	0.77	323.7	41.6	313.2	6.7	314.3	7.7	0.4	313.1	6.7
North Tinos psammite	17TL43	17TL 43.34		bd	234468	14004	14378	299439	2326343	0.19	68.6	147.6	771.8	10.83	1.07	0.0590	0.75	0.7508	1.31	0.0923	1.07	0.82	567.2	32.7	569.3	11.6	568.7	11.3	-0.1	569.3	11.6
North Tinos psammite	17TL43	17TL 43.35		bd	488303	28381	117454	4132670	9362601	0.66	165.6	2037.5	3106.2	20.57	1.26	0.0575	1.14	0.3851	1.70	0.0486	1.26	0.74	510.7	50.1	305.9	7.5	330.8	9.6	7.5	304.1	7.4
North Tinos psammite	17TL43	17TL 43.36		bd	458142	26555	28357	728191	5669495	0.19	134.0	359.0	1881.0	13.25	1.09	0.0574	0.60	0.5971	1.24	0.0755	1.09	0.88	506.7	26.5	469.1	9.9	475.4	9.4	1.3	468.6	9.8
North Tinos psammite	17TL43	17TL 43.37		bd	411657	25869	85971	1608743	3533440	0.68	136.7	793.2	1172.3	9.29	1.00	0.0618	0.58	0.9172	1.15	0.1076	1.00	0.86	668.4	24.9	659.0	12.5	660.9	11.2	0.3	658.8	12.5
North Tinos psammite	17TL43	17TL 43.38		bd	562026	29635	87514	3429898	######	0.49	177.4	1691.0	3473.0	20.02	1.14	0.0522	0.71	0.3597	1.34	0.0500	1.14	0.85	296.2	32.3	314.3	7.0	312.0	7.2	-0.7	314.4	7.0
North Tinos psammite	17TL43	17TL 43.39		bd	180914	11192	50093	979552	1656322	0.88	63.3	483.0	549.5	9.85	1.14	0.0609	0.60	0.8523	1.29	0.1016	1.14	0.89	635.4	25.8	623.6	13.6	625.9	12.0	0.4	623.3	13.6
North Tinos psammite	17TL43	17TL 43.40		bd	103683	5683	2858	87019	1626347	0.08	29.3	42.9	539.6	16.98	1.12	0.0533	0.86	0.4328	1.41	0.0589	1.12	0.79	342.4	38.9	369.0	8.0	365.2	8.6	-1.0	369.2	8.0
North Tinos psammite	17TL43	17TL 43.41		bd	141154	8078	3727	94101	1786072	0.08	39.9	46.4	592.6	13.65	1.09	0.0559	0.85	0.5642	1.39	0.0733	1.09	0.79	447.6	37.9	455.8	9.6	454.3	10.1	-0.3	455.9	9.6
North Tinos psammite	17TL43	17TL 43.42		bd	329611	18328	7270	195403	4999842	0.06	92.8	96.3	1658.8	16.41	1.07	0.0542	0.60	0.4556	1.23	0.0609	1.07	0.87	381.1	27.1	381.4	7.9	381.2	7.8	0.0	381.4	7.9
North Tinos psammite	17TL43	17TL 43.43		bd	381421	21534	10603	369867	6307118	0.09	108.0	182.4	2092.5	17.60	1.17	0.0544	0.67	0.4260	1.35	0.0568	1.17	0.87	387.7	30.0	356.2	8.1	360.3	8.1	1.1	355.9	8.1
North Tinos psammite	17TL43	17TL 43.44		bd	69870	4359	16792	314310	617011	0.76	23.8	155.0	204.7	9.55	1.22	0.0618	1.09	0.8922	1.63	0.1047	1.22	0.75	668.9	46.5	641.7	14.9	647.5	15.5	0.9	641.1	14.9
North Tinos psammite	17TL43	17TL 43.45		bd	214085	12740	5641	133788	2363091	0.08	60.7	66.0	784.0	12.10	1.15	0.0585	0.71	0.6665	1.35	0.0827	1.15	0.85	548.9	31.1	512.0	11.3	518.6	10.9	1.3	511.4	11.3
North Tinos psammite	17TL43	17TL 43.46		bd	182776	10401	22688	557527	2225998	0.37	56.4	274.9	738.5	13.09	1.28	0.0560	0.68	0.5898	1.44	0.0764	1.28	0.88	452.8	30.1	474.6	11.7	470.8	10.8	-0.8	475.0	11.7
North Tinos psammite	17TL43	17TL 43.47		bd	492347	28256	36761	892480	5992182	0.22	145.6	440.0	1988.0	13.14	1.13	0.0567	0.59	0.5945	1.28	0.0761	1.13	0.89	478.3	25.9	473.0	10.3	473.7	9.6	0.2	472.9	10.3
North Tinos psammite	17TL43	17TL 43.48		bd	133517	7705	9424	215954	1533970	0.21	39.3	106.5	508.9	12.48	1.15	0.0574	0.94	0.6335	1.49	0.0801	1.15	0.77	505.5	41.5	496.9	11.0	498.3	11.7	0.3	496.8	11.0
North Tinos psammite	17TL43	17TL 43.49		bd	96721	5584	15180	403096	1217126	0.49	30.7	198.7	403.8	13.68	1.21	0.0569	0.90	0.5736	1.51	0.0731	1.21	0.80	489.5	39.6	454.7	10.7	460.3	11.1	1.2	454.2	10.6
North Tinos psammite	17TL43	17TL 43.50		bd	125218	6732	17200	690692	2338188	0.44	39.0	340.5	775.7	20.50	1.13	0.0533	0.78	0.3585	1.37	0.0488	1.13	0.82	343.2	35.2	307.0	6.8	311.1	7.3	1.3	306.7	6.8
North Tinos psammite	17TL43	17TL 43.51		bd	167662	9794	6302	149021	2025701	0.11	48.0	73.5	672.1	12.98	1.12	0.0569	0.76	0.6041	1.36	0.0770	1.12	0.83	487.8	33.6	478.4	10.3	479.8	10.3	0.3	478.2	10.3
North Tinos psammite	17TL43	17TL 43.52		bd	95900	5916	12325	230627	834714	0.41	29.8	113.7	276.9	9.40	1.13	0.0609	0.95	0.8932	1.48	0.1063	1.13	0.77	637.2	40.9	651.5	14.0	648.1	14.0	-0.5	651.8	14.0
North Tinos psammite	17TL43	17TL 43.53		bd	120969	6925	6444	165214	1569533	0.16	35.1	81.5	520.7	14.30	1.12	0.0572	0.87	0.5512	1.42	0.0699	1.12	0.79	499.1	38.1	435.7	9.4	445.8	10.2	2.3	434.9	9.4
North Tinos psammite	17TL43	17TL 43.54		bd	169787	9221	4172	140834	2755453	0.08	47.8	69.4	914.2	17.63	1.04	0.0535	0.68	0.4180	1.25	0.0567	1.04	0.84	349.3	30.8	355.6	7.2	354.7	7.4	-0.3	355.7	7.2
North Tinos psammite	17TL43	17TL 43.55		bd	118455	6490	134	4343	1897734	0.00	32.7	2.1	629.6	17.19	1.20	0.0535	0.88	0.4290	1.49	0.0582	1.20	0.81	350.9	39.6	364.5	8.5	362.5	9.0	-0.5	364.6	8.5
North Tinos psammite	17TL43	17TL 43.56		bd	185099	9941	25782	1016444	3506589	0.43	57.7	501.1	1163.4	20.28	1.27	0.0525	0.76	0.3567	1.48	0.0493	1.27	0.86	307.2	34.8	310.2	7.7	309.7	7.9	-0.2	310.2	7.7
North Tinos psammite	17TL43	17TL 43.57		bd	133228	7432	4428	122391	2078159	0.09	37.9	60.3	689.5	16.74	1.20	0.0548	0.95	0.4509	1.53	0.0597	1.20	0.78	403.5	42.4	373.9	8.7	377.9	9.6	1.1	373.6	8.7
North Tinos psammite	17TL43	17TL 43.58		bd	254433	13436	34290	1375144	4835173	0.42	78.9	678.0	1604.2	20.65	1.10	0.0519	0.73	0.3465	1.32	0.0484	1.10	0.83	281.8	33.2	304.9	6.5	302.1	6.9	-0.9	305.1	6.6
North Tinos psammite	17TL43	17TL 43.59		bd	229557	12189	24672	879196	4240698	0.31	69.6	433.5	1406.9	20.05	1.22	0.0520	0.88	0.3572	1.50	0.0499	1.22	0.81	283.6	40.4	313.8	7.4	310.1	8.0	-1.2	314.1	7.5
North Tinos psammite	17TL43	17TL 43.60		bd	313262	17034	20730	795802	5921294	0.20	91.7	392.4	1964.5	20.36	1.11	0.0532	0.70	0.3605	1.31	0.0491	1.11	0.85	339.5	31.5	309.1	6.7	312.6	7.0	1.1	308.9	6.7
North Tinos psammite	17TL43	17TL 43.61		bd	202926	11748	26260	696096	2500068	0.30	62.9	327.2	829.4	13.39	1.15	0.0573	0.86	0.5895	1.44	0.0747	1.15	0.80	502.6	37.8	464.2	10.3	470.6	10.8	1.3	463.7	10.3
North Tinos psammite	17TL43	17TL 43.62		bd	755509	85926	134368	877210	2859524	0.46	254.9	432.5	948.7	4.09	1.21	0.1118	0.66	3.7649	1.38	0.2444	1.21	0.88	1828.4	23.9	1409.6	30.6	1585.3	21.9	11.1	1373.7	29.1
North Tinos psammite	17TL43	17TL 43.63		bd	383113	47365	43895	294833	1196090	0.37	123.9	145.4	396.8	3.41	1.25	0.1211	0.71	4.8974	1.44	0.2934	1.25	0.87	1972.5	25.2	1658.6	36.6	1801.8	24.0	7.9	1622.8	35.0
North Tinos psammite	17TL43	17TL 43.64		bd	907714	49152	18665	661705	15912260	0.06	254.8	326.2	5279.2	19.04	1.18	0.0533	0.75	0.3859	1.40	0.0525	1.18	0.84	342.4	34.1	330.0	7.6	331.4	7.9	0.4	329.9	7.6
North Tinos psammite	17TL43	17TL 43.65		bd	207434	11025	27369	1082783	3956884	0.41	64.2	533.8	1312.8	20.91	1.13	0.0523	0.77	0.3448	1.37	0.0478	1.13	0.82	299.2	35.3	301.2	6.6	300.8	7.1	-0.1	301.2	6.6
North Tinos psammite	17TL43	17TL 43.66		bd	223947	12956	49867	1330339	2851148	0.69	74.9	655.9	945.9	13.84	1.15	0.0568	0.72	0.5656	1.36	0.0723	1.15	0.85	483.3	31.9	449.8	10.0	455.1	9.9	1.2	449.3	10.0
North Tinos psammite	17TL43	17TL 43.67		bd	64220	3571	9948	348826	1097618	0.47	20.3	172.0	364.2	18.45	1.21	0.0544	0.99	0.4068	1.56	0.0542	1.21	0.77	389.4	44.4	340.3	8.0	346.5	9.1	1.8	339.8	8.0
North Tinos psammite	17TL43	17TL 43.68		bd	97746	5284	2858	98713	1605690	0.09	27.7	48.7	532.7	17.95	1.11	0.0534	0.88	0.4100	1.42	0.0557	1.11	0.78	346.1	39.7	349.4	7.5	348.8	8.3	-0.2	349.4	7.5
North Tinos psammite	17TL43	17TL 43.69		bd	260621	15037	32922	813674	3571902	0.34	80.6	401.2	1185.0	14.91	1.11	0.0565	0.73	0.5226	1.33	0.0671	1.11	0.83	473.5	32.5	418.5	9.0	426.9	9.2	2.0	417.8	9.0
North Tinos psammite	17TL43	17TL 43.70		bd	293209	17926	97687	1964416	2948697	0.99	106.8	968.5	978.3	10.94	1.63	0.0598	0.73	0.7533	1.79	0.0914	1.63	0.91	595.9	31.5	563.9	17.6	570.1	15.5	1.1	563.3	17.6
North Tinos psammite	17TL43	17TL 43.71		bd	48850	2635	6153	219282	826342	0.39	15.1	108.1	274.2	18.54	1.25	0.0539	1.24	0.4004	1.76	0.0539	1.25	0.71	365.7	55.9	338.6	8.3	342.0	10.2	1.0	338.4	8.2
North Tinos psammite	17TL43	17TL 43.72		bd	54553	3121	10768	281861	708157	0.59	17.9	139.0	234.9	14.14	1.31	0.0561	1.16	0.5474	1.75	0.0707	1.31	0.75	458.1	51.7	440.6	11.1	443.3	12.5	0.6	440.4	11.1
North Tinos psammite	17TL43	17TL 43.73		bd	9113	512	2718	93184	152473	0.91	3.2	45.9	50.6	18.57	1.74	0.0548	1.96	0.4065	2.62	0.0538	1.74	0.66	403.3	88.0	338.1	11.4	346.4	15.3	2.4	337.5	11.4
North Tinos psammite	17TL43	17TL 43.74		bd	37112	2004	4955	190462	686440	0.41	11.5	93.9	227.7	20.46	1.27	0.0536	1.11	0.3614	1.69	0.0489	1.27	0.75	356.3	50.3	307.6	7.6	313.3	9.1	1.8	307.2	7.6
North Tinos psammite	17TL43	17TL 43.75		bd	31848	1832	2169	55496	376526	0.22	9.4	27.4	124.9	12.90	1.56	0.0571	1.33	0.6104	2.05	0.0775	1.56	0.76	496.9	58.7	481.2	14.4	483.8	15.6	0.5	481.0	14.4
North Tinos psammite	17TL43	17TL 43.76		bd	300933	16288	62479	2563802	5760982	0.66	99.2	1264.0	1911.3	21.10	1.07	0.0530	0.68	0.3462	1.26	0.0474	1.07	0.84	328.8	30.9	298.6	6.2	301.9	6.6	1.1	298.3	6.2
North Tinos psammite	17TL43	17TL 43.77		bd	39776	2592	8332	172326	412497	0.62	13.2	85.0	136.9	11.39	1.21	0.0641	1.26	0.7757	1.75	0.0878	1.21	0.69	745.9	53.4	542.3	12.6	583.0	15.4	7.0	538.6	12.4
North Tinos psammite	17TL43	17TL 43.78		bd	220490	11759	30026	1266832	4249794	0.44	68.5	624.6	1410.0	20.81	1.16	0.0524	0.70	0.3467	1.35	0.0480	1.16	0.86	301.5	32.0	302.5	6.8	302.3	7.0	-0.1	302.5	6.8
North Tinos psammite	17TL43	17TL 43.79		bd	174464	9865	13301	351862	2104151	0.25	51.6	173.5	698.1	13.36	1.11	0.0557	0.93	0.5744	1.45	0.0748	1.11	0.77	440.1	41.3	465.2	10.0	460.8	10.7	-0.9	465.6	10.0
North Tinos psammite	17TL43	17TL 43.80		bd	598124	32872	68473	2731158	11057230	0.37	182.7	1346.5	3668.5	19.99	1.17	0.0535	0.69	0.3686	1.36	0.0500	1.17	0.86	348.4	31.4	314.7	7.2	318.6	7.4	1.2	314.4	7.1

Table 2.14: Sample 17TL43: North Tinos meta-psammite

Appendix 3: Whole Rock Geochemistry

3.1 Whole Rock Geochemistry

3.1.1 Geochemical sample preparation and methods

All samples were thoroughly washed and cleaned then crushed into a $<$ 80-micron powder using a Jaw crusher, followed by running through a Tema Mill using a steel crucible to avoid contamination by tungsten carbide. The crucible was thoroughly cleaned and run through separately with in house sand and the resultant powder was then passed through an 80-micron sieve. Some of the resultant powders were then sent off to the Franklin and Marshall College, Pennsylvania, USA, for X-ray fluorescence (XRF) by Dr Stanley Mertzman. The remaining powder was weighed and prepared for ICP-MS in house at the Department of Earth Sciences, University of Oxford. Full descriptions for each method are outlined below.

3.1.2 X-Ray Fluorescence

XRF was carried out by weighing 0.4000 $\pm$ 0.0001 grams of crushed rock powder and mixing with lithium tetraborate (3.6000 $\pm$ 0.0002 grams). The subsequent solution was then placed in a platinum crucible and heated with a meeker burner until molten. The molten material was transferred to a platinum casting dish and quenched. This procedure produced a glass disk that is used for XRF analysis of SiO_2, Al_2O_3, CaO,

K_2O, P_2O_5, TiO_2, total iron reported as Fe_2O_3T, MnO, Na_2O and MgO. Trace element analysis was achieved by weighing 7.0000 ± 0.0004 grams of whole rock powder and adding 1.4000±0.0002 of high purity copolywax powder. This was mixed for 10 minutes, and the powder was pressed into a briquette. Data are reported as parts per million (ppm) for Rb, Sr, Y, Zr, Nb, Ni, Ga, Cu, Zn, U, Th, Co, Pb, Sc, Cr, V, La, Ce, and Ba. Working curves for each element were determined by analyzing geochemical rock standards Abbey (1983) and Govindaraju (1994). Between 30 and 50 data points were gathered for each working curve; various element interferences are also taken into account. Results were calculated and presented as percent oxide. The amount of ferrous Fe was determined by the titration using a modified Reichen and Fahey (1962) method which includes weighing out 0.5000 ± 0.0002 grams of sample powder and transfer to a large alumina crucible and cover, 5 ml of deionized H_2O, 5 ml of concentrated H_2SO_4, were added followed by 5 ml of HF directly into each alumina crucible which were immediately covered and heated over Meker burner until felt to be boiling. Once sufficiently boiling, the crucible was removed and allowed to stand for 10 minutes. 450 ml of the boric acid solution was then added to an 800 ml plastic beaker, one beaker for each crucible, then 3-5 drops of 3.0% Sodium diphenylamine sulfonate solution was added as an indicator. After the crucible was heated for 10 minutes, it was picked up and placed to the bottom of the beaker so it is covered by solution. This solution was then promptly titrated using a standard solution of $K_2Cr_2Cr_7$ (potassium dichromate) to a purple end point, the amount of $K_2Cr_2Cr_7$ used in ml*0.8 is the weight % FeO of the sample, weight $\%Fe_2O_3$ was determined by division by 1.111348 to give % FeO_T, then % FeO_T-%FeO (titrated) = Fe_2O_3, then Fe_2O_3*1.111348 = weight $\%Fe_2O_3$. Loss on ignition is determined by heating an exact aliquot of the sample at 950°C for one hour.

3.1.3 Trace element geochemistry (ICP-MS)

All sample powders were weighed to approximately 100 ± 0.1 mg and then diluted and digested over 7 days in vials using 2 ml of concentrated HF and 4ml of HNO_3 at

80 °C and evaporated at 90 °C. Two 2 ml's of HNO_3 was then added and evaporated to dry then 1-3 ml of 16 M HNO_3 was added with MilliQ under the supervision of Dr Steve Wyatt. The samples were then heated overnight and diluted to 10 ml making a concentration of 2 M HNO_3 in the final solution. 2 M HNO_3 was then added to make up 48 ml of solution. Stock calibrations for standards A were made by adding 0.5 ml of 10 ppm solutions of transition, alkali, REE's and HFS standards making a result solution of 50 g. Stock calibration for standards B were made by using 48.5 ml of 2 M HNO_3 with 0.5 ml of stock calibration standard A then 0.5 ml of each QCA and QCB were added to make up to 50 ml. Three internal standards were used including In, Rh and Re, and six runs of all element standards was collected. The subsequent standard results are presented in Table 3.1 and reported data as ppm concentrations. A spectrum of trace elements was collected on a Perkin Elmer 6100DRC Quadrupole inductively coupled plasma mass spectrometer (ICP-MS) with a dynamic reaction cell at the Department of Earth Sciences, University of Oxford. Measured elements from whole rock samples include V, Cr, Mn, Co, Ni, Cu, Zn, Rb, Sr, Cd, In, Ba, Sc, Y, Cs, La, Ce, Pr, Nd, Sm, Eu, Gd, Tb, Dy, Ho, Er, Tm, Yb, Lu, Th, U, Co, Ga, Ta, Nb, Mo, Hf, W, Pb, Re.

All XRF analyses

Standards data	Sc 45 ng/g	Y 89 ng/g	In 115 (IS) IS	Cs 133 ng/g	La 139 ng/g	Ce 140 ng/g	Pr 141 ng/g	Nd 143 ng/g	Sm 147 ng/g	Eu 153 ng/g	Gd 157 ng/g	Tb 159 ng/g	Dy 163 ng/g	Ho 165 ng/g	Er 166 ng/g	Tm 169 ng/g	Yb 173 ng/g	Lu 175 ng/g	Th 232 ng/g	U 238 ng/g	Co 59 ng/g	Ga 69 ng/g	Nb 93 ng/g	Mo 98 ng/g	Rh 103 (IS) IS	Hf 178 ng/g	W 182 ng/g	Re 185 (IS) IS	Pb 208 ng/g
S7_R1	2.23189	2.12256	0.95859	1.99721	2.10434	2.13118	2.05070	2.03105	2.07463	2.12847	2.03198	2.07067	2.05250	2.09948	2.05135	2.07743	2.07928	2.08074	1.99093	1.96080	2.06698	2.01803	2.04911	2.02212	0.96318	1.96496	2.03276	0.98058	2.00775
S7_R2	2.29585	2.15303	0.97428	1.98981	2.14026	2.15226	2.05217	2.01212	2.10287	2.16759	2.05832	2.11047	2.08219	2.13980	2.07474	2.09847	2.11434	2.10355	2.01888	1.98845	2.11039	2.05012	2.10089	2.11239	0.97257	2.06856	2.06857	0.98015	2.02596
S7_R3	2.17058	2.06831	0.97481	2.00193	2.09096	2.11257	2.02768	2.03948	2.03855	2.10821	1.99033	2.05810	2.01083	2.07621	2.03931	2.05753	2.03019	2.04705	1.93240	1.91341	2.01031	2.01237	2.03181	2.01988	0.98083	1.98163	1.65249	0.98173	1.97203
S7_R4	2.15955	2.16036	0.98668	2.01298	2.12063	2.12246	2.05548	2.07542	2.07381	2.13512	2.01031	2.07614	2.04403	2.13129	2.06576	2.08546	2.08106	2.07429	1.95992	1.93681	2.06401	2.03817	2.06354	2.05236	0.98697	2.04543	1.61265	0.99959	1.99152
S7_R5	2.20374	2.16287	0.98535	1.99965	2.11632	2.12012	2.05952	2.08417	2.10603	2.13282	2.03274	2.07306	2.03881	2.11836	2.08116	2.07307	2.11042	2.06808	1.94343	1.92620	2.08132	2.02864	2.09403	2.08655	0.97804	2.02235	1.82121	0.98253	2.02221
S7_R6	2.16727	2.10186	0.97290	1.98527	2.08619	2.09555	2.01406	2.01496	2.02217	2.08632	2.01250	2.03081	2.00375	2.08123	2.01258	2.03213	2.05449	2.03437	1.91739	1.89943	2.05658	2.04002	2.02427	2.02277	0.96808	2.00170	1.74613	0.98525	1.93630
Precision	ng/g	ng/g	IS	ng/g	ng/g	ng/g	ng/g	ng/g	ng/g	ng/g	ng/g	ng/g	ng/g	ng/g	ng/g	ng/g	ng/g	ng/g	ng/g	ng/g	ng/g	ng/g	ng/g	ng/g	IS	ng/g	ng/g	IS	ng/g
AVG	2.20	2.13		2.00	2.11	2.12	2.04	2.04	2.07	2.13	2.02	2.07	2.04	2.11	2.05	2.07	2.08	2.07	1.96	1.94	2.06	2.03	2.06	2.05		2.01	1.82		1.99
STD	0.05	0.04		0.01	0.02	0.02	0.02	0.03	0.03	0.03	0.02	0.03	0.03	0.03	0.03	0.02	0.03	0.02	0.04	0.03	0.03	0.01	0.03	0.04		0.04	0.19		0.03
RSD%	2.37	1.78		0.49	0.96	0.89	0.89	1.49	1.63	1.29	1.16	1.25	1.41	1.25	1.24	1.12	1.55	1.19	1.95	1.68	1.59	0.70	1.54	1.90		1.94	10.51		1.71
2*RSD%	4.74	3.56		0.97	1.91	1.78	1.77	2.98	3.26	2.58	2.32	2.51	2.81	2.50	2.48	2.25	3.11	2.38	3.89	3.36	3.18	1.41	3.08	3.80		3.88	21.03		3.42
Accuracy	ng/g	ng/g	IS	ng/g	ng/g	ng/g	ng/g	ng/g	ng/g	ng/g	ng/g	ng/g	ng/g	ng/g	ng/g	ng/g	ng/g	ng/g	ng/g	ng/g	ng/g	ng/g	ng/g	ng/g	IS	ng/g	ng/g	IS	ng/g
Check std conc	2.09429	2.04943		1.99892	2.08386	2.12121	2.05193	2.04003	2.08260	2.11015	2.04880	2.08761	2.06236	2.12789	2.07509	2.08866	2.09575	2.10639	2.02981	2.03203	2.02458	2.00829	2.04909	2.03973		2.03302	2.03973		2.01332
Percentage of theoretical	105.28	103.84		99.94	101.24	100.05	99.58	100.14	99.38	100.77	98.73	99.15	98.85	99.05	98.99	99.14	99.17	98.18	96.58	95.35	101.99	101.14	100.56	100.63		99.07	89.34		98.97
Accuracy %	5.28	3.84		0.06	1.24	0.05	0.42	0.14	0.62	0.77	1.27	0.85	1.15	0.95	1.01	0.86	0.83	1.82	3.42	4.65	1.99	1.14	0.56	0.63		0.93	10.66		1.03

Table 3.15: ICP-MS Standards Data

	Eclogite Tinos	Tsiknas Gabbro	Tsiknas Gabbro	Tsiknas Gabbro	Gabbro	Plagiogranite	Plagiogranite	Amp sole	Amp Sole	Amp Sole	Tsiknas sole	S-type Livada	S-type Livada	S-type Livada	Tinos I-type	Tinos I-type	Naxos S-type marbles	Naxos S-type	Naxos S-type	Naxos S-type	Naxos S-type	Naxos S-type	Tinos Sole meta-sediment	Meta-chert	Tinos Sole Meta-sediment	Dacite dyke	Dacite dyke	Dacite dyke	Delos Leucogranite	Cross-cutting leucogranite dyke	Naxos leucogranite sill in Granodiorite
Specimen	TLTN-24	17TL-23	17TL24	17TL-27	TLT-26	17TL-35	TLT-63	TLT-7	TLTN-10	TLTN-12	17TL-26	TLTN-13	TLTN-14	TLTN-15	TLTN-34	TLTN-36	TLN-8	TLN-37	TL-58	TL-63	TL-64	TL-72	TLT-1	TLT-13	TLT-15	17TL-05	TLT-64	17TL-36	17TL-95	17TL-100	17TL-106
SiO2	52.53	48.69	56.41	49.24	50.36	73.04	74.89	56.13	55.14	49.25	61.03	76.73	77.03	76.45	70.88	71.37	67.46	73.58	75.29	75.14	74.98	74.39	77.55	81.78	77.57	70.32	67.82	67.66	64.86	76.53	74.78
TiO2	1.08	0.12	0.57	1.39	0.14	0.23	0.15	0.64	0.54	1.71	0.00	0.01	0.00	0.00	0.34	0.34	0.46	0.00	0.00	0.00	0.00	0.01	0.31	0.23	0.30	0.51	0.48	0.49	1.00	0.01	0.02
Al2O3	16.73	18.57	15.07	16.26	16.70	13.36	13.67	17.72	18.41	16.38	23.61	13.63	13.41	13.81	15.44	14.98	16.28	16.16	15.02	14.49	14.38	15.06	10.48	5.72	9.50	15.93	16.07	16.04	14.97	13.37	14.33
Fe2O3T	13.29	6.02	7.54	10.14	7.61	3.10	1.99	6.64	5.09	10.49	0.47	0.55	0.53	0.47	2.53	2.79	4.27	0.45	0.98	0.70	0.65	0.65	3.50	4.87	4.61	4.38	3.82	3.81	5.35	0.82	0.85
MnO	0.25	0.12	0.25	0.19	0.16	0.04	0.02	0.16	0.14	0.18	0.02	0.16	0.20	0.12	0.07	0.07	0.07	0.02	0.05	0.09	0.07	0.11	0.11	1.49	0.98	0.09	0.09	0.09	0.10	0.02	0.02
MgO	4.59	9.80	7.03	6.55	11.21	0.48	0.23	4.50	4.74	6.87	0.34	0.11	0.08	0.08	1.07	1.09	1.72	0.25	0.18	0.07	0.07	0.26	1.58	1.51	1.33	1.58	2.26	2.35	1.51	0.07	0.14
CaO	5.06	14.93	8.25	11.42	10.71	4.13	2.26	9.28	9.55	10.72	5.69	1.11	0.73	0.77	2.83	2.79	1.76	3.30	0.42	0.56	0.48	0.91	2.58	3.26	2.16	0.57	2.98	2.77	5.25	0.74	1.00
Na2O	6.23	1.38	4.11	3.56	3.01	5.67	6.67	4.53	5.51	3.82	8.51	4.99	5.19	5.92	3.57	3.54	3.62	5.84	2.93	5.43	4.95	5.15	2.28	0.87	3.16	3.16	3.85	3.85	3.04	3.69	3.84
K2O	0.20	0.09	0.32	0.53	0.19	0.06	0.08	0.53	0.40	0.38	0.66	2.66	2.98	2.13	3.28	3.10	4.19	0.35	4.97	3.25	4.03	3.23	1.22	0.27	0.40	3.24	2.63	2.62	3.56	4.78	4.97
P2O5	0.12	0.02	0.07	0.28	0.03	0.07	0.03	0.14	0.13	0.19	0.02	0.02	0.03	0.02	0.10	0.10	0.17	0.02	0.06	0.06	0.05	0.05	0.08	0.07	0.20	0.14	0.12	0.12	0.19	0.02	0.03
Total	100.08	99.74	99.62	99.56	100.12	100.18	99.99	100.27	99.65	99.99	100.35	99.97	100.18	99.77	100.11	100.17	100.00	99.97	99.90	99.79	99.66	99.82	99.69	100.07	100.21	99.92	100.12	99.80	99.83	100.05	99.98
LOI	2.03	1.49	1.70	1.39	3.77	0.82	0.76	1.51	2.36	2.37	1.10	0.38	0.41	0.48	1.09	1.04	1.80	1.09	1.06	0.38	0.35	0.52	1.11	1.05	1.33	2.86	1.68	1.85	1.18	0.51	0.79
FeO	7.83	3.95	5.39	6.81	5.03	0.48	0.41	2.57	3.06	6.42	0.19	0.26	0.19	0.16	1.49	1.51	3.15	0.15	0.21	0.36	0.25	0.40	1.81	3.84	1.54	1.09	2.32	2.08	3.52	0.29	0.12
Fe2O3	4.59	1.63	1.55	2.57	2.02	2.57	1.53	3.78	1.69	3.36	0.26	0.26	0.32	0.29	0.87	1.11	0.77	0.28	0.75	0.30	0.37	0.21	1.49	0.60	2.90	3.17	1.24	1.50	1.44	0.50	0.72
Rb	4.40	1.60	6.80	3.90	4.10	1.00	1.00	25.60	16.10	24.40	25.60	251.50	271.60	213.80	190.60	183.40	164.00	26.30	303.10	372.60	458.80	521.90	51.20	11.10	17.40	153.30	139.50	130.80	117.40	347.70	344.40
Sr	183.00	118.00	135.00	763.00	59.00	156.00	113.00	245.00	229.00	237.00	267.00	18.00	16.00	18.00	288.00	280.00	179.00	520.00	24.00	5.00	5.00	24.00	149.00	158.00	142.00	301.00	603.00	578.00	465.00	35.00	81.00
Y	33.20	5.00	41.60	29.90	9.70	50.40	69.40	32.90	18.90	45.40	0.70	61.20	50.10	72.10	13.80	13.70	26.40	16.30	j0.5	j0.5	j0.5	37.60	32.10	29.70	34.20	20.80	17.80	18.10	4.80	1.10	6.30
Zr	68.00	11.00	67.00	117.00	12.00	116.00	157.00	62.00	46.00	133.00	13.00	90.00	102.00	100.00	184.00	187.00	144.00	41.00	21.00	22.00	18.00	33.00	134.00	6.00	44.00	212.00	172.00	178.00	392.00	63.00	88.00
V	372.00	189.00	145.00	226.00	150.00	51.00	23.00	155.00	127.00	289.00	3.00	8.00	13.00	7.00	43.00	41.00	91.00	6.00	7.00	8.00	3.00	8.00	52.00	103.00	64.00	67.00	93.00	85.00	53.00	6.00	8.00
Ni	18.00	141.00	323.00	146.00	145.00	19.00	25.00	106.00	79.00	106.00	4.00	25.00	8.00	8.00	7.00	7.00	35.00	16.00	5.00	4.00	4.00	12.00	13.00	73.00	40.00	25.00	154.00	187.00	9.00	6.00	3.00
Cr	36.00	396.00	551.00	369.00	301.00	45.00	60.00	184.00	175.00	231.00	14.00	54.00	10.00	29.00	21.00	22.00	66.00	9.00	19.00	11.00	8.00	18.00	18.00	147.00	138.00	32.00	97.00	57.00	35.00	22.00	15.00
Nb	j0.5	j0.5	3.50	22.00	j0.5	0.60	1.40	10.70	j0.5	0.70	j0.5	61.30	78.80	81.20	15.80	16.80	9.60	28.60	22.40	37.90	35.70	39.30	7.70	2.80	8.80	14.40	12.80	14.20	48.30	23.80	36.90
Ga	19.20	11.80	14.40	16.80	10.90	19.80	18.10	16.00	10.90	17.10	11.70	26.00	27.90	27.10	21.30	21.20	19.60	23.90	25.70	30.20	29.20	38.70	13.20	8.80	13.40	20.10	21.40	20.90	22.90	24.60	28.50
Cu	53.00	40.00	35.00	58.00	31.00	15.00	17.00	62.00	84.00	64.00	42.00	17.00	19.00	16.00	14.00	8.00	51.00	23.00	13.00	13.00	15.00	12.00	25.00	13.00	40.00	46.00	23.00	21.00	25.00	13.00	42.00
Zn	129.00	34.00	138.00	110.00	43.00	8.00	8.00	66.00	72.00	78.00	14.00	14.00	9.00	13.00	39.00	39.00	74.00	17.00	18.00	26.00	26.00	36.00	63.00	49.00	61.00	351.00	45.00	52.00	72.00	32.00	12.00
Co	49.00	50.00	51.00	60.00	43.00	22.00	j1	24.00	17.00	40.00	52.00	j1	j1	j1	j1	j1	7.00	j1	j1	j1	j1	j1	2.00	13.00	9.00	42.00	5.00	31.00	58.00	13.00	27.00
Ba	112.00	j3	92.00	77.00	15.00	29.00	19.00	44.00	20.00	23.00	13.00	28.00	8.00	16.00	442.00	400.00	1297.00	198.00	45.00	4.00	3.00	22.00	309.00	36.00	124.00	616.00	673.00	711.00	629.00	33.00	43.00
La	18.00	11.00	19.00	18.00	9.00	18.00	17.00	13.00	10.00	7.00	13.00	16.00	15.00	19.00	25.00	21.00	23.00	18.00	13.00	12.00	13.00	17.00	30.00	29.00	33.00	35.00	29.00	30.00	36.00	17.00	18.00
Ce	18.00	9.00	45.00	36.00	8.00	21.00	25.00	16.00	15.00	11.00	8.00	19.00	20.00	17.00	46.00	38.00	43.00	17.00	12.00	13.00	14.00	25.00	43.00	28.00	44.00	70.00	58.00	59.00	73.00	15.00	26.00
U	j0.5	j0.5	j0.5	j0.5	j0.5	0.50	1.20	0.60	j0.5	j0.5	j0.5	5.20	5.70	6.40	3.20	2.50	1.10	6.50	0.90	j0.5	j0.5	4.30	0.90	j0.5	j0.5	1.50	4.20	2.50	4.60	j0.5	4.30
Th	7.30	j0.5	6.60	j0.5	j0.5	3.10	7.30	4.70	j0.5	j0.5	j0.5	43.80	37.45	36.70	20.70	17.50	11.70	5.10	3.60	7.70	7.00	17.80	15.70	2.70	11.30	81.00	18.90	20.20	17.10	25.10	43.40
Sc	34.00	41.00	19.00	34.00	36.00	8.00	6.00	22.00	19.00	35.00	j1	3.00	j1	1.00	5.00	5.00	10.00	1.00	j1	j1	j1	j1	10.00	4.00	7.00	4.00	8.00	5.00	5.00	j1	j1
Pb	j1	j1	3.00	j1	j1	j1	j1	7.00	5.00	j1	5.00	80.00	70.00	90.00	31.00	49.00	27.00	23.00	7.00	5.00	13.00	36.00	j1	5.00	2.00	254.00	30.00	36.00	25.00	72.00	95.00

Table 3.16: All XRF whole rock analyses